

# The Science of Solar System Ices

# Astrophysics and Space Science Library

---

## EDITORIAL BOARD

### *Chairman*

W. B. BURTON, *National Radio Astronomy Observatory, Charlottesville, Virginia, U.S.A.*  
*(bburton@nrao.edu); University of Leiden, The Netherlands*  
*(burton@strw.leidenuniv.nl)*

F. BERTOLA, *University of Padua, Italy*  
J. P. CASSINELLI, *University of Wisconsin, Madison, U.S.A.*  
C. J. CESARSKY, *Commission for Atomic Energy, Saclay, France*  
P. EHRENFREUND, *Leiden University, The Netherlands*  
O. ENGVOLD, *University of Oslo, Norway*  
A. HECK, *Strasbourg Astronomical Observatory, France*  
E. P. J. VAN DEN HEUVEL, *University of Amsterdam, The Netherlands*  
V. M. KASPI, *McGill University, Montreal, Canada*  
J. M. E. KUIJPERS, *University of Nijmegen, The Netherlands*  
H. VAN DER LAAN, *University of Utrecht, The Netherlands*  
P. G. MURDIN, *Institute of Astronomy, Cambridge, UK*  
F. PACINI, *Istituto Astronomia Arcetri, Firenze, Italy*  
V. RADHAKRISHNAN, *Raman Research Institute, Bangalore, India*  
B. V. SOMOV, *Astronomical Institute, Moscow State University, Russia*  
R. A. SUNYAEV, *Space Research Institute, Moscow, Russia*

For further volumes:  
<http://www.springer.com/series/5664>

Murthy S. Gudipati • Julie Castillo-Rogez  
Editors

# The Science of Solar System Ices



Springer

*Editors*

Murthy S. Gudipati  
NASA Jet Propulsion Laboratory  
California Institute of Technology  
Oak Grove Drive 4800  
Pasadena 91109-8099  
CA, USA

Julie Castillo-Rogez  
NASA Jet Propulsion Laboratory  
California Institute of Technology  
Oak Grove Drive 4800  
Pasadena 91109-8099  
CA, USA

ISSN 0067-0057

ISBN 978-1-4614-3075-9

ISBN 978-1-4614-3076-6 (eBook)

DOI 10.1007/978-1-4614-3076-6

Springer New York Heidelberg Dordrecht London

Library of Congress Control Number: 2012935695

© Springer Science+Business Media New York 2013

This work is subject to copyright. All rights are reserved by the Publisher, whether the whole or part of the material is concerned, specifically the rights of translation, reprinting, reuse of illustrations, recitation, broadcasting, reproduction on microfilms or in any other physical way, and transmission or information storage and retrieval, electronic adaptation, computer software, or by similar or dissimilar methodology now known or hereafter developed. Exempted from this legal reservation are brief excerpts in connection with reviews or scholarly analysis or material supplied specifically for the purpose of being entered and executed on a computer system, for exclusive use by the purchaser of the work. Duplication of this publication or parts thereof is permitted only under the provisions of the Copyright Law of the Publisher's location, in its current version, and permission for use must always be obtained from Springer. Permissions for use may be obtained through RightsLink at the Copyright Clearance Center. Violations are liable to prosecution under the respective Copyright Law.

The use of general descriptive names, registered names, trademarks, service marks, etc. in this publication does not imply, even in the absence of a specific statement, that such names are exempt from the relevant protective laws and regulations and therefore free for general use.

While the advice and information in this book are believed to be true and accurate at the date of publication, neither the authors nor the editors nor the publisher can accept any legal responsibility for any errors or omissions that may be made. The publisher makes no warranty, express or implied, with respect to the material contained herein.

Printed on acid-free paper

Springer is part of Springer Science+Business Media ([www.springer.com](http://www.springer.com))

# Foreword

Ices play a key role in the chemistry and physics of planet and star formation. When the solar system formed, the most commonly found solid materials were ices. Although much of that icy material ended up in giant planets, ices are key to the formation and evolution of many smaller bodies. They moderated the early chemistry on those primordial planets and moons and today drive atmospheric and geologic processes on the objects spanning the solar system. Planetary ice is often largely water, but there is a startling richness of other species, forming their own “pure” ices or mixtures with water ice. Each of these ices has unique properties, with the interplay between atmospheric gases, radiation, thermal fluctuations, etc., controlling many of the processes on planetary surfaces. Given that the physical and thermodynamic properties of water ice alone are incredibly complex, with chemistry and kinetics adding even more complexity, much work is needed before we can begin to fully interpret telescopic observations and data returned from landers and rovers sent to explore the different ices in the solar system. Pioneering exploratory missions in the 1960s, 1970s, and 1980s, coupled with observations in new wavelength regions, revealed a richness of ices far beyond what was previously imagined.

Since studies of ices under realistic extraterrestrial conditions did not exist at the time, the 1970s saw the advent of dedicated laboratory work and theoretical model development to understand these new discoveries. Phase diagrams were improved or even measured for the first time. Nonequilibrium processes (thermal conductivity, rheology, grain growth kinetics, differential desorption, photo- and thermal processing, etc.) were studied. So emerged the new field of extraterrestrial ice analog studies.

The wide-ranging studies described in this book (not only the observations but also the chemistry and physics of extraterrestrial ices in many environments) show how this field has blossomed over the years and completely revolutionized our understanding and appreciation of the many ways in which ices exist and evolve. The cosmic ice frontier has now moved far beyond the spectral matching and albedo measurements of the early days to probing the processes that occur on a molecular level both within and on the surfaces of these ices. Today’s goal is to

understand how these processes affect the chemistry and physics of the ice and, in the case of planetary-sized objects, the geology and atmosphere of the body itself. These processes are driven by a complex interplay of condensation history, radiation exposure, thermal fluctuation, pressure, and so on. It is clear from the work described in this book that this is both a rich and challenging field. The deeper understanding of ice physics and chemistry that these data provide will play a central, essential role as we extend our exploration to the icy bodies in the solar system, out into our galaxy, and to galaxies across the universe.

CA, USA

Lou Allamandola  
David Stevenson

# Preface

This book, *The Science of Solar System Ices*, has its origins at The Oxnard Workshop, organized in Oxnard, California, May 5–8, 2008, entitled “The Science of Solar System Ices: A Cross-Disciplinary Workshop.” The long delay in publishing the proceedings of this conference is a consequence of the large number of activities that have kept the planetary ice community busy for the last 3 years, heavily involved in planetary flagship mission reviews (2009), planetary decadal survey white papers and reviews (2009–2010), and finally the planetary decadal survey report (March 7, 2011). We thank the authors who were the first to submit their chapters for their patience and those authors who submitted their chapters last for their persistence. With due apologies for the delay, we are very pleased to present you with this book, which, we hope, would help the solar system ice community in the coming decade, or further, as a single source of reference, similar to the earlier book *Solar System Ices* (Schmitt, de Bergh, Festou, Kluwer, 1998), a result of an international symposium “Solar System Ices” held in Toulouse, France in 1995. About a decade earlier was the NATO international workshop on “ices in the solar system” held in Nice, France.

The Oxnard Workshop was unique in several aspects. It marked the first attempt to focus on the importance of laboratory work in bringing the three different communities (observers, modelers, and laboratory experimentalists) together into a small group of close to 120 international participants and give them a platform to talk to each other. This workshop covered all fields related to ice properties in the context of planetary science and solar system exploration: surface chemistry, volatile trapping, optical properties, planetary surface characterization, physical properties, and geophysics and geology of icy bodies. There were successive talks from an observer, a modeler, and a laboratory experimentalist on the same or similar topic. This method enabled rigorous discussions, new ideas, and a focused approach to future directions and needs. It was immediately clear at the end of the workshop that a book should be published that could cater to the needs of the wider solar system ice community. In its final form today, this book is a compilation of 18 chapters that crystallize the state of the art in ice physics and ice chemistry as of 2011. The review of the field is particularly timely, as the National Research

Council has highlighted experimental work as a major component of planetary exploration in the decadal survey “Visions and Voyages for Planetary Science in the Decade 2013–2022” and other advocacy groups are also emphasizing the importance of experimental research as an instrumental component of space exploration. We felt the need for this in 2007, which resulted in The Oxnard Workshop. We also felt the importance of how different communities learn to understand and speak the “science language of each other” and collaborate with colleagues with complementary expertise. We are pleased that we achieved this during the workshop and hope such cross-cutting meetings continue in the future.

The need for laboratory measurements on ices is tied to new discoveries by Earth-based and spaceborne observations. We know that the majority of solar system bodies contain icy materials. Increasing our knowledge of ice properties at the laboratory scale is necessary to increase the science return of past and ongoing space missions and support the definition and planning of future missions. Recent technological advances in instruments and their performance have made the unthinkable a realistic goal in space sciences and the exploration of previously uncharted conditions increasingly relevant to icy bodies in the solar system and beyond. In order to undertake next-generation exploration of solar system icy bodies, which may have more secrets pertaining to the birth and death of stars, solar systems, and habitability within these bodies, we need stronger laboratory research (and support) and sustainable programs that fund and encourage collaboration among the three communities of solar system explorations: the observers, the modelers, and the laboratory experimentalists.

In order to sustain and encourage space exploration, the science and technology that took humanity beyond the imaginable in the past 65 years (to mention a few, the Voyagers crossing the solar system, Spirit and Opportunity tweeting from Mars, Cassini diving less than 50 km into Enceladus plumes from its surface at 10 AU and sniffing the plume molecules, and Hubble reaching to the beginning of the universe), we need to stress on three vital “game change” plans:

1. Providing strong and healthy support to basic research that builds on the past and leads us into the future.
2. Strengthening the programs that support new “out of the box” instrument concepts from very low technology readiness levels (TRL) for future space explorations.
3. Bringing nations and people of this world together – through their partnership in expanding our horizons through science, knowledge, and creativity.

Let the space sciences be the common grounds for humanity to ride planet Earth, and perhaps other planets, comets, asteroids through robotic or human explorations, together in peace.

Pasadena, CA, USA

Murthy S. Gudipati  
Julie C. Castillo-Rogez

## About the Editors

**Murthy S. Gudipati** is a principal scientist in the Planetary Ices Group, Science Division, Jet Propulsion Laboratory, California Institute of Technology, Pasadena, California. Gudipati's research interests can be broadly defined as understanding the physics and chemistry of interstellar and solar system ices through laboratory simulations, observations, and instrumentation or simply the evolution of ices in the Universe. The three wings of this space endeavor are the physics and chemistry of ices with applications to biology, chemistry, atmosphere, and astrophysics; space instrumentation to analyze organic matter on planets such as Mars, Europa, Titan, and Enceladus; and observations and analysis of in situ and remote data. Gudipati's research in the recent past has focused on the physics and chemistry of cryogenic ices. This research builds on the over 15 years of earlier expertise on chemical physics/physical chemistry, spectroscopy, and photochemistry of atmospheric and organic molecules in cryogenic matrices.

**Julie Castillo-Rogez** is a planetary scientist in the Planetary Ices Group, Science Division, Jet Propulsion Laboratory, California Institute of Technology, Pasadena, California. Her main interest lies in material physics, applied to the modeling of icy satellite and asteroid geophysical evolution and the design and planning of future spaceborne and in situ observations of these objects. Castillo-Rogez is involved hands-on in the measurements of the mechanical properties of ice in JPL's Ice Physics Laboratory, which she cofounded. She is a consultant for the definition and design of frozen astromaterial simulants, simulation chambers, and instrument test beds. Her technical publications over the last 10 years cover a variety of topics, ranging from the geophysics and dynamics of icy satellites to the astrobiology of asteroids and the development of strategies to explore these objects with small spacecrafts.



# Acknowledgments

The editors are very grateful to the following colleagues who have volunteered their time reviewing and ensuring the quality of the material presented in this book.

Michael Bland  
Christopher Boxe  
Mathieu Choukroun  
Deborah Domingue  
Robert Hodyss  
William Grundy  
Reggie Hudson  
Shun-Ichiro Karato  
Mark Laufer  
Rachel Mastrapa  
Ted Roush  
Denis Samyn  
Throstur Thorsteinsson  
Catherine De Bergh

We are also grateful to the Lunar and Planetary Institute staff who supported the organization of *The Science of Solar System Ices* workshop and to Maury Solomon for her efficient handling of the publication of this book.



# Contents

## Part I Optical Remote Sensing of Planetary Ices

<b>1 Observed Ices in the Solar System .....</b>	3
Roger N. Clark, Robert Carlson, Will Grundy, and Keith Noll	
<b>2 Photometric Properties of Solar System Ices.....</b>	47
A.J. Verbiscer, P. Helfenstein, and B.J. Buratti	
<b>3 Ultraviolet Properties of Planetary Ices .....</b>	73
A.R. Hendrix, D.L. Domingue, and K.S. Noll	
<b>4 The Ices on Transneptunian Objects and Centaurs.....</b>	107
C. de Bergh, E.L. Schaller, M.E. Brown, R. Brunetto, D.P. Cruikshank, and B. Schmitt	

## Part II Ice Physical Properties and Planetary Applications

<b>5 First-Principles Calculations of Physical Properties of Planetary Ices .....</b>	149
Razvan Caracas	
<b>6 Frictional Sliding of Cold Ice: A Fundamental Process Underlying Tectonic Activity Within Icy Satellites .....</b>	171
Erland M. Schulson	
<b>7 Planetary Ices Attenuation Properties.....</b>	183
Christine McCarthy and Julie C. Castillo-Rogez	
<b>8 Creep Behavior of Ice in Polar Ice Sheets.....</b>	227
Paul Duval	

<b>9</b>	<b>Cratering on Icy Bodies.....</b>	253
	M.J. Burchell	
<b>10</b>	<b>Geology of Icy Bodies.....</b>	279
	Katrin Stephan, Ralf Jaumann, and Roland Wagner	

### Part III Volatiles in Ices

<b>11</b>	<b>Amorphous and Crystalline H<sub>2</sub>O-Ice.....</b>	371
	Rachel M.E. Mastrapa, William M. Grundy, and Murthy S. Gudipati	
<b>12</b>	<b>Clathrate Hydrates: Implications for Exchange Processes in the Outer Solar System.....</b>	409
	Mathieu Choukroun, Susan W. Kieffer, Xinli Lu, and Gabriel Tobie	
<b>13</b>	<b>Cometary Ices.....</b>	455
	Carey Lisse, Akiva Bar-Nun, Diana Laufer, Michael Belton, Walter Harris, Henry Hsieh, and David Jewitt	
<b>14</b>	<b>Gas Trapping in Ice and Its Release upon Warming.....</b>	487
	Akiva Bar-Nun, Diana Laufer, Oscar Rebolledo, Serguei Malyk, Hanna Reisler, and Curt Wittig	

### Part IV Surface Ice Chemistry

<b>15</b>	<b>Chemistry in Water Ices: From Fundamentals to Planetary Applications.....</b>	503
	Murthy S. Gudipati and Paul D. Cooper	
<b>16</b>	<b>Radiation Effects in Water Ice in the Outer Solar System.....</b>	527
	R.A. Baragiola, M.A. Famá, M.J. Loeffler, M.E. Palumbo, U. Raut, J. Shi, and G. Strazzulla	
<b>17</b>	<b>Sputtering of Ices.....</b>	551
	Robert E. Johnson, Robert W. Carlson, Timothy A. Cassidy, and Marcello Fama	
<b>18</b>	<b>Photochemistry in Terrestrial Ices.....</b>	583
	Cort Anastasio, Michael Hoffmann, Petr Klán, and John Sodeau	
<b>Index.....</b>		645

**Part I**

**Optical Remote Sensing of Planetary Ices**

# Chapter 1

## Observed Ices in the Solar System

Roger N. Clark, Robert Carlson, Will Grundy, and Keith Noll

**Abstract** Ices have been detected and mapped on the Earth and all planets and/or their satellites further from the sun. Water ice is the most common frozen volatile observed and is also unambiguously detected or inferred in every planet and/or their moon(s) except Venus. Carbon dioxide is also extensively found in all systems beyond the Earth except Pluto although it sometimes appears to be trapped rather than as an ice on some objects. The largest deposits of carbon dioxide ice is on Mars. Sulfur dioxide ice is found in the Jupiter system. Nitrogen and methane ices are common beyond the Uranian system. Saturn's moon Titan probably has the most complex active chemistry involving ices, with benzene ( $C_6H_6$ ) and many tentative or inferred compounds including ices of Cyanoacetylene ( $HC_3N$ ), Toluene ( $C_7H_8$ ), Cyanogen ( $C_2N_2$ ), Acetonitrile ( $CH_3CN$ ),  $H_2O$ ,  $CO_2$ , and  $NH_3$ . Confirming compounds on Titan is hampered by its thick smoggy atmosphere. Ammonia was predicted on many icy moons but is notably absent among the definitively detected ices with the possible exception of Enceladus. Comets, storehouses of many compounds that could exist as ices in their

---

R.N. Clark (✉)

U.S. Geological Survey, Federal Center, MS964, Box 25046, Denver,  
CO 80225, USA

e-mail: [rclark@usgs.gov](mailto:rclark@usgs.gov)

R. Carlson

Jet Propulsion Laboratory, 183-601, California Institute of Technology, Pasadena,  
CA 91109, USA

e-mail: [tassie@earthlink.net](mailto:tassie@earthlink.net)

W. Grundy

Lowell Observatory, 1400 West Mars Hill Road, Flagstaff, AZ 86001, USA  
e-mail: [W.Grundy@lowell.edu](mailto:W.Grundy@lowell.edu)

K. Noll

Space Telescope Science Institute, 3700 San Martin Dr, Baltimore, MD 21218, USA  
e-mail: [noll@stsci.edu](mailto:noll@stsci.edu)

nuclei, have only had small amounts of water ice definitively detected on their surfaces. Only one asteroid has had a direct detection of surface water ice, although its presence can be inferred in others. This chapter reviews some of the properties of ices that lead to their detection, and surveys the ices that have been observed on solid surfaces throughout the Solar System.

## 1.1 Introduction

Ice technically refers to the mineral ice, solid H<sub>2</sub>O, which is found naturally on the Earth. In the planetary sciences “ice” has become known as any volatile material that is frozen. Thus, in the planetary literature we discuss water ice, CO<sub>2</sub> ice, SO<sub>2</sub> ice, benzene ice, methane ice, etc. This chapter will review such ices found on the surfaces of planets and their satellites in the Solar System.

The major elements forming the solar system were hydrogen, carbon, nitrogen, and oxygen, often referred to as CHON material. When chemically combined, these elements produce molecules with low condensation temperatures – volatiles- with H<sub>2</sub>O being the most refractory of these. Sulfur can also contribute to the volatile inventory, and the abundances of CHON + S material can be appreciable. For comets, the molar elemental abundances, relative to hydrogen, of O, C, N, and S are 0.33, 0.15, 0.04, and 0.01, respectively (Anders and Grevesse 1989).

Under the reducing conditions produced by the presence of H<sub>2</sub>, the expected closed-shell molecules are H<sub>2</sub>O, CH<sub>4</sub>, NH<sub>3</sub>, and H<sub>2</sub>S and these are observed as volatile gases or condensates in the atmospheres of the giant planets. Depending on thermal and chemical conditions in protoplanetary and protosolar nebulae, some or all of the above molecules, as well as those formed in more oxidizing conditions, will be incorporated in the forming satellites, comet nuclei, and dwarf planets. Examples of some stable volatiles formed under oxidizing conditions are CO, CO<sub>2</sub>, N<sub>2</sub>, and SO<sub>2</sub>. Minor species may include CH<sub>3</sub>OH, HCN, HCNO, etc. These volatiles condense in varying proportions at rates that are highly dependent on temperature and molecular interaction energies, ultimately forming the diverse ices that constitute outer solar system bodies.

In their pure states, these molecules can exist in crystalline or amorphous forms, with each molecule generally having a variety of phases for both their amorphous and crystalline cases. The occurrence of particular phase of depends on the formation conditions, particularly the temperature and starting state (gaseous or liquid), and the subsequent thermal and irradiation history. For example, the freezing of liquid water produces hexagonal ice whereas amorphous, cubic, or hexagonal ice can be produced by condensation of the vapor at different temperatures. Irreversible phase changes are produced by heating, and ultraviolet and ionizing radiation can amorphize crystalline ice (Jenniskens et al. 1998; Chapter by Mastrapa et al. [this volume](#)).

Many ices on and within solar system bodies are not pure, but contain other ices or impurities. These mixed ices can exist in many forms. The minor constituent can be randomly dispersed as isolated molecules within the crystalline or amorphous

matrix (a solid solution). These molecules can be substitutional or interstitial, or trapped within defects or closed channels, sometimes existing as micro-atmospheres in voids (e. g., spectroscopically) interacting O<sub>2</sub> molecules in H<sub>2</sub>O ice, (Johnson and Jesser 1997; Loeffler et al. 2006). Inclusions of one ice mixed within the other is another possibility and can be temperature dependent as in the case of CO<sub>2</sub> in H<sub>2</sub>O ice (Hodyss et al. 2008). Complexes such as hydrates can be formed. An example is SO<sub>2</sub> as a minor constituent in H<sub>2</sub>O ice, wherein the SO<sub>2</sub> bonds to H<sub>2</sub>O to form isolated SO<sub>2</sub>•2H<sub>2</sub>O hydrates or larger aggregates (SO<sub>2</sub>)<sub>x</sub>(H<sub>2</sub>O)<sub>y</sub> (Schriever et al. 1988; Schriever-Mazzuoli et al. 2003a). Macroscopic crystalline or amorphous forms of hydrates are also possible; possible examples are hydrated sulfuric salts and acids on Europa (McCord et al. 1998b; Carlson et al. 1999b). In some cases, the molecular components can interact and act as anions and cations, forming salts such as ammonium hydrosulfide NH<sub>4</sub>SH, formed when NH<sub>3</sub> and H<sub>2</sub>S gas co-condense. The OCN<sup>-</sup> anion is prevalent in astrophysical ice grains (Hudson et al. 2001). Another potentially important class of ice structure is clathrates, crystalline forms of condensed volatiles that produce cages around trapped (guest) molecules. Although many molecules can form clathrates, the important cases for planetary and astrophysical conditions are the clathrate hydrates, a term used to describe clathrates formed by H<sub>2</sub>O molecules (and different than the molecular hydrates discussed above). Only certain guest molecules can support the host cages from collapse; for clathrate hydrates some important stabilizing guest molecules are O<sub>2</sub>, H<sub>2</sub>, N<sub>2</sub>, CO, CH<sub>4</sub>, CO<sub>2</sub>, SO<sub>2</sub>, and CH<sub>3</sub>OH. Clathrates can contain a single type of guest molecule or a mixture of different molecules, termed a mixed clathrate. Many clathrates are only produced at high confinement pressures, forcing the enclathrating molecules to accommodate the trapped guest molecules within cages; examples are terrestrial deep-sea methane clathrate hydrates and air clathrate hydrates in ice cores extracted from depth. Enceladus's plumes may arise from mixed clathrate hydrate disruption from the satellite's deep, high-pressure interior (Kieffer et al. 2006). Some clathrates can be produced at very low or even zero pressure. Sulfur dioxide clathrate hydrates can be produced at or near the surfaces of cold, icy satellites (Hand et al. 2006) and CH<sub>3</sub>OH and H<sub>2</sub>S can each form clathrate hydrates under mild heating (to ~120 K) in vacuum. These low-pressure forms may be important for some icy body surfaces.

## 1.2 Detection of Ices and Their Spectral Properties

The main method for detecting water ice, as well as other ices and compounds is by studying sunlight reflected from the surface under study (reflectance spectroscopy), and/or the heat emitted in the thermal infrared (thermal emission spectroscopy). The chemical bonds of a compound absorb light at specific wavelengths, thus spectroscopy can be used to directly and unambiguously detect a compound (given sufficient spectral range, resolution and signal-to-noise ratio). Other

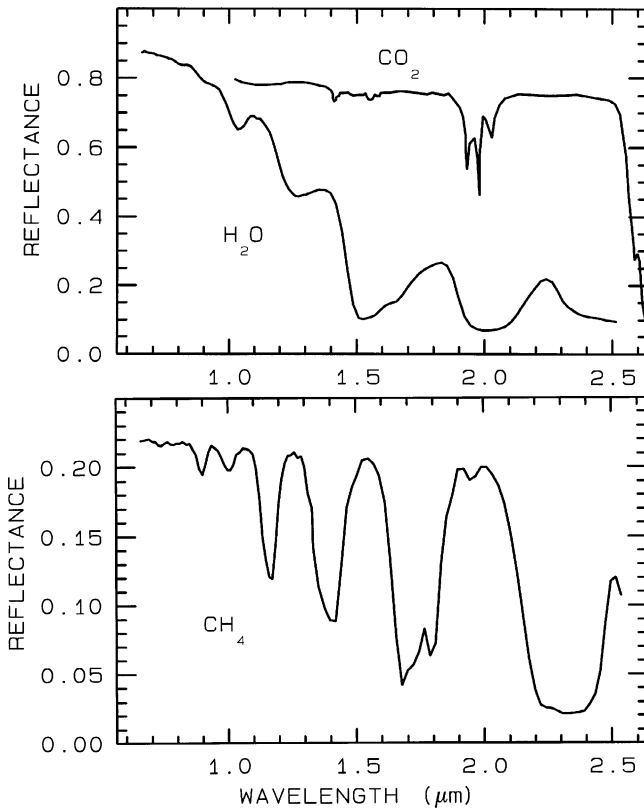


**Fig. 1.1** Spectral reflectance of solid methane, water and carbon dioxide. The strength of an absorption depends on the fundamental strength of a transition, and the mean photon path length through the material. The mean photon path depends on the material abundance and the grain size, thus both affect the appearance of the resulting spectrum (From Clark et al. (1986))

methods of remote sensing, such as neutron absorption only sense the presence of atoms, so do not directly detect a specific chemical compound, and require instrumentation in close proximity to the surface (e.g. low orbit). Reflectance spectroscopy, however, can be used to probe surfaces both near and to the outer reaches of the Solar System from the Earth's surface as well as from spacecraft. See Clark (1999) for a review of methods and causes of absorption features in spectra. In reflectance, scattering controls the light returned from the surface to the detector, and scattering can occur from ice-vacuum interfaces (grain boundaries or crystal imperfections) or from impurities mixed in the surface such as a particulate mineral. Thus, even in a pure ice, the effective grain size greatly controls the strength of absorptions, and the overall shape of the near-infrared reflectance spectrum (Figs. 1.1 and 1.2).

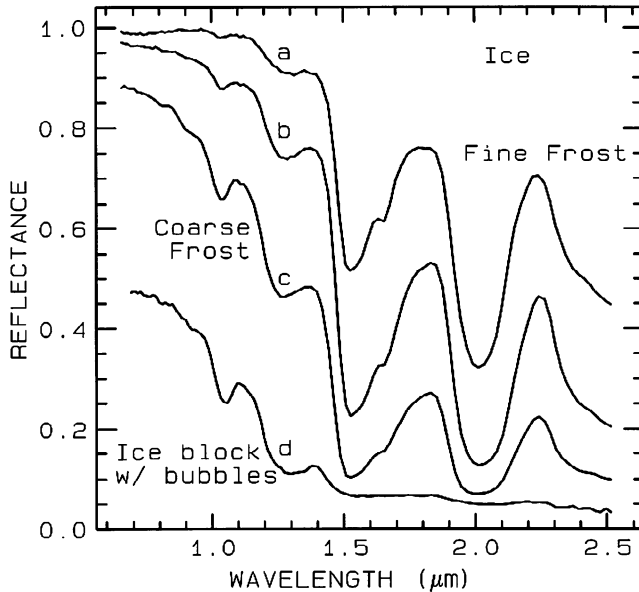


**Fig. 1.2** Illustration of changing absorption band shapes and strengths with grain size. The near-infrared spectral reflectance of (a) a fine grained ( $\sim 50 \mu\text{m}$ ) water frost, (b) medium grained ( $\sim 200 \mu\text{m}$ ) frost, (c) coarse grained ( $400\text{--}2,000 \mu\text{m}$ ) frost and (d) an ice block containing abundant microbubbles. The larger the effective grain size, the greater the mean photon path that photons travel in the ice, and the deeper the absorptions become. Curve D is very low in reflectance because of the large path length in ice. The ice temperatures for these spectra are 112–140 K (From Clark et al. (1986))

### 1.3 H<sub>2</sub>O (Ice)

Water ice phases and spectral effects as a function of temperature are discussed in detail by Mastrapa et al. ([This Volume](#)). Ice forms multiple crystal structures, including cubic (Ic) or hexagonal (Ih), and amorphous (Hobbs 1975 and references therein) which might be encountered on planetary surfaces in the solar system. The spectra of water ice display particularly broad absorptions because the water molecules are orientationally disordered. In hexagonal or cubic ice, the oxygen atoms are in a well-defined crystal structure, but the hydrogen bonds point randomly toward neighboring oxygen atoms.

The water molecule (H<sub>2</sub>O) has three fundamental vibrations, all infrared active. In the isolated molecule (vapor phase) they occur at 2.738 ( $v_1$ , symmetric OH stretch), 6.270 ( $v_2$ , H-O-H bend), and 2.663  $\mu\text{m}$  ( $v_3$ , asymmetric OH stretch). In liquid water, the frequencies shift due to hydrogen bonding:  $v_1 = 3.106 \mu\text{m}$ ,  $v_2 = 6.079 \mu\text{m}$ , and  $v_3 = 2.903 \mu\text{m}$ . H<sub>2</sub>O ice contains absorptions in the infrared owing to O-H stretches (3  $\mu\text{m}$ ), H-O-H bend (6  $\mu\text{m}$ ), and many translation and rotational modes at longer wavelengths. In the spectral region of reflected solar

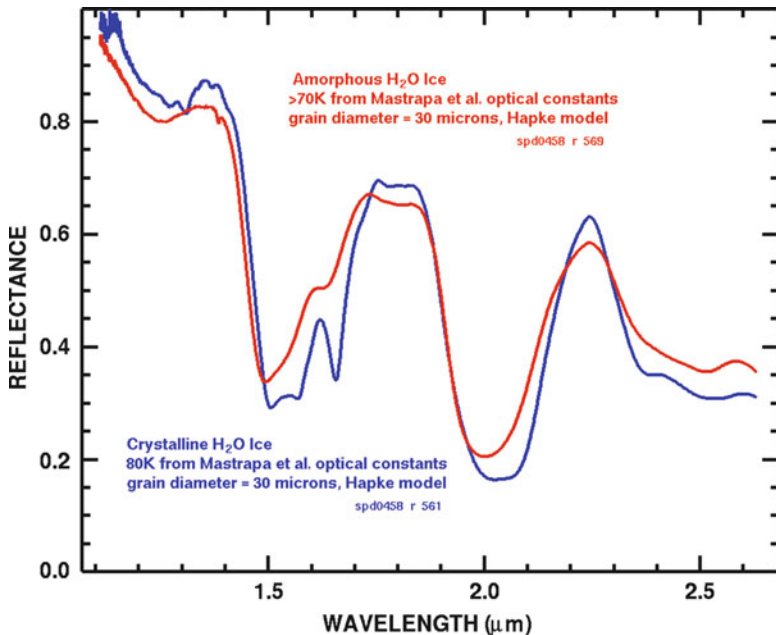


**Fig. 1.3** Amorphous versus crystalline ice (From Clark et al. 2010a))

radiation,  $\sim 0.4\text{--}3.0 \mu\text{m}$ , ice displays overtones and combinations of the above modes at 2.02, 1.52, 1.25, 1.04, 0.90, and  $0.81 \mu\text{m}$ . The first overtones of the OH stretches occur at about  $1.4 \mu\text{m}$  and the combinations of the H-O-H bend with the OH stretches are found near  $1.9 \mu\text{m}$ .

Mastrapa et al. (2008) measured the optical constants of crystalline and amorphous ice from 20 to 120 K and reviews conditions for amorphous versus crystalline water ice. Below about 135 K, amorphous ice is expected to condense from the vapor phase if the rate of growth is slow. Thus we might expect amorphous ice to be present in the Jupiter system and beyond. However, as we will see, with the probably exception of the Jupiter system where surfaces are being irradiated by particles caught in Jupiter's magnetic field, outer solar system surfaces are dominated by crystalline  $\text{H}_2\text{O}$ .

The detection of amorphous versus crystalline ice is illustrated by the change in reflectance spectra in Fig. 1.3. In amorphous ice, the absorptions shift to shorter wavelengths. The Fresnel peak near  $3.1 \mu\text{m}$  also shifts to shorter wavelengths, and the temperature sensitive  $1.65\text{-}\mu\text{m}$  absorption becomes very weak.

Spectra of icy surfaces in the Saturn system were found to have ice spectra displaying a  $2\text{-}\mu\text{m}$  absorption that was asymmetric and shifted longer than that observed in laboratory spectra of crystalline ice (Clark et al. 2008a). This puzzle was solved by Clark et al. (2010a) by the effects of diffraction by sub-micron ice grains (Fig. 1.4a, b). Sub-micron ice grains show several diagnostic indicators: (1) the  $2\text{-}\mu\text{m}$  absorption is made asymmetric and the band minimum is shifted to a

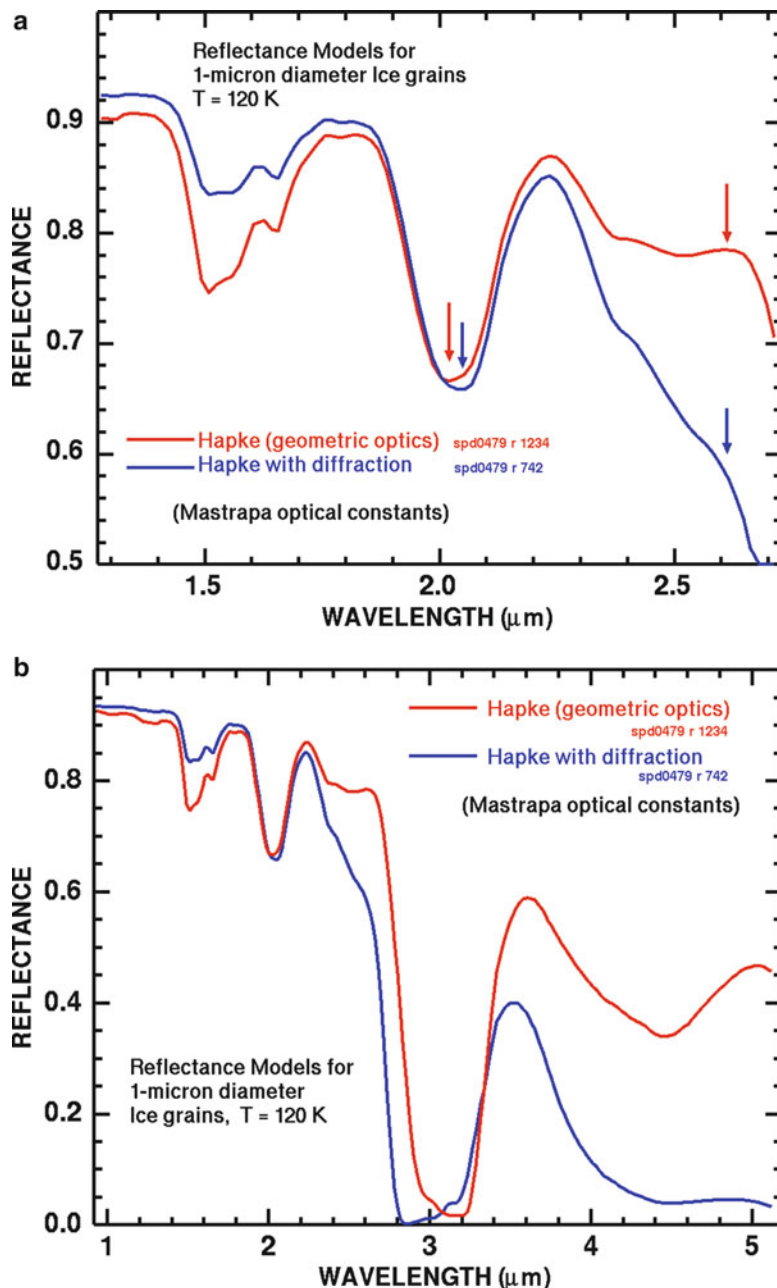


**Fig. 1.4** (a) Effects of diffraction on spectra of small ice grains. (b) Effects of diffraction on spectra of small ice grains (From Clark et al. (2010a))

slightly longer wavelength, (2) the 1.5- $\mu\text{m}$  to 2- $\mu\text{m}$  band depth ratio decreases, (3) the 2.6- $\mu\text{m}$  peak is decreased, (4) the 3.1- $\mu\text{m}$  Fresnel reflection peak is suppressed, and (5) the 5- $\mu\text{m}$  reflectance is decreased relative to the 3.6- $\mu\text{m}$  reflectance peak. In sections below, we will discuss the evidence for sub-micron crystalline ice as well as amorphous ice and larger grains of crystalline ice. At wavelengths shorter than 1- $\mu\text{m}$ , sub-micron and nanophase particles will cause Rayleigh scattering in the surfaces, and these effects are observed in the Saturn system (Clark et al. 2008a, 2010a).

## 1.4 SO<sub>2</sub> Ice

SO<sub>2</sub>, a colorless gas at room temperature, is a common terrestrial volcanic (and industrial) effluent and also present in Venus's atmosphere. SO<sub>2</sub> is a bent molecule of the form O-S-O and is a stable form of sulfoxides, SO and S<sub>2</sub>O being much less stable. Oxidation of SO<sub>2</sub> in the presence of H<sub>2</sub>O produces sulfuric acid, evident in the Earth's atmosphere as acid rain and in Venus's atmosphere as the ubiquitous sulfuric acid clouds and haze.

SO<sub>2</sub> is more refractory than NH<sub>3</sub> and liquefies at  $\sim$ 263 K and freezes at  $\sim$ 200 K. Within the temperature range of 90–120 K, appropriate for Jovian satellites, the SO<sub>2</sub> vapor pressure varies by five orders, from about 10<sup>-4</sup> nbar to 10 nbar. SO<sub>2</sub> is amorphous when condensed at temperatures  $<70$  K, but crystallizes for temperatures  $>70$  K (Schmitt et al. 1994). Condensed SO<sub>2</sub> forms many different textures (Nash and Betts 1998). The condensation, evaporation, and metamorphism of pure SO<sub>2</sub> and mixed ices have been discussed by Sanford and Allamandola (Sandford and Allamandola 1993).

Ultraviolet photolysis of SO<sub>2</sub> produces SO + O for wavelengths less than 2,179 Å and S + O<sub>2</sub> for wavelengths below 2,080 Å. The atomic oxygen can attach to SO<sub>2</sub>, forming SO<sub>3</sub>. In the presence of H<sub>2</sub>O, SO<sub>3</sub> reacts to yield H<sub>2</sub>SO<sub>4</sub> (Schriverr-Mazzuoli et al. 2003b). Ion bombardment of SO<sub>2</sub> ice produces SO<sub>3</sub> (monomeric and polymeric), sulfur, and sulfate (Moore 1984). SO<sub>2</sub> subjected to electrical discharge produces SO<sub>3</sub>, S<sub>2</sub>O, S<sub>3</sub>, S<sub>4</sub>, O<sub>3</sub>, and polysulfur oxides (Hopkins et al. 1973).

Useful reviews of SO<sub>2</sub> properties by Schmitt et al. (1998b) and Nash and Betts (1998) are found in the Solar System Ices book (Schmitt et al. 1998a). Infrared and ultraviolet spectroscopy of SO<sub>2</sub> is summarized in (Carlson et al. 2007).

## 1.5 Nitrogen Ice (N<sub>2</sub>)

Although nitrogen is cosmochemically abundant, the high volatility of N<sub>2</sub> ice makes it unstable except at extremely low temperatures characteristic of the outer edge of the Solar System. There are two low-pressure phases of N<sub>2</sub> ice. Above 35.61 K, the stable form is beta N<sub>2</sub> ice, an orientationally-disordered hcp solid (Scott 1976). It is difficult

to detect spectroscopically, because N<sub>2</sub> is a non-polar molecule in which vibrational absorptions are not easily excited. Only when an N<sub>2</sub> molecule collides with another molecule is a dipole moment temporarily induced, enabling a photon around 4.25 μm to excite its 1-0 fundamental vibrational mode (e.g., Shapiro and Gush 1966). This collision-induced absorption is relatively broad ( $\sim$ 100 cm<sup>-1</sup> in wavenumber units), compared with gas-phase absorptions due to fixed dipole moments, owing to the modulation of the vibrational transition by the translational motion of the colliding pair. The integrated absorption of the band depends sensitively on the fraction of molecules involved in collisions, and thus on the density and temperature of the gas (Sheng and Ewing 1971). A 2-0 overtone band is observed around 2.15 μm, exhibiting behavior like that of the 1-0 fundamental, albeit with much weaker absorption (McKellar 1989). Similar-looking 1-0 and 2-0 absorption bands are also seen in liquid N<sub>2</sub> (Grundy and Fink 1991; Brodyanski et al. 2002) and in the higher-temperature beta N<sub>2</sub> ice (Grundy et al. 1993; Tryka et al. 1995), suggesting an analogous role for induced molecular dipole moments in these condensed phases. Peak Lambert absorption coefficients of the 1-0 and 2-0 bands in beta N<sub>2</sub> ice are of the order of 1 and 0.01 cm<sup>-1</sup>, respectively (Schmitt et al. 1998b), far weaker than the near-infrared absorption coefficients of other ices discussed previously in this chapter. These weak absorptions require substantial optical pathlengths to produce observable absorption in beta N<sub>2</sub>. The shape of the beta N<sub>2</sub> absorption band changes with temperature, becoming narrower at lower temperatures, with a shoulder appearing on the long wavelength side of the band below about 41 K.

The lower temperature alpha phase of N<sub>2</sub> is an orientationally-ordered fcc solid, stable below 35.61 K (Scott 1976). Like beta N<sub>2</sub>, alpha N<sub>2</sub> has absorptions around 4.25 and 2.15 μm, but the shapes of the bands in alpha N<sub>2</sub> differ considerably from their counterparts in beta and liquid N<sub>2</sub> (Grundy et al. 1993; Tryka et al. 1995; Schmitt et al. 1998; Brodyanski et al. 2002). Alpha N<sub>2</sub> has not been observationally detected on any outer Solar System body, but it could occur seasonally where temperatures drop below 35.61 K (e.g., Duxbury and Brown 1993). It would be readily distinguishable from beta N<sub>2</sub> via near-infrared reflectance spectroscopy, through its distinctly structured absorption bands. Specifically, alpha N<sub>2</sub> has a very sharp absorption peak at 2.148 μm with a width less than 1 cm<sup>-1</sup>, which has been interpreted as a simultaneous excitation of two vibron modes of the alpha N<sub>2</sub> crystal by one photon (Brodyanski et al. 2002). At 2.166 μm, a weaker, narrow feature is attributed to simultaneous excitation of a fundamental vibration of <sup>15</sup>N<sup>14</sup>N plus a vibron mode in the <sup>14</sup>N<sub>2</sub> crystal, and weaker, broader, nearby features are attributed to phonon sidebands (Brodyanski et al. 2002).

## 1.6 Hydrocarbon and Other Ices

Hydrocarbons are a diverse category of organic compounds, comprising numerous families without heteroatoms and with functional groups of solely hydrogen and carbon atoms. The simplest hydrocarbons are the alkanes – singly bonded

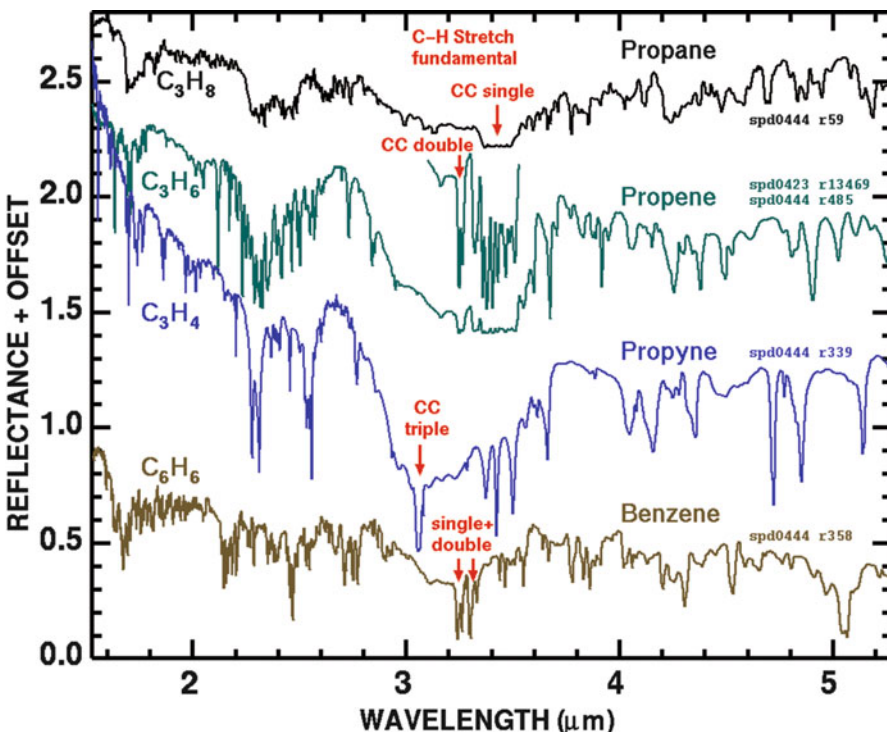


**Fig. 1.5** Spectra of propane, propene, propyne and benzene ices (From Clark et al. (2009))

molecules with no reactive functional groups. Hence, they tend to combust at relatively high temperatures, even though composed entirely of low atomic weight atoms, and have a generic chemical formula of  $C_nH_{2n+2}$ . If the carbon backbone contains a C-C double bond, the hydrocarbon is termed an alkene, and it has a formula of  $C_nH_{2n}$  (e.g. propene,  $C_3H_6$ ); with a C-C triple bond, it is called an alkyne whose formula is  $C_nH_{2n-2}$  (e.g. propyne,  $C_3H_4$ ). In the singly bonded alkanes, hydrogen atoms will bond to all the remaining positions on the carbon atom, and they are known as saturated hydrocarbons. Unsaturated hydrocarbons then, are those with doubly or triply bonded carbon atoms, and they will have less than their ‘full’ complement of hydrogen atoms. Together, these straight (or branched) chain hydrocarbons are known as ‘aliphatic’ compounds, and also include such derivatives as fatty acids (Wade 2005).

In general, spectra of different families share different spectral characteristics while spectral properties are similar within a family (also called group or series). For example, Fig. 1.5 shows spectral differences among ices in the alkane, alkene, and alkyne groups from Clark et al. (2009). In alkanes, the C-H stretch fundamental occurs near  $3.4\text{ }\mu\text{m}$ , whereas in the C-C double bonded alkenes, the C-H stretch shifts closer to  $3.2\text{ }\mu\text{m}$ , and in the C-C triply bonded alkynes, the C-H stretch shifts to nearly  $3.0\text{ }\mu\text{m}$  (Fig. 1.5).

The carbon skeleton can close in on itself in two ways: by creating a ring of singly-bonded carbons of any length equal to or greater than three (cycloalkanes, known as alicyclic hydrocarbons), *or* by the overlapping of p orbitals from adjacent carbon atoms into pi ( $\pi$ ) bonds to create a benzene ring ( $C_6H_6$ ). The benzene ring with overlapping p orbitals is particularly stable, and forms the basis of the aromatic hydrocarbon family. The C-H stretch fundamental of aromatic hydrocarbons occurs near  $3.3\text{ }\mu\text{m}$  (Fig. 1.5) and benzene ice is detected on Saturn’s moon Titan. Most organic molecules are infrared active, displaying stretching and bending vibrations. Because these transitions are specific to the atoms and their chemical bonds, and are similar regardless of the type of larger molecule within which they are contained, an examination of the IR spectrum will reveal an enormous amount of information about an unknown compound (e.g. as seen in Fig. 1.5). Clark et al. (2009) observed that the spectral complexity of organic ices first increases as molecular weight increases, then decreases at higher molecular weights. The loss of spectral structure at high molecular weights is probably due to many overlapping absorptions averaging out small details.

Reflectance spectra of cyanoacetylene (2-propynenitrile, IUPAC nomenclature),  $HC_3N$  ice was studied by Curchin et al. 2010. The reflectance spectrum of  $HC_3N$  ice is rich in spectral features in the reflected solar range (0.8 to  $>5\text{ }\mu\text{m}$ ), which should allow detection with imaging spectrometers currently flying in the solar system, and it has been detected on Titan (see below). Reflectance spectra of other ices, such as cyanogen and other observed compounds in Titan’s atmosphere have yet to be studied at temperatures relevant to our solar system surfaces.

## 1.7 Methane Ice ( $CH_4$ )

Methane deserves special attention as the smallest and simplest alkane, as well as being the hydrocarbon most ubiquitously observed as an ice on solar system bodies. It is readily detected spectroscopically by means of numerous overtones and combinations of four fundamental vibrational transitions. These are a symmetric mode  $v_1(A_1)$  at  $2,914\text{ cm}^{-1}$  ( $3.43\text{ }\mu\text{m}$ ), a doubly degenerate  $v_2(E)$  bending mode at  $1,526\text{ cm}^{-1}$  ( $6.55\text{ }\mu\text{m}$ ), and triply degenerate stretching  $v_3(F_2)$  and bending  $v_4(F_2)$  modes at  $3,020$  and  $1,306\text{ cm}^{-1}$  ( $3.31$  and  $7.66\text{ }\mu\text{m}$ ), respectively (Grundy et al. 2002). Two different phases occur at zero pressure. At temperatures below  $20.4\text{ K}$ ,  $CH_4$  exists as a cubic crystal, while above that temperature, it loses its orientational order and long-range coordination, resulting in broadened bands similar to (but not identical to) those of liquid methane (e.g., Ramaprasad et al. 1978; Martonchik and Orton 1994). Temperature-dependent spectra have been measured for methane ice between  $0.7$  and  $5\text{ }\mu\text{m}$ , revealing subtle changes with temperature that offer an as-yet unexploited potential for remote sensing of  $CH_4$  ice temperatures (Grundy et al. 2002). Methane molecules dispersed in nitrogen ice exhibit slightly different spectral behavior, characterized by subtle wavelength shifts toward blue wavelengths as well as the loss of a weak transition at  $1.69\text{ }\mu\text{m}$  (Quirico et al. 1997). This property

provides a way to remotely distinguish diluted from pure CH<sub>4</sub>, as well as the potential to detect smaller quantities of nitrogen ice than can be readily detected through observation of the much weaker N<sub>2</sub> ice absorptions, with specific applications discussed later in this chapter.

## 1.8 Observed Ices in the Solar System

We will now discuss the detections of icy planets and their satellites in our Solar System.

### 1.8.1 Terrestrial Planets

Of the terrestrial planets Mercury, Venus, Earth and Mars, only Earth and Mars have ice on their surfaces. The surfaces of Mercury and Venus are too hot for any ice to exist, although ice has been inferred to exist in the poles of Mercury from radar reflectivity, ice has not been confirmed.

The Earth is the only planet whose temperature is near the melting point of water where both liquid and solid water exists. This condition enables a complex hydrologic cycle of both solid and liquid water eroding and reshaping the surface. Saturn's moon Titan has a close analogy where instead of liquid water, liquid methane and ethane exist at the surface and instead of liquid water lakes and rivers on the Earth, Tiran has liquid methane and ethane lakes and rivers in a current active hydrolic cycle. These two bodies are unique in the Solar System in that regard. See Hobbs (1975) for discussions of ice on the Earth's surface and in the atmosphere.

The Earth's surface is dominated by liquid and solid water. Where temperatures are low and pressures high, methane clathrate hydrates exist and are ubiquitous on the ocean floor and in permafrost regions (Sloan 1998). Methane clathrate hydrates may exist on outer solar system bodies but there is no definitive detection of them beyond the Earth.

Water ice is thought to exist in the permanently shadowed craters on the moon and neutron spectrometer data from Lunar Prospector (Feldman et al. 1998, 2000, 2001) showed that hydrogen is present in the lunar polar regions. More recently Clark (2009), Pieters et al. (2009), and Sunshine et al. (2009) reported that adsorbed water is extensive in the lunar surface raising the likelihood that some of it has migrated and is trapped in the polar regions. Press releases from the NASA LCROSS impact into south pole crater Cabeus A indicates water ice was detected but research papers have yet to be published.

#### 1.8.1.1 Mars

Mars has seasonal and remnant polar caps of H<sub>2</sub>O and CO<sub>2</sub> ices, as well as permafrost and geologic features indicative glacial flow and sublimation of water ice from below the surface. Mars' seasonal polar caps extend down to about

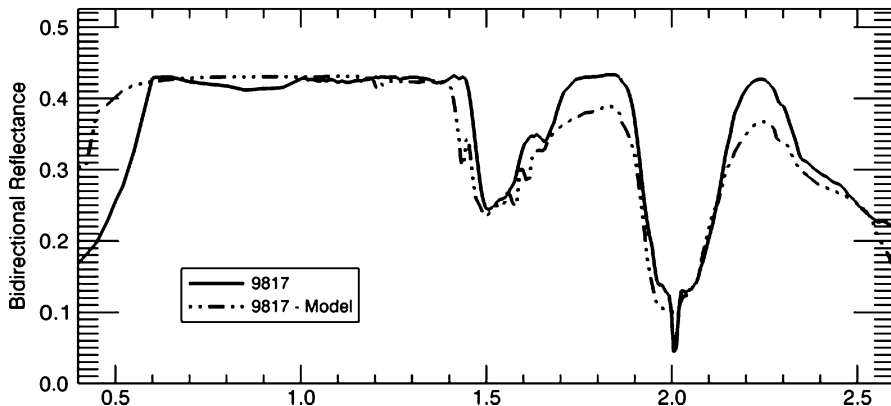


**Fig. 1.6** CRISM spectrum of the Mars Phoenix landing site (*solid line*) and model results (*dotted lines*) obtained at  $L_s \sim 19.3^\circ$ . Water ice dominates the spectrum with smaller amounts of  $\text{CO}_2$  ice (From Cull et al. (2010))

50° latitude (e.g. James et al. 1993 and references therein). Due to present day obliquity, the southern hemisphere is drier than the northern hemisphere. The southern residual cap is dominated by  $\text{CO}_2$  ice while the northern residual cap is dominated by  $\text{H}_2\text{O}$  ice (Farmer et al. 1976; Kieffer et al. 1976), but recently confirmed that an  $\text{H}_2\text{O}$  cap underlies the southern  $\text{CO}_2$  remnant cap (Byrne and Ingersoll 2003; Bibring et al. 2004).

More than 25% of the atmospheric  $\text{CO}_2$  condenses each year to form the seasonal caps (Forget et al. 1995; Kieffer and Titus 2001). The NASA Phoenix lander and Mars Reconnaissance Orbiter, Compact Reconnaissance Imaging Spectrometer for Mars (CRISM), and the High-Resolution Imaging Science Experiment (HIRIS) instruments have quantified growth of the northern seasonal polar cap of  $\text{H}_2\text{O}$  and  $\text{CO}_2$  at 68° N latitude (e.g. Cull et al. 2010; Fig. 1.6). During winter, the  $\text{CO}_2$  ice grows to a depth of about 0.35 m with a thin layer of  $\text{H}_2\text{O}$  ice on the surface.

The sub-surface of Mars apparently contains significant amount of ice (Picardi et al. 2005). During periods of high obliquity, water ice in the poles and the subsurface may move to lower latitudes. There is evidence for such movement with geomorphic features such as thin mantling units at high latitudes, possible ice deposits on poleward-facing slopes, and evidence of glacial flow (Carr 2006).

Images of Mars' surface show large flood channels, ancient seas and lakes, indicating large amounts of water at the surface. Where the water went is a major mystery. Perhaps it was lost to space, or locked up in a many kilometer-thick cryosphere (Clifford 1993). Ice is presently stable on in the sub-surface above about latitude 40° below a fraction of a meter depth. Much of Mars' surface between 30° and 60° latitudes have an stippled appearance at scales of a few meters, which has been interpreted as sublimation of ice that accumulated in these regions during times of higher obliquity (Carr (2006), and references therein).

Carr also discusses many other geologic features that point to large reservoirs of sub-surface ice, some of which has sublimed. Thus, Mars is an ice-rich world and a world scarred by ice processes, including sublimation and glacial flow.

### 1.8.2 Asteroids and Comets

To date there is only one asteroid, 24 Themis, with a reported detection of ice (Rivkin and Emery (2008) and confirmed by Campins et al. (2009)). Both teams detected a weak absorption at 3- $\mu\text{m}$  best described by water ice. However, strongly hydrogen bonded water can also display absorptions at the wavelengths where ice absorbs and higher signal-to-noise ratio spectra are needed to confirm this weak absorption. Indeed, Clark (2009) show absorption at 3-  $\mu\text{m}$  due to adsorbed water in the sunlit surface Moon.

Comets are presumed to be made of dirty ice. Davies et al. (1997) detected weak absorptions attributed to water ice in comet Hale-Bopp but the spectra included the coma. They also showed possible evidence for the ice being amorphous, but the low signal-to-noise ratio and weak absorption strength precludes a definitive detection of amorphous versus crystalline ice. Lellouch et al. (1998) also reported detection of ice in the coma of Comet Hale-Bopp. The temperatures they derived, 170 K, for their observations are too high for amorphous ice. The only detection of ice on a comet nucleus without interference from the coma, comet Tempel 1, was by Sunshine et al. (2006) using the Deep Impact spacecraft where small exposures of ice were seen by the imaging spectrometer. While water ice has been detected on comets, to date, no other ices have been definitively detected.

### 1.8.3 Jupiter System

Of Jupiter's four large moons, discovered 400 years ago by Galileo, three of these (Europa, Ganymede, and Callisto) were found to have water ice surfaces (Kuiper 1957; Moroz 1965; Johnson and McCord 1971; Pilcher et al. 1972; Fink et al. 1973), subsequently studied using airborne and ground-based spectroscopy by (Pollack et al. 1978; Clark 1980; Clark and McCord 1980) and others, and more recently by infrared spectroscopy from the *Galileo* spacecraft (Fig. 1.7) in orbit around Jupiter. While no water ice was found on the innermost of the Galilean satellites – Io –sulfur dioxide ice was identified by (Fanale et al. 1979; Hapke 1979; Smythe et al. 1979) on the surface of this moon, the most volcanically active object in the solar system. The vigorous heating that powers Io's volcanoes is the periodic solid-body tidal flexing arising from this moon's orbital eccentricity.

Gravity data shows that Io is a differentiated silicate body with an Fe or Fe + FeS core, whereas the outer three Galileans contain water ice, with increasing H<sub>2</sub>O content as one moves outward from Jupiter. Europa is differentiated and may have an internal structure similar to Io's but with an overlying 100–200 km H<sub>2</sub>O mantle

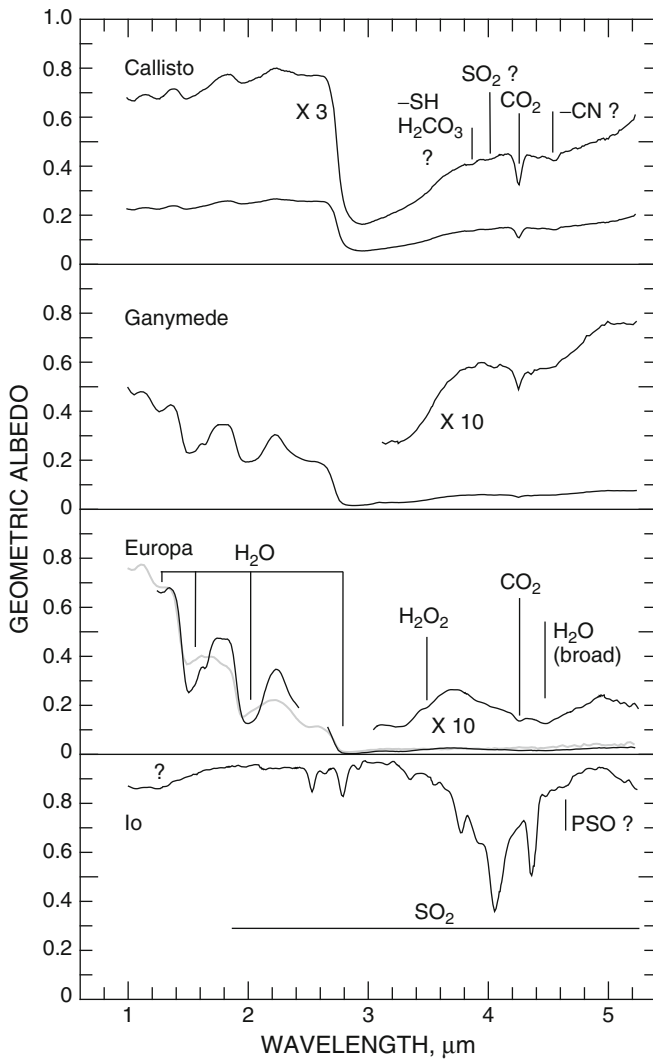


**Fig. 1.7** Infrared Spectra of the Galilean Satellites. Geometric albedo spectra derived from Galileo NIMS observations show the rich spectrum of  $\text{SO}_2$  on Io (bottom panel) with possible polysulfur oxide absorption present. The broad 1- $\mu\text{m}$  absorption is unidentified as is a weak feature at  $3.15 \mu\text{m}$ . Nearly pure water ice indicated on Europa's leading side (black line) while a hydrate is present on the trailing side (grey line) and produces distorted  $\text{H}_2\text{O}$  bands. Hydrogen peroxide and carbon dioxide are also apparent in Europa's spectrum. Ganymede has less exposed ice and the geometric albedo is less due to broad non-ice absorption. Callisto is almost completely covered with dark non-ice compounds and both Callisto and Ganymede show spectral features possibly due to a hydrosulfide or carbonic acid, possibly  $\text{SO}_2$ , and potentially a CN compound

that comprises 10% of the satellite's mass. This H<sub>2</sub>O cover is thought to consist of a 2–20 km icy crust covering an ocean of up to 100 km thick. As in the case of Io, tidal flexing provides the heat to sustain a liquid ocean which is likely in contact with the rocky mantle. Ganymede, the largest satellite in the solar system and larger than Mercury, has more water than Europa, contributing to approximately half of the satellites mass. An outer icy crust and mantle, about 200 km thick, are thought to cover an ocean that is sandwiched between layers of high-pressure ice in different phases. Beneath the H<sub>2</sub>O mantle is a differentiated rocky body with a Fe-containing liquid core acting as a magnetic dynamo. Callisto is less differentiated than his sibling satellites, but has about the same relative water content and likely an ocean also, based on Galileo magnetic field data. However, due to their distance from Jupiter, tidal heating is much less efficient for these outer two satellites compared to Io and Europa.

In the classical solar nebula description, carbon and nitrogen compounds are reduced in the formation regions of the giant-planets, in which case the CHON material that forms outer solar system planets and satellites would consist of H<sub>2</sub>O, CH<sub>4</sub>, and NH<sub>3</sub> (Prinn and Fegley 1981, 1989). Inclusion of NH<sub>3</sub> within Ganymede and Callisto could facilitate the existence of liquid oceans deep inside these moons since ammonia can reduce the melting point of water to about 180 K (Kargel 1998). However, recent models (Canup and Ward 2002) suggest that instead of warm and dense nebular conditions, the circum-Jovian accretion disk was cold and gas-starved. In this case the reduction of CO and N<sub>2</sub> to hydrides is incomplete and little ammonia would be expected to have been incorporated in any of the Galilean satellites. However, Ganymede and Callisto may have formed in outer regions that were richer in NH<sub>3</sub> hydrates and N<sub>2</sub>, CO, and CH<sub>4</sub> clathrate hydrates, thereby providing the “anti-freeze” for their oceans (Mousis and Gautier 2004). The gas-starved nebula model is favored by Galileo measurements and predicts that little water or hydrated material would be incorporated within or on Io, although a thin ice veneer could have been deposited during late stages (McKinnon 2007). Some amount of hydrated minerals may also have been incorporated, as suggested by the presence of hydrous minerals on Amalthea (Takato et al. 2004), a Jovian satellite interior to Io's orbit. In the gas-starved formation scenario, Io is expected to be composed of solar mixtures of silicates, oxides and sulfides (McKinnon 2007). Differentiation into a Fe-containing core can deplete the mantle of iron compounds. In the following paragraphs we discuss the icy (SO<sub>2</sub> and H<sub>2</sub>O) surface compositions of Jupiter's Galilean satellites. General reviews can be found in recent books (Bagenal et al. 2004; Lopes et al. 2007; Pappalardo et al. 2009). Io and Europa's surface compositions are reviewed in (Carlson et al. 2007) and (Carlson et al. 2009), respectively.

### 1.8.3.1 Io

Io is the Innermost of the four Galilean satellites and exhibits a young, volcanically active surface that is rapidly resurfaced at an average rate of about 1 cm per year. The surface is nearly completely covered by sulfur dioxide ice and elemental sulfur,

the exceptions being in the hot volcanic areas and fresh lava flows where silicates may be exposed.  $\text{SO}_2$  is a volcanic effluent, derived from the degassing of hot magma, and is the dominant volcanic gas, accompanied by minor amounts of SO and  $\text{S}_2$  (Zolotov and Fegley 1998, 1999, 2000) and other species such as NaCl (Lellouch et al. 2003).  $\text{SO}_2$  contributes nearly all of the absorption features in Io's spectra (Fanale et al. 1979; Hapke 1979; Smythe et al. 1979; Schmitt et al. 1994; Nash and Betts 1995; Carlson et al. 1997). The global abundance and grain sizes of the  $\text{SO}_2$  snow indicate that optically thick  $\text{SO}_2$  deposits of mm-size grains are concentrated in Io's equatorial regions (Carlson et al. 1997; Laver and de Pater 2008, 2009) and confirm earlier measurements of (McEwen et al. 1988), who studied Io's surface using ultraviolet and visible Voyager images. These equatorial deposits are strongly associated with active volcanoes and arise from volcanic venting of gaseous  $\text{SO}_2$  into the plumes and atmosphere with subsequently deposition onto colder surfaces as frost. The relatively large grain sizes indicate sublimation and condensation metamorphism for these deposits.

In contrast, fine grained  $\text{SO}_2$  frost was found at mid-and high-latitudes (Carlson et al. 1997; Doute et al. 2001; Laver and de Pater 2008, 2009).  $\text{SO}_2$  frost sublimates during the day due to relatively high surface temperatures. Although most of it re-condenses locally during the nighttime,  $\text{SO}_2$  molecules slowly migrate toward higher latitudes and colder regions (Matson and Nash 1983). The high-latitude  $\text{SO}_2$  deposits appear transparent under normal-incidence illumination and therefore are thought to be optically thin (Geissler et al. 2001). They tend to remain as small grains as originally condensed because of the colder environment and rapid radiolytic destruction of the  $\text{SO}_2$  grains in higher latitudes (Wong and Johnson 1996). The poles of Io appear red due to the radiolytic destruction of  $\text{SO}_2$  and the production of elemental sulfur.

$\text{SO}_2$  is a thermochemical product of hot magmas and its presence is indicative of volcanic conditions. The ratios of SO and  $\text{S}_2$  to  $\text{SO}_2$  in the volcanic plumes are consistent with high-temperature volcanism in a silicate mantle that is deficient in Fe-metal (Zolotov and Fegley 2000). Being a high-temperature chemical product,  $\text{SO}_2$  probably represents a very minor contribution to the satellite's total mass. Since it is a very volatile, it is likely that most of Io's  $\text{SO}_2$  is at or near the surface. The solid and gaseous forms of  $\text{SO}_2$  are evident in the surficial ices and the overlying sublimational and plume-derived atmosphere, but there is evidence that liquid  $\text{SO}_2$  forms a near-surface “aquifer”. Sapping channels and scarps provide one line of evidence (McCauley et al. 1979; McEwen et al. 2000; Moore et al. 2001) and uniform topographic infilling of a crater by  $\text{SO}_2$  (Lopes et al. 2001) provides further evidence for  $\text{SO}_2$  “ground water” (Fig. 1.8). It has been estimated that the upper 1 km of Io is rich in the volatiles  $\text{SO}_2$  and sulfur (McEwen et al. 2000).

Io undergoes intense radiation from Jupiter's magnetosphere, and a byproduct of  $\text{SO}_2$  ice radiolysis is sulfur trioxide. A signature of  $\text{SO}_3$ , as well as  $\text{S}_8$  and  $\text{SO}_2$ , may be present in thermal emission spectra of Io (Khanna et al. 1995; Hanel et al. 2003). A related species, disulfur monoxide  $\text{S}_2\text{O}$ , was investigated by (Baklouti et al. 2008) but interference by strong  $\text{SO}_2$  bands precluded its observation. Polysulfur oxides may be present on Io and produce a broad absorption in the 4.5- $\mu\text{m}$  region

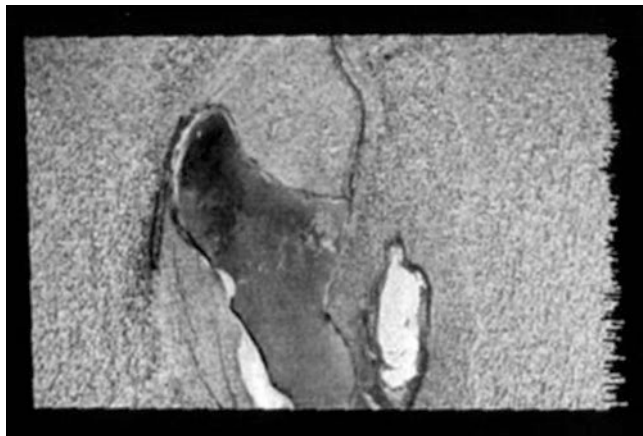


**Fig. 1.8** The interior of a caldera near Chaac, to the *right* of the flow feature, is filled with very pure SO<sub>2</sub> that appears to be topographically controlled, suggestive of liquid flow

(Baklouti et al. 2008). Ion irradiation can also sputter surface atoms and molecules into an atmosphere around Io and into escape orbits. Neutral and ionized toroidal clouds are formed around Jupiter and provide a source of sulfur, oxygen, sodium, potassium, and other species to other satellites. This is particularly important for Europa, where the torri strike the trailing hemisphere and provide a source of sulfur and metals.

### 1.8.3.2 Europa

Europa orbits Jupiter at about twice the distance from Jupiter as Io and is the innermost of the water ice containing Galilean satellites. Although it contains less H<sub>2</sub>O than Ganymede or Callisto, the surface exhibits much more exposed water ice and hydrate than the other H<sub>2</sub>O-ice Galileans due to its much more active surface activity, a consequence of tidal heating (the crater age is a mere 50 My (Zahnle et al. 2003)). The leading hemisphere of Europa, in the sense of orbital motion, presents the purest ice as determined by infrared spectroscopy which probes the upper sub-mm depths. Both amorphous and crystalline ice are present, with a greater proportion being the amorphous form compared to crystalline (Hansen and McCord 2004). The presence of amorphous and crystalline phases are the result of two competing processes – the increase in disorder and amorphization of ice crystals by energetic particle bombardment, and thermally-induced phase transformation of amorphous ice to the lower energy cubic ice form or the even lower energy hexagonal ice phase.

The second major “ice” on Europa is actually a hydrated species, predominant on the trailing side and associated with the dark material that produces Europa’s

hemispherical color dichotomy – the red, trailing hemisphere and the white, leading hemisphere. This icy hydrate is a complex of some molecule X (or groups of molecules) surrounded by hydration shells of water, often in stoichiometric proportions, as  $Xn \cdot mH_2O$ . One suggested source of this hydrate is a salty subsurface ocean the X being a salt such as  $MgSO_4$ , forming hydrates such as epsomite  $MgSO_4 \cdot 7H_2O$  and others (McCord et al. 1998b; McCord et al. 1999). A second hypothesis is that radiolysis of exogenic (Iogenic) sulfur implanted on Europa's trailing hemisphere produces hydrated sulfuric acid (Carlson et al. 1999b, 2002, 2005). The associated dark material is thought to be polymeric sulfur (Carlson et al. 1999b) since most salts and acids are colorless in the visible. The association of hydrate and dark material with geological features on the trailing side implies an endogenic process, either emplacement of material from the subsurface ocean or thermal modification of exogenically-derived material, forming lag deposits.

The magnetospheric environment at Europa is almost as damaging as at Io, and several radiolytic species are observed. Molecular oxygen is found on Europa (Spencer and Calvin 2002), and is radiolytically formed and trapped in  $H_2O$  ice, as is hydrogen peroxide  $H_2O_2$  (Carlson et al. 1999a).  $SO_2$  is observed and is a radiolytic product of sulfate decomposition (Johnson et al. 2004; Carlson et al. 2009).  $CO_2$  is also found (Smythe et al. 1998; Hand et al. 2007; Hansen and McCord 2008) and this ubiquitous molecule could be from endogenic or exogenic sources (see discussions below). These minor species may exist in Europa's near surface as mixed clathrate hydrates (Hand et al. 2006).

### 1.8.3.3 Ganymede

Ganymede, like Io and Europa, is a differentiated body but is unique because it has an intrinsic magnetic field arising from dynamo motions within a molten iron core. Ganymede and Callisto contain more ice than Europa, but both exhibit darker, less icy surfaces than does Europa. The major source of this dark material is probably meteoritic infall, which should also occur on Europa, but Europa's vigorous current or recent surface activity has diluted and buried the meteoritic material within the ice shell.

Ganymede has roughly equal proportions of amorphous and crystalline ice (Hansen and McCord 2004); the small proportion of amorphous ice compared to Europa is presumably due to the lower incident flux of high-energy magnetospheric radiation and shielding by Ganymede's magnetic field. Bright, icy polar caps are observed on this satellite and the boundary between the icy polar regions and the less icy lower latitudes closely coincides with the transition from open to closed magnetic field lines. This suggests surface brightening by energetic magnetospheric particles streaming in on open striking field lines and striking Ganymede's polar surfaces. This brightening may be produced by ice grain disruption (Johnson 1997), creating smaller grains and more scattering sites, which decreases the absorption and increases the albedo, or by sputtering and thermal segregation (Khurana et al. 2007).

A hydrate, possibly similar to Europa's, has been identified on Ganymede and suggested to have been from  $\text{MgSO}_4$ -rich brine emplaced from the ocean below (McCord et al. 2001). Ganymede once had an active surface but any such emplacement must have occurred in the distant past since the surface age is  $\sim 2$  Gy (Zahnle et al. 2003). With subsequent meteoritic infall and gardening, it is unclear how these salt minerals could be present in the high concentrations that were observed. The geological process that erupts material from a 200-km deep ocean is also unclear. A second class of hydrate, associated with dark crater rays, has been identified by (Hibbits and Hansen 2007) and found to be similar to C-type asteroid or Callisto non-ice materials. This hydrate may be material from, or modified by, the impactor.

Three water-related radiolytic species are found on Ganymede: molecular oxygen (Spencer et al. 1995; Calvin et al. 1996), ozone (Noll et al. 1996), and hydrogen peroxide (Hendrix et al. 1999). Transient, localized  $\text{SO}_2$  concentrations have been suggested (Domingue et al. 1998) and spectral information indicates the presence of other species. Since these features are similar to those found in spectra of Callisto, they are described in the following section.

#### 1.8.3.4 Callisto

Callisto is the outermost icy Galilean satellite, with a composition that is about half  $\text{H}_2\text{O}$  and half rocky silicates. In contrast to the inner Galilean satellites, Callisto is only partly differentiated, with the denser rocky components having slowly settled, or currently settling, to the center (Schubert et al. 2004). The lack of tidal heating and the low rate of gravitational settling may not provide sufficient energy to cause geological activity on the surface. Callisto has a very old surface, mostly covered with a layer of dark material, presumably from meteoritic infall. Both impact cratering and mass wasting have exposed the icy “bedrock” over approximately 10% of this ancient surface, showing the presence of water ice that is predominantly crystalline with grain sizes (diameters) of  $\sim 200$ – $400$   $\mu\text{m}$  (Hansen and McCord 2004). Water molecules tend to segregate by sublimation and condensation on cold, bright ice surfaces, but the dark material also has an  $\text{H}_2\text{O}$  component, probably including adsorbed  $\text{H}_2\text{O}$ . Because the temperatures attained by the dark material are high ( $\sim 150$ – $160$  K). Some of these water molecules sublime during the day and re-condense at night, so thermal segregation is not complete. The radiolysis product  $\text{O}_2$  has been observed on Callisto (Spencer and Calvin 2002) and  $\text{H}_2\text{O}_2$  has been suggested (Hendrix et al. 1999).

$\text{NH}_3$  has not been observed on the surface, but  $\text{CO}_2$  is found on the surfaces of Callisto and Ganymede (Carlson et al. 1996; McCord et al. 1997, 1998a; Hibbitts et al. 2000, 2002; Hibbitts et al. 2003) as well as on Europa as noted above. A tenuous  $\text{CO}_2$  atm. has also been found on Callisto, indicating loss from the surface. The surficial  $\text{CO}_2$  is not an ice, based on the spectral position of the absorption feature, and  $\text{CO}_2$  ice is too volatile to be stable at Galilean satellite temperatures; instead the molecules appear to be trapped in the dark material.

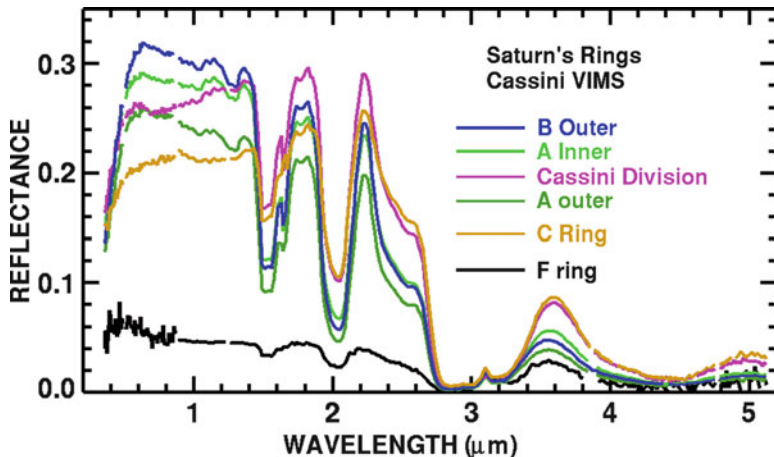


**Fig. 1.9** Spectra of Saturn's rings corrected for fill factor (From Cuzzi et al. (2009))

The source of CO<sub>2</sub> could be degassing from the interior (Moore et al. 1999) or an exogenic source or production mechanism. SO<sub>2</sub> has been suggested as a surface component base on ultraviolet (Lane and Domingue 1997; Noll et al. 1997) and infrared spectra (McCord et al. 1997, 1998a; Hibbitts et al. 2000). SO<sub>2</sub> is also quite volatile, and cannot exist as a frost but could be trapped similar to CO<sub>2</sub>. (Hendrix and Johnson 2008) have questioned the ultraviolet SO<sub>2</sub> identification and interpreted Galileo ultraviolet spectra as absorption by carbonized organics. Infra-red evidence for the presence of aliphatic hydrocarbons has been suggested by (McCord et al. 1997, 1998a). Two other spectral features have been identified on both Callisto and Ganymede, one at 3.88 μm and thought to be due to a hydrosulfide compound (-SH) (McCord et al. 1997, 1998a) or the CO<sub>2</sub>-related compound, carbonic acid (H<sub>2</sub>CO<sub>3</sub>) (Hage et al. 1998). Another common feature for these two satellites occurs at 4.57 μm and possibly due to a -CN-containing tholin (McCord et al. 1997, 1998a).

#### 1.8.4 Saturn System

It has long been known that the surfaces of Saturn's rings and major satellites, Mimas, Enceladus, Tethys, Dione, Rhea, Hyperion, Iapetus, and Phoebe are predominantly icy objects (e.g., Fink et al. 1975; Clark et al. 1984, 1986, 2005, 2008a, b 2012; Roush et al. 1995; Cruikshank et al. 1988, 1998, 2005; Grundy et al. 1999; Cruikshank et al. 1998 Owen et al. 2001; Filacchione et al. 2007, 2008; Cuzzi et al. 2009). While the reflectance spectra of these objects (Figs. 1.9, 1.10, 1.11, and 1.12) in the visible range indicate that a coloring agent is present on all surfaces,

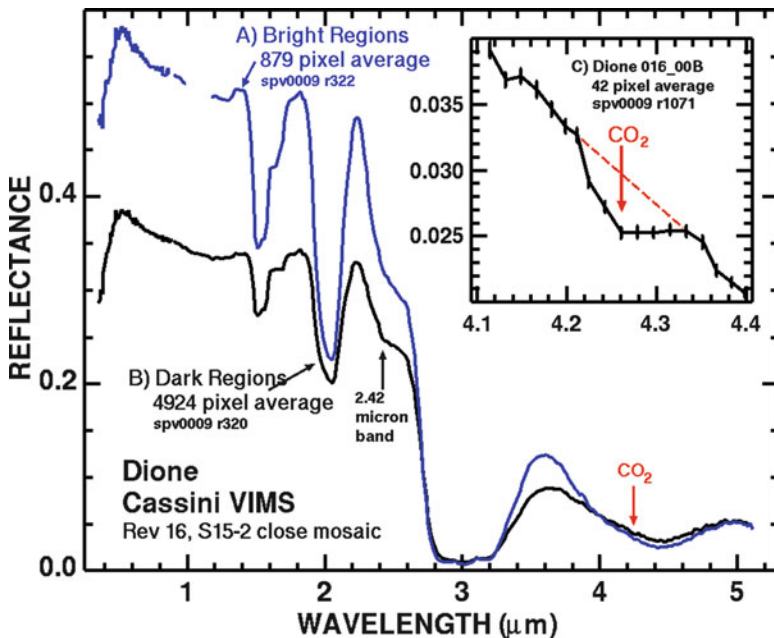


**Fig. 1.10** Spectra of Saturn's satellite Dione (From Clark et al. (2008a))

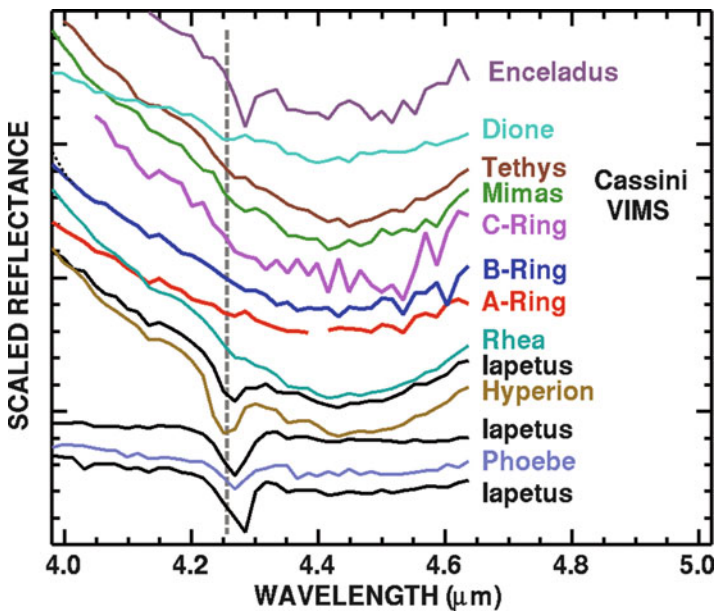


**Fig. 1.11** CO<sub>2</sub> on icy objects in the Saturn system (From Cuzzi et al. (2010))

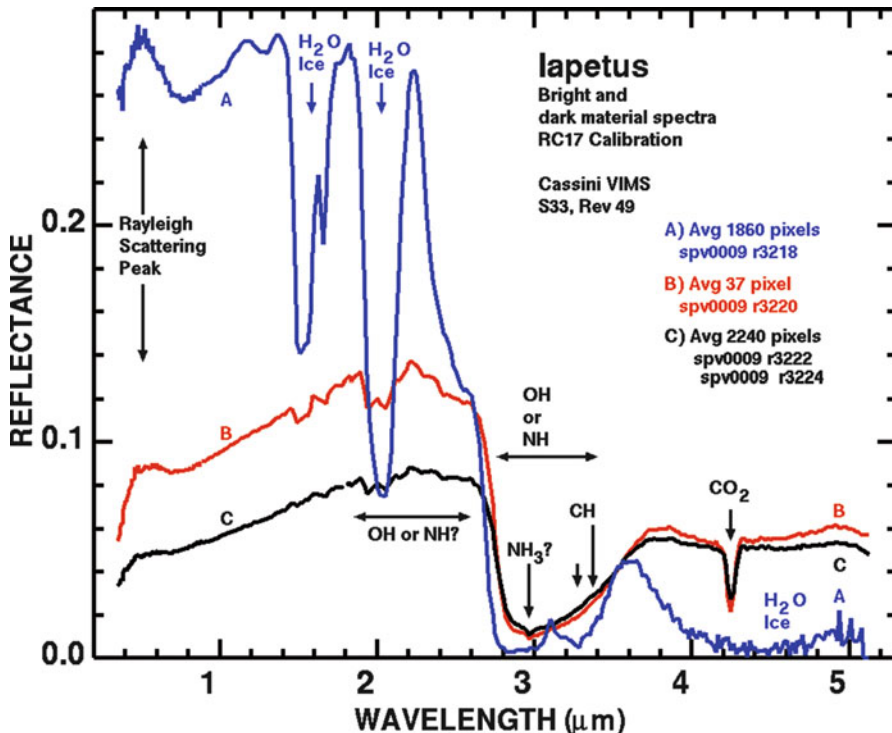


**Fig. 1.12** Spectra of Iapetus (From Clark et al. (2012))

only Phoebe and the dark hemisphere of Iapetus display spectra markedly different from very pure water ice (e.g. Cruikshank et al. 2005; Clark et al. 2005; Jaumann et al. 2009; and references therein, Clark et al. 2010a).

Dark material was first inferred in the Saturn system by Cassini (1672), and verified by Murphy et al. 1972 and Zellner 1972. The nature of the dark material has been studied by numerous authors, sometimes with conflicting conclusions, including Cruikshank et al. (1983), Vilas et al. (1996), Jarvis et al. (2000), Owen et al. (2001), Buratti et al. (2002), and Villas et al. (2004). The new Cassini VIMS data provide a greater spectral range in reflected solar radiation, with higher precision, and show new absorption features not previously seen in these bodies (e.g. Buratti et al. 2005; Cruikshank et al. 2007, 2008; Clark et al. 2005, 2008a). These new observations allow new insights into the nature of the icy satellite surfaces to be made.

The Cassini spacecraft entered the Saturn system in 2004, and the Visual and Infrared Mapping Spectrometer (VIMS) began obtaining spatially resolved spectra of Saturn's satellites and rings (Broen et al. 2004); Figs. 1.9, 1.10, 1.11, and 1.12). The VIMS has provided a wealth of spatially resolved compositional data on the satellites (e.g., Phoebe: Clark et al. (2005); Iapetus: Buratti et al. (2005), Cruikshank et al. (2007, 2008); Enceladus: Brown et al. (2006), Jaumann et al. (2006); Dione: Clark et al. (2008a, 2010a), Jaumann et al. (2009)) and rings (e.g. Nicholson et al.

(2008), Cuzzi et al. (2009)). The satellites and rings are dominated by crystalline H<sub>2</sub>O ice with trace amounts of CO<sub>2</sub> (Fig. 1.11) and dark material (e.g. Fig. 1.12) although it is not clear if the CO<sub>2</sub> is an ice, trapped, or both. Trace organics and ammonia absorptions are seen in some satellites but again, it is not clear if the absorptions are due to ices or trapped molecules. Unusual colors and spectral shapes of the satellites and rings in the UV to visible are currently explained by a combination of Rayleigh scattering by small particles (ice grains as well as contaminants) and a UV absorber by one of the contaminants (Clark et al. (2008a, 2010a); see reviews by Jaumann et al. (2009), Cuzzi et al. (2009), Hendrix et al. (this volume)).

The surface composition of Titan is still enshrouded in a cloud of mystery despite the initial flood of data from the Cassini spacecraft and the Huygens probe. While the composition of Titan's atmosphere is known (Coudren et al. (2003, 2006a, b, 2007), Coudren (2005), Flasar et al. (2005), Teanby et al. (2009) and references therein), with most of the observed gases having been predicted using models of UV photolysis and reactions of atmospheric methane and nitrogen (Yung and DeMore (1999), Vuitton et al. (2008) and references therein), the many less volatile molecules that coat and/or make up the solid surface have yet to be identified. Tholins are the solid end products of photolysis and electron discharge experiments done in terrestrial laboratories with gases common in Titan's atmosphere and are one type of mixture of compounds theorized to exist on Titan (Sagan et al. 1992). Table 1b in Clark et al. (2010b) lists known solid compounds on Titan through 2009, and include benzene (firm), with many tentative or inferred compounds including ices of Cyanoacetylene (HC<sub>3</sub>N), Toluene (C<sub>7</sub>H<sub>8</sub>), Cyanogen (C<sub>2</sub>N<sub>2</sub>), Acetonitrile (CH<sub>3</sub>CN), H<sub>2</sub>O, CO<sub>2</sub>, and NH<sub>3</sub>.

The Cassini RADAR has provided the highest spatial resolution images of Titan's surface from Saturn orbit but is a mono-frequency system that provides compositional information only through the dielectric constant of the surface at its operating wavelength of 2.16 cm (Elachi et al. 2005). Only the Descent Imager-Spectral Radiometer, DISR, on the Huygens probe and VIMS from the Cassini Saturn orbiter have the capability to provide combined spectral plus spatial information about the surface (Tomasko et al. 2005; Schroder and Keller 2008; Sotin et al. 2005; Barnes et al. 2005, 2007, 2008; McCord et al. 2006, 2008; Brown et al. 2008; Rodriguez et al. 2006; Nelson et al. 2009; Soderblom et al. 2009). The DISR is limited in wavelength range out to 1.7 μm but obtained very high spatial resolution over a limited area; VIMS measures out to 5.1 μm (Fig. 1.13) and can cover large parts of the surface of Titan but at much more limited spatial resolution. Terrestrially synthesized tholins do not match the spectral slope in data from the Huygens DISR (Tomasko et al. 2005; Schroder and Keller 2008) or Cassini VIMS (McCord et al. 2006). The DISR spectra of Titan's surface show a blue spectral slope from 1 to 1.6 μm that is distinctly "un-tholin" like and show what qualitatively appears to be a water-ice absorption, but the complete H<sub>2</sub>O feature was not covered by the spectrometer (Tomasko et al. 2005; Schroder and Keller 2008) and Schroeder and Keller concluded the absorption did not match water ice. Also, the 1.25-μm H<sub>2</sub>O absorption was not observed even though expected in the models presented by Tomasko et al. (2005) and Schroder and Keller (2008). In situ analyses

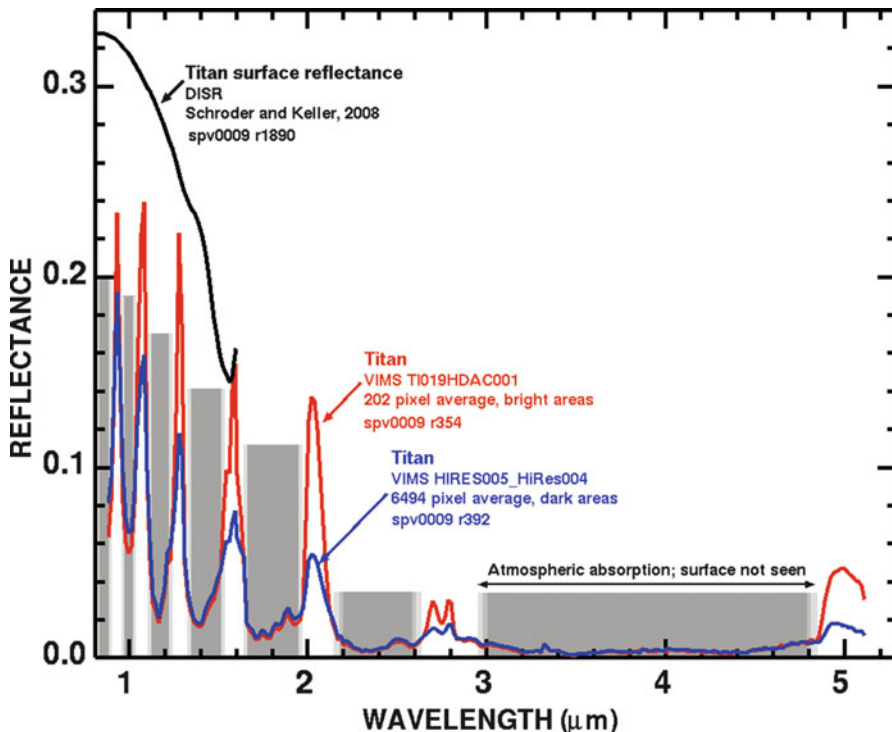


**Fig. 1.13** Spectra of Titan (From Clark et al. (2010b))

have detected methane, ethane, and tentatively identified cyanogen, benzene, and carbon dioxide on the surface from the Huygens GCMS (Niemann et al. 2005). Ammonia and hydrogen cyanide were the main pyrolysis products of the aerosols measured by the Huygens in situ pyrolysis experiment during its descent (Israel, et al. 2005) and those aerosols could rain down to the surface, but pyrolysis products are not necessarily compounds in the aerosols. Higher in Titan's thermosphere, benzene was first detected in the stratosphere of Titan by ISO and CIRS (Coudé du Foresto et al. 2003, 2007), and the Cassini Ion and Neutral Mass Spectrometer (INMS) instrument has detected high abundances of benzene along with toluene (Waite et al. 2007) above 900 km. Toluene is an interesting molecule after benzene because toluene consists of a benzene ring with a methyl functional group,  $-\text{CH}_3$ , replacing one of the hydrogen atoms attached to the benzene ring, thus it is a possible larger organic molecule that may be compatible with observed VIMS surface spectra.

Clark et al. (2010b) presented evidence for surface deposits of solid benzene, ( $\text{C}_6\text{H}_6$ ) (Fig. 1.14), solid and/or liquid ethane, ( $\text{C}_2\text{H}_6$ ), or methane ( $\text{CH}_4$ ), and clouds of hydrogen cyanide (HCN) aerosols using diagnostic spectral features in data from the Cassini Visual and Infrared Mapping Spectrometer (VIMS). Cyanoacetylene (2-propynenitrile, IUPAC nomenclature,  $\text{HC}_3\text{N}$ ) is indicated in spectra of some

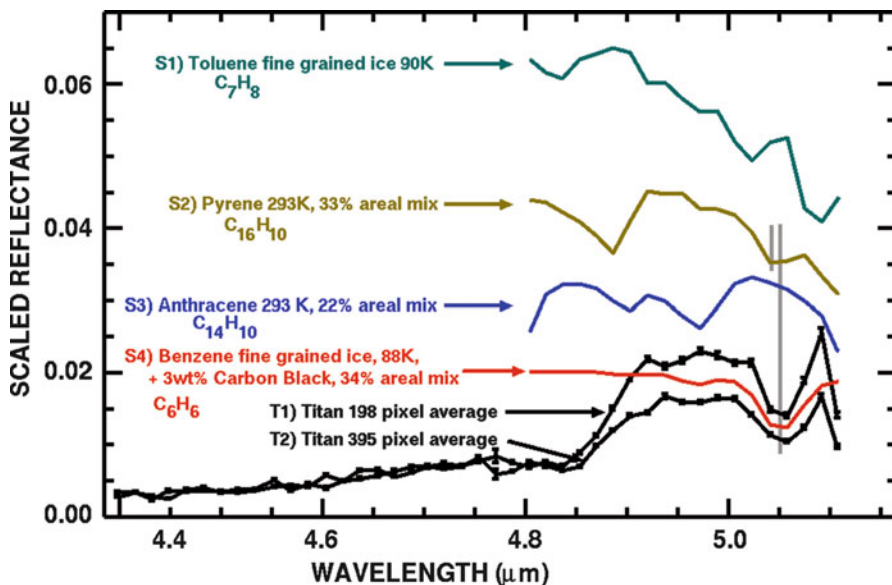


**Fig. 1.14** Spectral of Titan showing an absorption attributed to benzene ice (From Clark et al. (2010b))

bright regions, but the spectral resolution of VIMS is insufficient to make a unique identification although it is a closer match to the feature previously attributed to CO<sub>2</sub>. Acetylene (C<sub>2</sub>H<sub>2</sub>), expected to be more abundant on Titan according to some models than benzene, was not detected. Water ice, if present, must be covered with organic compounds to the depth probed by 1–5- $\mu\text{m}$  photons: a few millimeters to centimeters. While many organic compounds have now been detected in the atmosphere and on Titan’s surface, we still have only a small spectral database of organic compounds to compare to spectra of Titan. Spectra of additional compounds are needed, along with higher spatial and spectral resolution data on Titan’s surface in order to better understand the full compositional range of compounds on Titan.

### 1.8.5 *Uranus System*

The Uranus system was investigated by the Voyager II spacecraft in 1986, but that probe had no near-infrared spectral-imaging capability. Accordingly, compositional studies of the Uranian satellites and rings have relied on ground-based telescopic observations, progressing in parallel with advances in infrared instrumentation technology. Prior to the Voyager encounter, low spectral resolution circular-variable filter (CVF) spectrophotometry led to detection of broad water ice absorptions at 1.5 and 2  $\mu\text{m}$  on the five major satellites of Uranus: Miranda, Ariel, Umbriel, Titania,

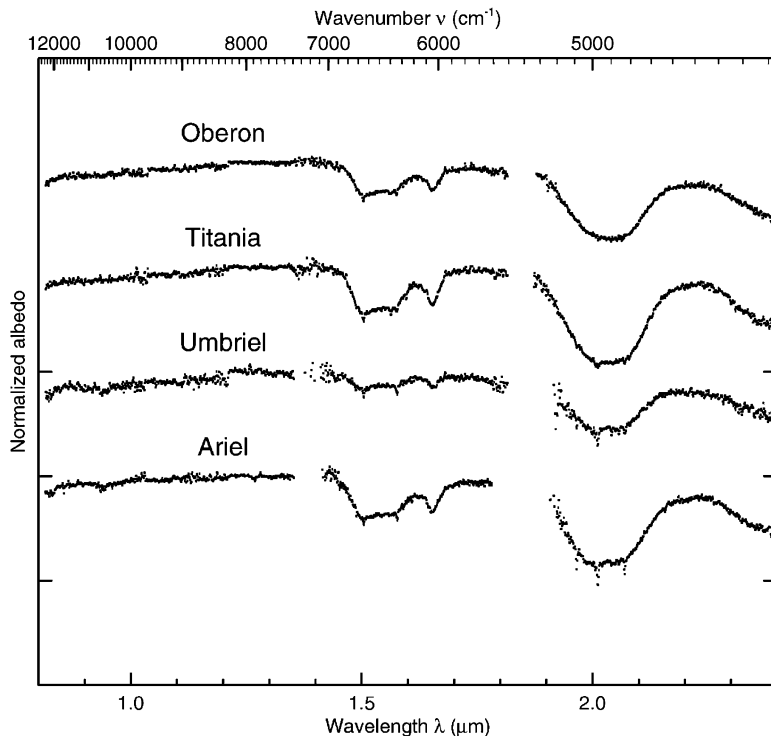


**Fig. 1.15** Spectra of the Uranian satellites (From Grundy et al. (2006))

and Oberon (Cruikshank 1980; Cruikshank and Brown 1981; Soifer et al. 1981; Brown 1983; Brown and Clark 1984; Brown et al. 1991). Spectrometers based on infrared detector arrays enabled higher quality near-infrared spectra to be obtained (Fig. 1.15), revealing the  $1.65\text{-}\mu\text{m}$  water ice band on all five satellites, indicative of cold crystalline  $\text{H}_2\text{O}$  ice (Grundy et al. 1999; Bauer et al. 2002). An apparent dip in Miranda's spectrum near  $2.2\text{ }\mu\text{m}$  has been tentatively attributed to ammonia ice (Bauer et al. 2002) but this identification has not yet been confirmed. Repeated observations of the other four satellites have shown no comparable  $2.2\text{-}\mu\text{m}$  dips, but did reveal the presence of a narrow triplet of  $\text{CO}_2$  ice absorptions near  $2\text{ }\mu\text{m}$  on Ariel, Umbriel, and Titania, but not Oberon (Grundy et al. 2003, 2006). Interestingly, the strengths of these  $\text{CO}_2$  ice absorptions were found to be spatially variable, being strongest on the trailing hemispheres of the satellites, and also on the satellites closer to Uranus (whether or not Miranda fits this pattern remains to be tested). This spatial pattern is consistent with in situ production of  $\text{CO}_2$  from local  $\text{H}_2\text{O}$  plus carbonaceous materials driven by Uranian magnetosphere charged particle radiolysis, balanced by relatively rapid sublimation loss (Grundy et al. 2006). Water ice absorptions were seen to exhibit the opposite pattern, being deepest on the leading hemispheres of Ariel, Umbriel, and Titania (although perhaps not Oberon; Grundy et al. 2006). This pattern of deeper water ice absorptions on leading hemispheres is also seen in the Jovian and Saturnian satellite systems, but the cause remains

uncertain. Possibilities include preferential gardening of icy regoliths by impactors impinging on leading hemispheres (Zahnle et al. 2003), and preferential sputtering removal of H<sub>2</sub>O ice via magnetospheric charged particle bombardment on trailing hemispheres (e.g., Cheng et al. 1986; Eviatar and Richardson 1986; Pospieszalska and Johnson 1989; Johnson 1990). No ices have been identified to date in spectra of the Uranian rings (e.g., Soifer et al. 1981; Pang and Nicholson 1984; Baines et al. 1998). The low albedos of Uranian satellites and ring particles implies the presence of a darkening agent, which has long been presumed to be carbonaceous in nature, although its precise composition remains unknown.

### **1.8.6 *The Neptune System and Beyond***

The Neptune system was explored by Voyager 2 in 1989, providing a wealth of physical details. But, as with the Uranus system, almost all compositional information about ices in the Neptune system came from Earth-based observations. The largest satellite Triton provides particularly interesting and complex examples of outer solar system ice geology. Early Triton results came from a series of near-infrared CVF observations during the 1970s and 1980s, leading to the discovery of methane, nitrogen, and water ice absorptions (Cruikshank and Silvaggio 1979; Cruikshank and Apt 1984; Rieke et al. 1985; Cruikshank et al. 1984, 1988, 1989).

The advent of array spectrometers with cryogenic optics resulted in much higher quality spectra (Fig. 1.16), leading to the discovery of CO, CO<sub>2</sub>, and C<sub>2</sub>H<sub>6</sub> ices (Cruikshank et al. 1993; Bohn et al. 1994; DeMeo et al. 2010). The higher spectral resolution and signal precision enabled by these instruments revealed subtle wavelength shifts in the methane bands consistent with the CH<sub>4</sub> molecules being dispersed in nitrogen ice (Cruikshank et al. 1993; Quirico et al. 1999), a situation anticipated from thermodynamic arguments (Lunine and Stevenson 1985). They also revealed the phase of Triton's water ice to be predominantly crystalline (Grundy and Young 2004).

A picture emerged of a solar-powered, active world in which volatile N<sub>2</sub>, CO, and CH<sub>4</sub> ices sublime and condense in response to seasonal insolation on a substrate of H<sub>2</sub>O and CO<sub>2</sub> ices (which are non-volatile at Triton surface temperatures), leading to an array of bizarre landforms and even jetting of sublimated nitrogen gas out of fissures, with possible aeolian transport of non-volatile H<sub>2</sub>O and CO<sub>2</sub> ice dust (e.g., Brown et al. 1990; Hansen and Paige 1992; Stansberry et al. 1996; Grundy et al. 2002). Evidence for short-term changes in the visible wavelength parts of Triton's spectrum reinforced the perception of an active Triton (Hicks and Buratti 2004), as did the paucity of impact craters in Voyager images (Schenk and Zahnle 2007). To explain the large optical path-lengths required by the observed 2.15-μm N<sub>2</sub> absorption band, Triton's N<sub>2</sub> ice could have an unusually compacted texture, perhaps more like a sintered slab than the usual particulate soils encountered on planetary surfaces (e.g., Eluszkiewicz (1991), Grundy and Stansberry (2000)). Based on seasonal models, latitudinal heterogeneity in the spatial distribution of Triton's ices is expected, but time-resolved spectroscopy reveals a longitudinal

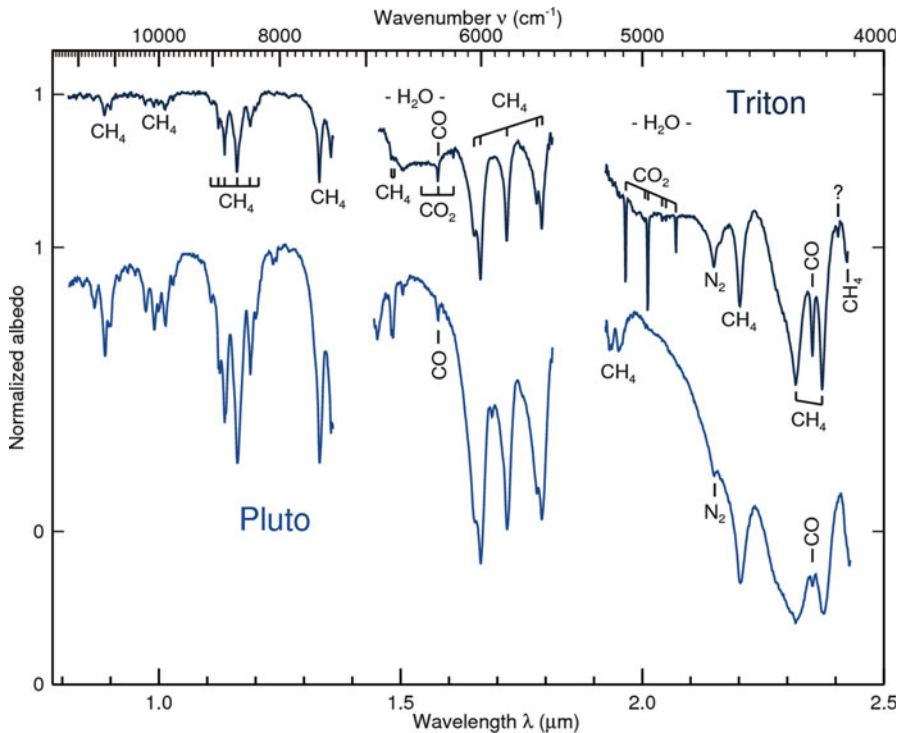


**Fig. 1.16** Near infrared spectra of Triton and Pluto are compared in this figure (Grundy et al. 2009). Features arising from CH<sub>4</sub>, CO, CO<sub>2</sub>, and N<sub>2</sub> are identified

heterogeneity as well (Grundy et al. 2010). The N<sub>2</sub> and CO ices seem to co-occur, and to be much more abundant on Triton’s Neptune-facing hemisphere. Despite being mostly dissolved in N<sub>2</sub> ice, Triton’s CH<sub>4</sub> shows a very different longitudinal pattern, with strongest absorption seen on Triton’s trailing hemisphere. The H<sub>2</sub>O and CO<sub>2</sub> ice absorptions show little or no longitudinal variation, as if they are globally distributed, perhaps as wind-blown dust.

To date, H<sub>2</sub>O ice has only been detected on one other body in the Neptune system, the satellite Nereid (M.E. Brown et al. 1998; R.H. Brown et al. 1999). Little is known beyond photometric colors regarding compositions of Neptune’s other satellites and rings (e.g., Dumas et al. (2002)).

Objects at Neptune’s heliocentric distance and beyond (the transneptunian region, also known as the Kuiper belt) have surface temperatures sufficiently low ( $<\sim 50$  K) for multiple ices to condense on their surfaces. The equilibrium temperature,  $T_{\text{eq}}$ , of a solid body is a function of both the heliocentric distance of objects and their albedos,  $q$ , following the relation  $T_{\text{eq}} = 280 \text{ K} ((1-q)/a^2)^{1/4}$ . For an object at 30 AU with an albedo of 0.04 this gives  $T_{\text{eq}} = 50.6$  K. Larger heliocentric distances,  $a$ , and/or higher geometric albedos,  $q$ , lead to even lower temperatures. For objects near condensation thresholds, there is a positive feedback favoring the

stability of icy surfaces once the threshold for formation is met. The stability of ices is also a function of surface gravity and the ability of a body to limit atmospheric escape. Schaller and Brown (2007) have calculated the expected stability for CH<sub>4</sub>, N<sub>2</sub> and CO ices in outer solar system bodies and find that objects with diameters below 1,000–1,500 km are not expected to have retained significant amounts of these ices on their surfaces. The handful of larger objects in the Kuiper Belt can, and apparently have retained these materials.

Methane ice was first detected as a solid in the solar system in an infrared spectrum of Pluto (Cruikshank et al. 1976). More recently, solid CH<sub>4</sub> has been identified in the large Kuiper Belt Objects Eris (Brown et al. 2005), Sedna (Barucci et al. 2005), and Makemake (Licandro et al. 2006). The S/N and spectral coverage of spectra of small outer solar system objects have steadily improved. The chapter by de Bergh et al. (*this volume*) provides more detail on these remote objects.

For Pluto in particular, high S/N spectra show it shares many spectral features with Triton (Fig. 1.16) including multiple discrete features of CH<sub>4</sub>, although the two clusters of features due to CO<sub>2</sub> ice in Triton’s spectrum are absent from Pluto’s spectrum. The quality and detail of the spectra allow for detailed analyses comparing band strengths and positions to constrain the detailed physical state of the ices on the surface. As with Triton, the beta N<sub>2</sub> 2-0 absorption is interpreted as arising from optical path lengths in beta N<sub>2</sub> ice of the order of many centimeters, implying unusually coarse particle sizes or perhaps a fused glaze of N<sub>2</sub> ice (e.g., Eluszkiewicz (1991); Grundy and Stansberry (2000)). The existence of the ~2.16-μm side band in spectra of both Pluto and Triton has been used to place upper limits on the temperature of N<sub>2</sub> ice on those bodies (Grundy et al. 1993; Tryka et al. 1993, 1994).

Even without directly detecting its absorption bands, it may be possible to infer the presence of N<sub>2</sub> ice from its effect on absorptions by other species. For instance, when CH<sub>4</sub> is dispersed in N<sub>2</sub> ice, the much stronger CH<sub>4</sub> bands are shifted to slightly shorter wavelengths (Quirico and Schmitt 1997a), an effect which has been reported in spectra of Eris and Makemake, in addition to Pluto and Triton. Unfortunately, details of how the distinct CH<sub>4</sub> bands shift depend on the relative concentrations of N<sub>2</sub> and CH<sub>4</sub> are not yet fully understood (e.g., Brunetto et al. (2008), Cornelison et al. (2008)), and the uniqueness of N<sub>2</sub> in its ability to shift CH<sub>4</sub> absorption bands has yet to be established.

Pluto shows evidence for time-varying albedo features on its surface (Buie et al. 2010). Seasonal effects are expected to result in redistribution of surface ices over time. Grundy et al. (2009) have recently shown what appears to be seasonal evolution of features on Pluto over a decade of observation. Differing longitudinal variations of CH<sub>4</sub> and N<sub>2</sub> ices suggest that these two ices may be physically segregated on the surface. In contrast, CO and N<sub>2</sub> vary together with longitude, implying they are intimately mixed. Ethane ice has also been reported in spectra of Pluto, notably by bands at 2.27, 2.405, 2.457, and 2.461 μm (DeMeo et al. 2010), where it presumably forms through radiolysis and/or photolysis of CH<sub>4</sub>.

Water ice has been detected on numerous Kuiper belt objects and Centaurs, both small and large (e.g., Dotto et al. (2003), Barkume et al. (2008), Guillet et al. (2009)). However, it seems to be absent from some of them. For most of the smaller objects, the

bands are fairly shallow, consistent with their low albedos. Systematic changes in albedo and color from the Kuiper belt through the inner solar system could be linked to the sublimation loss of H<sub>2</sub>O ice (Grundy 2009; Lamy and Toth 2009).

The dwarf planet Haumea along with its largest satellite Hi'iaka are noteworthy for their particularly deep water ice bands (e.g., Barkume et al. (2006), Trujillo et al. (2007), Pinilla-Alonso et al. (2009)). Members of the Haumea collisional family have similar water-rich spectral characteristics, suggesting they could be fragments of the icy mantle of a differentiated target body (Brown et al. 2007).

A similar catastrophic impact scenario may apply in the Pluto system (Canup 2005), but unlike Pluto, Charon has a water ice dominated surface (Buie et al. 1987). Additionally, Charon's spectrum shows strong evidence for NH<sub>3</sub> ice (Cook et al. 2007). Charon may represent a sample of Pluto's mantle material which was too small to retain the more volatile CH<sub>4</sub>, N<sub>2</sub>, and CO ices which mask Pluto's own mantle from view.

## 1.9 Summary

Ices are ubiquitous in the solar system, from Earth and further from the sun. As our observational technology has improved, we have found more ices in more locations. If water ice in the poles of Mercury can be confirmed, water ice would be found throughout the solar system on every planet and/or their moons with the exception of Venus.

There are outstanding issues. Some small absorptions seen in spectra of outer solar system objects have yet to be identified. For example, possible SO<sub>2</sub> absorptions on the Galilean satellites needs confirmation. A 2.42-μm absorption seen in spectra of Saturn's satellites, and a 5.01-μm absorption seen in spectra of Titan all remain unidentified.

Water ice dominates most icy objects. But why is the ice so pure in Saturn's rings and most satellites, yet Titan is covered in organics? Similarly, Pluto is covered in organics yet its moon Charon displays a relatively pure water ice surface. What drives most surfaces to show such pure water surfaces with few other ices is unknown. Where are the expected signatures of ammonia or ammonia-water mixtures? If methane is so abundant on Pluto, Triton and Titan, why not other objects?

Not addressed in detail in this chapter are the contaminants in the icy surfaces of the solar system. Why are some objects very high albedo with relatively pure ice surfaces while others are very dark (e.g. Phoebe, the two faced of Iapetus, brighter Hyperion, dark Callisto versus brighter Ganymede and Europa). Some of the answers certainly relate to resurfacing (e.g. Europa and Enceladus), while others display ancient heavily cratered surfaces that are still bright (e.g. Rhea) while other ancient surfaces are dark (e.g. Phoebe). The mechanisms for these selections are not completely understood, although there is a trend in the Jupiter and Saturn systems

for increasing darkening on moons further from the planet, implying dark dust preferentially coating the outer moons.

If water condenses below 135 K, it is expected to be amorphous. Yet the spectra of water ice throughout the solar system is dominated by crystalline ice (where our spectra are of sufficient quality to distinguish between amorphous versus crystalline water ice), with the possible exception of the trailing side of Europa where intense radiation can destroy the ice crystal structure. Even in the outer solar system beyond Saturn, where temperatures are well below 90 K, observed water ices are crystalline. Why we do not observe amorphous ice is a mystery.

A major outstanding question relates to the compositional heterogeneity of the protoplanetary nebula, as well as the sub-nebulae around the giant planets. Did distinct zones result from condensation of volatiles other than water? One can imagine ammonia, carbon dioxide, or methane “snow lines.” Another possible source of heterogeneity could involve variable degrees of processing of icy pre-solar grains. If there were distinct nebular zones, can we identify bodies which inherited different bulk compositions as a result of accreting in these regions, and can compositional studies of those bodies advance understanding of conditions in the nebula?

## References

- Anders E, Grevesse N (1989) Abundances of the elements: meteoritic and solar. *Geochim Cosmochim Acta* 53:197–214
- Apt J, Carleton NP, Mackay CD (1983) Methane on Triton and Pluto: new CCD spectra. *Astrophys J* 270:342–350
- Bagenal F, Dowling TE, McKinnon WB (eds) (2004) Jupiter. Cambridge University Press, Cambridge
- Baines KH, Yanamandra-Fisher PA, Lebofsky LA, Momary TW, Golisch W, Kaminski C, Wild WJ (1998) Near-infrared absolute photometric imaging of the uranian system. *Icarus* 132:266–284
- Baklouti D, Schmitt B, Brissaud O (2008) S<sub>2</sub>O, polysulfur oxide and sulfur polymer on Io’s surface? *Icarus* 194:647–659
- Barkume KM, Brown ME, Schaller EL (2006) Water ice on the satellite of Kuiper belt object 2003 EL61. *Astrophys J* 640:L87–L89
- Barkume KM, Brown ME, Schaller EL (2008) Near-infrared spectra of Centaurs and Kuiper belt objects. *Astron J* 135:55–67
- Barnes JW, Brown RH, Turtle EP, McEwen AS, Lorenz RD, Janssen M, Schaller EL, Brown ME, Buratti BJ, Sotin C, Griffith C, Clark R, Perry J, Fussner S, Barbara J, West R, Elachi C, Bouchez AH, Roe HG, Baines KH, Bellucci G, Bibring J-P, Capaccioni F, Cerroni P, Combes M, Coradini A, Cruikshank DP, Drossart P, Formisano V, Jaumann R, Langevin Y, Matson DL, McCord TB, Nicholson PD, Sicardy B (2005) A 5-μm bright spot on Titan: evidence for surface diversity. *Science* 310:92–94, <http://www.sciencemag.org/cgi/content/full/310/5745/92>
- Barnes JW, Radebaugh J, Brown RH, Wall S, Soderblom L, Lunine J, Burr D, Sotin C, Le Mouélic S, Rodriguez S, Buratti BJ, Clark RN, Baines KH, Jaumann R, Nicholson PD, Kirk RL, Lopes R, Lorenz R, Mitchell K, Wood CA (2007) Near-infrared spectral mapping of Titan’s mountains and channels. *J Geophys Res* 112:E11006. doi:[10.1029/2007JE002932](https://doi.org/10.1029/2007JE002932)

- Barnes JW, Brown RH, Soderblom L, Sotin C, Le Mouélic S, Rodriguez S, Jaumann R, Beyer RA, Buratti BJ, Pitman K, Baines KH, Clark R, Nicholson P (2008) Spectroscopy, morphometry, and photoinmetry of Titans Dunefields from Cassini/VIMS. *Icarus* 195:400–414. doi:[10.1016/j.icarus.2007.12.006](https://doi.org/10.1016/j.icarus.2007.12.006)
- Barucci MA, Cruikshank DP, Dotto E, Merlin F, Poulet F, Dalle Ore C, Fornasier S, de Bergh C (2005) Is Sedna another Triton? *Astron Astrophys* 439:L1–L4
- Bauer JM, Roush TL, Geballe TR, Meech KJ, Owen TC, Vacca WD, Rayner JT, Jim KTC (2002) The near infrared spectrum of Miranda: evidence of crystalline water ice. *Icarus* 158:178–190
- Bibring JP et al (2004) Perennial water ice identified in the south polar cap of Mars. *Nature* 428:627–630
- Bohn RB, Sandford SA, Allamandola LJ, Cruikshank DP (1994) Infrared spectroscopy of Triton and Pluto ice analogs: the case for saturated hydrocarbons. *Icarus* 111:151–173
- Brodyanski AP, Medvedev SA, Vetter M, Kreutz J, Jodl HJ (2002) Nature of infrared-active phonon sidebands to internal vibrations: spectroscopic studies of solid oxygen and nitrogen. *Phys Rev B* 66:104301, 1–19
- Brown RH (1983) The uranian satellites and Hyperion: new spectrophotometry and compositional implications. *Icarus* 56:414–425
- Brown RH, Clark RN (1984) Surface of Miranda: identification of water ice. *Icarus* 58:288–292
- Brown RH, Kirk RL, Johnson TV, Soderblom LA (1990) Energy sources for Triton's geyser-like plumes. *Science* 250:431–435
- Brown RH, Johnson TV, Synnott S, Anderson JD, Jacobson RA, Dermott SF, Thomas PC (1991) Physical properties of the Uranian satellites. In: Bergstrahl JT, Miner ED, Matthews MS (eds) *Uranus*. University of Arizona Press, Tucson, pp 513–527
- Brown ME, Koresko CD, Blake GA (1998) Detection of water ice on Nereid. *Astrophys J* 508: L175–L176
- Brown RH, Cruikshank DP, Pendleton Y, Veeder GJ (1999) Water ice on Nereid. *Icarus* 139:374–378
- Brown ME, Trujillo CA, Rabinowitz DL (2005) Discovery of a planetary-sized object in the scattered Kuiper belt. *Astrophys J* 635:L97–L100
- Brown RH, Baines KH, Bellucci JP, Bibring BJ, Buratti E, Bussoletti F, Capaccioni P, Cerroni P, Clark RN, Coradini DP, Cruikshank P, Drossart Y, Formisano R, Jaumann Y, Langevin DJ, Matson TR (2005) The Cassini visual and infrared mapping spectrometer investigation: Space Science Reviews 115(1–4):111–168
- Brown RH, Clark RN, Buratti BJ, Cruikshank DP, Barnes JW, Mastrapa RME, Bauer J, Newman S, Momary T, Baines KH, Bellucci G, Capaccioni F, Cerroni P, Combes M, Coradini A, Drossart P, Formisano V, Jaumann R, Langevin Y, Matson DL, McCord TB, Nelson RM, Nicholson PD, Sicardi B, Sotin C (2006) Composition and physical properties of Enceladus surface. *Science* 311:1425–1428, <http://www.sciencemag.org/cgi/content/abstract/311/5766/1425>
- Brown ME, Barkume KM, Blake GA, Schaller EL, Rabinowitz DL, Roe HG, Trujillo CA (2007) Methane and ethane on the bright Kuiper belt object 2005 FY9. *Astron J* 133:284–289
- Brown RH, Soderblom LA, Soderblom JM, Clark RN, Jaumann R, Barnes JW, Sotin C, Buratti B, Baines KH, Nicholson PD (2008) The identification of liquid ethane in Titan's Ontario Lacus. *Nature* 454:607–610
- Brunetto R, Caniglia G, Baratta GA, Palumbo ME (2008) Integrated near-infrared band strengths of solid CH<sub>4</sub> and its mixtures with N<sub>2</sub>. *Astrophys J* 686:1480–1485
- Buie MW, Cruikshank DP, Lebofsky LA, Tedesco EF (1987) Water frost on Charon. *Nature* 329:522–523
- Buie MW, Grundy WM, Young EF, Young LA, Stern SA (2010) Pluto and Charon with the hubble space telescope. II. Resolving changes on Pluto's surface and a map for Charon. *Astron J* 139:1128–1143
- Buratti BJ, Hicks MD, Tryka KA, Sittig MS, Newburn RL (2002) High-resolution 0.33–0.92 micron spectra of Iapetus, Hyperion, Phoebe, Rhea, Dione, and D-type asteroids: how are they related? *Icarus* 155:375–381

- Buratti BJ, Cruikshank DP, Brown RH, Clark RN, Bauer JM, Jaumann R, McCord TB, Simonelli DP, Hibbitts CA, Hansen GA, Owen TC, Baines KH, Bellucci G, Bibring J-P, Capaccioni F, Cerroni P, Coradini A, Drossart P, Formisano V, Langevin Y, Matson DL, Mennella V, Nelson RM, Nicholson PD, Sicardy B, Sotin C, Roush TL, Soderlund K, Muradyan A (2005) Cassini visual and infrared mapping spectrometer observations of Iapetus: detection of CO<sub>2</sub>. *Astrophys J* 622:L149–L152
- Byrne S, Ingersoll AP (2003) A sublimation model for martian south polar ice features. *Science* 299:1051–1053
- Calvin WM, Johnson RE, Spencer JR (1996) O<sub>2</sub> on Ganymede: spectral characteristics and plasma formation mechanisms. *Geophys Res Lett* 23:673–676
- Campins H, Hargrove K, Howell ES, Kelley MS, Licandro J, Mothi-Diniz T, Ziffer J, Fernandez Y, Pinilla-Alonso N (2009) Confirming water ice on the surface of Asteroid 24 Themis, In: American Astronomical Society, DPS meeting #41, #32.05, Puerto Rico. <http://adsabs.harvard.edu/abs/2009DPS....41.3205C>
- Canup RM (2005) A giant impact origin of Pluto-Charon. *Science* 307:546–550
- Canup RM, Ward WR (2002) Formation of the Galilean satellites: conditions of accretion. *Astron J* 124:3404–3423
- Carlson RW, Smythe W, Baines K, Barbinis E, Becker K, Burns R, Calcutt S, Calvin W, Clark R, Danielson G, Davies A, Drossart P, Encrenaz T, Fanale F, Granahan J, Hansen G, Herrera P, Hibbitts C, Hui J, Irwin P, Johnson T, Kamp L, Kieffer H, Leader F, Lellouch E, LopesGautier R, Matson D, McCord T, Mehlman R, Ocampo A, Orton G, RoosSerote M, Segura M, Shirley J, Soderblom L, Stevenson A, Taylor F, Torson J, Weir A, Weissman P (1996) Near-infrared spectroscopy and spectral mapping of Jupiter and the Galilean satellites: results from Galileo's initial orbit. *Science* 274:385–388
- Carlson RW, Smythe WD, LopesGautier RMC, Davies AG, Kamp LW, Mosher JA, Soderblom LA, Leader FE, Mehlman R, Clark RN, Fanale FP (1997) The distribution of sulfur dioxide and other infrared absorbers on the surface of Io. *Geophys Res Lett* 24:2479–2482
- Carlson RW, Anderson MS, Johnson RE, Smythe WD, Hendrix AR, Barth CA, Soderblom LA, Hansen GB, McCord TB, Dalton JB, Clark RN, Shirley JH, Ocampo AC, Matson DL (1999a) Hydrogen peroxide on the surface of Europa. *Science* 283:2062–2064
- Carlson RW, Johnson RE, Anderson MS (1999b) Sulfuric acid on Europa and the radiolytic sulfur cycle. *Science* 286:97–99
- Carlson RW, Anderson MS, Johnson RE, Schulman MB, Yavrouian AH (2002) Sulfuric acid production on Europa: the radiolysis of sulfur in water ice. *Icarus* 157:456–463
- Carlson RW, Anderson MS, Mehlman R, Johnson RE (2005) Distribution of hydrate on Europa: further evidence for sulfuric acid hydrate. *Icarus* 177:461–471
- Carlson RW, Kargel JS, Doute S, Soderblom LA, Dalton B (2007) Io's surface composition. In: Lopes RMC, Spencer JR (eds) *Io after Galileo*. Springer/Praxis, Chester, pp 193–229
- Carlson RW, Calvin WM, Dalton JB, Hansen GB, Hudson RL, Johnson RE, McCord TB, Moore MH (2009) Europa's Surface Composition. In: Pappalardo RT, McKinnon WB, Khurana KK (eds) *Europa*. University of Arizona Press, Tucson
- Carr MH (2006) *The surface of Mars*. Cambridge University Press, New York, p 307
- Cassini GD (1672) Phil. Trans. 12, 831. Quoted in Alexander, A. F. O'D., 1962. *The planet Saturn*. McMillan, New York, p 474
- Cheng AF, Haff PK, Johnson RE, Lanzerotti LJ (1986) Interactions of magnetospheres with icy satellite surfaces. In: Burns JA, Matthews MS (eds) *Satellites*. University of Arizona Press, Tucson, pp 403–436
- Clark RN (1980) Ganymede, Europa, Callisto, and Saturns rings – compositional analysis from reflectance spectroscopy. *Icarus* 44:388–409
- Clark RN (1999) Chapter 1: spectroscopy of rocks and minerals and principles of spectroscopy. In: Rencz AN (ed) *Manual of remote sensing*. Wiley, New York, pp 3–58
- Clark RN (2009) Detection of adsorbed water and hydroxyl on the moon. *Science* 326:562–564. doi:[10.1126/science.1178105](https://doi.org/10.1126/science.1178105)

- Clark RN, McCord TB (1980) The Galilean satellites: new near-infrared spectral reflectance measurements (0.65–2.5  $\mu\text{m}$ ) and a 0.325–5  $\mu\text{m}$  summary. *Icarus* 41:323–329
- Clark RN, Brown RH, Owensby PD, Steele A (1984) Saturn's satellites: near-infrared spectrophotometry (0.65–2.5  $\mu\text{m}$ ) of the leading and trailing sides and compositional implications. *Icarus* 58:265–281
- Clark RN, Fanale FP, Gaffey MJ (1986) Surface composition of natural satellites. In: Burns JA, Matthews MS (eds) *Satellites*. University of Arizona Press, Tucson, pp 437–491
- Clark RN, Brown RH, Jaumann R, Cruikshank DP, Nelson RM, Buratti BJ, McCord TB, Lunine J, Baines KH, Bellucci G, Bibring J-P, Capaccioni F, Cerroni P, Coradini A, Formisano F, Langevin Y, Matson DL, Mennella V, Nicholson PD, Sicardy B, Sotin C, Hoefen TM, Curchin JM, Hansen G, Hibbits K, Matz K-D (2005) Compositional maps of Saturn's moon Phoebe from imaging spectroscopy. *Nature*. doi:[10.1038/nature03558](https://doi.org/10.1038/nature03558)
- Clark RN, Curchin JM, Jaumann R, Cruikshank DP, Brown RH, Hoefen TM, Stephan K, Moore JM, Buratti BJ, Baines KH, Nicholson PD, Nelson RM (2008a) Compositional mapping of Saturn's satellite Dione with Cassini VIMS and implications of dark material in the Saturn system. *Icarus* 193:372–386
- Clark RN, Cruikshank DP, Jaumann R, Filacchione G, Nicholson PD, Brown RH, Stephan K, Hedman M, Buratti BJ, Curchin JM, Hoefen TM, Baines KH, Nelson R (2008b) Compositional mapping of Saturn's rings and icy satellites with Cassini VIMS. *Saturn after Cassini-Huygens*, London, July 2008
- Clark RN, Curchin JM, Hoefen TM, Swayze GA (2009) Reflectance spectroscopy of organic compounds I: alkanes. *J Geophys Res* 114:E03001. doi:[10.1029/2008JE003150](https://doi.org/10.1029/2008JE003150)
- Clark RN, Cruikshank DP, Jaumann R, Brown RH, Curchin JM, Hoefen TM, Stephan K, Dalle Ore CM, Buratti BJ, Filacchione G, Baines KH, Nicholson PD (2010a) The composition of Iapetus: mapping results from Cassini VIMS. *Icarus*, in review
- Clark RN, Curchin JM, Barnes JW, Jaumann R, Soderblom L, Cruikshank DP, Lunine J, Stephan K, Hoefen TM, Le Mouelic S, Sotin C, Baines KH, Buratti B, Nicholson P (2010b) Detection and mapping of hydrocarbon deposits on Titan. *J Geophys Res*, in press
- Clifford SM (1993) A model for the hydrologic and climate behaviour of water on Mars. *J Geophys Res* 98:10973–11016
- Cook JC, Desch SJ, Roush TL, Trujillo CA, Geballe TR (2007) Near-infrared spectroscopy of Charon: possible evidence for cryovolcanism on kuiper belt objects. *Astrophys J* 663:1406–1419
- Cornelison DM, Tegler SC, Grundy W, Abernathy M (2008) Near-infrared laboratory spectroscopy of  $\text{CH}_4/\text{N}_2$  ice mixtures: implications for icy dwarf planets. Paper presented at the science of solar system ices (ScSSI): a cross-disciplinary workshop, Oxnard, 5–8 May 2008
- Coustenis A (2005) Formation and evolution of Titan's atmosphere. *Space Sci Rev* 116:171–184
- Coustenis A, Salama A, Schultz B, Ott S, Lellouch E, Encrenaz T, Gautier D, Feuchtgruber H (2003) Titan's atmosphere from ISO mid-infrared spectroscopy. *Icarus* 161:383–403
- Coustenis A, Achterberg R, Conrath B, Jennings D, Marten A, Gautier D, Nixon C, Flasar M, Teanby N, Bezard B, Samuelson RE, Carlson R, Lellouch E, Bjoraker G, Romani P, Taylor FW, Irwin P, Fouchet Th, Hubert A, Orton G, Kunde V, Vinatier S, Mondellini J, Abbas M, Courtin R (2006a) The composition of Titan's stratosphere from Cassini/CIRS mid-infrared spectra. *Icarus* 189:35–62
- Coustenis A, Negrão A, Salama A, Schulz B, Lellouch E, Rannou P, Drossart P, Encrenaz T, Schmitt B, Boudon V, Nikitin A (2006b) Titan's 3- $\mu\text{m}$  spectral region from ISO high-resolution spectroscopy. *Icarus* 180:176–185. doi:[10.1016/j.icarus.2005.08.007](https://doi.org/10.1016/j.icarus.2005.08.007)
- Coustenis A et al (2007) The composition of Titan's stratosphere from Cassini/CIRS mid-infrared spectra. *Icarus* 189:35–62
- Cruikshank DP (1980) Near infrared studies of the satellites of Saturn and Uranus. *Icarus* 41:246–258
- Cruikshank DP, Apt J (1984) Methane on Triton: physical state and distribution. *Icarus* 58:306–311

- Cruikshank DP, Brown RH (1981) The Uranian satellites: water ice on Ariel and Umbriel. *Icarus* 45:607–611
- Cruikshank DP, Silvaggio PM (1979) Triton: a satellite with an atmosphere. *Astrophys J* 233:1016–1020
- Cruikshank DP, Pilcher CB, Morrison D (1976) Pluto – evidence for methane frost. *Science* 194:835–837
- Cruikshank DP, Bell JF, Gaffey MJ, Brown RH, Howell R, Beerman C, Rognstad M (1983) The dark side of Iapetus. *Icarus* 53:90–104
- Cruikshank DP, Brown RH, Clark RN (1984) Nitrogen on Triton. *Icarus* 58:293–305
- Cruikshank DP, Brown RH, Tokunaga AT, Smith RG, Piscitelli JR (1988) Volatiles on Triton: the infrared spectral evidence, 2.0–2.5 microns. *Icarus* 74:413–423
- Cruikshank DP, Brown RH, Giver LP, Tokunaga AT (1989) Triton: do we see the surface? *Science* 245:283–286
- Cruikshank DP, Roush TL, Owen TC, Geballe TR, de Bergh C, Schmitt B, Brown RH, Bartholomew MJ (1993) Ices on the surface of Triton. *Science* 261:742–745
- Cruikshank DP, Brown RH, Calvin W, Roush TL, Bartholomew MJ (1998) Ices on the satellites of Jupiter, Saturn, and Uranus. In: Schmitt B, de Bergh C, Festou M (eds) *Solar system ices*. Kluwer, Dordrecht, pp 579–606
- Cruikshank DP, Schmitt B, Roush TL, Owen TC, Quirico E, Geballe TR, de Bergh C, Bartholomew MJ, Dalle Ore CM, Doute S, Meier R (2000) Water ice on Triton. *Icarus* 147:309–316
- Cruikshank DP, Owen TC, Ore CD, Geballe TR, Roush TL, de Bergh C, Sandford SA, Poulet F, Benedito GK, Emery JP (2005) A spectroscopic study of the surfaces of Saturn's large satellites: H<sub>2</sub>O ice, tholins, and minor constituents. *Icarus* 175:268–283
- Cruikshank DP, Dalton JB, Dalle Ore CM, Bauer J, Stephan K, Filacchione G, Hendrix CJ, Hansen CJ, Coradini A, Cerroni P, Tosi F, Capaccioni F, Jaumann R, Buratti BJ, Clark RN, Brown RH, Nelson RM, McCord TB, Baines KH, Nicholson PD, Sotin C, Meyer AW, Bellucci G, Combes M, Bibring J-P, Langevin Y, Sicardy B, Matson DL, Formisano V, Drossart P, Mennella V (2007) Surface composition of Hyperion. *Nature* 448:54–57. doi:[10.1038/nature05948](https://doi.org/10.1038/nature05948)
- Cruikshank DP, Wegryn E, Dalle Ore CM, Brown RH, Baines KH, Bibring J-P, Buratti BJ, Clark RN, McCord TB, Nicholson PD, Pendleton YJ, Owen TC, Filacchionej G, the VIMS Team (2008) Hydrocarbons on Saturn's satellites Iapetus and Phoebe. *Icarus* 193:334–343. doi:[10.1016/j.icarus.2007.04.036](https://doi.org/10.1016/j.icarus.2007.04.036)
- Cull S, Arvidson RE, Mellon MT, Wiseman SJ, Clark RN, Titus TN, Morris RV, McGuire P (2010) Seasonal H<sub>2</sub>O and CO<sub>2</sub> ice cycles at the Mars Phoenix landing site: 1. Prelanding CRISM and HiRISE observations. *J Geophys Res.* doi:[10.1029/2009JE003340](https://doi.org/10.1029/2009JE003340), in press
- Curchin JM, Shaffer CJ, Clark RN, McMahon J, Hoefen TM (2010) Reflectance spectroscopy of 2-propynenitrile, cyanoacetylene (HC3N). *Icarus*, submitted
- Cuzzi JN, Burns JA, Charnoz S, Clark RN, Colwell JE, Dones L, Esposito LW, Filacchione G, French RG, Hedman MM, Kempf S, Marouf EA, Murray CD, Nicholson PD, Porco CC, Schmidt J, Showalter MR, Spilker LJ, Spitale JN, Srama R, Sremcevic M, Tiscareno MS, Weiss J (2010) *Science*, 327:1470–1475 doi: 10.1126/science.1179118
- Davies JK, Roush TL, Cruikshank DP, Bartholomew MJ, Geballe TR, Owen TC, de Bergh C (1997) The detection of water ice in comet Hale-Bopp. *Icarus* 127:238–245
- de Bergh C, Schaller EL, Brown ME, Brunetto R, Cruikshank DP, Schmitt B (2010) The ices on transneptunian objects and Centaurs (this volume)
- DeMeo FE, Dumas C, de Bergh C, Protopapa S, Cruikshank DP, Geballe TR, Alvarez-Candal A, Merlin F, Barucci MA (2010) A search for ethane on Pluto and Triton. *Icarus* (in press)
- Domingue DL, Lane AL, Beyer RA (1998) IUE's detection of tenuous SO<sub>2</sub> frost on Ganymede and its rapid time variability. *Geophys Res Lett* 25:3117–3120
- Dotto E, Barucci MA, Boehnhardt H, Romon J, Doressoundiram A, Peixinho N, de Bergh C, Lazzarin M (2003) Searching for water ice on 47171 1999 TC36, 1998 SG35, and 2000 QC243: ESO large program on TNOs and Centaurs. *Icarus* 162:408–414

- Doute S, Schmitt B, Lopes-Gautier R, Carlson R, Soderblom L, Shirley J (2001) Mapping SO<sub>2</sub> frost on Io by the modeling of NIMS hyperspectral images. *Icarus* 149:107–132
- Dumas C, Terrile RJ, Smith BA, Schneider G (2002) Astrometry and near-infrared photometry of Neptune's inner satellites and ring arcs. *Astron J* 123:1776–1783
- Duxbury NS, Brown RH (1993) The phase composition of Triton's polar caps. *Science* 261:748–751
- Elachi CS, Wall M, Allison Y, Anderson R, Boehmer P, Callahan P, Encrenaz E, Flamini G, Franceschetti Y, Gim G, Hamilton S, Hensley M, Janssen W, Johnson K, Kelleher R, Kirk R, Lopes R, Lorenz J, Lunine D, Muhleman S, Ostro F, Paganelli G, Picardi F, Posa L, Roth R, Seu S, Shaffer L, Soderblom B, Stiles E, Stofan S, Vetrella R, West C, Wood L, Wye HZ (2005) Cassini radar views the surface of Titan. *Science* 308:970–974
- Eluszkiewicz J (1991) On the microphysical state of the surface of Triton. *J Geophys Res* 96:19217–19229
- Eviatar A, Richardson JD (1986) Predicted satellite plasma tori in the magnetosphere of Uranus. *Astrophys J* 300:L99–L102
- Fanale FP, Brown RH, Cruikshank DP, Clark RN (1979) Significance of absorption features in Io's IR absorption spectrum. *Nature* 280:761–763
- Farmer CB, Davies DW, Laporte DD (1976) Mars: Northern summer ice cap – water vapor observations from Viking 2. *Science* 194:1339–1341. doi:[10.1126/science.194.4271.1339](https://doi.org/10.1126/science.194.4271.1339)
- Feldman WC, Maurice S, Binder AB, Barraclough BL, Elphic RC, Lawrence DJ (1998) Fluxes of fast and epithermal neutrons from lunar prospector: evidence for water ice at the lunar poles. *Science* 281:1496–1500
- Feldman WC, Lawrence DJ, Elphic RC, Barraclough BL, Maurice S, Genetay I, Binder AB (2000) Polar hydrogen deposits on the Moon. *J Geophys Res* 105:4175–4195
- Feldman WC, Maurice S, Lawrence DJ, Little RC, Lawson SL, Gasnault O, Wiens RC, Barraclough BL, Elphic RC, Prettyman TH (2001) Evidence for water ice near the lunar poles. *J Geophys Res* 106:23231–23251
- Filacchione G, Capaccioni F, McCord TB, Coradini A, Cerroni P, Bellucci G, Tosi F, D'Aversa E, Formisano V, Brown RH, Baines KH, Bibring J-P, Buratti BJ, Clark RN, Combes M, Cruikshank DP, Drossart P, Jaumann R, Langevin Y, Matson DL, Mennella V, Nelson RM, Nicholson PD, Sicardy B, Sotin C, Hansen G, Hibbitts K, Showalter M, Newmann S (2007) Saturn's icy satellites investigated by Cassini VIMS. I. Full-disk properties: 350–5100 nm reflectance spectra and phase curves. *Icarus* 186:259–290
- Filacchione G, Capaccioni F, Tosi F, Cerroni P, McCord TB, Baines KH, Bellucci G, Brown RH, Buratti BJ, Clark RN, Cruikshank DP, Cuzzi JN, Jaumann R, Stephan K, Matson DL, Nelson RM, Nicholson PD (2008) Analysis of the Saturnian icy satellites full-disk spectra by Cassini-VIMS, *Saturn After Cassini-Huygens*, London, July 2008
- Fink U, Larson HP (1975) Temperature dependence of the water-ice spectrum between 1 and 4 microns: application to Europa, Ganymede, and Saturn's rings. *Icarus* 24:411–420
- Fink U, Dekkers NH, Larson HP (1973) Infrared spectra of the Galilean satellites of Jupiter. *Astrophys J* 179:L155–L159
- Flasar FM et al (2005) Titan's atmospheric temperatures, winds, and composition. *Science* 308:975–978
- Forget F, Hansen GB, Pollack JB (1995) Low brightness temperatures of Martian polar caps: CO<sub>2</sub> clouds or low surface emissivity? *J Geophys Res* 100(E10):21219–21234
- Geissler P, McEwen AS, Keszthelyi L, Lopes-Gautier RMC, Granahan J, Simonelli DP (2001) Galileo imaging of SO<sub>2</sub> frosts on Io. *J Geophys Res* 106:33253–33266
- Grundy WM, Fink U (1991) The absorption coefficient of the liquid N<sub>2</sub> 2.15 micron band and application to Triton. *Icarus* 93:169–173
- Grundy WM, Stansberry JA (2000) Solar gardening and the seasonal evolution of nitrogen ice on Triton and Pluto. *Icarus* 148:340–346
- Grundy WM, Young LA (2004) Near infrared spectral monitoring of Triton with IRTF/SpeX I: establishing a baseline. *Icarus* 172:455–465

- Grundy WM, Schmitt B, Quirico E (1993) The temperature dependent spectra of alpha and beta nitrogen ice with application to Triton. *Icarus* 105:254–258
- Grundy WM, Buie MW, Stansberry JA, Spencer JR, Schmitt B (1999) Near-infrared spectra of icy outer solar system surfaces: remote determination of H<sub>2</sub>O ice temperatures. *Icarus* 142:536–549
- Grundy WM, Buie MW, Spencer JR (2002) Spectroscopy of Pluto and Triton at 3–4 microns: possible evidence for wide distribution of nonvolatile solids. *Astron J* 124:2273–2278
- Grundy WM, Young LA, Young EF (2003) Discovery of CO<sub>2</sub> ice and leading-trailing spectral asymmetry on the Uranian satellite Ariel. *Icarus* 162:222–229
- Grundy WM, Young LA, Spencer JR, Johnson RE, Young EF, Buie MW (2006) Distributions of H<sub>2</sub>O and CO<sub>2</sub> ices on Ariel, Umbriel, Titania, and Oberon from IRTF/SpeX observations. *Icarus* 184:543–555
- Grundy WM (2009) Is the missing ultra-red material colorless ice? *Icarus* 199:560–563
- Grundy WM, Young LA, Olkin CB, Buie MW, Stansberry JA (2009) Observed spatial distribution and secular evolution of ices on Pluto and Triton. *Bull Am Astron Soc* 41:6.01
- Grundy WM, Young LA, Stansberry JA, Buie MW, Olkin CB, Young EF (2010) Near-infrared spectral monitoring of Triton with IRTF/SpeX II: spatial distribution and evolution of ices. *Icarus* 205:594–604
- Guilbert A, Alvarez-Candal A, Merlin F, Barucci MA, Dumas C, de Bergh C, Delsanti A (2009) ESO-large program on TNOs: near-infrared spectroscopy with SINFONI. *Icarus* 201:272–283
- Hage W, Liedl KR, Hallbrucker A, Mayer E (1998) Carbonic acid in the gas phase and its astrophysical relevance. *Science* 279:1332–1335
- Hand KP, Carlson RW, Cooper JF, Chyba CF (2006) Clathrate hydrates of oxidants in the europaen ice shell. *Astrobiology* 6:463–482
- Hand KP, Carlson RW, Chyba CF (2007) Energy, chemical disequilibrium, and geological constraints on Europa. *Astrobiology* 7:1006–1022
- Hanel RA, Conrath BJ, Jennings DE, Samuelson RE (2003) Exploration of the solar system by infrared remote sensing. Cambridge University Press, Cambridge
- Hansen GB, McCord TB (2004) Amorphous and crystalline ice on the Galilean satellites: a balance between thermal and radiolytic processes. *J Geophys Res* 109(E01012):1–19, [10.1029/2003JE002149](https://doi.org/10.1029/2003JE002149)
- Hansen GB, McCord TB (2008) Widespread CO<sub>2</sub> and other non-ice compounds on the anti-Jovian and trailing sides of Europa from Galileo/NIMS observations. *Geophys Res Lett* 35:L01202
- Hansen CJ, Paige DA (1992) A thermal model for the seasonal nitrogen cycle on Triton. *Icarus* 99:273–288
- Hapke B (1979) Io's surface and environs: a magmatic-volatile model. *Geophys Res Lett* 6:799–802
- Hendrix AR, Domingue D, Noll KS (2010) Ultraviolet properties of planetary ices (this volume)
- Hendrix AR, Johnson RE (2008) Callisto: new insights from Galileo disk-resolved UV measurements. *Astrophys J* 687:706–713
- Hendrix AR, Barth CA, Stewart AIF, Hord CW, Lane AL (1999) Hydrogen peroxide on the icy Galilean satellites. In: Lunar and planetary science conference XXX, Vol. LPI Contribution 964. Lunar and Planetary Institute, Houston (CD-ROM), pp Abstract #2043
- Hibbitts CA, Hansen GB (2007) The other non-ice material on Ganymede: dark ray ejecta (abstract). *Bull Am Astron Soc* 39:428
- Hibbitts CA, Pappalardo RT, Hansen GB, McCord TB (2003) Carbon dioxide on Ganymede. *J Geophys Res* 108:2-1–2-21. doi:[10.1029/2002JE001956](https://doi.org/10.1029/2002JE001956), 5084
- Hibbitts CA, McCord TB, Hansen GB (2000) The distributions of CO<sub>2</sub> and SO<sub>2</sub> on the surface of Callisto. *J Geophys Res* 105:22541–22557
- Hibbitts CA, Klemaszewski JE, McCord TB, Hansen GB, Greeley R (2002) CO<sub>2</sub>-rich impact craters on Callisto. *J Geophys Res* 107:14-1–14-12. doi:[10.1029/2000JE001412](https://doi.org/10.1029/2000JE001412), 5084
- Hicks MD, Buratti BJ (2004) The spectral variability of Triton from 1997–2000. *Icarus* 171:210–218

- Hobbs PV (1975) Ice physics. Oxford University Press, Hardcover, 856p
- Hodyss R, Johnson PV, Orzechowska GE, Goguen JD, Kanik I (2008) Carbon dioxide segregation in 1:4 and 1:9 CO<sub>2</sub>:H<sub>2</sub>O ices. *Icarus* 194:836–842
- Hopkins AG, Tang S-Y, Brown CW (1973) Infrared and Raman spectra of the low-temperature products from discharged sulfur dioxide. *J Amer Chem Soc* 95:3486–3490
- Hudson RL, Moore MH, Gerakines PA (2001) The formation of cyanate ion (OCN<sup>-</sup>) in interstellar ice analogs. *Astrophys J* 550:1140–1150
- Israel G, Szopa C, Raulin F, Cabane M, Niemann H, Atreya S, Bauer S, Brun J-F, Chassefiere E, Coll P, Conde E, Coscia D, Hauchecorne A, Millian P, Nguyen M-J, Owen T, Riedler W, Samuelson R, Siguier J-M, Steller M, Sternberg R, Vidal-Madjar C (2005) Complex organic matter in Titan's atmospheric aerosols from in situ pyrolysis and analysis. *Nature* 438:796–798
- James PB, Kieffer HH, Paige DA (1993) The Seasonal Cycle of Carbon Dioxide on Mars, in MARS. Kieffer, Jakosky, Snyder, Matthews, eds., University of Arizona Press.
- Jarvis KS, Vilas F, Larson SM, Gaffey MJ (2000) Are Hyperion and Phoebe linked to Iapetus? *Icarus* 146:125–132
- Jaumann R, Stephan K, Buratti BJ, Hansen GB, Clark RN, Brown RH, Baines KH, Bellucci G, Coradini A, Cruikshank DP, Griffith CA, Hibbitts CA, McCord TB, Nelson RM, Nicholson PD, Sotin C, Wagner R (2006) Distribution of icy particles across Enceladus' surface as derived from Cassini VIMS measurements. *Icarus* 193(2008):407–419. doi:[10.1016/j.icarus.2007.09.013](https://doi.org/10.1016/j.icarus.2007.09.013)
- Jaumann R, Clark RN, Nimmo F, Hendrix AR, Buratti BJ, Denk T, Moore JM, Schenk PM, Ostro SJ, Srama R (2009) Icy satellites: geological evolution and surface processes. In: Dougherty MK et al (eds) Saturn after Cassini/Huygens. Springer, doi: 10.1007/978-1-4020-9215-2, pp 637–681
- Jenniskens P, Blake DF, Kouchi A (1998) Amorphous water ice. In: Schmitt B, De Bergh C, Festou M (eds) Solar system ices. Kluwer, Boston, pp 199–240
- Johnson RE (1990) Energetic charged-particle interactions with atmospheres and surfaces. Springer, New York
- Johnson RE (1997) Polar “caps” on Ganymede and Io revisited. *Icarus* 128:469–471
- Johnson RE, Jesser WA (1997) O<sub>2</sub>/O<sub>3</sub> microatmospheres in the surface of Ganymede. *Astrophys J* 480:L79–L82
- Johnson TV, McCord TB (1971) Spectral geometric albedo of the Galilean satellites 0.3–2.5 microns. *Astrophys J* 169:589–593
- Johnson RE, Carlson RW, Cooper JF, Paranicas C, Moore MH, Wong M (2004) Radiation effects on the surfaces of the Galilean satellites. In: Bagenal F, McKinnon W (eds) Jupiter. Cambridge University Press, Cambridge
- Kargel JS (1998) Physical chemistry of ices in the solar system. In: Schmitt B, de Bergh C, Festou M (eds) Solar system ices. Kluwer, Dordrecht, pp 3–32
- Khanna RK, Pearl JC, Dahmani R (1995) Infrared-spectra and structure of solid-phases of sulfur-trioxide – possible identification of solid SO<sub>3</sub> on Io surface. *Icarus* 115:250–257
- Khurana KK, Pappalardo RT, Murphy N, Denk T (2007) The origin of Ganymede’s polar caps. *Icarus* 191:193–202
- Kieffer HH, Titus TN (2001) TES mapping of Mars’ northern seasonal cap. *Icarus* 154:162–180
- Kieffer S, Chase C Jr, Martin TZ, Miner ED, Palluconi FD (1976) Martian North Pole summer temperatures: dirty water ice. *Science* 194:1341–1344. doi:[10.1126/science.194.4271.1341](https://doi.org/10.1126/science.194.4271.1341)
- Kieffer SW, Lu XL, Bethke CM, Spencer JR, Marshak S, Navrotksy A (2006) A clathrate reservoir hypothesis for Enceladus’ south polar plume. *Science* 314:1764–1766. doi:[10.1126/science.1133519](https://doi.org/10.1126/science.1133519)
- Kuiper GP (1957) Infrared observations of planets and satellites (abstract). *Astron J* 62:245
- Lamy P, Toth I (2009) The colors of cometary nuclei: comparison with other primitive bodies of the Solar System and implications for their origin. *Icarus* 201:674–713
- Lane AL, Domingue DL (1997) IUE’s view of Callisto: detection of an SO<sub>2</sub> absorption correlated to possible torus neutral wind alterations. *Geophys Res Lett* 24:1143–1146

- Laver C, de Pater I (2008) Spatially resolved SO<sub>2</sub> ice on Io, observed in the near IR. *Icarus* 195:752–757. doi:[10.1016/j.icarus.2007.12.023](https://doi.org/10.1016/j.icarus.2007.12.023)
- Laver C, de Pater I (2009) The global distribution of sulfur dioxide ice on Io, observed with OSIRIS on the WM Keck telescope. *Icarus* 201:172–181. doi:[10.1016/j.icarus.2008.12.037](https://doi.org/10.1016/j.icarus.2008.12.037)
- Lee P, Helfenstein P, Everka J, McCarthy D (1992) Anomalous-scattering region on Triton. *Icarus* 99:82–97
- Lellouch E, Crovisier J, Lim T, Bockelee-Morvan D, Leech K, Hanner MS, Altieri B, Schmitt B, Trotta F, Keller HU (1998) Evidence for water ice and estimate of dust production rate in comet Hale-Bopp at 2.9 AU from the Sun. *Astron Astrophys* 339:L9–L12
- Lellouch E, Paubert G, Moses JI, Schneider NM, Strobel DF (2003) Volcanically emitted sodium chloride as a source for Io's neutral clouds and plasma torus. *Nature* 421:45–47
- Licandro J, Pinilla-Alonso N, Pedani M, Oliva E, Tozzi GP, Grundy WM (2006) The methane ice rich surface of large TNO 2005 FY9: a Pluto-twin in the trans-neptunian belt? *Astron Astrophys* 445:L35–L38
- Loeffler MJ, Teolis BD, Baragiola RA (2006) A model study of the thermal evolution of astrophysical ices. *Astrophys J* 639:L103–L106
- Lopes RMC, Spencer JR (eds) (2007) Io after Galileo. Springer/Praxis, Chichester
- Lopes RMC, Kamp LW, Doute S, Smythe WD, Carlson RW, McEwen AS, Geissler PE, Kieffer SW, Leader FE, Davies AG, Barbinis E, Mehlman R, Segura M, Shirley J, Soderblom LA (2001) Io in the near infrared: near-infrared mapping spectrometer (NIMS) results from the Galileo flybys in 1999 and 2000. *J Geophys Res* 106:33053–33078
- Lunine JI, Stevenson DJ (1985) Physical state of volatiles on the surface of Triton. *Nature* 317:238–240
- Martonchik JV, Orton GS (1994) Optical constants of solid and liquid methane. *Appl Opt* 33:8306–8317
- Mastrappa RM, Bernstein MP, Sandford SA, Roush TL, Cruikshank DP, Dalle Ore CM (2008) Optical constants of amorphous and crystalline H<sub>2</sub>O-ice in the near infrared from 1.1 to 2.6 μm. *Icarus* 197:307–320
- Mastrappa RM et al. This Volume
- Matson DL, Nash DB (1983) Ios atmosphere – pressure control by regolith cold trapping and surface venting. *J Geophys Res* 88:4771–4783
- McCauley JF, Smith BA, Soderblom LA (1979) Erosional scarps on Io. *Nature* 280:736–738
- McCord TB, Carlson RW, Smythe WD, Hansen GB, Clark RN, Hibbitts CA, Fanale FP, Granahan JC, Segura M, Matson DL, Johnson TV, Martin PD (1997) Organics and other molecules in the surfaces of Callisto and Ganymede. *Science* 278:271–275
- McCord TB, Hansen GB, Fanale FP, Carlson RW, Matson DL, Johnson TV, Smythe WD, Crowley JK, Martin PD, Ocampo A, Hibbitts CA, Granahan JC (1998a) Salts on Europa's surface detected by Galileo's near infrared mapping spectrometer. *Science* 280:1242–1245
- McCord TB, Hansen GB, Clark RN, Martin PD, Hibbitts CA, Fanale FP, Granahan JC, Segura M, Matson DL, Johnson TV, Carlson RW, Smythe WD, Danielson GE, Team TN (1998b) Non-water-ice constituents in the surface material of the icy Galilean satellites from the Galileo near infrared mapping spectrometer investigation. *J Geophys Res* 103:8603–8626
- McCord TB, Hansen GB, Matson DL, Johnson TV, Crowley JK, Fanale FP, Carlson RW, Smythe WD, Martin PD, Hibbitts CA, Granahan JC, Ocampo A, Team, a. t. N. (1999) Hydrated salt minerals on Europa's surface from the Galileo NIMS investigation. *J Geophys Res Planets* 104:11827–11851
- McCord TB, Hansen GB, Hibbitts CA (2001) Hydrated salt minerals on Ganymede's surface: evidence of an ocean below. *Science* 292:1523–1525
- McCord TB, Hansen GB, Buratti BJ, Clark RN, Cruikshank DP, D'Aversa E, Griffith CA, Baines KH, Brown RH, Dalle Ore CM, Filacchione G, Formisano V, Hibbitts CA, Jaumann R, Lunine JI, Nelson RM, Sotin C, the Cassini VIMS Team (2006) Composition of Titan's surface from Cassini VIMS. *Planet Space Sci* 54:1524–1539

- McCord TB, Hayne P, Combe J-P, Hnasen G, Barnes J, Rodriguez S, Le Mouelic S, Baines K, Buratti B, Sotin C, Nicholson P, Jaumann R, Nelson R, the Cassini VIMS Team (2008) Titan's surface: search for spectral diversity and composition using the Cassini VIMS investigation. *Icarus* 194:212–242
- McEwen AS, Johnson TV, Matson DL, Soderblom LA (1988) The global distribution, abundance, and stability of SO<sub>2</sub> on Io. *Icarus* 75:450–478
- McEwen AS, Belton MJS, Breneman HH, Fagents SA, Geissler P, Greeley R, Head JW, Hoppa G, Jaeger WL, Johnson TV, Keszthelyi L, Klaasen KP, Lopes-Gautier R, Magee KP, Milazzo MP, Moore JM, Pappalardo RT, Phillips CB, Radebaugh J, Schubert G, Schuster P, Simonelli DP, Sullivan R, Thomas PC, Turtle EP, Williams DA (2000) Galileo at Io: results from high-resolution imaging. *Science* 288:1193–1198. doi:[10.1126/science.288.5469.1193](https://doi.org/10.1126/science.288.5469.1193)
- McKellar ARW (1989) Low-temperature infrared absorption of gaseous N<sub>2</sub> and N<sub>2</sub> + H<sub>2</sub> in the 2.0–2.5 micron region: application to the atmospheres of Titan and Triton. *Icarus* 80:361–369
- McKinnon WB (2007) Formation and early evolution of Io. In: Lopes RMC, Spencer JR (eds) *Io after Galileo*. Chichester, Springer, pp 61–88
- Moore MH (1984) Studies of proton-irradiated SO<sub>2</sub> at low-temperatures – implications for Io. *Icarus* 59:114–128
- Moore MH, Hudson RL (2003) Infrared study of ion-irradiated N<sub>2</sub>-dominated ices relevant to Triton and Pluto: formation of HCN and HNC. *Icarus* 161:486–500
- Moore JM, Asphaug E, Morrison D, Spencer JR, Chapman CR, Bierhaus B, Sullivan RJ, Chuang FC, Klemaszewski JE, Greeley R, Bender KC, Geissler PE, Helfenstein P, Pilcher CB (1999) Mass movement and landform degradation on the icy Galilean satellites: results of the Galileo nominal mission. *Icarus* 140:294–312
- Moore JM, Sullivan RJ, Chuang FC, Head JW III, McEwen AS, Milazzo MP, Nixon BE, Pappalardo RT, Schenk PM, Turtle EP (2001) Landform degradation and slope processes on Io: the Galileo view. *J Geophys Res* 106:33223–33240. doi:[10.1029/2000je001375](https://doi.org/10.1029/2000je001375)
- Moroz VI (1965) Infrared spectrophotometry of the Moon and the Galilean satellites of Jupiter. *Sov Astron* 9:999–1006
- Mousis O, Gautier D (2004) Constraints on the presence of volatiles in Ganymede and Callisto from an evolutionary turbulent model of the Jovian subnubula. *Planet Space Sci* 52:361–370
- Murphy RE, Cruikshank DP, Morrison D (1972) Radii, albedos, and 20-micron brightness temperatures of Iapetus and Rhea. *Astrophys J Lett* 177:L93–L96
- Nash DB, Betts BH (1995) Laboratory infrared spectra (2.3–23 μm) of SO<sub>2</sub> phases: applications to Io surface analysis. *Icarus* 117:402–419
- Nash DB, Betts BH (1998) Ices on Io – composition and texture. In: Schmitt B, de Bergh C, Festou M (eds) *Solar system ices*. Kluwer, Dordrecht, pp 607–638
- Nelson RM, Kamp LW, Matson DL, Irwin PGJ, Baines KH, Boryta MD, Leader FE, Jaumann R, Smythe WD, Sotin C, Clark RN, Cruikshank DP, Drossart P, Pearl JC, Hapke BW, Lunine J, Combes M, Bellucci G, Bibring J-P, Capaccioni F, Cerroni P, Coradini A, Formisano V, Filacchione G, Langevin RY, McCord TB, Mennella V, Nicholson PD, Sicardy B (2009) Saturn's Titan: surface change, ammonia, and implications for atmospheric and tectonic activity. *Icarus* 199:429–441
- Nicholson PD, Hedman MM, Clark RN, Showalter MR, Cruikshank DP, Cuzzi JN, Filacchione G, Capaccioni F, Cerroni P, Hansen GB, Sicardy B, Drossart P, Brown RH, Buratti BJ, Baines KH (2008) Angioletta Coradini, a close look at Saturn's rings with Cassini VIMS. *Icarus* 193:182–212. doi:[10.1016/j.icarus.2007.08.036](https://doi.org/10.1016/j.icarus.2007.08.036)
- Niemann HB, Atreya S, Bauer S, Carignan G, Demick J, Frost R, Gautier D, Haberman J, Harpold D, Hunten D, Israel G, Lunine J, Kasprzak W, Owen T, Paulkovich M, Raulin F, Raaen E, Way S (2005) The abundance of constituents of Titan's atmosphere from the GCMS instrument on the Huygens probe. *Nature* 438:779–784
- Noll KS, Johnson RE, Lane AL, Domingue DL, Weaver HA (1996) Detection of ozone on Ganymede. *Science* 273:341–343
- Noll KS, Johnson RE, McGrath MA, Caldwell JJ (1997) Detection of SO<sub>2</sub> on Callisto with the Hubble space telescope. *Geophys Res Lett* 24:1139–1142

- Owen TC, Cruikshank DP, Dalle Ore CM, Geballe TR, Roush TL, de Bergh C, Pendleton YJ, Khare BN (2001) Decoding the domino: the dark side of Iapetus. *Icarus* 149:160–172
- Pang KD, Nicholson PD (1984) Composition and size of Uranian ring particles. *LPSC XV*:627–628 (abstract)
- Pappalardo RT, McKinnon WB, Khurana K (eds) (2009) EUROPA. University of Arizona Press, Tucson
- Picardi G, Plaut JJ, Biccari D, Bombaci O, Calabrese D, Cartacci M, Cicchetti A, Clifford SM, Edenhofer P, Farrell WM, Federico C, Frigeri A, Gurnett DA, Hagfors T, Heggy E, Herique A, Huff RL, Ivanov AB, Johnson WTK, Jordan RL, Kirchner DL, Kofman W, Leuschen CJ, Nielsen E, Orosei R, Pettinelli E, Phillips RJ, Plettnermeier D, Safaeinili A, Seu R, Stofan ER, Vannaroni G, Watters TR, Zampolini E (2005) Radar soundings of the subsurface of Mars. *Science* 310:1925–1928. doi:[10.1126/science.1122165](https://doi.org/10.1126/science.1122165)
- Pieters CM, Goswami JN, Clark RN, Annadurai M, Boardman J, Buratti B, Combe J-P, Dyar MD, Green R, Head JW, Hibbitts C, Hicks M, Isaacson P, Klima R, Kramer G, Kumar S, Livo E, Lundein S, Malaret E, McCord T, Mustard J, Nettles J, Petro N, Runyon C, Staid M, Sunshine J, Taylor LA, Tompkins S, Varanasi P (2009) Character and spatial distribution of OH/H<sub>2</sub>O on the surface of the Moon seen by M3 on Chandrayaan-1. *Science* 326:568–572. doi:[10.1126/science.1178658](https://doi.org/10.1126/science.1178658)
- Pilcher CB, Ridgeway ST, McCord TB (1972) Galilean satellites: identification of water frost. *Science* 178:1087–1089
- Pinilla-Alonso N, Brunetto R, Licandro J, Gil-Hutton R, Roush TL, Strazzulla G (2009) The surface of (136108) Haumea (2003 EL61), the largest carbon-depleted object in the trans-Neptunian belt. *Astron Astrophys* 496:547–556
- Pollack JB, Witteborn FC, Erickson EF, Strecker DW, Baldwin BJ, Bunch TE (1978) Near-infrared spectra of the Galilean satellites: observations and compositional implications. *Icarus* 36:271–303
- Pospieszalska MK, Johnson RE (1989) Magnetospheric ion bombardment profiles of satellites: Europa and Dione. *Icarus* 78:1–13
- Prinn RG, Fegley B (1981) Kinetic inhibition of CO and N<sub>2</sub> reduction in circumplanetary nebulae – implications for satellite compositions. *Astrophys J* 249:308–317
- Prinn RG, Fegley B Jr (1989) Origin of planetary, satellite, and cometary volatiles. In: Atreya SK, Pollack JB, Mathews MS (eds) *Origin and evolution of planetary and satellite atmospheres*. University of Arizona Press, Tucson, pp 8–136
- Quirico E, Schmitt B (1997a) Near-infrared spectroscopy of simple hydrocarbons and carbon oxides diluted in solid N<sub>2</sub> and as pure ices: implications for Triton and Pluto. *Icarus* 127:354–378
- Quirico E, Schmitt B (1997b) A spectroscopic study of CO diluted in N<sub>2</sub> ice: applications for Triton and Pluto. *Icarus* 128:181–188
- Quirico E, Doute S, Schmitt B, de Bergh C, Cruikshank DP, Owen TC, Geballe TR, Roush TL (1999) Composition, physical state, and distribution of ices at the surface of Triton. *Icarus* 139:159–178
- Ramaprasad KR, Caldwell J, McClure DS (1978) The vibrational overtone spectrum of liquid methane in the visible and near infrared: applications to planetary studies. *Icarus* 35:400–409
- Rieke GH, Lebofsky LA, Lebofsky MJ (1985) A search for nitrogen on Triton. *Icarus* 64:153–155
- Rivkin AS, Emery JP (2008) Water ice on 24 Themis? asteroids, comets, meteors, (abstract), Baltimore. <http://www.lpi.usra.edu/meetings/acm2008/pdf/8099.pdf>
- Rodriguez S, Le Mouélic S, Sotin C, Clenet H, Clark R, Buratti B, Brown R, McCord T, Nicholson P, Baines K, the VIMS Science Team (2006) Cassini/VIMS hyperspectral observations of the HUYGENS landing site on Titan. *Planet Space Sci* 54:1510–1523
- Roush TL, Cruikshank DP, Owen TC (1995) Surface ices in the outer solar system. In: Farley KA (eds) *AIP conference proceedings 341: volatiles in the Earth and solar system*, The American Institute of Physics, New York, pp 143–153
- Sagan C, Thompson WR, Khare B (1992) Titan: a laboratory for pre-biological organic chemistry. *Acc Chem Res* 25:286–292

- Sandford SA, Allamandola LJ (1993) The condensation and vaporization behaviour of ices containing SO<sub>2</sub>, H<sub>2</sub>S, and CO<sub>2</sub>: implications for Io. *Icarus* 106:478–488
- Schaller EL, Brown ME (2007) Volatile loss and retention on Kuiper belt objects. *Astrophys J* 659: L61–L64
- Schenk PM, Zahnle K (2007) On the negligible surface age of Triton. *Icarus* 192:135–149
- Schmitt B, de Bergh C, Lellouch E, Maillard J-P, Barbe A, Doute S (1994) Identification of three absorption bands in the 2-mm spectrum of Io. *Icarus* 111:79–105
- Schmitt B, de Bergh C, Festou M (eds) (1998a) Solar system ices. Kluwer, Dordrecht
- Schmitt B, Quirica E, Trotta F, Grundy WM (1998b) Optical properties of ices from the UV to infrared. In: Schmitt B, De Bergh C, Festou M (eds) Solar system ices. Kluwer, Dordrecht, pp 199–240
- Schriver A, Schriver L, Perchard JP (1988) Infrared matrix isolation studies of complexes between water and sulfur dioxide: identification and structure of the 1:1, 1:2, and 2:1 species. *J Mol Spectr* 127:125–142
- Schriver-Mazzuoli L, Chaabouni H, Schriver A (2003a) Infrared spectra of SO<sub>2</sub> and SO<sub>2</sub>: H<sub>2</sub>O ices at low temperature. *J Mol Struct* 644:151–164
- Schriver-Mazzuoli L, Schriver A, Chaabouni H (2003b) Photo-oxidation of SO<sub>2</sub> and of SO<sub>2</sub> trapped in amorphous water ice studied by IR spectroscopy. Implications for Jupiter's satellite Europa. *Can J Phys* 81:301–309
- Schroder SE, Keller HU (2008) The reflectance spectrum of Titan's surface at the Huygens landing site determined by the descent imager/spectral radiometer. *Planet Space Sci* 56:753–769
- Schubert G, Anderson JD, Spohn T, McKinnon WB (2004) Interior composition, structure, and dynamics of the Galilean satellites. In: Bagenal F, Dowling TE, McKinnon W (eds) Jupiter: the atmosphere, satellites, and magnetosphere. Cambridge University Press, Cambridge, pp 281–306
- Scott TA (1976) Solid and liquid nitrogen. *Phys Rep* 27:89–157
- Shapiro MM, Gush HP (1966) The collision-induced fundamental and first overtone bands of oxygen and nitrogen. *Can J Phys* 44:949–963
- Sheng DT, Ewing GE (1971) Collision induced infrared absorption of gaseous nitrogen at low temperatures. *J Chem Phys* 55:5425–5430
- Sloan ED Jr (1998) Clathrate hydrates of natural gases. Taylor and Francis, New York, p 705
- Smythe WD, Nelson RM, Nash DB (1979) Spectral evidence for SO<sub>2</sub> frost or adsorbate on Io's surface. *Nature* 280:766
- Smythe WD, Carlson RW, Ocampo A, Matson D, Johnson TV, McCord TB, Hansen GE, Soderblom LA, Clark RN (1998) Absorption bands in the spectrum of Europa detected by the Galileo NIMS instrument. In: XXIX lunar and planetary science conference, Vol. CD. Lunar and Planetary Institute, Houston
- Soderblom LA, Barnes JW, Brown RH, Clark RN, Janssen MA, McCord TB, Niemann HB, Tomasko MG (2009) Composition of Titan's surface, chapter 6. In: Brown RH, Lebreton J-P, Waite JH (eds) Titan from Cassini-Huygens. Springer, Dordrecht/New York, pp 141–175. doi:[10.1007/978-1-4020-9215-2](https://doi.org/10.1007/978-1-4020-9215-2)
- Soifer BT, Neugebauer G, Matthews K (1981) Near-infrared photometry of the satellites and rings of Uranus. *Icarus* 45:612–617
- Sotin C, Jaumann R, Buratti BJ, Brown RH, Clark RN, Soderblom LA, Baines KH, Bellucci G, Bibring J-P, Capaccioni F, Cerroni P, Combes M, Coradini A, Cruikshank DP, Drossart P, Formisano V, Langevin Y, Matson DL, McCord TB, Nelson RM, Nicholson PD, Sicardy B, LeMouelic S, Rodriguez S, Stephan K, Scholz CK (2005) Release of volatiles from a possible cryovolcano from near-infrared imaging of Titan. *Nature* 435. doi:[10.1038/nature03596](https://doi.org/10.1038/nature03596), <http://www.nature.com/nature/journal/v435/n7043/full/nature03596.html>
- Spencer JR, Calvin WM (2002) Condensed O<sub>2</sub> on Europa and Callisto. *Astron J* 124:3400–3403
- Spencer JR, Buie MW, Bajoraker GL (1990) Solid methane on Triton and Pluto- 3- to 4-micron spectrophotometry. *Icarus* 88:491–496

- Spencer JR, Calvin WM, Person MJ (1995) Charge-coupled-device spectra of the galilean satellites: molecular-oxygen on Ganymede. *J Geophys Res* 100:19049–19056
- Stansberry JA, Pisano DJ, Yelle RV (1996) The emissivity of volatile ices on Triton and Pluto. *Planet Space Sci* 44:945–955
- Sunshine JM, A'Hearn MF, Groussin O, Li JY, Belton MJS, Delamere WA, Kissel J, Klaasen KP, McFadden LA, Meech KJ, 13 co-authors (2006) Exposed water ice deposits on the surface of Comet 9P/Tempel 1. *Science* 311:1453–1455
- Sunshine JS, Farnham TL, Feaga LM, Groussin O, Merlin F, Milliken RE, A'Hearn MF (2009) Temporal and spatial variability of Lunar hydration as observed by the deep impact spacecraft. *Science* 326:565–568. doi:[10.1126/science.1179788](https://doi.org/10.1126/science.1179788)
- Takato N, Bus SJ, Terada H, Pyo T-S, Kobayashi N (2004) Detection of a deep 3- $\mu$ m absorption feature in the spectrum of Amalthea (JV). *Science* 306:2224–2227. doi:[10.1126/science.1105427](https://doi.org/10.1126/science.1105427)
- Teanby NA, Irwin PGJ, de Kok R, Jolly A, Bezard B, Nixon CA, Calcutt SB (2009) Titan's stratospheric C<sub>2</sub>N<sub>2</sub>, C<sub>3</sub>H<sub>4</sub>, and C<sub>4</sub>H<sub>2</sub> abundances from Cassini/CIRS far-infrared spectra. *Icarus* 202:620–631
- Tomasko MG, Archinal B, Becker T, Bezard B, Bushroe M, Combes M, Cook D, Coustenis A, de Bergh C, Dafoe L, Doose L, Doute S, Eibl A, Engel S, Gliem F, Grieger B, Holso K, Howington-Kraus E, Karkoschka E, Keller HU, Kirk R, Kramm R, Kuppens M, Lanagan P, Lellouch E, Lemmon M, Lunine J, McFarlane E, Moores J, Prout GM, Rizk B, Rosiek M, Rueff P, Schroder SE, Schmitt B, See C, Smith P, Soderblom L, Thomas N, West R (2005) Rain, wind and haze during the Huygens probe's descent to Titan's surface. *Nature* 438:765–778
- Trujillo CA, Brown ME, Barkume KM, Schaller EL, Rabinowitz DL (2007) The surface of 2003 EL61 in the near-infrared. *Astrophys J* 655:1172–1178
- Tryka KA, Brown RH, Anicich V, Cruikshank DP, Owen TC (1993) Spectroscopic determination of the phase composition and temperature of nitrogen ice on Triton. *Science* 261:751–754
- Tryka KA, Brown RH, Cruikshank DP, Owen TC, Geballe TR, de Bergh C (1994) Temperature of nitrogen ice on Pluto and its implications for flux measurements. *Icarus* 112:513–527
- Tryka KA, Brown RH, Anicich V (1995) Near-infrared absorption coefficients of solid nitrogen as a function of temperature. *Icarus* 116:409–414
- Vilas F, Larson SM, Stockstill KR, Gaffey J (1996) Unraveling the zebra: clues to the Iapetus dark material composition. *Icarus* 124:262–267
- Vilas F, Jarvis KS, Barker ES, Lederer SM, Kelley MS, Owen TC (2004) Iapetus dark and bright material: giving compositional interpretation some latitude. *Icarus* 170:125–130
- Vuitton V, Yelle RV, Cui J (2008) Formation and distribution of benzene on Titan. *J Geophys Res* 113:E05007. doi:[10.1029/2007JE002997](https://doi.org/10.1029/2007JE002997)
- Wade LG (2005) Organic chemistry, 5th edn. Prentice Hall, Englewood Cliffs
- Waite H, Young D, Cravens T, Coates A, Crary F, Magee B, Westlake J (2007) The process of Tholin formation in Titan's upper atmosphere. *Science* 316:870–875
- Wong MC, Johnson RE (1996) A three-dimensional azimuthally symmetric model atmosphere for Io.2. Plasma effect on the surface. *J Geophys Res* 101:23255–23259
- Yung YL, DeMore WB (1999) Photochemistry of planetary atmospheres. Oxford University Press, New York, pp 201–234
- Zahnle K, Schenk P, Levison H, Dones L (2003) Cratering rates in the outer solar system. *Icarus* 163:263–289
- Zellner B (1972) On the nature of Iapetus. *Astrophys J Lett* 174:L107–L109
- Zolotov MY, Fegley B (1998) Volcanic production of sulfur monoxide (SO) on Io. *Icarus* 132:431–434
- Zolotov MY, Fegley B Jr (1999) Oxidation state of volcanic gases and the interior of Io. *Icarus* 141:40–52
- Zolotov MY, Fegley B (2000) Eruption condition of Pele volcano on Io inferred from chemistry of its volcanic plume. *Geophys Res Lett* 27:2789–2792

# Chapter 2

## Photometric Properties of Solar System Ices

A.J. Verbiscer, P. Helfenstein, and B.J. Buratti

**Abstract** We present an overview of fundamental photometric properties of icy surfaces throughout the Solar System and investigate the extent to which these properties reflect the evolution of the bodies on which they reside. We review photometric models and their parameters and discuss the physical interpretability of those parameters. We focus on those fundamental photometric properties, primarily albedo and the near-opposition phase function, which are independent of any interpretation from the application of a photometric model. Finally, we offer suggestions for future work, both observational and laboratory measurements, which will enhance the scientific return from continued photometric studies of icy bodies in the Solar System.

### 2.1 Introduction

Planetary photometry is the quantitative measurement of reflected and emitted radiation from solar system bodies. Over the past three decades, the observational data set of icy planetary surfaces has expanded considerably. Spacecraft imaging systems have returned hundreds of thousands of multi-wavelength images of giant planet satellites, rings, and even comet nuclei. These platforms have delivered spatial resolutions and access to viewing geometries unattainable from Earth. In addition, the advent of larger aperture ground-based telescopes combined with advances in detector technology

---

A.J. Verbiscer (✉)

Department of Astronomy, University of Virginia, Charlottesville, VA, USA  
e-mail: [verbiscer@virginia.edu](mailto:verbiscer@virginia.edu)

P. Helfenstein

Department of Astronomy and Space Sciences, Cornell University, Ithaca, NY, USA  
e-mail: [helfenstein@astro.cornell.edu](mailto:helfenstein@astro.cornell.edu)

B.J. Buratti

Jet Propulsion Laboratory, California Institute of Technology, Pasadena, CA, USA  
e-mail: [buratti@jpl.nasa.gov](mailto:buratti@jpl.nasa.gov)

have yielded photometric measurements (albedo, color, and phase function) from an entirely new classification of icy bodies, the transneptunian objects (TNOs), and an expanded collection of irregular satellites and Jupiter and Neptune Trojan asteroids.

An important goal of planetary photometry is to infer physical surface properties from the variation in the intensity of reflected sunlight as a function of illumination and viewing geometry. Physically motivated photometric models relate this behavior to properties such as roughness, particle structure, and compaction state. This technique is a valuable means of discerning surface characteristics even on scales below the resolution limit of the telescopes observing them. In general, robust estimates of surface properties from photometric analyses require observations which span the broadest possible range of viewing and illumination angles. Although the size of the Earth's orbit restricts this range for ground-based observations, surface characteristics of objects not visited by spacecraft can be inferred from similarities between the photometric properties of those bodies for which spacecraft observations do exist. Thus spacecraft images provide not only photometric measurements of their direct targets but they may also supply context for similarly classified objects.

Since the last review of the photometric properties of ices in the Solar System (Verbiscer and Helfenstein 1998) several advances in photometric models have improved our ability to reproduce the scattering behavior exhibited by planetary surfaces. For example, models available in the mid-1990s could not fully account for the dramatic, non-linear increase in reflectance seen at opposition, whereas subsequent versions incorporating coherent backscatter successfully replicate this phenomenon.

In this chapter, we present an overview of fundamental photometric properties of icy surfaces throughout the Solar System and investigate the extent to which these properties reflect the evolution of the bodies on which they reside. We review photometric models and their parameters and discuss the physical interpretability of those parameters. At present, no photometric model accurately retrieves physical characteristics of icy surfaces that can be reproduced in a laboratory setting. Parameters such as albedo, roughness, and porosity are intimately linked, and their degeneracy has not been broken. Owing to this current limitation, we do not provide any model-dependent photometric parameters previously derived for icy surfaces. Instead, we focus on those fundamental photometric properties, primarily albedo and the near-opposition phase function, which are independent of any interpretation from the application of a photometric model. Finally, we offer suggestions for future work, both observational and laboratory measurements, which will enhance the scientific return from continued photometric studies of icy bodies in the Solar System.

## 2.2 Fundamental Photometric Properties

Several important photometric quantities characterize the energy balance on a planetary surface. These include the geometric albedo, the spherical albedo, the bolometric Bond albedo, and the phase integral. For icy bodies, these are especially important because they direct the nature of volatile transport.

The geometric albedo  $p_\lambda$  at wavelength  $\lambda$  is the ratio of the scattered, integrated flux at opposition to that of a perfectly diffuse, flat disk of the same apparent size.

Geometric albedos are sometimes misleadingly cited as percentages; however, since  $p_\lambda$  is simply a ratio, there is no upper limit on its value. Furthermore, geometric albedos greater than unity invoke no violations of conservation of energy. The bolometric Bond albedo, however, is the total scattered energy from a body divided by the incident energy. It is thus a measure of the total energy balance, and unless a planetary body is self-luminous, the bolometric Bond albedo cannot exceed unity. Recently, the *Cassini* spacecraft measured the bolometric Bond albedos of several saturnian satellites (Howett et al. 2010; Pitman et al. 2010).

The phase integral is given by  $q_\lambda = 2 \int_0^\pi \Phi_\lambda(\alpha)$  where  $\alpha$  is the solar phase angle and  $\Phi_\lambda(\alpha)$  is the disk-integrated reflectance normalized to unity at  $\alpha = 0^\circ$ . The solar phase angle is the angle subtended at the detector between a planetary body and the Sun. The spherical albedo  $A_\lambda$  is the product of the geometric albedo and phase integral and is sometimes referred to as the Bond albedo.

Table 2.1 lists the geometric albedo, phase integral, and spherical albedo measured in the broadband *V* filter (centered at 0.55  $\mu\text{m}$ ) for several giant planet satellites and rings, jovian Trojan asteroids, TNOs (segregated according to the classification of Gladman et al. 2008), comet nuclei, and the icy main-belt asteroid 24 Themis. Although photometric measurements exist for many more objects than those listed here, we only include those of known diameters for which at least rudimentary phase curves are available in the *V* band. Because the geometric albedo relates the reflectance to that of a diffuse disk of the same apparent size, the diameter of the object must be known in order to determine its geometric albedo. Stansberry et al. (2008) and Müller et al. (2010) applied the standard thermal model (Lebofsky and Spencer 1989) to mid-infrared (24–160  $\mu\text{m}$ ) observations acquired by the *Spitzer Space Telescope* and *Herschel Space Observatory*, respectively, to determine the size and albedo of several TNOs.

### 2.2.1 Geometric Albedo and Phase Function

At opposition, the observer is directly aligned between the planetary body and the Sun, and the solar phase angle reaches a minimum. Since the Sun is not a point source and has a finite angular size, no planetary body can be observed at precisely  $\alpha = 0^\circ$ . Near opposition, many different phase angles are observed simultaneously due to the angular extent of the solar disk, and the resulting reflectance is a weighted combination of the reflectances measured at all phase angles across the Sun. Therefore, the angular radius of the solar disk seen from a planetary body defines the minimum phase angle at which the object can be observed. Owing to solar limb darkening, phase angles smaller than the angular solar radius are observable during node crossings. Therefore, although the angular size of half the solar disk at 9.5 AU is 0.028°, the minimum phase angle at which a saturnian satellite can be observed is  $\sim 0.010^\circ$ . The large heliocentric distances of TNOs make it possible to observe them at even smaller phase angles and probe regions of the solar phase curve (reflectance vs. solar phase angle) inaccessible to giant planet satellites. The angular size of the solar radius at 50 AU is 0.005° and solar limb darkening permits access to

**Table 2.1** Fundamental photometric quantities for icy surfaces in the solar system<sup>a</sup>

Object	Geometric albedo $p_V$	Phase integral $q_V$	Spherical albedo $A_V$	$S_V$ (mag)	Minimum $\alpha$ observed (angular solar radius) ( $^{\circ}$ )	Refs <sup>b</sup>
<b>Jovian satellites</b>						
Europa	1.02	0.69	0.70	0.24	0.02 <sup>c</sup>	1
Ganymede (L)	0.61	0.69	0.42	0.277	0.4	2
Ganymede (T)	0.42	0.64	0.27	0.027	1.4	2
Callisto (L)	0.22	0.59	0.13	0.115	0.4	2
Callisto (T)	0.25	0.52	0.13	0.113	0.6	2
<b>Jovian trojans</b>						
Achilles	0.038–0.051			0.045	0.08 (0.052)	3,5
<b>Saturnian rings</b>						
A Ring	0.52			0.404	0.01	6
B Ring	0.79			0.363	0.01	6
C Ring	0.083			0.498	0.01	6
<b>Saturnian satellites</b>						
Janus	0.71			0.352 <sup>U</sup>	0.01	7
Epimetheus	0.73			0.229 <sup>U</sup>	0.01	7
Mimas	0.962	0.62	0.60	0.331	0.01	7
Enceladus	1.375	0.68	0.93	0.271	0.01	7
Tethys	1.233	0.52	0.64	0.321	0.01	7
Calypso	1.34				0.01	7
Dione	0.998	0.70	0.70	0.302	0.01	7
Helene	1.67				0.01	7
Rhea	0.949	0.63	0.60	0.374	0.01	7
Iapetus	0.30				0.01	7
Phoebe	0.086	0.32	0.03	0.243	0.01	8
<b>Uranian rings</b>						
<b>Uranian satellites</b>						
Portia group <sup>d</sup>	0.080	0.33	0.026	0.225	0.034	9
Puck	0.104	0.34	0.035	0.219	0.034	9
Miranda	0.464	0.44	0.200	0.410	0.034	9
Ariel	0.533	0.43	0.230	0.441	0.034	9
Umbriel	0.258	0.39	0.100	0.321	0.034	9
Titania	0.350	0.46	0.170	0.357	0.034	9
Oberon	0.309	0.44	0.140	0.359	0.034	9
<b>Neptunian satellites</b>						
Triton	0.77	1.16	0.89	0.21	0.004	10, 11
Nereid	0.26			0.203	0.005	12
<b>Dwarf planets</b>						
Pluto	0.61			0.0355	0.361 (0.007)	13
Charon	0.431			0.265	0.361 (0.007)	13
Eris	0.96			0.105	0.16 (0.003)	14, 15
Haumea	0.84			0.11	0.51 (0.005)	16
Makemake	0.8			0.054	0.69 (0.005)	17, 15
<b>Classical KBOs</b>						
Quaoar	0.172			0.159	0.17 (0.006)	18, 15
Varuna	0.16			0.278	0.06 (0.006)	17, 15
Sila-Nunam	0.06–0.14			0.98 <sup>R</sup>	0.006 (0.006)	19, 20

(continued)

**Table 2.1** (continued)

Object	Geometric albedo $p_V$	Phase integral $q_V$	Spherical albedo $A_V$	$S_V$ (mag)	Minimum $\alpha$ observed (angular solar radius) ( $^{\circ}$ )	Refs <sup>b</sup>
1999 DE <sub>9</sub>	0.0685			0.128	0.17 (0.007)	<i>17, 15</i>
2002 KX <sub>14</sub>	0.60			0.159	0.09 (0.007)	<i>18, 15</i>
2002 AW <sub>197</sub>	0.1177			0.128	0.17 (0.006)	<i>17, 15</i>
2002 UX <sub>25</sub>	0.115			0.158	0.02 (0.006)	<i>17, 15</i>
<b><i>Scattered Disk TNOs</i></b>						
1999 TD <sub>10</sub>	0.044			0.15	0.26 (0.013)	<i>17, 15</i>
<b><i>Detached TNOs</i></b>						
Sedna	0.16			0.114	0.27 (0.003)	<i>17, 15</i>
<b><i>Centaurs</i></b>						
Chiron	0.0757			0.1	0.64 (0.016)	<i>17, 21</i>
Chariklo	0.0573			0.05	4.0 (0.019)	<i>17, 22</i>
Bienor	0.0344			0.095	0.33 (0.014)	<i>17, 15</i>
2002 PN <sub>34</sub>	0.0425			0.043	0.33 (0.020)	<i>17, 15</i>
Asbolus	0.0546			0.05	1.97 (0.018)	<i>17, 15</i>
Thereus	0.0428			0.072	0.22 (0.022)	<i>17, 15</i>
Hylonome	0.062			0.206 <sup>R</sup>	0.09 (0.012)	<i>23, 24</i>
Echeclus	0.0383			0.22	0.11 (0.034)	<i>17, 25</i>
Typhon	0.051			0.126	0.19 (0.014)	<i>17, 15</i>
<b><i>Plutinos</i></b>						
Ixion	0.12			0.133	0.03 (0.006)	<i>17, 15</i>
Huya	0.0504			0.155	0.28 (0.009)	<i>17, 15</i>
1999 TC <sub>36</sub>	0.0718			0.131	0.28 (0.009)	<i>17, 15</i>
2000 GN <sub>171</sub>	0.0568			0.143	0.02 (0.009)	<i>17, 15</i>
Orcus	0.1972			0.114	0.39 (0.006)	<i>17, 15</i>
<b><i>Comets</i></b>						
19P/Borrelly	0.072	0.26	0.019	0.043	1.9 (0.046)	<i>26</i>
2P/Encke	0.047			0.05	4.01 (0.134)	<i>27</i>
9P/Tempel 1	0.056	0.23	0.013	0.046	3.24 (0.134)	<i>28</i>
81P/Wild 2	0.059	0.16	0.0093	0.0513	13.1 (0.089)	<i>29</i>
<b><i>Main Belt asteroids</i></b>						
24 Themis	0.074			0.1	0.34 (0.084)	<i>30,31</i>

<sup>a</sup>All observations at V-band, 0.55  $\mu\text{m}$ , except those noted with<sup>U</sup> which are U-band at 0.34  $\mu\text{m}$  and<sup>R</sup> which are R-band at 0.65  $\mu\text{m}$ . Unless noted by L (leading hemisphere) and T (trailing hemisphere), all parameters are global averages from rotationally corrected phase curves. Some TNO phase curves have not been corrected for light curve variations

<sup>b</sup>References: *1* Helfenstein and Shkuratov (2011), in preparation, *2* Domingue and Verbiscer (1997), *3* Fernandez et al. (2003), *4* Schaefer et al. (2010), *5* Shevchenko et al. (2009), *6* French et al. (2007), *7* Verbiscer et al. (2007), *8* Miller et al. (2011), *9* Karkoschka (2001), *10* Buratti et al. (2011), *11* Hillier et al. (1990), *12* Schaefer et al. (2008), *13* Buie et al. (2010), *14* Sicardy et al. (2011), *15* Rabinowitz et al. (2007), *16* Rabinowitz et al. (2006), *17* Stansberry et al. (2008), *18* Brucker et al. (2009), *19* Müller et al. (2010), *20* Rabinowitz et al. (2009), *21* Lazzaro et al. (1997), *22* Davies et al. (1998), *23* Luu and Jewitt (1996), *24* Bauer et al. (2003), *25* Rousselot et al. (2005), *26* Li et al. (2007a), *27* Boehnhardt et al. (2008), *28* Li et al. (2007b), *29* Li et al. (2009), *30* Chernova et al. (1994), *31* Harris et al. (1989)

<sup>c</sup>Italicized phase angles are smaller than the solar radius seen from the icy surface

<sup>d</sup>Includes the seven innermost satellites of Uranus: Bianca, Cressida, Desdemona, Juliet, Portia, Rosalind, and Belinda

phase angles as small as  $\sim 0.002^\circ$ . These configurations describe *true* opposition when the Earth (or spacecraft) actually transits the solar disk as seen from the object.

Traditionally, geometric albedos are determined by extrapolating solar phase curves to opposition, or zero phase. If solar phase curves were simply linear functions, this technique would yield accurate results; however, as phase angles approach zero, phase curves of most particulate surfaces exhibit a dramatic, non-linear increase in reflectance. (We discuss this opposition effect, or surge, in detail in Sect. 2.3.1.4) The best estimates of  $p_V$  are therefore achieved when the surface is observed at phase angles close to zero, limited by the angular size of the solar radius seen from the object. Table 2.1 also lists the minimum phase angle at which each icy body has been observed as well as the angular size of the solar radius seen from each. The likelihood that an estimated  $p_V$  is close to the actual  $p_V$  can be gauged from the minimum observed phase angle. The minimum phase angles at which comet nuclei have been observed, for instance, are rather large ( $1.9\text{--}13.1^\circ$ ); therefore, their geometric albedos are likely underestimates. On the other hand, *Hubble Space Telescope* observations of the uranian satellites and rings (Karkoschka 2001) were obtained at a phase angle ( $\alpha = 0.034^\circ$ ) so close to zero that their measured geometric albedos will probably not significantly exceed these extrapolated values. A growing number of icy bodies have been observed at or near node crossings, enabling *measurement* rather than estimation of their geometric albedo. These include most saturnian satellites (Verbiscer et al. 2007), Nereid (Schaefer et al. 2008), Triton (Buratti et al. 2011), the classical TNO Sila-Nunam (provisionally designated 1997 CS<sub>29</sub>) (Rabinowitz et al. 2009; Verbiscer et al. 2010), and a few objects for which we do not have geometric albedos, e.g. Tithonus (a Jupiter Trojan (Schaefer et al. 2010)).

A phase function parameter  $S_V$  (fifth column in Table 2.1) is simply the difference in reflectance (in magnitudes) observed at solar phase angle  $1^\circ$  and the best estimate (in most cases) of the reflectance at the minimum phase angle at which the body can be observed. Traditionally, the phase coefficient  $\beta$  measures the slope of the phase curve (in magnitudes/degree) over a specified range of phase angles. The phase function parameter  $S_V$  may not necessarily be the slope of the phase curve between  $\alpha = 0^\circ$  and  $\alpha = 1^\circ$ , since some phase curves become non-linear at phase angles less than  $1^\circ$ . The parameter  $S_V$  simply provides a quantitative measure of the amount by which the reflectance of these icy surfaces increases as they reach opposition. As we discuss in detail below, comparisons between  $S_V$  and  $p_V$  among icy surfaces throughout the Solar System suggest correlations between their fundamental photometric properties and weathering and thermal histories.

### 2.2.2 Discussion

At visible wavelengths, geometric albedos of icy bodies throughout the Solar System appear to span a broad range, from 0.03 to 1.4. Closer inspection reveals, however, that only the major satellites closest to the giant planets and the dwarf planets have  $p_V > 0.2$  and the surfaces of most other icy bodies are dark ( $p_V < 0.2$ ). The major satellites of the outer Solar System orbit within giant planet magnetospheres in

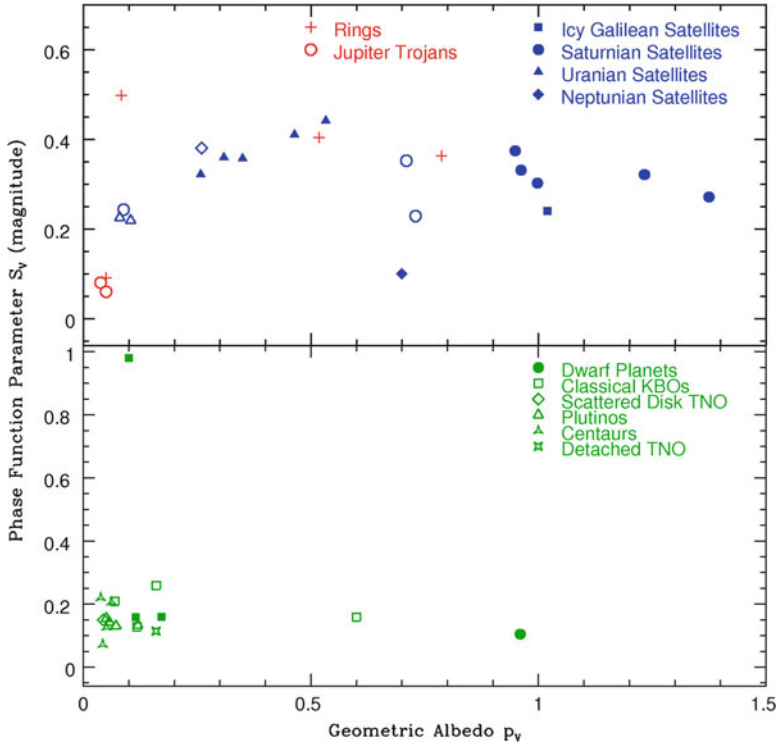


**Fig. 2.1** Geometric albedo  $p_V$  and a phase function parameter  $S_V$  for icy surfaces in Table 2.1 which have been observed at phase angles smaller than  $0.3^\circ$ .  $S_V$  is the slope of the phase curve between  $\alpha = 1^\circ$  and  $\alpha = 0^\circ$ , measured in magnitudes. In most cases the reflectance at  $\alpha = 0^\circ$  is derived from extrapolating the phase curve to opposition. For the saturnian satellites, Nereid, Triton, and Sila-Nunam the reflectance at true opposition was measured rather than extrapolated from solar phase curves. For the objects in the *upper box*, *solid symbols* denote objects larger than 300 km in diameter; for the TNOs in the *lower box*, solid symbols represent binary systems

regions populated by dust and charged particles. These environments alter physical surface properties through processes such as sputtering and desorption (e.g. Paranicas et al. 2009), micrometeoroid impacts (e.g. Verbiscer et al. 2007), and sublimation (cf. Spencer 1987). As a result, these satellite surfaces exhibit a wide variety of albedos, colors, and phase functions on both global and small scales while most TNOs, irregular satellites and Trojans, have more uniform colors, or at least groupings of colors, albedos, and phase functions.

To investigate the correlation of albedo and phase function with various types of icy surfaces, Fig. 2.1 shows both quantities for those objects which have been observed at phase angles smaller than  $0.3^\circ$ . Icy surfaces which have not been observed at  $\alpha < 0.3^\circ$  are excluded because their geometric albedos and phase functions are likely underestimates and their placement on Fig. 2.1 would be misleading. Several groupings appear, most notably the major saturnian and uranian satellites. The satellites residing within Saturn's tenuous E ring all have

geometric albedos at or above unity, and Mimas, Enceladus, Tethys, and Dione have  $S_V > 0.25$  mag due to continuous bombardment by E ring particles (Verbiscer et al. 2007). Janus and Epimetheus also orbit Saturn within their own dusty ring which accounts for their high geometric albedos and steep phase functions. Although Phoebe also orbits Saturn within its own dusty ring (Verbiscer et al. 2009), the relatively lower impact velocities between Saturn’s darkest satellite and ring particles produce a shallower phase function than that seen on moons closer to the planet. While there is no apparent correlation between size and phase function  $S_V$ , icy bodies larger than 300 km in diameter (solid symbols at the top of Fig. 2.1) are brighter ( $p_V > 0.25$ ) than smaller objects.

The exceptionally high geometric albedo of Enceladus is consistent with the fact that it is geologically active (Spencer et al. 2006). Triton also has a high geometric albedo (Buratti et al. 2011) and is geologically active (Soderblom et al. 1990). Even with substantial magnetospheric bombardment and darkening, Europa’s high albedo indicates that its surface has far more fresh exposed water ice and less surface contaminants than Ganymede and Callisto. Full-disk observations of the icy Galilean satellites do not exist at phase angles smaller than  $0.2^\circ$ ; therefore, their geometric albedos are likely not accurately extrapolated from their phase curves. The geometric albedo of Europa is derived from a “hybrid” phase curve comprised of disk-resolved *Galileo* spacecraft observations and full-disk reflectances (discussed in detail in Sect. 2.3.1.5). The geometric albedo of the classical Kuiper belt object (KBO) 2002 KX<sub>14</sub> is unusually high ( $p_V = 0.6$ ); however, the uncertainties in this measurement are also large  $+0.36 - 0.23$  (Brucker et al. 2009). The only other bodies with  $p_V > 0.5$  are dwarf planets Pluto, Eris, Makemake, and Haumea, yet it is not currently known if any of these bodies is geologically active. Only Eris has been observed at  $\alpha < 0.3^\circ$ , so it’s possible that the other dwarf planets have even higher geometric albedos and steeper phase functions. Most distant, irregular satellites, including Phoebe, are dark. When considered along with their retrograde orbits, the low albedo of these objects suggests that they were captured and did not originate with their parent planet but elsewhere in the Solar System.

The Solar System’s most reflective satellites, Enceladus and Tethys, interestingly, do not have the steepest phase functions. Although the major uranian satellites (Miranda, Ariel, Umbriel, Titania, and Oberon) are substantially darker than their saturnian counterparts, they exhibit comparable phase functions  $S_V$ . Miranda and Ariel have the steepest phase functions of any icy satellites, yet the exact mechanism by which their phase functions are enhanced is not currently known. Only particles in Saturn’s C-ring demonstrate a more dramatic increase in reflectance as the phase angle decreases from  $1^\circ$ . The phase functions of the saturnian rings are anti-correlated with albedo. Section 2.3.1.4 discusses the relationship between albedo and the coherent backscatter opposition effect.

Aside from Saturn’s C ring, the darkest objects in the Solar System have relatively shallow phase functions  $S_V < 0.25$ . These include comet nuclei, Centaurs, jovian Trojans and particles comprising the uranian rings. The Centaurs and jovian Trojans are the darkest objects ( $0.03 < p_V < 0.08$ ). The surfaces of Plutinos, objects in a 3:2 mean motion resonance with Neptune, and comet nuclei

are similarly dark. Among the TNOs, a handful of classical KBOs (Varuna, Sila-Nunam, 2002 KX<sub>14</sub>, and 2002 UX<sub>25</sub>), two Centaurs (Hylonome and Echeclus), and two Plutinos (Ixion and 2000 GN<sub>171</sub>) have been observed at phase angles smaller than  $\alpha \approx 0.1^\circ$ . Interestingly, some jovian Trojans have been observed at phase angles close to the angular solar radius at their heliocentric distance, yet they have very small  $S_V$ . Other objects with comparably small  $S_V$  have not been observed at phase angles near the minimum as the jovian Trojans have, thus, their phase functions are likely underestimated.

The rest of the objects in these groups will likely move slightly upward and to the right in Fig. 2.1 as they are observed at smaller phase angles. The classical KBOs in dynamically “cold” orbits with low inclinations and low eccentricities have generally higher geometric albedos than Sedna, a “detached” object (having no influence from Neptune or any other giant planet), and 1999 TD<sub>10</sub>, a TNO from the scattered disk. However, more detached TNOs and objects from the scattered disk need to be observed at small phase angles to reach statistically valid conclusions. Except for the dwarf planets, all TNOs exhibit roughly similar  $S_V$ . Sila-Nunam, the classical binary KBO which has been observed at the smallest (but not minimum) phase angle, also has the steepest phase function. Rabinowitz et al. (2009) and Verbiscer et al. (2010) suggest that ejecta exchange between binary or multiple components of TNOs (Stern 2009) can produce the surface microtextures capable of enhancing the reflectance at opposition. Solid symbols in the lower portion of Fig. 2.1 represent binary or multiple TNO systems. Excluding Sila-Nunam, however, there does not currently appear to be a strong correlation between TNOs with multiple components and phase function.

## 2.3 Photometric Models and Their Parameters

Photometric models have been widely applied to icy bodies in the Solar System for many years. They all strive to relate viewing geometry to the radiance factor  $R_\lambda$ , where  $R_\lambda = I_\lambda/F_\lambda$ .  $I_\lambda$  is the specific intensity of light at wavelength  $\lambda$  scattered from a surface and  $\pi F_\lambda$  is the plane-parallel specific incident solar flux. The radiance factor itself is dimensionless since  $I_\lambda$  and  $\pi F_\lambda$  both have units W/m<sup>2</sup>/sr. Typically, radiance factors range from 0 to 1. Most often, broadband photometry is obtained from spacecraft imaging cameras and telescopes, and the radiance and flux quantities are then integrated over the specific optical filter bandpass being used for the observation.

Empirical equations, such as that of Lambert (1760), Minnaert (1941) and Kaasalainen (2003), relate the reflectance from a particulate surface to viewing geometry in a simple manner as functions of the incidence, emission and solar phase angles. The incidence angle  $i$  is the angle between the surface normal and the incident radiation, while the emission angle  $e$  is the angle between the surface normal and emergent ray. The solar phase angle  $\alpha$  is the angle between the incident and emergent ray, measured from the scattering surface. (See Verbiscer and Helfenstein (1998) for a detailed review of empirical models.) Analytical models,

such as that of Hapke (1981, 1984, 1986, 2002, 2008), Goguen (1981), Lumme and Bowell (1981, 1985), and Shkuratov et al. (1999) approximate the solution for radiative transfer from a rough, particulate surface.

An analytical photometric model can be best considered as an assemblage of mathematical components, each of which describes a functional dependence of directional light scattering on a different parameterized quasi-physical property, or a group of related properties that act in concert. The main functional components of typical models rely on (1) a component to describe albedo and directional singly scattered light by an average regolith grain, (2) a component to describe how photons are multiply scattered among and from an aggregate volume of average grains, (3) a parameterized component to describe the effects of macroscopic surface texture on reflected light, and (4) component functions to describe the opposition effect – a conspicuous non-linear surge in brightness with decreasing phase angle that is observed at small phase angles on particulate covered bodies. So complex are these interactions that even the best available analytical models remain incomplete and inadequately verified. They have continued to evolve over a span of at least three decades as laboratory testing and refinement of theory identify new deficiencies and new corrections, respectively. One of the most difficult aspects of summarizing the results of photometric analyses from a wide variety of icy surfaces is that over the past few decades, different versions of the models have been used to analyze different icy body data sets. Since the last review of the photometric properties of solar system ices (Verbiscer and Helfenstein 1998), there have been a number of advances in the theories used to interpret photometric data and observations as well as advances in the analysis and realization of the limits of currently available models (Shepard and Helfenstein 2007). Among the analytical models, the Hapke (1981, 1984, 1986, 2002, 2008) model and the Shkuratov et al. (1999) model have seen the widest application to both photometric and spectroscopic data. We discuss below recent modifications to the Hapke model and a model based on that of Shkuratov et al., presenting their parameters and the physical interpretability of those parameters.

### 2.3.1 *The Hapke Model*

Among the analytical models, Hapke's (1981, 1984, 1986, 2002, 2008) equation has seen the widest application to icy surfaces. In general, the Hapke function yields useful, high-fidelity modeling of the photometric behavior of planetary regoliths. It is well-suited to image processing tasks such as correcting for systematic photometric shading gradients across the disk in spacecraft images so that they can be used as panels in global albedo maps, or for estimating radiometric Bond albedos. However, despite numerous revisions and refinements to overcome deficiencies and improve its physical realism, the Hapke model has yet to be fully validated as a tool for retrieving accurate estimates of the physical and geological properties of planetary regoliths. Until accurate soil physical properties can be verifiably retrieved

from fits of Hapke's model to well-characterized laboratory samples, the validity of many published studies that adopt this approach remains in doubt. Further, few published planetary photometric analyses make use of the most recent version (Hapke 2008) that corrects a fundamental flaw in earlier treatments of the effects of regolith porosity on reflectance. Consequently, nearly all published applications of Hapke's model to planetary objects are obsolete and mutually inconsistent.

Only limited success has been realized in attempts to validate Hapke theory by comparing the known characteristics of laboratory samples to those predicted by fits of the model parameters to photometric observations of the samples. Gunderson et al. (2006) performed fits of Hapke's (2002) model to a sample of JSC-1 lunar soil stimulant. While they obtained excellent fits to fixed incidence angle, variable emission angle data sets, the models extrapolated poorly to fixed, near-zero phase angle data at varying incidence angles, and no solutions provided simultaneous, high quality fits to the two types of data sets. Strong correlations were found between single-scattering albedo and the particle phase function parameters and, to a lesser extent, the small-scale mean surface roughness. Shepard and Helfenstein (2007) performed fits of Hapke's (2002) model to spectrophotometric measurements covering a wide range of photometric geometries of soil analogs for 29 separate particulate samples (both natural and artificial) and compared their results to the known composition, compaction state, grain-size distribution and particle structure of the samples. They found no compelling evidence that individual photometric parameters could be uniquely interpreted to reveal the physical state of the samples, either in an absolute or relative sense. Instead, combinations of physical properties such as particle single-scattering albedo, roughness, and porosity were convolved within each retrieved photometric parameter. Shkuratov et al. (2007) tested the validity of Hapke (2002) model inversions for natural particulate sample surfaces when the directional scattering behavior (that is, the particle phase functions) of isolated natural soil grains are independently known from polar nephelometer measurements. Like Shepard and Helfenstein (2007), they found that retrieved values of particle single-scattering albedo depended on the compaction state of the soil samples, contrary to model predictions. They also found a wavelength-dependence for Hapke model parameters that, in theory, should not depend on wavelength.

In the most recent and promising attempt to validate Hapke's (2008) model, Helfenstein and Shepard (2011) updated Hapke's (1986) model of the shadow-hiding opposition surge to be consistent with the 2008 correction for porosity. In a preliminary test, the refined model was fit separately to three samples from Shepard and Helfenstein's (2007) suite of laboratory photometric measurements representing respectively, a low-albedo, a medium albedo, and a very high-albedo surface. The test suggests that the revised Hapke model significantly improves the fidelity of model parameters retrieved for low- to moderate-albedo materials. However, as predicted by Hapke's (2008) theory, the porosity correction has little effect on high-albedo surfaces for which no improvements were observed in the test. Much more thorough testing is needed, but for application to icy satellite surfaces, the preliminary tests imply that reliable results can be obtained only at spectral wavelengths where ice particles are dark, for example, in the ultraviolet range.

### 2.3.1.1 Single Scattering by Average Regolith Grains

Light that is scattered once by an average regolith grain is generally described by the product  $\omega_o P(\alpha)$  where  $\omega_o$  is the average particle single scattering albedo and  $P(\alpha)$  is known as the average particle single scattering phase function. The single scattering albedo is the ratio of a particle's scattering efficiency to its extinction efficiency, or the probability that a photon will be scattered rather than absorbed. Hapke's models prior to 2008 do not properly treat how the effective scattering cross sections of regolith grains in mutual contact change with changing packing density or porosity. As a result, estimates of  $\omega_o$  retrieved from fits of the earlier models to photometric data can be significantly in error.

As noted above, the single particle phase function describes the directional scattering behavior of average regolith grains. Although Hapke (1981) initially proposed using a two-parameter Legendre polynomial representation, typically the empirical one-term Henyey-Greenstein (1941) phase function (1THG) is used:

$$P(\alpha) = (1 - g^2) / (1 + 2g \cos(\alpha) + g^2)^{3/2}$$

The asymmetry parameter  $g$  is the average cosine of the scattering angle  $\Theta$ , and  $\Theta = \pi - \alpha$ . By convention,  $g$  ranges from  $-1$  to  $+1$ , with negative values representing backscattering and positive values representing forward scattering behavior. Particles which scatter isotropically have  $g = 0$ . To data sets which span nearly the full range of phase angles, a double Henyey-Greenstein function is sometimes used to describe anisotropic particle scattering. This can be a three-term Henyey-Greenstein function (3THG) which is a linear combination of two 1THG's (cf. Kattawar 1975):

$$P(\alpha) = (1-f) \frac{(1-g_1^2)}{(1+2g_1 \cos(\alpha) + g_1^2)^{3/2}} + (f) \frac{(1-g_2^2)}{(1+2g_2 \cos(\alpha) + g_2^2)^{3/2}} \quad (2.1)$$

where  $g_1$  and  $g_2$  are separate asymmetry parameters that, most often, describe backward and forward scattering lobes, respectively, of different angular widths, and the partition parameter  $f$  controls the relative amplitude of each contribution. In two-term simplifications (2THG) of the Henyey-Greenstein models, the forward and backscattering components have the same angular widths but different amplitudes. The most often used representation is that from McGuire and Hapke (1995)<sup>1</sup>:

$$P(\alpha) = \frac{(1+c)}{2} \frac{(1-b^2)}{(1-2b \cos(\alpha) + b^2)^{3/2}} + \frac{(1-c)}{2} \frac{(1-b^2)}{(1+2b \cos(\alpha) + b^2)^{3/2}} \quad (2.2)$$

In relation to the 3THG parameters from Eq. 2.1,  $g_1 = -g_2 = -b$  and  $f = (1-c)/2$ . Most icy bodies in the Solar System are dominantly backscattering

---

<sup>1</sup> Domingue et al. (1991) and Souchon et al. (2011) adopted a slightly different version of the 2THG in which coefficients  $c$  and  $(1-c)$ , respectively, replace  $(1+c)/2$  and  $(1-c)/2$  in Eq. 2.2.

(Verbiscer et al. 1990); although, those to which a double Henyey-Greenstein phase function has been applied also exhibit a forward scattering component (Hillier et al. 1990; Domingue and Verbiscer 1997; Buratti et al. 2008).

*Physical interpretability:* For macroscopic regolith grains in mutual contact (as in a regolith), the directional scattering of light is sensitive to the shape, microscopic texture, internal mechanical structure, and optical constants of the materials composing the particles. McGuire and Hapke (1995) attempted to map out the relationship between parameters of their 2THG particle phase function and the well-characterized structural properties of analog regolith particles in the laboratory. In theory, their results provide a framework for interpreting the physical structure of average regolith grains from fits of the 2THG retrieved from photometric phase curves of planetary surfaces. However, in their laboratory test, Shepard and Helfenstein's (2007) retrievals of the 2THG parameters only crudely reflected the characteristics of grains making up the samples. Souchon et al. (2011), on the other hand, tested Hapke's (1993) model and found good qualitative agreement between the observed microstructure of natural soil grains and the physical interpretation of retrieved particle phase function model parameters when the range of photometric geometries of the samples were optimized to exclude the opposition effect and observations at large incidence and emission angles.

### 2.3.1.2 Multiple Scattering

Many of the changes in Hapke's model as it has been applied to icy satellites have come through refinement of the function to describe the contribution of multiply-scattered photons between grains in the regolith. Hapke's (1981, 1984, 1986) model approximated multiple scattering with an analytical simplification of Chandrasekhar's (1960) H-functions for isotropically scattering grains. This approximation was considered adequate for relatively low to moderate albedo bodies for which the contribution of multiply scattered light was small compared to the emitted singly scattered signal. It was also applied in early Voyager-spacecraft based studies of icy satellites (Helfenstein 1986; Verbiscer and Veverka 1989; Domingue et al. 1991). During the 1990s some icy satellite studies improved the Hapke model by substituting the exact calculation for anisotropic scatterers (Verbiscer 1991; Verbiscer and Veverka 1992, 1994). As more complete phase coverage of icy satellites became available through *Galileo* and *Cassini* spacecraft data, Hapke (2002) anticipated the need for a rigorous treatment of multiple scattering for strongly anisotropic grains and introduced such an improvement as well as more accurate analytical approximations for multiple scattering by isotropic scatterers.

### 2.3.1.3 Macroscopic Roughness

Hapke's (1984) macroscopic roughness parameter  $\theta$  encompasses topographic facets ranging in size from aggregates of particles to mountains, craters, and ridges, up to the spatial resolution limit of the detector on the surface (Helfenstein 1988;

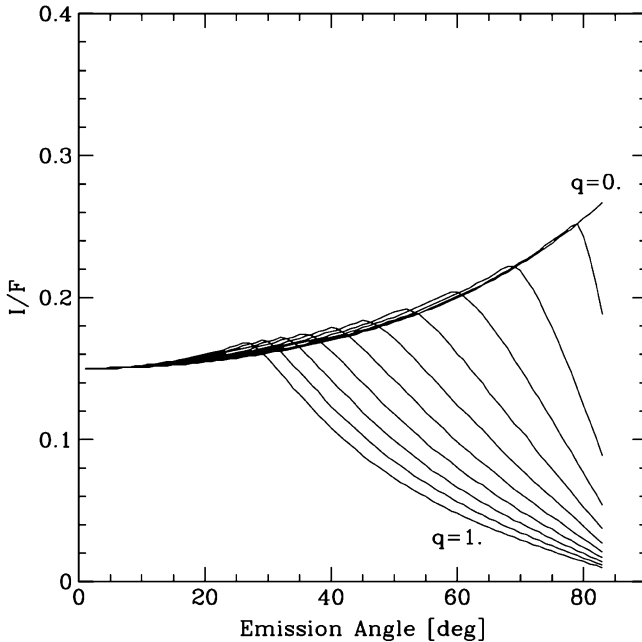


**Fig. 2.2** Scans of the radiance factor ( $I/F$ ) along the photometric equator for a solar phase angle of  $24^\circ$  and for a variety of crater depth-to-radius ratios ( $q$ ) ranging from 0 (smooth) to 1 (rough). An inflection point occurs in the scan that is characteristic of the roughness: fitting observations to disk-resolved observations from spacecraft can effectively derive surface roughness

Shepard and Campbell 1998; Helfenstein and Shepard 1999). These topographic features alter the specific intensity of an icy surface by changing the local incidence and emission angles from that of a smooth locally flat surface, by removing radiation from the scene from cast shadows, and through occultation of some surface facets by others. In addition to the analytical mean slope model used by Hapke, numerical models such as the crater roughness model (Buratti and Veverka 1985) and the S-matrix model (Goguen et al. 2010) describe this effect quantitatively. Figure 2.2 shows an example of how a rough facet alters the reflected intensity at the photometric equator.

Three main problems exist in deriving macroscopic roughness from spacecraft and ground-based observations: (1) the non-uniqueness of the formal fits, (2) the treatment of volumetric multiple scattering, including the absence of a treatment for multiple reflection at macroscopic scales, and (3) the improper treatment of the effects of porosity in formulations prior to Hapke (2008). The difficulty with obtaining a unique determination of roughness can be minimized by obtaining observations over a range of solar phase angles and by fitting models to both disk-integrated and disk-resolved measurements (Helfenstein et al. 1988). In general, the effects of macroscopic roughness are most pronounced at large solar phase angles. However, it is difficult to derive separately the single particle phase function

and roughness, since both quantities show the largest effects at large solar phase angles. In disk-resolved observations, roughness is most strongly manifested by limb-darkening behavior and it is most reliably distinguished on low-albedo surfaces. Unfortunately, in high-albedo surfaces, multiple-scattering of light between regolith grains, introduces additional limb-darkening effects that can complicate the recognition of effects due to roughness. Especially for very high albedo objects, like Enceladus and Europa, one might expect that different roughness estimates could be obtained depending on which model of volumetric multiple scattering was assumed.

*Physical Interpretability:* Two critical obstacles to the meaningful interpretation of photometric roughness are necessarily limited by the extent to which idealized shapes conform to actual geological features and the tendency of multiply-reflected light to mute the detectable roughness selectively at different size scales depending on the albedo of the surface. No model fully replicates the full range of features found on a planetary surface. Roughness models peer into the topography of the surface *below the resolution limit of the camera*. However the smallest-sized features that contribute to detectable photometric roughness effects depend on the size scale at which projected shadows become dark. Recent work shows that for low-albedo objects like the moon, small sub-millimeter scale features dominate (Helfenstein and Shepard 1999). For high-albedo surfaces, the size-scale at which projected shadows become dark is likely significantly larger. One consequence of this albedo selection effect is that high-albedo surfaces have a tendency to exhibit smaller amplitude photometric roughness than low-albedo surfaces. Shepard and Helfenstein (2007) observed this effect in laboratory tests on a variety of soil samples and found a systematic decrease of photometrically derived values of  $\theta$  with increasing  $\omega_o$ . A further consequence is that the types of geological structures that dominate photometric roughness likely change with size scale. On low albedo surfaces, these appear to be aggregates of regolith grains; however, on bright icy satellites, they may be tiny (perhaps centimeter or larger) impact craters.

### 2.3.1.4 Opposition Effect

Airless planetary bodies typically exhibit a sharp increase in brightness as the phase angle approaches zero. This ‘opposition effect’ is due to both shadow hiding and a constructive interference phenomenon known as coherent backscatter. The disappearance of mutual shadows cast by particles comprising the regolith (Irvine 1966; Hapke 1986) is most pronounced at phase angles less than  $20^\circ$  (cf. Helfenstein et al. 1988) and is related to the size distribution of regolith grains, their transparency, the porosity of the surface, and the rate at which porosity changes with depth. At the smallest phase angles ( $\alpha < 20^\circ$ ), the coherent backscatter opposition effect (CBOE) occurs when photons following identical but reversed paths in the regolith interfere constructively in the backscattering direction to increase the brightness by up to a factor of two (Shkuratov 1988; Muinonen 1990; Hapke 1990; Mishchenko 1992; Ozrin 1992). While the shadow hiding opposition effect (SHOE) affects only singly

scattered photons, coherent backscatter affects multiply scattered photons, but because multiple scattering can occur within the internal structure of single particles, the Hapke model allows it to amplify both the singly and multiply scattered light (Hapke 2002; Hapke et al. 2009; Helfenstein et al. 1997; Helfenstein and Shepard 2011). If whole regolith grains are the dominant fundamental scatterers of light in a regolith, then CBOE should be important mostly for bright icy surfaces such as Europa and Enceladus. Yet while they are dark in comparison to those objects, the uranian satellites (Karkoschka 2001) and Phoebe (Miller et al. 2011) also have strong opposition surges (Fig. 2.1) attributed to CBOE, and a significant CBOE contribution is seen even in lunar soils (Hapke et al. 1993, 1998; Helfenstein et al. 1997; Shkuratov et al. 1999). In Hapke's 2002 treatment, both CBOE and SHOE are each characterized by an amplitude and an angular width term:  $B_{o,sh}$  and  $h_{sh}$  for the SHOE respectively, and  $B_{o,cb}$  and  $h_{cb}$  for CBOE.

*Physical Interpretability:* The SHOE amplitude, can be interpreted as a measure of regolith grain transparency. The value of  $B_{o,sh}$  can range from unity for perfectly opaque grains, to nearly zero for ideally transparent grains. While the SHOE angular width depends on a variety of aspects of grain packing and size distribution, to simplify interpretation in planetary photometric analyses, it is often assumed that over the shallow depth to which optical radiation probes, regolith grains have a uniform size and packing with depth. Under these assumptions,  $h_{sh}$  is strictly a function of the porosity: In Hapke (1986),  $h_{SH} = -0.375 \ln(1-\phi)$ , where  $\phi$  is known as the packing-factor and porosity  $p = (1-\phi)$ . However, Hapke (2008) noted that this expression is only partly correct. After updating to be consistent with Hapke's porosity correction, Helfenstein and Shepard (2011) determined that

$$h_{SH} = -0.3102 \phi^{1/3} \ln(1 - 1.209\phi^{2/3}) \quad (2.3)$$

The angular width parameter of the CBOE,  $h_{cb}$ , is primarily sensitive to the mean optical path length of a photon through the regolith. It is thus sensitive to the optical transparency of regolith grain materials, and the arrangement of scatterers both within the regolith and within individual grains in the regolith. Relatively long path lengths are needed to produce a narrow CBOE. The amplitude of the CBOE is sensitive to the intensity of multiple scattering, and to first order should be largest for regoliths (or regolith grains) containing high densities of high-albedo scatterers.

### 2.3.1.5 Summary of Current Limitations of the Hapke Model

At present, there has been only one published laboratory validation (Helfenstein and Shepard 2011) of Hapke's (2008) correction for the effects of porosity. That study successfully predicted reflectances of well-characterized powders composed of spherical particles with known optical properties given *a priori* knowledge of the packing and size-distribution. However, to date, no blind test that demonstrates successful accurate retrieval of optical and physical sample properties using the Hapke (2008)

**Table 2.2** Fits of different Hapke model versions to Europa's (0.55  $\mu\text{m}$ ) phase curve<sup>a</sup>

Hapke model	$\omega_o$	$h_{sh}$	$B_{0,sh}$	$h_{cb}$	$B_{0,cb}$	$g$	$\theta$	Residual
1986	0.966	0.00054	1.000	NA	NA	-0.39	16°	0.00119
1993	0.965	0.00053	0.97	NA	NA	-0.39	17°	0.00114
2002	0.952	0.625	1.00	0.0016	0.49	-0.25	18°	0.000993
2008	0.917	0.237	0.49	0.0013	0.47	-0.21	22°	0.000634

<sup>a</sup>Adapted from Helfenstein et al. (in preparation)

correction has been published. Hence, the validity of any physical interpretations of Hapke model fits to icy satellite surfaces to date remains questionable.

It is interesting to compare how different versions of the Hapke model perform on a well-defined phase curve, Table 2.2 and Fig. 2.3 show a preliminary fit of Hapke (2008) to phase curve data for Europa in comparison to fits using earlier versions of the Hapke model to the same data set. Hapke (2008) fits the data better than any of the previous models. All of the fits to the Europa phase curve similarly require a moderately rough surface ( $16^\circ \leq \theta \leq 22^\circ$ ) composed of relatively high-albedo ice grains ( $0.952 \leq \omega_o \leq 0.975$ ). However, the fits differ most significantly in terms of the way they resolve the opposition effect and the particle phase function. The 2008 and 2002 models both incorporate the same physical description of CBOE and SHOE. Both resolve the total opposition effect into a narrow angular contribution from CBOE and a relatively broad contribution from SHOE. For the 2008 model, the SHOE angular width is only about 49% as wide and only 38% as intense as for the 2002 model fit. In terms of implied regolith properties, the 2008 model is consistent with a porosity of about 53% among transparent particles, while the 2002 model predicts a more compacted regolith with a porosity of less than 20% among opaque particles. Both of these models work with a moderately backscattering ( $-0.25 \leq g \leq -0.27$ ) ice grains. Modeling only the SHOE, the Hapke 1981, 1984, and 1986 equations all lack a description of CBOE. Consequently, they manage to fit the Europa data set by forcing the SHOE angular width to fit the narrow (i.e. CBOE) component and by forcing the particle phase function to be strongly backscattering enough to describe the broad SHOE behavior (that was described by SHOE in the 2002 and 2008 models). In other words, the introduction of a separate CBOE model in 2002 provided the SHOE model the freedom to describe a broader component of the opposition effect (cf. Helfenstein et al. 1997; Hapke et al. 1998). In terms of implied regolith properties, these older models predict an unrealistically large porosity (>99%) among opaque regolith grains (cf. Domingue et al. 1991). In summary, among all four model fits, Hapke (2008) is intuitively most realistic because it best describes scattering among bright transparent ice particles (as opposed to implausible opaque grains), and does not require an exotic regolith porosity.

The above demonstration is by no means proof that the Hapke (2008) model is fully correct. As described previously, even with the correction from Hapke (2008), a primary remaining deficiency is the failure of the macroscopic roughness model to account for the effects of multiple reflections from topographic facets. More critical

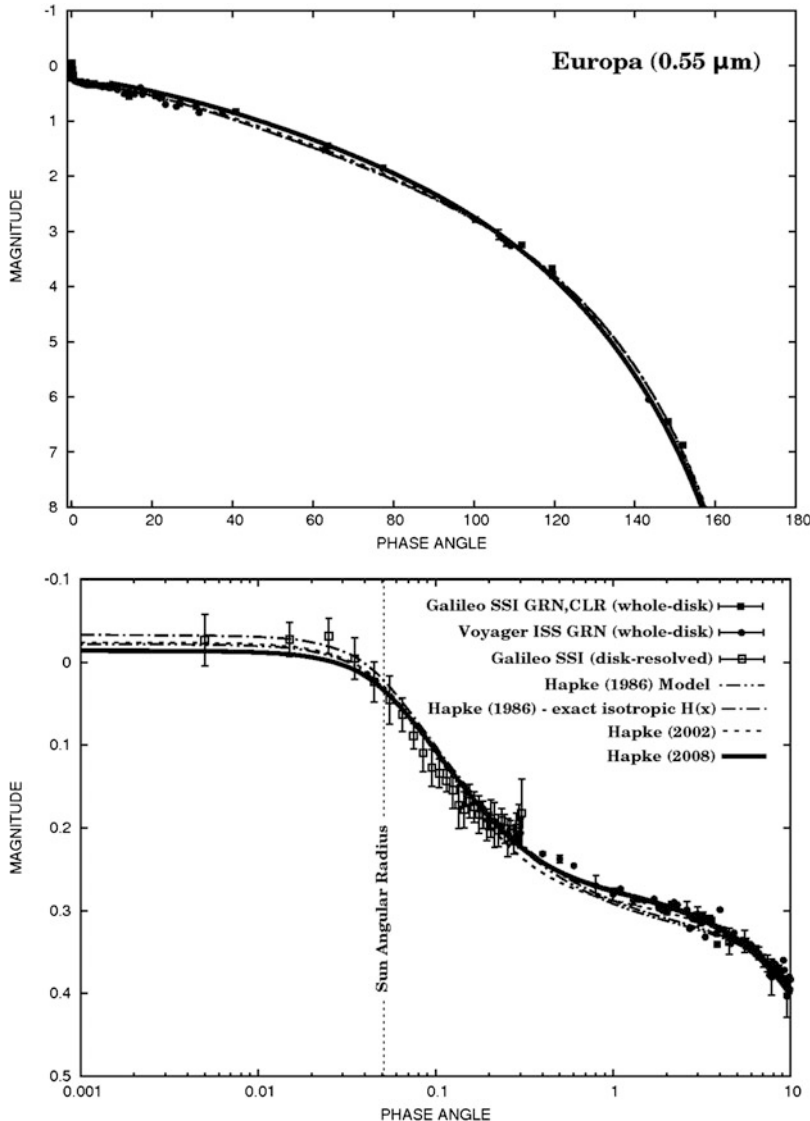


**Fig. 2.3** Fits of different versions of Hapke’s photometric model (Table 2.2) to Europa’s phase curve (Helfenstein et al. in preparation). Observations combine Voyager ISS, Galileo SSI, and Earth based telescopic data. (top) Section of phase curve at phase angles less than  $10^\circ$  show details of the opposition effect (note logarithmic scale for phase angles). (bottom) Phase curve plotted out to large phase angles. Differences in the phase curve behavior predicted by the different model fits are relatively small

is the potentially fundamental flaw in the Hapke model revealed by laboratory work (Piatek et al. 2004): the Hapke model treats whole regolith grains as the fundamental light-scattering units in planetary soils. Laboratory work by Piatek et al. suggests that the smaller constituents of regolith particles (particle inclusions, crystal

defects, voids, particle surface asperities, and minute dust particles that coat larger grains) may play a more fundamental role in controlling light scattering from typical regolith surfaces.

### 2.3.2 Quasi-fractal Photometric Models

At submillimeter size scales, undisturbed lunar regoliths and presumably regoliths on other airless bodies, exhibit a fractal architecture (cf. Helfenstein and Shepard 1999). It is thus not surprising that photometric models which attempt to treat regolith surfaces realistically as fractal structures have recently been under development (Drossart 1993; Shkuratov et al. 1999; Shkuratov and Helfenstein 2001). The most recent of these sought to develop a realistic model that can account for the simultaneous contributions of SHOE and CBOE in planetary regoliths. By their nature, these models overcome an important limitation of the Hapke model by allowing for the possibility that microscopic dust coating regolith grains, grain imperfections, surface asperities, inclusions may be important fundamental scatterers in regoliths. Shkuratov et al. (1999) introduced a semi-empirical three-parameter photometric model that treats the regolith as a topographically faceted structure with roughness that varies with size scale according to fractal-like statistics (see also Shkuratov et al. 1991). The three model parameters are  $d$ , the approximate diameter of an individual scatterer in the regolith,  $k$ , a semi-empirical parameter that characterizes the shape of the shadow-hiding opposition surge, and a coherent-backscatter parameter  $L$  that represents the diffusion scale-length of photons through the regolith. The model accurately described the lunar opposition effect seen by the *Clementine* spacecraft, as well as the opposition phase curves of asteroids, Phobos, and laboratory analogs. Perhaps the most valuable aspect of this study was its robust model for the CBOE.

#### 2.3.2.1 The Shkuratov-Helfenstein (S-H) Model

Shkuratov and Helfenstein (2001), building on Shkuratov et al. (1999), developed an improved fractal-based light-scattering model that incorporates parts of the Hapke model to replace some of the semi-empirical components. While they adopted the fairly rigorous coherent-backscatter model and the treatment of a fractally faceted surface at large scales from Shkuratov et al. (1991), they more realistically treat regolith grains as fractally-structured aggregates composed of minute “elemental” scatterers. They also incorporate Hapke’s (1986) more rigorous treatment of SHOE.

The elemental scatterers in their analytical approximation of a regolith aggregate are assumed to be isotropically scattering grains with a model average single-scattering albedo,  $\omega_o$ . The relative size and structural complexity of the regolith is characterized by a number of hierarchical generations,  $\eta$ , that must be assembled

to form a regolith with the correct albedo and directional scattering behavior.<sup>2</sup> In this fractal model, the parameter  $\eta$  need not be an integer and can have values less than unity (for example, for icy regolith aggregates that are not perfectly opaque). The model also combines the CBOE and SHOE and describes the way SHOE is manifested on a fractally arranged surface. It employs Hapke's  $h$  parameters to describe the angular width of the SHOE and Shkuratov's coherent backscatter parameter  $L$ .

*Physical Interpretability of S-H Parameters:* As stated earlier, the single scattering albedo parameter,  $\omega_o$ , in this model differs from that in the Hapke model in that it characterizes elemental scatterers from which whole regolith grains are composed. In the Hapke model, the single-scattering albedo refers to the albedo of an average whole regolith grain. The equivalent quantity can be computed in the S-H model (see Fig. 2.4 in Shkuratov and Helfenstein 2001) given the other three S-H parameters. The  $h$ -parameter has the same meaning and interpretation as it does in Hapke (1986). It measures the angular width of the SHOE and is related to the compaction state of the regolith. The characteristic diffusion length,  $L$ , is analogous to the mean optical path length of a photon in the aggregate. In general, larger values of  $L$  correspond to narrower CBOE angular widths and greater permeability of regolith materials to scattered photons. Finally, the fractal generation number,  $\eta$ , is a measure of the structural complexity of the regolith. When  $\eta \geq 1$ , the aggregates are large and structurally complex enough to be opaque. The case where  $\eta = 0$  is the limiting condition most like the Hapke model because it represents a regolith in which the elemental scatterers are not aggregated at all, but instead they scatter as whole particles. For bright icy satellites, we often expect the case where  $0 < h < 1$ , because this represents an aggregate that is not large and complex enough to be opaque (that is, in this case the regolith grains are partially transparent or translucent).

To date, the S-H model has not been extensively applied to planetary objects for two main reasons. First, until recently, relatively few photometric data sets offered sufficiently detailed phase angle coverage. Meaningful fits of the S-H model require observations at phase angles small enough to detect the CBOE (usually seen at  $\alpha < 2^\circ$ ), and the coverage need so extend far enough beyond the SHOE to characterize its shape fully (generally through  $\alpha > 20^\circ$ ). In addition, the model needs further refinement to improve its accuracy for describing photometric behavior at very large phase angles ( $\alpha > 120^\circ$ ).

Figure 2.4 and Table 2.2 show trial fits of the S-H model to several objects that cover a range of albedos. These include fits using a revised model that incorporates Hapke's (2008) porosity correction and elemental scatterers that are slightly

---

<sup>2</sup> In Shkuratov and Helfenstein (2001), the symbol  $q$  was used to represent the fractal generation number of the regolith. To avoid confusion with the symbol for phase integral, we adopt the symbol  $\eta$  here.

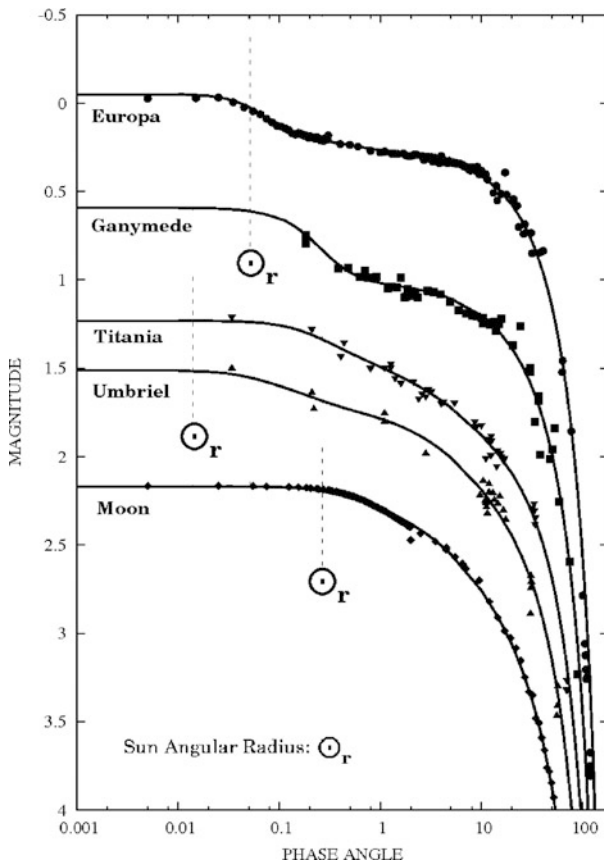


**Fig. 2.4** Fits of the Shkuratov-Helfenstein model (Table 2.3) to five objects that have different albedos. Details of fits to the opposition effect are shown (note logarithmic scale for phase angle). Good fits to the opposition effect portion of each phase curve were achieved in all cases. Phase curves and fits plotted to large phase angles show that the model seldom fits well at phase angles larger than 90°. Plots adapted from Helfenstein and Shkuratov (in preparation)

**Table 2.3** Example values of Shkuratov-Helfenstein model parameters for selected objects<sup>a</sup>

Object	$\omega_o$	$h_{sh}$	$L$	$\eta$	$(g_1, g_2, f)$
<b>Shkuratov and Helfenstein (2001)</b>					
<b>Moon</b>	0.66	0.05	25	1.50	0,0,0
<b>Titania</b>	0.85	0.05	69	0.56	0,0,0
<b>Helfenstein and Shkuratov (2011)</b>					
<b>Moon</b>	0.633	0.077	12	1.18	0, -0.995, $1.0 \times 10^{-6}$
<b>Umbriel</b>	0.881	0.065	100	0.93	0, -0.995, $1.0 \times 10^{-5}$
<b>Titania</b>	0.913	0.101	6.8	0.43	0, -0.995, $1.0 \times 10^{-5}$
<b>Ganymede</b>	>0.999998	0.243	2414	0.35	0, -0.995, $1.0 \times 10^{-5}$
<b>Europa</b>	>0.999998	0.507	12	0.34	0, -0.999, $2.5 \times 10^{-7}$

<sup>a</sup>Adapted from Helfenstein and Shkuratov (in preparation)

non-isotropic<sup>3</sup> (Helfenstein and Shepard, in preparation). These improvements were especially needed to obtain good fits to Europa’s phase curve. Unfortunately, this approach introduced ambiguity between what portion of the CBOE is due to scattering in the aggregate and what part is intrinsic to the elemental scatterers.

Table 2.2 indicates that the elemental scatterers have relatively large values of  $\omega_o$  even for dark objects like the Moon and Umbriel, although they are systematically lower than for the brighter icy satellites (Titania, Ganymede, and Europa). Values of the fractal parameter  $\eta$  are near or greater than unity for the darkest objects (the Moon and Umbriel) implying opaque, complexly structured aggregates. In contrast, for the bright icy satellites (Europa, Ganymede, Titania),  $\eta$  is significantly less than unity, implying that the bright icy aggregates are not large or structurally complex enough to become completely opaque. The angular width of the SHOE systematically gets wider for brighter objects than for darker ones. A naïve interpretation would be that regoliths on brighter icy objects are systematically more compacted than on low-albedo bodies. However, a more plausible explanation is that the much greater amount of multiply-scattered light in high-albedo regoliths mutes or renders undetectable the SHOE, except perhaps at very large size scales where surface structures can become opaque. There appears to be no clear systematic dependence of  $L$  on regolith type. This differs from results in Shkuratov et al. (1999) and Shkuratov and Helfenstein (2001), where  $L$  in general, is found to be systematically longer for brighter objects than for darker objects (presumably because bright relatively transparent ice grains are generally more permeable to photons than dark absorbing ones). However, in the new fits in Table 2.2, the result is likely due to ambiguities resulting both from allowing elemental scatterers to exhibit their own opposition surges and the limited ability to detect the SHOE on bright objects.

## 2.4 Implications for Planetary Science

Given the recent challenges to the utility of photometry as a tool to discern actual physical surface properties, what can we learn about icy surfaces from the application of the best available photometric models? We can assess the populations of icy bodies in the Solar System in terms of the albedo, color, and phase function and connect these fundamental physical properties to their thermal and weathering histories. Impacts with dusty ring particles serve to enhance the phase functions of the saturnian satellites, yet the process by which the uranian satellite phase functions are enhanced is not known. Do the major satellites of Uranus reside within a tenuous, dark ring? Ejecta exchange between binary (or more) TNO

---

<sup>3</sup> Helfenstein and Shkuratov’s (in preparation) fits from Table 2.3 use a 3THG function for the elemental scatterers, modeling scatterers that are almost entirely isotropic ( $g_1=0$ ), with only a small fraction ( $1\times 10^{-7}$ – $1\times 10^{-5}$ ) contributed from a non-isotropic extremely narrow backscattering spike (i.e.  $g_2 \leq -0.995$ ).

systems may be an alternative mechanism by which phase functions are enhanced (Stern 2009; Rabinowitz et al. 2009). What conclusions can we draw from the fact that several dwarf planets are as bright as the major giant planet satellites and nowhere near as dark as the “typical” residents in the classical Kuiper belt? Do they also have steep phase functions like the giant planet satellites? Only observations at phase angles close to zero will tell; however, node crossings for these bodies do not occur until decades from now.

## 2.5 Summary and Future Work

Future laboratory work will certainly advance the application of photometric models to observations of icy surfaces in the Solar System. The Hapke (2008) correction for the effects of porosity should follow the preliminary test published by Helfenstein and Shepard (2011).

The successful completion of several upcoming spacecraft missions will supply key observations of icy surfaces not yet seen at spatial resolutions exceeding those attainable by the newly refurbished *Hubble Space Telescope*. Foremost among these are the images anticipated from the *New Horizons* spacecraft as it makes the first reconnaissance of a dwarf planet, Pluto and its satellites Charon, Nix, and Hydra in 2015. Following the Pluto flyby, *New Horizons* plans to target at least one additional Kuiper belt object.

The *Cassini* spacecraft has begun the final phase of its exploration of the Saturn system which will continue until the next Saturn solstice in 2017. To date, the mission has returned hundreds of thousands of images of Saturn’s rings and satellites; the “Solstice” mission will add to an already incredibly rich data set, expanding the coverage in illumination and viewing angles across the visible and near-infrared spectrum for the icy surfaces in Saturn’s realm.

The Atacama Large Millimeter Array (ALMA) will measure diameters for hundreds of TNOs, making possible determinations of their geometric albedos and ultimately the distribution of mass throughout the Solar System beyond the orbit of Neptune.

## References

- Bauer J et al (2003) Physical survey of 24 Centaurs with visible photometry. *Icarus* 166:195  
Boehnhardt H et al (2008) Photometry and polarimetry of the nucleus of comet 2P/Encke. *Astron Astrophys* 489:1337  
Brucker MJ et al (2009) High albedos of low inclination classical Kuiper belt objects. *Icarus* 201:284  
Buie MW, Grundy WM, Young EF, Young LA, Stern SA (2010) Pluto and Charon with the *Hubble Space Telescope*. I. Monitoring global change and improved surface properties from light curves. *Astron J* 139:1117  
Buratti BJ, Veverka J (1985) Photometry of rough planetary surfaces – the role of multiple scattering. *Icarus* 64:320

- Buratti BJ et al (2008) Infrared (0.83–5.1  $\mu\text{m}$ ) photometry of Phoebe from the Cassini visual infrared mapping spectrometer. *Icarus* 193:309
- Buratti BJ et al (2011) Photometry of Triton 1992–2004: Surface volatile transport and discovery of a remarkable opposition surge. *Icarus* 212:835
- Chandrasekhar S (1960) Radiative transfer. Dover, New York
- Chernova GP, Lupishko DF, Shevchenko VG (1994) Photometry and polarimetry of the asteroid 24 Themis. *Kinemat Phys Neb Tel* 10:45
- Davies JK, McBride N, Ellison SL, Green SF, Ballantyne DR (1998) Visible and infrared photometry of six Centaurs. *Icarus* 134:213
- Domingue D, Verbiscer A (1997) Re-analysis of the solar phase curves of the icy Galilean satellites. *Icarus* 128:49
- Domingue DL, Hapke BW, Lockwood GW, Thompson DT (1991) Europa's phase curve – implications for surface structure. *Icarus* 90:30
- Drossart P (1993) Optics on a fractal surface and the photometry of the regoliths. *Plan Space Sci* 41:381
- Fernandez Y, Sheppard SS, Jewitt DC (2003) The albedo distribution of Jovian Trojan asteroids. *Astron J* 126:1563
- French RG et al (2007) Saturn's rings at true opposition. *Pub Astron Soc Pacific* 119:623
- Gladman B, Marsden BG, Vanlaerhoven C (2008) Nomenclature in the outer solar system. In: Barucci MA et al (eds) University of Arizona Press, Tucson, p 43
- Goguen J (1981) A theoretical and experimental investigation of the photometric functions of particulate surfaces. Ph.D. Thesis, Cornell University, Ithaca
- Goguen JD, Stone TC, Kieffer HH, Buratti BJ (2010) A new look at photometry of the Moon. *Icarus* 208:548
- Gunderson K, Thomas N, Whitby JA (2006) First measurements with the Physikalisch Institut Radiometric Experiment (PHIRE). *Plan Space Sci* 54:1046
- Hapke B (1981) Bidirectional reflectance spectroscopy. 1. Theory. *J Geophys Res* 86:565
- Hapke B (1984) Bidirectional reflectance spectroscopy. III – Correction for macroscopic roughness. *Icarus* 59:41
- Hapke B (1986) Bidirectional reflectance spectroscopy. IV – The extinction coefficient and the opposition effect. *Icarus* 67:264
- Hapke B (1990) Coherent backscatter and the radar characteristics of outer planet satellites. *Icarus* 88:407
- Hapke B (1993) Theory of reflectance and emittance spectroscopy. Cambridge University Press, New York
- Hapke B (2002) Bidirectional reflectance spectroscopy. 5. The coherent backscatter opposition effect and anisotropic scattering. *Icarus* 157:523
- Hapke B (2008) Bidirectional reflectance spectroscopy. 6. Effects of porosity. *Icarus* 195:918
- Hapke BW, Nelson RM, Smythe WD (1993) The opposition effect of the moon – the contribution of coherent backscatter. *Science* 260:509
- Hapke B, Nelson R, Smythe W (1998) The opposition effect of the Moon: coherent backscatter and shadow hiding. *Icarus* 133:89
- Hapke B, Shepard MK, Nelson RM, Smythe W, Piatek J (2009) A quantitative test of the ability of models based on the equation of radiative transfer to predict the bidirectional reflectance of a well-characterized medium. *Icarus* 199:210
- Harris AW et al (1989) Photoelectric observations of asteroids 3, 24, 60, 261, and 863. *Icarus* 77:171
- Helfenstein P (1986) Derivation and analysis of geological constraints on the emplacement and evolution of terrains on Ganymede from applied differential photometry. PhD thesis, Brown University, Providence
- Helfenstein P (1988) The geological interpretation of photometric surface roughness. *Icarus* 73:462
- Helfenstein P, Shepard MK (1999) Submillimeter-scale topography of the lunar regolith. *Icarus* 141:107
- Helfenstein P, Shepard MK (2011) Testing the Hapke photometric model: Improved inversion and the porosity correction. *Icarus* 215:83

- Helfenstein P, Veverka J, Thomas PC (1988) Uranus satellites – Hapke parameters from Voyager disk-integrated photometry. *Icarus* 74:231
- Helfenstein P, Veverka J, Hillier J (1997) The lunar opposition effect: a test of alternative models. *Icarus* 128:2
- Heney C, Greenstein J (1941) Diffuse radiation in the galaxy. *Ap J* 93:70
- Hillier J et al (1990) Voyager disk-integrated photometry of Triton. *Science* 250:419
- Howett CJA, Spencer JR, Pearl JC, Segura ME (2010) Thermal inertia and bolometric Bond albedo values for Mimas, Enceladus, Tethys, Dione, Rhea and Iapetus as derived from Cassini/CIRS measurements. *Icarus* 206:573
- Irvine WM (1966) The shadowing effect in diffuse reflection. *J Geophys Res* 71:2931
- Kaasalainen S et al (2003) Asteroid photometric and polarimetric phase curves: empirical interpretation. *Icarus* 161:34
- Karkoschka E (2001) Comprehensive photometry of the rings and 16 satellites of Uranus with the Hubble Space Telescope. *Icarus* 151:51
- Kattawar GW (1975) A three-parameter analytic phase function for multiple scattering calculations. *J Quant Spectr Rad Trans* 15:839
- Lambert JH (1760) *Photometria*. W. Engelmann, Leipzig
- Lazzaro D et al (1997) Photometric monitoring of 2060 Chiron's brightness at perihelion. *Plan Space Sci* 45:1607
- Lebofsky LA, Spencer JR (1989) Systematic biases in radiometric diameter determinations. In: Binzel RP et al (eds) *Asteroids II*. University of Arizona Press, Tucson, p 128
- Li J-Y et al (2007a) Deep Impact photometry of Comet 9P/Tempel 1. *Icarus* 187:41
- Li J-Y, A'Hearn MF, McFadden LA, Belton MJS (2007b) Photometric analysis and disk-resolved thermal modeling of Comet 19P/Borrelly from Deep Space 1 data. *Icarus* 188:195
- Li J-Y, A'Hearn MF, Farnham TL, McFadden LA (2009) Photometric analysis of the nucleus of Comet 81P/Wild 2 from Stardust images. *Icarus* 204:209
- Lumme K, Bowell E (1981) Radiative transfer in the surfaces of atmosphere less bodies. I – Theory. II – Interpretation of phase curves. *Astron J* 86:1694
- Lumme K, Bowell E (1985) Photometric properties of zodiacal light particles. *Icarus* 62:54
- Luu J, Jewitt D (1996) Color diversity among the Centaurs and Kuiper belt objects. *Astron J* 112:2310
- McGuire A, Hapke B (1995) An experimental study of light scattering by large, irregular particles. *Icarus* 113:134
- Miller C, Verbiscer AJ, Chanover N, Holtzman J, Helfenstein P (2011) Comparing Phoebe's 2005 opposition surge in four visible light filters. *Icarus* 212:819
- Minnaert M (1941) The reciprocity principle in lunar photometry. *Ap J* 93:403
- Mishchenko MI (1992) The angular width of the coherent back-scatter opposition effect - an application to icy outer planet satellites. *Astrophys Space Sci* 194:327
- Muinonen K (1990) Light scattering by inhomogeneous media: backward enhancement and reversal of linear polarization. PhD thesis, Helsinki University, Helsinki
- Müller TG et al (2010) "TNOs are cool": A survey of the trans-Neptunian region. I. Results from the Herschel science demonstration phase (SDP). *Astron Astrophys* 518:146
- Ozrin VD (1992) Exact solution for coherent backscattering of polarized light from a random medium of Rayleigh scatterers. *Waves Random Med* 2:141
- Paranicas C, Cooper JF, Garrett HB, Johnson RE, Sturmer SJ (2009) Europa's radiation environment and its effects on the surface. In: Pappalardo RT et al (eds) *Europa*. University of Arizona Press, Tucson, p 529
- Piatek J, Hapke BW, Nelson RM, Smythe WD, Hale AS (2004) Scattering properties of planetary regolith analogs. *Icarus* 171:531
- Pitman KM, Buratti BJ, Mosher JA (2010) Disk-integrated bolometric Bond albedos and rotational light curves of Saturnian satellites from Cassini Visual and Infrared Mapping Spectrometer. *Icarus* 206:537
- Rabinowitz DL et al (2006) Photometric observations constraining the size, shape, and albedo of 2003 EL61, a rapidly rotating, Pluto-sized object in the Kuiper belt. *Ap J* 639:1238

- Rabinowitz DL, Schaefer BE, Tourtellotte SW (2007) The diverse solar phase curves of distant icy bodies. I. Photometric observations of 18 trans-Neptunian objects, 7 Centaurs, and Nereid. *Astron J* 133:26
- Rabinowitz DL, Schaefer B, Schaefer M, Tourtellotte S (2009) Evidence for recent resurfacing of the binary Kuiper belt object 1997 CS29. *BAAS* 41:6509
- Rousselot P, Petit JM, Poulet F, Sergeev A (2005) Photometric study of Centaur (60558) 2000 EC98 and trans-Neptunian object (55637) 2002 UX25 at different phase angles. *Icarus* 176:478
- Schaefer BE, Tourtellotte SW, Rabinowitz DL, Schaefer MW (2008) Nereid: Light curve for 1999 2006 and a scenario for its variations. *Icarus* 196:225
- Schaefer MW, Schaefer BE, Rabinowitz DL, Tourtellotte SW (2010) Phase curves of nine Trojan asteroids over a wide range of phase angles. *Icarus* 207:699
- Shepard MK, Campbell BA (1998) Shadows on a planetary surface and implications for photometric roughness. *Icarus* 134:279
- Shepard MK, Helfenstein P (2007) A test of the Hapke photometric model. *J Geophys Res* 112: E03001
- Shevchenko VG et al (2009) Do Trojan asteroids have the brightness opposition effect? *Lunar Plan Sci Conf* 40:1391
- Shkuratov YG (1988) A diffraction mechanism for the formation of the opposition effect of the brightness of surfaces having a complex structure. *Kinemat Phys Neb Tel* 4:33
- Shkuratov Y, Helfenstein P (2001) The opposition effect and the quasi-fractal structure of regolith: I. Theory. *Icarus* 152:96
- Shkuratov Y et al (1991) A possible interpretation of bright features on the surface of Phobos. *Plan Space Sci* 39:341
- Shkuratov Y, Starukhina L, Hoffman H, Arnold G (1999) A model of spectral albedo of particulate surfaces: implications for optical properties of the Moon. *Icarus* 137:235
- Shkuratov Y et al (2007) Photometry and polarimetry of particulate surfaces and aerosol particles over a wide range of phase angles. *J Quan Spectr Rad Trans* 106:487
- Sicardy B et al (2011) A Pluto-like radius and a high albedo for the dwarf planet Eris from an occultation. *Nature* 478:493
- Soderblom LA et al (1990) Triton's geyser-like plumes – discovery and basic characterization. *Science* 250:410
- Souchon A et al (2011) An experimental study of Hapke's modeling of natural granular surface samples. *Icarus* 215:313
- Spencer JR (1987) Thermal segregation of water ice on the Galilean satellites. *Icarus* 69:297
- Spencer JR et al (2006) Cassini encounters Enceladus: background and the discovery of a south polar hot spot. *Science* 311:1401
- Stansberry J et al (2008) Physical properties of Kuiper belt and Centaur objects: constraints from the Spitzer Space Telescope. In: Barucci MA et al (eds) *The solar system beyond Neptune*. University of Arizona Press, Tucson, p 592
- Stern SA (2009) Ejecta exchange and satellite color evolution in the Pluto system, with implications for KBOs and asteroids with satellites. *Icarus* 199:571
- Verbiscer A (1991) Photometry of icy satellite surfaces, Ph.D. Thesis, Cornell University, Ithaca
- Verbiscer A, Helfenstein P (1998) Reflectance spectroscopy of icy surfaces. In: Schmitt B et al (eds) *Solar system ices*. Kluwer, Dordrecht, p 157
- Verbiscer A, Veverka J (1989) Albedo dichotomy of Rhea – Hapke analysis of Voyager photometry. *Icarus* 82:336
- Verbiscer A, Veverka J (1992) Mimas – photometric roughness and albedo map. *Icarus* 99:63
- Verbiscer A, Veverka J (1994) A photometric study of Enceladus. *Icarus* 110:115
- Verbiscer A, Helfenstein P, Veverka J (1990) Backscattering from frost on icy satellites in the outer solar system. *Nature* 347:162
- Verbiscer A, French RG, Showalter M, Helfenstein P (2007) Enceladus: Cosmic graffiti artist caught in the act. *Science* 315:815
- Verbiscer AJ, Skrutskie MF, Hamilton DP (2009) Saturn's largest ring. *Nature* 461:1098
- Verbiscer AJ, Fisher TM, French RG (2010) The strongest opposition surges: products of ejecta exchange? *BAAS* 42:957

# Chapter 3

## Ultraviolet Properties of Planetary Ices

A.R. Hendrix, D.L. Domingue, and K.S. Noll

**Abstract** Ultraviolet measurements of planetary ices have been pursued since the earliest days of the space program and have proved useful and enlightening, particularly when combined with measurements at longer wavelengths. This chapter provides a brief history of spacecraft measurements of planetary ices in the UV, a review of laboratory experiments and measurements, and an overview of the significant results from solar system observations.

### 3.1 Introduction

Ultraviolet measurements of planetary ices have been pursued since the earliest days of the space program. While UV observations have often focused on gases and emission processes, measurements of icy surfaces have proved useful and enlightening, particularly when combined with measurements at longer wavelengths. This chapter provides a brief history of spacecraft measurements of planetary ices in the UV, a review of laboratory experiments and measurements, and an overview of the significant results from solar system observations. For reference, we define the wavelength ranges used in this report in Table 3.1, using the ISO definitions (ISO report 2007).

---

A.R. Hendrix (✉)

Jet Propulsion Laboratory, California Institute of Technology, Pasadena, CA 91109, USA  
e-mail: [arh@jpl.nasa.gov](mailto:arh@jpl.nasa.gov)

D.L. Domingue

Planetary Science Institute, 1700 E. Fort Lowell, Suite 106, Tucson, AZ 85719-2395, USA  
e-mail: [domingue@psi.edu](mailto:domingue@psi.edu)

K.S. Noll

Space Telescope Science Institute, Baltimore, MD, USA

**Table 3.1** Ultraviolet spectral ranges

Name	Wavelength range (nm)
EUV (extreme ultraviolet)	10–121
FUV (far ultraviolet)	122–200
MUV (middle ultraviolet)	200–300
NUV (near ultraviolet)	300–400

## 3.2 History of UV Observations of Icy Surfaces and Instrumentation

Prior to the dawn of the space age, spectrophotometry of solar system objects at wavelengths shorter than  $\sim 300$  nm had long been desired in order to complement observations made by ground-based telescopes at longer wavelengths. However, the presence of ozone in Earth’s atmosphere, a strong absorber of ultraviolet light between 200 and 300 nm, and molecular oxygen ( $O_2$ ), which is the dominant ultraviolet absorber below 200 nm, prevented astronomers of the 1950s and earlier from observing the universe in this important spectral region.

The ultraviolet wavelengths of astronomical sources became observable midway through the last century when instruments could be deployed above Earth’s atmosphere. For the first time, by utilizing a rocket or spacecraft platform, astronomical measurements were made above the atmosphere. Thus, the space revolution dramatically enhanced the ability of astronomers to observe the solar system with the full electromagnetic spectrum. Here we focus on instrumentation that has contributed to our understanding of solar system ices.

The Orbiting Astronomical Observatory (OAO) series of satellites, launched in the 1960s and early 1970s, made critical early measurements of many solar system objects in the UV. OAO-2 made the first-ever broad-band UV measurements (as short as 211 nm) of the icy Galilean satellites (Caldwell 1975). Those measurements showed the moons to be dark in the UV relative to the visible, and when combined with the infrared measurements indicating the presence of water ice, allowed for some early constraints on surface compositions.

The International Ultraviolet Explorer (IUE) spacecraft, a joint U.S.–European collaboration, was launched in 1978 into a geosynchronous orbit. It functioned continuously from launch until it was terminated in 1996 and its capabilities were taken over by instruments on the Hubble Space Telescope. IUE spectra were recorded in two wavelength ranges of 115–195 and 190–320 nm, with no imaging capability. IUE observations were made of a range of icy objects in the solar system, including comets and moons of Saturn. However, its measurements of the Galilean satellites stand out as being particularly significant. They helped to establish the fundamental nature of the surface compositions of these icy moons, the importance of Io’s sulfurous volcanoes and their impact on the rest of the system, and the hemispheric-scale spectral variations, with implications for exogenic processes.

The joint U.S.–European Hubble Space Telescope (HST) was launched in 1990. HST is in a low-Earth orbit, allowing upgrades to the facilities by astronauts; the low orbit reduces the observational duty cycle to 50–60% of that of IUE in high orbit.

UV spectroscopy with HST has been performed with the Goddard High-Resolution Spectrograph (GHRS), the Faint-Object Spectrograph (FOS), the Space Telescope Imaging Spectrograph (STIS), and the Advanced Camera for Surveys (ACS). The Cosmic Origins Spectrograph (COS), installed in May 2009, is now also available for observations of solar system targets. Ultraviolet HST instruments have made measurements of icy objects including the Galilean and Saturnian moons and Triton. These were the first UV spectra of these objects, and established the spectral characters of the ices and extended the wavelength coverage of IUE. These HST measurements helped to confirm the importance of radiolysis in the outer solar system, by establishing the presence of radiation products such as O<sub>3</sub> in some of these surfaces.

Many interplanetary spacecraft missions have included in their payloads ultraviolet instruments that have made measurements of solar system ices. The primary purpose of these space-bound UV instruments has been for atmospheric measurements; however, their capability in studying icy surfaces has proven extremely valuable. The Voyager project sent two spacecraft, both launched in 1977, to the outer solar system. The payload of Voyager 2 included the Ultraviolet Spectrometer (UVS) and the Photopolarimeter Experiment (PPS) (Lillie et al. 1977), which included a channel centered on 250 nm. Voyager 2 was the first spacecraft to fly by all four of the Jovian planets (Jupiter, Saturn, Uranus, and Neptune) and provided the first UV observations of the icy moons of Uranus, as well as Triton. In 1989 the Galileo spacecraft was launched. This spacecraft was the first dedicated mission to the Jupiter system and it included within its scientific instrument payload two ultraviolet spectrometers, the EUV (extreme ultraviolet spectrometer, which operated between 50 and 140 nm) and the UVS (the ultraviolet spectrometer that covered the 115–430 nm wavelength range). The UVS allowed for the first disk-resolved observations of the Galilean satellites that were critical in understanding the spatial distributions in radiation products across the surfaces of the icy moons. The Cassini mission, launched in 1997, includes the Ultraviolet Imaging Spectrograph (UVIS) and arrived at Saturn in June 2004; the mission is planned to end in 2017. The Cassini UVIS continues to make measurements of the icy moons and rings of Saturn, investigating composition and ice grain sizes. In 2004, Rosetta with its ALICE ultraviolet instrument (covering 70–205 nm) was launched en route to comet 67P/Churyumov-Gerasimenko, set to enter orbit in 2014. The New Horizons mission to Pluto, launched in January 2006, also carries an ALICE instrument, covering 52–187 nm.

### 3.3 Laboratory Measurements of Ices

Here we present a review of the current understanding of the UV spectral properties of several ice species, as measured in the laboratory. These include measurements made in absorption and in reflectance. Reflectance measurements are useful for observing the spectral properties of a particular ice sample (e.g., for a particular grain size and temperature). Measurements made in absorption can be particularly useful because the optical constants can then be derived, which are critical for spectral modeling purposes.

The ultraviolet absorption features in ices are driven by electronic transitions. For all of the species discussed here, the solid phase spectrum is more subdued compared to the gas phase spectrum due to the absence of Rydberg series in the solid phase; however, as discussed by Mason et al. (2006), pockets of crystallinity in amorphous ice can lead to fine structure in the absorption spectrum. In some ices such as NH<sub>3</sub>, and particularly H<sub>2</sub>O, the major UV absorption is blue-shifted from its position in the gas phase.

### 3.3.1 Water Ice

Water ice exhibits a strong absorption edge in the far-UV. The earliest measurement of this feature was reported by Cassel (1936), who measured ice in absorption; they measured a sharp onset in absorption at 167 nm, independent of sample thickness. This absorption peaks near 144 nm and corresponds to the A-X band in H<sub>2</sub>O vapor; another absorption peak is present near 78 nm. The measurements of Lu et al. (2008) demonstrate an increase in absorption with decreasing wavelength shortward of the 144 nm absorption peak (~110–135 nm), consistent with the Seki et al. (1981) 80 K results; Mason et al. (2006) indicate that the cross section remains roughly constant with wavelength in the ~120–127 nm region. Absorption by ice in the near- and mid-UV (~200–400 nm) is very weak. The transparent nature of ice in this spectral region makes laboratory measurements very difficult, as very thick samples are required to measure any attenuation; therefore there is a lack of optical constant information in this region of the ultraviolet. Water ice laboratory measurements in the UV that have been reported in the literature are summarized in Table 3.2.

Warren (1984) and Warren and Brandt (2008) provided compilations of optical constants derived from transmission measurements for hexagonal ice. They reviewed the results of Dressler and Schnepp (1960), Onaka and Takahashi (1968), Otto and Lynch (1970), Minton (1971), Daniels (1971), Browell and Anderson (1975) and Shibaguchi et al. (1977). In their compilation, Warren (1984) and Warren and Brandt (2008) ultimately use the data from Seki et al. (1981) for 80 K crystalline water ice in the 45–161 nm region, along with the data from Minton (1971) for ice at 223–263 K in the 180–185 nm region. As a result of the lack of optical constant information in the ultraviolet, the Warren (1984) and Warren and Brandt (2008) compilations include an interpolation between 161 and 180 nm; the Warren (1984) compilation also interpolates between 185 and 400 nm, and the Warren and Brandt (2008) compilation extrapolates between 180 and 200 nm. The Warren and Brandt (2008) compilation leaves a gap in the 200–390 nm range. These experimental results are summarized in Fig. 3.1, where we show the wavelength dependence of imaginary index of refraction  $k$  in the far-UV (after Warren 1984); we also include in this figure the results of Irvine and Pollack, whose data were included in Greenberg (1968) with no description of the experimental technique. More recent work has focused on the absorbing region shortward of ~170 nm, and the absorption peak near 144 nm: Mason et al. (2006) deposited water vapor

**Table 3.2** Ultraviolet laboratory measurements of ices: summary

Species	Publication	Wavelength range	Temperature	Measurement type	Notes
H <sub>2</sub> O	Cassel (1936)	140–180 nm	0°C	Absorption	Film thickness ~3–4 μm
	Dressler and Schnepf (1960)	140–172 nm	175 K, 77 K	Transmission	Cubic and amorphous samples
	Onaka and Takahashi (1968)	124–177 nm	133–153 K,	Transmission	Cubic and amorphous samples
			123–163 K		
Taub and Eiben (1968)		200–700 nm	–5–196°C	Irradiation	
Greenberg (1968); Irvine and Pollack (unpublished)		0.5–180 nm	?	Determination of k	
Otto and Lynch (1970)		35–248 nm	263 K	Dielectric constants measurements	Poly-crystalline hexagonal samples
Daniels (1971)		44–150 nm	78 K	Dielectric constants measurements	Amorphous sample
Minton (1971)		181–185 nm	223–263 K		Poly-crystalline hexagonal samples
Pipes et al. (1974)		140–300 nm	77 K	Reflectance	Amorphous and hexagonal samples
Browell and Anderson (1975)		147.5 nm, 161–320 nm	77 K, 155 K	Reflectance (to determine index of refraction)	Hexagonal and amorphous samples
Shibaguchi et al. (1977)		173–178 K	103 K, 253 K	Transmission	Hexagonal sample
Seki et al. (1981), Kobayashi (1983)		44–248 nm	80 K	Reflectivity of single crystal	Hexagonal, amorphous
Warren (1984)		44–2,270 nm	Within 60 K of melting point	Compilation	
Hapke et al. (1981), Wagner et al. (1987)		100–2,400 nm	?		
Sack et al. (1991)		220–550 nm	20–100 K	Reflectance	
Mason et al. (2006)		120–320 nm	25 K	Irradiation	
Warren and Brandt (2008)		44–2,270 nm	Within 60 K of melting point	Transmission Compilation	Amorphous

(continued)

**Table 3.2** (continued)

Species	Publication	Wavelength range	Temperature	Measurement type	Notes
$\text{NH}_3$	Lu et al. (2008)	110–192 nm	10 K	Transmission	
	Goguen et al. (unpublished)	11–200 nm	100 K	Reflectance	
	Dressler and Schnepp (1960)	140–220 nm	125 K, 77 K	Transmission	Cubic and amorphous samples
	Martonchik et al. (1984)			Compilation	
	Pipes et al. (1974)	140–300 nm	77 K	Reflectance	Amorphous and cubic samples
	Browell and Anderson (1975)	140–320 nm	77 K, 155 K	Reflectance (to determine index of refraction)	
$\text{CO}_2$	Hapke et al. (1981), Wagner et al. (1987)	100–2,400 nm	?	Reflectance	
	Davies et al. (2007), Mason et al. (2006)	130–205 nm	25, 75, 80, 90 K	Transmission	
	Warren (1986)			Compilation	
$\text{CH}_4$	Hansen (2005)	174–1800 nm		Transmission	
	Dressler and Schnepp (1960)	130–155 nm	175 K, 77 K	Transmission	
$\text{SO}_2$	Hapke et al. (1981), Wagner et al. (1987)	100–2,400 nm	?	Reflectance	

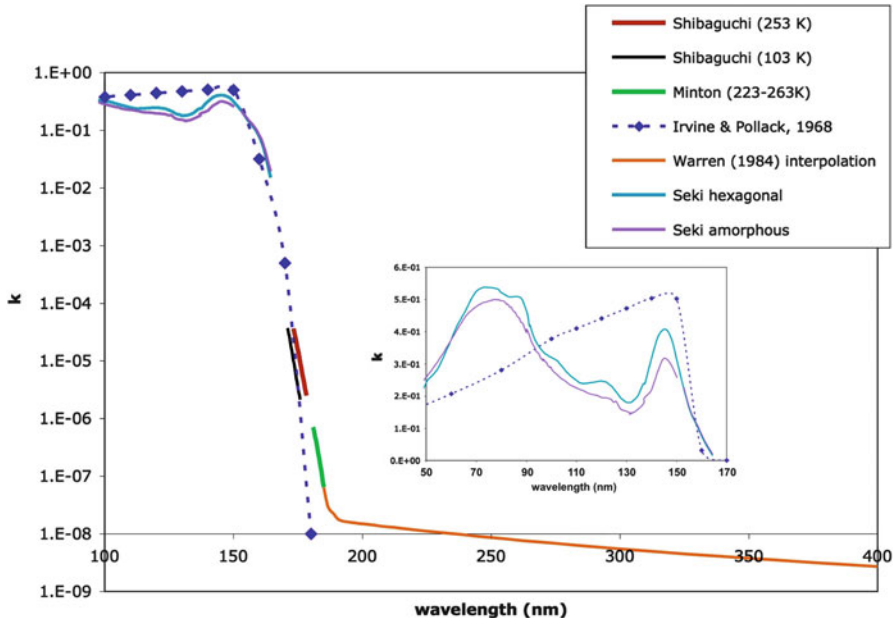


**Fig. 3.1** Reproduction of Fig. 3.2 of Warren (1984), showing measurements of the  $\text{H}_2\text{O}$  imaginary refractive index  $k$ . Included are data from Seki et al. (1981), Shibaguchi et al. (1977), Minton (1971), and the *orange* Warren (1984) interpolation line

at 25 K (expected to be amorphous) and published a cross section spectrum in the 120–177 nm range; Lu et al. (2008) measured amorphous water ice in transmission at 10 K in the far-UV. Hodyss et al. have more recently been making transmission measurements of water ice and other ices at varying temperatures in the 100–200 nm range (R. Hodyss, personal communication).

Water ice has also been measured in the laboratory in reflectance experiments. Pipes et al. (1974) measured the directional-hemispherical reflectance of ~5 mm thick samples of both hexagonal and amorphous water frosts at 77 K. Hapke et al. (1981) measured the bidirectional reflectance of water ice which was likely amorphous; the temperature of the ice was not reported. Jay Goguen and JPL colleagues (*pers. comm.*) measured the reflectance of a sample (~cm thick) of pure water ice at 100 K at phase and emission angles of  $45^\circ$  under vacuum. All reflectance measurements display the absorption edge at ~165 nm (see Fig. 3.2); the precise wavelength of the edge is grain size dependent. Both the Hapke and the Goguen spectra are higher than expected at the shorter wavelengths, possibly due to a red leak or to non-ice contaminants in the sample; Hapke et al. (1981) suggest that the reflectance maximum centered near 130 nm is due to surface scattering related to an absorption maximum in water vapor at that wavelength. Pipes et al. (1974) report that the reflectance in the 140–170 nm range is <2%. A model reflectance spectrum of pure water ice, derived using the Hapke model with the Warren and Brandt (2008) optical constants, is also shown in Fig. 3.2. The model predicts a strong absorption edge at 165 nm, and a flat spectrum throughout the MUV and visible.

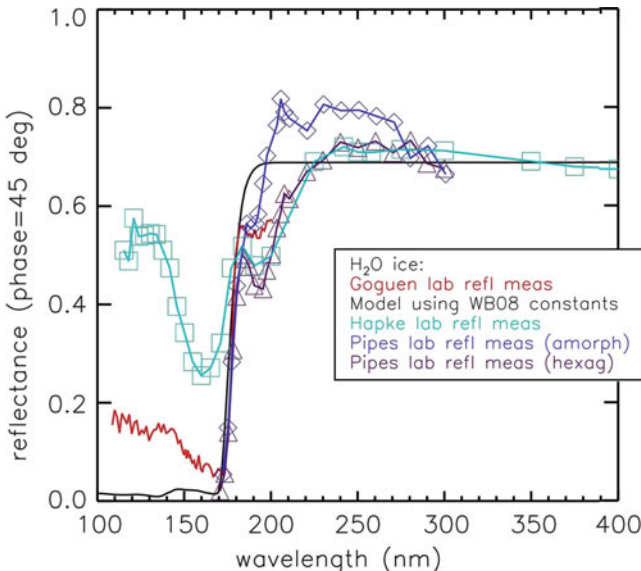


**Fig. 3.2** Reflectance spectra of water ice. The Goguen measurement was made at  $45^\circ$  phase,  $45^\circ$  emission angle. Hapke models were derived for the Goguen geometry using the optical constants from Warren and Brandt (2008) (WB08); a grain size of 200 microns agrees with the Goguen measurement. The Hapke et al. (1981) reflectance data and Pipes et al. (1974) reflectance data (for both hexagonal and amorphous ice samples) are also shown, scaled to approximately agree with the model in the near-UV. Pipes et al. (1974) report that the reflectance in the 140–170 nm range is <2% (From Hendrix et al. (2010))

### 3.3.1.1 Amorphous and Crystalline Ice

A few measurements have been made to study spectral variations between crystalline and amorphous water ice in the UV. Seki et al. (1981) measured hexagonal and amorphous ice in reflectance at 80 K in the 7–28 eV (44–177 nm) range. The hexagonal sample was prepared by cooling at 80 K; the amorphous sample was prepared by deposition of water vapor at 80 K. Seki et al. (1981) (also Kobayashi 1983) found that the amorphous ice exhibited somewhat broader features than the hexagonal ice, with any fine structure in the hexagonal ice spectrum missing in the amorphous ice spectrum. Seki et al. (1981) found that the absorptions at 78 and 144 nm were weaker in the amorphous samples than in the crystalline samples.

Dressler and Schnepf (1960) deposited water vapor at 175 and 77 K. The 175 K sample was cooled to 77 K prior to spectral measurements and is assumed to have hexagonal crystal structure; the 77 K sample is assumed to be amorphous. No difference was detected between the transmission spectra of the two ice samples at different temperatures. A rapid increase in absorption coefficient was measured between 170 and 150 nm. A region of weak, continuous absorption with a shallow maximum near 195 nm was found in the 175 K (cubic) deposits, extending from approximately 180–210 nm; however, the intensity of the absorption was not seen

to increase with increasing layer thickness and so it was not regarded by the authors as being characteristic of the bulk of the material.

Pipes et al. (1974) measured H<sub>2</sub>O frosts in reflectance. Amorphous frosts, grown at <113 K, were fine-grained while the hexagonal frosts, formed by annealing the amorphous frosts at 180 K, were large grained. In the hexagonal frost sample there was a “precursor absorption feature” centered at about 195 nm with a half-width of 10 nm. The feature was observed to some extent in the amorphous frost but could not be determined whether it was due to the presence of a small quantity of cubic or hexagonal crystals. The 195 nm feature in the hexagonal frosts could be enhanced by annealing the frost and was deemed to be associated with the bonding of the H<sub>2</sub>O molecules in the solid.

It is noted that all reflectance measurements (Fig. 3.2) display this “dip” or “trough” (corresponding to an absorption peak), which varies in depth and wavelength, centered at ~186 nm (Goguen), ~190 nm (Hapke), ~187.5 nm (Pipes amorphous), and 193 nm (Pipes hexagonal). The variation in this trough is unclear—it may be due to differences in sample preparation, measurement temperature, and/or crystallinity of the sample. As discussed in the next section, a similar spectral feature has been noted in laboratory spectra of NH<sub>3</sub>; but whether the mechanism that produces the NH<sub>3</sub> feature also produces the apparent H<sub>2</sub>O feature is not clear. The trough is not seen in the model spectrum based on the Warren and Brandt (2008) optical constants (Fig. 3.2), possibly due to a paucity of optical constants measurements in this wavelength range. Because a feature does not appear in the gaseous H<sub>2</sub>O spectrum near this wavelength, it is possible that it appears due to some unknown contaminant.

### 3.3.1.2 Radiolysis Effects

Many measurements have been made to study the effects of irradiation on water ice (e.g., Strazzulla et al. 1988; Moore and Hudson 2000); such irradiation can damage the ice, cause chemical changes, result in desorption or sputtering of atomic and molecular particles, and amorphize the ice (Baragiola 2003). However, few laboratory measurements have been made to investigate the ultraviolet spectral effects of irradiation of water ice (or other ices), though this is a significant area of interest pertaining to the satellites of the outer solar system, which orbit within the magnetospheres of their parent planets.

Sack et al. (1991) grew ice films by vapor deposition on a copper block cooled to 20 K; the sample could be warmed to above 100 K. The sample was bombarded with 33 keV non-reactive (He<sup>+</sup> and Ar<sup>+</sup> ions). The reflectance spectrum was measured in the ~250–550 nm range. The samples were found to darken in a wavelength-dependent fashion, with much stronger darkening occurring at the shorter wavelengths. However, the darkening was seen to occur with both with warming (due to annealing of scattering centers) and with irradiation.

Irradiation of H<sub>2</sub>O ice results in chemical products such as O<sub>3</sub> (Johnson and Quickenden 1997; Teolis et al. 2006) and H<sub>2</sub>O<sub>2</sub> (e.g., Cooper et al. 2003; Gomis

et al. (2004), which are detectable in the UV and have been found at the surfaces of some outer solar system moons. Taub and Eiben (1968) measured the spectral response of water ice to irradiation by electron doses. Their results indicated the creation of absorption bands at 230 and 280 nm; OH and HO<sub>2</sub> were suggested to be the source of these absorptions. Moore and Hudson (2000) studied the creation of H<sub>2</sub>O<sub>2</sub> by 800 keV proton irradiation and found it to be produced in 16 K samples but not in 80 K samples; H<sub>2</sub>O<sub>2</sub> was produced in 80 K mixtures of H<sub>2</sub>O and O<sub>2</sub> or CO<sub>2</sub>. However, Gomis et al. (2004) irradiated pure ice samples with 30 keV ions (H<sup>+</sup>, C<sup>+</sup>, N<sup>+</sup>, O<sup>+</sup>, Ar<sup>+</sup>) and produced H<sub>2</sub>O<sub>2</sub> at both 16 and 77 K, suggesting that a non-H<sub>2</sub>O species is not needed to produce H<sub>2</sub>O<sub>2</sub> at warmer temperatures.

Teolis et al. (2006) measured the 260 nm ozone Hartley band in irradiated water ice samples. They achieved this by irradiating H<sub>2</sub>O ice with 100 keV Ar<sup>+</sup> (to simulate the heavy magnetospheric ions at Jupiter and Saturn such as O and S) while simultaneously depositing fresh water, to simulate redeposition of sputtered water molecules and allow trapping of O<sub>2</sub>. They measured the UV spectrum of the irradiated samples and found a significantly deeper O<sub>3</sub> absorption band after performing the simultaneous deposition of H<sub>2</sub>O, suggesting that the retention of O<sub>2</sub> is required to create O<sub>3</sub>. These results also suggest that heavy ions are required to produce the O<sub>2</sub> (and thus O<sub>3</sub>); 100 keV protons do not provide enough energy. This study is important for understanding the UV signatures at many icy bodies in the solar system – though the Ganymede 260 nm absorption band is significantly broader than that produced in the laboratory by Teolis et al. (2006), so this needs to be further investigated.

### 3.3.2 Ammonia Ice

Ammonia ice exhibits a very strong absorption edge at ~200 nm, with an absorption peak near 180 nm. Dressler and Schnepp (1960) made measurements by depositing ammonia vapor at 77 K and at 125 K and measuring the solid ammonia at 77 K. The higher-temperature deposit was assumed to have the cubic crystal structure; absorption was found to set in between 188 and 178 nm and to be very intense and uniform below 178 nm. In the deposit formed at 77 K (amorphous), the long-wavelength onset of absorption is marked by a very intense and comparatively narrow absorption band at 194 nm. This band is followed to shorter wavelengths by uniformly strong absorption. The long-wavelength onset of absorption in the cubic (125 K) sample is 186 ±4 nm while the absorption onset in the amorphous (77 K) sample is 199±4 nm. This is in contrast to their measurements of H<sub>2</sub>O ice, in which they found no measurable difference between cubic and amorphous samples.

Martonchik et al. (1984) compiled measurements of the ammonia ice optical constants n and k. In the 140–210 nm region, the Martonchik et al. compilation includes the 77 K data of Dressler and Schnepp (1960), scaled to match the data of Browell and Anderson (1975) at 176 nm. Martonchik et al. noted that early

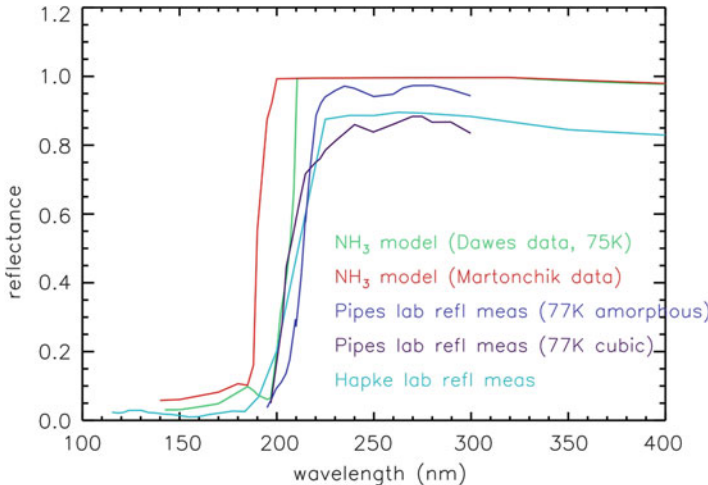


**Fig. 3.3** Ammonia ice: comparisons between Hapke models using optical constants from Martonchik et al. (1984) and Dawes et al. (2007; samples deposited at 75 K) and reflectance measurements from Pipes et al. (1974) and Hapke et al. (1981). The difference in wavelength of the absorption edge between the spectral models and the laboratory-measured reflectance spectra could be due to differences in crystallinity and/or temperature in the samples. Pipes et al. (1974) report that the reflectance in the 140–170 nm range is <2% (After Hendrix et al. (2010))

measurements showed that no absorption was present in the 210–770 nm region; no recent measurements have been made in that wavelength range.

Dawes et al. (2007) produced photoabsorbance spectra of solid  $\text{NH}_3$  in the ~130–205 nm range, for samples condensed at 25, 75, 80 and 90 K; they also presented the spectrum of a sample deposited at 25 K and annealed to 75 K. Dawes et al. (2007) measured distinct spectral differences that were the result of temperature-related structural changes in the ice. In the 75 K sample, a narrow absorption maximum at 194 nm was measured and was attributed to an exciton peak. (Dressler and Schnepp (1960) also measured the 194 nm absorption peak in their crystalline sample at 77 K, but not at 125 K.) Samples deposited at temperatures >85 K were found to be crystalline (cubic) or large-grain polycrystalline, with much weaker 194 nm exciton absorption peaks. Lu et al. (2008) measured  $\text{NH}_3$  in absorption at 10 K and published an absorption spectrum; the sample thickness is unknown. Similar to the Dawes et al. (2007) results at 25 K, the Lu et al. results show a peak in absorption near 180 nm, a local minimum in absorption near 150 nm; absorption increases with decreasing wavelength between 150 and 110 nm. Lu et al. (2008) did not measure a feature at 194 nm.

Pipes et al. (1974) measured the directional-hemispherical reflectance of both hexagonal and amorphous ammonia frosts ~5 mm thick at 77 K. Hapke et al. (1981) measured the bidirectional reflectance of ammonia frost which was likely amorphous; the temperature of the ice was not reported. Figure 3.3 displays these reflectance measurements along with Hapke models derived using optical constants from

Martonchik et al. (1984) and the Dawes et al. (2007) data at 75 K. The longest wavelength of the Dawes *et al.* data is  $\sim$ 205 nm, so at wavelengths longer than this, we use the Martonchik et al. data; negligible absorption is expected in the NUV-visible.

### 3.3.3 Carbon Dioxide

Limited measurements have been made of CO<sub>2</sub> in the ultraviolet, and we find that the published data produce conflicting stories on the shape of the absorption profile. Warren (1986) discussed and compiled earlier measurements of the optical constants of carbon dioxide ice. There is a gap in the Warren (1986) compilation in the 130–330 nm range due to a lack of measurements, and there are discrepancies in the existing measurements. Hansen (2005) measured the transmission of UV light through CO<sub>2</sub> ice samples of varying thicknesses to determine the absorption coefficient ( $\alpha$ ) for wavelengths as short as 174 nm, at  $\sim$ 160 K. The absorption coefficient increases weakly with decreasing wavelength between 200 and 240 nm, and increases sharply with decreasing wavelength between 174 and 200 nm.

Measurements in absorption by Lu et al. (2008) suggest very little absorption by CO<sub>2</sub> at 10 K in the 135–217 nm range; a small absorption peak is centered near 126 nm, as well as a strong absorption edge near 119 nm. There is thus a large discrepancy between the results of Hansen (2005) and those of Lu et al. (2008). Furthermore, the measurements discussed by Warren (1986) suggest a narrow peak in absorption near 120 nm, whereas the Lu et al. results show continuing absorption shortward of this peak. Recent unpublished work at JPL indicates that CO<sub>2</sub> is not strongly absorbing enough in the far-UV to be detectable on planetary surface, unless present in large quantities (*R. Hodyss, pers. comm.*).

### 3.3.4 Sulfur Dioxide

Sulfur dioxide frost exhibits a very strong absorption edge in the mid-UV. Shortward of  $\sim$ 310 nm, SO<sub>2</sub> is very dark; longward of this region SO<sub>2</sub> is quite bright and spectrally featureless throughout the near UV and visible. Nash et al. (1980) provided the first spectrum of SO<sub>2</sub> frost extending into the UV, highlighting the strong UV absorption edge and demonstrating its importance in explaining the spectrum of the Jovian moon Io.

Mason et al. (2006) published spectra of solid SO<sub>2</sub> in the 138–310 nm range and identified absorptions corresponding to those that occur in the vapor phase, namely an absorption near 275.9 nm with a stronger absorption maximum at 197.7 nm. They noted that rapid deposition of the SO<sub>2</sub> vapor results in glassy, amorphous ices whereas slower deposition produces pockets of crystallinity, where fine vibrational structure is measured in the spectra.

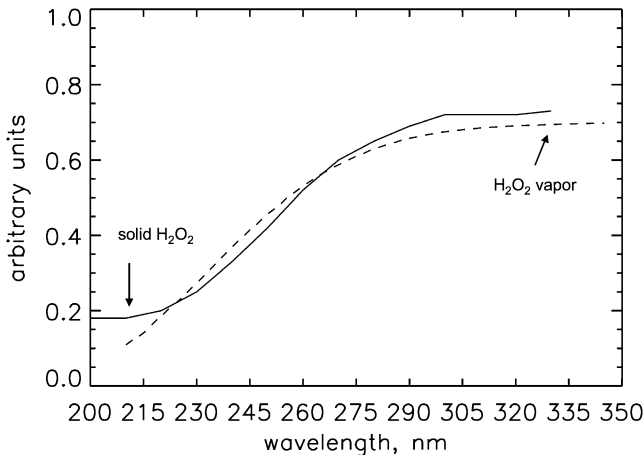


**Fig. 3.4** Reflectance spectrum of solid hydrogen peroxide (after Carlson et al. 1999) compared with gaseous H<sub>2</sub>O<sub>2</sub> transmission spectrum (using the cross section of Vaghjiani and Ravishankara (1989), with column density of 5e18 cm<sup>-2</sup>)

### 3.3.5 Other Ices

Solid methane was measured in transmission by Dressler and Schnepf (1960), who derived absorption coefficients. They found that CH<sub>4</sub> exhibits a strong absorption edge between 139 and 131 nm; weak absorption continued to as long as 200 nm but they could not rule out the contribution from impurities to their sample.

Berland et al. (1996) measured mixtures of H<sub>2</sub>O and nitric acid (HNO<sub>3</sub>) for applications to polar stratospheric clouds. A 1:1 H<sub>2</sub>O:HNO<sub>3</sub> mixture exhibits a strong absorption maximum centered at 200 nm; the absorption maximum shifts toward slightly longer wavelengths with increasing amounts of H<sub>2</sub>O.

Ozone was measured by Vaida et al. (1989) 77 K in solution with O<sub>2</sub>, H<sub>2</sub>O and CCl<sub>4</sub> and also condensed in a film. In both the solid O<sub>3</sub> and the O<sub>3</sub> in O<sub>2</sub>, the Hartley band was measured to shift from the gas phase wavelength of 253 nm to 220–245 nm. In solution with H<sub>2</sub>O and CCl<sub>4</sub>, the band was seen to shift by ~6 nm to the red. In all cases, the band is seen to broaden.

Hydrogen peroxide was measured in the solid phase at ultraviolet wavelengths in order to compare with the Galileo UVS spectrum of Europa (Carlson et al. 1999). The spectrum is similar to that of vaporous H<sub>2</sub>O<sub>2</sub>, displaying a slow absorption in the mid-UV range, between ~300 and ~220 nm (Fig. 3.4); outside of this range the spectrum is largely flat and featureless.

Several species have been measured in absorption at 10 K, such as methanol (H<sub>3</sub>COH) (Kuo et al. 2007) and CO (Lu et al. 2005, 2008) measured O<sub>2</sub>, NO, and N<sub>2</sub>O in addition to the CO<sub>2</sub>, H<sub>2</sub>O and NH<sub>3</sub> previously discussed, in the ~110–250 nm range. Solid carbon monoxide displays the pronounced vibrational

structure seen in gaseous CO in the 130–155 nm range, although the vibrational structure accompanying electronic transitions of greater energy is lost. For solid methanol at 10 K there is a smooth, fairly steady absorption that sets in near 185 nm and continues through 110 nm. The curve of pure solid nitrogen oxide contains two broad absorption features; the most prominent feature occurs with a maximum near 208 nm; another feature with maximum near 150 nm is much broader but weaker, and the absorption continues through 110 nm. The spectrum of pure solid dioxygen contains apparently two broad lines, with maxima near 140 and 170 nm. Solid dinitrogen dioxide exhibits a prominent absorption maximum near 130 nm.

## 3.4 Measurements of Solar System Ices

### 3.4.1 *Ultraviolet Observations of the Galilean Satellites*

#### 3.4.1.1 Introduction/History

The Galilean satellites (Io, Europa, Ganymede, Callisto) represent an interconnected system. Interactions between their surfaces and Jupiter's magnetic field produce thin atmospheres and irradiation chemistry within the surface ices. Many of the key processes operating to modify their surfaces are exogenic in nature, such as irradiation from jovian magnetospheric ions and neutral wind particles, micrometeorite bombardment, and photolysis. Each process works to leave a distinctive spectral signature on the satellite surfaces, many of which are detectable in the ultraviolet.

Io is part of a complex system that involves volcanic activity (plumes and outgassing from hotspots), irradiation by Jupiter's magnetic field (which sputters material from the surface and atmosphere and, in conjunction with the volcanism on the surface, is key in creating a plasma torus centered on this satellite), and sublimation of volatile materials. As a consequence of this complex system, Io retains an SO<sub>2</sub> atmosphere. Dissociation of the SO<sub>2</sub> surface frost and atmospheric gas, along with ionization of the sulfur and oxygen atoms, creates ionized materials that become entrained within Jupiter's magnetic field. This material, in both ionized and neutral form, then interacts with the surfaces of the remaining Galilean satellites to produce a complex surface chemistry.

Water ice on the surfaces of Europa, Ganymede, and Callisto has been identified predominately on the basis of its absorption characteristics in the visible to infrared wavelengths, with the relative amount of water decreasing with the satellite's distance from Jupiter (Pilcher et al. 1972). Earth-based observations from the near-ultraviolet to near-infrared have long noted an albedo asymmetry between the leading and trailing hemispheres on these three satellites (Stebbins and Jacobsen 1928; Johnson 1971; Millis and Thompson 1975; Morrison et al. 1974; McFadden et al. 1980). These hemispherical albedo dichotomies were also seen in the Voyager

near-ultraviolet to visible images (Johnson et al. 1983; McEwen 1986; Nelson et al. 1986) and ultraviolet observations from the IUE (Nelson et al. 1987). On Europa, the trailing hemisphere albedo is darker than the leading hemisphere. Ganymede displays a similar hemispherical albedo dichotomy as Europa with the trailing hemisphere darker than the leading hemisphere. The longitudinal variations in albedo on Europa and Ganymede have been correlated to the preferential bombardment of the trailing hemisphere by magnetospheric ions. Jupiter's magnetic field rotates more quickly than the Galilean satellites, thus ions entrained within the field preferentially sweep into the trailing hemisphere of these satellites. The longitudinal albedo variations, which are most pronounced in the ultraviolet, show a distinctive cosine signature commensurate with magnetospheric interactions. However, the interactions between the surface and co-rotating jovian magnetosphere on Ganymede are complicated by the presence of an intrinsic magnetic field (Kivelson et al. 1996; Gurnett et al. 1996), where the polar regions are open to Jupiter's magnetospheric plasma and the equator is shielded to low energy ions. Cooper et al. (2001) have shown that particles of sufficient energy can cross the closed field lines at the equator to interact with the surface; among these particles are  $S^+$  ions with energies  $>400$  keV and  $O^+$  ions with energies  $>800$  keV.

Callisto, like her sister icy satellites, displays a hemispherical albedo dichotomy, however it is in the opposite sense as that of Europa and Ganymede; its leading hemisphere is darker than the trailing hemisphere. The visible rotation curves of Callisto are not commensurate with a surface modification due to magnetospheric ion bombardment; the albedo variations do not show a smooth sinusoidal function with longitude centered on either the leading or trailing hemisphere. The local minimum in the visible rotation curve occurs at  $60^\circ$  longitude, on the jovian quadrant of the leading hemisphere which is also associated with the Valhalla impact basin.

Micrometeorite bombardment on these satellites preferentially impacts the leading hemisphere of these satellites. Dust and grains trapped within Jupiter's gravity well are preferentially swept up by the leading hemisphere. The hemispherical albedo differences on Callisto imply this is a dominate exogenic process operating on this satellite. In contrast, ion bombardment appears to be the dominate exogenic process altering the surfaces of Europa and Ganymede.

Ions neutralized in the plasma, in addition to neutrals escaping from Io's outgassing, travel radially from Jupiter. These neutrals then interact preferentially with the joivan-facing hemispheres of the icy Galilean satellites.

All of these processes work to modify the surface through sputtering, volatilization, and implantation. Sputtering and volatilization alter grain sizes and preferentially remove materials. The sputtered material is either lost to space, possibly as part of the satellite's atmosphere, or re-deposited into cold-traps at the poles or on the leading hemisphere (Sieveka and Johnson 1982). Sputtering also preferentially destroys small grains, thus contributing to the relative darkening between the two hemispheres (Johnson et al. 1988; Calvin et al. 1995). Ion and neutral implantation within the surface water ice produces absorption signatures indicative of radiation chemistry.

Many of the diagnostic signatures of the icy composition of the surfaces of the Galilean satellites have been derived from observations performed in the ultraviolet

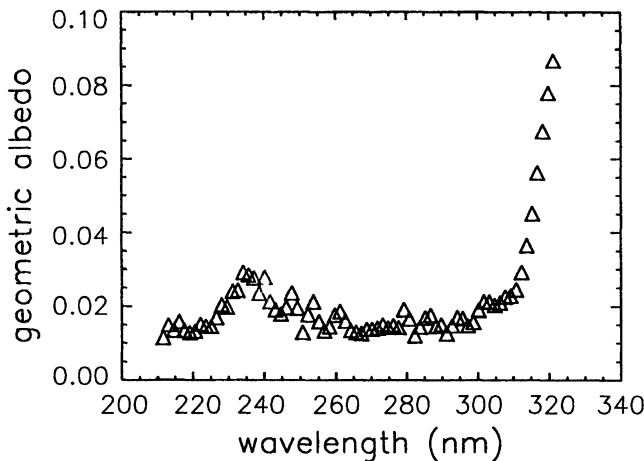


**Fig. 3.5** Galileo UVS albedo spectrum of Io, showing the strong SO<sub>2</sub> frost absorption near 310 nm (from Hendrix et al. 1999a). The bump near 235 nm has been attributed to SO<sub>2</sub> gas

especially those associated with surface radiation chemistry. Examinations of these systems in the ultraviolet have played a key role in understanding the complex interactions and interconnections between the satellite surfaces, their atmospheres, and the radiation chemistry of the surface ices. Observations from ground-based telescopes, orbital telescopes (such as IUE and HST), and spacecraft (Voyager, Galileo, Cassini, and New Horizons) have all contributed towards our understanding of these satellites.

### 3.4.1.2 Io

The first reports of the presence of SO<sub>2</sub> frost on Io were from ground-based telescopic observations in the near-ultraviolet and visible wavelength ranges, 320–860 nm (Nelson and Hapke 1978; Smythe et al. 1979). A spectral edge at  $\sim 330$  nm, was reported in these observations commensurate with the spectral downturn in the visible to ultraviolet seen in laboratory spectra of sulfur compounds (Nelson and Hapke 1978). These were later followed by IUE observations between 240 and 340 nm, which mapped the longitudinal distribution of this surface constituent (Nelson et al. 1987); it was noted that the SO<sub>2</sub> abundance was greater on the leading hemisphere. Voyager imaging observations in the near-ultraviolet and visible were also commensurate with the longitudinal albedo variations observed in the IUE observations (McEwen et al. 1988). Spectra from the Galileo UVS showed the presence of both SO<sub>2</sub> gas and the strong SO<sub>2</sub> frost absorption edge (Fig. 3.5). Alternate or additional surface components, based on infrared measurements, include such materials as S<sub>2</sub>O (Hapke 1989), Na and K polysulfides, H<sub>2</sub>S (Nash and Howell 1989; Salama et al. 1990), H<sub>2</sub>O (Salama et al. 1990), and CO<sub>2</sub> (Trafton et al. 1991). HST observations in the ultraviolet, taken at 285 nm with

the Faint Object Camera (FOC) mapped comparative regions of high and low SO<sub>2</sub> concentration in addition to searching for temporal variations in the SO<sub>2</sub> surface abundance (Paresce et al. 1992).

### 3.4.1.3 Europa

Ratios of leading versus trailing hemisphere ultraviolet spectra of Europa's surface taken with IUE and HST show an enhanced absorption at 280 nm on the trailing hemisphere (Lane et al. 1981; Ockert et al. 1987; Noll et al. 1995). Interpretation of the original disk-integrated IUE and HST observations was that the ultraviolet absorption is commensurate with SO<sub>2</sub> signatures created by the implantation of sulfur into the water ice matrix, where the sulfur interacts with the oxygen bonds to produce the SO<sub>2</sub>-like signature (Lane et al. 1981; Ockert et al. 1987; Noll et al. 1995). The sulfur ions, originally from Io are entrained within Jupiter's magnetic field and are preferentially implanted into the satellite's trailing hemisphere. Examination of the Voyager images (especially in ratios of ultraviolet (350 nm) to visible filter (590 nm) albedos) demonstrate a direct correlation between albedo ratio and models of magnetospheric ion implantation (McEwen 1986; Johnson et al. 1988; Pospieszalska and Johnson 1989), where the implantation models predict a pattern related to the cosine of the angle (latitude or longitude) from the trailing hemisphere apex. An absorption seen in the Voyager UV filter images (attributed to H-S or S-S band) was correlated to the predicted ion bombardment longitudinal distribution (Johnson et al. 1988). Studies of the longitudinal distribution of this feature from IUE measurements show it is present between 225° and 315° longitude, but noticeably absent within leading hemisphere longitudes (Lane and Domingue 1997). Disk-resolved Galileo UVS observations demonstrate that this absorption feature generally decreases with distance from the center of the trailing hemisphere (Hendrix et al. 1998), consistent with magnetospheric interactions. An alternate interpretation of the origin of the 280 nm sulfur feature, offered by Noll et al. (1995), suggests that the SO<sub>2</sub> is endogenic in origin, originating from Europa's non-ice surface component. A more recent analysis of the highest-resolution Galileo UVS observations suggests that much of the UV SO<sub>2</sub> absorption is related to the dark, geologically young regions on the trailing hemisphere (Hendrix et al. 2010).

Bombardment of Europa's surface from neutrals would produce a jovian versus anti-jovian hemisphere dichotomy. The source of these neutrals would be particles emanating from Io or from dust from Jupiter's gossamer ring (Horanyi and Cravens 1996). Examination of the IUE observations show temporal changes in the jovian hemisphere that have been attributed to variability in the neutral bombardment of the jovian hemisphere (Lane and Domingue 1997).

Observations in the infrared have also shown correlations with hydrogen peroxide, sulfuric acid, and sulfuric acid hydrate (Carlson et al. 1999, 2005) within the water ice matrix. Galileo UVS observations also support the presence of hydrogen peroxide (Carlson et al. 1999; Hendrix et al. 1999c).

### 3.4.1.4 Ganymede

Ultraviolet observations of Ganymede from IUE, HST, and the Galileo UVS all show the presence of an absorber at  $\sim 260$  nm on the trailing hemisphere in leading versus trailing hemisphere spectral ratios (Nelson et al. 1987; Noll et al. 1996; Hendrix et al. 1999b). The position of this absorption indicates an absorber other than sulfur is needed to produce this feature. Nelson et al. (1987) proposed ozone as the possible absorber, which was confirmed by the later HST observations (Noll et al. 1996). Noll et al. (1996) showed that the ultraviolet absorption is well described by the Hartley band of ozone (broadened and shifted), where the ozone is trapped within the surface ice. This is consistent with HST observations at visible wavelengths that show the presence of O<sub>2</sub> within the water ice (Spencer et al. 1995; Calvin et al. 1996; Johnson and Jesser 1997). Both the oxygen and ozone are thought to be “atmospheres” trapped within bubbles or small voids within the surface ice (Noll et al. 1996; Johnson and Jesser 1997). Disk-resolved measurements of the 260 nm absorption feature from Galileo UVS observations show that the ozone abundance is correlated with longitude, latitude, and solar zenith angle (Hendrix et al. 1999b). These correlations imply a complex interchange between creation mechanisms (ion bombardment of the surface, photolysis of oxygen to ozone) and destruction mechanisms (dissociation of the ozone by ultraviolet radiation). The bombardment of the water ice by charged particles produces H, OH, O, H<sub>2</sub>, and O<sub>2</sub> (Johnson et al. 1998). It also produces defects in the ice, and annealing of the ice can create larger bubbles in which the O<sub>2</sub> can accumulate (Johnson and Quickenden 1997). Subsequent radiolysis of the trapped O<sub>2</sub> then produces the observed ozone (Johnson and Quickenden 1997). This explains the correlation of the 260 nm feature with the trailing hemisphere and is commensurate with no detection of either O<sub>2</sub> or O<sub>3</sub> on the leading hemisphere (Spencer et al. 1995; Calvin et al. 1996), despite the presence of Ganymede’s intrinsic magnetic field. However, Cooper et al. (2001) have shown that particles of sufficient energy can cross the closed field lines at the equator to interact with the surface. The correlation with solar zenith angle observed in the disk-resolved Galileo UVS observations (Fig. 3.6) suggests that the ozone is dissociated by ultraviolet radiation when the surface is well illuminated by the sun (Hendrix et al. 1999b).

The tenuous detection of SO<sub>2</sub> frost on Ganymede was indicated in an analysis of the IUE data set (Domingue et al. 1998). The presence of a sharp slope above 0.32  $\mu$ m in observations taken in 1985 was interpreted as indicative of SO<sub>2</sub> frost. The feature was seen in disk-integrated observations centered at 272° longitude. Observations centered at this same longitude taken in 1996 do not show this diagnostic slope between the ultraviolet and visible, suggesting that this frost has a strong temporal component.

### 3.4.1.5 Callisto

While water ice has been definitively identified on Callisto by ground-based observations (Pilcher et al. 1972), the surface contains at least one non-water ice

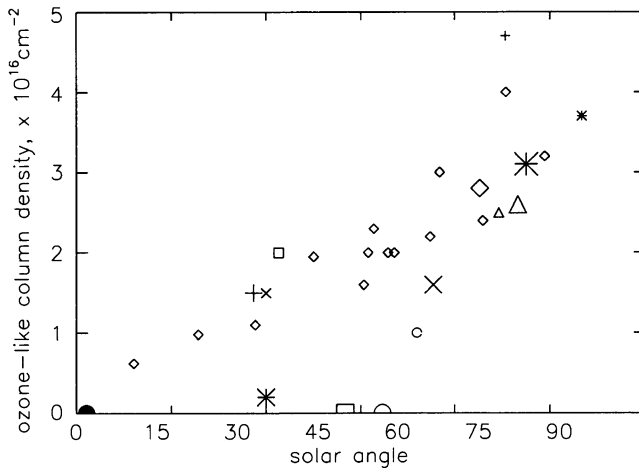


**Fig. 3.6** Galileo UVS measurements of ozone column density at Ganymede, related to solar angle (from Hendrix et al. 1999b). The different symbols refer to different observations

component. Suggested candidates for the non-ice component include phyllosilicates (Roush et al. 1990; Calvin and Clark 1991) and organics (McCord et al. 1997; Hendrix and Johnson 2008). Carbon dioxide, seen in dark regions as detected by its IR absorption feature, is believed to be adsorbed or trapped in grains of the non-ice material (Hibbitts et al. 2000).

Ultraviolet observations from IUE, HST, and the Galileo UVS provide some insight into the links between the surface composition and the exogenic surface alteration processes. Disk-integrated observations from IUE and HST detected an absorption band at 280 nm on the leading hemisphere of Callisto that is similar to that observed on the trailing hemisphere of Europa (Lane and Domingue 1997; Noll et al. 1997a), an example shown in Fig. 3.7. For each satellite the absorption feature is seen in ratio spectra of one hemisphere to the other. The 280 nm feature on Europa has been ascribed to S-O band vibrations producing an SO<sub>2</sub> signature from sulfur ions implanted into the surface water ice lattice (Lane et al. 1981; Noll et al. 1995). This is supported by the detection of this feature on the trailing side. While this feature on Callisto's leading side has also been interpreted as S implanted within the water ice matrix, a different mechanism for producing it on the leading hemisphere is required. Lane and Domingue (1997) put forth two possible source mechanisms. In one they postulate that this absorption is the result of the implantation of neutral sulfur from the Io torus. This is commensurate with their detection of this feature on the jovian quadrant of the leading hemisphere. Alternately they hypothesize that the SO<sub>2</sub> is part of the material that was excavated during the Valhalla impact event. Noll et al. (1995, 1997a) offer an alternate source for the SO<sub>2</sub> on both Europa and Callisto, suggesting that SO<sub>2</sub> is native to each satellite. Noll et al. (1997a) postulate that on Callisto it is the preferential bombardment of the leading hemisphere by micrometeorites that sputters the water and enhances the concentration of SO<sub>2</sub>.

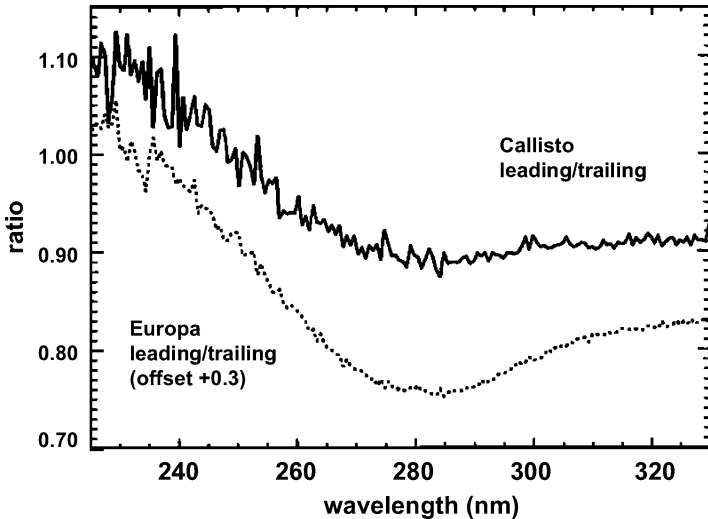


**Fig. 3.7** HST measurements of Callisto and Europa (from Noll et al. 1997a). The Callisto spectrum is a ratio of the leading hemisphere to the trailing hemisphere; the Europa spectrum is a ratio of the trailing hemisphere to the leading hemisphere, highlighting an absorption feature centered near 280 nm the different

Detection of  $\text{SO}_2$  and  $\text{CO}_2$  spectral signatures in Galileo NIMS observations support an endogenic or native component to the origin of the  $\text{SO}_2$  on Callisto and Ganymede (Carlson et al. 1996). Galileo UVS measurements of Callisto do not show the 280 nm feature (Hendrix and Johnson 2008), though at low resolution, the leading hemisphere is somewhat redder than the trailing hemisphere at  $\lambda > 280$  nm. At higher resolutions, regions at high latitudes are spectrally blue at wavelengths longer than 280 nm, suggesting the shoulder of an absorption band centered near 350 nm; Hendrix and Johnson (2008) suggested organic species could be responsible for the absorption, and that they would be destroyed by radiolysis at lower latitudes.

### 3.4.2 Satellites and Rings of Saturn

The Saturn system is dominated by the near-ubiquitous presence of water and water ice (see Clark et al. 2012, *this volume*, and references therein). At nearly all wavelengths, the Saturnian satellites (Mimas, Enceladus, Tethys, Dione and Rhea) are brighter than the Galilean moons, reflective of differing large-scale compositional and/or exogenic processes in the two systems. The rings of Saturn were first measured in the ultraviolet using IUE (Wagener and Caldwell 1988) and were shown to exhibit a strong UV absorption edge near 165 nm. Observations of the rings by the Cassini UVIS (Bradley et al. 2010) provide further spatial information and higher

quality spectral albedos in the far-UV; the  $\sim$ 165 nm H<sub>2</sub>O ice absorption edge is the most striking spectral feature, and Bradley et al. use this feature to gain insights into path lengths with implications for ring grain particle structure.

The surface of Titan, Saturn's largest satellite, is inaccessible at ultraviolet wavelengths because of its dense atmosphere. Water ice is inferred on its surface from infrared observations in windows of low opacity and data from the Huygens probe (see Clark et al. 2012). Several of Saturn's larger icy satellites, however, have had their ultraviolet spectra measured. Enceladus, Tethys, Dione, Rhea, and Iapetus range in diameter from 500 to 1,500 km and have been observed with the Hubble Space Telescope (HST). Nearly all of Saturn's moons have been measured at far-UV wavelengths using the Cassini UVIS.

Noll et al. (1997b) reported the detection of an albedo minimum in spectra of Rhea and Dione centered at 260 nm in UV spectra obtained with the Faint Object Spectrograph (FOS). Because these surfaces are known to be dominated by water ice and because both satellites are immersed in Saturn's magnetosphere, Noll et al. concluded that trapped O<sub>3</sub> was the source of this absorption feature by analogy with Ganymede. The required column abundance was estimated to be in the range N(O<sub>3</sub>) = 1–6  $\times$  10<sup>16</sup> cm<sup>-2</sup>. The spectrum of Iapetus did not show a prominent band at 260 nm with an upper limit for ozone of N(O<sub>3</sub>) < 0.5  $\times$  10<sup>16</sup> cm<sup>-2</sup>.

Near ultraviolet to near infrared spectra of Enceladus and Tethys were obtained with the Space Telescope Imaging Spectrometer (STIS) in 1999 and 2000. Absolute albedos determined from HST observations are in good agreement with observations at opposition obtained by Verbiscer et al. (2007) to which the data in Fig. 3.8 have been scaled. The progressively higher albedos with proximity to Enceladus suggests ongoing resurfacing with material originating in Enceladus, perhaps redeposited from the E ring (Verbiscer et al. 2007). Interestingly, the broad  $\sim$ 260 nm feature is seen in Tethys, but is apparently absent in Enceladus. It is possible that the ice on Enceladus is too fresh to allow for the retention of significant amounts of trapped radiolytic by-products.

All of Saturn's satellites require the presence of UV absorbers other than water ice and ozone. Mixtures of a few percent of organic residues derived from irradiated mixtures of water and ethane ices are sufficient to match the red slope seen in all of Saturn's satellites shortward of 500 nm and the low albedos seen shortward of 220 nm (Noll et al. 1997b). The sharp drop in Enceladus' albedo shortward of 220 nm and the low albedo observed in the far UV by Cassini UVIS (Fig. 3.9a) have been interpreted by Hendrix et al. (2010) as evidence for a small amount of NH<sub>3</sub> ice mixed with H<sub>2</sub>O ice, possibly along with a small amount of a red organic material. This hypothesis is consistent with measured species in the Enceladus plumes (Waite et al. 2009). The visible albedos of the Saturnian moons have been compared with the E-ring grain brightness, suggesting a direct relationship; however, in the far-UV, the large-scale albedo pattern is different and is not consistent exclusively with the E-ring (Fig. 3.9b). Neutral gases from Enceladus' plume (e.g., H<sub>2</sub>O, NH<sub>3</sub>) may be more important in driving the UV albedos. We expect that organic residues or possibly silicates or nanophase iron (Clark et al. this volume) also play a role, especially at Dione and Rhea.

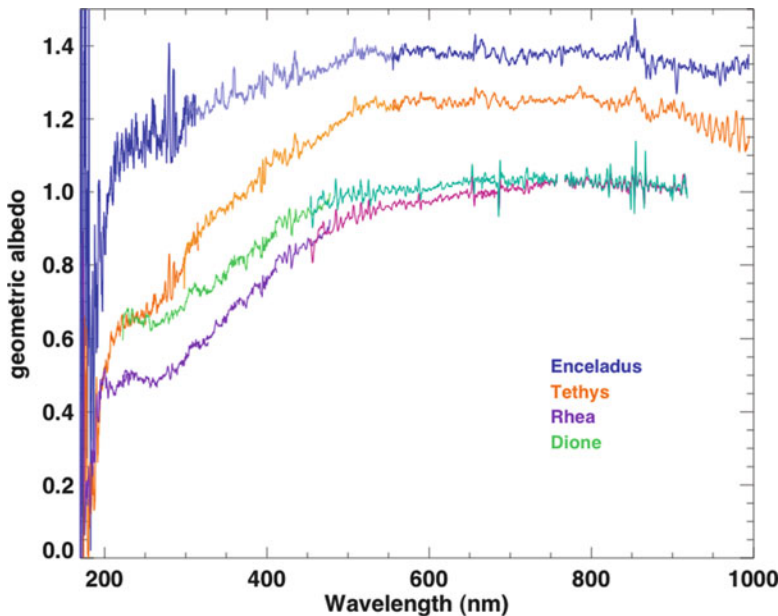


**Fig. 3.8** Ultraviolet and visible spectra of Enceladus, Tethys, Rhea, and Dione. The UV data are from HST as described in the text. For Rhea and Dione, the visible wavelength spectra longward of 450 nm are from Buratti (*private communication*). The data are all scaled to match geometric albedos observed by Verbiscer et al. (2007). The UV spectra show a steep drop in albedo at 210 nm in Enceladus, Tethys, and possibly Rhea; the data for Dione do not extend to short enough wavelengths

### 3.4.3 Satellites of Uranus

Titania, Oberon, Ariel, Umbriel, and Miranda are the five largest satellites of Uranus, ranging in diameter from 472 to 1,578 km. All five regular satellites have infrared spectra that show water ice absorption bands with relative band strengths indicative of crystalline water ice (Grundy et al. 2006, Clark et al. this volume). The water ice band depths show a hemispheric asymmetry, with deeper bands on the leading hemispheres, possibly a signature of magnetospheric charged particle interactions with the surface ices. Infrared spectra have also identified CO<sub>2</sub> ice absorption features in Ariel, Umbriel and Titania (Grundy et al. 2003, 2006). The CO<sub>2</sub> ice bands are strongest on the trailing hemispheres of these satellites and are strengthen at decreasing separation from Uranus (Grundy et al. 2006). This behavior is again indicative of a connection between surface ices and magnetospheric charged particles.

Initial UV observations of the Uranian moons were made with the Voyager 2 PPS instrument. Nelson et al. (1987) reported geometric albedos at 250 nm for Miranda, Ariel, Umbriel, Titania and Oberon, and noted the distinct groupings of the Uranian, Jovian and Saturnian satellites when considering their UV and IR albedos, with implications for weathering and/or formation histories. The Uranian

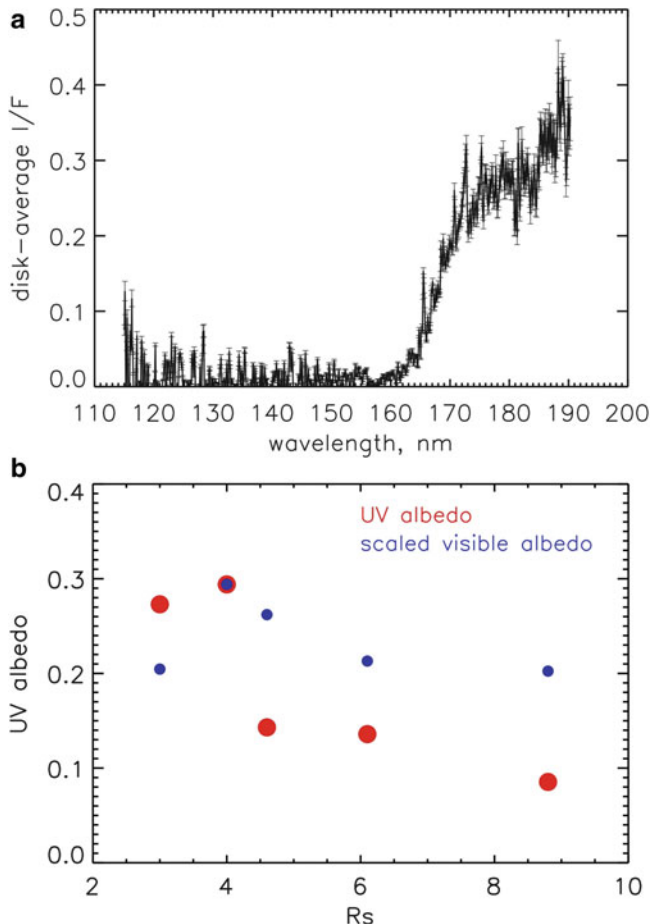


**Fig. 3.9** (a) Cassini UVIS-measured disk-integrated reflectance spectrum of Enceladus at phase angle =  $2^\circ$ . From Hendrix et al. (2010). The magnitude of the spectrum is consistent with the large UV drop-off measured by HST (Fig. 3.8). (b) Cassini UVIS-measured disk-integrated reflectance spectrum of the Saturnian moons at phase angle  $\sim 10^\circ$ . Overplotted are the visible geometric albedo values from Verbiscer et al. (2007), scaled to the Enceladus UV value. In the UV, the other moons are yet darker than Enceladus. The trend with radial distance from Saturn is different in the two wavelength regimes, suggesting different processes and/or species controlling the albedos

moons have UV albedos similar to the darker Saturnian satellites, (higher than the Jovian satellites), and the greatest UV/IR color ratios. Indeed, Buratti et al. (1990) demonstrated using Voyager broad-band data that the moons have strikingly flat spectra, with very little UV absorption.

Spectra at near ultraviolet wavelengths can be used to search for possible magnetospherically induced spectral features in these satellites. Roush et al. (1998) used the Hubble Space Telescope's Faint Object Spectrometer (FOS) to obtain moderate resolution spectra of Ariel, Titania, and Oberon from 220 to 480 nm (Fig. 3.10). The albedo in the near-UV continues the bland, nearly featureless trend

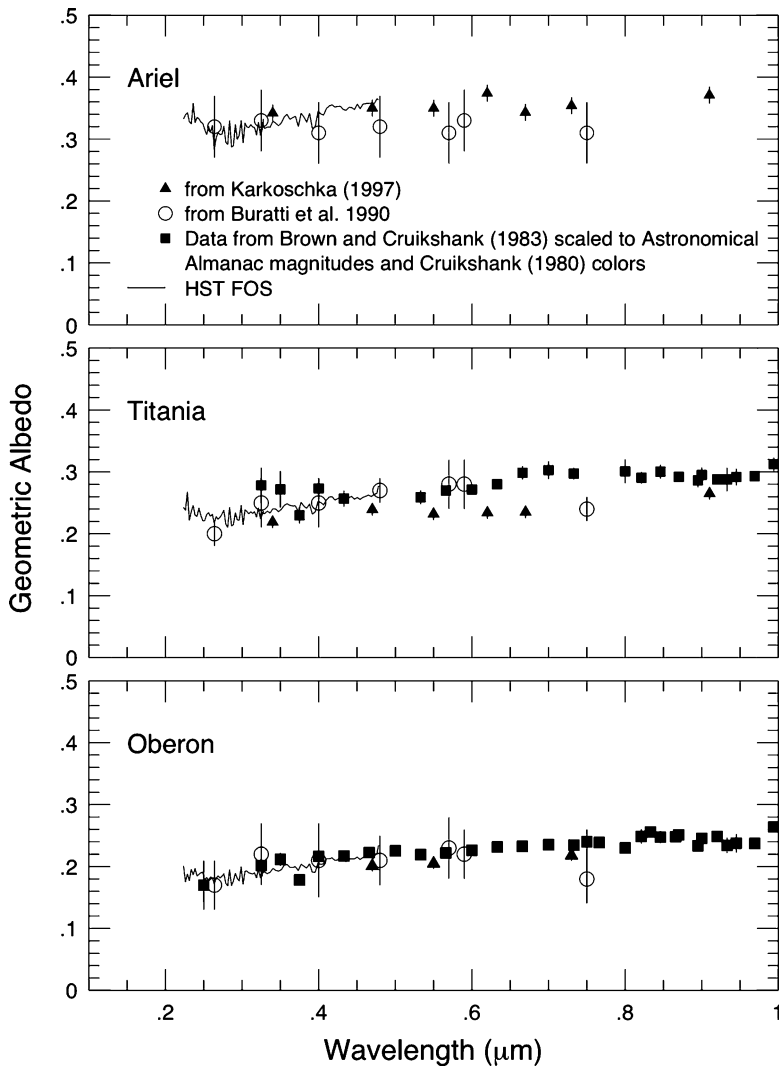


**Fig. 3.10** FOS near-ultraviolet spectra of Ariel, Titania, and Oberon (Roush et al. 1998) are shown as solid curves and compared to spectrophotometry (Brown and Cruikshank 1983; Buratti et al. 1990; Karkoschka 1997). All three satellites have minima near 280 nm. The source of this subtle feature may be entrapped OH in ice (Roush et al. 1998) although other sources are possible

seen at visible wavelengths in these objects. A subtle minimum is seen in all three satellites centered at 280 nm. The feature is strongest in Ariel and decreases with increasing distance from Uranus becoming weaker in Titania and weakest in Oberon. Whether or not hemispheric differences exist is unclear from these data because the sub-Earth latitude at the time of these observations in August 1996 was approximately 45°S. Sub-Earth longitudes at the single epoch of observation were approximately 90° for Ariel, 310° for Titania, and 130° for Oberon.

A 280 nm near-UV absorption feature is present at Europa where it is interpreted as a signature of either SO<sub>2</sub> or sulfur ions in ice (Sect. 3.4.1.3). Roush et al. (1998), however, interpreted the 280 nm minimum in Ariel, Titania and Oberon as being due to trapped OH in ice (Taub and Eiben 1968). The lower temperatures of the uranusian satellites allow for OH to remain trapped in an ice lattice unlike the situation in the jovian system. This fact and the lack of an obvious source of sulfur ions similar to Io in the jovian system led the authors to prefer this interpretation over SO<sub>2</sub>. However, sulfur present in surface brines processed by magnetospheric charged particle radiolysis could provide an endogenic source of this species. An attempt to fit the observed feature with OH alone proved incomplete.

### 3.4.4 Triton

In the Neptune system, only Triton is bright enough for observations in the ultraviolet from Earth. Initial observations in the UV were made with the Voyager 2 PPS UV channel (250 nm) (Lane et al. 1989); a geometric albedo of 0.59 was obtained for Triton, 0.12 for Nereid and 0.06 for Larissa, highlighting the uniqueness of Triton and its relatively high UV albedo.

Stern and Trafton (1994) obtained a spectrum from 220 to 330 nm with the HST FOS that extended earlier work with IUE and Voyager. These data showed an inflection in the albedo curve flattens at 285 nm transitioning from a red slope at longer wavelengths to a flat slope at shorter wavelengths. The spectrum is otherwise featureless. Stern et al. (1995) interpreted the inflection as a weak band centered at 275 nm with a depth of ~6% relative to a flat continuum bridging their observed spectral range. Because the band did not appear to vary with rotation, Stern et al. inferred that it could be due to a non-icy contaminant. No compositional constraints on surface ices were inferred from these spectra.

Young and Stern (2001) reported changes in Triton's UV albedo from observations made with the STIS instrument in 1997. They noted that the albedo increased by ~20% in the 250–320 nm interval but not at shorter wavelengths with the overall effect being a reddening of the UV spectrum. Young and Stern also noted that the light curve amplitude was less pronounced than predicted by Voyager-based models. Both of these changes were interpreted as being due to seasonal effects, although the details of the mechanism involved remain unknown.

### 3.4.5 Pluto and Charon

The ultraviolet spectrum of Pluto, measured using HST's FOS in 1992–93, was analyzed down to 250 nm by Trafton and Stern (1996). Multiple longitudes, all with Charon out of the aperture, were measured in order to evaluate light curve variability. Krasnopolsky (2001) extended the analysis of these same data to

200 nm. Like Triton, the spectrum of Pluto is featureless except for a possible very weak minimum or change of slope near 260 nm. Pluto's mean geometric albedo over the 200–330 nm range is approximately 0.225–0.25, significantly lower than Triton's. From the UV albedo, Krasnopolsky derived upper limits for ices on Pluto's surface:  $\text{H}_2\text{O} < 20\%$ ,  $\text{CO}_2 < 13\%$ ,  $\text{NH}_3 < 10\%$ , and  $\text{SO}_2 < 4\%$ .

Krasnopolsky (2001) also reported the ultraviolet spectrum of Charon, derived from FOS data obtained in 1993. After correcting for background and scattered light from Pluto, Krasnopolsky was able to extract spectra of the leading and trailing hemispheres of Charon observed near maximum elongation. The spectra extended from 225 to 320 nm with reasonable S/N and shows a mostly flat spectrum with an albedo range similar to Pluto's.

Longitudinal variations in Pluto follow the visible lightcurve, with some small differences. The absolute amplitude is very similar at UV and visible wavelengths, but the fractional amplitude increases at shorter wavelengths as the albedo decreases. These observations suggest that the lightcurve is controlled primarily by the non-ice component of the surface (Trafton and Stern 1996).

### 3.5 Application of Laboratory Data to Spacecraft Measurements

As an example of an application of laboratory-measured properties of ices to spacecraft measurements of an icy surface, we discuss a Cassini UVIS measurement of Enceladus (Fig. 3.9a). Some of the Saturnian moons exhibit lower visible albedos and demonstrate obvious spectral slopes in the near-UV and visible, suggestive of a non-water ice species. Enceladus, however, from visible-near infrared wavelength observations, exhibits little spectral evidence of surface constituents other than water ice. As discussed, the UVIS measurements of Enceladus show this body to be darker at far-UV wavelengths than expected from a pure water ice surface. Hendrix et al. (2010) modeled the spectrum with an intimate mixing model (Hapke 2002) consisting of 98% water ice (using the Warren and Brandt 2008 optical constants used in Fig. 3.2), 1% ice tholin (Khare et al. 1993) and 1%  $\text{NH}_3$  ice (using the Dawes et al. 2007 optical constants used in Fig. 3.3). Model results are shown in Fig. 3.11; this mixture provides an adequate representation of the UVIS spectrum while simulating the general spectral shape of Enceladus at near-UV and visible wavelengths as well. As noted, the STIS spectrum of Enceladus (Fig. 3.8) shows a sharp decline in brightness near 210 nm and is consistent with the low UVIS-measured albedo as well as the identification of  $\text{NH}_3$  ice (Fig. 3.3). A small amount of ice tholin, a species produced by irradiation of a 6:1  $\text{H}_2\text{O:C}_2\text{H}_6$  mixture, was needed in the model to produce a slight red slope in the near-UV.

Ammonia (or a related species) could be present on the other satellites in the Saturn system, and could help explain their low far-UV albedos. However, as those

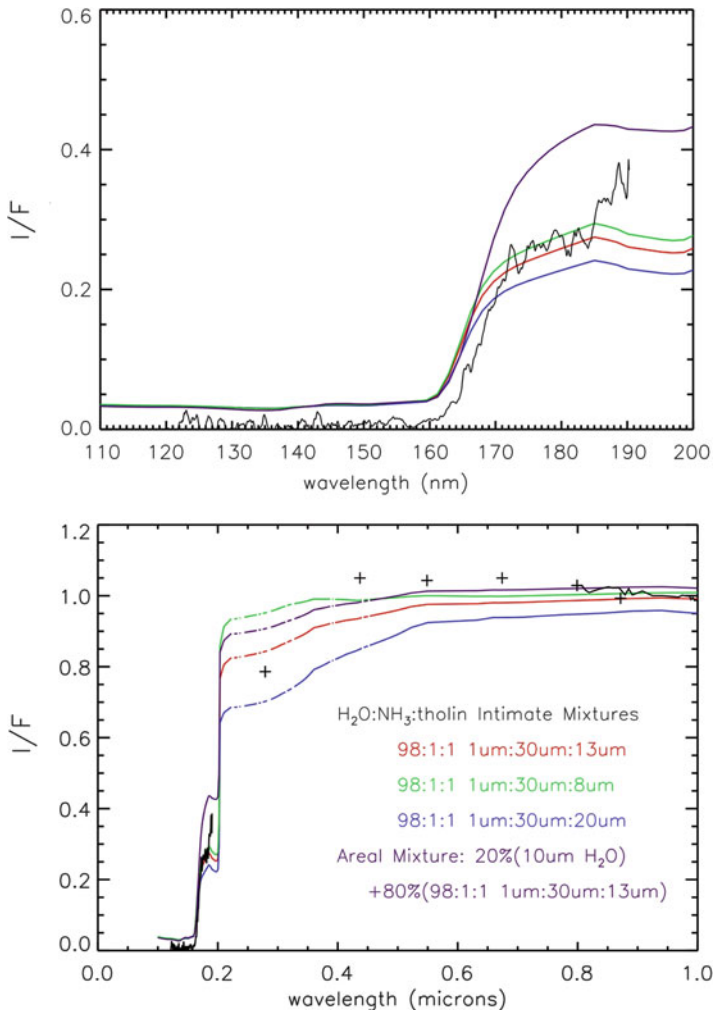


**Fig. 3.11** Enceladus data (from Fig. 3.9a) compared with spectral mixing models. (top) Cassini UVIS spectrum. (bottom) UVIS spectrum plus HST broad band data from Verbiscer et al. (2005) at solar phase angle = 2°. Shown are intimate mixtures of H<sub>2</sub>O, ice tholin (1%) and NH<sub>3</sub> (1%). Also shown is an areal mixture of 20% H<sub>2</sub>O and 80% of an intimate mixture of H<sub>2</sub>O, ice tholin and NH<sub>3</sub>. Models use NH<sub>3</sub> data from Dawes et al. (2007) (From Hendrix et al. (2010))

moons do not exhibit such a high near-UV-visible albedo along with the sharp 210 nm drop-off of Enceladus, we expect that another species (such as a tholin) dominates the characteristics of this part of the spectrum.

In the Enceladus situation, it is plausible that pure NH<sub>3</sub> is present as part of the surface ice in these amounts, because ammonia has been detected in the plume as a neutral gas (Waite et al. 2009) and is likely consistently replenished on the surface.

In other regions of the Saturn (and solar) system, we expect that NH<sub>3</sub> would be rapidly processed and converted to ammonia hydrate and other related species. With such a strong absorption edge in NH<sub>3</sub>, it is plausible that a related species would exhibit a strong absorption as well, but this is unknown. It is therefore critical that UV laboratory measurements of these species be studied.

### 3.6 Conclusions and Needed Measurements

Our understanding of solar system surfaces and processes has been greatly enhanced during the last four decades by the use of ultraviolet measurements, both by combining with longer-wavelength datasets and by studying the UV data sets on their own. The ultraviolet range has been significantly utilized in studying the varying radiolytic and space weathering processes and effects in different regions in the solar system. Many more measurements have yet to be made to realize the potential of this wavelength range in investigating solar system ices.

Interpretation of ultraviolet spacecraft data suffers from a severe lack of laboratory data at appropriate temperatures. Modern measurements of pure water ice and mixtures of ices, both pure and irradiated, are critical. Further irradiation studies are needed, for instance, to understand the 260 nm absorption feature at Ganymede, which is broader than the ozone feature produced from irradiation of pure ice in the laboratory (Teolis et al. 2006) and may be the result of other species. Similarly, the H<sub>2</sub>O<sub>2</sub> feature, which appears to be present on all the Galilean satellites (Hendrix et al. 1999c), has not been replicated in the laboratory via irradiation experiments; this would be a valuable measurement to fully understand the Galileo data and to prepare for a future flagship mission to Jupiter. Laboratory experiments measuring ammonia hydrate in transmission or reflectance in the UV at outer solar system-appropriate temperatures have not been reported in the literature, but would be exceedingly helpful in interpreting Cassini data from the Saturnian system. Laboratory studies of ice-rich carbonaceous species, including tholins, would be useful for analysis of bodies in the Saturnian system as well as other outer solar system objects, by New Horizons and future spacecraft missions. Sulfur-ice mixtures, both pure and irradiated, are critical for interpretation of spacecraft data from the Jovian system, particularly in light of the upcoming Europa mission. Laboratory studies of photolysis of ice mixtures have yielded potentially biologically significant amino groups (e.g., Bernstein et al. 2002; Munoz Caro et al. 2002) – which may be detectable at UV wavelengths on other bodies, but the spectroscopy work must be done in the laboratory.

**Acknowledgements** The research was carried out at the Jet Propulsion Laboratory, California Institute of Technology, under a contract with the National Aeronautics and Space Administration. © 2011. All rights reserved.

## References

- Baragiola RA (2003) Water ice on outer solar system surfaces: basic properties and radiation effects. *Planet Space Sci* 51:953–961
- Berland BS, Foster KL, Tolbert MA, George SM (1996) UV absorption spectra of H<sub>2</sub>O/HNO<sub>3</sub> films. *Geophys Res Lett* 23:2757–2760
- Bernstein MP, Elsila JE, Dworkin JP, Sandford SA, Allamandola LJ, Zare RN (2002) Side group addition to the polycyclic aromatic hydrocarbon coronene by ultraviolet photolysis in cosmic ice analogs. *Astrophys J* 576:1115–1120
- Bradley ET, Colwell JE, Esposito LW, Cuzzi JN, Tollerud H, Chambers L (2010) Far ultraviolet spectral properties of Saturn's rings from Cassini UVIS. *Icarus* 206:458–466
- Browell EV, Anderson RC (1975) Ultraviolet optical constants of water and ammonia ices. *J Opt Soc Am* 65:919–926
- Brown RH, Cruikshank DP (1983) The uranus satellites: surface compositions and opposition brightness surges. *Icarus* 55:83–92
- Buratti B, Wong F, Mosher J (1990) Surface properties and photometry of the uranian satellites. *Icarus* 84:203–214
- Caldwell J (1975) Ultraviolet observations of small bodies in the solar system by OAO-2. *Icarus* 25:384–396
- Calvin WM, Clark RN (1991) Modeling the reflectance spectrum of Callisto 0.25 to 4.1 μm. *Icarus* 89:305–317
- Calvin WM, Clark RN, Brown RH, Spencer JR (1995) Spectra of the icy Galilean satellites from 0.2 to 5 μm: a compilation, new observations, and a recent summary. *J Geophys Res* 100:19041–19048
- Calvin WM, Johnson RE, Spencer JR (1996) O<sub>2</sub> on Ganymede: spectral characteristics and plasma formation mechanisms. *Geophys Res Lett* 23:673–676
- Carlson R et al (1996) Near-Infrared Spectroscopy and Spectral mapping of Jupiter and the Galilean Satellites: results from Galileo's initial orbit. *Science* 274:385–388
- Carlson RW, Anderson MS, Johnson RE, Smythe WD, Hendrix AR, Barth CA, Soderblom LA, Hansen GB, McCord TB, Dalton JB, Clark RN, Shirley JH, Ocampo AC, Matson DL (1999) Hydrogen peroxide on the surface of Europa. *Science* 283:2062–2064
- Carlson RW, Anderson MS, Mehlman R, Johnson RE (2005) Distribution of hydrate on Europa: further evidence for sulfuric acid hydrate. *Icarus* 177:461–471
- Cassel EJ (1936) Ultra-violet absorption of ice. *Proc R Soc* 153:534–541
- Clark RN, Cruikshank DP, Jaumann R, Brown RH, Stephan K, Dalle Ore CM, Livo KE, Pearson N, Curchin JM, Hoefen TM, Buratti BJ, Filacchione G, Baines KH, Nicholson PD (2012) The Composition of Iapetus: Mapping Results from Cassini VIMS. *Icarus* 218:831–860
- Cooper JF, Johnson RE, Mauk BH, Garrett HB, Gehrels N (2001) Energetic ion and electron irradiation of the icy Galilean satellites. *Icarus* 149:133–159
- Cooper PD, Johnson RE, Quickenden TI (2003) Hydrogen peroxide dimers and the production of O<sub>2</sub> in icy satellite surfaces. *Icarus* 166:444–446
- Daniels J (1971) Bestimmung der optischen konstanten von eis aus energie – verlustmessungen von schnellen elektronen. *Opt Commun* 3:240
- Dawes A, Mukerji RJ, Davis MP, Holtom PD, Webb SM, Sivaraman B, Hoffmann SV, Shaw DA, Mason NJ (2007) Morphological study into the temperature dependence of solid ammonia under astrochemical conditions using vacuum ultraviolet and Fourier-transform infrared spectroscopy. *J Chem Phys* 126:244711-1–244711-12
- Domingue DL, Lockwood GW, Kubala AE (1998) Supplementary analysis of Io's disk-integrated solar phase curve. *Icarus* 134:113–136
- Dressler K, Schnepf O (1960) Absorption spectra of solid methane, ammonia, and ice in the vacuum ultraviolet. *J Chem Phys* 33:270–274

- Gomis O, Satorre MA, Strazzulla G, Leto G (2004) Hydrogen peroxide formation by ion implantation in water ice and its relevance to the Galilean satellites. *Planet Space Sci* 52:371–378
- Grundy WM, Young LA, Young EF (2003) Discovery of CO<sub>2</sub> ice and leading-trailing spectral asymmetry on the uranus satellite Ariel. *Icarus* 162:222–229
- Grundy WM, Young LA, Spencer JR, Johnson RE, Young EF, Buie MW (2006) Distributions of H<sub>2</sub>O and CO<sub>2</sub> ices on Ariel, Umbriel, Titania, and Oberon from IRTF/SpeX observations. *Icarus* 184:543–555
- Gurnett DA, Kurth WS, Roux A, Bolton SJ, Kennel CF (1996) Evidence for a magnetosphere at Ganymede from plasma-wave observations by the Galileo spacecraft. *Nature* 384:535–537
- Greenberg, JM (1968) Nebulae and Interstellar Matter. In: Middlehurst BM, Aller LH (eds) Stars and stellar systems, Vol 7, University of Chicago Press, Chicago, p 221
- Hansen GB (2005) Ultraviolet to near-infrared absorption spectrum of carbon dioxide ice from 0.174 to 1.8 μm. *J Geophys Res* 110:E110033. doi:[10.1029/2005JE002531](https://doi.org/10.1029/2005JE002531)
- Hapke B (1989) The surface of Io – a new model. *Icarus* 79:56–74
- Hapke BW (2002) Bidirectional reflectance spectroscopy 5. The coherent backscatter opposition effect and anisotropic scattering. *Icarus* 157:523–534
- Hapke B, Wells E, Wagner J, Partlow W (1981) Far-UV, visible, and near-IR reflectance spectra of frosts of H<sub>2</sub>O, CO<sub>2</sub>, NH<sub>3</sub>, and SO<sub>2</sub>. *Icarus* 47:361–367
- Hendrix AR, Johnson RE (2008) Callisto: new insights from Galileo disk-resolved UV measurements. *Astrophys J* 687:706
- Hendrix AR, Barth CA, Hord CW, Lane AL (1998) Europa: disk-resolved ultraviolet measurements using the Galileo ultraviolet spectrometer. *Icarus* 135:79–84
- Hendrix AR, Barth CA, Hord CW (1999a) Io's patchy SO<sub>2</sub> atmosphere as measured by the Galileo ultraviolet spectrometer. *J Geophys Res* 104:11817–11826
- Hendrix AR, Barth CA, Hord CW (1999b) Ganymede's ozone-like absorber: observations by the Galileo ultraviolet spectrometer. *J Geophys Res* 104:14169–14178
- Hendrix AR, Barth CA, Stewart AIF, Hord CW, Lane AL (1999c) Hydrogen peroxide on the icy Galilean satellites. *LPSC XXX #2043*
- Hendrix AR, Hansen CJ, Holsclaw GM (2010) The ultraviolet reflectance of enceladus: implications for surface composition. *Icarus* 206:608–617
- Hibbitts CA, McCord TB, Hansen GB (2000) Distributions of CO<sub>2</sub> and SO<sub>2</sub> on the surface of Callisto. *J Geophys Res* 105:22541–22557
- Horanyi M, Cravens TE (1996) The structure and dynamics of Jupiter's ring. *Nature* 381:293–295
- ISO 21348-2007(E) Space environment (natural and artificial) – process for determining solar irradiances
- Johnson TV (1971) Galilean satellites: narrowband photometry 0.3–1.1 microns. *Icarus* 14:94–111
- Johnson RE, Jesser WA (1997) O<sub>2</sub>/O<sub>3</sub> microatmospheres in the surface of Ganymede. *Astrophys J* 480:L79–L82
- Johnson RE, Quickenden TI (1997) Photolysis and radiolysis of water ice. *J Geophys Res* 102:10985–10996
- Johnson TV, Soderblom LA, Mosher JA, Danielson GE, Cook AF, Kupferman P (1983) Global multispectral mosaics of the icy Galilean satellites. *J Geophys Res* 88:5789–5805
- Johnson RE, Nelson ML, McCord TB, Gradie JC (1988) Analysis of Voyager images of Europa: plasma bombardment. *Icarus* 75:423–436
- Johnson RE, Killen RM, Waite JH Jr, Lewis WS (1998) Europa's surface composition and sputter-produced atmosphere. *Geophys Res Lett* 25:3257–3260
- Karkoschka E (1997) Rings and satellites of Uranus: colorful and not so dark. *Icarus* 125:348–363
- Khare BN, Thompson WR, Cheng L, Chyba C, Sagan C, Arakawa ET, Meisse C, Tuminello PS (1993) Production and optical constants of ice tholin from charged particle irradiation of (1:6) C<sub>2</sub>H<sub>6</sub>/H<sub>2</sub>O at 77K. *Icarus* 103:290–300

- Kivelson MG, Khurana KK, Russell CT, Walker RJ, Warnecke J, Coroniti FV, Polanskey C, Southwood DJ, Schubert G (1996) Discovery of Ganymede's magnetic field by the Galileo spacecraft. *Nature* 384:537–541
- Kobayashi K (1983) Optical and electronic structure of ice. *J Phys Chem* 87:4317–4321
- Krasnopolsky VA (2001) Middle ultraviolet spectroscopy of Pluto and Charon. *Icarus* 153:277–284
- Kuo Y-P, Lu H-C, Wu Y-J, Cheng B-M, Ogilvie JF (2007) Absorption spectra in the vacuum ultraviolet region of methanol in condensed phases. *Chem Phys Lett* 447:168–174
- Lane AL, Domingue DL (1997) IUE's view of Callisto: detection of an SO<sub>2</sub> absorption correlated to possible torus neutral wind alterations. *Geophys Res Lett* 24:1143
- Lane AL, Nelson RM, Matson DL (1981) Evidence for sulphur implantation in Europa's UV absorption band. *Nature* 292:38–39
- Lane AL et al (1989) Photometry from Voyager 2: initial results from the Neptunian atmosphere, satellites, and rings. *Science* 246:1450–1454
- Lillie CF, Hord CW, Pang K, Coffee DL, Hansen JE (1977) The Voyager mission photopolarimeter experiment. *Space Sci Rev* 21:159–181
- Lu H-C, Chen H-K, Cheng B-M, Kuo Y-P, Ogilvie JF (2005) Spectra in the vacuum ultraviolet region of CO in gaseous and solid phases and dispersed in solid argon at 10 K. *J Phys B-At Mol Opt* 38:3693–3704
- Lu H-C, Chen H-K, Cheng B-M, Ogilvie JF (2008) Absorption spectra in the vacuum ultraviolet region of small molecules in condensed phases. *Spectrochim Acta A* 71:1485–1491
- Martonchik JV, Orton GS, Appleby JF (1984) Optical properties of NH<sub>3</sub> ice from the far infrared to the near ultraviolet. *Appl Optics* 23:541–547
- Mason NJ, Dawes A, Holtom PD, Mukerji RJ, Davis MP, Sivaraman B, Kaiser RI, Hoffmann SV, Shaw DA (2006) VUV spectroscopy of extraterrestrial ices. In: Kaiser RI, Bernath P, Osamura Y, Petrie S, Mebel AM (eds) *Astrochemistry, from laboratory studies to astronomical observations*. American Institute of Physics, Melville
- McCord TB et al (1997) Organics and other molecules in the surfaces of Callisto and Ganymede. *Science* 278:271
- McEwen AS (1986) Exogenic and endogenic albedo and color patterns on Europa. *J Geophys Res* 91:8077–8097
- McEwen AS, Johnson TV, Matson DL, Soderblom LA (1988) The global distribution, abundance and stability of SO<sub>2</sub> on Io. *Icarus* 75:450–478
- McFadden LA, Bell JF, McCord TB (1980) Visible spectral reflectance measurements (0.33–1.1 μm) of the Galilean satellites at many orbital phase angles. *Icarus* 44:410–430
- Millis RL, Thompson DT (1975) UVB photometry of the Galilean satellites. *Icarus* 26:408–419
- Minton AP (1971) The far-ultraviolet spectrum of ice. *J Phys Chem* 75:1162–1164
- Moore MH, Hudson RL (2000) IR detection of H<sub>2</sub>O<sub>2</sub> at 80 K in ion-irradiated laboratory ices relevant to Europa. *Icarus* 145:282–288
- Morrison D, Morrison ND, Lazarewicz AR (1974) Four-color photometry of the Galilean satellites. *Icarus* 23:399–416
- Munoz Caro GM, Meierhenrich UJ, Schutte WA, Barbier B, Arcones Segovia A, Rosenbauer H, Thiemann WH-P, Brack A, Greenberg JM (2002) Amino acids from ultraviolet irradiation of interstellar ice analogues. *Nature* 416:403–406
- Nash DB, Howell RR (1989) Hydrogen sulfide on Io – evidence from telescopic and laboratory infrared spectra. *Science* 244:454–457
- Nash DB, Fanale FP, Nelson RM (1980) SO<sub>2</sub> frost: UV-visible reflectivity and Io surface coverage. *Geophys Res Lett* 7:665–668
- Nelson RM, Hapke BW (1978) Spectral reflectivities of the Galilean satellites and Titan, 0.32 to 0.86 micrometers. *Icarus* 36:304–329
- Nelson ML, McCord TB, Clark RN, Johnson TV, Matson DL, Mosher JA, Soderblom LA (1986) Europa: characterization and interpretation of global spectral surface units. *Icarus* 65:129–151

- Nelson RM, Buratti BJ, Wallis BD, Lane AL, West RA, Simmons KE, Hord CW, Esposito LW (1987) Voyager 2 photopolarimeter observations of the Uranian satellites. *Icarus* 92:14905–14910
- Noll KS, Weaver HA, Gonnella AM (1995) The albedo spectrum of Europa from 2200 to 3300 Å. *J Geophys Res* 100:19057–19059
- Noll KS, Johnson RE, Lane AL, Domingue DL, Weaver HA (1996) Detection of ozone on Ganymede. *Science* 273:341–343
- Noll KS, Johnson RE, McGrath MA, Caldwell JJ (1997a) Detection of SO<sub>2</sub> on Callisto with the Hubble Space Telescope. *Geophys Res Lett* 24:1139–1142
- Noll KS, Roush TL, Cruikshank DP, Johnson RE, Pendleton YJ (1997b) Detection of ozone on Saturn's satellites Rhea and Dione. *Nature* 388:45–47
- Ockert ME, Nelson RM, Lane AL, Matson DL (1987) Europa's ultraviolet absorption band (260 to 320 nm) – temporal and spatial evidence from IUE. *Icarus* 70:499–505
- Onaka R, Takahashi T (1968) Vacuum UV absorption spectra of liquid water and ice. *J Phys Soc Jpn* 24:548–550
- Otto A, Lynch MJ (1970) Characteristic electron energy losses of solid benzene and ice. *Aust J Phys* 23:609–612
- Paresce F et al (1992) Near-ultraviolet imaging of Jupiter's satellite Io with the Hubble Space Telescope. *Astron Astrophys* 262:617–620
- Pilcher CB, Ridgway ST, McCord TB (1972) Galilean satellites: identification of water frost. *Science* 178:1087–1089
- Pipes JG, Browell EV, Anderson RC (1974) Reflectance of amorphous-cubic NH<sub>3</sub> frosts and amorphous-hexagonal H<sub>2</sub>O frosts at 77 K from 1400 to 3000 Å. *Icarus* 21:283–291
- Pospieszczyk MK, Johnson RE (1989) Magnetospheric ion bombardment profiles of satellites: Europa and Dione. *Icarus* 78:1–13
- Roush TL, Pollack JB, Witteborn FC, Bregman JD, Simpson JP (1990) Ice and minerals on Callisto – a reassessment of the reflectance spectra. *Icarus* 86:355
- Roush TL, Noll KS, Cruikshank DP, Pendleton Y (1998) Ultraviolet spectra of Ariel, Titania, and Oberon: evidence for trapped OH from Hubble Space Telescope Observations. *LPSC Abstracts* 29:1636
- Sack NJ, Boring JW, Johnson RE, Baragiola RA, Shi M (1991) Alteration of the UV-visible reflectance spectra of H<sub>2</sub>O ice by ion bombardment. *J Geophys Res* 96:17535–17539
- Salama F, Allamandola LJ, Witteborn FC, Cruikshank DP, Sanford SA, Bregman JD (1990) The 2.5–5.0 micron spectra of Io – evidence for H<sub>2</sub>S and H<sub>2</sub>O frozen in SO<sub>2</sub>. *Icarus* 83:66–82
- Seki M, Kobayashi K, Nakahara J (1981) Optical spectra of hexagonal ice. *J Phys Soc Jpn* 50:2643–2648
- Shibaguchi T, Onuki H, Onaka R (1977) Electronic structures of water and ice. *J Phys Soc Jpn* 42:152–158
- Sieveka EM, Johnson RE (1982) Thermal- and plasma-induced molecular redistribution on the icy satellites. *Icarus* 51:528–548
- Smythe WD, Nelson RM, Nash DB (1979) Spectral evidence for SO<sub>2</sub> frost or adsorbate on Io's surface. *Nature* 280:766
- Spencer JR, Calvin WM, Person MJ (1995) Charge-coupled device spectra of the Galilean satellites: molecular oxygen on Ganymede. *J Geophys Res* 100:19049–19056
- Stebbins J, Jacobsen TS (1928) Further photometric measures of Jupiter's satellites and Uranus, with tests for the solar constant. *Lick Obs Bull* 13:180–195
- Stern SA, Trafton LM (1994) The ultraviolet spectrum of Triton from HST: first results. *Icarus* 112:533–536
- Stern SA, Trafton LM, Flynn B (1995) Rotationally resolved studies of the mid-ultraviolet spectrum of Triton. II. HST surface and atmospheric results. *Astron J* 109:2855–2868
- Strazzulla G, Massimino P, Spinella F, Calcagno L, Foti AM (1988) IR spectra of irradiated organic materials. *Infrared Phys* 28:183–188

- Taub IA, Eiben K (1968) Transient solvated electron, hydroxyl, and hydroperoxy radicals in pulse-irradiated crystalline ice. *J Chem Phys* 49:2499–2513
- Teolis BD, Loeffler MJ, Raut U, Fama M, Baragiola RA (2006) Ozone synthesis on the icy satellites. *Astrophys J* 644:L141–L144
- Trafton LM, Stern SA (1996) Rotationally resolved spectral studies of Pluto from 2500 to 4800 Å obtained with HST. *Astron J* 112:1212–1224
- Trafton LM, Lester DF, Ramseyer TF, Salama F, Sanford SA, Allamandola LJ (1991) A new class of absorption feature in Io's near-infrared spectrum. *Icarus* 89:264–276
- Vaghjiani GL, Ravishankara AR (1989) Absorption cross sections of  $\text{CH}_3\text{OOH}$ ,  $\text{H}_2\text{O}_2$  and  $\text{D}_2\text{O}_2$  vapors between 210 and 365 nm at 297 K. *J Geophys Res* 94:3487–3492
- Vaida V, Donaldson DJ, Strickler SJ, Stephens SL, Birks JW (1989) Reinvestigation of the electronic spectra of ozone: condensed-phase effects. *J Phys Chem* 93:506–508
- Verbiscer AJ, French RG, McGhee CA (2005) The opposition surge of Enceladus: HST observations 338–1022 nm. *Icarus* 173:66–83
- Verbiscer A, French R, Showalter M, Helfenstein P (2007) Enceladus: cosmic graffiti artist caught in the act. *Science* 315:815
- Wagner JK, Hapke BW, Wells EN (1987) Atlas of reflectance spectra of terrestrial, lunar, and meteoritic powders and frosts from 92 to 1800 nm. *Icarus* 69:14–28
- Wagener R, Caldwell J (1988) On the abundance of micron-sized particles in Saturn's A and B rings. A Decade of UV Astronomy with the IUE Satellite. In: Proceedings of the celebratory symposium held at Goddard Space Flight Center, Vol 1, pp 85–88. European Space Agency, Greenbelt, 12–15 April 1988
- Waite JH Jr et al (2009) Liquid water on Enceladus from observations of ammonia and 40Ar in the plume. *Nature* 460:487–490
- Warren SG (1984) Optical constants of ice from the ultraviolet to the microwave. *Appl Optics* 23:1206–1225
- Warren SG (1986) Optical constants of carbon dioxide ice. *Appl Optics* 25:2650–2674
- Warren SG, Brandt RE (2008) Optical constants of ice from the ultraviolet to the microwave: a revised compilation. *J Geophys Res* 113:D14220. doi:[10.1029/2007JD009744](https://doi.org/10.1029/2007JD009744)
- Young LA, Stern SA (2001) Ultraviolet observations of Triton in 1999 with the space telescope imaging spectrograph: 2150–3180 Å spectroscopy and disk-integrated photometry. *Astron J* 122:449–456

# Chapter 4

## The Ices on Transneptunian Objects and Centaurs

C. de Bergh, E.L. Schaller, M.E. Brown, R. Brunetto,  
D.P. Cruikshank, and B. Schmitt

**Abstract** Transneptunian objects (TNOs) and Centaurs are small bodies orbiting the Sun in the cold outer regions of the Solar System. TNOs include Pluto and its satellite Charon, and Neptune's large satellite Triton is thought to have been captured from the TNO population. Visible and near-infrared spectroscopy of a number of the brightest of these bodies shows surface ices of H<sub>2</sub>O, CH<sub>4</sub>, N<sub>2</sub>, CH<sub>3</sub>OH, C<sub>2</sub>H<sub>6</sub>, CO, CO<sub>2</sub>, NH<sub>3</sub>•nH<sub>2</sub>O, and possibly HCN, in various combinations; water ice is by far the most common. Silicate minerals and solid complex carbonaceous materials are thought to occur on these bodies, but their spectral signatures have not yet been positively identified. The pronounced red color of several TNOs and Centaurs is presumed to result from the presence of carbonaceous materials. In all, the TNOs and Centaurs are thought to be primitive bodies in the sense that they have undergone relatively little modification by heating and by the space environment since their condensation in the volatile-rich outer regions of the solar nebula. As such, they hold the potential to yield important information on the chemical and physical conditions of the solar nebula. Continued and expanded studies of

---

C. de Bergh (✉)

LESIA, Observatoire de Paris, Meudon, France

e-mail: [catherine.debergh@obspm.fr](mailto:catherine.debergh@obspm.fr)

E.L. Schaller

Lunar and Planetary Laboratory, University of Arizona, Tucson, USA

M.E. Brown

California Institute of Technology, California, USA

R. Brunetto

Institut d'Astrophysique Spatiale, Univ. Paris-Sud, CNRS, UMR-8617 Orsay, France

D.P. Cruikshank

NASA Ames Research Center, California, USA

B. Schmitt

Laboratoire de Planétologie de Grenoble, Université Joseph Fourier, CNRS-INSU, Grenoble, France

TNOs and Centaurs require additional basic laboratory data on the physical and the optical properties of the ices already identified and those candidate materials that have not yet been confirmed. New sky surveys and large telescopes projected for operation in the near future will reveal many more objects in the outer Solar System for detailed study.

## 4.1 Introduction

A large number of Solar System bodies called transneptunian objects (TNOs), or Kuiper Belt objects (KBOs), orbit around the Sun beyond Neptune, therefore in regions of the Solar System where ices must be predominant. Pluto belongs to this population. The first TNO (Pluto excluded) was discovered only in 1992 (Jewitt and Luu 1993) and more than 1,200 of them have now been found.

Various approaches are used to get information on the composition and nature of these bodies. Among them, spectroscopy is the most efficient one. However, as these objects are very faint, such observations are challenging. This is why only a limited number of objects have been observed spectroscopically so far, and, furthermore, why the spectra are not all of high quality. The generally brighter objects called Centaurs, whose orbits are located in between those of the giant planets, are studied in parallel as they most probably originated as TNOs. Triton, which is believed to be an escaped TNO which has been captured by Neptune (e.g., McCord 1966; McKinnon 1984; Agnor and Hamilton 2006), is also considered in this chapter, but more details on Triton (as well as on Pluto) can be found in the chapter by Clark et al. (2012).

A fraction of these objects have water ice on their surface. This water ice is often observed in the crystalline state. As concerns the largest TNOs, their spectra are dominated by methane ice, as is the case for Pluto and Triton. Although nitrogen ice (present on Pluto and Triton) has not been firmly identified on these objects its presence is indirectly inferred. These peculiar objects belong to the newly defined class of dwarf planets. The other ices identified on TNOs are: ethane, and, possibly, methanol and some ammonia hydrate, as well as carbon monoxide which is seen only on Pluto and Triton, however, and carbon dioxide detected only on Triton. In addition, hydrogen cyanide may be present on Triton. Some of these ices may be present as mixtures. Other compounds such as silicates and carbonaceous materials are present as well, either as impurities in the ices or coexisting with them in separate entities (areal mixtures) (See Sect. 3). They are however much more difficult to identify.

After providing some general information on TNOs and Centaurs, we present the models and laboratory data available to interpret the spectra of these objects, as well as specific needs for new laboratory measurements on ices. We then present results on the surface composition based on spectral modelling and other known properties of these objects. In the last part, before concluding, we discuss the possible states of alteration of the observed surfaces, given the various alteration processes that could be at work.

## 4.2 Brief Overview of the Properties of TNOs and Centaurs

The TNOs discovered so far orbit the Sun in the region between about 30 AU and several hundred AU. Some have relatively circular orbits while others have very elliptic orbits. Furthermore the orbital inclinations over the ecliptic have a wide range of values. It is clear that this region of the Solar System has been dynamically highly perturbed with time, leading to objects with very different orbits that have been classified in several main classes: the classical objects which have, for the majority of them, semi-major axes between about 42 and 48 AU and low orbital eccentricities, the resonant objects which are trapped in mean-motion resonances with Neptune, the scattered disk objects which have high-eccentricity and high-inclination orbits and perihelion distances near 35 AU, and the detached (or extended scattered disk) objects which have pericenters decoupled from Neptune (see Gladman et al. 2008 for more details). Among the resonant objects, those that are in 3:2 resonance with Neptune, as is Pluto, are called Plutinos. Some of these objects must have formed in a region different from where they are now. Outer planet migration, with possibly an episode of strong resonance between Jupiter and Saturn, and maybe additional effects due to passing stars or planet-size embryos could have shaped the transneptunian region (see, e.g. Morbidelli et al. 2008).

Many TNOs have near-similar sized satellites. A few have satellites that are much smaller than the main body, probably indicating a different formation mechanism (see Noll et al. 2008 for a review).

The Centaurs have orbits that cross those of the giant planets. They must have originated in the transneptunian region, but they have escaped Neptune's influence and have been ejected into (unstable) planet-crossing orbits with perihelia closer to the Sun. Some of them may become Jupiter-family comets or those ejected to very large perihelia may have become scattered disk objects (e.g., Levison and Duncan 1997; Horner et al. 2004).

Size estimates, when available, indicate bodies with diameters in the 50–3,000 km range. Not that many bodies have had their size estimated, however. Indeed, a direct size estimate has been possible for only the brightest TNOs. For other objects, we need to know not only the magnitude and distance of the object but also its surface albedo. The albedo is the percentage of sunlight reflected by a surface. To measure a surface albedo it is necessary to have access to measurements in the thermal infrared range. Wherever TNOs originated from<sup>1</sup>, at present Solar System conditions they have temperatures between 20 and 60 K. They therefore emit very little thermal radiation. This is why only a few albedo measurements are available. Those that exist mostly come from recent observations

---

<sup>1</sup> Some TNOs may have originated in cold regions of the solar nebula and incorporated pre-solar materials, others may have incorporated grains which were reprocessed close to the sun (such as crystalline silicates detected in comets), due to a huge radial mixing during the early stages of the solar nebula and before the accretion of the planetesimals.

with the Spitzer Space Telescope. Many albedos are in the 0.04–0.2 range. However, some objects, and particularly the large ones, have very high albedos most probably related to the predominance of ices on their surfaces (Stansberry et al. 2008).

By studying the orbits of TNOs satellites it is possible to get good estimates of their masses and therefore some constraints on their densities. For some other objects, information on their densities is derived from the observed light-curves (studies of the brightness variations with the rotation of the object). The densities were found to vary between about 0.6 and 2.6 g/cm<sup>3</sup>, with a tendency for larger bodies to have a higher density (Sheppard et al. 2008), therefore smaller than that of asteroids of comparable size, indicating a significant ice fraction in their interiors. More recently, a much higher density (of the order of 4.2 g/cm<sup>3</sup>) has been measured for the classical object Quaoar, making us question its origin (Fraser and Brown 2010). About 40 objects have well-known rotational periods that range between 3.4 and 18 h (Sheppard et al. 2008).

Detailed information on the physical nature of TNOs and Centaurs is hard to obtain as these objects are very faint (visual magnitudes generally between 19 and 27) because of their large distances from the Sun, their small size and their generally low surface albedo. Among the more than 1,200 objects discovered, only about 130 of them have been observed by spectro-photometry (broad-band photometry at different wavelengths) and many fewer (only about 60) by spectroscopy. Spectro-photometric observations have revealed a very surprising wide range of colors, as well as the existence of very red objects (Doressoundiram et al. 2008). Among them are found the reddest small Solar System bodies. In particular, they are much redder than Trojan asteroids and Jupiter-family comets (Luu and Jewitt 1996). This unique property is still not completely understood, although it may have some connection with different space weathering conditions, or perhaps reflects intrinsic differences in composition.

Spectroscopy of TNOs and Centaurs has proven to be quite difficult. Indeed, not only are the objects very faint, the composition and nature of their surfaces are such that, in many cases, the spectra are featureless. Existing spectra are essentially ground-based data in the visible and near-IR ranges (up to 2.5 μm) acquired with the Keck, Subaru, ESO-VLT and ESO-NTT, Gemini or TNG telescopes. Spectra in the visible and near-IR probe only the upper surface layers, probably no deeper than a few centimeters below the surface, in the most favourable cases.

The species detected in spectra of TNOs and Centaurs are essentially ices. The most common signatures detected are those of water ice at 1.5 and 2 μm. In addition, very clear signatures of solid methane have been detected in visible and near-IR spectra of two large TNOs (Eris and Makemake) (Brown et al. 2005; Licandro et al. 2006a, b), making them very similar to Pluto in terms of surface composition, with, however, some interesting differences that will be discussed in Sect. 5. Much weaker signatures of methane ice are seen (only in the near-IR) in spectra of two other TNOs (Quaoar, and Sedna) (Schaller and Brown 2007b; Barucci et al. 2005a). Nitrogen ice has been searched for on these objects, but there is no firm detection of this ice so far. It could be present on all four TNOs, however (see further). Ethane ice is also detected on Makemake and Quaoar (Brown et al. 2008;

Dalle Ore et al. 2009), and may be present on Pluto (DeMeo et al. 2010; Merlin et al. 2010b). Two objects (one Centaur and one TNO) show the presence of a feature at 2.27  $\mu\text{m}$  in their spectra that has been attributed to methanol ice (or a similar species) (Cruikshank et al. 1998; Barucci et al. 2006). A feature around 2.2  $\mu\text{m}$ , also seen in Charon spectra, has been attributed to some ammonia hydrate in the solid state. This is however a tentative identification (see further). Carbon monoxide ice is detected in near infrared spectra of Pluto and Triton, not on any other TNO so far. Carbon dioxide is seen only on Triton.

Observations with the Spitzer Space telescope, which are essentially broad-band photometric observations in the far-IR, are very useful to complement the ground-based spectroscopic observations at shorter wavelengths, providing additional constraints on the surface composition (e.g. Emery et al. 2007). In addition, very interesting spectroscopic observations have been obtained with Spitzer on the bright Centaurs Asbolus and Elatus (Barucci et al. 2008a). They have shown the presence of fine-grained silicates, without any specific identification of the minerals so far. There is also some indication for the presence of hydrated silicates at the surface of some TNOs, based on the existence of very weak bands in visible spectra. However, this needs confirmation (see Barucci et al. 2008a for a review).

To explain other characteristics of TNOs and Centaurs (overall spectral shape, very red colors of some of the objects, and low surface albedos) it is generally assumed that the surfaces contain, in addition to ices and silicates, some refractory carbonaceous compounds. This assumption is made by analogy with what is found in meteorites, comets, interplanetary dust particles and the interstellar medium, and is also based on our knowledge of the effects of irradiation on carbon-containing ices as observed in the laboratory (see Sect. 4). Due to a lack of specific signatures of such compounds in the spectra of TNOs and Centaurs, and to a lack of available optical constants, models of TNOs and Centaurs spectra generally include species such as tholins (Titan, Triton, or Ice tholins), HCN polymers, kerogens and amorphous carbons. Titan and Triton tholins are products of irradiation of gaseous mixtures of methane and nitrogen in different proportions that are made in the laboratory. Ice tholins are produced by irradiation of mixtures of ices. These compounds can have very red spectral slopes in the visible, especially fine-grained tholins. No known silicates are as red as these tholins. Small (nano-phase) metallic iron particles are another compound known to produce very red visible spectral slopes in asteroids (see e.g. Hapke 2001). These particles can be produced by surface space weathering of silicates, as a consequence of low energy solar wind particle irradiation or micrometeoritic impacts. Some nano-phase iron could also be present in primordial TNO materials, in analogy with what is observed in primitive interplanetary dust particles. However, Brunetto et al. (2007) demonstrated that weathered silicates alone are not able to reproduce the extremely red spectral color observed for some TNOs and Centaurs (e.g. Pholus), and that a tholin-like component is in fact necessary.

Amorphous carbons are introduced in models to lower the albedo without introducing any spectral signature or significant slope in the spectra. However, it should be noted that all these compounds are used for convenience and, in no way,

have been specifically identified. On the other hand, spectral signatures (3.2–3.5  $\mu\text{m}$ ) of hydrocarbons (aromatic and aliphatic) have been found in the red, low-albedo material covering the leading hemisphere of Saturn’s satellite Iapetus (Cruikshank et al. 2008). This finding supports, but does not prove, the contention that hydrocarbons are a significant component of the red-colored, low-albedo material on many small Solar System bodies, as has long been expected. More details on TNOs compositions can be found in the review chapter by de Bergh et al. (2008).

TNOs and Centaurs have unique properties that make them particularly exciting to study. They are quite small, therefore not as prone to internal evolution than most satellites of the outer planets, and they are relatively isolated (not under the influence of a magnetosphere, as is the case for the major satellites of the giant planets). They are therefore considered as some of the most pristine bodies in the Solar System. However, it is not excluded that some of the largest objects (of the dwarf planet class or even smaller) have differentiated interiors (McKinnon et al. 2008). Furthermore, the surfaces of the largest of them are most probably periodically rejuvenated by sublimation and condensation of volatile surface ices, and smaller objects would have lost some of the most volatile material present at formation. In addition, irradiation by solar UV and the solar wind (but the Sun is quite far) and cosmic rays must have altered some of the “old” surfaces (see Sect. 4). Particle irradiation of ices induces the formation of new molecular species, sputtering of the surface, alteration of the structure (e.g. amorphization), and can modify the spectral signatures of pre-existing species; it can induce the formation of a de-hydrogenated refractory residue starting from simple C-rich ices. Furthermore, collisions must have been important in the transneptunian region early in the evolution of the Solar System and must still be significant, and they could affect their surfaces in an important way: the resurfacing produced by collisions can bring more pristine material to the surface, but it can also re-arrange and modify the surface (for instance it can induce the formation of crystalline ice). By studying these bodies we can therefore have access to the early times of Solar System formation and to further evolutionary processes in the outer part of the Solar System.

In the next two Sections we discuss the scattering models and laboratory data on ices relevant to TNOs and Centaurs spectroscopy.

### 4.3 Scattering Models

Icy bodies in the Solar System are most often studied by spectroscopic measurements of the diffusely reflected sunlight emanating from their surfaces. For small bodies in the outer Solar System, these objects are usually seen as unresolved point sources, and the light received from them is the average of the sunlight scattered from each surface element over the hemisphere facing the observer. The reflectance spectra thus obtained can be analyzed by means of synthetic spectra computed with realistic models that account for the composition and scattering properties of the surface components identified or suspected to occur. The principal utility of models is in the

investigation of the composition (ices, minerals, organic solids), scattering properties of the individual surface particles, and the nature of the mixing of components of different compositions and particle sizes.

Two scattering theories have been widely used in the calculation of synthetic spectra for comparison with astronomical sources, the Hapke theory (Hapke 1981, 1984, 1993) and the Shkuratov theory (Shkuratov et al. 1999). Other approaches have been taken by Goguen (1981), Lumme and Bowell (1981), Mischenko (e.g., 1994), and other investigators. Very useful discussions of scattering and scattering theories include Verbiscer and Helfenstein (1998), Douté and Schmitt (1998), and Shkuratov and Grynko (2005). The Hapke and Shkuratov theories are compared using both methods to model two icy Centaur objects in the paper by Poulet et al. (2002), to which we return below.

All modeling theories attempt to calculate the reflectance of an airless particulate surface at every wavelength within the spectral range of interest, accounting for all of the singly and multiply scattered solar photons emerging from the surface. This requires expressions for the photometric properties of the individual particles and particle clusters making up the surface, some of which are opaque and some are transparent or semi-transparent. Irregular particle shapes, particle albedo, interparticle shadowing, coherent backscattering, packing density, and particle composition all affect the photometric properties. In the work of various investigators over the years, photometric properties have been described by several empirical expressions based on a range of simplifying assumptions, notably those by Lambert, Minnaert, Lommel and Seeliger, etc., all reviewed by Verbiscer and Helfenstein (1998). The following discussion is adapted from Cruikshank et al. (2003)

Photometric models basically describe the dependence of the bidirectional reflectance,  $R_t$  on the photometric geometry of a surface, where  $R_t = I_t/\pi F$ .  $R_t$  is also called the radiance factor,  $I_t$  is the intensity of light scattered from a surface element with a particular orientation (incident angle  $i$ , emission angle  $e$ , and phase angle  $\alpha$ ), and  $\pi F$  is the plane-parallel luminous flux.

The models of Hapke (1981, 1993) and Shkuratov et al. (1999) are widely used to match plausible, natural materials, including ices, to observational data on the surfaces of TNOs and Centaurs. These models, which are based on geometric optics, incorporate specific ices, minerals, and organic solids by means of the complex refractive indices (optical constants) of those materials at every wavelength interval of the computed spectrum (see Sect. 4 below, and Mastrapa et al. 2008). The models are applicable in the visible and near-infrared regions of the spectrum because the typical size range of the particles and other structures encountered or expected in planetary regoliths are significantly larger (tens of  $\mu\text{m}$ ) than the wavelength of the light (see below).

Applications of the Hapke model to quantitative analysis of (intimate) laboratory mineral mixtures give mass abundance estimates better than 10% if the particle sizes of the components of the mixture are known (Mustard and Pieters 1987, 1989; Hiroi and Pieters 1994). When the Shkuratov theory is applied to laboratory reflectance spectra of mixtures, the abundance estimates are accurate to within

5–10%. At the same time, the calculated particle sizes fall within the range of actual sizes of the materials used in the mixtures (Poulet and Erard 2004).

Hapke's model (1981, 1993) for the calculation of the reflectance of a particulate surface uses as input parameters the illumination geometry, particle size distribution, porosity, and complex refractive indices of the constituent material(s). The model accommodates mixtures of particles of different sizes and compositions that are thoroughly mixed at the micrometer scale (intimate mixtures). In intimate mixtures, an incident solar photon encounters grains of all composition before emerging from the surface.

Another surface configuration consists of materials of different composition and/or microphysical properties that are laterally isolated from one another. With this configuration an incident solar photon encounters only one surface component, but the emergent flux of scattered sunlight integrated over the whole illuminated surface includes light scattered from each kind of surface, weighted by the fraction of the surface covered with each kind. A third type of physical configuration consists of plane-parallel homogeneous layers, where one material overlies another; each layer can present different textures and compositions. The Douté and Schmitt layer model (1998) uses analytical expressions with a non-isotropic phase function to give realistic contributions for single and double scattering.

The Shkuratov theory is based on the slab model for the local scattering properties and on the principle of invariant imbedding for the derivation of the reflectance of the particulate surface. The Shkuratov model incorporates the phase function as a dependent variable that is calculated directly from the refractive indices as a function of grain size and composition in a self-consistent way. For a discussion of this and other differences between the Hapke and Shkuratov models, see Cruikshank et al. (2003).

### **4.3.1 Model Calculations of the Spectrum of 5145 Pholus**

The choice of scattering theory, as well as the choice of the mixing modes and other parameters of the scattering particles, has a significant effect on the calculated abundances of the components. To illustrate some differences in the abundances of a complex surface derived in the Shkuratov and Hapke models, we show in Fig. 4.1 the spectral reflectance of the Centaur object 5145 Pholus together with both Hapke and Shkuratov models, each using the same five component materials (Cruikshank et al. 1998; Poulet et al. 2002).

With the Hapke theory, the model consists of two principal components. The first component, covering 38.5 ( $\pm 5\%$ ) of the surface, is an intimate mixture of olivine, Titan tholin,  $\text{H}_2\text{O}$  ice, and  $\text{CH}_3\text{OH}$  ice. The second component is carbon black, covering 61.5 ( $\pm 5\%$ ) of the surface, spatially isolated from the first component. The Shkuratov model uses Titan tholin incorporated as inclusions in the  $\text{H}_2\text{O}$  ice as well as in independent grains. This technique avoids the problem of grains that are

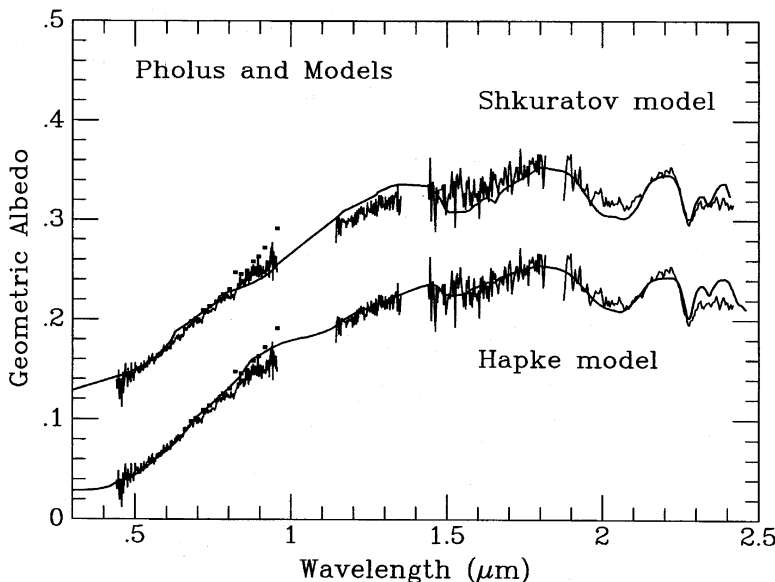


**Fig. 4.1** Hapke and Shkuratov models of the Centaur 5,145 Pholus. The data and the Shkuratov model are offset upward by 0.1 in geometric albedo. The Hapke model has the following components (composition, grain size, relative abundance): H<sub>2</sub>O ice, 10 μm, 0.06; Titan tholin, 1 μm, 0.06; CH<sub>3</sub>OH ice, 10 μm, 0.10; olivine, 20 μm, 0.205; carbon, N/A, 0.615. The Shkuratov model has (in the same format) H<sub>2</sub>O ice (with 16% small inclusions of Titan tholin), 10 μm, 0.42; Titan tholin, 50 μm, 0.26; CH<sub>3</sub>OH ice, 50 μm, 0.12; olivine, 100 μm, 0.05; carbon, ≥10 μm, 0.15 (Figure reproduced from Cruikshank et al. 2003, reproduced with permission of Académie des sciences)

too small, yet it produces the required amount of absorption at the short wavelengths to match the observational data.

As noted by Poulet et al. (2002), the Shkuratov model achieves the spectral fit and low overall albedo with much less carbon by using significantly larger grains for most components, but uses substantially more Titan tholin to achieve the strong absorption toward the violet. This comparison effectively illustrates the variation in the abundances of the components that results from the choice of modeling technique, as well as the choices of grain sizes.

#### 4.4 Appropriate Laboratory Data on Ices

To identify the ices present at the surface of TNOs, determine their relative abundances and get information on their physical state (pure or mixed, crystallographic phase, . . .), temperature, texture (grain size), as well as information on the alteration processes to which they may have been subjected (e.g. irradiation and impacts), we need extensive laboratory data.

Laboratory data on ices can be recorded in: (1) visible and IR transmission spectroscopy; (2) visible and IR transmission-reflection-transmission spectroscopy; (3) visible and IR diffuse reflectance spectroscopy. The samples can be prepared as thin layers (typically less than one micrometer) deposited on a cold substrate, or as crystals grown in closed cryogenic cells (either from the liquid or from the solid phase). Thin films allow to study spectral regions dominated by strong absorption bands (fundamental vibrations, typically in the mid-IR), whereas thick films are more suitable for analysing weaker bands (overtones and combinations, typically in the visible and near-IR). For more discussion on this, see Schmitt et al. 1998 and references therein, and Clark et al. (2012).

The comparison between laboratory transmission or reflectance spectra and observations can be used for a first spectral identification of the ices. However, to fit the observed spectra and to constrain and retrieve quantitative information (abundances of surface components, grain sizes, etc.) a radiative transfer model must be used (such as Hapke's or Shkuratov's models), as described in Sect. 3. The optical constants of the considered components (real and imaginary parts of the index of refraction,  $\tilde{n} = n + ik$ ) are fundamental input parameters for these models, and they are usually derived from laboratory transmission spectra. The imaginary part of the index,  $k$ , is related to the absorption coefficient alpha through:  $k = \lambda \alpha / 4\pi$ . To get accurate optical constants over a wide spectral range requires spectra recorded for widely different thicknesses to deal with both weak and strong absorptions as well as samples with a high optical quality, and this is a very difficult and demanding task. Approximate optical constants can also be extracted from reflectance measurements, but they must be used with care. However, diffuse reflectance spectra can be used in geographic (or spatial) mixtures, but with a grain size fixed by the specific experiment.

Many of the measurements made so far on ices in the laboratory have been made for applications to icy mantles on grains in the dense interstellar medium (ISM), therefore at very low temperatures (around 10 K) and, most often in the mid-IR range. For TNOs and Centaurs, the visible and near-IR ranges, which correspond to the reflected solar spectrum, are essential, and data at  $T$  higher than 20 K (in the 20–80 K range) are more appropriate. Data well adapted to the study of planetary satellites are often not suitable, mainly because they have been acquired at too high  $T$  (above 100 K).

A major step forward of interest in the study of TNOs was accomplished a number of years ago through the interpretation of near infrared spectra of Pluto and Triton obtained with a new instrument at the UKIRT telescope that allowed the detection of new ices at the surface of these two bodies: N<sub>2</sub> and CO on Pluto (Owen et al. 1993) and CO and CO<sub>2</sub> on Triton (Cruikshank et al. 1993). This led to a series of special experiments in the laboratory, particularly at the Laboratoire de Glaciologie (then at Laboratoire de Planétologie) de Grenoble (France), that involved the development of new cells, but also at Jet Propulsion Laboratory (USA). Since then, several other laboratories have contributed.

Review papers on available laboratory data on unirradiated ices for Solar System bodies have been published by Schmitt et al. in 1998 and, more recently, by de Bergh et al. (2008). In the latter, only data concerning TNOs and Centaurs were

considered. In what follows, we give a short overview of the data that have been used to interpret spectra of TNOs, and we identify some important missing data. We also refer to the chapters by Clark et al. (2012) and Mastrapa et al. (2012).

**Water ice:** Reliable absorption coefficients for crystalline (hexagonal) water ice (using monocrystals grown in closed cells) were published by Grundy and Schmitt (1998) for the spectral range 1–2.7  $\mu\text{m}$ , and the temperature range 20–270 K. Optical constants have been computed for  $T = 60$  K and 145 K in the mid-IR and between 33 and 150 K in the far-IR (Trotta 1996; Schmitt et al. 1998). More recent optical constants are those of Mastrapa et al. (2008) and Mastrapa et al. (2009) that cover the ranges 1.1–2.6 and 3–20  $\mu\text{m}$ , respectively, using vapor-condensed thin films for temperatures between 20 and 150 K (at 10 K intervals) and corresponding to a mixture of hexagonal and cubic ice. The presence of a band around 1.65  $\mu\text{m}$  is a good indicator for the presence of crystalline water ice at low temperature; its exact wavelength and intensity relative to the 1.5  $\mu\text{m}$  band is a good indicator of temperature. No data at low temperatures exist for the visible range. Consequently, data for ice near the melting temperature are used instead (e.g. Warren 1984). Data for amorphous water ice are somewhat more difficult to obtain (they cannot be obtained with closed cells). Absorption coefficients at 40 and 140 K in the 1–2.7  $\mu\text{m}$  range were published by Schmitt et al. (1998), at 15 K in the mid-infrared (Trotta 1996) and 33 and 110 K in the far-IR (Schmitt et al. 1998). New data by Mastrapa et al. (2008) and Mastrapa et al. (2009) are optical constants in the 1.1–2.6 and 3–20  $\mu\text{m}$  ranges for temperatures between 25 and 100 K. More details on all these data can be found in the chapter by Mastrapa et al. (2012).

**Pure methane:** In the mid-far IR, optical constants at 20 and 30 K (obtained with thin films) have been published by Hudgins et al. (1993). Reliable optical constants exist in the near-IR for pure methane ice (phases I and II) at appropriate temperatures for TNOs (Grundy et al. 2002). The spectral range covered is 0.7–5  $\mu\text{m}$  and they were recorded for temperatures between 20 and 90 K (at 10 K intervals) using crystals grown in a closed cell. A good indicator for the existence of pure methane ice on the surface of a TNO is the band at 1.69  $\mu\text{m}$  which appears only for pure ice (not in methane diluted in nitrogen). These data are suitable for Pluto (and Triton) except for some weak bands in the near-IR that are not accounted for with the existing data (see Douté et al. 1999), but they are not sufficient for Eris or Makemake for which absorptions are detected below 0.7  $\mu\text{m}$  that are not measured in the laboratory spectra. Laboratory data for thicker samples of  $\text{CH}_4$ , for instance using closed cells that allow the formation of samples thicker than 1 cm, are necessary, although difficult to achieve. In addition, some TNOs (e.g. outer scattered disk objects and inner Oort cloud objects) may have surface  $T$  around 20 K, so one must consider also  $\text{CH}_4$  in phase II (cubic phase I forms above 20.4 K and cubic phase II below), and this phase has not yet been thoroughly studied in the visible-NIR range.

**Methane diluted in nitrogen:** Methane absorption bands in the near-infrared spectra of Triton (Cruikshank et al. 1993; Quirico et al. 1999) and Pluto (Owen et al. 1993; Douté et al. 1999) are systematically shifted by  $\sim 10 \text{ cm}^{-1}$  to shorter

wavelengths with respect to the corresponding bands of pure CH<sub>4</sub> ice in the laboratory, depending on the degree of dilution. This shift arises from the fact that some (or most) of the CH<sub>4</sub> on Triton and Pluto is dissolved or diluted in solid N<sub>2</sub>, resulting in an effect called the matrix shift. The matrix effect of CH<sub>4</sub>:N<sub>2</sub> mixtures at low methane concentration has been investigated in the laboratory by Quirico and Schmitt (1997a), and in higher concentrations by Quirico et al. (1996), Schmitt et al. (1998), and Brunetto et al. (2008), although optical constants for the higher concentration mixtures are not yet available. Methane bands in spectra of Eris and Makemake are significantly stronger than those on Triton and Pluto, indicating higher concentrations in the CH<sub>4</sub>:N<sub>2</sub> mixture.

**Nitrogen:** Both phases of nitrogen, alpha (cubic) and beta (hexagonal), may be present on TNOs (transition temperature: 35.6 K at zero pressure). Reliable optical constants around 2.15 μm have been published by Grundy et al. (1993) in the temperature range 20–63 K. The bands of alpha-nitrogen are very narrow at these wavelengths, although its integrated intensity is the same as for beta-nitrogen, so it would be very difficult to detect nitrogen in the alpha phase at the surface of TNOs. Some more limited data, but over a larger spectral range (2–5 μm), are those by Tryka et al. (1995) that were obtained for temperatures between 35 and 60 K for both the fundamental and first harmonic bands. The fundamental band around 4.3 μm has also been studied in both phases by Quirico et al. (1996).

**Carbon monoxide:** CO has been detected in Pluto and Triton from near-IR spectra, but not on any other TNO; this may due to insufficient spectral resolution as the bands are quite narrow. In the near IR, optical constants at T = 21 K exist for pure CO ice in the alpha phase (Quirico and Schmitt 1997a) and some work has been done on CO diluted in N<sub>2</sub> ice (alpha and beta phases) at temperatures between 34 and 60 K (Quirico and Schmitt 1997b). The shift in band position when CO is diluted in nitrogen is very small, so with the Pluto spectra recorded so far it has not been possible to see if CO is diluted in nitrogen or not. In the mid-IR, optical constants are available only at very low T (10–15 K, e.g. Hudgins et al. 1993; Quirico and Schmitt 1997b; Palumbo et al. 2006).

**Carbon dioxide:** Very narrow bands of CO<sub>2</sub> were detected in near-IR spectra of Triton, but not on Pluto or any other TNO. The fact that CO<sub>2</sub> is seen on Triton but not Pluto is an interesting puzzle, since both objects have otherwise rather similar surface compositions. From the perspective of our limited knowledge of both of these objects, the principal difference between them is that at some seasons Triton travels through Neptune's field of charged particles, while Pluto is unlikely to experience anything similar. Radiolytic reactions on Triton's surface and in the atmosphere may produce the substantial quantity of solid CO<sub>2</sub> found on the surface, and such production and deposition must be occurring in the present epoch, owing to the youth of the surface (judged from a dearth of impact craters and other factors).

In the mid-IR, optical constants of CO<sub>2</sub> ice have been derived at a few T between 10 and 160 K by several teams (e.g. Hudgins et al. 1993; Trotta 1996; Baratta and Palumbo 1998), but large differences exist among these data sets, mainly because different methods were used to extract the optical constants. In the near-IR, there

exist many reflectance spectra of CO<sub>2</sub> ice, but only a few papers have derived the absorption coefficient of CO<sub>2</sub> ice and CO<sub>2</sub> diluted in nitrogen ice (Quirico and Schmitt 1997a; Hansen 1997; Hansen 2005) since the compilation of the first measurements by Warren (1986).

**Methanol:** The absorption observed at 2.27 μm in spectra of one Centaur and one TNO could be due to methanol or to a photolytic product of methanol (Cruikshank et al. 1998; Barucci et al. 2006). The spectra of methanol from different laboratories differ significantly. Optical constants of methanol were measured in the mid-IR by Hudgins et al. 1993. In the near-IR, optical constants were derived from a single transmission spectrum at 90 K (Cruikshank et al. 1998) and should be remeasured more carefully. Furthermore, lower temperatures and mixtures with water ice would be more appropriate for TNOs, so more laboratory data are necessary.

**Ammonia/ammonia hydrates:** After a first review of the spectroscopic measurements on NH<sub>3</sub> ice by Taylor (1973) and derivation of its optical constants in the infrared, a more detailed work by Martonchik et al. (1984) covered the near UV to the far infrared. However, data on pure ammonia are still incomplete and some data sets display a strong absorption slope in the visible, although ammonia is transparent in that range. Pure ammonia has not been detected on TNOs, but on these bodies ammonia may exist in a hydrated state. NH<sub>3</sub> and H<sub>2</sub>O ices are thermodynamically unstable in the presence of one another and combine to form the NH<sub>3</sub> hydrates according to the relative proportions of the two components. Ammonia hydrates include NH<sub>3</sub>•H<sub>2</sub>O, 2NH<sub>3</sub>•H<sub>2</sub>O, and NH<sub>3</sub>•2H<sub>2</sub>O, all of which are stoichiometric compounds (not clathrates) that have lower NH<sub>3</sub> vapour pressures than pure NH<sub>3</sub> ice. A band at 2.2 μm detected in spectra of Charon and Orcus has indeed been tentatively assigned to an ammonia hydrate. Spectra of ammonia hydrates recorded by different teams differ. The optical constants available are very limited. They have been determined only from spectra with 1% and 3% of ammonia in an NH<sub>3</sub>•H<sub>2</sub>O mixture, and at a temperature of 77 K (data from Clark; optical constants from Roush; see Brown et al. 1988). Although extensive work has been done recently on ammonia hydrates by Moore et al. (2007), who recorded spectra between 1.8 and 20 μm in the 10–165 K range, there are no new optical constants available.

**Ethane:** Optical constants of ethane at 30 K over part of the near-IR range were first computed by Pearl et al. (1991). These data were then completed by Quirico and Schmitt (1997a) who measured absorption coefficients in the near-IR of ethane and ethane diluted in alpha-nitrogen ice at 21 K. Significant shifts have been observed between these two states (Quirico and Schmitt 1997a). New optical constants have been obtained by Mastrapa (private communication) from spectra deposited at 40 K and covering the spectral range 0.91–3.5 μm.

**Hydrogen cyanide:** Mid- and far-IR spectra of HCN have been recorded for temperatures between 35 and 95 K (Masterson and Khanna 1990; Dello Russo and Khanna 1996). Optical constants in the mid-IR at 60 K have been published by Masterson and Khanna (1990).

**Other icy mixtures.** As mentioned above, the band position, strength, and width of ices may be strongly affected by the presence of other species, especially by other ices. For instance, it is known that mixing CH<sub>4</sub> with N<sub>2</sub> in the solid phase produces variations in the peak position and shape of methane bands from the visible to the IR range (Quirico and Schmitt 1997a). Since this effect cannot be simulated using radiative transfer models, specific experiments must be performed.

Generally speaking, it has been shown that in some instances the ice band strengths strongly depend on the composition of the ice matrix (Bernstein and Sandford 1999; Öberg et al. 2007). The strength of the N<sub>2</sub> bands can increase when nitrogen is mixed with another compound, but this effect has been studied only for the fundamental vibration band of N<sub>2</sub>. Brunetto et al. (2008) found that band strengths of methane remain constant when methane is mixed with nitrogen. This demonstrates that dedicated experiments must be performed case by case. Near-IR studies would be very relevant.

Some work has been done on mixtures of H<sub>2</sub>O with components such as CH<sub>4</sub>, CO<sub>2</sub> (see below), HCN and NH<sub>3</sub>, but there are no available optical constants suitable for TNOs spectroscopy. More data on water ice mixed with other compounds are required. CO<sub>2</sub> diluted in nitrogen was studied by Quirico and Schmitt (1997a) and CO<sub>2</sub> diluted in water and methanol ices was studied by Bernstein et al. (2005). A new band (2v<sub>3</sub>) appears in diluted CO<sub>2</sub> around 2.134 μm that is not seen in pure CO<sub>2</sub> ice spectra.

More laboratory data on CO diluted in N<sub>2</sub> (alpha and beta phases) are needed, in particular for the interpretation of the New Horizons mission that will reach Pluto in 2015. One of the main scientific goal of New Horizons mission is to determine, via infrared observations, the distribution of solid N<sub>2</sub>, CH<sub>4</sub>, H<sub>2</sub>O and CO on Pluto surface. Mixtures of H<sub>2</sub>O highly diluted in N<sub>2</sub>, CH<sub>4</sub>, or CO have been performed by Satorre et al. (2001) and Fulvio et al. (2010): these show the presence of a very narrow band at about 1.89 μm, easily distinguishable from the large 2 μm feature of pure H<sub>2</sub>O ice, that can be a strong diagnostic tool to study the distribution of these volatiles on large TNOs and dwarf planets.

**Ices intimately mixed with non-icy materials (impurities).** In the case of ices mixed with non-icy materials (e.g. silicates, carbons), radiative transfer models can give a reasonable estimate of the associated spectral effects. The general result (see e.g., Cruikshank et al. 1998) is that refractory carbonaceous components (e.g. amorphous carbon, tholins, organic residues, soot, etc.) dominate the absorption in the visible and near-IR, even when present as small inclusions, subduing the ice and silicate<sup>2</sup> features (see, e.g., Clark 1981). In most cases, to interpret the visible colours of TNOs and

---

<sup>2</sup> So far, it has been difficult to detect silicate features in the VNIR spectra of TNOs and Centaurs, although their presence is deduced mainly thanks to our knowledge of the composition of cometary dust and “cometary” (anhydrous “chondritic porous”) interplanetary dust particles. Such difficulty may be either due to the opacity of associated carbonaceous species and sulfides in this spectral region, or to the lack of Fe<sup>2+</sup> (which may be partly responsible for the visible absorption) in the silicates.

Centaurs, it is necessary to consider ices “contaminated” by low-abundant inclusions of those carbonaceous refractory materials, with grain sizes that are smaller than the wavelength. This violates the “optical geometry” assumption in most scattering models, and suggests that more experimental work needs to be performed to better characterise the spectral and photometric properties of such “dirty ices” (see below).

**Irradiated ices** [see also chapters by Hudson et al. (2008) and Baragiola et al. (2012)]. In addition to the species discussed above, several other ices (e.g. H<sub>2</sub>CO<sub>3</sub>, C<sub>3</sub>O<sub>2</sub>, C<sub>2</sub>O, C<sub>3</sub>O, N<sub>2</sub>O, NO, NO<sub>2</sub>, HCN, HNCO, other hydrocarbons, etc.) can be present on the surface of TNOs and Centaurs, in particular due to a complex surface chemistry induced by energetic ions and/or UV photons on simpler ices. Burgdorf et al. (2010) have recently reported the detection of the 4.76 μm band of HCN on Triton. In a study of Pluto’s spectrum, Protopapa et al. (2009) report an unresolved spectral band complex at this wavelength and suggest that it is due to nitriles, which should include HCN. Although not yet detectable on TNOs, such species could be identified by forthcoming space missions or extremely large telescopes, which would need adequate support by laboratory measurements. We emphasize the importance of estimating optical constants for higher order hydrocarbons at relevant temperatures and spectral range.

In the spectral interpretation of TNOs and Centaurs observation, one should also consider that, in addition to the formation of new molecular species, ion irradiation can modify the spectral signatures (band strength, profiles, etc.) of pre-existing species. As mentioned above, for a given molecular species the shape, peak position, and the intensity of the IR bands depend on the chemical composition and the structure of its solid or matrix. For instance, ion irradiation of pure methanol ice (which induces the production of CO and CH<sub>4</sub>) and methanol mixed with water has shown that the methanol band at 2.34 μm strongly decreases with respect to the one at 2.27 μm (Brunetto et al. 2005). Cruikshank et al. (1998) observed the methanol band around 2.27 μm in the spectrum of Centaur Pholus, although the band at 2.34 μm was not observed. The fact that the 2.34 μm band has not been observed could be indicative of ion irradiation processes.

Ion irradiation of simple ices (methane, methanol, benzene, mixture containing C-rich molecules), using doses up to hundreds of eV/molecule, induces the formation of an organic refractory residue (e.g. Strazzulla et al. 1991, 2001), and eventually the formation of amorphous carbon (e.g. Ferini et al. 2004; Palumbo et al. 2004). These modifications are accompanied by changes in colours, in particular a strong reddening and darkening of the visible and near-IR spectra (Brunetto et al. 2006) of the original sample (unprocessed ices are usually flat and bright), related to the total dose released to the target (elastic plus inelastic contributions), differently from the case of silicates (e.g. Brunetto and Strazzulla 2005) and bitumens (e.g. Moroz et al. 2004), in which reddening effects are due to the elastic collisions between ions and target nuclei.

The competition between compositional and space weathering effects (Moroz et al. 2004; Brunetto et al. 2006) and rejuvenating processes, such as impacts or internal activity of the object (Stern 2002; Cook et al. 2007), can perhaps explain the great

variety of spectral colours observed in the outer Solar System (e.g. Doressoundiram et al. 2002; Delsanti et al. 2004; Barucci et al. 2005b; Barucci and Peixinho 2006; Benecchi et al. 2009). Concerning space weathering, one can speculate that a large number of objects possess a mantle enriched in refractory organics developed after prolonged irradiation of their carbon-containing surfaces by cosmic ions, by analogy with what was previously suggested for Oort cloud comets (Strazzulla et al. 1991). The red coloured surfaces could correspond to radiation doses between 10 and 100 eV/molecule (Brunetto et al. 2006), while more-neutral-coloured objects could have accumulated much higher doses (Moroz et al. 2004).

The presence of an irradiation mantle could spectrally mask the pristine molecules underneath, such as water or methane. While estimating the optical constants of irradiated methane, Brunetto and Roush (2008) have indeed found that a relatively thin (tens of  $\mu\text{m}$ ) layer of irradiated methane ice could mask the water ice bands in the spectrum, while a much thicker layer of tholins would be required to produce a similar effect<sup>3</sup>.

The orbital elements of the objects and their evolution are critical parameters to the formation of an irradiation mantle. Estimates of the radiation doses for different ice-processing environments can be found in Hudson et al. (2008): objects in a broad zone of the middle heliosphere, around 40 AU, would experience moderate irradiation from galactic cosmic-ray ions at micrometer-to-meter depths. With respect to objects at 40 AU, Centaurs would accumulate higher surface doses due to higher fluxes of solar energetic ions. In present Solar System conditions, the classical Kuiper belt resides far sunward of the termination shock<sup>4</sup>. Thus, on the antisunward side there are rising fluxes of energetic ions diffusing inward from the heliosheath and perhaps also from the local interstellar medium. The result is that Scattered Disk objects could be more irradiated than classical TNOs, and bodies in the Oort Cloud could accumulate even higher doses (the process of crust formation and volatile ice masking would therefore be more efficient there).

In future studies, efforts should concentrate on the estimation of optical constants of refractory material synthesized from icy mixtures relevant to the chemistry of TNOs, e.g. CH<sub>4</sub>, H<sub>2</sub>O, N<sub>2</sub>, CO, CH<sub>3</sub>OH.

#### 4.4.1 Data Banks Available

A compilation of the papers (up to 1998) in which optical constants of ices, organics, carbon species and silicates have been published is available at the Heidelberg-Jena-St Petersburg Database of Optical Constants (HJPDOC: <http://www.mpa-hd.mpg.de/HJPDOC/>). However, there are currently very few ice spectra and optical constant

---

<sup>3</sup> Note that a layer of at least 200  $\mu\text{m}$  of non-absorbing very fine grained ice is required to mask the presence of refractory materials in the visible range (e.g. Gil-Hutton et al. 2009).

<sup>4</sup> The position of the termination shock may have changed during Solar System history, in response to changes in the local interstellar environment of the Sun and solar activity. Occasionally, it may have moved further inward producing higher irradiation doses for the classical TNOs.

data available on the web. A first set of mid-IR spectra on CO and CO<sub>2</sub> mixed with a few other species and first order derived optical constants (At Leiden Institute of Chemistry/Leiden University) is available at <http://www.strw.leidenuniv.nl/~lab/databases/databases%202007.htm>. Some other absorbance spectra can be found at “The Cosmic Ice Laboratory” (NASA/Goddard) at <http://www-691.gsfc.nasa.gov/cosmic.ice.lab/spectra.htm>.

To fill this gap, a new database, GhosST (“Grenoble Astrophysics and Planetology Solid Spectroscopy and Thermodynamics” database) is now starting at Laboratoire de Planétologie de Grenoble (<http://ghosst.obs.ujf-grenoble.fr/>). It will contain most of the transmission and reflectance spectra of ices, organics and minerals measured at LPG and their derived absorption coefficients and optical constants, as well as a searchable band list of these species.

## 4.5 Results on Surface Composition and Spectral Interpretation

As discussed above, spectro-photometric observations of TNOs and Centaurs show that these objects have a wide diversity of colors. This diversity extends to the near-IR range. Therefore, visible-near infrared reflectance spectra of TNOs and Centaurs can have very different general shapes (see examples in Fig. 4.2). There have been some attempts to classify the objects, depending on their spectral shapes (Barucci et al. 2005b; Fuchignoni et al. 2008). Four main classes have been defined so far (see caption of Table 4.1). In addition, TNOs and Centaurs have a wide range of albedos (see Table 4.1 for a sample of them).

The differences in the general shapes of the spectra and albedos of TNOs and Centaurs must indicate, *a priori*, different surface compositions and/or textures. The eventual goal of all of the spectral and photometric observations of objects in the outer Solar System is to gain an understanding of the physical and chemical characteristics of the surfaces, to help determine the important processes which operate on these bodies, to learn about the history and origin of the objects, and to discern important clues about the formation and evolution of the Solar System. To date we must admit that these broad goals are, for the most part, unmet. Nonetheless, by combining all the observations available, we have developed at least a preliminary understanding of some of the aspects of the physical characteristics of these objects. In what follows, we describe in more details the observed spectra of TNOs and Centaurs and their interpretation.

### 4.5.1 Objects with Volatile Ices

Pluto and Neptune’s satellite Triton have surfaces coated with methane, molecular nitrogen, and carbon monoxide (Cruikshank et al. 1976, 1993; Cruikshank and Silvaggio 1979; Owen et al. 1993). These three ices have significant vapor

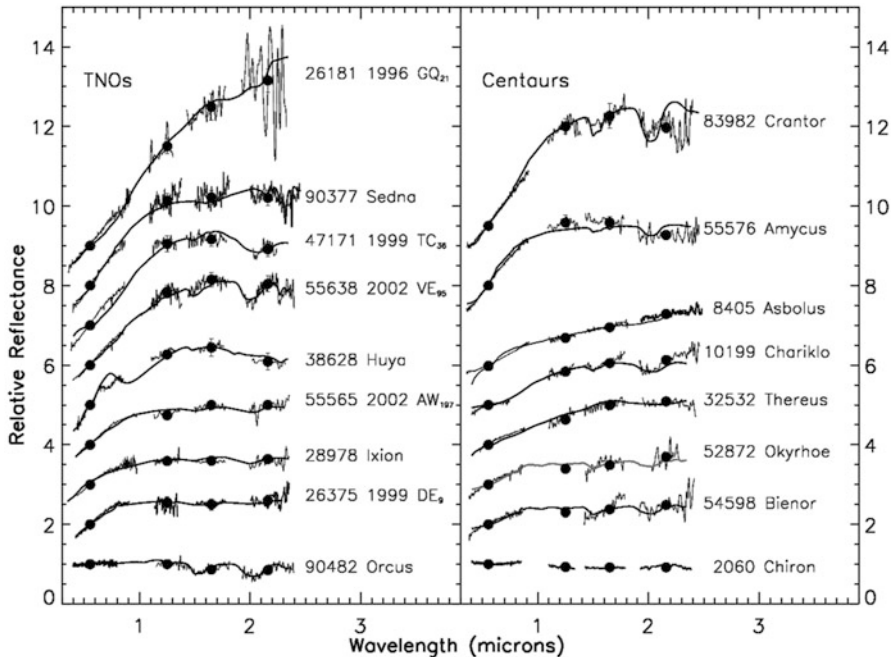


**Fig. 4.2** Combined visible-near infrared spectra of some TNOs and Centaurs recorded at the ESO-VLT in Chile and models (black lines). The references for most spectra and models can be found in Barucci et al. (2008a). For TNOs Ixion and 55638, see Merlin et al. (2010a) (Figure adapted from Fig. 4.3 in Barucci et al. 2008a. Courtesy of Frédéric Merlin)

pressures at the low (<50 K) surface temperatures found on objects in the outer Solar System and sublime to form Pluto and Triton's tenuous atmospheres. Other ices, volatile in the mid and inner Solar System (such as ammonia, carbon dioxide, and water), are completely involatile at distances past 30 AU. Thus, in this discussion, volatile refers only to N<sub>2</sub>, CO, and CH<sub>4</sub> ices. Though N<sub>2</sub> ice is a very important surface constituent on both Pluto and Triton, CH<sub>4</sub> ice is most easily detected due to several strong and broad absorption features in the near infrared (Quirico et al. 1999; Grundy et al. 2010; and Fig. 4.3 for Pluto). The visible and near infrared spectra of Pluto and Triton resemble spectra of methane ice with small absorption features due to N<sub>2</sub> and CO ice (plus absorptions of CO<sub>2</sub> and H<sub>2</sub>O for Triton) superposed (see the chapter by Clark et al. in 2011).

There exist, so far, four other TNOs on which volatile ices have been detected: 136199 Eris, 136472 Makemake, 50000 Quaoar and 90377 Sedna. They are all very large (Eris was thought to be slightly larger than Pluto, but results from a recent stellar occultation indicate that it may be slightly smaller; Sicardy et al., in preparation) or moderately large TNOs (see Table 4.1). The spectrum of Eris (Fig. 4.3) is, like those of Pluto and Triton, dominated by absorptions due to methane ice (Brown et al. 2005; Licandro et al. 2006a; Dumas et al. 2007). Though N<sub>2</sub> has not been detected, shifts in the locations of some of the CH<sub>4</sub> bands (compared to the locations

**Table 4.1** List of objects for which good near-infrared spectra are available, with their dynamical class, orbital inclination, visible gradient (in % per 100 nm, computed between 500 and 800 nm), taxonomic group, measured albedos and diameters, and the species that have been detected in their spectra (ices or silicates)

Object	Dy. cl.	i ( $^{\circ}$ )	Vis. gr.	Tax.	Albedo (%)	Diam. (km)	Species detected
<i>Centaurs</i>							
2060 Chiron	Ce	6.9	-0.1	BB	7.6 $^{+1}_{-0.9}$	233 $^{+14}_{-14}$	H <sub>2</sub> O(var.)
5145 Pholus	Ce	24.7	48	RR	8 $^{+7}_{-3}$	140 $^{+40}_{-40}$	H <sub>2</sub> O(m), CH <sub>3</sub> OH
8405 Asbolus	Ce	17.6	14	BR	5.5 $^{+1.3}_{-0.9}$	84 $^{+8}_{-8}$	Silicates
10199 Chariklo	Ce	23.4	13	BR	5.7 $^{+0.5}_{-0.4}$	259 $^{+10}_{-10}$	H <sub>2</sub> O(var.)
31824 Elatus	Ce.	5.2	26	RR	10 $^{+4}_{-3}$	30 $^{+8}_{-8}$	H <sub>2</sub> O(w), silic.
32532 Thereus	Ce	20.4	12	BR	4.3 $^{+1.1}_{-0.8}$	88 $^{+9}_{-9}$	H <sub>2</sub> O(var.)
52872 Okyrhoe	Ce.	15.6	11	BR	2.5 $^{+0.8}_{-0.5}$	52 $^{+7}_{-7}$	H <sub>2</sub> O?
55576 Amycus	Ce	13.3	37	RR	18 $^{+7.8}_{-4.7}$	76 $^{+12}_{-12}$	H <sub>2</sub> O?
63252 (2001BL <sub>41</sub> )	Ce	12.4		BR	3.9 $^{+2.5}_{-1.3}$	35 $^{+7}_{-8}$	None
83982 Crantor	Ce	12.8	39	RR	11 $^{+7}_{-4}$	60 $^{+15}_{-13}$	H <sub>2</sub> O(m)
<i>TNOs</i>							
15789 (1993SC)	Re	5.2		RR	3.5 $^{+1.4}_{-1.4}$	298 $^{+140}_{-140}$	None
15874 (1996TL <sub>66</sub> )	Sc	24		BB	3.5 $^{+2}_{-1}$	575 $^{+116}_{-115}$	H <sub>2</sub> O
15875 (1996TP <sub>66</sub> )	Re	5.7	31	RR	7.4 $^{+7}_{-3}$	160 $^{+45}_{-45}$	None
19521 Chaos	Cl	12	23	IR	>5.8	<747	None
20000 Varuna	Cl	17.2	27	IR	8.8 $^{+4.2}_{-3.1}$	714 $^{+178}_{-128}$	H <sub>2</sub> O?
26181 (1996GQ <sub>21</sub> )	Sc	13.4	37	RR	6.8 $^{+1.6}_{-1.2}$	461 $^{+46}_{-45}$	H <sub>2</sub> O(m)
26375 (1999DE <sub>9</sub> )	Re	7.6	20	IR	6.8 $^{+1.6}_{-1.2}$	461 $^{+46}_{-45}$	H <sub>2</sub> O(w)
28978 Ixion	Re	19.6	23	IR/RR	12 $^{+14}_{-6}$	650 $^{+260}_{-220}$	H <sub>2</sub> O?
29981 (1999TD <sub>10</sub> )	Sc	5.96		BR	4.4 $^{+1.4}_{-0.96}$	104 $^{+13}_{-13}$	H <sub>2</sub> O(w)
38628 Huya	Re	15.4	24	IR	5 $^{+0.5}_{-0.4}$	533 $^{+25}_{-24}$	H <sub>2</sub> O?
42301 (2001UR <sub>163</sub> )	Sc	0.8	53	RR		620	None
42355 Typhon	Sc	2.4	12	BR	5.1 $^{+1.3}_{-0.9}$	175 $^{+17}_{-20}$	H <sub>2</sub> O(w)
47171 (1999TC <sub>36</sub> )	Re	8.4	32	RR	7.2 $^{+1.5}_{-1.2}$ 6.5–8.5*	414 $^{+39}_{-38}$ 134–154	H <sub>2</sub> O(m)
47932 (2000GN <sub>171</sub> )	Re	10.8	25	IR	5.7 $^{+2.5}_{-1.6}$	321 $^{+57}_{-54}$	None
50000 Quaoar	Cl	7.98	27	RR?	17 $^{+5.5}_{-3.6}$ 9 $^{+3}_{-3}$ (image)	908 $^{+112}_{-118}$ 1,260 $^{+190}_{-190}$	H <sub>2</sub> O(m), CH <sub>4</sub> , C <sub>2</sub> H <sub>6</sub>
54598 Bienor	Sc	20.7	8	BR	3.4 $^{+1.3}_{-0.8}$	206 $^{+30}_{-30}$	H <sub>2</sub> O(m)
55565 (2002AW <sub>197</sub> )	Cl	24.4	22	IR	11 $^{+4.1}_{-2.5}$	742 $^{+98}_{-104}$	H <sub>2</sub> O?
55637 (2002UX <sub>25</sub> )	Cl	19.5	21	IR	11.1 $^{+4.9}_{-3}$	680 $^{+106}_{-108}$	None
55638 (2002VE <sub>95</sub> )	Re	16.3	39	RR		400	H <sub>2</sub> O(m), CH <sub>3</sub> OH

(continued)

**Table 4.1** (continued)

Object	Dy. cl.	i (°)	Vis. gr.	Tax.	Albedo (%)	Diam. (km)	Species detected
65489 Ceto	De.	22.2	21	?	7.7 <sup>+1.4</sup> <sub>-1.1</sub>	230 <sup>+18</sup> <sub>-18</sub>	H <sub>2</sub> O(m)
66652 Borasisi	Cl	0.6	29	RR	29 <sup>+12</sup> <sub>-12</sub>	170 <sup>+39</sup> <sub>-39</sub>	None
79360 (1997CS <sub>29</sub> )	Cl	2.3		RR	6–14*	250–420	None
84522 (2002TC <sub>302</sub> )	Sc	35.1	34	?	3.1 <sup>+2.9</sup> <sub>-1.2</sub>	1,150 <sup>+337</sup> <sub>-325</sub>	None
84922 (2003VS <sub>2</sub> )	Re	14.8	24	?	5.8 <sup>+4.8</sup> <sub>-2.2</sub>	725 <sup>+199</sup> <sub>-188</sub>	H <sub>2</sub> O?
90377 Sedna	De	11.9	40	RR	>16	<1,600	CH <sub>4</sub> , N <sub>2</sub> ?
90482 Orcus	Re	20.6	1.6	BB	19.7 <sup>+3.4</sup> <sub>-2.8</sub>	946 <sup>+74</sup> <sub>-72</sub>	H <sub>2</sub> O(s), NH <sub>3</sub> ?
					27 <sup>+7</sup> <sub>-5</sub>	850 <sup>+90</sup> <sub>-90</sub>	
90568 (2004GV <sub>9</sub> )	Cl	22		?	7.3 <sup>+4.9</sup> <sub>-2.9</sub>	684 <sup>+68</sup> <sub>-74</sub>	None
119951 (2002KX <sub>14</sub> )	Cl	0.4	26	?	6 <sup>+3.6</sup> <sub>-2.3</sub>	180 <sup>+50</sup> <sub>-38</sub>	None
136199 Eris	De	44	4.4	BB	70 <sup>+15</sup> <sub>-20</sub>	2,600 <sup>+400</sup> <sub>-200</sub>	CH <sub>4</sub> , C <sub>2</sub> H <sub>6</sub> ,
					86 <sup>+7</sup> <sub>-7</sub> (image)	2400 <sup>+100</sup> <sub>-100</sub>	N <sub>2</sub> ?
136472 Makemake	Cl	29		?	80 <sup>+10</sup> <sub>-20</sub>	1,500 <sup>+400</sup> <sub>-200</sub>	CH <sub>4</sub> , N <sub>2</sub> ?
					Dark + bright*	1,360–1,480	
145451 (2005RM <sub>43</sub> )	Sc	28.8	2.2	?			None
145452 (2005RN <sub>43</sub> )	Cl	19.3	23	?		220	None
208996 (2003AZ <sub>84</sub> )	Cl	13.5	2.2	BB	12.3 <sup>+4.3</sup> <sub>-2.9</sub>	686 <sup>+99</sup> <sub>-95</sub>	H <sub>2</sub> O(m)
					5–9*	850–970	
<i>Collisional family</i>							
136108 Haumea	Cl	28.2	−0.2	BB	84 <sup>+10</sup> <sub>-20</sub>	1,150 <sup>+250</sup> <sub>-100</sub>	H <sub>2</sub> O(s)
					0.70–0.75*	~1,300	
Satellite Hi'iaka	Cl			BB?			
19308 (1996TO <sub>66</sub> )	Cl	27.6	2.4	BB	>17 <sup>+20</sup> <sub>-8</sub>	<641 <sup>+250</sup> <sub>-206</sub>	H <sub>2</sub> O(s)
24835(1995 SM <sub>55</sub> )	Cl	27	2.4	BB		140	H <sub>2</sub> O(s)
55636(2002 TX <sub>300</sub> )	Cl	25.9	0	BB	>10	<800	H <sub>2</sub> O(s)
120178(2003 OP <sub>32</sub> )	Cl	27.2	−1	BB		850	H <sub>2</sub> O(s)
145453 (2005RR <sub>43</sub> )	Cl	28.6	1.6	BB		200	H <sub>2</sub> O(s)
<i>Pluto</i>	Re	17.2			61	2,350	CH <sub>4</sub> , CO, N <sub>2</sub>
<i>Charon</i>	Re	17.2		BB?	38	1,208	H <sub>2</sub> O(s), NH <sub>3</sub> ?

For the H<sub>2</sub>O absorption bands, “w”, “m”, and “s” correspond to “weak”, “medium” or “strong” (with the fraction of water ice “f” in the simulations of Barkume et al. (2008) less than 10%, between 10% and 50%, and more than 80%, respectively – see text for more details). Albedos and diameters come from Spitzer observations, Herschel observations (for six objects in this list; the

(continued)

**Table 4.1** (continued)

albedos are denoted by an asterisk. For Makemake, the dark terrain albedo is 0.02–0.12, and the bright terrain albedo 0.78–0.90), direct imaging measurements (for Eris and Quaoar), ISO measurements (for 15789), ground-based millimeter measurements (for 19308 and 19521), or binary mass plus density assumptions (for Borasisi). For references see Stansberry et al. (2008), Brucker et al. (2009), Lellouch et al. (2010), Lim et al. (2010) and Müller et al. (2010). Diameters without any corresponding albedo have been estimated assuming an albedo of 0.1 (see Barucci et al. 2008a). References for the measured visible gradients (with error bars) can be found in Barkume et al. (2008), Pinilla-Alonso et al. (2008) and Fornasier et al. (2009). The taxonomic groups are from Fulchignoni et al. (2008), except the one for 42355 Typhon which is from DeMeo et al. (2009). Four main classes have been defined based on combined visible and near-IR colors: the BB, BR, IR, and RR classes, where the BB objects have a neutral color (relative to the Sun) and the RR objects are the reddest ones (steep spectral slopes). The BR and IR objects have intermediate spectral slopes in the visible and near-IR (see Barucci et al. 2005b for more details)  
*Ce* centaur, *Re* resonant object, *Sc* scattered disk object, *C* classical object, *De* detached object

of bands of pure CH<sub>4</sub> ice in the laboratory) indicate that some of the CH<sub>4</sub> could be dissolved in N<sub>2</sub> (Licandro et al. 2006a; Tegler et al. 2007; Merlin et al. 2009; Abernathy et al. 2009), with possibly stratification in the upper surface layers (a more recent work by Tegler et al. 2010 does not support stratification). Models of Eris spectra include, in addition to methane ice, some tholins.

The spectrum of Makemake (Fig. 4.3) is also dominated by methane (Licandro et al. 2006b; Brown et al. 2007; Tegler et al. 2007, 2008). Some of the methane bands are slightly shifted in wavelength compared to those of pure methane, which suggests that some of the methane could be diluted in nitrogen, as may be the case for Eris. However, in contrast to Pluto, Eris, and Triton, the methane bands are much broader and more saturated on Makemake, indicating that the methane is present in large (cm sized) grains. In addition, absorption features due to ethane ice, and possibly other higher order hydrocarbons, have also been detected (Brown et al. 2007). The large grain sizes of methane and the presence of higher order hydrocarbons on the surface can all be explained if it is methane, rather than molecular nitrogen, that is the dominant surface constituent (Brown et al. 2007).

The spectrum of Quaoar is dominated by absorption bands of crystalline water ice (see discussion of water ice objects in the next subsection), but also contains several features in the infrared (1.8, 2.2, 2.32, 2.37 μm) which have been attributed to the presence of a small amount of methane ice on its surface (Schaller and Brown 2007b; Guillet et al. 2009a). Detections of additional bands in the 2.2–2.4 μm range (not belonging to methane) may also indicate the presence of higher order hydrocarbons such as ethane (Fig. 4.4). Broad-band Spitzer Space Telescope photometry at 3.6 and 4.5 μm can be modeled by inclusion of N<sub>2</sub> and amorphous H<sub>2</sub>O ices (Dalle Ore et al. 2009), but, while intriguing, firm detections of specific ices cannot be made from such broad-band observations.

Sedna is a peculiar object. With a perihelion of 76 AU and an aphelion of 927 AU, the orbit of Sedna is far beyond that of most other TNOs. Due to its faintness, spectroscopy of Sedna is extremely difficult. A tentative detection of methane from near-IR spectra recorded at the VLT has been reported, as well as the suggestion of

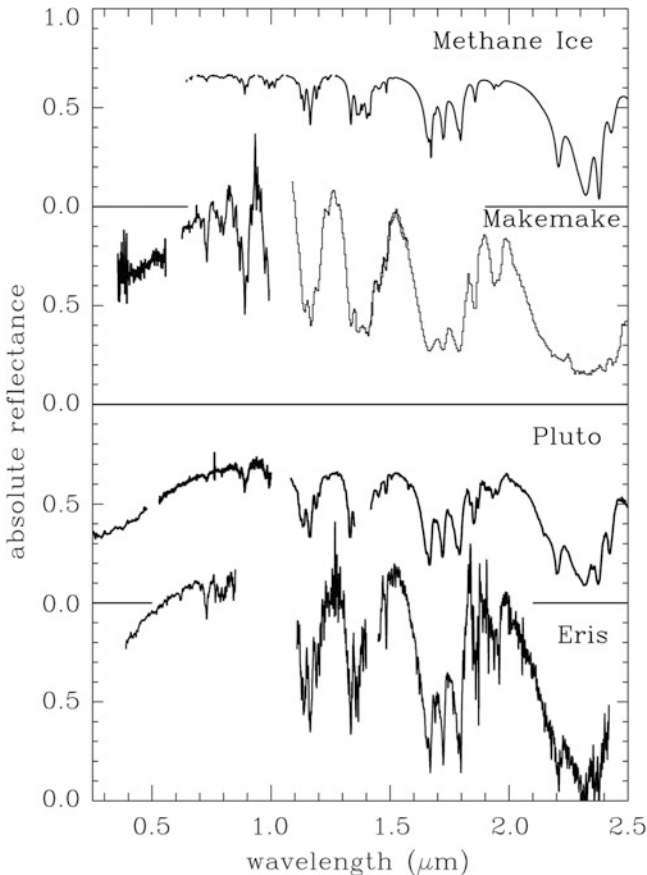


**Fig. 4.3** Visible and near-infrared reflectance spectra of Makemake (Brown et al. 2007; spectra recorded at the Keck telescope), Pluto (compiled from Trafton and Stern 1996; Grundy and Fink 1996; Rudy et al. 2003; Douté et al. 1999), and Eris (Merlin et al. 2009; spectra recorded at the VLT) along with a spectrum of pure methane ice with 100- $\mu\text{m}$  grains (absorption coefficients from Grundy et al. 2002). The main absorption features seen in the spectra of all three TNOs are due to methane ice. The methane absorption features of Eris and Makemake are broader and more saturated than those of Pluto and the methane laboratory spectrum indicating larger methane grain sizes for Eris and Makemake (mm-sized for Eris and cm-sized for Makemake) (Brown et al. 2007; Licandro et al. 2006a,b; Merlin et al. 2009). The 2.15  $\mu\text{m}$  absorption feature due to  $\text{N}_2$  ice is present in spectrum of Pluto but has not been detected on Eris or Makemake. However, the presence of molecular nitrogen on Eris has been inferred because of slight shifts in the wavelengths of the methane absorption bands. Such shifts could be explained if the methane were dissolved in molecular nitrogen (Brown et al. 2005; Licandro et al. 2006a; Merlin et al. 2009) (Figure adapted from Brown 2008)

the presence of molecular nitrogen (Barucci et al. 2005a). By combining the spectra of Barucci et al. with Spitzer Space Telescope photometric data at 3.6 and 4.5  $\mu\text{m}$ , Emery et al. (2007) find that ices of methane and nitrogen, with, in addition, some water ice, provide a satisfactory fit to the combined VLT-Spitzer data, though, again,

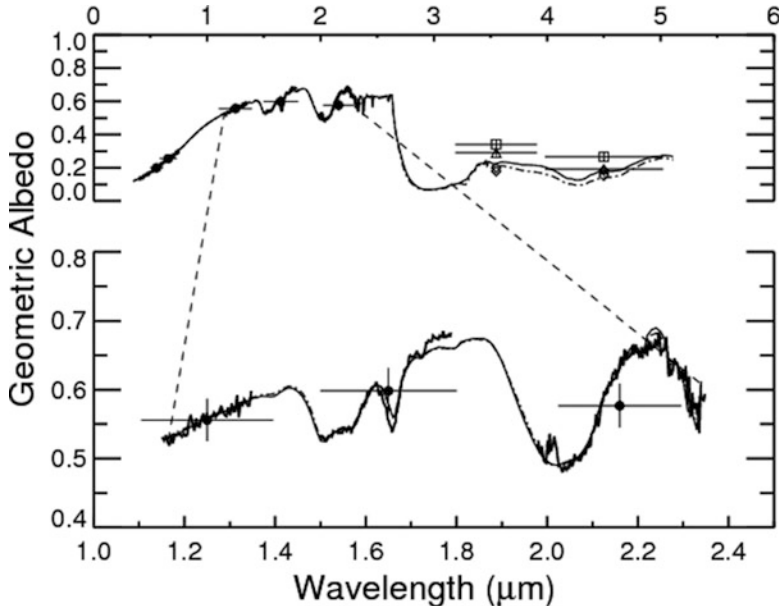


**Fig. 4.4** Spectra of Quaoar with best fitting model (in grey). *Top:* Combined VLT spectroscopic data in the visible and near-infrared and Spitzer broad-band photometric data points in the extended infrared (at 3.6 and 4.5  $\mu\text{m}$ ), with model. *Bottom:* an enlargement of the visible-near-infrared VLT spectrum with some photometric data that have been used to connect the visible and near-infrared parts that were recorded with different spectrometers. The best fitting model includes the three surface species previously detected: crystalline water ice, methane ice, and ethane ice, as well as some nitrogen and amorphous water ice that help improve the fit in the extended infrared but for which there is no detection, and some tholins to account for the red slope in the visible (From Dalle Ore et al. 2009, reproduced with permission © ESO)

the broad-band photometry cannot be used to detect specific ices. Sedna is a very red object, redder than Pluto, Eris and Makemake. Tholins (Triton tholin, with, in addition, some Titan tholin embedded in water ice in the best fit model of Emery et al.) were introduced in surface models to account for the red spectral slope between 0.4 and 1  $\mu\text{m}$ .

The presence of volatiles on the surfaces of only the largest and most distant objects is because these objects have sufficient gravity to retain their atmospheres against thermal escape over the age of the Solar System (Schaller and Brown 2007a). Triton, Eris, Pluto, Makemake, Sedna, and Quaoar all have indication of some volatile surface ices (always methane, in some cases  $\text{N}_2$  and CO, also). The atmospheric loss model even predicts that a few objects can exist in a transition regime where nitrogen is lost but methane is maintained. Makemake and Quaoar are both predicted and observed to be in such a regime (Brown et al. 2007; Schaller and Brown 2008).

There is no clear detection of hydrocarbons other than methane on Pluto and Triton. Very small amounts of ethane may be present on Pluto, however. On nitrogen-rich objects like Triton and Pluto (and possibly Eris; see Merlin et al. 2009) irradiation

processing of hydrocarbons on the surface leading to high-order hydrocarbons may be limited, as the bulk of the methane molecules appear to be isolated in a relatively inert nitrogen matrix. On objects such as Makemake and Quaoar, however, the relative lack of nitrogen could allow methane irradiation chemistry to proceed quickly, leading to easily detectable ethane and also to possible higher-order hydrocarbon species.

Products of photochemistry in the presumed thin atmospheres of TNOs can be modeled along the lines of studies of the photochemistry of the microbar atmospheres of Triton and Pluto e.g., Krasnopolsky and Cruikshank (1995, 1999). This work shows that the C<sub>2</sub> hydrocarbons and HCN form and precipitate to the surface in significant quantities over the age of the Solar System. While the possible detection of HCN on Triton has recently been reported (Burgdorf et al. 2010), other such materials should contribute to the surface ice chemistry, though none have been detected.

The surfaces of the largest objects are replenished on something like a seasonal time scale as volatiles migrate from warm to cold areas throughout the year, with some surface areas possibly maintaining an annual deposit of volatiles (Hansen and Paige 1996). In most cases the significant eccentricities – and thus extreme temperature variations – of these objects aids in resurfacing.

The two objects for which the resurfacing timescale remain mysterious are Sedna and Quaoar. Spectrally, Sedna looks little like the other methane-rich objects. The absorption features are shallow and only marginally detected. Even at Sedna's 76 AU perihelion, methane has little volatility, so it is possible that methane resurfacing happens rarely or never on Sedna. In this case continued irradiation would have destroyed much of the methane even in the presence of nitrogen. It is possible that Sedna's surface contains mostly higher-order hydrocarbons or, even, the final end state of this processing long carbon chains or nitrogen-bearing tholins. Quaoar, on the other hand, is on a near-circular orbit with an unknown polar orientation. The fact that methane has been observed shows that it has not all migrated to a cold dark pole, but understanding seasonal cycling on Quaoar will require better modelling and understanding of this body.

The volatile rich bodies range in optical colors from extremely red (Sedna) to nearly neutral (Eris). Though the numbers are small, it appears that a correlation exists between the color and the albedo, with the reddest volatile-rich objects being the darkest, and the least red being the brightest. The interpretation would be that exposed processed hydrocarbons are both dark and red while volatiles covering these hydrocarbons are bright and neutrally colored. In the case of Eris, which is thought to be nearly uniformly covered in volatile ice with little or no exposed processed hydrocarbon, this hypothesis explains the color, spectrum, lack of significant light curve, and exceedingly high albedo.

#### **4.5.2 Other Objects**

Until the recent discoveries of large objects rivaling or exceeding the size of Pluto, the near infrared spectra of all other small and mid-sized transneptunian objects and Centaurs lay on a continuum between those whose spectra were essentially

featureless to those whose spectra resembled pure crystalline water ice. These objects have diverse spectral shapes. Water ice is detected on these objects by the presence of the 1.5 and 2.0  $\mu\text{m}$  absorption features. Its crystallinity is detected by the presence of an absorption feature at 1.65  $\mu\text{m}$ .

To first order, the surfaces of small and midsized TNOs and Centaurs can be described with a two component model consisting of dark (likely carbon-rich) deposits and exposed crystalline water ice (Luu and Jewitt 1996; Barkume et al. 2008). The spectra of these objects (considering only the near-IR part) can be parameterized as a linear mixture between a featureless continuum component with a variable slope and crystalline water ice (Luu and Jewitt 1996; Barkume et al. 2008). The fraction,  $f$ , of water ice in the spectra can then be compared with object size, orbital properties and object color. For a useful comparison between the different objects, a fixed grain size of 50  $\mu\text{m}$  was used for the crystalline water ice in their model. It should be mentioned that, while this approach is very useful to classify the infrared spectra of these objects, a more complete modelling including the visible part of the spectra and the geometric albedo of the objects (when available) is needed to derive more information on the surface components. However, such modelling has been possible only in a limited number of cases, so far.

#### 4.5.2.1 Objects with Featureless to Nearly Featureless Spectra ( $f < 10\%$ )

Many small TNOs and Centaurs show no or very weak absorption features in the infrared, even at moderate signal-to-noise, (Barkume et al. 2008; Guilbert et al. 2009a) but do show a diversity of visible colors. These objects must have little or no fresh ices on their surfaces, although we note that mixing water ice with dark materials quickly erases the water ice spectral signature. Models of their composition include essentially refractory carbonaceous compounds to account for their low albedos and overall spectral shapes.

#### 4.5.2.2 Objects with Moderate Water Ice Spectra ( $10\% < f < 50\%$ )

Many mid-sized (400–1,000 km diameter) TNOs and a few Centaurs show moderate absorptions due to the presence of crystalline water ice on their surfaces (see, e.g., Cruikshank et al. 1998; Luu et al. 2000; de Bergh et al. 2005; Barucci et al. 2006; Barkume et al. 2008; Guilbert et al. 2009a). Barkume et al. (2008) found a weak correlation between object size and the fraction of water ice detected on the surfaces of the TNOs in their sample indicating that larger objects generally show stronger water ice absorption features. However, no such correlation was found for the Centaurs (Barkume et al. 2008). The degree of exposed water ice detected on the surfaces of all of these objects may be related to initial abundances, subsequent irradiation, impacts, or perhaps cryovolcanism (see next Sect. 5.3).

Three of these objects present some peculiarities: 90482 Orcus, 5145 Pholus, and 2002 VE<sub>95</sub>. Orcus' spectrum shows, in addition to the water ice absorption bands, a small absorption feature at 2.2  $\mu\text{m}$  that has been attributed to either ammonia hydrate

or methane ice (de Bergh et al. 2005; Barucci et al. 2008b). As methane is not expected to survive to the present day on the surface of Orcus due to its small size (Schaller and Brown 2007a; Levi and Podolak 2009) this feature has been generally interpreted as ammonia hydrate. Spectra of Pholus and 2002 VE<sub>95</sub> (one is a Centaur and the other one a Plutino) show, in addition to water ice signatures, an absorption feature at 2.27  $\mu\text{m}$  that has been attributed to methanol ice or an irradiation product of methanol ice (Cruikshank et al. 1998; Barucci et al. 2006). The spectrum of 5145 Pholus has been discussed in Sect. 4. That of 55638 (2002 VE<sub>95</sub>), although of not as high quality, presents additional similarities with that of Pholus. Indeed, the general shapes are very similar, and both objects are among the reddest objects. Their spectra have been modelled with Titan and Triton tholins as well as amorphous carbon. The albedo of 2002 VE<sub>95</sub> is however unknown.

A few of these objects – exclusively Centaurs – also present *variable* spectra in the near-infrared. This is the case, for instance, of the Centaur 2060 Chiron for which the water ice bands are not always present in its spectrum. Some correlation has been found between the activity of the object (presence of a coma) and the absence of the water ice bands. It has been suggested that the coma “hides” the water ice at the surface when the body is active (Luu et al. 2000). Spectra of two other Centaurs, 32532 Thereus and 10199 Chariklo, around which no coma has ever been detected and which have a larger perihelion distance than Chiron, present the same kind of variability, but with weaker water ice bands than for Chiron, when present (see Licandro and Pinilla-Alonso 2005; Merlin et al. 2005; Guilbert et al. 2009b). In the case of Thereus, this is explained by heterogeneities over the surface of the object. In the case of Chariklo, it is less certain as its rotation period is not known; temporal variations due to a weak cometary-like activity are not completely excluded.

#### 4.5.2.3 Objects with Strong Water Ice Spectra ( $f > 80\%$ )

In contrast to the near infrared spectra of the non-volatile rich TNOs and Centaurs discussed above, the near infrared spectra of 136108 Haumea (2003 EL<sub>61</sub>), its two satellites, and several other small TNOs (1996 TO<sub>66</sub>, 2002 TX<sub>300</sub>, 1995 SM<sub>55</sub>, 2003 OP<sub>32</sub>, 2005 RR<sub>43</sub>, 2003 UZ<sub>117</sub>, 2005 CB<sub>79</sub>) resemble laboratory spectra of pure crystalline water ice with modeled fractions of water ice greater than 80% (Brown et al. 1999; Barkume et al. 2006; Trujillo et al. 2007; Merlin et al. 2007; Brown et al. 2007; Barkume et al. 2008; Schaller and Brown 2008; Pinilla-Alonso et al. 2009; Fraser and Brown 2009). Remarkably, these objects are also relatively clustered in orbital element space. The largest object, Haumea, had been previously suggested to have experienced a massive collision that imparted its fast (4-h) rotation, stripped off most of its icy mantle leaving it with a density close to rock (2.7 g/cm<sup>3</sup>), and formed its two satellites (Rabinowitz et al. 2006; Brown et al. 2006). Brown et al. (2007) concluded that the extremely water ice rich TNOs and the satellites of Haumea were in fact fragments of the icy mantle of the proto-Haumea that had been ejected during a massive collision. The strong water ice spectral signature has been used as a tracer of this collision.

It should be noted that, while the first spectral models of Haumea that were published (Trujillo et al. 2007) included only crystalline water ice, both Merlin et al. (2007) and Pinilla-Alonso et al. (2009) found a better fit with the data using a mixture of amorphous and crystalline water ice (see Fig. 4.5). Carbonaceous compounds, if present, must be very minor surface constituents. Indeed, only 3% of amorphous carbon is included in the best fit model of Merlin et al., and none in the best fit model of Pinilla-Alonso et al.

The existence of Haumea and its family not only allows us to categorize some of the known spectra in the Kuiper belt, but it also serves as a test-bed for some of the processes long thought relevant in the outer Solar System such as cryovolcanism and the effects of irradiation and impacts on water ice surfaces.

From laboratory irradiation studies, it is known that crystalline water ice can be transformed into amorphous ice. The amorphization rate of irradiated crystalline water ice depends on temperature. Although the exact temperature dependence of the amorphization efficiency is still debated in the laboratory community (Strazzulla et al. 1992; Moore and Hudson 1992; Mastrapa and Brown 2006; Zheng et al. 2009), for most TNOs (in particular those that have surface temperature below 40 K<sup>5</sup>), the amorphization efficiency should be very high (about 90%). For these bodies, the irradiation timescale can be as fast as 100–1,000 million years due to particle irradiation (the amorphization timescale for objects approaching the termination shock is shorter than for objects orbiting around 40 AU). As an example, the first 200 μm ice layers of Haumea’s surface (i.e. the ones responsible for the visible-NIR spectra, Gil-Hutton et al. 2009) may accumulate a dose of 10 eV/molecule in about 1 Gyr.<sup>6</sup>

The initial discovery of crystalline water ice on Charon was thus somewhat surprising, but Brown and Calvin (2000) argued that some likely mundane surface processing mechanism was continuously refreshing the water ice on the surface. Jewitt and Luu (2004), however, noticing crystalline water ice on Quaoar, suggested that the crystalline water ice was due to currently active cryovolcanism. Quaoar is indeed large enough that subsurface liquid is possible, particular with some agent such as ammonia that depresses the freezing temperature (e.g., Kargel 1992). If the subsurface liquid, which would be quite deeply buried, could somehow reach the surface, current activity might indeed be possible. But the realization that crystalline water ice was seen on Haumea, which has such a thin layer of ice that subsurface liquid is difficult to imagine (Trujillo et al. 2007) and that crystalline

---

<sup>5</sup> For Haumea, using the Stefan-Boltzmann law, Merlin et al. (2007) estimated a mean surface temperature of about 30 K, and using the peak position of the 1.65-μm band they estimated an upper limit of 40 K.

<sup>6</sup> This value can be obtained using the estimates of the dose by Strazzulla et al. (2003). According to several authors (Strazzulla et al. 1992; Moore and Hudson 1992; Leto and Baratta 2003; Mastrapa and Brown 2006), 10 eV/molecule is the dose at which the saturation level of amorphous ice is reached after irradiation. The error bar on this estimate can reasonably be of 20%, so that the amorphization timescale should be considered to be in the range 0.8–1.2 Gyr.

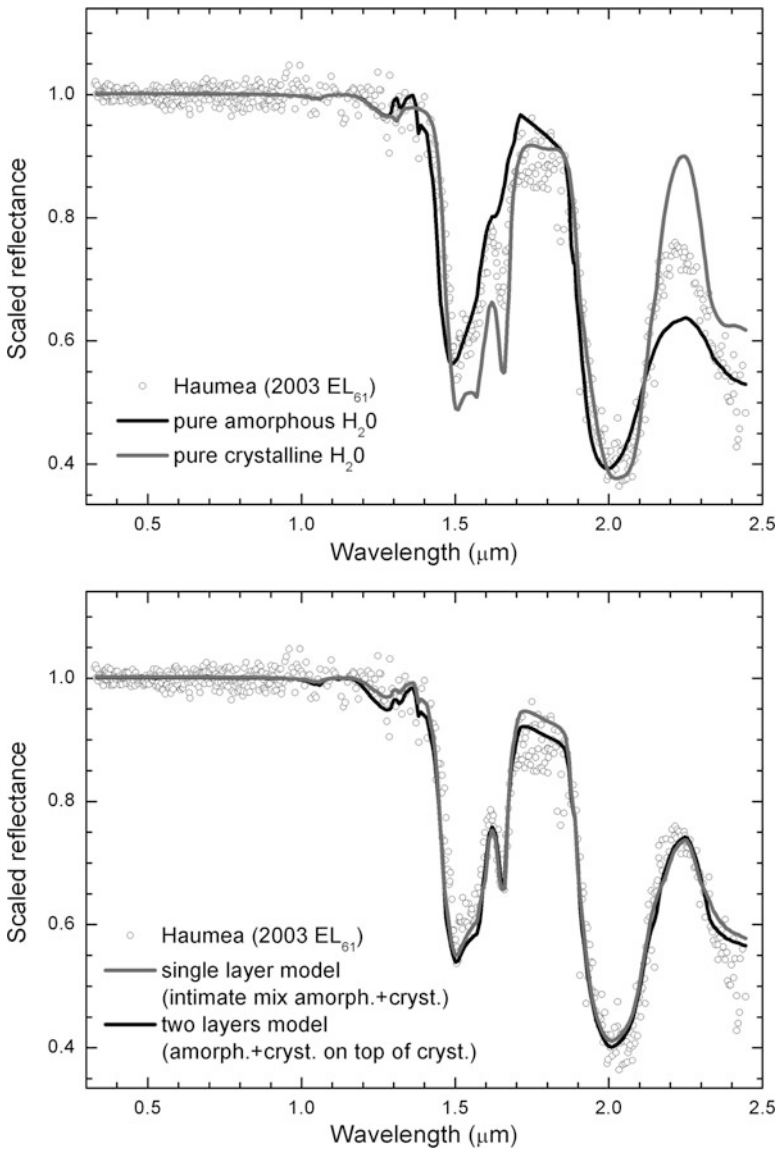


**Fig. 4.5** Composite reflectance spectrum of Haumea (2003 EL<sub>61</sub>) with models (thick lines). An average visible-near-infrared spectrum from TNG and WHT observations by Pinilla-Alonso et al. (2009) has been combined with near-infrared spectra of Trujillo et al. (2007) recorded at the Keck and Gemini telescopes. However, in this figure, the Pinilla-Alonso et al. spectrum is considered only up to 2.2  $\mu\text{m}$ , as beyond it is too noisy. *Top*: models with pure amorphous ice and pure crystalline ice (grain size diameters: 15  $\mu\text{m}$ ) which show the shifts in the positions of the main bands of water ice between the two different states, the 1.65  $\mu\text{m}$  band characteristic of ice in the crystalline state, and the important drop in reflectance around 2.35  $\mu\text{m}$  for amorphous ice. *Bottom*: some attempt to better model the spectra. The best fit (thick black line) is obtained with a single layer consisting of an intimate mixture of crystalline and amorphous water ice (about 1:1) above a layer of pure crystalline water ice. This model is obviously not unique. Spectra of higher quality are required to better evaluate the contribution of amorphous water ice to the absorption (Figure adapted from Pinilla-Alonso et al. 2009)

water ice is seen on even quite small Haumea family members where there is little chance of a subsurface ocean (Barkume et al. 2008) drives home the point that crystalline water ice is ubiquitous in the outer Solar System, and not just on the large potentially cryovolcanically active objects. The original suggestion that the explanation is more mundane therefore seems likely.

Haumea and its family also give a convincing demonstration of the effects of space weathering on Gyr timescales. Ragozzine and Brown (2007) demonstrate that the current dynamical configuration of the Haumea system suggests a formation time of at least a billion years ago; dynamical models suggest that the most likely formation time was at the beginning of the Solar System (Levison et al. 2008). Yet the surfaces of Haumea and its family appear like nearly fresh laboratory samples of water ice. How might this be possible? As mentioned above, the surface of Haumea, the parent body of the family, does not show the presence of C-rich ices such as methane, methanol, etc. Thus the irradiation-induced formation of complex organics (see Sect. 4) from simple C-rich ices is impossible. But why do we find water ice in the crystalline state on the cold surface of Haumea (and other TNOs) in spite of long-term exposure to irradiation? Is the surface warmer (or has it been warmer in the past) than expected, in which case thermal recrystallization could more easily balance irradiation amorphization? This does not seem very realistic.

Two other possibilities exist. Either irradiation does not have the expected effect on water ice surfaces over billions of years or the surface is continuously replenished. Water ice is thoroughly involatile at these temperatures, and, as argued above, internal resurfacing of the smallest of these objects seems unlikely, so if resurfacing of any sort were occurring it is likely that the only mechanism which could do it would be impacts on the surface. One could imagine a mechanism, for example, where impacts cause vaporization which subsequently coat the impacting material, leading to a preservation of a pristine appearing surface (Brown and Calvin 2000; Gil-Hutton et al. 2009).

#### 4.5.3 Relationships of Composition with Other Properties of the Objects

In Table 4.1 are shown all the objects for which good (or relatively good) spectra are available, along with their dynamical class, orbital inclination, and, when available, visible spectral gradient, taxonomic family, albedo and estimated size, as well as the major components detected or suspected to be present at their surface. As explained above, the taxonomic classification takes into account both the visible spectral gradient and the near-IR spectral gradient. For some of these objects, there is also information (not discussed here) on their opposition surge and polarimetric properties.

The most obvious difference is between the largest objects and the others, where only the spectra of the largest objects are dominated by methane ice and only these objects (with the exception of Haumea, and maybe also members of its

family) have very high albedos. There is also evidence for important similarities between objects belonging to the Haumea collisional family, as discussed above. The other TNO that resembles them spectrally the most is Charon, satellite of Pluto. Charon is also most probably the result of a collision (with the proto-Pluto). Charon, however, has an additional absorption in its spectrum around 2.2  $\mu\text{m}$ , like Orcus, that has been attributed to some ammonia hydrate which is not seen in Haumea spectra. Furthermore, Charon has a much lower albedo than Haumea. For the rest of the objects, although the sample is slightly enlarged in comparison to that of Barkume et al. (2008), the conclusions are essentially the same. In summary, there is a lack of correlation of the fraction of water ice detected with visible color, taxonomic designations, albedo and orbital parameters. However, for TNOs, but not for Centaurs, there is some correlation with diameter.

As already mentioned, while spectroscopy has been carried out for a very small sample of the objects discovered so far, colors (and especially visible colors, which are easier to obtain) have been measured for a much larger number of objects. When considering colors, better statistics can therefore be made.

**Cold classical Kuiper belt objects:** Once the volatile rich and Haumea family objects are excluded, the strongest remaining physically related objects are the dynamically cold classical Kuiper belt objects in low eccentricity low inclination orbits beyond 40 AU. While other populations appear mixed, the cold classical Kuiper belt objects are uniformly red in the visible. Some evidence also indicates that they have moderately higher albedos than the average of other populations. Unfortunately, this population also lacks the large objects found in the other populations, so no objects are currently bright enough for detailed spectroscopy, and no specific ices have been detected on any of these objects. Nonetheless the uniform red colors may give us important information on space weathering processes. Indeed, in the general view, an object whose surface includes carbon-bearing ices ( $\text{CH}_4$ ,  $\text{CH}_3\text{OH}$ , etc.) would start out neutrally colored and would redden over time due to solar and cosmic ion irradiation. Alternatively, the object may start red due to the presence of primordial organics. With even more elapsed time (i.e. at higher irradiation dose), however, the object would become darker but more neutrally colored. In this view, red surfaces would only appear at an early or intermediate state. The uniform red colors and possibly uniform moderate albedos of dynamically “cold” classical TNOs could indicate that these bodies did not accumulate a dose able to complete this last darkening step, which corresponds to carbonization. In the case of dynamically “hot” TNOs, due to their more eccentric orbits, some of them may have accumulated higher doses that could be responsible for some of the observed neutral colors; but this scenario is still rather speculative and needs to be investigated in more details.

**Medium-sized Kuiper belt objects:** Quaoar is the smallest known Kuiper belt object to have had volatiles detected on its surface, but its surface is mainly covered in water ice, of which a large but difficult to determine fraction is in crystalline form. While this crystalline water ice has prompted speculation of cryovolcanism, from the discussion of the Haumea family above it appears that the crystalline water ice component is most probably due to other mechanisms.

The group of medium-sized Kuiper belt objects, which we will define to be those with (perhaps poorly determined) diameters greater than about 500 km are the only known *distant* objects with moderate water ice absorption. Two of the largest of these objects, Charon and Orcus, have evidence for the presence of ammonia or ammonia hydrates on the surface. It is an open question whether or not ammonia-features are always present when water ice absorption is detected; the spectra of no other smaller objects are of sufficient quality to detect the features seen on the other objects.

The presence of moderate amounts of crystalline water ice mixed with ammonia on the surface of Charon (and perhaps by extension other medium-sized Kuiper belt objects) led Cook et al. (2007) to re-interpret the presence of ammonia as yet another signature of cryovolcanism. Like crystalline water ice can be transformed into amorphous ice by particle irradiation, the ammonia ices can be destroyed by irradiation with a relatively low dose (e.g. Strazzulla and Palumbo 1998; Loeffler et al. 2006; Moore et al. 2007). However, the efficiency of this process depends on the past and present orbital properties of the objects, so that for some objects ammonia could be more stable on the surface than originally expected. Charon, in particular, orbits in a region where the irradiation dose is minimum (see Hudson et al. 2008), leaving open the possibility of the original interpretation of Brown and Calvin (2000) for the water-ammonia surface of Charon – that the ammonia is a signature of past extrusion rather than current activity.

**Dynamically hot populations:** The typical small members of the dynamically hot populations, which include the scattered Kuiper belt, the resonant objects, and the hot classical Kuiper belt appear to be an uninterpretable melange. The only spectral signatures ever detected on these objects are occasional hints of weak water ice absorption, but often even water ice absorption can be ruled out to a high level. The optical colors vary, however, from the reddest to the bluest objects in the Kuiper belt. No clear correlation between color and albedo has appeared. No satisfying explanation for the spectral interpretation of these objects has emerged.

**The Centaurs:** The Centaurs have surface characteristics unique from the Kuiper belt population from which they were presumably derived. They thus provide one of the few opportunities to understand the effects of the thermal environment of these small bodies of the outer Solar System.

Colors of Centaurs appear bifurcated between a red and a neutral population. Contrary to what is usually assumed, there is some evidence that the red Centaurs generally have higher albedos than the blue Centaurs (Stansberry et al. 2008). Intriguingly, spectra of some Centaurs show the signature of moderate water ice absorption that is only otherwise seen in the medium-sized Kuiper belt objects. The presence of water ice absorption does not seem to be related to the optical colors (Barkume et al. 2008).

One of the difficulties in interpreting these spectral characteristics is that we cannot be certain that at least some of them are due to the fact that we are looking at smaller-sized objects in the Centaur population than we see in the Kuiper belt population. While the water ice absorption signature seems unlikely to be size related, it is not implausible that the Centaur-sized Kuiper belt objects have bifurcated colors and correlated albedos and that some size-related effect confuses

these correlations for the larger objects. It is also not implausible, however, that these effects are intrinsically related to the thermal environment in which Centaurs find themselves. A better connection between Centaur physical properties and dynamical lifetimes and histories is required to help our understanding of this important piece of the puzzle of the interpretation of outer solar system surfaces.

## 4.6 Conclusion and Perspectives

The diversity in surface composition among TNOs presents an opportunity to sample the range of materials preserved, to some unknown degree, since their condensation and aggregation in the early solar nebula. That diversity also presents a puzzle of considerable complexity in which is locked a wealth of information entangled in our ignorance of the physics and chemistry of the earliest materials and processes in the outer regions of the disk in which the Sun and planets originated. While studies of the dynamical history of the Solar System progress, expanded observational studies of the physical properties of transneptunian bodies can yield more information on surface compositions and thermal structures of individual objects within the range of the observational techniques currently available and those projected in the near future.

The basic icy components of TNO surfaces (including Pluto and extending to Triton) that are readily identified in high quality near-IR ( $\lambda \leq 2.5 \mu\text{m}$ ) spectra are H<sub>2</sub>O, CO, CO<sub>2</sub>, CH<sub>4</sub>, and N<sub>2</sub>, as noted earlier. Ethane (C<sub>2</sub>H<sub>6</sub>) and methanol (CH<sub>3</sub>OH) can also be found in the near-IR. The ices of hydrocarbons more complex than CH<sub>4</sub> present a confusion of absorption bands that are very difficult to distinguish from one another, as illustrated in the study of alkane ices by Clark et al. (2009). At longer wavelengths,  $2.5 \leq \lambda \leq \sim 8 \mu\text{m}$ , the diagnostic bands of hydrocarbons become a bit more easily distinguished. Thus, the extension of spectral observations of TNOs to wavelengths longer than 2.5  $\mu\text{m}$  will be beneficial in the identification of such new hydrocarbon species as may occur, including those produced *in situ* by photolysis. A similar situation applies to nitriles, including HCN, the most abundant product of photolysis of N<sub>2</sub>-CH<sub>4</sub> mixtures, as illustrated by the tentative detection of this species on Triton from spectra recorded around 4.8  $\mu\text{m}$  by the AKARI infrared satellite (Burgdorf et al. 2010).

Extending the wavelength region of TNO spectroscopic studies from Earth-based observatories is frustrated by the weakness of the sunlight reflected from these bodies and the interference of the Earth's atmosphere. Observations from space-based telescopes will overcome the latter problems, but the objects are still quite faint. The development of larger and more capable ground- and space-based telescopes will enable spectroscopy of increased quality for an increasingly large number of objects, facilitating the detection of new species and the balance between amorphous and crystalline H<sub>2</sub>O ice.

Beyond the volatile molecules, other materials that we can reasonably expect to find on at least some TNOs include silicates (absorption bands in the visible and

near-IR regions and emission bands at 10 and 20  $\mu\text{m}$ ) when data of sufficient quality can be obtained. Carbonaceous materials (aromatic and aliphatic hydrocarbons) that contribute to the colors and low albedos of TNOs may also appear when high-quality spectra of the 3- $\mu\text{m}$  region become available.

Additional laboratory studies, including optical constants, of frozen volatiles are needed for the further investigation of TNO and Centaur spectra at all available wavelengths. Mixtures of ices (and of ices mixed with silicates or carbonaceous compounds) are of particular interest, both before and after photolysis by ions and ultraviolet light. Since N<sub>2</sub> is an important component of several TNOs, in addition to Triton, the spectra of hydrocarbons and nitriles frozen in the N<sub>2</sub> matrix, both alpha and beta phases, are needed. In addition to ices, spectroscopic studies of adsorbed and enclathrated molecules such as CO<sub>2</sub> are needed. Some of the Saturn satellites having both ice and non-ice components, for example, show the presence of CO<sub>2</sub> as an adsorbed or otherwise complexed species, exhibiting shifted and broadened absorption bands (Cruikshank et al. 2010).

Further investigation of complex carbonaceous material from natural sources (the meteorites and comets) are needed to provide a more direct suite of probable materials for comparison with observations of TNOs. Optical constants are especially needed for modeling studies.

Continued and expanded investigations of comets, Centaur objects, and Trojan asteroids will help shed light on the compositions and physical properties of TNOs.

New facilities such as Herschel (now in flight), and ALMA (in construction) will bring greatly improved sensitivity at thermal infrared wavelengths for the determination of the dimensions and surface albedos of TNOs. As shown in Table 4.1, the first Herschel albedo measurements (Lellouch et al. 2010; Lim et al. 2010; Müller et al. 2010) have just become available. At the same time, greatly expanded deep sky surveys with facilities such as Pan-STARRS and the LSST are expected to multiply the number of known objects several-fold, with the possibility that many more relatively bright TNOs will be available for detailed study.

Finally, we note that the *New Horizons* mission launched in January, 2006, will fly by Pluto and Charon in July, 2015, and then proceed on into the Kuiper Belt region, with the possibility to observe one or more TNOs during fast flybys (Stern and Spencer 2004; Young et al. 2008).

## References

- Abernathy MR, Tegler SC, Grundy WM et al (2009) Digging into the surface of the icy dwarf planet Eris. *Icarus* 199:520
- Agnor CB, Hamilton DP (2006) Neptune's capture of its moon Triton in a binary-planet gravitational encounter. *Nature* 441:192
- Baragiola RA, Fama MA, Loeffler MJ et al (2012) Radiation effects in water ice in the outer solar system. (this volume)
- Baratta GA, Palumbo ME (1998) Infrared optical constants of CO and CO<sub>2</sub> thin icy films. *J Opt Soc Am A* 15:3076

- Barucci MA, Peixinho N (2006) Trans-neptunian objects' surface properties. In: Lazzaro D et al (eds) Asteroids, Comets, and Meteors: Proceedings of the 229th symposium International Astronomical Union, August 2005, Cambridge University Press, Buzios, p 171
- Barucci MA, Cruikshank DP, Dotto E et al (2005a) Is Sedna another Triton? *Astron Astrophys* 439:L1
- Barucci MA, Bel'skaya IN, Fulchignoni M et al (2005b) Taxonomy of Centaurs and trans-neptunian objects. *Astron J* 130:1291
- Barucci MA, Merlin F, Dotto E et al (2006) TNO surface ices. Observations of the TNO 55638, (2002 VE<sub>95</sub>) and analysis of the population's spectral properties. *Astron Astrophys* 455:725
- Barucci MA, Brown ME, Emery JP et al (2008a) Composition and surface properties of transneptunian objects and Centaurs. In: Barucci MA et al (eds) The solar system beyond Neptune. The University of Arizona Press, Tucson, p 143
- Barucci MA, Merlin F, Guillet A et al (2008b) Surface composition and temperature of the TNO Orcus. *Astron Astrophys* 479:L13
- Barkume KM, Brown ME, Schaller EL (2006) Water ice on the satellite of Kuiper belt object 2003 EL<sub>61</sub>. *Astrophys J Lett* 640:L87
- Barkume KM, Brown ME, Schaller EL (2008) Near-infrared spectra of Centaurs and Kuiper belt objects. *Astron J* 135:55
- Benecchi SD, Noll KS, Grundy WM et al (2009) The correlated colors of transneptunian binaries. *Icarus* 200:292
- Bernstein MP, Sandford SA (1999) Variations in the strength of the infrared forbidden 2328.2 cm<sup>-1</sup> fundamental of solid N<sub>2</sub> in binary mixtures. *Spectrochim Acta A* 55(12):2455
- Bernstein MP, Cruikshank DP, Sandford SA (2005) Near-infrared laboratory spectra of solid H<sub>2</sub>O/CO<sub>2</sub> and CH<sub>3</sub>OH/CO<sub>2</sub> ice mixtures. *Icarus* 179:527
- Brown ME (2008) The largest Kuiper belt objects. In: Barucci MA et al (eds) The solar system beyond Neptune. The University of Arizona Press, Tucson, p 335
- Brown ME, Calvin WM (2000) Evidence for crystalline water and ammonia ices on Pluto's satellite Charon. *Science* 287:107
- Brown RH, Cruikshank DP, Tokunaga AT et al (1988) Search for volatiles on icy satellites. I – Europa. *Icarus* 74:262
- Brown ME, Barkume KM, Blake GA et al (2007) Methane and ethane on the bright Kuiper belt object 2005 FY<sub>9</sub>. *Astron J* 133:284
- Brown ME, Trujillo CA, Rabinowitz DL (2005) Discovery of a planetary-sized object in the scattered Kuiper belt. *Astrophys J Lett* 635:L97
- Brown ME, Schaller EL, Roe HG et al (2006) Direct measurement of the size of 2003 UB<sub>313</sub> from the Hubble Space Telescope. *Astrophys J Lett* 643:L61
- Brown RH, Cruikshank DP, Pendleton Y (1999) Water ice on Kuiper belt object 1996 TO<sub>66</sub>. *Astron J Lett* 519:L101
- Brucker MJ, Grundy WM, Stansberry JA et al (2009) High albedos of low inclination classical Kuiper belt objects. *Icarus* 201:284
- Brunetto R, Roush TL (2008) Impact of irradiated methane ice crusts on compositional interpretations of TNOs. *Astron Astrophys* 481:879
- Brunetto R, Strazzulla G (2005) Elastic collisions in ion irradiation experiments: a mechanism for space weathering of silicates. *Icarus* 179:265
- Brunetto R, Baratta GA, Domingo M et al (2005) Reflectance and transmittance spectra (2.2–2.4 μm) of ion irradiated frozen methanol. *Icarus* 175:226
- Brunetto R, Barucci MA, Dotto E et al (2006) Ion irradiation of frozen methanol, methane, and benzene: linking to the colors of Centaurs and trans-neptunian objects. *Astrophys J* 644:646
- Brunetto R, Roush TL, Marra AC et al (2007) Optical characterization of laser ablated silicates. *Icarus* 191:381
- Brunetto R, Caniglia G, Baratta GA et al (2008) Integrated near-infrared band strengths of solid CH<sub>4</sub> and its mixtures with N<sub>2</sub>. *Astrophys J* 686:1480
- Burgdorf MJ, Cruikshank DP, Dalle Ore CM et al (2010) A tentative identification of HCN ice on Triton. *Astrophys J Lett* 718:L53

- Clark RN (1981) The spectral reflectance of water-mineral mixtures at low temperatures. *J Geophys Res* 86:3074
- Clark RN, Curchin JM, Hoefen TM et al (2009) Reflectance spectroscopy of organic compounds: 1. Alkanes. *J Geophys Res* 114(E3):E03001
- Clark RN, Carlson R, Grundy W et al (2012) Observed ices in the solar system. (this volume)
- Cook JC, Desch SJ, Roush TL et al (2007) Near-infrared spectroscopy of Charon: possible evidence for cryovolcanism on Kuiper belt objects. *Astrophys J* 663:1406
- Cruikshank DP, Silvaggio PM (1979) Triton: a satellite with an atmosphere. *Astrophys J* 233:1016
- Cruikshank DP, Meyer AW, Brown RH et al (2010) Carbon dioxide on the satellites of Saturn: results from the Cassini VIMS investigation and revisions to the VIMS wavelength scale. *Icarus* 206:561
- Cruikshank DP, Pilcher CB, Morrison D (1976) Pluto – evidence for methane frost. *Science* 194:835
- Cruikshank DP, Roush TL, Bartholomew MJ et al (1998) The composition of Centaur 5145 Pholus. *Icarus* 135:389
- Cruikshank DP, Roush TL, Owen TC et al (1993) Ices on the surface of Triton. *Science* 261:742
- Cruikshank DP, Roush TL, Poulet F (2003) Quantitative modelling of the spectral reflectance of Kuiper belt objects and Centaurs. *C R Phys Acad Sci Paris* 4:783
- Cruikshank DP, Wegryn E, Dalle Ore CM et al (2008) Hydrocarbons on Saturn's satellites Iapetus and Phoebe. *Icarus* 193:334
- Dalle Ore C, Barucci MA, Emery JP et al (2009) Composition of KBO (50000) Quaoar. *Astron Astrophys* 501:349
- de Bergh C, Delsanti A, Tozzi GP et al (2005) The surface of the transneptunian object 90482 Orcus. *Astron Astrophys* 437:1115
- de Bergh C, Schmitt B, Moroz LV et al (2008) Laboratory data on ices, refractory carbonaceous materials, and minerals relevant to transneptunian objects and Centaurs. In: Barucci MA et al (eds) *The solar system beyond Neptune*. The University of Arizona Press, Tucson, p 483
- Dello Russo N, Khanna RK (1996) Laboratory infrared spectroscopic studies of crystalline nitriles with relevance to outer planetary systems. *Icarus* 123:366
- Delsanti A, Hainaut O, Jourdeuil E et al (2004) Simultaneous visible-near IR photometric study of Kuiper belt object surfaces with the ESO/Very Large Telescopes. *Astron Astrophys* 417:1145
- DeMeo F, Fornasier S, Barucci MA et al (2009) Visible and near-infrared colors of transneptunian objects and Centaurs from the second ESO large program. *Astron Astrophys* 493:283
- DeMeo F, Dumas C, de Bergh C et al (2010) A search for ethane on Pluto and Triton. *Icarus* 208:412
- Doressoundiram A, Peixinho N, de Bergh C et al (2002) The color distribution in the Edgeworth-Kuiper belt. *Astron J* 124:2279
- Doressoundiram A, Boehnhardt H, Tegler SC et al (2008) Color properties and trends of the transneptunian objects. In: Barucci MA et al (eds) *The solar system beyond Neptune*. The University of Arizona Press, Tucson, p 91
- Douté S, Schmitt B, Quirico E et al (1999) Evidence for methane segregation at the surface of Pluto. *Icarus* 142:421
- Douté S, Schmitt B (1998) A multilayer bidirectional reflectance model for the analysis of planetary surface hyperspectral images at visible and near-infrared wavelengths. *J Geophys Res* 103:31367
- Dumas C, Merlin F, Barucci MA et al (2007) Surface composition of the largest dwarf planet 136199 Eris (2003 UB<sub>313</sub>). *Astron Astrophys* 471:331
- Emery JP, Dalle Ore CM, Cruikshank DP et al (2007) Ices on (90377) Sedna: confirmation and compositional constraints. *Astron Astrophys* 466:395
- Ferini G, Baratta GA, Palumbo ME (2004) A Raman study of ion irradiated icy mixtures. *Astron Astrophys* 414:757
- Fornasier S, Barucci MA, de Bergh C et al (2009) Visible spectroscopy of the new ESO large programme on trans-neptunian objects and Centaurs: final results. *Astron Astrophys* 508:457

- Fraser WC, Brown ME (2009) NICMOS Photometry of the unusual dwarf planet Haumea and its satellites. *Astrophys J Lett* 695:L1
- Fraser WC, Brown ME (2010) Quaoar: a rock in the Kuiper belt. *Astrophys J* 714:1547
- Fuchignoni M, Belskaya I, Barucci MA et al (2008) Transneptunian object taxonomy. In: Barucci MA et al (eds) *The solar system beyond Neptune*. The University of Arizona Press, Tucson, p 181
- Fulvio D, Guglielmino S, Favone T et al (2010) Near-infrared laboratory spectra of H<sub>2</sub>O trapped in N<sub>2</sub>, CH<sub>4</sub>, and CO: hints for trans-Neptunian objects' observations. *Astron Astrophys* 511:A62
- Gil-Hutton R, Licandro J, Pinilla-Alonso N et al (2009) The trans-neptunian object size distribution at small sizes. *Astron Astrophys* 500:909
- Gladman B, Marsden BG, VanLaerhoven C (2008) Nomenclature in the outer solar system. In: Barucci MA et al (eds) *The solar system beyond Neptune*. The University of Arizona Press, Tucson, p 43
- Goguen J (1981) A theoretical and experimental investigation of the photometric functions of particulate surfaces. Ph.D. thesis, Cornell University, Ithaca
- Grundy WM, Fink U (1996) Synoptic CCD spectrophotometry of Pluto over the past 15 years. *Icarus* 124:329
- Grundy WM, Schmitt B (1998) The temperature-dependent near-infrared absorption spectrum of hexagonal H<sub>2</sub>O ice. *J Geophys Res (E)* 103:25809
- Grundy WM, Schmitt B, Quirico E (1993) The temperature-dependent spectra of  $\alpha$  and  $\beta$  nitrogen ice with application to Triton. *Icarus* 105:254
- Grundy WM, Schmitt B, Quirico E (2002) The temperature-dependent spectrum of methane ice I between 0.7 and 5  $\mu\text{m}$  and opportunities for near-infrared remote thermometry. *Icarus* 155:486
- Grundy WM, Young LA, Stansberry JA et al (2010) Near-infrared spectral monitoring of Triton with IRTF/SpeX II: spatial distribution and evolution of ices. *Icarus* 205:594
- Guilbert A, Alvarez-Candal A, Merlin F et al (2009a) ESO-large program on TNOs: near-infrared spectroscopy with SINFONI. *Icarus* 201:272
- Guilbert A, Barucci MA, Brunetto R et al (2009b) A portrait of Centaur 10199 Chariklo. *Astron Astrophys* 501:777
- Hansen GB (1997) The infrared absorption spectrum of carbon dioxide ice from 1.8 to 333  $\mu\text{m}$ . *J Geophys Res (E)* 102:21569
- Hansen CJ, Paige DA (1996) Seasonal nitrogen cycles on Pluto. *Icarus* 120:247
- Hansen GB (2005) Ultraviolet to near-infrared absorption spectrum of carbon dioxide ice from 0.174 to 1.8  $\mu\text{m}$ . *J Geophys Res (E)* 110:E11003
- Hapke B (1981) Bidirectional reflectance spectroscopy. I – theory. *J Geophys Res* 86:3039
- Hapke B (1984) Bidirectional reflectance spectroscopy. III – correction for macroscopic roughness. *Icarus* 59:41
- Hapke B (1993) Theory of reflectance and emittance spectroscopy. Cambridge University Press, New York
- Hapke B (2001) Space weathering from Mercury to the asteroid belt. *J Geophys Res* 106:10039
- Hiroi T, Pieters C (1994) Estimation of grain sizes and mixing ratios of fine powder mixtures of common geologic minerals. *J Geophys Res* 99:10867
- Horner J, Evans NW, Bailey ME (2004) Simulations of the population of Centaurs – I. The bulk statistics. *Mon Not R Astron Soc* 354:798
- Hudgins DM, Sandford SA, Allamandola LJ et al (1993) Mid- and far-infrared spectroscopy of ices – optical constants and integrated absorbances. *Astrophys J Suppl S* 86:713
- Hudson RL, Palumbo ME, Strazzulla G et al (2008) Laboratory studies of the chemistry of transneptunian object surface materials. In: Barucci MA et al (eds) *The solar system beyond Neptune*. The University of Arizona Press, Tucson, p 507
- Jewitt DC, Luu JX (1993) Discovery of the candidate Kuiper belt object 1992 QB<sub>1</sub>. *Nature* 362:730
- Jewitt DC, Luu J (2004) Crystalline water ice on the Kuiper belt object (50000) Quaoar. *Nature* 432:731

- Kargel JS (1992) Ammonia-water volcanism on icy satellites – phase relations at 1 atmosphere. *Icarus* 100:556
- Krasnopolsky VA, Cruikshank DP (1995) Photochemistry of Triton's atmosphere and ionosphere. *J Geophys Res Planet* 100:21271
- Krasnopolsky VA, Cruikshank DP (1999) Photochemistry of Pluto's atmosphere and ionosphere near perihelion. *J Geophys Res* 104:21979
- Lellouch E, Kiss C, Santos-Sanz P et al (2010) “TNOs are cool”: a survey of the trans-neptunian region. II. The thermal lightcurve of (136108) Haumea. *Astron Astrophys* 518:L147
- Leto G, Baratta GA (2003) Ly-alpha photon induced amorphization of Ic water ice at 16 Kelvin. Effects and quantitative comparison with ion irradiation. *Astron Astrophys* 397:7
- Levi A, Podolak M (2009) Corona-like atmospheric escape from KBOs. I. Gas dynamics. *Icarus* 202:681
- Levison HF, Duncan MJ (1997) From the Kuiper belt to Jupiter-family comets: the spatial distribution of ecliptic comets. *Icarus* 127:13
- Levison HF, Morbidelli A, Vokrouhlický D et al (2008) On a scattered-disk origin for the 2003 EL<sub>61</sub> collisional family – an example of the importance of collisions on the dynamics of small bodies. *Astron J* 136:1079
- Licandro J, Pinilla-Alonso N (2005) The inhomogeneous surface of Centaur 32522 Thereus (2001 PT<sub>13</sub>). *Astrophys J* 630:L93
- Licandro J, Grundy WM, Pinilla-Alonso N et al (2006a) Visible spectroscopy of 2003 UB<sub>313</sub>: evidence for N<sub>2</sub> ice on the surface of the largest TNO? *Astron Astrophys* 458:L5
- Licandro J, Pinilla-Alonso N, Pedani M et al (2006b) The methane ice rich surface of large TNO 2005 FY<sub>9</sub>: a Pluto-twin in the trans-neptunian belt? *Astron Astrophys* 445:L35
- Lim TL, Stansberry J, Müller M et al (2010) “TNOs are cool”: a survey of the trans-neptunian region. III. Thermophysical properties of 90482 Orcus and 136472 Makemake. *Astron Astrophys* 518:L148
- Loeffler MJ, Raut U, Baragiola RA (2006) Enceladus: a source of nitrogen and an explanation for the water vapor plume observed by Cassini. *Astrophys J Lett* 649:L133
- Lumme K, Bowell E (1981) Radiative transfer in the surfaces of atmosphereless bodies. I – theory. *Astron J* 86:1694
- Luu J, Jewitt D (1996) Color diversity among the Centaurs and Kuiper belt objects. *Astron J* 112:2310
- Luu J, Jewitt DC, Trujillo C (2000) Water ice in 2060 Chiron and its implications for Centaurs and Kuiper belt objects. *Astrophys J Lett* 531:L151
- Martonchik JV, Orton GS, Appleby JF (1984) Optical properties of NH<sub>3</sub> ice from the far infrared to the near ultraviolet. *Appl Opt* 23:541
- Masterson CM, Khanna RK (1990) Absorption intensities and complex refractive indices of crystalline HCN, HC<sub>3</sub>N, and C<sub>4</sub>N<sub>2</sub> in the infrared region. *Icarus* 83:83
- Mastrappa RME, Brown RH (2006) Ion irradiation of crystalline H<sub>2</sub>O ice: effect on the 1.65-μm band. *Icarus* 183:207
- Mastrappa RM, Bernstein MP, Sandford SA et al (2008) Optical constants of amorphous and crystalline H<sub>2</sub>O-ice in the near infrared from 1.1 to 2.6 μm. *Icarus* 197:307
- Mastrappa RM, Sandford SA, Roush TL et al (2009) Optical constants of amorphous and crystalline H<sub>2</sub>O-ice: 2.5–22 μm (4000–455 cm<sup>-1</sup>) optical constants of H<sub>2</sub>O-ice. *Astrophys J* 701:1347
- Mastrappa RME, Grundy WM, Gudipati MS (2012) Amorphous and crystalline H<sub>2</sub>O ice. (this volume)
- McCord TB (1966) Dynamical evolution of the neptunian system. *Astron J* 71:585
- McKinnon WB (1984) On the origin of Triton and Pluto. *Nature* 311:355
- McKinnon WB, Prialnik D, Stern SA et al (2008) Structure and evolution of Kuiper belt objects and dwarf planets. In: Barucci MA et al (eds) *The solar system beyond Neptune*. The University of Arizona Press, Tucson, p 213
- Merlin F, Barucci MA, Dotto E et al (2005) Search for surface variations on TNO 47171 and Centaur 32532. *Astron Astrophys* 444:977

- Merlin F, Guillet A, Dumas C et al (2007) Properties of the icy surface of the TNO 136108 (2003 EL<sub>61</sub>). *Astron Astrophys* 466:1185
- Merlin F, Alvarez-Candal A, Delsanti A et al (2009) Stratification of methane ice on Eris' surface. *Astron J* 137:315
- Merlin F, Barucci MA, de Bergh C et al (2010a) Surface composition and physical properties of several trans-neptunian objects from the Hapke scattering theory and Shkuratov model. *Icarus* 208:945
- Merlin F, Barucci MA, de Bergh C et al (2010b) Chemical and physical properties of the variegated Pluto and Charon surfaces. *Icarus* 210:930
- Mishchenko MI (1994) Asymmetry parameters of the phase function for densely packed scattering grains. *J Quant Spectrosc Radiat Transf* 52:95
- Moore MH, Hudson RL (1992) Far-infrared spectral studies of phase changes in water ice induced by proton irradiation. *Astrophys J* 401:353
- Moore MH, Ferrante RF, Hudson RL et al (2007) Ammonia water ice laboratory studies relevant to outer solar system surfaces. *Icarus* 190:260
- Morbidelli A, Levison HF, Gomes R (2008) The dynamical structure of the Kuiper belt and its primordial origin. In: Barucci MA et al (eds) *The solar system beyond Neptune*. The University of Arizona Press, Tucson, p 275
- Moroz L, Baratta G, Strazzulla G et al (2004) Optical alteration of complex organics induced by ion irradiation: 1. Laboratory experiments suggest unusual space weathering trend. *Icarus* 170:214
- Müller TG, Lellouch E, Stansberry J et al (2010) "TNOs are cool": a survey of the trans-neptunian region. I. Results from the Herschel science demonstration phase (SDP). *Astron Astrophys* 518:L146
- Mustard JF, Pieters CM (1987) Quantitative abundance estimates from bidirectional reflectance measurements. *J Geophys Res* 92:617
- Mustard JF, Pieters CM (1989) Photometric phase functions of common geologic minerals and applications to quantitative analysis of mineral mixture reflectance spectra. *J Geophys Res* 94:13619
- Noll KS, Grundy WM, Chiang EI et al (2008) Binaries in the Kuiper belt. In: Barucci MA et al (eds) *The solar system beyond Neptune*. The University of Arizona Press, Tucson, p 345
- Öberg KI, Fraser HJ, Boogert ACA et al (2007) Effects of CO<sub>2</sub> on H<sub>2</sub>O band profiles and band strengths in mixed H<sub>2</sub>O:CO<sub>2</sub> ices. *Astron Astrophys* 462:1187
- Owen TC, Cruikshank DP, Roush T et al (1993) Surface ices and the atmospheric composition of Pluto. *Science* 261:745
- Palumbo ME, Ferini G, Baratta GA (2004) Infrared and Raman spectroscopies of refractory residues left over after ion irradiation of nitrogen-bearing icy mixtures. *Adv Space Res* 33:49
- Palumbo ME, Baratta GA, Collings MP et al (2006) The profile of the 2140 cm<sup>-1</sup> solid CO band on different substrates. *Phys Chem Chem Phys Inc Faraday Trans* 8:279
- Pearl J, Ngoh M, Ospina M et al (1991) Optical constants of solid methane and ethane from 10,000 to 450 cm<sup>-1</sup>. *J Geophys Res* 96:17477
- Pinilla-Alonso N, Licandro J, Lorenzi V (2008) Visible spectroscopy in the neighborhood of 2003EL<sub>61</sub>. *Astron Astrophys* 489:455
- Pinilla-Alonso N, Brunetto R, Licandro J et al (2009) The surface of (136108) Haumea (2003 EL<sub>61</sub>), the largest carbon-depleted object in the trans-neptunian belt. *Astron Astrophys* 496:547
- Poulet F, Cuzzi JN, Cruikshank DP et al (2002) Comparison between the Shkuratov and Hapke scattering theories for solid planetary surfaces: application to the surface composition of two Centaurs. *Icarus* 160:313
- Poulet F, Erard S (2004) Nonlinear spectral mixing: quantitative analysis of laboratory mineral mixtures. *J Geophys Res* 109(E2):E02009
- Protopapa S, Boehnhardt H, Herbst TM et al (2009) Surface characterization of Pluto, Charon, and Triton using NACO observations. *EPSC Abstracts*, 4, EPSC2009-103
- Quirico E, Schmitt B, Bini R et al (1996) Spectroscopy of some ices of astrophysical interest: SO<sub>2</sub>, N<sub>2</sub> and N<sub>2</sub>:CH<sub>4</sub> mixtures. *Planet Sp Sci* 44:973

- Quirico E, Schmitt B (1997a) Near-infrared spectroscopy of simple hydrocarbons and carbon oxides diluted in solid N<sub>2</sub> and as pure ices: implications for Triton and Pluto. *Icarus* 127:354
- Quirico E, Schmitt B (1997b) A spectroscopic study of CO diluted in N<sub>2</sub> ice: applications for Triton and Pluto. *Icarus* 128:181
- Quirico E, Douté S, Schmitt B et al (1999) Composition, physical state, and distribution of ices at the surface of Triton. *Icarus* 139:159
- Rabinowitz DL, Barkume K, Brown ME (2006) Photometric observations constraining the size, shape, and albedo of 2003 EL<sub>61</sub>, a rapidly rotating, Pluto-sized object in the Kuiper belt. *Astrophys J* 639:1238
- Ragozzine D, Brown ME (2007) Candidate members and age estimate of the family of Kuiper belt object 2003 EL<sub>61</sub>. *Astrophys J* 134:2160
- Rudy RJ, Venturini CC, Lynch DK et al (2003) 0.8–2.5 micron reflectance spectroscopy of Pluto. *Publ Astron Soc Pac* 115:484
- Satorre MA, Palumbo ME, Strazzulla G (2001) Infrared spectra of N<sub>2</sub>-rich ice mixtures. *J Geophys Res* 106:33363
- Schaller EL, Brown ME (2007a) Volatile loss and retention on Kuiper belt objects. *Astrophys J* 659:L61
- Schaller EL, Brown ME (2007b) Detection of methane on Kuiper belt object (50000) Quaoar. *Astrophys J Lett* 670:L49
- Schaller EL, Brown ME (2008) Detection of additional members of the 2003 EL<sub>61</sub> collisional family via near-infrared spectroscopy. *Astrophys J* 684:L107
- Schmitt B, Quirico E, Trotta F et al (1998) Optical properties of ices from UV to infrared. In: Schmitt B et al (eds) Solar system ices. Kluwer, Boston, p 199
- Sheppard SS, Lacerda P, Ortiz JL (2008) Photometric lightcurves of transneptunian objects and Centaurs: rotations, shapes, and densities. In: Barucci MA et al (eds) The solar system beyond Neptune. The University of Arizona Press, Tucson, p 129
- Shkuratov Y, Starukhina L, Hoffmann HI et al (1999) A model of spectral albedo of particulate surfaces: implications for optical properties of the Moon. *Icarus* 137:235
- Shkuratov YG, Gryko YS (2005) Light scattering by media composed of semitransparent particles of different shapes in ray optics approximation: consequences for spectroscopy, photometry, and polarimetry of planetary regoliths. *Icarus* 173:16
- Stansberry JA, Grundy W, Brown M et al (2008) Physical properties of Kuiper belt and Centaur objects: constraints from the Spitzer Space Telescope. In: Barucci MA et al (eds) The solar system beyond Neptune. The University of Arizona Press, Tucson, p 161
- Stern SA (2002) Evidence for a collisional mechanism affecting Kuiper belt object colors. *Astron J* 124:2297
- Stern SA, Spencer J (2004) New Horizons: the first reconnaissance mission to bodies in the Kuiper belt. *Earth Moon Planet* 92:477
- Strazzulla G, Baratta GA, Johnson RE et al (1991) Primordial comet mantle – irradiation production of a stable, organic crust. *Icarus* 91:101
- Strazzulla G, Baratta GA, Leto G et al (1992) Ion-beam-induced amorphization of crystalline water ice. *Europhys Lett* 18:517
- Strazzulla G, Palumbo ME (1998) Evolution of icy surfaces: an experimental approach. *Planet Sp Sci* 46:1339
- Strazzulla G, Baratta GA, Palumbo ME (2001) Vibrational spectroscopy of ion-irradiated ices. *Spectrochim Acta A* 57(4):825
- Strazzulla G, Cooper JF, Christian ER et al (2003) Ion irradiation of TNOs: from the fluxes measured in space to the laboratory experiments. *C R Phys Acad Sci Paris* 4:791
- Taylor FW (1973) Preliminary data on the optical properties of solid ammonia and scattering parameters for ammonia cloud particles. *J Atmos Sci* 30:677
- Tegler SC, Grundy WM, Romanishin W et al (2007) Optical spectroscopy of the large Kuiper belt objects 136472 (2005 FY<sub>9</sub>) and 136108 (2003 EL<sub>61</sub>). *Astron J* 133:526
- Tegler SC, Grundy WM, Vilas F et al (2008) Evidence of N<sub>2</sub>-ice on the surface of the icy dwarf planet 136472 (2005 FY<sub>9</sub>). *Icarus* 195:844

- Tegler SC, Cornelison DM, Grundy WM et al (2010) Methane and nitrogen abundances on Pluto and Eris. *Astrophys J* 725:1296
- Trafton LM, Stern SA (1996) Rotationally resolved spectral studies of Pluto from 2500 to 4800 angstroms obtained with HST. *Astron J* 112:1212
- Trotta F (1996) Détermination des constantes optiques de glaces dans l'infrarouge moyen et lointain. Application aux grains du milieu interstellaire et des enveloppes circumstellaires. Thesis, LGGE-University Joseph Fourier, Grenoble
- Trujillo CA, Brown ME, Barkume KM et al (2007) The surface of 2003 EL<sub>61</sub> in the near-infrared. *Astrophys J* 655:1172
- Tryka KA, Brown RH, Anicich V (1995) Near-infrared absorption coefficients of solid nitrogen as a function of temperature. *Icarus* 116:409
- Verbiscer A, Helfenstein P (1998) Reflectance spectroscopy of icy surfaces. In: Schmitt B et al (eds) Solar system ices. Kluwer, Boston, p 157
- Warren SG (1984) Optical constants of ice from the ultraviolet to the microwave. *Appl Opt* 23:1206
- Warren SG (1986) Optical constants of carbon dioxide ice. *Appl Opt* 25:2650
- Young LA, Stern SA, Weaver HA et al (2008) New Horizons: anticipated scientific investigations at the Pluto system. *Space Sci Rev* 140:93
- Zheng W, Jewitt D, Kaiser RI (2009) On the state of water ice on Saturn's moon Titan and implications to icy bodies in the outer solar system. *J Phys Chem A* 113:11174

**Part II**

**Ice Physical Properties**

**and Planetary Applications**

# Chapter 5

# First-Principles Calculations of Physical Properties of Planetary Ices

Razvan Caracas

**Abstract** We review specific aspects from computational condensed-matter physics with particular interest to the study of physical properties of the planetary ices. We describe the most widespread technique in use today, the density-functional theory and its derivative, the density-functional perturbation theory. We show the basic theoretical formalism and then discuss and exemplify the most important physical properties that can be computed today and that are relevant for the community of planetary ices.

## 5.1 Introduction

The last decades saw the rise of computational physics as a new branch of physics intermediate between the two traditional main branches: theoretical physics and experimental physics. This evolution is continuously triggered by the exponential rise of the computational power, together with the development of performant algorithms and the larger availability of software implementations. Nowadays, numerical physics evolved into a tool of investigation fully complementary to experiments in a large numbers of disciplines associated with physics. Amongst these disciplines the Earth sciences and the mineral physics had a privileged place. Today is the turn of planetary sciences to fully enter in the big family of physical disciplines that benefit from these numerical developments.

Here from all the possible numerical studies of condensed matter we discuss only the atomistic calculations performed using the density-functional theory and its extensions. This might look restrictive at first, but these techniques, called

---

R. Caracas (✉)

Centre National de la Recherche Scientifique, Laboratoire de Sciences de la Terre,  
Ecole Normale Supérieure de Lyon, 46 allée d'Italie, Lyon cedex 07 69364, France  
e-mail: [razvan.caracas@ens-lyon.fr](mailto:razvan.caracas@ens-lyon.fr)

first-principles or *ab initio* simulations, are powerful enough to allow us to determine a wide range of physical properties of minerals and ices.

For bulk solids, static physical properties, e.g. equilibrium structure, compressibility and elasticity, are the easiest to determine. On a second level of complexity, and thus more demanding computationally are the dielectric and dynamical properties. Their computation requires the determination of first- and second-order derivatives of the energy. Classical examples of such properties are: dielectric tensors, dynamical charges and phonons. More recently, computation of the Raman tensors, which require third order derivatives of the energy, are also available. Transport properties, like the thermal and electrical conductivity, and excited electronic states are hard to calculate. For bulk fluids, recent studies reported the determination of structural and transport properties. Calculations involving interfaces, either between two solids or between a solid and a melt, though possible, usually require much larger computational efforts. In the following we will briefly survey the methodology involved to determine numerically these properties.

This chapter is organized as follows. In Sect. 5.2 the theoretical basics of the density-functional theory and its main extension the density-functional perturbation theory are presented. Sect. 5.3 treats with the treatment of thermodynamics. Of course there is an impressive amount of dedicated literature on these subject; here we will only give a brief overview. Potential applications with a special focus on the study of planetary ices are discussed in Sect. 5.4 and Sect. 5.5 gives a small discussion of possible further developments of computational studies in the near future.

## 5.2 Methodology

### 5.2.1 Density-Functional Theory

As usual in electronic structure calculations the electronic ground-state energy of a system of nuclei and electrons in density-functional theory (DFT) is described, according to the Kohn-Sham equation (Eq. 5.1), as a sum of kinetic energy ( $T$ ) plus all the coulombian interactions between the nuclei and the electrons that corresponds to the Hartree term  $E_H$ , plus the energy due to interaction with external fields, like electric fields, magnetic fields, strains, etc.,  $E_{ext}$  plus the exchange-correlation energy (Hohenberg and Kohn 1964; Kohn and Sham 1965):

$$E[n(\vec{r})] = T[n(\vec{r})] + \int v_{ext}(\vec{r}) n(\vec{r}) dr + E_H[n(\vec{r})] + E_{xc} n(\vec{r}) \quad (5.1)$$

The electron density is defined as follows:

$$n(\vec{r}) = \sum_i [\Psi_i(\vec{r})]^2 \quad (5.2)$$

In this system of equations we make use of the adiabatic approximation (the Born-Oppenheimer approximation): the electrons instantaneously follow the movement of the nuclei.

The first three terms in Eq. 5.1 have analytical solutions and can be computed exactly. The last term, the exchange-correlation energy is not analytical; it corresponds roughly to the balance between two electrons with opposite spins to occupy the same energetic level and two electrons with the same spin to avoid each other on the same energetic levels (Payne et al. 1992). From these two terms, the first one is favorable and the second one unfavorable energetically. This energy term is approximated as the energy per electron of a homogeneous electron gas, described within the local density approximation (LDA). When the gradient of the electronic density is also taken into account then one makes use of an extension of LDA like the generalized gradient approximation (GGA).

The aim of a standard DFT calculation is to find the electronic density, which minimizes the energy from Eq. 5.1. This is a matricial system of equations that can be solved using usual diagonalization procedures. The result is a set of electronic eigenvalues,  $E_i$ , the Khon-Sham energies and electronic eigenfunctions, the Khon-Sham wavefunctions. The eigenvalues are not the electronic energies, but there is a one-to-one correspondence between the relative distance to the Fermi level of the Khon-Sham eigenvalues and of the real electronic energies.

The implementation of DFT comes in different flavors, from all-electron developments, where the Khon-Sham equation is solved for all the electrons in the system to pseudopotential-based developments where the electrons are divided into two parts: the core and the valence electrons. The former ones are not solved explicitly but their effect on the valence electrons is taken into account using pseudopotentials. They must be highly localized, not extending beyond a well-defined part of the space, usually spherical, and centered on the atomic nuclei. They do not participate to the chemical bonds. The wavefunctions of the valence electrons are computed explicitly using for example planewaves or some variation of atomic orbitals. They are delocalized and they participate to the chemical bonds. Please note that especially under pressure electrons from the inner electronic levels tend to delocalize as the interatomic distances decrease and they start to participate to the chemical bonds. In this case one has to pay attention to the pseudopotential that should not consider anymore these states as core states. These states called semi-core states should be treated as valence states.

Most often the Khon-Sham equation is solved in the reciprocal space. One computes the electronic density in the reciprocal space and uses fast-Fourier techniques to represent it in the real space. The reciprocal space is sampled on a set of reciprocal unit cell vectors, the  $\mathbf{G}$  vectors, and within each unit cell one defines a usually regular grid of so called  $\mathbf{k}$ -points (Monkhorst and Pack 1976).

In the planewave implementations a set of planewaves are defined on the grid obtained from the  $\mathbf{G} + \mathbf{k}$  vectors. The electron density is then computed adjusting iteratively the parameters  $C_{i,m,k}$ , of the planewaves  $\varphi_m(k)$  until the Khon-Sham equation finds its minimum. The Khon-Sham wavefunctions,  $\psi_i(\vec{r})$ , are then defined as:

$$\psi_i(\vec{r}) = \sum_{k,G} \sum_{m=1}^M -e^{(k+G)} \vec{r} c_{i,m,k} \varphi_m(k) \quad (5.3)$$

Critical parameters in standard DFT calculations with planewaves and pseudopotentials are: (1) the size of the basis, namely the number M of planewaves, m; (2) the definition of the special grid of  $\mathbf{k}$  points; (3) the completeness and quality of the pseudopotential, namely the electrons that are considered in the electronic core should be highly localized and should not participate into the chemical bonds.

### 5.2.2 *Ab Initio Molecular Dynamics*

Molecular dynamics (MD) has been used for decades to investigate dynamical properties of molecules, solids, and liquids by numerical simulations. In these simulations the atoms are allowed to move according to Newtonian equations of motion, whose parameters (forces, velocities and accelerations) are determined from the interatomic forces.

In the conventional (or classical) molecular dynamics approach, a model of interatomic interactions must be provided as input before a simulation can be carried out. Such models, or interatomic potentials, are based on a priori knowledge of the physical system studied. By contrast, First-Principles Molecular Dynamics does not require any a priori knowledge of interatomic interactions. Ionic forces are instead computed directly from the electronic structure of the system, which is obtained by solving an approximate form of the Schrödinger equation, like the Kohn-Sham equation of DFT. This feature is important for simulations involving the formation and breaking of chemical bonds. First-principles (or ab initio) molecular dynamics is thus a microscopic description of matter that relies entirely on fundamental physical quantities and on the laws of quantum mechanics. The resulting approach is free of empirical assumptions specific to the system under study and is therefore applicable to a wide variety of problems, ranging from high-pressure physics to solvation chemistry to molecular biology.

For a wide range of technical and less technical details, see for example the classical books of Allen and Tildesley (1989), Frenkel and Smit (2001), etc.

### 5.2.3 *Density-Functional Perturbation Theory*

The crystal lattice is not rigid. With respect to the periodic arrangement of nuclei, corresponding to the perfect classical crystal at zero temperature, small perturbations can occur due to a series of external or internal factors, like electric or magnetic fields, temperature, strains and so on. Consequently the energy of the

crystal can be expressed as a Taylor expansion as a function of these small perturbations  $\lambda_i$ :

$$\begin{aligned} F_{e+i}[\lambda] = & F_{e+i}^{(0)}[\lambda] + \sum_i \left( \frac{\partial F_{e+i}}{\partial \lambda_i} \right) \lambda_i + \frac{1}{2} \sum_{ij} \left( \frac{\partial^2 F_{e+i}}{\partial \lambda_i \partial \lambda_j} \right) \lambda_i \lambda_j + \\ & \frac{1}{6} \sum_{ijk} \left( \frac{\partial^3 F_{e+i}}{\partial \lambda_i \partial \lambda_j \partial \lambda_k} \right) \lambda_i \lambda_j \lambda_k + \dots \end{aligned} \quad (5.4)$$

The above equation can be solved analytically using the Hellman-Feynman description of the forces and the  $2n + 1$  theorem, which together allow us to compute the  $(2n + 1)$ th order derivatives and their respective terms of the Taylor expansion knowing the  $n$ th order derivatives of the wavefunctions (Gonze and Lee 1997; Baroni et al. 2001; Gonze et al. 2005b).

If we consider the atomic displacements,  $\tau$ , and the electric fields,  $\epsilon$ , as perturbations then the full expansion up to the third order is as follows (Veithen et al. 2005; Gonze et al. 2005b; Caracas and Gonze 2010), where each of the different terms corresponds to a (measurable) physical property:

$$\begin{aligned} F_{e+i}[\mathbf{R}_k, E] = & F_{e+i}[\mathbf{R}_k, E] \\ & - \Omega_0 \sum_{\alpha} \text{polarization} \quad P_{\alpha}^s \quad \epsilon_{\alpha} - \sum_{\alpha} \sum_k \text{forces} \quad F_{\alpha}^0 \tau_{\kappa \alpha} \\ & - \Omega_0/2 \sum_{\alpha \beta} \text{dielectric tensor} \quad \chi_{\alpha \beta}^{\infty(1)} \epsilon_{\alpha} \epsilon_{\beta} - \sum_{\alpha \beta} \sum_{\kappa} \text{dynamical charges} \quad Z_{\kappa, \alpha \beta}^* \tau_{\kappa \alpha} \epsilon_{\beta} \\ & + 1/2 \sum_{\alpha \beta} \sum_{\kappa' \kappa} \text{interatomic force cts.} \quad C_{\alpha \beta}(\kappa, \kappa') \tau_{\kappa \alpha} \tau_{\kappa' \beta} \\ & - \Omega_0/3 \sum_{\alpha \beta} \text{Non-linear opt. coeff.} \quad \chi_{\alpha \beta \gamma}^{\infty(2)} \epsilon_{\alpha} \epsilon_{\beta} \epsilon_{\gamma} - \Omega_0/2 \sum_{\kappa} \sum_{\alpha \beta} \frac{\partial \chi_{\alpha \beta}^{\infty(1)}}{\partial \tau_{\kappa \gamma}} \epsilon_{\alpha} \epsilon_{\beta} \tau_{\kappa \gamma} \\ & - 1/2 \sum_{\kappa \kappa'} \sum_{\alpha \beta} \frac{\partial Z_{\kappa, \alpha \beta}^*}{\partial \tau_{\kappa' \gamma}} \tau_{\kappa \alpha} \tau_{\kappa' \gamma} \epsilon_{\beta} + 1/3 \sum_{\kappa \kappa' \kappa''} \sum_{\alpha \beta} \Xi(\kappa, \kappa', \kappa'') \tau_{\kappa \alpha} \tau_{\kappa' \beta} \tau_{\kappa'' \gamma} + \dots \quad (5.5) \end{aligned}$$

$\kappa, \kappa', \kappa''$  stand for translation vectors of the unit cells,  $\alpha, \beta, \gamma$  stand for Cartesian directions and  $\Omega_0$  is the unit cell volume. The complexity of the exact expression for each higher-order term of the Kohn-Sham equations and consequently the complexity of the implementation increase with the order of the derivation.

By inverting this equation one can obtain the different physical properties of interest. The first order properties are vectorial properties and all the higher order properties are tensorial.

The first order terms correspond to the polarization,  $P$ , and forces,  $F$ , defined as the derivative of the energy respectively to one electric field and to the one atomic displacement. The centrosymmetric structures have a zero residual spontaneous polarization and the relaxed structures have zero forces.

The second order terms consist of the first order dielectric tensor,  $\chi^{\infty(1)}$ , which is the derivative of the energy with respect to two electric fields; the Born effective charges,  $Z^*$ , defined as the mixed derivative to atomic displacements and electric fields; and the interatomic force constants tensor, C, obtained as the change in energy due to two atomic displacements in two unit cells separated by the phonon wavevector  $q = \kappa - \kappa'$ . The dielectric tensors can be static or frequency dependent. The square roots of the static dielectric tensor give the refractive index tensor. The Born effective charges can also be seen as the change in polarization due to atomic displacements and can be related to the amount of charge exchanged by neighboring atoms during vibrations. The interatomic force constants when normalized with the masses yield the dynamical matrices.

The phonon frequencies are obtained by diagonalizing the dynamical matrices. The Raman and infrared modes are obtained from the center-zone dynamical matrices, characterized by  $q = 0$ . Selection rules based on the crystal symmetry and on its effect on the vibrational pattern associated to a specific mode determine whether that mode is Raman-active, infrared-active or silent.

Understanding the stability of the crystalline structures from the phonon analysis is realized looking at the energy variation, i.e. potential wells, described by the atoms during vibrations (Fig. 5.1). According to Eqs. 5.4 and 5.5 the second derivative of the energy to small atomic displacements yields the dynamical matrix whose eigenvalues are the square of the phonon frequencies, as already stated above. If the energy increases as the atoms move away from their equilibrium positions then the structure is stable, as in this case the atoms tend to fall back in the minimum of the potential wells. Then the dynamical matrices have positive eigenvalues and the phonons have positive frequencies. If there is no energy increase because of an atomic displacement then the corresponding dynamical matrix element is zero. In this case the phonon frequency is also zero and the structure can be distorted without energy loss or gain. If the energy decreases as the atoms move away from their equilibrium positions then the structure is unstable, as in this case the atoms tend to fall in new minima of the potential wells. Then the dynamical matrices have negative eigenvalues and the phonons have imaginary frequencies. The energy variations in the three cases correspond respectively to a (an)harmonic single-minimum potential well, a flat potential and a double (or multiple) potential well. The acoustic modes are an exception as they represent translational modes of the whole crystal, so there is no energy gain or loss and the corresponding frequencies are zero in the zone center.

The third order terms in the Eq. 5.3 correspond to non-linear effects: the non-linear optical coefficients,  $\chi^{\infty(2)}$ , are the derivative of the energy with respect to three electric fields, and the Raman coefficients are the derivative of the energy with respect to two electric field and one atomic displacement. The third term of the third order derivative of the energy, i.e. with respect to one electric field and two atomic displacements participates to the width of the infrared and Raman peaks, while the very last term of the expression yields anharmonicities, related to the phonon time of life, the line broadening of Raman and infrared spectra and thermal transport due to phonon scattering.

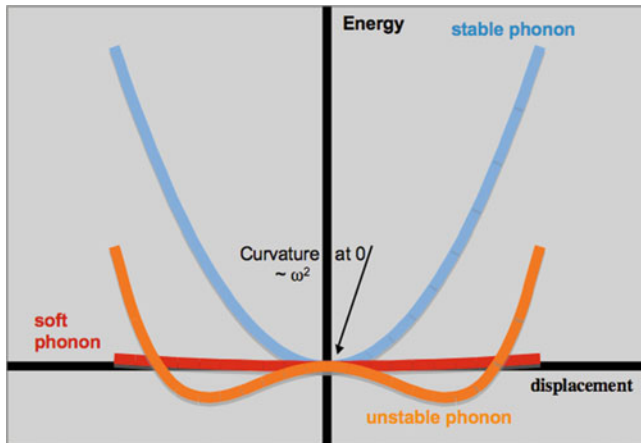


**Fig. 5.1** Energy variation during the atomic vibrations around equilibrium positions

The values of the Raman tensors are:

$$\alpha_{\alpha\beta} = \sum_{\kappa} \frac{\partial \chi_{\alpha\beta}^{\infty(1)}}{\partial \tau_{\kappa\gamma}} \varepsilon_{\alpha} \varepsilon_{\beta} \tau_{\kappa\gamma} \quad (5.6)$$

For non-centrosymmetric crystals, some modes are active in both Raman and infrared. In this case, the same formalism as above holds for the TO component, while a supplementary correction is needed for the modes in LO geometry that accounts for the coupling between the incident laser and the mode dipole.

Currently there are two DFT packages, quantum espresso (Baroni and Resta 1986; Baroni et al. 1987, 2001; Lazzari and Mauri 2003; Scandolo et al. 2005) and ABINIT (Gonze and Vigneron 1989; Gonze et al. 1992, 2002, 2005a, b, 2009; Gonze and Lee 1997; Veithen et al. 2005) where the Raman tensors are implemented within density-functional perturbation theory (DFPT).

### 5.2.4 Thermodynamics

Starting from the results of the density functional perturbation theory we may calculate the thermodynamic functions of a given structure: the Helmholtz free energy, the internal energy, the constant-volume specific heat, and the entropy as functions of temperature. These properties are related to the vibrational degrees of freedom of the lattice, because the electronic degrees of freedom play a noticeable

role only for metals at very low temperatures (Landau and Lifshitz 1960). However, the complete knowledge of the phonon band structure, with sufficient accuracy, is required for the calculation of these thermodynamic functions. The formulas presented in the following assume a truncation of the Taylor series (Eq. 5.1) at the second order, which corresponds to neglecting all the anharmonic effects. For most solids, the harmonic approximation will be accurate for a temperature smaller than a significant fraction of the melting temperature or the temperature of the lowest solid-solid phase transition, usually two third of the melting. On the other hand, the quantum effects are correctly included, unlike in an approach based on the classical dynamics of nuclei.

If one knows the phonon density of states  $g(\omega)$ , defined as the phonon population in the energy range  $\omega$  to  $\omega + d\omega$ , then one can calculate the phonon contribution to the thermodynamical functions as:

$$\begin{aligned}\Delta F &= 3Nk_B T \int_0^{\omega} \{\ln(e^x - 1) - x/2\} g(\omega) d\omega \\ \Delta E &= 3N \int_0^{\omega L} \frac{(e^x + -1)}{(e^x - 1)} - \frac{\hbar\omega}{2} g(\omega) d\omega \\ C_v &= 3Nk_B \int_0^{\omega L} \left( \frac{x}{e^{\frac{x}{2}} - e^{-\frac{x}{2}}} \right)^2 g(\omega) d\omega \\ S &= 3Nk_B \int_0^{\omega L} \left[ \frac{xe^x}{e^x - 1} - \ln(e^x - 1) \right] g(\omega) d\omega\end{aligned}\quad (5.7)$$

Here  $\Delta F$ ,  $\Delta E$ ,  $C_v$  and  $S$  are respectively the Helmholtz free energy, the internal energy, the constant-volume specific heat, and the entropy. They are evaluated at temperature  $T$ , and  $x = \frac{\hbar\omega}{k_B T}$ , where  $k_B$  is the Boltzmann constant.

Then, if we compute the free energy  $U(T) = E^{(0)} + \Delta F = E^{(0)} + \Delta E - ST$  at several volumes,  $V$ , for two structures (or chemical phases) the common tangent of the each pair of  $U(T)$  of  $V$  curves gives the phase transition pressure,  $P$ , between the corresponding two structures (or chemical phases) at the temperature  $T$ . If we repeat this procedure at several temperatures we can determine the two-phase stability region in the  $P - T$  thermodynamic space for that given pair of structures (or chemical phases). Doing this all over again for all the different structures (or chemical phases) of that system allows us to eventually build the full phase diagram.

The same free energy calculated at several volumes can be used to fit an equation of state, namely the variation of the energy with volume. It is then straightforward to obtain the variation of the volume (i.e. density) with pressure. Performing the fits at several temperatures we are able to build the thermal equation of state as well as the thermal dilatation.

## 5.3 Physical Properties

In the following we will briefly discuss the most common physical properties that are currently obtainable from DFT and DFPT calculations and which may be of interest to the investigation of planetary ices. We can first separate static properties, like electronic, structural and mechanical properties. These properties are computed within the DFT in the static approximation for a lattice of fixed nuclei at absolute zero temperature. These properties define the groundstate, where the electrons populate the electronic bands that have the lowest energy. Then, the other properties, like dielectric and vibrational require the treatment of the response of the lattice with respect to different perturbations. These properties are computed within the DFPT.

### 5.3.1 *Static properties: Electronic, Structural and Mechanical*

The electronic wavefunctions and eigenvalues as well as the electronic density are obtained at the end of any fully converged DFT calculation. Just like for molecular crystals, the planetary ices are characterized by regions of high electron density, inside the molecules and by regions of low electron density, the intermolecular space. From a classical chemical point of view this distribution of the electron density defines strong covalent bonds in the former case and weak van der Waals-like bonds in the latter case. Static ionic charges can be also determined in a variety of formalisms, like the Bader (1991) and Hirshfeld (1977) charges, the Mulliken population analysis (Mulliken 1955), etc.

One of the major limitations of the DFT is the underestimation of the electronic gap. This makes unreliable the quantitative calculation of the electronic contributions to the optical properties of materials, like the optical spectra, so important for the observation and identification of planetary ices. However several corrections to the gap problem of DFT have been developed and implemented over the last years, like the GW approximation (Hedin 1965; Onida et al. 2002) or the time-dependent DFT (Runge and Gross 1984). Both these methods now give a good agreement with respect to experimental measurements but they are very computationally intensive and so far their applications were usually limited to systems of less than two dozen atoms per unit cell.

Understanding the behavior of the crystal structures at varying thermodynamic conditions is of course the basis for understanding the rest of the physical properties. Nowadays the forces on the atoms and the strains on the unit cell are currently obtained in a standard way in DFT calculations. They are used in determining the theoretical crystal structures by minimization of the residual forces on the atoms and the non-hydrostatic stresses on the cell. Then equations of states can be computed by chaining constant-volume or constant-pressure calculations.

For crystals and glasses, there are two types of mechanical properties currently computed today: elasticity and plasticity.

The elastic constants tensor can be obtained assuming a linear relation between applied strains and residual stresses or from the derivative of the energy with respect to strains. Both these approaches have been used on a variety of minerals and the common agreement is remarkable.

For the plasticity calculations one needs to determine the energy surface corresponding to various structural dislocations. Then application of finite-differences-like methods integrates the results from the first-principles calculations into a generalized flow-model of the solid that can be related to plasticity and macroscopic rheology (Hamann et al. 2005).

For liquids and melts computing the atomic mean square displacements is straightforward from the trajectories of the particles. Their derivatives as a function of time yield the diffusion coefficients. Then various viscosity measurements (bulk, shear, etc.) can be defined and analyzed from the autocorrelation functions.

### **5.3.2 Dielectric Properties**

The first set of perturbational properties is obtained from the derivatives of the energy with respect to electric fields, yielding the Born effective charges and the dielectric tensors.

The Born effective charges, also called dynamical charges, are tensors that correspond to the energy derivative with respect to atomic displacements and electric fields or, equivalently, to the change in atomic force due to an electric field: The sum of the Born effective charges of all nuclei in one cell must vanish, element by element, along each of the three directions of the space. The value of the Born effective charges gives an indication about the amount of hybridization and charge transfer occurring during atomic vibrations: larger is the deviation of these charges with respect to the nominal charge values larger is the charge transfer between neighboring vibrating atoms (Ghosez et al. 1998).

The dielectric tensors represent the derivative of the energy with respect to two electric fields. They also relate the induced polarization to the external electric field. The square root of the electronic component of the dielectric tensor gives the refractive index (Baroni et al. 2001; Gonze et al. 2005b; Caracas and Gonze 2010).

The dielectric tensor is frequency dependent. Specifically it contains an electronic contribution, approximated as frequency-independent in the infrared regime, and contributions from each possible phonon modes at the Brillouin zone center.

### **5.3.3 Dynamical Properties**

The second set of perturbation properties is obtained from the derivatives of the energy with respect to atomic displacements, yielding the dynamical matrices.

Each entry in the dynamical matrix represents the change in energy associated with two atomic displacements along Cartesian directions. Its elements can be computed either analytically using density functional perturbation theory, as explained in Sect. 5.2.3, or numerically using the frozen phonons approach. The latter one involves computing the energy for different structures distorted according to the atomic displacements of each entry in the dynamical matrix.

The diagonalization of the dynamical matrices yields eventually the phonon frequencies and the corresponding atomic vibrational pattern. In order to build a phonon band dispersion diagram, we usually compute the phonons on a regular, high-symmetry grid of  $\mathbf{q}$  points and then apply Fourier interpolation techniques (Gonze et al. 1994; Baroni et al. 2001) to obtain the dynamical matrices at any arbitrary  $\mathbf{q}$  point. The integration of the phonons band structure yields the phonon density of states used in thermodynamics.

The Raman- and infrared- active modes are directly accessible by the corresponding vibrational spectroscopies and comparison with experimental measurements are straightforward. The intensities of the Raman peaks are computed via the Raman tensors, and the intensities of the infrared peaks via the dielectric tensors (Caracas and Cohen 2006; Caracas and Banigan 2009; Cardona 1982; Cohen 2007; Hayes and Loudon 1978; Hermet et al. 2007).

## 5.4 Examples

In the following we exemplify the application of density functional perturbation theory with the analysis of the computation of the phonon band structure and the spectroscopic and thermodynamical properties of two molecular solids: nitrogen and ice. Based on the dynamical instabilities we are able to interpret the transition between the molecular and ionic phases of ice and to predict a post-ice X phase stable at ultrahigh-pressure. We then give a few examples of application of DFT techniques to other ices. We finalize with a brief report on the WURM project and discuss its implications on the planetary ices community.

### 5.4.1 Nitrogen

Crystalline nitrogen undergoes a series of phase transitions under pressure that compact its structure and reduce the degrees of freedom of molecules. At low pressures, in the  $\alpha$  phase the free rotation of the molecules describes spheres, while in the  $\beta$  phase this rotation is follows two-dimensional disks. At higher pressure, the degree of freedom of the molecular motions is further reduced and partial disorder or complete order occurs, as exhibited by different crystalline structures such as the  $\delta$  or  $\varepsilon$  (Bini et al. 2000; Tassini et al. 2005). All these phases have molecular structures. From 10 to 20 GPa up to about 100 GPa there are several crystalline

phases obtained experimentally whose structures and stabilities are not yet fully understood. Above about 100 GPa, first-principles calculations suggested that crystalline atomic polymeric structures should develop, where the integrality of the nitrogen molecules is lost. Several structures have been predicted theoretically (McMahan and LeSar 1985; Martin and Needs 1986; Caracas and Hemley 2007), and the most stable one, named “cubic gauche,” has been experimentally confirmed experimentally (Eremets et al. 2004, 2007). These experiments that lead to the formation of the cubic gauche structure passed through a high-temperature amorphous state as an intermediate state.

The cubic gauche structure is cubic, with  $I\bar{2}_13$  space group, and the atoms in the special  $8a(x \ x \ x)$  Wyckhoff positions. Each nitrogen atom has three nearest neighbors at equal distance. The topology thus yields an atomic character to the structure, with the nitrogen atoms polymerizing in left-handed spiral chains parallel to the [111] directions. The chains delimit void spaces with quasi-trigonal cross-sections in the (111) planes or quasi-hexagonal in the (110) planes. The strong covalent bonding and the three-dimensional framework topology of the structure qualify this material as high-energy and ultra-hard.

Figure 5.2 illustrates the dispersion of the phonon bands at 0 and 250 GPa (Caracas 2007). All the modes have positive frequencies over this wide pressure range, thus the cubic gauche structure of nitrogen is dynamically stable. The 12 optical phonon modes decompose in the zone center as  $A + E + 2T$  according to group theory. The  $T$  modes are both Raman and infrared active, and the  $A$  and  $E$  modes are only Raman active. Then we compute the Raman spectra for the cubic gauche structure of nitrogen (Caracas 2007). As this structure is stable at high pressures Raman spectroscopy is the usual tool used for identification. The theoretical Raman spectra are dominated by the  $A$  mode. The intensity of the other modes is less than 10% and they would be hardly observable in a measurement. Our theoretical prediction (Caracas 2007) is in excellent agreement with the experimental measurements (Eremets et al. 2004), in terms of both peak position and intensity, as shown in Fig. 5.3.

### 5.4.2 Water Ice

There are fifteen different crystalline structures of water ice and a few more metastable, amorphous, or modulated structures obtained during different experiments or theoretical investigations so far (Fortes 2004; Fortes and Choukroun 2010; Johari and Andersson 2007; Abascal et al. 2009; Vega et al. 2010). Above about 3 GPa the phase diagram of water ice is dominated by the phases VII, VIII and X (Hemley et al. 1987; Hemley 2000; Pruzan et al. 2003). The structure of these three ices is similar and consists of a body-centered cubic lattice of oxygen atoms with the hydrogen atoms staying in-between. In ice VII and ice VIII the structure is molecular and the integrality of the molecules is preserved. Ice VII is disordered with molecules pointing randomly in all Cartesian directions. Ice VIII is ordered

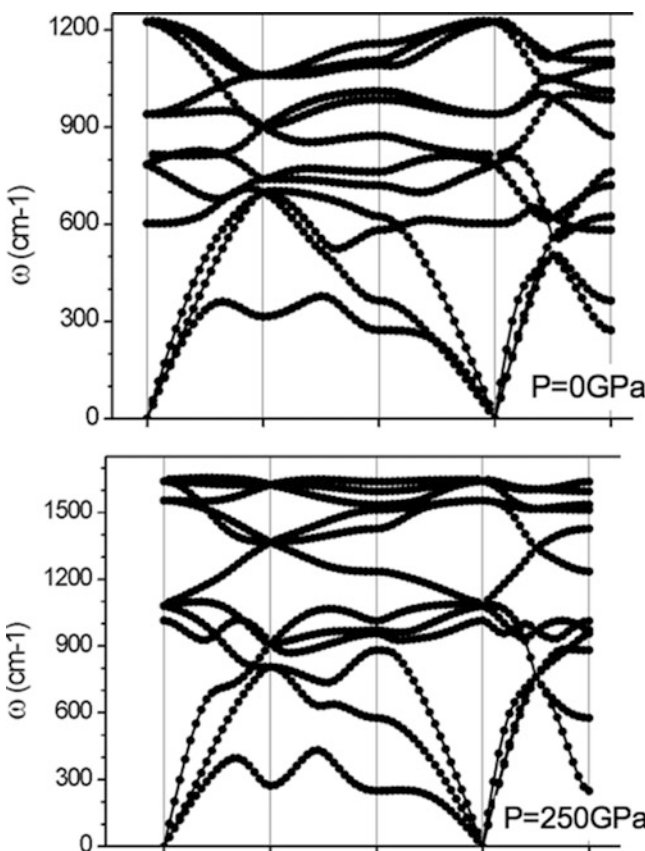


**Fig. 5.2** Phonon band structure of the cubic gauche nitrogen at low and high pressures

with the molecules pointing only around the c direction. The structure has tetragonal symmetry with a center of inversion. In ice X the integrality of the molecules is lost. The hydrogen atoms lay between every two neighboring oxygen atoms at equal distance. The structure has an ionic character and has been named the “symmetric hydrogen bond” structure.

As much experimental effort has been dedicated to the study of the phase boundaries and the physical properties of these three ices we have recently performed a dynamical analysis of ice X by computing the phonons at different pressures (Caracas 2008). Phonon band dispersions at several representative pressures are shown in Fig. 5.4.

At pressures below about 114 GPa ice X exhibits an unstable phonon mode. This mode is weakly dispersive: we retrieve it unstable around the same frequency all over the Brillouin zone. This feature suggests a highly localized character in the direct space of the atomic displacement pattern. Indeed when looking at the corresponding vibration in the direct space we observe that this mode corresponds

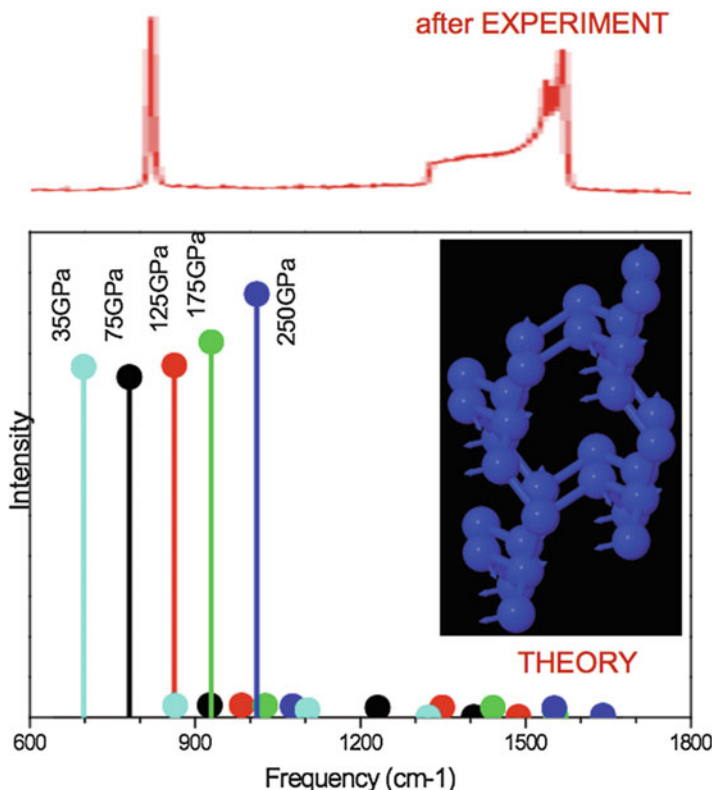


**Fig. 5.3** Theoretical and experimental Raman spectra of the cubic gauche

to the bouncing back and forth of the hydrogen atoms between their two oxygen neighbors (Fig. 5.4).

At low pressures the distance between the two oxygen atoms is large and thus the energy variation with respect to atomic vibrations opens up and forms the characteristic two-well shape of the unstable modes. The hydrogen atoms oscillate between these two minima, which are energetically equivalent positions. The structure that results from the condensation of this unstable phonon mode is disordered ice X. Independent experimental evidence (Goncharov et al. 1996) shows that the transition between ices VII or VIII and X goes through an intermediate phase, which is disordered.

As the pressure increases the distance between the oxygen atoms decreases and the double-well potential closes and transforms into a normal potential well with the minimum at the mid-distance between the two oxygen atoms. The hydrogen atoms are stabilized and vibrate around this minimum, situated at equal distance to both oxygen neighbors. This is the stable configuration of ice X, which can be found in a pressure range extending from about 114 GPa up to 430 GPa.

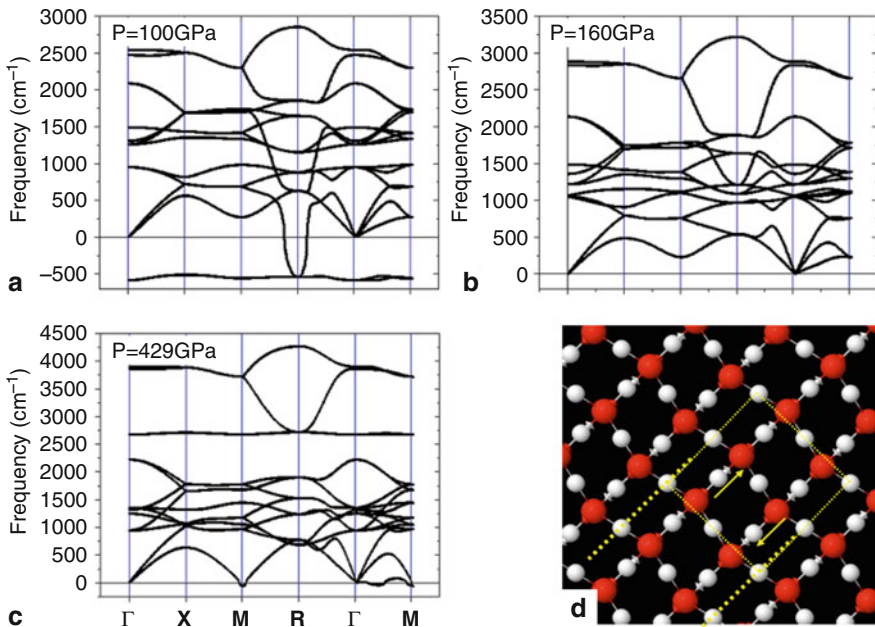


**Fig. 5.4** Phonon band structure of the ionic phase ice X at low (a), intermediate (b) and high (c) pressures. The dynamical instability at high pressures determines a phase transition towards a first post-ice X phase with orthorhombic symmetry (d)

Towards the upper part of this stability range another phonon softens, at and around the M point of the reciprocal space. This phonon mode corresponds to displacements of both hydrogen and oxygen atoms parallel to the diagonal (110) planes. The result of this displacement is shear of the OH<sub>4</sub> tetrahedral and a breaking of the symmetry. This is the phase transition to the post-ice X phase of ice, with Pbcm symmetry (Fig. 5.4), which has been independently predicted in a molecular-dynamics study (Benoit et al. 1996) and in another phonon analysis (Militzer and Wilson 2010).

It is important to note that the analysis of the phonon modes in ice X allows us to explain the experimental Raman observations up to 100 GPa by the disordered ice X and to confirm previous ab initio molecular dynamics calculations (Benoit et al. 1996).

However, the field of application of the phonon analysis is restricted by the quasi-harmonic approximation, i.e. the neglect of third- and higher-order derivatives in the Taylor expansion of the energy (Eq. 5.4). Consequently the high-temperature thermodynamic regime can be investigated only using molecular-dynamics calculations. For example, for ice, these simulations showed that the high-dense ices VII and X exhibit a superionic state at temperatures above about 2,000 K (Cavazza et al. 1999; Goldman et al. 2005) up to the melting curve (Schwegler et al. 2008).

### **5.4.3 Hydrous and Anhydrous Salts as Planetary Ices**

The ab initio investigation of planetary ices, in the large sense as hydrous and anhydrous salts, is just at its beginning. One of the major handicaps to overcome is the absence of accurate chemical and geochemical information from the remote icy bodies of the solar system, which removes clear constraints of the possible chemical systems. This leaves the field of cryomineralogy and cryopetrology extremely broad and largely uncharted.

The determination of the crystal structure and compressibility of planetary ices has been the largest application of the ab initio methods to ices so far. For example an isosymmetrical phase transition has been predicted in mirabilite,  $\text{Na}_2\text{SO}_4 \cdot 10\text{H}_2\text{O}$ , which involves changes in the Na coordination by water molecules (Brand et al. 2009). A combination of neutron diffraction data and ab initio relaxations allowed the determination of the crystal structure of ammonia monohydrate (Fortes et al. 2009).

The determination of the vibrational spectrum and the subsequent analysis of the unstable phonon modes allowed the prediction of a low-temperature phase transition in bischofite,  $\text{MgCl}_2 \cdot 6\text{H}_2\text{O}$  (Bobocioiu and Caracas 2010). Determination of dielectric properties showed the formation of a strong dipole in the bulk and on the surface of methanol monohydrate (Martinez et al. 2009), an ice that presents also an amazing negative linear compressibility – i.e. expansion under compression along one of the crystallographic directions – computed first by Martinez et al. (2009) and later investigated experimentally in extenso by Fortes et al. (2011).

### **5.4.4 The WURM Project**

The WURM project (Caracas and Bobocioiu 2011) aims to build a database of computed physical properties for known minerals, planetary ices, aerosols and any other inorganic chemicals that are related to the mineral realm existent or susceptible to naturally exist on Earth or in another place of the Solar System 2. The WURM project is the computational sister of the RRUFF project (Downs 2006), with which it shares many similarities.

The database provides for each phase (1) all the structural information relevant to the calculations, (2) the various parameters used to obtain the results, (3) the Born effective charges and the dielectric tensors, and (4) the Raman spectra with both peak position and peak intensities and the list of all the phonon modes in the center of the Brillouin zone.

The WURM project is thus a repository of reference vibrational spectra that can be used as an identification tool for various Earth and planetary materials.

The database is freely accessible at the <http://www.wurm.info> website (Fig. 5.5). The results of the calculations are stored as xml files. A series of javascripts and php scripts read and process the content of the xml files. They ensure a highly interactive way of displaying the information where the users are able to personalize the content they are viewing. The website is in a continuous up-date state with new



**Fig. 5.5** The WURM project is a repository of computed physical properties for minerals

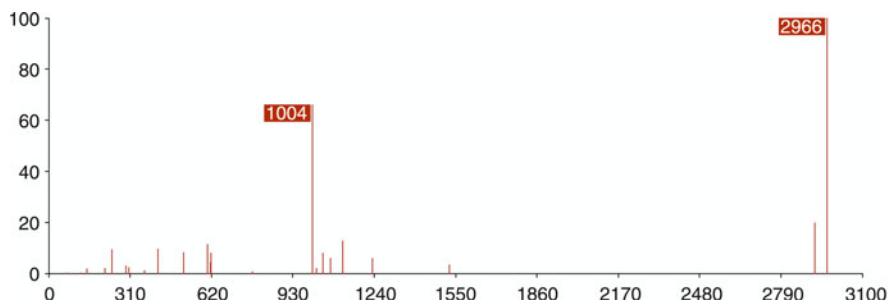


**Fig. 5.6** The computed Raman spectrum of kieserite and reported in the WURM website is dominated by the OH stretching modes and the SO<sub>4</sub> breathing modes

features added on a regular basis, following a flexible structure, detailed below. The website features an internal search engine, a full index of spectra as well as general information about the project and the data hosted.

For example for kieserite, a major hydrated magnesium silicate phase identified on Mars (Gellert et al. 2004) the computed Raman spectrum (Fig. 5.6) is dominated by the OH vibrations at 2,966 cm<sup>-1</sup>, followed by the breathing modes of the SO<sub>4</sub> tetrahedra combined with a rocking mode of the H-O-H molecules at 1,004 cm<sup>-1</sup>. The low frequency modes are various lattice modes and modes affecting the MgO<sub>6</sub> octahedra. This behavior is expected from the character of the structure: with large cations and molecular anionic group. The Raman spectrum of hydrohalite, a major phase in the H<sub>2</sub>O–NaCl system is characterized by four groups of peaks, which in order of increasing frequency correspond to lattice modes, OH rocking modes, OH bending modes and OH breathing modes.

Apart from continuously increasing the size of the database with new spectra in the foreseeable future new visualization tools and new mineral properties are to be added, like displaying the infrared spectra, the dynamic visualization of the single-crystal spectra or reporting the elastic properties.

## 5.5 A Few Words About Limitations

After this brief overview of the DFT and the few successful examples of its application to the study of the planetary ices it is worthwhile noting its limitations as well. These are twofold: restrictions imposed by the available hardware and by (missing) implementations and theoretical developments and/or approximations.

In the first category, related to hardware, main factors are the memory and the computing time. It is good to know that standard DFT calculations scale up to  $O(N^3)$ , where  $N$  is the system size. This restricts the field of applicability to systems with usually not more than a couple hundred atoms (per translationally-identical structural unit). In the second category, one of the major limitations are the failure of DFT to reproduce the electronic gap, because of the missing proper treatment of the many-body interactions. Though corrections to DFT were developed recently (e.g. Onida et al. 2002) large-scale calculations of optical constants of planetary ices, despite its huge interest, are still lacking. DFT also fails to correctly describe weak interatomic bonds, like van der Waals. This is usually reflected in wrong structures and largely overestimated compressibilities. Several corrections are proposed (e.g. Lein et al. 1999; Grimme 2004; Silvestrelli 2009, etc.) dealing with the long-term correlation, but there is still a lot of room for improvement.

Despite these limitations, there is no doubt that ab initio simulations applied to the study of planetary ices will be thriving in the future. Determination of the crystal structures, of the dielectric tensors and atomic dynamical charges, computation of the Raman and infrared spectra, of the phonon band dispersion and the subsequent calculation of the thermodynamic properties and the analysis of the possible unstable phonon modes, construction of the phase diagrams and prediction of the phase transitions are just a few examples of the successful and promising use of first-principles calculations based on the density-functional theory and density-functional perturbation theory.

## References

- Abascal JLF, Sanz E, Vega C (2009) Triple points and coexistence properties of the dense phases of water calculated using computer simulation. *Phys Chem Chem Phys* 11:556–562
- Allen MP, Tildesley DJ (1989) Computer simulation of liquids. Clarendon, Oxford, p 408
- Bader R (1991) A quantum theory of molecular structure and its applications. *Chem Rev* 91:893–928
- Baroni S, Resta R (1986) Ab initio calculation of the low-frequency Raman cross section in silicon. *Phys Rev B* 33:5969–5971
- Baroni S, Giannozzi P, Testa A (1987) Green's-function approach to linear response in solids. *Phys Rev Lett* 58:1861–1864
- Baroni S, de Gironcoli S, Dal Corso A, Giannozzi P (2001) Phonons and related crystal properties from density-functional perturbation theory. *Rev Mod Phys* 73:515–562
- Benoit M, Bernasconi M, Focher P, Parrinello M (1996) New high-pressure phase of ice. *Phys Rev Lett* 76:2934
- Bini R, Ulivi L, Kreutz J, Jodl H (2000) High pressure phases of solid nitrogen by Raman and infrared spectroscopy. *J Chem Phys* 112:8522

- Bobociou E, Caracas R (2010) Complexity in low-temperature phase diagrams of planetary ices: phase transition in bischofite,  $MgCl_2 \cdot 6H_2O$ . In: Abstract MR11C-1890P presented at 2010 fall meeting, AGU, San Francisco, 13–17 Dec 2010
- Brand HEA, Fortes DA, Wood IG, Vocablo L (2009) Equation of state and pressure-induced structural changes in mirabilite ( $Na_2SO_4 \cdot 10H_2O$ ) determined from ab initio density functional theory calculations. *Phys Chem Miner* 37:265–282
- Caracas R (2007) Raman spectra and lattice dynamics of cubic gauche nitrogen. *J Chem Phys* 127:144510
- Caracas R (2008) Dynamical instabilities of ice X. *Phys Rev Lett* 101:085502
- Caracas R, Banigan E (2009) Elasticity and Raman and infrared spectra of  $MgAl_2O_4$  spinel from density-functional perturbation theory. *Phys Earth Planet Inter* 174:113–121
- Caracas R, Bobociou E (2011) The WURM project – a freely available web-based repository of computed physical data for minerals. *Amer Miner* 96:437–443
- Caracas R, Cohen RE (2006) Theoretical determination of the Raman spectra of  $MgSiO_3$  perovskite and post-perovskite at high pressure. *Geophys Res Lett* 33:L12S05. doi:[10.1029/2006GL025736](https://doi.org/10.1029/2006GL025736)
- Caracas R, Gonze X (2010) Lattice dynamics and thermodynamical properties. In: Chaplot SL, Mittal R, Choudhury N (eds) *Thermodynamic properties of solids: experiment and modeling*. Wiley-VCH, Weinheim
- Caracas R, Hemley RJ (2007) New structures of dense nitrogen: pathways to the polymeric phase. *Chem Phys Lett* 442:65–70
- Cardona M (1982) Light scattering in solids II. In: Cardona M, Güntherodt G (eds) *Basic concepts and instrumentation*, vol 50, *Topics in applied physics*. Springer, New York, pp 19–168
- Cavazzoni C, Ghioro GL, Scandolo S, Tosatti E, Bernasconi M, Parrinello M (1999) Superionic and metallic states of water and ammonia at giant planet conditions. *Science* 283:44–46
- Downs RT (2006) The RRUFF project: an integrated study of the chemistry, crystallography, Raman and infrared spectroscopy of minerals. In: Program and abstracts of the 19th general meeting of the international mineralogical association in Kobe, International Mineralogical Association, Kobe, 3–13 Oct 2006
- Eremets M, Gavriliuk AG, Trojan IA, Dzvienko DA, Boehler R (2004) Single-bonded cubic form of nitrogen. *Nat Mater* 3:558
- Eremets M, Gavriliuk AG, Trojan IA (2007) Single-crystalline polymeric nitrogen. *Appl Phys Lett* 90:171904
- Fortes AD (2004) Computational & experimental studies of solids in the ammonia-water system. Ph.D. thesis, University College of London/University of London
- Fortes AD, Choukroun M (2010) Phase behaviour of ices and hydrates. ISSI special publication on exchange processes in icy satellites. *Space Sci Rev* 153:185–218
- Fortes AD, Suard E, Lemée-Cailleau MH, Pickard CJ, Needs RJ (2009) Crystal structure of ammonia monohydrate phase II. *J Am Chem Soc* 131:13508–13515
- Fortes AD, Suard E, Knight KS (2011) Negative linear compressibility and massive anisotropic thermal expansion in methanol monohydrate. *Science* 331:742–746
- Frenkel D, Smit B (2001) *Understanding molecular simulation: from algorithms to applications*. Academic, San Diego, 664 pp
- Gellert R, Rieder R, Anderson RC, Bruckner J, Clark BC, Dreibus C, Economou T, Klingelhöfer G, Lugmair GW, Ming DW, Squyres SW, d'Uston C, Wänke H, Yen A, Zipfel J (2004) Chemistry of rocks and soils in Gusev Crater from the alpha particle X-ray spectrometer. *Science* 305:829–832
- Ghosez Ph, Michenaud J-P, Gonze X (1998) Dynamical atomic charges: the case of  $ABO_3$  compounds. *Phys Rev B* 58:6224–6240
- Goldman N, Fried LE, Kuo IFW, Mundy CJ (2005) Bonding in the superionic phase of water. *Phys Rev Lett* 94:217801
- Goncharov AF, Struzhkin VV, Somayazulu MS, Hemley RJ, Mao HK (1996) Compression of ice to 210 gigapascals: infrared evidence for a symmetric hydrogen-bonded phase. *Science* 273:218

- Gonze X, Lee C (1997) Dynamical matrices, born effective charges, dielectric permittivity tensors, and interatomic force constants from density-functional perturbation theory. *Phys Rev B* 55:10355–10368
- Gonze X, Vigneron J-P (1989) Density-functional approach to nonlinear-response coefficients of solids. *Phys Rev B* 49:13120–13128
- Gonze X, Allan DC, Teter MP (1992) Dielectric tensor, effective charges and phonon in  $\alpha$ -quartz by variational density-functional perturbation theory. *Phys Rev Lett* 68:3603–3606
- Gonze X, Charlier J-C, Allan DC, Teter MP (1994) Interatomic force constants from first principles the case of  $\alpha$ -quartz. *Phys Rev B* 50:13035–13038
- Gonze X, Beuken J-M, Caracas R, Detraux F, Fuchs M, Rignanese G-M, Sindic L, Verstraete M, Zerah G, Jollet F, Torrent M, Roy A, Mikami M, Ghosez Ph, Raty J-Y, Allan DC (2002) First-principle computation of material properties the ABINIT software project. *Comput Mater Sci* 25:478–492, <http://www.abinit.org>
- Gonze X, Rignanese G-M, Verstraete M, Beuken J-M, Pouillon Y, Caracas R, Jollet F, Torrent M, Zerah G, Mikami M, Ghosez Ph, Veithen M, Raty J-Y, Olevano V, Bruneval F, Reining L, Godby R, Onida G, Hamann DR, Allan DC (2005a) A brief introduction to the ABINIT software package. *Zeitschrift für Kristallographie* 220:558–562
- Gonze X, Rignanese G-M, Caracas R (2005b) First-principles studies of the lattice dynamics of crystals, and related properties. *Zeitschrift für Kristallographie* 220:458–472
- Gonze X, Amadon B, Anglade P-M, Beuken J-M, Bottin F, Boulanger P, Bruneval F, Caliste D, Caracas R, Côté M, Deutsch T, Genovesi L, Ghosez Ph, Giantomassi M, Goedecker S, Hamann DR, Hermet P, Jollet F, Jomard G, Leroux S, Mancini M, Mazevedt S, Oliveira MJT, Onida G, Pouillon Y, Rangel T, Rignanese G-M, Sangalli D, Shaltaf R, Torrent M, Verstraete MJ, Zerah G, Zwanziger JW (2009) ABINIT: first-principles approach to material and nanosystem properties. *Comput Phys Commun* 180:2582–2615
- Grimme S (2004) Accurate description of van der Waals complexes by density functional theory including empirical corrections. *J Comput Chem* 25:1463–1473
- Hamann D, Wu X, Rabe KM, Vanderbilt D (2005) Metric tensor formulation of strain in density-functional perturbation theory. *Phys Rev B* 71:035117
- Hayes W, Loudon R (1978) Scattering of light by crystals. Wiley, Hoboken, 113 pp
- Hedin L (1965) New method for calculating the one-particle green's function with application to the electron-gas problem. *Phys Rev* 139:A796–A823
- Hemley RJ (2000) Effects of high pressure on molecules. *Annu Rev Phys Chem* 51:763–800
- Hemley RJ, Jephcoat AP, Mao HK, Zha CS, Finger LW, Cox DE (1987) Static compression of H<sub>2</sub>O-ice to 128 GPa (1.28 Mbar). *Nature* 330:737–740
- Hermet P, Goffinet M, Kreisel J, Ghosez Ph (2007) Raman and infrared spectra of multiferroic bismuth ferrite from first-principles. *Phys Rev B* 75:220102(R)
- Hirshfeld FH (1977) *Theoret. Chim Acta (Berl)* 44:129
- Hohenberg P, Kohn W (1964) Inhomogeneous electron gas. *Phys Rev* 136:B864–B871
- Jmol: an open-source Java viewer for chemical structures in 3D. <http://www.jmol.org/>
- Johari GP, Andersson O (2007) Vibrational and relaxational properties of crystalline and amorphous ices. *Thermochim Acta* 461:14–43
- Kohn W, Sham LJ (1965) Self-consistent equations including exchange and correlation effects. *Phys Rev* 140:A1133–A1138
- Landau L, Lifshitz E (1960) Electrodynamics of continuous media. Pergamon Press, Oxford
- Lazzeri M, Mauri F (2003) First-principles calculation of vibrational Raman spectra in large systems: signature of small rings in crystalline SiO<sub>2</sub>. *Phys Rev Lett* 90:36–401
- Lein M, Dobson JF, Gross EKU (1999) Toward the description of van der Waals interactions within density functional theory. *J Comput Chem* 20:12–22
- Maradudin AA, Montroll EW, Weiss GH, Ipatova IP (1971) Theory of lattice dynamics in the harmonic approximation. In: Ehrenreich HE, Seitz F, Turnbull D (eds) Solid state physics. Academic, New York
- Martin RM, Needs RJ (1986) Theoretical study of the molecular-to-nomolecular transformation of nitrogen at high pressures. *Phys Rev B* 34:5082–5092

- Martinez RD, Caracas R, Humberto AH (2009) Organic ices: methanol monohydrate, *Eos Transactions AGU*, 90(52), Fall meeting supplement, Abstract MR23A-1680, San Francisco
- McMahan AK, LeSar P (1985) Pressure dissociation of solid nitrogen under 1 mbar. *Phys Rev Lett* 54:1929–1932
- Militzer B, Wilson HF (2010) New phases of water ice predicted at megabar pressures. *Phys Rev Lett* 105:19570
- Monkhorst HJ, Pack JD (1976) Special points for Brillouin-zone integrations. *Phys Rev B* 13:5188–5192
- Mulliken RS (1955) Electronic population analysis on LCAO-MO molecular wave functions. *I. J Chem Phys* 23:1833–1840
- Nickel EH (1995) The definition of a mineral. *Can Miner* 33:689–690
- Onida G, Reining L, Rubio A (2002) Electronic excitations: density-functional versus many-body Green's-function approaches. *Rev Mod Phys* 74:601–659
- Payne MC, Teter MP, Allan DC, Arias TA, Joannopoulos JD (1992) Iterative minimization techniques for ab initio total-energy calculations: molecular dynamics and conjugate gradients. *Rev Mod Phys* 64:1045–1097
- Placzek G (1934) Rayleigh-Streuung und Raman-Effekt. In: Marx G (ed) *Handbuch der Radiologie*, vol 6. Akademische, Frankfurt-Main, pp 205–374
- Prosandeev SA, Waghmare U, Levin I, Maslar J (2005) First-order Raman spectra of  $\text{AB}'_{1/2}\text{B}''_{1/2}\text{O}_3$  double perovskites. *Phys Rev B* 71:214–307
- Pruzan Ph, Chervin JC, Wolanin E, Canny B, Gauthier M, Hanfland M (2003) Phase diagram of ice in the VII–VIII–X domain. Vibrational and structural data for strongly compressed ice VIII. *J Raman Spectrosc* 34:591–591
- Runge E, Gross EKU (1984) Density-functional theory for time-dependent systems. *Phys Rev Lett* 52:997–1000
- Scandolo S, Giannozzi P, Cavazzoni C, de Gironcoli S, Pasquarello A, Baroni S (2005) First-principles codes for computational crystallography in the Quantum-ESPRESSO package. *Zeitschrift für Kristallographie* 220:574–579, <http://www.pwscf.org>
- Schwegler E, Sharma M, Gygi F, Galli G (2008) Melting of ice under pressure. *Proc Nat Acad Sci USA* 105:14779–14783
- Silvestrelli PL (2009) van der Waals interactions in density functional theory using Wannier functions. *J Phys Chem A* 113:5224–5234
- Tassini L, Gorelli F, Ulivi F (2005) High temperature structures and orientational disorder in compressed solid nitrogen. *J Chem Phys* 122:074701
- Teter M (1993) Additional condition for transferability in pseudopotentials. *Phys Rev B* 48:5031–5041
- Troullier N, Martins JL (1991) Efficient pseudopotentials for plane-wave calculations. *Phys Rev B* 43:1993–2006
- Vega C, Conde MM, McBride C, Abascal JLF, Noya EG, Ramirez R, Sesé LM (2010) Heat capacity of water: a signature of nuclear quantum effects. *J Chem Phys* 132:046101
- Veithen M, Gonze X, Ghosez Ph (2005) Non-linear optical susceptibilities, Raman efficiencies and electrooptic tensors from first-principles density functional perturbation theory. *Phys Rev B* 71:125107
- Wang Z, Zhao Y, Zha CS, Xue Q, Downs RT, Duan RG, Caracas R, Liao X (2008) X-Ray induced synthesis of 8 H diamond. *Adv Mater* 20:3303–3307

# Chapter 6

## Frictional Sliding of Cold Ice: A Fundamental Process Underlying Tectonic Activity Within Icy Satellites

Erland M. Schulson

**Abstract** Frictional sliding is a fundamental process underlying tectonic activity within the crusts of Enceladus, Europa and other icy satellites. Provided that the coefficient of friction is not too high, sliding can account for the generation of active plumes within Enceladus "tiger stripes" and for the development of certain fracture features on Europa. This paper reviews current knowledge of frictional sliding in water ice Ih, and then raises a number of questions relevant to tectonic modeling.

### 6.1 Introduction

Frictional sliding is a fundamental process underlying tectonic activity within the icy crusts of Saturn's Enceladus, Jupiter's Europa and Neptune's Triton. This is evident from a variety of features. For instance, active plumes emanating from localized "tiger stripe" rifts within the south polar region of Enceladus (Porco et al. 2006; Hansen et al. 2006) could be energized through frictional sliding and attendant heating that accompany diurnal-stress-driven cyclical shear deformation along the fractures/faults (Nimmo et al. 2007). The plumes, whose activity is expected to vary periodically and may affect the injection of material into Saturn's E-ring (Hurford et al. 2007), may originate from either sub-surface water vaporization (Porco et al. 2006; Spencer et al. 2006) or clathrate decomposition (Kieffer et al. 2006). Similarly, lateral offsets along long lineaments/fractures that lace through Europa (Schenk and McKinnon 1989; Greenberg et al. 1998; Hoppa et al. 1999; Prockter et al. 1999; Tufts et al. 1999; Kattenhorn 2004) indicate that frictional sliding plays a role in their development, particularly should such features be formed under compressive stresses as suggested by the orientation of near-equatorial lineaments (Spaun et al. 2001) and by the wing-like character of a

---

E.M. Schulson (✉)

Thayer School of Engineering, Dartmouth College, Hanover, NH 03755, USA  
e-mail: [erland.schulson@dartmouth.edu](mailto:erland.schulson@dartmouth.edu)

wedge crack (Schulson 2002a). Other noteworthy features are Europa's double ridges (Hoppa et al. 2000) and the Europa-like ridges on Neptune's Triton (Smith 1989): in both cases, frictional sliding and attendant heating might lead to upwelling of warm material (Nimmo and Gaidos 2002; Prockter et al. 2005). Thus, the coefficients of static friction  $\mu_s$  and kinetic (or dynamic) friction  $\mu_k$  become important factors in modeling, the former in determining whether the driving shear stress is great enough to effect sliding and the latter in both maintaining sliding and generating heat.

The purpose of this paper is to review current knowledge of the friction of ice on ice. We focus on low-speed ( $< 0.05 \text{ ms}^{-1}$ ) behavior, since that is the kind relevant to extra-terrestrial tectonics. Friction at higher speeds ( $0.5\text{--}10 \text{ ms}^{-1}$ ) and between ice and other materials is discussed by Barnes et al. (1971), Evans et al. (1976), Oksanen and Keinonen (1982), Casassa et al. (1991) and by Persson (1998).

## 6.2 Limit on Friction Coefficients for Sliding and Heating

The issue in relation to icy satellites is the magnitude of the friction coefficients: if too high, then sliding and heating will not occur. How high is too high? That depends on the driving shear stress and the normal stress across the fault as well as the hydrostatic pressure and hence its depth. Upon incorporating both the shear and normal stresses and pressure, Coulomb's failure criterion dictates that failure occurs when the applied shear stress exceeds the frictional resistance of a fault. Or, as discussed by Dombard and McKinnon (2006) in terms of "Byerlee's rule" (1978), the yield strength increases with increasing hydrostatic stress. The failure stress also depends upon the cohesion across the fault/fracture.

For instance, in modeling the behavior of a vertically-oriented, brittle fault on Enceladus, assumed to be 2 km deep within a spherically symmetric icy shell 24 km thick, Smith-Konter and Pappalardo (2008) found, upon invoking Coulomb's failure criterion and assuming both zero cohesion and a coefficient of static friction  $\mu_s = 0.2$ , that the fault exhibits "*slip windows*" when loaded by a combination of diurnal tidal shear stress of amplitude  $\sim 45 \text{ kPa}$ , of diurnal normal stress of amplitude  $\sim 70 \text{ kPa}$  and of an overburden pressure of  $\sim 200 \text{ kPa}$ . (That combination was obtained from a numerical code (Wahr et al. 2008) that gives tidal-induced stresses at any point on the surface of a satellite for both diurnal and non-synchronous rotation). That is, under the assumed conditions Enceladus' tiger stripe faults are expected to slide during two parts of the  $360^\circ$  diurnal cycle, from  $\sim 55^\circ$  to  $\sim 105^\circ$  and again from  $\sim 195^\circ$  to  $\sim 255^\circ$ , not necessarily in the same direction. The windows are expected to open for lower values of the friction coefficient, but to close for  $\mu_s > 0.3$ . The closure limit would be lower should the fault possess cohesion, and it would be still lower for deeper faults. Similarly, for shear heating to account for the origin of plumes and heat flux on Enceladus (Nimmo et al. 2007) and for the origin of ridges on Triton (Prockter et al. 2005), relatively low values of the kinetic friction coefficient ( $\mu_k = 0.1\text{--}0.3$ ) are necessary (Nimmo et al. 2007).

### 6.3 Measured Friction Coefficients

Actual values probably depend upon a number of factors, including the chemical composition and structure of the crust as well as temperature and sliding speed. On composition, it seems reasonable to assume from spectroscopic evidence that water ice, if not the only constituent, is probably a primary one, even though such evidence indicates the presence of hydrated salts, frozen gases, clathrates and possibly other minerals (Kargel 1991; Dalton et al. 2005). The relevant crystallographic variant of water ice is the low-pressure form ice Ih ( $h = \text{hexagonal}$ ) of density  $\rho \sim 10^3 \text{ kg m}^{-3}$ . This is the form of interest because the pressure within the brittle zone, Table 6.1, where frictional sliding is expected to operate, is less than  $\sim 200 \text{ MPa}$ , which is the nearly temperature-independent equilibrium pressure under which ice I transforms to a higher density phase (Petrenko and Whitworth 1999). On temperature and sliding speeds, the ranges of interest, respectively, are approximately 100–270 K and  $10^{-8}$ – $10^{-5} \text{ ms}^{-1}$  (Nimmo and Gaidos 2002). Thus, the coefficients of interest within the context of current modeling, and the ones we review, are those for “pure” ice Ih sliding slowly over itself at homologous temperatures that range from  $T_h \sim 0.35$ –0.95. There are no data for two other candidates,  $\text{MgSO}_4 \cdot 11\text{H}_2\text{O}$  and  $\text{Na}_2\text{SO}_4 \cdot 10\text{H}_2\text{O}$ , and none for ice containing particles of silica. Water ice, in other words, is all we have to go on.

The literature offers insight, as well as contradictions. Specifically, from confined compression tests on indium-sheathed, cylindrically shaped specimens of fresh-water granular ice sliding slowly ( $3 \times 10^{-7}$ – $3 \times 10^{-5} \text{ ms}^{-1}$ ) upon itself across  $45^\circ$  saw-cuts, Beeman et al. (1988) obtained a (kinetic) coefficient of friction of either  $\mu_k = 0.2$  or  $\mu_k = 0.55$  for cold (77–115 K) material loaded under a range of confining pressure (0.3–250 MPa). The lower value was obtained under higher pressures ( $> 10 \text{ MPa}$ ). Over the experimental ranges examined, neither temperature nor sliding speed appeared to affect the behavior. Through another set of high-pressure (10–50 MPa) tests on similar material, Rist et al. (1994) and Rist (1997) obtained the value  $\mu_k = 0.4$ –0.8 upon sliding ice across a deformation-induced plastic shear fault<sup>1</sup> at a speed of  $\sim 10^{-3} \text{ ms}^{-1}$  at temperatures of 233 and 253 K. Again, the behavior appeared to be independent of temperature.

<sup>1</sup> When loaded to terminal failure under triaxial confinement, ice exhibits two kinds of shear fault (Schulson 2002b). Under low confinement, faults are comprised of bands of damage oriented at an angle  $\theta$  to the maximum (i.e., most compressive) principal stress  $\sigma_I$ , where  $\theta = \frac{1}{2} \arctan \frac{1}{\mu}$  and where  $\mu$  is the internal friction coefficient whose value is similar to the dynamic coefficient of friction (Schulson et al. 2006a, b); typically,  $\theta = 25$ – $30^\circ$ . Such faults are termed *Coulombic faults*. Under high confinement, frictional sliding is suppressed. Faulting still occurs, but the faults are now comprised of narrow bands of plastically deformed/recrystallized material oriented along planes of maximum applied shear stress; i.e., at  $\sim 45^\circ$  to  $\sigma_I$ . Such faults are termed *plastic faults*.

**Table 6.1** Pressure  $p_{BD} = \rho g z_{BD}$  at depth of brittle-ductile (BD) transition in icy satellites

Satellite	Gravitational constant, g ( $\text{ms}^{-2}$ )	BD depth $z_{BD}$ (km)	Reference for $z_{BD}$	Pressure at $z_{BD}$ (MPa)
Enceladus	0.11	4	Nimmo et al. (2007)	0.4
Europa	1.31	~10	Billings and Kattenhorn (2005)	13
Triton	0.78	9.5	Prockter et al. (2005)	7

Jones (1989) and Kennedy et al. (2000), in apparent contradiction, found that temperature is an important factor. Using a double-shear device, they slid at low speeds ( $5 \times 10^{-7}$  to  $5 \times 10^{-2} \text{ ms}^{-1}$ ) plate-shaped specimens of warmer (233–270 K) fresh-water granular ice across smooth ( $\sim 3 \mu\text{m}$ ) surfaces of the same material loaded under relatively low normal stresses (0.007 and 1.0 MPa). They obtained coefficients that varied between  $\mu_k = 0.05$  and  $\mu_k = 0.8$ , Fig. 6.1. The higher values ( $\mu_k > 0.5$ ) generally correlated with lower temperatures and with lower sliding speeds ( $< 10^{-4} \text{ ms}^{-1}$ ). At 233 K the coefficient exhibited a maximum at an intermediate speed of  $\sim 10^{-4} \text{ ms}^{-1}$ . Yasutome et al. (1999), Kanazawa et al. (2003) and Maeno et al. (2003) corroborated these findings. Through similar experiments, also on fresh-water granular ice sliding against itself across a smooth interface loaded under low normal stresses (0.001–.37 MPa), they found using the double-shear method that the (kinetic) friction coefficient varied from  $\mu_k \sim 0.02$ – $\sim 1.0$ , Fig. 6.2. Again, it exhibited a complicated dependence on temperature and sliding speed over the ranges examined (243–273 K;  $10^{-7}$ – $10^1 \text{ ms}^{-1}$ ).

Through a different kind of experiment, one that bears directly on sliding across natural shear faults, Fortt and Schulson (2007) found that, again, temperature and sliding speed are important factors. They examined the resistance to sliding across Coulombic shear faults (roughness  $\sim 1 \text{ mm}$ ) loaded under low pressure ( $< 2 \text{ MPa}$ ). The faults had been introduced into plate-shaped specimens of fresh-water columnar ice through across-column, biaxial loading to terminal failure at 263 K. The rougher surface exhibited greater friction, owing most likely to the interlocking of asperities. Over the ranges of temperature (233–270 K) and sliding speed ( $8 \times 10^{-7}$  to  $4 \times 10^{-3} \text{ ms}^{-1}$ ) examined, the friction coefficients varied between  $\mu_s \sim \mu_k = 0.4$ –1.6, Fig. 6.3. The coefficients generally increased with decreasing temperature, independent of normal stress across the fault. Also, they depended upon sliding speed: the coefficients reached a maximum at an intermediate speed around  $10^{-5} \text{ ms}^{-1}$ . At lower speeds, below the point of maximum friction, sliding is quiet. At higher speeds, it is noisy and is generally characterized by slip–stick behavior.

## 6.4 Interpretation

The interpretation of this behavior is challenging. All investigators noted that ice exhibits stick–slip character when sliding upon itself at higher speeds ( $\gtrsim 10^{-5} \text{ m s}^{-1}$ ). This is a manifestation of the formation (up load) and then breaking (down load) of

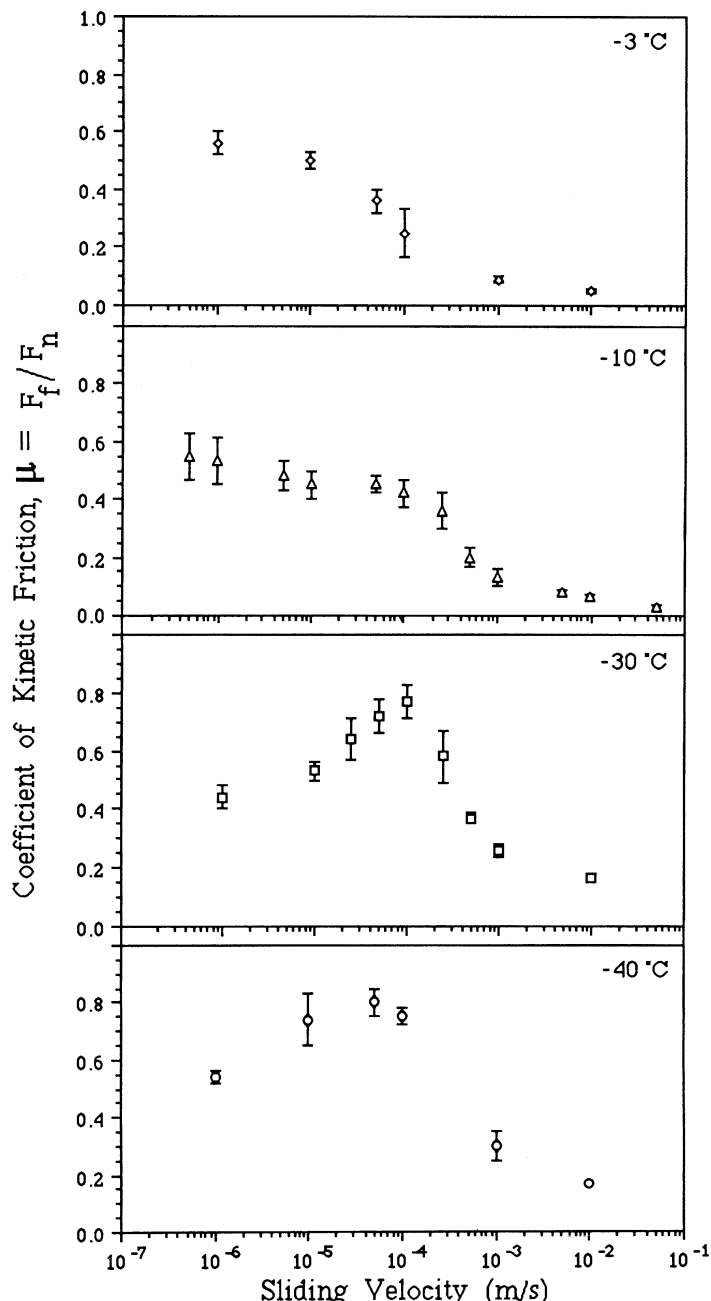


**Fig. 6.1** The kinetic friction coefficient of fresh-water ice sliding across itself along a smooth interface at low speeds (From Kennedy et al. 2000)

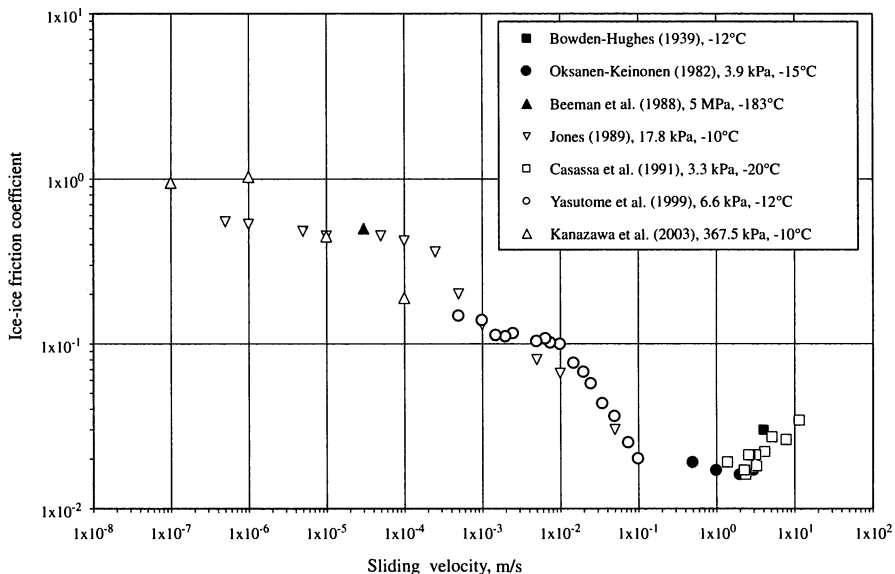


**Fig. 6.2** Compilation of the kinetic friction coefficient of fresh-water ice sliding across itself versus sliding speed (From Maeno et al. 2003)

bonds within points of contact the sum of which constitutes the real area of contact (Kennedy 1991; Williams 1994; Kennedy et al. 2000). When sliding commences, the combination of contact stresses and those that arise through surface traction imparts significant inelastic deformation within a narrow region adjacent to the interface, as evident from the presence of microcracks and other deformation features (Kennedy et al. 2000; Montagnat and Schulson 2003). Inelastic deformation, therefore, would appear to contribute significantly to (and perhaps even dominate) the frictional resistance to sliding. Melting, when it occurs, is expected to lower the friction coefficient (Bowden and Hughes 1939; Kennedy et al. 2000) and this could account for the general decrease in friction coefficient of warm ice with increasing velocity at sliding speeds above  $\sim 10^{-5} \text{ ms}^{-1}$ . In other words, barring melting as an ameliorating process, energy consumed during plastic flow and fracture of the localized adhesive zones/contact points, as well as subsequent deformation of wear debris (or gouge) entrapped between the sliding faces, may well account for much of the frictional force. Kennedy et al. (2000) proposed that the general effects noted above of both thermal weakening and velocity strengthening (over the low-speed range) could be accounted for semi-quantitatively by power-law creep, where the creep rate is set by the ratio of sliding speed to the thickness of the deformation region adjacent to the interface  $\dot{\varepsilon} \sim v/w$  and where the friction force is governed by the shear stress driving creep. On this model, both the thermal and the rate effect become extinguished once the sliding speed reaches a critical level at which point the stress to drive creep exceeds the fracture stress. At that point and beyond (again barring melting), fracture toughness – a property that is essentially independent of loading rate and temperature, at least of

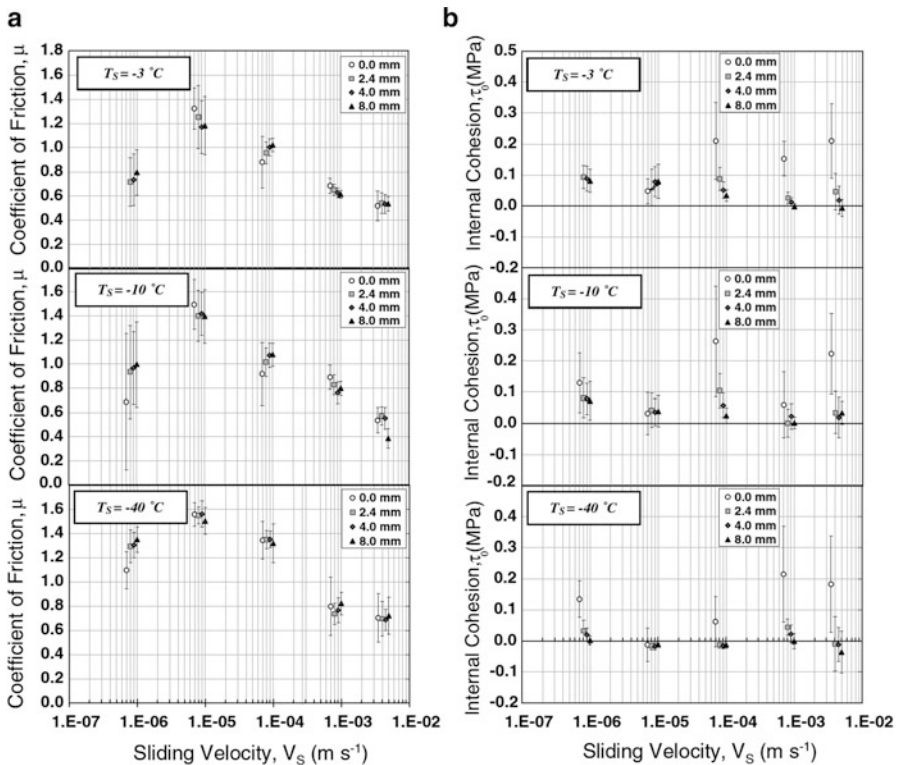


**Fig. 6.3** Graphs showing (a) the kinetic coefficient of friction across Coulombic shear faults and (b) the internal cohesion versus sliding velocity at  $-3^\circ\text{C}$ ,  $-10^\circ\text{C}$  and  $-40^\circ\text{C}$  for displacements across the fault from 0 to 8 mm. Note: points are displaced on velocity scale to avoid overlap (From Fortt and Schulson 2007)

relatively warm ice (Schulson and Duval 2009) – is expected to control the frictional force. Within the fracture-controlled regime, Montagnat and Schulson (2003) modeled the friction force in terms of fracture toughness and the size of stress concentrators.

This interpretation, then, implies a transition from ductile-like to brittle-like behavior within the near-surface deformation region once the sliding speed reaches a critical speed, analogous to the ductile-brittle transition that occurs within bulk ice when deformed at a critical strain rate (Schulson 1990, 2001). Indeed, Fortt and Schulson (2007) showed that the velocity that marks the suppression of velocity-strengthening across Coulombic shear faults and correspondingly marks the transition from quiet to noisy sliding, when expressed in terms of the strain rate within the surface region, is similar to the transition strain rate within bulk material, thus providing further support for the above interpretation.

This kind of thinking leads to a hypothesis and to a rationalization of the apparent contradiction noted above. Schulson's (1990, 2001) model of the ductile-brittle transition holds that the strain rate marking the transition scales as  $\dot{\varepsilon}_t \sim K_{Ic}^n A e^{-Q/RT}$  where  $K_{Ic}$  denotes fracture toughness and  $A$  and  $n$  are constants in the power-law creep equation ( $\dot{\varepsilon} = A\bar{\sigma}^n e^{-Q/RT}$  where  $\bar{\sigma}$  is the effective stress that takes into account the multiaxiality of the stress state),  $Q$  is the apparent activation energy for creep,  $T$  is absolute temperature and  $R$  is the gas constant. If we assume that most of the temperature dependence resides within the exponential term, and if we take for the activation energy a value between 31 and 61 kJ mol<sup>-1</sup> (Durham and Stern 2001), the exact value depending upon the creep mechanism, then upon reducing the temperature from 233 K to say 100 K we would expect the transition velocity to fall by at least a factor of about 10<sup>9</sup> (taking the lower limit on  $Q$ ). Given that within warm ice ( $T_h > 0.85$ ) the transition velocity  $v_t \sim 10^{-5}$  ms<sup>-1</sup> (Kennedy et al. 2000; Fortt and Schulson 2007) then within cold ice ( $T_h \sim 0.35$ ) the transition velocity could be as low as 10<sup>-14</sup> ms<sup>-1</sup> or lower. This calculation is at best a rough estimate, and so should not be taken too seriously. Yet, it leads to the *hypothesis* that at the lower temperatures of interest to tectonic activity on Enceladus and other icy satellites, frictional sliding may fall within the regime of brittle-like behavior, in which case velocity strengthening would not be expected at rates easily explored experimentally. This, then, provides a theoretical foundation for the observation of Beeman et al. (1988) and helps to reconcile the apparent contradiction noted above.

## 6.5 Questions Arising

In relation to the modeling of tectonic activity on Europa and Enceladus and other icy satellites, several questions arise:

- Under exactly what conditions of temperature and sliding speed do those factors begin to affect frictional resistance to sliding of pure water ice Ih?
- Do those conditions depend upon the character of the sliding surface (i.e., Coulombic fault, saw cut, smooth surface)?
- What are the values of the friction coefficients of other candidate materials (e.g., MgSO<sub>4</sub>.11H<sub>2</sub>O, Na<sub>2</sub>SO<sub>4</sub>.10H<sub>2</sub>O) that may comprise icy satellites?
- Is the friction coefficient that is obtained from measurements on relatively small test specimens in the laboratory applicable to the larger scale of the field?

The fourth question is difficult to examine experimentally. However, we can offer the following comment based upon the deformation of winter sea ice on the Arctic Ocean where frictional sliding is now recognized as a major geophysical process (Schulson and Hibler 1991; Hibler and Schulson 2000; Schulson 2004; Wilchinsky and Feltham 2004; Sammonds et al. 2005; Hopkins and Thorndike 2006; Schreyer et al. 2006; Weiss et al. 2007). Within that domain, there is evidence that the friction

coefficient is scale independent. The evidence comes from brittle compressive failure envelopes, particularly from the slope  $q$  that is governed by the coefficient of internal friction  $\mu_i$  (Jaeger and Cook 1979; Schulson et al. 2006a, b). The slope turns out to have the same value for the sea ice cover as a whole as it does for laboratory specimens harvested from the cover (Schulson et al. 2006b; Weiss et al. 2007). It also turns out that the internal friction coefficient is practically indistinguishable from the kinetic coefficient of friction described above (Schulson et al. 2006a, b). It appears, therefore, that the friction coefficient of sea ice is a scale independent mechanical property. Our sense is that the same may be true of the material of icy satellites.

## References

- Barnes P, Tabor D, Walker JCS et al (1971) The friction and creep of polycrystalline ice. Proc R Soc Lond 1557:127–155
- Beaman M, Durham WB, Kirby SH (1988) Friction of ice. J Geophys Res 93:7625–7633
- Billings SE, Kattenhorn SA (2005) The great thickness debate: ice shell models for Europa and comparisons with estimates based on flexure at ridges. Icarus 177:397–412
- Bowden FP, Hughes TP (1939) The mechanism of sliding on ice and snow. Proc R Soc Lond A 172:280–298
- Byerlee J (1978) Friction of rocks. Pure Appl Geophys 116:615–626
- Casassa G, Narita H, Maeno N (1991) Shear cell experiments of snow and ice friction. J Appl Phys 69:3745–3756
- Dalton JB, Prieto-Ballesteros O, Kargel JS et al (2005) Spectral comparison of heavily hydrated salts with disrupted terrains on Europa. Icarus 177:472–490
- Dombard AJ, McKinnon WB (2006) Elastoviscoplastic relaxation of impact crater topography with application to Ganymede and Callisto. J Geophys Res. doi:[10.1029/2005JE002445](https://doi.org/10.1029/2005JE002445)
- Durham WB, Stern LA (2001) Rheological properties of water ice – applications to satellites of the outer planets. Annu Rev Earth Plant Sci 29:295–330
- Evans DCB, Nye JF, Cheeseman KJ (1976) Kinetic friction of ice. Proc R Soc Lond A 347:493
- Fortt AL, Schulson EM (2007) The resistance to sliding along coulombic shear faults in ice. Acta Mater 55:2253–2264
- Greenberg R, Geissler P, Hoppa G et al (1998) Tectonic processes on Europa: tidal stresses, mechanical response, and visible features. Icarus 135:64–78
- Hansen CJ, Esposito L, Stewart AIF, Colwell J, Hendrix A, Pryor W, Shemansky D, West R (2006) Enceladus' water vapour plume. Science 311:1422–1425
- Hibler WD, Schulson EM (2000) On modeling the anisotropic failure and flow of flawed sea ice. J Geophys Res 105:17105–17120
- Hopkins MA, Thorndike AS (2006) Floe formation in Arctic sea ice. J Geophys Res 111:1–9, Art. No. C11S23 Sep 13 2006
- Hoppa G, Tufts BR, Greenberg R et al (1999) Strike-slip faults on Europa: global shear patterns driven by tidal stress. Icarus 141:287–298
- Hoppa G, Greenberg R, Tufts BR, Geissler P, Phillips C, Milazzo M (2000) Distribution of strike-slip faults on Europa. J Geophys Res 105:22617–22627
- Hurford TA, Helfenstein P, Hoppa GV et al (2007) Eruptions arising from tidally controlled periodic openings of rifts on Enceladus. Nature 447:292–294
- Jaeger JC, Cook NGW (1979) Fundamentals of rock mechanics. Chapman and Hall, London
- Jones DE (1989) Ice friction: effects of temperature, sliding velocity and ice type. M.Eng. thesis, Thayer School of Engineering, Dartmouth College

- Kanazawa S, Arakawa M, Maeno N (2003) Measurements of ice-ice friction coefficients at low sliding velocities. *Seppyo* 65:389–397
- Kargel JS (1991) Brine volcanism and the interior structures of asteroids and icy satellites. *Icarus* 94:368–390
- Kattenhorn SA (2004) Strike-slip fault evolution on Europa: evidence from tailcrack geometries. *Icarus* 172:582–602
- Kennedy FE (1991) Encyclopedia of physics. VCH, New York
- Kennedy FE, Schulson EM, Jones D (2000) Friction of ice on ice at low sliding velocities. *Philos Mag A* 80:1093–1110
- Kieffer SW, Lu X, Bethke CM et al (2006) A clathrate reservoir hypothesis for Enceladus' south polar plume. *Science* 314:1764–1766
- Maeno N, Arakawa M, Yasutome A et al (2003) Ice-ice friction measurements, and water lubrication and adhesion-shear mechanisms. *Can J Phys* 81:241–249
- Montagnat M, Schulson EM (2003) On friction and surface cracking during sliding. *J Glaciol* 49:391–396
- Nimmo F, Gaidos E (2002) Strike-slip motion and double ridge formation on Europa. *J Geophys Res.* doi:[10.1029/2000JE001476](https://doi.org/10.1029/2000JE001476)
- Nimmo F, Spencer JR, Pappalardo RT et al (2007) Shear heating as the origin of the plumes and heat flux on Enceladus. *Nature* 447:289–291
- Oksanen P, Keinonen J (1982) The mechanism of friction of ice. *Wear* 78:315–324
- Persson BNJ (1998) Sliding friction: physical principles and applications. Springer, New York
- Petrenko VF, Whitworth RW (1999) Physics of ice. Oxford University Press, New York
- Porco CC, Helfenstein P, Thomas PC (2006) Cassini observes the active south pole of Enceladus. *Science* 311:1393–1401
- Prockter LM, Antman AM, Pappalardo RT et al (1999) Europa: stratigraphy and geological history of the anti-Jovian region from Galileo E14 solid-state imaging data. *J Geophys Res Planet* 104:16531–16540
- Prockter LM, Nimmo F, Pappalardo RT (2005) A shear heating origin for ridges on triton. *Geophys Res Lett.* doi:[10.1029/2005GL022832](https://doi.org/10.1029/2005GL022832)
- Rist MA (1997) High stress ice fracture and friction. *J Phys Chem B* 101:6263–6266
- Rist MA, Jones SJ, Slade TD (1994) Microcracking and shear fracture in ice. *Ann Glaciol* 19:131–137
- Sammonds P, Hatton D, Feltham D et al (2005) Experimental study of sliding friction and stick-slip on faults in floating ice sheets. In: Dempsey JP (ed) Proceedings of the 18th international conference on POAC'05, Potsdam
- Schenk PM, McKinnon WB (1989) Fault offsets and lateral crustal movement on Europa for a mobile ice shell. *Icarus* 79:75–100
- Schreyer HL, Sulsky DL, Munday LB et al (2006) Elastic-decohesive constitutive model for sea ice. *J Geophys Res* 111:C11S26
- Schulson EM (1990) The brittle compressive fracture of ice. *Acta Metall Mater* 38:1963–1976
- Schulson EM (2001) Brittle failure of ice. *Eng Fract Mech* 68:1839–1887
- Schulson EM (2002a) On the origin of a wedge-crack within the icy crust of Europa. *J Geophys Res.* doi:[10.1029/2001JE001586](https://doi.org/10.1029/2001JE001586)
- Schulson EM (2002b) Compressive shear faulting in ice: Plastic vs. Coulombic faults. *Acta Mater* 50:3415–3424
- Schulson EM (2004) Compressive shear faults within the arctic sea ice cover on scales large and small. *J Geophys Res* 109:1–23
- Schulson EM, Hibler WD (1991) The fracture of ice on scales large and small: arctic leads and wing cracks. *J Glaciol* 37:319–323
- Schulson EM, Duval P (2009) Creep and fracture of ice. Cambridge University Press, Cambridge
- Schulson EM, Fortt A, Iliescu D et al (2006a) On the role of frictional sliding in the compressive fracture of ice and granite: terminal vs. post-terminal failure. *Acta Mater* 54:3923–3932

- Schluson EM, Fortt A, Iliescu D et al (2006b) Failure envelope of first-year arctic sea ice: the role of friction in compressive fracture. *J Geophys Res.* doi:[10.1029/2005JC003234](https://doi.org/10.1029/2005JC003234)[186](https://doi.org/10.1029/2005JC003234186)
- Smith BA (1989) Voyager-2 at neptune – imaging science results. *Science* 246:1422–1449
- Smith-Konter B, Pappalardo RT (2008) Tidally driven stress accumulation and shear failure of Enceladus's tiger stripes. *Icarus* 198:435–451
- Spaun NA, Pappalardo RT, Head JW et al (2001) Characteristics of the trailing equatorial quadrant of europa from Galileo imaging data: evidence for shear failure in forming linea. In: *Lunar and planet science conference*, CD-ROM:1228, Houston
- Spencer J, Pearl J, Segura M et al (2006) Cassini encounters Enceladus: background and the discovery of a south polar hot spot. *Science* 311:1401–1405
- Tufts BR, Greenberg R, Hoppa G et al (1999) Astypalaea linea: a large-scale strike-slip fault on Europa. *Icarus* 141:53–64
- Wahr J, Selvans ZA, Mullen ME et al (2008) Modeling stresses on satellites due to nonsynchronous rotation and orbital eccentricity using gravitational potential theory. *Icarus*. doi:[10.1016/j.icarus.2008.1011.1002](https://doi.org/10.1016/j.icarus.2008.1011.1002)
- Weiss J, Schulson EM, Stern HL (2007) Sea ice rheology in-situ, satellite and laboratory observations: fracture and friction. *Earth Planet Sci Lett* 255:1–8
- Wilchinsky AV, Feltham DL (2004) A continuum anisotropic model of sea-ice dynamics. *Proc R Soc Lond A* 460:2105–1240
- Williams JA (1994) *Engineering tribology*. Oxford University Press, Oxford
- Yasutome A, Arakawa M, Maeno N (1999) Measurements of ice-ice friction coefficients. *Seopyo* 61:437–443

# Chapter 7

## Planetary Ices Attenuation Properties

Christine McCarthy and Julie C. Castillo-Rogez

**Abstract** In this chapter, we review the topic of energy dissipation in the context of icy satellites experiencing tidal forcing. We describe the physics of mechanical dissipation, also known as attenuation, in polycrystalline ice and discuss the history of laboratory methods used to measure and understand it. Because many factors – such as microstructure, composition and defect state – can influence rheological behavior, we review what is known about the mechanisms responsible for attenuation in ice and what can be inferred from the properties of rocks, metals and ceramics. Since attenuation measured in the laboratory must be carefully scaled to geologic time and to planetary conditions in order to provide realistic extrapolation, we discuss various mechanical models that have been used, with varying degrees of success, to describe attenuation as a function of forcing frequency and temperature. We review the literature in which these models have been used to describe dissipation in the moons of Jupiter and Saturn. Finally, we address gaps in our present knowledge of planetary ice attenuation and provide suggestions for future inquiry.

### 7.1 Introduction

Planetary satellites are subject to periodic deformation in response to the tides exerted by their primaries. This deformation is driven by the eccentricities of their orbits and by the physical librations of the satellites' shapes. Depending on the internal structure and material properties of these objects, deformation can result in the dissipation of tidal energy in the form of heat, impacting the geophysical

---

C. McCarthy (✉)

Lamont-Doherty Earth Observatory, Columbia University, Palisades, NY, USA  
e-mail: [mccarthy@ldeo.columbia.edu](mailto:mccarthy@ldeo.columbia.edu)

J.C. Castillo-Rogez

Jet Propulsion Laboratory, California Institute of Technology, Pasadena, CA, USA

evolution of the object. Loss of mechanical energy results in tidal evolution of a satellite's orbital and spin properties.

Properly modeling the tidal response of planetary objects is important for two reasons. First, tidal heating can be a significant heat source; it is thought to drive cryovolcanism on Enceladus (Barr and Milkovich 2008) and to be involved in the preservation of a deep ocean in Europa (Tobie et al. 2003), for instance. Second, the tidal response of icy bodies can potentially be measured, in which case the characterization of its amplitude and phase provides direct constraints on the internal and thermal structures of these objects. Methods to measure that tidal response include physical librations of the shape (e.g., Williams et al. 2001), radial deformation of the equatorial bulge (Castillo et al. 2000), secular acceleration (e.g., Aksnes and Franklin 2001), and phase lag (Rappaport et al. 2008). Dynamical models of resonant interactions between satellites may also lead to constraints on their dissipative properties (Zhang and Nimmo 2009). Another aspect of the problem is that the periodic deformation of the shape can promote significant geological activity, for example, by: (1) tectonic stresses leading to crack nucleation and faulting (e.g., terrestrial ice shelves (Rothrock 1975) and cycloid features on Europa (Greenberg et al. 1998)); (2) promotion of motion along faults (e.g., on Earth (Cochran et al. 2004) or on Enceladus, at the Tiger stripes (Hurford et al. 2007)); and (3) volcanic activity (e.g., on Io (Peale et al. 1979)).

In order to infer constraints on the evolution and current state of icy bodies from these various observations, it is necessary to develop models that properly account for the behavior of planetary material subject to tidal stressing in the relevant conditions of frequency, temperature and stress amplitudes. This chapter focuses on the internal friction properties of icy materials – in the viscous and anelastic regimes. Solid-solid friction, another mechanism that can accommodate the response of material to tidal stress, is addressed in the chapter by Erland Schulson.

The response of ice to cyclic deformation has been much studied in conditions relevant to terrestrial ice sheets with geotechnical applications (e.g., Johari et al. 1995) or to model the tidal response of ice shelves and the resulting fatigue-induced cracks (e.g., Cole and Durell 1995). There are very few experiments that have considered the response of ice in conditions relevant to outer planet satellites. Such experiments are technically challenging as they require work in cryogenic conditions, at relatively low stress (below 0.1 MPa) and at frequencies below  $10^{-4}$  Hz (Fig. 7.1). As a result, most tidal models have relied on the extrapolation of data obtained in conditions that may significantly depart from those relevant to icy satellites.

In this chapter, we review the literature available for the mechanical properties of water ice at low frequency approaching conditions in icy satellites, including the mechanisms responsible for dissipation (Sect. 7.2) and examine the variables that can affect the material response in the geologic context (Sect. 7.3). We then look at the models that have been suggested to extrapolate these measurements to conditions relevant to Solar system bodies (Sect. 7.4). Finally, we address the expression of tidal response and its consequences in icy bodies, based on observations and interpretation (Sect. 7.5) and, in light of these considerations, we address a list of related issues and measurements necessary to solve these questions (Sect. 7.6).

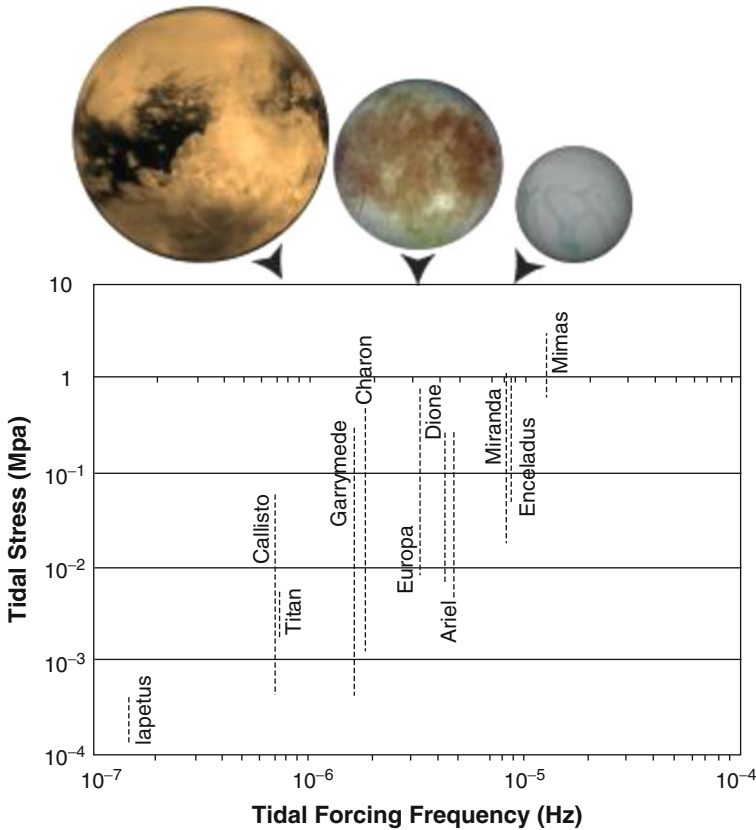


**Fig. 7.1** Tidal forcing frequency and cyclic peak stress for the orbital tides at all outer planet satellites. The range of values reflects the possible internal structure models for these objects (*Lower bound* corresponds to models without a deep ocean; *upper bounds* correspond to models with a deep ocean) (Note: satellites figures are not to scale)

## 7.2 The Physics of Attenuation Under Mechanical Forcing

The study of planetary material anelasticity started in the mid-1950s, mainly focusing on rocky material with the primary goal to support the interpretation of seismic studies (e.g., Faul and Jackson 2005). Our understanding of ice dissipative properties borrows significantly from that research, and we refer the readers to some of the many key papers on the topic: e.g., Jackson (1993), Weertman (1983), Cooper (2002), Karato (2008).

### 7.2.1 A Few Definitions

Like many materials, ice exhibits viscoelastic behavior. That is, in response to some deviatoric stress, it will respond with a combination of instantaneous elastic

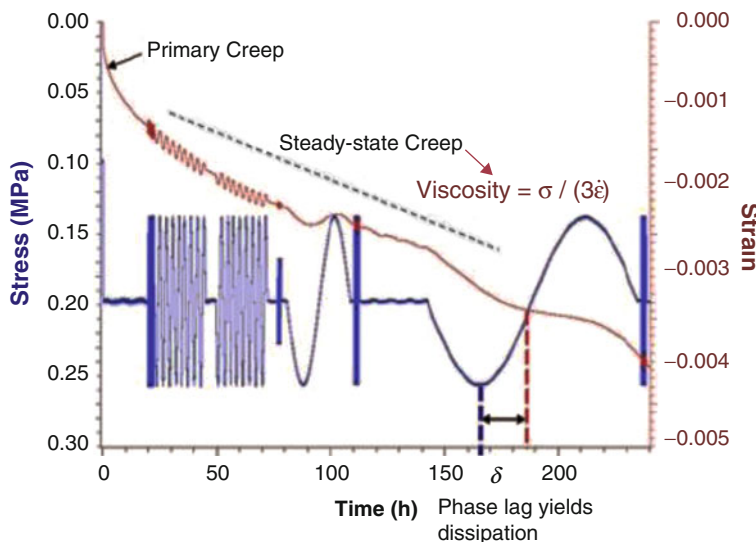


**Fig. 7.2** Example of the strain response to a median, or offset, stress in addition to a periodic stress. The response to the offset stress is a typical creep curve with an instantaneous elastic response, a decelerating transient and finally a steady-state response indicated by the monotonic downward trend of the strain data (compression negative). The response to the periodic stress is a periodic strain at the same frequency as the forcing frequency, but lagging behind by  $\delta$

behavior and time-dependent inelastic behavior. The characteristic feature of elasticity is that it is completely recoverable; the elastic response merely involves the stretching and contracting of atomic bonds so that, when stress is removed, atoms return to their previous positions. Inelasticity, however, involves time dependent motion of point, line, and planar defects within the crystal. The inelastic response can be broken into two parts: fully recoverable anelastic deformation and permanent viscous (or plastic) creep.<sup>1</sup> These processes are illustrated in Fig. 7.2, which shows the response of a sample of synthetic ice subjected to a constant uniaxial stress, in addition to a periodic stress. The material first exhibits an instantaneous change in length as a consequence of elastic deformation. That first step is followed by a phase of primary creep, during which the strain rate decelerates, until steady-state creep is reached. Primary creep, which is also referred to as “transient creep”, may last from a few hours to several tens of hours, depending on the properties of the material and temperature.

It is the inelastic behavior that causes a stressed material to experience a relaxation of elastic strain energy until that energy is fully dissipated. In the case of periodic loading of a viscoelastic material, the dynamic relationship between stress and strain, specifically in terms of the ratio of strain energy dissipated to the energy stored, is described by the term “internal friction”, or inverse quality factor  $Q^{-1}$ , which is also commonly called attenuation in the earth sciences. Since the various mechanisms responsible for attenuation each have a characteristic time-scale related to the mobility of that defect, the dissipation is very much a function of

the temperature and the frequency of mechanical forcing. A material subject to low temperature and/or rapid forcing has a response that is essentially elastic. On the other hand, a material stressed over a very long period of time at relatively high-temperature has its overall response dominated by its viscosity. Between these two limits is a response that combines a mixture of recoverable and irrecoverable strain, the timescale of which is generally taken as the Maxwell time, that is, the ratio of the material viscosity to its elasticity.

### 7.2.2 *Principles of Laboratory Measurements*

Various methods have been used to study viscoelasticity in materials. At high frequencies, resonance methods that measure the decay of free vibrations of a system following a perturbation are typically used. Here, the quality factor is determined from the width of a resonant peak. One resonance method uses ultrasound spectroscopy, in which a specimen is held between two ultrasonic transducers, one acting as a transmitter and the other as a receiver (Lakes 2004). The frequency range of such tests is typically 50 kHz to 20 MHz. It is this technique that has been used extensively to study the internal friction of ice at very low temperature at which point-defect related mechanisms were found to act (Sect. 7.2.4). It is also the only approach used so far that has yielded constraints on the attenuation properties of amorphous ice as a function of its nanoporosity (Sect. 7.3.5).

At conditions applicable to icy satellites (i.e. subresonant, low-frequency conditions of tidal forcing), the desired mode of testing is forced oscillation. Such tests can have either a torsional or longitudinal geometry, and can be either *reversed*, meaning the applied stress (compression-tension) oscillates about zero, or *non-reversed*, in which a median stress is applied in addition to the periodic stress (compression-compression). Longitudinal forced oscillation tests on ice are often conducted with commercial testing machines, where the upper limit in frequency is the instrument resonance and the lower limit is determined by control of drift in electronics and temperature (Lakes 2004). Torsional forced oscillation pendulums have also been used to measure dissipation at subresonant frequencies. In such devices, torque is generated by a motor or an electromagnetic drive and angular displacement of the gripped specimen is measured (i.e., Ké 1947; Woirmard et al. 1977; Vassouille et al. 1978).

In addition to dynamic experiments, the attenuation response of planetary materials has been studied through quasi-static transient microcreep tests. Provided that the rheology is linear, the attenuation spectrum can be determined from the time-dependent creep function using Laplace transform techniques (e.g., Findley et al. 1976; Jackson 1993). As shown in Sect. 7.4.1, microcreep measurements and forced oscillation provide complementary information. Microcreep is an attractive method to probe attenuation properties with a single creep test. However, due to a lack of resolution in microcreep data at short time scales, static methods do not reveal the high frequency dissipation maxima observed in dynamic testing. Additionally, the low frequency transition to purely viscous (permanent) dissipation

predicted by microcreep tests has not been observed, or is possibly not available, from forced oscillation tests. (See Webb and Jackson 2003, e.g., for a comparison between datasets obtained on the same material from these two methods).

### 7.2.3 *Brief History of the Research on Ice Attenuation Properties*

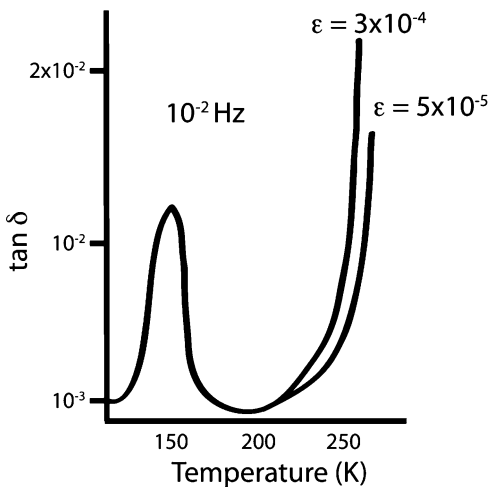
The majority of our understanding of ice properties has been obtained from studies on ice shelves and sea ice, focused on geotechnical applications or aimed at understanding the mechanical behavior of ice packs. To the best of our knowledge the first attenuation estimates on ice were obtained in the mid-1950s from analysis of primary creep measurements (Ladanyi and Saint-Pierre 1978; Brill and Camp 1961; Jellinek and Brill 1956). A number of experimental studies also focused on the relaxation of ice at high frequency (e.g., Kuroiwa 1964; Tamura et al. 1986).

The first low-frequency forced oscillation measurements were obtained during the mid-1970s in the Laboratory of Glaciology of Grenoble (e.g., Vassouille et al. 1978; Tatibout et al. 1981, 1983, 1987). These were torsional measurements obtained over a wide range of temperatures, from 120 to 273 K, and frequencies as low as  $10^{-4}$  Hz. These first experiments probed a regime of attenuation driven by proton reorientation and a grain-boundary absorption mechanism. More recently, the significant bulk of work on dissipation in both laboratory grown and natural sea ice to date has been conducted by David Cole and various coworkers (e.g. Cole 1995, 2001; Cole et al. 1998; Cole and Durell 1995, 2001). A key contribution from Cole (1995) is the development of an empirically-based model to describe relaxation in ice that is specifically tied to microstructure and defect state. This so-called Cole model will be the subject of Sect. 7.4.5.3.

### 7.2.4 *The Physics of Viscoelastic Dissipation in Ice*

Energy dissipation within a crystalline material occurs by physical mechanisms that include thermoelasticity, which is relaxation caused by thermal expansion/contraction anisotropy between grains (Zener 1948), and by motion of various types of defects: point-defects within the lattice, linear defects (dislocations), and planar defects (grain, subgrain and phase boundaries). The defect-related mechanisms are the same mechanisms that are responsible for steady-state creep, and as such, are influenced by the same factors: defect density and mobility, temperature, grain size, and stress amplitude, as well as composition and the nature of defects at all scales (including porosity). Evidence that the same defects are involved in the two different responses comes from the determination of activation energies of these processes (e.g., Webb and Jackson 2003). In addition to the mechanisms regularly associated with plasticity and anelasticity in polycrystalline material, ice experiences a large relaxation attributed to its unique and highly disordered structure. The following mechanisms have been associated with viscoelastic dissipation in ice.

**Fig. 7.3** Attenuation versus temperature of single crystal ice displaying a Debye peak at  $\sim 150$  K associated with proton rearrangement and high-temperature absorption that is strain amplitude dependent at  $T > 200$  K  
(After Tatibouet et al. 1981)



#### 7.2.4.1 Proton Reorientation

The structure of ordinary Ih ice is such that each H<sub>2</sub>O molecule is linked to others by hydrogen bonds in any of six different configurations, meaning that no long-range order in the orientation of H<sub>2</sub>O molecules exists (Pauling 1935). Statistically, there are a large number of configurations that the ice structure can take with respect to the orientation of the molecules. A change from one configuration to another comes about either by rotation of molecules or by movement of protons from one oxygen atom to another (Bjerrum 1952). Studies on single crystal ice have revealed a low-temperature (or high frequency) relaxation peak associated with this rearrangement of water molecules by rotational defects (e.g. Vassouille et al. 1978; Hiki and Tamura 1983; Tatibouet et al. 1981). The relaxation is analogous to a Zener relaxation (Zener 1947) in that it occurs because of a change in local atomic order that is affected by the presence of defects (Snoek 1939; Nowick and Berry 1972; p. 349). It takes the form of a Debye peak (seen in Fig. 7.3 centered at  $\sim 150$  K for  $f = 10^{-2}$  Hz), such that there is exponential energy decay associated with (1) a fixed length scale and (2) some loss of bond-energy wrought by application of a deviatoric stress. The presence of dopants has been found to very much affect the motion of protonic point defects, resulting in a shifting of the dissipation peak to lower temperature (Perez et al. 1986) and the creation of a second dissipation peak whose origin remains to be explained (Oguro 2001). The occurrence of proton-reorientation relaxation is expected in cold planetary material ( $T < 150$  K) subject to tidal stress at frequencies between  $10^{-5}$  and  $10^{-4}$  Hz (Castillo-Rogez et al. 2011).

### 7.2.4.2 Dislocation-Driven Attenuation

An additional influential feature of the Ih ice crystal structure is that the molecules are concentrated close to a series of parallel planes known as the *basal planes*. With the development of the X-ray topographic method in the 1970s, dislocations located on various planes within single ice crystals were observed (e.g., Webb and Hayes 1967; Fukuda et al. 1987; Duval et al. 1983; Baker 1997). The most significant finding from these studies was the remarkable anisotropy in the plastic deformation of ice, such that the creep rate by slip on the basal plane (in particular, the so-called *glide* set of basal planes; Whitworth 1980) is roughly  $10^4$  times faster, at a given stress, than creep by non-basal slip. Dislocation mobility, which is very low in ice compared to other materials, is related to the level of the Peierls barrier, which is believed to be due in part to the proton disorder described above (e.g., Louchet 2004; Song 2008; Schulson and Duval 2009).

On basal planes, where the Peierls stress is high, attenuation occurs by motion of dislocations (and dissociated partials) via nucleation and migration of geometrical kinks over a Peierls potential hill (e.g., Karato and Spetzler 1990; Karato 1998; Jackson 2007). The simple schematic in Fig. 7.4a demonstrates this type of attenuation mechanism, though, in reality, dislocation loops in the basal plane expand under stress into screw and  $60^\circ$  orientations to take up a hexagonal form, as seen at A in Fig. 7.4b (Ahmad and Whitworth 1988). The purely anelastic relaxation due to the nucleation and migration of a pair of kinks should result in a *Bordoni peak* that is independent of strain amplitude and broader than a peak with a single relaxation time (e.g., Niblett and Zein 1980). The height and shape of the peak are expected to be sensitive to the degree of strain, with a sharper, more defined peak occurring with increased deformation (Nowick and Berry 1972, p. 378). In experiments on polycrystalline ice, Cole and his colleagues applied a uniaxial load that cycled between compression and tension. The zero-mean-stress of their method implied that no plastic deformation occurred during testing, such that no new dislocations were created. They determined, therefore, that observed loss, which showed a shallow frequency dependence and slight drop at the lowest frequency, was due almost entirely to motion of existing dislocations on basal planes, the density of which they controlled by applying various amounts of pre-strain to samples (Cole and Durell 2001).

In more realistic geologic settings, however, relaxation will also be sensitive to the long-term stress. At very low frequency (or high temperature) pinning mechanisms become ineffective and there will be a gradual transition from anelastic to viscous behavior (Karato and Spetzler 1990; Jackson 2007). The transition occurs when single kink nucleations lead to successive nucleation and/or unpinning of dislocations (Karato 1998).

Although the bulk of deformation in polycrystalline ice occurs by slip on basal glide planes, not every grain can be kinematically oriented favorably. On non-basal planes, where the Peierls stress is low, dislocations are instead curved, as seen at S in Fig. 7.4d (Ahmad and Whitworth 1988). Although edge dislocations can move

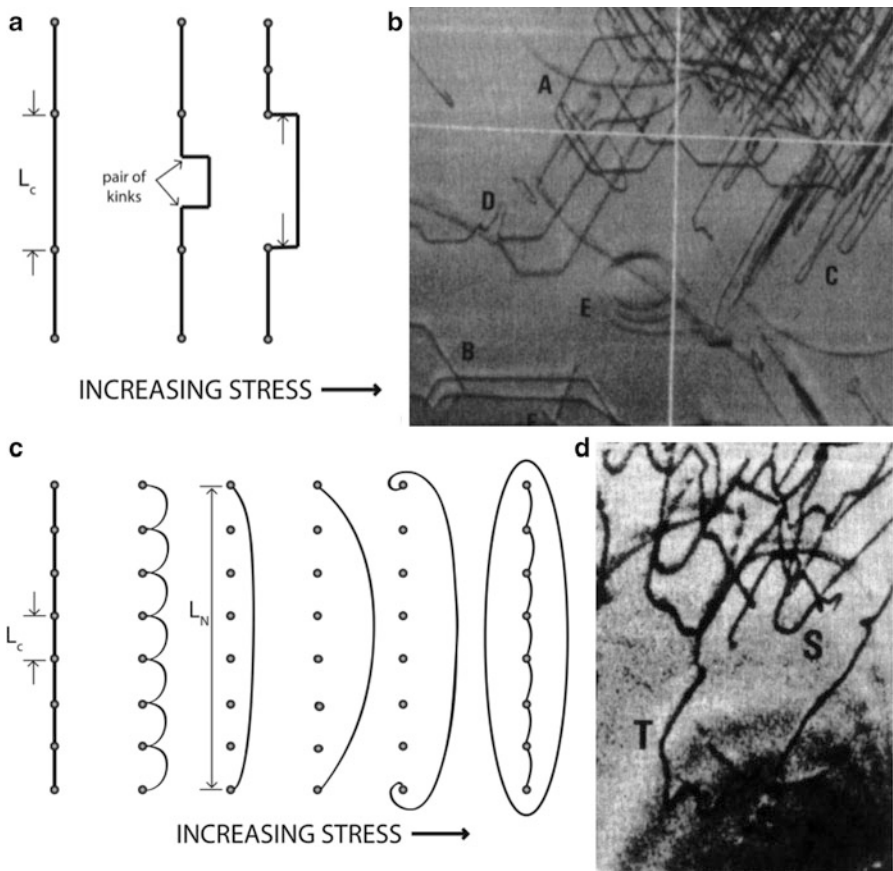


**Fig. 7.4** Schematics of dislocation-based dissipation mechanisms and examples of such dislocations in X-ray topography images of single crystals of ice: (a) the formation and migration of kink pairs on basal planes where Peierls stress is high, as described by Karato (2008); (b) straight and hexagonal loop (A) dislocation segments on the basal plane (Ahmad and Whitworth 1988); (c) the bowing out and eventual breakaway of a dislocation segment in a glide plane with low Peierls stress, as described by the Granato-Lücke model (1945), and (d) curved dislocation segments in non-basal (possibly pyramidal) planes (Ahmad and Whitworth 1988) with permission from Taylor & Francis Ltd. <http://www.tandfonline.com>

very fast on non-basal planes, screw dislocations cannot glide at all. Therefore, macroscopic slip on non-basal planes is extremely difficult. However, small-scale anelastic relaxation from oscillating dislocations on these planes is likely an additional contribution to attenuation. The prevailing model for this type of low Peierls stress, dislocation-based damping is that proposed by Granato and Lücke (1956), which describes a three-dimensional network of pinned dislocations behaving like stretched vibrating strings that are pinned at the ends (a distance  $L_N$  apart), perhaps by other quasi-immobile dislocations (Tatibouet et al. 1986). They are also pinned at various points along their lengths, the average distance between which is  $L_C$  (Fig. 7.4c).

The pinned dislocations oscillate between one equilibrium position and another under alternating stress. With increasing stress amplitude, motion of the dislocation segments transitions from bowing out between pinners to partial breakaway to eventual catastrophic breakaway (Burdett and Queen 1970). Although the Granato-Lücke model has not been well constrained in ice, some form of dislocation breakaway and multiplication is needed to explain the high-temperature, strain-amplitude-dependent attenuation that is observed in ice (Fig. 7.3).

#### 7.2.4.3 Grain-Boundary Sliding (GBS)

Grain boundaries are planar defects in polycrystalline materials that have long been identified as important players in both plastic deformation and energy dissipation. In reality, grain boundaries are far from planar and instead are curved or jagged interfaces. Sliding on nonplanar surfaces can only occur for very small distances before configurational incompatibilities cause stress concentrations at triple junctions to develop (Ké 1946; Raj and Ashby 1971; Raj 1975). Further sliding requires accommodation by one or more of the following: localized elastic deformation of grains (described below); grain-scale diffusive flux of atoms (Ashby and Verrall 1973) or by motion of lattice dislocations (e.g., Ké 1999). For the diffusional mechanism, a rapid flux of matter away from high-traction triple junctions occurs in response to the steep stress gradient along grain boundaries. When diffusive flux is responsible for dissipation, the attenuation spectra takes on a weak frequency dependence that persists for many decades of frequency. Often called the “high-temperature background,” this power law absorption (i.e.  $Q^{-1} \propto f^{-m}$  where  $m$  is between 1/2 and 1/3) has been observed for many materials at high homologous temperature and has been attributed to the diffusion-effected evolution of normal traction on grain, subgrain and/or phase boundaries (Gribb and Cooper 1998; McMillan et al. 2003; McCarthy et al. 2011b).

Recent experimental studies on polycrystalline ice in which samples experienced both a periodic and a long-term constant stress observed moderate power law relationship similar in form to that of silicates (e.g., McCarthy et al. 2008). Because the diffusivity of ice at its melting point is three to four orders of magnitude less than values found for silicate minerals and metals, diffusion-driven relaxation of stress is slow, and the mechanism only becomes dominant when the stress and material geometry become less favorable for other deformation mechanisms. Although diffusion-based creep mechanisms have not been directly observed in water ice at laboratory conditions, such mechanisms are predicted by theory to be expressed under very low stress and in very fine-grained samples (e.g., Goldsby and Kohlstedt 2001). That the dynamic response of polycrystalline ice simultaneously deforming with non-Newtonian rheology revealed a high-temperature background of the same form found in silicate minerals (with Newtonian rheology) is therefore remarkable. It suggests that, despite creeping by non-Newtonian deformation mechanisms of dislocation-accommodated grain boundary sliding and dislocation creep, the small periodic stress potential of forced oscillation experiments samples

an additional mechanism, that of chemical diffusion at grain (or subgrain) boundaries, or by some mechanism that supplies a distribution of compliances to give the characteristic broad band of attenuation. This needs to be moderated however by the presence of impurities and partial melt, which are expected to modify the material geometry and effect the expression of grain boundary sliding (see further details in Sect. 7.5).

An additional dissipation mechanism attributed to grain boundaries has been observed in the form of a plateau in the high frequency range of attenuation spectra in some materials. The shape of the spectra has commonly been attributed to the superposition of a Debye peak associated with “elastically-accommodated grain boundary sliding” (e.g., Ké 1947). According to classical theory, grain boundary sliding at high frequency and/or low temperature is accommodated not by diffusion but instead by local elastic deformation of grains (Raj and Ashby 1971). In that sense, this mechanism may be the geometrically needed first step to long-range diffusionaly accommodated grain boundary sliding discussed above (Barnhoorn et al. 2007; Sundberg and Cooper 2010). The mechanism is considered to be rate-limited by grain boundary viscosity.

Dynamic studies on non-deformed and annealed samples of polycrystalline ice have confirmed the presence of an attenuation peak at high temperatures attributed to grain boundary sliding (Cole et al. 1998). Interestingly, samples that were strained to 1% showed an increase in the high-temperature background attenuation that caused the grain boundary peak to nearly disappear (Tatibouet et al. 1987). These works suggest that the anelastic response of polycrystalline ice at high temperature is due to a combined effect of dislocation and grain boundary sliding-based mechanisms, such that strain history is critical to the response.

### 7.2.5 Shear Versus Bulk Viscoelasticity

Outer planet satellites are subject to both compression-extension and shear stresses that result from the combination of a radial component and a librational component (phase lag of the equatorial bulge) (Murray and Dermott 2000; Greenberg et al. 1998, their Figure 1). The radial component is a function of the material attenuation properties under compression while the librational component produces shear deformation of the material, and the associated dissipated energy is thus a function of the shear dissipation factor.

Most forced oscillation experiments on polycrystalline ice have used uniaxial loading and, thus, measured the Young’s modulus E dissipation,  $Q_E^{-1}$ , which is a combination of bulk  $k$  and shear  $\mu$  moduli dissipation according to:

$$Q_E^{-1} = \frac{\mu}{3k + \mu} Q_k^{-1} + \frac{3k}{3k + \mu} Q_\mu^{-1}. \quad (7.1)$$

Using the standard relationships between elastic moduli and the Poisson's ratio of ice (0.325) means that Young's modulus type experiments on polycrystalline ice measure  $Q_E^{-1} \cong 0.12 Q_k^{-1} + 0.88 Q_\mu^{-1}$ . Therefore, care must be taken to use the appropriate loading mode of dissipation when applying laboratory data to tidal stress modeling and when comparing ice attenuation measurements to those of rocky materials, which are traditionally obtained in a torsional geometry (i.e., 100%  $Q_\mu^{-1}$ ).

Another consideration is related to the significant anisotropy of monocrystalline ice (Young's modulus of  $\sim 8$  GPa along the  $a$ -axis vs. 11.5 GPa along the  $c$ -axis) and how this is expected to influence anelastic properties. Although an aggregate with randomly dispersed grains can be treated as an isotropic solid behaving independently from orientation, ice that has aligned grains, i.e. a fabric, cannot be treated so simply. Strain-induced anisotropy in polar ice, for instance, is known to significantly affect shear viscosity (e.g., Staroszczyk and Morland 1999). Studies on unidirectionally solidified first-year sea ice found that anisotropy affects attenuation as well. Specifically, the magnitude of dissipation was found to be proportional to an orientation factor, which is determined by the average shear stress resolved on basal planes (Cole et al. 1998). So application of attenuation measurements made on laboratory prepared isotropic ice to actively deforming icy shells (where fabric formation is certainly possible) is not straightforward.

### **7.2.6 Linear and Non-linear Deformation**

At high enough levels of strain, all materials will display some nonlinear effect or strain amplitude-dependence. Single crystals of ice tested at laboratory conditions have shown a distinct nonlinearity at strains as low as  $2 \times 10^{-5}$  (Fig. 7.3). The higher the temperature and lower the frequency, the more pronounced the strain-amplitude dependence (Tatibouet et al. 1986). Amplitude-dependent attenuation has been observed in polycrystalline ice as well (Cole and Durell 1995; Tatibouet et al. 1981). For the temperatures and frequencies tested by Cole and Durell (1995), decreasing anelasticity with decreasing peak stress that was quasi-linear for stresses smaller than 0.3 MPa was observed and tended toward zero as stress decreased.

Strains as high as  $2 \times 10^{-5}$  are expected in the icy shells of outer planet satellites such as Europa (Tobie et al. 2003) and Enceladus (Nimmo et al. 2007). Therefore it is reasonable to expect some nonlinearity in the response of the shell material. In that case, some basic assumptions about viscoelasticity break down. For instance, the transition to fully viscous behavior does not necessarily correspond to the Maxwell time. Thus, it is possible that, even if the tidal forcing frequency is close to the material's Maxwell frequency, a Maxwell solid model (Sect. 7.4.4.1) may underestimate the amount of dissipation resulting from cyclic stressing.

## 7.3 Laboratory Measurements on Planetary Ices: State of the Art

In the previous section we addressed the state of knowledge of attenuation in crystalline water ice. However, planetary ices encompass a wide range of composition in the form of second-phase impurities. Of specific relevance is the presence of a variety of hydrates: ammonia and methanol hydrates, hydrated salts, clathrate hydrates (see chapters by de Bergh et al. and Choukroun et al. in this book). The influence of these species on the overall behavior of a mixture of icy material depends on the form under which they condensed in the ice: soluble species at the grain boundaries, dopants within the ice lattice, or condensates within the ice matrix. Another important problem addressed in this section is the role of microstructure on attenuation and its evolution as a consequence of accumulated strain. We also briefly address the state of knowledge about dissipation properties of amorphous ice, because of its relevance to binary Kuiper Belt Objects.

### 7.3.1 *Dopants and Soluble Impurities*

Impurities in ice may be present within the crystal lattice as dopants or localized at grain boundaries. Dopants of relevance to icy satellites are ammonia and various chlorides. These particles can enter the lattice and increase the dissipation at a given temperature. The impact of various impurities on the attenuation associated with proton reorientation has been studied. Dopants (both KOH and HF) tend to decrease the temperature at which the proton-ordering associated maximum of dissipation is encountered at a given frequency (Perez et al. 1986; Oguro 2001; see also a review by Petrenko and Whitworth 1999). Studies have also focused on the influence of doping on dislocation-based damping in single crystal and polycrystalline ice. The bonding environment in the presence of HF molecules is such that dislocations can move more rapidly, thus weakening the ice and resulting in higher attenuation and larger strain-amplitude dependence (Perez et al. 1986; Tatibouet et al. 1986). Additionally, HF-doping of polycrystalline ice causes a peak associated with grain boundaries to move to higher temperature (Tatibouet et al. 1987).

### 7.3.2 *Partial Melting and Slurries*

The role of partial melt in the dissipation of planetary materials has been investigated experimentally for a variety of silicates and oxides in an effort to link seismic observation with a partially molten, low seismic velocity zone in the earth. In the case of terrestrial rocks, various studies have shown that a few percent of melt is sufficient to significantly increase dissipation (e.g., James et al. 2004;

Fountaine et al. 2005). The mechanisms by which melt influences wave velocity, modulus and attenuation are known as the “poroelastic effect” and the “anelastic effect”. Poroelastic effects are due to the large compressibility and little to no rigidity in the melt phase resulting in a decrease in elastic moduli of the solid-liquid composite. Energy dissipation occurs via “squirt flow” of viscous melt between neighboring pores (Mavko 1980). Extensive theoretical studies have been performed on this poroelastic effect to determine the modulus reduction and timescale of relaxation based on the geometry of the system and the melt fraction and viscosity (e.g., O’Connell and Budiansky 1977; Mavko et al. 1998). Unless the pore aspect ratio is very small, the characteristic frequency for the poroelastic effect on  $Q^{-1}$  is much higher than the seismic frequency range.

The anelastic effect of partial melt is the enhancement of grain boundary sliding. The specific anelastic response of partially molten systems is believed to be strongly influenced by melt geometry (e.g., Mavko 1980), that is, by the wetting behavior of the melt with respect to the crystalline solid, which is determined by the interfacial energies of the solid/melt system (e.g., Nye and Frank 1973; Waff and Bulau 1979). In the case of silicate partial melt systems, the general consensus is that melt resides in an interconnected network of triple grain junctions. Several studies found that the presence of a texturally equilibrated melt phase does little to the steady-state Newtonian (Cooper and Kohlstedt 1984) and non-Newtonian (power law) (Beeman and Kohlstedt 1993) creep behavior, other than create a minor enhancement of creep rate due to the reduction in diffusive path length. The increase in attenuation in specimens with such melt geometry was solely attributed to the viscosity decrease; the melt-bearing samples presented the same attenuation “band” observed in melt-free samples (Gribb and Cooper 2000).

(1) When interfacial energies instead dictate a completely wetted grain boundary, (2) where lenses and larger pockets of melt are present (Faul et al. 2004), or (3) in the case of non-equilibrium geometries (Fountaine et al. 2005), a broad dissipation peak superimposed on the background has additionally been observed and attributed to enhancement of elastically-accommodated grain boundary sliding (see Sect. 7.2.4) (Faul et al. 2004; Jackson et al. 2006). The relaxation timescale is dependent on melt viscosity and the aspect ratio of grain boundary regions such that the position and dimensions of the absorption peak evolve as the fraction of melt increases. Dissipation has been found to increase as the melt fraction increases up to 25% (Fountaine et al. 2005).

The dihedral angle of ice and water is approximately 20° and thus the equilibrium form should consist of channels of water at three-grain intersections (Nye and Frank 1973). However, significant variation in equilibrium geometry (e.g., Mader 1992) and thin films at grain boundaries (Dash et al. 2006) have also been observed in polycrystalline ice, even at subsolidus temperatures. Small amounts of impurities, which are driven from grains during crystallization and therefore concentrate at grain boundaries, are known to greatly enhance complete surface melting. Though a thorough examination of attenuation in ice + melt systems has not yet been conducted, Cole and Durell (1995) observed a decrease in modulus and increase in anelasticity above the eutectic melting temperature in laboratory-grown saline samples.

Both the elastic and anelastic responses were amplified with increased salt content, consistent with previous observations made via resonance techniques (Spetzler and Anderson 1968). The effect of partial melt on ice properties is particularly significant in planetary settings where the auxiliary phase results in a deep eutectic with ice, such as with sulfuric acid or ammonia. The icy shells of satellites with such chemistry could consist of a significant melt phase. Thus the effect of partial melt on the attenuation of ice is a topic of continued interest.

### 7.3.3 *Solid Particles and Second Phases*

Solid particles, such as silicates, and second phases, such as hydrates, located at the grain boundary region may play a significant role in grain boundary sliding. Theoretical studies determined that unless solid particles are of the order of a few nanometers, they most likely inhibit diffusion at the grain boundaries (Raj and Ashby 1971). Experimentally, it has been found that second phases impede grain boundary sliding, increase viscosity, and thus limit internal friction at low stress (e.g., Jackson et al. 2002 for silicates; Song et al. 2006 for ice). Although inhibition of GBS is expected to decrease attenuation in a two-phase system at low stress, this is countered by the increase of dislocation density and an additional mechanism of dissipation at heterophase boundaries (Buechner et al. 1999). However, above a certain stress, pile-ups of dislocations at phase boundaries cause local stress concentrations that result in multiplication of dislocations and/or fracture of second phases, thus enhancing the creep rate (McCarthy et al. 2011a). The idea that softening can occur at high stress raises an important question as to the applicability to icy satellites. It implies that the impact of silicates and other second phases on the rheology of icy satellite material is a function of tidal stress amplitudes. In general, the increase of viscosity due to silicates is inferred from empirical relationships established by measurements obtained at relatively large stress (e.g., Friedson and Stevenson 1983) in comparison to the tidal stress amplitude of icy satellites. These authors considered a low content of silicate grains (<4 vol%). For a high content of silicates, jamming between silicate grains may become the main feature limiting creep, as demonstrated by the experimental work of Durham et al. (2009). Silicate particles also act in preventing grain growth, which indirectly influences the mechanical properties of the material (Goodman et al. 1977; Barr and Milkovich 2008).

### 7.3.4 *Porosity*

Several theoretical studies have been developed to estimate the decrease in elastic moduli due to porosity and/or cracks based on the geometry and volume fraction of cavities (e.g., Kuster and Toksöz 1974; Wu 1966; Mavko et al. 1998). The analysis is identical to the case of fluid-filled pores but, here, the modulus of the dry or empty

inclusion is zero. For both saline and non-saline low porosity ice ( $\phi < 0.1$ ), a decrease in effective Young's modulus has been observed (Cole 1995; Cole and Durell 1995) and found to follow the form:  $E(\text{GPa}) = 10.0\text{--}35.1\phi$  (Langleben and Pounder 1963). It has been posited that in small icy satellites (<1000 km in radius), modest self-gravitation further decreases effective modulus, which should enhance the tidal evolution of binary asteroids (Goldreich and Sari 2009).

Studies have also investigated the influence of porosity on energy dissipation. One source of relaxation for cracked or porous solids is related to relaxation of shear stress within each pore. The characteristic relaxation frequency for the mechanisms is  $\omega \approx (\mu/\eta)(c/a)$  where  $\mu$  is the shear modulus of the solid,  $\eta$  of the fluid (or zero viscosity void) and  $c/a$  is the aspect ratio of the void, so that, unless the aspect ratio of voids is extremely small, the characteristic frequency is in the MHz range (O'Connell and Budiansky 1977). That an increase in attenuation with increased porosity was observed at low frequencies in saline ice (Cole and Durell 1995) suggests that the relaxation was due, not to gas filled pores, but to fluid moving through very small aspect ratio cracks or brine channels. Since the measurements were made on saline ice at temperatures well above the eutectic melting temperature, this can reasonably assumed to be the case. Increased attenuation in 1% saline ice in the kHz range has been interpreted as flow between fluid pockets with aspect ratio  $10^{-3}$  (Spetzler and Anderson 1968; O'Connell and Budiansky 1977).

Other studies on porosity consider the case of a granular (i.e., unsintered) material typical of rubble-piles (e.g., Pilbeam and Vaisnys 1973). For these cohesionless soils, energy dissipation is caused by friction at grain-to-grain contacts and is sensitive to confining pressure. If the shear stress amplitude is less than the product of the normal force and the coefficient of friction, then the main source of mechanical loss is by static friction at the grain boundaries (e.g., Mindlin 1954; Pilbeam and Vaisnys 1973; Winkler and Murphy 1995). Experimental data gathered in the final reference indicates that the effective dissipation factor corresponding to static friction is on the order of 100–1000 under pressure conditions ( $P < 10 \text{ MPa}$ ) relevant to small irregular satellites, like Janus and Epimetheus. Porosity in such settings would greatly influence the acoustic properties of the icy shell and possibly the attenuation at seismic frequencies, depending on the shape of cavities. Acoustic methods have been very successful in measuring porosity in geologic and engineering materials. However, at frequencies relevant to tidal forcing of icy satellites, there is no reason to expect anelastic dissipation due to porosity.

However, when shear stress exceeds the confining pressure, macroscopic frictional sliding between grains results in dissipation that is strain amplitude dependent and that decreases with confining pressure. Details about the physics driving frictional sliding can be found in the chapter by Erland Schulson. That problem has been approached by Nimmo et al. (2007) in the case of friction along Enceladus' Tiger stripes.

### 7.3.5 *Amorphous Ice*

Constraints on the mechanical properties of amorphous ice are scarce. To the best of our knowledge, no data has been obtained on the attenuation properties of amorphous ice under conditions relevant to planetary bodies. As amorphous ice is difficult to produce in laboratory and is mostly handled in the form of thin films formed under a low-vapor atmosphere on a cold plate at temperatures below 100 K, the only method so far to test their attenuation properties is with a vibrating plate in the kHz-MHz frequency range (see Sect. 7.2.2). Such experiments carried out by Hessinger et al. (1996) proved a very useful approach for constraining the amount of nanoporosity in low-density amorphous ice. At these frequencies, the quality factor is very sensitive to nanoporosity so that a freshly deposited amorphous ice sample is characterized by a small value of Q (on the order of 10). That parameter increased as the sample was warmed up and the porosity annealed, as indicated by an increase of the ice density.

Attenuation data are also lacking for other rare forms of ice that are believed to be present in planetary bodies but are difficult to produce in the lab, such as cubic ice and high-density forms of amorphous ice.

### 7.3.6 *Material Aging*

In polycrystalline material, various mechanisms are expected to play a role in the aging of the samples: grain growth, recrystallization, and rearrangement of dislocations (e.g., Taupin et al. 2008). The effect of aging is a common phenomenon largely studied in materials science. Tatibouet et al. (1981) studied the effects of both thermal aging and plastic aging and found that thermal aging of monocrystalline ice is characterized by an increase in internal friction (under torsion) and that plastic aging enhances the total aging rate. Plastic aging results from the multiplication of dislocations as a consequence of Frank-Read source mechanisms (e.g., Tatibouet et al. 1981) and their accumulation as an effect of viscous strain. The stress at which these dislocations form decreases with increasing temperature (e.g., Goldsby 2007).

Tatibouet et al. (1981) also show that accumulation of dislocations during aging can lead to polygranulation of the ice. Johari et al. (1995) measured the complex Young's modulus of aged polycrystalline ice samples and observed a decrease in effective modulus by 30% after only ~30 h of sample aging, after which that modulus reached equilibrium. For their coarse-grain samples and temperatures in the 240–260 K range, phase lag continuously increased for the first ~50 h of testing; this parameter then decreased and seemed to reach an equilibrium (or at least evolve slowly) by the end of the 240-h long test. Thus, while the change in elastic properties rapidly reached equilibrium, the internal friction in these samples evolved on a longer timescale. However, after several hundred hours of aging (thermal or plastic), these authors observed a decrease in internal friction, which they interpreted as a result of a change in dislocation density. Cole and Durell (2001) interpreted the decrease in internal friction as dynamic recovery under low stress.

## 7.4 Quantifying Viscoelasticity and Attenuation

Deformation in a geologic setting involves mechanisms acting over a range of time scales. Some mechanisms can be easily captured by steady-state creep experiments. Others, which represent only small deviations from purely elastic behavior, involve strains so small as to be nearly undetectable by creep experiments. Instead, attenuation experiments “tickle” a material by applying a very small dynamic load. Here we supply the mathematical relationships between the static (creep) response and dynamic response and provide a summary of various mechanical models that have been used to describe the viscoelasticity of ice and other planetary materials.

### 7.4.1 Stress–Strain Relationships in the Time Domain

The steady-state creep response of water ice has been studied a great deal, and several decades of laboratory measurements have led to the identification of empirical relationships that can predict the viscosity of water ice for a wide range of conditions. It is beyond the scope of this chapter to address the origin and development of these relationships, and we refer readers to key references and detailed reviews on the topic: Goodman et al. (1981), Duval et al. (1983), Weertman (1983), Goldsby and Kohlstedt (2001), Durham and Stern (2001), Castelnau et al. (2008).

The relationship between strain rate and differential stress, temperature, and grain size is generally quantified by the semi-empirical power law:

$$\dot{\varepsilon} = A \frac{\sigma^n}{d^p} \exp\left(\frac{-E_a^*}{RT}\right), \quad (7.2)$$

where  $A$  is a factor associated with aspects of microstructure (exclusive of grain size), chemical potentials and geometry,  $n$  and  $p$  are constants that reflect the (power law) sensitivities to  $\sigma$  the stress,  $d$  the grain size,  $E_a$  corresponds to the activation energy,  $R$  is the gas constant, and  $T$  the temperature. Although all thermally activated mechanisms will be operating simultaneously in a stressed system, at a given set of conditions, only one will dominate and will be characterized by a unique combination of values for  $n$ ,  $p$  and  $E_a$ . Thus the flow of ice over a broad range of conditions can be described by a composite “flow law” (e.g., Goldsby and Kohlstedt 2001):

$$\dot{\varepsilon} = \dot{\varepsilon}_{BD} + \dot{\varepsilon}_{VD} + \left( \frac{1}{\dot{\varepsilon}_{GBS}} + \frac{1}{\dot{\varepsilon}_{BS}} \right)^{-1} + \dot{\varepsilon}_{DC} \quad (7.3)$$

where each term is a power law of the form in Eq. 7.2 and the subscripts correspond to:  $BD$  for grain boundary diffusion (or Coble creep),  $VD$  for volume diffusion

(or Nabarro-Herring creep), *GBS* for grain-boundary sliding, *BS* for basal slip, and *DC* for dislocation creep.

The time dependent behavior of viscoelastic materials can be described by a *creep compliance*  $J(t)$ :

$$J(t) = J_U + F(t) + \frac{t}{\eta_{ss}}, \quad (7.4)$$

where  $J(0) \equiv J_U$  is defined as the unrelaxed compliance, which represents the immediate response to forcing,  $F(t)$  is some function of time (examples of which are described in Sect. 7.4.5) and  $\eta_{ss}$  is the steady-state viscosity.

Stress relaxation is the compliment to creep; it is the time dependent response to a fixed amount of strain that is applied instantaneously and held constant. The gradual decrease of stress that results is the stress relaxation function  $M(t)$ , from which is defined  $M(0) \equiv M_U$ , the unrelaxed modulus (Nowick and Berry 1972). Because there is a unique relationship between stress and strain, the relaxed modulus and compliance are reciprocal, i.e.,

$$M_R = \frac{1}{J_R}. \quad (7.5)$$

#### 7.4.2 Stress–Strain Relationships in the Frequency Domain

The dynamic, or frequency-dependent, behavior of viscoelastic materials is described by the *complex compliance*  $J^*(\omega)$  and the *complex modulus*  $M^*(\omega)$ . When a small periodic stress is applied, it follows the form  $\sigma(t) = \sigma_0 \cos \omega t$ , where angular frequency  $\omega = 2\pi t$ . In complex notation, this stress can be expressed as  $\sigma^* = \sigma_0 e^{i\omega t}$  and the material response, by requirement of linearity, will be at the same frequency. The complex compliance, which is the ratio of periodic strain to stress, is related to the time domain response by transform according to:

$$J^*(\omega) = i\omega \int_0^\infty J(t) \exp(-i\omega t) dt \quad (7.6)$$

where  $s = i\omega$  is the transform variable (e.g. Findley et al. 1976; Karato 2008). The complex compliance can also be written:

$$J^*(\omega) = \frac{\varepsilon_0}{\sigma_0} = J_1(\omega) - iJ_2(\omega) \quad (7.7)$$

where the real part,  $J_1(\omega)$ , is called the “storage compliance”, and the imaginary part,  $J_2(\omega)$ , the “loss compliance” with:

$$\begin{cases} J_1(\omega) = J_U + \omega \int_0^\infty (J(t) - J_U) \sin \omega t dt \\ J_2(\omega) = -\omega \int_0^\infty (J(t) - J_U) \cos \omega t dt \end{cases} \quad (7.8)$$

Similarly, the *complex modulus* is defined as

$$M^*(\omega) = \frac{\sigma_0}{\varepsilon_0} = [J^*(\omega)]^{-1} = [J_1^2(\omega) + J_2^2]^{-\frac{1}{2}} \quad (7.9)$$

Since the periodic strain can be expressed as  $\varepsilon^* = \varepsilon_0 e^{i(\omega t - \delta)} = J^*(\omega) \sigma_0 e^{i\omega t}$ , then

$$\begin{aligned} J_1(\omega) &= \frac{\varepsilon_0}{\sigma_0} \cos \delta \\ \text{and} \\ J_2(\omega) &= \frac{\varepsilon_0}{\sigma_0} \sin \delta \end{aligned} \quad (7.10)$$

where  $\delta$  is the phase lag between stress and strain, also known as the loss angle, and:

$$\tan \delta = \frac{J_2(\omega)}{J_1(\omega)} = \frac{M_2(\omega)}{M_1(\omega)}. \quad (7.11)$$

The real and imaginary parts of  $J^*$  and  $M^*$  are not independent but are related such that if either  $J_1(\omega)$  or  $J_2(\omega)$  (or either  $M_1(\omega)$  or  $M_2(\omega)$ ) is known for all frequency ranges (or at least for a very wide range), then the other can be calculated according to a mathematical property called the Kramers-Krönig relation.

### 7.4.3 Phase Lag and Attenuation

When the sinusoidally time-varying stress of a viscoelastic material is plotted against the sinusoidally time-varying strain of the same frequency, a hysteresis loop is formed, the dimensions of which represent various material properties (Fig. 7.5). The slope of the diagonal line bisecting the ellipse, for instance, is the absolute dynamic modulus  $|M^*(\omega)|$ . The area within the ellipse represents the energy per volume per cycle dissipated in the material,  $\Delta W$  (e.g., Lakes 1999).

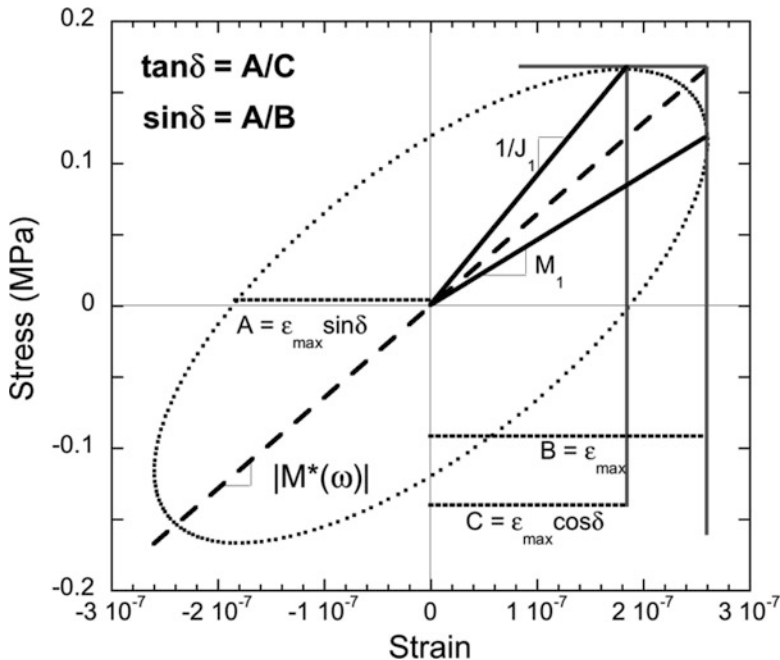


**Fig. 7.5** Plot of cyclic stress versus cyclic strain, known as a Lissajous, or hysteresis loop. The dimensions of the elliptical loop provide values for various material properties (After Lakes 2004). In particular, the width of the figure is a measure of the phase lag  $\delta$ , such that a purely elastic material would plot as a straight diagonal line with zero thickness. The figure shown here was generated using data from a particularly “lossy” material, ice + MS11 eutectic mixture, at 240 K and 0.1 Hz

The ratio of  $\Delta W$  to the maximum elastic energy stored,  $W$ , for a given amplitude is equivalent to the inverse ratio of the real and imaginary parts of the complex compliance. According to the most commonly used definition, these ratios are related to the phase lag by:

$$\tan \delta = \frac{J_2}{J_1} = \frac{\Delta W}{2\pi W} = Q^{-1} \quad (7.12)$$

where  $Q$  is called the quality factor and its inverse is attenuation, the commonly adopted measure of damping in experimental studies (e.g., Nowick and Berry 1972; O’Connell and Budiansky 1978). However, it should be noted that within the context of tidal forcing, Eq. 7.12 assumes small dissipation. When considering a particularly lossy response, where phase lag is quite large, the simple relation of  $\tan \delta$  with  $Q^{-1}$  breaks down and a more precise definition should instead be employed (please see the Appendix of Efroimsky and Williams 2009 for a detailed derivation of  $Q^{-1}$ ).

### 7.4.4 Simple Dissipation Models

A major goal of the research on material attenuation properties is to establish empirical relationships between quality factor and frequency. Such a relationship is important in order to extrapolate attenuation to conditions that cannot be probed by experimental techniques. This is especially relevant in the case of tidal forcing as it spans a frequency range from  $10^{-4}$  down to  $10^{-6}$  Hz (Fig. 7.1), which is difficult to obtain with existing techniques.

Many mechanical models have been proposed to describe material response. For purposes of visualization, these are often depicted as a collection of elastic springs and viscous dashpots, which, following the *Boltzmann superposition principle*, can be summed to represent an overall response. As previous researchers have admonished, however, these models should serve solely as a pedagogical device and are not truly representative of mechanical behavior (Lakes 1999; Cooper 2002).

A well-established method to evaluate mechanical behavior is to fit one of these models to a material's observed creep compliance  $J(t)$ . From this, the complex properties of  $J^*(\omega)$  and  $M^*(\omega)$  can be obtainable by application of the Laplace transform in Eq. 7.6. Here we present various phenomenological models of compliance that have been used, with varying degrees of success, to represent the mechanical response of a material to an applied stress. All of these models have known transforms tabulated in various references (e.g. Findley et al. 1976; Karato 2008). A review of the various relationships used in the literature on satellite dissipation can be found in Efroimsky and Lainey (2007) and Castillo-Rogez et al. (2011).

#### 7.4.4.1 The Maxwell Model: Advantages and Limits

Most of the planetary studies on solid bodies have relied on the Maxwell model to describe dissipation. The Maxwell model (e.g., Maxwell 1867; Zschau 1978) offers the primary advantage that the phase lag can be expressed by two intrinsic properties: elasticity and viscosity. These two properties are represented in Fig. 7.6 by an ideal elastic spring (energy storage element) and a purely viscous dashpot (dissipation element). For a Maxwell model, the two elements are arranged in series. The single relaxation time represents the amount of time required for the energy stored in the spring to shift to and be dissipated by the dashpot. The real and imaginary components of the complex compliance for the Maxwell model are:

$$\begin{cases} J_1^{Max}(\omega) = \frac{1}{k} \\ J_2^{Max}(\omega) = \frac{1}{\eta\omega} \end{cases} \quad (7.13)$$

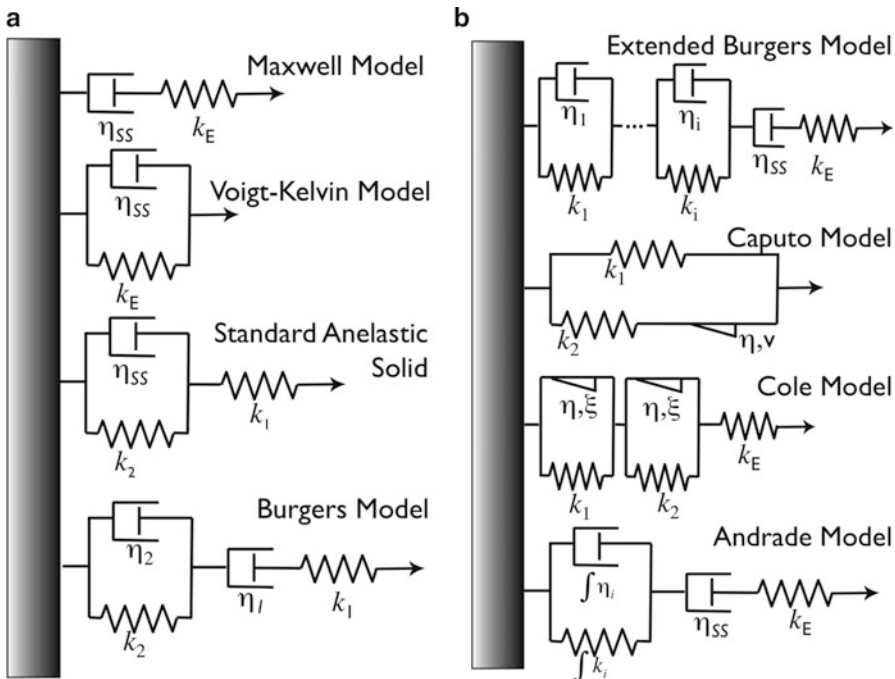


**Fig. 7.6** Simple spring-and-dashpot models used to illustrate the components of various viscoelastic solid models, where a spring represents the elastic response, a dashpot the viscosity, and a spring-pot (triangle) is a fractional order response

As a result, it is possible to express the dependence of attenuation directly as a function of the angular frequency, so that  $\tan\delta = k/\eta\omega \propto \omega^{-1}$ .

A major historical reason that the Maxwell model has been the preferred model in planetary science is that it has relatively simple expressions for calculating attenuation and it renders reliable quantification of attenuation in some metals and rocks at high frequency (in the Hz to kHz range, e.g., Coyner and Randolph 1988). The Maxwell model has also been found to properly match the behavior of Earth's terrestrial material relaxed over long time scales, such as glacial rebound (e.g., Romanowicz 1994). More generally, the Maxwell model has been used to describe ice frequency-dependent anelasticity when forcing periods approximate the Maxwell time (e.g., Tobie et al. 2005 and references therein). However, the attenuation spectrum yielded by the Maxwell model significantly departs from experimental observations at frequencies greater than the Maxwell frequency.

The Maxwell model yields dissipation models that are infinitely large as temperature decreases. Simply put, the Maxwell model is not built to properly describe the mechanical properties of ice because it lacks a component accounting for anelasticity. However, the systematic application of the Maxwell model has been justified by the lack of comprehensive appreciation of ice anelasticity.

#### 7.4.4.2 Voigt/Kelvin Model

Whereas a Maxwell model describes a spring and dashpot in mechanical series, the Voigt/Kelvin model takes those two elements and places them instead in mechanical parallel, so that both elements experience the same stress. When stress is first applied, the response is almost entirely viscous, but with time, the viscous element elongates and stress is gradually transferred to the elastic element. This model, often called delayed elasticity, does not contain a term for the initial elastic response on loading, nor does it contain a term for permanent plastic response. Thus, like the Maxwell model, by itself the Voigt/Kelvin model cannot describe the phenomenological behavior of viscoelastic materials over the full range of time.

### 7.4.5 Models Accounting for a Transient Creep Component

#### 7.4.5.1 Standard Anelastic Solid

To closer approximate the response of solids, a three parameter mechanical model employs a Voigt/Kelvin unit in mechanical series with a single spring  $k_1$  (Fig. 7.6a). This combination (also called a Zener model) describes an initial response entirely by  $k_1$  at  $t = 0$  followed by an anelastic response from the Voigt/Kelvin element. The corresponding real and imaginary parts obtained from inversion of  $J(t)$  are:

$$\begin{cases} J_1^{SAS}(\omega) = \frac{1}{k_1} + \frac{k_2}{k_2^2 + \eta^2\omega^2} \\ J_2^{SAS}(\omega) = \frac{\eta\omega}{k_2^2 + \eta^2\omega^2} \end{cases}. \quad (7.14)$$

Although the standard anelastic solid model can better approximate the transient response of solids, it has no viscous (non-recoverable) component and thus does not provide for a very long period response. Furthermore, its simplistic description of anelasticity relies on a single relaxation time. For that reason it has been found to be appropriate for representing attenuation due to proton reorientation and is commonly used in electrical studies, but it cannot account for complex microstructure of the material as do other models that include a broader range of relaxation times.

#### 7.4.5.2 Burgers Model

The simplest mechanical model that captures all of the basic elements of material response is the Burgers or Four-element Model, which is created by placing a Maxwell unit and a Voigt/Kelvin unit in mechanical series (Fig. 7.6a). The creep

compliance for the Burgers model, then, is just the sum of the Maxwell and Voigt/Kelvin models:

$$J(t) = \frac{1}{k_1} + \frac{1}{k_2} \left[ 1 - \exp\left(\frac{-t}{\tau}\right) \right] + \frac{t}{\eta_{ss}} \quad (7.15)$$

where the three terms represent the elastic  $k_1$ , anelastic, and plastic  $\eta_{ss}$  responses, respectively, and  $\tau$  is the relaxation time (e.g. Findley et al. 1976). Inversion of the Burgers model produces a Debye-type peak in the frequency domain, which is associated with the characteristic relaxation time of the Voigt/Kelvin element, superimposed onto the background attenuation of the Maxwell element. Thus the Burgers model, like the SAS model, describes attenuation in a material with only one relaxation time, whereas many materials have a far more complex response. For this reason, the Burgers model in its simple form is generally not used in geophysical applications (e.g., Jackson 1993; Jellinek and Brill 1956).

#### 7.4.5.3 Extended Burgers Model

In order to reflect the complexity of planetary materials, some researchers replace the single relaxation time  $\tau$  in the simple Burgers model with a suitably broad distribution  $D(\tau)$  of relaxation times to more accurately describe the response in both the time and frequency domains (Tan et al. 2001; Jackson et al. 2004). The components of the complex compliance of this “extended” Burgers model are given by:

$$\begin{cases} J_1^{EB}(\omega) = \frac{1}{k_E} \left[ 1 + \Delta \int_0^\infty D(\tau) d\tau / (1 + \omega^2 \tau^2) \right], \\ J_2^{EB}(\omega) = \frac{\omega}{k_E} \Delta \int_0^\infty \tau D(\tau) / (1 + \omega^2 \tau^2) + \frac{1}{\eta_{ss} \omega}, \end{cases} \quad (7.16)$$

where the parameter  $\Delta$  is anelastic relaxation strength, which is a direct function of the concentration, mobility and geometry of the defect(s) accommodating the relaxation (Jackson et al. 2002). Expressions of  $\Delta$  for various deformation mechanisms can be found in Karato and Spetzler (1990).  $D(\tau)$  is a function representing the distribution of relaxation times characterizing the broad plateau in the frequency dependence of  $Q^{-1}$ :

$$D(\tau) = \frac{\alpha \tau^{-(1-\alpha)} H(\tau - \tau_m) H(\tau_M - \tau)}{\tau_M^\alpha - \tau_m^\alpha} \quad (7.17)$$

where  $H$  is the Heaviside step function,  $\tau_M$  and  $\tau_m$  bound the absorption band in which the frequency-dependence of the dissipation factor is characterized by a slope  $\alpha$  (positive and lower than 1). Inversion of the Extended Burgers model has been found to fit laboratory spectra of rocky material in frequency range  $1\text{--}10^{-3}$  Hz (e.g., Tan et al. 2001; Jackson et al. 2002).

#### 7.4.5.4 Caputo Model

Another model that seeks to describe the weak frequency dependence observed over a wide frequency range is the Caputo model (Caputo 1966, 1967; Minster and Anderson 1981). The Caputo body improves upon the SAS model by employing a special stress-strain relation that has a memory mechanism in the form of a fractional derivative and a long-time scale transient creep. For this purpose, the model replaces a dashpot with a *spring-pot*, which relies on viscosity and a scaling term  $v$ , such that the spring-pot has an intermediate order  $1 > v > 0$  between pure elastic and pure viscous behavior (Fig. 7.6b). The storage and loss components of the Caputo model are:

$$\begin{cases} J_1^{Ca} = \frac{k_2 - k_1}{k_1 k_2} \omega^v \sin(v\pi/2) \\ J_2^{Ca} = \left[ 1 + \frac{\omega^v}{k_1 k_2} + \omega^v \frac{(k_1 + k_2)}{k_1 k_2} \cos(v\pi/2) \right] \end{cases} \quad (7.18)$$

where  $k_1$  and  $k_2$  are functions of the elasticity of the material.

Although the Caputo model proved to describe well the attenuation associated with Earth's free oscillations and torsional modes (Caputo and Mainardi 1979), it is generally deemed to have limited applicability (e.g., Bagdassarov 1999; Han et al. 2007) and is rarely used in the planetary science literature (e.g., Wieczorkowski and Wolff 1998). However, the observation that  $Q$  can come close to a constant over a wide frequency range has been extensively used in planetary models developed in the 1970s and 1980s, so we provide this model for reference (see Sect. 7.5).

#### 7.4.5.5 Cole Model

This model was introduced by Cole (1995) in order to quantify the experimental observations of attenuation in saline ice and isolate the relaxation due to dislocation motion (Cole and Durell 1995). As such, it is the only model developed specifically to characterize the response of ice. Like the Extended Burgers model, the Cole model seeks to explain the broad attenuation plateau and also the low-frequency modulus asymptote observed in the experimental data. In this case, the Debye-peak producing Voigt/Kelvin element is replaced with an adjustable parameter  $\xi$  to control the peak width while keeping its area constant (e.g.,  $\xi = 1$  for a Debye peak). The storage and loss components of the dislocation-dominated compliance of the Cole model are:

$$\begin{cases} J_1^{Cole} = \frac{1}{k_E} + \delta D \left[ 1 - \frac{2}{\pi} \tan^{-1}(\exp(\xi s)) \right] \\ J_2^{Cole} = \xi \delta D \frac{1}{\exp(\xi s) + \exp(-\xi s)} \end{cases} \quad (7.19)$$

where the quantity  $\delta D = \rho\Omega b^2/\sigma_r$  and  $s = \ln(\tau_C\omega)$ . The Cole model is based on the theory of oscillatory motion of basal plane dislocations (e.g., Weertman 1955; 1983; see also Sect. 7.2.4) and thus uses the mobile dislocation density  $\rho$ , the length of the Burgers vector  $b$ , and the restoring stress constant  $\sigma_r$ , which is the force the dislocation segment “feels” in its Peierls potential trough. The orientation factor  $\Omega$  is a geometry term related to the degree of alignment between ice grains. The model was further developed by Cole (1995) and Cole and Durell (2001), to describe relaxation by grain boundary sliding and to include the effect of strain history, salinity and porosity as they are incorporated into  $\rho$  and  $\Omega$ . Cole and his collaborators demonstrated the applicability of the model to describe the anelastic response of natural and laboratory grown ice. However, its ability to model the response of ice at frequencies of planetary significance is questionable. At the very low frequencies of tidal forcing, viscoelasticity, *in addition to* anelasticity, is expected to be responsible for relaxation (e.g. Karato and Spetzer 1990). Unlike the Extended Burgers model, the Cole model provides no term for low frequency viscous relaxation. Another limitation is that the model uses a fixed value for the parameter  $\xi$  that is only based on fittings to empirical data so that alterations based on the context and nature of the microstructure cannot be made. Still, the wealth of data collected by that group is significant and the Cole model’s ability to isolate and model the dislocation-based dissipation mechanism in ice is significant.

#### 7.4.5.6 Andrade Model

The Andrade creep function was introduced by Andrade (1910) to describe transient creep in metals. In its initial form, it was expressed as:

$$J(t) = \frac{1}{\mu} + \beta t^m. \quad (7.20)$$

The full form of the Andrade creep function as applied to ice was introduced by Duval (1976, 1978):

$$J(t) = \frac{1}{k_E} + \beta t^m + \frac{t}{\eta_{ss}} \quad (7.21)$$

where  $\beta$  is a constant determined by the properties of the defects driving attenuation (i.e., their density and mobility) and, as such, that parameter is a direct function of the viscosity of the material (Castillo-Rogez et al. 2011). Shown in Fig. 7.6b, the transient element  $\beta t^m$  represents an infinite number of Voigt/Kelvin elements possessing a continuous distribution of relaxation times (Andrade 1910; Duval et al. 1983; Cooper 2002). The parameter  $m$  has been measured for a variety of materials, including polycrystalline ice (Ladanyi and Saint-Pierre 1978; McCarthy et al. 2007) and monocrystalline ice (Castillo-Rogez et al. 2011), and is generally

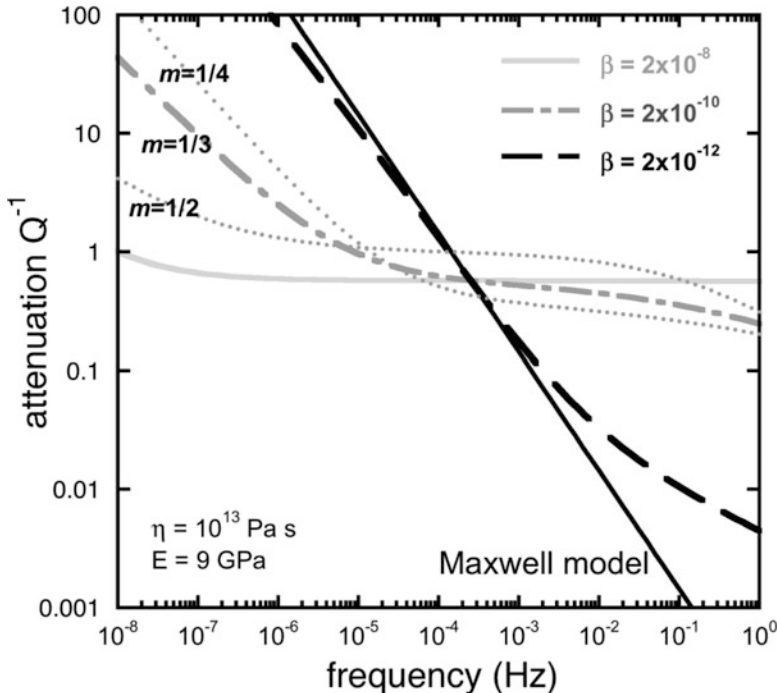


**Fig. 7.7** A comparison of the Andrade-based model to the Maxwell model. The various lined curves represent different listed values for the parameter of  $\beta$  (while assuming constant  $m = 1/3$ ). The dotted lines represent the effect of changing  $m$  (while keeping constant  $\beta = 2 \times 10^{-10}$ ). Only at very small  $\beta$  does the Andrade-based model transition toward the Maxwell model

found to be between 1/3 and 2/3 (cf. Weertman and Weertman 1975). The dependence of  $m$  on experimental conditions or material properties is not clear. In the case of silicates, it has been suggested that the value of  $m$  is primarily determined by the lack of uniformity in grain shapes and the presence of impurities (e.g., Lee and Morris 2010). When the Andrade creep function is transformed, the storage and loss components are:

$$\begin{aligned} J_1^{And}(\omega) &= \frac{1}{k_E} + \beta \Gamma(1+m) \omega^{-m} \cos\left(\frac{m\pi}{2}\right) \\ J_2^{And}(\omega) &= \beta \Gamma(1+m) \omega^{-m} \sin\left(\frac{m\pi}{2}\right) + \frac{1}{\eta_{ss}\omega}, \end{aligned} \quad (7.22)$$

where  $\Gamma(m+1)$  is the gamma function. The spectra predicted by the Andrade creep function is such that at very low frequencies,  $Q^{-1} \propto f^{-(1-m)}$  and the slope of the intermediate band (i.e. the  $\alpha$ -term of the Extended Burgers model) can be any value between 0 and  $-(1-m)$ . The length, slope and location in frequency space of the band are determined by the relative magnitudes of modulus, viscosity and  $\beta$  (Fig. 7.7).

A point worth noting about this model is that at frequencies lower than the Maxwell frequency (where viscoelastic theory predicts anelastic behavior to end and purely viscous behavior to dominate), the model can continue to have a moderate slope. This may be an indication that a mathematical model based on the Andrade creep function loses physical meaning at very low frequency. However, the fact that no experimental studies on planetary materials have yet demonstrated the predicted sharp transition to purely viscous behavior (a slope of  $-1$  in log-log plot) may instead suggest that real materials continue to sample additional anelastic mechanisms beyond the Maxwell frequency. The degree of departure from the Maxwell model has been proposed to be a function of the value of  $\beta$  (Castillo-Rogez et al. 2011). As shown in Fig. 7.7, if beta is small (e.g.,  $\sim 10^{-12}$  as found in olivine; Jackson et al. 2002), then the attenuation spectrum approaches that predicted for a Maxwell model. On the other hand, the larger the value of  $\beta$ , due to increased defect density, the greater departure is to be expected.

## 7.5 Applications to Solar System Objects

The effect of tidal stress in outer planet satellites plays a major role in the geophysical, geological, and orbital evolution of these objects. Orbital evolution and tidal heating depend on the tidal Love number  $h_2$ , which expresses the amplitude of deformation in response to the tidal potential and the friction coefficient  $Q^{-1}$ .

### 7.5.1 *Historical Approach to Tidal Dissipation Modeling in Planetary Satellites*

Many studies over the past five decades have assumed that icy monoliths are characterized by a dissipation factor on the order of 100. That suggestion was based on available acoustic measurements, which also showed that the dissipation factor of ice and rock was frequency independent at ultrasonic frequency (Knopoff 1964; Goldreich and Soter 1966). Peale et al. (1980) justified a value of  $Q$  equal to 100 based on measurements obtained on ice by Nakamura and Abe (1980). However, the latter measurements were performed at seismic frequencies. Still, that rough estimate proved consistent in modeling the orbital evolution of Saturn's satellite Mimas from the synchronous orbit to its present location (Goldreich and Soter 1966). A value of  $Q = 100$  has also been used for representing the dissipation factor of very porous bodies (e.g., Phobos, Yoder 1982; binary asteroids, Margot et al. 2002), as a step toward inferring the rigidity of these objects.

However, the assumption that ice dissipation factor is not frequency-dependent and equal to 100 finds its limit when modeling satellites large enough to have undergone some internal evolution. For example, Peale (1986) noted that in such a framework, it

is not possible to explain the spin-orbit resonance of Saturn's satellite Iapetus (see discussion in Sect. 7.5.5). Nor is it adequate to explain the intense heating measured on Enceladus (Spencer et al. 2006), which is believed to be due in large part to tidal heating. Although a few recent studies have used such an assumption (e.g., Meyer and Wisdom 2007), most of the satellite dissipation studies developed since the mid-1980s have relied on the application of a Maxwell solid model to approximate  $Q$  at satellite forcing frequencies. That approach has shaped our understanding of icy satellite thermal and orbital evolution for the past two decades (Sect. 7.5.2). As described above, despite its convenience, the Maxwell model fails to account for planetary material anelasticity, which may be the main attenuation mechanism expressed at the forcing frequencies relevant to satellite tides. A few studies have also attempted to compare the dissipation obtained from various models: Maxwell body, Caputo model, SAS, and Burgers model (e.g., Wieczkowski and Wolf 1998; Hussmann and Spohn 2004; Robuchon et al. 2010). However, the latter models fail to describe the full range of viscoelastic behavior.

A novel approach to the problem is emerging, starting with the introduction of the Andrade-based model as potentially a better approach for describing planetary ice attenuation properties by McCarthy et al. (2007) and with its first application to modeling of Enceladus' tidal response by Rambaux et al. (2010). However, as noted by Castillo-Rogez et al. (2011), the lossy nature of polycrystalline ice requires that care must be taken in the application of laboratory attenuation data (which is expressed as the tangent of the phase lag) to models of tidal torque (which utilize the sine of phase lag) (Goldreich and Peale 1966; Efroimsky and Williams 2009). The approximation of  $\sin \delta \sim \tan \delta = Q^{-1}$  that is often used for materials with  $Q$  greater than 10 will not hold with highly dissipative materials such as ice. We refer readers to Efroimsky and Williams (2009) and Tobie et al. (2005) for details on the calculation of torque and of the tidal response of icy bodies.

### 7.5.2 Mechanisms Driving Dissipation in Icy Satellites

Similar to that discussed in Sect. 7.4, the mechanisms in the viscoelastic regime that drive dissipation in solid bodies also depend on the nature, density, and mobility of defects, which are functions of temperature, stress, grain size, and impurity content. The dominant creep mechanisms expected in pure water ice can be mapped as a function of stress and grain size (Fig. 7.8 after Goodman et al. 1981; Goldsby and Kohlstedt 2001). That map shows that in most satellites, tidal stress is on the order of a few hundred or thousand Pascal, such that tidal stress is primarily accommodated by the diffusion of defects within the lattice. A few objects are subject to greater tidal stress peak amplitudes: the Galilean satellite Europa, the Kronian satellites Enceladus, and Uranus' Mimas, Ariel and Miranda. With the exception of Mimas, these satellites share the characteristic of having recently been geologically active (and possibly still active) as evidenced by their complete lack of large craters.

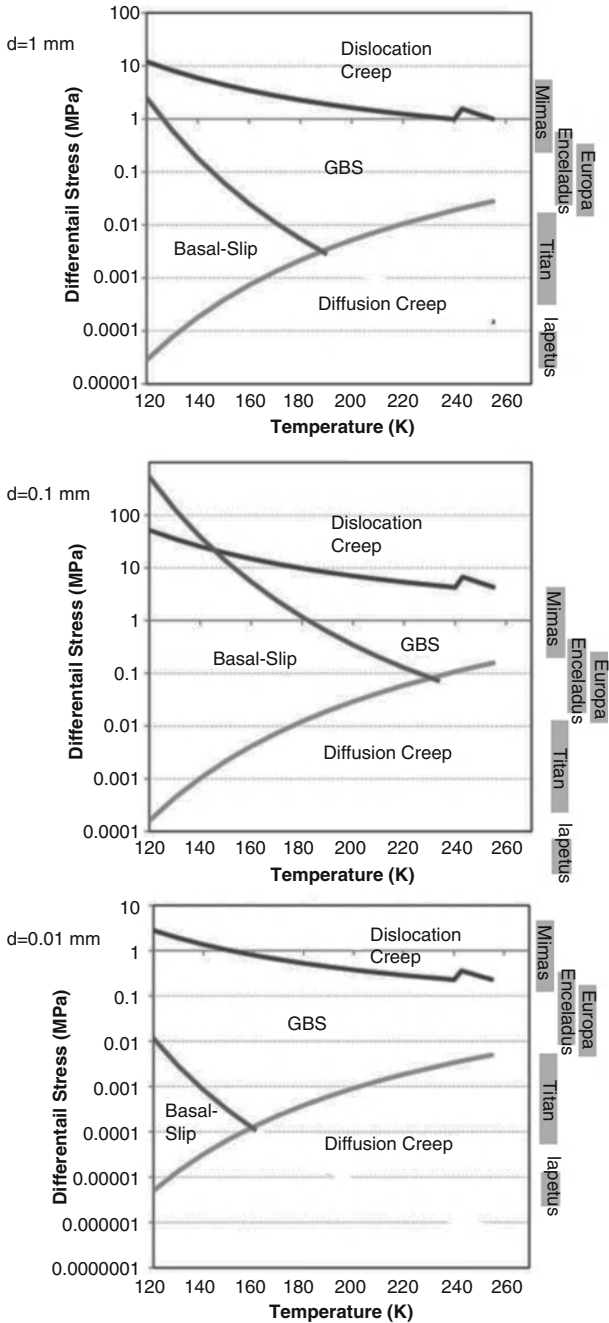


**Fig. 7.8** Deformation mechanisms preferentially expressed in ice as a function of stress and temperature conditions, and for different grain sizes (assuming homogeneous grain size). The right-hand column shows the range of cyclic peak stress amplitudes expected in various icy satellites (see Fig. 7.1). This figure is built after the approach presented in Barr and Pappalardo (2005) using input parameters to Eq. 7.2 taken from Goldsby and Kohlstedt (2001). The mechanisms expected to accommodate stress are dislocation creep, dislocation-accommodated grain-boundary sliding (GBS), basal-slip accommodated grain-boundary sliding, and diffusion creep

The role of tidal heating in preserving a deep ocean in Europa and promoting intense geological activity on Enceladus is a topic of primary interest as these objects are the current target of the ongoing *Cassini-Huygens* Mission and the prospective *Europa and Jupiter System Mission*. It has been suggested that the tidal strain in icy satellites is so small that the response of the object is non-linear (Montagnat and Duval 2004). The situation may be different in the case of Enceladus and Europa, subject to stresses greater than 0.1 MPa and possible stress concentration, as suggested by the model of Tobie et al. (2008).

Also, satellites' orbital properties have evolved as a consequence of the tides they are subject to and the tides they exert on their primaries. It is expected that, in their early history, outer planet satellites were closer to their primaries (e.g., Zhang and Nimmo 2009), had higher eccentricity, and possibly possessed deep oceans. Thus, at least for a short period of time, they could have undergone significant tidal stress and increased tidal heating.

### 7.5.3 Key Results from the Maxwell Body Approximation

Since the unrelaxed modulus of ice shows little dependence on temperature for the conditions encountered in icy satellites (Parameswaran 1987), the attenuation spectrum predicted by the Maxwell model mostly depends on the viscosity of the material. In the frame of the Maxwell model, there is an important coupling between internal friction and the occurrence of convective heat transfer through the viscosity of the material. In other words, if the conditions (temperature, grain size) are such that material defects can easily move, then they can also be involved in anelastic dissipation. This observation is at the origin of numerous studies that have highlighted convective regions in icy satellites as preferential regions for tidal heating (e.g., Sotin et al. 2002; Fig. 7.9).

In this framework, tidal dissipation reaches a peak when the Maxwell time of the material, i.e., the ratio of its viscosity to elastic modulus, equals the tidal forcing period (e.g., the orbital period in the case of satellites in spin-orbit resonance). In this context, tidal dissipation is a runaway phenomenon. It contributes to increasing the temperature and, thus, decreasing the material viscosity, which then promotes further dissipation. However, if the viscosity becomes too low and the ice volume too small, the tidal dissipation becomes less efficient, and the ice starts cooling down. The threshold between the two trends is determined by the Maxwell time of the dissipative material. Tidal dissipation is in steady-state if that property is equal to the forcing period. The consequent interplay between the thermal and orbital states of planetary satellites was integrated in detailed geophysical models by Hussmann and Spohn (2004). These authors suggested that Europa and Io have been the probable objects of oscillatory phases of runaway heating and cooling associated with large changes in orbital eccentricity, alternating with quasi-steady state periods. They also demonstrated that departure from the equilibrium

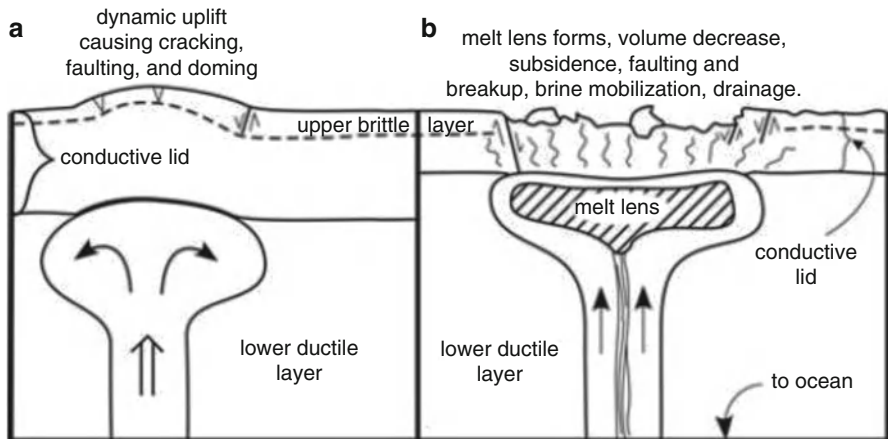


**Fig. 7.9** Illustration of the impact of tidal dissipation on the geological activity of Europa driven by convective upwelling (Reprinted with authorization from the American Geophysical Union)

state is transitory, as the satellites tend to rapidly return to equilibrium. At present, most satellites, except Enceladus (Meyer and Wisdom 2008), should be at or close to equilibrium.

#### 7.5.4 Impact of Anelasticity on the Tidal Response of Icy Satellites

Recent studies have suggested that an Andrade-based model may be more appropriate to the modeling of satellite tidal response than the Maxwell model (e.g., Nimmo 2008; Roberts and Nimmo 2008). At the time of this chapter's preparation, a few studies have been working with a complex compliance based on the Andrade creep model in geophysical modeling of icy satellites (e.g., Rambaux et al. 2010). Castillo-Rogez et al. (2011) have attempted to develop a hybrid model that combines (a) at high frequency: the distribution of characteristic times in the anelastic regime, as formulated in the Andrade model, and (b) at low frequency: a purely viscous response expressed with the Maxwell body. The transitional region between the purely anelastic and viscous regimes is not well understood and needs to be further studied in laboratory.

The theoretical attenuation spectrum presented in Fig. 7.10 features a strong change in the frequency dependence of attenuation around the inverse of the Maxwell time. That threshold is a function of the mechanism involved in the dissipation. Since ice viscosity shows a strong dependence on temperature,  $1/\tau$  is commonly outside the range of forcing frequencies relevant to satellite tides. Taking Enceladus as an example, for an ice shear modulus of 3.3 GPa (e.g., Parameswaran 1987),  $\tau$  equals the orbital period for a viscosity of  $\sim 4 \times 10^{14}$  Pas.

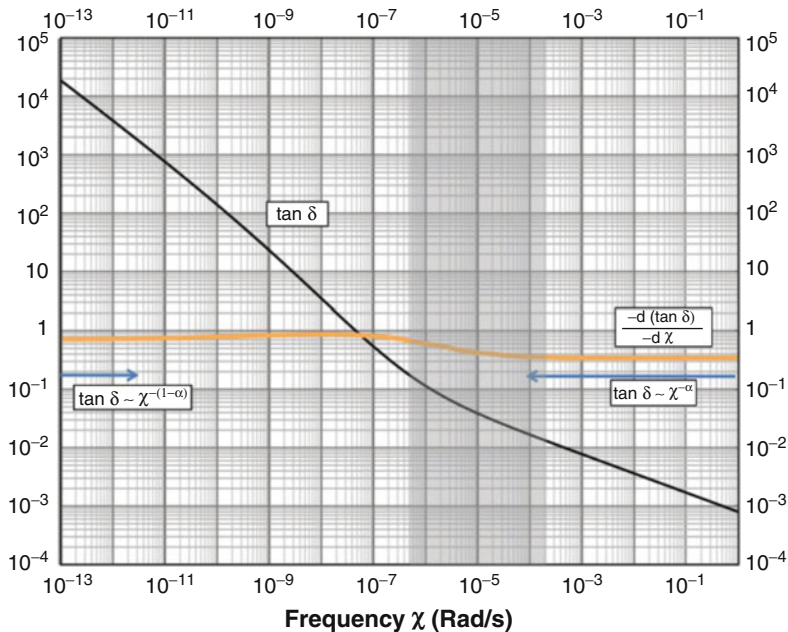


**Fig. 7.10** Examples of attenuation spectra for the Andrade model for  $\alpha = 0.5$  and  $\beta = 5 \times 10^{-13}$

This means that material with larger viscosity will be dominated by the anelastic response, whereas warmer material may be dominated by purely viscous behavior and thus well approximated by a Maxwell solid model. However, in general, the frequency range of direct interest to icy satellite modeling coincides with anelastic-dominated behavior. If the icy satellites accreted cold (e.g., Ellsworth and Schubert 1983; Matson et al. 2009), their dissipative behavior must have been primarily governed by their material anelasticity (until the contribution of viscosity became increasingly significant as a consequence of satellite warming). In such conditions the material is expected to be more dissipative than that modeled with a Maxwell solid model. Related to that issue, the evolving tidal forcing amplitudes and frequencies resulting from the inward/outward evolution of the satellites orbits (e.g., Meyer and Wisdom 2007; Zhang and Nimmo 2009) must have also affected the style of attenuation in these objects. To illustrate these considerations, the dissipation factor for a homogeneous ice sphere is plotted as a function of period and viscosity in Fig. 7.11 in the frame of the Maxwell body (Fig. 7.11a) and Andrade-based model (Fig. 7.11b). Both approaches yield a maximum of dissipation as the Maxwell time of the material and the tidal period coincide. At low viscosities, both models tend to overlap. However, the departure of the Maxwell body from the Andrade-based model increases for increasing ice viscosities and decreasing forcing periods. The significance of that change in approach to modeling the geophysical and dynamical evolution of planetary satellites remains to be evaluated.

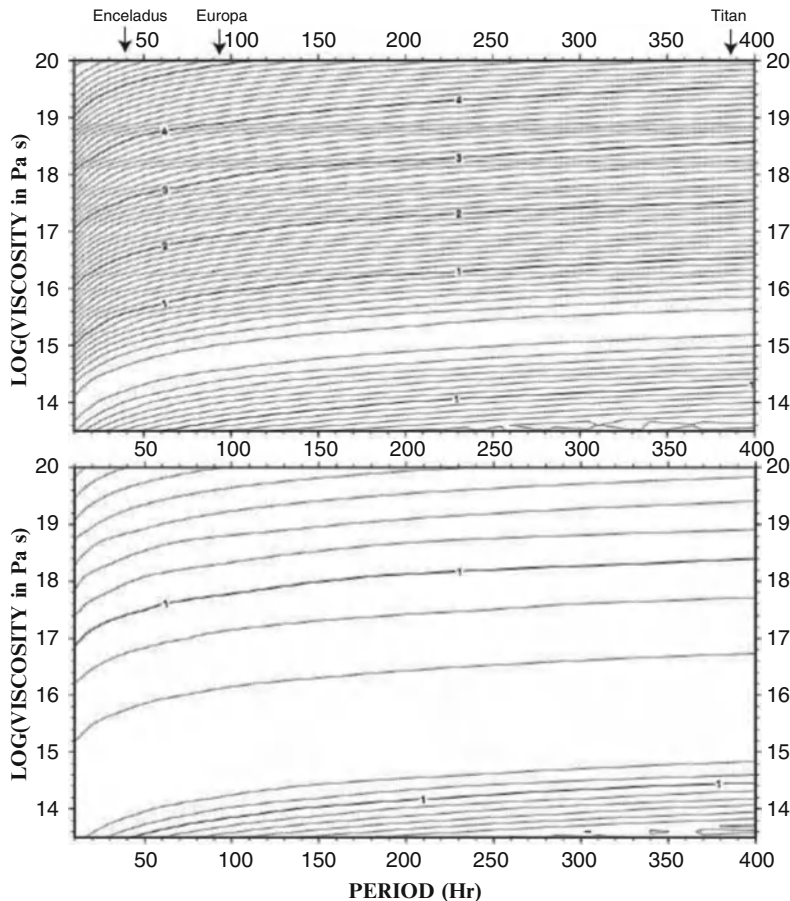


**Fig. 7.11** Decimal logarithm of the quality factor  $Q$  for a homogeneous sphere of pure water ice as a function of viscosity and forcing period (see Castillo-Rogez et al. (2011) for details about the calculation of these figures). *Top:* for the Maxwell model; *Bottom:* for the Andrade creep function assuming a parameter  $\alpha$  equal to 0.3

### 7.5.5 Application: Iapetus' Evolution to Spin-Orbit Resonance

Due to its unusual orbital and geological properties, the Saturnian satellite Iapetus has been the focus of several recent studies aimed at modeling its despinning to synchronous rotation. Peale (1986) pointed out the apparent inconsistency between Iapetus' synchronous rotation and the dissipative properties assumed at the time. Using a dissipation factor equal to 100, Peale et al. (1979) inferred a despinning timescale of 14 Gy for Iapetus. From coupling thermal and dynamical evolution, Castillo-Rogez et al. (2007) suggested that Iapetus could achieve despinning on a shorter timescale, on the order of 1 Gy. However, that study relied on the Maxwell

model, such that the temperature had to reach the water ice melting point for despinning to become significant and complete in a few thousand years. That scenario was found to be problematic because solid-state convection was ignored. As described above, due to the strong coupling between attenuation and viscosity, significant tidal dissipation implies that the material can deform in a way suitable to promote convective heat transfer. Such a possibility was demonstrated in the case of Iapetus with the application of a Four-Element model (Burgers) to account for the transient properties of the material (Robuchon et al. 2010). However, that study fully decoupled transient and steady-state creep, which is inconsistent with experimental observations and theoretical considerations. The most recent take on the topic was to apply an Andrade-based model using an empirical relationship between the Andrade parameter  $\beta$  and the steady-state creep (Castillo-Rogez et al. 2011). In such a framework, convection and tidal dissipation are still coupled, but to a lesser extent (to the power of the Andrade parameter  $\alpha$ ). As a result, these authors found geophysical models in which convection onset and tidal dissipation were not mutually exclusive.

## 7.6 Conclusions and Roadmap for Future Research

We have reviewed the state of knowledge of ice attenuation properties as of 2010. At this time, the identification of ice mechanical properties over a range of forcing frequencies relevant to the tides of icy satellites is in progress. There seems to be a general understanding in the recent literature that the simple Maxwell model may not be suited to describing the tidal response of icy satellites. At this stage, there is no definitive answer as to which alternative model is best, especially between the Andrade-based and the Extended Burgers models, for describing the response of planetary materials over a wide range of frequencies encompassing satellite tides.

There is a good chance that in the next decade, significant advances from an experimental and theoretical point of view will lead to a better understanding of attenuation in icy materials as there is a strong interest in that research to support ongoing and prospective missions to icy bodies: e.g., *New Horizons* Mission to Pluto and Charon, *Dawn* Mission to Ceres, etc.

As discussed above, attenuation can be quantified as a function of material defect properties. The challenge posed to future geophysical models is to progress from using “black-box” input parameters to considering the material’s thermal history, from accretion or freezing from a deep salty ocean, to its possible upwelling to the surface as a consequence of solid-state convection. Processes of importance include defect annealing (e.g., recrystallization), the role played by tidal stress in keeping the grain size small, and the segregation of impurities.

Future research should focus on a variety of frozen volatile compositions, including: ammonia hydrates, clathrate hydrates, and hydrated salts, as well as mixtures of ice and silicates. The importance of focusing on multiphase compositions is not limited to the problems addressed in this study but is also relevant to a more general

understanding of planetary material mechanical properties with geological and geophysical applications (Castillo-Rogez et al. 2009).

Aside from composition, the impact of microstructure and its evolution as a result of thermal and mechanical aging require dedicated studies. Although the role of impurities in preventing grain growth has become an important feature of recent models, the actual impact on material microphysics remains to be implemented.

Most satellites experience tidal stresses at least one order of magnitude smaller than the stresses currently achieved by laboratory experiment. Proper extrapolation to planetary conditions requires a more detailed knowledge of the mechanisms controlling dissipation and the conditions under which the response becomes non-linear. There is also a need to better characterize how tidal stress affects the stress distribution in icy satellites, and especially how tidal and convective straining interact and influence one another. Of crucial importance, attenuation under pure shear conditions has to be properly characterized in order to develop geophysical models approaching as closely as possible the conditions expected in icy satellites.

**Acknowledgements** We would like to thank several people for discussions that contributed to this chapter, including Reid Cooper and Yasuko Takei. The authors would also like to thank Shun Karato and Michael Efroimsky for their thorough reviews. Part of this review chapter was prepared at the Jet Propulsion Laboratory, California Institute of Technology, under contract with NASA. All rights reserved. Government sponsorship acknowledged.

## References

- Ahmad S, Whitworth RW (1988) Dislocation motion in ice: a study by synchrotron X-ray topography. *Philos Mag A* 57(5):749–766
- Aksnes K, Franklin FA (2001) Secular acceleration of Io derived from mutual satellite events. *Astron J* 122:2734–2739. doi:[10.1086/323708](https://doi.org/10.1086/323708)
- Andrade END (1910) On the viscous flow in metals and allied phenomena. *Proc R Soc Lond Ser-A* 84:1–12
- Ashby MF, Verrall RA (1973) Diffusion-accommodated flow and superplasticity. *Acta Metall Mater* 21:149–163. doi:[10.1016/0001-6160\(73\)90057-6](https://doi.org/10.1016/0001-6160(73)90057-6)
- Bagdassarov NS (1999) Viscoelastic behavior of mica-based glass-ceramic aggregate. *Phys Chem Miner* 26:513–520
- Baker I (1997) Observation of dislocations in ice. *J Phys Chem B* 101:6158–6162
- Barnhoorn A, Jackson I, Fitz Gerald JD, Aizawa Y (2007) Suppression of elastically accommodated grain-boundary sliding in high-purity MgO. *J Eur Ceram Soc* 27:4697–4703
- Barr AC, Milkovich SM (2008) Ice grain size and the rheology of the Martian polar deposits. *Icarus* 194:513–518. doi:[10.1016/j.icarus.2007.11.018](https://doi.org/10.1016/j.icarus.2007.11.018)
- Barr AC, Pappalardo RT (2005) Onset of convection in the icy Galilean satellites: influence of rheology. *J Geophys Res* 110:E12005. doi:[10.1029/2004JE002371](https://doi.org/10.1029/2004JE002371)
- Beeman ML, Kohlstedt DL (1993) Deformation of fine-grained aggregates of olivine plus melt at high temperatures and pressures. *J Geophys Res* 98(4):6443–6452
- Bjerrum N (1952) Structure and properties of ice I. *Science* 115(2989):385–390
- Brill R, Camp PR (1961) Properties of ice. Research report no 68 of the SIPRE snow, ice, and permafrost research establishment. US Army Terrestrial Science Center, Hanover

- Buechner PM, Stone D, Lakes RS (1999) Viscoelastic behavior of superplastic 37 wt% Pb 63 wt% Sn over a wide range of frequency and time. *Scr Mater* 41(5):561–567
- Burdett CF, Queen TJ (1970) The role of dislocations in damping. *Metall Rev* 143(1):65–78
- Caputo M (1966) Linear models of dissipation whose Q is almost frequency independent. *Ann Geophys* 19:383–393
- Caputo M (1967) Linear models of dissipation whose Q is almost frequency independent – II. *Geophys J R Astron Soc* 13:529–539
- Caputo M, Mainardi F (1979) A new dissipation model based on memory mechanism. *Pure Appl Geophys* 91(1):134–147
- Castelnau O, Duval P, Montagnat M, Brenner R (2008) Elastoviscoplastic micromechanical modeling of the transient creep of ice. *J Geophys Res* 113:B11203. doi:[10.1029/2008JB005751](https://doi.org/10.1029/2008JB005751)
- Castillo JC, Mocquet A, Sotin C (2000) Déetecter la présence d'un océan dans Europe à partir de mesures altimétriques et gravimétriques. *CR Acad Sci IIA-Earth Planet Sci* 330:659–666
- Castillo-Rogez J, Matson DL, Sotin C, Johnson TV, Lunine JI, Thomas PC (2007) Iapetus' geophysics: rotation rate, shape, and equatorial ridge. *Icarus*. doi:[10.1016/j.icarus.2007.02.018](https://doi.org/10.1016/j.icarus.2007.02.018)
- Castillo-Rogez JC, Durham WB et al (2009) Laboratory studies in support of planetary geophysics. White paper to the decadal survey solar system 2012
- Castillo-Rogez JC, Efroimsky M, Lainey V (2011) The tidal history of Iapetus. Dissipative spin dynamics in the light of a refined geophysical model. *J Geophys Res* 116:E09008. doi:[10.1029/2010JE003664](https://doi.org/10.1029/2010JE003664)
- Cochran ES, Vidale JE, Tanaka S (2004) Earth tides can trigger shallow thrust fault earthquakes. *Science* 306:1164–1166. doi:[10.1126/science.1103961](https://doi.org/10.1126/science.1103961)
- Cole DM (1995) A model for the anelastic straining of saline ice subjected to cyclic loading. *Philos Mag A* 72(1):231–248
- Cole DM (2001) The microstructure of ice and its influence on mechanical properties. *Eng Fract Mech* 68:1797–1822
- Cole DM, Durell GD (1995) The cyclic loading of saline ice. *Philos Mag A* 72(1):209–229
- Cole DM, Durell GD (2001) A dislocation-based analysis of strain-history effects in ice. *Philos Mag A* 81(7):1849–1872
- Cole DM, Johnson RA, Durell GD (1998) Cyclic loading and creep response of aligned first-year sea ice. *J Geophys Res* 103(C10):21, 751–21,758
- Cooper RF (2002) Seismic wave attenuation: energy dissipation in viscoelastic crystalline solids. In: Karato S, Wenk HR (eds) Plastic deformation of minerals and rocks, vol 51, Reviews in mineralogy and geochemistry. Mineralogical Society of America, Washington, DC, pp 253–290
- Cooper RF, Kohlstedt DL (1984) Rheology and structure of olivine-basalt partial melts. *J Geophys Res* 91(B9):9315–9324
- Coyner KB, Randolph RJ (1988) Frequency-dependent attenuation in rocks. Technical report A672502
- Dash JG, Rempel AW, Wettlaufer JS (2006) The physics of premelted ice and its geophysical consequences. *Rev Mod Phys* 78:695
- Durham WB, Stern LA (2001) Rheological properties of water ice – applications to satellites of the outer planets. *Annu Rev Earth Planet Sci* 29:295–330
- Durham WB, Pathare AV, Stern LA, Lendferink HJ (2009) Mobility of icy sand packs, with application to Martian permafrost. *Geophys Res Lett* 36:L23203
- Duval P (1976) Temporary or permanent creep laws of polycrystalline ice for different stress conditions. *Ann Geophys* 32:335–350
- Duval P (1978) Anelastic behaviour of polycrystalline ice. *J Glaciol* 21(85):621–628
- Duval P, Ashby MF, Anderman I (1983) Rate-controlling processes in the creep of polycrystalline ice. *J Phys Chem* 87:4066–4074
- Efroimsky M, Lainey V (2007) On the theory of bodily tides. In: Belbruno E (ed) New trends in astrodynamics and applications III. American Institute of Physics, Melville, pp 131–138
- Efroimsky M, Williams JG (2009) Tidal torques. A critical review of some techniques. *Celest Mech Dynam Astr* 104:257–289, arXiv:0803.3299 1230

- Ellsworth K, Schubert G (1983) Saturn's icy satellites: thermal and structural models. *Icarus* 54:490–510
- Paul UH, Jackson I (2005) The seismological signature of temperature and grain size variations in the upper mantle. *Earth Planet Sci Lett* 234:119–134
- Paul UH, FitzGerald JD, Jackson I (2004) Shear wave attenuation and dispersion in melt-bearing olivine polycrystals: 1. Microstructural interpretation and seismological implications. *J Geophys Res* 109:B06202
- Findley WN, Lai JS, Onaran K (1976) Creep and relaxation of nonlinear viscoelastic materials. Dover, New York
- Fountaine FR, Ildefonse B, Bagdassarov NS (2005) Temperature dependence of shear wave attenuation in partially molten gabbronorite at seismic frequencies. *Geophys J Int* 163:1025–1038
- Friedson AJ, Stevenson DJ (1983) Viscosity of rock-ice mixtures and applications to the evolution of icy satellites. *Icarus* 56(1):1–14
- Fukuda A, Hondoh T, Higashi A (1987) Dislocation mechanisms of plastic deformation in ice. *J Phys C* 48(3):163–173
- Goldreich P, Peale S (1966) Spin-orbit coupling in the Solar system. *Astron J* 71:425–438
- Goldreich P, Sari R (2009) Tidal evolution of rubble piles. *Astrophys J* 691:54
- Goldreich P, Soter S (1966) Q in the Solar system. *Icarus* 5:375–389
- Goldsby DL (2007) Diffusion creep of ice: constraints from laboratory creep experiments. *LPS* 38:2186
- Goldsby DL, Kohlstedt DL (2001) Superplastic deformation of ice: experimental observations. *J Geophys Res-Solid Earth* 106:B11017–B11030. doi:[10.1029/2000JB900336](https://doi.org/10.1029/2000JB900336)
- Goodman DJ, Frost HJ, Ashby MF (1977) The effect of impurities on the creep of ice Ih and its illustration by the construction of deformation maps, isotopes and impurities in snow and ice. *Int Assoc Sci Hydrol, Int Union Geod Geophys* 118:29–33, IASH Publication
- Goodman DJ, Frost HJ, Ashby MF (1981) The plasticity of polycrystalline ice. *Philos Mag A* 43:665–695
- Granato AV, Lücke K (1956) Theory of mechanical damping due to dislocations. *J Appl Phys* 27:582
- Greenberg R, Geissler P, Hoppa G, Tufts BR, Durda DD, Pappalardo R, Head JW, Greeley R, Sullivan R, Carr MH (1998) Tectonic processes on Europa: tidal stresses, mechanical response, and visible features. *Icarus* 135:64–78
- Gribb TT, Cooper RF (1998) Low-frequency shear attenuation in polycrystalline olivine: grain boundary diffusion and the physical significance of the Andrade model for viscoelastic rheology. *J Geophys Res* 103:B11, 27, 267–27, 279
- Gribb TT, Cooper RF (2000) The effect of an equilibrated melt phase on the shear creep and attenuation behavior of polycrystalline olivine. *Geophys Res Lett* 27(15):2341–2344
- Han DH, Liu J, Batzle M (2007) Shear velocity as the function of frequency in heavy oils, *Soc. Exploration Geophys. Expanded Abstracts* 26(1) doi:<http://dx.doi.org/10.1190/1.2792824>
- Hessinger J, White BE Jr, Pohl RO (1996) Elastic properties of amorphous and crystalline ice films. *Planet Space Sci* 44:937–944. doi:[10.1016/0032-0633\(95\)00112-3](https://doi.org/10.1016/0032-0633(95)00112-3)
- Hiki Y, Tamura J (1983) Internal friction in ice crystals. *J Phys Chem* 87:4054–4059. doi:[10.1021/j100244a011](https://doi.org/10.1021/j100244a011)
- Hurford TA, Helfenstein P, Hoppa GV, Greenberg R, Bills BG (2007) Eruptions arising from tidally controlled periodic openings of rifts on Enceladus. *Nature* 447:292–294. doi:[10.1038/nature05821](https://doi.org/10.1038/nature05821)
- Hussmann H, Spohn T (2004) Thermal-orbital evolution of Io and Europa. *Icarus* 171:391–410. doi:[10.1016/j.icarus.2004.05.020](https://doi.org/10.1016/j.icarus.2004.05.020)
- Jackson I (1993) Progress in the experimental study of seismic wave attenuation. *Annu Rev Earth Planet Sci* 21:375–406

- Jackson I (2007) Physical origins of anelasticity and attenuation in rock. In: Schubert G (ed) Treatise of geophysics, vol 2, Mineral physics: properties of rocks and minerals. Elsevier, Amsterdam, pp 496–522, Chapter 2.17
- Jackson I, Fitz Gerald JD, Faul UH, Tan BH (2002) Grain-size-sensitive wave attenuation in polycrystalline olivine. *J Geophys Res* 107(B12):2360. doi:[10.1029/2001JB001225](https://doi.org/10.1029/2001JB001225)
- Jackson I, Faul UH, Fitz Gerald JD, Tan BH (2004) Shear wave attenuation and dispersion in melt-bearing olivine polycrystals: specimen fabrication and mechanical testing. *J Geophys Res* 109: B06201
- Jackson I, Faul UH, Fitz Gerald JD, Morris SJS (2006) Contrasting viscoelastic behavior of melt-free and melt-bearing olivine: implications for the nature of grain-boundary sliding. *Mat Sci Eng A* 442:170–174
- James MR, Bagdassarov N, Müller K, Pinkerton H (2004) Viscoelastic behaviour of basalt lavas. *J Volcanol Geotherm Res* 132:99–113
- Jellinek HHG, Brill R (1956) Viscoelastic properties of ice. *J Appl Phys* 27:1198–1209
- Johari GP, Pascheto W, Jones SJ (1995) Anelasticity and grain boundary relaxation of ice at high temperatures. *J Phys D-Appl Phys* 28:112–119
- Karato S (1998) A dislocation model of seismic wave attenuation and micro-creep in the Earth: Harold Jeffreys and the rheology of the solid earth. *Pure Appl Geophys* 153:239–256
- Karato S (2008) Deformation of earth materials. Cambridge University Press, Cambridge, UK
- Karato S, Spetzler HA (1990) Defect microdynamics in minerals and solid-state mechanisms of seismic wave attenuation and velocity dispersion in the mantle. *Rev Geophys* 28(4):399–421
- Ké TS (1946) Experimental evidence of the viscous behavior of grain boundaries in metals. *Phys Rev* 71(8):533–546
- Ké TS (1947) Experimental evidence of the viscous behavior of grain boundaries in metals. *Phys Rev* 71(8):533–546
- Ké TS (1999) Fifty-year study of grain boundary relaxation. *Metall Mater Trans A* 30A:2267–2295
- Knopoff L (1964) Q. *Rev Geophys* 4:625–660
- Kuroiwa, D (1964) Internal friction of ice. I; The internal friction of H<sub>2</sub>O and D<sub>2</sub>O ice, and the influence of chemical impurities on mechanical damping. *Contributions from the Institute of Low Temperature Science* A18:1–37
- Kuster GT, Toksöz MN (1974) Velocity and attenuation of seismic waves in two-phase media Part 1. Theoretical formulations. *Geophysics* 39:587
- Ladanyi B, Saint-Pierre R (1978) Evaluation of creep properties of sea ice by means of a borehole dilatometer. In: Proceedings of the international association of hydraulic research symposium on ice problems, Part I, Lulea, pp 97–115
- Lakes RS (1999) Viscoelastic solids. CRC Press, Boca Raton
- Lakes RS (2004) Viscoelastic measurement techniques. *Rev Sci Instrum* 75(4):797–809
- Langleben MP, Pounder ER (1963) Elastic parameters of sea ice, in ice and snow: properties, processes and applications. MIT Press, Cambridge, pp 69–78
- Lee LC, Morris SJS (2010) Anelasticity and grain boundary sliding. *Proc R Soc A*. doi: [10.1088/1361-6403/365/1862/0624v1](https://doi.org/10.1088/1361-6403/365/1862/0624v1)
- Louchet F (2004) Dislocations and plasticity in ice. *CR Phys* 5:687–698
- Mader HM (1992) Observations of the water-vein system in polycrystalline ice. *J Glaciol* 38 (130):333–347
- Margot JL, Nolan MC, Benner LAM, Ostro SJ, Jurgens RF, Giorgini JD, Slade MA, Campbell DB (2002) Binary asteroids in the near-earth object population. *Sci Exp.* doi:[10.1126/science.1072094](https://doi.org/10.1126/science.1072094)
- Matson DL, Castillo-Rogez JC, McKinnon WB, Sotin C, Schubert G (2009) The thermal evolution and internal structure of Saturn's midsize icy satellites. In: Brown R, Dougherty M, Esposito L, Krimigis T, Waite H (eds) *Saturn after Cassini-Huygens*, Springer, Chapter 19, doi:[10.1007/978-1-4020-9217-6\\_18](https://doi.org/10.1007/978-1-4020-9217-6_18)

- Mavko GM (1980) Velocity and attenuation in partially melted rocks. *J Geophys Res* 85:5173–5189
- Mavko G, Mukerji T, Dvorkin J (1998) The rock physics handbook: tools for seismic analysis of porous media. Cambridge University Press, Cambridge
- Maxwell JC (1867) On the dynamical theory of gases. *Philos Trans* 157:49–83
- McCarthy C, Goldsby DL, Cooper RF, Durham WB, Kirby SH (2007) Steady-state creep response of ice-I/magnesium sulfate hydrate. Workshop on ices, oceans, and fire: satellites of the outer Solar system, Boulder, 13–15 Aug 2007, pp 88–89
- McCarthy C, Berglund SR, Cooper RF, Goldsby DL (2008) Influence of strain history and strain amplitude on the internal friction of ice-I and two-phase ice/salt hydrate aggregates, AGU fall meeting, American Geophysical Union
- McCarthy C, Cooper RF, Goldsby DL, Durham WB, Kirby S (2011a) Transient and steady-state creep responses of ice-I and magnesium sulfate hydrate eutectic aggregates. *J Geophys Res.* doi:[10.1029/2010JE003689](https://doi.org/10.1029/2010JE003689)
- McCarthy C, Takei Y, Hiraga T (2011b) Experimental study of attenuation and dispersion over a broad frequency range: 2. The universal scaling of polycrystalline materials. *J Geophys Res* 116:1–18
- McMillan KM, Lakes RS, Cooper RF, Lee T (2003) The viscoelastic behavior of  $\beta$ -In<sub>3</sub>Sn and the nature of the high-temperature background. *J Mater Sci* 38:2747–2754
- Meyer J, Wisdom J (2007) Tidal heating in Enceladus. *Icarus* 188:535–539
- Meyer J, Wisdom J (2008) Episodic volcanism on Enceladus: Application of the Ojakangas-Stevenson model. *Icarus* 198:178–180
- Mindlin RD (1954) Mechanics of granular media, Office of naval research project NR-064-388, Technical report no. 14, CU-IA-i-i-ONR-266(09) –CE
- Minster JB, Anderson DL (1981) A model of dislocation-controlled rheology for the mantle. *Philos Trans Roy Soc Lond* 299(1449):319–356
- Montagnat M, Duval P (2004) Dislocations in ice and deformation mechanisms: from single crystals to polar ice. *Defects Diffus Forum* 229:43–54
- Murray CD, Dermott SF (2000) Solar system dynamics. Cambridge University Press, Cambridge, UK, p 592
- Nakamura T, Abe O (1980) A grain-boundary relaxation peak of antarctic mizuho ice observed in internal friction measurements at low frequency. *J Fac Sci, Hokkaido University. Series 7, Geophysics* 6(1):165–171
- Niblett DH, Zein M (1980) The Bordoni peak in copper single crystals at megahertz frequencies. *J Phys F Met Phys* 10:773–780
- Nimmo F (2008) Tidal dissipation and faulting, or a tale of Q and f. The science of Solar system ices workshop, Oxnard, 5–8 May 2008
- Nimmo F, Spencer JR, Pappalardo RT, Mullen ME (2007) Shear heating as the origin of the plumes and heat flux on Enceladus. *Nature* 447:289–291
- Nowick AS, Berry BS (1972) Anelastic relaxation in crystalline solids. Academic, New York
- Nye JF, Frank FC (1973) Hydrology of the intergranular veins in a temperate glacier In: Symposium on the hydrology of glaciers, vol 95. Cambridge (1969), International Association of Scientific Hydrology Publication, pp 157–161
- O'Connell RJ, Budiansky B (1977) Viscoelastic properties of fluid-saturated cracked solids. *J Geophys Res* 82:5719–5735
- O'Connell RJ, Budiansky B (1978) Measures of dissipation in viscoelastic media. *Geophys Res Lett* 5(1):5–8
- Oguro M (2001) Anelastic behavior of H<sub>2</sub>O ice single crystals doped with KOH. *J Phys Chem Solids* 62:897–902. doi:[10.1016/S0022-3697\(00\)00247-X](https://doi.org/10.1016/S0022-3697(00)00247-X)
- Parameswaran VR (1987) Orientation dependence of elastic constants for ice. *Def Sci J* 37:367–375
- Pauling L (1935) The structure and entropy of ice and other crystals with some randomness of atomic structure. *J Am Chem Soc* 57:2680–2684

- Peale SJ (1986) Orbital resonances, unusual configurations and exotic rotation states among planetary satellites. In: Burns JA, Matthews MS (eds) *Satellites*. University of Arizona Press, Tucson
- Peale SJ, Cassen P, Reynolds RT (1979) Melting of Io by tidal dissipation. *Science* 203:892–894
- Peale SJ, Cassen P, Reynolds RT (1980) Tidal dissipation, orbital evolution, and the nature of Saturn's inner satellites. *Icarus* 43:65–72
- Perez J, Maï C, Tatibouët J, Vassouille R (1986) Dynamic behaviour of dislocations in HF-doped ice Ih. *J Glaciol* 25(91):133–149
- Petrenko VF, Whitworth RW (1999) *Physics of ice*. Oxford University Press, Oxford, UK
- Pilbeam CC, Vaisnys JR (1973) Acoustic velocities and energy losses in granular aggregates. *J Geophys Res* 78(5):810–824
- Raj R (1975) Transient behavior of diffusion-induced creep and creep rupture. *Metall Trans* 6A:1499–1509
- Raj R, Ashby MF (1971) On grain boundary sliding and diffusion creep. *Metall Trans* 2:1113–1127
- Rambaux N, Castillo-Rogez JC, Williams JG, Karatekin O (2010) The librational response of Enceladus. *Geophys Res Lett* 37:L04202. doi:[10.1029/2009GL041465](https://doi.org/10.1029/2009GL041465)
- Rappaport NJ, Iess L, Wahr J, Lunine JI, Armstrong JW, Asmar SW, Tortora P, di Benedetto M, Racopoppa P (2008) Can Cassini detect a subsurface ocean in Titan from gravity measurements? *Icarus* 194:711–720. doi:[10.1016/j.icarus.2007.11.024](https://doi.org/10.1016/j.icarus.2007.11.024)
- Roberts JH, Nimmo F (2008) Tidal heating and the long-term stability of a subsurface ocean on Enceladus. *Icarus* 193:675–689
- Robuchon G, Choblet G, Tobie G, Cadek O, Sotin C, Grasset O (2010) Coupling of thermal evolution and despinning of early Iapetus. *Icarus* 207:959–971. doi:[10.1016/j.icarus.2009.12.002](https://doi.org/10.1016/j.icarus.2009.12.002)
- Romanowicz B (1994) Anelastic tomography: a new perspective on upper-mantle thermal structure. *Earth Planet Sci Lett* 128:113–121
- Rothrock DA (1975) Mechanical behavior of pack ice (invited review paper). *Annu Rev Earth Planet Sci* 3:317–342
- Schlüson EM, Duval P (2009) *Creep and fracture of ice*. Cambridge University Press, Cambridge, UK
- Snoek J (1939) Letter to the editor. *Physica* 6(7–12):591–592. doi:[10.1016/S0031-8914\(39\)90061-3](https://doi.org/10.1016/S0031-8914(39)90061-3)
- Song M (2008) An evaluation of the rate-controlling flow process in Newtonian creep of polycrystalline ice. *Mater Sci Eng A Struct Mater Propert Microstr Process* 486:27–31
- Song M, Cole DM, Baker I (2006) Investigation of Newtonian creep in polycrystalline ice. *Philos Mag Lett* 86:763–771
- Sotin C, Head JW, Tobie G (2002) Europa: tidal heating of upwelling thermal plumes and the origin of lenticulae and chaos melting. *Geophys Res Lett* 29:74-1. doi:[10.1029/2001GL013844](https://doi.org/10.1029/2001GL013844), CiteID 1233
- Spencer JR, Pearl JC, Segura M, Flasar FM, Mamoutkine A, Romani P, Buratti BJ, Hendrix AR, Spilker LJ, Lopes RMC (2006) Cassini encounters Enceladus: background and the discovery of a South Polar hot spot. *Science* 311:1401–1405
- Spetzler H, Anderson DL (1968) The effect of temperature and partial melting on velocity and attenuation in a simple binary system. *J Geophys Res* 73:6051–6060
- Staroszczyk R, Morland L (1999) Orthotropic viscous model for ice, Lecture notes in physics, technological, environmental, and climatological impact. In: Proceedings of the 6th international symposium, Darmstadt, 22–25 Aug 1999, pp 249–258, doi:[10.1007/BFb0104166](https://doi.org/10.1007/BFb0104166)
- Sundberg M, Cooper RF (2010) A composite viscoelastic model for incorporating grain boundary sliding and transient diffusion creep; correlating creep and attenuation responses for materials with a fine grain size. *Philos Mag* 90(20):2817–2840
- Tamura J, Kogure Y, Hiki Y (1986) Ultrasonic attenuation and dislocation damping in crystals of ice. *J Phys Soc Jpn* 55(10):3445–3461
- Tan BH, Jackson I, Fitz Gerald JD (2001) High-temperature viscoelasticity of fine-grained polycrystalline olivine. *Phys Chem Miner* 28:641–664

- Tatiboutet J, Perez J, Vassouille R (1981) Very low frequencies internal friction measurements of ice Ih. *J Phys Colloq C5*(42):541–546
- Tatiboutet J, Perez J, Vassouille R (1983) Study of lattice defects in ice Ih by very-low-frequency internal friction measurements. *J Phys Chem* 87:4050–4054
- Tatiboutet J, Perez J, Vassouille R (1986) High-temperature internal friction and dislocations in ice Ih. *J Phys* 47:51–60
- Tatiboutet J, Perez J, Vassouille R (1987) Study of grain boundaries in ice by internal friction measurement. *J Phys* 48(suppl 3):C1-197–C1-203
- Taupin V, Richeton T, Chevy J, Fressengeas C, Weiss J, Louchet F, Carmen-Miguel M (2008) Rearrangement of dislocation structures in the aging of ice single crystals. *Acta Mater* 56:1555–1563
- Tobie G, Choblet G, Sotin C (2003) Tidally heated convection: constraints on Europa's ice shell thickness. *J Geophys Res* 108:5124. doi:[10.1029/2003JE002099](https://doi.org/10.1029/2003JE002099)
- Tobie G, Mocquet A, Sotin C (2005) Tidal dissipation within large icy satellites: applications to Europa and Titan. *Icarus* 177:534–549
- Tobie G, Cadek O, Sotin C (2008) Solid tidal friction above a liquid water reservoir as the origin of the south pole hotspot on Enceladus. *Icarus* 196:642–652
- Vassouille R, Mai C, Perez J (1978) Inelastic behavior of ice Ih single crystals in the low-frequency range due to dislocations. *J Glaciol* 21(85):375–384
- Waff HS, Bulau JR (1979) Equilibrium fluid distribution in an ultramafic partial melt under hydrostatic stress conditions. *J Geophys Res* 84:6109–6114
- Webb WW, Hayes CE (1967) Dislocations and plastic deformation of ice. *Philos Mag* 16:909–925
- Webb S, Jackson I (2003) Anelasticity and microcreep in polycrystalline MgO at high temperature: an exploratory study. *Phys Chem Miner* 30:157–166. doi:[10.1007/s00269-003-0299-1](https://doi.org/10.1007/s00269-003-0299-1)
- Weertman J (1955) Internal friction of metal single crystals. *J Appl Phys* 26(2):202–210
- Weertman J (1983) Creep deformation of ice. *Annu Rev Earth Planet Sci* 11:215–240
- Weertman J, Weertman JR (1975) High temperature creep of rock and mantle viscosity. *Annu Rev Earth Planet Sci* 3:293–315
- Whitworth RW (1980) The influence of the choice of glide plane on the theory of the velocity of dislocations in ice. *Philos Mag A* 41(4):521–528
- Wieczkowski K, Wolf D (1998) Modelling of stresses in the Fennoscandian lithosphere induced by Pleistocene glaciations. *Tectonophysics* 294(3–4):291–303
- Williams JG, Boggs DH, Yoder CF, Ratcliff JT, Dickey JO (2001) Lunar rotational dissipation in solid body and molten core. *J Geophys Res-Planet* 106:27933–27968
- Winkler KW, Murphy WF III (1995) Acoustic velocity and attenuation in porous rocks. In: Ahrens TJ (ed) *Rock physics and phase relations: A handbook of physical constants*. American Geophysical Union, Washington, DC
- Woigard J, Sarrazin Y, Chaumet H (1977) Apparatus for the measurement of internal friction as a function of frequency between  $10^{-5}$  and 10 Hz. *Rev Sci Instrum* 48(10):1322–1325
- Wu TT (1966) The effect of inclusion shape on the elastic moduli of a two-phase material. *Int J Solids Struct* 2:1–8
- Yoder CF (1982) Tidal rigidity of Phobos. *Icarus* 49:327–346
- Zener C (1947) Theory of the elasticity of polycrystals with viscous grain boundaries. *Phys Rev* 60:906–908
- Zener C (1948) Elasticity and anelasticity of metals. University of Chicago Press, Chicago
- Zhang K, Nimmo F (2009) Recent orbital evolution and the internal structures of Enceladus and Dione. *Icarus* 204:597–609. doi:[10.1016/j.icarus.2009.07.007](https://doi.org/10.1016/j.icarus.2009.07.007)
- Zschau J (1978) Tidal friction in the solid earth: loading tides versus body tides. In: Brosche P, Sundermann J (eds) *Tidal friction and the Earth's rotation*. Springer, New-York, pp 62–94

# Chapter 8

## Creep Behavior of Ice in Polar Ice Sheets

Paul Duval

**Abstract** Major advances in the understanding of the plasticity of ice Ih have been made with the development of studies of the flow of glaciers and, recently, with the analysis of deep ice cores in Antarctica and Greenland. Evidence is presented that indicates deformation, in glaciers and ice sheets, is essentially produced by basal slip. Other deformation modes are required for compatibility reasons: non-basal slip, dislocation climb, cross-slip and/or grain boundary sliding. Diffusion processes cannot be invoked as a significant deformation mode, even at low stresses. A grain size effect is expected for secondary creep, as soon as the stress exponent of the flow law is lower than 2. A threshold stress could explain the apparent high stress exponent found at the ice divides in polar ice sheets. It is shown that the presence of a liquid phase at grain boundaries or around particles significantly reduces the ice viscosity. Dynamic recrystallization is very active in glaciers and ice sheets. Grain boundary migration associated with normal grain growth and dynamic recrystallization is considered as an efficient accommodation process of basal slip. Migration recrystallization, which is associated with tertiary creep and with the rapid migration of grain boundaries between dislocation-free nuclei and deformed grains, produces an interlocking grain structure and grains well oriented for basal slip.

### 8.1 Introduction

The ductile rheology of ice Ih has a strong impact on the flow of glaciers and polar ice sheets. The ice stored within the Greenland and the Antarctic ice sheets, should it flow into the sea, would raise the level by about 7 m and about 60 m, respectively. The creep of ice sheets, which can impart strains that exceed unity in several hundreds of thousand years, is also relevant to paleoclimatology. The determination

---

P. Duval (✉)

LGGE/CNRS, BP 96, 38402 Saint Martin d'Hères Cedex, France

e-mail: [duval@lgge.obs.ujf-grenoble.fr](mailto:duval@lgge.obs.ujf-grenoble.fr)

of the age of ice depends in part upon constitutive laws that describe the deformation behavior, laws that must incorporate plastic anisotropy, the presence of water near the bottom and sliding. Ice in polar ice sheets is generally clean, with a concentration of atmospheric particles typically of the order of 1,000 ng/g in ice from glacial periods and 50 ng/g in ice from interglacial periods (Duval and Montagnat 2006). In the basal layers, ice can pick up dirt and rocks as it moves over the bedrock and a concentration of impurities higher than 20% by volume can be found.

The brittle and ductile rheology of water ices has a primary influence on the evolution and dynamics of icy moons of the outer solar system and several high-pressure phases exist (Sotin et al. 1998). A review of essential results on the rheology of high-pressure ices can be found in Durham et al. (1998). Concerning ice Ih, data on the flow behavior of terrestrial ice sheets are needed to constraint the governing parameters of the flow behavior of icy satellites even if some extrapolations can be required. In any case, the applicable deformation regime to icy satellites interiors is always in question. The main reason is the difficulty to reproduce in the laboratory the *in situ* conditions. For example, convective stresses in the Europa ice shell deduced from thermal convection models are between  $10^{-4}$  and  $10^{-3}$  MPa whereas tidal stresses would be between  $10^{-2}$  and  $10^{-1}$  MPa (Tobie et al. 2003). At these low stresses, the time required to reach a steady state or a strain higher than 1% can be longer than several centuries. Based on laboratory experiments performed by Goldsby and Kohlstedt (1997), a grain-size dependence of the ice viscosity was deduced for these low-stresses conditions, but by means of extrapolation of grain size and temperature (Goldsby and Kohlstedt 2001). This grain size effect is associated with a stress exponent lower than 2. The decrease of the stress exponent at deviatoric stresses lower than 0.1 MPa was deduced from several laboratory experiments (Mellor and Testa 1969; Duval 1973) and also from *in situ* measurements (Holdsworth and Bull 1970; Lipenkov et al. 1997; Cuffey et al. 2000; Pettit and Waddington 2003). But, deformation modes associated with this grain-size effect are not definitively clarified (Duval and Montagnat 2002; Goldsby and Kohlstedt 2002).

This work focuses on the deformation modes of polycrystalline ice for conditions prevailing in polar ice sheets. The analysis is made by taking into account the evolution of the ice microstructure along deep ice cores recovered in the coldest parts of East Antarctica. Emphasis is placed on the influence of grain size, impurities and liquid phase on the ice viscosity in the low-stress conditions of polar ice sheets. Considering the direct relation between the behavior of the ice crystal and the polycrystal, analysis of deformation modes of single ice crystals is made with emphasis on its exceptional anisotropy and dislocation dynamics.

## 8.2 Polar Ice Sheets and Deep Ice Cores

Deep ice cores provide the most direct and highly resolved records of climate and the atmospheric composition over the past 800,000 years. Several ice cores have been retrieved in Greenland and Antarctica the last 50 years. The analysis of these ices also gives information on their physical properties such as texture, crystal orientation and, thus, the deformation history of these ice sheets, the past thickness and sea level.

### 8.2.1 *The Antarctic Ice Sheet*

The Antarctic ice sheet covers an area of about 14 million km<sup>2</sup>. Its thickness is higher than 3 km on a large part of East Antarctica. If melted, this ice sheet would cause sea level to rise by more than 60 m. Mean annual Temperature is lower than  $-57^{\circ}\text{C}$  in East Antarctica where the thickness can reach 4,000 m. Three deep ice cores of more than 3,000 long have provided the past climate over several climatic cycles: the 3,700 m Vostok ice core (Petit et al. 1999), the 3,270 m EPICA ice core (Augustin et al. 2004) and the 3,035 m Dome Fuji ice core (Motoyama 2007). The flat surface on East Antarctica gives a low horizontal shear stress and deformation is essentially induced by axial stresses with a vertical strain rate along the major part of the cores, which is about  $2.5 \times 10^{-13} \text{ s}^{-1}$  at Vostok (De La Chapelle et al. 1998). More detailed information on the last climatic cycle has been obtained from the analysis of ice cores retrieved in West Antarctica where the accumulation rate is much higher. Information on the ice structure of the 2,164 m Byrd ice core retrieved in 1968 can be found in Gow and Williamson (1976).

### 8.2.2 *The Greenland Ice Sheet*

The Greenland ice sheet covers an area of about 1.7 million of km<sup>2</sup>. Its thickness is higher than 3,000 m in the central part of the ice sheet and if melted, this ice sheet would cause sea level to rise by about 7 m. Several deep ice cores have been retrieved these last 20 years. The GRIP and GISP2 ice cores, of about 3,000 m length, have given climatic information on about 120,000 years. Information on the ice structure along these two deep ice cores can be found in Gow et al. (1997) and Thorsteinsson et al. (1997).

## 8.3 Viscoplastic Behavior of Single Ice Crystals

### 8.3.1 *Basal and Non-basal Slip*

Single crystals undergo plastic deformation as soon as there is a component of shear stress on the basal plane. Basal slip is observed for shear stresses in the basal plane lower than 0.02 MPa (Chevy 2008). It takes place due the motion of basal dislocations with the  $a/3<11\bar{2}0>$  Burgers' vector (Hobbs 1974). The macroscopic slip direction corresponds to the maximum shear direction in the basal plane (Glen and Perutz 1954).

The creep of single crystals deformed so that basal slip can take place is characterized by a continuously increasing strain rate. The multiplication of mobile dislocations is at the origin of this softening and hardening by dislocation interactions is not significant even at strain higher than 50% (Chevy 2008). The

double cross-slip of basal screw dislocations on prismatic or pyramidal planes appears to be an efficient mechanism for dislocation multiplication (Chevy 2008). The dislocation density during a creep test can increase from less than  $10^8$  to more than  $10^{12} \text{ m}^{-2}$ .

Non-basal slip can be studied when ice crystals are loaded such that there is no resolved shear stress on the basal plane. But, those tests are difficult to perform, since a slight misorientation ( $\leq 1^\circ$ ) can rise to basal slip. Though some prismatic glide is observed for orientations close to those that inhibit basal slip, no clear observation of any deformation is reported in crystals loaded along the [0001] direction, that inhibits both basal and prismatic slip. Figure 8.1 shows the relationship between strain rate and stress for basal and non-basal slip. The non-basal deformation of ice crystals requires a stress at least 60 times larger than that for basal slip at the same strain rate.

### 8.3.2 *Dynamics of Dislocations*

High quality measurements have been made of the velocity at which individual dislocations glide on both basal and prismatic planes in ice (Ahmad and Whitworth 1988; Shearwood and Whitworth 1991; Okada et al. 1999). Results obtained for stresses lower than 1 MPa show that the average velocity on the basal plane scales linearly with the shear stress resolved on that plane (Petrenko and Whitworth 1999). Under a shear stress of 0.1 MPa on the basal plane, the velocity of basal screw dislocations at  $-10^\circ\text{C}$  is about  $1 \mu\text{m s}^{-1}$  (Shearwood and Whitworth 1991).

Investigation of the plastic deformation of ice crystals in terms of the dynamics of dislocations generally involve computing the velocity of one dislocation segment under stress in the presence of various obstacles and the macroscopic plasticity is directly related to the uncorrelated motion of a large number of dislocations (Weertman 1973). Recent work questions the concept of uncorrelated motion and the modelling that stems from it. Experiments on ice single crystals revealed that the strain response to a constant load consists of a series of dislocation avalanches (Miguel et al. 2001). A relatively large number of dislocations appears to move cooperatively in an intermittent fashion and the movement is correlated over large distances. This collective behaviour manifests itself in the form of dislocation patterns. The motion of dislocations in ice crystals is associated with the formation of slip lines and slip bands with a scale invariance in their spatial distribution (Chevy et al. 2010). These large-scale correlations are the fingerprint of strong interactions between dislocations and the formation of long-range internal stresses (Montagnat et al. 2006).

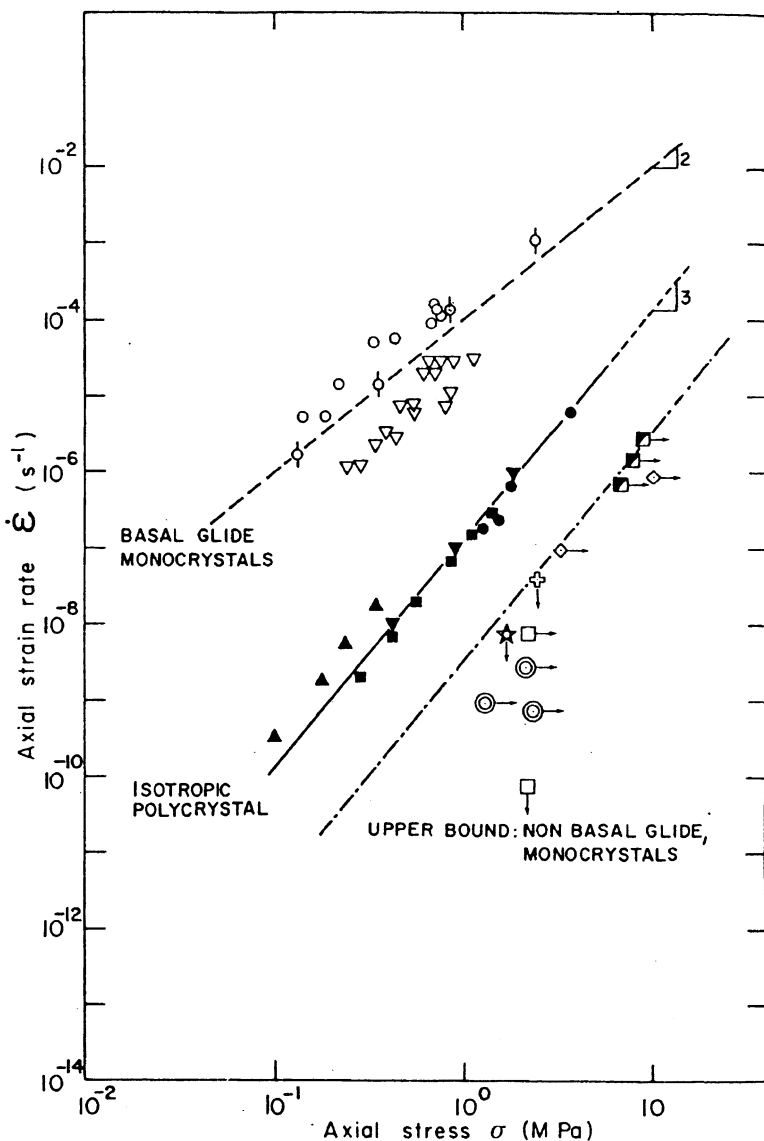


**Fig. 8.1** Stress-strain rate relationship for basal and non-basal slip in single crystals at  $-10^{\circ}\text{C}$ , and for isotropic polycrystals (From Duval et al. 1983)

### 8.3.3 Internal Friction

When subjected to small stresses and for short time, an ice crystal may not suffer permanent deformation. The reversible motion of dislocations can induce energy dissipation. The associated internal friction  $\delta$  is given by:

$$\delta = \frac{1}{2\pi} \frac{\Delta W}{W} \quad (8.1)$$

where  $\Delta W$  and  $W$ , respectively, are the dissipated energy during one cycle of the loading stress and the maximum elastic energy during this cycle.

Internal friction experiments performed over wide frequency range and at high temperature have been used to study the dynamics of dislocations in a single crystal oriented for basal slip (Tatibouet et al. 1986). There is a large increase of the internal friction above 200 K at frequencies lower than 1 Hz that is related to the motion of basal dislocations (Tatibouet et al. 1986). The non-linear dependence of internal friction on the inverse of frequency is explained by a distribution in dislocation relaxation time, associated with interactions between basal and non-basal dislocations segments. For a given frequency, high temperature internal friction increases with the strain amplitude (applied stress) and dislocation density. These results are related to the Orowan's equation, which gives strain rate as a function of the mobile dislocation density and dislocation velocity. It is worth noting that dislocation multiplication was not observed at  $10^{-3}$  Hz with strain amplitude less than  $10^{-4}$  (Tatibouet et al. 1986). The experiments of Tatibouet et al. (1986) were performed for a dislocation density less than  $5 \times 10^9 \text{ m}^{-2}$ . Measurements on highly deformed single crystals would be useful to determine variation of internal friction with dislocation density. Values higher than  $10^{11} \text{ m}^{-2}$  are expected in deformed single crystals (Chevy 2008).

### 8.3.4 The Flow Law and Rate-Controlling Processes for Basal Slip of Single Ice Crystals

The strain rate determined in creep tests can be expressed by:

$$\dot{\varepsilon} = A\sigma^n \exp(-Q/RT) \quad (8.2)$$

where R is the gas constant and T the temperature. Almost all authors report a stress exponent  $n$ , of  $2 \pm 0.3$  and an activation energy  $Q$  close to 65 kJ/mole (Jones and Glen 1969). It is important to point out that the value of  $n$  has been determined for finite strain between 3% and 20%. It is worth noting that steady state was probably not reached in these experiments (Chevy 2008).

Rate-controlling processes for basal slip could be directly related to the mobility of basal dislocations. But, values of the activation energy for basal slip are significantly less than those for the motion of basal dislocations (Hondoh 2000). Considering the possible role of cross-slip in dislocation multiplication, the activation energy for basal slip would not be related to the mobility of basal dislocations, but rather to this mechanism which would induce the multiplication of mobile dislocations (Schulson and Duval 2009).

## 8.4 Ductile Behavior of Isotropic Polycrystalline Ice

### 8.4.1 Creep Behavior

A typical creep curve, giving strain rate as a function of strain, is shown in Fig. 8.2. After an initial instantaneous elastic strain, there is a period of primary or transient creep where the creep rate decreases continuously. A minimum creep rate can be determined in the range of strain of 1–2%. This secondary creep corresponds to the transition between the decelerating primary creep and the accelerating tertiary creep. Beyond about 10% strain, a steady state can be reached if cracking does not occur; this stage corresponds to tertiary creep.

#### 8.4.1.1 Primary Creep

The primary creep strain  $\varepsilon_p$  is generally well described by the Andrade law (Duval 1976):

$$\varepsilon_p = \varepsilon_0 + \beta t^{1/3} + \varepsilon \dot{Y}_{\min} t \quad (8.3)$$

where  $\varepsilon_0$  is “instantaneous” strain,  $t$  the time and  $\varepsilon \dot{Y}_{\min}$  is the secondary creep rate. The transient strain  $\varepsilon_t = \beta t^{1/3}$  is made up of a recoverable “delayed elastic” strain  $\varepsilon_d$  plus an irreversible viscous strain. The strain  $\varepsilon_d$  can be one order of magnitude higher than the theoretical elastic strain (Duval 1978) whereas the transient creep strain can be more than 50 times the elastic strain (Ashby and Duval 1985). It is worth noting that the transient strain is sometimes considered as fully recoverable by some authors, which can be the case as long as the transient strain is lower than  $10^{-4}$  (Tatibouet et al. 1986; Cole and Durell 1995). As shown in Fig. 8.3, the initial strain rate can be 100 times the minimum strain rate. Deformation by basal slip in each grain explains the high initial strain rate. Due to the mismatch of slip at grain boundaries, an increasingly non-uniform state of long-range internal stress develops, which promotes the cooperative glide of dislocations and dislocations avalanches, as observed in monocrystals. The hardening associated with primary creep is essentially kinematic or directional: it is represented by a tensor and it is

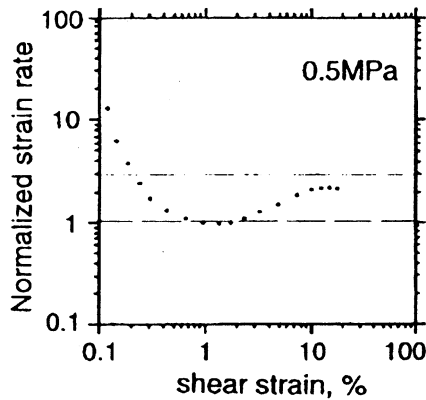


**Fig. 8.2** Normalized strain rate plotted against strain for isotropic polycrystalline ice deformed in uniaxial compression at  $-15^{\circ}\text{C}$ . Horizontal lines indicate secondary and tertiary creep (From Jacka and Li Jun 2000)

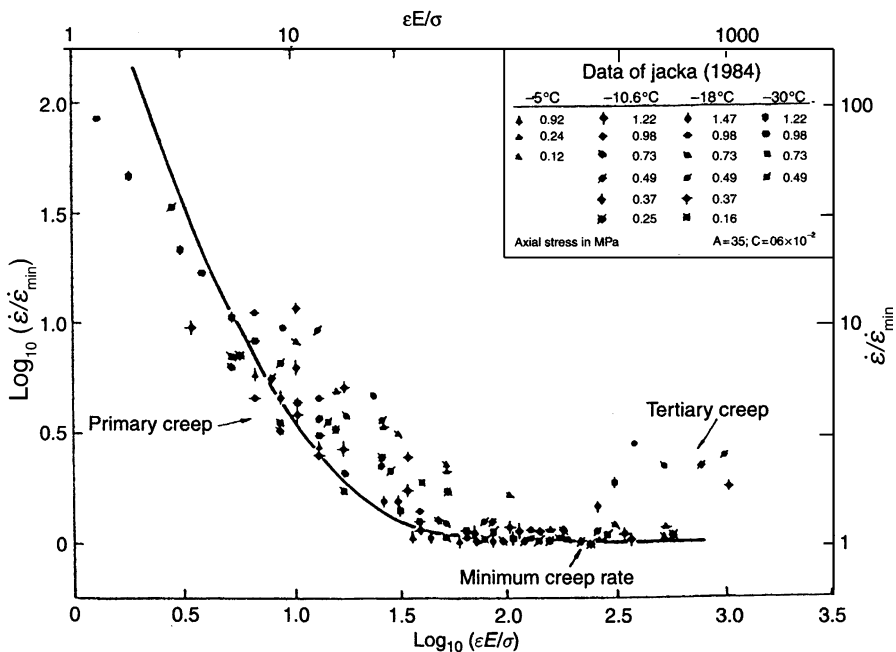


**Fig. 8.3** Strain rate plotted against strain using the reduced variables  $\frac{\dot{\varepsilon}}{\dot{\varepsilon}_{\min}}$  and  $\varepsilon E / \sigma$  (From Ashby and Duval 1985)

responsible for the large deformation recovered after unloading (Duval 1978). Transient creep has been modeled by using a mean-field self-consistent theory (Castelnau et al. 2008). In this model, in which the ice crystal was assumed to deform by basal, prismatic and pyramidal slip, the hardening kinetic of primary creep was attributed to the hardening of the hard glide prismatic systems.

#### 8.4.1.2 Internal Friction

Internal friction experiments on polycrystalline ice are suitable for the study of both grain and grain boundary behavior. At frequencies lower than 1 Hz, a grain boundary (GB) relaxation peak is observed at a temperature higher than 220 K (Tatibouet et al. 1987). The temperature at the peak increases with frequency and it is about 250 K at 1 Hz. However, internal friction is dominated by intracrystalline dislocation slip at low frequencies, as observed in ice single crystals. The effect of strain amplitude for the GB relaxation is important. For a given frequency, the height of the GB peak decreases with the increase of the imposed strain amplitude whereas the intracrystalline internal friction increases. This result would be due to the progressive accumulation of dislocations near grain boundaries, impeding the dynamics of GB dislocations at the origin of the GB relaxation (Tatibouet et al. 1987). As a consequence, internal friction at high temperature would be mainly associated with dislocation slip within grains when polycrystals are deformed. As shown in Fig. 8.3, viscosity strongly increases during transient creep and mainly by directional hardening (Duval et al. 1983). Since the amplitude of deformation during internal friction is relatively low, the ice viscosity should be much lower than that corresponding to secondary creep whatever the deformation microstructure.

#### 8.4.1.3 Secondary Creep

There is general agreement on the form of the constitutive law for the minimum creep rate. It is well described by Glen's law (Glen 1955) and is known in the engineering literature as Norton's law. For multiaxial stress states, the strain rate  $\dot{\epsilon}^Y_{ij}$  is related to the deviatoric stresses  $\sigma'_{ij}$  by:

$$\dot{\epsilon}^Y_{ij} = \frac{B}{2} \tau^{n-1} \sigma'_{ij} \quad (8.4)$$

where  $B$  and  $n$  are creep constants and  $\tau$  the effective shear stress defined by  $\tau^2 = 1/2 \sum_{ij} (\sigma'_{ij})^2$ . Data for axial stresses in the range of 0.2–2 MPa on clean ice suggest a stress exponent  $n = 3$  (Barnes et al. 1971; Budd and Jacka 1989). Equation 8.4 was verified with tests performed in shear and compression (Duval 1976; Budd and Jacka 1989).

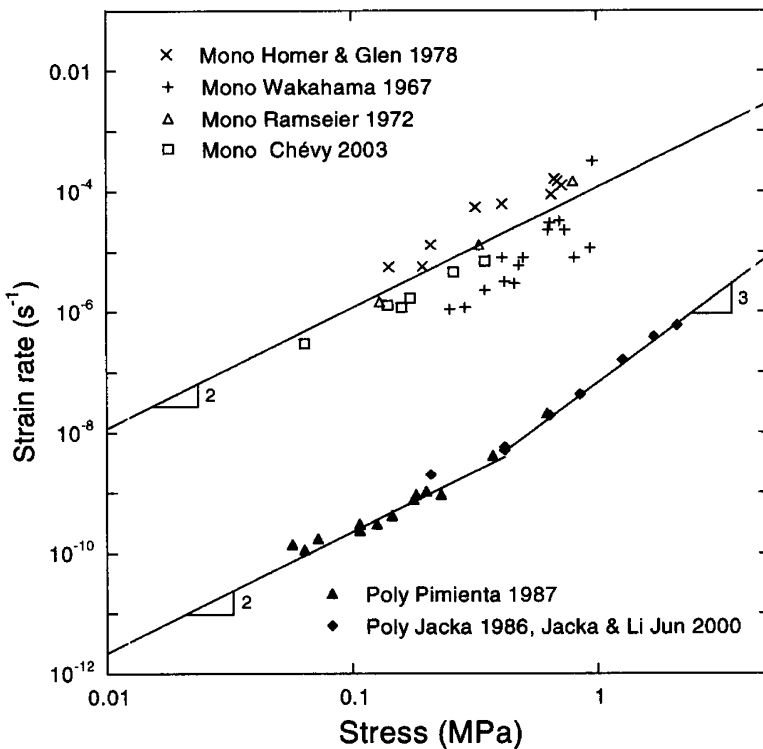


**Fig. 8.4** Equivalent secondary strain rate  $\dot{\varepsilon}'_{eq}$  plotted against equivalent stress  $\sigma_{eq}$  for single crystals deformed by basal slip and for isotropic polycrystalline ice at  $-10^{\circ}\text{C}$ ;  $\dot{\varepsilon}_{eq}^2 = 2/3\dot{\varepsilon}_{ij}\dot{\varepsilon}_{ij}$  and  $\sigma_{eq}^2 = 3/2\dot{\sigma}_{ij}'\dot{\sigma}_{ij}'$  (From Montagnat and Duval 2004)

### Behavior at Low Stresses

The behavior of ice at stresses lower than 0.2 MPa has been the subject of extensive studies over several decades. This interest is mainly related to the flow of ice sheets for which deviatoric stresses are generally lower than 0.1 MPa and to the deformation of ice Ih in planetary conditions (Durham et al. 2001). The difficulty in obtaining reliable data at strain rates lower than  $10^{-10} \text{ s}^{-1}$  is at the origin of contradictory results. But, a clear indication of the decrease of the stress exponent for deviatoric stress below 0.1 MPa was found from both laboratory tests and the analysis of field data (Mellor and Testa 1969; Dahl-Jensen and Gundestrup 1987; Lipenkov et al. 1997). Figure 8.4 shows this transition between a behavior with a stress exponent of about 3 at *high stresses* and a behavior with  $n \leq 2$  at *low stresses*. This figure also shows the large difference between the behavior of single crystals oriented for basal slip and the isotropic polycrystal. It should be noted that a regime with  $n = 1.8$  was obtained on finely-grained ice ( $<200 \mu\text{m}$ ) by Goldsby and Kohlstedt (1997, 2001), from compression creep tests performed at 236 K.

A Newtonian viscosity  $\eta = \sigma'_{ij}/2 \dot{\varepsilon}_{ij}$  was assumed for effective shear stresses less than 0.1 MPa. (Langdon 1973; Doake and Wolff 1985). But, there is no evidence of this behavior even if polynomial laws with three exponents from  $n = 1$  to  $n = 5$  were suggested for glacier flow modeling (Lliboutry 1969; Hutter 1983; Pettit and Waddington 2003). A grain size sensitive creep regime with  $n = 1$  was however suggested for shear stresses lower than 75 kPa from measurements of the tilting of several boreholes in an isothermal temperate glacier (Marshall et al. 2002). The trend of the increasing stress exponent with decreasing stress observed under ice divides and ridges (Gillet-Chaulet et al. 2011) could be ascribed to the existence of a threshold stress. This is a crucial question for the behaviour of ice at low stresses, and, specially, for planetary ices.

### Effect of Temperature and a Liquid Phase

The variation of the material constant  $B$  (Eq. 8.4) with temperature has been studied by many authors in the regime with  $n = 3$ . The activation energy, determined between  $-10^{\circ}\text{C}$  and  $-48^{\circ}\text{C}$  and for an axial stress of 1 MPa. by Barnes et al. (1971), is about 78 kJ/mole. This value is in agreement with several studies (cf. Hooke LeB 1981). At  $-10^{\circ}\text{C}$ , depending on several parameters (grain size, density, impurity content, etc),  $B$  is typically between  $5 \times 10^{-7}$  and  $2 \times 10^{-6} (\text{MPa})^{-3} \text{ s}^{-1}$  for pure isotropic granular ice. Values outside this range for pure glacier ice are questionable.

Above about  $-10^{\circ}\text{C}$ , creep rate becomes more temperature-dependent and only an apparent activation energy can be determined. For example, a value of 120 kJ/mole was found by Barnes et al. (1971) between  $-8^{\circ}\text{C}$  and  $-2^{\circ}\text{C}$ . Measurements made at the melting point can be used to determine variation of the creep rate with the amount of liquid present within the ice sample. Duval (1977) showed that creep rate increases of a factor 4 when the water content rises from less than 0.1% to 1%. The viscosity of ice at the melting point can be lower than  $10^{12} \text{ Pa s}^{-1}$  at an equivalent stress of 0.1 MPa. Creep data on melt-free pure ice and on saline ice with 7% melt are shown in Fig. 8.5. Results obtained over a range of axial stresses between 0.1 and 0.7 MPa show that secondary creep rates are enhanced by more than one order of magnitude by the presence of the liquid phase (de La Chapelle et al. 1999), in keeping with the observation by Cole (1995) that sea ice of  $\sim 3\%$  brine content creeps faster by an order-of-magnitude than fresh-water ice of the same grain size and shape. The increase of the activation energy above  $-10^{\circ}\text{C}$  is not found in ice single crystals (Jones and Brunet 1978). This shows that processes at grain boundaries must be invoked to explain these results.

From experiments performed by Goldsby and Kohlsted (2001), the activation energy in the  $n \sim 1.8$  regime would be about  $49 \text{ kJ mole}^{-1}$  below 260 K.

### Effect of Grain Size

Grain size in glaciers and ice sheets is typically in the range of 1–10 mm. In the stress-range with  $n = 3$  and providing that the sample size is more than about

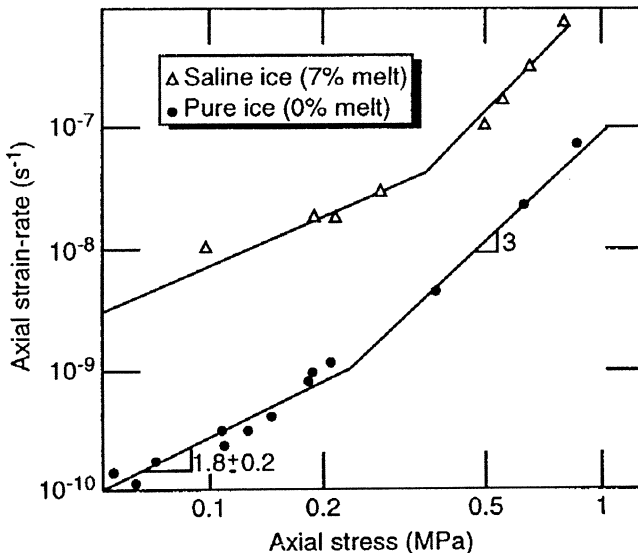


**Fig. 8.5** Equivalent secondary strain rate plotted against equivalent stress for pure and saline polycrystalline ice at  $-13^{\circ}\text{C}$ . The creep rate was determined for a strain of about 1%. (From de La Chapelle et al. 1999)

12 times greater than grain size, secondary creep does not depend on grain size (Duval and Le Gac 1980; Jones and Chew 1981; Jacka 1994). In the  $n = 1.8$  regime, the minimum creep rate appears to increase with decreasing grain size (Duval 1973; Goldsby and Kohlstedt 1997). This result is in agreement with in situ deformation measurements obtained by Cuffey et al. (2000). Considering that several deformation mechanisms imply a grain-size effect, flow-laws incorporating a grain-size dependence were suggested (Cuffey et al. 2000; Goldsby and Kohlstedt 2001; Durham and Stern 2001). From Goldsby and Kohlstedt (2001), the grain size exponent  $p$  is equal to 1.4 (with  $\dot{\varepsilon} \propto d_g^{-p}$ ) in the grain size range 26–175  $\mu\text{m}$  at 248 K. A good agreement with results given in Fig. 8.4 is found by these authors, but at the expense of extrapolations to larger grain sizes and higher temperature. It is worth noting that an inverse grain size effect was observed by Duval and LeGac (1980) for primary creep. The Andrade creep appears to increase with grain size.

### Effect of Particles and Impurities

The issue of the mechanical behavior of ice containing particles and soluble impurities is highly significant for glaciers dynamics and for the study of ice of the outer solar system (Paterson 1991; Durham et al. 1992; Mangold et al. 2002). The effect of particles on the creep behavior is dependent on both the concentration and the size.

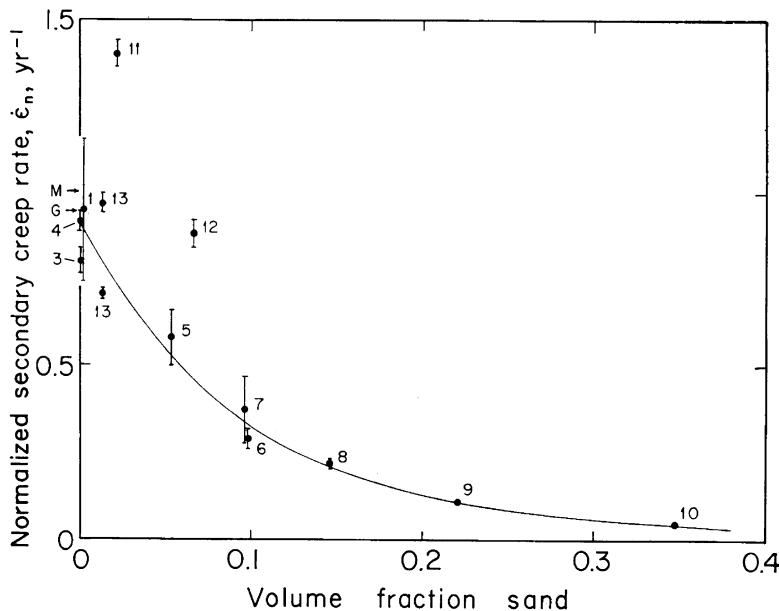


**Fig. 8.6** Secondary creep rate against volume sand concentration at  $-9.1^\circ\text{C}$ . Numbers correspond to runs (From Hooke et al. 1972)

Insoluble atmospheric impurities in polar ice sheets typically consist of particles in the size range 0.1–5  $\mu\text{m}$  with a concentration between 10 and 5,000 ng per gram of ice. For these “low” impurity concentrations, the effect on creep is difficult to assess. Indeed, glacial ice, which contains many more particles than ice from interglacial ice, has also a higher concentration of soluble impurities. On the other hand, the size and the orientation of crystals are also well correlated with climate (Paterson 1991). All these parameters are interdependent. Thus, particles exert a retarding force on moving grain boundaries and has a profound effect on grain growth in polar ice sheets (Alley et al. 1986; Durand et al. 2006). Considering the increase of strain rate with decreasing grain size, the development of a preferential orientation of grains (*fabrics*) associated with the lattice rotation by dislocation slip would be enhanced by small grain size and, in turn, by particles (Paterson 1991; Thorsteinsson et al. 1999). Based on the only correlation between particles concentration and the ice viscosity, Fischer and Koerner (1986) assert that atmospheric particles induce an increase creep rate in polar ice sheets.

At the base of glaciers and ice sheets, debris-laden ice can contain more than 70% particles by weight with particle sizes between 1  $\mu\text{m}$  and 1 mm (Echelmeyer and Zhongxiang 1987). The effect of a high concentration of fine particles on the creep behavior is well documented. The creep rate generally decreases with increasing volume fraction of particles (Hooke LeB et al. 1972; Durham et al. 1992; Mangold et al. 2002). For example, the secondary creep rate of ice samples with 0.35 volume fraction fine sand tested in uniaxial compression at  $-9.1^\circ\text{C}$  was about a factor of ten times lower than that determined with clean ice (Fig. 8.6).

Strengthening by dispersed *fine* particles can be explained by the interaction between dislocations and particles (Ashby 1966). For a high volume fraction of relatively *large* non-deformable particles, results can be interpreted in the context of the effect of hard phases in composite materials (Durham et al. 1992).

Several studies indicate that particles with a size between 1 and 100  $\mu\text{m}$  and a concentration higher than 0.5 by weight increase creep rate as soon as temperature is above  $-20^\circ\text{C}$  (Baker and Gerberich 1979; Cuffey et al. 1999). From deformation measurements at the base of a sub-polar glacier, the effective viscosity of debris-laden ice at  $-4^\circ\text{C}$ , containing 21–39% ice by weight, was found to be lower, by a factor of about 100, than that of adjacent clean ice (Echelmeyer and Zhongxiang 1987). The softening of ice above  $-10^\circ\text{C}$  by such a high concentration of sediment particles was found in several glaciers (Lawson 1996; Fitzsimons et al. 1999; Cohen 2000). From these authors, the presence of a liquid-like layer surrounding solid particles is probably at the origin of the reduction of the viscosity.

### Effect of Confining Pressure

The effect of hydrostatic pressure  $P$  on the mechanical behavior of ice deserves some interest when considering the deformation in ice sheets where the ice pressure can be higher than 30 MPa in East Antarctica. The creep of ice Ih at planetary conditions involves hydrostatic pressures that can reach 200 MPa, which is near the transition between ice I, ice II and ice III. High confining pressures are also found during the interaction between ice and marine structures (oil platforms, lighthouses..). Pressures can be as high as 50 MPa in the central zone of damaged ice with interacting cracks (Jordaan 2001).

In spite of the paucity of data, the behavior of ice under confining pressure can be described in a way that can be easily understood. The secondary creep rate is found to slightly decrease as the hydrostatic pressure increases at lower levels and then to increase at higher levels of pressure (Jones and Chew 1983; Barrette and Jordaan 2003). Taking into account the hydrostatic pressure, the minimum creep rate can be given by:

$$\dot{\varepsilon} = A\sigma^n \exp[-(E + PV)/RT] \quad (8.5)$$

where  $E$  is the activation energy and  $V$  the activation volume. In uniaxial compression,  $\sigma$  corresponds to the equivalent stress  $\sigma_{eq}$  defined by  $\sigma_{eq}^2 = 3/2\sigma'_{ij}\sigma'_{ij}$  and  $P$  the confining pressure. To conform to the behavior,  $V$  should be positive at low pressures and negative at high pressures. At high pressure, the variation of the melting temperature with pressure and some melting at grain boundaries explain the increase of creep rate with pressure (Jones and Chew 1983). From Kirby et al. (1987), this pressure effect is consistent with a negative activation volume for creep of  $-13 \times 10^{-6} \text{ m}^3 \text{ mol}^{-1}$ . A value higher than  $50 \times 10^{-6} \text{ m}^3 \text{ mol}^{-1}$  is given by Jones and Chew (1983) at  $-10^\circ\text{C}$ . This positive value of  $V$  at low pressure should be related to the activation volume of the rate-controlling process. But, data at low pressure are too scarce to permit a precise estimation of this volume.

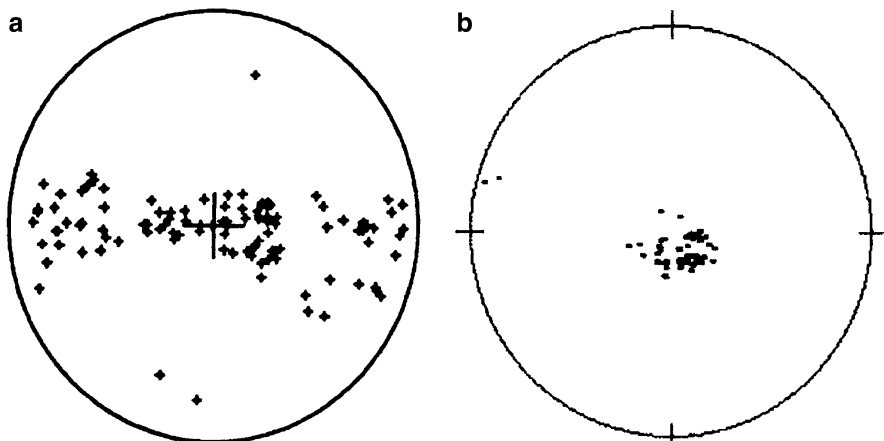


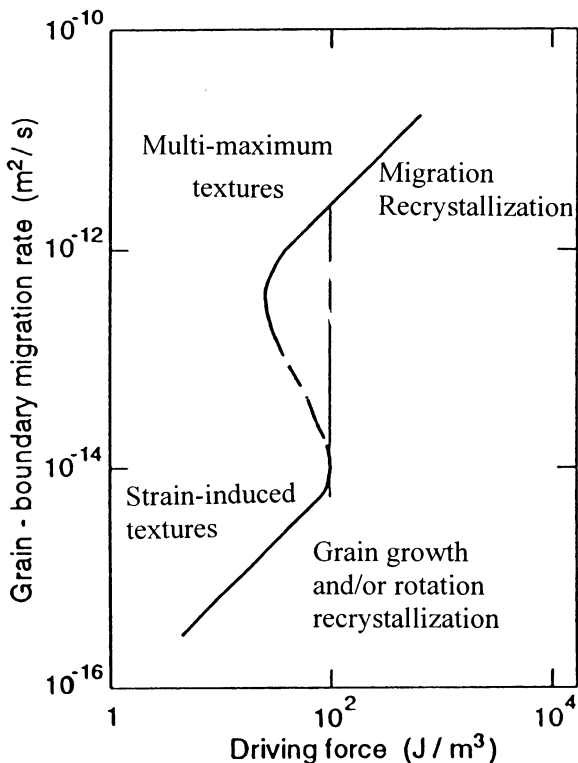
**Fig. 8.7** (a)  $c$ -axes fabric of ice of the Vostok core at the depth of 2,047 m; ice is assumed to be deformed in tension along a horizontal direction (From Castelnau et al. 1996). (b)  $c$ -axes fabric of ice of the Dome Fuji core at the depth of 2,500 m; ice is assumed to be deformed in compression along the vertical direction or by horizontal shear (From Azuma et al. 1999). The center of the diagrams represents the vertical direction

### Anisotropy of Ices

The viscous behavior of polycrystalline ice depends on the mechanical properties of individual grains in the aggregate, the orientation of such anisotropic grains and the interaction between grains. Initially isotropic ice near the surface of polar ice sheets progressively becomes anisotropic with the development of fabrics ( $c$ -axes distribution). The orientation changes that take place during deformation are related to the lattice rotation by intracrystalline slip. Figure 8.7 shows typical tension and compression fabrics observed along the Vostok and Dome Fuji ice cores. When looking for the evolution of fabrics along these ice cores, there is conclusive relation between the strength of fabrics and the final strain, in the absence of recrystallization processes (Castelnau et al. 1996). It is worth noting that ice, with the very high anisotropy of the crystal, is considered as a model material to validate polycrystals models (self-consistent and full-field approaches) established to simulate the behavior of anisotropic materials (Lebensohn et al. 2004, 2007).

Very large variations of strain rates with the applied stress direction have been found with both laboratory and in situ measurements. The directional viscosity of anisotropic polycrystalline ices such those exhibiting fabrics shown in Fig. 8.7 can differ by more than one order of magnitude depending on the direction of the applied stress (Castelnau et al. 1996; Thorsteinsson 2001).

**Fig. 8.8** Grain boundary migration rate as a function of driving force in the temperature range  $-10^{\circ}\text{C}$  to  $-15^{\circ}\text{C}$  (From Duval and Castelnau 1995). The grain boundary velocity is given by  $V = MF$ , where  $M$  is the intrinsic GB mobility and  $F$  the driving force



#### 8.4.1.4 Tertiary Creep

After the minimum creep rate corresponding to secondary creep, strain rate increases into tertiary creep. At high temperature, typically above  $-15^{\circ}\text{C}$ , and at mechanical conditions impeding cracking, a quasi steady state is reached at a strain slightly above 0.1 (Fig. 8.2). The increase of strain rate during tertiary creep is explained by softening processes directly associated with recrystallization processes and by the formation of “recrystallization fabrics” (Duval 1981; Alley 1992). The finite plastic strain is far too small to produce any important rotation of the crystal lattice and thus, the observed fabrics form by recrystallization (de La Chapelle et al. 1998). It is worth noting that ice must be considered as isotropic, since, in this case, recrystallization fabrics develop quickly with changing stress state. Thus, fabrics are stress-controlled.

Tertiary creep is associated with the rapid migration of grain boundaries between dislocation-free nuclei and deformed grains, inducing a new bulk orientation of grains. This recrystallization regime is termed “*migration recrystallization*”. Grain boundary migration rates are typically between  $10^{-12} \text{ m}^2 \text{ s}^{-1}$  and  $10^{-10} \text{ m}^2 \text{ s}^{-1}$  at  $-10^{\circ}\text{C}$  (Fig. 8.8), corresponding to grain boundary velocity between  $10^{-10} \text{ m.s}^{-1}$

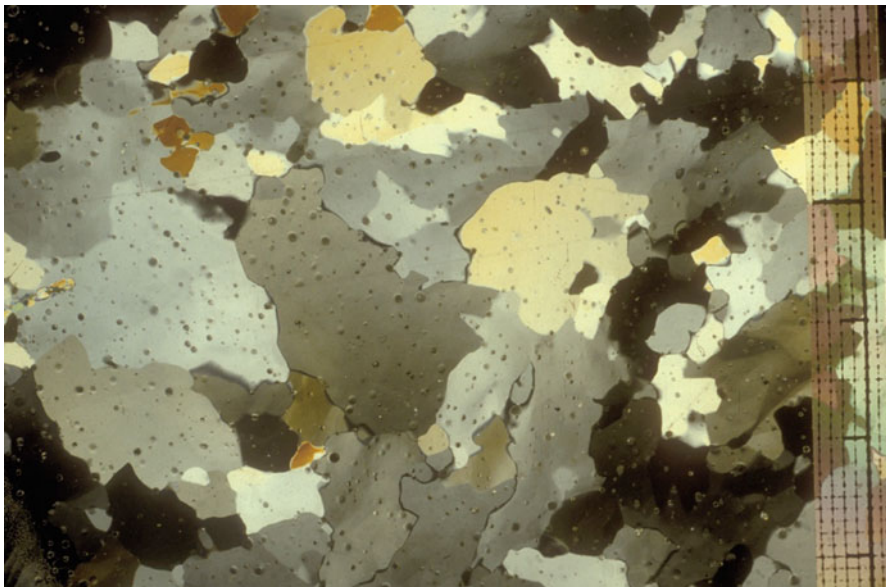


**Fig. 8.9** Thin section of ice photographed between crossed polaroids from Terre Adélie (East Antarctica) at the depth of 70 m; bubbles can be seen within grains; scale in mm (From Duval and Castelnau, 1995)

and  $10^{-8}$  m.s $^{-1}$  with a mean grain size of  $5 \times 10^{-3}$  m. This relatively high velocity of grain boundaries tends to produce an interlocking grain structure (Fig. 8.9). Migration recrystallization extensively occurs in temperate glaciers and in polar ice sheets near the bottom where temperature above  $-15^{\circ}\text{C}$  is found (Gow and Williamson 1976; Samyn et al. 2008). But, the stored energy associated with dislocations must be high enough to induce this recrystallization regime. Thus, there is no evidence of migration recrystallization along the Vostok ice core even though temperature reaches the melting point in the deepest layers of the ice sheet (de La Chapelle et al. 1998). Figure 8.10 shows typical ice microstructure at two depths at Vostok, which clearly shows that migration recrystallization is not active at these two depths. The presence of the lake beneath Vostok station probably explains the low strain rate along the whole core ( $<10^{-12}$  s $^{-1}$ ) and, thus, a stored energy too low to initiate migration recrystallization (Montagnat et al. 2001).

A value of the stress exponent  $n$  higher than 3 was deduced from tests performed in compression at  $-11.5^{\circ}\text{C}$  by Steinemann (1958). A value of  $n = 4$  also obtained by Kirby et al. (1987) from tests performed in triaxial compression at constant displacement rates in the temperature range 240–258 K and under a confining pressure of 50 MPa. Steady state strain rates, between  $3.5 \times 10^{-7}$  and  $3.5 \times 10^{-4}$  s $^{-1}$ , were determined after a finite strain generally higher than 10%. These results unambiguously correspond to tertiary creep.



**Fig. 8.10** Thin sections of ice photographed between crossed polaroids from the Vostok ice core (East Antarctica) at the depths of 200 and 3,206 m; scale in mm (Courtesy of V. Lipenkov)

In spite of the lack of reliable data on tertiary creep, there is, however, a clear indication that steady state is associated with an equilibrium grain size depending on stress (Jacka and Jun 1994). A dynamical balance between grain nucleation and grain boundary migration rate can explain this universal relationship. But, it must yet be considered as empirical in spite of a good physical basis (Poirier 1985).

## 8.5 Rate-Controlling Processes in the Creep of Polycrystalline Ice

### 8.5.1 Secondary Creep with $n = 3$

Power-law creep or Glen's flow law with a stress exponent of about three characterizes secondary creep at stresses higher than 0.1 MPa (Barnes et al. 1971; Budd and Jacka 1989). This *natural* creep law with  $n = 3$  can be derived by assuming that a density  $(\sigma/Gb)^2$  of dislocations moves at the velocity of climb,  $D\Omega\sigma/bkT$  (Poirier 1985). This velocity calculated at  $-10^\circ\text{C}$  with  $D = 1.5 \times 10^{-15} \text{ m}^2 \text{ s}^{-1}$  (Petrenko and Whitworth 1999) and 0.1 MPa is about  $10^{-9} \text{ ms}^{-1}$ . This climb velocity is more than two orders of magnitude lower than that for the glide of basal dislocations. This is in qualitative agreement with the large difference between basal slip and the behavior of the isotropic polycrystal (Fig. 8.4). Then, basal slip could be accommodated by the climb of basal dislocations on prismatic planes. Shear on the basal plane generates dislocations, which then climb on planes normal to the basal plane. Cross-slip of dislocations on the prismatic or pyramidal planes induced by the internal stress field of basal dislocations could be also invoked to accommodate basal slip (Taupin et al. 2007).

In conclusion, a combination of deformation systems operates during the deformation of polycrystalline ice in the power-law creep regime with  $n = 3$ . On first

loading, the stress state is uniform. As creep relaxes the resolved shear stress on the basal plane on each grain, load is transferred to the harder non-basal systems. An increasingly non-uniform state of internal stress develops. These internal stresses impede further deformation; that is, they give directional or kinematic hardening. They can be relieved by reversing the stress, so they are responsible for the large recoverable strain, which appears when ice is unloaded (Duval 1978). The development of this internal stress field during primary creep is associated with a creep rate decrease by a factor of 100 or more (Fig. 8.3). The initial creep rate is largely determined by that of the softest system, i.e. basal slip. The steady-state creep rate is determined by an appropriate average of the resistances of all systems. For this reason, the creep rate of polycrystals lies between the extremes of the single crystal (Fig. 8.1).

### 8.5.2 Secondary Creep with $n \leq 2$

The creep regime with a stress exponent of about  $n = 1.8$  is in agreement with the behavior of superplastic materials subjected to a tensile stress corresponding to region II in the stress–strain rate relationship (Langdon 1994). Grain boundary sliding (GBS) appears to account for essentially all of the strain in this region II (Langdon 1994). GBS would be accommodated by slip in the grains and finally by the climb of dislocations into grain boundaries. From Goldsby and Kohlstedt (1997), results obtained on fine-grained ice with  $d_g \leq 89 \mu\text{m}$  are in agreement with this deformation mode. Considering easy basal slip (Fig. 8.4) and fabric development in polar ice sheets, GBS does not appear to be a significant deformation mode in glaciers and ice sheets. It may be invoked to accommodate basal slip as suggested by Goldsby and Kohlstedt (2002). In this case, GBS should account for a small part of the strain (Duval and Montagnat 2002). An efficient recovery or softening process in polar ice sheets is grain boundary migration associated with normal grain growth and dynamic recrystallization (de La Chapelle et al. 1998; Samyn et al. 2008). The mismatch of slip at grain boundaries, which is associated with the development of a large internal stress field (cf. Sect. 8.4.1.1), can be relieved by grain boundary migration. From values of the grain boundary migration rate in polar ice sheets, this process appears to be efficient to accommodate basal slip (Montagnat and Duval 2000). Considering the reduction in dislocation density by grain boundary migration and the formation of new grains, strain rate should increase with decreasing grain size as suggested from in situ measurements (Cuffey et al. 2000) and laboratory tests (Duval 1973). However, the value of the grain size parameter remains to be determined. It is worth noting that GBS, even if this deformation process can be considered as minor in polar ice sheets, could be associated with these observed recovery processes.

### 8.5.3 *Tertiary Creep*

The acceleration of creep rate after secondary creep is caused by dynamic recrystallization. The enhancement factor defined by the ratio between strain rate during tertiary creep and strain rate during secondary creep is about 3 in compression or pure shear and between 8 and 10 in simple shear (Duval 1981; Li Jun et al. 1996). Softening processes directly associated with recrystallization give an enhancement factor between 2 and 3 whatever the stress state (Duval 1981). The preferential orientation of grains induced by recrystallization explains the remainder. Accommodation of basal slip during tertiary creep would be therefore produced by recrystallization and the climb and/or cross slip of basal dislocations.

Recrystallization fabrics appear to reflect stress state with grains well oriented for basal slip (Duval 1981). Since the behavior of each grain is related to the orientation of each grain in the polycrystal, recrystallization fabrics should be seen to be those that minimize the long-range internal stress field, which develops during primary creep. The nucleation of one grain modifies the spatial distribution of the stored energy in the whole polycrystal. Recrystallization would be therefore associated with self-organized criticality like dislocation dynamics. Accordingly, the classic view on the direct relationship between the orientation of recrystallized grains, the applied stress and local dislocation density should be revised.

A question not yet answered concerns the occurrence of grain nucleation when steady state is reached. Since the orientation of each grain in the polycrystal is related to the orientation of all grains in reducing lattice incompatibility, the stored energy near grain boundaries should decrease when reaching steady state tertiary creep. Grain nucleation would not occur after the formation of recrystallization fabrics. Only grain boundary migration driven by deformation gradients could locally occur and give this interlocking grain structure (Fig. 8.9). This recrystallization process obviously requires the great grain boundary mobility associated with migration recrystallization.

In the laboratory, there was no clear evidence of the occurrence of migration recrystallization at low stresses. The stored strain energy might not reach a critical value to allow migration recrystallization to occur. As discussed above, slow grain boundary migration, associated with normal grain growth (driven by the only free energy of grain boundaries) and rotation recrystallization (essentially driven by the stored energy within grains), would impede the accumulation of dislocations within grains (Alley 1992). But, migration recrystallization was observed below 2,800 m along the GRIP ice core (Greenland) in interglacial ice containing less than 100 ng/g of fine particles (Thorsteinsson et al. 1997; de La Chapelle et al. 1998). A critical point is the intrinsic mobility of grain boundaries, which depends on temperature, but, also, on the structure of grain boundaries. A high mobility of grain boundaries has been observed along the Siple ice core (West Antarctica) in spite of a temperature lower than  $-20^{\circ}\text{C}$  (Diprinzio et al. 2005).

## 8.6 Conclusions

In the low stress conditions of polar ice sheets, the viscosity of polycrystalline ice is several orders of magnitude higher than that of the ice crystal oriented for basal slip. Thus, basal slip can be considered as the dominant deformation mode in polar ice sheets. Deformation and recrystallization fabrics, commonly found in deep polar ice sheets, are in accordance with this assertion. The activity of basal slip systems, given by micro–macro polycrystals models, is more than 80% of the activity of all slip systems. Additional deformation modes could be non-basal slip, dislocation climb, dislocation cross-slip or grain boundary sliding. Grain boundary migration associated with normal grain growth and/or dynamic recrystallization, which is observed to occur along the whole deep ice cores, is an efficient process to relieve the long internal stress field induced by the mismatch of slip at grain boundaries.

A grain size effect is expected from in situ measurements, laboratory tests and theoretical analyses at stresses associated with a stress exponent  $\sim 1.8$ . Large variations of the ice viscosity can be induced by variations in grain size, impurity distribution, water content and the orientation of grains. A threshold stress could be invoked for the mechanical behaviour at very low stresses.

**Acknowledgments** The author is grateful to Murthy Gudipati and Julie Castillo-Rogez for the invitation. I acknowledge Denis Samyn and Throstar Thorsteinsson for their constructive review work and encouragement. This work was supported by CNRS (Institute des Sciences de l'ingénierie et des systèmes).

## References

- Ahmad S, Whitworth RW (1988) Dislocation motion in ice: a study by synchrotron X-ray topography. *Philos Mag* A57:749–766
- Alley RB (1992) Flow-law hypotheses for ice-sheet modeling. *J Glaciol* 38:245–256
- Alley RB, Perepezko JH, Bentley CR (1986) Grain growth in polar ice: II application. *J Glaciol* 32:425–433
- Ashby MF (1966) Work hardening of dispersion-hardened crystals. *Philos Mag* 14:1157–1178
- Ashby MF, Duval P (1985) The creep of polycrystalline ice. *Cold Reg Sci Technol* 11:285–300
- Augustin L et al (2004) Eight glacial cycles from an Antarctic ice core. *Nature* 429:623–628
- Azuma N et al (1999) Textures and fabrics in the Dome F (Antarctica) ice core. *Ann Glaciol* 29:163–168
- Baker RW, Gerberich WW (1979) The effect of crystal size and dispersed-solid inclusions on the activation energy for creep of ice. *J Glaciol* 24:179–194
- Barnes P, Tabor D, Walker JCF (1971) The friction and creep of polycrystalline ice. *Proc Roy Soc Lond A* 324:127–155
- Barrette PD, Jordaan IJ (2003) Pressure-temperature effects on the compressive behavior of laboratory-grown and iceberg ice. *Cold Reg Sci Technol* 36:25–36
- Budd WF, Jacka TH (1989) A review of ice rheology for ice sheet modelling. *Cold Reg Sci Technol* 16:107–144
- Castelnau O, Duval P, Lebensohn R, Canova GR (1996) Viscoplastic modelling of texture development in polycrystalline ice with a self-consistent approach: comparison with bound estimates. *J Geophys Res* 101(B6)

- Castelnau O, Duval P, Montagnat M, Brenner R (2008) Micromechanical modelling of the transient creep of ice. *J Geophys Res* 113(B11203):1–14
- Chevy J (2008) Viscoplasticité et hétérogénéités de déformation du monocrystal de glace expériences et simulations. Thèse de l' Université Joseph Fourier, Grenoble, France
- Chevy J, Fressengeas C, Lebyodkin M, Taupin V, Bastie P, Duval P (2010) Characterizing short-range vs. long-range spatial correlations in dislocation distributions. *Acta Mater* 58:1837–1849
- Cohen D (2000) Rheology of ice at the bed of Engabreen, Norway. *J Glaciol* 46:611–621
- Cole DM (1995) A model for the anelastic straining of saline ice subjected to cyclic loading. *Philos Mag A* 72(1):231–248
- Cole DM, Durell GD (1995) The cyclic loading of saline ice. *Philos Mag* 72:209–229
- Cuffey KM, Conway H, Hallet B, Gades AM, Raymond CF (1999) Interfacial water in polar glaciers and glacier sliding at  $-17^{\circ}\text{C}$ . *Geophys Res Lett* 26:751–754
- Cuffey KM, Thorsteinsson T, Waddington ED (2000) A renewed argument for crystal size control of ice sheet strain rates. *J Geophys Res* 105(B12):27,889–27,894
- Dahl-Jensen D, Gundestrup NS (1987) Constitutive properties of ice at Dye 3, Greenland. In: Waddington ED, Walder JS (eds) *The physical basis of ice sheet modeling*, vol 170. IAHS Publication, Vancouver, pp 31–43
- de La Chapelle S, Castelnau O, Lipenkov V, Duval P (1998) Dynamic recrystallization and texture development in ice as revealed by the study of deep ice cores in Antarctica and Greenland. *J Geophys Res* 103(B3):5091–5105
- de La Chapelle S, Milsch H, Castelnau O, Duval P (1999) Compressive creep of ice containing a liquid intergranular phase: rate-controlling processes in the dislocation creep regime. *Geophys Res Lett* 26:251–254
- Diprinzio CL et al (2005) Fabric and texture at simple Dome. *J Glaciol* 51:281–290
- Doake CSM, Wolff EW (1985) Flow law for ice in polar ice sheets. *Nature* 314:255–257
- Durand G et al (2006) Effect of impurities on grain growth in cold ice sheets. *J Geophys Res* 111 (FO1015):1–18
- Durham WB, Stern LA (2001) Rheological properties of water ice-applications to satellites of the outer planets. *Ann Rev Earth Planet Sci* 29:295–330
- Durham WB, Kirby SH, Stern LA (1992) Effect of dispersed particulates on the rheology of water ice at planetary conditions. *J Geophys Res* 97(E12):20883–20897
- Durham WB, Kirby SH, Stern LA (1998) Rheology of planetary ices. In: Schmitt B, De Bergh C, Festou M (eds) *Solar system ices*. Kluwer Academic, Dordrecht, pp 63–78
- Durham WB, Stern LA, Kirby SH (2001) Rheology of ice I at low stresses and elevated confining pressure. *J Geophys Res* 106:11031–11042
- Duval P (1973) Fluage de la glace polycristalline pour les faibles contraintes. *CR Acad Sci Paris* 277:703–706
- Duval P (1976) Lois de fluage transitoire ou permanent de la glace polycristalline pour divers états de contrainte. *Annales de Géophysique*, fasc. IV, t. 32:335–350
- Duval P (1977) The role of the water content on the creep rate of polycrystalline ice. In: Isotopes and impurities in snow and ice, vol 118. IAHS Publication, pp 29–33
- Duval P (1978) Anelastic behavior of polycrystalline ice. *J Glaciol* 21:621–628
- Duval P (1981) Creep and fabrics of polycrystalline ice under shear and compression. *J Glaciol* 27:129–140
- Duval P, Castelnau O (1995) Dynamic recrystallization of ice in polar ice sheets. *Journal de Physique IV*, 5 (Colloque N°3):C3-197-C3-205
- Duval P, Le Gac H (1980) Does the permanent creep-rate of polycrystalline ice increase with crystal size? *J Glaciol* 25:151–157
- Duval P, Montagnat M (2002) Comments on superplastic deformation of ice: experimental observations by DL Goldsby and Kohlstedt DL. *J Geophys Res* 107B, ECV4:1–2
- Duval P, Montagnat M (2006) Physical deformation modes of ice in glaciers and ice sheets. In: Knight P (ed) *Glaciology and Earth's changing environment*. Blackwell, Oxford, pp 303–307

- Duval P, Ashby MF, Anderman I (1983) Rate-controlling processes in the creep of polycrystalline ice. *J Phys Chem* 87:4066–4074
- Echelmeyer K, Zhongxiang W (1987) Direct observation of basal sliding and deformation of basal drift at sub-freezing temperatures. *J Glaciol* 33:83–98
- Fischer DA, Koerner RM (1986) On the special rheological properties of ancient microparticles-laden Northern Hemisphere ice as derived from bore-hole and core measurements. *J Glaciol* 32:501–510
- Fitzsimons SJ, Lorrain R, McManus KJ (1999) Structure and strength of basal ice and substrate of a dry-based glacier: evidence for substrate deformation at sub-freezing temperatures. *Ann Glaciol* 28:236–240
- Gillet-Chaulet F, Hindmarsh RCA, Corr HFJ, King EC, Jenkins A (2011) In-situ quantification of ice rheology and direct measurement of the Raymond effect at summit, Greenland using a phase-sensitive radar. *Geophys Res Lett* 38:L24503
- Glen JW (1955) The creep of polycrystalline ice. *Proc Roy Soc Lond* A228:519–538
- Glen JW, Perutz MF (1954) The growth and deformation of ice crystals. *J Glaciol* 2:397–403
- Goldsby DL, Kohlstedt DL (1997) Grain boundary sliding in fine-grained ice I. *Scr Mater* 37:1399–1406
- Goldsby DL, Kohlstedt DL (2001) Superplastic deformation of ice: experimental observations. *J Geophys Res* 106(B6):11017–11030
- Goldsby DL, Kohlstedt DL (2002) Reply to comment by P. Duval and M. Montagnat on Superplastic deformation of ice: experimental observations. *J of Geophys Res* 107B:2313. doi:[10.1029/2002JB001842](https://doi.org/10.1029/2002JB001842)
- Gow AJ, Williamson T (1976) Rheological implications of the internal structure and crystal fabrics of the West Antarctic ice sheet as revealed by deep core drilling at Byrd Station. Report 76–35, Cold Region Research and Laboratory, Hanover
- Gow AJ, Meese DA, Alley RB, Fitzpatrick JJ, Anandakrishnan S, Woods GA, Elder BC (1997) Physical and structural properties of the Greenland ice sheet project: a review. *J Geophys Res* 102(C12):26,559–26575
- Hobbs PV (1974) *Ice physics*. Clarendon, Oxford
- Holdsworth G, Bull C (1970) The flow law of cold ice: investigations on Meserve Glacier, Antarctica. *IAHS Publ* 86:204–216
- Hondoh T (2000) Nature and behavior of dislocations in ice. In: Hondoh T (ed) *Physics of ice core records*. Hokkaido University Press, Sapporo, pp 3–24
- Hooke LR (1981) Flow law for polycrystalline ice in glaciers: comparison of theoretical predictions, laboratory data and field measurements. *Rev Geophys Space Phys* 19:664–672
- Hooke LR, Dahlin BB, Kauper MT (1972) Creep of ice containing dispersed fine sand. *J Glaciol* 11:327–336
- Hutter K (1983) *Theoretical glaciology*. Reidel, Dordrecht
- Jacka TH (1994) Investigations of discrepancies between laboratory studies on the flow of ice: density, sample shape and size, and grain size. *Ann Glaciol* 19:146–154
- Jacka TH, Jun L (1994) The steady state crystal size of deforming ice. *Ann Glaciol* 20:13–18
- Jacka TH, Li Jun (2000) Flow rates and crystal orientation fabrics in compression of polycrystalline ice at low temperatures and stresses. In: Hondoh T (ed) *Physics of ice core records*. Hokkaido University Press, Sapporo, pp 83–102
- Jones SJ, Brunet JG (1978) Deformation of ice single crystals close to the melting point. *J Glaciol* 21:445–455
- Jones SJ, Chew HAM (1981) On the grain-size dependence of secondary creep. *J Glaciol* 27:517–518
- Jones SJ, Chew HAM (1983) Creep of ice as a function of hydrostatic pressure. *J Phys Chem* 87:4064–4066
- Jones SJ, Glen JW (1969) The mechanical properties of single crystals of pure ice. *J Glaciol* 8:463–473
- Jordan IJ (2001) Mechanics of ice-structure interaction. *Eng Fract Mech* 68:1923–1960

- Jun L, Jacka TH, Budd WF (1996) Deformation rates in combined compression and shear for ice which is initially isotropic and after the development of strong anisotropy. *Ann Glaciol* 23:247–252
- Kirby SH, Durham WB, Beeman ML, Heard HC, Daley MA (1987) Inelastic properties of ice Ih at low temperatures and high pressures. *Journal de Physique, Colloque C1*, 48:C1-227-C1-232
- Langdon TG (1973) Creep mechanisms in ice. In: Whalley E, Jones SJ, Gold LW (eds) *Physics and chemistry of ice*. Royal Society of Canada, Ottawa, pp 356–361
- Langdon TG (1994) A unified approach to grain boundary sliding in creep and superplasticity. *Acta Metall Mater* 42:2437–2443
- Lawson W (1996) The relative strength of debris-laden basal ice and clean glacier ice: some evidence from Taylor Glacier, Antarctica. *Ann Glaciol* 23:270–276
- Lebensohn RA, Liu Y, Ponte Castaneda P (2004) On the accuracy of the self-consistent approximation for polycrystals: comparison with full-field numerical simulations. *Acta Mater* 52:5347–5361
- Lebensohn RA, Tomé CN, Ponte Castaneda P (2007) Self-consistent modeling of the mechanical behavior of viscoplastic polycrystals incorporating intragranular field fluctuations. *Philos Mag* 87:4287–4322
- Lipenkov V, Salamatin A, Duval P (1997) Bubbly-ice densification in ice sheets: applications. *J Glaciol* 43:397–407
- Lliboutry L (1969) The dynamics of temperate glaciers from the detailed viewpoint. *J Glaciol* 8:185–205
- Mangold N, Allemand P, Duval P, Geraud Y, Thomas P (2002) Experimental and theoretical deformation of ice-rock mixtures: implications on rheology and ice content of Martian permafrost. *Planet Space Sci* 50:385–401
- Marshall HP, Harper JT, Pfeffer WT, Humphrey NF (2002) Depth-varying constitutive properties observed in an isothermal glacier. *Geophys Res Lett* 29. doi:[10.1029/2002GL015412](https://doi.org/10.1029/2002GL015412)
- Mellor M, Testa R (1969) Creep of ice under low stress. *J Glaciol* 8:147–152
- Miguel CM, Vespignani A, Zapperi S, Weiss J, Grasso JR (2001) Intermittent dislocation flow in viscoplastic deformation. *Nature* 410:667–671
- Montagnat M, Duval P (2000) Rate controlling processes in the creep of polar ice, influence of grain boundary migration associated with recrystallization. *Earth Planet Sci Lett* 183:179–186
- Montagnat M, Duval P (2004) The viscoplastic behavior of ice in polar ice sheets: experimental results and modelling. *CR Physique* 5:699–708
- Montagnat M et al (2001) High crystalline quality of large single crystals of subglacial ice above Lake Vostok (Antarctica) revealed by hard X-ray diffraction. *CR Acad Sci Paris* 333:419–425
- Montagnat M, Weiss J, Duval P, Brunjail H, Bastie P, Gil Sevillano J (2006) The heterogeneous nature of slip in ice single crystals deformed under torsion. *Philos Mag* 86:4259–4270
- Motoyama H (2007) The second deep ice core coring project at Dome Fuji, Antarctica. *Sci Drill* 5:41–43
- Okada Y, Hondoh T, Mae S (1999) Basal glide of dislocations in ice observed by synchrotron radiation topography. *Philos Mag* 79:2853–2868
- Paterson WSB (1991) Why ice-age ice is sometimes “soft”? *Cold reg Sci Technol* 20:75–98
- Petit JR (1999) Climate and atmospheric history of the past 420,000 years from the Vostok ice core, Antarctica. *Nature* 399:429436
- Petrenko VF, Whitworth RW (1999) Physics of ice. Oxford University Press, Oxford
- Pettit EC, Waddington ED (2003) Ice flow at low deviatoric stress. *J Glaciol* 49:359–369
- Poirier JP (1985) Creep of crystals: high temperature deformation processes in metals, ceramics and minerals. Cambridge University Press, Cambridge
- Samyn D, Svensson A, Fitzimons SJ (2008) Dynamic implications of discontinuous recrystallization in cold basal ice: Taylor Glacier, Antarctica. *J Geophys Res* 113. doi:[10.1029/2006JF000600](https://doi.org/10.1029/2006JF000600)
- Schlüslon EM, Duval P (2009) Creep and fracture of ice. Cambridge University Press, Cambridge
- Shearwood C, Whitworth RW (1991) The velocity of dislocations in ice. *Philos Mag* A64:289–302

- Sotin C, Grasset O, Beauchesne S (1998) Thermodynamics properties of high pressure ices: implications for the dynamics and internal structure of large icy satellites. In: Schmitt B, De Bergh C, Festou M (eds) Solar system ices. Kluwer Academic, Dordrecht, pp 79–96
- Steinemann S (1958) Experimentelle Untersuchungen Zur Plastizität von Eis. Beiträge Zur Geologie Der Schweiz. Hydrologie 10:1–72
- Tatiboutet J, Perez J, Vassollo R (1986) High-temperature internal friction and dislocations in ice Ih. *J de Physique* 47:51–60
- Tatiboutet J, Perez J, Vassollo R (1987) Study of grain boundaries in ice by internal friction measurement. *J de Physique* 48:C1-197–C1-203
- Taupin V, Varadhan S, Chevy J, Fressengeas C, Beaudoin AJ, Montagnat M, Duval P (2007) Effects of size on the dynamics of dislocations in ice single crystals. *Phy Rev Lett* 99:155507-1–155507-4
- Thorsteinsson Th (2001) Deformation of strongly anisotropic materials. *J Glaciol* 47:507–516
- Thorsteinsson TH, Kipfstuhl J, Miller H (1997) Textures and fabrics in the GRIP ice core. *J Geophys Res* 107(B1):26,583–26599
- Thorsteinsson Th, Waddington ED, Taylor KC, Alley RB, Blankenship DD (1999) Strain-rate enhancement at Dye 3, Greenland. *J Glaciol* 45:338–345
- Tobie C, Choblet G, Sotin C et al (2003) Tidally heated convection: constraints on Europa's ice shell thickness. *J Geophys Res* 108:5124. doi:[10.1029/2003JE002099](https://doi.org/10.1029/2003JE002099)
- Weertman J (1973) Creep of ice. In: Whalley E, Jones SJ, Gold LW (eds) Physics and chemistry of ice. Royal Society of Canada, Ottawa, pp 320–337

# Chapter 9

## Cratering on Icy Bodies

M.J. Burchell

**Abstract** This chapter covers impacts on ices. Possible outcomes of impacts include both cratering and catastrophic disruption (i.e., where the target body breaks apart in the impact). Both of these are described in laboratory experiments and discussed in a Solar System context. Other physical phenomena that occur during impact (light flash and ionization) are briefly described. As well as this, a general description of cratering is given, along with examples of the impact speeds typical of those for icy bodies in space. Also included is a discussion of how laboratory experiments and modelling are carried out (what type of facilities are used and what they can achieve). This is followed by discussion of real impacts on icy bodies such as satellites of outer planets and comet nuclei. Physical problems that complicate the outcomes of impact events such as the porosity of target bodies (e.g. impacts on comets) are discussed.

### 9.1 Introduction

Impact processes are ubiquitous throughout the Solar System. The intersection of the orbits of two bodies results in what is usually a high speed impact, at an encounter speed typically measured in many  $\text{km s}^{-1}$ . These “hypervelocity” impacts result in (relatively) large craters, high speed ejecta and heavily shocked materials found at the impact site (e.g. (Melosh 1989)). Here on Earth, such impacts from space are called “giant impacts” and result in large (km + scale) craters. However, this is rather misleading as it is a very specific picture focussed on the Earth. In the wider Solar System it fails for several reasons. For example, the Earth’s atmosphere shields the Earth’s surface from high speed impacts by

---

M.J. Burchell (✉)

Centre for Astrophysics and Planetary Science, School of Physical Sciences

University of Kent, Canterbury, Kent CT2 7NH, UK

e-mail: [M.J.Burchell@kent.ac.uk](mailto:M.J.Burchell@kent.ac.uk)

bodies smaller than about 50 m in size (Bland et al. 1996). Thus the many atmosphere-less bodies in the outer solar system will be much more frequently impacted by the more numerous smaller bodies found in space, so there will be many small craters present on their surfaces (rather like on the Moon). Indeed, even at the micrometre scale surfaces will be peppered with impact craters made by dust particles. The second major difference lies in the nature of the target body. On Earth this is some usually taken as rock (even though currently 2/3rds of the Earth's surface is covered in water, making an impact in a shallow or deep ocean more likely (Dypvik and Jansa 2003; Kyte et al. 1981)). By contrast, in the outer Solar System, ice is an important component of many solid bodies (see other chapters in this book) and the temperature, type, porosity etc. of the ice can vary from body to body. All this has important consequences for the results of impact processes.

As stated, the classical description of impact cratering (e.g. (Melosh 1989)) is mostly given in terms of rock (or metal) targets. Three stages are usually described: an initial contact phase (i.e. where the projectile impacts and penetrates the target), an excavation phase (where the crater grows by bulk movement of target material set into motion by the shock event) and a modification phase (where gravity causes crater walls to slump, some ejecta falls back into the crater and there may also be litho-static rebound of the crater floor). This is for large scale events. The key processes are referred to as *hydrodynamic*, as at the high speeds involved the peak shock pressures that arise from the impact are typically of order 10–100 GPa (or more), whereas the strength of the targets is typically measured in 10s or 100s of MPa. Thus the material strength is negligible until late in the crater growth phase. The target material in effect flows during the impact as if it were a material with no shear strength. Rim walls pile up around the crater during the growth phase, and when the shock pressure has fallen such that resistance to motion becomes significant (this may be due to material strength or gravity), crater growth stops with an excavated crater surrounded by a raised rim (e.g. Fig. 9.1b).

At small size scales (up to m scale) a similar process occurs for ductile materials with the lack of a modification stage (Fig. 9.1a). However, at small sizes, target strength plays an important role in the later stages of crater growth for brittle materials like ice (and indeed rock), with large scale spallation of material occurring around the initial impact crater (Fig. 9.2a). This prevents formation of the raised rim associated with the craters described above, by removing material from the target surface around the crater, and the resulting spall zone can more than double the diameter of the impact feature.

For impacts in ice at larger size scales (10s and 100s of m and above) it is common to assume that cratering proceeds in the same way as the classical model resulting in a bowl shaped crater with a raised rim wall around it (Fig. 9.2b, but note the low rim around the crater and the shallow interior in this example). For larger craters, in the classical model a central peak (or uplift) will occur (Figs. 9.1c – rock and 9.2c – ice); the scale for the on-set of formation of this peak depends not just on material properties, but also on the magnitude of the local gravity. As craters get bigger, this central peak evolves into a central ring and finally for the largest impacts there is the onset of formation of multi-ring impact basins. It is often

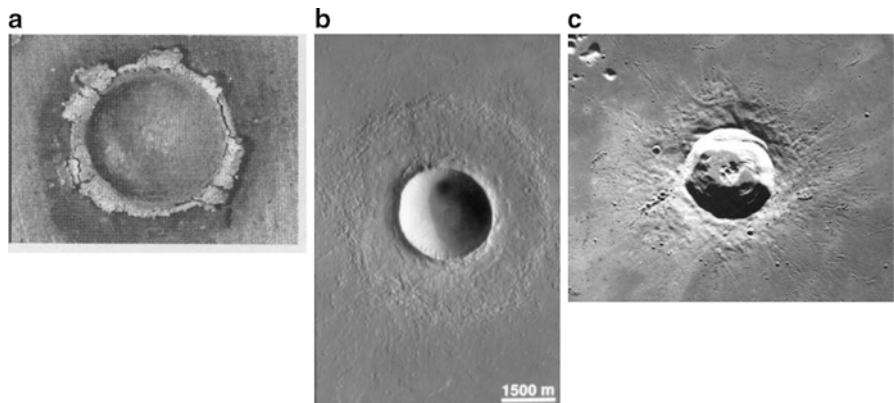


**Fig. 9.1** Traditional view of impact cratering as a function of size. (a) cm scale crater in ductile metal (Source: Univ. of Kent), (b) km sized bowl-shaped crater on Mars (Source NASA), (c) Euler lunar crater, (approx. 25 km dia.) with central uplift (Source NASA Apollo 17, AS17-2923)

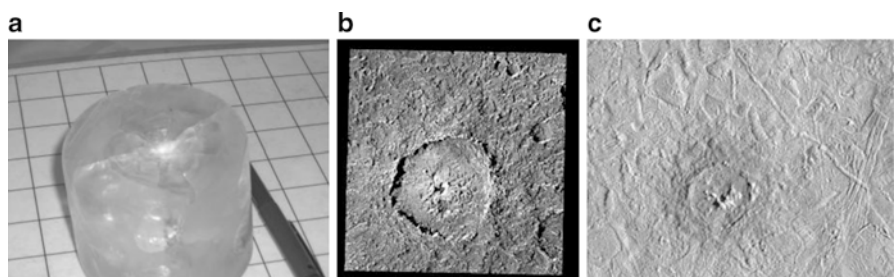


**Fig. 9.2** Sequence of impact craters in ice. (a) cm scale crater showing spallation zone around a deeper central pit (Source: Univ. of Kent), (b) km sized bowl-shaped crater with low relief rim walls and central pit (Source: NASA), (c) crater Pywll, approx. 24 km dia. with central uplift (Source: NASA)

assumed that any differences (in ice) compared to large scale craters in rock arise solely from the different properties of the materials at high strain rates and are minor in nature. As is discussed later however, there is wide-spread observational evidence to suggest that there are more serious changes in crater formation arising from the difference between rock and ice. And viscous relaxation of the ice may alter the morphology of the crater with time.

There will also be differences arising due to layering in the target surface. On Mars for example, sub-surface ice may be mixed in with rocky material, and when shocked and heated during an impact may alter the behaviour of outward flow of the surface material away from the crater. And in the outer solar system itself, the icy surface may have a sub-surface ocean beneath it. A large impact may penetrate this icy crust or, where non-penetrating, there may be subtle features of crater formation which are influenced by the finite thickness of the icy surface layer.

A further complication is that icy bodies may not be made of just ice. A substantial component may be silicates for example. This could be distributed in two ways. It could, on small bodies, be uniformly distributed throughout the body. Or, if the body were larger, it may be differentiated and have a higher silicate content at the core (e.g. Pluto has a mean density of 1.7–1.8 g cm<sup>3</sup>, suggesting a large silicate content, but spectroscopy of its surface suggests the surface is predominantly icy).

The question of porosity is also important. Small icy bodies such as comet nuclei, can be of order 10 km across. This is insufficient for the local gravity to have collapsed all the pore space in such a body, resulting in a target which may have significant porosity at the microscopic scale (i.e. estimates of comet nuclei density are not certain but 0.5 g cm<sup>3</sup> is not un-common, suggesting that even if made of pure water ice the bodies are 50% void space). Macroscopic porosity is also possible, in that, like asteroids, if broken apart as a result of a previous impact, an icy body may reassemble under self-gravitation and gaps may occur between the fragments.

A discussion of the influence of all of these factors on cratering in ices is given in the rest of this chapter.

## 9.2 Ice as a Geological Material and the Consequences for Impact Studies

When studying a material, knowledge of its key relevant properties is vital. It should be borne in mind that even after decades of studies, many crucial parameters of rocky materials are still poorly known with regards to impact studies. Those for ice are even less well known (see other Chapters in this book). The density of a material is a good starting point. But for ice the density needs to be specified as a function of temperature, as the icy bodies in the outer solar system will be at low temperatures. Next the phase diagram for ice needs to be well known. Then the strength of the material is required. However, in high speed impacts the strain rate is of order 10<sup>6</sup>–10<sup>8</sup> s<sup>-1</sup>, so the strength required is not that obtained from static laboratory testing. Also the type of strength needs to be specified, tensile, compressive, shear, etc.

Moving on from these, the details of what is referred to as the shock Hugoniot are required. This is based on the idea that a single shock is applied uniformly to a material (with initial pressure  $P_0$ , density  $\rho_0$  and temperature  $T_0$ ) which is instantly shocked to a new state of ( $P$ ,  $\rho$  and  $T$ ). The locus of values of ( $P$ ,  $\rho$  and  $T$ ) to which a material can be shocked are referred to as the Hugoniot. In a strong shock it is assumed that the jump to the shocked state is instantaneous and the speed of the propagation of the shock front in a material is given as  $U$ . If the shock is being provided by a “pusher” of some sort, which has impacted the original surface which was initially at rest, then the speed of this “pusher” is  $u$  (i.e. the speed of the shocked material).

In this strong shock regime  $U > u$ . Application of the conservation laws for mass, momentum and energy across the shock front then permit derivation of relationships between the initial and shocked values of density and pressure. The change in the (specific) internal energy ( $E$ ) of the material can also be found in terms of the pressure and specific volume  $V$  (which is the inverse of density). These basic relations are derived in many texts (e.g. (Melosh 1989)) and can be written as:

$$\rho(U - u) = \rho_o U, \quad (9.1)$$

$$P - P_o = \rho_o u U, \quad (9.2)$$

$$E - E_o = (P + P_o)(V_o - V)/2. \quad (9.3)$$

However, these relations do not fully define the condition of the material on both sides of the shock, an equation of state (EOS) is also required, often of the form  $P = P(V, E)$ . The EOS contains details of the microscopic nature and behaviour of the materials down to the atomic scale (rather than the simpler bulk properties). In addition, some impact models also require a further strain-rate dependent constitutive equation, relating the shocked and un-shocked material (note; an EOS is a constitutive model without any strain rate dependence and where the materials pre- and post-shock are in thermodynamic equilibrium).

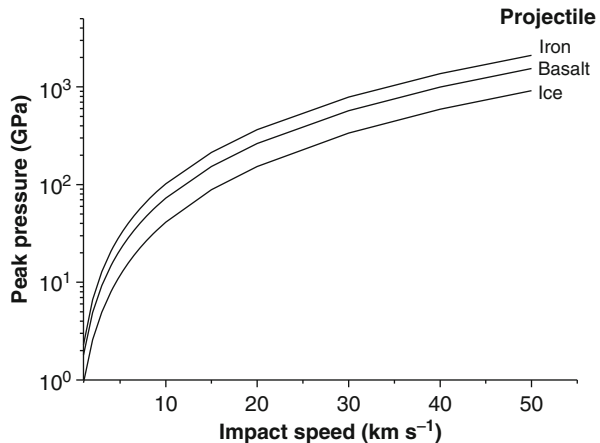
The Hugoniot data for a material are often shown in graphical form. However, since graphs only have two axes, a choice of which two parameters to plot has to be made. As a result, two graphs are often shown, a  $P$ - $V$  graph and a  $U$ - $u$  graph. In the case of the  $U$ - $u$  graph, once the shock regime has been entered, the relation is often found to be linear, and is expressed as

$$U = C + S u. \quad (9.4)$$

Experimental shock work is often focussed on obtaining the data to obtain the Hugoniot data or obtain the coefficients  $C$  and  $S$  (see other Chapters in this book). For example, values for  $C$  and  $S$  are tabulated for many materials on page 232 of (Melosh 1989) where the values for ice are given as  $C = 1.28$  (km s<sup>-1</sup>) and  $S = 1.56$ . This information is rarely obtainable from first principles calculations and without it the results of any estimates of the results of a shock event are unlikely to be realistic. Thus a major part of modelling impacts on icy bodies lies in understanding the properties of ice under shock compression (e.g. see (Stewart and Ahrens 2005a; Feistel and Wagner 2006; Wagner and Pruss 2002; Frank et al. 2004; Senft and Stewart 2008)). One key property in accurate modelling is the shock pressure needed to melt ice (e.g. see (Stewart and Ahrens 2005a)), it can perhaps intuitively be appreciated that this is important for a material such as ice, but melt production is also an uncertain topic even in impacts on rock (Osinski et al. 2008).

One simple way to obtain estimates of shock pressures in impacts is via the Planar Impact Approximation (PIA) method which is described in Chap. 4 of (Melosh 1989) for example. Using just the values of  $C$  and  $S$  (values for both

**Fig. 9.3** Peak shock pressure in impacts in ice by a variety of projectiles. The estimates were made using the Planar Impact Approximation and values for  $C$  and  $S$  in the linear wave speed approximation from (Melosh 1989). Curves for three types of impactor are shown



projectile and target are required), combined with the impact speed, the peak shock pressure can be predicted in an impact; this is shown for impacts on ice in Fig. 9.3. As can be seen, the peak shock pressure rises rapidly at impact speeds up to  $\sim 10 \text{ km s}^{-1}$ , but then increases at a slower rate. The shock pressures needed for melting and vaporisation of various materials are tabulated in Chap. 3 of (Melosh 1989), and for ice, the onset of melting is given as 3 GPa with complete melting at 10 GPa, vaporisation starts at 26 GPa and is complete at  $>100$  GPa. It should be remembered however that the graph in Fig. 9.3 is based on an approximate method, and that the peak shock pressures only apply in a small region of the target, more complete simulations based on a fuller knowledge of the shock Hugoniot are required to fully explore the phenomenon of melting for example. Nevertheless, it can be appreciated from Fig. 9.3, that the results of impact cratering on ice will contain a strong dependence on impact speed. The impact speeds that are expected in the outer solar system are discussed below, but do cover the full range shown in Fig. 9.3.

### 9.3 Impact Speeds in the Outer Solar System

The simple model for finding impact speeds is to compute the orbits of both objects, find the relative speed at the intersection of the orbits and add a term for their mutual gravitational attraction. The result will typically be in units of  $\text{km s}^{-1}$ . People familiar with impacts in the inner Solar System usually have a rule of thumb that impact speeds increase nearer the sun and are lower further out. But it should be remembered however, that the orbits do not need to be heliocentric, one or both of the bodies can be orbiting a planet such as Jupiter for example (or a giant planet may be the target in the impact). In the case of the gas giant planets the in-fall speed due to their gravitational attraction can be high. In addition, if the target is a satellite, the contribution from the orbital speed of the target satellite can also be

**Table 9.1** Mean impact speeds on outer solar system bodies (Adapted from (Zahnle et al. 2003))

Target	$\langle v \rangle$ km s <sup>-1</sup>
Jupiter	
Io	32
Europa	26
Ganymede	20
Himalia	6.1
Saturn	
Enceladus	24
Titan	10.5
Phoebe	3.2
Pluto	1.9
Charon	1.8

significant. Thus collisional speeds in the outer solar system are not low as popularly believed, but cover a wide range.

One model for calculating impacts speeds is that of (Zahnle et al. 1998, 2003), which was developed specifically for consideration of cratering rates on planetary satellites in the outer solar system. Tables of mean impact speeds on various bodies are given in (Zahnle et al. 2003) with an abbreviated version given here in Table 9.1. A simplified version of this model gives the mean impact speed  $\langle v \rangle$  as:

$$\langle v \rangle = \sqrt{3v_{orb}^2 + v_\infty^2 + v_{esc}^2} \quad (9.5)$$

where  $v_{orb}$ , and  $v_{esc}$  are the orbital speed and escape velocity of the satellite, and  $v_\infty$  is the distant encounter velocity of the impactor with the planet. For the case of elliptical comets, in (Zahnle et al. 2003)  $v_\infty$  is approximated as  $\sqrt{[e^2 + i^2]}V_{orb}$ , where  $e$  and  $i$  are the eccentricity and inclination of the comet, but  $V_{orb}$  is now the orbital velocity of the planet. This approximation gives mean impact speeds equal to about 95% of those obtained from a fuller calculation (Zahnle et al. 2003). As can be seen in Table 9.1, impact speeds on icy satellites of the outer planets can cover a wide range of values.

It is also possible to model impact speeds on planets and small bodies (other than satellites) in the outer solar system. For Kuiper Belt Objects (KBOs) impacting other KBOs, impact speeds of 0.5–3.5 km s<sup>-1</sup> are suggested by (Dell’Oro et al. 2001). This encompasses the mean impact velocity for Pluto given in Table 9.1. For comparison, mean impact speeds in the asteroid belt are estimated as 5.3 km s<sup>-1</sup> (Bottke et al. 1994) and impacts on the Earth have a mode speed often given as around 20 km s<sup>-1</sup>, but the full range of speeds is from 11.1 to 70 km s<sup>-1</sup> depending on the orbit of the impactor (e.g., see (Hughes and Williams 2000)). It should also be recalled that comet nuclei can have highly elliptical orbits that bring them into the inner solar system. Thus impact speeds on cometary surfaces can cover a wide range of values and will vary depending on where in the Solar System the comet nucleus is when it is struck. However, given that these bodies spend most of their life in the outer solar system, mean impact speeds will be closer to 1 km s<sup>-1</sup> than 10 km s<sup>-1</sup> or above.

## 9.4 Laboratory Experiments on Impact Cratering in Ice Targets

There are two main types of laboratory experiments of interest, those which seek to obtain information about the shock Hugoniot data, and those which seek insights into impact processes via observation of cratering or disruption events under controlled conditions at laboratory scales.

### 9.4.1 Shock Hugoniot Measurements

To obtain data relevant to the shock Hugoniot for a material, a planar shock is often passed through a sample of the material. Several methods exist for this. One method often used is that of the flyer plate. Here a plate is set into high speed motion, either by an explosion or by firing a projectile carrying the plate in a large gun. The plate then strikes a target (the upper surface of which is also usually a plate, beneath which is located the sample). A uniform shock is thus transmitted into the sample. If the sample is mounted in a capsule and surrounded by appropriately matched materials, multiple reverberations of the shock can build up in the sample, shocking it to a higher pressure than from the passage of the initial single shock. Observation of the speeds of the driver plate and the shock wave in the material (via X-rays for example, or via optical means for transparent materials) permits measurement of the necessary parameters. Examples of such experimental studies for ice are (Kato et al. 2001; Stewart and Ahrens 2003; Larson 1984; Iijima et al. 1995).

### 9.4.2 Impact Cratering Experiments

Here a different approach is taken, a projectile (dimensions much smaller than the target) is fired at high speed into the target and the resulting crater (or disrupted target fragments) observed. A variety of means are available to accelerate projectiles to high speeds. Particles up to a micrometre in size can be electrostatically accelerated to speeds above  $1 \text{ km s}^{-1}$  (provided they can be charged). An early description of this technique is given in (Friichtenicht 1962) and a more recent example of such an electrostatic accelerator is (Burchell et al. 1999). In electrostatic acceleration the projectile velocity ( $v$ ) is given by:

$$v = \sqrt{(2QV/m)} \quad (9.6)$$

where  $Q$  and  $m$  are the particle charge and mass respectively and  $V$  (usually of order a few MV) is the accelerating voltage. The particles are usually charged to their maximum surface charge density and thus  $Q$  is not readily variable and only

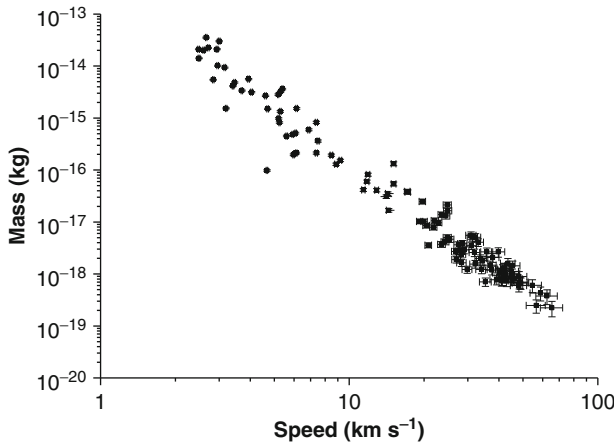


**Fig. 9.4** Example of particle mass versus speed in an electrostatic accelerator (See (Burchell et al. 1996, 1999) for more details)

depends on size (and typically ranges from 0.1 to 100 fC). The result is that there is an inverse relationship between particle speed and mass, this is shown in Fig. 9.4 for the electrostatic accelerator described in (Burchell et al. 1999).

A variety of means are available for acceleration of larger particles. Two-stage light gas guns, plasma guns and rail guns are the most common. Two-stage light gas guns were originally developed in the 1940s and 50s (Crozier and Hume 1957). An initial stage uses a normal gun-powder charge to drive a piston (usually nylon) down a barrel. In front of the piston is a light gas (e.g. hydrogen) and the end of the barrel is sealed by a thin disk of metal (a bursting disk) which leads into a second barrel (called the launch tube) which has a narrower internal diameter. As the light gas is compressed, the pressure on the confining barrel walls increases, and the bursting disk causes it to rupture, suddenly releasing the high pressure gas. Just behind the bursting disk (in the launch tube) is a sabot (often made of a polyurethane resin so it has a low coefficient of friction but sufficient strength to survive the shock it is subject to) carrying the projectile. The sudden release of the highly compressed light gas accelerates the sabot down the launch tube to a higher speed than would have been obtained from a single stage gun with its (relatively) slow burning, heavy mean molecular mass gun-powder. A typical (small) modern gun is described in (Burchell et al. 1999). Such guns can achieve speeds in the range 1–8 or 9 km s<sup>-1</sup>, and can fire sabots from mm to cm scale in diameter. In some guns, the sabot can be discarded in flight, allowing just the projectile loaded within it to impact the target. In others both the projectile and the sabot strike the target. By loading small projectiles, or even large numbers of very small projectiles (down to micrometer size), in the sabot, these guns can fire projectiles in sizes from a micrometer up to cm scale. It is possible to measure projectile speed in flight by flash X-rays or passage through light curtains for example. Such guns are workhorse tools in impact studies. Although the speeds obtainable are generally slightly too low for terrestrial impact

studies, they significantly overlap the range of impact speeds applicable to some icy bodies in the outer solar system. However, in general, the projectile size is still smaller than that required for cratering at most scales of interest.

Higher impact speeds can be achieved by use of electrostatic rail guns (Upshaw and Kajs 1991) or plasma drag accelerator (Best and Rose 1999). Rail guns use a projectile launched along an electromagnetic accelerator and can achieve speeds up to  $15 \text{ km s}^{-1}$ . Exploding wire guns use a high charge applied to a wire to heat it and explode it generating a fast expanding plasma which picks up small particles near by and accelerates them to high speeds (up to  $15 \text{ km s}^{-1}$ ). Again however, projectile sizes are still small.

### 9.4.3 Experimental Results

A wide range of experiments have been performed relating to impacts on icy bodies. As well as impact cratering, outcomes that have been observed include impact-generated light flash, plasma, ejecta etc. Impact light flash has been observed since the early days of hypervelocity impact experiments (Atkins 1955). A variety of reports of light flash for impacts on ice exist. The earliest report seems to be (Burchell et al. 1996) where light flash from impacts onto water ice of sub-micrometer sized iron particles were reported for speeds of  $2\text{--}70 \text{ km s}^{-1}$ . It was found that the energy in the light flash varied with  $mv^{3.65}$  (where  $m$  and  $v$  were the mass and speed of the projectile), i.e. the fraction of the incident kinetic energy that went into the light flash (called the luminous efficiency –  $\eta$ ) was not constant but increased as impact speed increased. The same work (Burchell et al. 1996) also reported on impact ionization yields from impacts on ice and found that the ionized charge varied with  $mv^{4.1}$  (again not scaling linearly with impact kinetic energy). Note however, that in both cases the experiments were at the micrometer scale (i.e. masses of  $10^{-14}$  to  $10^{-19} \text{ kg}$ ) and it is not clear how this scales to significantly larger mass scales.

Impact cratering experiments on ice targets have been carried out using (mostly) light gas guns with a variety of target types and impact speeds. Typical experiments are reported in Table 9.2; most give fits to crater size  $x$  (depth, diameter, volume) of the form  $x - aE^b$ , where  $E$  is impact kinetic energy and  $a$  and  $b$  are obtained from the data. As well as low and high speed impacts, data have been taken under a range of ice temperatures (as low as 81 K) and at oblique incidence. Several papers attempt to extrapolate results to larger scales, either by direct scaling with energy (e.g. (Eichhorn and Grun 1993)), late-stage energy scaling (e.g. (Kawakami et al. 1983)) or via use of dimensionless ratios ( $\pi$ -scaling) (e.g. (Lange and Ahrens 1987; Burchell and Johnson 2005)). However, when carrying out scaling it is not clear if the results can reasonably be extrapolated from energies of 1–1,000 J up to greater than  $10^9 \text{ J}$  or above (e.g., a 2,000 kg object travelling at  $1 \text{ km s}^{-1}$  has of order  $10^9 \text{ J}$  of energy), particularly as this will involve moving from a strength dominated impact process to one controlled by gravity. In addition to pure water ice targets, targets containing mixtures of minerals and water ice and ammonia and water ice, as

**Table 9.2** Summary of various laboratory impact cratering experiments on ice targets. Unless otherwise stated, Target temperature was typically 255–265 K and impacts were at normal incidence (Note: p.c. stands for polycarbonate)

Target ice	Impact speed (km s <sup>-1</sup> )	Projectile type	Comment	
H <sub>2</sub> O	0.04–0.85	Various including ice, al. and p.c.	Both cratering and target fragmentation reported	Kato et al. (1995)
H <sub>2</sub> O	0.1–0.64	P.c.	Ice temperature 81–257 K	Lange and Ahrens (1987)
H <sub>2</sub> O	0.13–0.54	P.c., Teflon, pyrophyllite and al.	Both cratering and target fragmentation reported	Kawakami et al. (1983)
H <sub>2</sub> O	0.18–0.41	Polyethylene and al.	Cratering and ejecta fragment size are given	Cintala et al. (1985a)
H <sub>2</sub> O	1–18	Iron	Use an electrostatic accelerator and found crater volume from vapour release	Eichhorn and Grun (1993)
H <sub>2</sub> O	1.1–7	Copper	50% porous ice targets. Crater volume was double that of non-porous ice but excavated mass was unchanged	Burchell et al. (2002)
H <sub>2</sub> O	2.3–6.3	Polyethylene	Impacts in ice and ice-saturated sand	Croft (1981)
H <sub>2</sub> O	2.9–5.5	Various: al. to tungsten carbide	Showed variation of cratering efficiency with projectile density and included modelling of porosity effects	Burchell and Johnson (2005)
H <sub>2</sub> O	~5	Al.	Ice temperature 100–253 K	Grey and Burchell (2003)
H <sub>2</sub> O	~5	Al.	Oblique incidence (normal to grazing incidence)	Grey et al. (2002)
H <sub>2</sub> O	~5	Al. and porous ceramic	Ejecta size distribution as function of angle of ejection	Burchell et al. (2003)
Ammonia rich H <sub>2</sub> O ice	~4.8	St. st.	Crater size reduces as ammonia content increases	Grey and Burchell (2004)
H <sub>2</sub> O-silicate	0.9–11.8	Glass and nylon	Plasma drag accelerator was used. Craters in pure ice were 100× larger than in pure silicates	Koschny and Grun (2001a)
H <sub>2</sub> O-silicate	0.9–11.8	Glass and nylon	Plasma drag accelerator was used. Ejecta quantity and size distribution given	Koschny and Grun (2001b)
H <sub>2</sub> O – CO <sub>2</sub> – Mineral	0.1–0.6	Water ice	Layered, thermally processed targets	Arakawa et al. (2000)
CO <sub>2</sub>	~5	St. st.	Craters and ejecta were measured	Burchell et al. (1998)
CO <sub>2</sub>	~5	Various, e.g. nylon–copper	Craters same dia. as in water ice targets but are shallower	Burchell et al. (2005)

well as pure CO<sub>2</sub> ice have been used (see Table 9.2 for details). Several of the papers in the table include details on the size distribution of the ejecta from the impacts.

A series of light gas gun experiments was also carried out in preparation for the Deep Impact mission to comet 9P/Temple 1 (see below), but mostly featured impacts on granular materials such as perlite rather than ice (Schultz et al. 2007) (i.e. those involved decided that the particular properties of ice were of less interest in determining the result that properties such as porosity etc.). Earlier experiments had reported impact flash and vapour plumes from impacts on CO<sub>2</sub> ice (Schultz 1996).

## 9.5 Hydrocode Modelling of Impacts on Icy Bodies

A variety of applications of hydrocode modelling of impacts have been made to icy bodies. Three general types of impacts can be considered, (1) impacts resulting in craters with only local significance, (2) impacts resulting in large craters with global consequences and (3) disruption events (see Sect. 9.8).

There are relatively few hydrocode simulations of ice cratering events and work is still on-going to generate a fully detailed, appropriate EOS (e.g. see (Stewart and Ahrens 2005b; Leinhardt and Stewart 2009)). However, some results are significant. The modelling of large impact craters on Ganymede shows formation of central peaks in ice craters in line with the observations (Bray et al. 2008). Hydrocode modelling of impact craters can also explicitly include target porosity and simulations suggest impacts in porous small bodies may produce either craters or cavities, depending on the degree of porosity (Burchell and Johnson 2005). Cratering into layered surfaces has also been modelled. In the case of Mars where sub-surface ice may be present, modelling (Senft and Stewart 2008) suggests that the low strength of ice and the contrast between ice and rock layers in terms of a shock impedance mis-match, can significantly alter the outcome of a cratering event. Subsurface flow is particularly altered as is the nature of the ejecta. Further, changes in the efficiency of excavation can alter the overall crater morphology. Another example is (Moore et al. 1998) where impacts on a solid ice target are contrasted with those on an ice surface over a liquid interior.

An example of hydrocode studies of impacts with global significance is that of (Bruesch and Asphaug 2004). Here large (1,000 km diameter) icy bodies are modelled with a pure ice surface and a silicate core (typically a 13 km diameter, solid, pure ice body was modelled impacting the target at a speed of 20 km s<sup>-1</sup>). This scenario was considered to be sufficient to not only produce a large impact crater, but also to couple into global seismic activity, with disruption occurring at the antipodes, and which was potentially sensitive to the interior structure of the target. This reflects observation of large craters on icy Saturnian satellites such as Tethys, Mimas and Rhea and the results are scaled to these bodies. For Mimas and Rhea, the model results do not result in antipodal stresses sufficient to rupture ice, but for Tethys there is the possibility (in some of the model scenarios) for rupture of the ice at the antipode. This reflects that Odysseus, the relevant impact crater on

Tethys, is relatively larger compared to Tethys (crater diameter 0.76 times Tethys radius) than the relevant craters on Mimas and Rhea (Herschel and Tirawa respectively). Overall, these results were at the limit of model resolution, and any resulting effects on the surfaces of the icy bodies were held to be small (and at the limit of image resolution from the Cassini mission images so far). Nevertheless, impacts may well have a global effect on a body (short of disruption) and understanding such impacts (based on the observed craters) will be one of the ways of obtaining information on internal structures of the icy satellites.

Several papers have modelled cometary impacts on icy satellites for the purpose of considering various outcomes other than just cratering. One possibility is determining the thickness of the ice crust on bodies with a subsurface ocean. Based on the observation that some craters on Europa have a central peak, it is possible to assume that these impacts did not penetrate the ice surface layer on Europa, which was uplifted during the impact to form the observed peak. Modelling of impacts onto ice layers of different thicknesses suggests that on Europa, where these craters are observed the ice layer is at least 3–4 km deep (Turtle and Pierazzo 2001). It should however be noted that models of ice thickness based on flexure under loading produce smaller estimates of the ice thickness. Other simulations concern possible survival of organic material delivered in the impact of a comet on an icy satellite (Pierazzo and Chyba 1999, 2002). For the case of Europa, even at  $30 \text{ km s}^{-1}$  impacts by non-porous icy comets deliver about 20% of the impactor to the target, but for porous comets this is only true at the lowest impact speeds modelled ( $16 \text{ km s}^{-1}$ , compared to the mean impact speed of  $26 \text{ km s}^{-1}$  predicted in Table 9.1 above). Survival of the bulk impactor material in such impacts, has to be combined with the shock processing of any organic content. Nevertheless, over geologic time scales, significant amounts of complex organic materials are predicted to have been delivered to Europa in this fashion.

Impact crater modelling has also been applied to Titan. Here the influence of a dense atmosphere prevents small bodies impacting the surface at high speed. In one example of such modelling, impacts onto Titan's surface of 2 km diameter icy objects at  $7 \text{ km s}^{-1}$  (slightly slower speed than predicted in Table 9.1 above) were held not only to result in impact craters, but the heat retained at the impact site would sustain liquid water at the site for hundreds of years (Artemieva and Lunine 2003). Later modelling suggested that no impact sufficient to generate a global liquid water ocean can be expected to have occurred on Titan, but confirmed that local lakes in impact craters would occur and larger impacts may have penetrated the surface crust into the proposed subsurface liquid reservoirs (Artemieva and Lunine 2005).

## 9.6 Observations of Craters on Icy Solar System Bodies

The study of craters on icy bodies came into focus with the second generation of space missions which flew past the outer planets and their satellites (after the first missions by Pioneer 10 and 11). Data from these missions (Voyager I and II)

included images of the icy surfaces of some of the satellites of Jupiter, Saturn, Uranus and Neptune. The subsequent Galileo mission to Jupiter and the on-going Cassini mission to Saturn have greatly increased the coverage of these icy bodies; during their lengthy times spent orbiting their target planets, they have also had many fly-bys of the various satellites. Most of these satellites are atmosphere-less and readily provide evidence for impact cratering. In the case of the Saturnian satellite Titan however, there is a dense atmosphere, comparable to the Earth's, nevertheless craters have been found there as well (Elachi et al. 2006). Another feature of the Jovian and Saturnian satellites is that in some cases the ice surface overlies an interior ocean. This can influence crater formation in a variety of ways. Finally, there is no reason to suspect that the surfaces of Pluto and Charon do not feature impact craters (unless some re-surfacing process has covered them up). The current NASA new Horizons mission is (at the time of writing) already beyond Jupiter and will pass Pluto in 2015, allowing imaging of any large craters.

The surfaces of the Galilean satellites of Jupiter show extensive evidence of cratering which can be used for a variety of purposes such as dating the surfaces (e.g. (Schenk et al. 2007)). More than just diameter can be measured for these craters. For example, use of stereo imagery and photoclinometry permit slopes and heights (or depths) of features to be found. Profiles across craters can show how the slope varies from rim walls to central peaks. Comparison of the craters on Ganymede and Callisto to those on rocky bodies found a variety of differences (Schenk 1991). The transition from simple to more complex crater morphologies occurred at a smaller diameter on icy bodies than similar sized rocky ones (e.g. compared to the Moon). For the complex craters, the rim wall heights and crater depths were 60–70% of those on equivalent rocky bodies, showing that despite viscous relaxation of the ice, topographical relief could be sustained in general. In larger craters, the central peak heights and widths were greater than those found in rocky craters on the Moon. For craters on Ganymede, the slope of the crater walls is typically half that found in similar sized craters on the Moon (e.g. Bray et al. 2008). There was also evidence for several new crater types, namely pit and dome craters on Ganymede and Callisto (Schenk 1993). Bright domes in craters are held to be caused by uplift of previous buried ice-rich deposits. The pit craters are considered to represent impacts into mechanically weak surfaces. Similarly, studies of craters on icy satellites of Saturn and Uranus (e.g. (Schenk 1989; Moore et al. 2004)) found many examples of various crater morphologies compared to those in rocky bodies. Much of the difference was because the craters were shallower than their rocky counterparts, assigned to litho-static rebound rather than viscous relaxation.

One new class of crater found on icy bodies was the “palimpsest” craters found on Ganymede and Callisto. These were relatively flat blemishes on the icy surfaces. Originally the low resolution Voyager images showed these features but could not definitively assign an impact origin to them (Smith et al. 1979). More detailed studies on the higher resolution Galileo data more positively identified these as craters and suggested they arose from fluid-ejecta deposits from impacts into ice-rich targets (Jones et al. 2003).

Studies of Europa have found a variety of craters (Moore et al. 1998). One population (<30 km diameter) is similar to the classic craters seen on the Moon (e.g. bowl shaped, some of the larger ones with central peaks), albeit with more subdued topography reflecting relaxation of the ice (Pwyll is an example – see Fig. 9.1c). Some of these craters are even more subdued than those on other icy bodies, suggesting a different degree of viscous relaxation (implying a different thermal gradient in the ice). The second population of (larger craters) lacks almost all vertical relief, with no raised rim walls, no central pits etc. and is often compared to the palimpsest craters on Ganymede and Callisto. These large, flat craters on Europa (e.g. Callanish, with diameter ~50–10 km but vertical relief limited to order 100 m) are held to have formed in a finite thickness (relative to crater size) ice layer over a liquid interior, with interaction between the two influencing the shape of the resultant craters (unlike the case of Ganymede with a thicker ice crust). During formation, the floor crater would have penetrated the ice crust and a liquid interior formed which filled the crater. Thus the current appearance is not that arising from subsequent relaxation or processing, but reflects the appearance shortly after formation.

The maximum crater size on a solid body before it is disrupted can be found by examining the known large craters on various bodies. For small icy bodies (<400 km diameter), this has been done by (Leliwa-Kopystynski et al. 2008) who find that  $D_{cr} \sim 1.2R$  holds (where  $D_{cr}$  is crater diameter, and  $R$  is the radius of the target body), smaller than the  $D_{cr} \sim 1.6R$  found for rocky bodies. Whilst these limits may increase slightly as more complete coverage of the surfaces of more icy bodies is obtained, the absence of craters above these limits is a good indicator of the scale of an impact which breaks an icy body apart. In decimetre scale laboratory experiments on ice targets, a limit of  $D_{cr} \sim 1.64R$  was found (Leliwa-Kopystynski et al. 2008).

## 9.7 Real Craters on Porous Icy Bodies (i.e., Comet Nuclei)

Comet nuclei are held to be low density, highly porous bodies. It is therefore interesting to compare craters on these objects to craters on other icy bodies. Several problems arise however. These bodies are small and very dark (amongst the darkest objects in the Solar System with an albedo of just 3 or 4%). It is therefore not possible to image them from the Earth in high enough resolution to see craters on their surfaces. Fortunately, several space missions have now flown past comet nuclei, providing images of their surfaces (see Fig. 9.5). In chronological order, the imaged comet nuclei are: 1P/Halley (in 1986 by the Rosetta spacecraft), 19P/Borrelly (in 2001 by the Deep Space 1 spacecraft), 81P/Wild 2 (in 2004 by the Stardust spacecraft) and 9P/Tempel 1 (in 2005 by the Deep Impact spacecraft). In addition, the Rosetta spacecraft is on its way to rendezvous with 67P/Churyumov-Gerasimenko in 2014. The Deep Impact spacecraft is still operational and is now targeted at 103P/Hartley 2 (with a fly-by scheduled for Oct. 2010) and the extended

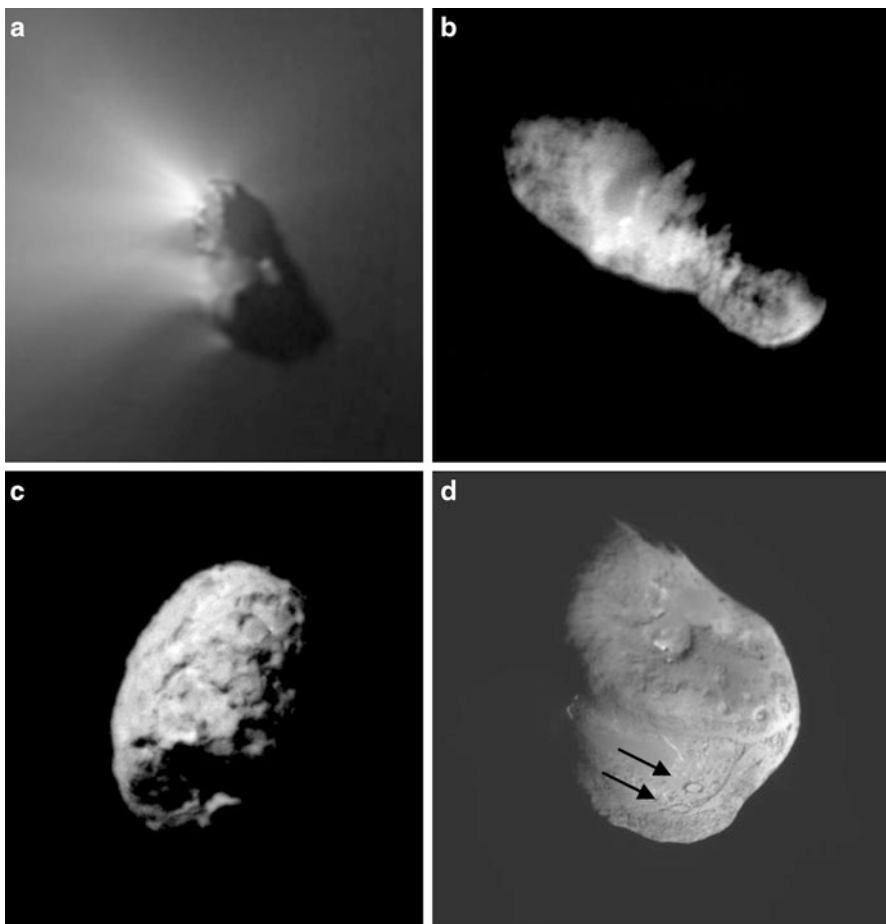


**Fig. 9.5** Images of comet nuclei: (a) 1P/Halley, radii of  $7.6 \times 3.6 \times 3.6$  km (Source: ESA), (b) 19P/Borelly, radii  $4 \times 1.6 \times 1.6$  km (Source NASA), (c) 81P/Wild 2, radii  $2.75 \times 2 \times 1.65$  km (Source NASA) and (d) 9P/Tempel 1, radii of  $3 \times 3$  km (Source: NASA). Classical appearing impact craters are shown *arrowed* in (d)

mission of the Stardust spacecraft will take it past 9P/Tempel 1 in 2011 (permitting observation of the crater made by the Deep Impact mission in 2005).

It can be seen from Fig. 9.5, that the lighting conditions and resolution make it hard to see craters on the surface of 1P/Halley and only the largest structures are visible on 19P/Borelly. However, the lighting and image resolution during the fly-bys of 81P/Wild 2 and 9P/Tempel 1 have provided excellent detail of their surface structure. After the fly-by of 81P/Wild 2, it was noted (Brownlee et al. 2004) that no images showed craters with classical rim walls and bowl shaped interiors and it was suggested this was due to the porous nature of the nucleus altering the classical appearance of impact craters, rather than due to a lack of impacts (even though there is a low density of material in the outer solar system, modelling suggests there

will be a significant impact flux over the lifetime of these bodies). This argument was taken further in a comparison of 1P/Halley, 19P/Borelly and 81P/Wild 2 which suggested different modification histories as a result of repeated passages through the inner solar system (Basilevsky and Keller 2006). However, in the case of 9P/Tempel 1, classical looking impact craters (shown arrowed in Fig. 9.5d) were observed on its surface. This may indicate that the nature of impact cratering on porous icy bodies with varying silicate contents is a subtle one, especially when the surfaces may have undergone wildly differing degrees of subsequent erosion. It should be remembered however, that not all circular features observed on a surface are necessarily impact craters. They may reflect sub-surface collapse, blow-outs of surface material in some eruptive process, growth of originally smaller features by preferential sublimation of crater walls etc.

Whether all the observed features on 81P/Wild 2 are impact craters is discussed in (Burchell and Kearsley 2009). If they are accepted as craters, then combined with the predicted impact flux, it is suggested in (Burchell and Kearsley 2009) that the surface of 81P/Wild 2 is several billion years old. There is a lack of small craters observed on both 81P/Wild 2 and 9P/Tempel 1. This may be due to loss of surface material during passage through the inner Solar System, although estimates of such loss suggest it may only correspond to depths of 10s of cm for 81P/Wild 2 during each perihelion passage and of order 1 m in all its passages through the inner Solar System since its orbital interaction with Jupiter pushed it into its present orbital path in 1974 (Brownlee et al. 2004).

The surface of 9P/Tempel 1 (A'Hearn et al. 2005) by contrast shows what appear to be classical impact crater shapes, with raised circular rims (shown arrowed in Fig. 9.5d). These craters are shallow, as if the interiors have been in-filled somehow. The purpose of the Deep Impact mission was to make its own impact crater on the comet nucleus. To do this, a 385 kg mass was flown into the comet at  $10.1 \text{ km s}^{-1}$ , which resulted in an impact event witnessed from both the spacecraft and the Earth (Schultz et al. 2007; A'Hearn et al. 2005; Sugita et al. 2005) and even from other spacecraft (Keller et al. 2005). However, although the impact produced an impact light flash and large ejecta cloud, the crater was not imaged directly before the main Deep Impact spacecraft moved beyond the necessary angle for viewing the impact site. The crater size and shape thus have to be inferred from information obtained from a variety of sources combined with highly processed images taken during the fly-by (Schultz et al. 2007). The interpretation of this data makes allowance for possible inhomogeneities in the ice, porosity, sub-surface layering, presence of loosely consolidated fine dust, angle of impact and so on. The deduced crater shape is that of an inverted sombrero-hat, i.e. a shallow region surrounding a deeper central pit.

Overall, studies of the cratering on the surface of comet nuclei, should still be considered as being in its infancy. A wide variety of forms has been observed on the two comets imaged in high resolution (81P/Wild 2 and 9P/Tempel 1). The classical crater shape with a raised rim is absent on one comet but present on the other. Indeed, the study of 81P/Wild 2 raised the difficult issue of whether or not all circular features observed on planetary surfaces are craters. Even here on Earth, this is a difficult topic which can lead to mis-identification of features as impact craters (Reimold 2007). Nevertheless, if such problems can be resolved (or are simply

ignored) the use of crater counts per unit surface area, combined with models of impact flux rates can lead to estimates of the ages of the cometary surfaces. In the case of 81P/Wild 2, this leads to an estimate of several billion years for the age of the comet's surface (Burchell and Kearsley 2009). This issue of cratering on comet nuclei will undoubtedly re-revisited when the Stardust and Deep Impact main spacecraft visit their new targets, and when the Rosetta spacecraft finally encounters and orbits comet 67P/Churyumov-Gerasimenko in 2014.

## 9.8 Catastrophic Disruption of Icy Bodies (Experiment and Modelling)

Whilst cratering is usually taken as the outcome of an impact, it is not the only possible result. The key parameter is energy density ( $Q$ ) in the impact (the kinetic energy of the impactor divided by the combined mass of the two bodies), given by

$$Q = \frac{1}{2}mv^2 / (m + M). \quad (9.6)$$

Here  $m$  is the mass of the impactor and  $M$  that of the target body with  $v$  the impact speed. If  $Q$  is sufficiently large, then the target body can break apart during the impact. Note that in the definition of  $Q$ , the  $m$  term in the denominator is often neglected, as, due to the relatively high impact speeds, the condition  $M \gg m$  still results in a sufficiently high energy density for a break up event. The critical value of  $Q$  above which break-up occurs is referred to as  $Q^*$ . Once broken up, the fragments do not necessarily disperse, they have to possess a velocity sufficient to overcome the self gravity of the body. Thus many large bodies reassemble after a break-up event into what for asteroids is referred to as a “rubble-pile”. As is the case with cratering, much of the literature on what is referred to as catastrophic disruption events pertains to asteroids (metal or rocky bodies), rather than icy bodies.

A schematic showing the cratering vs. disruption regimes as a function of  $Q$  is given in Fig. 9.6. Note that the vertical axis is given in terms of  $M_f/M_i$ , where  $M_f$  is the mass of the largest fragment after impact and  $M_i$  is the original target mass. By convention, the critical value for the threshold between cratering and disruption is given by  $M_f/M_i = 0.5$ , and it is the corresponding value of  $Q$  that is taken as  $Q^*$ . As  $Q$  increases above  $Q^*$ , the value of  $M_f/M_i$  continues to fall, i.e. the mass of the largest surviving fragment gets smaller. The size distribution of the fragments inside a single event also changes. If ordered by size, the cumulative size of fragments (for asteroid break-up) has long been held to behave as illustrated in Fig. 9.7. Note that for  $Q$  close to  $Q^*$  and for  $Q$  much greater than  $Q^*$ , two types of behaviour pertain. In the former case there is a much more rapid fall off in fragment size (reflecting the presence of only a few large fragments after the break up), whereas in the latter case there are many similar sized small fragments. This is illustrated for asteroid break-up in (Durda et al. 2007) and the same may well hold true for break-up of icy bodies.

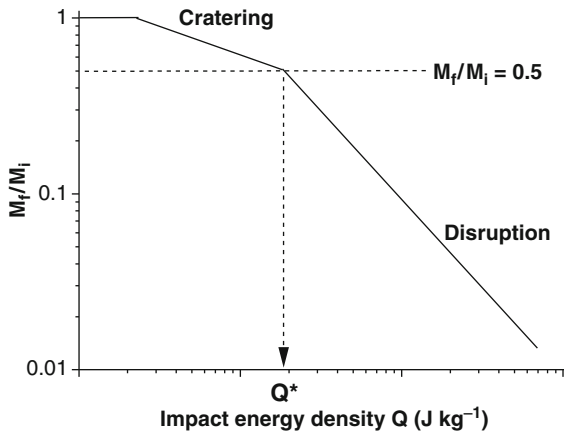


**Fig. 9.6** Schematic diagram showing evolution of the mass of the largest target fragment remaining after an impact ( $M_f$ ) normalised to the total initial mass ( $M_i$ ) versus the impact energy density  $Q$ . As  $Q$  increases the impact crater becomes larger and larger, until it removes more than  $\frac{1}{2}$  the mass of the target in the impact. When  $M_f/M_i = 0.5$ , the transition from the cratering to the disruption regime is taken to occur and the associated value of  $Q$  is called  $Q^*$

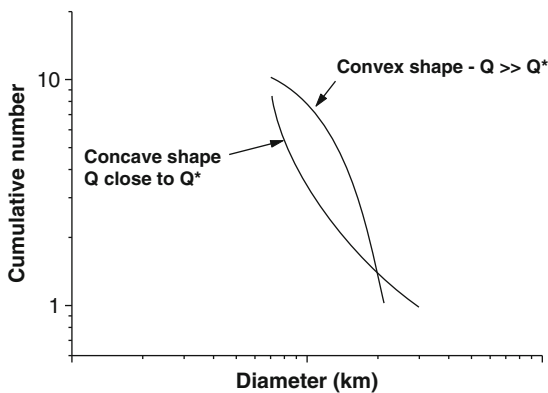


**Fig. 9.7** Schematic diagram showing size frequency distribution (SFD) of fragments of a catastrophically disrupted body. The shape of the distribution (concave or convex) can indicate how close to critical the impact event was. A concave distribution indicates a just sub-critical or near critical impact, whereas a convex shape indicates that  $Q$  was much greater than  $Q^*$ , i.e. a supercritical disruption event

It would be nice to know the exact form of  $Q^*$  as a function of the size of the target body. However, it can only be measured at laboratory scales, and has to be obtained at larger sizes by a variety of modelling methods (via scaling, analytical models or hydrocodes). In laboratory experiments  $Q^*$  for ice has been found to be of order  $1-100 \text{ J kg}^{-1}$  at cm to decimetre sizes (see Table 9.3). There is some evidence that the values obtained in experiments may depend on projectile density. However, the values obtained are significantly lower than the  $\sim 1,000 \text{ J kg}^{-1}$  found in similar

**Table 9.3** Summary of various laboratory impact disruption experiments on ice targets. Most experiments feature ice targets of cm to a few 10s of size and at temperatures of 255–265 K

Target type	Impact speed (km s <sup>-1</sup> )	Projectile type	Q* (J kg <sup>-1</sup> )	Comment
H <sub>2</sub> O	0.04–0.85	Various including ice, al. and polycarbonate projectiles)	30 (al. projectiles)–60 (ice projectiles)	Both cratering and fragmentation were reported Kato et al. (1995)
H <sub>2</sub> O	0.09–0.15	Ice	21	Giblin et al. (2004)
H <sub>2</sub> O	0.11–0.18	Al.	~10	Ryan et al. (1999)
H <sub>2</sub> O	0.14–0.68	Not given	3	~50% porous ice targets A later paper suggested this may be an artificially low value (Giblin et al. 2004)
H <sub>2</sub> O	0.15–0.67	Ice	40 (non-porous ice) and 137 (37–55% porous ice)	Kawakami et al. (1983)
H <sub>2</sub> O	0.16–1.05	Polyethylene, al. and st. st.	15	Mean grain size after disruption also given Arakawa et al. (2002)
H <sub>2</sub> O	1–7	Copper	4.9–9 (solid ice) 708 (50% porous ice)	Cintala et al. (1985b)
H <sub>2</sub> O	1–7.9	Al. and st. st.	2–18	Porous were made from large ice flakes bigger than the projectile Also determines limits on largest possible craters on small bodies Leliwa- Kopystynski et al. (2008)
H <sub>2</sub> O	2.3–4.7	Nylon	50–60	Fragment size distribution also given Arakawa (1999)
H <sub>2</sub> O-silicate	0.15–0.67	Ice	99	38% porous target. Mass of ice: silicate 1:1 Arakawa et al. (2002)
H <sub>2</sub> O-silicate	0.15–0.67	Ice	40–120	Silicate content and target porosity were varied Arakawa and Tomizuka (2004)
H <sub>2</sub> O-silicate	1.2–7.3	Copper	120–160	Mass ratio ice: silicate is 1:4 Lightwing and Burchell (2006)

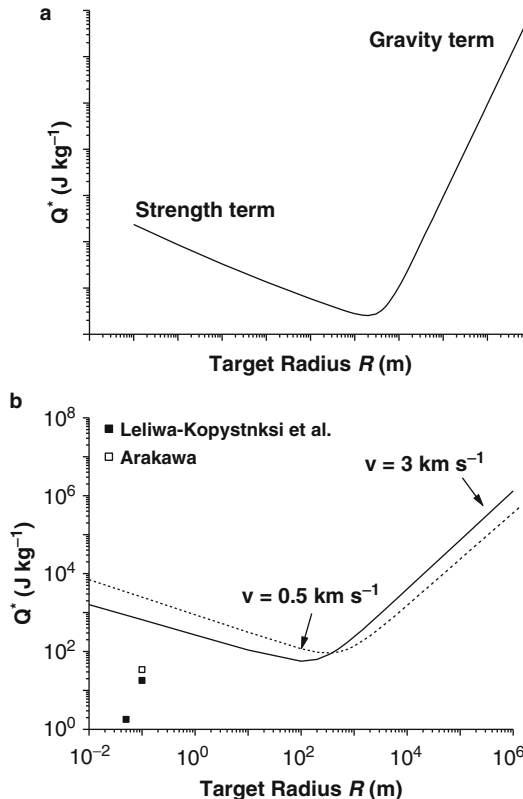


**Fig. 9.8** Evolution of  $Q^*$  with size of body ( $r$ ). (a) Schematic diagram showing  $Q^*$  initially falls as  $r$  increases from laboratory scales to approximately 100–1,000 m, then starts to rise again as the energy needed to disperse the body against gravity becomes significant and dominates. (b) The curves shown here are from a widely used hydrocode simulation for two impact speeds ( $0.5$  and  $3\text{ km s}^{-1}$ ) (Benz and Asphaug 1999). The general trend of the predictions agrees with the idealised case shown in (a), but does not agree with the experimental data shown for laboratory scale experiments (Leliwa-Kopystynski et al. 2008) and Arakawa is (Arakawa 1999))

experiments on rock targets.  $Q^*$  is found to increase significantly if the ice target is porous, with energy flowing into compression of the pores rather than propagation of cracks. The addition of silicates into the ice target also increases  $Q^*$ .

According to models of catastrophic disruption, as target size increases,  $Q^*$  initially falls (Fig. 9.8a). Thus effectively, larger targets are weaker. This is a well known result in impact mechanics. However, as target mass increases further, the self-gravity of the body also increases, and it is harder for the fragments to disperse. The ability to avoid re-accumulation of the target fragments after impact is thus dependent on the velocity imparted to the fragments and the total mass. This requires an increasing projectile impact energy as target mass increases, and, for bodies at size scales above a few 100–1,000 m, this increase in  $Q^*$  dominates the decrease due to decreasing target strength. The result is the evolution of  $Q^*$  with  $r$  shown in Fig. 9.8a at larger target sizes.

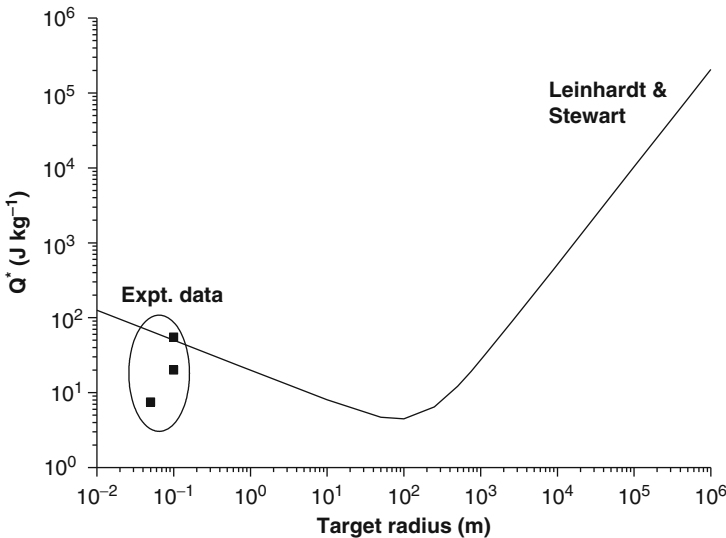


**Fig. 9.9**  $Q^*$  versus target body size. Sample experimental data from Table 9.3 are shown (lower left). The curve labelled Leinhardt & Stewart is (Leinhardt and Stewart 2009) and is for impacts at  $1 \text{ km s}^{-1}$

One of the better known predictions of  $Q^*$  for icy bodies is (Benz and Asphaug 1999) and is shown in Fig. 9.8b. However, such predictions should be treated with caution. They are usually obtained for pure water ice, homogeneous bodies. The effect of impact angle or rotating target bodies is also often ignored (although it is given in (Benz and Asphaug 1999)). And at lower size scales, porosity may be important (e.g. in cometary nuclei). In addition, it can be seen in Fig. 9.8b, that the most widely used hydrocode model for disruption of icy bodies (Benz and Asphaug 1999), significantly overestimates  $Q^*$  at laboratory scales where it can be directly measured. A more recent hydrocode simulation for impacts on ice (Leinhardt and Stewart 2009) lowers the predictions of  $Q^*$  at small sizes (in agreement with laboratory data, see Fig. 9.9) but keeps the same form of the dependence of  $Q^*$  on gravity at larger scales where it is broadly in agreement with the earlier predictions. However, this does not allow for oblique incidence impacts which result in higher  $Q^*$  values; for example, in (Benz and Asphaug 1999) the simulations suggest that an impact at  $45^\circ$  increases  $Q^*$  by a factor of 2 compared to an impact at normal incidence.

The transition from strength to gravity dominated regimes for icy bodies occurs at around 100 m to 1 km, suggesting that comet nuclei for example (typical sizes 5–10 km) are in the gravity regime. However, such bodies still have significant porosity which, according to (Dawe et al. 2005) can increase  $Q^*$  at decimetre (laboratory) scales by a factor of  $\sim 100$ . It is thus not clear how this will alter the form of  $Q^*$  with  $r$  in Fig. 9.9. It may well be that comet nuclei are of a size and composition that places them at the boundary between strength and gravity dominated regimes for disruption. Similarly, it is not clear what value  $Q^*$  should apply for larger bodies with a differentiated core (e.g. Pluto, which may have a silicate rich core with a pure ice mantle).

## 9.9 Summary

The study of cratering on icy bodies in the Solar System is an increasingly sophisticated one. Craters have been observed on bodies such as comet nuclei and icy satellites. There is also evidence that the formation of at least some craters on Mars have been significantly influenced by the presence of sub-surface ice. These observations are increasingly backed up by insights gained from laboratory experimentation and hydrocode modelling. Thus in the Solar System, trying to understand impact cratering solely by reference to impacts on rocky bodies is no longer an appropriate method: icy bodies also undergo impacts whose consequences need to be understood.

Understanding the mechanics of impacts on ice not only provides an explanation for the observed impact features, but can also provide insights into the interiors and histories of these bodies. For example, the thickness of icy surfaces over interior oceans or the size of a differentiated core can be modelled based on observed crater sizes. The presence of a differentiated core may also increase the energy density needed for catastrophic disruption, increasing the life-time of a body against impact disruption. Finally, one significant impact on an icy body we only have indirect evidence for is a giant impact on Pluto. The evidence is the presence of Charon orbiting Pluto, which is held to have formed after a giant impact in a similar way to our Moon forming after a giant impact on the Earth.

## References

- A'Hearn M et al (2005) Deep impact: excavating comet tempel 1. *Science* 310:258
- Arakawa M (1999) Collisional disruption of ice by high-velocity impact. *Icarus* 142:34
- Arakawa M, Tomizuka D (2004) Ice-silicate fractionation among icy bodies due to the difference of impact strength between ice and ice-silicate mixture. *Icarus* 170:193
- Arakawa M et al (2000) Impact cratering of granular mixture targets of H<sub>2</sub>O ice-CO<sub>2</sub> ice-pyrophylite. *Planet Sp Sci* 48:1437
- Arakawa M, Leliwa-Kopystynski J, Maeno N (2002) Impact experiments on porous icy-silicate cylindrical blocks and the implication for disruption and accumulation of small icy bodies. *Icarus* 158:516
- Artemieva N, Lunine J (2003) Cratering on Titan: impact melt, ejecta, and the fate of surface organics. *Icarus* 164:471
- Artemieva N, Lunine J (2005) Impact cratering on Titan II. Global melt, escaping ejecta, and aqueous alteration of surface organics. *Icarus* 175:522
- Atkins WW (1955) Flash associated with high velocity impact on aluminium. *J Appl Phys* 26: L126
- Basilevsky AT, Keller HU (2006) Comet nuclei: morphology and implied processes of surface modification. *Planet Sp Sci* 54:808
- Benz W, Asphaug E (1999) Catastrophic disruption revisited. *Icarus* 142:5
- Best S, Rose MF (1999) A plasma drag hypervelocity particle accelerator (HYPER). *Int J Impact Eng* 23:67
- Bland PA et al (1996) The flux of meteorites to the Earth over the last 50,000 years. *Mon Not R Astron Soc* 283:551

- Bottke WF Jr, Nolan MC, Greenberg R, Loolword RA (1994) Velocity distributions among colliding asteroids. *Icarus* 107:255
- Bray VJ et al (2008) The effect of target properties on crater morphology: comparison of central peak craters on the moon and Ganymede. *Meteorit Planet Sci* 43:1979
- Brownlee DE et al (2004) Surface of young Jupiter family comet 81P/Wild 2: view from the Stardust Spacecraft. *Science* 304:1764
- Bruesch LS, Asphaug E (2004) Modeling global impact effects on middle-sized icy bodies: applications to Saturn's moons. *Icarus* 168:457
- Burchell MJ, Johnson E (2005) Impact craters on small icy bodies such as icy satellites and comet nuclei. *Mon Not R Astron Soc* 360:769
- Burchell MJ, Kearsley AT (2009) Short period Jupiter family comets after Stardust. *Planet Sp Sci* 57:1146
- Burchell MJ, Cole MJ, Ratcliff PR (1996) Light flash and ionization from hypervelocity impacts on ice. *Icarus* 122:359
- Burchell MJ et al (1998) Hypervelocity impact experiments on solid CO<sub>2</sub> targets. *Icarus* 131:210
- Burchell MJ et al (1999) Hypervelocity impact studies using the 2 MV Van de Graaff dust accelerator and two stage light gas gun of the university of Kent at Canterbury. *Meas Sci Technol* 10:41
- Burchell MJ, Johnson E, Grey IDS (2002) Hypervelocity impacts on porous ices. In: Proceedings of asteroids, comets and meteors – ACM 2002, ESA-SP500, Berlin, p 859
- Burchell MJ et al (2003) Survivability of bacteria ejected from icy surfaces after hypervelocity impact. *Org Life Evol Biosp* 33:53
- Burchell MJ, Leliwa-Kopystynski J, Arakawa M (2005) Cratering of icy targets by different impactors: laboratory experiments and implications for cratering in the Solar system. *Icarus* 179:274
- Cintala MJ et al (1985a) Impact experiments in H<sub>2</sub>O ice II: collisional disruption. In: Lunar and planetary science conference XVI (Houston), p 129
- Cintala MJ et al (1985b) Impact experiments in H<sub>2</sub>O ice. In: Lunar and planetary science conference XVI (Houston), p 131
- Croft SK (1981) Hypervelocity impact craters in icy media. In: Lunar and planetary science conference XII (Houston), p 190
- Crozier WD, Hume W (1957) High-velocity, light-gas gun. *J Appl Phys* 28:892
- Dawe W, Murray M, Burchell MJ (2005) Catastrophic disruption of porous and solid ice bodies. In: Lunar and planetary science conference XXXVI (Houston), #1096
- Dell'Oro A et al (2001) Updated collision probabilities of minor body populations. *Astron Astrophys* 366:1053
- Durda DD et al (2007) Size-frequency distributions of fragments from SPH/N-body simulations of asteroid impacts: comparison with observed asteroid families. *Icarus* 186:498
- Dypvik H, Jansa LF (2003) Sedimentary signatures and processes during marine bolide impacts: a review. *Sediment Geol* 161:309
- Eichhorn K, Grun E (1993) High velocity impacts of dust particles in low temperature ice. *Planet Sp Sci* 41:429
- Elachi C et al (2006) Titan Radar Mapper observations from Cassini's T3 fly-by. *Science* 441:709
- Feistel R, Wagner W (2006) A new equation of state for H<sub>2</sub>O ice Ih. *J Phys Chem Ref Data* 35:1021
- Frank MR, Fei YW, Hu JZ (2004) Constraining the equation of state of fluid H<sub>2</sub>O to 80 GPa using the melting curve, bulk modulus, and thermal expansivity of ice VII. *Geochim Cosmochim Acta* 68:2781
- Friichtenicht JF (1962) Two million volt electrostatic accelerator for hypervelocity research. *Rev Sci Instrum* 33:209
- Giblin I, Davis DR, Ryan EV (2004) Collisional disruption of porous icy targets simulating Kuiper belt objects. *Icarus* 171:487
- Grey IDS, Burchell MJ (2003) Hypervelocity impact cratering on water ice targets at temperatures ranging from 100 K to 253 K. *J Geophys Res* 108(E3):6.1. doi:[10.1029/2002JE001899](https://doi.org/10.1029/2002JE001899)
- Grey IDS, Burchell MJ (2004) Hypervelocity impact craters in ammonia rich ice. *Icarus* 168:467

- Grey IDS, Burchell MJ, Shrine NRG (2002) Scaling of hypervelocity impact craters in ice with impact angle. *J Geophys Res* 107(E10), 6.1, doi:10.1029/2001JE001515
- Hughes DW, Williams IP (2000) The velocity distributions of periodic comets and stream meteoroids. *Mon Not R Astron Soc* 315:629
- Iijima Y et al (1995) Cratering experiments on ice: dependence of crater formation on projectile materials and scaling parameter. *Geophys Res Lett* 22:2005
- Jones KB et al (2003) Morphology and origin of palimpsests on Ganymede based on Galileo observations. *Icarus* 164:197
- Kato M et al (1995) Ice-on-ice impact experiments. *Icarus* 113:423
- Kato M et al (2001) Shock pressure attenuation in water ice at a pressure below 1 GPA. *J Geophys Res* 106(E8):17567
- Kawakami S et al (1983) Impact experiments on ice. *J Geophys Res* 88:5806
- Keller HU et al (2005) Deep impact observations by OSIRIS onboard the Rosetta spacecraft. *Science* 310:281
- Koschny D, Grun E (2001a) Impacts into ice-silicate mixtures: crater morphologies, volumes and depth-diameter ratios, and yield. *Icarus* 154:391
- Koschny D, Grun E (2001b) Impacts into ice-silicates mixtures: ejecta mass and size distributions. *Icarus* 154:402
- Kyte FT, Zhou Z, Wasson JT (1981) High noble-metal concentrations in a late Pliocene sediment. *Science* 292:417
- Lange M, Ahrens TJ (1987) Impact experiments in low-temperature ice. *Icarus* 69:506
- Larson DB (1984) Shock-wave studies of ice under uniaxial strain conditions. *J Glaciol* 30:235
- Leinhardt ZM, Stewart ST (2009) Full numerical simulations of catastrophic small body collisions. *Icarus* 199:542
- Leliwa-Kopystynski J, Burchell MJ, Lowen D (2008) Impact cratering and break up of the small bodies of the Solar system. *Icarus* 195:817
- Lightwing A, Burchell MJ (2006) Catastrophic disruption of mixed ice:sand bodies. In: Lunar and planetary science conference XXXVII (Houston), #1565
- Melosh HJ (1989) Impact cratering: a geologic process. Oxford University Press, Oxford
- Moore JM et al (1998) Large impact features on Europa: results of the Galileo nominal mission. *Icarus* 135:127
- Moore JM et al (2004) Large impact features on middle-sized icy satellites. *Icarus* 171:421
- Osinski GR et al (2008) The effect of target lithology on the products of impact melting. *Meteorit Planet Sci* 43:1939
- Pierazzo E, Chyba CF (1999) Amino acid survival in large cometary impacts. *Meteorit Planet Sci* 34:909
- Pierazzo E, Chyba CF (2002) Cometary delivery of biogenic elements to Europa. *Icarus* 157:120
- Reimold WU (2007) The impact crater Bandwagon: (Some problems with the terrestrial impact cratering record). *Meteorit Planet Sci* 42:1467
- Ryan EV, Davis DR, Giblin I (1999) A laboratory impact study of simulated Edgeworth–Kuiper belt objects. *Icarus* 142:56
- Schenk PM (1989) Crater morphology and modification on the icy satellites of Uranus and Saturn: depth/diameter and central peak occurrence. *J Geophys Res* 94:3815
- Schenk PM (1991) Ganymede and Callisto – complex crater formation and planetary crusts. *J Geophys Res (The Planets)* 96:15635
- Schenk PM (1993) Central pit and dome craters – exposing the interiors of Ganymede and Callisto. *J Geophys Res (The Planets)* 98:7475
- Schenk PM et al (2007) Ages and interiors: the cratering record of the galilean satellites. In: Bagenal F (ed) Jupiter. Cambridge University Press, Cambridge, pp 427–456
- Schultz PH (1996) Effect of impact angle on vaporization. *J Geophys Res* 101(E9):21117
- Schultz PH et al (2007) The deep impact oblique impact cratering experiment. *Icarus* 190:295
- Senft LE, Stewart ST (2008) Impact crater formation in icy layered terrains on Mars. *Meteorit Planet Sci* 43:1993

- Smith BA et al (1979) The Galilean satellites and Jupiter: Voyager 2 imaging science results. *Science* 206:927
- Stewart ST, Ahrens TJ (2003) Shock Hugoniot of H<sub>2</sub>O ice. *Geophys Res Lett* 30:1332
- Stewart ST, Ahrens TJ (2005) Shock properties of H<sub>2</sub>O ice. *J Geophys Res* 110. doi:[10.1029/2004JE002305](https://doi.org/10.1029/2004JE002305), E03005
- Sugita S et al (2005) Subaru telescope observation of deep impact. *Science* 310:274
- Turtle EP, Pierazzo E (2001) Thickness of a European ice shell from impact crater simulations. *Science* 294:1326
- Upshaw JL, Kajs JP (1991) Micrometeoroid impact simulations using a railgun electromagnetic accelerator. *IEEE Trans Magn* 27:607
- Wagner WM, Pruss A (2002) The IAPWS formulation 1995 for the thermodynamic properties of ordinary water substance for general and scientific use. *J Phys Chem Ref Data* 31:387
- Zahnle K, Dones L, Levison H (1998) Cratering rates on the Galilean satellites. *Icarus* 136(202):723
- Zahnle K et al (2003) Cratering rates in the outer Solar system. *Icarus* 163:263

# Chapter 10

## Geology of Icy Bodies

Katrin Stephan, Ralf Jaumann, and Roland Wagner

**Abstract** The exploration of the outer solar system in the last decades revealed an exotic icy world with surfaces showing the most diverse geology, sometimes exceptional to these icy bodies due to the peculiar rheology of ice. Each of these icy bodies exhibits unique characteristics and its own fascinating geological history – formed by the competition of external and internal forces.

Some satellites are still geologically active today while others appear to be mostly inactive at present time. Geologically old surfaces are heavily cratered. Some projectiles which created large craters or basins were massive enough that they could have destroyed the target body, like in the case of the impact crater Herschel on the Saturnian satellite Mimas. The observed impact crater morphologies are often exclusive to icy bodies like impact craters on the Galilean satellites Ganymede and Callisto. They mirror the target properties at the time of impact and thus help to understand the satellite's geological evolution. They also reflect the external influence of the space environment onto the surface material since the impact occurred, which is of major importance since most of these icy bodies do not exhibit an atmosphere. Tectonic resurfacing can often be observed as widely distributed simple extensional fractures. Satellites that experienced a more intricate tectonic resurfacing also show more complex tectonic features like double ridges on the Jovian satellite Europa, the Saturnian satellite Enceladus as well as Neptun's satellite Triton. Peculiar tectonic features that are restricted to a single

---

K. Stephan (✉) • R. Wagner

German Aerospace Center, Institute of Planetary Research, Rutherfordstrasse 2,  
14489 Berlin, Germany

e-mail: [Katrin.Stephan@dlr.de](mailto:Katrin.Stephan@dlr.de)

R. Jaumann

German Aerospace Center, Institute of Planetary Research, Rutherfordstrasse 2,  
14489 Berlin, Germany

Freie Universität Berlin, Institute of Geological Sciences, Malteserstrasse 74-100,  
12249 Berlin, Germany

satellite include Europa's bands and chaotic terrain as well as Miranda's coronae indicating outstanding geological evolutions of these two bodies. These complex features are far from being fully understood. They are, at least partly, expected to be associated with recent and/or past cryovolcanism. Current volcanism, however, has been detected only on the two satellites Enceladus and Triton, finding its peak in geysers on Enceladus originating from its south pole forming vapor plumes that reach up to 500 km into space.

## 10.1 Introduction

The two Voyager spacecraft that flew through the outer Solar System in the decade between 1979 and 1989 allowed a first look at the icy satellites of Jupiter and Saturn and have also provided our only view of the regions farther out so far, i.e. the satellite systems of Uranus and Neptune. The recent Galileo mission offered a more detailed look at Jupiter's satellites, monitoring changes on their surfaces with the spacecraft orbiting through the system over a period of no less than 8 years (1996–2003).

In a similar way, the Cassini spacecraft has been in orbit about Saturn since July 2004, until 2005 in combination with Huygens probing Titan's surface which is hidden from the visible eye by its dense atmosphere. Cassini completed its initial 4-year tour in June 2008 and its first extended mission, called the Cassini Equinox Mission, in September 2010. Since Cassini arrived at Saturn shortly after the planet's northern winter solstice, the second extension called Cassini Solstice Mission is planned to continue until September 2017 (end of mission) and will allow to study a complete seasonal period in the Saturnian system for the first time.

Although similar geological processes driven by both internal or external forces influence the geological evolution of each satellite in the outer solar system, these bodies experienced most variable geological histories. Occurrence and importance of specific processes in modifying the surfaces vary greatly between icy bodies, depending on major characteristics of a specific body (size, composition), but are also influenced by a specific space environment, as well as thermal and orbital evolution. The diversity of features observed on the icy satellites reflects the diversity of the processes that have molded their surfaces. They are often very different from those observed on terrestrial bodies due to the unique behavior of  $\text{H}_2\text{O}$  ice, which represents the most abundant material. Observations of surface features made by remote sensing instruments describing their morphology and distribution on a planetary surface are extremely important to put constraints on the mechanisms responsible for these features and provide more detailed information that are useful as parameters for theoretical models or laboratory experiments (Collins et al. 2009).

Exogenic modification of planetary surfaces is primarily caused by impact events affecting essentially all surfaces. Interplanetary dust, solar UV radiation, and partly energetic particles originating from planetary magnetospheres, however, also cause significant alteration of the physical and chemical properties of the surface material. Endogenic modification includes tectonic resurfacing as well as icy volcanism (cryovolcanism) of several sorts.

Several recent in-depth reviews of the current knowledge of the geology specific icy bodies exist including: Jupiter: the Planet, Satellites, and Magnetosphere (2004) (Eds.: F. Bagenal, T. Dowling, and W. McKinnon); Saturn from Cassini-Huygens (2009) (Eds.: M. K. Dougherty, L.W. Esposito, S. Krimigis); Titan from Cassini-Huygens (2009) (Eds.: R. H. Brown, J.-P. Lebreton, H. Waite), and Planetary Tectonics (2009) (Eds.: T. R. Watters and R. A. Schultz). In order to recognize the uniqueness of surface features in the outer Solar System but also in order to emphasize the partly striking similarity of surface features on some bodies of different satellite systems, this chapter will focus on the presentation of geological surface features observed on icy satellites, rather than describing each individual body separately. Thus, surface features of similar appearance on different icy satellites will be discussed in direct comparison to each other with respect to geological processes responsible for their formation and the evolution of the corresponding satellite.

## 10.2 Impact Cratering on Icy Bodies

Impact craters on planets and their satellites are created by hypervelocity collisions with minor bodies (Melosh 1989). These bodies, generally termed projectiles or impactors, range in size from dust grains (micrometeorites) to large bolides with diameters of several tens or hundreds of kilometers. Candidate impactors include (a) asteroids from the Main Belt, (b) comets and other trans-Neptunian objects from the Kuiper Belt or from the Oort cloud, (c) planetocentric debris, or (d) remnants of planetary accretion, e.g., planetesimals from the formation zone of the terrestrial planets, or from the region near Uranus and Neptune (Wetherill 1975; Chapman and McKinnon 1986; Neukum and Ivanov 1994; Strom et al. 2005; Ivanov and Hartmann 2007).

The craters on a solid planetary surface record the time interval during which the surface was exposed to the influx of impactors: the more craters, the older the surface (Öpik 1960). On the other hand, size and morphology of each crater reflect a specific impact condition like size of the projectile, impact velocity and impact angle are directly translated into crater size. Physical properties of the projectile as well as of the target body, such as surface gravity, density and rheological parameters also control the crater form (Croft 1985; Holsapple 1987; Schmidt and Housen 1987; Melosh 1989). Influences of impact conditions, impactor and surface properties on size and form of the final crater are summarized as *crater scaling*. They are empirically described by a number of crater scaling laws (e.g., Holsapple 1987; Schmidt and Housen 1987; Melosh 1989).

Special attention is given to the rheological properties of icy surfaces because crater forms on icy satellites deviate from those observed on the terrestrial planets (Schenk et al. 2004, and references therein). The widest range in crater morphologies is observed on the icy Galilean satellites of Jupiter, Callisto, Ganymede, and Europa. Craters on the satellites of Saturn, Uranus and Neptune resemble those on the terrestrial planets (Chapman and McKinnon 1986). Detailed analyses

of craters on the Uranian and Neptunian satellites are impeded by the comparably low image resolution of the Voyager 2 images achieved during the flybys in 1986 and 1989 (Smith et al. 1986, 1989). In general, the following classes of crater forms are found on icy satellites: (1) simple craters at small sizes, (2) regular complex craters, (3) craters with central pits, (4) craters with central domes, (5) palimpsests, and (6) impact basins and multi-ring structures.

### **10.2.1 Simple Craters**

Small craters up to several kilometers in diameter are characterized by a bowl or paraboloid shape of the crater interior (Fig. 10.1). The morphology of simple craters on icy satellites and on the terrestrial planets is similar (Chapman and McKinnon 1986; Schenk et al. 2004). The depth-to-diameter ( $d/D$ ) ratio of simple craters on the icy Galilean satellites is comparable to those of simple craters on the terrestrial planets, on the order of 0.2 (Schenk et al. 2004). Examples for simple craters on various icy satellites are shown in Fig. 10.1.

### **10.2.2 Regular Complex Craters**

With increasing diameter, crater forms become complex. The simple-to-complex transition diameter is dependent on target body surface properties and approximately scales inversely with its surface gravity (e.g., Pike 1980; Melosh 1989). Simple craters (Sect. 10.2.1) form in a regime dominated by the strength of surface material while complex craters larger than the transition diameter form by collapse of an initially simple, bowl-shaped crater (or, more precisely, of a transient cavity) under the influence of gravity (e.g., Melosh 1989). In addition to gravity, the amount of volatiles in the surface and subsurface of icy satellites and, partly, of Mars provides a further significant influence on the simple-to-complex transition on these bodies (e.g., Schenk et al. 2004).

Complex craters on the icy satellites of Saturn, Uranus and Neptune are similar to those on the terrestrial planets. Complex crater morphologies reminiscent of those on the terrestrial planets are also found on the icy Galilean satellites (see next Sect. 10.2.3 for a detailed description). Regular complex craters exhibit (a) central peaks or peak complexes, (b) flat floors, (c) rim wall terraces, or (d) bright ejecta. Central peaks could form by elastic rebound of the material beneath a crater when compressive stress induced by the impact is relieved (Baldwin 1963; Melosh 1989). Another mode of central peak origin could be a hydrodynamic process: Upon impact, a central peak may rise out of material with Bingham rheology (i.e., material with a plastic yield stress which may behave as a viscous fluid) and “freeze” once the shear stress has become lower than the cohesion of the material (Melosh 1989). Impact experiments showed that, dependent of impact energy and

## Simple craters

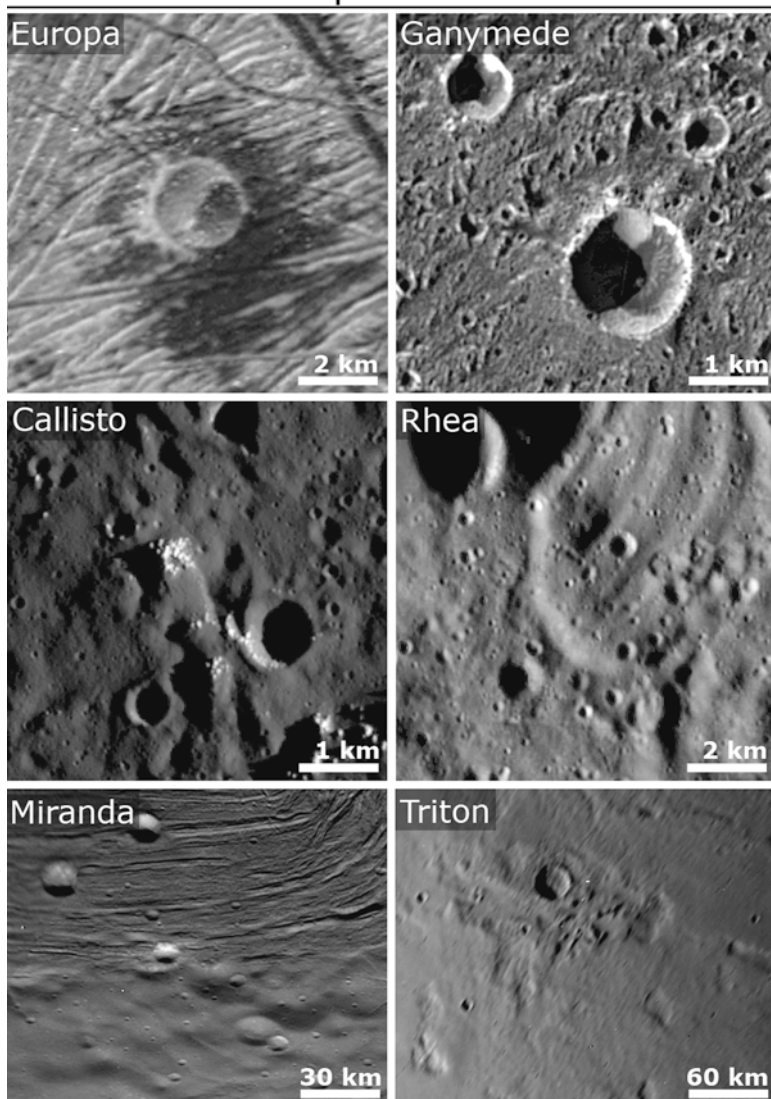


**Fig. 10.1** Simple craters on icy satellites. The shadow of the crater wall in the interior enhances their paraboloid or bowl shape (except for the high-sun image of crater *Mael Duin* on Europa which shows dark deposits on its floor and dark ejecta). Craters on Europa, Ganymede and Callisto are shown in Galileo SSI image data with spatial resolution of 20 m/pxl (Europa; scaled up from originally 55 m/pxl) and 10 m/pxl (Ganymede, Callisto). Data of Rhea are from the Cassini ISS narrow angle camera (NAC), shown at a resolution of 20 m/pxl. Image data of Miranda and Triton were taken by the Voyager 2 narrow angle camera at 300 and 600 m/pxl resolution respectively. The 30-km diameter crater on Triton is of the complex type

## Regular complex craters

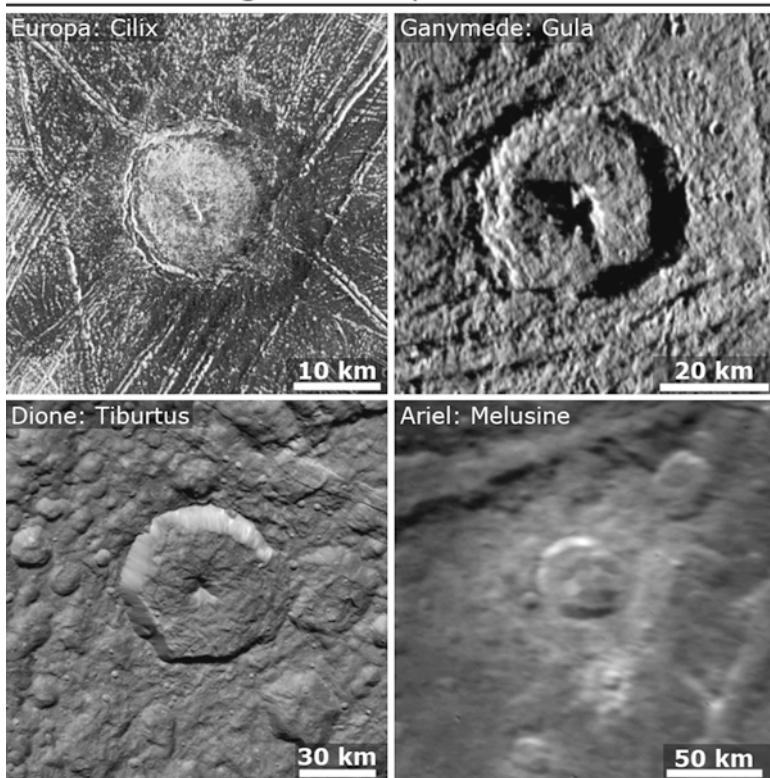


**Fig. 10.2** Examples of regular complex craters on icy satellites. The two craters *Cilius* (15 km diameter, lat.  $2.6^{\circ}$  N, long.  $181.9^{\circ}$  W) on Europa and *Gula* (38 km, lat.  $64.1^{\circ}$  N, long.  $12.3^{\circ}$  W) on Ganymede were imaged by the Galileo SSI camera. *Tiburtus* on Dione (59 km, lat.  $29.11^{\circ}$  N, long.  $189.73^{\circ}$  W) was captured by the Cassini ISS narrow angle camera (NAC). *Melusine* (50 km, lat.  $52.9^{\circ}$  S, long.  $8.9^{\circ}$  E) on Uranus' satellite Ariel was imaged at comparably low resolution by Voyager 2 during its flyby in Jan. 1986

target properties, several oscillations can occur producing central peaks or mounds with decaying height in each oscillation, eventually leaving a final peak or mound after all impact energy has been dissipated (Greeley et al. 1980).

Compared to craters on the silicate surfaces of the terrestrial planets formation of rimwall terraces is less abundant on icy satellites (e.g., Schenk and Moore 2007; Schenk et al. 2004). Some complex craters, such as *Tiburtus* on Dione (Fig. 10.2), do not show terraces at all. On the satellites of Saturn and Uranus, the simple-to-complex transition ranges over crater diameters of approximately 10–25 km, comparable to transition diameters on the Moon and Mercury (Chapman and McKinnon 1986; Pike 1988; Schenk 1989). On Neptune, the largest simple craters are observed up to a diameter of 12 km (Smith et al. 1989). Examples for regular complex craters are shown in Fig. 10.2.

Cassini ISS data revealed new details on craters of the satellites of Saturn. Central peaks are common in complex craters on the mid-sized moons (e.g., Wagner et al. 2006, 2007a,b, 2008, 2010; Schenk and Moore 2007; Jaumann et al. 2009a; Prockter et al. 2010). On Enceladus, tectonic resurfacing has largely affected crater morphology (e.g., Prockter et al. 2010). A substantial number of craters are transected or crisscrossed by lineaments, fractures or troughs (Bray et al. 2007). Also, many craters on Enceladus have undergone viscous relaxation, documented in up-domed floors (Smith et al. 2007). On Titan, the number of impact craters is comparably small due to intense geologic activity on the largest moon of Saturn (Lopes et al. 2010). Cassini RADAR data revealed 5 certain and 44 probable impact features (Wood et al. 2010). The five certain craters are of the complex type and show comparable morphologies to complex craters on rocky bodies (Wood et al. 2010).

### 10.2.3 Complex Craters on the Icy Galilean Satellites

Complex craters on the three icy Galilean satellites of Jupiter, Europa, Ganymede and Callisto, are characterized by a wide range of morphologies, including forms uncommon on other icy satellites or on the terrestrial planets. Schenk et al. (2004) observed three major trends in crater morphology with increasing size on these three satellites: (1) Similar to craters on the terrestrial planets, the complexity of crater forms increases with increasing diameter. (2) With the diameter further increasing, crater forms begin to deviate from forms known from the silicate surfaces of the terrestrial planets. (3) The depth-to-diameter ratio first increases with increasing crater diameter. After having reached a maximum diameter which is specific for each satellite, the depth-to-diameter ratio decreases with increasing diameter. Compared to complex craters on the terrestrial planets and on the icy satellites of Saturn, Uranus and Neptune, these craters are much flatter (e.g., Schenk et al. 2004). The simple-to-complex transition diameters are on the order of ~5 km (Europa) and ~3 km (Ganymede, Callisto), lower than on the Moon and Mercury, but comparable to transition diameters on Earth, Venus or Mars (e.g., Pike 1988; Schenk et al. 2004). At crater sizes larger than these transition diameters, the occurrence of central peaks is common (e.g., Schenk et al. 2004).

Continuous ejecta of some complex craters on the icy Galilean satellites may exhibit an outward-facing steep slope or scarp about half a crater diameter away from the crater rim, a feature termed a *pedestal* (Horner and Greeley 1982; Moore et al. 1998, 2004b). Typical pedestal craters are Pwyll on Europa and Achelous on Ganymede which are shown in Fig. 10.3. At Pwyll, the pedestal coincides with an albedo boundary between a dark region interior of the pedestal and bright, far-reaching rayed ejecta. The pedestals of Pwyll and Achelous are indicated by arrows in Fig. 10.3. Pedestal craters on Ganymede occur mostly within a size range of 6–40 km (which includes sizes of pedestal craters on Europa), but larger craters up to 89 km were also observed (Horner and Greeley 1982). Pedestal craters in the same range as those found on Ganymede have also been observed on Saturn's

## Complex craters on Europa and Ganymede

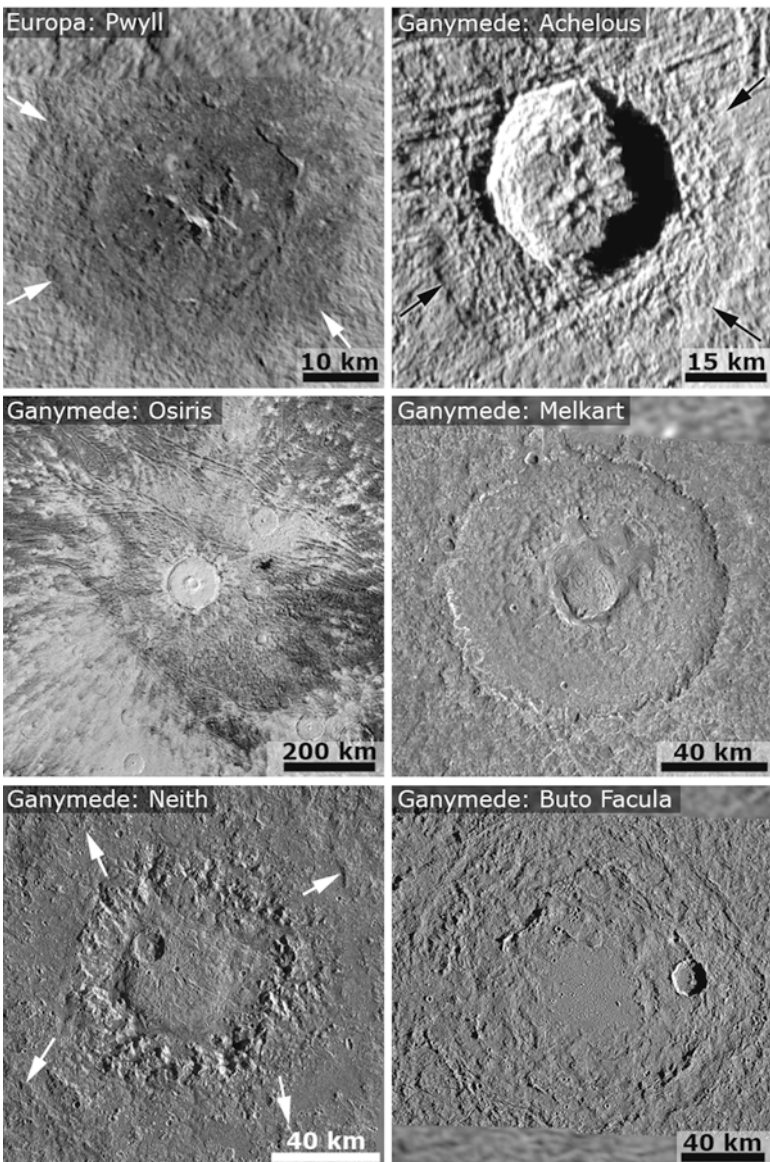


**Fig. 10.3** Complex crater types unique to the icy Galilean satellites Europa and Ganymede. Crater forms on Ganymede are also representative for craters on Callisto which are not shown here. All craters except Osiris were imaged by Galileo SSI. Pedestal craters *Pwyll* on Europa (27 km diameter, lat.  $25.2^{\circ}$  S, long.  $271.4^{\circ}$  W) and *Achelous* on Ganymede (35 km, lat.  $61.8^{\circ}$  N, long.  $11.7^{\circ}$  W). The pedestals are indicated by arrows. Central dome craters *Osiris* (Voyager 2 images, 104 km, lat.  $38.1^{\circ}$  S, long.  $107.7^{\circ}$  W) and *Melkart* (105 km, lat.  $9.9^{\circ}$  S, long.  $186.2^{\circ}$  W). These four craters also exhibit bright rayed ejecta (as shown for Osiris). Anomalous dome crater (pene-palimpsest) *Neith* (lat.  $29.4^{\circ}$  N, long.  $7.0^{\circ}$  W). Arrows indicate the location of the crater rim which has an approximate diameter of 135–140 km. Palimpsest *Buto Facula* (lat.  $13.2^{\circ}$  N, long.  $203.5^{\circ}$  W) with concentric structures. Total diameter of the structure is 245 km

satellite Dione (Wagner et al. 2006). Ejecta pedestals which resemble rampart craters on Mars infer the presence of subsurface volatiles and were explained to be the result of an ejecta flow mechanism (Horner and Greeley 1982). Impact experiments showed that target viscosity plays an important role in the formation of pedestal craters (Gault and Greeley 1978). Higher-resolution Galileo SSI images of pedestal craters revealed that the continuous ejecta deposits in pedestal craters consist of two facies: (1) an inner facies terminated by the pedestal, and (2) a radial outer facies bounded by the onset of secondary crater fields (Schenk and Ridolfi 2002). Moore et al. (1998) inferred that pedestal craters formed by plastic deformation of initially warm ice which became halted as this material stiffened during emplacement.

At diameters larger than approximately 25 km, central peaks and peak complexes in complex craters on Ganymede and Callisto are replaced by craters with rimmed central pits (Passey and Shoemaker 1982; Schenk et al. 2004). While central pits also occur in craters on the terrestrial planet, on Mars (e.g., Hodges et al. 1980; Barlow 2009) and also on the Earth (e.g., Greeley et al. 1982), this crater type is otherwise unique to Ganymede and Callisto among the icy satellites. Several models of central pit formation exist (summarized by Alzate and Barlow (2011)): (1) Central pits may form by collapse of a central peak in a weak layered target if the stress at the base of the peak exceeds the strength of the material (Passey and Shoemaker 1982). The much lower strength of ice compared to rock explains why more central pit craters exist on Ganymede and Callisto than on the terrestrial planets (Schenk 1993). (2) Central pits could also form by outgassing processes if volatiles coalesced beneath the updomed crater floor upon impact and penetrated the crater, creating a central depression (Hodges et al. 1980; Greeley et al. 1982). (3) Impact experiments showed that, in general, central pits formed by impacts into targets stratified into a stronger upper substrate underlain by weaker material (Greeley et al. 1982). (4) Another mode of origin in discussion, brought up for the first time by Croft (1981) and reassessed recently (Alzate and Barlow 2011, and references therein), is collapse of brecciated material in a central peak creating a pit which may be more prominent if the central peak contains liquid material.

With increasing crater diameter larger than 50–60 km, domes within central pits become characteristic features in craters on Ganymede and Callisto (Passey and Shoemaker 1982; Schenk 1993; Schenk et al. 2004). A typical dome crater is Melkart on Ganymede which is shown in Fig. 10.3. The pit-to-crater as well as the dome-to-crater ratio increases with increasing crater diameter, and domes in general occur at crater diameters.

In this size range up to approximately 250 km, craters with an anomalously large dome can occur. The dome is surrounded by a wreath of rugged terrain rather than by a distinct pit rim (as, e.g., Melkart). Also, these impact structures lack a coherent crater rim. A typical example is the impact structure Neith (Fig. 10.3). Arrows indicate the inward-facing scarps representing the crater rim which is much less prominent compared to the central dome and the rugged terrain around it. These craters were termed *anomalous dome craters* by Schenk et al. (2004, and references therein). Other terms used are *anomalous pit craters* (Croft 1983), *large dome craters* (Moore and

Malin 1988), or *moat craters* (Lucchitta and Ferguson 1988). Another term created by Passey and Shoemaker (1982) was *pene-palimpsests type II*. The origin of central domes is not well understood. Several modes of formation are discussed: (1) refreezing of impact melt (Croft 1983), (2) post-impact diapirism (Moore and Malin 1988), or (3) rapid uplift of ductile material during impact (Schenk 1993).

#### 10.2.4 Palimpsests on Ganymede and Callisto

On Ganymede, bright, circular or elliptical patches were observed in the dark cratered terrain. These features are, in general, more than 50 km up to 390 km in diameter and were interpreted as impact structures (Smith et al. 1979a, b; Passey and Shoemaker 1982). Morphologic characteristics indicative of impact craters, such as a distinct crater rim, cannot be distinguished at Voyager image resolution. Smith et al. (1979b) coined the term *palimpsests* or *palimpsest craters* to describe these features. In some of these forms, however, some concentric structures can be distinguished at Voyager resolution. These features were called *pene-palimpsests type I* (in contrast to *pene-palimpsests type II* described in Sect. 10.2.3) by Passey and Shoemaker (1982).

Galileo SSI imaged some of these palimpsests at higher resolution. A typical example is Buto Facula located in dark terrain of Marius Regio (Fig. 10.3). The SSI images revealed much more structure than did the Voyager images and allowed to identify morphologic and geologic units such as (a) a circular, flat area in the center, (b) concentric massifs, representing a degraded pit and/or crater rim, (c) continuous ejecta, and (d) secondary crater chains (Moore et al. 1998). The identification of these morphologic and geologic units in SSI images helped to unequivocally verify an impact origin for palimpsests, as has been envisaged earlier (e.g., Smith et al. 1979a, b; Passey and Shoemaker 1982; Lucchitta and Ferguson 1988).

Palimpsests do not only occur in dark terrain on Ganymede, but also, although rarely, in bright terrain. Examples for bright terrain palimpsests are Zakar and Epigeus which were both imaged by Galileo SSI.

Palimpsests are also abundant in the dark cratered plains of Callisto. Compared to the number of palimpsests on Ganymede, a much smaller number of palimpsests on Callisto was discussed (Schenk et al. 2004). However, it could be shown that the number of palimpsests on Callisto is much higher and comparable to that on Ganymede, but most of these features are heavily degraded and therefore not easy to discern (Wagner 2007).

The origin of palimpsests is, like that of dome craters poorly understood. Before the Voyager encounters and in the Voyager era between 1979 and 1989, viscous relaxation was thought to be responsible for flat crater forms and palimpsests (Smith et al. 1979a, b; Passey and Shoemaker 1982). An alternative explanation was relaxation by enhanced rim and floor collaps in icy material of low strength (Schenk et al. 2004, and references therein). Additional modes of origin were reviewed and summarized by Jones et al. (2003), including (a) extrusion of liquid material, triggered by the impact, (b) emplacement of fluidized ejecta, or (c) emplacement of dry and solid ejecta.

### 10.2.5 Impact Basins

Large complex craters, generally several hundreds of kilometers across, are termed impact basins (e.g., Melosh 1989; Spudis 1993). Their occurrence was first verified on the surface of the Moon by Hartmann and Kuiper in 1962 (summarized by Hartmann et al. (1981)). In the original definition by these authors, basins are characterized not only by one crater rim but by at least two or more concentric “rings” which are either raised rims or furrows. Therefore these impact features were termed *multi-ring basins* (Hartmann et al. 1981, and references therein) Impact basins on the terrestrial planets as well as on icy satellites are mostly old features which were formed in the early history of planets and satellites, possibly during a period of intense bombardment, by large projectiles several tens of kilometers in diameter (e.g., Wetherill 1975, 1981; Spudis 1993). In many respects, they are important features for understanding the early geologic and thermal evolution of a planet or satellite (e.g., Spudis 1993): (1) In a large basin-forming impact event, vast amounts of material are ejected and redistributed over a wide range across a planet or satellite. (2) Volcanic processes can be initiated by large impact events. (3) Tectonic deformation takes place as a consequence of a large impact, creating concentric and/or radial structural features, such as ridges, scarps, or furrows. (4) The number and spacing of rings in such impact basins are strong indicators of target properties and rheological parameters, of the depth of the brittle/ductile boundary, and of the heat flow in the early history of a planetary body. (5) They are also important stratigraphic markers, and the various geologic units mappable in a basin (e.g., continuous ejecta materials, impact melt materials, secondary crater chains) can be used to subdivide the geologic history of a planet into distinct time-stratigraphic systems, as has been done for all major terrestrial planets (e.g., Moon: Wilhelms 1987, and references therein; Mars: Tanaka 1986).

The largest impact basins on icy satellites are found on Callisto and Ganymede (Passey and Shoemaker 1982). Despite the high state of degradation of all landforms on Callisto (e.g., Moore et al. 2004a), some of its basins are well-preserved due to the lack of widespread tectonic or cryovolcanic resurfacing on the outermost Galilean satellite. The two largest of these structures are Valhalla (centered at lat. 14–7° N, long. 56° W) and Asgard (lat. 32.2° N, long. 139.9° W) with maximum diameters of ~3,800 and ~1,900 km respectively (Schenk 1995; Schenk et al. 2004). Unlike basins on terrestrial planets, these impact structures have numerous “rings” of ridges, scarps and graben, up to 24 in the case of Valhalla, surrounding a bright, circular plain in the center, reminiscent of a palimpsest which is several hundred kilometers across (Schenk 1995; Greeley et al. 2000). Valhalla, including a detail of its concentric graben system, is shown in Fig. 10.4. Smaller ring structures can be discerned but are heavily degraded. Only a small number of arcs of total ring structures are still preserved (Greeley et al. 2000; Schenk et al. 2004).

On Ganymede, concentric rings of graben or furrows can also be observed in its old dark terrain, which likely represent multi-ring impact basins, but tectonic resurfacing has heavily obliterated the original form of the total ring structure

## Impact basins on icy satellites

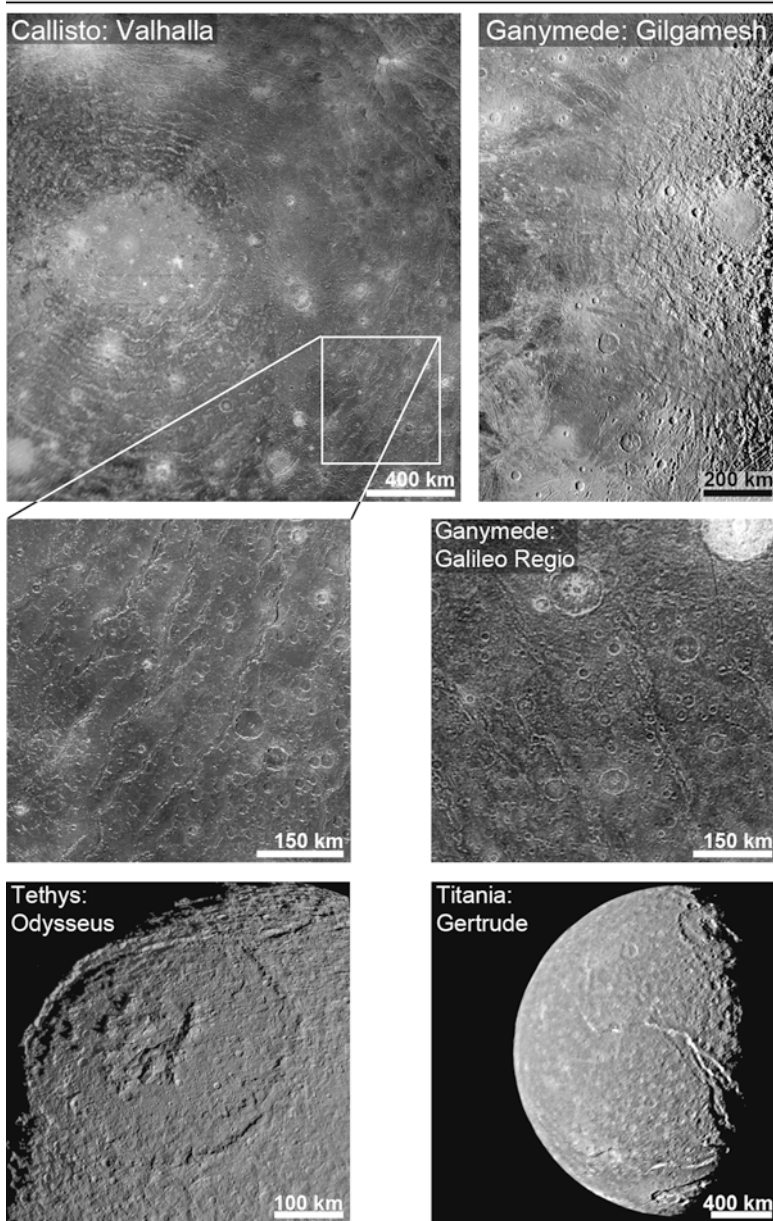


**Fig. 10.4** Impact basins on icy satellites of Jupiter, Saturn, and Uranus. Valhalla and Galileo Regio were imaged by the Galileo SSI camera, Odysseus by Cassini ISS (NAC). Gilgamesh and Gertrude are shown in images taken by Voyager 2

(Passey and Shoemaker 1982). Alternatively, endogenic processes such as mantle plumes in Ganymede's icy interior have been proposed as possible origin (Casacchia and Strom 1984). A typical example is the concentric furrow system named Lakhmu Fossae in Galileo Regio which is depicted in Fig. 10.4 (middle right panel) in comparison to Valhalla ring graben (Fig. 10.4, middle left) at comparable resolution. A much better preserved type of basin on Ganymede is Gilgamesh (center lat.  $62.8^{\circ}$  S and long.  $125^{\circ}$  W), which was formed by a large impact into bright terrain at later time than the degraded basins in the dark terrain (Schenk et al. 2004). This feature has fewer rings which are mostly furrows, graben or scarps surrounding a circular area which is more or less smooth at Voyager resolution (Galileo SSI could image Gilgamesh only at high sun which is not well suitable for morphologic analysis).

Europa's relatively young surface is only lightly cratered and lacks the characteristic imprint of a more intense higher bombardment early in its history (Moore et al. 1998; Schenk et al. 2004). The two largest craters are Tyre (center lat.  $33.6^{\circ}$  N and long.  $146.6^{\circ}$  W) and Callanish (center lat.  $16.7^{\circ}$  S and long.  $334.5^{\circ}$  W). They are characterized by distinct multi-ring features which, however, are one order of magnitude smaller than those on Ganymede or Callisto. Their transient crater diameters, representing the crater formed prior to crater modification processes, are 43 and 35 km respectively (Turtle et al. 1999). The existence of clusters and chains of small secondary craters extending radially from the centers of the two impact structures helped to exclude a non-impact origin for these two features (Moore et al. 2001).

The mid-sized satellites of Saturn, Mimas, Tethys, Dione, Rhea and Iapetus host several large impact basins of which some have been known prior to the Cassini mission (e.g., Stooke 2001, 2002; Moore et al. 2004b). Enceladus is devoid of large impact features as a consequence of its intense surface activity that has persisted into the present (e.g., Porco et al. 2006).

The most remarkable impact structure in Mimas' densely cratered plains is the large impact basin Herschel with a diameter of 139 km, about one third of the diameter of the satellite, centered at  $1.4^{\circ}$  S and  $111.8^{\circ}$  W (Smith et al. 1981; Moore et al. 2004b). The feature is up to 12 km deep and exhibits a large central peak up to 8 km in height (Moore et al. 2004b). Grooves and troughs on global scale could indicate the beginning of a breakup of the satellite upon impact (Moore et al. 2004b, and references therein).

Tethys features a huge impact basin termed Odysseus (Fig. 10.4), more than one third of the satellite diameter, with 445 km from rim to rim and up to 9 km height from rim to floor the largest impact structure across this satellite (Smith et al. 1981, 1982; Moore et al. 2004b). The center of the Odysseus basin is at lat.  $32.82^{\circ}$  N and long.  $128.89^{\circ}$  W. Ithaca Chasma, an almost satellite-wide huge graben system (Smith et al. 1981, 1982), is aligned along a great circle at a right angle to the Odysseus impact site. It has been proposed that the formation of this graben system was somehow related to deformation created by the Odysseus impact, but other, non impact-related processes could also be possible (Moore et al. 2004b; Giese et al. 2007a) (see Sect. 10.3.1). Smaller, degraded large craters and basins were found in the Cassini ISS images from Tethys (Giese et al. 2007a).

Evander, 350 km in diameter from rim to rim, is the largest impact basin on Dione (center lat. 57° S, center long. 145° W) (Wagner et al. 2006). Prior to Cassini, this basin could be distinguished in Voyager data (Stooke 2002). Evander is a highly relaxed basin featuring a flat floor that follows the satellite's limb curvature (Moore et al. 2004b; Wagner et al. 2006). Evander is a two-ring basin; it exhibits a central peak complex, surrounded by a rim-like ring several kilometers high (Wagner et al. 2006).

The largest and most numerous impact basins, some of them 400–600 km across, are abundant on the old, densely cratered plains of Rhea and Iapetus but the majority of these basins is heavily degraded and can only be discerned by using digital terrain models derived from stereo images (Giese et al. 2007b, 2008; Wagner et al. 2007a, 2008). Several basins, such as the second-largest basin on Rhea, Tirawa (370 km diameter, centered at 34.2° N and 151.7° W) were reported to occur on Rhea but not all of those conjectured in Voyager images could be confirmed with Cassini ISS data (Moore et al. 1985, 2004b; Stooke 2001; Giese et al. 2007b; Wagner et al. 2007b). Tirawa superimposes the older much more degraded largest basin (480 km) on Rhea named Mamaldi (Wagner et al. 2007b).

Iapetus features several large basins several hundred kilometers across which occur both in its dark and bright terrain (Giese et al. 2007b, 2008; Denk et al. 2010). As Evander on Dione, some of them exhibit two rings, such as Turgis (580 km outer ring diameter, centered at 16.9° N and 28.4° W). Unlike the highly degraded basins on Rhea, those on Iapetus still have preserved their original topography. (Giese et al. 2008) reported that seven basins were found on Iapetus using digital elevation models. The basins have complex morphologies, involving central peak complexes and slumping of crater walls, including landslides (Giese et al. 2008; Singer et al. 2009). Giese et al. (2008) measured maximum depths on the order of 10 km. Basins on Iapetus are characterized by only one ring, indicating a thick lithosphere at the time of basin formation but depth-to-diameter ratios infer that viscous relaxation of the basin floors has taken place (Giese et al. 2008).

Except for the basin Gertrude on Titania (see. Fig. 10.4), most large impact features on the Uranian satellites are putative which is mostly due to the low spatial resolution and incomplete image coverage obtained from these satellites (Smith et al. 1986; Moore et al. 2004b). Miranda and Ariel lack large impact structures. However, an impact origin has been discussed for an ovoid-shaped feature termed Arden Corona on Miranda (Croft and Soderblom 1991). Umbriel, the least-imaged Uranian satellite, has a dark densely cratered surface with numerous large craters (Smith et al. 1986). Limb profiles indicate the presence of at least one large impact basin approximately 400 km in diameter but other processes involving tectonism could also be possible (Helfenstein et al. 1989; Croft and Soderblom 1991). Figure 10.4 shows the ~400 km basin Gertrude (center lat. 15.8° S, center long. 287.1° E) on Titania near the terminator. The feature has a central ring or dome some 150 km in diameter (Smith et al. 1986). Limb images of Oberon revealed a bright, conically-shaped dome which possibly represents the central peak of a large impact feature (Smith et al. 1986; Croft and Soderblom 1991). The peak could be up to 11 km high and represent the center of a large impact basin ~375 km in diameter (Thomas 1988; Croft and Soderblom 1991; Moore et al. 2004b).

The origin of multi-ring structures is described by several models, but only two of them can sufficiently explain their morphologies: (1) In the Tsunami model (Van Dorn 1968; Spudis 1993), a massive impactor fluidizes the target material. Wave-like features appear which are topographically expressed as ridges, scarps and/or troughs. (2) In the ring model (McKinnon and Melosh 1980), a massive projectile impacts into a kilometers to tens of kilometers thick, brittle lithosphere and penetrates into a ductile, plastic or partly fluid asthenosphere. By gravitational flow of plastic or fluid material towards the impact center extensional stress create concentric troughs or graben. From the width and spacing of these troughs, the brittle-to-ductile boundary can be inferred (McKinnon and Melosh 1980). At the time of formation of basins on the two largest Galilean satellites, this transition zone was at depths of 15–20 km on Callisto, inferred from average widths and spacing of Valhalla and Asgard ring graben, and at ~10 km in Galileo Regio on Ganymede, assuming that the normal faults forming the ring graben have dip angles on the order of 60° (McKinnon and Melosh 1980). Using topographic profiles based on stereo data from the Galileo SSI camera, and interpreting the furrows as features associated with flexural uplift rather than normal faulting, Nimmo and Pappalardo (2004) derived values on the order of 2–3 km and a possible heat flow of 60–80  $\text{mW m}^{-2}$  for the dark terrain at Galileo Regio on Ganymede. On Europa, the two ring structures Tyre and Callanish were formed in an icy crust overlying either a low-viscosity zone or a brine-rich zone in convecting ice which could overly a liquid water layer (Moore et al. 2001, and references therein). The satellites of Saturn and Uranus lack multi-ring structures because either there was no ductile material in the subsurface, or the impactors did not penetrate to the brittle-to-ductile boundary.

## 10.2.6 Crater Chains

Linear or slightly arcuate chains of craters, termed *catenae*, can be observed on the Jovian and Saturnian moons. Crater chains can reach lengths up to several hundred kilometers. Callisto features many of these unusually long crater chains, e.g., Gipul Catena with a length of 641 km, or Gomul Catena (343 km) (Passey and Shoemaker 1982; Schenk 1995; Greeley et al. 2000). Gomul Catena is superimposed on ring graben of the Valhalla impact basin and is centered at 35.5° N and 47.1° W. Gomul Catena and a detail of this crater chain are shown in Galileo SSI data in Fig. 10.5.

Long chains of craters also occur on Ganymede, like Enki Catena which was imaged by Galileo SSI (Fig. 10.5). The chain is centered at 38.8° N and 13.6° W and is 161 km long.

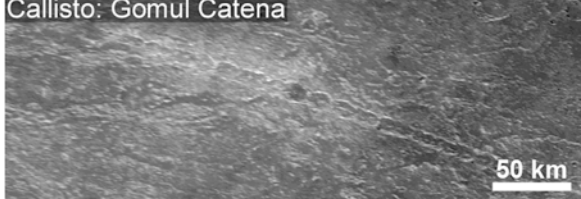
On the Saturnian satellites, e.g. on Dione or Rhea, crater chains several tens of kilometers long are abundant. Groups of parallel chains could be observed, such as the features named Pantagias Catenae on Dione (Wagner et al. 2010).

Some of these chains are radial to impact basins or large craters and can therefore be interpreted as secondary craters (e.g., Greeley et al. 2000). The majority of the large chains on Ganymede and Callisto were formed by projectiles fragmented

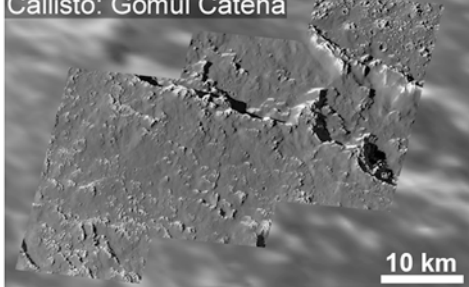
**Fig. 10.5** Typical examples of crater chains (*catenae*). Gomul Catena (Callisto) and Enki Catena (Ganymede) are shown in Galileo SSI data. The small inserted image in Enki Catena was taken by the Voyager 1 narrow angle camera at high sun. See text for further explanation

### Crater chains on Callisto and Ganymede

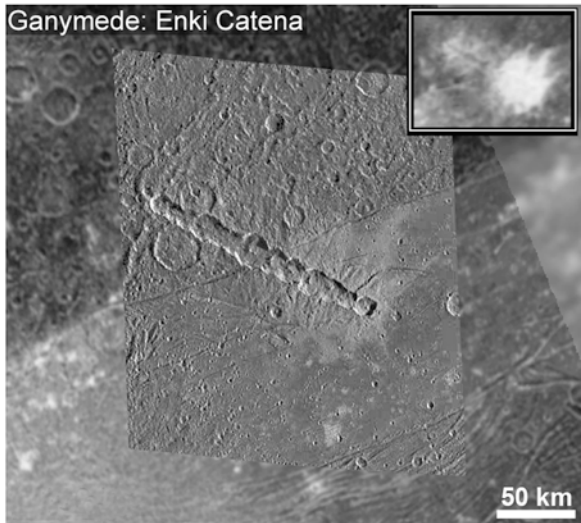
Callisto: Gomul Catena



Callisto: Gomul Catena



Ganymede: Enki Catena



into a string of bolides hitting the surfaces, similar to the break-up and impact of comet Shoemaker-Levy-9 which impacted Jupiter in July 1994 (McKinnon and Schenk 1995; Greeley 2000).

The occurrence of crater chains and multiple craters provides implications on projectile strengths and compositions. Schenk et al. (1996) discussed that the impactors creating the long crater chains on Callisto and Ganymede most likely were rubble pile cometary nuclei, consisting of fragments of varying sizes. Jupiter's gravitational field was strong enough to initiate the breakup of such cometary

bodies by tidal forces (Schenk et al. 1996). Such a process was deemed to be less likely for Saturn due to the lower encounter velocities at Saturn and its satellites as a consequence of the greater distance from the Sun, the lower density of Saturn, and the much smaller satellites compared to the sizes and masses of Callisto and Ganymede (Asphaug and Benz 1996). However, double craters, chains and clusters of craters were reported from some of the mid-sized satellites of Saturn, e.g., Rhea and Dione (Moore et al. 1985; Wagner et al. 2010). These craters could have been formed by binary impactors, by fragmentation of a low-strength (cometary) impactor, or by material ejected from an impact on another moon (Wagner et al. 2010, and references therein).

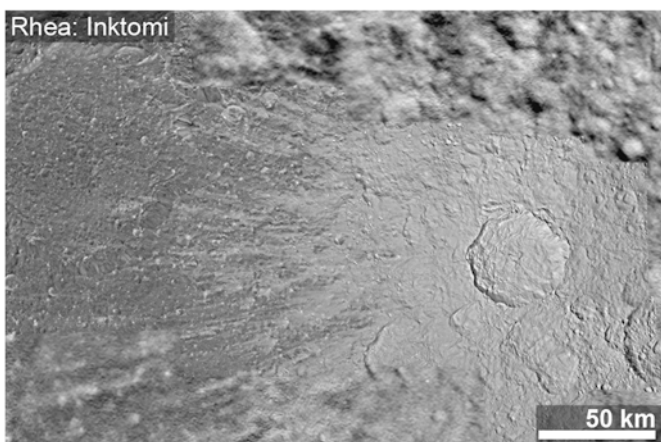
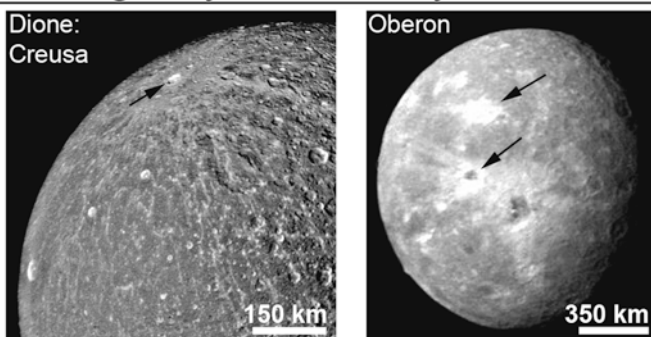
### 10.2.7 Ray Craters

Rayed ejecta, either bright or, more rarely, dark, are a characteristic feature of a number of stratigraphically young impact craters (e.g., Melosh 1989). Also, all known ray craters are fresh and their ejecta rays are superimposed on older geologic units indicating that they were formed in comparably recent time. Prominent examples on the Earth's moon are the bright ray craters Copernicus or Tycho.

Bright rayed ejecta occur at craters of all sizes on the icy satellites. The surface of Ganymede hosts the largest number of bright ray craters on all icy satellites. A typical example is the dome crater Osiris (108 km diameter, centered at 38.1° S and 166.4° W), shown in Fig. 10.3, whose bright ejecta extend several hundreds of kilometers outward from the impact center. On icy satellites, the albedo of the substrate influences how strong bright ejecta are discernible (e.g., Passey and Shoemaker 1982): A bright substrate enhances the bright albedo of the ejecta and the rays, as revealed in the ejecta of Osiris (Fig. 10.3). Their albedo increases significantly where the ejecta rays cross the dark-bright terrain boundary. The crater chain Enki Catena (161.3 km length, centered at 38.8° N and 13.6° W) also crosses the dark-bright terrain boundary (Fig. 10.5), with the albedo being significantly higher on the bright substrate. This feature is even more enhanced in the Voyager images of the catena which were taken at high sun (small panel).

The largest impact structures where bright rays occur are basins such as Heimdall and Lofn on Callisto (Greeley et al. 2000). Towards the lower end of the size range, small, kilometer-sized craters with bright ejecta or rays are observed on the Saturnian satellites in Cassini ISS images taken at high sun elevation. Large ray craters several tens of kilometers in diameter, however, are less common on the Saturnian satellites. Figure 10.6 shows examples from the Saturnian satellites Dione (upper left panel) and Rhea (middle panel), and from the Uranian satellite Oberon (upper right panel). Some ray craters could only be distinguished in images taken through color filters or in data of the VIMS spectrometer (Stephan et al. 2010; Schenk and Murphy 2011). While a number of these ray craters appears to remain observable in color data only (Schenk and Murphy 2011), others could now also be identified in images taken through one filter under high sun (Wagner et al. 2011).

### Bright ray craters on icy satellites



### Dark ray craters on Ganymede

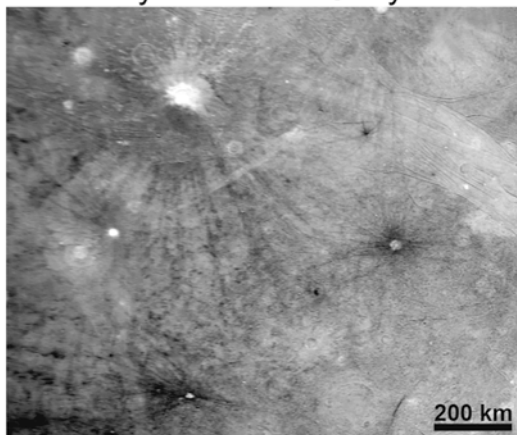


**Fig. 10.6** Examples for ray craters on icy satellites. The ray craters Creusa on Dione (*arrow*) and Inktomi on Rhea were imaged by the Cassini ISS NAC camera, the ray craters on Oberon and the dark ray craters on Ganymede by Voyager 2

Creusa is the largest bright ray crater on Dione, has a diameter of 36.2 km and is located at lat. 49.2° N and 76.3° W (Fig. 10.6, upper left panel). Its bright rays extend more than thousand kilometers. It was first identified as a ray crater in multispectral Cassini ISS images (Stephan et al. 2010). VIMS data revealed the deepest H<sub>2</sub>O absorption bands measured on Dione which infer pure water ice and large particles (Stephan et al. 2010). Large particles in turn are indicators of fresh and geologically young materials (Jaumann et al. 2008). Dating Creusa with its superimposed crater frequency, however, has not been possible so far because the crater was imaged only at low resolution or at oblique viewing angle. The largest bright ray crater on Rhea is a 47.2-km crater, centered at 14.1° S and 112.1° W, which was observed at high spatial resolution in a close flyby of Cassini at Rhea on Aug. 30, 2007 (Wagner et al. 2008) (Fig. 10.6, middle panel). The crater is a remarkable surface feature on the leading hemisphere of Rhea because of its extended bright ray system which is easily distinguishable even on low-resolution global. Therefore it was selected for nomenclature and was assigned the name Inktomi (Roatsch et al. 2009). The bright ray system features a strong butterfly-wing pattern which indicates an oblique impact angle of a west-east-moving projectile (Wagner et al. 2008, 2011). Inktomi is characterized by the deepest H<sub>2</sub>O absorption bands measured in Cassini-VIMS data from Rhea characteristic for young geologic features (Stephan et al. 2011). By measuring the superimposed crater frequency in the continuous ejecta of Inktomi the crater was also shown to be young, on the order of ~280 to ~8 Ma, depending of the cratering model (Wagner et al. 2008; Stephan et al. 2011) (see Sect. 10.2.9).

Bright ejecta and rays can also be discerned on the surfaces of the Uranian moons Ariel, Titania and Oberon. Examples for ray craters on Oberon are shown in Fig. 10.6 (upper right panel, indicated by arrows).

Bright, ray-like ejecta of small craters can be explained by penetration of a small projectile through a surface layer only a few tens of meters thick with a mixture of ice and darker, non-ice material into a more ice-rich regime (e.g., Denk et al. 2010). Material consisting of cleaner ice is excavated and deposited at and near the impact site. The occurrence of bright rays with tens or hundreds of kilometers spatial extension on terrestrial planets as well as on icy bodies is more difficult to explain. Possible modes of origin are (a) thin deposits of fine-grained material ejected at high velocity from the spall zone close to the projectile at the impact site, and/or (b) impact-gardening of the substrate by secondary crater material (Chapman and McKinnon 1986; Melosh 1989). The latter mode could explain why ray craters on Ganymede appear darker when emplaced on the dark terrain substrate, but brighter on bright substrate (Shoemaker et al. 1982).

Material which creates secondary craters is believed to originate in the spall zone, ejected at high speed, like material forming rays (Chapman and McKinnon 1986; Melosh 1989). However, the highly dispersed material forming rays not always creates secondary craters, which explains why not all bright ray craters are associated with secondary craters (Chapman and McKinnon 1986; Melosh 1989). An alternative origin of ray-forming material, supported by, e.g., spectral data, is that ray material is lifted and ejected from deeper stratigraphic levels during

the growth of the crater (Pieters et al. 1982; Chapman and McKinnon 1986). The high ejection velocities of ray-forming material could be responsible that rays do not occur on the smaller Saturnian satellites because most of this material leaves the satellite if ejection velocities exceed the escape velocity of a specific satellite. Escape velocities on the major satellites of Saturn (except Titan) range between  $\sim$ 160 m/s on Mimas and  $\sim$ 630 m/s on Rhea. Currently, ray crater abundance on the satellites of Saturn is subject of detailed investigations (e.g., Schenk and Murphy 2011; Wagner et al. 2011). Ray craters are subject to weathering processes and have retention times on the order of 1–2 Ga, however, time-scales of fading crater rays are highly model-dependent (Passey and Shoemaker 1982).

Craters with dark rays are exclusively abundant on Ganymede, and their occurrence is restricted to an area on the trailing hemisphere approximately ranging from latitudes  $25^{\circ}$  N to  $15^{\circ}$  S, and longitudes  $200$ – $250^{\circ}$  W, except for crater Kittu which is located at  $0.4^{\circ}$  N and  $334^{\circ}$  W (Conca 1981; Chapman and McKinnon 1986; Schenk and McKinnon 1991; Stephan 2006). Conca (1981) conjectured that the dark albedo of these ray craters is derived from a contamination by impactor material and that their preferential location on the trailing hemisphere is caused by magnetospheric sputtering. Schenk and McKinnon (1991) explained the occurrence of dark ray craters in the equatorial region with impacts of C- and D-type asteroids or comets and, in addition, the impact of magnetospheric particles as the dominant factors for the formation of dark rays. The existence of an internal magnetic field at Ganymede discovered by the Galileo magnetometer, however, is an indication that particle bombardment in the equatorial regions is less significant than anticipated (Cooper et al. 2001). Using Galileo NIMS data, Stephan (2006) suggested that the concentration of impact-induced reworking of surface material, rather than impactor material alone, and a significant contribution of excavated pre-existing dark material in the subsurface could be a likely origin for dark crater rays on Ganymede.

### 10.2.8 Craters on Titan

Titan's surface is covered by a dense nitrogen atmosphere which is opaque at visible wavelengths and accessible to remote sensing instruments only in the near infrared and at centimeter wavelengths used by radar instruments. Numbers of 5 certain craters and 44 nearly certain to probable craters were reported by Wood et al. (2010) which they could identify in the Cassini RADAR data on approximately 22% of Titan's surface. The diameters of these craters range from 3 km to basin size (444 km) (Wood et al. 2010). Recently, eight more (4 nearly certain, 4 probable craters) were found in additional 11% of Titan's surface coverage by the RADAR instrument (Neish and Lorenz 2012).

Craters on Titan have morphologies comparable to craters both on icy and rocky objects (Wood et al. 2010). Figure 10.7 shows three examples of craters on Titan in various states of degradation. Ksa (Fig. 10.7, left panel) is a fresh crater

## Craters on Titan

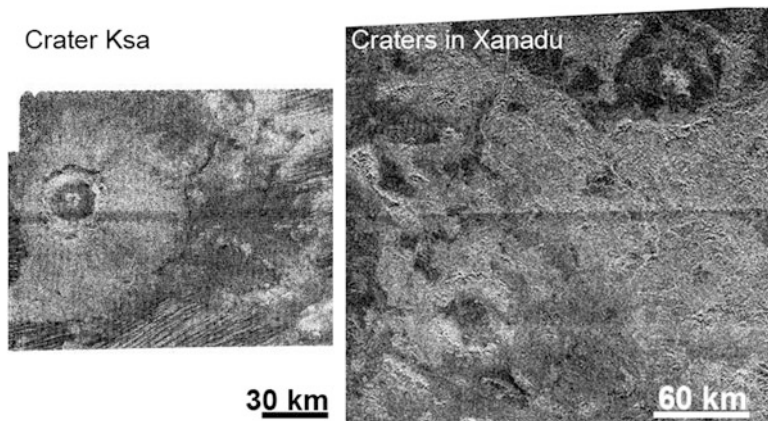


**Fig. 10.7** Examples for craters on Titan. Left panel: crater Ksa, 30 km diameter. Parts of the bright ejecta are covered by linear dark dunes. Right panel: nearly certain (unnamed) impact craters (Wood et al. 2010), 45 and 63 km in diameter. Both features are located in a region dissected by narrow meandering river channels (Cassini RADAR data)

with 30 km diameter and a central peak. The two craters in the right panel in Fig. 10.7 are 45 km and 63 km in diameter and of the nearly certain type in Wood et al. (2010) (listed as No. 25 and 26, Wood et al. 2010). These two craters are much more degraded, most likely by mass wasting, aeolian and fluvial processes, are characterized by partial crater rims, and the larger of the two craters has a central peak.

The low frequency of craters on Titan implies a young surface age and reflects active geologic processes at present (Wood et al. 2010). Absolute ages range from a few 100 Ma to approximately 1 Ga (Jaumann and Neukum 2009; Wood et al. 2010), depending of cratering chronologies (see next section), but the oldest terrain could be as old as ~3.9 Ga (Jaumann and Neukum 2009).

### 10.2.9 Impact Cratering Chronology Models

Impact craters provide information about the origin of projectiles, physical properties of a planetary or satellite surface, and their change in time. In addition, impact craters also record the time that has passed since the formation of a geologic unit: the higher the frequency of impact craters superimposed on the unit, the higher its age because of the longer exposition time towards the flux of incoming projectiles, compared to a less densely cratered unit (e.g., Öpik 1960; Baldwin 1964; Hartmann 1966; Neukum 1975, 1977).

The crater frequency measured on a geologic unit is representative of its relative age (Arvidson et al. 1979). In order to derive an absolute age for a specific unit, there are two different methods: (1) calibration of crater frequency with radiometric

ages of rock samples which were collected on the unit where the frequency was measured, and (2) calibration of crater frequencies with crater forming rates (e.g., Hartmann et al. 1981).

The Moon is the only body where the first method can be applied. Apollo and Luna rock and soil samples were used to derive a chronology model for the Moon (Hartmann et al. 1981; Wilhelms 1987; Neukum and Ivanov 1994). Based on these ages, a lunar cratering chronology was derived, characterized by an early period of heavy bombardment with an exponential decline in cratering rate in the first ~800 Ma, and a constant cratering rate since ~3.3–3 Ga ago (Wetherill 1975; Neukum and Ivanov 1994; Neukum et al. 2001; Ivanov and Hartmann 2007). Several groups of investigators concluded, however, that a peak at ~3.9 Ga in radiometric ages corresponded to a strong peak in impact and cratering rate, indicating a terminal lunar cataclysm or Late Heavy Bombardment (LHB), rather than a smooth exponential decay (e.g., Tera et al. 1974; Hartmann et al. 2000; Ivanov and Hartmann 2007). The terminal lunar cataclysm is still in debate (e.g., Baldwin 2006).

Because no surface materials are available from bodies other than the Moon until today, the surfaces of the terrestrial planets and of the icy satellites in the outer solar system can only be dated with the second method. The most likely bombardment history of a planet is inferred from the shape of crater size-frequency distributions measured on the surface which reflects the size-frequency distributions of impactors.

For the terrestrial planets, the shapes of crater distributions are similar to those on the Moon as well as to the size distribution of Main Belt asteroids which is a strong indication that these planets, including the Moon, were bombarded preferentially by asteroidal bodies (Durda et al. 1998; Neukum and Ivanov 1994; Neukum et al. 2001; Ivanov et al. 2001; Ivanov and Hartmann 2007). Strom et al. (2005) also concluded preferentially asteroidal bodies but discussed evidence for different asteroidal families with different size distributions responsible for cratering the terrestrial planets at different times.

For each of the terrestrial planets, impact chronology models with a lunar-like bombardment history were derived (summarized by, e.g. Neukum et al. 2001). For the icy satellites in the outer solar system, there is much less agreement about the nature and origin of projectiles which bombarded their surfaces. Currently, the largest data set of crater size-frequency distributions from any satellite in the outer solar system is available for the moons of Saturn, provided by imaging data returned of the ISS camera aboard the Cassini spacecraft.

Three model chronologies exist for the moons in the outer solar system (Dones et al. 2009, and references therein):

*Model I*, the Neukum *lunar-like impact chronology* in which Main Belt asteroids captured into planetocentric orbits are assumed to be the preferential impactors, is based on the following three findings (Horedt and Neukum 1984a, b; Neukum 1985, 1997; Neukum et al. 1998, 2005, 2006): (1) A strong similarity between the shapes of crater size-frequency distributions measured on the Earth's moon and on the icy satellites of Jupiter and Saturn; (2) the lack of an apex-antapex asymmetry on these bodies which should be characteristic in the case of primarily heliocentric impactors; (3) a lower impact velocity on the icy moons required for planetocentric

orbits, inferred from a left-ward shift in log-D (D: crater diameter) of the crater distributions on icy satellites with respect to lunar crater distributions. A yet unsolved issue of this model, however, is the capture of asteroids into orbits about Jupiter or Saturn as a regular mechanism. As for the lunar case (e.g., Neukum and Ivanov 1994), Neukum and co-workers assume a lunar-like time dependence of the cratering rate which was characterized by an exponential decay prior to 3–3.3 Ga and a constant cratering rate since 3.0 Ga. Model chronologies with a similar time dependence by comets instead of asteroids were derived by Shoemaker and Wolfe (1982) for the Jovian satellites, and by Plescia and Boyce (1985) for the Saturnian moons.

Contrarily, several groups of investigators discussed impactor populations radically different from those in the inner solar system (Strom et al. 1981; Woronow et al. 1982; Zahnle et al. 1998, 2003; Kirchoff and Schenk 2009). *Model II*, the *cometary impact chronology*, was established by Zahnle et al. (1998, 2003) for all icy satellites in the outer solar system, based on cometary bodies as primary impactors. They derived constant cratering rates for each moon, with a possibly higher cratering rate prior to ~4 Ga, based on the assumption of a time-inversed decline in the population of bodies crossing the orbits of the giant planets since the time when the solar system formed 4.56 Ga ago. The preferential family of impactors in Model II are ecliptic comets (previously termed short-period comets (Zahnle et al. 1998)) and Kuiper Belt objects (KBOs). Ecliptic comets captured by Jupiter are termed Jupiter Family Comets (JFC); ecliptic comets between Saturn and Neptune are termed Centaurs (Zahnle et al. 2003). Asteroids are deemed negligible as potential impactors in the outer solar system at present times and, possibly, in the past 3 Ga but could have played a more important role prior to 4 Ga ago (Zahnle et al. 1998). The nearly-isotropic comets (or long-period comets) also do not contribute significantly to the present cratering rates in the outer solar system (Zahnle et al. 1998, 2003).

*Model III*, the *Nice impact chronology model*, is based on the assumption of significant changes in the orbits of the four giant planets in the early solar system. The Nice model was first established at the Observatoire de la Côte d'Azur in Nice (France) and discussed in a series of papers (Gomes et al. 2005; Morbidelli et al. 2005; Tsiganis et al. 2005). According to this model, Jupiter and Saturn crossed the 2:1 resonance approximately 3.9 Ga ago, causing a solar-system wide spike in impact and cratering rate around that time termed the Late Heavy Bombardment. The spike in cratering rate in the Nice model could be a possible explanation for the clustering of radiometric ages in the lunar rocks ~3.9 Ga and hence for the terminal lunar cataclysm discussed by Tera et al. (1974).

Currently, cratering model ages from measured crater frequencies can only be calculated for the cases of Model I and II, using equations given by Neukum (1997) and (Neukum et al. 1998, 2006), and Zahnle et al. (1998, 2003). For the old, densely cratered units on the Jovian and Saturnian satellites, both sets of models produce comparable model ages. There is much more disagreement for younger, less densely cratered units. While Zahnle et al. (2003) estimated the surface of Europa to be on the order of 50–70 Ma years old, the average age of the European surface is

~1 Ga according to Neukum et al. (1998), with individual units having ages of 200–500 Ma. The widest range of ages was measured in the geologic units on Enceladus (Porco et al. 2006). Densely cratered plains have ages on the order of 4.1 Ga in Model I, and 1.6 Ga in Model II. Tectonized units (Sect. 10.3) range in age from 3.8 Ga to 110 Ma (Model I), versus 230 to 1 Ma (Model II). The estimated age of the cryovolcanically active south polar region (Sect. 10.4) is less than 4 Ma old in Model I, and less than 0.5 Ma in Model II.

#### **10.2.10 *Laboratory Experiments of Impact Cratering into Icy Material***

Even prior to the Voyager flybys at Jupiter, it was argued by e.g. Johnson and McGetchin (1973) that impact crater morphology on icy satellites could be significantly different from crater forms on the silicate surfaces of the terrestrial planets, a view which, at least to some degree, was confirmed by images returned from these bodies (e.g., Smith et al. 1979a, b; Passey and Shoemaker 1982).

An overview of recent studies of impact experiments and implications for impact cratering in the outer solar system is given in (Arakawa et al. this issue). The following properties and/or processes have influence on crater morphology (Greeley et al. 1982; Melosh 1989): (1) impactor properties, including its mass (or size) and density, and impact velocity and angle; (2) target properties, including composition, rheologic parameters, and stratification; (3) processes active subsequent to crater formation, either endo- or exogenic. Theoretical modeling as well as impact cratering experiments in the laboratory were carried out by several groups of investigators in order to explain the crater forms on icy satellites described above and the processes involved in the impact cratering in ice (e.g., Greeley et al. 1982; Kato et al. 1995; Burchell et al. 2001; Grey and Burchell 2003 and references therein) including ammonia ice (Grey and Burchell 2004) as well as in ice-solid particle mixtures (Yasui and Arakawa 2008).

### **10.3 Tectonic Resurfacing on Icy Satellites**

Many of the outer icy satellites display evidence that tectonic activity formed their surfaces, although in different relative importance. A detailed review of tectonics on icy satellites with implications for their geological history can be found in Collins et al. (2009) and Kattenhorn and Hurford (2009). Recent result derived for the Saturnian satellites based on new Cassini data are summarized in Jaumann et al. (2009a, b) and Spencer et al. (2009), respectively.

Tectonic landforms have been found on at least two icy Galilean satellites, seven of the nine major Saturnian satellites, including Titan, on all five major satellites of Uranus, and the Neptunian satellite Triton. Most of these satellites show

predominately extensional deformation resulting most commonly from normal faulting (Pappalardo and Davis 2007). Some satellite surfaces also exhibit strike-slip faulting (Collins et al. 2009). Instead contraction apparently plays a minor role. Possibly, however, contractional surface features are just harder to identify (Pappalardo and Davis 2007).

Europa and Enceladus exhibit pervasively tectonized surfaces, covered with a great variety of tectonic features that are partly unique to the outer solar system, but which are still far from being fully understood. Ganymede and Miranda both are characterized by geologically old heavily cratered terrain that has been disrupted by extensional deformation. On Ganymede the tectonically resurfaced regions form a global network (Pappalardo et al. 2004), while they are restricted to regional provinces called “coronae” on Miranda (Smith et al. 1986). Although less dominant compared to Ganymede and Miranda but still distinct, systems of normal faults also cut across the surfaces of Dione, Tethys, Rhea (Plescia 1983; Moore 1984; Wagner et al. 2006; Moore and Schenk 2007; Stephan et al. 2010), Ariel and Titania (Smith et al. 1986). To date, contractional surface structures have been inferred only on Europa (Prockter and Pappalardo 2000), Dione (Moore 1984) and may play a more important role in the tectonics of Enceladus (Helfenstein et al. 2010). Iapetus exhibits a giant equatorial ridge whose origin is still a mystery and might be not tectonic in origin at all (Ip 2006).

Based on their morphologies observed tectonic structures on the icy satellites’ surfaces can be divided into seven basic assemblages: (1) regional and global isolated fractures and horst-and-graben like structures, (2) sets of sub-parallel fractures, normal faults, and horst-and-graben structures named grooves, (3) linear to curvilinear ridges, (4) bands, special regional appearances like (5) coronae on Miranda and (6) lenticulae and chaotic terrain on Europa, and (7) rare but nevertheless existent contractional structures such as folds.

The nature, distribution and orientation of these tectonic features provide a first indication, which mechanisms could be responsible for their formation and clues to the satellite’s geological and orbital history. Thus, in addition to physical properties of the satellite and its central planet, and the rheological and thermal properties of icy material, a detailed description of the tectonic surface features is an important input for any theoretical model and laboratory experiments (Collins et al. 2009).

Based on recent knowledge, the formation of tectonic structures on icy satellites may have resulted from different mechanisms including: (1) impact-related processes, (2) tidal deformation, (3) variations in rotation rate, rotation and/or tidal axis orientation, (4) global volume change due to internal temperature change, H<sub>2</sub>O-ice phase changes, or ice-silicate differentiation, and (5) mantle convection driven by thermal or compositional heterogeneities. For a detailed discussion of these mechanisms the reader is referred to Collins et al. (2009). We only present the most important aspects regarding these processes here.

For example, major basin-forming impact events often include the formation of fracture systems due to seismic disruption, which appears in areas antipodal to impact sites and collapse of impact basins (Smith et al. 1982; Moore and Ahern 1983; Pappalardo et al. 2004; Moore et al. 2004a, b; Giese et al. 2007a; Moore and

Schenk 2007; Jaumann et al. 2009a). Satellites, however, are mainly distorted due to external forces such as rotation and tides (Collins et al. 2009; Hussmann et al. 2010). If the rotation rate or the magnitude of the tide changes the shape of the satellite will change and cause global stresses. Whereas the variations in the rotation rate changes the satellite's shape on a very long timescale leading to a permanent deformation, the frequency of tidal forces can change on the order of days and weeks associated with continuous variations of the tidal potential (Matsuyama and Nimmo 2007; Hussmann et al. 2010).

If a satellite is initially rotating faster than its orbital period, it will reduce its rotation rate due to the gravitational forces of the central planet until it exactly matches its orbital period, i.e. despins within a few million years (e.g. Murray and Dermott 1999). That means the satellite's shape will be less rotationally flattened, which causes global stresses that are compressive at the equator and tensile at the poles (Melosh 1977; Collins et al. 2009). The maximum stress reached during despinning depends mainly on the satellite radius and the differences between the initial and the final rotation velocities (Melosh 1977). A summary of the expected despinning time scales of icy satellites can be found in Hussmann et al. (2010). In contrast, tidal stresses result in flattening of the rotating satellite at its poles, an equatorial tidal bulge centered on the side facing the planet and an equal bulge centered on the opposite hemisphere. Global and axial symmetric stress patterns are expected in this case (Melosh 1977) with the symmetry axis directed along the rotation axis, the highest strain rate at the poles and the lowest on the tidal axis (Collins et al. 2009). Large impacts and non-synchronous rotation of a floating icy shell on an ocean (Melosh 1977; Chapman and McKinnon 1986; Murchie and Head 1986; Nimmo and Matsuyama 2007; Collins et al. 2009), however, can also cause changes in the rotational and tidal axis (Melosh 1977; Helfenstein and Parmentier 1985; Leith and McKinnon 1996; Greenberg et al. 1998; Nimmo and Matsuyama 2007) resulting in a wide variety of tectonic patterns for different reorientation geometries (Matsuyama and Nimmo 2007).

Gravitational forces of the central planet drag a satellite into a synchronous, circular orbit in its equatorial plane and tidal stresses should become constant. Many satellite's orbits, however, are still elliptical, even with synchronous rotation (Hussmann et al. 2010). This is because every satellite interacts with its neighbors, especially when these adjacent satellites are in a situation of orbital resonance with a periodic gravitational influence on each other. One example is the 1:2:4 resonance of Jupiter's moons Ganymede, Europa (see Sects. 10.3.1 and 10.3.2) and Io, that significantly forces the eccentricities of their orbits around Jupiter (Hussmann et al. 2010). This can keep tidal stresses ongoing on geological timescales. As the distance between planet and satellite continually changes due to the orbital eccentricity (optical libration), the strength of the tidal force producing the tidal bulges also varies accordingly with a relatively higher bulge when the satellite is closer to the planet and a lower when it is further away. In addition, a satellite's rotation velocity varies with its distance from the planet, although the rate of the satellite's axial spin remains constant. Thus, although for every orbit completed the satellite rotates exactly once, during the closest part of its orbit its rotation lags slightly

behind its orbital motion, and during the furthest part of its orbit its rotation is slightly ahead of its orbital motion. Consequently, as seen from the planet, the satellite does not show exactly the same hemisphere throughout its orbit; rather it swings slightly from side to side (physical libration). Thus the locations of the tidal bulges oscillate east and west across the satellite's surface as well. A summary of the present day shapes of the outer solar system satellites, orbital and tidal characteristics is given in Collins et al. (2009) and references therein. Murray and Dermott (1999) provide a general description of tidal and rotational deformation of satellites. Especially, large tidal deformations are expected on Europa, Enceladus and possibly on Triton (Hussmann et al. 2010).

Several other mechanisms that are discussed in detail in Collins et al. (2009) can lead to volume changes within a satellite and thus cause significant tectonic deformation resulting in extensional or compressional features on the surface (Squyres and Croft 1986; Kirk and Stevenson 1987; Mueller and McKinnon 1988). Such volume changes can reach several percent (esp. in the case of Ganymede as described in Squyres 1980; Mueller and McKinnon 1988) and will generate isotropic stress fields on the surface.

Although most of the observed tectonic surface features on the icy bodies in the outer solar system have counterparts on Earth and other terrestrial bodies (Collins et al. 2009), the appearance of some of them is different from those observed on the surfaces of terrestrial bodies and can only be found exclusively on icy satellites due to the unique behavior of H<sub>2</sub>O ice. For a detailed discussion of the complex rheology of H<sub>2</sub>O i.e. its elastic, brittle and viscous properties the reader is referred to the excellent reviews provided by Petrenko and Whitworth (1999), Beaman et al. (1988) and Durham and Stern (2001), Collins et al. (2009), Durham et al. (1998, 2010), respectively. Although H<sub>2</sub>O ice is a brittle material at the sufficiently low temperatures in the outer solar system (<150 K), the amount of energy that is necessary to reach its melting point is lower than for terrestrial bodies (Collins et al. 2009). Therefore, some tectonic features on icy satellites may be influenced by near-surface ductile or liquid H<sub>2</sub>O. Thus, understanding the formation of these surface features is important for the implication of the presence and the distribution of H<sub>2</sub>O in the subsurface (Pappalardo et al. 1999; Greeley et al. 2000, 2004).

In the following, we present a comparison of the most important tectonic landforms observed on the icy satellites starting with the simplest tectonic structures and progress with increasing degree of their complexity and summarize the favored explanations for their formation, which may lead to some understanding of the relationship of volcanic and tectonic features to the endogenic and exogenic processes that have affected icy satellites.

### 10.3.1 *Fractures and Graben-Like Structures*

The simplest tectonic landforms that occur on almost every icy body are single fractures without any vertical movements, normal faults with vertical movements as

well as an inclined fault plane that sometimes form narrow graben i.e. a down-dropped block bounded on both sides by two antithetic normal faults. These features are often the only tectonic features on icy satellites that experienced no more than minor amounts of tectonic influence but were also observed on icy bodies like Europa and Enceladus with a complex tectonic history. These tectonic features occur either on a regional scale often related to impact processes or a global scale indicating processes affecting the whole satellite like described above.

### 10.3.1.1 Fractures Related to Impact Processes

Regional occurrences of fractures are often related to impact processes where older zones of weakness in the satellite's lithosphere become re-activated. This kind of tectonic features is the most obvious one on the outermost Galilean satellite Callisto and is seen as concentric arcuate graben-like features created by basin-forming impact events, such as the multi-ring impact basins Asgard and Valhalla (see detailed description and explanation of these features in Sect. 10.2.5 and Fig. 10.4) (Schenk 1995; Moore et al. 2004a).

They are similar to the furrows, the oldest recognized tectonic features observed in the dark terrain on the neighboring satellite Ganymede termed "fossae" (Smith et al. 1979b; Passey and Shoemaker 1982). These fossae are 6–20 km wide and characterized by flat floors and raised rims with a maximum vertical distance of 1,400 m between rim and floor (Murchie and Head 1988; Giese et al. 1998; Prockter et al. 1998). Most of them are arranged in sub-concentric sets with more or less regular spacing of ~50 km between individual furrows (Shoemaker et al. 1982) similar in appearance to the multi-ringed structures on Europa and Callisto (Prockter et al. 2010). Thus, the furrows have been interpreted to be graben-like features formed by huge, basin-forming impacts that have undergone topographic relaxation caused by a higher heat flow and a thinner lithosphere in an early period of Ganymede's history (McKinnon and Melosh 1980). Although, this origin of Ganymede's furrows is now favored (Pappalardo et al. 2004), other mechanisms like extensional tectonism that occurred during crustal solidification before large craters could be retained (Casacchia and Strom 1984; Zuber and Parmentier 1984) cannot be ruled out.

Possible relationships between tectonic structures and impacts are also suspected on several Saturnian satellites, especially on Mimas, Tethys, Dione and Rhea. The surface of Mimas, despite its little geologic diversity (Stooke 1989), shows a global pattern of linear-to-arcuate, sub-parallel troughs across the surface. These features were interpreted to be related to the impact event that forms the 139-km large impact crater Herschel that dominates one hemisphere of Mimas (Moore et al. 2004a; Jaumann et al. 2009a). On Tethys, the main tectonic feature is a large, wide graben complex called Ithaca Chasma, which extends approximately 270° around the satellite (Fig. 10.8). Cassini images show that the graben system is roughly 2–3 km deep with a raised rim up to 6 km high (Giese et al. 2007a; Moore and Schenk 2007). The origin of Ithaca Chasma is still controversial. Either it could have been formed by

## Fractures and graben-like structures (I)

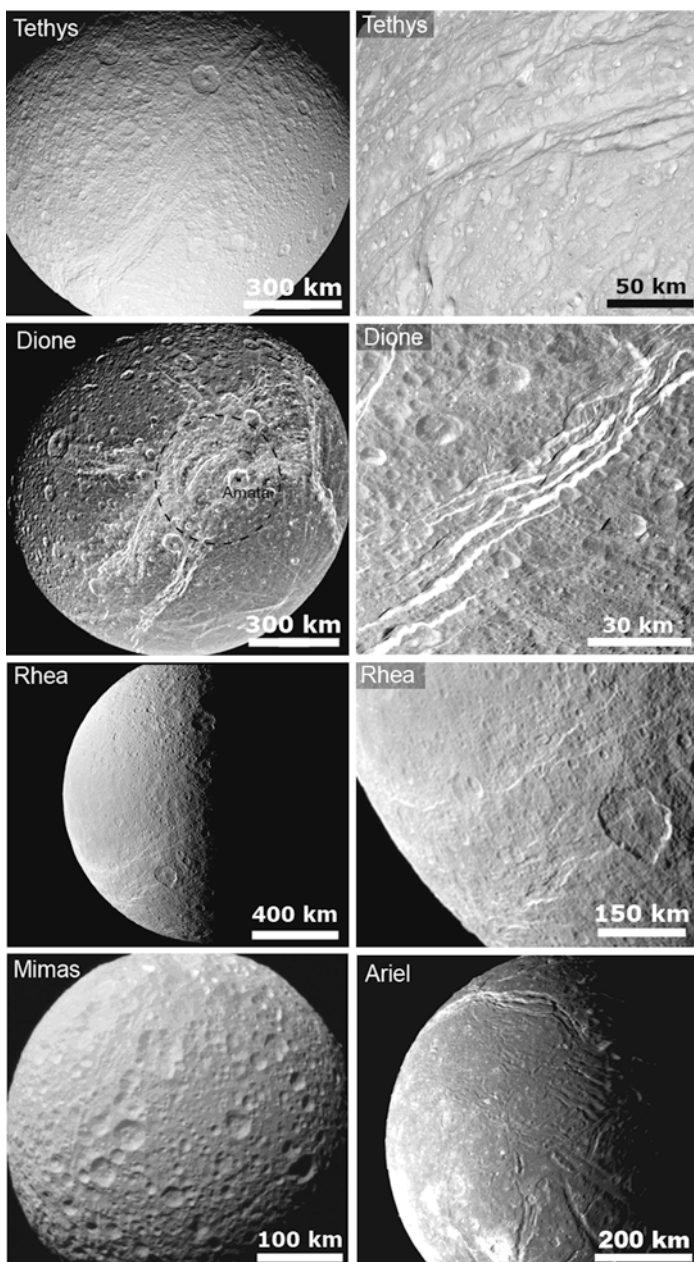


**Fig. 10.8** Examples of tectonic fracturing on icy satellites due to impact events (Tethys, Mimas), global fracturing (Ariel) or both processes (Dione and Rhea). Note that all of these satellites experienced only moderate or minor amount of tectonic resurfacing. The dashed circle in the global image of Dione marks the rim of a degraded impact basin identified by Schenk and Moore (2007)

freeze expansion of Tethys' interior (Smith et al. 1982) or tectonic activity due to a 2:3 orbital resonance between Dione and Tethys early in the solar system's history leading to orbital eccentricity and tidal heating (Hussmann et al. 2010). Alternatively, Ithaca Chasma could be tectonically associated to Odysseus (Fig. 10.4 in Sect. 10.2.5), the largest (~450 km wide) impact basin on the satellite (Moore and Ahern 1983; Moore et al. 2004b). The latter hypothesis is supported by the observation that Ithaca Chasma is confined within a great circle that is roughly concentric with Odysseus (e.g., Moore and Ahern 1983; Moore et al. 2004b).

At least two cases of tectonic orientation regionally influenced by a pre-existing but very degraded large impact basin could be identified on Dione, one centered on the smaller impact crater Amata (Fig. 10.8) as well as the 90 km large impact crater Turnus (Moore et al. 2004b; Schenk and Moore 2007). Large basins 400–600 km in diameter are also common on Iapetus and Rhea (Jaumann et al. 2009a).

Impacts not quite large enough to completely disrupt a satellite are expected to do considerable damage in the form of global fracturing (Jaumann et al. 2009a) and/or induce incipient breakup fracturing on Iapetus, Rhea, and the smaller Saturnian inner satellites (Smith et al. 1981; Collins et al. 2009). However, it cannot be completely ruled out that these fractures are caused by global effects like tidal stresses or volume changes (see below) during which older zones of weakness, in this case the impact basins, become reactivated. Especially, the fresh-appearing crater walls of relatively small impact craters on Dione in the vicinity of fractured terrain are believed to be the result of reactivation during Dione's periods of tectonic activity (Wagner et al. 2006; Stephan et al. 2009). In addition, Giese et al. (2007a) pointed out that crater counts on Tethys i.e. on the floor of Odysseus and the bottom of Ithaca Chasma imply a relatively younger age of the impact basin.

### 10.3.1.2 Networks of Fractures Related to Global Processes

Coherent networks of fractures or graben-like structures that extend over large portions of their respective satellites with simple symmetries about the satellite's rotational and tidal axes are evident on many of the outer planets satellites. Often parallel to sub-parallel sets of normal faults and graben-like structures can be observed.

Near-global networks of fractures divide Dione's surface into large polygons (Plescia 1983; Moore 1984; Wagner et al. 2006). Cassini images show them morphologically fresh exhibiting some bright scarps (Fig. 10.8), which, as noted before, imply that extensional deformation continued into geologically recent times (Wagner et al. 2006; Stephan et al. 2010). This also includes linear features, termed “wispy terrain” that were mapped on Dione's as well as on Rhea's surface based on Voyager images (Smith et al. 1981; Plescia 1983) and were revealed to be sets of faults by Cassini (Wagner et al. 2006; Moore and Schenk 2007). The main sets of faults on Dione appear to roughly follow a great circle, tilted with respect to the equator (Miller et al. 2007), and Moore and Schenk (2007) found north-south trending

## Fractures and graben-like structures (II)

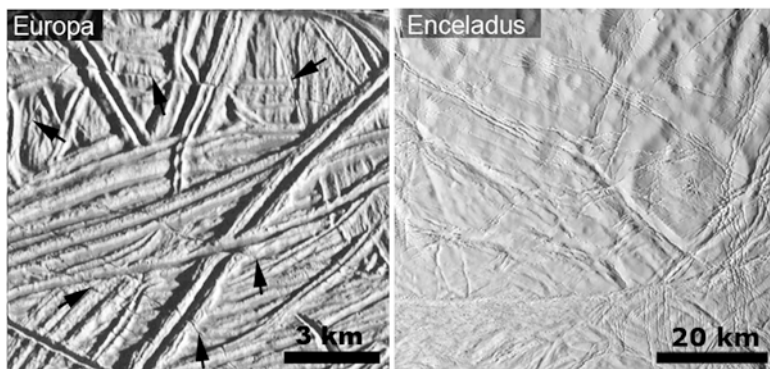


**Fig. 10.9** Close up view of fracturing on satellites with a complex tectonic history and numerous styles of tectonic resurfacing i.e. Europa and Enceladus with individual fractures representing the basic tectonic feature. Note that in contrast to fractures on the other satellites fractures on Europa (indicated by *black arrows*) and Enceladus occur only at sub-kilometer scale

ridges along the western boundary of a resurfaced plain that might have been formed by compression. Also, graben and extensional normal fault systems on Rhea, along with several large and broad ridges or scarps identified in both Voyager and Cassini images trend dominantly north-south (Moore et al. 1985; Moore and Schenk 2007; Wagner et al. 2007a).

The surfaces of the Jovian satellite Europa and the Saturnian satellite Enceladus reveal a complex tectonic history with numerous different tectonic styles (Sects. 10.3.2 and 10.3.4) that overprinted each other. Enceladus was known as the satellite with the highest geologic diversity since the two Voyager flybys implying tectonic and even cryovolcanic (Sect. 10.3.7) activity which could persist until present times (Smith et al. 1981, 1982; Kargel 1995). Nevertheless, complex networks of simple fractures or narrow graben are evident and criss-cross the surfaces representing the basic tectonic features on these two satellites (Figueroedo and Greeley 2000, 2004; Kadel et al. 2000; Prockter et al. 2000; Kattenhorn 2002; Greeley et al. 2004; Miller et al. 2007) (Fig. 10.9). On either satellite they appear as single or sets of sub-parallel fractures that can be several to hundreds of kilometers long with their rims sometimes raised with respect to the surrounding terrain (Greeley et al. 2004; Miller et al. 2007). Fractures also appear within Europa's bands (Figueroedo and Greeley 2000; Prockter et al. 2002; Kattenhorn 2002; Kattenhorn and Hurford 2009; Prockter and Patterson 2009) possibly caused by tension along anticlinal fold hinges (see Sect. 10.3.4). On Europa these fractures are generally ~100–300 m wide and were interpreted to have widened subsequently to the original fracturing due to mass wasting of debris from the sides of the initial fracture and/or due to tectonic movement along them possibly due to upbowing or strike-slip movement (Kattenhorn and Hurford 2009). Similar observations can be made on Enceladus where sub-kilometer scale parallel cracks, which can only

be seen in the highest-resolution Cassini images, crisscross the whole satellite's surface (Miller et al. 2007; Spencer et al. 2009).

Networks of fractures were also identified on the Uranian satellites (Smith et al. 1986). Their extent and origin, however, is unknown, due largely to the lack of a global coverage and image resolution of the Voyager data. On Titania fractures and graben are between 20 and 50 km wide and 2–5 km deep, which cut across most of the craters on the surface (Smith et al. 1986). Ariel's surface shows systems of graben-like features, interconnected to each other, that are hundreds of kilometers long and more than 10 km deep (Fig. 10.8). They are similar to, but much larger and more extensive than on Titania.

At least in case of Mimas, Tethys, Dione, Rhea diurnal tidal stresses are rather small (Collins et al. 2009). Therefore, despinning, volume changes or reorientation are more likely to be responsible for the observed fractures than present-day tidal stresses (Melosh 1977, 1980; Moore 1984; Pollack and Consolmagno 1984; Hillier and Squyres 1991; Nimmo and Matsuyama 2007; Jaumann et al. 2009a). Especially Dione's tectonic fabric exhibits patterns consistent with a decline in oblateness due to either despinning or orbital recession (Melosh 1977, 1980). Moore (1984) proposed a tectonic history of extension followed at least regional by compression. Similar processes are expected on Rhea (Jaumann et al. 2009a). While the troughs observed on Rhea suggest mainly extensional and (minor) compressional tectonics (Thomas 1988), the en-echelon pattern of the scarps and troughs that could be observed on the trailing hemisphere of Rhea suggests shear stress (Wagner et al. 2007b). This pattern also may have been influenced by the possible presence of large, degraded impact basins (Moore et al. 1985).

In contrast, the global fracture pattern on Europa was found to be consistent with diurnal tidal stresses and probably a non-synchronous rotation of the stress field (Helfenstein and Parmentier 1980; Geissler et al. 1998; Figueredo and Greeley 2000; Kattenhorn 2002; Sarid et al. 2004, 2005, 2006; Pappalardo et al. 2005; Groenleer and Kattenhorn 2008; Kattenhorn and Hurford 2009). Isolated fractures represent the youngest tectonic features on Europa and may transform into more complex features like ridges and bands (Sect. 10.3.4) (Kattenhorn 2002; Kattenhorn and Hurford 2009). This is also expected for Enceladus, although the analysis of the data is still preliminary (Miller et al. 2007). Thus, relationships between the dimension of the fracture networks and ongoing short-time-scale tidal stresses could be an explanation of the sub-kilometer scale fractures on both satellites – whereas the fractures and graben on the other satellites' surfaces present the result of the permanent deformation due to long-term mechanisms like despinning and/or volume changes in their early history.

### 10.3.2 Grooves

Tectonically resurfaced regions observed on icy satellites that are characterized by extensive tilt block faulting (called grooved terrain) are the dominant tectonic

structure on the Jovian satellite Ganymede. A detailed review of the grooved terrain is given in Pappalardo et al. (2004) and references therein.

These linear or curved *sulci* (singular *sulcus*) cover about two thirds of Ganymede's total surface area (Patterson et al. 2010). They consist of a complex patchwork of intersecting structural cells of bright grooved terrain and cut the old dark and heavily cratered terrain on Ganymede into discrete polygons (Fig. 10.10). As seen at higher image resolution (Fig. 10.10) each of the individual structural cells of grooved terrain show numerous closely spaced grooves subparallel to its elongated axis (Smith et al. 1979b; Smith et al. 1982; Shoemaker et al. 1982), while the general trends of the cells within Ganymede's bright grooved terrain differ greatly from one another reflecting a complex stress and strain history (Lucchitta 1980; Shoemaker et al. 1982; Murchie and Head 1986). In addition, swaths of geologically older grooved terrain are often cross-cut and presumably destroyed by younger grooved terrain (Fig. 10.10) (Collins et al. 1998; Pappalardo et al. 2004) pointing to a formation of the grooved terrain on Ganymede during a relatively long time period. Crater frequency statistics imply that the grooved terrain may have formed between 400 Ma and 4 Ga ago (Neukum et al. 1998; Zahnle et al. 1998, 2003).

Prior to the Galileo mission, the formation of grooved terrain on Ganymede was believed to take place in a combination of tectonic and cryovolcanic processes (e.g. Golombek and Allison 1981; Shoemaker et al. 1982) but observations by Galileo showed that cryovolcanism has played a minor role in creating grooved terrain on Ganymede (Pappalardo et al. 2004). The bright terrain units were rather formed predominantly at the expense of dark terrain through a process termed tectonic resurfacing, causing the partial or total transformation of dark terrain by pervasive tectonism (Head et al. 1997).

Because ridges and troughs of Ganymede's grooved terrain are periodically spaced (Grimm and Squyres 1985; Patel et al. 1999b) with gently rolling surface exhibiting average slopes of about 6° (Squyres 1981), extensional deformation of a brittle surface layer underlain by a viscous substrate is now the favored mechanism responsible for their formation (e.g., Herrick and Stevenson 1990; Pappalardo et al. 1998b; Collins et al. 1998; Dombard and McKinnon 2001; Bland and Showman 2007) (Fig. 10.11). Generally, grooved terrain is expected to be created by several episodes of extensional stress (Collins et al. 1998; Pappalardo et al. 2004) and the local tectonic style appears to be related to the amount of strain accommodated onto each structural cell (Pappalardo et al. 1998b; Collins et al. 2009). Whereas at an extensional strain of less than 5% the grooved terrain consists of parallel faults arranged in a graben-like morphology, at higher strain these parallel normal faults all dip in one direction (Pappalardo and Collins 2005). Pappalardo and Collins (2005) found impact craters within the grooved terrain that had been cut by tilt-block faulting zones about 10–20 km in width. Using the craters as strain markers, they estimated that these sets of faults had accommodated from 50% up to 180% extensional strain and concluded that the strain was high enough to resurface the region through tectonism alone to a degree that no features from the preexisting surface can be recognized within the fault zone.

## Grooves on Ganymede and Enceladus

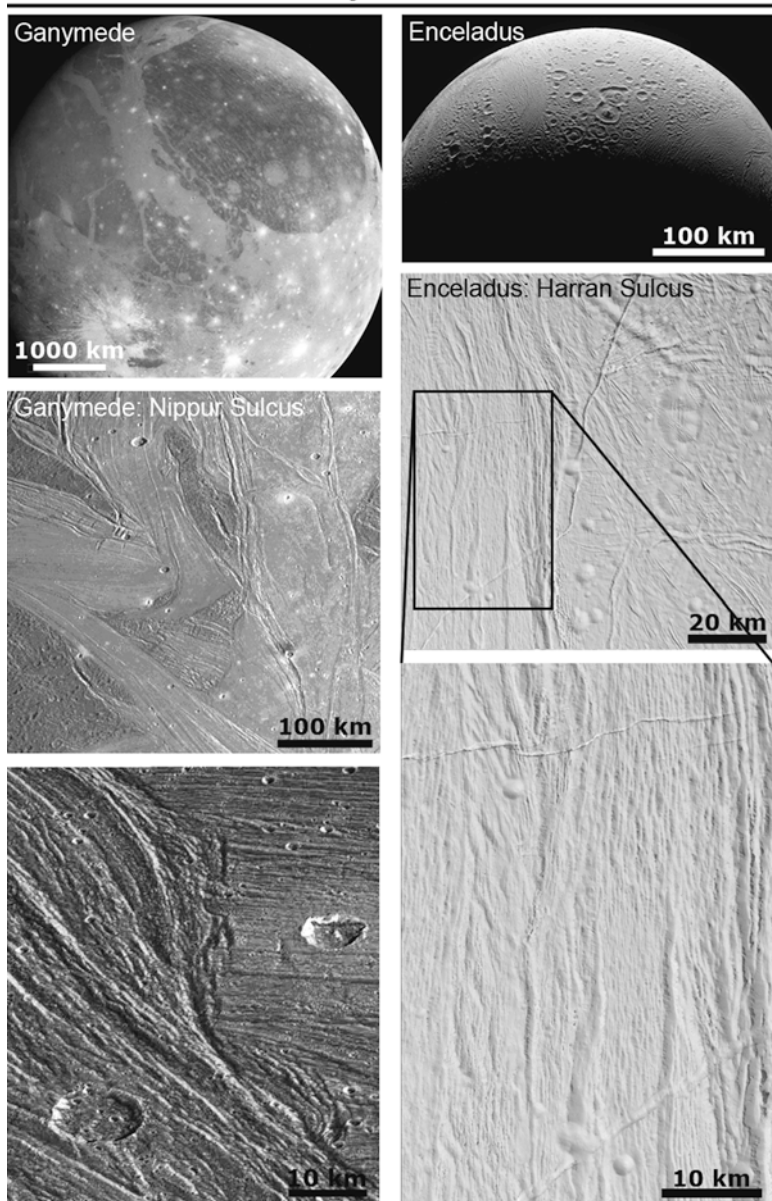


**Fig. 10.10** Grooved terrain on Ganymede and Enceladus that intersects old heavily cratered regions seen at different levels of image resolution as seen by Galileo and Cassini, respectively

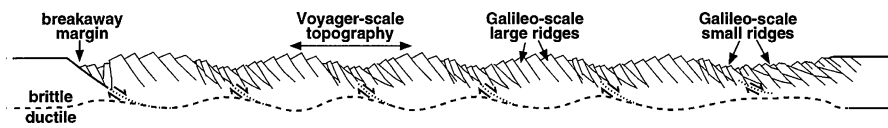


**Fig. 10.11** Schematic profile through the grooved terrain named Uruk Sulcus on Ganymede from Pappalardo et al. (1998b) illustrating possible normal-tilt faulting due to extensional stresses. Small-scale deformation in the range of 1–2 km with a relief of 100–200 km (identified in high-resolution Galileo images) is superimposed on 5–10 km large scale features (known from lower resolved Voyager images) (Squyres 1981; Giese et al. 1998; Patel et al. 1999b; Pappalardo et al. 1998b, 2004). The left margin of the profile marks the origin of the rift zone that is progressing to the right characterized by highly imbricated fault blocks. Near the brittle–ductile transition (dashed line) large scale shear zones (dotted lines) with the direction of the shear stress marked by (half arrows) are suspected. (Reproduced from Pappalardo et al. (1998b), with permission from Elsevier)

Some of the sets of faults in the grooved terrain on Ganymede had also accommodated a few kilometers of strike-slip motion in addition to the extension normal to the faults (Lucchitta 1980; Murchie and Head 1988; Pappalardo and Collins 2005) and higher resolution observations show several fault zones in which normal faults are organized into en echelon segments, indicating transtension (Pappalardo et al. 1998b; Collins et al. 1998; DeRemer and Pappalardo 2003). Lateral movement can be up to several hundreds of kilometers (Murchie and Head 1988; Head et al. 2002). There is much less evidence for contractional features (Pappalardo et al. 1998b, 2004).

Initial estimates of the amount of global expansion represented by all grooved terrain on Ganymede is significantly higher than would be expected from heating and melting due to tidal forces (Showman et al. 1997; Bland et al. 2009) as well as non-synchronous rotation alone, and is closer to the amount expected from a heat pulse due to interior differentiation (Collins 2006). Since Ganymede is so large, there would be a large volume of high-pressure ice phases in the interior displaced to the outside, which would cause significant volume change (Squyres 1980; Mueller and McKinnon 1988). Volume change would cause isotropic tensile stress over the entire surface, which could be an explanation for the large amount of extensional deformation observed, although there is still the question to be answered how Ganymede would remain undifferentiated for the initial part of its history (Friedson and Stevenson 1983) until the grooved terrain was formed.

Terrain similar to the grooved terrain on Ganymede could also be observed in the equatorial region on the Saturnian satellite Enceladus (Helfenstein et al. 2010), although, grooved topography on Enceladus is generally much more complex (Fig. 10.10). A detailed description of Enceladus' surface geology based on the latest Cassini results can be found in Spencer et al. (2009) and references therein.

As seen on Ganymede, grooved terrain on Enceladus such as *Harran Sulcus* shown in Fig. 10.10 consists of lanes of curvilinear grooves, which are oriented in north–south direction and separate smooth plains (called *planitia*) from old densely cratered regions (Rothery 1999; Bland et al. 2007). The *planitia* themselves,

however, also show extensive sets of parallel, north-south trending linear features. At least two deformation wavelengths could be measured (Bland et al. 2007) that are strikingly similar to the observations made on Ganymede. Smaller-scale deformation appears in the range of about  $\sim 4$  km, whereas larger-scale deformation occurs between 8 and 10 km predominantly in case of larger scale graben-like features.

Because of the similarity to the archetypical example of Ganymede's grooved terrain the grooved terrain observed on Enceladus also could have formed by extension of a brittle surface layer underlain by a viscous substrate (Pappalardo and Greeley 1995) resulting in parallel, periodically spaced, fault blocks (Fletcher and Hallet 1983). Furthermore, extensional deformation has been suggested to be responsible for ridge and trough terrains throughout the icy satellites (Herrick and Stevenson 1990).

### **10.3.3 Coronae**

Oval- to square-shaped tectonic processes called “coronae” mark the surface of the Uranian satellite Miranda (Smith et al. 1986). Similar features were only observed on the terrestrial planet Venus. Miranda's geologically old cratered terrain is cut by three “coronae” that extend up to several hundreds of kilometers (Fig. 10.12) and exhibit relatively straight boundaries and rounded corners. Each of these coronae consists of an inner core with smooth material and/or chaotically intersecting ridges and troughs and outer belts of predominantly subparallel ridges (Smith et al. 1986; Greenberg et al. 1991; Pappalardo 1994).

Currently, Miranda's coronae are believed to have been formed by extension and associated cryovolcanism (Croft and Soderblom 1991; Greenberg et al. 1991; Collins et al. 2009) rather than by a breakup and re-accretion of the satellite. The morphologies of the outer parts of Arden (Fig. 10.12c) and Inverness Coronae indicate a formation due to normal faulting (Plescia 1988; Thomas 1988; Greenberg et al. 1991; Pappalardo 1994; Pappalardo et al. 1997) similar to the grooved terrain on Ganymede (Sect. 10.3.5). The reconstruction of apparent tilt-block style normal faults in the outer belt of Arden Corona (Fig. 10.12d) performed by Pappalardo et al. (1997) suggests that tens of percent extension has occurred, along faults with initial dips of  $\sim 50^\circ$ .

Currently favored models suggest that the coronae were probably formed over plumes of material from the core of Miranda (Croft and Soderblom 1991; Greenberg et al. 1991), fracturing the crust expressed as graben-like structures in combination with (1) linear extrusion of viscous volcanic material through pre-existing fractures (Schenk 1991) or (2) solid-state diapirism (Jankowski and Squyres 1988; McKinnon 1988; Janes and Melosh 1990; Greenberg et al. 1991).

The geologic complexity of this tiny satellite (372 km in diameter), however, is still a mystery (Collins et al. 2009) but may be the result of tidal interactions with Uranus itself or its neighboring satellites like (1) a temporarily tidal resonance with Umbriel, which is implied from the current-day relative high inclination of Miranda's orbit, or (2) Ariel and/or Umbriel (Dermott et al. 1988; Tittemore and Wisdom 1990; Peale 1999; Moons and Henrard 1994). The relatively straight sides

## Coronae on Miranda

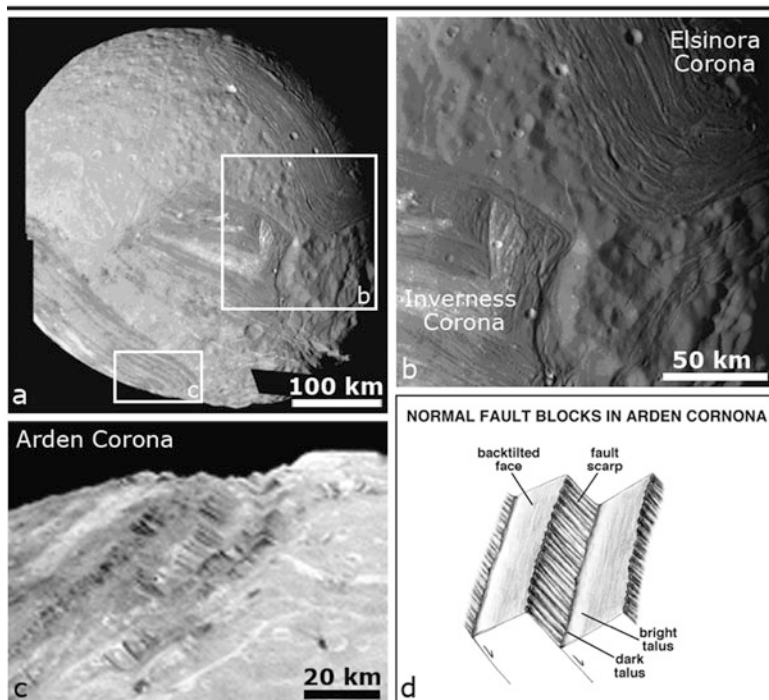


**Fig. 10.12** Miranda's surface at different image resolution: (a) a global view centered at the south pole showing the cratered terrain cut by three tectonic provinces called *coronae* (b) Inverness Corona and Elsinora Corona and (c) Arden Corona observed by Voyager in oblique viewing geometry showing tilt-block style normal faults in the outer belt like shown in (d) the schematic view of the tilt-block-style (Reproduced from Pappalardo et al. (1997), with permission of American Geophysical Union)

and rounded corners of the coronae may be the result of structural control by more ancient structures (Collins et al. 2009).

### 10.3.4 Ridges

On Europa and Triton, which show evidence for a more complex tectonic history, ridges are the most ubiquitous tectonic features (Pappalardo et al. 1999; Greeley et al. 2000, 2004; Greenberg 2005; Patel et al. 1999a; Prockter et al. 2005; Prockter and Patterson 2009) and make up a global network of cross-cutting ridges all over the satellite's surfaces (Fig. 10.13). They most commonly occur as pairs of parallel ridges flanking both sides of a medial trough, thus called a *double ridge* (Fig. 10.13). Although on both satellites these ridges can be several hundreds of kilometers long and only a couple of 100 m high (Croft et al. 1995; Giese et al.

## Ridges on Europa and Triton

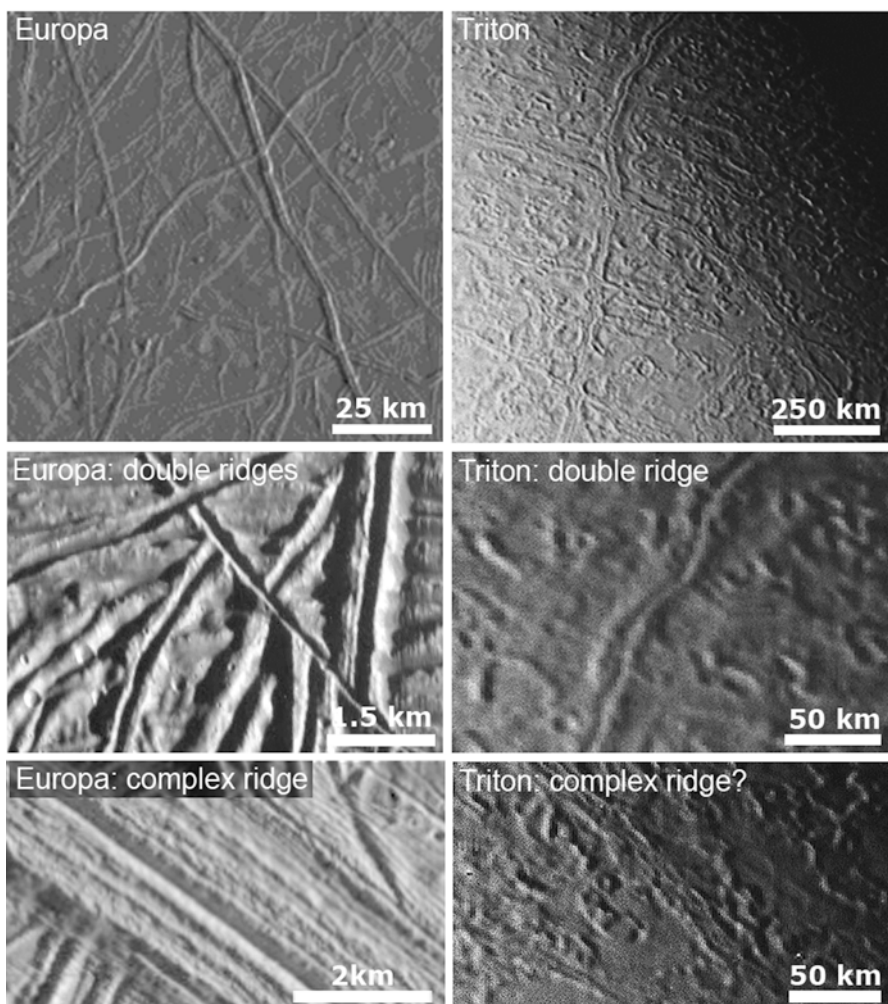


**Fig. 10.13** Ridge-dominated surfaces of Europa and Triton. Ridge morphologies appear mostly as double ridges (that probably formed from isolated fractures), which transform into more complex ridges i.e. with increasing numbers of ridges sub-parallel to each other (see text). Note the strike-slip motion of Europa's ridges along isolated troughs (*left column, center image*)

1999; Greeley et al. 2004), significant differences occur with respect to their widths. Whereas on Europa prominent double ridges are commonly a few hundred meters up to about 2 km wide, ridges on Triton reach dimensions between 15 and 20 km (Collins et al. 2009) (Fig. 10.13). The much greater widths of Triton's ridges compared to ridges on Europa are likely due to the lower surface temperature, and thus to a greater brittle-ductile transition depth.

Ridges on Europa and Triton that exhibit more complex ridge morphologies are described by Pappalardo et al. (1999), Greeley et al. (2004) and references therein. These ridge complexes are mostly composed of three and more subparallel ridges (Fig. 10.13) (Prockter and Patterson, 2009), which can interweave or merge along their trends (e.g. Greeley et al. 1998; Figueiredo and Greeley 2000). However, by examining these complex ridges over their full length, they could also represent several generations of double ridges that run at least partly parallel with a limited range or overprint each other (Fig. 10.13). Many double ridges and complex ridges show evidence for strike-slip motion along isolated troughs (Fig. 10.13) described in Sect. 10.3.1 (Hoppe et al. 1999; Sarid et al. 2002; Kattenhorn 2004; Rhoden et al. 2011). Partly, the double ridges on Europa exhibit a cycloidal pattern (Greeley et al. 2004) (Fig. 10.13). Apparently, ridge formation has continued throughout Europa's visible history and could be ongoing even today (Prockter and Patterson 2009). The majority of Europa's surface is comprised of relatively old ridged structures (e.g. Greeley et al. 2004) crosscut and overprinted by numerous younger double ridges and ridge complexes (Prockter and Patterson 2009).

Given the strong resemblance of the ridges on the two satellites, it is reasonable that similar formation mechanisms are responsible on both. Classifications of ridge morphologies on Europa and Triton presented by Head et al. (1999) and Pappalardo et al. (1999) imply a gradual transition from simple to complex features inferring that isolated fractures develop into troughs, which further can develop into double and wider complex ridges and possibly even into Europa's prominent tectonic bands (Sect. 10.3.4). In this case varying morphologies would represent an evolutionary sequence possibly including intrusive upwelling of liquid material along initial fractures, followed by extrusion and minor spreading (Head et al. 1999; Pappalardo et al. 1999; Prockter et al. 2002).

Understanding their mode of formation is important for the implication of the presence, depth and the distribution of a liquid H<sub>2</sub>O layer underneath (Pappalardo et al. 1999; Greeley et al. 2000). Proposed models are discussed in detail in Greeley et al. (2004), Collins et al. (2009), which include: (1) liquid material and icy debris to be pumped toward the surface due to diurnal tidal stresses (possibly enhanced through nonsynchronous rotation of Europa's icy crust (Greenberg et al. 1999b); (2) cryovolcanic (possibly gas-driven) extrusion into fractures or graben (Kadel et al. 1998; Smith et al. 1989; Croft et al. 1995) similar to terrestrial volcanic ridges; (3) intrusion of melt into shallow vertical cracks/dikes (Melosh and Turtle 2004); (4) cracking and diapirism of warm subsurface (Head et al. 1999); as well as (5) strike-slip motion along fractures creating frictional and viscous heating (Gaidos and Nimmo 2000; Nimmo and Gaidos 2002; Prockter et al. 2005).

A volcano-tectonic origin of ridges similar in morphology to the European ridges is at least partly supported by observations made by Cassini on the Saturnian satellite Enceladus. Although ridges are not globally distributed on Enceladus' surface they dominate its South Polar Region (SPT) (Fig. 10.14). These ridges, which are informally called *tiger stripes*, show a striking morphologically similarity to the double ridges on Europa (Fig. 10.14). The tiger stripes were identified to

## Ridges on Europa and Enceladus

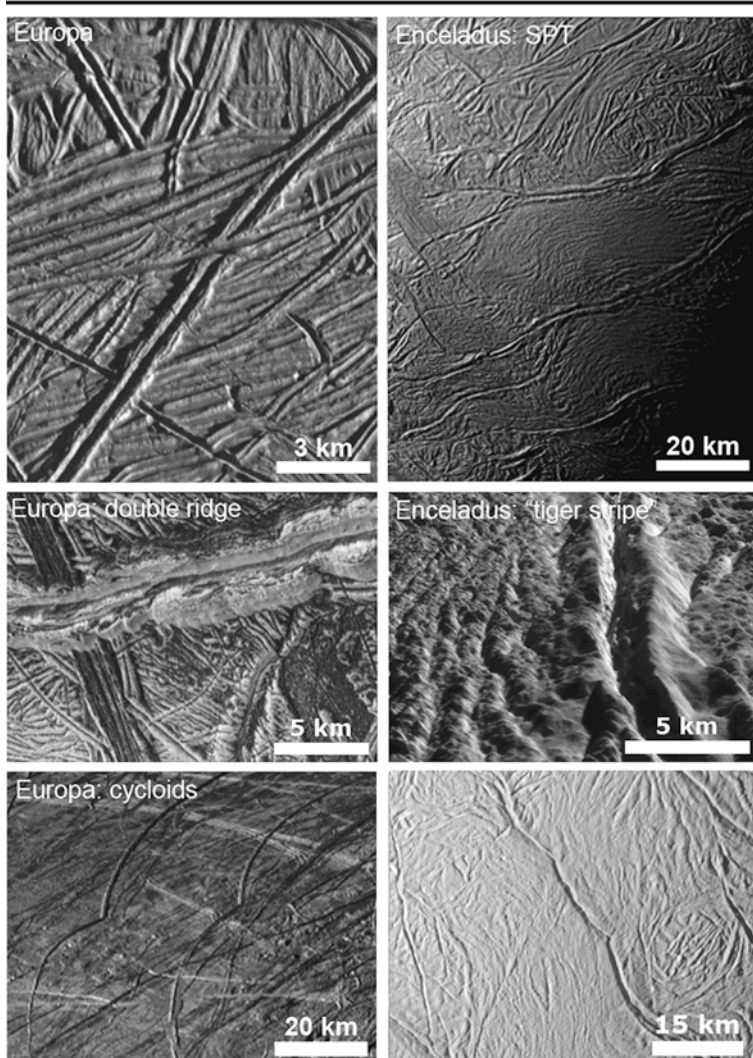


**Fig. 10.14** Comparison of the double ridges on Europa to ridges in the South Polar Terrain (SPT) of Enceladus including a three dimensional perspective of an E-W running about 300 m high double ridge on Europa ( $\sim 16^{\circ}\text{S}/195^{\circ}\text{W}$ ) (Adapted from Giese et al. 1999) and of Damascus Sulcus (NASA photojournal, PIA12207) one of the “tiger stripes” with a 200–250 m deep medial trough as well as cycloidal ridges on both satellites

be the source of thermal emission (Spencer et al. 2006) and the center of Enceladus’ recent volcanic activity (Sect. 10.3.7) (Spitale and Porco 2007). For a detailed review of the results achieved during the nominal Cassini mission the reader is referred to Spencer et al. (2009).

Cassini images show these tiger stripes as linear depressions with comparable dimensions as seen on Europa i.e. typically flanked on both sides by prominent 100-m-high ridges, about 500 m deep and 2 km wide, but limited to about 130 km in length (Fig. 10.14) (Porco et al. 2006). Partly, the ridges in Enceladus' SPT exhibit a cycloidal pattern (Spencer et al. 2009), which was also observed on Europa (Greeley et al. 2004). Although the driving source might be different on Europa and Enceladus, the observations made at least imply a possibly similar mechanism of formation.

### 10.3.5 Bands

In addition to ridges, straight, curved, dark or bright (gray), smooth or ridged zones called bands are another exceptional morphological feature on Europa's surface (Fig. 10.15). Europa is the only place in our solar system where these surface features could be observed so far. These bands crisscross its surface separating bright plains predominantly near the anti-Jovian point termed “pull-apart terrain” (Greeley et al. 1998; Figueiredo and Greeley 2000, 2004; Prockter et al. 2002). It has been found that bands cover over half of the surface in the anti-Jovian region of Europa (Prockter et al. 2002). Thus, processes responsible for the band formation play a significant role in the resurfacing of Europa's crust (Schenk and McKinnon 1989; Pappalardo and Sullivan 1996; Prockter and Patterson 2009). A detailed description and interpretation of the different band morphologies seen in Galileo images as well as implications for their formation is given in Prockter et al. (2002), Prockter and Patterson (2009), Greeley et al. (2004), Collins et al. (2009), and Kattenhorn and Hurford (2009).

Morphology and albedo of Europa's ridges (Sect. 10.3.3) and bands changes with time (Geissler et al. 1998). Dark bands were interpreted to be stratigraphically young, whereas the stratigraphically oldest bands appear as bright as their surrounding ridged plains (Geissler et al. 1998; Prockter et al. 2002) (Fig. 10.15). Regional-scale Galileo images of bands show an overall bilateral symmetry, with a narrow central and a hummocky textured zone on either side of it (Prockter and Patterson 2009). Toward the margins of some bands regularly spaced subparallel ridges and troughs could be observed, which are probably tilted normal fault blocks of the hummocky unit (Figueiredo and Greeley 2000; Prockter et al. 2002; Prockter and Patterson 2009) (Fig. 10.16).

Maximum band widths do not exceed 30 km, suggesting that some geophysical process limits the band formation (Prockter et al. 2002, 2010). A detailed treatment of possible formation mechanism of Europa's tectonic features is presented in Kattenhorn and Hurford (2009). In summary, bands as well as Europa's ridges described above appear to initiate as fractures in the satellite's brittle lithosphere and are subsequently modified to produce the observed morphologies. Primarily, Europa's bands were interpreted as a possible indication of crustal spreading analogous to terrestrial oceanic-spreading (e.g. Macdonald 1982; Prockter and Patterson 2009) caused by

## Europa's band morphologies (I)

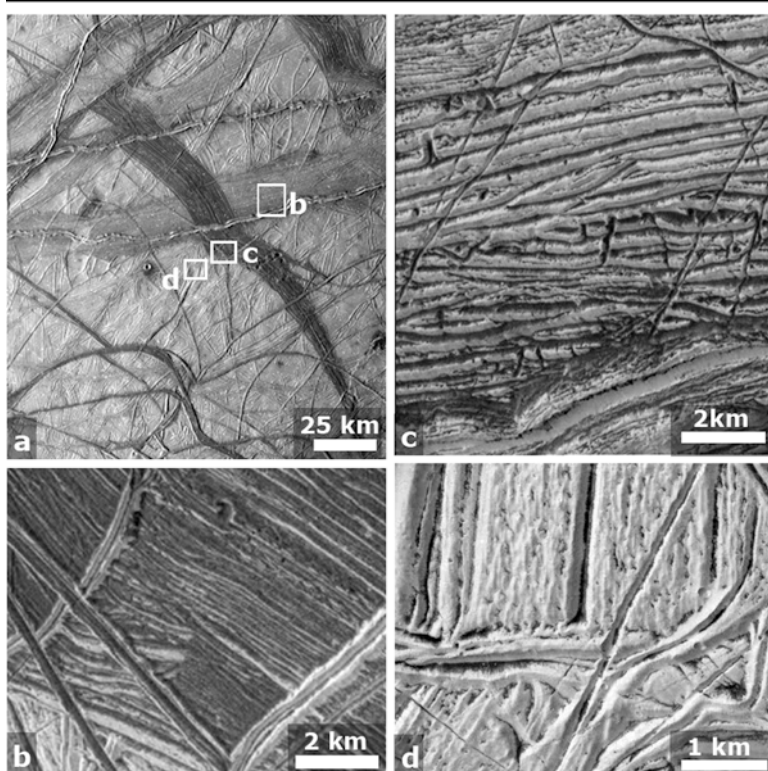


**Fig. 10.15** Band morphologies on Europa: (a) global view of the pull-apart terrain on Europa's anti-Jovian hemisphere that can be subdivided at higher spatial resolution into (b) stratigraphically *younger* dark ridged bands and (c) *older* gray ridged bands with (d) the oldest bands exhibiting similar albedo as the surrounding *bright* terrain. Locations of the local areas shown in the panels (b), (c) and (d) are indicated by frames in panel (a)

tidal stresses and possibly non-synchronous rotation of a brittle surface ice layer moving on a warmer, low-viscosity subsurface material (e.g. Sullivan et al. 1998; Prockter et al. 2002; Greeley et al. 2004). The medial trough could represent the possible site of plate separation and where cryovolcanic material was emplaced symmetrically on either side of the band axis. This is supported by the fact that the opposing sides of bands on Europa can be reconstructed and structures that were split and displaced as these bands opened along fractures can be restored (Schenk and McKinnon 1989; Pappalardo and Sullivan 1996; Sullivan et al. 1998). Further, the equatorial region of isotropic tension west of the antijovian point, predicted by non-synchronous rotation, correlates to the zone of pull-apart bands originally recognized in Voyager images (Helfenstein and Parmentier 1980; Pieri 1981; Lucchitta and Soderblom 1982; Schenk and McKinnon 1989), and recognized in Galileo images, extending westward to  $\sim 250^\circ$  longitude (Sullivan et al. 1998). Finally, laboratory experiments using wax analogue models show that cyclic

## Europa's band morphologies (II)

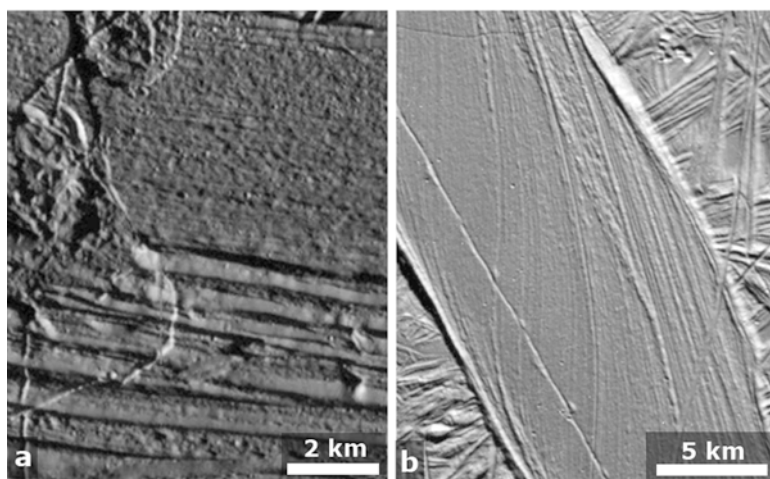


**Fig. 10.16** Bands in some places exhibit normal faulting near their margins (a) and partly show evidence for strike-slip motion like observed by Galileo in Astypalaea Linea (b)

strain on an opening rift zone can form band-like features in a thin brittle layer on top of a ductile substrate (Manga and Sinton 2004).

Geologic mapping has shown that bands postdate the ridged planes but even the youngest bands are commonly crosscut by chaos regions and lenticulae (Prockter et al. 2009). The latter represent another extraordinary group of features unique to Europa's surface which are described in the next section. Thus, bands formed at a time that was intermediate in Europa's history and, in contrast to the formation of Europa's ridges, processes responsible for the band formation are no longer active. Thus the process of ridge formation likely differs from that of band formation: ridge formation appears to require ongoing tidal stresses while band formation requires conditions that allow significant dilation of the surface with upwelling of relatively mobile material from the subsurface. This observation suggests that the style of surface deformation has changed through time from horizontal (bands) to vertical (chaos) tectonic (Prockter and Patterson 2009; Prockter et al. 2010).

### 10.3.6 Lenticulae and Chaotic Terrain

Nearly half of Europa's surface has been disrupted into isolated plates of preexisting material, such as ridged plains, with lumpy matrix material between the plates (e.g. Greeley et al. 2004; Greenberg 2005; Collins and Nimmo 2009) (Fig. 10.17). This disrupted terrain appears as larger disrupted regions described as *chaotic terrain* intermixed with local features known as *lenticulae* where the original surface has not been disrupted (Pappalardo et al. 1998a). Lenticulae have

## Lenticulae and Chaotic Terrain on Europa

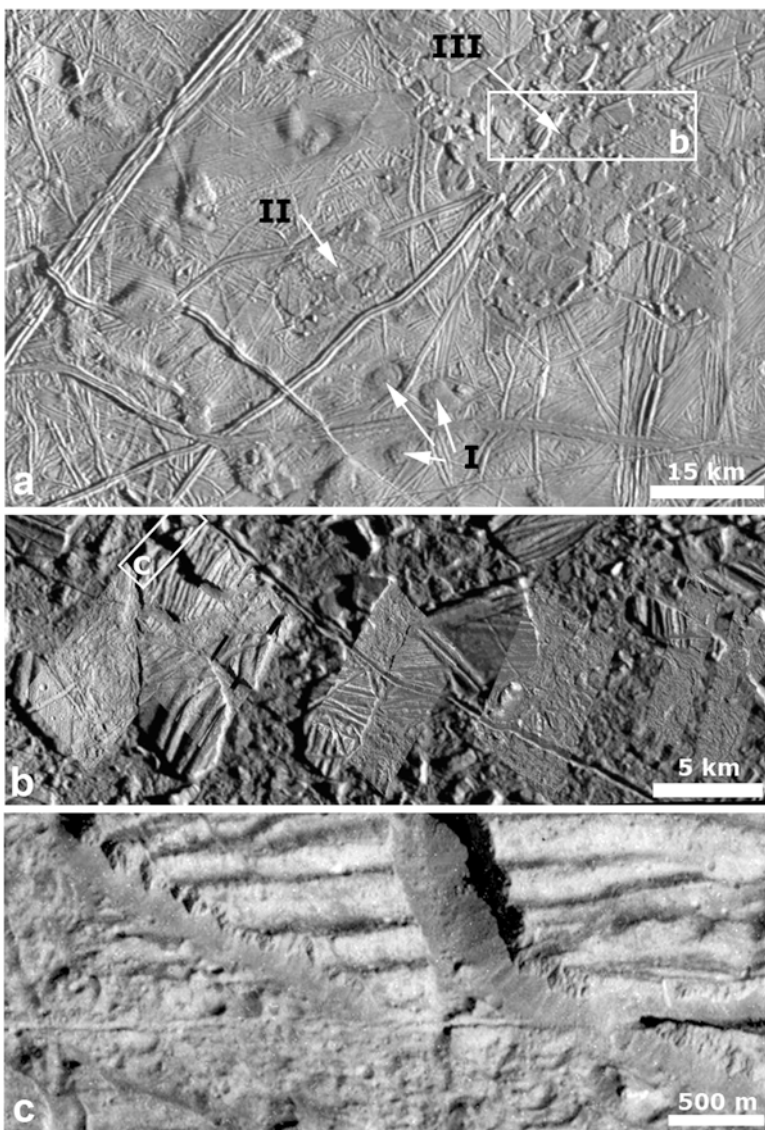


**Fig. 10.17** (a) Chaotic terrain ( $\sim 8^\circ\text{N}/275^\circ\text{W}$ ) in the trailing hemisphere of Europa indicating a possible transition of local lenticulae (step I) into chaotic terrain (step III) i.e. the progressing destruction of the pre-existing ridged plains and (b + c) close-up view of the chaotic terrain of Conamaros Chaos in Galileo high-resolution images. Note the frames included in the images for the location of the image subsets

been divided into three major classes including subcircular pits, dark spots, and domes, (Pappalardo et al. 1998a; Greeley et al. 2004; Collins and Nimmo 2009).

Sizes of chaotic terrains range from kilometer-scale features to regions of more than 1,300 km across with up to 20 km large blocks of existing ridged plains material, which were sometimes tilted, shifted and rotated with respect to one another by as much as several kilometers (Spaun et al. 1998; Collins and Nimmo 2009). Domes, pits and spot sizes predominantly range between 5 and 20 km (Carr et al. 1998; Spaun et al. 1999; Pappalardo et al. 1998a; Greeley et al. 2004) (Fig. 10.17a). The matrix material can be low-lying or high-standing relative to the surrounding plains (Prockter et al. 2010). In contrast, chaotic terrains and lenticulae are high-standing by 100–200 m above their surrounding regions (Schenk and Pappalardo 2004; Nimmo and Giese 2005).

The proportion of plates with respect to matrix material varies between the different chaos regions. Some, such as Conamara chaos, have distinct plates that can be partially pieced together allowing reconstruction of their original location relative to the surrounding terrain and to each other (Spaun et al. 1998). Other chaos regions, such as Thrace Macula, are predominantly comprised of matrix material and show only traces of preexisting structures (Fagents 2003; Prockter et al. 2010). Others, such as Murias Chaos, consist almost exclusively of matrix material at the resolutions available from Galileo images (Prockter et al. 2010). Geological mapping of Europa generally shows that the youngest chaos regions crosscut almost all other features (e.g. Greenberg et al. 1999b; Prockter et al. 1999; Figueiredo and Greeley 2000) and thus puts it at or near the top of the time sequence of feature formation. This suggests that the formation of chaos terrain may be a relatively recent phenomenon (Collins and Nimmo 2009). Thus, in addition to Europa's ridges chaos formation probably represent continuous and ongoing processes throughout the European history (Hoppa et al. 2001).

Morphological transitions from the lenticulae (Fig. 10.17a, I) to the chaotic terrain (Fig. 10.17a, III) rather suggests a related formation (Spaun et al. 1999; Riley et al. 2000; Collins and Nimmo 2009). Nevertheless, the origin of Europa's chaotic terrain including the lenticulae is far from being fully understood. A detailed discussion of the models proposed in the literature so far can be found in Greeley et al. (2004), Collins et al. (2000, 2009), and Collins and Nimmo (2009). Favored models for the formation include local melting of the ice shell (Greenberg et al. 1999a) and diapirism (Pappalardo et al. 1998a).

Most commonly, Europa's chaotic terrain is seen as unmelted pieces of a pre-existing icy crust that moved on a substrate of warm, mobile ice (e.g. Spaun et al. 1998), or that floated like icebergs on liquid water at some shallow depth, possibly a subsurface ocean (Carr et al. 1998; Greenberg et al. 1998). Thus, chaos regions have been interpreted as places of enhanced internal heat flow and perhaps melting (Carr et al. 1998; Williams and Greeley 1998; Greenberg et al. 1999b) requiring that Europa has a very thin (<10 km) ice shell, exposing the ocean below (O'Brien et al. 2002; Collins and Nimmo 2009). In case of a thicker ice shell the warm liquid material at the base of the ice shell would flow to maintain its thickness faster than the ice shell could melt through from below (Prockter et al. 2010).

Alternately, in the diapiric model, which was initially proposed for the formation of the lenticulae, solid-state convection occurs at the base of an ice layer when the temperature is near the solidus, causing ice diapirs to rise buoyantly to the surface that disrupt the relatively cold and rigid lithosphere (Pappalardo et al. 1998a). This mechanism has been modeled as thermal and compositional in origin and has been used to explain the formation of small and larger dome features that stand several hundred meters above the surrounding plains (Rathbun et al. 1998; Figueredo et al. 2002; Spaun et al. 2004; Mével and Mercier 2007; Singer et al. 2010). It still has its difficulties, however, to explain the wide range of larger, roughly asymmetric chaos regions on Europa's surface (Collins and Nimmo 2009).

### 10.3.7 Folds

As described above, tectonics on icy satellites were identified to be predominantly due to extensional deformation. In contrast surface features formed by compressive stresses, such as folds, are rare. But nevertheless these features are existent and were at any rate observed locally on Europa (Figueredo and Greeley 2000; Prockter and Pappalardo 2000; Prockter et al. 2002), Enceladus (Spencer et al. 2009), and possibly on Rhea (Moore et al. 1985; Moore and Schenk 2007), which could at least partly accommodate for the extensional deformation observed on the surfaces of these satellites. Possible evidence for contractional surface features is also reported for Titan (Miti et al. 2010). Compressive stresses are also in discussion to be responsible for the giant equatorial ridge on Iapetus (Porco et al. 2005a, b; Castillo-Rogez et al. 2007; Sandwell and Schubert 2010).

The strongest evidence for contraction on Europa was the identification of several parallel folds within the dilatational band associated with the right-lateral strike slip fault Astypalaea Linea (Prockter and Pappalardo 2000) that exhibit a wavelength of about 25 km and an amplitude of  $250 \pm 50$  m (Dombard and McKinnon 2006) (Fig. 10.18a). In adjacent ridged terrain, the folds gradually disappear or are not resolvable, suggesting that dilatational band material is more easily folded, possibly due to a localized high heat flow (Prockter 2001) combined with a reduced ice thickness (Billings and Kattenhorn 2005). This causes dilatational bands to become localized zones of crustal weakness that may be able to accommodate contraction by folding. In contrast, Mével and Mercier (2002) suggest that late transpressive motion along Astypalaea Linea may have caused the localized folding.

Nevertheless, the distinct scarcity of visible folding on Europa suggests that it is not a significant accommodator of crustal contraction and/or is difficult to recognize in existing images, and is certainly insufficient to balance out the amount of extension (Kattenhorn and Hurford 2009). Although Europa has likely undergone some amount of expansion due to cooling and thickening of the icy shell, the likely maximum extensional strain after even 100 Ma of cooling (~0.35%, Nimmo 2004) would be insufficient to account for the amount of new

## Contractional surface features

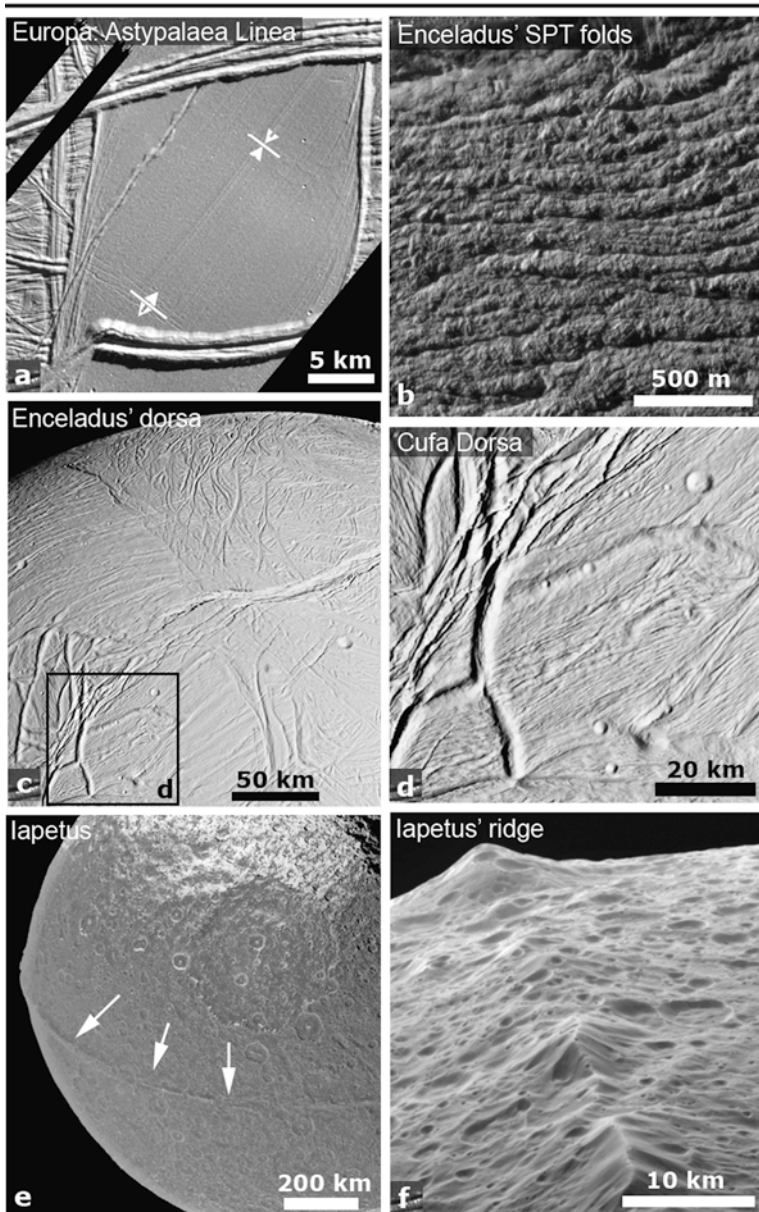


**Fig. 10.18** Examples of compressive tectonics on the icy satellites: (a) Europa's long-wavelength folds in the region of Astypalaea Linea (Prockter and Pappalardo 2000), (b) intensely folded terrain in the South Polar Terrain (SPT) of Enceladus between the tiger stripes, (c) the peculiar dorsa of Enceladus' trailing hemisphere (Mitri et al. 2010) with (d) a close view onto Cufa Dorsa, and (e) the equatorial ridge of Iapetus (f) showing an old impact battered surface (Porco et al. 2005a, b)

surface area created at spreading bands, which occupy about 5% of the surface area (Figueredo and Greeley 2004). Hence, some amount of contraction must have occurred during the visible tectonic history in order to create a balanced surface area budget. Given this need, contractional features might be expected to be as common on the surface as extensional features. In actuality, contractional deformation on Europa is visibly sparse and by no means obvious (Kattenhorn and Hurford 2009).

A second candidate feature for possible localized contraction, which might help to accommodate the strain from extensional bands on Europa, is represented by convergence bands (Greenberg et al. 2002; Sarid et al. 2002; Greenberg 2004; Kattenhorn and Marshall 2006; Patterson et al. 2006). Tectonic reconstruction across these bands reveal a zone of “missing” crust leading to the interpretation that these bands represent zones of convergence driven by lateral motion along adjacent strike-slip faults or along zones of preexisting weakness in the icy shell such as dilational bands and dilational strike-slip faults (Kattenhorn and Hurford 2009). Convergence band-like features might be common on Europa and potentially important tectonic features for balancing Europa’s surface area budget. These features, however, are not well studied. Thus, additional work is needed to prove this hypothesis (Kattenhorn and Hurford 2009).

Only one other unequivocal example of compressional morphology like the folds on Europa could be observed on an icy satellite so far. Regions between the extensionally formed tiger stripes in the South Polar Terrain (SPT) of Enceladus (Sect. 10.3.4) are characterized by numerous closely spaced parallel features (Fig. 10.18b) exhibiting morphologies that are distinctly different from other tectonic features observed on this satellite (Spencer et al. 2009; Barr and Preuss 2010). High-resolution Cassini images reveal an intensely folded terrain analogous to compressional folds on terrestrial lava flows (Fink 1980) with the folds exhibiting wavelengths of about 1.1 km (Barr and Preuss 2010).

Other surface features on Enceladus that might result from compressional tectonism also include a peculiar polygonal system of about 2.5 km wide rounded ridges called “dorsa”, which are located within a tectonically deformed region of the trailing hemisphere (Kargel and Pozio 1996; Miller et al. 2007; Spencer et al. 2009; Helfenstein et al. 2010) (Fig. 10.18c, d). Although these features have remained poorly understood, their morphology suggests that they represent compressional features and were most likely formed by thrust faulting resulting from multi-directional contraction (Kargel and Pozio 1996; Helfenstein et al. 2010; Crow-Willard and Pappalardo 2009; Pappalardo et al. 2010).

Possible evidence of contractional surface features occurring in the equatorial region of Titan is also described by Radebaugh et al. (2007) and Mitri et al. (2010) based on the examination of Radar images obtained by Cassini, although the moderate resolution of the Cassini Synthetic Aperture Radar (SAR) does not permit an unambiguous geological interpretation.

The most bizarre surface feature possibly formed by compression, however, is the equatorial ridge on Iapetus (Porco et al. 2005a; Giese et al. 2008). It runs exactly along the equator for at least one third of the satellite’s circumference and gives the

satellite a walnut-like appearance (Fig. 10.18e). The ridge forms a complex system including isolated peaks, segments of more than 200 km in length and sections with three near parallel ridges (Porco et al. 2005b). The ridge is about 10 km wide, and, although the ridge is variable in height, it rises partly to more than 20 km (Porco et al. 2005b). The ridge is most pronounced on Iapetus' dark leading hemisphere, whereas there is no ridge within the bright regions, only a series of isolated about 10 km high peaks along the equator (Fig. 10.18f). The ridge system is heavily cratered, indicating that it is ancient and comparable in age to other terrains on Iapetus (Schmedemann et al. 2008).

It is not resolved yet how the ridge was formed, why it follows the equator almost perfectly and why the ridge is confined to the dark terrain on Iapetus, named Cassini Regio. It is believed, however, that the equatorial ridge is likely a consequence of the same phenomenon that produced the oblateness of Iapetus global shape (Thomas et al. 2007; Sandwell and Schubert 2010). Proposed models include that the ring represents accreted material from an ancient ring system orbiting Iapetus (Ip 2006; Dombard et al. 2010), upwarping of the surface by tectonic faulting due to extensional forces (Giese et al. 2008), convection inside Iapetus that might have resulted in equatorial extension and diking (Czechowski and Leliwa-Kopystynski 2008; Roberts and Nimmo 2009; Melosh and Nimmo 2009), despinning (Porco et al. 2005b; Castillo-Rogez et al. 2009) or rearrangement of the material of Iapetus' lithosphere due to compaction of the interior accompanying the buckling failure of the lithosphere that is focused at the equator (Sandwell and Schubert 2010).

The ridge appears too solid to be the result of a collapsed ring (Giese et al. 2008). Furthermore, the mass of the ridge was estimated to be about  $10^{18}$  kg, comparable to the C-ring of Saturn, which makes it questionable that Iapetus could be encircled by such a massive ring (Dombard and Cheng 2008). The rings position exactly at the equator as well as the fact that it is extremely localized and that very little other tectonic deformation is observed on the satellite makes it difficult to explain the formation of the ridge tectonically (Singer and McKinnon 2010). Dombard and Cheng (2008) also point out difficulties to explain a convective origin of the ridge. They argue that for a convective upwelling to deform an overlying lithosphere on a scale comparable to the width of the ridge (100–200 km) would require a relatively thin lithosphere (<500 km), which would not be sufficient, however, to maintain the ridge after loss of the convective support.

Although, the highly oblate shape suggests an earlier, more rapid spin rate, despinning alone cannot explain the equatorial ridge (Castillo-Rogez et al. 2007). Whether a satellite is spinning down or spinning up, compressional features can be expected to be oriented perpendicular to the equator, making it difficult to explain the ridge with despinning (Melosh 1977; Pechmann and Melosh 1979; Jaumann et al. 2009a). Although the ridge represents such a large mass that, if it had formed in another location, it would almost certainly have re-oriented to the equator anyway (Castillo-Rogez et al. 2007). Reorientation, however, would cause significant stresses across the satellite (not just at the equator), yet few tectonic features have been observed (Singer and McKinnon 2010).

Sandwell and Schubert (2010) suggest an alternative scenario in which Iapetus had a relatively high initial porosity ( $>10\%$ ). Due to radioactive heating early in Iapetus' evolution the temperature of its interior reaches about 200 K, the material becomes ductile and the satellite compacts by 10%, while the icy shell remains strong. The authors propose a thickness of Iapetus' lithosphere of at least 120 km, which would be necessary to maintain its shape and then deforms to match the reduced volume of the satellite and fails by the buckling instability in the equatorial region.

## 10.4 Cryovolcanism on Icy Satellites

In contrast to silicate volcanism on the terrestrial planets, cryovolcanism in the outer solar system is driven by lava made of liquid or vapour phase of H<sub>2</sub>O probably including other volatiles such as NH<sub>3</sub>, CH<sub>4</sub> and N<sub>2</sub> that would be frozen solid at the normal temperature of these icy satellite's surfaces (Kargel 1990, 1998; Geissler 2000; Zhong et al. 2009). Detailed discussion of cryovolcanism is given in (Kargel 1998 and references therein). Here we summarize the major aspects.

Cryovolcanism is thought to include effusive eruptions of icy slurries and explosive eruptions consisting primarily of vapor (Fagents 2003). The main difference between cryovolcanism and silicate volcanism is that in the former, the melt is denser than the solid by  $\sim 10\%$  (Jaumann et al. 2009a). This means that special circumstances must exist for an eruption of non-vapor cryovolcanic materials to occur including: (1) the melt includes dissolved volatiles, which reduce the bulk melt density of the cryovolcanic material (Crawford and Stevenson 1988); (2) the melt is driven upwards by pressure differences caused by tidal effects, as proposed for the Jovian satellite Europa (Greenberg et al. 1999a), surface topography (Showman et al. 2004) or freezing (Fagents 2003; Manga and Wang 2007) or (3) local compositional differences resulting in a locally dense ice shell and a less dense melt possibly due to the addition of NH<sub>4</sub> (Kargel 1992, 1995). Erupted cryovolcanic material consisting of primarily liquid and solid H<sub>2</sub>O will immediately freeze under surface conditions, or boil at least until a sufficiently thick ice cover is formed (Allison and Clifford 1987). If the erupted material is dominated by the vapor phase, the vapor plume will expand outwards (Kargel et al. 1991; Wilson et al. 1997; Miyamoto et al. 2005; Tian et al. 2007) and escape entirely if the molecular thermal velocities exceed the escape velocity. Any associated solid material will follow ballistic trajectories, ultimately forming deposits centered on the eruption vents (Melosh and Janes 1989; Fagents et al. 2000).

During the Voyager 1 and 2 missions many resurfaced smooth and sparsely cratered terrains were identified on Europa and Ganymede (Squyres 1980; Lucchitta and Soderblom 1982; Squyres et al. 1983; Allison and Clifford 1987; Schenk and Moore 1995), Enceladus, Dione, Tethys, Iapetus (Smith et al. 1982; Stevenson 1982; Kargel and Pozio 1996), Miranda and Ariel (Smith et al. 1986; Plescia 1987; Jankowski and Squyres 1988; Croft and Soderblom 1991; Schenk 1991), and several other icy satellites. These were widely interpreted as due to cryovolcanism

(e.g. Lucchitta and Soderblom 1982; Smith et al. 1979a, b, 1982; Kargel 1995; Jankowski and Squyres 1988; Schenk 1991; Schenk and Moore 1995, 1998). Upon closer inspection by the Galileo and Cassini missions, however, many of these surface features on the Jovian and Saturnian satellites turned out to be resurfaced due to mass wasting (Prockter et al. 1998), tectonics (Johnson 2005; Collins et al. 2009), viscous flow and diapiric rise (Head et al. 1998a; Collins et al. 2009) or may be the result of viscous relaxation of topography causing the gradual disappearance of the surface features such as impact craters; the surface eventually refreezes appearing relatively scratch-free.

Nevertheless, surface features associated to cryovolcanism were observed indicating that cryovolcanism could have occurred in the past and may still go on. The best evidence of past cryovolcanism on Ganymede was found in form of multiple scalloped depressions called *paterae* adjacent to Ganymede's bright terrain (Sect. 10.3.2), which could represent caldera-like source vents for icy volcanism (Lucchitta 1980; Schenk and Moore 1995; Head et al. 1998b; Kay and Head 1999; McKinnon et al. 2001; Spaun et al. 2001). Giese et al. (2001) reported smooth, low-lying flat plains within the grooved terrain of Ganymede resembling tectonic structures (graben) which were flooded by low-viscosity icy lava (Pappalardo et al. 2004). This suggests that cryovolcanism in combination with tectonic processes (Sect. 10.3.2) may have played some role in the formation of bright terrain (Head et al. 1998b). It remains for further studies, however, to unravel the global distribution, timing, and relative importance of cryovolcanism with respect to tectonism, and its contribution to bright terrain formation (McKinnon et al. 2001).

Active volcanism is still believed to occur on Europa but could not be detected so far (see Greeley et al. 2004 and Pappalardo et al. 2004). Either cryovolcanism takes place at a scale not distinguishable in Galileo data (Fagents et al. 2000; Figueiredo and Greeley 2003), or this activity is episodic rather than continuous (Phillips et al. 2000). Nevertheless, cryovolcanism could be associated with tectonic processes that form Europa's prominent ridges and bands, possibly similar to what occurs along terrestrial oceanic spreading zones (Sects. 10.3.4 and 10.3.5).

Enceladus is the only icy body in the solar system known to be substantially volcanically active today. Since the Voyager encounters with Enceladus its geological activity was postulated based on its young, reflective surface and its location near the core of Saturn's E ring (Rothery 1999). However, the Voyager missions failed to provide conclusive evidence that Enceladus was recently active. In 2005, the Cassini spacecraft actually observed numerous jets of liquid H<sub>2</sub>O, volatiles including N<sub>2</sub> and CO<sub>2</sub> as well as simple hydrocarbons erupting from vents near Enceladus' south pole (*tiger stripes*) extending out nearly 500 km from the surface (Porco et al. 2006; Hansen et al. 2006; Waite et al. 2006) (Fig. 10.19a–c). Substantial heat is emanating from the surrounding areas (Spencer et al. 2006). This discovery not only confirmed Enceladus' recent geologic activity but also attested its primary source for Saturn's E ring (Spahn et al. 2006). It is still a mystery, however, why this small satellite is volcanically active today and why this activity is concentrated in Enceladus' southern polar region. See a detailed review of the recent interpretations in Spencer et al. (2009) and references therein.

## Cryovolcanism on Enceladus and Triton

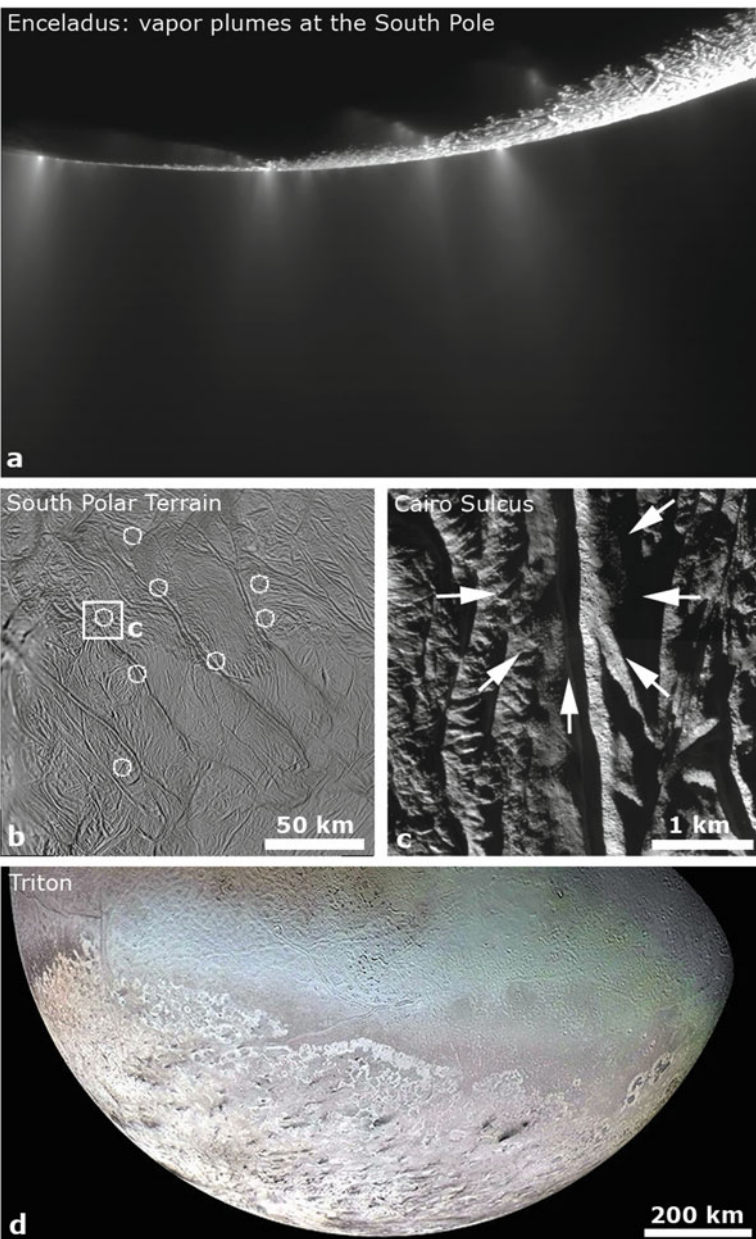


**Fig. 10.19** Regions of volcanic activity on Enceladus and Triton with (a) vapor plumes observed on Enceladus originating from (b) local spots within the ‘tiger stripes’ in its South Polar Terrain like (c) Cairo Sulcus and (d) dark streaks in Triton’s southern hemisphere interpreted as cryovolcanic plumes

That Triton, like Enceladus, is a volcanically active body at present times could be verified during the Voyager-2 flyby in 1989. Two active dark plumes rising vertically up to 8 km above the surface and then extending horizontally over a distance of more than 100 km were detected in high-emission angle views of the satellite's limb (Smith et al. 1989; Soderblom et al. 1990; Kirk et al. 1995) suggestive of geyser-like activity. These plumes originate from two dark spots on the surface close to Triton's South Pole. In addition to these, Voyager images show more than 100 additional dark streaks crossing the polar region between 50° and 57°S (Kirk et al. 1995) (Fig. 10.19d), the part of Triton's surface close to the subsolar point.

Gaseous N<sub>2</sub> and/or CH<sub>4</sub> were discussed as the major compounds driving Triton's geyser-like activity (Smith et al. 1989). Non-volcanic origins for the plumes were also discussed, such as solar insolation and sublimation, or sublimation due to intrusion of liquid material into volatile-rich material in the upper crust (Kirk et al. 1990; Brown et al. 1990). Ingersoll and Tryka (1990) suggested that the plumes are an atmospheric rather than a surface phenomenon similar to terrestrial dust devils. Triton's southern hemisphere was just approaching its summer solstice during the Voyager flyby implying that the activity might be seasonal. One year for Triton equals about 165 years on Earth; moreover its orbit is not circular and opposite to the rotation of Neptune, making it the only major satellite in the solar system to do so. This indicates that solar heating, although very weak at Triton's great distance from the Sun, could play a crucial role. Possibly dark carbon-based ices trapped within or beneath a semi-transparent layer of frozen N<sub>2</sub> absorb light and trap heat until enough N<sub>2</sub> gas pressure accumulates for it to erupt through the crust (McKinnon and Kirk 2007; Smith et al. 1989). A temperature increase of just 4 K above the extremely low surface temperature of 37 K on Triton would cause an expansion of the N<sub>2</sub> gas that could drive eruptions to the heights observed.

In addition to the dark streaks, extensive hummocky plains with flow fronts, domes and ridges (see Fig. 10.13 in Sect. 10.3.4) of the so called "cantaloupe terrain", which is known to exist on Triton only, was reported to be of cryovolcanic origin possibly in connection with subsequent modification by erosion and degradation (Smith et al. 1989), but this is still uncertain (Boyce 1993; Schenk and Jackson 1993). Further smooth to undulating plains that extend over several hundreds of kilometers originate at an 80-km wide caldera-like structure named Leviathan Patera (Smith et al. 1989; Croft et al. 1995). Clusters of pits near the centers of these plains could represent source vents where liquid material extruded.

Although not observed yet, cryovolcanism may occur on other satellites in the outer solar system where no high-resolution images are available yet. Both Saturnian satellites Tethys and Dione show evidence for weak plasma tori (Burch et al. 2007) somewhat analogous to the much more pronounced feature at Enceladus, which is caused by the geysers (Porco et al. 2006). It is not yet clear whether surface activity or some other process is generating these tori. Although no surface processes associated to these plasma streams could be identified on Dione so far (Stephan et al. 2010), Clark et al. (2008) reported a possible, but currently unconfirmed, detection of material around Dione, which may also indicate some surface activity.

Although the surface features on Saturn's largest satellite Titan are hidden beneath a dense nitrogen atmosphere, landforms indicative of cryovolcanic activity are expected to occur (e.g., Jaumann et al. 2009b). An exotic chemistry and the high atmospheric pressure on Titan lead to complex rheologies of cryovolcanic materials and a tendency towards effusive rather than explosive eruptions, as, e.g., observed on Enceladus and Triton (Lopes et al. 2007, and references therein). It is thought that ammonia could have been erupted, thus providing a potential source for the atmospheric nitrogen by photolytically dissolving ammonia into nitrogen and hydrogen which is emitted (Zhong et al. 2009). Like nitrogen, methane is destroyed by photolysis as well. The fact that it still exists in great quantities on Titan indicates that it may still be erupting today. In pre-Cassini studies by, e.g., Kargel (1991, 1992) and Kargel et al. (1991), the authors suggested that effusive eruptions of material with rheological properties akin to the rheology of material in terrestrial basaltic eruptions might have occurred on Titan. Some support for cryovolcanic features is given by recent Cassini RADAR observations that report flow-like structures and a possible shield volcano on Titan's surface (Lopes et al. 2007; Fortes et al. 2007) although these features seem suspect in the light of recent topographic data (Kirk et al. 2009).

## 10.5 Surface Erosion and Degradation on Icy Satellites

The surfaces of all icy satellites show evidence of mass movement and landform degradation including any process, erosional and/or depositional that causes the alteration of a planetary surface (Greeley 1985). In particular, geologically old surfaces of icy satellites that do not exhibit an atmosphere show widespread abundance of erosional processes, probably employing a variety of mechanisms (Moore et al. 1999). At least four processes can be distinguished, which contribute to surface degradation on airless satellites, including (1) mass wasting by gravity, causing downslope movement of surface materials to a lower gravitational potential and resulting in the reduction of the topographic relief of surface features, (2) bombardment of (micro-) meteorites, (3) irradiation, sputtering and implantation of particles from planetary magnetospheres or from the solar wind and cosmic rays, as well as (4) sublimation and redeposition of surface materials due to diurnal variations of surface temperatures (Greeley 1985; Moore et al. 1999). The importance of each of these processes varies from satellite to satellite depending on the position of the satellite in the solar system and within the specific planetary system, which is manifested in a range of landforms on their surfaces. Thus, erosion and degradation play a major role in the evolution of the surficial layers of icy satellites (Moore et al. 1999) and provide important implications for the interpretation of remotely sensed data, whether obtained telescopically or by spacecraft (Clark and Johnson 1996).

Erosion is also an important geological process on the Saturnian satellite Titan. Of all icy satellites Titan is the only one with a substantial atmosphere, enabling interactions between the surface and atmosphere, which is unique in the sense that

methane seems to play a role in erosional processes that water plays on Earth (Lunine and Atreya 2008). Titan's surface shows unequivocal evidence of fluvial, lacustrine, and eolian processes analogous to Earth (Prockter et al. 2010).

### 10.5.1 Mass Wasting on Icy Satellites

Mass wasting occurs on any icy satellite with substantial topography on the order of at least several tens or hundreds of meters in height. Gravity is the primary agent to move material downslope and to deposit it at the lowest gravitational potential (Greeley 1985), typically at the base of positive relief features such as tectonic scarps (Stephan et al. 2010), ridges and crater rims (Chuang and Greeley 2000).

Landslides are the most conspicuous landforms implying mass wasting. They range in lengths from several tens or hundreds of meters (distinguishable only in high-resolution images) to several tens of kilometers. Examples for landslides on the icy satellites of Jupiter and Saturn are shown in Fig. 10.20. Landslides are tongue-, fan- or pancake-shaped bounded by a distinct scarp, as forms observable on Callisto, Tethys or Rhea, or are represented by an irregularly-shaped slump-like hill, or groups of hills, as on Iapetus and Phoebe (Fig. 10.20) (Prockter et al. 1998; Moore et al. 1999; Chuang and Greeley 2000; Wagner et al. 2006, 2008; Singer et al. 2009). In some cases, material moves downslope and fills topographic depressions, e.g., craters, without slump-like accumulations of material, as shown in the example from Hyperion.

In the icy satellites of Uranus, landforms of mass wasting are not easily discernible because of the low image resolution. Landslides at canyon walls could be identified on Ariel (Croft and Soderblom 1991). Features interpreted as talus deposits occur at the base of tectonic features on Oberon, Titania and Miranda (Croft and Soderblom 1991).

Mass wasting processes require oversteepened slopes and triggering mechanisms to set material into downslope motion: (a) comminution of, or lowering of cohesion in, surface materials by mechanical “weathering”, either by solar insolation over diurnal periods, or by impacts of micrometeorites or larger projectiles; and (b) seismic effects, caused by tectonic stress or by impacts (Chuang and Greeley 2000). The processes, which are often prerequisite for mass wasting, such as impact gardening, sputtering, or sublimation, are described in the following in more detail.

### 10.5.2 Impact Gardening

Gardening and contamination of the surface by impacting material, i.e. infalling (micro-) meteoritic debris or secondary debris from larger impacts, is a dominant surface process on airless icy satellites, forming a regolith of pulverized and mixed surface materials (Shoemaker et al. 1982). Impacts erode pre-existing craters or

## Surface degradation on icy satellites (I)

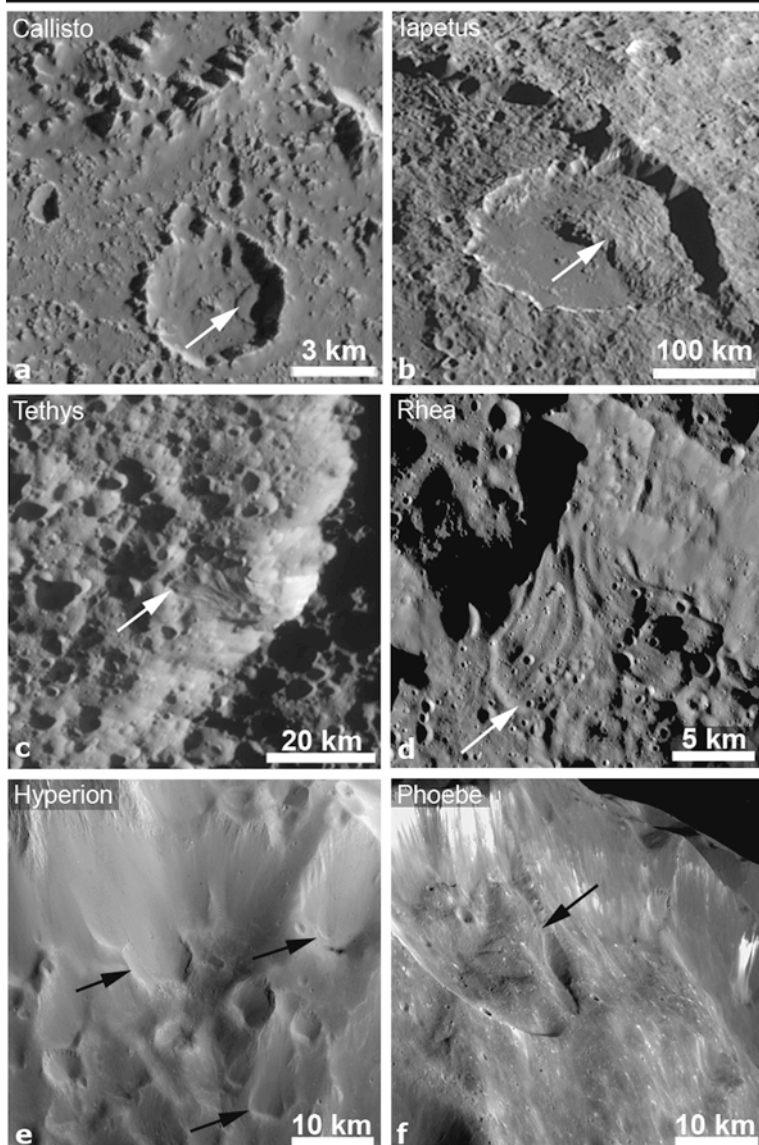


**Fig. 10.20** Examples of mass wasting on airless satellites of Jupiter and Saturn (indicated by arrows): (a) Landslides at the interior wall of impact craters on (a) Callisto, (b) Iapetus, (c) Tethys (crater Penelope), (d) Rhea; as well as mass wasting on inner walls of large craters on (e) Hyperion and (f) Phoebe (Crater Erginus)

## Surface degradation on icy satellites (II)

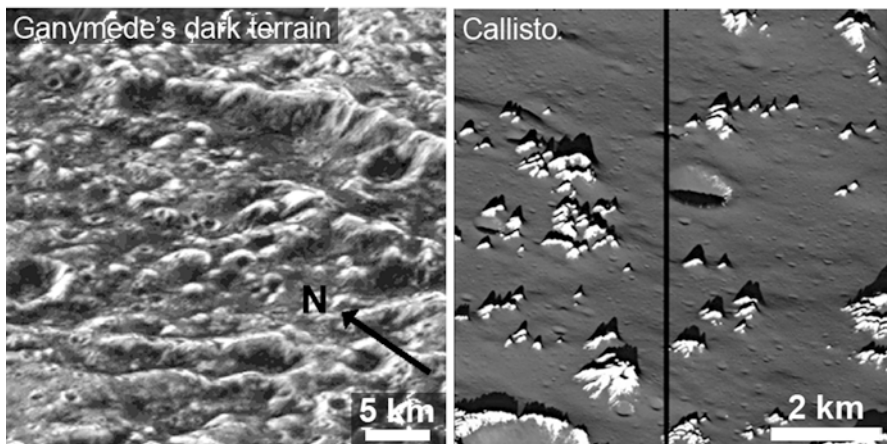


**Fig. 10.21** Surface degradation on Ganymede (left) and Callisto (right)

other, topographically high-standing landforms, cover them by redistribution of ejecta, or subdue underlying surface features (Moore et al. 1999).

Impact gardening affects all icy satellite surfaces but can be observed primarily in geologically old regions. Thus, on Europa’s young surface, which appears sufficiently uncratered, the effects of impact gardening would not be seen (Moore et al. 1999). In contrast, the topography of the geologically old dark terrain on Ganymede appears “softened” at small scales (Fig. 10.21) when compared to younger grooved terrain (Sect. 10.3.2), particularly in the rounded crests of crater rims and furrows, which Prockter et al. (1998) attributed to micrometeoritic bombardment. Although impact cratering appears to be the dominant process in the evolution of Callisto’s surface, it cannot account for the highly degraded surface of Callisto (Moore et al. 1999) (Fig. 10.21). Callistoan mass movements are probably caused by sublimation-driven landform modification (Moore et al. 1999; Chuang and Greeley 2000), which is described below.

Impact gardening probably plays a more important role on the Saturnian satellites characterized by geologically old, densely cratered surfaces like Mimas, Tethys, Dione, Rhea and probably also Hyperion and Phoebe causing the pulverization of surface material resulting in a fine regolith that covers the surfaces of these bodies (Wagner et al. 2006, 2007a, b; Jaumann et al. 2009a; Stephan et al. 2010; Spencer and Denk 2010).

### 10.5.3 Sputtering

Collisions of high-energy ions from planetary magnetospheres; solar wind particles and/or cosmic rays causes sputtering, i.e. the ejection and redistribution of

molecules (predominantly H<sub>2</sub>O ice molecules) in the upper layer of the surface material. The potential effect of sputtering due to magnetospheric particles decreases substantially with increasing distance from the planet (Moore et al. 1999). Satellites orbiting outside the magnetospheres are rather influenced by the solar wind.

Thus, sputtering should be strongest on Europa compared to Ganymede and Callisto. The sputter ablation rate was estimated to be of the order of roughly 200 m/Ga (Ip et al. 1998). If the age of Europa's landscape is not greater than 10<sup>8</sup> years as suggested by Zahnle et al. (2003) and Chapman et al. (1998), then sputtering could only play a role detectable at small scales (Moore et al. 1999). The effectiveness of sputtering on H<sub>2</sub>O ice is 20 times less at Ganymede and 100 times less at Callisto than at Europa (Johnson 1990). The magnetic field of Ganymede (Kivelson et al. 1996) probably further shields this satellite from the effects of sputtering. Estimates of particle fluxes and H<sub>2</sub>O ice sputtering rates suggest an erosion rate of ~80 cm/Ga in Ganymede's equatorial region, which is two orders of magnitude less than the expected sublimation rate (Cooper et al. 2001). Sputter ablation will be reduced by the presence of a refractory lag deposit, and impact gardening would distribute sputter-produced chemical products throughout the regolith. If sputtering rates were greater than the rate of thermal sublimation, the surface should be rehomogenized at timescales faster than those required to segregate it into dark and bright patches (Spencer 1987). Therefore, the presence of extreme albedo variations within dark terrain implies that sublimation does occur at a significantly higher rate than sputtering. It is therefore unlikely that sputtering is a major influence on dark terrain surface morphology, at least in the non-polar regions (Pappalardo et al. 2004). Sputter ablation rates on Callisto are presumably lower than on Ganymede and of minor importance (Moore et al. 2004b).

Although the net energy flux into the icy surfaces in the Saturnian magnetosphere is smaller than that at Europa and Ganymede (Johnson et al. 1982, 2008; Mauk et al. 2009), the surfaces of the inner Saturnian satellites up to the orbit of Rhea are eroded by the incident plasma. Evidence for the interaction of the magnetospheric particles and the icy surfaces are often manifested in albedo variations across the surfaces (Schenk et al. 2011), distribution of dark material on the trailing hemispheres of Dione (Clark et al. 2008; Stephan et al. 2010) and Rhea (Stephan et al. 2011) but also in the existence of radiolytic products like O<sub>3</sub> within the surface material, similar to what has been found on Europa (Spencer and Calvin 2002) and Ganymede (Noll et al. 1997), and/or in the form of a tenuous atmospheres of O<sub>2</sub> around Dione and Rhea (Teolis et al. 2010) resulting from the radiation-induced decomposition of the surface ice. Recently, a tenuous atmosphere of CO<sub>2</sub> around Rhea could be identified that possibly results from the decomposition of organic material on Rhea's trailing hemisphere (Teolis et al. 2010). It is questionable, however, if sputter ablation has a significant effect onto landform degradation on the surfaces of the Saturnian satellites. Probably, the only process relevant for this is impact gardening (see above Sect. 10.5.2).

### 10.5.4 Sublimation

Landform degradation due to sublimation has been proposed in particular for the icy Galilean satellites (Moore et al. 1996, 1999; Prockter et al. 1998). Thermal segregation models (Spencer 1987) predict that dirty ice, as it occurs on the icy Galilean satellites, will evolve rapidly due to the high sublimation rate (meters per million years) of dark warm ice (Spencer et al. 1998). Spencer (1987) stated that micrometeorite bombardment and charged-particle sputtering are probably insufficiently rapid to prevent segregation from happening.

Sublimation was used to explain the local albedo variations in the northern polar regions of Callisto (Spencer and Maloney 1984) and Ganymede's dark terrain (Fig. 10.21) (Prockter et al. 1998) with poleward-facing slopes at high latitudes covered by a thin H<sub>2</sub>O frost veneer, which are colder and their surroundings. Thus slopes are the preferred location for ice accumulation in contrast to the opposite sun-facing slopes that show a concentration of dark material. Impact gardening competes with sublimation, mixing lag deposits or recondensed frosts back into the subsurface. Prockter et al. (1998) concluded that sublimation is the primary process responsible for the albedo heterogeneity of the dark terrain Galileo Regio at small scales, and it may add in mass wasting, but they doubt that sublimation contributes significantly to the degradation of large-scale morphology at that location, which they rather relate to impact gardening (see above). Possibly, sublimation plays a role in the formation of Ganymede's polar caps, although detailed studies showed that because of extremely low temperatures in the polar regions, thermal migration is incapable of transporting water beyond a latitude of ~50° (Purves and Pilcher 1980; Shaya and Pilcher 1984).

Of all icy satellites, Callisto's surface is the most degraded one, featuring landforms unique to this body (Fig. 10.21) (Moore et al. 1999). At high resolution, Callisto's surface is dominated by two primary landforms: (a) bright hummocks or massifs, or groups of massifs, and (b) a globally abundant blanket of smooth, undulating dark material (Moore et al. 1999, 2004b; Greeley et al. 2000). The massifs give the surface a knobby appearance. Erosion and surface degradation on Callisto is dominated by sublimation which is caused by (a) solar insolation in a diurnal cycle, (b) compositional differences in the icy crust, and (c) possibly pre-existing zones of weakness created by early tectonism (Moore et al. 1999, 2004a; Wagner 2007). Sublimation on Callisto may be triggered by the presence of material more volatile than H<sub>2</sub>O-ice, with CO<sub>2</sub> being the most likely candidate species (Moore et al. 1999). An abundance of CO<sub>2</sub> in Callisto's crust is supported by the presence of a tenuous carbon dioxide atmosphere created by outgassing (Carlson et al. 1999). The following sequence of events could have caused the evolution of landforms by sublimation degradation on Callisto (Moore et al. 1999, 2004b; Wagner 2007): The host material is a bright mixture of ice-/non-ice species (McCord et al. 1998). On-going sublimation causes the separation of more volatile from less volatile materials. Due to spatial differences in the physical properties of the host material which as a consequence resists differently to sublimation, bright material evolves into massifs and hummocks, surrounded by debris aprons of dark

material. With continuing sublimation, hummocks and massifs degrade with time. Eventually, hummocks and massifs can disappear, and the aprons around former massifs coalesce and create a uniform blanket of dark material which embays the most resistant massifs (Wagner 2007). The apparent rarity of large-scale sublimation-driven landform modification of Ganymede relative to Callisto may be the consequence of fewer near-surface deposits containing substantial amounts of CO<sub>2</sub> (Moore et al. 1999).

It is expected that for Rhea and all colder objects (maximum diurnal temperature <100 K) as well as for Enceladus due to its extremely high albedo (0.81), H<sub>2</sub>O sublimation is negligible (Spencer and Denk 2010). The interplay of sublimation and impact gardening might be more complex on Phoebe and the bright side of Iapetus. Their long rotation periods (~79 and ~550 days) yield substantially higher daytime temperatures for a given albedo than on the Saturnian satellites. Because there is more time for temperatures to equilibrate with sunlight a smaller fraction of the absorbed sunlight is reradiated from the night side (Spencer and Denk 2010).

The only place in the Saturnian system, where sublimation is expected to play an important role at least in the production of a residual regolith covering the surface, is on the leading hemisphere of Iapetus (Spencer and Denk 2010). Even though, the dark material concentrated here might originate either from a heliocentric source or, more probably, from Saturn's outer retrograde satellites, its deposition further increases surface temperatures there up to ~130 K, and has by far the highest sublimation rate of H<sub>2</sub>O ice (>100 m/Ga) on any Saturnian satellite until sublimation is cut off by a formation of a dark, ice-free lag deposit on the leading hemisphere (Spencer and Denk 2010).

A surface unit unique to Triton is termed *cantaloupe terrain* and is composed of pits and dimples, with a spatial extent of several kilometers up to 25 km across (Smith et al. 1989; Stone et al. 1989). Collapse and degradation by extensive sublimation of surface materials has been invoked as a likely process for the formation of these landforms (Smith et al. 1989). Sublimation of matrix-forming material also has caused mechanical weakening of material exposed in scarp resulting in the recession of these scarp with time (Moore et al. 1996, 1999).

### **10.5.5 Interaction Between Surface and Atmosphere**

Titan is the only satellite that exhibits a substantial atmosphere enabling the interaction between the surface and the atmosphere not seen on any other satellite (Prockter et al. 2010). Remarkably, Titan shows all major exogenic geological processes that are known to cause surface erosion and degradation on Earth either caused by wind or liquids and which are still going on. Sediments on Titan are believed to consist of H<sub>2</sub>O-ice, derived from Titan's lithosphere, mass wasting and fluvial processes (Lorenz and Lunine 1996; Griffith et al. 2003) and organic material, which settles from the atmosphere after formation by photochemical reactions of hydrocarbons (Khare et al. 1978; Tran et al. 2003; Lorenz and Lunine 2005).

It has been long predicted that lakes or even seas of liquid hydrocarbons exist on Titan's surface (e.g., Lunine et al. 1983; Lunine 1993), which would be necessary as a reservoir to resupply Titan's atmospheric methane (Yung et al. 1984). First evidence of surface liquids provided images taken by the DISR instrument aboard the Huygens probe showing a dendritic drainage system of channels similar to terrestrial river systems (Fig. 10.22b) (e.g. Tomasko et al. 2005; Soderblom et al. 2007; Lorenz et al. 2008a), which are presumed to be formed by precipitation and runoff of methane rainfall out of frequently occurring tropospheric clouds (e.g. Griffith et al. 1998, 2005, 2006; Porco et al. 2005b; Schaller et al. 2006a, b; Jaumann et al. 2008; Turtle et al. 2009). The river system terminates in a large basin, which did not seem to contain liquids at present since Huygens landed on a solid surface. Images of the landing site showed a number of rounded pebbles, which conclusively indicate transportation and deposition by fluid material (Keller et al. 2008). Since then, features resulting from fluvial erosion are distributed across the entire surface of Titan. The only regions where fluvial features are almost entirely missing are the vast dune fields in the equatorial region (Elachi et al. 2006; Porco et al. 2005b; Lunine and Atreya 2008; Lorenz et al. 2008b; Jaumann et al. 2008). Cassini RADAR data indicate very shallow channels with almost no apparent depth suggesting an easily erodible substrate, as well as channel systems cutting more than 100 m deep into an apparently more resistant bedrock (Lorenz et al. 2008b).

Next to the fluvial systems Cassini revealed a myriad of surface features in the northern polar region of Titan that morphologically resemble lakes on Earth (e.g. Stofan et al. 2007; Lopes et al. 2007). Their low radar backscatter signal is indicative of an exceedingly low-dielectric material such as liquid methane, likely mixed with liquid ethane (Fig. 10.22c) (e.g. Stofan et al. 2007; Lopes et al. 2007). Spectroscopic evidence that these lakes are actually filled with liquid ethane could be confirmed for one of the few lake-like features in the southern polar region, named Ontario Lacus (Brown et al. 2008). Further evidence confirming the presence of liquids on Titan's surface was the detection of a specular glint from one of Titan's northern lakes (Stephan et al. 2010). All of the lakes identified to date occur at high latitudes ( $\geq\sim 55^\circ$ , e.g. Stofan et al. 2007; Hayes et al. 2008; Brown et al. 1990; Turtle et al. 2009). This is consistent with the atmospheric models, which suggest that over a Saturnian year, liquid is transported from the equatorial region to the poles, where it falls as rain (Mitchell 2008). Intriguingly, repeated imaging of Titan's surface illustrates ongoing changes in the lake level (Turtle et al. 2009) including ponding of liquids on the surface in the south polar region due to precipitation from methane rain and retreating of the shoreline of Ontario Lacus of more than several kilometers (Turtle et al. 2009; Hayes et al. 2008), and even the disappearing of lakes during southern summer (Hayes et al. 2010). So far, Cassini's observations only extend through Titan's southern autumnal equinox – it will be interesting to follow seasonal changes in weather patterns, especially the precipitation at lower latitudes as northern spring processes.

Transport and deposition of eroded material on Titan is indicated by the presence of elongated dark subparallel surface features (Fig. 10.22 a), which were interpreted

## Surface degradation on Titan

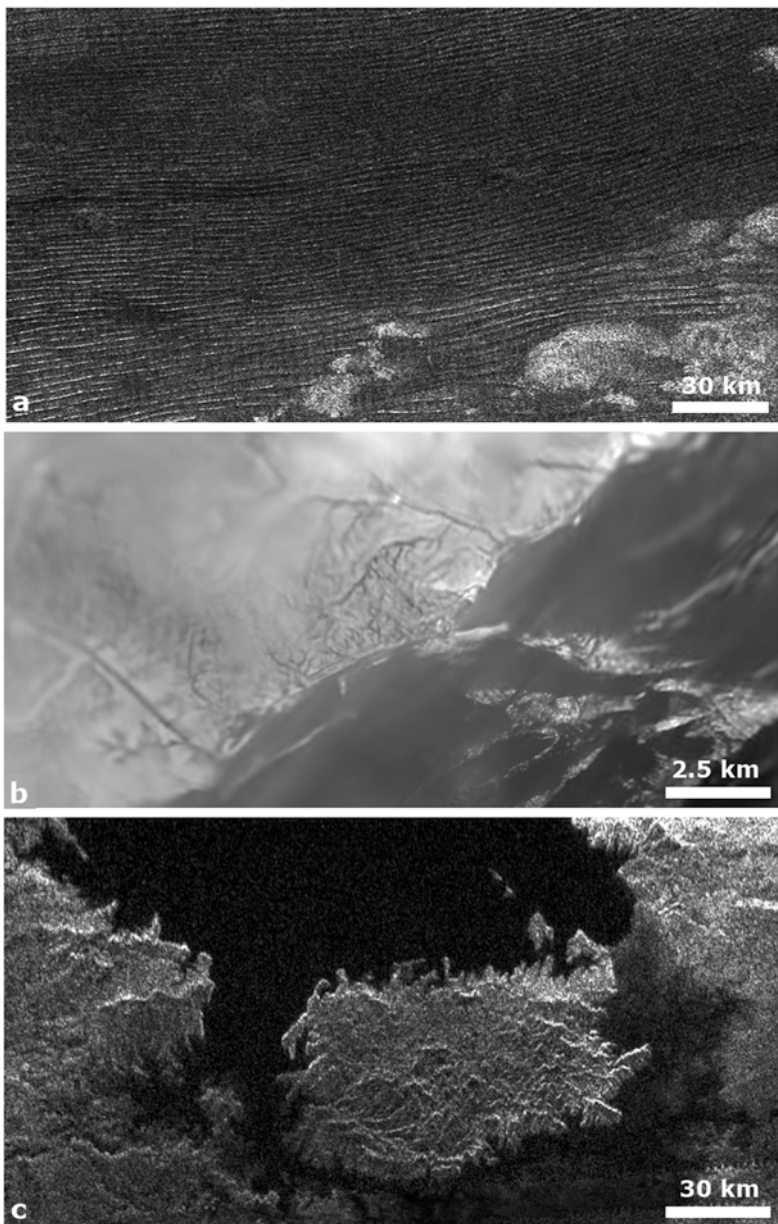


**Fig. 10.22** Evidence for aeolian and fluvial processes on Titan's surface: (a) Titan's longitudinal dunes, which cover most of Titan's equatorial regions. The dunes embay high-standing topographic obstacles (*bright* features) following the prevailing wind pattern; (b) a dendritic system of channels that incise the *bright* highlands, as viewed by the Descent Imager/Spectral Radiometer (DISR) during the descent of the Huygens probe, debouching into the *dark*, probably dry lakebed, where the Huygens probe landed (Tomasko et al. 2005) and (c) that shows *rounded pebbles* with sizes of ~15–20 cm indicating transport and deposition by a fluid; (d) a part of one of Titan's large radar-dark features (Kraken Mare) in the northern polar region indicating lakes filled with hydrocarbons

as vast fields of dunes made of organic material and deposited onto a bright substrate (Elachi et al. 2006; Lorenz et al. 2006). The predominantly longitudinal dunes cover large areas of the equatorial region between 30° N and S. The limited extent of river channels (see above) cannot account for this large volume of sediments, and the large-scale sediment transport processes on Titan remain an enigma (Lorenz et al. 2008b). A photochemical origin is now predicted for the dune material i.e. it is supposed to originate from atmospheric haze particles (Lorenz et al. 2008b; Prockter et al. 2010) and transported by a global wind system to the equator (Radebaugh et al. 2008). These dunes are typically 2 km wide and between 30 and 70 m high (Lorenz and Radebaugh 2009). They are primarily E-W oriented, which implies a material transport from W to E (Porco et al. 2005b; Radebaugh 2009). Although meteorological models support a “dry” equatorial region (e.g. Mitchell 2008), a W-E oriented wind regime is still difficult to explain with the atmospheric circulation models, which suggest a predominance of westward flows at low latitudes (Tokano 2008; Prockter et al. 2010).

The only satellite other than Titan, where evidence of erosion, transport and deposition by wind could be identified is Triton. Triton’s atmosphere is also dominated by N<sub>2</sub>, with traces of other compounds such as CH<sub>4</sub> at low latitudes near the surface (Stone et al. 1989). Dark streaks that were interpreted as volcanic plumes (Smith et al. 1989; Stone et al. 1989) or dust devils (Ingersoll and Tryka 1990) are abundant in the southern polar ice cap (see Sect. 10.4 and Fig. 10.19d). The streaks extend over several 10’s of kilometers up to 100 km. They are concentrated between 10° and 30° S and are preferentially oriented SW-NE indicative of a dominant wind direction (Smith et al. 1989).

## 10.6 Summary and Geological Evolution of Icy Satellites

Compared to terrestrial planets, the icy satellites in the outer Solar system show a great and unanticipated variety of surface features with (1) geologically old surfaces dominated by impact craters of varying size and morphologies, (2) tectonized regions expressed by diverse, mostly extensional, styles of deformation, as well as (3) present-day cryovolcanic activity. Geyser-type cryovolcanism on Enceladus ejecting icy material hundreds of kilometers into space forms Saturn’s E ring.

Impact events as well as surface degradation are observed on all of these satellites. The geologically oldest surfaces, such as those on Callisto, are heavily cratered and show a wealth of different impact crater morphologies (Sect. 10.2). Some of these impact crater morphologies are unique to outer solar system bodies owing their appearance to the rheological properties of H<sub>2</sub>O ice. Large impact basins several hundreds or even thousands of kilometers in diameter are common in the old surfaces. Younger, morphologically fresh craters superimposed on these oldest units in some cases feature bright rays which may extend several hundreds of kilometers. Differences in crater morphologies and relaxation state provide

information about crustal thickness and internal heat flow at the time of the impact event (e.g., Schenk et al. 2004, and references therein).

The degree of erosion and degradation on the airless satellites varies from body to body (Prockter et al. 2010, and references therein). Best indicators for such processes are variabilities in impact crater freshness, such as, e.g., eroded ejecta materials, or partial crater rims. Mass wasting on crater walls or tectonic features also imply surface degradation. In addition, sublimation processes driven by solar insolation during day-night cycles cause the degradation of landforms. On Titan with its dense atmosphere erosion and degradation by wind and by liquids as on Earth can be observed (Prockter et al. 2010).

The frequency of tectonic forms also varies from satellite to satellite. Whereas compressional deformation is rare, extensional deformation is common on the icy satellites. The wide variety in the extent of extensional tectonic activity on the icy satellites is accompanied by a variety of their distribution in time, suggestive of tectonic period(s), that defies a simple explanation. The total extent of tectonic deformation varies (siehe oben 43,3,4) (Prockter et al. 2010, and references therein): (a) The surfaces of Callisto, Mimas and Iapetus are barely deformed. (b) Horst-and-graben systems often extend across a whole satellite, such as on Tethys, Dione, Rhea, and on the Uranian satellites Ariel, Umbriel, Titania and Oberon. (c) Complex systems of grooves and ridges characterize the bright terrain on Ganymede, or the regions termed *coronae* on Miranda. (d) Peculiar ridges and bands were possibly formed in association with cryovolcanism on the heavily deformed and probably currently active satellites Europa, Enceladus and Triton.

Sources of stresses which created these forms also vary from satellite to satellite. There is no straight-forward relationship between the degree of geological activity and tidal stresses (e.g. Nimmo and Pappalardo 2006; Matsuyama and Nimmo 2007, 2008; Schenk et al. 2008; Spencer et al. 2009; Hussmann et al. 2010). Present-day diurnal tidal stresses are less important except on Europa, Enceladus and probably Triton (Collins et al. 2009; Spencer et al. 2009; Hussmann et al. 2010). Global expansion due to phase changes of ice and, as a consequence, volume changes may explain the formation of Ganymede's bright terrain (Pappalardo et al. 1998b). The coherent global tectonic networks on Dione and Rhea (and possibly Tethys), and on some Uranian satellites are suggestive of global mechanisms such as tidal despinning, reorientation, or global expansion due to volume changes which probably occurred early in the histories of these satellites (Thomas et al. 2007; Jaumann et al. 2009a).

Except for Enceladus and Triton there is no unquestionable evidence of cryovolcanic activity in the outer solar system from surface imaging, topographic measurements, or from remote sensing of satellite atmospheres. Smooth plains with lower superimposed crater frequency, such as those on Dione were assumed to originate from cryovolcanism (e.g., Plescia 1983). Cassini ISS data, however, could not support a cryovolcanic origin for these units (Wagner et al. 2006). A possible volcano-tectonic origin of smooth plains associated with fractures on Dione has been re-assessed by Schenk and Moore (2009).

Although there have been some attempts to put all the observed geological processes into a time sequence by correlating crater frequencies with impact rates

of potential impactors, e.g., comets or asteroids, no consistent interpretation of the crater chronology in the outer solar system has been developed so far to update the existing model chronologies i.e. the lunar-like impact chronology model (Neukum et al. 1998) and the cometary, constant-rate bombardment history model (Zahnle et al. 1998, 2003; Dones et al. 2009). To date, no formula exists to calculate absolute ages from crater frequencies for the Nice impact cratering chronology (Model III).

However, these models may help to compare the geological histories of the icy satellites in a stratigraphic sense. Thus, chronology models I and II (Neukum et al. 1998, 2005; Zahnle et al. 1998, 2003) were included in the diagram of Fig. 10.23, which shows a summary of the current knowledge of how the major geological processes evolved through time on each of the icy satellite, separate for impact processes, erosion and degradation, tectonism, and cryovolcanism. Because of the strong dependence of ages of the model chronologies applied, and also because of differences in crater counts (and their interpretation) performed by various groups we did not include absolute model ages at the abscissa of these diagrams.

As noted before, all satellites are influenced by impact events throughout their history. The lunar-like model (Neukum 1985, 1997; Neukum et al. 1998, 2005, 2006) with an exponentially declining cratering rate in the first ~800 Ma is reflected in the thicker bar merging into a thinner bar, representing the constant cratering rate since ~3.3–3 Ga continuing to the present. The thin bar also represents the constant cratering rate model by Zahnle et al. (1998, 2003) (continued as a dashed line towards the earliest times). Note that for simplicity, we used the same bar thickness for constant cratering rates but these are different in the two models.

Despite the discrepancies between these chronology models, most heavily cratered surfaces are stratigraphically old with the oldest surfaces on the icy satellites i.e. the heavily cratered plains exhibiting ages of about 4 Ga years, which is similar throughout the outer solar system and consistent between Model I and II (Neukum et al. 1998; Zahnle et al. 1998, 2003).

The dark densely cratered plains on Callisto and Ganymede are on the order of 4 Ga and older in Model I and II (Neukum et al. 1998; Zahnle et al. 1998, 2003; Pappalardo et al. 2004; Schenk et al. 2004). Based on the lunar-like impact chronology models the ages of the densely cratered surfaces of the icy Saturnian satellites were estimated to be on the order of 3.8–4 Ga old (Plescia and Boyce 1983; Boyce and Plescia 1985; Neukum 1985; Neukum et al. 2006), and high ages (>4 Ga) were implied for the heavily cratered regions on each satellite using the cometary, constant-rate bombardment history model (Zahnle et al. 2003; Dones et al. 2009). Also the surface ages of heavily cratered regions on the five major Uranian satellites Miranda, Ariel, Umbriel, Titania and Oberon, which were obtained from Voyager images are mostly old (order of 4 Ga), keeping in mind that, except for Miranda and Ariel, the resolution of the Voyager images is low (Plescia 1987, 1988; Zahnle et al. 2003).

On the Jovian satellite Callisto as well as on the Saturnian satellites Mimas, Hyperion and Phoebe impact cratering and degradational processes driven by sublimation, radiation, and micrometeoroid bombardment are the dominant processes that have shaped the surface with time (Schenk 1995; Greeley et al. 2000; Moore et al. 2004a; Wagner 2007; Jaumann et al. 2009a). Tectonism was possibly

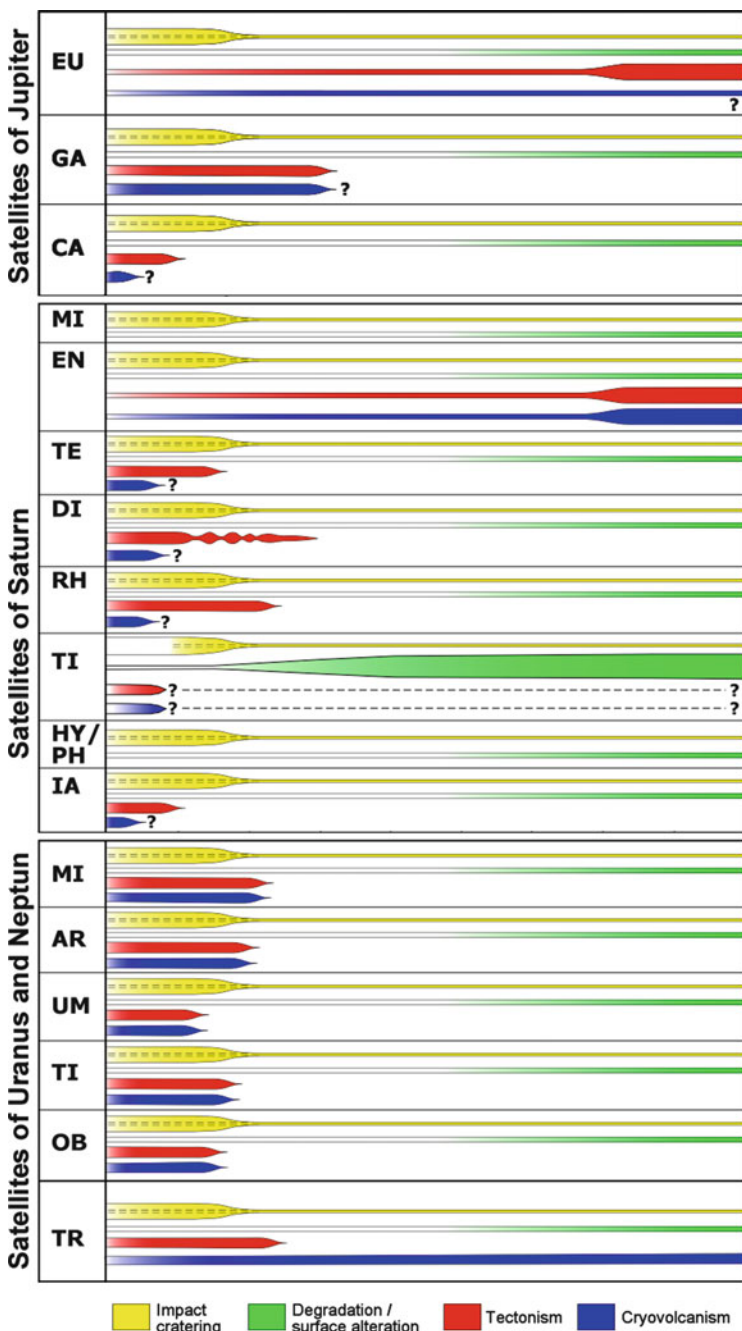


**Fig. 10.23** Comparison of the relative timing of the major geologic processes on the icy outer planet satellites. A detailed explanation of the diagrams is given in text. The abscissa represents a relative time scale, with the earliest history of the satellites at the *left* (after their formation 4.4–4.5 Ga ago) and the present at the *right*

active in the early history of these bodies and created a fracture system which provided zones of weakness for erosion and degradation (Moore et al. 2004a; Wagner 2007). If ever cryovolcanism took place on Callisto, which is questionable, it is no longer recorded (Moore et al. 2004b; Wagner 2007). Mimas also shows local evidence for tectonism, but this may have been linked to large impact events, such as the formation of the 139-km basin Herschel (tectonic processes on Mimas were therefore not included in the diagram) (Jaumann et al. 2009a).

In contrast to the geologically old surfaces, greater variety in surface ages as well as in the disparity between chronology models I and II exists for the geologically younger tectonically resurfaced regions on Ganymede (taking into account that the derivation of accurate (upper) ages is strongly dependent on the available image data). Tectonism has lasted for a longer time and may have been active until 1–2 Ga ago (Schenk et al. 2004). The role of cryovolcanism has been reported to be less than anticipated from Voyager data (e.g., Pappalardo et al. 2004). Cryovolcanic processes could have been linked to tectonism and may have ceased at about the same time (indicated by a question mark). As on all Galilean satellites, landforms indicating erosional and degradational processes can be observed. These processes most likely were active throughout their histories (Moore et al. 1998; Greeley et al. 2000, 2004; Moore et al. 2004b; Pappalardo et al. 2004).

Voyager data revealed that Tethys, Dione and Rhea have experienced tectonism in the past, with varying degree from satellite to satellite (Moore 1984; Moore and Ahern 1983; Moore et al. 1985; Plescia 1983). Among these three satellites, Dione appears to be the most evolved satellite. Cassini ISS imaged these tectonized regions on these three satellites at much higher resolution and revealed several episodes of tectonic deformation on Dione (Wagner et al. 2006; Stephan et al. 2009). The almost satellite-encircling graben system, Ithaca Chasma, dominates the surface of Tethys (Moore and Ahern 1983). It was discussed that its formation could have been caused by the major impact event of the large basin Odysseus (e.g., Moore et al. 2004a). Detailed investigation of Tethys using stereo images showed, however, that Ithaca Chasma appears to predate Odysseus and hence could not have been created by the impact (Giese et al. 2007a). On Rhea, new imaging data obtained by Cassini in November 2009 revealed that tectonic activity on the trailing hemisphere has persisted for an unexpectedly longer time than anticipated, despite the globally abundant dense crater distribution, inferring a high surface age and little geologic evolution of Saturn's second-largest satellite (Wagner et al. 2010).

Cryovolcanism has been invoked to be responsible for smooth plains observed on these three satellites and for the *wispy terrain* on the trailing hemispheres of Dione and Rhea (Moore 1984; Moore and Ahern 1983; Moore et al. 1985; Plescia 1983). Moore and others (1984) mapped troughs in the *wispy terrain*, implying that tectonism is associated with cryovolcanic processes in this region. ISS images do not show unequivocal evidence for cryovolcanism on these satellites; instead, a predominantly tectonic origin of the *wispy terrain* could be confirmed by ISS images (Wagner et al. 2006, 2007b, 2008, 2010).

Iapetus is dominated by impact cratering but also by the equatorial ridge indicating early tectonism. Cryovolcanism could have taken place, like on the

other satellites, but is questionable (e.g., Jaumann et al. 2009a). Based on the lunar-like impact chronology models the resurfaced terrains, e.g. on Dione (as well as Enceladus), may have formed less than 1.5 Ga ago (Boyce and Plescia 1985; Neukum 1985; Neukum et al. 2006). The cometary, constant-rate bombardment history model (Zahnle et al. 2003) implies very young ages for the resurfaced terrains on e.g. Enceladus (order of  $<< 1$  Ga) (Dones et al. 2009).

Much less is known about the time scale of geological processes on the satellites of Uranus because of the lack in global image coverage at medium or high resolution. Figure 10.23 shows that Miranda and Ariel appear to be the most evolved ones of the major Uranian satellites and have experienced tectonic deformation as well as, possibly, have undergone cryovolcanic activity (Croft and Soderblom 1991, and references therein). These processes could have taken place on the other three satellites Titania, Umbriel and Oberon also but are difficult to verify because these three satellites were the least ones imaged by Voyager 2. Titania shows a younger resurfaced terrain with ages of 2–3 Ga (Zahnle et al. 2003). The tectonically and/or cryovolcanically resurfaced units on Ariel and Miranda could be much younger, possibly only several 100 Ma (Zahnle et al. 2003).

Europa in the Jovian system, Enceladus (and Titan) orbiting Saturn and Triton, the largest satellite of Neptune show the highest complexity of geologically resurfacing. For Europa a possibly higher cratering rate (heavy bombardment) in its history is included in Fig. 10.23, as for Ganymede and Callisto, but all of this record is lost in its crater distribution because of the intense tectonic deformation at more recent times (e.g., Greeley et al. 2004; Schenk et al. 2004). The low frequency of craters superimposed on the surface of Europa implies an even much younger surface age much younger than the surfaces of its neighbors Ganymede and Callisto (Smith et al. 1979b; Lucchitta and Soderblom 1982). The average age of Europa could be 30–70 Ma in the comet impact chronology model II (Zahnle et al. 2003). With the asteroid/lunar-like chronology model I, much higher average surface ages on the order of 1 Ga are obtained for Europa, but individual geological units can also be as young as ~200 Ma or less (Neukum et al. 1998). Tectonism has played a major role at recent times on Europa, indicated by a thicker bar towards the present. Tectonism could have been more or even less intense in the past, but none of this intensity is recorded. Therefore we used a thinner bar back to the earliest history, but this representation of tectonic activity is open to debate. Cryovolcanic features on Europa are observed. The search for active cryovolcanism at present, e.g., plume vents, was not successful, but its existence cannot be ruled out and therefore remains an open issue (indicated by the question mark) (Phillips et al. 2000; Greeley et al. 2004, and references therein). On Saturn's largest satellite Titan, Cassini RADAR data show only a small number of large impact features, implying that most of the ~20–30% of its surface investigated by radar to date is very young (Stofan et al. 2006; Jaumann and Neukum 2009; Wood et al. 2010).

Triton exhibits a surface with very low crater frequency implying a comparably young age (Croft et al. 1995). Several groups have worked on crater distribution on Neptun's satellite Triton and concluded that its surface could be not older than

several Ma up to 600 Ma (Zahnle et al. 2003, and references therein), or surface ages in specific ages could even be negligible, as pointed out by Schenk and Zahnle (2007). The bodies in the Neptunian system may have experienced a heavy bombardment period which is recorded on the smaller satellites, but it is lost on Triton due to geologic activity at later times and even at present on the largest satellite of Neptune. Cryovolcanism, confirmed by the presence of geyser-like activity, could have taken place throughout its history (Croft et al. 1995). Tectonic features reminiscent of ridges and fractures on Europa or Enceladus could be comparably young.

Enceladus is the geologically most active one of the airless icy moons of Saturn. As for Europa, it cannot be verified if cryovolcanism and tectonism were more or less intense in the past than they are today. However, a period of more intense impact bombardment is, at least to some degree, recorded in some areas on Enceladus.

Much work remains to be done to fully understand the geologic history and ongoing geologic processes of the icy outer planet satellites. For many satellites, we still lack complete global imaging coverage at a resolution sufficient to distinguish geologic features on their surfaces.

The next few years of the Cassini mission, as well as plans for new flagship missions into the outer solar system which are currently in discussion will hopefully provide a continuing flood of data helping to map and characterize in detail the surface features presented and discussed in this chapter. Understanding the origins of these structures and the histories of the satellites will require geological (including compositional) and geophysical investigations which would give us more solid foundation for understanding the behavior of icy lithospheres and the forces shaping them. In particular, ongoing observations of Europa, Enceladus or of other modified bodies provide the possibility to study geologic processes like impact cratering, tectonics and active cryovolcanism and their occurrence and importance in the histories of these outer solar system bodies. In the context of comparative satellite geology, this may lead to a better understanding of icy satellites which were more active in a distant past than at recent times or even today and also may improve the understanding of their composition (including the possible existence of liquid material underneath their surfaces), their thermal and as well as their orbital evolution, including possible tidal stress.

**Acknowledgments** We thank H. Hussmann for his valuable comments and an anonymous reviewer for his careful review that significantly improved this chapter. This work has been partly supported by DLR and the Helmholtz Alliance ‘Planetary Evolution and Life’.

## References

- Allison ML, Clifford SM (1987) Ice-covered water volcanism on Ganymede. *J Geophys Res* 92:7865–7876  
Alzate N, Barlow NG (2011) Central pit craters on Ganymede. *Icarus* 211:1274–1283

- Arvidson RE, Boyce J, Chapman C, Cintala M, Fulchignoni M, Moore H, Neukum G, Schultz P, Soderblom L, Strom R, Woronow A, Young R (1979) Standard techniques for presentation and analysis of crater size-frequency data. *Icarus* 37(2):467–474
- Asphaug E, Benz W (1996) Size, density, and structure of Comet Shoemaker-Levy 9 inferred from the physics of tidal breakup. *Icarus* 121(2):225–248
- Baldwin RB (1963) *The measure of the Moon*. University of Chicago Press, Chicago
- Baldwin RB (1964) Lunar crater counts. *Astron J* 69(5):377–392
- Baldwin RB (2006) Was there ever a Terminal Lunar Cataclysm? With lunar viscosity arguments. *Icarus* 184(2):308–318
- Barlow NG (2009) Martian central pit craters: summary of Northern Hemisphere results. In: *Lunar and planetary science conference*, The Woodlands, Texas, XL. Abstract 1915, 23–27 March 2009
- Barr AC, Preuss LJ (2010) On the origin of south polar folds on Enceladus. *Icarus* 208:499–503
- Beeman M, Durham WB, Kirby SH (1988) Friction of ice. *J Geophys Res* 93:7625–7633
- Billings SE, Kattenhorn SA (2005) The great thickness debate: ice shell thickness models for Europa and comparisons with estimates based on flexure at ridges. *Icarus* 177:397–412
- Bland MT, Showman AP (2007) The formation of Ganymede's grooved terrain: numerical modeling of extensional necking instabilities. *Icarus* 189(2):439–456
- Bland MT, Beyer RA, Showman AP (2007) Unstable extension of Enceladus' lithosphere. *Icarus* 192(1):92–105
- Bland MT, Showman AP, Tobie G (2009) The orbital–thermal evolution and global expansion of Ganymede. *Icarus* 200(1):207–221
- Boyce JM (1993) A structural origin for the cantaloupe terrain of Triton. In: *Lunar and planetary science conference*, Houston, Texas, XXIV. 24(Part 1: A-F (SEE N94-12015 01-91)), pp 165–166, 15–19 March 1993
- Boyce JM, Plescia JB (1985) Chronology of surface units on the icy satellites of Saturn. In: *Ices in the solar system. Proceedings of the advanced research workshop*, Nice, 16–19 Jan 1984 edited, D. Reidel, Dordrecht, pp 791–804
- Bray VJ, Smith DE, Turtle E, Perry J, Rathbun J, Barnash AN, Helfenstein P, Porco CC (2007) Impact crater morphology variations on Enceladus, In: *Lunar and planetary science conference*, League City, Texas, XXXVIII. LPI contribution no. 1338, p 1873, 12–17 March 2007
- Brown RH, Kirk RL, Johnson TV, Soderblom LA (1990) Energy sources for Triton's geyser-like plumes. *Science* 250:431–435
- Brown RH, Soderblom LA, Soderblom JM, Clark RN, Jaumann R, Barnes JW, Sotin C, Buratti B, Baines KH, Nicholson PD (2008) The identification of liquid ethane in Titan's Ontario Lacus. *Nature* 454(7204):607–610
- Burch JL, Goldstein J, Lewis WS, Young DT, Coates AJ, Dougherty MK, André N (2007) Tethys and Dione as sources of outward-flowing plasma in Saturn's magnetosphere. *Nature* 447 (7146):833–835
- Burchell MJ, Grey IDS, Shrine NRG (2001) Laboratory investigations of hypervelocity impact cratering in ice. *Adv Space Res* 28(10):1521–1526
- Carr MH, Belton MJS, Chapman CR, Davies ME, Geissler P, Greenberg R, McEwen AS, Tufts BR, Greeley R, Sullivan R, Head JW, Pappalardo RT, Klaasen KP, Johnson TV, Kaufman J, Senske D, Moore J, Neukum G, Schubert G, Burns JA, Thomas P, Veverka J (1998) Evidence for a subsurface ocean on Europa. *Nature* 391:363–365
- Carlson RW, Anderson MS, Johnson RE, Smythe WD, Hendrix AR, Barth CA, Soderblom LA, Hansen GB, McCord TB, Dalton JB, Clark RN, Shirley JH, Ocampo AC, Matson DL (1999) Hydrogen peroxide on the surface of Europa. *Science* 283(5410):2062–2064
- Casacchia R, Strom RG (1984) Geologic evolution of Galileo Regio, Ganymede. *J Geophys Res* 89(S2):B419–B428
- Castillo-Rogez JC, Matson DL, Sotin C, Johnson TV, Lunine JI, Thomas PC (2007) Iapetus' geophysics: rotation rate, shape and equatorial ridge. *Icarus* 190(1):179–202

- Castillo-Rogez J, Johnson TV, Lee MH, Turner NJ, Matson DL, Lunine J (2009) 26Al decay: heat production and a revised age for Iapetus. *Icarus* 204(2):658–662
- Chapman CR, McKinnon WB (1986) Cratering of planetary satellites. In: Burns J, Matthews MS (eds) *Satellites*. University of Arizona Press, Tucson, pp 492–580
- Chapman CR, Merline WJ, Bierhaus B, Brooks S, Galileo Imaging Team (1998) Cratering in the jovian system: intersatellite comparisons, LPSC XXIX, 16–20 March, Houston, 1927
- Chuang FC, Greeley R (2000) Large mass movements on Callisto. *J Geophys Res* 105 (E8):20227–20244
- Clark BE, Johnson RE (1996) Interplanetary weathering: surface erosion in outer space. *Eos Trans Am Geophys Union* 77(15):141. doi:[10.1029/96EO00094](https://doi.org/10.1029/96EO00094)
- Clark RN, Curchin JM, Jaumann R, Cruikshank DP, Brown RH, Hoefer TM, Stephan K, Moore JM, Buratti BJ, Baines KH, Nicholson PD, Nelson RM (2008) Compositional mapping of Saturn's satellite Dione with Cassini VIMS and implications of dark material in the Saturn system. *Icarus* 193(2):372–386
- Collins GC (2006) Global expansion of Ganymede derived from strain measurements in grooved terrain. In: *Lunar and planetary science conference*, Houston, Texas, XXXVII. Abstract no. 2077, 13–17 March 2006
- Collins G, Nimmo F (2009) Chaotic terrain on Europa. In: Pappalardo RT, McKinnon WB, Khurana KK (eds) *Europa*. The University of Arizona space science series. University of Arizona Press, Tucson, pp 259–281
- Collins GC, Head JW, Pappalardo RT (1998) Formation of Ganymede grooved terrain by sequential extensional episodes: implications of Galileo observations for regional stratigraphy. *Icarus* 135(1):345–359
- Collins GC, Head JW III, Pappalardo RT, Spaun NA (2000) Evaluation of models for the formation of chaotic terrain on Europa. *J Geophys Res* 105(E1):1709–1716
- Collins GC, McKinnon WB, Moore JM, Nimmo F, Pappalardo RT, Prockter LM, Schenk PM (2009) Tectonics of the outer planet satellites. In: Schultz RA, Watters TR (eds) *Planetary tectonics*. Cambridge University Press, Leiden, pp 264–350
- Conca J (1981) Dark-ray craters on Ganymede. *Lunar Planet. Sci. Conf.* XII: Houston, TX, Pergamon Press, p. 1599–1606, 16–20 March 1981
- Cooper JF, Johnson RE, Mauk BH, Garrett HB, Gehrels N (2001) Energetic ion and electron irradiation of the icy Galilean satellites. *Icarus* 149:133–159
- Crawford GD, Stevenson DJ (1988) Gas-driven water volcanism and the resurfacing of Europa. *Icarus* 73(1):66–79
- Croft SK (1981) On the origin of pit craters. In: *Lunar and planetary science conference*, XII: Houston, Texas, Abstract no. 1070, 16–20 March 1981
- Croft SK (1983) A proposed origin for palimpsests and anomalous pit craters on Ganymede and Callisto. *J Geophys Res* 88:B71–B89
- Croft SK (1985) The scaling of complex craters. *J Geophys Res* 90:C828–C842
- Croft SK, Soderblom LA (1991) Geology of the uranian satellites. In: Bergstrahl JT, Miner ED, Matthews MS (eds) *Uranus*. University of Arizona Press, Tucson, pp 561–628
- Croft SK, Kargel JS, Kirk RL, Moore JM, Schenk PM, Strom RG (1995) The geology of Triton. In: Cruikshank DP (ed) *Neptune and Triton*. University of Arizona Press, Tucson, pp 879–947
- Crow-Willard EN, Pappalardo RT (2009) Geological mapping of tectonized terrains in the trailing hemisphere of Enceladus. Spring meeting 2009, American Geophysical Union, Toronto, Ontario, Canada, 24–27 May 2009
- Czechowski L, Leliwa-Kopystynski J (2008) The Iapetus's ridge: possible explanations of its origin. *Adv Space Res* 42:61–69
- Denk T, Neukum G, Roatsch T, Porco CC, Burns JA, Galuba GG, Schmedemann N, Helfenstein P, Thomas PC, Wagner RJ, West RA (2010) Iapetus: unique surface properties and a global color dichotomy from Cassini imaging. *Science* 327(5964):435–439

- DeRemer LC, Pappalardo RT (2003) Manifestations of strike slip faulting on Ganymede. In: Lunar and planetary science conference, XXXIV, Houston, Texas. Abstract no. 2033, 17–21 March 2003
- Dermott SF, Malhotra R, Murray CD (1988) Dynamics of the Uranian and Saturnian satellite systems: a chaotic route to melting Miranda? *Icarus* 76(2):295–334
- Dombard A, McKinnon W (2006) Folding of Europa's icy lithosphere: an analysis of viscous-plastic buckling and subsequent topographic relaxation. *J Struct Geol* 28(12):2259–2269
- Dombard AJ, Cheng AF (2008) Constraints on the evolution of Iapetus from simulations of its ridge and bulge. In: Lunar and planetary science conference, XXXIX, League City, Texas, Abstract no. 2262, 10–14 March 2008
- Dombard AJ, McKinnon WB (2001) Formation of grooved Terrain on Ganymede: extensional instability mediated by cold, superplastic creep. *Icarus* 154(2):321–336
- Dombard AJ, Cheng AF, McKinnon WB, Kay JP (2010) The weirdest topography in the outer solar system: the ridge on Iapetus and its possible formation via giant impact. AGU fall meeting 2010, San Francisco, California. Abstract no. P31D-01, 5–9 December 2010
- Dones L, Chapman CR, McKinnon WB, Melosh HJ, Kirchoff MR, Neukum G, Zahnle KJ (2009) Icy satellites of Saturn: impact cratering and age determination. In: Dougherty MK, Esposito LW, Krimigis SM (eds) *Saturn from Cassini-Huygens*. Springer, Netherlands, pp 613–635
- Durda DD, Greenberg R, Jedicke R (1998) Collisional models and scaling laws: a new interpretation of the shape of the main-belt asteroid size distribution. *Icarus* 135(2):431–440
- Durham WB, Stern LA (2001) Rheological properties of water ice – application to satellites of the outer planets. *Ann Rev Earth Pl Sc* 29(1):295–330
- Durham WB, Prieto-Ballesteros O, Goldsby D, Kargel J (2010) Rheological and thermal properties of icy materials. *Space Sci Rev* 153(1):273–298
- Elachi C, Wall S, Janssen M, Stofan E, Lopes R, Kirk R, Lorenz R, Lunine J, Paganelli F, Soderblom L, Wood C, Wye L, Zebker H, Anderson Y, Ostro S, Allison M, Boehmer R, Callahan P, Encrenaz P, Flaminii E, Francescetti G, Gim Y, Hamilton G, Hensley S, Johnson W, Kelleher K, Muhleman D, Picardi G, Posa F, Roth L, Seu R, Shaffer S, Stiles B, Vettrella S, West R (2006) Titan Radar Mapper observations from Cassini's T3 fly-by. *Nature* 441 (7094):709–713
- Fagents SA (2003) Considerations for effusive cryovolcanism on Europa: the post-Galileo perspective. *J Geophys Res* 108(E12):13–11–13–19
- Fagents SA, Greeley R, Sullivan RJ, Pappalardo RT, Prockter LM, The Galileo SSI Team (2000) Cryomagmatic mechanisms for the formation of Rhadamanthys Linea, triple band margins, and other low-albedo features on Europa. *Icarus* 144(1):54–88
- Figueredo PH, Greeley R (2000) Geologic mapping of the northern leading hemisphere of Europa from Galileo solid-state imaging data. *J Geophys Res* 105(E9):22629–22646
- Figueredo PH, Greeley R (2003) The emerging resurfacing history of Europa from pole-to-pole geologic mapping. In: Lunar and planetary science conference, XXXIV2003, Houston, Texas. Abstract no. 1017, 17–21 March 2003
- Figueredo PH, Greeley R (2004) Resurfacing history of Europa from pole-to-pole geological mapping. *Icarus* 167(2):287–312
- Figueredo PH, Chuang FC, Rathbun J, Kirk RL, Greeley R (2002) Geology and origin of Europa's “Mitten” feature (Murias Chaos). *J Geophys Res* 107:5026
- Fink JH (1980) Possible Rhyolite flows in the Arcadia Planitia region of Mars: evidence from surface ridge geometry. In: Lunar and planetary science conference, Houston, Texas. Abstract no. 285–287, 17–21 March 1980
- Fletcher RC, Hallet B (1983) Unstable extension of the lithosphere: a mechanical model for basin-and-range structure. *J Geophys Res* 88(B9):7457–7466
- Fortes AD, Grindrod PM, Trickett SK, Vocadlo L (2007) Ammonium sulfate on Titan: possible origin and role in cryovolcanism. *Icarus* 188(1):139–153
- Friedson AJ, Stevenson DJ (1983) Viscosity of rock-ice mixtures and applications to the evolution of icy satellites. *Icarus* 56(1):1–14

- Gaidos EJ, Nimmo F (2000) Planetary science: tectonics and water on Europa. *Nature* 405(6787):637
- Gault D, Greeley R (1978) Exploratory experiments of impact craters formed in viscous-liquid targets: analogs for Martian rampart craters? *Icarus* 34:486–495
- Geissler PE (2000) Cryovolcanism in the outer Solar System. In: Sigurdsson H, Houghton BF, McNutt SR, Rymer H, Stix J (eds) *Encyclopedia of volcanoes*. Academic, San Diego/San Francisco/New York/Boston/London/Sydney/Toronto, pp 785–800
- Geissler PE, Greenberg R, Hoppa G, McEwen A, Tufts R, Phillips C, Clark B, Ockert-Bell M, Helfenstein P, Burns J, Veverka J, Sullivan R, Greeley R, Pappalardo RT, Head JW, Belton MJS, Denk T (1998) Evolution of lineaments on Europa: clues from Galileo multispectral imaging observations. *Icarus* 135(1):107–126
- Giese B, Oberst J, Roatsch T, Neukum G, Head JW, Pappalardo RT (1998) The local topography of Uruk Sulcus and Galileo Regio obtained from stereo images. *Icarus* 135(1):303–316
- Giese B, Wagner R, Neukum G, Sullivan R (1999) Doublet ridge formation on Europa: evidence from topographic data. In: American Astronomical Society, DPS meeting #31, edited, p 62.08
- Giese B, Wagner R, Neukum G, Pappalardo R, Head JW III, The Galileo SSI Team (2001) In: Lunar and planetary science conference, XXXII, Houston, Texas. Abstract no. 1743, 12–16 March 2001
- Giese B, Wagner R, Neukum G, Helfenstein P, Thomas PC (2007a) Tethys: lithospheric thickness and heat flux from flexurally supported topography at Ithaca Chasma. *Geophys Res Lett* 34: L21203
- Giese, B., Wagner R, Roatsch T, Denk T, Neukum G (2007b) The topographies of Rhea and Iapetus in comparison. In: AGU, Fall meeting 2007, San Francisco, California, edited, AGU, 10–14 December 2007
- Giese B, Denk T, Neukum G, Roatsch T, Helfenstein P, Thomas PC, Turtle EP, McEwen A, Porco CC (2008) The topography of Iapetus' leading side. *Icarus* 193(2):359–371
- Golombek MP, Allison ML (1981) Sequential development of grooved terrain and polygons on Ganymede. Reports of planetary geology program, pp 54–56
- Gomes R, Levison HF, Tsiganis K, Morbidelli A (2005) Origin of the cataclysmic late heavy bombardment period of the terrestrial planets. *Nature* 435:466–469
- Greeley R, Fink J, Snyder DB, Gault DE, Guest JE, Schultz PH (1980) Impact cratering in viscous targets – laboratory experiments, vol 3. In: Lunar and planetary science conference, XI, League City, Texas. (A82-22351 09-91), pp 2075–2097, 10–14 March 2008
- Greeley R, Fink JH, Gault DE, Guest JE (1982) Experimental simulation of impact cratering on icy satellites. In: Morrison D (ed) *Satellites of Jupiter*. University of Arizona Press, Tucson, pp 340–378
- Greeley R (1985) Planetary landscapes. George Allen and Unwin, London/Boston, p 265
- Greeley R, Sullivan R, Coon MD, Geissler PE, Tufts BR, Head JW, Pappalardo RT, Moore JM (1998) Terrestrial sea ice morphology: considerations for Europa. *Icarus* 135(1):25–40
- Greeley R, Klemaszewski JE, Wagner R (2000) Galileo views of the geology of Callisto. *Planet Space Sci* 48(9):829–853
- Greeley R, Chyba CF, Head JW, McCord TB, McKinnon WB, Pappalardo RT, Figueiredo PH (2004) Geology of Europa. In: Bagenal F, Dowling TE, McKinnon WB (eds) *Jupiter: the planet, satellites, and magnetosphere*. Cambridge University Press, New York, pp 363–396
- Greenberg R, Geissler P, Hoppa G, Tufts BR (2002) Tidal-tectonic processes and their implications for the character of Europa's icy crust. *Rev Geophys* 40(2):1004
- Greenberg R (2004) The evil twin of Agenor: tectonic convergence on Europa. *Icarus* 167 (2):313–319
- Greenberg R (2005) Europa – the Ocean Moon: search for an alien biosphere. Springer, Chichester, p 380
- Greenberg R, Croft SK, Janes DM, Kargel JS, Lebofsky LA, Lunine JI, Marcialis RL, Melosh HJ, Ojakangas GW, Strom RG (1991) Miranda. In: Bergstrahl JT, Miner ED, Matthews MS (eds) *Uranus*. University of Arizona Press, Tucson, pp 693–735

- Greenberg R, Geissler P, Hoppa G, Tufts BR, Durda DD, Pappalardo R, Head JW, Greeley R, Sullivan R, Carr MH (1998) Tectonic processes on Europa: tidal stresses, mechanical response, and visible features. *Icarus* 135(1):64–78
- Greenberg R, Hoppa GV, Tufts BR, Geissler P, Riley J (1999a) Chaos, cracks and ridges: surface effects of thin ice over liquid water on Europa. In: Lunar and planetary science conference, XXX, Houston, Texas. Abstract no. 1421, 15–19 March 1999
- Greenberg R, Hoppa GV, Tufts BR, Geissler P, Riley J, Kadel S (1999b) Chaos on Europa. *Icarus* 141(2):263–286
- Grey IDS, Burchell MJ (2003) Hypervelocity impact cratering on water ice targets at temperatures ranging from 100 K to 253 K. *J Geophys Res* 108(E3):5019
- Grey IDS, Burchell MJ (2004) Hypervelocity impact craters in ammonia rich ice. *Icarus* 168 (2):467–474
- Griffith CA, Owen T, Miller GA, Geballe T (1998) Transient clouds in Titan's lower atmosphere. *Nature* 395(6702):575–578
- Griffith CA, Owen T, Geballe TR, Rayner J, Rannou P (2003) Evidence for the exposure of water ice on Titan's surface. *Science* 300(5619):628–630
- Griffith CA, Penteado P, Baines K, Drossart P, Barnes J, Bellucci G, Bibring J, Brown R, Buratti B, Capaccioni F, Cerroni P, Clark R, Combes M, Coradini A, Cruikshank D, Formisano V, Jaumann R, Langevin Y, Matson D, McCord T, Mennella V, Nelson R, Nicholson P, Sicardy B, Sotin C, Soderblom LA, Kursinski R (2005) The evolution of Titan's mid-latitude clouds. *Science* 310(5747):474–477
- Griffith CA, Penteado P, Rannou P, Brown R, Boudon V, Baines KH, Clark R, Drossart P, Buratti B, Nicholson P, McKay CP, Coustenis A, Negrao A, Jaumann R (2006) Evidence for a polar ethane cloud on Titan. *Science* 313(5793):1620–1622
- Grimm RE, Squyres SW (1985) Spectral analysis of groove spacing on Ganymede. *J Geophys Res* 90(B2):2013–2021
- Groenleer JM, Kattenhorn SA (2008) Cycloid crack sequences on Europa: relationship to stress history and constraints on growth mechanics based on cusp angles. *Icarus* 193:158–181
- Hansen CJ, Esposito L, Stewart AIF, Colwell J, Hendrix A, Pryor W, Shemansky D, West R (2006) Enceladus' water vapor plume. *Science* 311(5766):1422–1425
- Hartmann WK (1966) Early lunar cratering. *Icarus* 5(1–6):406–418
- Hartmann WK et al (1981) Chronology of planetary volcanism by comparative studies of planetary cratering. In: BVS Project (ed) Basaltic volcanism on the terrestrial planets, Pergamon, Elmsford, pp 1050–1127
- Hartmann WK, Ryder G, Dones L, Grinspoon D (2000) The time-dependent intense bombardment of the primordial Earth/Moon system. In: Canup RM, Righter K (eds) Origin of the Earth and Moon. University of Arizona Press, Tucson, pp 493–512
- Hayes A, Aharonson O, Callahan P, Elachi C, Gim Y, Kirk R, Lewis K, Lopes R, Lorenz R, Lunine J, Mitchell K, Mitri G, Stofan E, Wall S (2008) Hydrocarbon lakes on Titan: distribution and interaction with a porous regolith. *Geophys Res Lett* 35(9):L09204
- Hayes A, Aharonson O, Lunine J, Wolf A, Wye L, Zebker H, Lorenz R, Turtle E, Kirk R, Wall S, Elachi C (2010) Cassini RADAR observations of the nature and seasonal variability of Titan's lakes. In Proceedings of the 38th COSPAR scientific assembly, Bremen
- Head JW, Pappalardo RT, Greeley R, Sullivan R, and a. t. G. I. Team (1997) European pits, domes, spots and ridges: evidence for an origin through recent solid-state convection (abstract), GSA Abstract Programs, Madison, Wisconsin, 29, A-312
- Head JW, Pappalardo RT, Greeley R, Sullivan R, The Galileo Imaging Team (1998a) Origin of ridges and bands on Europa: morphologic characteristics and evidence for linear diapirism from Galileo data. In: Lunar and planetary science conference, XXIX, Houston, Texas, 16–20 March 1998
- Head JW, Pappalardo RT, Kay J, Collins G, Prockter L, Greeley R, Chapman C, Carr M, Belton MJS, The Galileo Imaging Team (1998b) Cryovolcanism on Ganymede: evidence in bright

- terrain from Galileo solid state imaging data. In: Lunar and planetary science conference, XXIX. Abstract no. 1666
- Head JW, Pappalardo RT, Sullivan R (1999) Europa: morphological characteristics of ridges and triple bands from Galileo data (E4 and E6) and assessment of a linear diapirism model. *J Geophys Res* 104(E10):24,223–24,236
- Head JW, Pappalardo R, Collins G, Belton MJS, Giese B, Wagner R, Breneman H, Spaun N, Nixon B, Neukum G, Moore J (2002) Evidence for Europa-like tectonic resurfacing styles on Ganymede. *Geophys Res Lett* 29(24):2151
- Helfenstein P, Parmentier EM (1980) Fractures on Europa: possible response of an ice crust to tidal deformation. In: Proceedings of the lunar and planetary science conference, XI, Houston, Texas. vol 3. (A82-22351 09-91), pp 1987–1998, 17–21 March 1980
- Helfenstein P, Parmentier EM (1985) Patterns of fracture and tidal stresses due to nonsynchronous rotation: implications for fracturing on Europa. *Icarus* 61(2):175–184
- Helfenstein P, Thomas PC, Everka J (1989) Evidence from Voyager II photometry for early resurfacing of Umbriel. *Nature* 338(6213):324–326
- Helfenstein P, Thomas P, Everka J, Burns J, Roatsch T, Giese B, Wagner R, Denk T, Neukum G, Turtle E, Perry J, Bray VJ, Rathbun J, Porco C (2010) Planetary science: Tectonic overturn on Enceladus. *Nat Geosci* 3(2):75–76
- Herrick DL, Stevenson DJ (1990) Extensional and compressional instabilities in icy satellite lithospheres. *Icarus* 85(1):191–204
- Hiiller J, Squyres SW (1991) Thermal stress tectonics on the Satellites of Saturn and Uranus. *J Geophys Res* 96(E1):15665–15674
- Hodges CA, Shew NB, Clow G (1980) Distribution of central pit craters on Mars. In: Lunar and planetary science conference, XI, Houston, Texas. Abstract no. 1160, pp 450–452, 17–21 March 1980
- Holsapple KA (1987) The scaling of impact phenomena. *Int J Impact Eng* 5(1–4):343–355
- Hoppa GV, Tufts BR, Greenberg R, Geissler PE (1999) Formation of cycloidal features on Europa. *Science* 285(5435):1899–1902
- Hoppa GV, Randall Tufts B, Greenberg R, Hurford TA, O'Brien DP, Geissler PE (2001) Europa's rate of rotation derived from the tectonic sequence in the Astypalaea region. *Icarus* 153:208–213
- Horedt GP, Neukum G (1984a) Cratering rate over the surface of a synchronous satellite. *Icarus* 60:700–717
- Horedt GP, Neukum G (1984b) Planetocentric versus heliocentric impacts in the Jovian and Saturnian satellite system. *J Geophys Res* 89:10,405–10,410
- Horner VM, Greeley R (1982) Pedestal craters on Ganymede. *Icarus* 51(3):549–562
- Hussmann H, Choblet G, Lainey V, Matson D, Sotin C, Tobie G, Van Hoolst T (2010) Implications of rotation, orbital states, energy sources, and heat transport for internal processes in icy satellites. *Space Sci Rev* 153(1):317–348
- Ingersoll AP, Tryka KA (1990) Triton's plumes: the dust devil hypothesis. *Science* 250 (4979):435–437
- Ip WH (2006) On a ring origin of the equatorial ridge of Iapetus. *Geophys Res Lett* 33(16):L16203
- Ip WH, Williams DJ, McEntire RW, Mauk BH (1998) Ion sputtering and surface erosion at Europa. *Geophys Res Lett* 25(6):829–832
- Ivanov BA, Hartmann WK (2007) Exogenic dynamics, cratering and surface ages. In: Spohn T (ed) *Planets and Moons*. Elsevier, Amsterdam, pp 207–242
- Ivanov BA, Neukum G, Wagner R (2001) Size-frequency distributions of planetary impact craters and asteroids. In: Marov MY, Rickman H (eds) *Collisional processes in the Solar System*. Kluwer Academic, Dordrecht, pp 1–34
- Janes DM, Melosh HJ (1990) Tectonics of planetary loading: a general model and results. *J Geophys Res* 95(B13):21345–21355
- Jankowski DG, Squyres SW (1988) Solid-state ice volcanism on the satellites of Uranus. *Science* 241:1322–1325

- Jaumann R, Neukum G (2009) The surface ages of Titan. In: Lunar and planetary science conference, XL, The Woodlands, Texas. Abstract no. 1641, 23–27 March 2009
- Jaumann R, Stephan K, Hansen GB, Clark RN, Buratti BJ, Brown RH, Baines KH, Newman SF, Bellucci G, Filacchione G, Coradini A, Cruikshank DP, Griffith CA, Hibbitts CA, McCord TB, Nelson RM, Nicholson PD, Sotin C, Wagner R (2008) Distribution of icy particles across Enceladus' surface as derived from Cassini-VIMS measurements. *Icarus* 193(2):407–419
- Jaumann R, Clark RN, Nimmo F, Hendrix AR, Buratti BJ, Denk T, Moore JM, Schenk PM, Ostro SJ, Srama R (2009a) Icy satellites: geological evolution and surface processes. In: Dougherty MK, Esposito LW, Krimigis SM (eds) *Saturn from Cassini-Huygens*. Springer, Dordrecht, pp 637–681
- Jaumann R, Kirk RL, Lorenz RD, Lopez RMG, Stofan ER, Turtle EP, Keller HU, Wood CA, Sotin C, Soderblom LA, Tomasko M (2009b) Geology and surface processes on Titan. In: Brown R, Lebreton J-P, Waite H (eds) *Titan from Cassini-Huygens*. Springer, Dordrecht, pp 75–140
- Johnson RE (1990) Energetic charged-particle interactions with atmospheres and surfaces. Springer, Berlin/Heidelberg/New York, p 230
- Johnson TV (2005) Geology of the icy satellites. *Space Sci Rev* 116(1):401–420
- Johnson RE, Famá M, Liu M, Baragiola RA, Sittler EC Jr, Smith HT (2008) Sputtering of ice grains and icy satellites in Saturn's inner magnetosphere. *Planet Sp Sci* 56(9):1238–1243
- Johnson TV, McGetchin TR (1973) Topography on satellite surfaces and the shape of asteroids. *Icarus* 18(4):612–620
- Johnson RE, Lanzaotti LJ, Brown WL (1982) Planetary applications of ion induced erosion of condensed-gas frosts. *Nucl Instrum Methods Phys Res* 198(1):147–157
- Jones KB, Head Iii JW, Pappalardo RT, Moore JM (2003) Morphology and origin of palimpsests on Ganymede based on Galileo observations. *Icarus* 164(1):197–212
- Kadel SD, Fagents SA, Greeley R, The Galileo SSI Team (1998) Trough-bounding ridge pairs on Europa: considerations for an endogenic model of formation (abstract). In: Lunar and planetary science conference, XXIX, Houston, Texas. Abstract no. 1078, 16–20 March 1998
- Kadel SD, Chuang FC, Greeley R, Moore JM, The Galileo SSIT (2000) Geological history of the Tyre region of Europa: a regional perspective on Europian surface features and ice thickness. *J Geophys Res* 105(E9):22657–22669
- Kargel JS (1990) Cryomagmatism in the outer Solar System. Ph.D. Thesis, Arizona University, Tucson
- Kargel JS (1991) Brine volcanism and the interior structures of asteroids and icy satellites. *Icarus* 94(2):368–390
- Kargel JS (1992) Ammonia-water volcanism on icy satellites: phase relations at 1 atmosphere. *Icarus* 100(2):556–574
- Kargel JS (1995) Cryovolcanism on the icy satellites. *Earth Moon Planets* 67(1–3):101–113
- Kargel JS (1998) Physical chemistry of ices in the outer solar system. In: Schmitt B, de Bergh C, Festou M (eds) *In: Solar system ices. Based on reviews presented at the international symposium "Solar system ices"*, Toulouse, Kluwer Academic, Dordrecht, 27–30 March 1995, p 3
- Kargel JS, Pozio S (1996) The volcanic and tectonic history of Enceladus. *Icarus* 119(2):385–404
- Kargel JS, Croft SK, Lunine JI, Lewis JS (1991) Rheological properties of ammonia-water liquids and crystal-liquid slurries: planetological applications. *Icarus* 89(1):93–112
- Kato M, Iijima Y-I, Arakawa M, Okimura Y, Fujimura A, Maeno N, Mizutani H (1995) Ice-on-ice impact experiments. *Icarus* 113(2):423–441
- Kattenhorn SA (2002) Nonsynchronous rotation evidence and fracture history in the bright plains region, Europa. *Icarus* 157(2):490–506
- Kattenhorn SA (2004) Strike-slip fault evolution on Europa: evidence from tailcrack geometries. *Icarus* 172(2):582–602
- Kattenhorn SA, Hurford T (2009) Tectonics of Europa. In: Pappalardo RT, McKinnon WB, Khurana KK (eds) *Europa, The University of Arizona space science series*. University of Arizona Press, Tucson, pp 199–236
- Kattenhorn SA, Marshall ST (2006) Fault-induced perturbed stress fields and associated tensile and compressive deformation at fault tips in the ice shell of Europa: implications for fault mechanics. *J Struct Geol* 28:2204–2221

- Kay JE, Head JW III (1999) Geologic mapping of the Ganymede G8 Calderas region: evidence for cryovolcanism. In: *Proceedings of the LPSC XXX*, Houston, 15–29 March 1999
- Keller HU, Grieber B, Küppers M, Schröder SE, Skorov YV, Tomasko MG (2008) The properties of Titan's surface at the Huygens landing site from DISR observations. *Planet Sp Sci* 56 (5):728–752
- Khare BN, Sagan C, Bandurski EL, Nagy B (1978) Ultraviolet-photoproduced organic solids synthesized under simulated jovian conditions. Molecular analysis. *Science* 199 (4334):1199–1201
- Kirchoff MR, Schenk PM (2009) Impactor populations in the Saturnian system: constraints from the cratering records. In: *Lunar and planetary science conference, XL*, The Woodlands, Texas. Abstract no. 2067, 23–27 March 2009
- Kirk RL, Stevenson DJ (1987) Thermal evolution of a differentiated Ganymede and implications for surface features. *Icarus* 69(1):91–134
- Kirk RL, Brown RH, Soderblom LA (1990) Subsurface energy storage and transport for solar-powered geysers on Triton. *Science* 250:424–429
- Kirk RL, Soderblom LA, Brown RH, Kieffer SW, Kargel JS (1995) Triton's plumes: discovery, characteristics, and models. In: Cruikshank DP (ed) *Neptune and Triton*. University of Arizona Press, Tucson, pp 949–989
- Kirk RL, Howington-Kraus E, Redding BL, Becker TL, Lee EM, Stiles BW, Hensley S, Hayes AG, Lopes RMC, Lorenz RD, Mitchell KL, Radebaugh J, Paganelli F, Soderblom LA, Stofan ER, Wood CA, Wall SD, Cassini Radar Team (2009) Three-dimensional views of Titan's diverse surface features from Cassini RADAR stereogrammetry. In: *Lunar and planetary science conference, XL*. Abstract no. 1413
- Kivelson MG, Khurana KK, Russell CT, Walker RJ, Warnecke J, Coroniti FV, Polanskey C, Southwood DJ, Schubert G (1996) Discovery of Ganymede's magnetic field by the Galileo spacecraft. *Nature* 384(6609):537–541
- Leith AC, McKinnon WB (1996) Is there evidence for polar wander on Europa? *Icarus* 120 (2):387–398
- Lopes RMC, Mitchell KL, Stofan ER, Lunine JI, Lorenz R, Paganelli F, Kirk RL, Wood CA, Wall SD, Robshaw LE, Fortes AD, Neish CD, Radebaugh J, Reffet E, Ostro SJ, Elachi C, Allison MD, Anderson Y, Boehmer R, Boubin G, Callahan P, Encrenaz P, Flamini E, Francescetti G, Gim Y, Hamilton G, Hensley S, Janssen MA, Johnson WTK, Kelleher K, Muhleman DO, Ori G, Orosei R, Picardi G, Posa F, Roth LE, Seu R, Shaffer S, Soderblom LA, Stiles B, Vettrella S, West RD, Wye L, Zebker HA (2007) Cryovolcanic features on Titan's surface as revealed by the Cassini Titan radar mapper. *Icarus* 186(2):395–412
- Lopes RMC, Stofan ER, Peckyno R, Radebaugh J, Mitchell KL, Mitri G, Wood CA, Kirk RL, Wall SD, Lunine JI, Hayes A, Lorenz R, Farr T, Wye L, Craig J, Ollerenshaw RJ, Janssen M, LeGall A, Paganelli F, West R, Stiles B, Callahan P, Anderson Y, Valora P, Soderblom L (2010) Distribution and interplay of geologic processes on Titan from Cassini radar data. *Icarus* 205(2):540–558
- Lorenz RD, Lunine JI (1996) Erosion on Titan: past and present. *Icarus* 122(1):79–91
- Lorenz RD, Lunine JI (2005) Titan's surface before Cassini. *Planet Sp Sci* 53(5):557–576
- Lorenz RD, Radebaugh J (2009) Global pattern of Titan's dunes: Radar survey from the Cassini prime mission. *Geophys Res Lett* 36(3):L03202
- Lorenz RD, Lopes RM, Paganelli F, Lunine JI, Kirk RL, Mitchell KL, Soderblom LA, Stofan ER, Ori G, Myers M, Miyamoto H, Radebaugh J, Stiles B, Wall SD, Wood CA (2008a) Fluvial channels on Titan: initial Cassini RADAR observations. *Planet Sp Sci* 56(8):1132–1144
- Lorenz RD, Mitchell KL, Kirk RL, Hayes AG, Aharonson O, Zebker HA, Paillou P, Radebaugh J, Lunine JI, Janssen MA, Wall SD, Lopes RM, Stiles B, Ostro S, Mitri G, Stofan ER (2008b) Titan's inventory of organic surface materials. *Geophys Res Lett* 35(2):L02206
- Lorenz RD, Wall S, Radebaugh J, Boubin G, Reffet E, Janssen M, Stofan E, Lopes R, Kirk R, Elachi C, Lunine J, Mitchell K, Paganelli F, Soderblom L, Wood C, Wye L, Zebker H, Anderson Y, Ostro S, Allison M, Boehmer R, Callahan P, Encrenaz P, Ori GG, Francescetti

- G, Gim Y, Hamilton G, Hensley S, Johnson W, Kelleher K, Muhleman D, Picardi G, Posa F, Roth L, Seu R, Shaffer S, Stiles B, Vetrella S, Flamini E, West R (2006) The sand seas of Titan: Cassini RADAR observations of longitudinal dunes. *Science* 312(5774):724–727
- Lucchitta BK (1980) Grooved terrain on Ganymede. *Icarus* 44(2):481–501
- Lucchitta BK, Ferguson HM (1988) Ganymede: “Moat” craters compared with palimpsests and basins. In: Lunar and planetary science conference, Houston, Texas. 19, pp 701–702, 14–18 March 1988
- Lucchitta BK, Soderblom LA (1982) Geology of Europa. In: Morrison D (ed) *Satellites of Jupiter*. University of Arizona Press, Tucson, pp 521–555, 940, 941
- Lunine JI (1993) Triton, Pluto, and the origin of the Solar system. *Science* 261(5122):697–698
- Lunine JI, Stevenson DJ, Yung YL (1983) Ethane ocean on Titan. *Science* 222(4629):1229–1230
- Lunine JI, Atreya SK (2008) The methane cycle on Titan. *Nat Geosci* 1:159–164
- Manga M, Sinton A (2004) Formation of bands and ridges on Europa by cyclic deformation: insights from analogue wax experiments. *J Geophys Res* 109(E9):E09001
- Manga M, Wang CY (2007) Pressurized oceans and the eruption of liquid water on Europa and Enceladus. *Geophys Res Lett* 34(7):L07202
- Matsuyama I, Nimmo F (2007) Rotational stability of tidally deformed planetary bodies. *J Geophys Res* 112(E11):E11003
- Matsuyama I, Nimmo F (2008) Tectonic patterns on reoriented and despun planetary bodies. *Icarus* 195(1):459–473
- Mauk BH, Hamilton DC, Hill TW, Hospodarsky GB, Johnson RE, Paranicas C, Roussos E, Russell CT, Shemansky DE, Sittler EC, Thorne RM (2009) Fundamental plasma processes in Saturn’s magnetosphere. In: Dougherty MK, Esposito LW, Krimigis SM (eds) *Saturn from Cassini-Huygens*. Springer, Netherlands, pp 281–331
- McCord TB, Hansen GB, Clark RN, Martin PD, Hibbitts CA, Fanale FP, Granahan JC, Segura M, Matson DL, Johnson TV, Carlson RW, Smythe WD, Danielson GE, The NT (1998) Non-water-ice constituents in the surface material of the icy Galilean satellites from the Galileo near-infrared mapping spectrometer investigation. *J Geophys Res* 103(E4):8603–8626
- McDonald KC (1982) Mid-ocean ridges: fine scale tectonic, volcanic and hydrothermal processes within the plate boundary zone. *Ann Rev Earth Planet Sci* 10:155–190
- McKinnon WB (1988) Odd tectonics of a rebuilt moon. *Nature* 333(6175):701–702
- McKinnon WB, Kirk RL (2007) Triton. In: Lucy-Ann M, Paul RW, Torrence VJ (eds) *Encyclopedia of the Solar System*, 2nd edn. Academic, San Diego, pp 483–502
- McKinnon WB, Melosh HJ (1980) Evolution of planetary lithospheres: evidence from multiringed structures on Ganymede and Callisto. *Icarus* 44(2):454–471
- McKinnon WB, Schenk PM (1995) Estimates of comet fragment masses from impact crater chains on Callisto and Ganymede. *Geophys Res Lett* 22(13):1829–1832
- McKinnon WB, Schenk PM, Moore JM (2001) Topographic and morphologic evidence for flooding of Ganymede’s resurfaced terrains by low-viscosity water-ice lavas. In: Lunar and planetary science conference, XXXII, Houston, Texas. Abstract no. 2179, 12–16 March 2001
- Melosh HJ (1977) Global tectonics of a despun planet. *Icarus* 31(2):221–243
- Melosh HJ (1980) Tectonic patterns on a tidally distorted planet. *Icarus* 43(3):334–337
- Melosh HJ (1989) Impact cratering: a geologic process. Oxford University Press, New York, p 245
- Melosh HJ, Janes DM (1989) Ice volcanism on Ariel. *Science* 245(4914):195–196
- Melosh HJ, Nimmo F (2009) An intrusive dike origin for Iapetus’ enigmatic ridge? In: Lunar and planetary science conference, XL, The Woodlands, Texas. Abstract no. 2478, 23–27 March 2009
- Melosh HJ, Turtle EP (2004) Ridges on Europa: origin by incremental ice-wedging. In: Lunar and planetary science conference, XXXV, Houston, Texas. Abstract no. 2029, 15–19 March 2004
- Mével L, Mercier E (2002) Geodynamics on Europa: evidence for a crustal resorption process. In: Lunar and planetary science conference, XXXIII, Houston, Texas. Abstract no. 1476, 11–15 March 2002

- Mével L, Mercier E (2007) Large-scale doming on Europa: a model of formation of Thera Macula. *Planet Space Sci* 55:915–927
- Miller DJ, Barnash AN, Bray VJ, Turtle EP, Helfenstein P, Squyres SW, Rathbun JA (2007) Interactions between impact craters and tectonic features on Enceladus and Dione. In: Paper presented at workshop on ices, oceans, and fire: satellites of the outer solar system, LPI Contribution, Boulder, 13–15 Aug 2007
- Mitchell JL (2008) The drying of Titan's dunes: Titan's methane hydrology and its impact on atmospheric circulation. *J Geophys Res* 113(E8):E08015
- Mitri G, Bland MT, Showman AP, Radebaugh J, Stiles B, Lopes RMC, Lunine JI, Pappalardo RT (2010) Mountains on Titan: modeling and observations. *J Geophys Res* 115:E10002
- Miyamoto H, Mitri G, Showman AP, Dohm JM (2005) Putative ice flows on Europa: geometric patterns and relation to topography collectively constrain material properties and effusion rates. *Icarus* 177(2):413–424
- Moons M, Henrard J (1994) Surfaces of section in the Miranda-Umbriel 3:1 inclination problem. *Celest Mech Dynam Astr* 59:129–148
- Moore JM (1984) The tectonic and volcanic history of Dione. *Icarus* 59(2):205–220
- Moore JM, Ahern JL (1983) The geology of Tethys. *J Geophys Res* 88(S2):A577–A584
- Moore JM, Malin MC (1988) Dome craters on Ganymede. *Geophys Res Lett* 15(3):225–228
- Moore JM, Schenk PM (2007) Topography of endogenic features on Saturnian mid-sized satellites. In: Lunar and planetary science, XXXVIII, Houston, Texas. LPI contribution no. 1338, p 2136, 12–16 March 2007
- Moore JM, Horner VM, Greeley R (1985) The geomorphology of RHEA – implications for geologic history and surface processes. *J Geophys Res* 90(Suppl):C785–C795
- Moore JM, Asphaug E, Morrison D, Spencer JR, Chapman CR, Bierhaus B, Sullivan RJ, Chuang FC, Klemaszewski JE, Greeley R, Bender KC, Geissler PE, Helfenstein P, Pilcher CB (1999) Mass movement and landform degradation on the icy Galilean Satellites: results of the Galileo nominal mission. *Icarus* 140(2):294–312
- Moore JM, Mellon MT, Zent AP (1996) Mass wasting and ground collapse in terrains of volatile-rich deposits as a Solar System-wide geological process: the pre-Galileo view. *Icarus* 122:63–78
- Moore JM, Asphaug E, Sullivan RJ, Klemaszewski JE, Bender KC, Greeley R, Geissler PE, McEwen AS, Turtle EP, Phillips CB, Tufts BR, Head JW, Pappalardo RT, Jones KB, Chapman CR, Belton MJS, Kirk RL, Morrison D (1998) Large impact features on Europa: results of the Galileo nominal mission. *Icarus* 135(1):127–145
- Moore JM, Asphaug E, Belton MJS, Bierhaus B, Breneman HH, Brooks SM, Chapman CR, Chuang FC, Collins GC, Giese B, Greeley R, Head JW, Kadel S, Klaasen KP, Klemaszewski JE, Magee KP, Moreau J, Morrison D, Neukum G, Pappalardo RT, Phillips CB, Schenk PM, Senske DA, Sullivan RJ, Turtle EP, Williams KK (2001) Impact features on Europa: results of the Galileo Europa Mission (GEM). *Icarus* 151(1):93–111
- Moore JM, Schenk PM, Bruesch LS, Asphaug E, McKinnon WB (2004a) Large impact features on middle-sized icy satellites. *Icarus* 171(2):421–443
- Moore JM, Chapman CR, Bierhaus EB, Greeley R, Chuang FC, Klemaszewski J, Clark RN, Dalton JB, Hibbitts CA, Schenk PM, Spencer JR, Wagner R (2004b) Callisto. In: Bagenal F, Dowling TE, McKinnon WB (eds) Jupiter: the planet, satellites, and magnetosphere. Cambridge University Press, Cambridge, UK, pp 397–426
- Morbidelli A, Levison HF, Tsiganis K, Gomes R (2005) Chaotic capture of Jupiter's Trojan asteroids in the early Solar System. *Nature* 435:462–465
- Mueller S, McKinnon WB (1988) Three-layered models of Ganymede and Callisto: compositions, structures, and aspects of evolution. *Icarus* 76(3):437–464
- Murchie SL, Head JW III (1986) Global reorientation and its effect on tectonic patterns on Ganymede. *Geophys Res Lett* 13(4):345–348
- Murchie SL, Head JW (1988) Possible breakup of dark terrain on Ganymede by large-scale shear faulting. *J Geophys Res* 93(B8):8795–8824

- Murray CD, Dermott SF (1999) Solar system dynamics. Cambridge University Press, Cambridge, NY
- Neish CD, Lorenz RD (2012) Titan's global crater population: A new assessment. *Planet Space Sci* 60, 26–33
- Neukum G (1975) Cratering in the Earth-Moon system – some comparison with other terrestrial planets. In: Proceedings of the international college Planet Geology (exp. abstracts), p 341
- Neukum G (1977) Lunar cratering. *Philos Trans R Soc Lond A* 285(1327):267–272
- Neukum G (1985) Cratering records of the satellites of Jupiter and Saturn. *Adv Space Res* 5(8):107–116
- Neukum G (1997) Bombardment history of the Jovian system. In: The three Galileos: the man, the spacecraft, the telescope. In: Proceedings of the conference held in Padova, Italy, edited, Kluwer Academic, Dordrecht, 7–10 Jan 1997
- Neukum G, Ivanov BA (1994) Crater size distributions and impact probabilities on Earth from lunar, terrestrial-type planets, and asteroid cratering data. In: Gehrels T (ed) Hazards due to comets and asteroids. University of Arizona Press, Tucson, pp 359–416
- Neukum G, Wagner R, Wolf U, Ivanov BA, Head JW, Pappalardo RT, Klemaszewski JE, Greeley R, Belton MJS, Galileo SSI Team (1998) Cratering chronology in the Jovian system and derivation of absolute ages. In: Lunar and planetary science conference, XXIX, Houston, Texas. Abstract no. 1742, 16–20 March 1998
- Neukum G, Ivanov BA, Hartmann WK (2001) Cratering records in the inner solar system in relation to the lunar reference system. In: Geiss J, Kallenbach R, Hartmann WK (eds) Chronology and evolution of Mars: proceedings from an ISSI workshop, 10–14 April 2000, Bern, Kluwer Academic, Boston, pp 55–86
- Neukum G, Wagner RJ, Denk T, Porco CC, The Cassini ISS Team (2005) The cratering record of the Saturnian satellites Phoebe, Tethys, Dione and Iapetus in comparison: first results from analysis of the Cassini ISS imaging data. In: Lunar and planetary science conference, XXXVI, Houston, Texas. Abstract no. 2034, 14–18 March 2005
- Neukum G, Wagner R, Denk T, Porco CC (2006) Cratering chronologies and ages of the major Saturnian satellites. *Geophys Res Abstr* 8(09252), EGU General Assembly, Vienna, Austria, 2–7 April 2006
- Nimmo F (2004) Stresses generated in cooling viscoelastic ice shells: application to Europa. *J Geophys Res* 109:E12001
- Nimmo F, Gaidos E (2002) Strike-slip motion and double ridge formation on Europa. *J Geophys Res* 107(E4):5021
- Nimmo F, Giese B (2005) Thermal and topographic tests of Europa chaos formation models from Galileo E15 observations. *Icarus* 177(2):327–340
- Nimmo F, Matsuyama I (2007) Reorientation of icy satellites by impact basins. *Geophys Res Lett* 34(19):L19203
- Nimmo F, Pappalardo RT (2004) Furrow flexure and ancient heat flux on Ganymede. *Geophys Res Lett* 31:L19701
- Nimmo F, Pappalardo RT (2006) Diapir-induced reorientation of Saturn's moon Enceladus. *Nature* 441(7093):614–616
- Noll KS, Roush TL, Cruikshank DP, Johnson RE, Pendleton YJ (1997) Detection of ozone on Saturn's satellites Rhea and Dione. *Nature* 388:45
- O'Brien DP, Geissler P, Greenberg R (2002) A melt-through model for Chaos formation on Europa. *Icarus* 156:152–161
- Öpik EJ (1960) The lunar surface as an impact counter. *Mon Not R Astron Soc* 120:404
- Pappalardo RT (1994) The origin and evolution of ridge and trough terrain and the geological history of Miranda. Arizona State University, Tempe
- Pappalardo RT, Collins GC (2005) Strained craters on Ganymede. *J Struct Geol* 27(5):827–838
- Pappalardo RT, Crawford Z, Gleeson D, Mullen M, Wahr J (2005) Europa's lineament history: combining nonsynchronous rotation and diurnal stresses. *Astrobiology* 5:315

- Pappalardo RT, Davis DM (2007) Where's the compression? Explaining the lack of contractional structures on icy satellites. *Lunar Planet Sci C* 1357:108–109
- Pappalardo RT, Greeley R (1995) A review of the origins of subparallel ridges and troughs: generalized morphological predictions from terrestrial models. *J Geophys Res* 100 (E9):18985–19007
- Pappalardo RT, Sullivan RJ (1996) Evidence for separation across a gray band on Europa. *Icarus* 123(2):557–567
- Pappalardo RT, Reynolds SJ, Greeley R (1997) Extensional tilt blocks on Miranda: evidence for an upwelling origin of Arden Corona. *J Geophys Res* 102(E6):13369–13380
- Pappalardo RT, Head JW, Greeley R, Sullivan RJ, Pilcher C, Schubert G, Moore WB, Carr MH, Moore JM, Belton MJS, Goldsby DL (1998a) Geological evidence for solid-state convection in Europa's ice shell. *Nature* 391(6665):365–368, 18–22 March 1996, 18–22 March 1996
- Pappalardo RT, Head JW, Collins GC, Kirk RL, Neukum G, Oberst J, Giese B, Greeley R, Chapman CR, Helfenstein P, Moore JM, McEwen A, Tufts BR, Senske DA, Breneman HH, Klaasen K (1998b) Grooved terrain on Ganymede: first results from Galileo high-resolution imaging. *Icarus* 135(1):276–302
- Pappalardo RT, Belton MJS, Breneman HH, Carr MH, Chapman CR, Collins GC, Denk T, Fagents S, Geissler PE, Giese B, Greeley R, Greenberg R, Head JW, Helfenstein P, Hoppe G, Kadel SD, Klaasen KP, Klemanzowski JE, Magee K, McEwen AS, Moore JM, Moore WB, Neukum G, Phillips CB, Prockter LM, Schubert G, Senske DA, Sullivan RJ, Tufts BR, Turtle EP, Wagner R, Williams KK (1999) Does Europa have a subsurface ocean? Evaluation of the geological evidence. *J Geophys Res* 104(E10):24015–24055
- Pappalardo RT, Collins GC, Head JW, Helfenstein P, McCord TB, Moore JM, Prockter LM, Schenk PM, Spencer JR (2004) Geology of Ganymede. In: Bagenal F, Dowling TE, McKinnon WB (eds) *Jupiter: the planet, satellites, and magnetosphere*. Cambridge University Press, Cambridge, UK
- Pappalardo RT, Crow-Willard E, Golombek M (2010) Thrust faulting as the origin of Dorsa in the trailing hemisphere of Enceladus. DPS meeting #42, Bulletin of the American Astronomical Society, DPS Meeting, Pasadena, California, 3–8 Oct 2010, p 976
- Passey QR, Shoemaker EM (1982) Craters and basins on Ganymede and Callisto – morphological indicators of crustal evolution. In: Morrison D (ed) *Satellites of Jupiter*. University of Arizona Press, Tucson, pp 379–434
- Patel JG, Pappalardo RT, Prockter LM, Collins GC, Head JW (1999a) Morphology of ridge and trough terrain on Europa: Fourier analysis and comparison to Ganymede. *Eos Trans AGU Fall Meeting*, San Francisco, California 80(17):210, 13–17 December 1999
- Patel JG, Pappalardo RT, Head JW, Collins GC, Hiesinger H, Sun J (1999b) Topographic wavelengths of Ganymede groove lanes from Fourier analysis of Galileo images. *J Geophys Res* 104(E10):24 057–24 074
- Patterson GW, Head JW, Pappalardo RT (2006) Plate motion on Europa and nonrigid behavior of the icy lithosphere: the Castalia Macula region. *J Struct Geol* 28:2237–2258
- Patterson GW, Collins GC, Head JW, Pappalardo RT, Prockter LM, Lucchitta BK, Kay JP (2010) Global geological mapping of Ganymede. *Icarus* 207(2):845–867
- Peale SJ (1999) Origin and evolution of the natural satellites. *Ann Rev Astron Astr* 37(1):533–602
- Pechmann JB, Melosh HJ (1979) Global fracture patterns of a despun planet: application to Mercury. *Icarus* 38:243–250
- Petrenko VF, Whitworth RW (1999) Physics of ice. Oxford University Press, Oxford, p 386
- Phillips CB, McEwen AS, Hoppe GV, Fagents SA, Greeley R, Klemanzowski JE, Pappalardo RT, Klaasen KP, Breneman HH (2000) The search for current geologic activity on Europa. *J Geophys Res* 105(E9):22579–22597
- Pieri DC (1981) Lineament and polygon patterns on Europa. *Nature* 289(5793):17–21
- Pieters CM, Adams JB, Head JW, McCord TB, Zisk SH (1982) Primary ejecta in crater rays: the Copernicus example. In: *Lunar and planetary science, XIII*, Houston, Texas. Abstract no. 1320, pp 623–624, 15–19 March 1982

- Pike RJ (1980) Control of crater morphology by gravity and target type – Mars, Earth, Moon. In: Proceedings of the lunar and planetary science conference, XI, Houston, Texas. vol 3. (A82-22351 09-91), pp 2159–2189, 17–21 March 1980
- Pike RJ (1988) Geomorphology of impact craters on Mercury. In: Vilas F, Chapman C, Matthews MS (eds) *Mercury*. University of Arizona Press, Tucson, pp 165–273
- Plescia JB (1983) The geology of Dione. *Icarus* 56(2):255–277
- Plescia JB (1987) Cratering history of the Uranian Satellites: Umbriel, Titania, and Oberon. *J Geophys Res* 92(A13):14918–14932
- Plescia JB (1988) Cratering history of Miranda: implications for geologic processes. *Icarus* 73 (3):442–461
- Plescia JB, Boyce JM (1983) Crater numbers and geological histories of Iapetus, Enceladus, Tethys and Hyperion. *Nature* 301(5902):666–670
- Plescia JB, Boyce JM (1985) Impact cratering history of the Saturnian satellites. *J Geophys Res* 90:2029–2037
- Pollack JB, Consolmagno G (1984) Origin and evolution of the Saturn system. In: Gehrels T, Matthews MS (eds) *Saturn*. University of Arizona Press, Tucson, pp 811–866
- Porco CC, Baker E, Barbara J, Beurle K, Brahic A, Burns JA, Charnoz S, Cooper N, Dawson DD, Del Genio AD, Denk T, Dones L, Dyudina U, Evans MW, Giese B, Grazier K, Helfenstein P, Ingersoll AP, Jacobson RA, Johnson TV, McEwen A, Murray CD, Neukum G, Owen WM, Perry J, Roatsch T, Spitale J, Squyres S, Thomas PC, Tiscareno M, Turtle E, Vasavada AR, Veverka J, Wagner R, West R (2005a) Cassini imaging science: initial results on Phoebe and Iapetus. *Science* 307(5713):1237–1242
- Porco CC, Baker E, Barbara J, Beurle K, Brahic A, Burns JA, Charnoz S, Cooper N, Dawson DD, Del Genio AD, Denk T, Dones L, Dyudina U, Evans MW, Fussner S, Giese B, Grazier K, Helfenstein P, Ingersoll AP, Jacobson RA, Johnson TV, McEwen A, Murray CD, Neukum G, Owen WM, Perry J, Roatsch T, Spitale J, Squyres S, Thomas P, Tiscareno M, Turtle EP, Vasavada AR, Veverka J, Wagner R, West R (2005b) Imaging of Titan from the Cassini spacecraft. *Nature* 434(7030):159–168
- Porco CC, Helfenstein P, Thomas PC, Ingersoll AP, Wisdom J, West R, Neukum G, Denk T, Wagner R, Roatsch T, Kieffer S, Turtle E, McEwen A, Johnson TV, Rathbun J, Veverka J, Wilson D, Perry J, Spitale J, Brahic A, Burns JA, DelGenio AD, Dones L, Murray CD, Squyres S (2006) Cassini observes the active south pole of Enceladus. *Science* 311(5766):1393–1401
- Prockter LM, Antman AM, Pappalardo RT, Head JW, Collins GC (1999) Europa: stratigraphy and geological history of the anti-Jovian region from Galileo E14 solid-state imaging data. *J Geophys Res* 104(E7):16531–16540
- Prockter LM, Pappalardo RT (2000) Folds on Europa: implications for crustal cycling and accommodation of extension. *Science* 289(5481):941–943
- Prockter LM (2001) Creation and destruction of lithosphere on Europa: from bands to folds. In: Lunar and planetary science conference, XXXII, Houston, Texas. Abstract no. 1452, 12–16 March 2001
- Prockter LM, Patterson GW (2009) Morphology and evolution of Europa's ridges and bands. In: Pappalardo RT, McKinnon WB, Khurana KK (eds) *Europa*. University of Arizona Press, Tucson, pp 237–258
- Prockter LM, Head JW, Pappalardo RT, Senske DA, Neukum G, Wagner R, Wolf U, Oberst JO, Giese B, Moore JM, Chapman CR, Helfenstein P, Greeley R, Breneman HH, Belton MJS (1998) Dark Terrain on Ganymede: geological mapping and interpretation of Galileo Regio at high resolution. *Icarus* 135(1):317–344
- Prockter LM, Head JW III, Pappalardo RT, Sullivan RJ, Clifton AE, Giese B, Wagner R, Neukum G (2002) Morphology of Europan bands at high resolution: a mid-ocean ridge-type rift mechanism. *J Geophys Res* 107:5028
- Prockter LM, Nimmo F, Pappalardo RT (2005) A shear heating origin for ridges on Triton. *Geophys Res Lett* 32(14):L14202

- Prockter LM, Lopes RMC, Giese B, Jaumann R, Lorenz RD, Pappalardo RT, Patterson GW, Thomas PC, Turtle EP, Wagner RJ (2010) Characteristics of icy surfaces in: satellites of the outer Solar system: exchange Processes involving the interiors. *Space Sci Rev* 211(1):63–111
- Purves NG, Pilcher CB (1980) Thermal migration of water on the Galilean satellites. *Icarus* 43(1):51–55
- Radebaugh J, Lorenz RD, Kirk RL, Lunine JI, Stofan ER, Lopes RMC, Wall SD (2007) Mountains on Titan observed by Cassini Radar. *Icarus* 192:77–91
- Radebaugh J, Lorenz RD, Lunine JI, Wall SD, Boubin G, Reffet E, Kirk RL, Lopes RM, Stofan ER, Soderblom L, Allison M, Janssen M, Paillou P, Callahan P, Spencer C, Cassini Radar T (2008) Dunes on Titan observed by Cassini Radar. *Icarus* 194(2):690–703
- Radebaugh J (2009) Planetary science: Titan's sticky dunes? *Nat Geosci* 2(9):608–609
- Rathbun JA, Musser GS Jr, Squyres SW (1998) Ice diapirs on Europa: implications for liquid water. *Geophys Res Lett* 25:4157–4160
- Riley J, Hoppa GV, Greenberg R, Tufts BR, Geissler P (2000) Distribution of chaotic terrain on Europa. *J Geophys Res* 105(E9):22599–22615
- Rhoden AR, Hurford TA, Manga M (2011) Strike-slip fault patterns on Europa: obliquity or polar wander? *Icarus* 211(1):636–647
- Roatsch T, Kersten E, Waehlisch M, Hoffmeister A, Neukum G, Porco CC (2009) High resolution Rhea Atlas derived from Cassini ISS images. European planetary science congress, Potsdam, Germany. Abstracts 4, abstract no. EPSC2009-61, 13–18 September
- Roberts JH, Nimmo F (2009) Tidal dissipation due to despinning and the equatorial ridge on Iapetus. In: Lunar and planetary science conference, The Woodlands, Texas, XL. Abstract no. 1927, 23–27 March 2009
- Rothery DA (1999) Satellites of the outer Planets: Worlds in their own right. Oxford University Press, New York, p 230
- Sandwell D, Schubert G (2010) A contraction model for the flattening and equatorial ridge of Iapetus. *Icarus* 210(2):817–822
- Sarid AR, Greenberg R, Hoppa GV, Hurford TA, Tufts BR, Geissler P (2002) Polar wander and surface convergence of Europa's ice shell: evidence from a survey of strike-slip displacement. *Icarus* 158:24–41
- Sarid AR, Greenberg R, Hoppa GV, Geissler P, Preblich B (2004) Crack azimuths on Europa: time sequence in the southern leading face. *Icarus* 168:144–157
- Sarid AR, Greenberg R, Hoppa GV, Brown JDM, Geissler P (2005) Crack azimuths on Europa: the G1 lineament sequence revisited. *Icarus* 173:469–479
- Sarid AR, Greenberg R, Hurford TA (2006) Crack azimuths on Europa: sequencing of the northern leading hemisphere. *J Geophys Res* 111:E08004
- Schaller EL, Brown ME, Roe HG, Bouchez AH (2006a) A large cloud outburst at Titan's south pole. *Icarus* 182(1):224–229
- Schaller EL, Brown ME, Roe HG, Bouchez AH, Trujillo CA (2006b) Dissipation of Titan's south polar clouds. *Icarus* 184(2):517–523
- Schenk PM (1989) Crater formation and modification on the icy satellites of Uranus and Saturn: depth/diameter and central peak occurrence. *J Geophys Res* 94(B4):3813–3832
- Schenk PM (1991) Fluid volcanism on Miranda and Ariel: flow morphology and composition. *J Geophys Res* 96(B2):1887–1906
- Schenk PM (1993) Central pit and dome craters: exposing the interiors of Ganymede and Callisto. *J Geophys Res* 98(E4):7475–7498
- Schenk PM (1995) The geology of Callisto. *J Geophys Res* 100(E9):19023–19040
- Schenk PM, Jackson MPA (1993) Diapirism on Triton: a record of crustal layering and instability. *Geology* 21(4):299–302
- Schenk PM, McKinnon WB (1989) Fault offsets and lateral crustal movement on Europa: evidence for a mobile ice shell. *Icarus* 79(1):75–100
- Schenk PM, McKinnon WB (1991) Dark-ray and dark-floor craters on Ganymede, and the provenance of large impactors in the Jovian system. *Icarus* 89:318–346

- Schenk PM, Moore JM (1995) Volcanic constructs on Ganymede and Enceladus: topographic evidence from stereo images and photoclinometry. *J Geophys Res* 100(E9):19009–19022
- Schenk PM, Moore JM (1998) Geologic landforms and processes on icy satellites. In: Schmitt B, de Bergh C, Festou M (eds) *Solar System ices*, based on reviews presented at the international symposium “Solar system ices”, Toulouse, Kluwer Academic, Dordrecht, 27–30 Mar 1998, p 551
- Schenk PM, Pappalardo RT (2004) Topographic variations in chaos on Europa: implications for diapiric formation. *Geophys Res Lett* 31(16):L16703
- Schenk PM, Moore JM (2007) Impact crater topography and morphology on Saturnian mid-sized satellites. In: Lunar and planetary science conference, XXXVIII, Houston, Texas. LPI contribution no. 1338, p 2305, 12–16 March 2007
- Schenk PM, Moore JM (2009) Eruptive volcanism on Saturn’s icy Moon Dione. In: Lunar and planetary science conference, The Woodlands, Texas, XL. Abstract no. 2465, 23–27 March 2007
- Schenk PM, Murphy SW (2011) The rayed craters of Saturn’s icy satellites (including Iapetus): current impactor populations and origins. In: Lunar and planetary science conference, XLII, The Woodlands, Texas. Abstract no. 2098, 7–11 March 2011
- Schenk P, Hamilton DP, Johnson RE, McKinnon WB, Paranicas C, Schmidt J, Showalter MR (2011) Plasma, plumes and rings: Saturn system dynamics as recorded in global color patterns on its midsize icy satellites. *Icarus* 211(1):740–757
- Schenk PM, Ridolfi FJ (2002) Morphology and scaling of ejecta deposits on icy satellites. *Geophys Res Lett* 29:31–34
- Schenk PM, Zahnle K (2007) On the negligible surface age of Triton. *Icarus* 192(1):135–149
- Schenk PM, Asphaug E, McKinnon WB, Melosh HJ, Weissman PR (1996) Cometary nuclei and tidal disruption: the geologic record of crater chains on Callisto and Ganymede. *Icarus* 121 (2):249–274
- Schenk PM, Chapman CR, Zahnle K, Moore JM (2004) Ages and interiors: the cratering record of the Galilean satellites. In: Bagenal F, Dowling TE, McKinnon WB (eds) *Jupiter: the planet, satellites, and magnetosphere*. Cambridge University Press, Cambridge, UK, pp 427–456
- Schenk PM, Matsuyama I, Nimmo F (2008) True polar wander on Europa from global-scale small-circle depressions. *Nature* 453(7193):368–371
- Schmedemann N, Neukum G, Denk T, Wagner R (2008) Stratigraphy and surface ages on Iapetus and other Saturnian satellites. In: Lunar and planetary science, XXXIX, League City, Texas, LPI contribution no. 1391, p 2070. 10–14 March 2008
- Schmidt RM, Housen KR (1987) Some recent advances in the scaling of impact and explosion cratering. *Int J Impact Eng* 5:543–560
- Shaya EJ, Pilcher CB (1984) Polar cap formation on Ganymede. *Icarus* 58(1):74–80
- Shoemaker EM, Wolfe RF (1982) Cratering time scales for the Galilean satellites. In: Morrison D (ed) *Satellites of Jupiter*. University of Arizona Press, Tucson, pp 277–339
- Shoemaker EM, Lucchitta BK, Wilhelms DE, Plescia JB, Squyres SW (1982) The geology of Ganymede. In: Morrison D (ed) *Satellites of Jupiter*. University of Arizona Press, Tucson, pp 435–520
- Showman AP, Stevenson DJ, Malhotra R (1997) Coupled orbital and thermal evolution of Ganymede. *Icarus* 129(2):367–383
- Showman AP, Mosqueira I, Head Iii JW (2004) On the resurfacing of Ganymede by liquid-water volcanism. *Icarus* 172(2):625–640
- Singer K, McKinnon WB (2010) Iapetian tectonics: despinning, respinning, contraction, or something completely different? DPS meeting #42, Bulletin of the American Astronomical Society: Pasadena, p 941
- Singer K, McKinnon WB, Schenk PM, Moore JM (2009) Large landslides on Iapetus: implications for crater and ridge modifications, Bulletin of the American Astronomical Society. DPS Meeting, Puerto Rico, USA, Abstract 38.01, 4–9 October 2009
- Singer KN, McKinnon WB, Schenk PM (2010) Pits, spots, uplifts, and small Chaos regions on Europa: evidence for diapiric upwelling from morphology and morphometry. In: Lunar and

- planetary science conference, The Woodlands, Texas, XXXXI. Abstract no. 2195, 1–5 March 2010
- Smith BA, Soderblom LA, Johnson TV, Ingersoll A, Collins SA, Shoemaker EM, Hunt GE, Masursky H, Carr M, Davies ME, Cook AF, Boyce J, Danielson GE, Owen T, Sagan C, Beebe R, Veverka J, Strom R, McCauley J, Morrison D, Briggs G, Suomi VE (1979a) The Jupiter system through the eyes of Voyager 1. *Science* 204(4396):951–972
- Smith BA, Soderblom LA, Beebe R, Boyce J, Briggs G, Carr M, Collins SA, Cook AF, Danielson GE, Davies ME, Hunt GE, Ingersoll A, Johnson TV, Masursky H, McCauley J, Morrison D, Owen T, Sagan C, Shoemaker EM, Strom R, Suomi VE, Veverka J (1979b) The Galilean satellites and Jupiter: Voyager 2 imaging science results. *Science* 206(4421):927–950
- Smith BA, Soderblom L, Beebe R, Boyce J, Briggs G, Bunker A, Collins SA, Hansen CJ, Johnson TV, Mitchell JL, Terrile RJ, Carr M, Cook AF, Cuzzi J, Pollack JB, Danielson GE, Ingersoll A, Davies ME, Hunt GE, Masursky H, Shoemaker E, Morrison D, Owen T, Sagan C, Veverka J, Strom R, Suomi VE (1981) Encounter with Saturn: Voyager 1 imaging science results. *Science* 212(4491):163–191
- Smith BA, Soderblom L, Batson R, Bridges P, Inge JAY, Masursky H, Shoemaker E, Beebe R, Boyce J, Briggs G, Bunker A, Collins SA, Hansen CJ, Johnson TV, Mitchell JL, Terrile RJ, Cook AF, Cuzzi J, Pollack JB, Danielson GE, Ingersoll AP, Davies ME, Hunt GE, Morrison D, Owen T, Sagan C, Veverka J, Strom R, Suomi VE (1982) A new look at the Saturn system: the Voyager 2 images. *Science* 215(4532):504–537
- Smith BA, Soderblom LA, Beebe RF, Bollinger K, Boyce JM, Brahic A, Briggs GA, Brown RH, Chyba C, Collins SA, Cook AF, Croft SK, Cruikshank D, Cuzzi JN, Danielson GE, Davies ME, Dowling TE, Godfrey D, Hansen CJ, Harris C, Helfenstein CP, Hunt GE, Ingersoll AP, Johnson TV, Krauss RJ, Masursky H, Morrison D, Owen T, Plescia JB, Pollack JB, Porco CC, Rages K, Sagan C, Schwartz J, Shoemaker EM, Sromovsky LA, Stoker C, Strom RG, Suomi VE, Synott SP, Terrile RJ, Thomas P, Thompson WR, Veverka J (1986) Voyager 2 in the Uranian system: imaging science results. *Science* 233(4759):43–64
- Smith BA, Soderblom LA, Banfield D, Barnet C, Basilevsky AT, Beebe RF, Bollinger K, Boyce JM, Brahic A, Briggs GA, Brown RH, Chyba C, Collins SA, Colvin T, Cook AF, Crisp D, Croft SK, Cruikshank D, Cuzzi JN, Danielson GE, Davies ME, De Jong E, Dones L, Godfrey D, Goguen J, Grenier I, Haemmerle VR, Hammel H, Hansen CJ, Helfenstein CP, Howell C, Hunt GE, Ingersoll AP, Johnson TV, Kargel J, Kirk R, Kuehn DI, Limaye S, Masursky H, McEwen A, Morrison D, Owen T, Owen W, Pollack JB, Porco CC, Rages K, Rogers P, Rudy D, Sagan C, Schwartz J, Shoemaker EM, Showalter M, Sicardi B, Simonelli D, Spencer J, Sromovsky LA, Stoker C, Strom RG, Suomi VE, Synott SP, Terrile RJ, Thomas P, Thompson WR, Verbiscer A, Veverka J (1989) Voyager 2 at Neptune: imaging science results. *Science* 246(4936):1422–1449
- Smith HT, Johnson RE, Sittler EC, Shappirio M, Reisenfeld D, Tucker OJ, Burger M, Crary FJ, McComas DJ, Young DT (2007) Enceladus: the likely dominant nitrogen source in Saturn's magnetosphere. *Icarus* 188(2):356–366
- Soderblom LA, Kieffer SW, Becker TL, Brown RH, Cook AF, Hansen CJ, Johnson TV, Kirk RL, Shoemaker EM (1990) Triton's geyser-like plumes: discovery and basic characterization. *Science* 250(4979):410–415
- Soderblom LA, Kirk RL, Lunine JI, Anderson JA, Baines KH, Barnes JW, Barrett JM, Brown RH, Buratti BJ, Clark RN, Cruikshank DP, Elachi C, Janssen MA, Jaumann R, Karkoschka E, Mouélic SL, Lopes RM, Lorenz RD, McCord TB, Nicholson PD, Radecbaugh J, Rizk B, Sotin C, Stofan ER, Sucharski TL, Tomasko MG, Wall SD (2007) Correlations between Cassini VIMS spectra and RADAR SAR images: implications for Titan's surface composition and the character of the Huygens probe landing site. *Planetary Science* 55(13):2025–2036
- Spahn F, Schmidt J, Albers N, Horning M, Makuch M, Seiss M, Kempf S, Srama R, Dikarev V, Helfert S, Moragas-Klostermeyer G, Krivov AV, Sremcevic M, Tuzzolino AJ, Economou T, Grun E (2006) Cassini dust measurements at Enceladus and implications for the origin of the E ring. *Science* 311(5766):1416–1418

- Spaun NA, Head JW, Collins GC, Prockter LM, Pappalardo RT (1998) Conamara Chaos region, Europa: reconstruction of mobile polygonal ice blocks. *Geophys Res Lett* 25:4277–4280
- Spaun NA, Head JW III, Pappalardo RT, The Galileo SSI Team (1999) Chaos and lenticulae on Europa: structure, morphology and comparative analysis. In: Lunar and planetary science conference, XXX, Houston, Texas. Abstract no. 1276, 15–19 March 1999
- Spaun NA, Head JW III, Pappalardo RT, The Galileo SSI Team (2001) Scalloped depressions on Ganymede from Galileo (G28) very high resolution imaging. In: Lunar and planetary science conference, XXXII, Houston, Texas. Abstract no. 1448, 12–16 March 2001
- Spaun NA, Head JW III, Pappalardo RT (2004) Europan Chaos and lenticulae: a synthesis of size, spacing, and areal density analyses. In: Lunar and planetary science conference, Houston, Texas, XXXV. Abstract no. 1409, 15–19 March 2004
- Spencer JR, Maloney PR (1984) Mobility of water ice on Callisto: evidence and implications. *Geophys Res Lett* 11(12):1223–1226
- Spencer JR (1987) Icy Galilean satellite reflectance spectra: less ice on Ganymede and Callisto? *Icarus* 70(1):99–110
- Spencer JR, Prockter L, Pappalardo R, Head J, Moore J, Galileo SSI Team (1998) Local volatile migration on Ganymede: Galileo SSI images, PPR radiometry, and theoretical considerations, LPSC XXIX, 16–20 March, Houston, 1149
- Spencer JR, Calvin WM (2002) Condensed O<sub>2</sub> on Europa and Callisto. *Astron J* 124(6):3400
- Spencer JR, Barr AC, Esposito LW, Helfenstein P, Ingersoll AP, Jaumann R, McKay CP, Nimmo F, Waite JH (2009) Enceladus: an active cryovolcanic satellite. In: Dougherty MK, Esposito LW, Krimigis SM (eds) *Saturn from Cassini-Huygens*. Springer, Dordrecht, pp 683–724
- Spencer JR, Pearl JC, Segura M, Flasar FM, Mamoutkine A, Romani P, Buratti BJ, Hendrix AR, Spilker LJ, Lopes RMC (2006) Cassini encounters enceladus: background and the discovery of a South polar hot spot. *Science* 311(5766):1401–1405
- Spencer JR, Denk T (2010) Formation of Iapetus' extreme Albedo Dichotomy by exogenically triggered thermal ice migration. *Science* 327(5964):432–435
- Spitale JN, Porco CC (2007) Association of the jets of enceladus with the warmest regions on its south-polar fractures. *Nature* 449(7163):695–697
- Stofan ER, Elachi C, Lunine JI, Lorenz RD, Stiles B, Mitchell KL, Ostro S, Soderblom L, Wood C, Zebker H, Wall S, Janssen M, Kirk R, Lopes R, Paganelli F, Radabaugh J, Wye L, Anderson Y, Allison M, Boehmer R, Callahan P, Encrenaz P, Flaminii E, Francescetti G, Gim Y, Hamilton G, Hensley S, Johnson WTK, Kelleher K, Muhleman D, Paillou P, Picardi G, Posa F, Roth L, Seu R, Shaffer S, Vettella S, West R (2007) The lakes of Titan. *Nature* 445(7123):61–64
- Stone EC, Cummings AC, Loooper MD, Selesnick RS, Lal N, McDonald FB, Trainor JH, Chenette DL (1989) Energetic charged particles in the magnetosphere of Neptune. *Science* 246(4936):1489–1494
- Spudis PD (1993) The geology of multi-ring impact basins: the Moon and other planets. Cambridge University Press, Cambridge, UK
- Squyres SW (1980) Volume changes in Ganymede and Callisto and the origin of grooved terrain. *Geophys Res Lett* 7(8):593–596
- Squyres SW (1981) The topography of Ganymede's grooved terrain. *Icarus* 46(2):156–168
- Squyres SW, Croft SK (1986) The tectonics of icy satellites. In: Burns J, Matthews MS (eds) *Satellites*. University of Arizona Press, Tucson, pp 293–341
- Squyres SW, Reynolds RT, Cassen PM, Peale SJ (1983) The evolution of Enceladus. *Icarus* 53 (2):319–331
- Stephan K (2006) Chemisch-physikalische Zusammensetzung der Ganymedoberfläche: Zusammenhänge mit geologischen Strukturen und deren Gestaltungsprozessen. Ph.D. Dissertation (in German) Thesis
- Stephan K, Hibbitts CA, Wagner R, Jaumann R, Hansen GB (2009) Ganymede's spectral properties: implications for further investigations in a future mission to Jupiter and its satellites, In: European planetary science congress, Potsdam, Germany, 4 EPSC2009-2633, 13–18 September

- Stephan K, Jaumann R, Wagner R, Clark RN, Cruikshank DP, Hibbitts CA, Roatsch T, Hoffmann H, Brown RH, Filacchione G, Buratti BJ, Hansen GB, McCord TB, Nicholson PD, Baines KH (2010) Dione's spectral and geological properties. *Icarus* 206(2):631–652
- Stephan K, Jaumann R, Wagner R, Clark RN, Cruikshank DP, Hibbitts CA, Roatsch T, Hoffmann H, Brown RH, Filacchione G, Buratti BJ, Hansen GB, Nicholson PD, Baines KH, Nelson RM, and Matson DL (2011) The Saturnian satellite Rhea as seen by Cassini VIMS. *Icarus* (submitted)
- Stevenson DJ (1982) Volcanism and igneous processes in small icy satellites. *Nature* 298 (5870):142–144
- Stofan ER, Lunine JI, Lopes R, Paganelli F, Lorenz RD, Wood CA, Kirk R, Wall S, Elachi C, Soderblom LA, Ostro S, Janssen M, Radebaugh J, Wye L, Zebker H, Anderson Y, Allison M, Boehmer R, Callahan P, Encrana P, Flamini E, Francescetti G, Gim Y, Hamilton G, Hensley S, Johnson WTK, Kelleher K, Muhleman D, Picardi G, Posa F, Roth L, Seu R, Shaffer S, Stiles B, Vetrella S, West R (2006) Mapping of Titan: results from the first Titan radar passes. *Icarus* 185(2):443–456
- Stooke PJ (1989) Geology of Mimas. In: Abstracts of the lunar and planetary science conference, Houston, Texas, 20, p 1069, 13–17 March 1989
- Stooke PJ (2001) Voyager images revisited: new views of the satellites of Saturn and Uranus. In: Lunar and planetary science conference, Houston, Texas, XXXII. Abstract no. 1074, 12–16 March 2001
- Stooke PJ (2002) Tethys and Dione: new geological interpretations. In: Lunar and planetary science conference, XXXIII, Houston, Texas. Abstract no. 1553, 11–15 March 2002
- Strom RG, Woronow A, Gurnis M (1981) Crater populations on Ganymede and Callisto. *J Geophys Res* 86(A10):8659–8674
- Strom RG, Malhotra R, Ito T, Yoshida F, Krings DA (2005) The origin of planetary impactors in the inner Solar System. *Science* 309(5742):1847–1850
- Sullivan R, Greeley R, Homan K, Klemaszewski J, Belton MJS, Carr MH, Chapman CR, Tufts R, Head JW, Pappalardo R, Moore J, Thomas P, The Galileo SSI Team (1998) Episodic plate separation and fracture infill on the surface of Europa. *Nature* 391(6665):371–373
- Tanaka KL (1986) The stratigraphy of Mars. *J Geophys Res* 91(B13):E139–E158
- Teolis BD, Jones GH, Miles PF, Tokar RL, Magee BA, Waite JH, Roussos E, Young DT, Crary FJ, Coates AJ, Johnson RE, Tseng WL, Baragiola RA (2010) Cassini finds an oxygen-carbon dioxide atmosphere at Saturn's icy moon Rhea. *Science* 330(6012):1813–1815
- Tera F, Papanastassiou DA, Wasserburg GJ (1974) Isotopic evidence for a terminal lunar cataclysm. *Earth Planet Sci Lett* 22(1):1–21
- Thomas PC (1988) Radii, shapes, and topography of the satellites of Uranus from limb coordinates. *Icarus* 73:427–441
- Thomas PC, Burns JA, Helfenstein P, Squyres S, Veverka J, Porco C, Turtle EP, McEwen A, Denk T, Giese B, Roatsch T, Johnson TV, Jacobson RA (2007) Shapes of the saturnian icy satellites and their significance. *Icarus* 190(2):573–584
- Tian F, Stewart AIF, Toon OB, Larsen KW, Esposito LW (2007) Monte Carlo simulations of the water vapor plumes on Enceladus. *Icarus* 188(1):154–161
- Tittemore WC, Wisdom J (1990) Tidal evolution of the Uranian satellites: III. Evolution through the Miranda-Umbriel 3:1, Miranda-Ariel 5:3, and Ariel-Umbriel 2:1 mean-motion commensurabilities. *Icarus* 85(2):394–443
- Tokano T (2008) Dune-forming winds on Titan and the influence of topography. *Icarus* 194 (1):243–262
- Tomasko MG, Archinal B, Becker T, Bezard B, Bushroe M, Combes M, Cook D, Coustenis A, de Bergh C, Dafoe LE, Doose L, Doute S, Eibl A, Engel S, Gliem F, Grieger B, Holso K, Howington-Kraus E, Karkoschka E, Keller HU, Kirk R, Kramm R, Kuppers M, Lanagan P, Lellouch E, Lemmon M, Lunine J, McFarlane E, Moores J, Prout GM, Rizk B, Rosiek M, Rueff P, Schroder SE, Schmitt B, See C, Smith P, Soderblom L, Thomas N, West R (2005) Rain, winds and haze during the Huygens probe's descent to Titan's surface. *Nature* 438 (7069):765–778

- Tran BN, Joseph JC, Ferris JP, Persans PD, Chera JJ (2003) Simulation of Titan haze formation using a photochemical flow reactor: the optical constants of the polymer. *Icarus* 165 (2):379–390
- Tsiganis K, Gomes R, Morbidelli A, Levison HF (2005) Origin of the orbital architecture of the giant planets of the Solar System. *Nature* 435:459–461
- Turtle EP, Phillips CB, Collins GC, McEwen AS, Moore JM, Pappalardo RT, Schenk PM, The Galileo Imaging Team (1999) Europan impact crater diameters and inferred transient crater dimensions and excavation depths. Lunar and planetary science conference, Houston, Texas, XXX. Abstract no. 1882, 15–19 March 1999
- Turtle EP, Perry JE, McEwen AS, DelGenio AD, Barbara J, West RA, Dawson DD, Porco CC (2009) Cassini imaging of Titan's high-latitude lakes, clouds, and south-polar surface changes. *Geophys Res Lett* 36(2):L02204
- Van Dorn WG (1968) Tsunamis on the Moon? *Nature* 220(5172):1102–1107
- Wagner RJ (2007) Untersuchungen zur Chronostratigraphie, Impaktchronologie und geologischen Entwicklung des Jupitersatelliten Callisto auf der Basis der Galileo-SSI-Kameradaten. Ph.D. Dissertation (in German) Thesis
- Wagner RJ, Neukum G, Giese B, Roatsch T, Wolf U, Denk T, The Cassini ISS Team (2006) Geology, ages and topography of Saturn's satellite Dione observed by the Cassini ISS camera. In: Lunar and planetary science conference, Houston, Texas, XXXVII. Abstract no. 1805, 13–17 March 2006
- Wagner RJ, Neukum G, Giese B, Roatsch T, Wolf U (2007a) The global geology of Rhea: preliminary implications from the Cassini ISS data. In: Lunar and planetary science, League City, Texas, XXXVIII. LPI contribution no. 1338, 1958, 12–17 March 2007
- Wagner RJ, Neukum G, Giese B, Roatsch T, Denk T (2007b) Geology and geomorphology of Rhea: a first look at the high-resolution Cassini images from the targeted flyby on Aug. 30, 2007. In: Paper presented at AGU Fall Meeting, 10–14 Dec 2007, San Francisco, California
- Wagner RJ, Neukum G, Giese B, Roatsch T, Denk T, Wolf U, Porco CC (2008) Geology of Saturn's satellite Rhea on the basis of the high-resolution images from the targeted flyby 049 on 30 Aug 2007. In: Lunar and Planetary Science Conf. XXXIX, 10–14 March 2008, League City, Texas. Abstr. No. 1930
- Wagner RJ, Neukum G, Giese B, Roatsch T, Denk T, Wolf U, Porco CC (2010) The geology of Rhea: a first look at the ISS camera data from orbit 121, 21 Nov 2009 in Cassini's extended mission. In: Lunar and Planetary Science Conf. XLI, 1–5 March 2010. The Woodlands, Texas. Abstr. No. 1672
- Wagner RJ, Neukum G, Wolf U, Schmedemann N, Denk T, Stephan K, Roatsch T, Porco CC (2011) Rayed craters on Dione and Rhea. In: Lunar and planetary science conference, The Woodlands, Texas, XLII. Abstract no. 2249, 7–11 March 2011
- Waite JH, Combi MR, Ip W-H, Cravens TE, McNutt RL, Kasprzak W, Yelle R, Luhmann J, Niemann H, Gell D, Magee B, Fletcher G, Lunine J, Tseng W-L (2006) Cassini ion and neutral mass spectrometer: Enceladus plume composition and structure. *Science* 311 (5766):1419–1422
- Wetherill GW (1975) Late heavy bombardment of the moon and terrestrial planets. In: Lunar science conference, Houston, Texas, VI, 2 (A78-46668 21-91), pp 1539–1561, 17–21 March 1975
- Wetherill GW (1981) Nature and origin of basin-forming projectiles, Multi-ring basins: formation and evolution. In: Proceedings of lunar and planetary science conference, Houston, Texas, vol 12A. pp 1–18, 16–20 March 1981
- Wilhelms DE (1987) The geologic history of the Moon, U.S.G.S. Professional paper 1349, Flagstaff, p 302
- Williams KK, Greeley R (1998) Estimates of ice thickness in the Conamara Chaos region of Europa. *Geophys Res Lett* 25(23):4273–4276
- Wilson L, Head JW, Pappalardo RT (1997) Eruption of lava flows on Europa: theory and application to Thrace Macula. *J Geophys Res* 102(E4):9263–9272

- Wood CA, Lorenz R, Kirk R, Lopes R, Mitchell K, Stofan E, The Cassini RADAR Team (2010) Impact craters on Titan. *Icarus* 206:334–344
- Woronow A, Strom RG, Gurnis M (1982) Interpreting the cratering record – mercury to Ganymede and Callisto. In: Morrison D (ed) *Satellites of Jupiter*. University of Arizona Press, Tucson, pp 237–276
- Yasui M, Arakawa M (2008) Experimental study on the rheology of ice-silica beads mixtures: effects of silica content and temperature on the flow law. In: Paper presented at the science of solar system ices (ScSSI): a cross-disciplinary workshop, Oxnard, 5–8 May 2008
- Yung YL, Allen M, Pinto JP (1984) Photochemistry of the atmosphere of Titan – comparison between model and observations. *Astrophys J Suppl Ser* 55:465–506 (ISSN 0067–0049)
- Zahnle K, Dones L, Levison HF (1998) Cratering rates on the Galilean Satellites. *Icarus* 136 (2):202–222
- Zahnle K, Schenk P, Levison H, Dones L (2003) Cratering rates in the outer Solar System. *Icarus* 163(2):263–289
- Zhong F, Mitchell KL, Hays CC, Choukroun M, Barmatz M, Kargel JS (2009) The rheology of cryovolcanic slurries: motivation and phenomenology of methanol-water slurries with implications for Titan. *Icarus* 202(2):607–619
- Zuber MT, Parmentier EM (1984) Lithospheric stresses due to radiogenic heating of an ice-silicate planetary body: implications for Ganymede's tectonic evolution. *J Geophys Res* 89: B429–B437

**Part III**  
**Volatiles in Ices**

# Chapter 11

## Amorphous and Crystalline H<sub>2</sub>O-Ice

Rachel M.E. Mastrapa, William M. Grundy, and Murthy S. Gudipati

**Abstract** On the surfaces of Solar System objects, H<sub>2</sub>O-ice can form in several different phases, including amorphous and crystalline. The stability of these phases as a function of thermal and radiation history is an active area of laboratory research. Meanwhile, remote detection of H<sub>2</sub>O-ice depends on the interpretation of infrared absorptions that are also dependent on phase and temperature. Surface processes, such as surface chemistry, micrometeorite gardening, and cryovolcanic resurfacing, on the surfaces of objects are linked to H<sub>2</sub>O-ice phase. We review the current state of laboratory measurements in the context of observations of Solar System objects and list the areas where new measurements are needed.

### 11.1 Introduction

Amorphous and crystalline phases of low-temperature and low-pressure H<sub>2</sub>O-ices play an important role in the evolution of Solar System icy objects, especially those subjected to local or wide-range thermal variations and high doses of radiation.

---

R.M.E. Mastrapa (✉)

SETI Institute, 189 Bernardo Ave, Suite 100, Mountain View, CA 94043, USA

NASA Ames Research Center, Moffett Field, CA 94035, USA

e-mail: [rachel.m.mastrapa@nasa.gov](mailto:rachel.m.mastrapa@nasa.gov)

W.M. Grundy

Lowell Observatory, 1400 West Mars Hill Road, Flagstaff, AZ 86001, USA

e-mail: [w.grundy@lowell.edu](mailto:w.grundy@lowell.edu)

M.S. Gudipati

Science Division, Jet Propulsion Laboratory, California Institute of Technology,  
Mail Stop 183-301, 4800 Oak Grove Drive, Pasadena, CA 91109, USA

Institute for Physical Sciences and Technology, University of Maryland,

Space Science Building, College Park, MD 27042, USA

e-mail: [gudipati@jpl.nasa.gov](mailto:gudipati@jpl.nasa.gov); [gudipati@umd.edu](mailto:gudipati@umd.edu)

The presence of H<sub>2</sub>O-ice in the outer Solar System has long been confirmed by remote sensing of the surfaces of icy objects and its ubiquity in the Solar System is not surprising considering its presence in the interstellar medium and dense clouds. Such a simple, common, and life-enabling material still has an interesting story to tell. In this chapter we will discuss the various phases of H<sub>2</sub>O-ice that are stable on outer Solar System objects and how the phase can be used to interpret the history of their surfaces. Although H<sub>2</sub>O in various forms has also been found on Mercury, Mars, and the Moon (Harmon and Slade 1992; Slade et al. 1992; Carr 1996; Feldman et al. 1998; Clark 2009; Sunshine et al. 2009), this chapter will focus on H<sub>2</sub>O-ice in the outer Solar System.

The stable phases of H<sub>2</sub>O-ice and their required conditions of formation have been identified by diffraction measurements of laboratory samples, with many follow up measurements using infrared spectroscopy. These studies, along with calorimetry measurements, have been used to calculate the reaction rates of the phase changes of H<sub>2</sub>O-ice. Phase changes as a result of radiation dose have been studied using both diffraction techniques and infrared spectroscopy, while some Solar System processes, such as micrometeorite bombardment, remain largely uninvestigated. The phase of H<sub>2</sub>O-ice on an icy surface has many implications for the dominant surface processes. The phase of H<sub>2</sub>O-ice can change how chemistry occurs within the ice, see Sect. 11.5.3.

The only current tool for remotely assessing H<sub>2</sub>O-ice phase is infrared spectroscopy, we will therefore restrict our review of laboratory spectra to that of low pressure phases that are observable on the surfaces of icy objects. The locations and profiles of the infrared absorptions of pure H<sub>2</sub>O-ice laboratory samples are highly dependent on temperature and phase. The shapes of the bands are further affected when by the mixing of phases through the creation of synthetic spectra.

Finally, we will discuss the current state of observations of H<sub>2</sub>O-ice in the outer Solar System and try to place them in the context of phase stability in relation to thermal and radiation environment.

## 11.2 Phases of H<sub>2</sub>O-Ice

Of the many phases of low temperature, low pressure H<sub>2</sub>O-ice, we limit our discussion to those that are likely to be detectable via remote sensing. Under Solar System surface conditions, the stable phase of H<sub>2</sub>O-ice is type I (one) (Fig. 11.1). There are two broad categories of ice I: amorphous and crystalline, each containing several sub-phases.

Amorphous H<sub>2</sub>O-ice is known by several names, such as I<sub>a</sub>, vitreous ice, and amorphous solid water (ASW). Some terms are restricted by the formation conditions of the laboratory ice such as vapor or liquid deposition. However, the terminology can be unclear. In this chapter, we will refer to vapor deposited amorphous H<sub>2</sub>O-ice as I<sub>a</sub>. Amorphous ice samples created from liquid droplets will be called hyper-quenched glassy water (HGW). Both of these formation conditions may

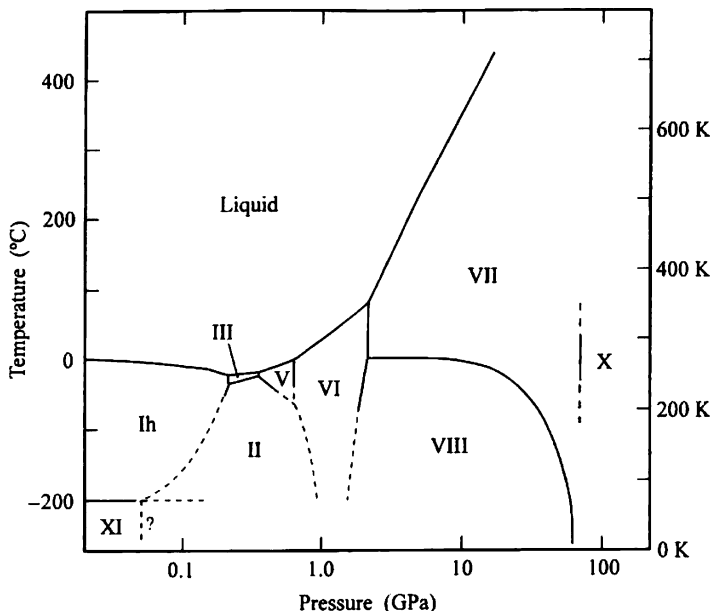


**Fig. 11.1** The stable phases of H<sub>2</sub>O-ice from Petrenko and Whitworth (1999). Note that cubic and amorphous phases are not included because they are not stable

be relevant to Solar System objects. The two main phases of amorphous ice are based on density: high (I<sub>ah</sub>) 1.1 g/cm<sup>3</sup> (Narten et al. 1976) and low (I<sub>al</sub>) 0.94 g/cm<sup>3</sup> (Jenniskens and Blake 1994). Note that these measurements of density are from diffraction measurements and therefore do not take porosity into account. Diffraction techniques will be discussed in Sect. 11.3.1. I<sub>ar</sub> is a relaxed phase of I<sub>al</sub> (Jenniskens and Blake 1996) and is referred to as restrained because it impedes the growth of cubic crystals (Jenniskens and Blake 1994). Two other forms of amorphous H<sub>2</sub>O-ice are formed by GPa compression of I<sub>h</sub>: High Density and Amorphous (HDA) and Low Density Amorphous (LDA). At this point, there are no laboratory measurements that can demonstrate that the infrared spectra of HDA and LDA are distinguishable from those of I<sub>ah</sub> and I<sub>al</sub>, so we will limit our discussion to the low-pressure phases.

H<sub>2</sub>O-ice has two stable crystalline phases hexagonal (I<sub>h</sub>) and cubic (I<sub>c</sub>) in the pressure and temperature range relevant to outer Solar System surfaces. The hexagonal phase of water ice, I<sub>h</sub>, is the most common form of water ice on Earth and is named after its crystallographic structure. The cubic phase of water ice, I<sub>c</sub>, is a metastable version of I<sub>h</sub> (e.g. Petrenko and Whitworth 1999). They have the same density, 0.9197 g/cm<sup>3</sup>, and the same hydrogen bond arrangement, and therefore similar coordination.

Ice XI has been offered as a possible surface component in the outer Solar System because of its stability at very low temperatures and pressures (McKinnon and Hofmeister 2005) (Fig. 11.1), but it is unknown if this phase would be

detectable via remote sensing since very few laboratory measurements have been made of its infrared spectrum.

Measurements of the shock properties of H<sub>2</sub>O have predicted the formation of the high-pressure phases, ices VI and VII and liquid H<sub>2</sub>O (Stewart and Ahrens 2005) (Fig. 11.1). Depending on the rate of cooling, the liquid could re-freeze into I<sub>h</sub> or HGW. Meanwhile, the high-pressure phases may decompose, see further discussion in Sect. 11.4.3.

### ***11.2.1 Review of Diffraction Techniques***

Multiple scattering of light (x-rays) or particles (neutrons, electrons) by atoms in a sample results in interference, which is manifested in the physical phenomenon of diffraction. The information conveyed by that diffraction pattern depends on the radiation source: x-rays sample electron density, neutrons interact with the nucleus, and electrons detect both. In H<sub>2</sub>O-ice, it is expected that the electron density around the O atom contributes to the intensities of electron and x-ray diffraction patterns. For accurate determination of hydrogen atom positions, neutron diffraction methods are widely used (Kuhs and Lehman 1983).

The most important aspect that must be remembered when interpreting x-ray or electron diffraction data of solids is that the electrons and x-rays see only atoms (electron density to be precise) that are next to each other by a given internal distance. However, this technique does not give any information on the voids, pores, and hollow space in the solid. The density of a material derived from diffraction measurements should be considered an average inter-atom distance, and not representative of bulk properties of the sample. For example, the density of HDA was predicted to be at 1.1 g/cm<sup>3</sup> from the x-ray diffraction spectra (Venkatesh et al. 1974). This needs to be kept in mind when interpreting the structures of amorphous material, where there is neither a short-range or long-range 3D structural order. Also, using diffraction techniques to measure the structure of ices is a problematic method since the sample can be damaged by irradiation.

The ultimate atomic resolution is governed by the wavelength of the x-rays, the shorter the wavelength, the higher the resolution. Normally Cu or Mo sources are used in traditional x-ray structural methods with 1.53 and 0.67 Å of wavelengths, respectively. Crystal structure analysis has recently benefited from advances in synchrotron radiation, where x-rays with photon fluxes close to laser fluxes can be achieved and the x-ray wavelengths can be tuned continuously, crystal structure analysis using x-rays of synchrotron radiation has taken a new dimension.

Diffraction measurements are preferentially made with single, mm-sized crystals, however powder diffraction analysis is used for solids, which either can't grow perfect macroscopic single crystals or where it is not easy to grow them. Similar to single crystal diffraction, microcrystalline powders or amorphous solids give diffraction patterns that reflect statistical averages of distances between electron densities in atoms of the solid. Fourier transformation of the laboratory

coordinate diffraction pattern (radial distance and intensity) gives the distribution of atoms or structures with internal reference coordinates. The broader the diffraction bands, the more inhomogeneous the interatomic vectors. Consequently, the peak width can give information on the grain size of polycrystalline powders. It is also expected that amorphous solids inherently result in broader diffraction patterns (Murthy et al. 1989). The diffraction pattern of warmed ice is similar to a powder since it does not have the discreet maxima of single crystals, unlike other ices such as methanol, which crystallize into a single-crystal sheet (Jenniskens and Blake 1996). The last decade has brought many improved measurements of the structure of H<sub>2</sub>O-ice, which have generally led to more questions. We will review the work of Jenniskens et al. and the most recent work.

## 11.2.2 *Structure and Formation Conditions of Relevant Phases*

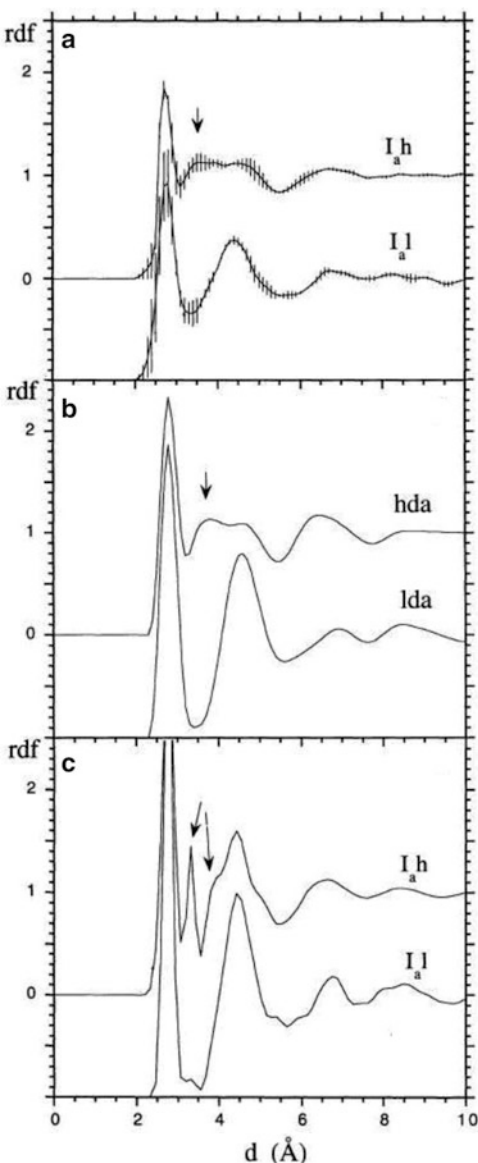
### 11.2.2.1 *Structure*

The structure of amorphous H<sub>2</sub>O-ice consists of a disordered, fully bonded, random network of H<sub>2</sub>O molecules where tetrahedral bonding is preferred (Jenniskens and Blake 1996). Any angular correlation between molecules vanishes over distances larger than 7 Å (Bergren et al. 1978). The surface of I<sub>a</sub>I can be described as a network of vertical cylindrical pores spaced 6 Å apart with diameters of 20 Å (Parent et al. 2002).

Electron diffraction results in a radial distribution function for the ice samples. It is interpreted as the probability of finding another oxygen atom at a given radial distance ( $r$ ). Both I<sub>a</sub>H and I<sub>a</sub>I have peaks near 2.75 Å and 4.25 Å. I<sub>a</sub>H also includes another peak near 3.25 Å (Fig. 11.2). These interstitial oxygens represent molecules that are somewhere between the two stable regions and it is interpreted that I<sub>a</sub>H is a collapsed form of I<sub>a</sub>I (Jenniskens et al. 1995). This network yields a local density of 1.1 g/cm<sup>3</sup> (Jenniskens et al. 1995). Inclusion of porosity may reduce this density significantly. For example, the I<sub>a</sub>H form is calculated to have a “structural density” of 1.07 g cm<sup>-3</sup> based on the diffraction pattern (Narten et al. 1976). However, the density of amorphous H<sub>2</sub>O-ice measured using a microbalance and interferometry is 0.82 g cm<sup>-3</sup> with a porosity of at least 13% (Westley et al. 1998). Other studies reported even more significant porosity of amorphous ices deposited at various angles on to a flat substrate (Stevenson et al. 1999; Dohnalek et al. 2003) leading to much lower bulk densities.

The structure of I<sub>h</sub> has been studied since the advent of X-ray diffraction. I<sub>h</sub> is arranged in a manner that follows the “ice rules” (1) there are two hydrogens adjacent to each oxygen and (2) there is only one hydrogen per bond (Bernal and Fowler 1933; Pauling 1935). Each H<sub>2</sub>O molecule resides at the corner of a tetrahedron, offering two hydrogens and accepting two hydrogen bonds. This leads to a disordered structure, where the hydrogens are free to take on several orientations so long as the ice rules are preserved. The H-O-H angle in a lone H<sub>2</sub>O molecule is 104.52°, slightly less than the 109.47° of a tetrahedral system, leading to slight shifts of the H<sub>2</sub>O molecules

**Fig. 11.2** Fourier transform of diffraction pattern showing radial distribution function (frequency of occurrence) vs. oxygen to oxygen distance for amorphous ices. For high-density amorphous ice, one observes an additional peak around 3–3.5 Å, which is absent in low-density amorphous ice (From Jenniskens et al. 1995. Reproduced by permission of the AAS)



from their average sites further contributing to the overall disorder of the structure (Petrenko and Whitworth 1999).  $I_c$  is arranged in a cubic structure with the same hydrogen disorder as  $I_h$  (Petrenko and Whitworth 1999). Near-edge x-ray absorption fine structure (NEXAFS) spectroscopy at the oxygen K-edge has been used to study bulk and surface properties of laboratory ices (Parent et al. 2002). The surface of the crystalline samples were well-ordered and had average  $H_2O-H_2O$  distances that are longer than that of the bulk ice (Parent et al. 2002).

### 11.2.2.2 Formation Conditions

Amorphous ice exists as high-density ( $I_{ah}$ ) below 70 K and low-density ( $I_{al}$ ) between 70 and 120 K. Above 120 K, restrained amorphous ( $I_{ar}$ ) and crystalline cubic ( $I_c$ ) coexist based on the thermal history and temperature of the ice, resulting in exclusive cubic crystalline ice at higher temperatures ().

The formation and structure of amorphous ice is highly dependent on deposition conditions. Amorphous H<sub>2</sub>O-ice samples have been created at 10 K with deposition rates ranging from 0.3 to 4  $\mu\text{m}/\text{h}$  via direct vapor deposition (Hagen et al. 1981), while at higher temperatures, a fractionally amorphous sample was created depositing at a rate of 1.5  $\mu\text{m}/\text{h}$  at 145 K by backfilling the chamber (Mitlin and Leung 2002). The formation of  $I_{ah}$  was originally confirmed at a low deposition temperature of 15 K (Jenniskens and Blake 1994).  $I_{ah}$  is formed by depositing H<sub>2</sub>O-ice at temperatures of less than 38 K at a rate of less than 100  $\mu\text{m}/\text{h}$  (Jenniskens et al. 1995). Higher deposition rates yielded samples with diffraction patterns similar to that of  $I_{al}$  (Jenniskens et al. 1995). There is also a minimum deposition rate of 1  $\mu\text{m}/\text{h}$  where the samples will also be  $I_{al}$ , possibly because the H<sub>2</sub>O molecules have enough time to re-align themselves before successive layers are deposited. Neutron scattering measurements of direct vapor deposited H<sub>2</sub>O-ice samples of up to 0.15 mm thickness failed to detect  $I_{ah}$  and were interpreted to mean that  $I_{ah}$  was perhaps a surface effect, or at least not seen in thick samples (Kolesnikov et al. 1997). Neutron scattering measurements confirmed that LDA formed by compressions of  $I_c$  or  $I_h$  has a different structure from  $I_{al}$  (Kolesnikov et al. 1997). Hyper-quenched glassy water (HGW) is formed by deposition of micrometer-size droplet of H<sub>2</sub>O sprayed onto a low temperature substrate, experiencing cooling rates of  $10^6$ – $10^7$  K/s. X-ray diffraction measurements of HGW confirmed that fully vitrified samples could be deposited at temperatures lower than 140 K (Kohl et al. 2000). Background vapor deposition of amorphous H<sub>2</sub>O-ice found that samples deposited below 120 K were microporous, while those over 120 K were non-porous (Parent et al. 2002).

The activation energy of  $I_c$  precludes its formation below 40 K (Jenniskens et al. 1995). The highest temperature for depositing  $I_c$  without  $I_h$  contamination is 190 K (Kohl et al. 2000).

### 11.2.3 Laboratory Needs

Since there are many phases of H<sub>2</sub>O-ice that could be stable in the Solar System, we will need to identify the phases that are most likely to form based on the environment. Vapor-deposited  $I_{ah}$  may be relevant near Pluto and  $I_{al}$  may be relevant on the satellites of Saturn, Uranus, and Neptune. However, there may also be conditions where HGW is flash-frozen from liquid H<sub>2</sub>O or LDA or HDA is formed by compression and release of an icy surface. Laboratory measurements are needed to detect distinguishable infrared features of these different types of amorphous phases, if any.

Many recent experiments have demonstrated differences in structure between the surface and the bulk of the sample. Surface structure is important for physical processes such as adsorption, spallation, and sublimation. Meanwhile, remote and *in situ* sensing techniques will mostly sample the bulk phase, except at the most strongly absorbing wavelengths near the vibrational fundamental modes.

There are many difficulties in interpreting phase from structural measurements (Soper 2008), especially with an amorphous material. This may be the source of the complicated and often-conflicting diffraction measurements of these ices, including the inability of other studies to confirm the formation of  $I_{a,r}$ .

## 11.3 Phase Changes

### 11.3.1 *Thermally Induced*

The specific transition temperature of amorphous to crystalline H<sub>2</sub>O-ice depends on the style of deposition, deposition rate, and the presence of impurities (Hagen and Tielens 1981). The heating rate and the time between deposition and the onset of cubic crystallization have a strong effect on the temperature at which phase changes occur (Jenniskens and Blake 1994). The average heating rates in the laboratory cover the range from 1 to 10 K/min, although most experiments are performed at 1–2 K/min. These phase changes are measured via diffraction or calorimetry experiments.

#### 11.3.1.1 Glass Transition

The glass transition precedes crystallization of an amorphous material and represents the temperature at which the molecules can begin to move. Upon heating  $I_{a,l}$ , the onset of structural relaxation occurs between 120 and 142 K, depending on the heating rate and time since deposition (Jenniskens and Blake 1996). During heating the first diffraction maximum increases in intensity while the second maximum remains unchanged. Low energy ion scattering (LES) measurements observed changes in the first few monolayers of amorphous H<sub>2</sub>O-ice at the glass transition. Reorganization of the surface leads to collapse of the pores and reduction in the number of dangling OH bonds (Cyriac and Pradeep 2008). Jenniskens and Blake (1996) interpreted the onset of the glass transition as a transformation to a new phase  $I_{a,r}$ . In this phase, the increasing temperature allows the relaxation of the structure and removes strained bonding angles. Recent calorimetry experiments question whether the glass transition is even detectable (Yue and Angell 2004). Although later measurements confirmed the glass transition at 136 K (Kohl et al. 2005). A detailed review of glass transition in pure and aqueous solutions, can be found in Angell (2002).

### 11.3.1.2 Amorphous-Amorphous

HDA formed by pressurization of I<sub>h</sub> to 12 kbar converts to LDA upon release of the pressure continuously over a series of amorphous forms that are intermediate and metastable for several hours at each annealing temperature (Tulk et al. 2002). The transition is initially rapid but then becomes kinetically inhibited (Tulk et al. 2002).

The I<sub>a</sub>h – I<sub>a</sub>l conversion occurs gradually over the temperature range from 38 to 80 K (Jenniskens and Blake 1994). The transition requires the breaking of one H-bond to relieve strain and reorder to I<sub>a</sub>l. This transition is irreversible, that is the ice sample remains I<sub>a</sub>l when cooled as identified by the shift in the transition peak (Fig. 11.3) (Jenniskens et al. 1995).

The I<sub>a</sub>l to I<sub>a</sub>r transition can occur between 122 and 136 K depending on the temperature history of the ice sample (Jenniskens and Blake 1994). The formation of I<sub>a</sub>r precedes the crystallization of I<sub>c</sub>, where changes in the diffraction pattern are seen well before the sample crystallizes. I<sub>c</sub> and I<sub>a</sub>r coexist in an intimate mixture at temperatures up to 188 K and for up to 16 h at 178 K (Jenniskens and Blake 1994). This agrees with previous work where some disordered regions remained,

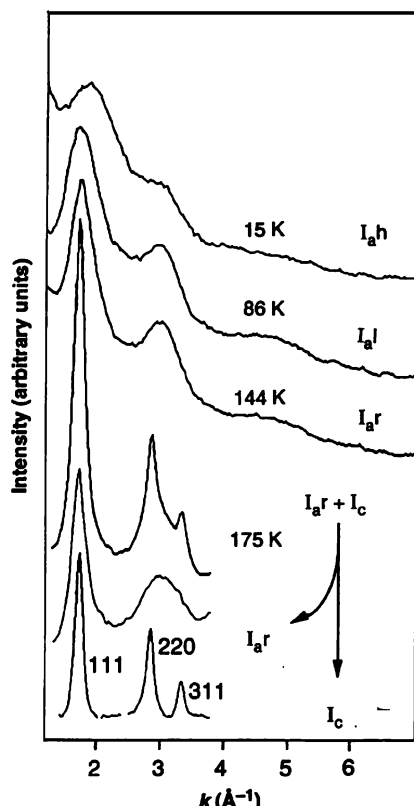


**Fig. 11.3** Electron diffraction patterns of vapor deposited water-ice at 15 K and subsequent warming up at 1–2 K per minute to various temperatures. Three amorphous forms (*high-density*, I<sub>a</sub>h; *low-density*, I<sub>a</sub>l; and *restrained*, I<sub>a</sub>r) as well as the cubic crystalline form (I<sub>c</sub>) are identified with increasing temperatures (From Jenniskens and Blake 1994. Reprinted with permission from AAAS)

inhibiting the growth of crystals (Dowell and Rinfrat 1960). The activation enthalpy of the I<sub>a</sub>r transition is  $\Delta H = 25 \pm 5$  kJ/mol (Jenniskens and Blake 1994).

### 11.3.1.3 Amorphous to Crystalline

The I<sub>a</sub>l to I<sub>c</sub> transition occurs over the range from 142 to 160 K. At this stage, small crystals form in only 30% of the ice (Jenniskens et al. 1998). The phase change is detected by diffraction peaks of cubic ice appearing for the crystallographic coordinates of [220] and [311] (Jenniskens and Blake 1994). The initiation of the transition and rate of conversion depends on the deposition temperature and heating rate. For an ice deposited at 14 K and heated at a rate of 1–3 K/min, the I<sub>c</sub> peaks appear at 145–160 K. The intensity of the peaks increases until 160–170 K. Meanwhile, an ice deposited at 86 K and heated at 10 K/min starts crystallizing at 142 K (Jenniskens and Blake 1996).

The fraction of crystallized material can be given by the Avrami equation:

$$x(T) = 1 - \exp[-k(T)t^n] \quad (11.1)$$

where x is the crystalline fraction, T is the temperature in K, t is time in s, k(T) is the rate constant, and n is dependent on the geometry of the particles and whether the limiting step is diffusion or reordering of molecules. Crystallization occurs in two zones, the first having fast crystal growth ( $n = 2$ ) and the second where crystal growth is slow ( $n = 0.8$ ) possibly impeded by regions of I<sub>a</sub>l (Jenniskens and Blake 1996). This can be used to calculate the timescale to the onset of crystallization:

$$\Delta t(s) = v_0 \exp\left(\frac{\Delta H_a}{RT}\right) \quad (11.2)$$

where  $v_0$  is the vibrational frequency of the molecule ( $3.3 \times 10^{15}$  s),  $\Delta H$  is the enthalpy, R is gas constant, T is the temperature in K.

From this calculation, I<sub>a</sub>h can persist at less than 19 K for  $45 \times 10^9$  year and at less than 22 K for  $10^5$  year (Jenniskens et al. 1995). I<sub>a</sub>l can persist at temperatures less than 90 K, however long term restructuring at just below the glass temperature would result in low-density ice and also remove micropores (Jenniskens and Blake 1996).

A purely theoretically study by Kouchi et al. (1994), gave the timescale to crystallization,  $t_c$ , as

$$t_c = \left(\frac{1}{2\pi\alpha}\right)^{1/4} \left(\frac{kT}{\sigma}\right) \frac{\Omega^{2/3}}{D_0} \exp\left[\frac{1}{kT} \left\{E_a + \frac{4\pi\sigma^3}{3L^2} \left(\frac{T_m}{T_m - T}\right)\right\}\right] \quad (11.3)$$

where  $\alpha$  is geometrical factor for crystal growth ( $\pi/3$  for spherical growth), k is the Boltzman constant, T is the temperature in Kelvin,  $\Omega$  is the volume of a water molecule,  $\sigma = \gamma\Omega^{2/3}$ ,  $D_0$  is the self-diffusion coefficient,  $E_a$  is the activation energy

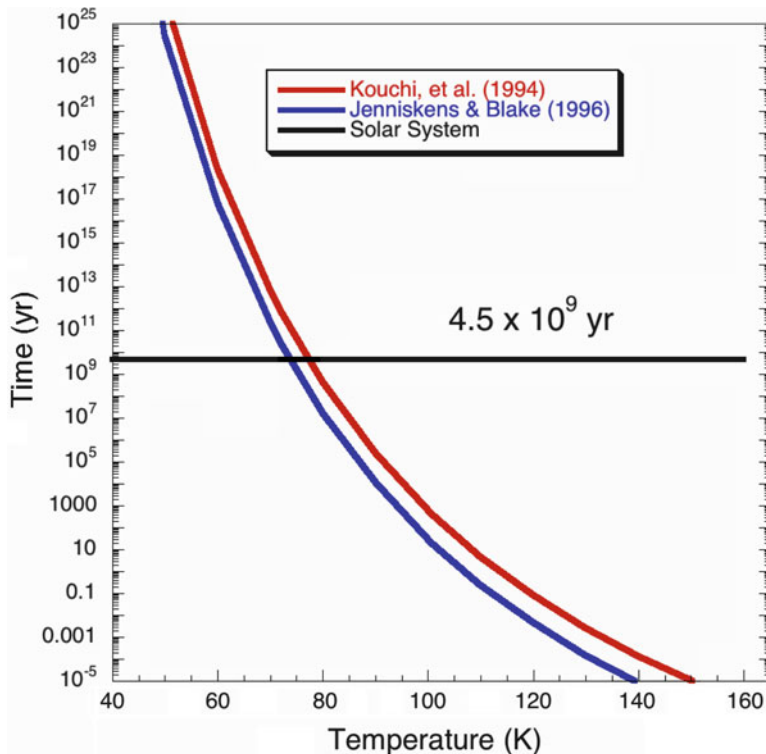


**Fig. 11.4** Crystallization rates for H<sub>2</sub>O-ice. In blue is the time to onset of crystallization (Jenniskens and Blake 1996) and red is the time to 100% crystallization (Kouchi et al. 1994). Please note that these curves are only theoretical estimates and extrapolations from experimental observations and should not be taken as proven

of self diffusion, L is the latent heat of crystallization per molecule for T = 0 K, and T<sub>m</sub> is the melting temperature of water ice (273 K).

We have calculated the timescale to onset of crystallization (Jenniskens and Blake 1996) and the timescale to 100% crystallization (Kouchi et al. 1994) and the results are shown in Fig. 11.4. In short, at 100 K amorphous ice will convert to crystalline in  $10^4$  years. Therefore, for Solar System timescales, amorphous ice would only be stable on surfaces that have always been much colder than 100 K.

Later work has tried to separate crystalline ice nucleation and growth during the crystallization of ASW. The nucleation activation energy is 168 kJ/mol while the activation energy of crystal growth is 47 kJ/mol (Safarik and Mullins 2004). It was suggested that nucleation occurs inside the bulk of the material and is unaffected by the substrate (Kondo et al. 2007) and that nucleation rates varied was based on location: bulk vs. surface interfaces (Backus and Bonn 2004).

Sugisaki et al. (1969) performed a calorimetric study of the conversion of amorphous to cubic ice at 135 K. They calculated a change of heat capacity of

35 J/mole-K with an exothermic effect of 1.64 kJ/mole. Jenniskens and Blake (1994) derived the activation enthalpy of the phase change  $\Delta H = 44 \pm 2$  kJ/mol. Sack and Baragiola (1993) calculated the activation energy of the reaction to be  $\Delta H = 42 \pm 4$  kJ/mol. Jenniskens and Blake (1996) noted two regimes of crystallization: the first had an activation enthalpy of  $\Delta H = 39 \pm 5$  kJ/mol and the second  $\Delta H = 58 \pm 10$  kJ/mole. They noted that these energies are equivalent to those for breaking two hydrogen bonds, i.e. 21 kJ/mol per bond.

#### 11.3.1.4 Crystalline to Crystalline

The cubic to hexagonal phase change occurs between 160 and 200 K in two steps with activation energies of 21.3 and 44.7 kJ/mole, respectively (Sugisaki et al. 1969). The exothermic effect is 160 J/mole. Both  $I_c$  and  $I_{ar}$  convert to  $I_h$  (Jenniskens and Blake 1994). The enthalpy of the  $I_c$ - $I_h$  conversation is  $\Delta H = 50$  kJ/mol (Jenniskens and Blake 1994). This is seen when ice samples are heated from 180 to 255 K and the ice converts to  $I_h$  (Kolesnikov et al. 1997). Under ultra-high vacuum conditions where the pressure is less than  $10^{-5}$  mbar and under continuous removal of residual gases (pumping), similar to of outer Solar System *airless* bodies, ice sublimation sets in around 155 K and is significant above 170 K (Gudipati and Allamandola 2006). Ice above 155 K can only be kept intact at relatively higher pressures (such as on Mars and on Earth), where significant exchange of material occurs between the surrounding gas-phase molecules and the ice surface.

#### 11.3.1.5 Other Phases

Recent work looked at diffraction measurements and differential scanning calorimetry (DSC) measurements of hyperquenched glassy water (HGW) and amorphous sold water (ASW) (Kohl et al. 2000). HGW was created by spraying an aerosol of  $H_2O$  droplets onto a cold substrate, while ASW was formed by vapor deposition. In the HGW samples, the fraction of amorphous ice depended strongly on the deposition temperature, since samples deposited at 130 K were only 5% crystalline while samples deposited at 150 K were 96% crystalline. HGW samples deposited at low temperatures could maintain at most 20% amorphous ice that persisted above 183 K until the sample converted to  $I_h$ . When heated to 200 K, HGW samples exhibited a grain size change in the  $I_c$  fraction of the sample. At 230 K, the sample converted to  $I_h$ . ASW samples deposited at 77 K were consistently 98% amorphous. ASW samples were not prepared at as many temperatures as HGW, but instead were deposited at 77 K, heated to 115 K and then exposed to nitrogen. Both ASW and HGW had identical diffractograms when heated to 183 K (Kohl et al. 2000).

Recent studies have also considered changes in the surface structure of ices during phase transitions. X-ray absorption spectroscopy of ice samples created by background-filling vapor deposition show the collapse of surface micropores in the temperature range from 38 to 147 K (Parent et al. 2002). Also, the  $H_2O$ - $H_2O$

distance on the surface increases from 2.77 to 2.80 Å, which is very different from that of the bulk (Parent et al. 2002).

Crystallization rates can change due to factors other than deposition temperature and heating rate. The reaction rate in an H<sub>2</sub>O-ice contaminated with CO<sub>2</sub> is endothermic (Kouchi and Sirono 2001). The crystallization rate is accelerated in an amorphous ice layered on crystalline H<sub>2</sub>O-ice compared to on an amorphous ice deposited on a Pt(111) surface (Dohnalek et al. 1999; Dohnalek et al. 2000).

### 11.3.2 *Radiation Induced*

Radiation can also change the structure of H<sub>2</sub>O-ice. During irradiation that deposits more than the dissociation energy into a water molecule, H<sub>2</sub>O molecules break down into H and OH. The H atoms can diffuse through the sample to recombine with OH or with other H (Baragiola 2003). This process also disrupts the structure of crystalline H<sub>2</sub>O-ice, amorphizing the sample. Early evidence of amorphization was interpreted from visible inspection of ice samples where they were seen to be more scattering than transparent after radiation exposure (Brown et al. 1978). In the three decades since this measurement was done, many experiments were performed with little agreement among them. The major difference between studies is the maximum temperature at which H<sub>2</sub>O-ice can be amorphized.

Different laboratories and different particle sources have produced different results. For example, 100 keV proton irradiation could amorphize samples up to 120 K (Golecki and Jaccard 1978). Amorphization of crystalline H<sub>2</sub>O-ice by ion irradiation has been detected in the mid infrared (MIR) region (Strazzulla et al. 1991; Strazzulla et al. 1992; Leto and Baratta 2003), far infrared (FIR) (Moore and Hudson 1992), and UV photolysis of ice samples studied by the MIR (Leto and Baratta 2003), NIR (Leto et al. 2005; Mastrapa and Brown 2006; Fama et al. 2010) and x-ray diffraction (XRD) spectra (Kouchi and Kuroda 1990), although the dose of the XRD results has been called into question (Jenniskens et al. 1995).

Electron beam irradiation of I<sub>a</sub>h samples can cause samples to flow but still maintain their structural character and convert I<sub>a</sub>l samples to I<sub>a</sub>h (Jenniskens et al. 1995). Electron irradiation can amorphize ice samples below 60 K, but is not effective at amorphizing samples at or above 70 K, while the dose needed to amorphize the sample at 60 K is over an order of magnitude larger than that needed at 8 K (Lepault et al. 1983; Heide 1984). Recent results claim that electrons cannot amorphize samples above 40 K (Zheng et al. 2009). To date, there is little consensus between different experiments utilizing electron sources.

In some cases, amorphous H<sub>2</sub>O-ice can be converted back to crystalline phase by irradiation. In the case of high-energy protons (Moore and Hudson 1992) this process was only seen at 13 K, while irradiation at higher temperatures did not produce crystalline H<sub>2</sub>O-ice. The conversion to crystalline H<sub>2</sub>O-ice coincided with bursts of gas release consisting of predominantly H<sub>2</sub>. After continued irradiation, the sample remained in the amorphous phase regardless of radiation dose. The fact that this occurs

at very low temperature would indicate that the crystallization is caused by the gas release and not heating by irradiation. Radiation-induced crystallization also depends on the incident charge density. For example, at 120 K, an amorphous H<sub>2</sub>O-ice sample needs an exposure of  $150 \times 10^3$  e<sup>-</sup>/nm<sup>2</sup> to crystallize (Dubochet et al. 1982). The necessary amount of exposure decreases with increasing temperature.

### ***11.3.3 Impact Induced***

Very little work has been done to measure the effect of impacts of the phase of H<sub>2</sub>O-ice. Models of micrometeorite impacts show that impact-induced crystallization may be competitive in the Solar System but in the Kuiper Belt (Porter et al. 2010). However, this model only examines the thermal input of an impact and does not include vaporization and re-condensation of H<sub>2</sub>O. Another study using a comet model required an impactor rate 1,000 times higher than that predicted for the current collisional environment (Marboeuf et al. 2009). However, recent measurements of phase changes in crystalline H<sub>2</sub>O-ice under shock conditions predict melting and vaporization from impactors with velocities as low as 1 km/s (Stewart et al. 2008). These shocks also produce multiple high-pressure phases. The high-pressure form of H<sub>2</sub>O-ice, VI, has been demonstrated to be stable after the shock-induced pressure is released (Stewart and Ahrens 2005). Further study of the long-term stability of these high-pressure phases, and the possibility of remote detection are required.

### ***11.3.4 Laboratory Needs***

There are a lot of contradictory results regarding the thermally induced transitions in H<sub>2</sub>O-ice. The main consensus is that the amorphous to crystalline transition occurs over a broad range of temperatures (120–150 K) depending on the rate of heating and the method used in preparation of the sample. As mentioned before, the physical properties of the ice seem to be strongly dependent on the method of sample preparation. We need to start tailoring our sample preparation to the appropriate environment. For example, vapor-deposited samples are appropriate for surfaces that have mobile volatiles. Meanwhile, liquid droplet sprays may be more appropriate for environments with active cryovolcanism.

Although it is clear that crystalline H<sub>2</sub>O-ice is amorphized under radiation, there are still many open questions that must still be answered, including the disparate results between different laboratories. The main point of contention is the maximum temperature at which crystalline H<sub>2</sub>O-ice can be amorphized, which ranges from as low as 40 K up to 90 K. This discrepancy is most likely due to the fact that each laboratory has a unique set of instrumentation, and we are often comparing infrared spectroscopy to diffraction measurements and proton irradiation to UV photolysis. What is needed is a series of experiments using multiple radiation

sources over a broad range of temperatures using multiple detection methods. Unfortunately, there are currently no laboratories that are capable of doing simultaneous diffraction and spectroscopic measurements. It would also be useful to analyze the materials escaping from the sample using mass spectroscopy.

Once it is clear how the radiation-induced amorphization process works for pure ices, we will have to study the effect of contamination on the amorphization. There are very few instances of pure H<sub>2</sub>O-ice in the Solar System, so a contaminated ice is more appropriate. One likely candidate is CO<sub>2</sub>, which has been studied before, but must be examined with the same rigor that is stated above.

Finally, no laboratory work has been done to study the effects of micrometeorite bombardment on H<sub>2</sub>O-ice. It would be very useful to be able create bulk samples and expose them to low energy impacts in a vacuum chamber that was well insulated from external thermal radiation.

## 11.4 Implications of Phase

### 11.4.1 Thermal/Radiation History

If we can place constraints on the temperature and radiation history of an object in the Solar System, we may be able to estimate the age of a given surface by determining the phase of H<sub>2</sub>O-ice on the surface. This estimate would be a result of balancing the dominant processes on the surface of these objects, including irradiation, impact-heating, and thermal variations, all of which are relevant on the surfaces of Kuiper Belt Objects (e.g. Stern 2003).

### 11.4.2 Thermal Properties

The thermal properties of amorphous and crystalline ice will be dealt elsewhere in this book. Briefly, the thermal conductivity of crystalline I<sub>h</sub> water ice has been more or less accurately determined to be around 5 W m<sup>-1</sup> K<sup>-1</sup> (Andersson et al. 2004). The same authors report thermal conductivity of ~0.1 W m<sup>-1</sup> K<sup>-1</sup> for amorphous ice. Other literature puts the amorphous ice thermal conductivity to be around 10<sup>-5</sup> W m<sup>-1</sup> K<sup>-1</sup> (Kouchi et al. 1992). Consistency among the different lab data on amorphous ice has not been so good – which is expected due to the above-mentioned wide range of porosity and structural diversity. In fact, it is expected that amorphous ices will have a wide variety of structural properties compared to their crystalline counterparts. Amorphous ices can be characterized by their porosity as the scaling factor. Influence of impurities and their concentration on the structural properties of amorphous ices is not well understood.

### 11.4.3 Chemistry

Surface chemistry properties of amorphous and crystalline H<sub>2</sub>O-ice are different, possibly due to higher hydrogen bond donor availability in amorphous ice (Schaff and Roberts 1996). Crystalline vapor deposited ice has unique surface structures that effect the type of chemistry that occurs on the surface (Sadchenko et al. 2000).

I<sub>ah</sub> is less efficient at trapping other materials, possibly because of the loss of dangling –OH bonds during the amorphous-crystalline transition (Cyriac and Pradeep 2008). The sublimation rate of amorphous H<sub>2</sub>O-ice is two orders of magnitude higher than crystalline H<sub>2</sub>O-ice and is strongly dependent on growth conditions (Sack and Baragiola 1993).

In crystalline or amorphous phases of H<sub>2</sub>O-ice, the flexibility or relaxability (Murthy et al. 1987) of the structure would determine how and whether radiation induced photochemistry occurs efficiently in these ices. Proton order-to-disorder transition occurs in crystalline ice at ~70 K, below which it is expected that the “rigidity of ice lattice” increases with decreasing temperature (Akiyama et al. 1997). Consequently, we expect low photochemical activity on KBOs and Oort cloud objects, should their ices exist in crystalline phase only.

Though there are extensive studies on radiation induced chemistry in/of ices, in amorphous as well as crystalline phases, detailed and systematic studies comparing the chemical reactivity in both amorphous and crystalline ices are sparse. For this reason, in this section we review what is known in other areas of solid-state chemistry and project these aspects to ice chemistry and derive logical predictions based on these studies.

There is extensive literature on the “consequence of lattice relaxability” (Murthy et al. 1987) of crystalline material for photochemical reactions as well as the “cage effect” (Wagner et al. 2000) of the host lattice in controlling the photochemical pathways. Past research of Gudipati has been focused on these aspects, from which two examples highlight the role of the “cavity” in photochemical transformations in condensed cryogenic solids, one representing the lattice relaxability and the other cavity volume or cage-effect.

#### 11.4.3.1 Cavity Volume/Cage Effect

When a molecule is confined in a surrounding cage, its orientational freedom will be constrained accordingly. Should there be no effect of the cage, the molecule behaves similar to a gas-phase molecule, some time even rotational transitions can be seen in the solid state. Though in ices these rotational transitions are not yet reported, methane rotations in high-pressure clathrates have been recently observed (Dartois and Deboffe 2008). Gudipati and co-workers (Gudipati 1997; Wagner et al. 2000) have observed that a CO<sub>2</sub> molecule embedded in an argon lattice takes up one of two different lattice positions (Fig. 11.5), either replacing a single Ar atom (single substitutional, SS) or replacing two Ar atoms (double substitutional,

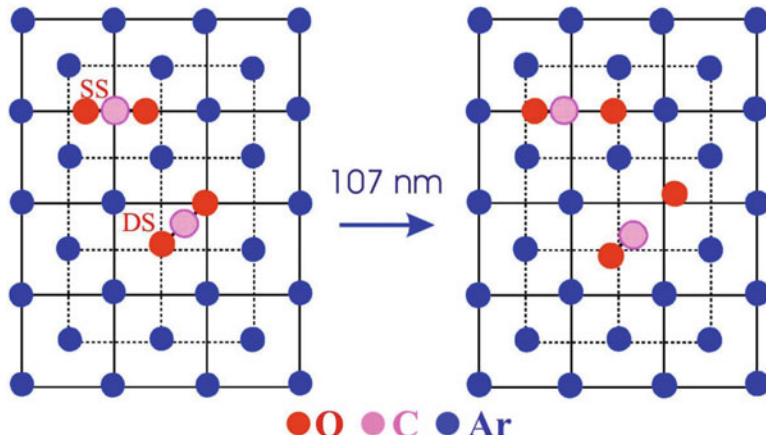


**Fig. 11.5** Orientation of trapped CO<sub>2</sub> molecules in face-centered cubic (FCC) Argon crystal lattice. Replacing one Ar by one CO<sub>2</sub> results in the tight single-substitutional (SS) cavity. When two Ar atoms are replaced, a more relaxed double-substitutional (DS) cavity is created for CO<sub>2</sub>. Spectroscopic and photochemical properties of CO<sub>2</sub> in DS are similar to those in the gas-phase, whereas strongly perturbed in SS cavity (Wagner et al. 2000) (Copyright (2000) American Chemical Society)

DS). In the SS site, CO<sub>2</sub> is tightly packed, whereas in the DS site it behaves similar to a gas-phase molecule. These two occupancy sites of CO<sub>2</sub> in the Ar lattice are also characterized by distinct infrared spectra at different temperatures. The infrared band due to the DS site is not affected significantly, subtle changes in volume show significant observable effects on the infrared band of CO<sub>2</sub> trapped in the SS site (Fig. 11.6). When photolyzed with VUV light at 107 nm, CO<sub>2</sub> dissociates into CO and O. In the Ar lattice, both SS and DS site cages confine the photolyzed CO and O atoms, while a Kr lattice allows escape of O atoms from the cage. Kr has more cage volume and the Kr lattice is less repulsive for O atoms so they escape more readily (Gudipati 1997; Wagner et al. 2000).

Similar behavior is expected for molecules embedded in amorphous ice cages. When the cages are large and allow molecular conformations and fragmentation (through dissociation and ionization), photochemical (radiation induced) reactions are expected to be dominant, whereas when the amorphous ice has been annealed at higher temperature closing up the cages, chemical processes are expected to be far less efficient. However, in crystalline ice, if enough energy is deposited through radiation (such as electron, ion, and cosmic ray bombardment), local crystal structure could be destroyed, boosting the efficiency of chemical reaction involving impurities.

In addition to thermal properties, a second major influence of amorphous vs. crystalline structure relates to the cavity volume and structure within the hydrogen bonded water molecules that form the amorphous solid water (ASW), another terminology used for amorphous water ice. Such cavities would be sparse in crystalline ice, their existence being limited to defect sites, grain boundaries, etc. Imagine we have an impurity; say CO<sub>2</sub> (or a large molecule such as an amino acid

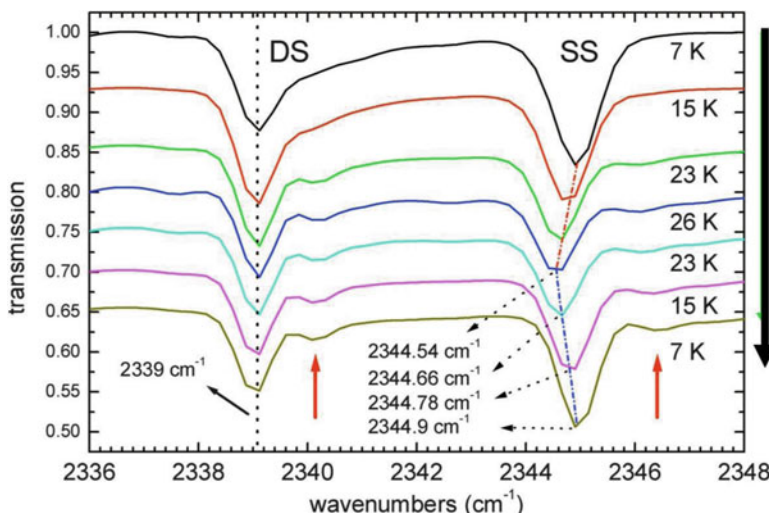


**Fig. 11.6** FTIR spectra of 0.1%  $\text{CO}_2$  trapped in Ar crystal lattice (Gudipati unpublished results). Two sites of trapping are shown. The IR frequency of  $\text{CO}_2$  trapped in DS is closer to the gas-phase frequency of  $2,339 \times \text{cm}^{-1}$ , whereas  $\text{CO}_2$  trapped in SS exhibits higher stretching frequency due to stronger cage confinement. Upon warming up from 7 to 26 K, a steady decrease in vibrational frequency of the SS site is seen due to expanding volume of the Ar crystal lattice

tryptophan) trapped in ice. In amorphous ice,  $\text{CO}_2$  will have enough cavity volume to reorient itself during photochemical processes, such as photodissociation into fragments or photoionization resulting in an electron-ion pair. Such photochemical reactions would either be extremely inefficient or it would disrupt the local structure when these molecules are trapped in crystalline ice. The rate of any given reaction should thus be different in amorphous and crystalline ice, with amorphous ice being a more accommodating host for radiation-induced chemistry. Photochemical or thermal processes, with insufficient excess energy to disrupt the crystal lattice around the impurity, should be less likely to occur in crystalline ices compared to the amorphous ices (Fig. 11.6)

#### 11.4.4 Laboratory Needs

Though phase transitions seem to be reasonably well understood, their consequences on properties such as thermal, electrical, and chemical behavior need further study. In particular, work is needed on radiation-induced chemistry on ice surfaces, reactive species survival within ice, and diffusion/transportation of volatile and non-volatile materials through ice. Future laboratory experiments should focus on better understanding of the physical and chemical properties of

the three distinguished amorphous phases: I<sub>ah</sub>, I<sub>al</sub>, and I<sub>ar</sub> as well as the interconversion among the high-temperature phases I<sub>ar</sub>, I<sub>c</sub>, and I<sub>h</sub>.

These are the most frequent questions raised by comet, KBO, and Oort cloud specialists. Physical properties of amorphous ices are sparse. Radiation-induced chemistry in amorphous ices has been extensively studied, but contrasting studies between amorphous and crystalline ice are rare. Similarly, a comparison among various forms of amorphous ices is also rare when it comes to their relative chemistry and physics. The role of restrained quasi-liquid phase of amorphous ice (I<sub>ar</sub>), that exists at higher than 120 K, in controlling and facilitating chemical reactions needs further detailed studies. Therefore, we need laboratory studies on chemical processes in ices comparing various amorphous and crystalline forms. These studies will enable us to better model the chemical evolution of comets, and other low-gravity objects.

## 11.5 Infrared Spectroscopy

H<sub>2</sub>O-ice is easily recognized by its broad absorptions in the infrared. Since remote diffraction measurements are not feasible, these absorptions are the only way to assess the phase of H<sub>2</sub>O-ice on other objects. Fortunately, the infrared spectra of H<sub>2</sub>O-ice have been studied in the laboratory for nearly a century and on a broad level, the changes in the spectra as a function of phase are well known. In the range from 1 to 5  $\mu\text{m}$ , the absorptions are caused by the vibration of the H<sub>2</sub>O molecule. The locations of the absorptions and assignments are given in Table 11.1. Bertie and Whalley (1964) confirmed the assignments of Ockman (1958) by creating mixtures of H<sub>2</sub>O and D<sub>2</sub>O ice and comparing the features to pure samples of both to distinguish the OH-OH interactions. These assignments were confirmed and further refined in more detail by Buch and Devlin (1999).

Whalley (1977) attempted a more physical model for assigning features from 2.5 to 4  $\mu\text{m}$ . His main assumption was that the spectral features of I<sub>c</sub> and I<sub>h</sub> are caused by the same vibrational modes even though the crystal structures are different. From this he also postulated that the similar features in amorphous ice are also caused by the same modes (Whalley 1977). Since the ices I<sub>c</sub> and I<sub>h</sub> are disordered crystals, that is, they do not have a perfect crystal lattice with an even distribution of protons, selection rules do not apply and all vibrations are active, effectively broadening the absorptions (Bertie and Whalley 1964). Intermolecular coupling also may cause the broadening of the infrared absorptions (Bertie and Whalley 1964; Whalley 1977; McGraw et al. 1978). Disordered ice is not completely without crystal structure, but it deviates just enough to negate some of the selection rules and weakly inhibit coupling (Bergren et al. 1978).

Two problems become apparent when reviewing the laboratory work. Few measurements included both diffraction and infrared spectroscopy. It has become standard practice to create ice samples at the appropriate temperature and assume that the phase is correct. Changes in the shape of the absorptions appear

**Table 11.1** Assignment of bands for amorphous and crystalline H<sub>2</sub>O-ice

Crystalline <sup>a</sup>		Amorphous <sup>b</sup>		Assignment, name
μm	cm <sup>-1</sup>	μm	cm <sup>-1</sup>	
0.80	12,500			3v1 + v3
0.90	11,100			2v1 + v2 + v3
1.05	9,667			2v1 + v3, 1 μm band
1.11	9,025			Multiple, 1.1 μm band
1.27	7,940			Multiple, 1.25 μm band
1.30	7,775	1.25 <sup>c</sup>	8,000	Multiple, 1.3 μm band
1.50	6,649	1.49	6,703	v1 + v3, 1.5 μm band
1.56	6,395	1.54	6,479	
1.65	6,048	1.64	6,087	
2.02	4,954	2.00	5,009	v <sub>2</sub> + v <sub>3</sub> , 2 μm band
2.96	3,380	2.97	3,367	v <sub>3</sub> LO, v <sub>1</sub> out-of-phase <sup>d</sup> 3 μm band
3.11	3,220	3.07	3,253	v <sub>3</sub> TO <sup>d</sup> 3 μm band
3.17	3,150	3.13	3,191	v <sub>1</sub> in-phase <sup>d</sup> 3 μm band
4.43	2,259	4.50	2,220	v <sub>2</sub> + v <sub>R</sub> <sup>e</sup> 4.5 μm band

<sup>a</sup>From Bertie and Whalley (1964) at 100 K<sup>b</sup>From Hardin and Harvey (1973) at 92 K<sup>c</sup>From Mastrapa et al. (2008)<sup>d</sup>From Ockman (1958)<sup>d</sup>From Whalley (1977)<sup>e</sup>From Hudgins et al. (1993)

Multiple – Multiple possible assignments

to correlate with the correct temperatures for phase transitions. Until future measurements are made, these results remain our only basis for comparison to Solar System spectra.

The other issue is that there are few measurements in the region that is most important to ground-based observations (1–2.5 μm) which also cover the broad range of temperatures seen in the outer Solar System (40–120 K). New measurements have been collected in the last 15 years, enabled by new laboratory capabilities (Grundy and Schmitt 1998; Mastrapa et al. 2008). Most importantly, these measurements produced absorption coefficients and optical constants used to create model spectra for comparison to observed spectra. Spacecraft instruments extend the range of relevant infrared measurements up to 5 μm. Future missions, such as JWST or SOFIA, may be able to observe thermal emission spectra of icy Solar System objects at wavelength >5 μm, but we will restrict our discussion to reflectance spectra from 1 to 5 μm.

### 11.5.1 Relevant Absorptions

In the wavelength range from 1 to 5 μm, only one of the absorptions of H<sub>2</sub>O-ice is a fundamental vibration, the one near 3 μm. The rest are overtones and combinations of bands at longer wavelengths and are significantly weaker than the 3 μm band.

Due to the breadth of the bands, and the fact that they shift position as a function of phase and temperature, we will refer to them by an average wavelength instead of a specific position (Table 11.1). For example, the band near 1.65 μm in crystalline H<sub>2</sub>O-ice can shift from 1.65 μm at 150 K to 1.66 μm at 20 K and is found at 1.64 μm in amorphous H<sub>2</sub>O-ice, but for consistency we refer to it as the 1.65 μm band.

Combination bands are exactly what their name suggests: they are combinations of features from longer wavelength. These are the features that will be studied throughout this chapter. Table 11.1 lists multiple assignments for the features in the region because it is very difficult to tell an exact assignment. The structures in this region are very complex and made up of multiple features. The main near-infrared features in water ice are near 1.3, 1.5, 1.56, 1.65 and 2 μm. They are very weak in intensity compared to the lattice and vibrational modes, and necessitate a thicker sample compared to those for the vibrational features to detect them.

### 11.5.2 *Amorphous H<sub>2</sub>O-Ice*

In the near-infrared, the shapes of the spectral bands in amorphous H<sub>2</sub>O-ice are consistent for temperatures lower than 70 K. Samples that were deposited below 70 K and that have never been heated above that temperature display absorptions that are shifted to shorter wavelength and are weaker than bands in spectra of samples deposited at T > 70 K (Mastrapa et al. 2008). For T > 70 K, the bands of the 1.5 and 2 μm bands are stronger and slightly shifted to longer wavelength. Spectra of samples deposited below 70 K and heated above that temperature shifted to resemble the higher temperature phase. When re-cooled, the bands remained at the higher temperature phase positions, suggesting that this is an irreversible transition. These different spectra could represent the transition between I<sub>a</sub>h at low temperature and I<sub>a</sub>l at high temperature (Narten et al. 1976; Jenniskens and Blake 1994; Westley et al. 1998). The spectral bands of amorphous H<sub>2</sub>O-ice show no other changes with temperature.

However, the shape of the 3-μm band is strongly dependent on the deposition temperature (Mukai and Krätschmer 1986; Hudgins et al. 1993): it grows stronger and shifts to longer wavelength as deposition occurs at higher temperatures (Mastrapa et al. 2009). Temperature cycling of the samples demonstrated that the changes in band shape are irreversible, that is, a sample deposited at 15 K, heated to 100 K, and cooled back to 15 K retains the band shape seen at 100 K.

### 11.5.3 *Crystalline H<sub>2</sub>O-Ice*

The infrared bands of crystalline H<sub>2</sub>O-ice are temperature dependent; they shift to shorter wavelength and decrease in absorption with temperature (Bertie and Whalley 1967; Hagen and Tielens 1982; Smith et al. 1994; Grundy and Schmitt 1998; Mastrapa and Brown 2006). Fink and Larson (1975) described a strong

inverse correlation between strength of the 1.65  $\mu\text{m}$  feature and temperature. They postulated that it was connected to decreased high-energy population of the librational modes, effectively narrowing and strengthening the features. Grundy and Schmitt (1998) performed a detailed study on monocrystalline samples and found that features at 1.5, 1.57, 1.65, and 2  $\mu\text{m}$  all shift to shorter wavelength with temperature. Also, the features at 1.31, 1.57, and 1.65  $\mu\text{m}$  lose intensity with increasing temperature. They compared these changes to temperature dependent changes of molecular and lattice vibrations, but refrained from making any comments on physical causes of these changes (Grundy and Schmitt 1998). Again, this behavior is similar to those of the vibrational features and probably dependent on the hydrogen bonding. The absorptions at 3.08 and 3.17  $\mu\text{m}$  are strongly temperature dependent, growing stronger and sharper as temperature decreases while the feature at 2.96  $\mu\text{m}$  band does not change very much (Hagen et al. 1981; Mastrapa et al. 2009). The absorption near 6  $\mu\text{m}$ , exhibits the opposite behavior of the other features, since it is broad and weak at low temperature and stronger and sharper at high temperature (Hagen et al. 1981; Mastrapa et al. 2009).

Although it has long been assumed that there are no spectral differences between  $I_h$  and  $I_c$  (Bertie and Whalley 1964), there may be slight differences in the band shapes (Hardin and Harvey 1973). The near-infrared absorptions of  $I_c$  (Mastrapa and Sandford 2008) are slightly stronger and shifted to longer wavelength when compared to  $I_h$  (Grundy and Schmitt 1998).

### 11.5.4 Comparing Phases

The infrared spectra of amorphous and crystalline H<sub>2</sub>O-ices are easily distinguishable (Ockman 1958; Bertie and Whalley 1964; Whalley 1977; Hagen and Tielens 1981, 1982; Smith et al. 1994). In the crystalline phase, the infrared bands are stronger, sharper, and shifted to longer wavelength compared to the amorphous-phase bands (Schmitt et al. 1998). Whalley (1977) attributes the broadness of the amorphous feature near 3  $\mu\text{m}$  to variable distortion of hydrogen bonds, which causes variation in the frequency of the OH oscillation. Madden et al. (1978) confirmed this in their model, showing that the changes were controlled mostly by variable stretching constants in the molecules. The  $v_2$  feature exhibits the opposite behavior, since it is strongest and sharpest in the amorphous spectrum (Hagen et al. 1981; Mastrapa et al. 2009).

Schmitt et al. (1998) described the change in the infrared features between amorphous and crystalline water ice, showing that the 1.5 and 2  $\mu\text{m}$  features shift to shorter wavelength by as much as 0.05  $\mu\text{m}$  in the amorphous spectrum. Also, the absorptions at 1.57 and 1.65  $\mu\text{m}$ , although weakly present in the amorphous spectrum, are much stronger in the crystalline spectrum (Schmitt et al. 1998). The shifts in position and changes in area between phases occur as a function of changes in the electric field based on ice configuration. There is therefore no single feature that can be used to easily differentiate between the phases. The 1.65  $\mu\text{m}$  band is present in both amorphous and crystalline H<sub>2</sub>O-ice, although it is weaker and shifted to shorter

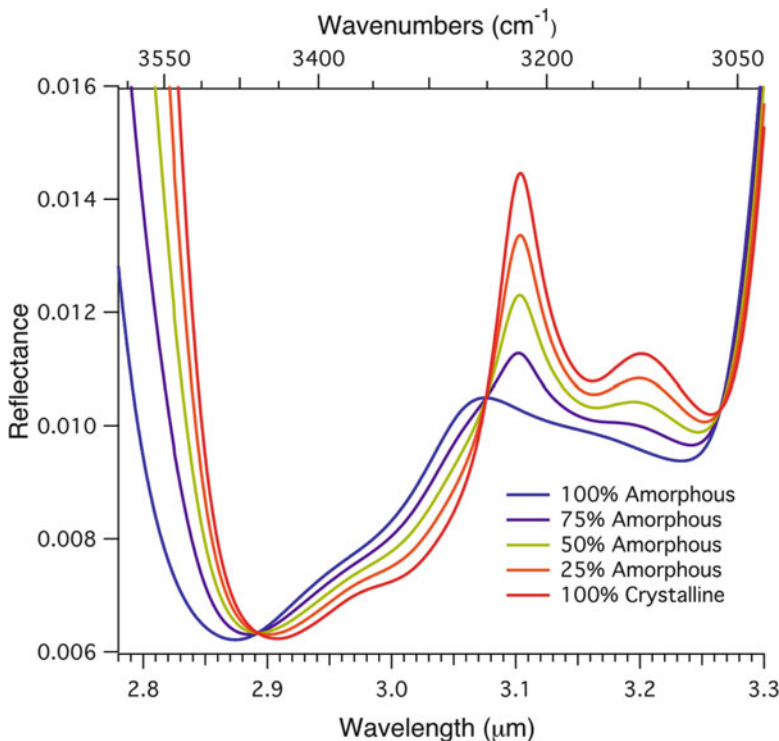


**Fig. 11.7** Model mixtures of amorphous and crystalline H<sub>2</sub>O-ice at 100 K, with grain sizes of 20  $\mu\text{m}$ . Mixtures ratios include: 100% amorphous (blue), 75% amorphous (purple), 50% amorphous (tan), 25% amorphous (orange), and 100% crystalline (red) (From Mastrapa et al. 2009. Reproduced by permission of the AAS)

wavelength in the amorphous ice (Fig. 11.7). Comparing amorphous to crystalline H<sub>2</sub>O-ice, the 2.0  $\mu\text{m}$  and 1.5  $\mu\text{m}$  bands shift to shorter wavelength, and the 1.65  $\mu\text{m}$ , 1.56  $\mu\text{m}$ , and 1.31  $\mu\text{m}$  bands decrease in strength. However, the 2.0  $\mu\text{m}$  band in the high temperature amorphous H<sub>2</sub>O-ice spectrum is slightly stronger than that of crystalline H<sub>2</sub>O-ice (Mastrapa et al. 2008). The band near 3  $\mu\text{m}$  is stronger and shifted to longer wavelength in crystalline H<sub>2</sub>O-ice compared to that of amorphous H<sub>2</sub>O-ice (Hagen et al. 1981; Mastrapa et al. 2009). This feature consists of one central component and two shoulders in the crystalline sample, while the amorphous spectrum shows a single broad feature.

### 11.5.5 Model Mixtures

We have used the optical constants to model single-scattering albedo spectra of different mixtures of amorphous and crystalline H<sub>2</sub>O-ice at 50 K following the

method described in Hapke (1993). The largest change seen in these mixtures is in the band near 1.65  $\mu\text{m}$ . As the amorphous fraction increases, the band shrinks. Also, the band near 1.56  $\mu\text{m}$  weakens, reducing the overall “boxiness” of the 1.5  $\mu\text{m}$  and 1.56  $\mu\text{m}$  bands together. There is also a significant shift in the 1.5  $\mu\text{m}$  band towards shorter wavelengths. The position of maximum absorption for the 2.0  $\mu\text{m}$  band also shifts to shorter wavelength with increasing amorphous content, although this change is not as obvious as with the other bands. Note that the 1.65  $\mu\text{m}$  band is clearly present in model spectra of up to 80% amorphous content. Therefore, the presence of this band cannot be used to interpret a surface as 100% crystalline. Also, model mixtures demonstrate that up to 25% amorphous mixtures fail to significantly dampen the strength of the 1.65  $\mu\text{m}$  band, and its position does not change noticeably until 75% amorphous.

Near 3  $\mu\text{m}$ , all model spectra demonstrate the Fresnel peak, but the pure crystalline spectrum has two peaks while the pure amorphous spectrum has one. The locations of the peaks are only weakly influenced by the amorphous end-member spectrum, and are generally the same as the crystalline end member. The strongest peak near 3.1  $\mu\text{m}$  does not shift from the pure crystalline position even when the content is 75% amorphous. The band near 3.2  $\mu\text{m}$  gets steadily weaker with increasing amorphous content until it disappears completely. The band near 4.5  $\mu\text{m}$  does not show a strong dependence on amorphous content (Fig. 11.8).

### 11.5.6 Laboratory Needs

The laboratory measurements needed include a method of confirming the phase of the ice. Ideally, we would be able to collect infrared spectra and diffraction measurements of the same sample. It would also be useful to be able to control the grain size of the sample. This would be a needed test of the optical constants and spectral models. The current data sets are well-constrained near the strong absorptions, but the transparent regions are poorly constrained due to the scattering of the sample. If the scattering properties of the sample could be measured and compensated for, then the transparent regions would be greatly improved. Finally, it is possible that there are some small differences in the infrared spectra of  $I_c$  and  $I_h$ . To fully study this,  $I_c$  and  $I_h$  samples should be made in the same laboratory and studied in detail.

## 11.6 H<sub>2</sub>O-Ice in the Solar System

The spectral identification of water ice on the surfaces of outer Solar System bodies is chronicled by Clark et al. (this volume). This history of discovery parallels dramatic improvements in telescopes and near-infrared spectrometers, with each new technological advance over the past half-century opening up smaller and more distant targets

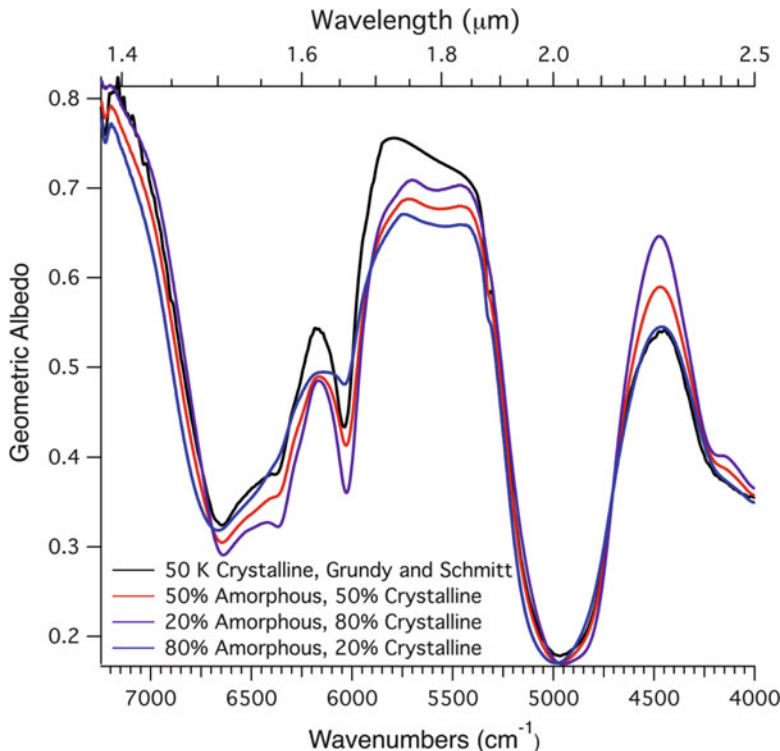


**Fig. 11.8** Geometric albedo model spectra of H<sub>2</sub>O ice. All spectra were generated using optical constants at 50 K. A model spectrum of crystalline H<sub>2</sub>O-ice generated from Grundy and Schmitt (1998) is provided for comparison (*solid line*). The remaining spectra are of mixtures of amorphous and crystalline H<sub>2</sub>O-ice as follows: 80–20% (*purple*), 50–50% (*red*), 20–80% (*blue*) (From Mastrapa et al. 2008, with permission from Elsevier)

to initial spectral reconnaissance. The same technological advances have also enabled successively more sophisticated spectral analyses of closer and larger bodies, including distinguishing between crystalline and amorphous ice phases.

The 1.65 μm band is the most commonly used tool for remotely assessing phase and temperature of H<sub>2</sub>O-ice. This feature is evident in spectra of almost all ice-bearing outer Solar System bodies for which sufficient quality spectra have been obtained, indicating that their surface ice is cold and at least partially crystalline at the ~ mm depths probed by reflectance spectroscopy at these wavelengths. Kieffer and Smythe (1974), Fink and Larson (1975), and Fink et al. (1976) employed this band to estimate the temperature of ice on various bodies. Clark (1981) pointed out that the texture of ice influences the shapes and depths of its absorption bands, and could thus frustrate the use of the 1.65 μm band for thermometry. Grundy et al. (1999) overcame this limitation by simultaneously fitting for temperature and texture, but pointed out a number of additional possible problems. In particular,

amorphous ice is spectrally similar to warm ice in having a suppressed 1.65  $\mu\text{m}$  band, so a mixture of partially amorphous and partially crystalline ice should spectrally resemble crystalline ice at a higher temperature. Despite this ambiguity, ice temperatures derived from 1.65  $\mu\text{m}$  spectra of jovian, saturnian, and uranus satellites are generally consistent with expectation from thermal models, suggesting that if amorphous ice is present at mm depths on those satellites, it must not be so abundant as to produce anomalous high apparent ice temperatures.

Is the fact that ice appears to be consistently crystalline at  $\sim$ mm depths in the surfaces of these bodies simply a consequence of the state of astronomical instrumentation being insufficiently advanced to permit infrared spectroscopy of small, inactive ones, or is it telling us that some other process acts to overcome the amorphizing effect of energetic radiation? It is possible that we need better spatial resolution on observed objects to locate isolated patches of amorphous ice.

### **11.6.1 Solar System Origin**

Since the detection of amorphous H<sub>2</sub>O-ice in interstellar clouds (Leger et al. 1979), it has been thought that the amorphous phase of H<sub>2</sub>O-ice is the most abundant in the universe. The question then becomes, at what stage of Solar System formation is the ice crystallized? Future observations of planetary disks in the process of coalescing, will help us answer this question. For now, and inventory of Solar System objects and the current interpretation of their surfaces are the only link we have between the rest of the universe and our Solar System.

### **11.6.2 Satellites**

Temperatures on jovian, saturnian, and possibly even uranus satellites get high enough (above  $\sim$ 80 K) to thermally crystallize amorphous ice on geologically short time scales. So despite the availability of many forms of energetic radiation capable of disrupting the crystal structure (as discussed in Sect. 11.4.2), it is perhaps not surprising to see predominantly crystalline ice at  $\sim$ mm depths on those satellites. However, that is not to say that amorphous ice does not exist at other depths. Much shallower depths are sampled by light reflected around 3.1 microns. At these wavelengths, ice absorbs a thousand times more strongly than it does at 1.65 microns, so observations of 3 micron reflected light probe  $\sim$ micron rather than  $\sim$ mm depths. Indeed, the absorption at 3.1 microns is so strong that a Fresnel reflectance peak appears, having a distinctive shape, depending on the phase of the ice. Hansen and McCord (2004) used this peak to show that at these much shallower depths, amorphous ice does exist on the surfaces of icy jovian satellites, despite their relatively warm temperatures. They found abundant surficial amorphous ice on Europa, a mixture of crystalline and amorphous ices on Ganymede, and predominantly

crystalline ice on Callisto, in contrast with the uniformly crystalline ice at  $\sim$ mm depths on all three satellites, from the 1.65 micron band. This distribution traces a balance between the intensity of bombardment by energetic radiation from the jovian magnetosphere and thermal recrystallization. Newman et al. (2008) have applied comparable techniques to mapping amorphous ice on the surface of the saturnian satellite Enceladus.

The identification of crystalline ice on Pluto's satellite Charon (Brown and Calvin 2000; Buie and Grundy 2000) presented more of a challenge, as Charon's surface should never get much warmer than around 60 K. Crystalline ice on Neptune's satellite Triton (Cruikshank et al. 2000; Grundy and Young 2004) presented similar difficulties, except that Voyager II images showed Triton's surface to be extremely youthful (Schenk and Zahnle 2007). The existence of crystalline ice in an environment where it should otherwise remain too cold for radiation-produced amorphous ice to re-crystallize has been interpreted as a possible indicator of very recent geological activity (Bauer et al. 2002; Jewitt and Luu 2004; Cook et al. 2007; Jewitt et al. 2007).

Icy outer Solar System bodies could certainly have had warm interiors soon after their accretion, due to decay of radioactive isotopes, especially short-lived <sup>26</sup>Al and <sup>60</sup>Fe (Prialnik et al. 2008). This heating could have crystallized initially amorphous ice, and even led to differentiation and resurfacing (De Sanctis et al. 2001; Choi et al. 2003; Prialnik and Merk 2008). It is possible that, like Triton, larger icy bodies remain geologically active today, perhaps even retaining interior oceans. But below some size threshold, they should have lost their internal heat long ago. The interiors of the smallest should never have become very warm in the first place. Threshold sizes for crystallization or for ongoing activity are sensitive functions of the initial inventory of radionuclides and of the thermal conductivity, neither of which are known with much certainty (McKinnon et al. 2008).

### 11.6.3 Transneptunian Objects (TNOs)

One might expect to see a transition from amorphous ice on the surfaces of small, inert bodies to crystalline ice on the surfaces of larger, still-active bodies. Such a threshold has, so far, evaded direct observational detection. Large TNOs certainly do have crystalline ice on their surfaces. Examples include Haumea (Barkume et al. 2006), Quaoar (Jewitt and Luu 2004), and Orcus (de Bergh et al. 2005; Barucci et al. 2008) with radii of roughly 750, 630, and 475 km, respectively (Brown et al. 2008). But several smaller TNOs appear to also have crystalline ice, although signal precision is often marginal for distinguishing the phase of their ice, and their sizes tend to be more uncertain. Examples include Haumea collisional family members (55636) 2003 TX<sub>300</sub>, (24835) 1995 SM<sub>55</sub>, (145453) 2005 RR<sub>43</sub>, (19308) 1996 TO<sub>66</sub>, (120178) 2003 OP<sub>32</sub> (Brown et al. 1999; Pinilla-Alonso et al. 2007; Barkume, Brown et al. 2008), and (208996) 2003 AZ<sub>84</sub> (Guilbert et al. 2009), as well as the

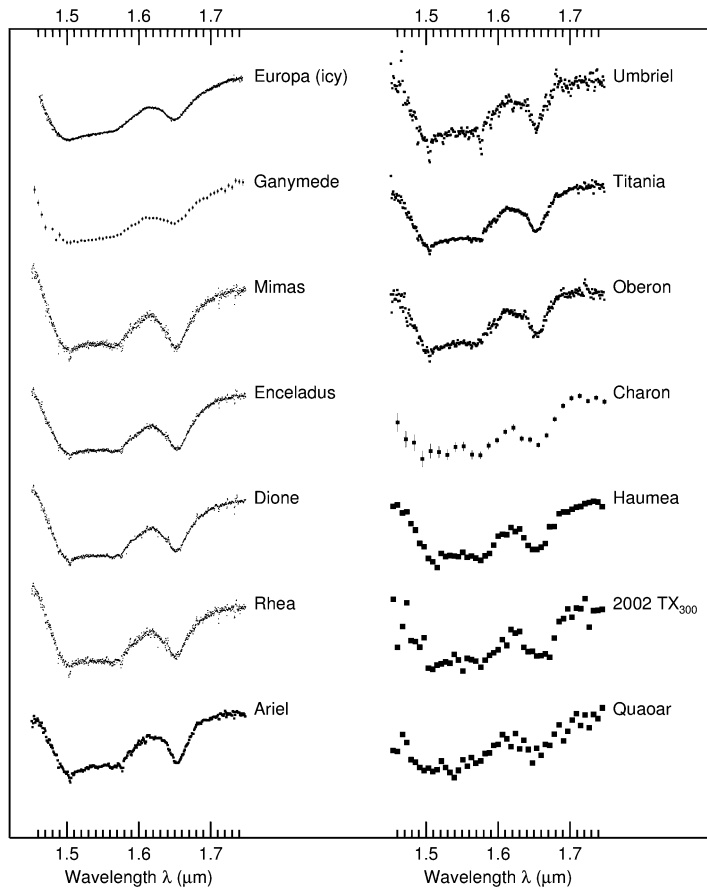


**Fig. 11.9** Examples of H-band reflectance spectra of outer Solar System objects, showing clear evidence for the characteristic features of cold, crystalline ice at the  $\sim$  mm depths probed by these wavelengths: a square-bottomed 1.50–1.58 micron band and a strong 1.65 micron side-band. Data are from Spencer et al. (2006; Europa – icy component), Grundy et al. (1999; Ganymede), Grundy et al. (unpublished IRTF data; Mimas, Enceladus, Dione, Rhea), Grundy et al. (2006; Ariel, Unbriel, Titania, Oberon), Buie and Grundy (2000; Charon), Barkume et al. (2008; Haumea, 2002 TX<sub>300</sub>, Quaoar)

Centaur Chariklo (Brown and Koresko 1998). Example spectra are shown in Fig. 11.9.

If ice in the interiors of comets is mostly amorphous, small TNOs and Oort cloud objects should be mostly amorphous as well. So far, only much larger TNOs have been spectroscopically studied, and their surfaces all look crystalline. Perhaps the size cut-off for continuing activity is smaller than had been anticipated? The higher bulk densities of larger TNOs (Lacerda and Jewitt 2007) do not require porosity, consistent with having experienced sufficient internal heating to have mobilized and crystallized their bulk ice. Smaller TNOs tell a somewhat different story (Fig. 11.6). Some, but not all, of their bulk densities are quite low, as shown in

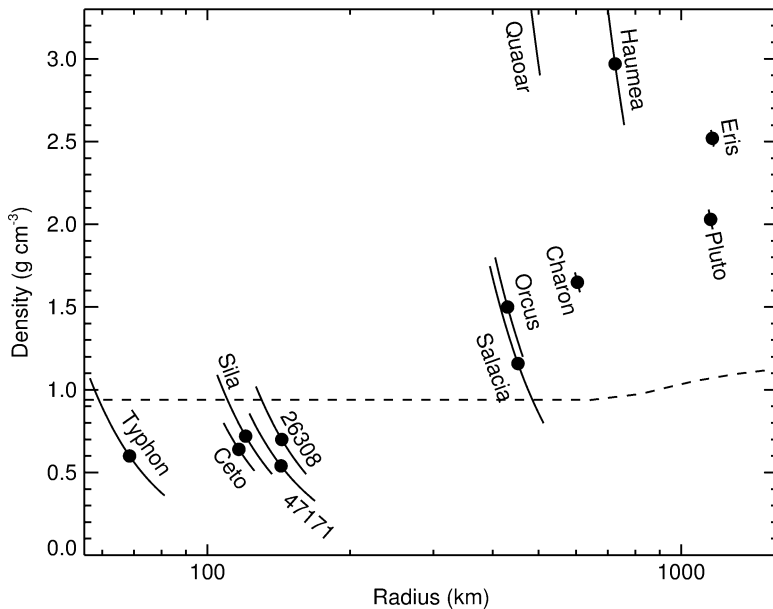


**Fig. 11.10** Bulk densities of TNOs computed from binary orbits and thermal radiometry, plotted versus sizes of the primary bodies (plus the density for Charon – densities for other satellites have yet to be determined). These results are drawn from Buie et al. (2006), Tholen et al. (2008), Stansberry et al. (2006, 2008, 2012), Grundy et al. (2007, 2008), Spencer et al. (2007), Rabinowitz et al. (2006), Benecchi et al. (2010), Brown et al. (2010), Fraser and Brown (2010), Sicardy et al. (2011), and Santos-Sanz et al. (2012). The *dashed curve* represents self-compression in cold H<sub>2</sub>O ice (Lupo and Lewis 1979)

Fig. 11.9 (Grundy et al. 2008), suggesting their interior temperatures never got high enough for the ice to deform itself and collapse interior void space. What temperature this compaction occurs at and how that compares with crystallization remains uncertain (McKinnon, Prialnik et al. 2008), but it would clearly be useful to determine the bulk densities of a larger sample to explore the nature of the boundary between the larger, compacted objects and the smaller, highly porous ones (Fig. 11.10).

#### 11.6.4 Comets

Although they would be compelling observational targets to address this question, much smaller outer Solar System bodies are challenging to even detect, let alone study spectroscopically. However, some do venture into the inner Solar System as comets. Jupiter family or ecliptic comets are thought to derive from the outer regions of the protoplanetary nebula, by way of the Kuiper belt, although it is not exactly

clear from which part(s) of that belt they derive (e.g. Volk and Malhotra 2008). Longer period, more isotropically-distributed comets are also thought to come from the giant planet forming part of the protoplanetary nebula, but by way of the Öort cloud instead. It is possible that the bodies scattered to the Öort cloud formed closer to the sun, on average, than those now occupying the Kuiper belt.

Compared with TNOs, comets can be studied up-close, but direct detection of spectral features of nuclear ice remains extremely challenging. Davies et al. (1997) reported a tentative detection of amorphous ice on the Öort cloud comet Hale-Bopp from the lack of a 1.65 micron band, while Lellouch et al. (1998) detected crystalline ice in the coma of the same comet from far-IR observations by ISO, when the comet was much closer to the Sun. Since this ice could have crystallized in the coma, this observation does not rule out amorphous ice in the nucleus. Other circumstantial evidence suggests that bulk cometary ice could be amorphous. For instance, the distant onset of activity in dynamically new comets has been interpreted as driven by crystallization or annealing of amorphous ice, expelling trapped volatiles such as CO in the process (e.g. Meech and Svoren 2004; Jewitt et al. 2007; Meech et al. 2009). Abundances of cometary volatiles (Bar-Nun et al. 2007), as well as the nuclear spin temperatures of molecules with multiple hydrogen atoms (Kawakita et al. 2004; Crovisier 2007) imply formation around a temperature of  $\sim$ 30 K, cold enough for amorphous ice to condense directly from the gas phase, and certainly too cold for amorphized ice to re-crystallize. Pre-solar particles in cold, dense clouds like the one in which the Solar System formed are clad in amorphous ice mantles (e.g., Irvine and Lunine 2004). Evidence for homogeneous composition of the fragments of comet 73P/Schwassmann-Wachmann 3 (Dello Russo et al. 2007) suggest that diverse volatile compositions of comets (A'Hearn et al. 1995; Fink 2009) reflect distinct bulk compositions, rather than the effects of subsequent processing. The fragility and low density of cometary nuclei is also consistent with having experienced very little post-formation processing (A'Hearn et al. 2005), as is the spectacular diversity of primitive particle types coexisting within comets (Hanner and Bradley 2004; Brownlee et al. 2006).

### 11.6.5 Future Observations

Studies sampling more of the size distribution of TNOs are needed. Bulk densities estimated from satellite orbits in conjunction with sizes from thermal radiometry or stellar occultations are needed to explore the transition between small, porous bodies and larger, more thermally processed ones. Near infrared spectroscopy of more TNOs could reveal whether the phase state of their surface water ice depends on object size. Spectra at higher signal precision could also reveal evidence of subtle ice absorptions in the spectra of otherwise featureless TNOs. Observations of the 3.1 micron band would be valuable for determining whether vertical crystallinity gradients exist on TNOs with strong 1.65 micron bands, providing key constraints on possible crystallization-promoting processes. They might also offer a sensitive probe for the existence of surface ice on objects having 1.5 and 2 micron

bands too weak to detect. 3.1 micron observations of TNOs are not yet quite feasible with existing instrumentation, but the James Webb Space Telescope should provide this capability within the next decade.

The proposed EJSM mission would include observations of Europa and Ganymede. The Europa spectra would have higher spatial resolution than Galileo, NIMS due to improved radiation shielding.

Additional valuable observations will occur when New Horizons flies through the Pluto system in 2015 (Young et al. 2008) revealing whether or not cold, crystalline ice on Charon's surface (and perhaps also on Pluto, Nix, or Hydra) is exclusively associated with recent geological features or occurs in ancient landscapes as well. If the latter is seen, it will prove that some other process is overcoming the amorphizing effects of energetic radiation.

Finally, when Rosetta explores the nucleus of comet Churyumov-Gerasimenko, it will reveal much about the comet's surface environment and interior, including perhaps the phase state of its ice. A particularly important question is whether material exposed at the surface of the nucleus is representative of the interior, as might be expected if material is removed faster than the solar heating thermal wave can propagate inward, or if the surface represents a devolatilized lag deposit, the end result of thermal processing.

## 11.7 Summary

Amorphous and crystalline form of H<sub>2</sub>O-ice, due to extreme contrast in their behavior, is expected to determine the physical properties of ices in our Solar System and dictate the chemical pathways they take. Amorphous ices due to their highly porous nature are expected to dominate low-gravity objects such as comets, asteroids, inter planetary dust particles, and interstellar ices, KBOs, Oort Clouds, etc. It is possible that high-gravity objects whose surface temperature remains below 80 K (trans-Saturnian objects) may accumulate amorphous ices on the surface. The long-term effect of impact-gardening on the phase of H<sub>2</sub>O-ice will need to be better understood to fully understand the stability of amorphous H<sub>2</sub>O-ice on these cold surfaces. All these objects are expected to undergo rich chemistry induced by radiation. Further laboratory measurements and observations are required to be able to use the phase of H<sub>2</sub>O-ice as a tool to interpret the history of Solar System objects.

**Acknowledgments** Mastrapa acknowledges funding from the NASA Outer Planet Research (OPR) and Planetary Geology & Geophysics (PG&G) programs. Grundy acknowledges support from funding from Spitzer Space Telescope, Hubble Space Telescope, and NASA PG&G. Gudipati acknowledges support from NASA PG&G, DDA, CDAP, and Astrobiology Institutes (Astrobiology of Icy Worlds, JPL; Titan as a Prebiotic Chemical System, JPL; Early Habitable Environments, NASA Ames), as well as internal funding from JPL through DRDF and R&TD programs. MSG's part of the research was carried out at the Jet Propulsion Laboratory, California Institute of Technology, under a contract with the National Aeronautics and Space Administration.

## References<sup>1</sup>

- A'Hearn MF, Millis RL et al (1995) The ensemble properties of comets: results from narrowband photometry of 85 comets, 1976–1992. *Icarus* 118:223–270
- A'Hearn MF, Belton MJS et al (2005) Deep impact: excavating comet tempel 1. *Science* 310:258–264
- Akiyama T, Sakamaki M et al (1997) Effects of proton motions on the fluorescence from 2-naphthol-doped ice IH and the proton ordering transition. *J Phys Chem B* 101:6205–6207
- Andersson O, Johari GP et al (2004) An ice phase of lowest thermal conductivity. *J Chem Phys* 120(20):9612–9617
- Angell CA (2002) Liquid fragility and the glass transition in water and aqueous solutions. *Chem Rev* 102(8):2627–2650
- Backus EHG, Bonn M (2004) Theory of bulk, surface and interface phase transition kinetics in thin films. *J Chem Phys* 121(2):1038–1049
- Baragiola RIA (2003) Water ice on outer solar system surfaces: basic properties and radiation effects. *Planet Space S* 51:953–961
- Barkume KM, Brown ME et al (2006) Water ice on the satellite of Kuiper belt object 2003 EL61. *Astrophys J* 640:L87–L89
- Barkume KM, Brown ME et al (2008) Near-infrared spectra of centaurs and Kuiper belt objects. *Astron J* 135:55–67
- Bar-Nun A, Notesco G et al (2007) Trapping of N<sub>2</sub>, CO and Ar in amorphous ice—Application to comets. *Icarus* 190:655–659
- Barucci MA, Merlin F et al (2008) Surface composition and temperature of the TNO Orcus. *Astron Astr* 479:L13–L16
- Bauer JM, Roush TL et al (2002) The near infrared spectrum of miranda: evidence of crystalline water ice. *Icarus* 158(1):178–190
- Benecchi SD, Noll KS, Grundy WM, Levison HF (2010) (47171)1999 TC36, a transneptunian triple. *Icarus* 207:978–991
- Bergren MS, Schuh D et al (1978) The OH stretching region infrared spectra of low density amorphous solid water and polycrystalline ice I<sub>h</sub>. *J Chem Phys* 69(8):3477–3482
- Bernal JD, Fowler RH (1933) A theory of water and ionic solution, with particular reference to hydrogen and hydroxyl ions. *J Chem Phys* 1(8):515–548
- Bertie JE, Whalley E (1964) Infrared spectra of ice I<sub>h</sub> and I<sub>c</sub> in the range 4000–350 cm<sup>-1</sup>. *J Chem Phys* 40(6):1637–1645
- Bertie JE, Whalley E (1967) Optical spectra of orientationally disordered crystals II. Infrared spectrum of ice I<sub>h</sub> and ice I<sub>c</sub> from 360 to 50 cm<sup>-1</sup>. *J Chem Phys* 46(4):1271–1284
- Brown ME, Calvin WM (2000) Evidence for crystalline water and ammonia ices on Pluto's satellite Charon. *Science* 287:107–109
- Brown ME, Koresko CC (1998) Detection of water ice on the Centaur 1997 CU 26. *Astrophys J* 505:L65
- Brown WL, Lanzerotti LJ et al (1978) "Sputtering" of ice by MeV light ions. *Phys Rev Lett* 40:1027–1030
- Brown RH, Cruikshank D et al (1999) Water ice on Kuiper belt object 1996 TO66. *Astrophys J* 519(1):L101–L104
- Brown RH, Soderblom LA et al (2008) The identification of liquid ethane in Titan's Ontario Lacus. *Nature* 454:607–610
- Brown ME, Ragozzine D, Stansberry J, Fraser WC (2010) The size, density, and formation of the Orcus-Vanth system in the Kuiper belt. *Astron J* 139:2700–2705
- Brownlee D, Tsou P et al (2006) Comet 81P/Wild 2 Under a Microscope. *Science* 314:1711

---

<sup>1</sup> Co-author Gudipati also published in the past as Gudipati S. Murthy

- Buch V, Devlin JP (1999) A new interpretation of the OH-stretch spectrum of ice. *J Chem Phys* 110(7):3437–3443
- Buie MW, Grundy WM (2000) The distribution and physical state of H<sub>2</sub>O on Charon. *Icarus* 148:324–339
- Buie MW, Grundy WM, Young EF, Young LY, Stern SA (2006) Orbits and photometry of Pluto's satellites: Charon, S/2005 P1, and S/2005 P2. *Astron J* 132:290–298
- Carr MH (1996) Water on Mars. Oxford University Press, New York
- Choi YJ, Brosch N et al (2003) Rotation and cometary activity of KBO (29981) 1999 TD<sub>10</sub>. *Icarus* 165:101–111
- Clark RN (1981) Water frost and ice: the near-infrared spectral reflectance 0.625–2.5 mm. *J Geophys Res* 86(B4):3087–3096
- Clark RN (2009) Detection of adsorbed water and hydroxyl on the moon. *Science* 326:562
- Cook JC, Desch SJ et al (2007) Near-infrared spectroscopy of Charon: possible evidence for cryovolcanism on Kuiper belt objects. *Astrophys J* 663:1406–1419
- Crovisier J (2007) Cometary diversity and cometary families
- Cruikshank DP, Schmitt B et al (2000) Water ice on triton. *Icarus* 147:309–316
- Cyriac J, Pradeep T (2008) Structural reorganization on amorphous ice films below 120 K revealed by near-thermal (1 eV) ion scattering. *J Phys Chem C* 112:5129–5135
- Dartois E, Deboffe D (2008) Methane clathrate hydrate FTIR spectrum Implications for its cometary and planetary detection. *Astron Astr* 490(3):L19–L22
- Davies JK, Roush TL et al (1997) The detection of water ice in Comet Hale-Bopp. *Icarus* 127:238–245
- de Bergh C, Delsanti A et al (2005) The surface of the transneptunian object 90482 Orcus. *Astron Astr* 437:1115–1120
- De Sanctis MC, Capria MT et al (2001) Thermal evolution and differentiation of Edgeworth-Kuiper belt objects. *Astron J* 121:2792–2799
- Dello Russo N, Vervack RJ et al (2007) Compositional homogeneity in the fragmented comet 73P/Schwassmann-Wachmann 3. *Nature* 448:172–175
- Dohnalek Z, Ciolfi RL et al (1999) Substrate induced crystallization of amorphous solid water at low temperatures. *J Chem Phys* 110(12):5489–5492
- Dohnalek Z, Kimmel GA et al (2000) The effect of the underlying substrate on the crystallization kinetics of dense amorphous solid water films. *J Chem Phys* 112(13):5932–5941
- Dohnalek Z, Kimmel GA et al (2003) The deposition angle-dependent density of amorphous solid water films. *J Chem Phys* 118(1):364–372
- Dowell LG, Rindefret AP (1960) Low-temperature forms of ice as studied by X-ray diffraction. *Nature* 188:1144–1148
- Dubochet J, Lepault J et al (1982) Electron microscopy of frozen water and aqueous solutions. *J Microsc* 128(3):219–237
- Fama M, Loeffler MJ et al (2010) Radiation-induced amorphization of crystalline ice. *Icarus* 207:314–319
- Feldman WC, Maurice S et al (1998) Fluxes of fast and epithermal neutrons from lunar prospector: evidence for water ice at the lunar poles. *Science* 281:1496
- Fink U (2009) A taxonomic survey of comet composition 1985–2004 using CCD spectroscopy. *Icarus* 201:311–334
- Fink U, Larson HP (1975) Temperature dependence of the water-ice spectrum between 1 and 4 microns: application to Europa, Ganymede, and Saturn's rings. *Icarus* 24:411–420
- Fink U, Larson HP et al (1976) Infrared spectra of the satellites of Saturn – Identification of water ice on Iapetus, Rhea, Dione, and Tethys. *Astrophys J* 207:L63–L67
- Fraser WC, Brown ME (2010) Quaoar: a rock in the Kuiper belt. *Astrophys J* 714:1547–1550
- Golecki I, Jaccard C (1978) Radiation damage in ice at low temperatures studied by proton channeling. *J Glaciol* 21(85):247–258
- Grundy WM, Schmitt B (1998) The temperature-dependent near-infrared absorption spectrum of hexagonal H<sub>2</sub>O-ice. *J Geophys Res* 103(E11):25809–25822

- Grundy WM, Young LA (2004) Near-infrared spectral monitoring of Triton with IRTF/SpeX I: establishing a baseline for rotational variability. *Icarus* 172:455–465
- Grundy WM, Buie MW et al (1999) Near-infrared spectra of icy outer solar system surfaces: determination of H<sub>2</sub>O ice temperatures. *Icarus* 142:536–549
- Grundy WM, Young LA et al (2006) Distributions of H<sub>2</sub>O and CO<sub>2</sub> ices on Ariel, Umbriel, Titania, and Oberon from IRTF/SpeX observations. *Icarus* 184:543–555
- Grundy WM, Stansberry JA, Noll KS, Stephens DC, Trilling DE, Kern SD, Spencer JR, Cruikshank DP, Levison HF (2007) The orbit, mass, size, albedo, and density of (65489) Ceto/Phorcys: a tidally-evolved binary Centaur. *Icarus* 191:286–297
- Grundy WM, Noll KS, Virtanen J, Muinonen K, Kern SD, Stephens DC, Stansberry JA, Levison HF, Spencer JR (2008) (42355) Typhon Echidna: scheduling observations for binary orbit determination. *Icarus* 197:260–268
- Gudipati MS (1997) Photochemically induced electronic-to-electronic energy transfer in geminate CO-O van der Waals pair generated through vacuum ultraviolet photolysis of CO<sub>2</sub> in Ar matrices. *J Phys Chem A* 101(11):2003–2009
- Gudipati MS, Allamandola L (2006) Unusual stability of PAH radical cations in amorphous water-ice up to 120 K: astronomical implications. *Astrophys J Lett* 638:286–292
- Guilbert A, Alvarez-Candal A et al (2009) ESO-Large program on TNOs: near-infrared spectroscopy with SINFONI. *Icarus* 201:272–283
- Hagen W, Tielens AGGM (1981) Infrared spectrum of H<sub>2</sub>O matrix isolated in CO at 10 K: evidence for bifurcated dimers. *J Chem Phys* 75:4198–4207
- Hagen W, Tielens AGGM (1982) The librational region in the spectrum of amorphous solid water and ice Ic between 10 and 140 K. *Spectrochim Acta* 38A:1089–1094
- Hagen W, Tielens AGGM et al (1981) The infrared spectra of amorphous solid water ice and ice I<sub>c</sub> between 10 K and 140 K. *Chem Phys* 56:367–379
- Hanner MS, Bradley JP (2004) Composition and mineralogy of cometary dust. *Comets II*:555–564
- Hansen GB, McCord TB (2004) Amorphous and crystalline ice on the Galilean satellites: a balance between thermal and radiolytic processes. *J Geophys Res (Planets)* 109:01012. doi:[10.1029/2003JE002149](https://doi.org/10.1029/2003JE002149)
- Hapke B (1993) Combined theory of reflectance and emittance spectroscopy. In: Pieters CM, Englert PAJ (eds) *Remote geochemical analysis: elemental and mineralogical composition*, vol 4. Cambridge University Press, Cambridge, pp 31–42
- Hardin AH, Harvey KB (1973) Temperature dependences of the ice I hydrogen bond spectral shifts- I. The vitreous to cubic ice I phase transformation. *Spectrochim Acta* 29A:1139–1151
- Harmon JK, Slade MA (1992) Radar mapping of Mercury – Full-disk images and polar anomalies. *Science* 258:640–643
- Heide H-G (1984) Observations on ice layers. *Ultramicroscopy* 14:271–278
- Hudgins D, Sandford SA et al (1993) Midinfrared and far-infrared spectroscopy of ices: optical-constants and integrated absorbances. *Astrophys J Sup Series* 86(2):713–870
- Irvine WM, Lunine JI (2004) The cycle of matter in our galaxy: from clouds to comets. *Comets II*:25–31
- Jenniskens P, Blake DF (1994) Structural transitions in amorphous water ice and astrophysical implications. *Science* 265:753–756
- Jenniskens P, Blake DF (1996) Crystallization of amorphous water ice in the solar system. *Astrophys J* 473:1104–1113
- Jenniskens P, Blake DF et al (1995) High-density amorphous ice, the frost on interstellar grains. *Astrophys J* 455:389–401
- Jenniskens P, Blake DF et al (1998) Amorphous water ice. A solar system material. In: Schmitt B, de Bergh C, Festou M (eds) *Solar system ices*. Kluwer Academic Publishers, Norwell, pp 139–156
- Jewitt DC, Luu J (2004) Crystalline water ice on the Kuiper belt object (50000) Quaoar. *Nature* 432:731–733

- Jewitt D, Chizmadia L et al (2007) Water in the small bodies of the Solar system. In: Reipurth B, Jewitt D, Keil K (eds) Protostars and Planets V. University of Arizona Press, Tucson, pp 863–878
- Kawakita H, Watanabe Ji et al (2004) Spin temperatures of ammonia and water molecules in Comets. *Astrophys J* 601:1152–1158
- Kieffer HH, Smythe WD (1974) Frost spectra: comparison with Jupiter's Satellites. *Icarus* 21:506–512
- Kohl I, Mayer E et al (2000) The glassy water-cubic ice system: a comparative study by X-ray diffraction and differential scanning calorimetry. *Phys Chem Chem Phys* 2:1579–1586
- Kohl I, Bachmann L et al (2005) Water behaviour glass transition in hyperquenched water? *Nature* 435(7041):E1–E1
- Kolesnikov AI, Li J-C et al (1997) Neutron scattering of vapor deposited amorphous. *Phys Rev Lett* 79(10):1869–1872
- Kondo T, Kato HS et al (2007) Deposition and crystallization studies of thin amorphous solid water films on Ru(0001) and on CO-precovered Ru(0001). *J Chem Phys* 127:094703
- Kouchi A, Kuroda T (1990) Amorphization of cubic ice by ultraviolet irradiation. *Nature* 344:134–135
- Kouchi A, Sirono S (2001) Crystallization heat of impure amorphous H<sub>2</sub>O ice. *Geophys Res Lett* 28(5):827–830
- Kouchi A, Greenberg JM et al (1992) Extremely low thermal conductivity of amorphous ice – Relevance to comet evolution. *Astrophys J* 388:L73–L76
- Kouchi A, Yamamoto T et al (1994) Conditions for condensation and preservation of amorphous ice and crystallinity of astrophysical ices. *Astron Astrophys* 290:1009–1018
- Kuhs WF, Lehman MS (1983) The structure of ice I<sub>h</sub> by neutron diffraction. *J Phys Chem* 87:4312–4313
- Lacerda P, Jewitt DC (2007) Densities of solar system objects from their rotational light curves. *Astron J* 133:1393
- Leger A, Klein S et al (1979) The 3.1 mm absorption in molecular clouds is probably due to amorphous H<sub>2</sub>O ice. *Astron Astrophys* 79:256–259
- Lellouch E, Crovisier J et al (1998) Evidence for water ice and estimate of dust production rate in comet Hale-Bopp at 2.9 AU from the sun. *Astron Astrophys* 339:L9–L12
- Lepault J, Freeman R et al (1983) Electron beam induced “Vitrified Ice”. *J Microsc* 132(3): RP3–RP4
- Leto G, Baratta GA (2003) Ly-alpha photon induced amorphization of Ic water ice at 16 Kelvin. Effects and quantitative comparison with ion irradiation. *Astron Astrophys* 397:7–13
- Leto G, Gomis O et al (2005) The reflectance spectrum of water ice: is the 1.65 μm msp peak a good temperature probe? *Memorie della Societa Astron Italiana Sup* 6:57–62
- Lupo MJ, Lewis JS (1979) Mass-radius relationships in icy satellites. *Icarus* 40:157–170
- Madden WG, Bergren MS et al (1978) A conjectured interpretation of the OH stretching spectrum of low density amorphous water. *J Chem Phys* 69(8):3497–3501
- Marboeuf U, Petit J-M et al (2009) Can collisional activity produce a crystallization of Edgeworth-Kuiper belt comets? *Mon Not R Astron Soc* 397:L74–L78
- Mastrapa RME, Brown RH (2006) Ion irradiation of crystalline H<sub>2</sub>O-ice: effect on the 1.65-μm band. *Icarus* 183:207–214
- Mastrapa RME, Sandford SA (2008) New optical constants of amorphous and crystalline H<sub>2</sub>O-ice, 3–20 μm. *AAS/Division for planetary sciences meeting abstracts*
- Mastrapa RM, Bernstein MP et al (2008) Optical constants of amorphous and crystalline H<sub>2</sub>O-ice in the near infrared from 1.1 to 2.6 μm. *Icarus* 197:307–320
- Mastrapa RM, Sandford SA et al (2009) Optical constants of amorphous and crystalline H<sub>2</sub>O-ice: 2.5–22 μm (4000–455 cm<sup>-1</sup>). *Astrophys J* 701:1347–1356
- McGraw R, Madden WG et al (1978) A theoretical study of the OH stretching region of the vibrational spectrum of ice I<sub>h</sub>. *J Chem Phys* 69(8):3483–3496

- McKinnon WB, Hofmeister AM (2005) Ice XI on Pluto and Charon? *Bull Am Astron Soc*, *Am Astron Soc* 37:732–733
- McKinnon WB, Prialnik D, Stern SA, Coradini A (2008) Structure and evolution of Kuiper belt objects and dwarf planets. In: Barucci A, Boehnhardt H, Cruikshank D, Morbidelli A (eds) *The Solar system beyond Neptune*. University of Arizona Press, Tucson, pp 213–241
- Meech KJ, Svoren J (2004) Using cometary activity to trace the physical and chemical evolution of cometary nuclei. *Comets II*:317–335
- Meech KJ, Pittichov J et al (2009) Activity of comets at large heliocentric distances pre-perihelion. *Icarus* 201:719–739
- Mitlin S, Leung KT (2002) Film growth of ice by vapor deposition at 128–185 K studied by Fourier transform infrared reflection – absorption spectroscopy: evolution of the OH stretch and the dangling bond with film thickness. *J Phys Chem B* 106:6234–6247
- Moore MH, Hudson RL (1992) Far-infrared spectral studies of phase changes in water ice induced by proton irradiation. *Astrophys J* 401:353–360
- Mukai T, Krätschmer W (1986) Optical constants of the mixture of ices. *Earth Moon and Planets* 36:145–155
- Murthy GS, Arjunan P et al (1987) consequences of Lattice relaxability in solid state photodimerizations. *Tetrahedron* 43:1225–1240
- Murthy GS, Hassenruck K et al (1989) [n]Staffanes: the parent hydrocarbons. *J Am Chem Soc* 111:7262–7264
- Narten AH, Venkatesh CG et al (1976) Diffraction pattern and structure of amorphous solid water at 10 and 77 K. *J Chem Phys* 64(3):1106–1121
- Newman SF, Buratti BJ et al (2008) Photometric and spectral analysis of the distribution of crystalline and amorphous ices on Enceladus as seen by Cassini. *Icarus* 193:397–406
- Ockman N (1958) The infra-red and Raman spectra of ice. *Adv Phys* 7:199–220
- Parent P, Laffon C et al (2002) Structure of the water ice surface studied by x-ray absorption of the O K-edge. *J Chem Phys* 117(23):10842–10851
- Pauling L (1935) The Structure and entropy of ice and of other crystals with some randomness of atomic arrangement. *J Am Chem Soc* 57(12):2680–2684
- Petrenko VF, Whitworth RW (1999) Physics of ice. England, Oxford University Press, Oxford
- Pinilla-Alonso N, Licandro J et al (2007) The water ice rich surface of (145453) 2005 RR43: a case for a carbon-depleted population of TNOs? *Astron Astrophys* 468:L25–L28
- Porter SB, Desch SJ, Cook JC (2010) Micrometeorite impact annealing of ice in the outer Solar system. *Icarus* 208:492–498
- Prialnik D, Merk R (2008) Growth and evolution of small porous icy bodies with an adaptive-grid thermal evolution code. I. Application to Kuiper belt objects and Enceladus. *Icarus* 197:211–220
- Prialnik D, Sarid G et al (2008) Thermal and chemical evolution of comet nuclei and Kuiper belt objects. *Space Sci Rev* 138:147–164
- Rabinowitz DL, Barkume K, Brown ME, Roe H, Schwartz M, Tourtellotte S, Trujillo C (2006) Photometric observations constraining the size, shape, and albedo of 2003 EL61, a rapidly rotating, Pluto-sized object in the Kuiper belt. *Astrophys J* 639:1238–1251
- Sack NJ, Baragiola RA (1993) Sublimation of vapor-deposited water ice below 170 K, and its dependence on the growth conditions. *Phys Rev B, Condensed Matter* 48(14):9973–9978
- Sadtchenko V, Giese CF et al (2000) Interaction of hydrogen chloride with thin ice films: the effect of ice morphology and evidence for unique surface species on crystalline vapor-deposited ice. *J Phys Chem B* 104(40):9421–9429
- Safarik DJ, Mullins CB (2004) The nucleation rate of crystalline ice in amorphous solid water. *J Chem Phys* 121(12):6003–6010
- Santos-Sanz P, Lellouch E, Fornasier S, Kiss C, Pal A, Muller TG, Vilenius E, Stansberry J, Mommert M, Delsanti A, Mueller M, Boehnhardt H, Peixinho N, Henry F, Ortiz JL, Thirouin A, Protopapa S, Duffard R, Szalai N, Lim T, Ejete C, Hartogh P, Harris AW, Rengel M (2012) “TNOs are Cool”: a survey of the transneptunian region. Size/albedo characterization of 15

- scattered disk and detached objects observed with Herschel Space Observatory-PACS. *Astron Astrophys* (in press)
- Schaff JE, Roberts JT (1996) Toward an understanding of the surface chemical properties of ice: differences between the amorphous and crystalline surfaces. *J Phys Chem* 100(33):14151–14160
- Schenk PM, Zahnle K (2007) On the negligible surface age of Triton. *Icarus* 192:135–149
- Schmitt B, Quirico E et al (1998) Optical properties of ices from UV to infrared. In: Schmitt B, de Bergh C, Festou M (eds) *Solar system ices*. Kluwer Academic Publishers, Norwell, pp 199–240
- Sicardy B et al (2011) A Pluto-like radius and a high albedo for the dwarf planet Eris from an occultation. *Nature* 478:493–496
- Slade MA, Butler BJ et al (1992) Mercury radar imaging – Evidence for polar ice. *Science* 258:635–640
- Smith RG, Robinson G et al (1994) Molecular ices as temperature indicators for interstellar dust: the 44- and 62- mm lattice features of H<sub>2</sub>O-ice. *Mon Not R Astron Soc* 271:481–489
- Soper AK (2008) Structural transformations in amorphous ice and supercooled water and their relevance to the phase diagram of water. *Mol Phys: Int J Interfac Chem Phys* 106(16):2053–2076
- Spencer JR, Grundy WM et al (2006) The nature of Europa's dark non-ice surface material: spatially-resolved high spectral resolution spectroscopy from the Keck telescope. *Icarus* 182:202–210
- Spencer JR, Stansberry JA, Grundy WM, Noll KS (2007) A low density for binary Kuiper belt object (26308) 1998 SM165. *Bull Am Astron Soc* 38:546 (abstract)
- Stansberry JA, Grundy WM, Margot JL, Cruikshank DP, Emery JP, Rieke GH, Trilling DE (2006) The albedo, size, and density of binary Kuiper belt object (47171) 1999 TC36. *Astrophys J* 643:556–566
- Stansberry J, Grundy W, Brown M, Cruikshank D, Spencer J, Trilling D, Margot JL (2008) Physical properties of Kuiper belt and Centaur objects: constraints from the Spitzer Space Telescope. In: Barucci A, Boehnhardt H, Cruikshank D, Morbidelli A (eds) *The Solar system beyond Neptune*. University of Arizona Press, Tucson, pp 161–179
- Stansberry JA, Grundy WM, Mueller M, Benecchi SD, Rieke GH, Noll KS, Buie MW, Levison HF, Porter SB, Roe HG (2012) Physical properties of transneptunian Binaries (120347) Salacia-Actaea and (42355) Typhon-Echidna. *Icarus* (in press)
- Stern SA (2003) The evolution of comets in the Oort cloud and Kuiper belt. *Nature* 424:639–642
- Stevenson KP, Kimmel GA et al (1999) Controlling the morphology of amorphous solid water. *Science* 283(5407):1505–1507
- Stewart ST, Ahrens TJ (2005) Shock properties of H<sub>2</sub>O ice. *J Geophys Res (Planets)* 110:03005
- Stewart ST, Seifter A et al (2008) Shocked H<sub>2</sub>O ice: thermal emission measurements and the criteria for phase changes during impact events. *Geophys Res Lett* 35:23203
- Strazzulla G, Baratta GA et al (1991) Primordial comet mantle: irradiation production of a stable, organic crust. *Icarus* 91:101–104
- Strazzulla G, Baratta GA et al (1992) Ion-beam-induced amorphization of crystalline water ice. *Europhys Lett* 18(6):517–522
- Sugisaki M, Suga H et al (1969) Calorimetric study of glass transition of the amorphous ice and of the phase transformation between the cubic and hexagonal ices. In: Riehl N (ed) *Physics of ice*. Platinum Press, New York, pp 329–343
- Sunshine JM, Farnham TL et al (2009) Temporal and spatial variability of Lunar hydration as observed by the deep impact spacecraft. *Science* 326:565
- Tholen DJ, Buie MW, Grundy WM, Elliott GT (2008) Masses of Nix and Hydra. *Astron J* 135:777–784
- Tulk CA, Benmore CJ et al (2002) Structural studies of several distance metastable forms of amorphous ice. *Science* 297:1320–1323
- Venkatesh CG, Rice SA et al (1974) Amorphous solid water – X-Ray diffraction study. *Science* 186(4167):927–928

- Volk K, Malhotra R (2008) The scattered disk as the source of the Jupiter family comets. *Astrophys J* 687:714–725
- Wagner R, Schouren F et al (2000) Photochemically induced energy transfer II: spectroscopic and photophysical aspects of the electronic-to-electronic energy transfer in geminate van der waals complexes. *J Phys Chem A* 104:3593–3602
- Westley MS, Baratta GA et al (1998) Density and index of refraction of water ice films vapor deposited at low temperatures. *J Chem Phys* 108(8):3321–3326
- Whalley E (1977) A detailed assignment of the O-H stretching bands of ice I. *Can J Chem* 55(19):3429–3441
- Young LA, Stern SA et al (2008) New horizons: anticipated scientific investigations at the Pluto system. *Space Sci Rev* 140:93–127
- Yue Y, Angell CA (2004) Clarifying the glass-transition behaviour of water by comparison with hyperquenched inorganic glasses. *Nature* 427(6976):717–720
- Zheng W, Jewitt D et al (2009) On the state of water ice on Saturn's Moon Titan and implications to icy bodies in the outer solar system. *J Phys Chem A* 113(42):11174–11181

# Chapter 12

## Clathrate Hydrates: Implications for Exchange Processes in the Outer Solar System

Mathieu Choukroun, Susan W. Kieffer, Xinli Lu, and Gabriel Tobie

**Abstract** Clathrate hydrates have unique physical and chemical properties because their crystalline structure contains voids that are filled by gas molecules. Their occurrence in many natural environments on Earth (deep-sea sediments, ice sheets) suggests their potential formation elsewhere in the Solar System where suitable pressure – temperature – gas composition conditions occur. This raises the question of their putative role in the storage and release of volatiles. This chapter first reviews the structure of clathrate hydrates, compares their thermo–physical properties with those of water ice, and addresses their stability and methods for estimating equilibria. Then we discuss their likely occurrence in Solar System objects and focus on the geophysical implications of their presence, from the perspectives of both the internal structure of and thermal transfer in icy Solar System bodies, as well as outgassing processes. A particular emphasis is placed on Titan and Enceladus, respectively the largest and the most geologically active satellites of Saturn, where the dissociation of clathrate hydrates could participate in atmospheric formation (Titan) and plume activity (Enceladus).

---

M. Choukroun (✉)

Jet Propulsion Laboratory, 4800 Oak Grove Dr, MS 79-24, Pasadena, CA 91109, USA  
e-mail: [mathieu.choukroun@jpl.nasa.gov](mailto:mathieu.choukroun@jpl.nasa.gov)

S.W. Kieffer

Department of Geology, University of Illinois, 1301 West Green St, Urbana, IL 61801, USA

X. Lu

Department of Geology, University of Illinois, 1301 West Green St, Urbana, IL 61801, USA  
Illinois Sustainable Technology Center, 1 Hazelwood Dr, Champaign, IL 61820, USA

G. Tobie

UMR-CNRS 6112 – Planétologie et Géodynamique, Université de Nantes, 2 rue de la Houssinière,  
Nantes 44322, France

## 12.1 Introduction

Clathrate hydrates are non-stoichiometric compounds, in which hydrogen-bonded H<sub>2</sub>O molecules form a crystalline skeleton. The three-dimensional framework leaves cage-like voids that trap gas molecules individually, via weak van der Waal interactions with the hydrate skeleton. The term “clathrate” is considered to be derived either from the Greek work “kleithra” or from the Latin word “clathratus”, both meaning a “cage.” While other clathrate-forming elements or molecules do exist, in this chapter we focus on hydrated structures that bear relevance to natural processes that occur throughout the Solar System. Many other hydrated solids may also exist within icy environments of the Solar System (sulfate salts, ammonia, methanol, etc.). We refer the reader in quest of further information on those hydrates to the recent reviews by Fortes and Choukroun (2010) and Durham et al. (2010).

First produced incidentally during low-temperature experiments on liquid water and dichlorine gas by Davy (1811), clathrate hydrates were not thought of as compounds occurring in nature until the work by Miller (1961). His equilibrium calculations suggested that clathrate hydrates may be stable on Earth, on Mars, and on various outer solar system objects (giant planets, Pluto, icy satellites, etc.). On Earth, the first observations of natural clathrate hydrates have been made in Northern Continental Russia in the 1960s (see Makogon 1981). Since then, the Deep Sea Drilling Program (DSDP) and the Ocean Drilling Program (ODP) discovered many locations where oceanic seafloor sediments host clathrate hydrates (e.g., Kvenvolden 1988, 1999). In fact, the total amounts of natural gas (primarily methane) trapped in oceanic clathrate hydrates and in the Siberian and Canadian permafrosts have been estimated to twice the amounts of fossil hydrocarbons (e.g., Kvenvolden 1988). These compounds amount to  $\sim 2.5 \times 10^{15} \text{ m}^3$ , although the variability in methods used for inferring the bulk abundance yields a high uncertainty on this estimate (e.g., Milkov 2004). Such a large abundance makes them simultaneously a potential energy resource of interest (e.g., Kvenvolden 1988, 1999) and a putative threat to Earth’s climate. Indeed, if the ocean temperature increases sufficiently for dissociation to occur to the extent that the release of methane in the atmosphere increases significantly the greenhouse effect, then positive feedback triggering further warming and dissociation has been suggested (Dickens 2001), leading to a catastrophic situation. Such an event has been tentatively related to a period of thermal maximum and major extinctions at the Paleocene-Eocene transition, 55 Million years ago (Dickens 2001, 2003). Besides the ocean seafloor, clathrate hydrates occur in terrestrial ice sheets: the paleontologic air trapped as bubbles in the accreting ice forms clathrate hydrate inclusions of a N<sub>2</sub>-O<sub>2</sub> mixture at depths of 1,000 m and more (e.g., Shoji and Langway 1982; Uchida et al. 1994), thus “fossilizing” the atmospheric record of our planet over geologic timescales. These various aspects of terrestrial clathrate hydrates are beyond the scope of this chapter, and we refer the reader seeking further information on these topics to the books by Max (2000) and Sloan and Koh (2007).

Nevertheless, the abundance of clathrate hydrates on Earth shows that, *wherever the thermodynamic context (i.e., pressure – temperature – gas composition conditions) is suitable for clathrate hydrate formation, these compounds do occur*. We know that conditions suitable for the formation of clathrate hydrates are met in a variety of extraterrestrial environments, so these compounds should be expected elsewhere in the Solar System, and possibly beyond.

Beyond our own planet, these compounds have been suggested as a potential storage medium for Mars' atmospheric methane in the permafrost by several studies, see the recent review by Chastain and Chevrier (2007). Also, CO<sub>2</sub> clathrate hydrates may exist at depth within the polar caps (e.g., Miller 1961; Kolb and Tanaka 2001; Greve and Mahajan 2005). We will not discuss further the Martian aspects of clathrate hydrate research because of the scope of this chapter. In the outer regions of our Solar System, the experimental and theoretical studies of Delsemme and Swings (1952) and Delsemme and Wenger (1970) suggested the occurrence of clathrate hydrates in comets, as well as more recent studies by Iro et al. (2003), Marboeuf et al. (2010). The relevance of clathrate hydrate species to the presolar nebula has also been advocated for (e.g., Lunine and Stevenson 1985; Gautier et al. 2001; Hersant et al. 2001, 2004, 2008; Gautier and Hersant 2005; Alibert and Mousis 2007; Mousis et al. 2009). Furthermore, the involvement of clathrate hydrates in exchange processes within icy satellites has been supported by several studies, whether to explain Titan's atmospheric replenishment (Lunine and Stevenson 1987; Tobie et al. 2006; Choukroun et al 2010a), or Enceladus' South Polar activity (e.g., Kieffer et al. 2006; Fortes 2007). These examples illustrate the relevance of clathrate hydrates in the storage and the release of volatiles in Solar System bodies.

Over six decades of extensive experimental work, thermodynamic modeling, and natural observations on Earth, have provided a fairly comprehensive view of the physical and chemical properties of these unique compounds. The purpose of this chapter is to use this extensive knowledge to discuss the relevance of clathrate hydrates to outer Solar System processes. We first present the current state of knowledge on clathrate hydrates' molecular structures and properties. Then we discuss their stability, in order to assess the extraterrestrial environments where these compounds can occur. From these considerations, we focus on their potential role on icy environments of the Solar System, with a specific emphasis on storage and outgassing.

## 12.2 Chemical Physics of Clathrate Hydrates

The molecular duality (or more in the case of gas mixtures) of clathrate hydrates and their intrinsic non-stoichiometry are certainly responsible for their very special physical and chemical properties. Indeed, the two types of chemical bonds that make the clathrate hydrate structure are: (1) hydrogen bonds, which sustain the icy skeleton and are known for driving the unique properties of the water molecule; and (2) van der Waals interactions, which are the repulsive interactions between the trapped

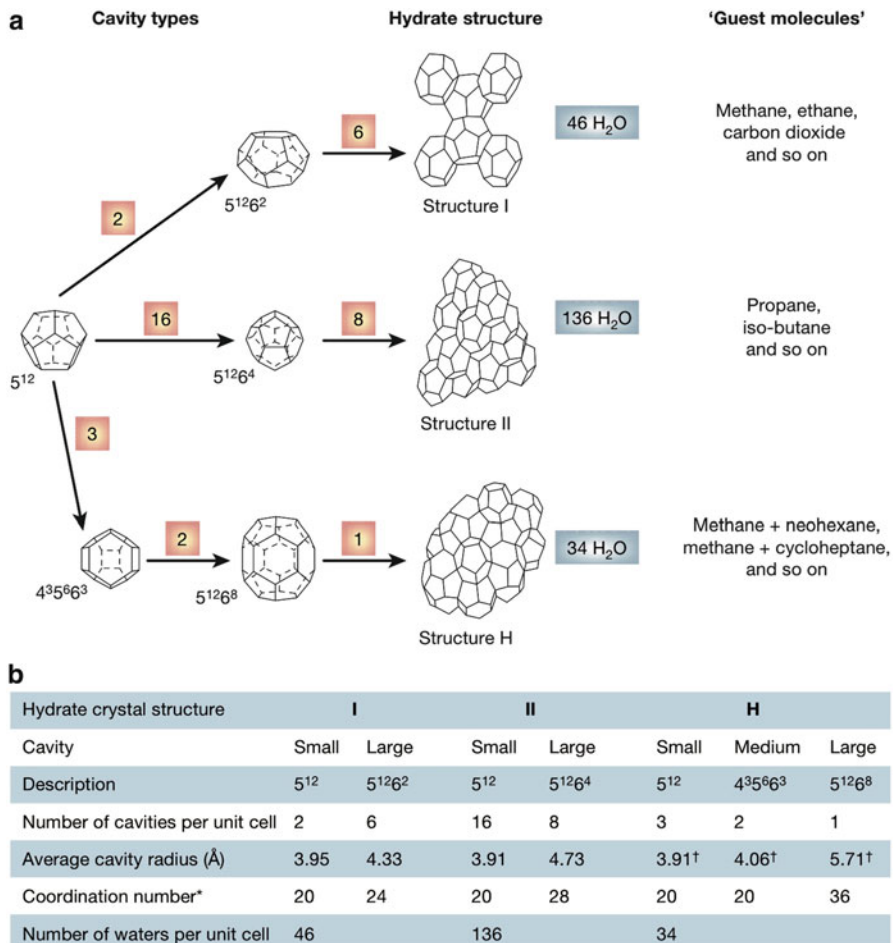
gas molecule(s) and the skeleton, needed to sustain the cage structure. Because the mere existence of this crystalline structure relies on these complex interactions, it should come as no surprise that the properties of clathrate hydrates are strongly dependent on pressure, temperature, and nature of the guest gas molecule(s).

### 12.2.1 Molecular Structure

As crystalline materials, clathrate hydrates consist of a periodic and three-dimensional stacking of unit cells. Unlike other crystalline compounds, the clathrate hydrate unit cell is itself an aggregate of hydrogen-bonded H<sub>2</sub>O molecules forming cavities (or cages) that are stabilized by the presence of the guest gas. Therefore, the unit cell configuration depends on the arrangement of cages within, and the structure of these cages. Five different types of cavities may exist in clathrate hydrates, which are referred to as  $x^y$ , with  $y$  the number of faces per cavity, each  $y$  face having  $x$  sides (e.g., Sloan and Koh 2007, and therein). The types of cages are: pentagonal dodecahedron ( $5^{12}$ ), tetrakaidecahedron ( $5^{12}6^2$ ), hexakaidecahedron ( $5^{12}6^4$ ), irregular dodecahedron ( $4^35^66^3$ ), and icosahedron ( $5^{12}6^8$ ). Three molecular structures of clathrate hydrates exist at near-ambient conditions: two cubic structures that are named structure I (hereafter CS-I) and structure II (CS-II), and a hexagonal structure (SH). They all consist of a specific arrangement of cages, most cage types being specific to one structure with the exception of the  $5^{12}$ , common to all structures. Figure 12.1 shows the cavity types and their arrangement in each clathrate hydrate structure; it gives some examples of molecules forming one structural type or another, and provides some quantitative crystallographic information (cavity number per unit cell, cavity radii, coordination, hydration).

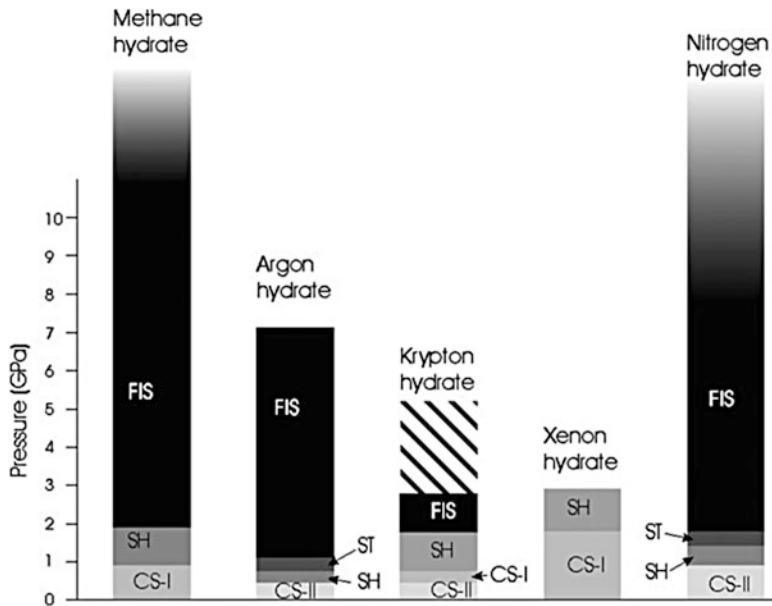
Figure 12.1 and the text above refer to clathrate hydrate structures that have been described at moderate pressures, i.e. below 500 MPa. However, pressure has a dramatic effect on the structure of clathrate hydrates: as the structure is being compressed, the decrease in radius of the cages makes the structure unstable, and triggers phase transitions to other hydrate structures. Pressures on the order of 0.1–100 GPa can be attained within optical sapphire-anvil or diamond-anvil cells, and with multi-anvil or Paris-Edinburgh presses in the low end of the range (<30 GPa). At high-pressure conditions, the techniques preferably used for crystallographic measurements are neutron diffraction, X-Ray diffraction, and Raman spectroscopy (although Raman does not provide unit cell characteristics, but gives information on vibrational energies of molecular bonds, i.e. bond length). Studies on the phase behavior and structure of clathrate hydrates up to pressures above 1 GPa have mostly taken place over the past decade. They have brought significant information on phase transitions and structural evolution of clathrate hydrates under pressure.

Figure 12.2 shows the structural transitions that take place upon compression of several clathrate hydrates. Specifically, high-pressure studies (Loveday et al. 2001a, b;



**Fig. 12.1** The three common clathrate hydrate crystal unit cell structures and their properties. (a) Cage structures, spatial arrangements, and guest examples for the unit cells. (b) Crystallographic characteristics of the clathrate hydrate structures CS-I, CS-II, and SH (Reproduced with permission from Sloan (2003))

Hirai et al. 2001, 2003; Shimizu et al. 2002; Kumazaki et al. 2004; Machida et al. 2006; Choukroun et al. 2007) have demonstrated the transformation from CS-I methane clathrate to a structure of unit-cell similar to SH around 1 GPa, and then to a structure referred to as “filled-ice” (FIS) above 2 GPa (Loveday et al 2001b). In the filled-ice structure, the water molecules are organized in sheets as in ice Ih (hexagonal ice I, the atmospheric pressure form of water ice), and the methane molecules occupy the voids between the sheets. The filled-ice structure of methane clathrate hydrates is stable up to 86 GPa, at least (Machida et al. 2006). Another clathrate hydrate structure has been observed upon compression of CS-II clathrate hydrates (e.g., Loveday and



**Fig. 12.2** The structural sequence adopted by the cage-forming gas hydrates that have been explored so far. The notations CS-I, CS-II, SH, ST, FIS, are explained in the text (Reproduced with permission from Loveday and Nelmes (2008))

Nelmes 2008, and therein), which, after transition via a CS-I or a SH stage, form a tetragonal structure (ST). This ST structure is the only clathrate hydrate structure that contains a single type of cages, which is an irregular tetrakaidecahedron with two tetragonal and four hexagonal faces ( $4^25^86^4$ ). Whichever clathrate hydrate guest gas is considered, it seems that the final stage of compression results in the formation of a filled-ice structure. For some species such as CO<sub>2</sub> the destabilization of the clathrate structure under pressure has been suggested (Manakov et al. 2009), however no consensus has been reached on this matter. Raman spectroscopic analyses within a sapphire-anvil cell by Choukroun (2007), and recent X-Ray diffraction measurements within a diamond-anvil cell by Hirai et al. (2010), instead suggest the existence of a phase transition to a high-pressure structure around 700–1,000 MPa. Yet, this high-pressure phase decomposes into solid CO<sub>2</sub> and ice VI above ~ 1.5 GPa. Further studies are needed to better understand the formation of filled-ice structure versus apparent decomposition.

### 12.2.2 Thermophysical Properties: Comparison with Water Ice

The unique crystalline structure of clathrate hydrates drives very peculiar properties. Indeed, on one hand the hydrogen-bonded H<sub>2</sub>O skeleton strongly resembles the ice Ih structure despite its cage-like organization. Furthermore, spectroscopic techniques (Raman, Infrared) show that the frequencies of vibrational modes of

O–O and O–H bonds within the clathrate hydrate structure are identical to those of ice *Ih* (e.g., Nakano et al. 1998; Choukroun et al. 2007; Dartois and Deboffle 2008; Dartois and Schmitt 2009). On the other hand, the presence of guest gases dramatically influences the possible molecular interactions and their intensities, which consequently affect the thermo–physical properties. Table 12.1 compares some properties of water ice and clathrate hydrates. These data indicate that clathrate hydrates of different structures have similar properties, despite some variability related to the guest gas composition, which may differ significantly from water ice.

The thermal conductivity of clathrate hydrates has been the subject of intensive laboratory experiments because of the dependence of this property on clathrate hydrate structure, guest gas, cage occupancy, pressure, and temperature (Ross et al. 1981; Ross and Andersson 1982; Cook and Leaist 1983; Handa and Cook 1987; Tse and White 1988). From a physical point of view, the temperature dependence of clathrate hydrates is extremely interesting because it shows a glass-like behavior, while these materials are crystalline. Later studies (Tse and White 1988; Tse et al. 1997; English and Tse 2010) suggest that the glass-like behavior is related to the rattling motion of the guest gas above 100 K, and show that the conductivity increases with decreasing temperature under 100 K, as expected from crystalline materials. On average, the thermal conductivity of clathrate hydrates is of 0.4–0.7  $\text{W} \cdot \text{m}^{-1} \cdot \text{K}^{-1}$  at pressures lower than 100 MPa and temperatures from 100 to 270 K. Experiments conducted on tetrahydrofuran (THF) clathrates to greater pressures up to 1.5 GPa yielded values up to 1.5  $\text{W} \cdot \text{m}^{-1} \cdot \text{K}^{-1}$  (Ross and Andersson 1982). However, these authors do not specify if THF clathrates undergo any phase transition in the high-pressure domain. THF clathrates are among the most extensively studied because they are very easy to synthesize, and the THF molecule only enters the large cages of the structure II. But THF clathrate hydrates have never been observed in nature, and their unusual cage occupancy relatively to clathrate species that may be expected in Solar System environments raises the issue of the relevance of their thermophysical properties. It seems thus appropriate to restrict the range of thermal conductivities applicable to planetary clathrate hydrates to the 0.4–0.7  $\text{W} \cdot \text{m}^{-1} \cdot \text{K}^{-1}$  reported above, until new studies provide further constraints.

The mechanical behavior of clathrate hydrates is very peculiar, compared to water ice. Despite elastic properties that are allegedly similar, the flow properties of clathrates have been the subject of few recent studies (Stern et al. 1996; Durham et al. 2003a, b, 2005). The first report on flow properties of clathrate hydrates (Stern et al. 1996) suggested an ice-like flow behavior. Further mechanical experiments conducted under high differential stress with a sustained gas pressure within the samples (Durham et al. 2003a, b, 2005), have demonstrated that: (1) the initial results were likely due to significant dissociation (up to 30%) within the samples; (2) methane clathrate hydrates and other gas hydrates exhibit a much greater strength than water ice, i.e. achieving a given strain rate requires applying a stress 10–30 times greater for clathrates than for water ice. The large difference in strength has been attributed to the slower diffusion time of  $\text{H}_2\text{O}$  in the clathrate hydrate lattice, see Table 12.1, which would thus restrict the flow rate (Durham et al. 2003b). More recently, it has been suggested (Lenferink et al. 2009) that

**Table 12.1** Comparison of some physical properties of water ice with clathrate hydrate structures I (CS-I) and II (CS-II). All values from<sup>a</sup> (Modified after Sloan and Koh (2007))

Property	H <sub>2</sub> O ice Ih	Structure I	Structure II
Structure and dynamics			
Lattice parameters at 273 K (Å)	a = 4.52, c = 7.36	12.0	17.3
Dielectric constant at 273 K	94	~58	~58
H <sub>2</sub> O reorientation time (μs)	21	~10	~10
H <sub>2</sub> O diffusion jump time (μs)	2.7	>200	>200
Elastic properties			
Young's modulus at 268 K (GPa)	8–9.5	~8.5 <sup>est</sup>	~8.5 <sup>est</sup>
Poisson's ratio	0.3301	0.31403	0.31119
Thermal properties			
Linear thermal expansion at 200 K ( $10^{-6}\text{ K}^{-1}$ )	56	77	52
Thermal conductivity at 263 K ( $\text{W.m}^{-1}.\text{K}^{-1}$ )	2.18	0.51	0.50
Heat capacity within 250–270 K ( $\text{J.kg}^{-1}.\text{K}^{-1}$ )	1,900 (250 K)–2, 100 (270 K)	2080	2130 +/- 40

<sup>a</sup>Davidson (1983), Davidson et al. (1986), Ripmeester et al. (1994)

concentrations of water ice as low as 10–15% within clathrate samples may also yield an ice-like flow behavior. However, all mechanical tests reported on clathrate hydrates have been conducted under differential stresses of several to tens of MPa, which are 2–3 orders of magnitude greater than the stresses expected on planetary bodies. This is of importance, as the flow regime at such conditions is likely dominated by dislocation creep, whereas grain-boundary sliding, basal slip, or volume-diffusion creep may be more relevant to planetary deformation scales (e.g., Durham et al. 2010, and references therein). Preliminary experimental data on the mechanical properties of clathrate hydrates have been obtained at stresses lower than 0.5 MPa (Choukroun et al. 2010b) and suggested a similar flow behavior as water ice in the grain-boundary sliding regime. Further experimental work is needed to understand the mechanical behavior of clathrate hydrates under low stress conditions, particularly in ice-bearing clathrates, to truly assert the behavior of a solid mixture.

Density values of clathrate hydrates have been voluntarily omitted from Table 12.1, due to the extreme variability of this physical parameter (e.g., Sloan and Koh 2007, and therein). Indeed, a clathrate density at given (P,T) conditions depends primarily on the nature, hence the density, of the guest gas(es) trapped, and on the degree of filling of the cages. As a result, the density of clathrate hydrates of planetary relevance at standard conditions ranges from ~900 kg.m<sup>-3</sup> (CH<sub>4</sub>) to ~1,800 kg.m<sup>-3</sup> (Xe). Methane clathrate hydrate is the only clathrate compound less dense than water ice. N<sub>2</sub> and CO<sub>2</sub> clathrate hydrates have densities close to pure liquid water, on the order of 950–1,000 to 1,100–1,150 kg.m<sup>-3</sup> (at pressures lower than 100 MPa), respectively, depending on the degree of filling of the cages. Most other clathrate hydrate species are denser than pure liquid water, at first

order. Considering that the abundances in hydrate-forming molecules in the Solar System are suitable for the presence of clathrates with a composition dominated by CH<sub>4</sub>, CO/CO<sub>2</sub>, and N<sub>2</sub> (plus potentially H<sub>2</sub>S), the bulk density of these compounds would *a priori* yield positive buoyancy from high-pressure ices and silicates, at least in the range 0–600 MPa within which no phase transitions have been reported. Little data are available on the density of high-pressure phases of clathrate hydrates, however high-pressure experiments yield specific volume variations upon compression of methane clathrates (e.g., Loveday et al. 2001a; Hirai et al. 2001). These experiments show that, along isothermal compression to 2 GPa, the density of methane clathrate increases only by ~10–15%. This variation is much lower than for water ice because of the numerous phases (4 phases in the 0–1 GPa range, e.g., Bridgman 1912; Choukroun and Grasset 2010, and therein) and significant jumps in density, which result in a variation of ~35% in density from 0 to 2 GPa (e.g., Fortes and Choukroun 2010, and therein). This comparison shows a much lower compressibility for clathrate hydrates, and suggests that the density contrast persists to higher pressures. Furthermore, the abrupt increases in density upon phase transition of water ice suggests that clathrate hydrates slightly denser (a few percents, e.g. N<sub>2</sub>) than ice Ih at low pressure could become less dense at high pressure than the polymorphs ice V and ice VI.

In summary, clathrate hydrates do share some physical properties with water ice. But the differences in thermal conductivity, mechanical behavior, and density are large and may play a crucial role in geologic processes of icy bodies of the Solar System. Furthermore, the guest gas composition of clathrate hydrates can affect these properties to the extent of inverting the density difference between clathrate hydrates and water ice/liquid water. This variability in clathrate hydrate physical properties relatively to water ice is rich in planetary implications, which are discussed further in Sect. 12.5.

## 12.3 Stability of Clathrate Hydrates

Three main factors influence the stability of clathrate hydrates: (1) the nature and the partial pressure of the guest gas; (2) the possible mixture of two or more gas molecules as guests; and (3) the presence of compounds that affect the stability of hydrogen bonds, such as ammonia, salts, and alcohols (methanol, ethanol, etc.). Due to these complex, superimposed factors, addressing the stability of clathrate hydrates in a given environment is a delicate endeavor. Extensive experimental literature is available on the stability of clathrate hydrates; most of it can be found in Sloan and Koh (2007) for hydrocarbons, N<sub>2</sub>, and CO<sub>2</sub> clathrates. Here we focus on clathrate hydrates of gas molecules relevant to planetary environments, including noble gases.

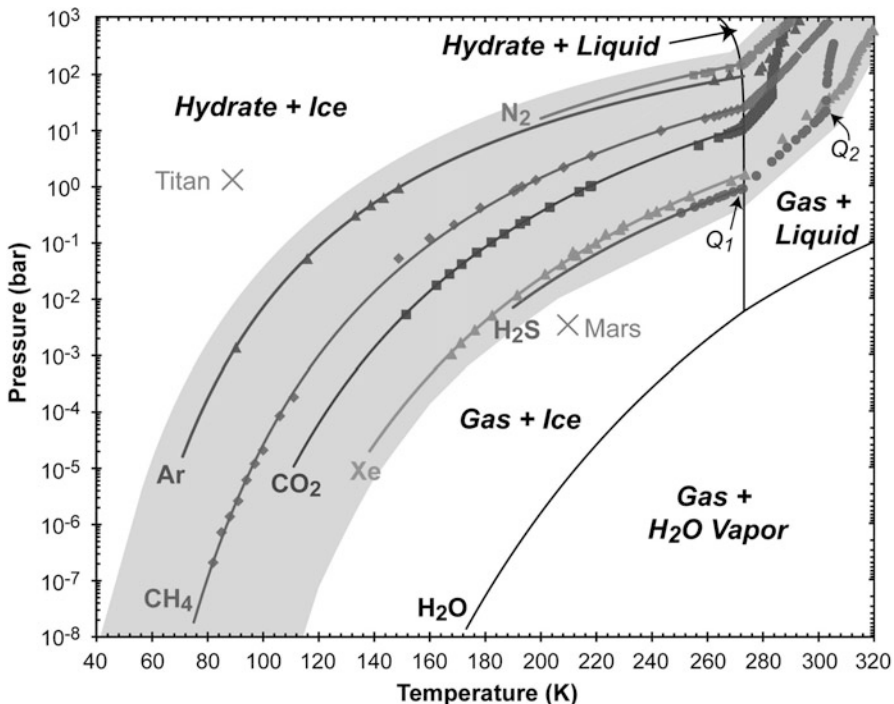


**Fig. 12.3** Pressure-temperature plot comparing the phase diagram of  $H_2O$  (black lines) with the stability curves of some major, single-guest, clathrate hydrate species.  $Q_1$ : quadruple point clathrate –  $H_2O$  ice –  $H_2O$  liquid – guest gas.  $Q_2$  ( $CO_2$ ,  $H_2S$ ): quadruple point clathrate –  $H_2O$  liquid – guest gas – guest liquid. The shaded area, which includes all the dissociation curves, separates the domains of stability and instability of clathrate hydrates in general

### 12.3.1 Experimental Data

The phase diagram of clathrate hydrates is complex, as compared with the phase diagram of  $H_2O$  shown in Fig. 12.3. Experimental data have been taken from: Roberts et al. (1940,  $CH_4$ ), Deaton and Frost (1946,  $CH_4$  and  $CO_2$ ), Kobayashi and Katz (1949,  $CH_4$ ), Unruh and Katz (1949,  $CO_2$ ), Selleck et al. (1952,  $H_2S$ ), Larson (1955,  $CO_2$ ), van Cleef and Diepen (1960,  $N_2$ ), McLeod and Campbell (1961,  $CH_4$ ), Jhaveri and Robinson (1965,  $N_2$  and  $CH_4$ ), Takenouchi and Kennedy (1965,  $CO_2$ ), Barrer and Edge (1967,  $Ar$  and  $Xe$ ), Delsemme and Wenger (1970,  $CH_4$ ) Galloway et al. (1970,  $CH_4$ ), Miller and Smythe (1970,  $CO_2$ ), Adamson and Jones (1971,  $CO_2$ ), Robinson and Mehta (1971,  $CO_2$ ), Verma (1974,  $CH_4$ ), Falabella (1975,  $CH_4$  and  $CO_2$ ), de Roo et al. (1983,  $CH_4$ ), Ng and Robinson (1985,  $CO_2$ ), Schmitt (1986,  $CO_2$ ), Thakore and Holder (1987,  $CH_4$ ), Adisasmito et al. (1991,  $CH_4$  and  $CO_2$ ), Makogon and Sloan (1994,  $CH_4$ ), Makogon et al. (1996,  $Xe$ ), Dyadin et al. (1997a,  $Ar$ ), Dyadin et al. (1997b,  $CH_4$ ), Dyadin et al. (1999b,  $Ar$  and  $Xe$ ),

Kuhs et al. (2000, N<sub>2</sub>), Mohammadi and Richon (2008, CO<sub>2</sub>), Yasuda and Ohmura (2008, CH<sub>4</sub> and CO<sub>2</sub>), Fray et al. (2010, CH<sub>4</sub>, CO<sub>2</sub>, and Xe), Mohammadi and Richon (2010, CH<sub>4</sub>). Recent data have been obtained on the CO clathrate hydrate – liquid water – gas equilibrium in the ranges 274.5–284.9 K and 13–40 MPa (Mohammadi et al. 2005), but are not shown in this figure for legibility. These results show that, in that range, the CO clathrate dissociation curve is roughly parallel to that of N<sub>2</sub>, shifted by 3 MPa to lower pressures.

Several equilibria, which correspond to different sections of the dissociation curve, involve clathrate hydrates: clathrate – ice Ih – guest gas, at temperatures and pressures lower than the first quadruple point  $Q_1$ ; clathrate – liquid water – guest gas between the quadruple points  $Q_1$  and  $Q_2$ ; clathrate – liquid water – liquid guest above  $Q_2$ . Other equilibria may exist (clathrate – liquid water – solid guest; clathrate – high-pressure ice polymorph – solid guest), although they are poorly documented so far. Overall, clathrate hydrates exhibit a very similar shape in their dissociation curves. Most dissociation curves of clathrate hydrate species are within a “band,” ~80 K wide, represented by the shaded area in Fig. 12.3. Therefore, a general clathrate hydrate stability domain can be distinguished, on the higher pressure – lower temperature side of the dissociation curve shown on Fig. 12.3. At these conditions, one should expect clathrate hydrates to be present. At higher temperatures and/or lower pressures, some clathrate hydrates may exist, depending on the guest gas(es), their partial pressure(s), and the presence of potential compounds that would decrease their stability, like salts, alcohols, ammonia, etc. The low-pressure side of Fig. 12.3 is of relevance to the presolar nebula condensation processes, which are discussed in Sect. 12.4.

Figure 12.3 does not show any experimental data on the stability of clathrate hydrates in multiple-guest systems. Extensive datasets do exist on hydrocarbon mixtures (e.g., Sloan and Koh 2007, and therein). The stability of mixed CH<sub>4</sub>–N<sub>2</sub> clathrate hydrates is also well constrained (Jhaveri and Robinson 1965). More recently, investigation of thermodynamic equilibria in the CO<sub>2</sub>–N<sub>2</sub>–H<sub>2</sub>O system have been conducted, to assess the potential of hydrates as storage medium to reduce industrial CO<sub>2</sub> emissions (e.g., Deschamps and Dalmazzone 2009; Chazallon 2010). All studies on mixed clathrate hydrates have shown that the clathrate hydrate in equilibrium with a multi-gas mixture may not contain the same fractions of gases as the original mixture, which implies that the stability of the mixed hydrate depends not only on the partial pressures of the gases, but also on their “affinity” for the clathrate hydrate structure. This is of particular importance for modeling the behavior of mixed hydrate systems, and one can use the example of the N<sub>2</sub>–CH<sub>4</sub> system: a clathrate hydrate in equilibrium with a 1:1 N<sub>2</sub>:CH<sub>4</sub> mixture has a dissociation curve that is only 3–4 K lower than the pure CH<sub>4</sub> clathrate dissociation curve at pressures above  $Q_1$  (Jhaveri and Robinson 1965). This implies that gas fugacities, not partial pressures, are equal in the liquid (or ice) and the clathrate phases at equilibrium; this fugacities equality provides a general method for predicting phase equilibria in complex systems, see Sect. 12.3.2.

Figure 12.4 shows the phase behavior of clathrate hydrates over a wide pressure range, compared to the phase diagram of H<sub>2</sub>O. Five stable ice polymorphs exist in

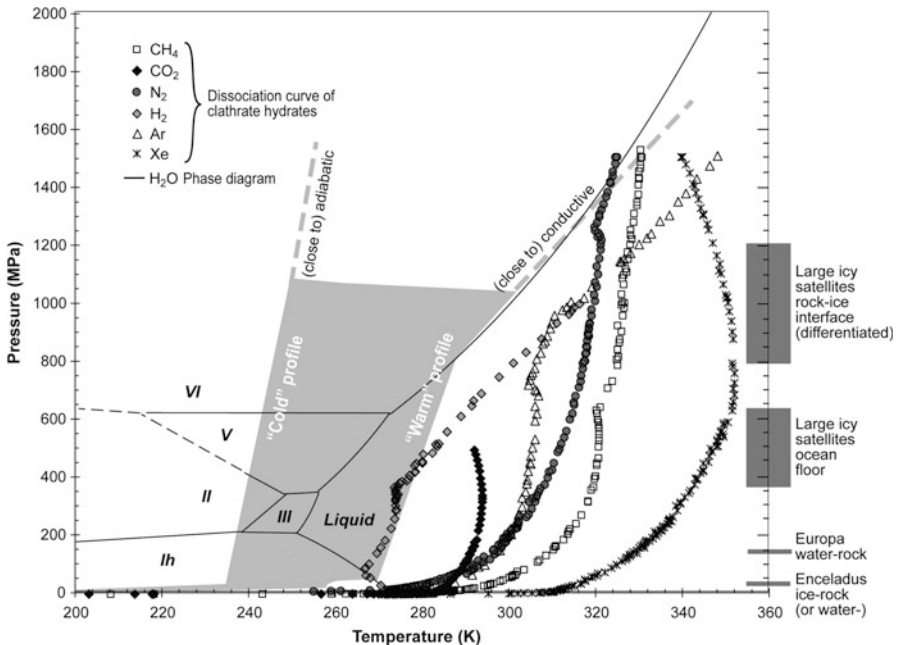


**Fig. 12.4** Comparison of the phase diagram of H<sub>2</sub>O, the stability curves of some clathrate hydrates, and two types of thermal profiles within icy satellites of the giant planets (Modified after Sohl et al. (2010))

this pressure–temperature range: ices Ih, II, III, V, and VI (Bridgman 1912). The dissociation data are shown for clathrate hydrates of CH<sub>4</sub>, CO<sub>2</sub>, N<sub>2</sub>, Ar, Xe, and H<sub>2</sub>, to represent the most and the least stable species. These data originate from: Roberts et al. (1940, CH<sub>4</sub>), Deaton and Frost (1946, CH<sub>4</sub> and CO<sub>2</sub>), Kobayashi and Katz (1949, CH<sub>4</sub>), Unruh and Katz (1949, CO<sub>2</sub>), Larson (1955, CO<sub>2</sub>), van Cleef and Diepen (1960, N<sub>2</sub>), McLeod and Campbell (1961, CH<sub>4</sub>), Marshall et al. (1964, N<sub>2</sub>), Jhaveri and Robinson (1965, N<sub>2</sub> and CH<sub>4</sub>), Takenouchi and Kennedy (1965, CO<sub>2</sub>), Galloway et al. (1970, CH<sub>4</sub>), Robinson and Mehta (1971, CO<sub>2</sub>), Verma (1974, CH<sub>4</sub>), Falabella (1975, CH<sub>4</sub> and CO<sub>2</sub>), de Roo et al. (1983, CH<sub>4</sub>), Ng and Robinson (1985, CO<sub>2</sub>), Thakore and Holder (1987, CH<sub>4</sub>), Adisasmito et al. (1991, CH<sub>4</sub> and CO<sub>2</sub>), Makogon and Sloan (1994, CH<sub>4</sub>), Dyadin et al. (1997a, Ar), Dyadin et al. (1997b, CH<sub>4</sub>), Nakano et al. (1998, CO<sub>2</sub>), Dyadin et al. (1999a, H<sub>2</sub>), Dyadin et al. (1999b, Ar and Xe), Kuhs et al. (2000, N<sub>2</sub>), Dyadin et al. (2001, N<sub>2</sub>).

The purpose of Figs. 12.3 and 12.4 is to show the variability in stability domains of pure clathrate hydrate species. We did not show the H<sub>2</sub> clathrate data on Fig. 12.3, for this species diffuses through the clathrate lattice at low pressures and can only be trapped in the cages above 100 MPa (Dyadin et al. 1999a). The phase transitions under pressure are also not shown in Fig. 12.4 for clarity, but they can be seen via inflections in the dissociation curves, and the pressures at which they occur are indicated in Fig. 12.2.

In Fig. 12.4, the shaded area represents the range of thermal profiles that may be expected within icy objects of the Solar System, as well as the pressures of some major interfaces in icy moons. These thermal profiles (Sohl et al. 2010), compared to the stability curves of clathrate hydrate species, suggest that most of these compounds are stable at depth in planetary objects, from a thermodynamic standpoint, in environmental conditions that include large amounts of water and gas, and low temperatures. On Fig. 12.3, the pressure–temperature conditions of Titan (Saturn’s largest satellite) and Mars surfaces are indicated, to demonstrate the likely stability of clathrate hydrates right on Titan’s surface, as an exception compared to other places such as Mars or Earth, where a depth of a few tens to hundreds of meters needs to be reached for clathrates to be stable. Notably, on Titan clathrate hydrates are stable from the surface, see Fig. 12.3, to the deepest interior (Choukroun et al. 2010a). Planetary implications of the thermal profiles and potential clathrate stability are evoked in Sohl et al. (2010), and discussed further in the present manuscript.

### 12.3.2 Thermodynamic Modeling of the Stability

A simple approach in modeling the phase diagram of clathrate hydrates consists of representing clathrate stability conditions by fitting experimental data with empirical functions. A commonly used expression is the August equation, a simplified version of the Antoine equation (Antoine 1888):

$$\log P_d = A + \frac{B}{T_d}$$

where  $P_d$  is the decomposition pressure of the clathrate as a function of temperature (see Sloan and Koh 2007, for a compilation of data). This kind of empirical function usually works on moderate pressure ranges. When phase transitions occur, different empirical laws and different sets of parameters must be used in order to describe the dissociation temperature on both sides of the transitions. For instance, above or below quadruple points, the parameters, A and B, are different (e.g., Sloan and Koh 2007, and therein). This equation, with parameters taken from Hersant et al. (2008), has been used to draw the dissociation curves of clathrate hydrates in Fig. 12.3.

The stability curves experimentally derived for single gas compound can also be used to approximate the stability curve of a mixed gas hydrate at first order, by assuming that clathrate hydrate behaves as an ideally dilute solution and that the ratio of occupancies for the small and large cages is constant and same for all guest molecules (e.g., Miller 1974; Lipenkov and Istomin 2001; McKay et al. 2003; Kieffer et al. 2006). The stability relations between gases dissolved in liquid water and clathrate, can be predicted from the dissociation pressure of the mixture,  $P_{d,mix}$ , using the simple following relationship:

$$P_{d,mix} = \left[ \sum \frac{y_i}{P_{d,i}} \right]^{-1}$$

where  $P_{d,i}$  is the dissociation pressure of each gas  $i$  contained in the mixture, and  $y_i$  is the mole fraction of each gas with respect to the total available gases. It is also possible from this simple approach to predict the relative partitioning of any two gas species within the clathrate from the dissociation pressure of each of these two gas species and their fugacity:

$$\frac{X_i \cdot P_{d,i}}{X_j \cdot P_{d,j}} = \frac{f_i}{f_j}$$

where  $X_i$  and  $X_j$  are the mole fraction of gases  $i$  and  $j$  in the clathrate, and  $f_i$  and  $f_j$  are the fugacities of the gases. For clathrates formed from a mixture of more than two species, this formula can also be applied as long as one of the gas species is dominant compared to the other gas species, i.e. as long as the ideal dilute solution theory applies. For clathrate-gas-ice equilibrium, the fugacity of the gas is equal to its partial pressure. For clathrate-gas-water, it is related to its fugacity in its pure phase or to its concentration in liquid water. At equilibrium, if there is sufficient amount of gas  $i$  in the system, its fugacity is equal to its equivalent fugacity in its pure phase. A variety of models have been proposed in the literature in order to describe the fugacity coefficients of pure phases at reference conditions and their extrapolation to a wide range of pressures and temperatures (see, for instance, Sloan 1998; Duan and Hu 2004). According to Henry's law, at equilibrium conditions the fugacity of a gas above a solution is proportional to the mole fraction of the gas dissolved in the liquid phase. If there is not a sufficient amount of gas in the system, the fugacity of the gas is smaller than its value in pure phase and can be estimated from its concentration in the liquid phase from Henry's law constant.

The simplified approach described above provides a reasonable approximation for multi-guest systems, but it is not able to describe the complexity of possible interactions between the different guest molecules. For instance, gas molecules do not enter the small and large cages with the same probability. A more rigorous thermodynamic description is required if one wants to properly describe the cage occupancy and its effects on the clathrate structure stability. Moreover, the effect of inhibitors cannot be properly included in the simplified approach. The statistical thermodynamic approach initially proposed by van der Waals and Platteeuw (1959) is able to include these different processes. This thermodynamic approach has been applied to a variety of problems in the Solar System: for instance to constrain the trapping mechanism of volatiles in the solar nebula (e.g., Lunine and Stevenson 1985; Iro et al. 2003), to determine the role of clathration on the composition of the atmosphere of Mars (e.g., Musselwhite and Lunine 1995) and Titan (e.g., Lunine and Stevenson 1985; Osegovic and Max 2005; Thomas et al. 2007).

In the statistical thermodynamic approach, the formation (or dissociation) of clathrate hydrates is represented by a thermodynamic equilibrium between three phases: the pure  $\text{H}_2\text{O}$  phase (liquid or solid), the vapor phase, and the clathrate phase. The vapor phase may consist of a mixture of gas molecules and the aqueous solution may contain several electrolytes besides dissolved gases. At equilibrium, the chemical potential of each component,  $\mu_i$ , must be equal for every phase in which that component is present. For clathrate modeling, only the chemical

potential of H<sub>2</sub>O in the different phases is considered. Assuming that the clathrate behaves as an ideally dilute solution, the chemical potential of H<sub>2</sub>O in the clathrate phase is equal to the chemical potential of a hypothetical empty clathrate reduced by the effect of cage occupancy by the guest molecules.

The fraction of cage occupancy by a guest molecule is determined by the Langmuir constant, which describes the strength of the molecule interaction with the clathrate cavity. At first order, the interaction can be described with a spherically symmetrical cell potential, depending on the coordination number of the cavity (number of oxygen atoms at the periphery of each cavity), the cavity radius, and two parameters depending on the guest molecule type, termed Kihara parameters. This first-order description neglects the possible distortion of the cavity induced by the guest molecule, and assumes single occupancy of the cavity. The Kihara parameters describing interactions between H<sub>2</sub>O and gas molecules in the clathrate structure is usually obtained from computations using the least-square criterion on minimizing the divergence between experimental and calculated dissociation pressure of clathrates (e.g., Bakker et al. 1996).

The chemical potential of pure H<sub>2</sub>O in liquid or solid phases as well as in a hypothetical empty clathrate phase can be determined from the enthalpy, entropy, molar volume, and heat capacity in each phase. All these quantities can be experimentally derived, and they depend on temperature and pressure. Moreover, in the case of aqueous solutions, the chemical potential in liquid phase must be corrected from the reduced activity of water due to the presence of dissolved gases, and also due to the presence of electrolytes- if any. The incorporation of solutes usually results in a reduction of the dissociation temperature relative to the temperature in the pure water system (e.g. Dickens and Quinby-Hunt 1997). From fitted Kihara potential parameters and from macroscopic thermodynamic parameters (enthalpy, entropy, capacity), it is thus possible to predict the structure of the formed clathrate, the formation (or dissociation) conditions of clathrate for various gas mixture compositions in equilibrium with water ice or aqueous solution, as well as the fraction of each gas component in large and small cages.

Figure 12.5 shows as an example the calculated curves for clathrate hydrates of several pure gas compounds (CO<sub>2</sub>, CH<sub>4</sub>, C<sub>2</sub>H<sub>4</sub>, C<sub>2</sub>H<sub>6</sub>, H<sub>2</sub>S, N<sub>2</sub>, and CO), and of a gas mixture corresponding to the composition of Enceladus' plumes as inferred by Waite et al. (2009). As the mass 28 in Enceladus' plumes is still unconstrained, solutions with different gas compound for mass 28 (C<sub>2</sub>H<sub>4</sub>, N<sub>2</sub>, CO) are considered. We can note that there is a very good agreement between the simplified approach and the full thermodynamic approach, whatever the considered composition. The stability curve of the mixture is mainly determined by the stability curve of CO<sub>2</sub>, and is shifted toward C<sub>2</sub>H<sub>4</sub>, or N<sub>2</sub>-CO, depending on the considered molecule for mass 28.

In summary, the clathrate hydrate research community now benefits from numerous experimental datasets and phase equilibrium calculation models (with various levels of complexity), which provide a very reasonable framework to estimate reliably the stability of clathrate hydrates, pure or mixed, at conditions from low to high temperatures, and over the pressure range  $\sim 10^2$  Pa to  $\sim 1$  GPa. Further developments are necessary to extend the applicable range of conditions to ultra-high vacuum (i.e., presolar nebula) and to the high-pressure phases of clathrate hydrates (which start to

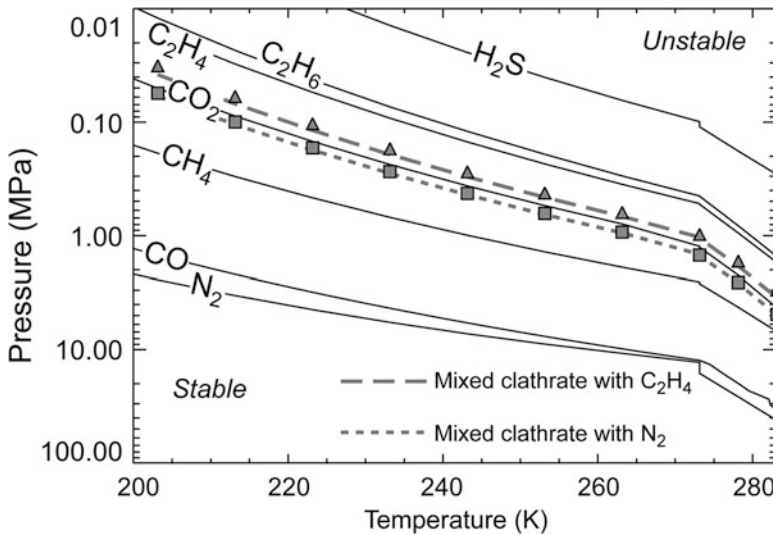


**Fig. 12.5** Stability curves for clathrate hydrates of pure gas compounds ( $\text{CO}_2$ ,  $\text{CH}_4$ ,  $\text{H}_2\text{S}$ ,  $\text{C}_2\text{H}_6$ ,  $\text{C}_2\text{H}_4$ ,  $\text{N}_2$  and  $\text{CO}$ ) and of a mixture of gas corresponding to the composition of Enceladus' plumes as inferred by Waite et al. (2009). The stability curves have been obtained with the CSMHYD software (Sloan 1998), except for the curve of  $\text{CO}$ , which is determined from the August equation provided by Hersant et al. (2004) for  $T < 273.15 \text{ K}$  and from experimental data for  $T > 273.15 \text{ K}$  (Mohammadi et al. 2005). For the gas mixture calculations, the simplified approach based on the stability curve of pure compound (Eq. 1) (dashed grey lines) and the full statistical thermodynamic approach (diamonds and squares) using the CSMHYD software (Sloan 1998) are compared. Two different solutions are shown assuming the unconstrained mass 28 in Enceladus' plumes (Waite et al. 2009) is either  $\text{C}_2\text{H}_4$  or  $\text{N}_2$ . Solutions with  $\text{CO}$  are very close to the solution with  $\text{N}_2$  and therefore it is not shown on the figure

form around GPa pressures, depending on the species, see Sect. 12.1). Another aspect of clathrate hydrate thermodynamics that requires further studies is the effect on inhibitors on the dissociation curve. So far, the effect of antifreeze agents is only described by empirical expressions, therefore experiments dedicated to measuring this inhibition by agents such as salts (although the effect of sodium chloride is fairly well known, e.g., Dickens and Quinby-Hunt 1997) and ammonia are needed to constrain the parameters (activity and fugacity coefficients) that will allow for taking these effects into account in the stability models.

## 12.4 Implications for the Early Outer Solar System

The “snow line”, which is the distance from the Sun at which water ice is stable due to sufficiently low surface temperatures under the solar flux, is located around 3.5–4 astronomical units from the Sun. This line separates the inner and the outer regions of our Solar System at present-day, and it was likely much closer to the colder Sun

in its early ages (<2 a.u. after 2 Million year of evolution, Dodson-Robinson et al. 2009). The bodies that formed beyond this line are very rich in water ice (up to 50%), as witnessed by the low densities of the satellites of the giant planets and their satellites, Kuiper Belt objects, Trans-Neptunian objects, and comets. The presence of such large amounts of H<sub>2</sub>O, throughout the history of outer Solar System objects, combined with temperatures that were once low enough for condensates of volatile compounds to form, entice the idea that clathrate hydrates may have played an active role in the formation, the thermal evolution, and the present-day structure and dynamics of these bodies.

During the condensation of the presolar nebula, three mechanisms have been proposed to explain the trapping of volatiles in planetary objects: (1) the direct condensation of the solid form from the nebular gas, (2) the trapping of gases in amorphous ice, and/or (3) the trapping of volatiles as their hydrates and clathrate hydrates. These theories have emerged from direct measurements of the composition of comets (e.g., Bockelée-Morvan et al. 2004), and of giant planets' atmospheres (e.g., Gautier et al. 1995; Atreya et al. 1999; Mahaffy et al. 2000), compared with models of nebula condensation and planet and satellite formation. For more information on that topics, we refer the reader to the review by Gautier and Hersant (2005), and more recent studies by Hersant et al. (2008) and Mousis et al. (2009).

Direct condensation of volatiles appears to be a poor contributor to the nebula condensation process, because (1) it can only occur at very cold temperatures, i.e. in the latest stages of nebula condensation, and (2) it is inconsistent with enrichments and depletions of volatile compounds in comets (e.g. Iro et al. 2003) and in the atmospheres of Jupiter and Saturn (e.g., Gautier et al. 2001) relative to their solar abundances (Anders and Grevesse 1989; Lodders 2003).

There is, however, a long-standing debate as to whether volatiles were trapped as gas-laden amorphous ice or as clathrate hydrates. The gas-laden amorphous ice model is based on several experimental studies (e.g., Bar-Nun et al. 1988; Notesco et al. 2003), which have demonstrated the great stability of gases trapped in amounts as high as 15 wt.% in a porous matrix of vapor-deposited amorphous ice. Other experimental studies (Barrer and Edge 1967; Miller and Smythe 1970; Delsemme and Wenger 1970; Falabella 1975) have also shown the stability of clathrate hydrates to very low pressure – temperature conditions (down to 10<sup>-2</sup> Pa = 10<sup>-5</sup> mtorr). Therefore, both hypotheses are plausible in the framework of the cooling presolar nebula. The major difference is that one involves co-deposition of amorphous ice and gases, while the other requires the pre-existence of crystalline ice and its conversion into a clathrate hydrate once the stability curve of given clathrate hydrate species is reached.

Models involving either clathrate hydrate formation or condensation of gas-laden amorphous ice have been proposed to explain the deficiency of N<sub>2</sub> relatively to CO in comets (Iro et al. 2003; Notesco et al. 2003), the general enrichments in volatiles in Jupiter (Gautier et al. 2001; Hersant et al. 2004) and in Saturn (Hersant et al. 2008; Mousis et al. 2009), as well as Titan's atmospheric budget measured by the Gas Chromatograph and Mass Spectrometer onboard the Huygens probe

(Niemann et al. 2005; Alibert and Mousis 2007; Owen and Niemann 2009). In the case of comets, the paradigm has historically shifted from clathrate hydrates in the nucleus (e.g., Delsemme and Swings 1952; Delsemme and Wenger 1970) to gas-laden amorphous ice (Bar-Nun et al. 1988; Notesco and Bar-Nun 2000; Notesco et al. 2003), with more recent models considering the crystallization of amorphous ice – which may have accreted as such – into clathrates because of the large amounts of gas present (Marboeuf et al. 2010).

The observation of protoplanetary disks shows that dust grains smaller than 1 mm may persist for several millions of years (e.g., Clampin et al. 2003), possibly because of intense collisions in the case of an optically thick disk (e.g., Benz 2000). Also, experimental measurements on water ice deposition and amorphous-crystalline transition by Kouchi et al. (1994) have shown that: (1) amorphous ice deposited on silicate grains within the molecular cloud from which the Sun originated likely reached temperatures high enough for recrystallization to occur, up to a distance  $\sim$ 12 a.u.; (2) throughout the presolar nebula, sublimation of ice would lead to its subsequent condensation in crystalline form as the nebula cooled down. If indeed small crystalline grains persisted for millions of years in the presolar nebula, clathrate hydrate formation could have taken place extensively (e.g., Gautier and Hersant 2005). However, the formation of gas-laden amorphous ice remains a possible alternative in cold, fast-condensing environments, like the outermost regions of the nebula where comets likely formed.

Determining which hypothesis is most likely, and/or constraining the locations and sequences within the presolar nebula, where the crystallization of clathrate hydrates or the condensation of gas-laden amorphous ice may occur, would require: (1) a better knowledge of the condensation timescales via improved models of nebula condensation and planetary formation; (2) new experimental constraints on the deposition of amorphous vs. crystalline ice as a function of temperature, at slow cooling rates applicable to the solar nebula, to complement the work by Kouchi et al. (1994); (3) further experimental data on the stability of clathrate hydrates at relevant conditions, to address the fairly large discrepancy among existing datasets and quantify the potential errors propagated upon extrapolation to presolar nebula conditions of expressions obtained at higher pressures and temperatures (Fray et al. 2010); (4) an understanding of amorphization rate of crystalline ice by cosmic rays, which would compete with the deposition rate of crystalline ice and affect its availability for conversion into clathrate hydrate; and (5) a good knowledge of the kinetics of clathrate formation by reaction of crystalline ice with low-pressure nebular gas, which would be a critical factor for assessing the likelihood and extent of clathrate hydrate formation. However, kinetic studies cannot be conducted at presolar conditions because of the timescales of reactions. Experimental data and molecular dynamics simulations do provide constraints on kinetics aspects at much higher pressures and temperatures. New experimental data are still necessary to obtain a better idea of the processes that are at play, and to determine how reliable the extrapolation down to solar nebula temperatures and pressures may be.

## 12.5 Clathrate Hydrates on Icy Satellites

Whether or not clathrate hydrates formed in the solar nebula or planetary subnebulae, and brought significant amounts of volatiles in non-solar proportions to the outer planets and their satellites and to comets, their persistence/formation in planetary environments after accretion is dependent on the initial chemical conditions and on the thermal evolution. In fact, we show in this section that the icy interiors of some giant planets' satellites likely harbor clathrate hydrates at present, whatever their origin may be.

### 12.5.1 *Contexts Suitable for Clathrate Hydrate Formation and/or Persistence*

Here we discuss the internal structure and thermal profiles within icy satellites in order to assess the environments where clathrate hydrates may be present, but the same processes are applicable to icy dwarf planets (e.g., Pluto-Charon), large Trans-Neptunian and Kuiper Belt Objects, and large icy asteroids (e.g., Ceres). The differences among these objects are the thickness of the putative icy mantle, and the presence/extent of deep liquid bodies.

Several datasets (gravity data, magnetic data, surface composition) obtained during the past *Galileo* mission at Jupiter and the ongoing *Cassini-Huygens* mission at Saturn suggest the presence of extensive liquid bodies in the interior of large icy satellites: Jupiter's Europa (e.g., Squyres et al. 1983a; Anderson et al. 1998; Khurana et al. 1998; Pappalardo et al. 1999; Spohn and Schubert 2003), Ganymede (e.g., Showman et al. 1997; Sohl et al. 2002; Spohn and Schubert 2003), Callisto (e.g., Khurana et al. 1998; Sohl et al. 2002; Spohn and Schubert 2003), and Saturn's Titan (e.g., Grasset and Sotin 1996; Grasset et al. 2000; Sohl et al. 2003; Tobie et al. 2005; Grasset and Pargamin 2005; Sotin et al. 2009, and therein; Nimmo and Bills 2010). Several models suggest a differentiated interior for Europa and Ganymede, with an icy mantle overlaying a silicate core (e.g., Anderson et al. 1996; Schubert et al. 1996; Sohl et al. 2002; Sotin and Tobie 2004). However, Callisto is probably only partially differentiated (Sohl et al. 2002; Sotin and Tobie 2004; Kuskov and Kronrod 2005), with an outer core containing a mixture of ice and silicates. Titan has a moment of inertia of 0.341, intermediate between Ganymede's and Callisto's, if hydrostatic equilibrium is assumed – which may be a debatable approximation –, and thus could be either differentiated or only partially differentiated (Sotin et al. 2009; Iess et al. 2010; Castillo-Rogez and Lunine 2010).

These large satellites, as well as the most volcanically active icy satellite, tiny Saturn's Enceladus, likely exhibit a deep-seated, water-based, liquid layer (which may not be a full layer decoupling the upper icy shell from what lies beneath it in Enceladus' case, Tobie et al. 2008). Besides being consistent with spacecraft data (see above), the existence of such internal oceans is predicted by thermal evolution models (e.g., Showman et al. 1997; Tobie et al. 2005; Moore 2006):

accretional heating, along with putative short-lived radiogenic heating, would have been sufficient to induce the melting of most of the icy fraction. Therefore, (at least some) partitioning of the H<sub>2</sub>O from the rocky component should have occurred easily owing to the low density and low viscosity of the liquid, which would have segregated as a liquid layer. Throughout the history of the icy satellite, radiogenic, tidal, and latent heat release heating, have controlled the evolution of the interior (e.g., Kirk and Stevenson 1987; Showman et al. 1997; Grasset et al. 2000; Tobie et al. 2005; Hussmann et al. 2006; Moore 2006; Grindrod et al. 2008). Many parameters are at play in this evolution: (1) the amounts of silicates and the proportion of radioactive elements (U, K, Th), which affect the heat production; (2) the amounts of anti-freeze constituents like hydrated sulfate or chloride salts and ammonia, which would generate a colder interior; (3) the cooling rate, i.e. how efficiently heat is transferred to the surface and is lost through radiation into space; (4) the extent of tidal heating within the various layers, which depends on viscosity, composition, and microstructure, among others.

Based on cosmochemical models, and reactions between hydrated phases and silicates (e.g., Zolotov and Kargel 2009, and therein), the volatile budgets within icy satellites can be predicted and incorporated in the evolution processes mentioned above. As shown in Fig. 12.4, clathrate hydrates are thermodynamically stable at depth in icy bodies, as long as pressure conditions and local gas contents (possibly dissolved in liquid) are high enough for the fugacity/activity to sustain the formation of the clathrate structure. The comparison between stability domains of clathrate hydrates and the thermal profiles within icy satellites suggests that clathrate hydrates of abundant cosmochemical gases may exist from shallow depths corresponding to pressures of ~1 MPa, up to the deepest parts of the interiors of large icy satellites. Hence, clathrate hydrates are not stable on the surface of airless bodies, and this thermodynamic fact possibly explains why clathrates have not been directly detected on planetary surfaces (besides their rather poor detectability via conventional techniques such as infrared spectroscopy, Dartois and Deboffle 2008; Dartois and Schmitt 2009). A notable exception to this statement is Titan, which is the only body in the Solar System where the atmosphere generates pressure-temperature conditions that allow clathrates to be stable right at the surface, see Fig. 12.3. The remaining of this section is dedicated to the discussion about the nature of clathrate hydrates that can be expected within icy satellites, and their implications for the geophysics of these bodies. Titan and Enceladus are the focus of separate sections because of the high relevance of clathrate hydrates to these icy moons, and the peculiar role they may play there.

### **12.5.2 Potential Influence on Internal Structure and Exchange Processes on Europa, Ganymede, and Callisto**

In the case of Europa, where the putative internal ocean may react directly with the silicate core underneath at pressures of 130–150 MPa (e.g., Khurana et al. 1998; Vance et al. 2007), the formation and/or the release of SO<sub>2</sub> and CO<sub>2</sub> that may form

$\text{CH}_4$  upon reduction by  $\text{H}_2$  produced by serpentinization probably lead to the formation of clathrate hydrates at the ocean–rock interface (Kargel et al. 2000; Prieto-Ballesteros et al. 2005). Depending on clathrate growth process, on cage occupancies, and on the composition of the liquid layer, two locations can be expected for these clathrates (see Sohl et al. 2010 for greater details). (1) If the clathrate hydrates form directly in the ocean or within a “mushy” layer at the ocean–rock interface, if they are  $\text{CH}_4$ -poor (density above  $1,050 \text{ kg.m}^{-3}$ ) and/or if the liquid layer is quite dilute in sulfate salts (density lower than  $1,100 \text{ kg.m}^{-3}$ ), they likely sink to the bottom of the liquid or remain trapped within “sediments” at the interface. (2) Conversely, if clathrate hydrates are  $\text{CH}_4$ -rich (density lower than  $\sim 1,050 \text{ kg.m}^{-3}$ ), in a dense (i.e. salty) liquid of  $1,050 \text{ kg.m}^{-3}$  and above, they would tend to float. This suggests that they may rise within the ocean all the way to the interface with the ice shell, and get entrained in the warm upwellings associated to convection with the shell (Sotin et al. 2002; Tobie et al. 2003; Barr and Pappalardo 2005). This scenario is particularly rich in astrobiological implications, as clathrate hydrates may act as the transporting agent of potential nutrients and products of biological activity, from the deep interior to the icy shell.

Similarly, the differentiation process in the early history of Ganymede and even Callisto (though it was incomplete for the latter), would have released volatiles along with the segregation of the water-rich fraction. The pressure of the high-pressure ice – rock interface is estimated to 0.8–1.2 GPa, where clathrate hydrates are extremely stable relatively to water ice, see Fig. 12.4. Volatiles may have been already trapped in clathrate hydrates if accreted as such and not destabilized as a consequence of accretional heating. Otherwise, the dissociation of clathrates at depth during accretion may also have released sufficient amounts of gas for new clathrate hydrates to form once in contact with the liquid. Whichever scenario is considered, clathrate hydrates would have segregated along with the water-rich fraction or formed within the liquid layer. Furthermore, clathrate hydrates may also have been released during the putative core overturn event (e.g., Kirk and Stevenson 1987), and remained trapped within the high pressure ices layer or transported by convective motions to the internal ocean. From there on, the same buoyancy considerations mentioned above for Europa would control the location of clathrate hydrates. With two major differences: (1) On large bodies like Ganymede, Callisto, and Titan (see Sect. 12.6), the pressures at the water–rock interface are so high that the residence time of  $\text{H}_2$  is likely large, creating a reduced environment. This environment could preclude the formation of oxidized compounds, and help the formation of aqueous solutions of lower density than liquid water, like ammonia–water. Such a context is less favorable for transport of clathrate hydrates up to the icy shell. (2) As shown in Fig. 12.2, most clathrate hydrate species are subject to a phase transition toward high-pressure structures around 0.6–1.0 GPa. It is therefore likely that clathrate hydrates initially present at these pressures relevant to large icy satellites were in those forms, which contain much less water than the low pressure phases (up to two times lower hydration number, Loveday et al., 2001a; Loveday and Nelmes 2008), and are obviously denser. This implies that the ascent of clathrates, shall it occur, during differentiation and core

overtake, is accompanied by their transition into the low-pressure structures. Such a phase transition can only happen in the presence of significant amounts of available water, and may well be kinetically and energetically limited. Furthermore, the contact of clathrate hydrates with extensive bodies of liquid water may result in their dissociation because of the necessary equilibrium of gas pressure within the clathrate with dissolved gas concentrations.

Several models suggest that volatiles are present in very large quantities (above 10% of the icy fraction of planetesimals) in the planetary subnebulae from which icy moons formed (e.g., Hersant et al. 2008; Mousis et al. 2009). It seems reasonable to consider the possibility that fugacity (and activity in the aqueous phase) of volatiles are therefore high enough to maintain favorable conditions for the formation/persistence of clathrate hydrates within these icy moons. Based on density contrast considerations and on the amounts of clathrate hydrates present, they may either form segregated layers within icy satellites, or be disseminated within layers of somewhat equivalent densities. Segregated clathrate hydrate layers may exist in the icy shell if an early dense atmosphere existed (Titan, see Sect. 12.6, Lunine et al. 1989, 2009; Tobie et al. 2009), or be located at the ice-ocean interfaces (Tobie et al. 2009). Disseminated clathrates would likely be mixed with water ice, in the outer icy shell (Europa, Enceladus, Titan) and/or within the high-pressure ice layer (Ganymede, Callisto, Titan) and the undifferentiated rock-ice mixture (Callisto).

Segregated clathrate hydrate layers, like salt hydrates layers evoked for Europa (Kargel et al. 2000; Spaun and Head 2001; Zolotov and Shock 2001; Zolotov and Kargel 2009), would have a dramatic influence on the thermal evolution of icy satellites. As such, clathrate layers would combine a much lower conductivity than water ice or liquid water (e.g., Ross et al. 1981; English and Tse 2010), with a mechanical strength about 1 order of magnitude larger than ice (Durham et al. 2003a, 2005, 2010), see Sect. 12.2.2. They would form insulating environments, not prone to initiate convective motions if one assumes that the viscosity contrast measured under large differential stresses remains valid at icy satellite conditions (which would require little variations when the deformation regimes change). Therefore, they would act as barriers against the transport of heat and matter, which would yield steeper thermal gradients and higher temperatures beneath. Over the course of thermal evolution, one may expect deep environments to release sufficient amounts of heat to destabilize these layers and trigger the release of water and gases. If this process occurs within the icy shell or at the internal ocean's interfaces, such events would initiate the release of volatiles from the interior (see the cases of Titan and Enceladus hereafter), and the dissolution of large amounts of gases within the liquid layer. Eventually, this reprocessing may also tend to disseminate water and gases within icy satellites' interior, which would form new clathrate hydrates mixed within the liquid/icy layers upon cooling.

Disseminated clathrate hydrates (as well as salts), unless present in large concentrations, would instead affect the heat transfer processes in a more passive manner. They would generate a decrease in the bulk thermal conductivity of icy layers, thereby increasing the thermal gradients across icy layers. However this effect should remain limited: a 20% concentration of clathrate hydrates within the

outer ice Ih layer would lower the thermal conductivity from ~2.5 to ~2.0 at 240 K, these values being strongly composition-, temperature-, and pressure-dependent. Across conductive layers, the presence of clathrate hydrates as impurities appears as a more thermally stable situation than segregated layers. From a mechanical point of view, the presence of clathrate hydrates and other impurities at low concentrations within the icy shell or other H<sub>2</sub>O-dominated layers is unlikely to modify significantly the response. Mechanical tests conducted on ice-clathrate mixtures under high differential stress, with clathrate concentrations as high as 70–90%, have shown a creep response similarly to pure water ice (Stern et al. 1996; Lenferink et al. 2009; Durham et al. 2010). This suggests that, in first approximation, the presence of low concentrations of clathrate hydrates disseminated within water ice layers would have a negligible impact on their mechanical response. Yet, the mechanical properties of clathrate hydrates mixed with ice are still poorly constrained, especially at the low-stress conditions of icy satellites. Experiments on the visco-elastic behavior of mixtures of ice with impurities such as clathrate hydrates and salts, as well as measurements of the attenuation properties of such mixtures, are needed to provide better constraints on the parameters used in geophysical models: elastic modulus, viscosity, dissipation factor, as a function of stress, temperature, and microstructure.

## 12.6 Titan: Replenishment of the Atmospheric Methane

### 12.6.1 *The Methane Problem*

Titan, Saturn's largest satellite (5150 km diameter), is the only known satellite bearing a 1.5-bar dense atmosphere, discovered by Kuiper (1944) via the detection of absorption features attributed to methane in its infrared spectrum. The atmosphere actually consists mostly of N<sub>2</sub> (~95%), which has no dipole moment and therefore cannot be seen at infrared wavelengths, and CH<sub>4</sub> (1.4% in the upper atmosphere, Waite et al. 2005, to ~ 5% near the surface, Niemann et al. 2005). These two compounds are involved in photochemical processes, owing to the atmosphere's interactions with the solar UV emissions, and are constantly dissociated and recombined in a complex series of nitriles, hydrocarbons, cyanides, and other organic compounds with high carbon-number (e.g., Yung et al. 1984; Coustenis et al. 2007). This photochemistry is so intense that the present amounts of atmospheric methane on Titan ( $2.8 \times 10^{17}$  kg, Niemann et al. 2005) would disappear entirely within 10–100 million years (e.g., Yung et al. 1984), which implies the existence of replenishment processes in order to sustain the presence of this compound in the atmosphere throughout Titan's history. Several possible reservoirs and mechanisms for allowing replenishment of atmospheric methane have been suggested before the first ground-based observations of Titan's surface, and prior to the arrival of the *Cassini* spacecraft and the *Huygens* probe in the

**Table 12.2** Comparison of the reservoirs and sources of methane for atmospheric replenishment on Titan foreseen before the Cassini-Huygens mission with the Cassini observations and relevant experimental work (Modified after Choukroun et al. (2010a))

Y/N	Reservoir/source	Location	Exchange	Cassini/experimental evidence	Comment
N	Global ocean/seas <sup>a,b</sup>	Surface	Evaporation	No oceans <sup>c</sup>	
N	Lakes <sup>d</sup>	Surface	Evaporation	Small lakes <sup>e</sup>	Present-day, <sup>f</sup> not sufficient
Y?	Porous regolith <sup>g</sup>	0–1 km	Compaction/Evap.	Gas release on landing <sup>h</sup>	Large porosity
Y?	Deep methane ocean <sup>i</sup>	0–2 km	Diffusion/Evap.	No relevant data	
Y?	CH <sub>4</sub> clathrate hydrates <sup>j</sup>	0–1,000 km	Cryovolcanism	Stable at depth <sup>k,l</sup> Potential cryovolcanic features <sup>m,n,o,p</sup>	Possible throughout history
N	Serpentization <sup>q</sup>	~1,000 km	CO <sub>2</sub> reduction	Outgassing of <sup>40</sup> Ar <sup>r,h</sup>	Early ages (before ~2 Gy?)
N	Comets <sup>s</sup>	Surface	Evaporation	Few impact craters at present <sup>t</sup>	Early ages (before ~1 Gy?)

<sup>a</sup>Sagan and Dermott (1982)

<sup>b</sup>Lunine et al. (1983)

<sup>c</sup>Tomasko et al. (2005)

<sup>d</sup>Flasar (1998)

<sup>e</sup>Stofan et al. (2007)

<sup>f</sup>Lorenz et al. (2008)

<sup>g</sup>Kossacki and Lorenz (1996)

<sup>h</sup>Niemann et al. (2005)

<sup>i</sup>Stevenson (1992)

<sup>j</sup>Lunine and Stevenson (1987)

<sup>k</sup>Loveday et al. (2001a)

<sup>l</sup>Hirai et al. (2001)

<sup>m</sup>Sotin et al. (2005)

<sup>n</sup>Lopes et al. (2007)

<sup>o</sup>Nelson et al. (2009)

<sup>p</sup>Wall et al. (2009)

<sup>q</sup>Atreya et al. (2006)

<sup>r</sup>Waite et al. (2005)

<sup>s</sup>Zahnle et al. (1992)

<sup>t</sup>Lorenz et al. (2007)

Saturn system. Table 12.2 summarizes these putative reservoirs and exchange processes, as well as experimental or observational (ground-based or *Cassini-Huygens* data) evidence obtained for or against them so far.

Some of these replenishment processes may have brought significant amounts of methane to Titan's atmosphere early in its history. Serpentization during the differentiation of the interior and/or as long as the icy mantle was entirely molten and liquid water could be in direct contact with rocks is a possible mechanism

(Atreya et al. 2006). However, hydrothermal circulations through cracks may be questionable at such high pressures, and some models suggest that the D/H ratio in Titan's methane is primordial (Glein et al. 2009). Furthermore, a serpentinization origin requires long-term storage of produced methane in Titan's interior, and therefore does not explain the outgassing process itself. Cometary impacts could be another source of methane (Zahnle et al. 1992; Griffith and Zahnle 1995). Such impacts likely occur at a low frequency nowadays, which suggests that this exogenic contribution of Titan's atmospheric methane budget is minor at present. Furthermore, the extent of hydrocarbon lakes is insufficient to sustain the abundance of methane in the atmosphere (Lorenz et al. 2008). Exchange processes between the interior and the atmosphere of Titan are thus necessary to explain the methane's replenishment.

Given the pressure–temperature conditions within Titan, two forms of storage of methane can be envisaged: (1) liquid methane at shallow depths, i.e. temperatures below 190 K (critical temperature of methane) or below the liquid–vapor equilibrium of CH<sub>4</sub> at pressures lower than 3 MPa; and (2) methane clathrate hydrates, which are thermodynamically stable from Titan's surface to the deep interior (Choukroun et al. 2010a). Liquid methane could be trapped in an icy regolith, whose self-compaction would release the liquid to the surface (Kossacki and Lorenz 1996) or re-supply hydrocarbon lakes if located nearby (Hayes et al. 2008). However, the storage capacity of such a regolith is very difficult to assess due to the lack of observational data (surface porosity, heat flux), of constraints on the thermal profile within the icy crust (which is thermal conductivity- and heat flux-dependent), and of laboratory data on the wetting properties and on the permeability of water ice to liquid hydrocarbons. Preliminary experiments on the wetting of water ice by liquid methane and ethane (Sotin et al. 2009) suggest that large amounts of hydrocarbons could remain trapped within pores and cracks of the ice, after the evaporation of liquid hydrocarbon bodies. Such wetting may contribute to the humidity level over seemingly dry areas of Titan's surface, like the *Huygens* probe landing site where methane has been released upon landing (Niemann et al. 2005). Further work is still needed to quantify the amounts of hydrocarbons that can be stored this way, and to assert the longevity of such a reservoir.

Much more extensive studies to date have investigated the stability of clathrate hydrates and their putative role on methane outgassing, both from a theoretical and an experimental perspective. Since the first study on this subject by Lunine and Stevenson (1987), which suggested a deep-seated dissociation of methane clathrates under high pressure, experimental works (Loveday et al. 2001a, b; Hirai et al. 2001, 2003; Machida et al. 2006; Choukroun et al. 2007) demonstrated an increasing stability with depth, and the occurrence of the phase transition to a high-pressure sH phase at the pressure where the thermodynamic calculations of Lunine and Stevenson (1987) predicted dissociation. However, dissociation of methane clathrates could also occur if the pressure-conditions did not promote their stability, and/or if ammonia (suggested to be the origin for the atmospheric nitrogen, Atreya et al. 1978) or ammonium-rich compounds, allegedly present in cryomagmas (Fortes et al. 2007), decreased the dissociation temperature sufficiently to induce dissociation.

## 12.6.2 Formation of an Early, Clathrate-Rich Crust

In principle, methane clathrate hydrates are thermodynamically stable from the very surface of Titan, see Fig. 12.3, to the deepest regions of the icy mantle (Grasset and Pargamin 2005; Choukroun et al. 2010a). However, at the time of accretion clathrate hydrates were likely mixed with silicate and ice particles. The accretional heat depends on the speed and size of particle collision, and an empirical factor that translates the fraction of kinetic energy that is actually converted into heat. The value of this factor is poorly constrained, and is typically estimated within the range 0.1–0.5 (e.g., Grasset et al. 2000; Tobie et al. 2006), which would have allowed significant melting of the icy fraction within accreting satellitesimals. This melting largely contributed to the early differentiation process, and the segregation of icy compounds from silicate mineral phases would have been eased at that time. An alternate model suggests that Titan remained undifferentiated after accretion (Barr et al. 2010), which would require all clathrates within Titan to be primordial. In that case, one would probably expect a different composition for these clathrates, as the first scenario involves significant chemical processing (see below). Regardless of the scenario, clathrate hydrates would have dissociated because of warm temperatures and decompression as they were rising through the liquid layer because of their positive buoyancy (assuming a composition rich in CH<sub>4</sub>, N<sub>2</sub>, CO<sub>2</sub>, and poor in heavy gases such as H<sub>2</sub>S and Xe), or as the impacts peak temperatures were reached. This process has been invoked as a potential origin for Titan’s atmosphere (Lunine et al. 1989, 2009). Soon after Titan’s accretion, a primitive atmosphere up to 200 bars of N<sub>2</sub> and CH<sub>4</sub> would have thus been in direct contact with a molten early liquid layer at a temperature of ~300 K. Upon cooling over a few million years, a CH<sub>4</sub>-rich clathrate layer ~3–5 km thick is expected to have formed at the interface, acting as a physical and chemical barrier, thermally insulating Titan’s interior (Lunine et al. 1989; Tobie et al. 2006; Lunine et al. 2009). In the undifferentiated accretion scenario, Barr et al. (2010) do not specify about the expected composition of the atmosphere nor its pressure conditions and evolution.

The early crust of methane-dominated clathrates would tremendously influence Titan’s thermal evolution, distribution of compounds, and potential for methane outgassing, as discussed in Sect. 12.5.2. Titan would cool slower through time, as can be seen by comparing an icy shell model (Tobie et al. 2005) with a clathrate crust model (Tobie et al. 2006): an underlying icy shell, up to 100 km thick and subject to convection (Tobie et al. 2005) would only appear in the last 500 Million year of Titan’s history. Prior to this shell’s formation, warm episodes related to core overturn and onset of silicate convection within the core may have induced sudden dissociation of part of the crust, releasing large amounts of methane in the atmosphere (Tobie et al. 2006). Furthermore, the growth of the early clathrate crust likely entrapped pockets of ammonia–water liquid from the primordial, 1–5 NH<sub>3</sub> wt.% ocean (Lunine et al. 2009; Choukroun et al. 2010a). These pockets eventually crystallized ice and ammonia hydrates below 176 K, or provided ammonia-rich liquids upon cooling if the solidus was not reached. Fortes et al. (2007) have

considered the trapping of ammonium sulfate solutions, which play a similar role although the densities of such solutions are larger than pure water, ice, or clathrates, requiring more energy than ammonia–water to allow cryovolcanic emissions. Further ammonia–water liquids may have been added to the icy shell beneath the clathrate crust after the onset of convection, by entrainment of these liquids within warm ice upwellings (Mitri et al. 2008). This lead Choukroun et al. (2010a) to suggest a clathrate-dominated upper icy shell, containing up to ~1–1.5% NH<sub>3</sub> in bulk, segregated in highly concentrated pockets with up to 15% NH<sub>3</sub>.

### 12.6.3 Cryovolcanic Release of Methane to the Atmosphere?

The thermal structure of the icy shell has been compared by Choukroun et al. (2010a) with new experimental data on the stability of clathrate hydrates in the H<sub>2</sub>O–NH<sub>3</sub>–CH<sub>4</sub> system, data that are compatible with other studies (Dong et al. 2008). This comparison has demonstrated the great stability of methane clathrate hydrates throughout Titan’s interior at thermal equilibrium, and little potential for clathrate dissociation. It has also been shown that a local geologic setting may be favorable for dissociation and cryovolcanic release of produced gases into the atmosphere. A new model of cryovolcanism of Titan has thus been proposed (Lunine et al. 2009; Choukroun et al. 2010a), and is shown on Fig. 12.6. In this model, a warm intrusion associated with upwelling in the ice shell heats up ammonia–water pockets, which melt or warm up sufficiently to induce the dissociation of surrounding clathrate hydrates if the heat flux is of ~40 mW.m<sup>-2</sup> (this value being on the high end of what might be expected in a convecting ice context). Subsequently, the increased buoyancy of the ammonia–water–methane cryomagma and the excess gas released allows for the rise of this cryomagma up to Titan’s surface.

One issue with the model of methane outgassing by clathrate dissociation is that, to date, no cryovolcanic activity has been formally and unambiguously detected on Titan. However, several features observed by the Visual and Infrared Mapping Spectrometer (Sotin et al. 2005; Nelson et al. 2009) and the Radar (Lopes et al. 2007; Wall et al. 2009) instruments onboard the *Cassini* spacecraft have been interpreted as possibly resulting from cryovolcanic activity. Choukroun et al. (2010a) have shown that the methane outgassed in their model may contribute to the sustenance of CH<sub>4</sub> in the atmosphere, at least for several thousands of years, based on the alleged activity. It must be borne in mind that the detection of cryovolcanic features may be impeded by the thick atmosphere through which the composition of the surface is very difficult to characterize at infrared wavelengths, by the important surface-atmosphere interaction, and by the very high cooling rate of cryomagmas on Titan’s surface, which would obliterate any thermal signature within ten days (Davies et al. 2010). As a consequence, it is unlikely that the *Cassini* data will provide a clear detection of cryovolcanic activity unless an event occurs during the course of the mission, although such direct observation would be desirable to confirm the proposed model. Until then, further

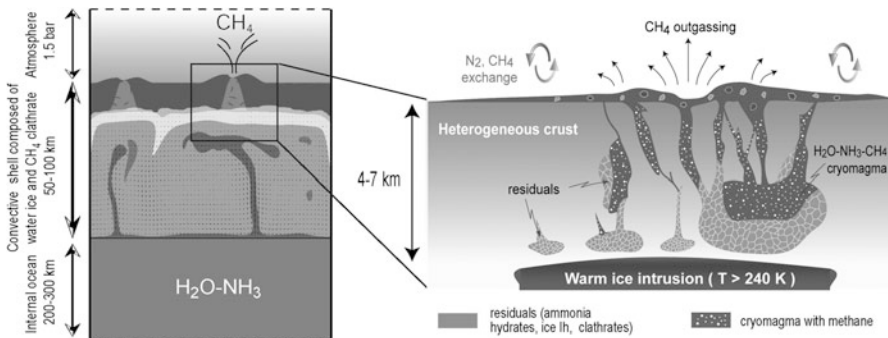


**Fig. 12.6** Conceptual model of recent and/or present-day cryovolcanism and associated release of methane. *Left:* cross-section of Titan's icy shell and computed convection motions within the ice underlaying the clathrate-rich upper crust. *Right:* at the tip of convective plumes, melting of ammonia hydrates generates a low-density, ammonia-rich cryomagma that dissociates the clathrates and may release methane in the atmosphere via direct effusive eruption or explosive eruptions by increase in gas pressure. See text for details (Modified after Lunine et al. (2009))

studies are required in order to address: (1) the effect of the mixing of methane with other compounds in the clathrate phase (ethane, N<sub>2</sub>, etc. . .); (2) the potential role that CO<sub>2</sub> may play in outgassing processes, either by itself or mixed with methane, given its tentative detection on Titan's surface (McCord et al. 2008); (3) the role of direct methane exchanges, from the liquid possibly trapped in the regolith, and how it would equilibrate with the atmosphere.

## 12.7 Enceladus: The Role of Clathrates in the Origin of the Plumes at the South Pole

Enceladus is one of the three bodies of the Solar System that exhibit on-going plume activity (Porco et al. 2006). It is warmer than Triton, the frigid satellite of Neptune, and much colder than Io, the hot, fiery satellite of Jupiter. Enceladus has risen high in visibility for astrobiological exploration for three reasons. (1) Compared to equatorial temperatures, the observation of unexpectedly high temperatures at the south pole (Spencer et al. 2006, 2009a, b) has led to inferences that liquid water might lie near the surface; (2) Some building blocks for life have been observed (compounds formed from C, H, O and possibly N, as well as simple and complex organic molecules (Waite et al. 2006, 2009). (3) Finally, the enormous radiated power, 15.8 GW (Howett et al. 2011), may or may not be in a form that organisms can use. It must be available in geological environments that bring together the necessary biogenic elements and liquid water in the presence of rock (Kieffer and Jakosky 2008).

The role of clathrates in the dynamics of the reservoir and plumes of Enceladus is very different in the two major end-member models proposed for the operation of

the plume system. In one set of models, clathrates play a passive role – providing gases to a liquid water-dominated system. In other models, they play the dominant role in storing the gases, driving the plumes, and controlling the tectonics by their stiff brittle nature.

### 12.7.1 Observations

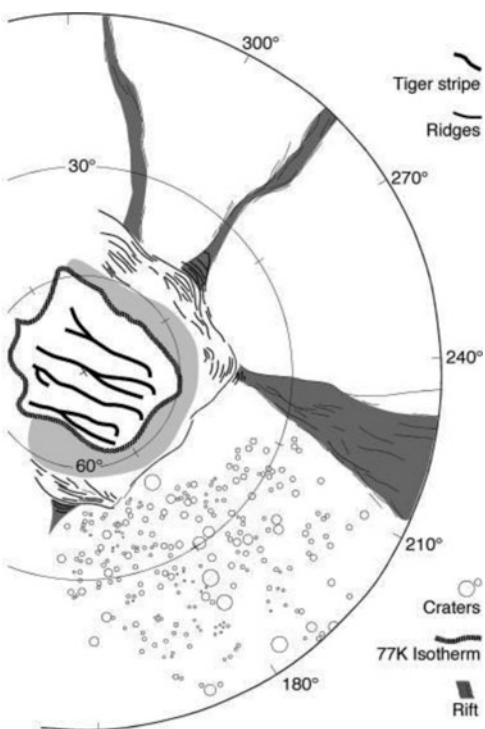
The geology of Enceladus is marvelously complex (Squyres et al. 1983b; Kargel and Pozio 1996; Porco et al. 2006; Spencer et al. 2009a, b), particularly in the region south of 60 S latitude, but the complexity can be simplified at a regional scale (Fig. 12.7). The role of clathrates in creating or controlling the geology is a subject of debate.

In the center of the south polar region are four prominent valleys, dubbed the “tiger stripes”, that have widths of about 2 km, depths of about 0.5 km, lengths of about 130 km, and spacings of about 35 km. Thirty or more individual plumes have been observed, carrying vapor, gases, and ice hundreds of kilometers above the surface and feeding ice particles into the E-ring of Saturn (Porco et al. 2006; Hansen et al. 2006). The number and activity of the plumes appears to be time-variable (Saur et al. 2008). Surrounding the tiger stripe terrain is a narrow annular terrain at latitude  $\sim$ 60°S that contains modest topography and no salient tectonic features (light gray area in Fig. 12.7). Surrounding this is another annular terrain that contains a “ring of ridges” with prominent compressional features. Radiating from these core terrains, at least three, and possibly four, tensile radial rifts propagate northward across the equator like the arms of a starfish.

The temperature of Enceladus at the equator is 76 K, but the south pole is warmer. The highest temperature reported in peer-reviewed literature is 167 K (Spencer et al. 2006; Spencer et al., 2009a, b), but the temperature may be as high as 190 K (Spencer, 2010, personal communication, press release <http://photojournal.jpl.nasa.gov/catalog/PIA13621>). The warm temperatures, as well as the plume source locations, occur along the tiger stripes (Spitale and Porco 2007; Abramov and Spencer 2009).

There is enormous power radiated from the south polar region. Initially reported as 3–7 GW (Spencer et al. 2009a, b), the estimate has been raised to 15.8 GW (Howett et al. 2011). Of two possible sources of heat production, radioactive decay has been shown to be insufficient (Porco et al. 2006; Meyer and Wisdom 2007). Tidal dissipation by strike-slip movement along the tiger stripes may be able to account for the initially observed 3–7 GW (Nimmo et al. 2007; Hurford et al. 2007), although the predictions of locations and time-variability of the plumes in these models were not matched by observations (Hansen et al. 2008; Spitale and Porco 2007). A tidal model based on clathrate dissociation (Halevy and Stewart 2008) predicted a variation in both mass flux and ratio of water vapor to gas for the October 9, 2008 flyby that was not observed, leading to the conclusion that the processes that produce the plume may be stationary rather than tidally controlled.

**Fig. 12.7** Map of the major tectonic features in the South Polar terrain of Enceladus. (From Gioia et al. (2007))



The nature and operation of the “heat source” below the south polar terrain remain a mystery at the time of this writing.

The plumes consist of ice particles, water vapor, and noncondensable gases. The gases in the plumes were observed on two separate flybys. In both, the dominant component was water vapor, ~90%. In 2005, the dominant noncondensable gases were reported as mass 28 (CO or N<sub>2</sub>; 3.3%), CO<sub>2</sub> (3.1%), and CH<sub>4</sub> (1.6%), plus traces of organics (Waite et al. 2006). In 2008, the dominant gases were CO<sub>2</sub> (5.3%), CO (4.4%), N<sub>2</sub> and CH<sub>4</sub> (<1%), with traces of NH<sub>3</sub> amounting to ~0.8% (Waite et al. 2009). Three classes of ice particles were detected in the E-ring of Saturn: pure ice, slightly dirty ice, and slightly salty ice (Postberg et al. 2009). These presumably reflect compositional differences at depth in Enceladus.

The ratio of ice particles to vapor (I/V) places a constraint on the single-component H<sub>2</sub>O models. Initially (Porco et al. 2006) I/V was reported to be ~1. Sublimation was ruled out as a process that could produce I/V ~1 from thermodynamic constraints, and so it was concluded that the reservoir contained boiling water. Subsequently, it was shown that this ratio had been miscalculated and should have been reported as ~0.2 (Kieffer et al. 2009), and that sublimation should not have been ruled out as a viable process that could produce the plume. A third refined analysis of the original data yielded I/V ~1 (Ingersoll and Ewald 2009).

### 12.7.2 Interpretations

To explain these observations, two different sets of assumptions have led to two very different end-member models for the plume dynamics, inferred reservoir conditions, and role for clathrates. In one model, referred to as the “Cold Faithful” model, the fluid driving the plumes is the single-component, H<sub>2</sub>O, and the gases and clathrates play a passive role (Porco et al. 2006, and subsequent papers). In an antithetical model referred to as the “Frigid Faithful” model, the driving fluid is a multi-component mixture of H<sub>2</sub>O-vapor and the other observed gases derived from an icy clathrate crust. In this model, the gases derived from the clathrates play an active, and dominant, role in driving the plumes. Variations on this model include gases that provide buoyancy to a liquid. For example, Kargel (2006, and earlier work referenced therein) speculated that a deep, gas-saturated ocean, or deep crustal pocket of water, exists in equilibrium with clathrates residing on the seafloor. Fortes (2007) proposed a hybrid model in which clathrates were formed in Enceladus as a result of hydrothermal activity of an aqueous cryomagma rising from the core through fractures in an icy crust. These clathrates are then carried upward by the rising fluids, like xenoliths in terrestrial volcanic eruptions, and upon ascent, break down to provide the gases and ice of the plumes.

In the single-component Cold Faithful system, the only options for production of vapor in the plume are (a) boiling, with droplets of liquid freezing to produce the ice/vapor (I/V) mixture of the plume, and (b) sublimation, with recondensation of vapor to produce the I/V mixture observed in the plume. The ratio of I/V thus provides a constraint on the process. If I/V ~ 1 as reported above the reservoir must be liquid water because sublimation and recondensation cannot produce this much ice (Porco et al. 2006).

In the single-component models, it has been suggested that liquid water exists in pockets close to the surface (Porco et al. 2006), in fractures and cracks that feed the plumes (Schmidt et al. 2008; Postberg et al. 2009), and in deep and large oceans (Collins and Goodman 2007; Glein and Shock 2010). The discovery of NaCl on ice particles in the E-ring of Saturn has been interpreted to indicate a saline subsurface reservoir (Postberg et al. 2009), but it is not clear whether such an ocean is present now or existed in the distant past (Glein and Shock 2010).

With the exception of the Fortes model, the noncondensable gases are incidental to the operation of the liquid water system and are transported passively from unspecified nonaqueous reservoirs, perhaps from clathrates somewhere else in the system (e.g., Kargel 2006). In the model of Fortes (2007) the clathrates are entrained in cool liquid water (250–270 K) cryomagmas, dissociating as they rise upward. The bubbling gas promotes the vigorous plume activity, akin to basaltic fire fountains propelled by volatile exsolution on earth.

Kieffer et al. (2006) noted that CO<sub>2</sub> could only be in solution in liquid water in the abundance reported by Waite et al. (2006) at depths greater than about 25 kilometers and could help drive geyser eruptions as on Earth (Lu et al. 2005, 2006). However, the other noncondensable gases could not be in solution in the

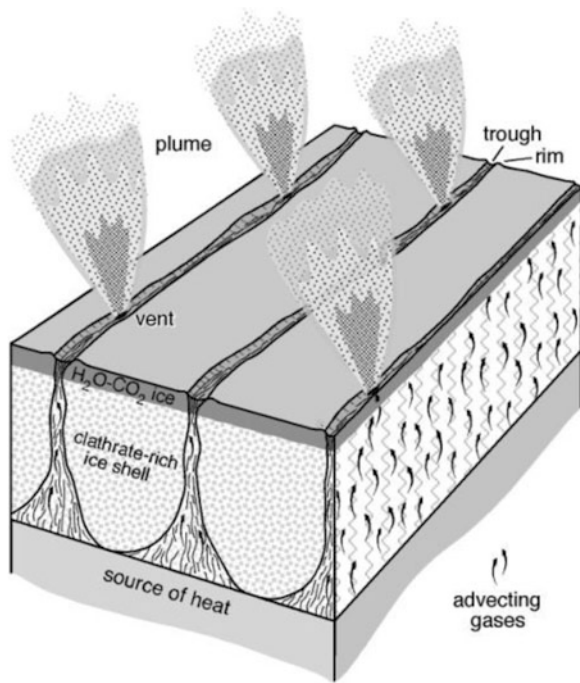
abundances observed even at the center of Enceladus. This motivated the proposal of the Frigid Faithful model in which the gases are stored in clathrates. The gases are more soluble in solid ice than in liquid water. Schenk and McKinnon (2009) have found that thermal isostasy requires a thermal expansion more consistent with clathrates than water ice and calculated that the crust could contain up to one third clathrates. The properties of clathrates are very important in the Frigid Faithful models because they are not only the source of gas and ice particles, but also influence the structural geology of the crust.

The proposed crust of Enceladus in the Frigid Faithful model consists of a leaky  $\text{H}_2\text{O}-\text{CO}_2$  ice cap “seal” on the order of 3–5 km thickness overlying an icy clathrate reservoir (Fig. 12.8). NaCl is not tolerated by the clathrate structure, but can exist in the icy part of the crust (Glein and Shock 2010). During times when the seal is relatively intact, there will be only minor leaks, the confining pressure is maintained, and the clathrates remain stable. Small leaks will be self-sealed by water vapor rising from depth. The seal is stressed tectonically by tidal distortions, causing confining pressure to be lost and exposing the clathrate reservoir to near-vacuum conditions. Alternatively, the clathrates could be heated to decomposition conditions; a mixture of the two processes is likely. With time, self-sealing resumes and the system returns to ambient conditions. New vents are continuously opened and closed by tidal stresses, producing variable fluxes into the plumes.

Heat is transported by vapor and gases rising through the crust as an “advection machine” (Kieffer et al. 2006; Gioia et al. 2007), an Enceladus version of a geologic heat pipe (McGuinness et al. 1993; Birkholzer 2006). Warm vapor and gases are advected toward the surface carrying the latent heat of vaporization, which is then redeposited at the cool end of the heat pipe by condensation in fractures as part of the self-sealing process. The dissociation of the clathrates generates gases that propel the plumes, as well as ice particles, and a small amount of water vapor (Lu and Kieffer 2009). Additionally, ice and salty ice are entrained into the plume. Pure ice may also be produced by the recondensation of sublimated  $\text{H}_2\text{O}$ , but is more plausibly produced as a byproduct of the violent decomposition of ices and clathrates as proposed for comets (Laufer et al. 2005). The I/V ratio constraints that apply to the single-component  $\text{H}_2\text{O}$  system do not apply to the multicomponent model because of the multiple possible sources of ice. The I/V ratio would be expected to be variable as new vents open and close.

In the Frigid Faithful model, the observed thermal anomaly at the south pole is a manifestation of a heat source buried under the tiger stripe terrain (Gioia et al. 2007). Thermal expansion of this heat source causes deformation of the surrounding cold icy shell. Hoop (circumferential) and radial stresses calculated from this model change across the region. On the tiger stripe terrain above the heat source, the hoop and radial stresses are both tensile, resulting in a tensile regime conducive to the formation of the tiger stripes (Fig. 12.7). At a distance of about 100 km from the South Pole, the radial stresses vanish and the hoop stresses are moderately tensile, resulting in the relatively unstressed, narrow annular region at 60 S that shows modest topography, the gray region in Fig. 12.7. At further distances, the radial stresses are compressive and the hoop stresses are tensile, resulting in a ring of compressive ridges (the “ring of ridges”) at about 140 km from the pole. At greater

**Fig. 12.8** Schematic of the Frigid Faithful advection machine (Modified from Gioia et al. (2007))



distances, the tensile hoop stresses act as tearing agents, and the radial stresses act as splitting agents, driving a set of radial rifts to open up north of the ring of ridges. These rifts cross the equator into the northern hemisphere (Fig. 12.7).

A well-known rule in structural geology is that the spacing of fractures near the surface of a layer is approximately equal to the thickness of that layer (Gioia et al. 2007). Therefore, in the Frigid Faithful model, the depth of the tiger stripes is taken to be approximately equal to their spacing, ~35 km. In systems dominated by advection, the crust remains close to the surface temperature to the depth of the advection, or, in this case, to 35 km. Such a cold crust would have negligible rates of deformation by creep and, since clathrates are intrinsically much stiffer than  $H_2O$  ice, there would be negligible solid-state convection.

In summary, clathrates play a much larger role in Frigid Faithful models than they do in Cold Faithful models because they control the structural geology of the south polar region and the gases that they provide upon dissociation are the major driver of the plumes out of their source region.

## 12.8 Conclusions and Remaining Questions

Clathrate hydrates are ubiquitous on Earth. Extensive literature data on the properties and the stability of clathrate hydrates, and detailed and complex thermodynamic models, provide a relatively solid basis for inferring the role of clathrate

hydrates on other planetary bodies. The strongest grounds for considering clathrate hydrates elsewhere, and particularly in the outer Solar System where ice may amount to >50% of the bulk composition of planetary bodies, are: (1) on our own planet, clathrate hydrates form wherever the pressure–temperature – chemical composition conditions are suitable; and (2) conditions thermodynamically favorable for clathrate hydrate formation exist in many environments throughout the Solar System. If present, clathrate hydrates are likely to influence geologic processes: (1) their putative stability within the presolar nebula suggests a role in the trapping of volatiles within planetesimals, satellitesimals, and comets; (2) their thermal conductivity five times lower than that of water ice can determine the thermal structure of a body, or at least affect significantly its thermal evolution; (3) their densities close to those of water ice and liquid water allow for various scenarios, with methane-rich clathrates preferentially located in the icy shell and at the ice-ocean interface, and/or methane-poor clathrates remaining trapped beneath the liquid layer; (4) the large amounts of gas they contain, combined with a thermodynamic behavior very different from water ice, can be related to outgassing processes observed at Enceladus and expected on Titan; and (5) as storage media for volatiles, they may affect the amounts of volatiles measured by ground-based or space observations, as well as isotopic composition.

Several key issues with clathrate hydrates in the Solar System still remain unanswered, because of the lack of sufficient laboratory data and integrative models at the relevant conditions. We propose here a non-exhaustive list of areas where further research appears highly desirable. (1) The stability of clathrate hydrates at presolar nebula conditions (pressure much lower than  $10^{-7}$  bar, temperature down to a few Kelvin degrees) remains an experimental “no-man’s-land,” and the paucity of experimental data on clathrate-ice-gas equilibria is such that condensation models at low temperature would greatly benefit from further constraints. A critical issue is the kinetics of clathrate formation at these conditions, which remains unexplored. The kinetics of formation and dissociation at the appropriate conditions are certainly too slow to be measured directly at the timescale of laboratory experiments; extrapolation from higher pressure and/or temperature through the measurement of activation energies could be the best approach to obtain constraints on these processes. (2) Although the stability of clathrates at pressures up to several tens of GPa has been demonstrated experimentally, statistical thermodynamic models are generally not applicable beyond 500 MPa to 1 GPa at most. Further developments, and reconsiderations of some assumptions such as the unicity of guest molecules in clathrate cages or long-distance interactions, would be needed to apply the commonly accepted theory to icy satellites or extrasolar planets. Integrative thermodynamic models, for example based on the model by Choukroun and Grasset (2007, 2010), allowing for the computation of clathrate hydrate equilibria up to 1–2 GPa, in presence of inhibitors of planetary relevance like salts and ammonia, would prove very helpful. (3) Mechanical properties of clathrate hydrates have only been investigated under differential stresses and strain rates that are orders of magnitude larger than on planetary bodies, and likely driven by dislocation creep. Further experimental work in other deformation regimes (grain-boundary sliding, diffusion

creep) may prove essential in characterizing the creep response of clathrate hydrates, pure or mixed with ice, for planetary applications. Dissipation measurements are also required, in order to assert the response of clathrate hydrates to tidal forcing.

Clathrate hydrates also bear some relevance to astrobiology. These compounds are very closely related to biological activity in terrestrial deep-sea sediments. They tend to form in regions where natural gas is produced in large amounts by the reduction of CO<sub>2</sub> into CH<sub>4</sub> by methanogenic bacteria (e.g., Charlou et al. 2004). Although we are not suggesting that this process takes place as such in outer Solar System bodies, this observation clearly raises a number of interesting prospects for research as to the mechanisms through which clathrate hydrates have formed and evolved within icy Solar System bodies. Further, most cosmochemical models suggest the occurrence of large quantities of primordial methane. Could clathrate hydrates play any role in the transport of potential nutrients such as methane in icy bodies? Could extraterrestrial organisms use clathrate hydrates to sustain their metabolism? Could the metabolic products form clathrate hydrates, which may be transported to the near-surface environment of icy bodies, and constitute a trace of this activity on bodies like Europa? Could their isotopic composition in carbon and hydrogen, and/or trace gases contents, be criteria to determine how those clathrates formed?

Finally, the detection, or rather the non-detection of clathrate hydrates on icy surfaces at present, may seem to question the relevance of these species to outer Solar System processes. However: (1) we have shown the thermodynamic instability of clathrate hydrate on most planetary surfaces, independently of their putative occurrence at depth; and (2) the detection of clathrate hydrates by techniques conventionally used in planetary science is very difficult, if not impossible at present, because of a lack of clearly discriminating data. Indeed, the infrared signature of clathrate hydrates is extremely close to that of water ice, some modifications of the peak associated to the hydrate forming gas being the only trace of the clathrate structure (Dartois and Deboffle 2008; Dartois and Schmitt 2009). Slight shifts in the position of the CO<sub>2</sub> band of some Saturnian satellites surfaces have been tentatively attributed to clathrate hydrates (Cruikshank et al. 2010), but other explanations cannot be totally ruled out, such as mixtures of solid CO<sub>2</sub> with other compounds, or radiolytic processes that may affect the signature of CO<sub>2</sub>. The dielectric constant of clathrate hydrates is about half the value of ice (Table 12.1), but the observation of such low dielectric constants in planetary Radar data may as well be interpreted in terms of volume scattering, porosity, or other compounds.

An in-situ planetary mission including a lander or rover, equipped with an X-Ray Diffractometer and/or a Raman spectrometer sent to an outer Solar System body likely to harbor clathrate hydrates close to or on its surface (i.e., Titan, Enceladus, possibly some comets), is needed to gather the observational evidence for clathrate hydrates outside Earth. Until then, further experimental and theoretical studies will bring new constraints on the planetary environments where clathrates should be expected, and on their role in astrophysical and geologic processes.

**Acknowledgments** MC acknowledges support from the NASA Outer Planets Research Program. The authors are grateful to Julie Castillo-Rogez for her review, which helped greatly improve on this chapter. Part of this work has been conducted at the Jet Propulsion Laboratory, California Institute of Technology, under contract with NASA. Part of the research leading to these results has received funding from the European Research Council under the European Community's Seventh Framework Programme (FP7/2007-2013 Grant Agreement no. 259285). Copyright 2011. All rights reserved. Government sponsorship acknowledged.

**Note added in proof** In the case of Titan, a recent study (Choukroun and Sotin, 2012) has shown that ethane-dominated precipitations around the poles would react with methane clathrate hydrates in the subsurface, yielding subsidence and releasing some methane in the atmosphere to sustain the hydrocarbon cycle.

Geologic / geomorphologic units on Titan, including potentially cryovolcanic areas, are detailed in Lopes et al. (2010). An alternative origin via hydrologic processes for these features is proposed in Moore and Pappalardo (2011).

Others?

## References

- Abramov O, Spencer JR (2009) Endogenic heat from Enceladus' South Polar fractures: new observations, and models of conductive surface heating. *Icarus* 199:189–196
- Adamson AW, Jones BR (1971) Physical adsorption of vapors on ice IV. Carbon dioxide. *J Colloid Interface Sci* 37:831–835
- Adisasmitho S, Frank RJ, Sloan ED (1991) Hydrates of carbon dioxide and methane mixtures. *J Chem Eng Data* 36:68–71
- Alibert Y, Mousis O (2007) Formation of Titan in Saturn's subnebula: constraints from Huygens probe measurements. *Astron Astrophys* 465:1051–1060
- Anders E, Grevesse N (1989) Abundances of the elements: meteoritic and solar. *Geochim Cosmochim Acta* 53:197–214
- Anderson JD, Lau EL, Sjogren WL, Schubert G, Moore WB (1996) Gravitational constraints on the internal structure of Ganymede. *Nature* 384:541–543
- Anderson JD, Schubert G, Jacobson RA, Lau EL, Moore WL, Sjogren WL (1998) Europa's differentiated internal structure: inferences from four Galileo encounters. *Science* 281:2019–2022
- Antoine C (1888) Tensions des vapeurs; nouvelle relation entre les tensions et les températures. *Comptes Rendus des Séances de l'Académie des Sciences* 107:681–684, 778–780, 836–837
- Atreya SK, Donahue TM, Kuhn WR (1978) Evolution of a nitrogen atmosphere on Titan. *Science* 201:611–613
- Atreya SK, Wong MH, Owen TC, Mahaffy PR, Niemann HB, de Pater I, Drossart P, Encrenaz Th (1999) A comparison of the atmospheres of Jupiter and Saturn: deep atmospheric composition, cloud structure, vertical mixing, and origin. *Planet Space Sci* 47:1243–1262
- Atreya SK, Adams EY, Niemann HB, Demick-Montelara JE, Owen TC, Fulchignoni M, Ferri F, Wilson EH (2006) Titan's methane cycle. *Planet Space Sci* 54:1177–1187
- Bakker RJ, Dubessy J, Cathelineau M (1996) Improvements in clathrate modelling: I. The H<sub>2</sub>O-CO<sub>2</sub> system with various salts. *Geochim Cosmochim Acta* 60:1657–1681
- Bar-Nun A, Kleinfeld I, Kochavi E (1988) Trapping of gas mixtures by amorphous water ice. *Phys Rev B* 38:7749–7754
- Barr AC, Pappalardo RT (2005) Onset of convection in the icy Galilean satellites: influence of rheology. *J Geophys Res* 110:E12005. doi:[10.1029/2004JE002371](https://doi.org/10.1029/2004JE002371)
- Barr AC, Citron RI, Canup RM (2010) Origin of a partially differentiated Titan. *Icarus* 209:858–862
- Barrer RM, Edge AVJ (1967) Gas hydrates containing Ar, Kr, and Ne: kinetics and energetics of formation and equilibria. *Proc R Soc Lond A* 300:1–24

- Benz W (2000) Low velocity collisions and the growth of planetesimals. *Space Sci Rev* 92:279–294
- Bockelée-Morvan D, Gautier D, Hersant F, Hure J-M, Robert F (2004) The composition of cometary volatiles. In: Festou M, Keller HU, Weaver HA (eds) Comets II. University of Arizona Press, Tucson, pp 391–423
- Birkholzer JT (2006) A temperature-profile method for estimating flow in geologic heat pipes. *J Contam Hydrol* 85:89–117
- Bridgman PW (1912) Water, in the liquid and five solid forms, under pressure. *Proc Am Acad Arts Sci* 47:441–558
- Castillo-Rogez JC, Lunine JI (2010) Evolution of Titan's rocky core constrained by Cassini observations. *Geophys Res Lett* 37:L20205. doi:[10.1029/2010GL044398](https://doi.org/10.1029/2010GL044398)
- Charlou J-L, Donval JP, Fouquet Y, Ondreas H, Knoery J, Cochonat P, Levaché D, Poirier Y, Jean-Baptiste P, Fourré E, Chazallon B, The ZAIROV Leg 2 Scientific Party (2004) Physical and chemical characterization of gas hydrates and associated methane plumes in the Congo-Angola Basin. *Chem Geol* 205:405–425
- Chastain BK, Chevrier V (2007) Methane clathrate hydrate as a potential source for Martian atmospheric methane. *Planet Space Sci* 55:1246–1256
- Chazallon B (2010) Capture of CO<sub>2</sub> by gas hydrates crystallization: investigation of equilibrium and compositional properties by micro-Raman spectroscopy. In: 12th International conference on the physics and chemistry of ice, abstract # 6-A2-1, Sapporo
- Choukroun M (2007) Etude expérimentale et thermodynamique des hydrates sous pression: applications à Titan. Ph.D. thesis, Université de Nantes, France
- Choukroun M, Morizet Y, Gasset O (2007) Raman study of methane clathrate hydrates under pressure: new evidence for the metastability of structure II. *J Raman Spectrosc* 38:440–451
- Choukroun M, Grasset O (2007) Thermodynamic model for water and high-pressure ices up to 2.2 GPa and down to the metastable domain. *J Chem Phys* 127:124506
- Choukroun M, Grasset O, Tobie G, Sotin C (2010a) Stability of methane clathrate hydrates under pressure: influence on outgassing processes of methane on Titan. *Icarus* 205:581–593. doi:[10.1016/j.icarus.2009.08.011](https://doi.org/10.1016/j.icarus.2009.08.011)
- Choukroun M, Castillo-Rogez JC, Young JB, Mielke RE (2010b) Preliminary comparison between the dissipation in CO<sub>2</sub> clathrate hydrates and water ice. In: Lunar planetary science conference XLI, abstract #2172, Houston, March 2010
- Choukroun M, Grasset O (2010) Thermodynamic data and modeling of the water and water-ammonia phase diagrams for planetary geophysics. *J Chem Phys* 133:144502
- Choukroun M, Sotin C (2012) Is Titan's shape caused by its meteorology and carbon cycle? *Geophys Res Lett* 39:L04201
- Clampin M, Krist JE, Ardila DR, Golimowski DA, Hartig GF, Ford HC, Illingworth GD, Bartko F, Benítez N, Blakeslee JP, Bouwens RJ, Broadhurst TJ, Brown RA, Burrows CJ, Cheng ES, Cross NJG, Feldman PD, Franx M, Gronwall C, Infante L, Kimble RA, Lesser MP, Martel AR, Menanteau F, Meurer GR, Miley GK, Postman M, Rosati P, Sirianni M, Sparks WB, Tran HD, Tsvetanov ZI, White RL, Zheng W (2003) Hubble space telescope ACS coronagraphic imaging of the circumstellar disk around HD 141569A. *Astron J* 126:385–392
- Collins GC, Goodman JC (2007) Enceladus' south polar sea. *Icarus* 189:72–82. doi:[10.1016/j.icarus.2007.01.010](https://doi.org/10.1016/j.icarus.2007.01.010)
- Cook JG, Leaist DJ (1983) Exploratory study of the thermal conductivity of methane hydrate. *Geophys Res Lett* 10(5):397–400
- Coustonis A, Achterberg RK, Conrath BJ, Jennings DE, Marten A, Gautier D, Nixon CA, Flasar FM, Teanby NA, Bézard B, Samuelson RE, Carlson RC, Lellouch E, Bjoraker GL, Romani PN, Taylor FW, Irwin PGJ, Fouchet T, Hubert A, Orton GA, Kunde VG, Vinatier S, Mondellini J, Abbas MM, Courtin R (2007) The composition of Titan's stratosphere from Cassini/CIRS mid-infrared spectra. *Icarus* 189:35–62
- Cruikshank DP, Meyer AL, Brown RH, Clark RN, Jaumann R, Stephan K, Hibbitts CA, Sandford SA, Mastrapa RME, Filacchione G, Dalle Ore CM, Nicholson PB, Buratti BJ, McCord TB,

- Nelson RM, Dalton JB, Baines KH, Matson DL (2010) Carbon dioxide on the satellites of Saturn: results from the Cassini VIMS investigation and revisions to the VIMS wavelength scale. *Icarus* 206(2):561–572
- Dartois E, Deboffe D (2008) Methane clathrate hydrate FTIR spectrum: implications for its cometary and planetary detection. *Astron Astrophys* 490:L19
- Dartois E, Schmitt B (2009) Carbon dioxide clathrate hydrate FTIR spectrum. *Astron Astrophys* 504:869–873
- Davies AG, Sotin C, Castillo-Rogez J, Matson DL, Johnson TV, Choukroun M, Baines KH (2010) Atmospheric control of the cooling rate of impact melts and Cryolavas on Titan's surface. *Icarus* 208:887–895. doi:[10.1016/j.icarus.2010.02.025](https://doi.org/10.1016/j.icarus.2010.02.025)
- Davidson DW (1983) Gas hydrates as clathrate ices. In: Cox JL (ed) *Natural gas hydrates*. Butterworths, Boston
- Davidson DW, Handa YP, Ripmeester JA (1986) Xenon-129 the NMR and thermodynamic parameters of xenon hydrate. *J Chem Phys* 90:6549–6552
- Davy H (1811) The Bakerian lecture: on some combination of oxymuriatic gas and oxygene, and on the chemical relation of these principles, to inflammable bodies. *Phil Trans R Soc Lond* 101:1–35
- Deaton WM, Frost EM (1946) Gas hydrates and their relation to the operation of natural-gas pipe lines. US Bureau of Mines Monogr 8:101
- Delsemme AH, Swings P (1952) Gas hydrates in cometary nuclei and interstellar grains. *Annu Astrophys* 15:1–6
- Delsemme AH, Wenger A (1970) Physico-chemical phenomena in comets I. Experimental study of snows in a cometary environment. *Planet Space Sci* 18:709–715
- Deschamps J, Dalmazzone D (2009) Dissociation enthalpies and phase equilibrium for TBAB semi-clathrate hydrates of N<sub>2</sub>, CO<sub>2</sub>, N<sub>2</sub> + CO<sub>2</sub> and CH<sub>4</sub> + CO<sub>2</sub>. *J Therm Anal Calorim* 98:113–118
- de Roo JL, Peter CJ, Lichtenhaller RN, Diepen GAM (1983) Occurrence of methane in hydrate-bearing sediments and undersaturated solutions of sodium chloride and water in dependence of temperature and pressure. *AIChE J* 29:651
- Dickens GR, Quinby-Hunt MS (1997) Methane hydrate stability in pore water: a simple theoretical approach for geophysical applications. *J Geophys Res* 102(B1):773–783
- Dickens GR (2001) The potential volume of ocean methane hydrates with variable external conditions. *Organ Geochem* 32:1179–1193
- Dickens GR (2003) A methane trigger for rapid warming? *Science* 299:1017
- Dodson-Robinson SE, Willacy K, Bodenheimer P, Turner NJ, Beichman CA (2009) Ice lines, planetesimal composition, and solid surface density in the solar nebula. *Icarus* 200:672–693
- Dong T, Wang L, Liu A, Guo X, Ma Q, Li G, Sun Q (2008) Experimental determination of methane hydrate formation in presence of ammonia. *Petrol Sci* 6:188–193
- Duan Z, Hu J (2004) A new cubic equation of state and its applications to the modeling of vapor-liquid equilibria and volumetric properties of natural fluids. *Geochim Cosmochim Acta* 68:2997–3009
- Durham WB, Kirby SH, Stern LA, Zhang W (2003a) The strength and rheology of methane clathrate hydrate. *J Geophys Res* 108(B4):2182. doi:[10.1029/2002jb001872](https://doi.org/10.1029/2002jb001872)
- Durham WB, Stern LA, Kirby SH (2003b) Ductile flow of methane hydrate. *Can J Phys* 81:373–380
- Durham WB, Stern LA, Kirby SH, Circone S (2005) Rheological comparison and structural imaging of sI and sII end-member gas hydrates and hydrate/sediments aggregates. In: Proceedings of 5th international conference on gas hydrates, Trondheim
- Durham WB, Prieto-Ballesteros O, Goldsby DL, Kargel JS (2010) Rheological and thermal properties of icy materials. *Space Sci Rev* 153:273–298. doi:[10.1007/s11214-009-9619-1](https://doi.org/10.1007/s11214-009-9619-1)
- Dyadin YA, Larionov EG, Mirinski DS, Mikina TV, Starostina LI (1997a) Clathrate formation in the Ar-H<sub>2</sub>O system under pressures up to 15,000 bar. *Mendel Commun* 1:32–34
- Dyadin YA, Aladko YE, Larionov EG (1997b) Decomposition of methane hydrates up to 15 kbar. *Mendel Commun* 1:34–35

- Dyadin YA, Larionov EG, Manakov AG, Zhurko FV, Aladko EY, Mikina TV, Komarov VY (1999a) Clathrate hydrates of hydrogen and neon. *Mendel Commun* 9(5):209–210
- Dyadin YA, Larionov EG, Aladko YE, Manakov AY, Zhurko FV, Mikina TV, Komarov VY, Gratchev EV (1999b) Clathrate hydrates in the water – noble gas (hydrogen) systems at high pressures. *J Struct Chem* 40(5):790–795
- Dyadin YA, Larionov EG, Aladko YE, Zhurko FV (2001) Clathrate nitrogen hydrates at pressures up to 15 kbar. *Dokl Phys Chem* 378(4–6):159–161
- English NJ, Tse JS (2010) Mechanisms of thermal conduction in clathrate hydrates. In: 12th International conference on the physics and chemistry of ice, abstract # 6-A3-1, Sapporo
- Falabella BJ (1975) A study of natural gas hydrates, Ph.D. thesis, University of Massachussets, University Microfilms, No. 76-5849, Ann Harbor
- Flasar FM (1998) Titan weather report. *Science* 395:541–542
- Fortes AD (2007) Metasomatic clathrate xenoliths as a possible source for the south polar plumes of Enceladus. *Icarus* 181:743–748. doi:[10.1016/j.icarus.2007.06.013](https://doi.org/10.1016/j.icarus.2007.06.013)
- Fortes AD, Grindrod PM, Trickett SK, Vočadlo L (2007) Ammonium sulfate on Titan: possible origin and role in cryovolcanism. *Icarus* 188(1):139–153
- Fortes AD, Choukroun M (2010) Phase behaviour of ices and hydrates. *Space Sci Rev* 153:185–218. doi:[10.1007/s11214-010-9633-3](https://doi.org/10.1007/s11214-010-9633-3)
- Fray N, Marboeuf U, Brissaud O, Schmitt B (2010) Equilibrium data of methane, carbon dioxide, and xenon clathrate hydrates below the freezing point of water. Applications of astrophysical environments. *J Chem Eng Data* 55:5101–5108. doi:[10.1021/je1006604](https://doi.org/10.1021/je1006604)
- Galloway TJ, Ruska W, Chappellear PS, Kobayashi R (1970) Experimental measurement of hydrate numbers for methane and ethane and comparison with theoretical values. *Ind Eng Chem Fundam* 9:237–243
- Gautier D, Conrath BJ, Owen T, de Pater I, Atreya SK (1995) The troposphere of Neptune. In: Cruikshank DP (ed) *Neptune and Triton*. The University of Arizona Press, Tucson, pp 547–611
- Gautier D, Hersant F, Mousis O, Lunine JI (2001) Enrichments in volatiles in Jupiter: a new interpretation of the Galileo measurements. *Astrophys J* 550:L227–L230
- Gautier D, Hersant F (2005) Formation and composition of planetesimals. *Space Sci Rev* 116:25–52
- Gioia G, Chakraborty P, Marshak S, Kieffer SW (2007) Unified model of tectonics and heat transport in a frigid Enceladus. *Proc Natl Acad Sci* 104(34):13578–13581. doi:[10.1073/pnas.0706018104](https://doi.org/10.1073/pnas.0706018104)
- Glein CR, Desch SJ, Shock EL (2009) The absence of endogenic methane on Titan and its implications for the origin of atmospheric nitrogen. *Icarus* 204:637–644
- Glein CR, Shock EL (2010) Sodium chloride as a geophysical probe of a subsurface ocean on Enceladus. *Geophys Res Lett* 37:L09204. doi:[10.1029/2010GL042446](https://doi.org/10.1029/2010GL042446)
- Grasset O, Sotin C (1996) The cooling rate of a liquid shell in Titan's interior. *Icarus* 123:101–112
- Grasset O, Sotin C, Deschamps F (2000) On the internal structure and dynamics of Titan. *Planet Space Sci* 48:617–636
- Grasset O, Pargamin J (2005) The ammonia-water system at high pressures: implications for the methane of Titan. *Planet Space Sci* 53:371–384
- Greve R, Mahajan RA (2005) Influence of ice rheology and dust content on the dynamics of the north-polar cap of Mars. *Icarus* 174:475–485
- Griffith CA, Zahnle K (1995) Influx of cometary volatiles to planetary moons: the atmospheres of 1000 possible Titans. *J Geophys Res* 100(E8):16907–16922
- Grindrod PM, Fortes AD, Nimmo F, Feltham DL, Brodholt JP, Vočadlo L (2008) The long-term stability of a possible aqueous ammonium sulfate ocean inside Titan. *Icarus* 197:137–151
- Halevy I, Stewart ST (2008) Is Enceladus' plume tidally controlled? *Geophys Res Lett* 35:L12203. doi:[10.1029/2008GL034349](https://doi.org/10.1029/2008GL034349)
- Handa YP, Cook JG (1987) Thermal conductivity of xenon hydrate. *J Phys Chem* 91(25):6327–6328
- Hansen CJ, Esposito L, Stewart AIF, Colwell J, Hendrix A, Pryor W, Shemansky D, West R (2006) Enceladus' water vapour plume. *Science* 311:1422–1425. doi:[10.1126/science.1121254](https://doi.org/10.1126/science.1121254)

- Hansen CJ, Esposito L, Stewart AIF, Meinke B, Wallis B, Colwell JE, Hendrix AR, Larsen K, Pryor W, Tian F (2008) Water vapour jets inside the plume of gas leaving Enceladus. *Nature* 456:477–479. doi:[10.1038/nature07542](https://doi.org/10.1038/nature07542)
- Hayes A, Aharonson O, Callahan P, Elachi C, Gim Y, Kirk R, Lewis K, Lopes R, Lorenz R, Lunine J, Mitchell K, Mitri G, Stofan E, Wall S (2008) Hydrocarbon lakes on Titan: distribution and interaction with a porous regolith. *Geophys Res Lett* 35:L09204. doi:[10.1029/2008GL033409](https://doi.org/10.1029/2008GL033409)
- Hersant F, Gautier D, Huré J-M (2001) A two-dimensional model for the primordial nebula constrained by D/H measurements in the solar system: implications for the formation of Giant planets. *Astrophys J* 554:391–407
- Hersant F, Gautier D, Lunine JI (2004) Enrichments I volatiles in the giant planets of the solar system. *Planet Space Sci* 52:623–641
- Hersant F, Gautier D, Tobie G, Lunine JI (2008) Interpretation of the carbon abundance in Saturn measured by Cassini. *Planet Space Sci* 56:1103–1111
- Hirai H, Uchihara Y, Fujihisa H, Sakashita M, Katoh E, Aoki K, Nagashima K, Yamamoto Y, Yagi T (2001) High-pressure structures of methane hydrate observed up to 8 GPa at room temperature. *J Chem Phys* 115(15):7066–7070
- Hirai H, Tanaka T, Kawamura T, Yamamoto Y, Yagi T (2003) Retention of methane hydrate up to 42 GPa. *Phys Rev B* 68:172102
- Hirai S, Komatsu K, Honda M, Kawamura T, Yamamoto Y, Yagi T (2010) Phase changes of CO<sub>2</sub> hydrate under high pressure and low temperature. *J Chem Phys* 133:124511
- Howett CJA, Spencer JR, Pearl J, Segura M (2011) High heat flow from Enceladus' South Polar Region measured using 10–600 cm<sup>-1</sup> Cassini/CIRS data. *J Geophys Res.* doi:[10.1029/2010JE003718](https://doi.org/10.1029/2010JE003718)
- Hurford TA, Helfenstein P, Hoppe GV, Greenberg R, Bills BG (2007) Eruptions arising from tidally controlled periodic openings of rifts on Enceladus controlled by periodic openings of rifts on Enceladus. *Nature* 447:292–294. doi:[10.1038/nature05821](https://doi.org/10.1038/nature05821)
- Hussmann H, Sohl F, Spohn T (2006) Subsurface oceans and deep interiors of medium-sized outer planet satellites and large trans-Neptunian objects. *Icarus* 185:258–273
- Iess L, Rappaport NJ, Jacobson RA, Racioppa P, Stevenson DJ, Tortora P, Armstrong JW, Asmar SW (2010) Gravity field, shape, and moment of inertia of Titan. *Science* 327:1367–1369
- Ingersoll AP, Ewald SP (2009) Ice/vapor ratio in the Enceladus plumes and the mass of Saturn's E ring. *Eos Trans. AGU*, 90(52), Fall meeting supplement, abstract P41D-01
- Iro N, Gautier D, Hersant F, Bockelée-Morvan D, Lunine JI (2003) An interpretation of the nitrogen deficiency in comets. *Icarus* 127:190–212
- Jhaveri J, Robinson DB (1965) Hydrates in the methane-nitrogen system. *Can J Chem Eng* 43:75–78
- Kargel J, Pozio S (1996) The volcanic and tectonic history of Enceladus. *Icarus* 119:385–404
- Kargel JS, Kaye JZ, Head JW, Marion GM, Sassen R, Crowley JK, Prieto-Ballesteros O, Grant SA, Hogenboom DL (2000) Europa's crust and ocean: origin, composition, and prospect for life. *Icarus* 148:226–265
- Kargel J (2006) Enceladus: cosmic gymnast, volatile miniworld. *Science* 311:1389–1391
- Khurana KK, Kivelson MG, Stevenson DJ, Schubert G, Russell CT, Walker RJ, Polanskey C (1998) Oceans in Europa and Callisto: independent evidence from magnetic perturbations. *Nature* 395:777–780
- Kieffer SW, Lu X, Bethke CM, Spencer JR, Marshak S, Navrotksy A (2006) A clathrate reservoir hypothesis for Enceladus South Polar Plume. *Science* 314:1764–1766. doi:[10.1126/science.1133519](https://doi.org/10.1126/science.1133519)
- Kieffer SW, Jakosky BM (2008) Enceladus – oasis or ice ball? *Science* 320(5882):1432–1433. doi:[10.1126/science.1159702](https://doi.org/10.1126/science.1159702)
- Kieffer SW, Lu X, McFarquhar G, Wohletz KH (2009) A redetermination of the ice/vapor ratio of Enceladus' plumes: implications for sublimation and the lack of a liquid water reservoir. *Icarus* 203:238–241. doi:[10.1016/j.icarus.2009.05.011](https://doi.org/10.1016/j.icarus.2009.05.011)

- Kirk RL, Stevenson DJ (1987) Thermal evolution of a differentiated Ganymede and implications for surface features. *Icarus* 69:91–134
- Kobayashi R, Katz DL (1949) Methane hydrate at high pressure. *Trans AIME* 186:66
- Kolb EJ, Tanaka KL (2001) Geologic history of the polar regions of Mars based on Mars global surveyor data. *Icarus* 154:22–39
- Kossacki KJ, Lorenz RD (1996) Hiding Titan's oceans: densification and hydrocarbon storage in an icy regolith. *Planet Space Sci* 44(9):1029–1037
- Kouchi A, Yamamoto T, Kozasa T, Kuroda T, Greenberg JM (1994) Conditions for condensation and preservation of amorphous ice and crystallinity of astrophysical ices. *Astron Astrophys* 290:1009–1018
- Kuhs WF, Klapproth AFG, Techmer K, Heinrichs T (2000) The formation of macroporous and mesoporous gas hydrates. *Geophys Res Lett* 27:2929–2932
- Kuiper GP (1944) Titan: a satellite with an atmosphere. *Astrophys J* 100:378–388
- Kumazaki T, Kito Y, Sasaki S, Kume T, Shimizu H (2004) Single-crystal growth of the high-pressure phase II of methane hydrate and its Raman scattering study. *Chem Phys Lett* 388:18
- Kuskov OL, Kronrod VA (2005) Internal structure of Europa and Callisto. *Icarus* 177:550–569
- Kvenvolden KA (1988) Methane hydrate – a major reservoir of carbon in the shallow geosphere? *Chem Geol* 71:41–51
- Kvenvolden KA (1999) Potential effects of gas hydrates on human welfare. *Proc Natl Acad Sci* 96(7):3420–3426
- Larson SD (1955) Phase studies of the two-component carbon dioxide-water system, involving the carbon dioxide hydrate. Ph.D. thesis, University of Illinois, Urbana
- Laufer D, Pat-El I, Bar-Nun A (2005) Experimental simulation of the formation of non-circular active depressions on Comet Wild-2 and of ice grain ejection from cometary surfaces. *Icarus* 178:248–252. doi:[10.1016/j.icarus.2005.04.019](https://doi.org/10.1016/j.icarus.2005.04.019)
- Lenferink HJ, Durham WB, Stern LA (2009) The strength of clathrate-rich mixtures of ice and methane clathrate hydrate. *Eos Trans AGU* 90 (52), Fall meeting supplement, abstract MR23A-1678, San Francisco
- Lipenkov VY, Istomin VA (2001) On the stability of air clathrate hydrate crystals in subglacial lake Vostok. Antarctica. *Mater Glyatsiol Issled* 91:1–30
- Lodders K (2003) Solar system abundances and condensation temperatures of the elements. *Astrophys J* 591:1220–1247
- Lopes RMC, Mitchell KL, Stofan ER, Lunine JI, Lorenz R, Paganelli F, Kirk RL, Wood CA, Wall SD, Robshaw LE, Fortes AD, Neish CD, Radebaugh J, Reffet E, Ostro SJ, Elachi C, Allison MD, Anderson Y, Boehmer R, Boubin G, Callahan P, Encrenaz P, Flaminii E, Francescetti G, Gim Y, Hamilton G, Hensley S, Janssen MA, Johnson WTK, Kelleher K, Muhleman DO, Ori G, Oroseir R, Picardi G, Posa F, Roth LE, Seu R, Shaffer S, Soderblom LA, Stiles B, Vettella S, West RD, Wye L, Zebker HA (2007) Cryovolcanic features on Titan's surface as revealed by the Cassini Titan Radar Mapper. *Icarus* 186:395–412
- Lopes RMC, Stofan ER, Peckyno R, Radebaugh J, Mitchell KL, Mitri G, Wood CA, Kirk RL, Wall SD, Lunine JI, Hayes A, Lorenz R, Farr T, Wye L, Craig J, Ollerenshaw RJ, Janssen M, LeGall A, Paganelli F, West R, Stiles B, Callahan P, Anderson Y, Valora P, Soderblom L et al (2010) Distribution and interplay of geological processes on Titan from Cassini radar data. *Icarus* 205:540–558
- Lorenz RD, Wood CA, Lunine JI, Wall SD, Lopes RM, Mitchell KL, Paganelli F, Anderson YZ, Wye L, Tsai C, Zebker H, Stofan ER (2007) Titan's young surface: initial impact crater survey by Cassini RADAR and model comparison. *Geophys Res Lett* 34:L07204. doi:[10.1029/2006GL028971](https://doi.org/10.1029/2006GL028971)
- Lorenz RD, Mitchell KL, Kirk RL, Hayes AG, Aharonson O, Zebker HA, Paillou P, Radebaugh J, Lunine JI, Janssen MA, Wall SD, Lopes RM, Stiles B, Ostro S, Mitri G, Stofan ER, The Cassini Radar Team (2008) Titan's inventory of organic surface materials. *Geophys Res Lett* 35:02206
- Loveday JS, Nelmes RJ, Guthrie M, Belmonte SA, Allan DR, Klug DD, Tse JS, Handa YP (2001a) Stable methane hydrate above 2 GPa and the source of Titan's atmospheric methane. *Nature* 410:661–663

- Loveday JS, Nelmes RJ, Guthrie M (2001b) Transition from cage clathrate to filled ice: the structure of methane hydrate III. *Chem Phys Lett* 350:459–465
- Loveday JS, Nelmes RJ (2008) High-pressure gas hydrates. *Phys Chem Chem Phys* 10:937–950
- Lu X, Watson A, Gorin AV, Deans J (2005) Measurements in a low temperature CO<sub>2</sub>-driven geysering well, viewed in relation to natural geysers. *Geothermics* 34:389–410. doi:[10.1016/j.geothermics.2005.05.001](https://doi.org/10.1016/j.geothermics.2005.05.001)
- Lu X, Watson A, Gorin AV, Deans J (2006) Experimental investigation and numerical modelling of transient two-phase flow in a geysering geothermal well. *Geothermics* 35:409–427. doi:[10.1016/j.geothermics.2006.07.001](https://doi.org/10.1016/j.geothermics.2006.07.001)
- Lu X, Kieffer S (2009) Thermodynamics and mass transport in multicomponent, multiphase H<sub>2</sub>O systems of planetary interest. *Annu Rev Earth Planet Sci* 37:449–477. doi:[10.1146/annurev.earth.031208.100109](https://doi.org/10.1146/annurev.earth.031208.100109)
- Lunine JI, Stevenson DJ, Yung YK (1983) Ethane ocean on Titan. *Science* 222(4629):1229–1230
- Lunine JI, Stevenson DJ (1985) Thermodynamics of clathrate hydrate at low and high pressures with application to the outer Solar system. *Astrophys J Suppl Ser* 58:493–531
- Lunine JI, Stevenson DJ (1987) Clathrate and ammonia hydrates at high pressure - Application to the origin of methane on Titan. *Icarus* 70:61–77
- Lunine JI, Atreya SK, Pollack JB (1989) Present state and chemical evolution of the atmospheres of Titan, Triton, and Pluto. In: Atreya SK, Pollack JB, Matthews MS (eds) *Origin and evolution of planetary and satellite atmospheres*. University of Arizona Press, Tucson
- Lunine JI, Choukroun M, Stevenson DJ, Tobie G (2009) Origin and evolution of Titan. In: Brown RH, Lebreton JP, Waite H (eds) *Titan from Cassini-Huygens*. Springer, New York, pp 35–59
- Machida S, Hirai H, Kawamura T, Yamamoto Y, Yagi T (2006) A new high-pressure structure of methane hydrate surviving to 86 GPa and its implications for the interiors of giant icy planets. *Phys Earth Planet Inter* 155:170–176
- Mahaffy PR, Niemann HB, Alpert A, Atreya SK, Demick J, Donahue TM, Harpold DN, Owen TC (2000) Noble gas abundance and isotope ratios in the atmosphere of Jupiter from the Galileo Probe Mass Spectrometer. *J Geophys Res* 105:15061–15072
- Makogon TY (1981) Hydrates of natural gas (trans: Cieslesicz J). Penn Well Books, Tulsa
- Makogon TY, Sloan ED (1994) Phase equilibrium for methane hydrate from 190 to 262 K. *J Chem Eng Data* 39:351–353
- Makogon TY, Mehta AP, Sloan ED (1996) Structure H and structure I hydrate equilibrium data for 2,2-dimethylbutane with methane and xenon. *J Chem Eng Data* 41:315–318
- Manakov AY, Dyadin YA, Ogiенко AG, Kurnosov AV, Aladko EY, Larionov EG, Zhurko FV, Voronin VI, Berger IF, Goryainov SV, Lihacheva AY, Anchakov AI (2009) Phase diagram and high-pressure boundary of hydrate formation in the carbon water system. *J Phys Chem B* 113:7257–7262
- Marboeuf U, Mousis O, Petit J-M, Schmitt B (2010) Clathrate hydrate formation in short-period comets. *Astrophys J* 708:812–816
- Marshall DR, Saito S, Kobayashi R (1964) Hydrates at high pressure: Part 1. methane-water, argon-water and nitrogen-water system. *AICHE J* 10(2):202–205
- Max MD (2000) Natural gas hydrates in oceanic and permafrost environments. Kluwer, Norwell
- McCord TB, Hayne P, Combe J-P, Hansen GB, Barnes JW, Rodriguez S, Le Mouélic S, Baines KH, Buratti BJ, Sotin C, Nicholson P, Jaumann R, Nelson R, The Cassini VIMS Team (2008) Titan's surface: search for spectral diversity and composition using the Cassini VIMS investigation. *Icarus* 194:212–242
- McGuinness MJ, Blakeley M, Pruess K, O'sullivan MJ (1993) Geothermal heat pipe stability: solution selection by upstreaming and boundary conditions. *Transp Porous Media* 11:71–100
- McKay CP, Hand KH, Doran PT, Anderson DT, Priscu J (2003) Clathrate formation and the fate of noble and biologically useful gases in Lake Vostok, Antarctica. *Geophys Res Lett* 30:1702. doi:[10.1029/2003GL017490](https://doi.org/10.1029/2003GL017490)
- McLeod HO, Campbell JM (1961) Natural gas hydrates at pressures to 10,000 psia. *J Pet Tech* 222:590–594

- Meyer J, Wisdom J (2007) Tidal heating in Enceladus. *Icarus* 188:535–539. doi:[10.1016/j.icarus.2007.03.001](https://doi.org/10.1016/j.icarus.2007.03.001)
- Miller SL (1961) The occurrence of gas hydrates in the solar system. *Proc Natl Acad Sci* 47 (11):1798–1808
- Miller SL, Smythe WD (1970) Carbon dioxide clathrate in the Martian ice cap. *Science* 170 (3957):531–533
- Miller SL (1974) The nature and occurrence of clathrate hydrates. In: Kaplan IR (ed) *Natural gas in marine sediments*. Plenum, New York, pp 151–177
- Milkov AV (2004) Global estimates of hydrate-bound gas in marine sediments: how much is really out there? *Earth Sci Rev* 66:183–197
- Mitri G, Showman AP, Lunine JI, Lopes RMC (2008) Resurfacing of Titan by ammonia-water cryomagma. *Icarus* 196:216–224
- Mohammadi AH, Anderson R, Tohidi B (2005) Carbon monoxide clathrate hydrates: equilibrium data and thermodynamic modeling. *AICHE J* 51:2825–2833
- Mohammadi AH, Richon D (2008) Equilibrium data of nitrous oxide and carbon dioxide clathrate hydrates. *J Chem Eng Data* 54:279–281
- Mohammadi AH, Richon D (2010) Ice-clathrate hydrate-gas phase equilibria for air, oxygen, nitrogen, carbon monoxide, methane, or ethane plus water system. *Ind Eng Chem Res* 48:3976–3979
- Moore WB (2006) Thermal equilibrium in Europa's ice shell. *Icarus* 180:141–146
- Moore JM, Pappalardo RT (2011) Titan: an exogenic world? *Icarus* 212:790–806
- Mousis O, Marboeuf U, Lunine JI, Alibert Y, Fletcher LN, Orton GS, Pauzat F, Ellinger Y (2009) Determination of the minimum masses of heavy elements in the envelopes of Jupiter and Saturn. *Astrophys J* 696:1348
- Musselwhite D, Lunine JI (1995) Alteration of volatile inventories by polar clathrate formation on Mars. *J Geophys Res* 100(E11):23301–23306
- Nakano S, Moritoki M, Ohgaki K (1998) High-pressure phase equilibrium and Raman microprobe spectroscopic study on CO<sub>2</sub> hydrate system. *J Chem Eng Data* 43:807–810
- Ng H-J, Robinson DB (1985) Hydrate formation in systems containing methane, ethane, propane, carbon dioxide or hydrogen sulfide in the presence of methanol. *Fluid Phase Equil* 21:145–155
- Niemann HB, Atreya SK, Bauer SJ, Carignan GR, Demick JE, Frost RL, Gautier D, Haberman JA, Harpold DN, Hunten DM, Israel G, Lunine JI, Kasprzak WT, Owen TC, Paulkovich M, Raulin F, Raeraen E, Way SH (2005) The abundances of constituents of Titan's atmosphere from the GCMS instrument on the Huygens probe. *Nature* 438:779–784
- Nimmo F, Spencer JR, Pappalardo RT, Mullen ME (2007) Shear heating as the origin of the plumes and heat flux on Enceladus. *Nature* 447:289–291. doi:[10.1038/nature05783](https://doi.org/10.1038/nature05783)
- Nimmo F, Bills BG (2010) Shell thickness variations and the long-wavelength topography of Titan. *Icarus* 208:896–904
- Nelson RM, Kamp LW, Matson DL, Irwin PGJ, Baines KH, Boryta MD, Leader FE, Jaumann R, Smythe WD, Sotin C, Clark RN, Cruikshank DP, Drossart P, Pearl JC, Hapke BW, Lunine JI, Combes M, Bellucci G, Bibring J-P, Capaccioni F, Cerroni P, Coradini A, Formisano V, Filacchione GR, Langevin Y, McCord TB, Mennella V, Nicholson PD, Sicardy B (2009) Saturn's Titan: surface change, ammonia, and implications for atmospheric and tectonic activity. *Icarus* 199:429–441
- Notesco G, Bar-Nun A (2000) The effect of methanol clathrate-hydrate formation and other gas-trapping mechanisms on the structure and dynamics of cometary ices. *Icarus* 148:456–463
- Notesco G, Bar-Nun A, Owen T (2003) Gas trapping in water ice at very low deposition rates and implications for comets. *Icarus* 162:183–189
- Osegovic JP, Max MD (2005) Compound clathrate hydrate on Titan's surface. *J Geophys Res* 110:8004
- Owen T, Niemann HB (2009) The origin of Titan's atmosphere: some recent advances. *Phil Trans R Soc A* 367:607–615
- Pappalardo R, Belton M, Breneman M, Carr M, Chapman C, Collins G, Denk T, Fagents S, Geissler P, Giese B, Greeley R, Greenberg R, Head J, Helfenstein P, Hoppa G, Kadel S,

- Klaasen K, Klemaszewski J, Magee K, McEwen A, Moore J, Moore M, Neukum G, Phillips C, Prockter L, Schubert G, Senske D, Sullivan R, Tufts B, Turtle E, Wagner R, Williams K (1999) Does Europa have a subsurface ocean? Evaluation of the geological evidence. *J Geophys Res* 104:24015–24056
- Porco C, Helfenstein P, Thomas PC, Ingersoll AP, Wisdom J, West R, Neukum G, Denk T, Wagner R, Roatsch T, Kieffer S, Turtle E, McEwen A, Johnson TV, Rathbun J, Veverka J, Wilson D, Perry J, Spitale J, Brahic A, Burns JA, DelGenio AD, Dones L, Murray CD, Squyres S (2006) Cassini observes the active south pole of Enceladus. *Science* 311:1393–1401. doi:[10.1126/science1123013](https://doi.org/10.1126/science1123013)
- Postberg F, Kempf S, Schmidt J, Brilliantov N, Beinsen A, Abel B, Buck U, Srama R (2009) Sodium salts in E-ring ice grains from an ocean below the surface of Enceladus. *Nature* 459:1098–1101. doi:[10.1038/nature08046](https://doi.org/10.1038/nature08046)
- Prieto-Ballesteros O, Kargel JS, Fernández-Sampedro M, Selsis F, Martínez EF, Hogenboom DL (2005) Evaluation of the possible presence of clathrate hydrates in Europa's icy shell or seafloor. *Icarus* 177:491–505
- Ripmeester JA, Ratcliffe CI, Klug DD, Tse JS (1994) Molecular perspectives on structure and dynamics in clathrate hydrates. *Ann NY Acad Sci* 715:161
- Roberts OL, Brownscombe ER, Howe LS (1940) Methane and ethane hydrates. *Oil Gas J* 39:37
- Robinson DB, Mehta BR (1971) Hydrate formation in systems containing methane, hydrogen sulphide, and carbon dioxide. *J Can Pet Tech* 10:33
- Ross RG, Andersson P, Backstrom G (1981) Unusual PT dependence of thermal conductivity for a clathrate hydrate. *Nature* 290:322–323
- Ross RG, Andersson P (1982) Clathrate and other solid phases in the tetrahydrofuran – water system: thermal conductivity and heat capacity under pressure. *Can J Chem* 60(7):881–892
- Sagan C, Dermott SF (1982) Tides in the seas of Titan. *Nature* 300:731–733
- Saur J, Schilling N, Neubauer FM, Strobel DF, Simon S, Dougherty M, Russell C, Pappalardo RT (2008) Evidence for temporal variability of Enceladus' gas jets: modeling of Cassini observations. *Geophys Res Lett* 35:L20105. doi:[10.1029/2008GL035811](https://doi.org/10.1029/2008GL035811)
- Schenk PM, McKinnon WB (2009) One-hundred-km-scale basins on Enceladus: evidence for an active ice shell. *Geophys Res Lett* 36:L16202. doi:[10.1029/2009GL039916](https://doi.org/10.1029/2009GL039916)
- Schmidt J, Brilliantov N, Spahn F, Kempf S (2008) Slow dust in Enceladus' plume from condensation and wall collisions in tiger stripe fractures. *Nature* 451:685–688. doi:[10.1038/nature06491](https://doi.org/10.1038/nature06491)
- Schmitt B (1986) La surface de la glace: structure, dynamique et interactions – implications astrophysiques. Ph.D. thesis, Université de Grenoble, France
- Schubert G, Zhang K, Kivelson MG, Anderson JD (1996) The magnetic field and internal structure of Ganymede. *Nature* 384:544–545
- Selleck FT, Carmichael LT, Sage BH (1952) Phase behavior in the hydrogen sulfide – water system. *Ind Eng Chem* 44:2219
- Shimizu H, Kumazaki T, Kume T, Sasaki S (2002) In situ observations of high-pressure phase transformations in a synthetic methane hydrate. *J Phys Chem B* 106:30–33
- Shoji H, Langwely CC (1982) Air hydrate inclusions in fresh ice core. *Nature* 298:548–550. doi:[10.1038/298548a0](https://doi.org/10.1038/298548a0)
- Showman AP, Stevenson DJ, Malhotra R (1997) Coupled orbital and thermal evolution of Ganymede. *Icarus* 129:367–383
- Sloan ED (1998) Clathrate hydrates of natural gases, 2nd edn. Marcel Dekker, New York
- Sloan ED (2003) Fundamental principles and applications of gas hydrates. *Nature* 426:353–363
- Sloan ED, Koh C (2007) Clathrate hydrates of natural gases, 3rd edn. CRC press, Boca Raton
- Sohl F, Spohn T, Breuer D, Nagel K (2002) Implications from Galileo observations on the internal structure and chemistry of the Galilean satellites. *Icarus* 157:104–119
- Sohl F, Hussmann H, Schwentker B, Spohn T, Lorenz RD (2003) Interior structure models and tidal Love numbers of Titan. *J Geophys Res* 108(E12):5130, CiteID
- Sohl F, Choukroun M, Kargel JS, Kimura J, Pappalardo R, Vance S, Zolotov M (2010) Oceans within icy moons. *Space Sci Rev* 153:485–510. doi:[10.1007/s11214-010-9646-y](https://doi.org/10.1007/s11214-010-9646-y)

- Sotin C, Head JW, Tobie G (2002) Europa: tidal heating of upwelling thermal plumes and the origin of lenticulae and chaos melting. *Geophys Res Lett* 29(8). doi:[10.1029/2001GL013844](https://doi.org/10.1029/2001GL013844)
- Sotin C, Tobie G (2004) Internal structure and dynamics of the large icy satellites. *CR Phys* 5:769–780
- Sotin C, Jaumann R, Buratti BJ, Brown RH, Clark RN, Soderblom LA, Baines KH, Bellucci G, Bibring J-P, Capaccioni P, Combes M, Coradini A, Cruikshank DP, Drossart P, Formisano V, Langevin Y, Matson DL, McCord TB, Nelson RM, Nicholson PD, Sicardy B, LeMouelic S, Rodriguez S, Stephan K, Scholz CK (2005) Release of volatiles from a possible cryovolcano from near-infrared imaging of Titan. *Nature* 435:786–789
- Sotin C, Mitri G, Rappaport N, Schubert G, Stevenson DJ (2009) The internal structure of Titan. In: Brown RH, Lebreton JP, Waite H (eds) *Titan from Cassini-Huygens*. Springer, New York, pp 61–73
- Spaun A, Head JW (2001) A model of Europa's crustal structure: recent Galileo results and implications for an ocean. *J Geophys Res* 106:7567–7576
- Spencer JR, Pearl JC, Segura M, Flasar FM, Mamoutkine A, Romani P, Buratti BJ, Hendrix AR, Spilker LJ, Lopes RMC (2006) Cassini encounters Enceladus: background and the discovery of a South Polar hot spot. *Science* 311:1401–1405. doi:[10.1126/science.1121661](https://doi.org/10.1126/science.1121661)
- Spencer J, Howett C, Pearl J, Segura M (2009a) High-resolution observations of Enceladus' endogenic thermal radiation in 2008. *EOS Trans. AGU*, 90(22), Joint Assembly Supplementary abstract P33A-04
- Spencer JR, Barr AC, Esposito LW, Helfenstein P, Ingersoll AP, Jaumann R, McKay CP, Nimmo F, Hunter JH (2009b) Enceladus: an active Cryovolcanic Satellite. In: Dougherty MK, Esposito LW, Krimigis SM (eds) *Saturn from Cassini-Huygens*. Springer, New York, pp 683–724
- Spitale JN, Porco CC (2007) Association of the jets of Enceladus with the warmest regions on its south-polar fractures. *Nature* 449:695–697. doi:[10.1038/nature06217](https://doi.org/10.1038/nature06217)
- Spohn T, Schubert G (2003) Oceans in the icy Galilean satellites of Jupiter? *Icarus* 161:456–467
- Squyres SW, Reynolds RT, Cassen PM, Peale SJ (1983a) Liquid water and active resurfacing on Europa. *Nature* 301:225–226
- Squyres SW, Reynolds RT, Cassen PM, Peale SJ (1983b) The evolution of Enceladus. *Icarus* 53:319–331
- Stern LA, Kirk SH, Durham WB (1996) Peculiarities of methane clathrate hydrate formation and solid-state deformation, including possible superheating of water ice. *Science* 273:1843–1848
- Stevenson DJ (1992) Interior of Titan. In: *Proceedings of the ESA's symposium on Titan*, Noordwijk, pp 29–33
- Stofan ER, Elachi C, Lunine JI, Lorenz RD, Stiles B, Mitchell KL, Ostro S, Soderblom L, Wood C, Zebker H, Wall S, Janssen M, Kirk R, Lopes R, Paganelli F, Radabaugh J, Wye L, Anderson Y, Allison M, Boehmer R, Callahan P, Encrenaz P, Flaminii E, Francescetti G, Gim Y, Hamilton G, Hensley S, Johnson WTK, Kelleher K, Muhleman D, Paillou P, Picardi G, Posa F, Roth L, Seu R, Shaffer S, Vetrella S, West R (2007) The lakes of Titan. *Nature* 445:61–64
- Takenouchi S, Kennedy GC (1965) Dissociation pressure of the phase CO<sub>2</sub>. 5 H<sub>2</sub>O. *J Geol* 73:38
- Thakore JL, Holder GD (1987) Solid vapor azeotropes in hydrate-forming systems. *Ind Eng Chem Res* 26:462
- Thomas C, Mousis O, Ballenegger V, Picaud S (2007) Clathrate hydrates as a sink of noble gases in Titan's atmosphere. *Astron Astrophys* 474:L17–L20
- Tobie G, Choblet G, Sotin C et al (2003) Tidally heated convection: Constraints on Europa's ice shell thickness. *J Geophys Res* 108:5124
- Tobie G, Grasset O, Lunine JI, Mocquet A, Sotin C (2005) Titan's internal structure inferred from a coupled thermal-orbital model. *Icarus* 175:496–502
- Tobie G, Lunine JI, Sotin C (2006) Episodic outgassing as the origin of atmospheric methane on Titan. *Nature* 440:61–64
- Tobie G, Cadek O, Sotin C (2008) Solid tidal friction above a liquid water reservoir as the origin of the South Pole hotspot on Enceladus. *Icarus* 196:642–652

- Tobie G, Choukroun M, Grasset O, Le Mouelic S, Lunine JI, Sotin C, Bourgeois O, Gautier D, Hirtzig M, Lebonnois S, Le Corre L (2009) Evolution of Titan and implications for its hydrocarbon cycle. *Philo Trans R Soc A* 367:619–631
- Tomasko MG, Archinal B, Becker T, Bézard B, Bushroe M, Combers M, Cook D, Coustenis A, de Bergh C, Dafoe LE, Doose L, Douté S, Eibl A, Engel S, Gliem F, Grieger B, Holso K, Howington-Kraus E, Karkoschka E, Keller HU, Kirk R, Kramm R, Küppers M, Lanagan P, Lellouch E, Lemmon M, Lunine JI, McFarlane E, Moores J, Prout GM, Rizk B, Rosiek M, Rueffer P, Schröder SE, Schmitt B, See C, Smith P, Soderblom LA, Thomas N, West R (2005) Rain, wind and haze during the Huygen's probe descent to Titan's surface. *Nature* 438:765–778
- Tse JS, White MA (1988) Origin of glassy crystalline behavior in the thermal properties of clathrate hydrates: a thermal conductivity study of tetrahydrofuran hydrate. *J Phys Chem* 92:5006–5011
- Tse JS, Shpakov VP, Murashov VV, Belosludov VR (1997) The low frequency vibrations in clathrate hydrates. *J Chem Phys* 107:9271–9274
- Uchida T, Hondoh T, Mae S, Lipenkov VY, Duval P (1994) Air-hydrate crystals in deep ice-core samples from Vostok Station, Antarctica. *J Glaciol* 40(134):79–86
- Unruh CH, Katz DL (1949) Gas hydrates of carbon dioxide – methane mixtures. *Trans AIME* 186:83
- Vance SD, Harnmeijer J, Kimura J, Hussmann H, deMartin B, Brown JM (2007) Hydrothermal circulation in small ocean-planets. *Astrobiology* 7:987–1005
- van Cleef A, Diepen GAM (1960) Gas hydrate of nitrogen and oxygen. *Rec Trav Chim* 79:582
- van der Waals JH, Platteuw JC (1959) Clathrate solutions, vol 2, *Advances in Chemical Physics*. Interscience, New York, pp 1–57
- Verma VK (1974) Gas hydrates from liquid hydrocarbon – water mixtures. Ph.D. thesis, University of Michigan, University Microfilms NO. 75–10,324, Ann Arbor
- Waite JH, Niemann H, Yelle RV, Kasprzak WT, Cravens TE, Luhmann JG, McNutt RL, Ip W-H, Gell D, De La Haye V, Müller-Wordag I, Magee B, Borggren N, Ledvina S, Fletcher G, Walter E, Miller R, Scherer S, Thorpe R, Xu J, Block B, Arnett K (2005) Ion neutral mass spectrometer results from the first flyby of Titan. *Science* 308:982–986
- Waite JH, Combi MR, Ip W-H, Craven TE, McNutt RL, Kasprzak W, Yelle R, Luhmann J, Niemann H, Gell D, Magee B, Fletcher G, Lunine J, Tseng W-L (2006) Cassini ion and neutral mass spectrometer: Enceladus plume composition and structure. *Science* 311:1419–1422. doi:[10.1126/science.1121290](https://doi.org/10.1126/science.1121290)
- Waite JH, Lewis WS, Magee BA, Lunine JI, McKinnon WB, Glein CR, Mousis O, Young DT, Brockwell T, Westlake J, Nguyen M-J, Teolis BD, Niemann HB, McNutt RL, Perry M, Ip W-H (2009) Liquid water on Enceladus from observations of ammonia and 40Ar in the plume. *Nature* 460:487–490. doi:[10.1038/nature08153](https://doi.org/10.1038/nature08153)
- Wall SD, Lopes RM, Stofan ER, Wood CA, Radebaugh JL, Horst SM, Stiles BW, Nelson RM, Kamp LW, Janssen MA, Lorenz RD, Lunine JI, Farr TG, Mitri G, Paillou P, Paganelli F, Mitchell KL (2009) Cassini RADAR at Hotei Arcus and Western Xanadu, Titan: evidence for geologically recent cryovolcanic activity. *Geophys Res Lett* 36:L04203. doi:[10.1029/2008GL036415](https://doi.org/10.1029/2008GL036415)
- Yasuda K, Ohmura R (2008) Phase equilibrium for clathrate hydrates formed with methane, ethane, propane, or carbon dioxide at temperatures below the freezing point of water. *J Chem Eng Data* 53:2182–2188
- Yung YL, Allen M, Pinto JP (1984) Photochemistry of the atmosphere of Titan – comparison between mode and observations. *Astrophys J Suppl Ser* 55:465–506
- Zahnle K, Pollack JB, Grinspoon D, Dones L (1992) Impact-generated atmospheres over Titan, Ganymede, and Callisto. *Icarus* 95(1):1–23
- Zolotov MY, Shock EL (2001) Composition and stability of salts on the surface of Europa and their oceanic origin. *J Geophys Res* 106:32815–32827
- Zolotov MY, Kargel JS (2009) On the composition of Europa's icy shell, ocean and underlying rocks. In: Pappalardo RT, McKinnon WB, Khurana K (eds) *Europa*. University of Arizona Press, Tucson

# Chapter 13

## Cometary Ices

**Carey Lisse, Akiva Bar-Nun, Diana Laufer, Michael Belton,  
Walter Harris, Henry Hsieh, and David Jewitt**

**Abstract** The purpose of this chapter is to survey the *empirical* situation of cometary ices, as they are known today – their location in the solar system, the discernable nature of the ices from remote sensing measurements, and the important physico-chemical properties of the ice known from previous laboratory studies. We then attempt to synthesize this phenomenological data into a framework for recognizing the most important unresolved issues in understanding the behavior of low temperature, porous, mixed amorphous/crystalline and radiation damaged ices together with their ability to trap gases and release them upon warming – with the hope of launching new, important laboratory studies of cometary ice analogues.

For an excellent earlier review discussing physico-chemical *models* of the origin of cometary ices in the ISM, dense cloud cores, and the proto-solar nebula, we suggest the reader examine Ehrenfreund et al. (2002).

---

C. Lisse (✉)

Applied Physics Laboratory, Johns Hopkins University, Baltimore, USA

e-mail: [carey.lisse@jhuapl.edu](mailto:carey.lisse@jhuapl.edu)

A. Bar-Nun • D. Laufer

Department of Geophysics and Planetary Sciences, Tel-Aviv University, Tel-Aviv, Israel

M. Belton

Belton Space Exploration Initiatives, LLC, Tucson, USA

W. Harris

University of California at Davis, Davis, USA

H. Hsieh

Queens University, Belfast, UK

D. Jewitt

University of California, Los Angeles, USA

### 13.1 The Main Reservoirs of Cometary Ice in the Solar System

Ice from the protoplanetary disk of the Sun now largely resides in several, distinct reservoirs in the modern Solar system.

The current paradigm of planetary system formation invokes the condensation of refractory materials (this term can be understood roughly as “rocky” materials) in the thick proto-solar disk, surrounded by a gaseous envelope. Eventually the solid grains settle into a thin disk, mix with local gas and ices (beyond the ice line), and aggregation into larger bodies begins. Dust grains grow to become pebbles, then boulders, then kilometer-sized and 100-kilometer-sized planetesimals – comets and asteroids – the building blocks of solid planets (e.g. Weidenschilling 2005). Planetesimals that formed in the region of the gas giants were either incorporated into the planets or rapidly ejected (Stern and Weissman 2001; Dones et al. 2004; Fernández 2007). Most escaped the Solar System entirely, but a large population was captured by stellar and galactic perturbations into the Oort cloud. Oort comets may be gravitationally scattered back into the inner Solar System to appear as dynamically new long-period comets, some of which are eventually captured into Halley-family short-period orbits.

The 50,000 AU – scale Oort cloud holds  $10^{11}$  constituent comets (Francis 2005) in a spherical swarm so large that external perturbations from the Milky Way galaxy and from the gravity of passing stars play a major destabilizing role. Comets deflected inwards from the Oort cloud enter the planetary region on eccentric, randomly-inclined orbits with large semimajor axes and long periods: these are the Long Period Comets (LPCs) or “Oort Cloud comets”. The total mass of the Oort cloud comets is  $\sim 10^1 M_\oplus$  (Hahn and Malhotra 1999): it could be an order of magnitude smaller but probably not an order of magnitude larger.

In the cool outer disk (beyond Jupiter’s orbit), the planetesimals incorporated frozen volatiles (Fig. 13.1) as well as refractory material. The trans-Neptunian region is occupied by numerous bodies with sizes up to several 1,000 km (Pluto and other dwarf planets). The Kuiper belt contains about 70,000 comets larger than 100 km in diameter, and perhaps 0.1–1 billion larger than 1 km in size (Chiang and Brown 2001; Levison and Morbidelli 2003; Vitense et al. 2010). The combined mass of Kuiper belt objects is  $(1-10) \times 10^{-2} M_\oplus$ . Collisions in this population generate fragments, some of which were scattered inwards by dynamical chaos to become intra-planet wanderers. These wanderers have short dynamical lifetimes, and are ejected from the Solar System entirely through gravitational interactions, or scatter further inward, where they begin to sublime and are re-classified first as Centaurs in the giant planet region, and then Jupiter-family short-period comets in the inner Solar System. The Kuiper belt is the local analog of the “debris” dust disks observed around many nearby main-sequence stars (dust in our own Kuiper belt has not been observed astronomically but dust impacts onto the Voyager spacecraft have been detected, Gurnett et al. 1997).

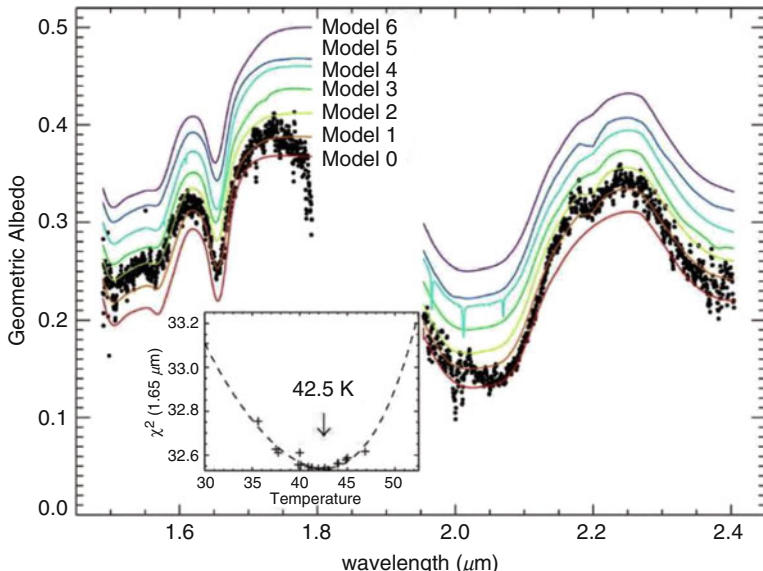


**Fig. 13.1** Near infrared spectrum of Charon, the satellite of large Kuiper belt object 134340 Pluto, with inset showing in greater detail the 1.65  $\mu\text{m}$  band diagnostic of crystalline water ice (From Cook et al. (2007))

Closer still, and discovered only in 2006, the outer regions of the asteroid belt contain icy objects that are, in all probability, left-overs from protoplanetary disk accretion just beyond the snow-line. To date, five objects, dynamically indistinguishable from main-belt asteroids (i.e., without strong dynamical interactions with Jupiter) which display cometary activity (indicating the likely presence of ice) are known: 133P/Elst-Pizarro (also 7968 Elst-Pizarro), P/2005 U1 (Read), 176P/LINEAR (also 118401 LINEAR), P/2008 R1 (Garradd), and P/2010 A2 (LINEAR). These objects have been dubbed “main-belt comets” (MBCs; Hsieh and Jewitt 2006). The closest MBC to the Sun (P/2010 A2) has a semimajor axis at 2.3 AU, while the next closest (P/2008 R1) is at 2.7 AU, and the remaining three have semimajor axes near 3.2 AU.

In using these objects as tracers of the primordial snow-line, it is important to consider their likely dynamical histories and whether their behavior does in fact indicate sublimation-driven activity. Indeed, dynamical modeling suggests that P/2008 R1 is not native to its current location and may have originated further from the Sun in the outer belt where the majority of currently-known MBCs are found (Jewitt et al. 2009). The nature of the newly discovered P/2010 A2 is as yet unclear, though preliminary results (Scotti et al. 2010a, b; Jewitt et al. 2010) suggest that its dust tail may have actually formed from ejecta from a high-velocity impact between two asteroids, rather than truly cometary (i.e. sublimation-driven) dust emission. These two examples aside, analyses of the remaining three MBCs (133P/Elst-Pizarro, P/2005 U1, and 176P/LINEAR) indicate that they all likely formed in

situ and exhibit activity characteristic of sublimating ice (Haghighipour 2009; Hsieh and Jewitt 2006; Hsieh et al. 2009).

It should be noted that ice is not completely unexpected in the asteroid belt. Evidence that asteroids may have contained water (likely in the form of ice) in the past is well-known. Spectroscopic evidence of hydrated minerals has been observed for main-belt asteroids in both infrared observations (e.g., Lebofsky 1980; Lebofsky et al. 1981; Feierberg et al. 1985; Jones et al. 1990; Vernazza et al. 2005) and visible observations (e.g., Vilas et al. 1994; Barucci et al. 1998). CI and CM carbonaceous chondrite meteorites linked with main-belt asteroids have also been shown to contain hydrated minerals (e.g., Hiroi et al. 1996; Burbine 1998; Keil 2000). Theoretical studies also show that the snow line (the boundary in the early solar system outside of which the protoplanetary disk was cold enough for water to freeze and be incorporated into accreting planetesimals) could have been as close to the Sun as the orbit of Mars, or even closer (e.g., Sasselov and Lecar 2000; Ciesla and Cuzzi 2006; Lecar et al. 2006). New results in the last year, e.g., the remote sensing detection of free water and hydrated minerals on the surfaces of 24 Themis (Campins et al. 2010; Rivkin and Emery 2010) and 65 Cybele (Licandro et al. 2011) have added to detection of asteroids containing water-associated materials in the main belt.

The case for *water ice currently* being present in the main belt has been made by investigators who noted that a decline in the abundance of aqueously altered minerals in more distant main-belt asteroids (beyond 3 AU, where the first three MBCs are found) could be evidence that water on those bodies never reached temperatures high enough to melt and drive hydration reactions, and thus could remain frozen today (Jones et al. 1990; Scott and Krot 2005). Thermal modeling of CM chondrite production additionally indicates that even for small parent bodies on which past aqueous alteration did take place, the bulk of each body's ice must have remained frozen given the temperature distribution dictated by the models (Grimm and McSween 1989). Likewise, modeling of Ceres has highlighted the critical role played by water (possibly constituting 15–30% of the body by mass) in the object's thermal evolution, and even suggested the possible existence of a once-liquid water mantle (McCord and Sotin 2005), though these results have been disputed by Zolotov (2009) who notes that the upcoming Dawn mission may resolve many of these questions.

In terms of survivability of ice in the asteroid belt, although surface ice is expected to be unstable over geologically long timescales (Hsieh et al. 2004), thermal models have shown that subsurface ice on main-belt objects could be stable against sublimation over the age of the solar system protected by little more than a few meters of dusty surface regolith (Fanale and Salvail 1984; Schorghofer 2008). The total mass of ice contained in main-belt objects is uncertain but very small: an informed guess would be  $10^{-5} M_{\oplus}$  (using the hypothesis that all main-belt asteroids beyond 3 AU are composed of perhaps 5–10% ice by mass).

The three cometary reservoirs, Oort cloud, Kuiper belt and MBCs, provide three distinct samples from the Sun's accretions disk. The MBCs and JFCs probably formed in-situ in the asteroid belt and Kuiper belt near 3 AU and 20–30 AU, respectively, while Oort cloud comets formed between Jupiter and Neptune and

were subsequently scattered out of the planetary region. Comets from the different reservoirs therefore sample the disk at radii different by an order of magnitude and accretion temperatures different by a factor of three or more.

[Separately from the three cometary reservoirs, solar system ice is also to be found in the satellites of the major planets. The satellites and the ice they contain have, in many cases, been accumulated by processes rather different from those that formed the comets. Accretion timescales in circum-planetary disks, for one thing, are much shorter than in the circum-solar disk, as a result of the smaller sizes and higher densities and shorter- orbital periods around the planets compared to the same quantities for bodies in much larger orbits about the Sun. Energy input from mass deposition was also much higher during their formation. The relatively recent discovery of significant tidal energy input has been shown to substantially alter many of these objects, with the effect being definitive for the structure of several (e.g. Europa, Ganymede, Enceladus). As a result, the ices have probably experienced different formation conditions and different thermal histories, and we leave a discussion of their icy makeup to other chapters in this book. An interesting exception is provided by the irregular satellites (which, although mostly small, actually outnumber the known regular satellites). The irregulars were almost certainly captured around their planets following formation in orbit about the Sun, probably at early times (Jewitt and Haghighipour 2007). Capture has also been suggested as a possible origin of the giant planet Trojans. Unfortunately, the ice content of these bodies has so-far eluded empirical determination].

## 13.2 The Expected Nature of Ices in Comets

We know something of the formation conditions for cometary ices from the measured abundances of gaseous species in the neutral atmosphere, or coma, surrounding an active comet. In order for comets to have a “classical” relative abundance of icy volatile species on the order of H<sub>2</sub>O:CO:CH<sub>3</sub>OH:H<sub>2</sub>CO:H<sub>2</sub>S:HCN:CS = 100:<10:2.7:<1.5:0.5:0.12:<0.13 (Biver et al. 2007), the ice grains which agglomerated to form the nucleus had to be formed at about 25 K (Notesco and Bar-Nun 2005). This is in good agreement with the 25–35 K estimates for the formation temperatures of water and ammonia in comets (Kawakita et al. 2001, 2002, 2004). At this temperature, the water molecules which form the grains stick wherever they hit, forming an open ice structure. The gas molecules, present when the porous ice structure is formed, enter the open pores and reside there by van der Waals forces between them and the dangling OH groups on the pore wall. If before leaving the pore, another ice layer is formed, the gas is trapped. The trapped gas begins to escape when the ice changes its structure: First during its slow annealing between 35–120 K (*b* and *d* in Fig. 13.2). Then, more vigorously between 120–140 K when the annealed ice transforms into cubic ice and restrained amorphous form (Jenniskens and Blake 1994; *e* in Fig. 13.2). This major shift in the position of the water molecules in the ice results in a major release of the gases that

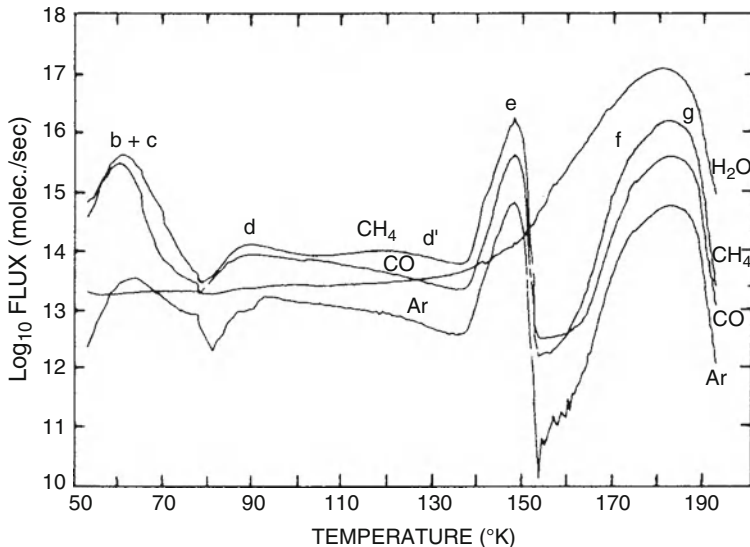


**Fig. 13.2** A plot of the fluxes of gas and water vapor versus temperature. The gas-rich amorphous ice was condensed at 50 K from a  $\text{H}_2\text{O}:\text{CH}_4:\text{CO}:\text{Ar}$  1:0.33:0.33:0.33 mixture. The various ranges of gas evolution (*b*–*g*) are labeled. Note the changes in gas evolution over six orders of magnitude (From Bar-Nun and Kliefeld (1989))

were trapped in the closed pores of the ice. Another phase of gas release occurs during the transformation into hexagonal ice at about 160 K (*f* in Fig. 13.2). All these movements of the water molecules in the ice both release some of the trapped gases but also close more tightly a fraction of these gases, which are released *only* when the ice itself sublimates. Below we show the experimentally observed gas release stages when a sample of gas-laden amorphous ice is warmed. A major point to be noted is that different gases such as  $\text{CH}_4$ ,  $\text{CO}$ ,  $\text{Ar}$  are all released from the ice at the same temperatures, which correspond to changes in the ice matrix and *not* to the sublimation of the gases themselves.

The strongest observational evidence for this process, as opposed to a composition dominated by a blending of materials in the ice phase, comes from the relatively constant mass ratios observed in outgassed materials as a function of heliocentric distance for the extremely active comet C/1995 O1 (Hale-Bopp), detected in many species at large distances from the Sun both pre- and post-perihelion (Biver et al. 1997; Fig. 13.3). A purely sublimation driven composition would have radical changes in mass fraction as the various surface ices sublimated following their individual vapor pressure relations.

Supporting evidence for this model is also provided by the results of the 2005 Deep Impact experiment, which showed little to no change in the ratio of emitted volatile abundances before and after impact (Biver et al. 2007; Cochran et al. 2007; Feldman et al. 2010 and references therein), and by the recent calculations of Marboeuf et al. (2010).

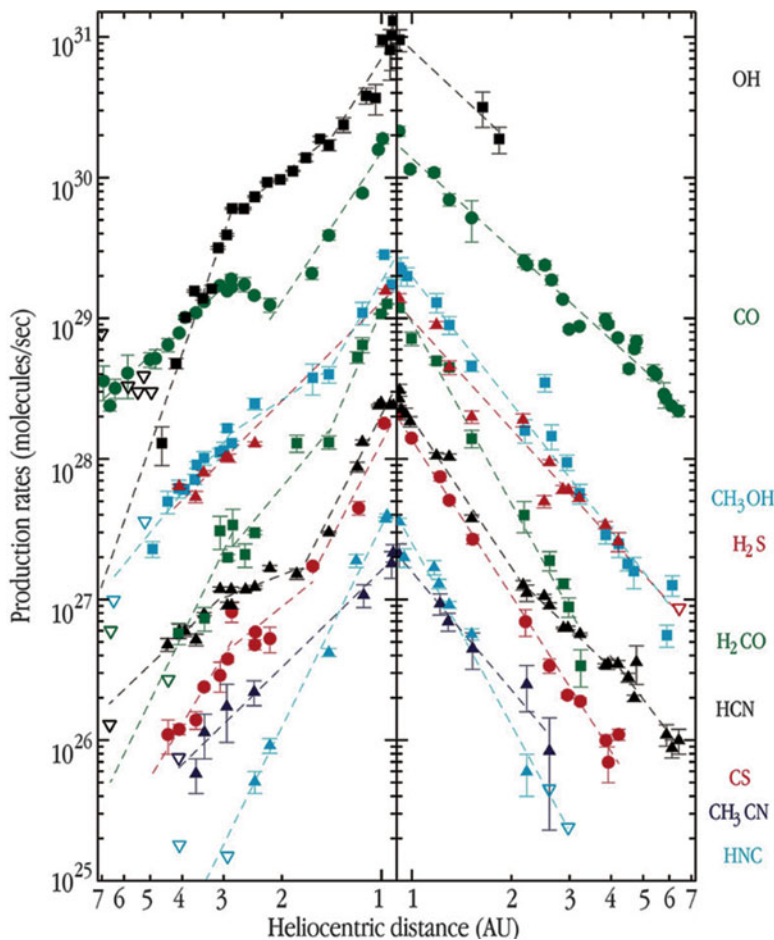


**Fig. 13.3** Changes in gas production rate as a function of heliocentric distance from comet C/1995 O1 (Hale-Bopp) show relatively constant mass fractions for the non-water bearing species despite their very different sublimation relations (After Biver et al. 1997, 2002)

**Crystalline State of the Ice.** One of the most basic issues concerns the crystalline vs. amorphous state of cometary ice. The crystallinity is important on at least two levels. First, amorphous ice can have an especially intricate physical structure with a large specific area ( $\sim 0.1 \text{ km}^2 \text{ kg}^{-1}$ ; Bar-Nun et al. 1987) and can be a very effective sponge for other molecules of cometary relevance (Bar-Nun et al. 2007). This is important both for understanding the compositions of the comets and related bodies in the source reservoirs and perhaps also for understanding the origin of the atmospheres of the Earth and other planets, since these might have been derived, in part, from the impact of comets (Owen 2007). Second, the crystallization of ice is exothermic, releasing about  $9 \times 10^4 \text{ J kg}^{-1}$ . This energy can provide a heat source in ice above and beyond that offered by the Sun. Under the right circumstances, it

might even drive a thermal runaway in which heat released from one parcel of amorphous ice triggers the crystallization of nearby ice. Models including such processes have met with success in fitting various observations of comets (Prialnik et al. 2004). The re-ordering of the bonds that occurs at crystallization results in the sudden release of the trapped gases, perhaps explaining outbursts and other features of the comets.

Amorphous ice (typically formed at low temperatures and densities) is never thermo-dynamically stable, but transforms to the crystalline state on the timescale

$$\tau_{cr} = 3.0 \times 10^{-21} \exp(\Delta E_{crystallization}/RT) \quad (13.1)$$

where  $\Delta E_{crystallization} = 44.6 \text{ kJ/mol}$  (or  $\Delta E_{crystallization}/R = 5370 \text{ K}$ , Schmitt et al. 1989),  $R = 8.31 \text{ J K}^{-1} \text{ mol}^{-1}$  is the ideal gas constant, and  $T [\text{K}]$  is the ice absolute temperature. Equation 13.1 gives the timescale in years. Setting  $\tau_{cr} = 4.5 \text{ Gyr}$  in Eq. 13.1, we find that ice colder than  $T \sim 77 \text{ K}$  can persist in the amorphous state for longer than the age of the Solar system, while ice held at a higher temperature should have already crystallized. The spherical blackbody temperature of an isothermal object (i.e. one of small size and/or high thermal conductivity) in orbit about the Sun is

$$T_{BB} = 280 R_{AU}^{-1/2} \quad (13.2)$$

where  $R_{AU}$  is the heliocentric distance in AU. From Eq. 13.2,  $T_{BB} = 77 \text{ K}$  corresponds to  $R_{AU} = 13 \text{ AU}$ . Assuming no other energy sources other than the Sun, we should expect that ice in the middle and outer solar system reservoirs should be amorphous, while ice in the main-belt comets must be crystalline.

### 13.3 Studies of Water Ice in Comets from Remote Sensing

**Amorphous and Crystalline Water Ice.** Direct observational evidence for amorphous or crystalline water ice in cometary bodies is weak to non-existent. No features attributable to water ice were found in the quick scans across the nucleus of 19P/Borrelley by the DS-1 MICAS near-IR spectrometer at 1.3–2.6  $\mu\text{m}$  (Soderblom et al. 2004). Weak signatures due to  $\sim 100 \mu\text{m}$  grains of recondensed water ice were found to cover a very small percentage ( $\sim 0.5\%$ ) of the surface of comet 9P/Tempel 1 by the Deep Impact HRI-IR spectrometer at  $\sim 1.5$  and  $\sim 2 \mu\text{m}$ , but no clear  $1.65 \mu\text{m}$  feature due to crystalline water ice was found (Sunshine et al. 2006). The amount of exposed water ice detected was much too small to support the observed coma outgassing from Tempel 1; this had to be supplied from subsurface ice. Grains in the comae of comets C/Hale-Bopp and C/2002 T7 (LINEAR) showed near-infrared bands due to water ice but the  $1.65 \mu\text{m}$  crystalline band was not clearly detected (Davies et al. 1997; Kawakita et al. 2004).

This is consistent with amorphous ice but still somewhat ambiguous because the scattering from optically small, possible dirty coma grains might not show the band as clearly as in a larger sample. Lellouch et al. (1998) inferred from their observations of Hale-Bopp that the NIR spectra do not match amorphous ice but are typical of crystalline ice.

Infrared spectra of Kuiper belt objects at 30 AU and beyond show a different result. In every case where the spectral resolution and signal-to-noise ratio are good, the spectra reveal a band at 1.65  $\mu\text{m}$  that is diagnostic of crystalline structure in water ice. This observation was surprising on two levels (Jewitt and Luu 2004). First, the crystallization of the ice implies that the temperature has been raised by an unknown process. Sources of such an increase include those that might act exclusively on surface layers (impacting micrometeorites, enhanced insolation during the T-Tauri phase, cosmic rays, etc.) and those that may affect the bulk properties of the nucleus (cryovolcanism, radioactive decay). In particular radioactive decay (e.g. from  $^{40}\text{K}$ ,  $^{235}\text{U}$ ,  $^{238}\text{U}$ ,  $^{235}\text{Th}$ ) is thought to be capable of raising internal temperature by amounts from 10s of degrees to substantially more if the objects formed on timescales short enough to incorporate  $^{26}\text{Al}$ . Depending on the internal thermal conductivity, these processes could effectively crystallize the entire nuclear interior (Prialnik and Podolak 1999). At the same time, bombardment by cosmic rays and energetic particles in the Solar wind is expected to amorphize exposed crystalline ice (Strazzulla et al. 1991), on a timescale of (1–10) Myr (Mastrapa and Brown 2006). This amorphization has been observed in the natural environment, notably on the Galilean satellites where the structural state of the ice varies with the fluence of energetic particles trapped within Jupiter's magnetosphere (Hansen and McCord 2004). Amorphization by impacting particles should destroy crystalline ice on Kuiper belt objects, leading to the inference that any exposed crystalline ice must have been recently emplaced or is being re-crystallized by some ongoing process.

There is considerable indirect evidence for the presence of amorphous water ice in comet-like bodies. For example, it has long been known that some comets and Centaurs (escaped Kuiper belt objects; see Fig. 13.4) lose mass even at distances where crystalline water is too cold to measurably sublime (i.e. beyond  $\sim 5$  AU). This has often been explained in terms of the exothermic crystallization of water ice (e.g. Prialnik et al. 2004, and references therein). A simple estimate of the heliocentric distance inside which crystallization is to be expected can be obtained by comparing the crystallization time (Eq. 13.1) with the orbital period, both as functions of distance. This result

$$\frac{3}{2} \ln R_c = -47.26 + E_A \sqrt{R_c} kT \quad (13.3)$$

gives a simple equation that can be solved numerically for  $R_c$ , with TBB from Eq. 13.2. Solution of Eq. 13.3 gives  $R_c \sim 7$  AU for the distance inside which crystallization is expected (Jewitt 2009). The higher temperatures (reaching up to about  $1.5T_{\text{BB}}$ ) expected near the subsolar point of a non-rotating nucleus can push  $R_c$  up to about 14 AU. These distances coincide well with the range of distances over which activity is observed in trans- Jovian objects (Fig. 13.4). Cometary

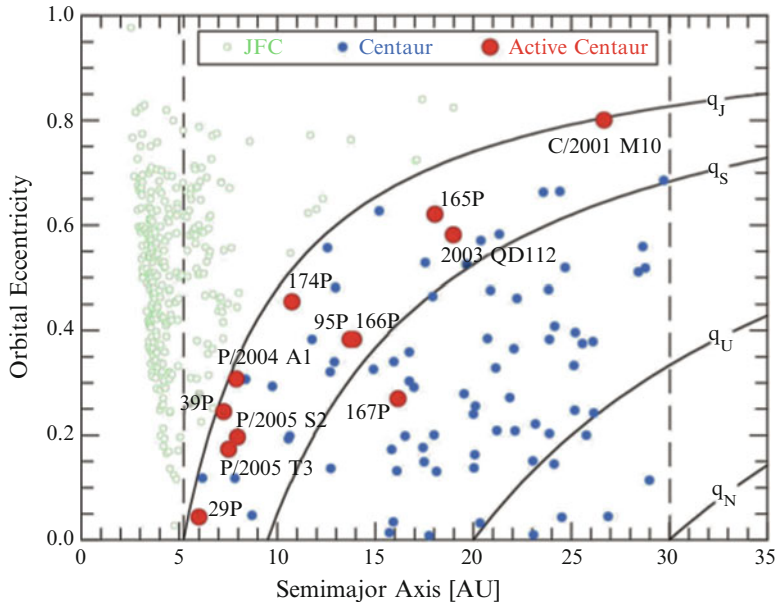


**Fig. 13.4** Distribution of the active and inactive Centaurs in the semimajor axis versus eccentricity plane. The *red dots* show active (mass-losing) Centaurs while *blue dots* show inactive Centaurs and *green diamonds* mark short-period (mostly Kuiper belt) comets. Diagonal arcs show the perihelion distances of the giant planets. The concentration of the active Centaurs between Jupiter and Saturn is consistent with triggering of the activity by the exothermic crystallization of water ice. Exposed supervolatiles (like CO) would sublimate to much larger distances than observed. (After Jewitt (2009))

activity at large heliocentric distances up to 14 AU pre-perihelion (Meech et al. 2008) has been attributed to the release of gases during the *annealing* of gas-laden amorphous ice. This observation is suggestive, albeit indirect, evidence for the existence of amorphous ice in the Centaurs. More detailed numerical models implicating crystallization often provide compelling fits to the data, but unfortunately they are founded upon the assumption of a large number of poorly known parameters, such as the location, heating rate, and petrology of the ices at depth leading to cometary and Centaur activity.

It should be noted that the exothermic character of ice crystallization, in the context of the comets, has been questioned by Kouchi and Sirono (2001). They argue that, in a realistic amorphous ice containing trapped volatile molecules (CO, CO<sub>2</sub>, CH<sub>4</sub>, etc.), heat released upon crystallization can be used to mobilize the volatiles, which then escape from the ice and result in a net loss of energy from the system (i.e. crystallization can even be endothermic when the impurity content exceeds about 2%). Nevertheless, in large scale laboratory experiments, (Bar-Nun and Laufer 2003) found no such decrease in temperature when a huge flux of gas was released from the large ice sample. The source of this disagreement is currently

not clear; mismatches between simple theory and scaled-up experiment are not uncommon in laboratory studies of physical chemistry models, and will likely take some time to resolve.

**Composition of Outgassed Ices.** An open question regarding ice structure in comets is the extent to which the known compositional differences among different comets (e.g. A'Hearn et al. 1995) are related to ice formation and the trapping of larger molecules. The fraction of carbon chain depleted objects is higher among short period comets tied to the Kuiper Belt, which implies a different formation history. However the classification scheme is by no means a complete description, since many KBO-tied short period comets are not depleted and many long-period Oort cloud objects *are*. There is also an evolutionary component, since the depleted short-period comets are also among the most processed objects, often having spent several hundred orbits in regions of the solar system where ice phase changes could have modified their interior composition. Could ice-formation modification lead to depletion of certain compounds in the trapped gas reservoirs of comets? Observations of the multiple fragments of Schwassmann-Wachmann 3 (Dello-Russo et al. 2008) indicate no variation with interior composition (i.e. complete structural homogeneity), although the observations used to demonstrate this occurred more than 12 years and two apparitions after the original breakup. More provocative is the recent identification of compositional heterogeneity among the different active regions of the long period comet C/1995O1 (Hale-Bopp) (Lederer et al. 2009), suggesting that the nucleus of this giant, highly active comet is composed of sub-units with different compositions. A similar result, indicating heterogeneity in the composition of evaporating ices, was found in the strong jets outgassing CO<sub>2</sub> and H<sub>2</sub>O from comet 9P/Tempel 1 (Feaga et al. 2008).

**Outbursts.** Abrupt increases in brightness, followed by a slow decay back to normal levels (and sometimes accompanied by the splitting of fragments from the nucleus) have been an established feature of cometary activity since physical studies of comets began in the nineteenth century (Sekanina 1982; Yeomans 1991). The origin of these *cometary outbursts* has been the source of wide ranging speculation that has remained unresolved because of the lack of observational constraints (Hughes 1991).

Theoretical work and laboratory simulations have suggested that gases are released from a constantly moving matrix of ice in the cometary nucleus, through a mechanism of dynamic percolation (Fig. 13.5). However, some of the water molecules sublimating from the surface migrate inward, building-up the ice and hindering further release of gases (Pat-El et al. 2009; Bar-Nun et al. 2009). Then, the gases bulge the overlying ice crust until it breaks, resulting in a huge flux of gas, which carries with it a similar huge flux of ice grains.

The *Deep Impact* mission has brought a new focus to the study of this phenomenon with the discovery of mini-outburst activity in the coma, wide spread layering of apparently global extent, and tongue-like shaped smooth terrains on the surface of comet 9P/Tempel 1 (A'Hearn et al. 2005; Fig. 13.6). These mini-outbursts have the same general character as the classical astronomical outbursts described by

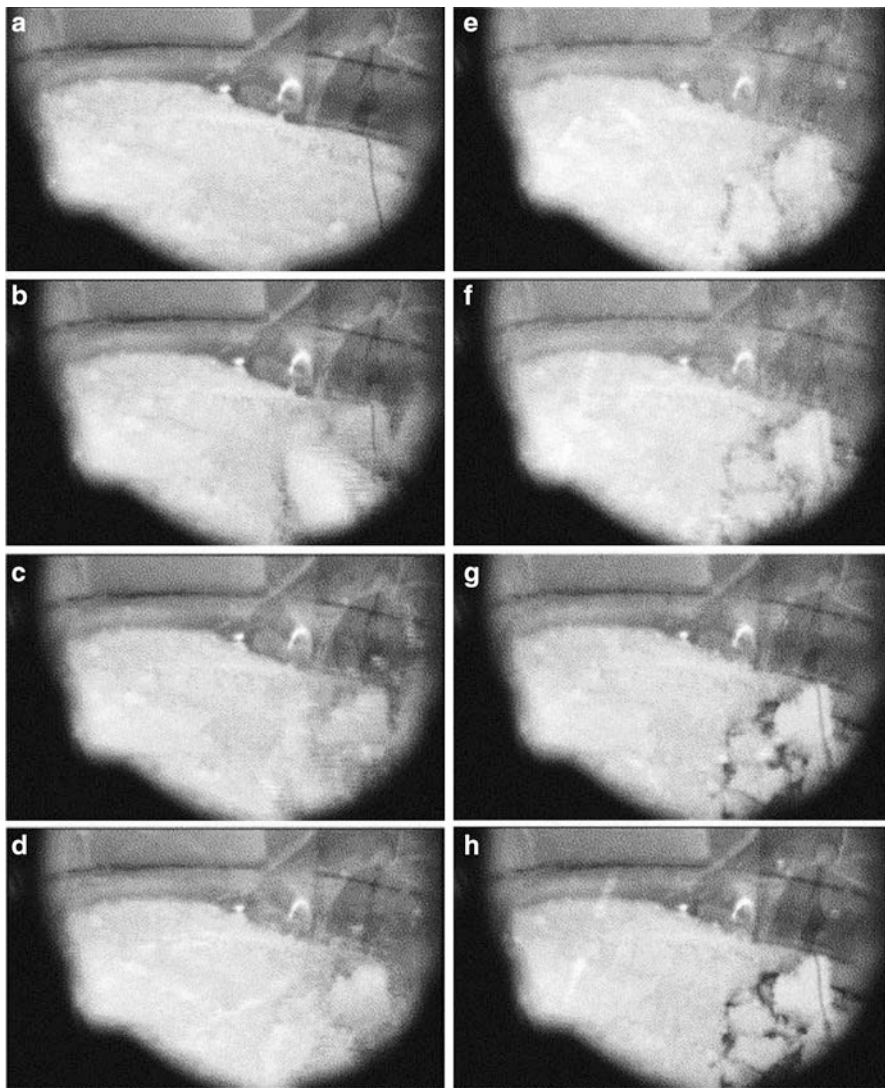


**Fig. 13.5** Time sequence of swelling (**b**), breakage, and collapse in 1.5-cm-thick ice samples. The magnitude of the collapse is best seen in (**h**). Note the ice grains seen as *white streaks* in (**f**) and (**h**). (From Laufer et al. (2005))

Hughes (1991), except that their brightness range is much smaller and they have been found to be approximately repetitive (Farnham et al. 2007; Belton et al. 2008).

Here we categorize these phenomena under the rubric of *cometary cryo-volcanism* because they have properties that bear a *prima facie* relationship to terrestrial volcanism even though they are physically entirely different. Cometary cryo-volcanism shows abrupt, explosive, sometimes episodic behavior but without the release of

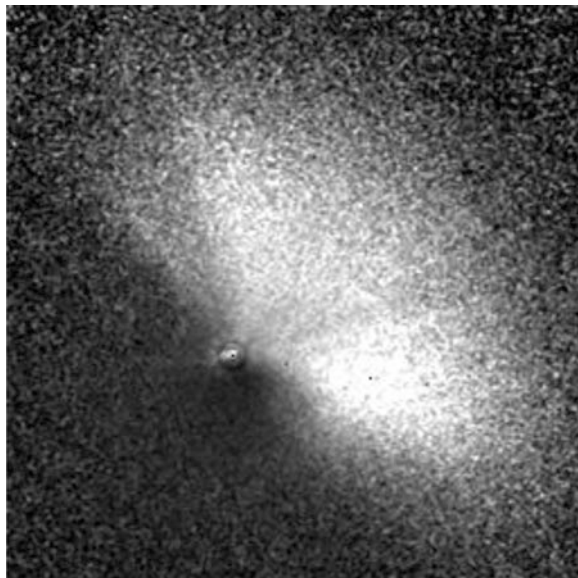


**Fig. 13.6** The June 14 2005 mini-outburst of 9P/Tempel 1 as seen from the Hubble Space Telescope (Courtesy of Feldman et al. 2007). The image shows the ratio of an image of the comet in outburst to an image just prior to outburst. This suppresses the brightness variations in the underlying coma. Note the increase in brightness towards the edges of the outburst material. This pattern has been found in several examples of mini-outbursts and has been interpreted as an ejecta curtain formed as material is excavated from the surface following an explosive event (Belton et al. (2008))

detectable heat. As in terrestrial volcanism, cometary volcanism may be accompanied with the emplacement of large volumes of material that can flow on the surface and its surface manifestations may include large superposed collapse features and localized fields of activity centers.

Outbursts cover a large range of cometary activity and include *mega-outbursts* that are marked by changes in brightness of the comet by a factor of  $\sim 10000$  or more, and, sometimes, fragmentation (i.e., splitting) of the nucleus. The result of such an event is shown in Fig. 13.6. More typical outbursts, what we call *normal-outbursts*, are less impressive (but may still involve fragmentation) with brightness increases of  $\sim 10$  and some comets are more susceptible to the phenomena than others. Finally, there are the newly discovered *mini-outbursts* that involve brightness increases of  $\sim 2$  that have the property of being approximately repetitive.

The *mega-* and *normal-outbursts* have the following observational properties:

1. The frequency of outbursts decreases with the brightness range of the outburst.
2. They are characterized by a rapid rise in brightness ( $\sim 2.5$  d) and a prolonged dispersal stage ( $\sim 20\text{--}30$  d) before falling to pre-outburst brightness levels (Hughes 1991).

3. The probability of their occurrence is random in the solar system and so does not depend on the surface temperature of the nucleus (Hughes 1991).
4. There is a higher probability for outbursts to occur on the post-perihelion leg of a comet's orbit (Hughes 1991).
5. All comets appear to partake of the outburst phenomena (Hughes 1991).
6. Some outbursts are accompanied by partial fragmentation of the nucleus.
7. Approximately 10% of dynamically new nuclei undergo catastrophic fragmentation (Weissman (1980) *Astronomy and Astrophysics*, vol. 85, no. 1–2, p. 191–196)
8. In some cases fragmentation is correlated with the occurrence of outburst activity (Sekanina 1997) but a causal relationship has not been observationally been established (Boehnhardt 2004).
9. Comet nuclei undergo fragmentation events at a rate of about once per century (Chen and Jewitt 1994).

*Mini-outbursts* have only been observed in a single comet, 9P/Tempel 1, as a result of the Deep Impact encounter and associated earth-based observations (Lara et al. 2006; Feldman et al. 2007). The repetitive outbursts of 29P/Schassmann-Wachmann 1 (Jewitt 1990) could be another case, but, so far, they have not been analyzed from this point-of-view. It is therefore not known how the statistics of their occurrence compares the mega- and normal varieties. Nevertheless, because of the extended time-base of the Deep Impact approach photometry and the possibility to perform stereoscopy on one of the outbursts with observations from the Hubble Space telescope on (Feldman et al. 2007; Farnham et al. 2007; Belton et al. 2008) much has been learned of their properties:

10. The outbursts occur in two groups that appear to repeat, on average, with the spin period indicating two locations on the surface of the nucleus.
11. The locations of the outbursts are in areas that are furthest from the center of figure of the nucleus.
12. The outbursts occur both during the day and night time.
13. None of the observed outbursts occurred near dawn or during the early morning. They seem to prefer times when the surface is cooling.
14. The outbursts form an ejecta sheet suggestive of the explosive excavation of a crater (Fig. 13.6).

An attempt to provide a self-consistent explanation of this array of observational facts in terms of a single mechanism has been made by Belton et al. (2008) under the assumption that there is a common physical process at work (Fig. 13.7). Of the published hypotheses collected by Hughes (1991) all of those that are stimulated by direct sunlight can be dismissed on the basis of items 11 and 3 above. The driving force behind the outbursts appears to be within the interior of the nucleus, modulated by processes that occur at, or near, the surface (item 12).

We mention one other form of “outburst activity” here for completeness – the case of the MBCs. For MBCs, activity is thought to be collisionally triggered, whereby the insulating inert layer of an ice-containing asteroid is penetrated by an impactor, exposing the ice below to direct solar heating. Following this collisional

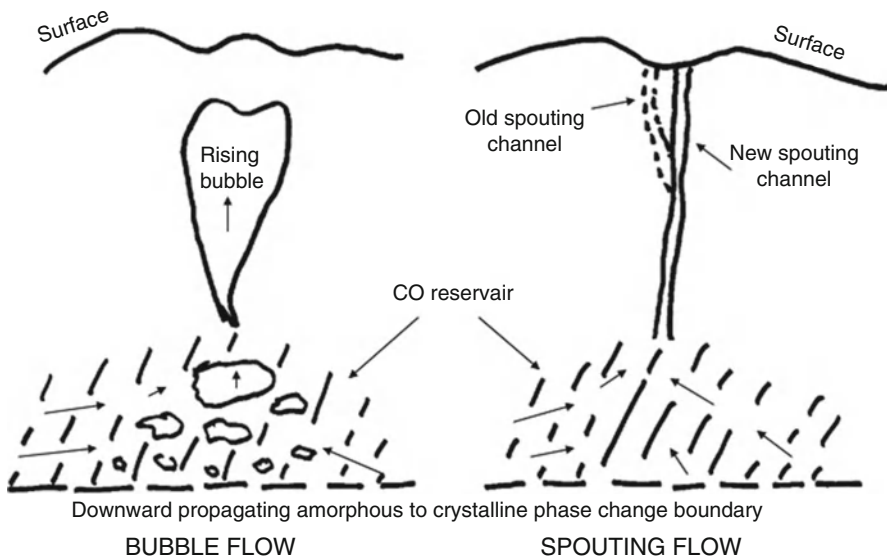


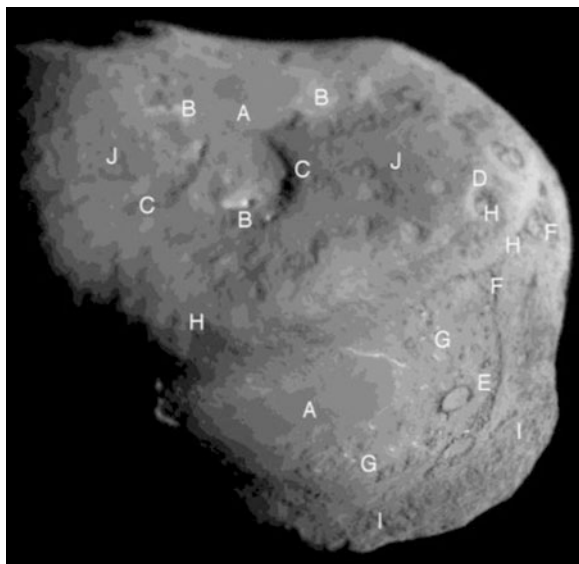
**Fig. 13.7** Possible mechanisms for the origin of cometary outbursts. On the *left* a large bubble of gas forms in the fluidized material that rises to the surface buoyantly. It reaches the surface only when the back pressure of sublimating H<sub>2</sub>O falls in the afternoon and night time. On the *right* gas is released only when the geometry of the *upper* regions of the CO reservoir is suitable for the formation of a spouting channel (Figure and explanation courtesy of Belton and Melosh (2009))

“activation”, comet-like sublimation-driven dust ejection ensues and continues until the ice content in the vicinity of the impact site is exhausted, a process which may occur over several orbit periods (cf. Hsieh and Jewitt 2006).

**Smooth Terrains.** Cometary smooth terrains (Fig. 13.8), which have been interpreted as geologically recent flows of material on the surface (e.g., Thomas et al. 2007; Belton and Melosh 2008) are an entirely new phenomena that have generated a wide range of ideas on the mechanisms that may have controlled their origin (Basilevsky and Keller 2007; Bar-Nun et al. 2008; Belton and Melosh 2009). With some hindsight, it has been suggested that such terrains may also exist on 19P/Borrelly and recorded, but at much lower spatial resolution, in the *DS-1* mission images (Britt et al. 2004). The globally pervasive layering has a different character from the smooth terrains. It may again be the result of recent geological processes like flows (Thomas et al. 2007) or, as Belton et al. (2007) have suggested, remnants that reflect sequential accretion processes that occurred during the accumulation of the cometary nucleus.

Three such regions have been discovered on 9P/Tempel 1 (Thomas et al. 2007). They are  $\sim 3$  km long and, except for faint dark linear markings, show no features down to the limit of resolution. When mapped on the nucleus shape model they are found to be downhill flows that terminate as a scarp on an uphill rise. They involve  $\sim 3 \times 10^7 \text{ m}^3$  of material (Belton and Melosh 2009).

**Fig. 13.8** The nucleus of 9P/Tempel 1 showing two of the smooth terrains discovered on its surface (marked as features A). Note that the northerly flow originates in a large circular depression near a higher albedo region that Sunshine et al. (2006) have found to be enhanced in water ice (Figure courtesy of Thomas et al. (2007))



Thomas et al. suggested that they were formed by the emplacement of very fluid material, while Gougen et al. (2008) pointed out that the material in the flow must have had substantial viscosity if the flow speed was to be less than the escape speed. Basilevsky and Keller (2007) advocated that the flows were analogous to an avalanche and proposed that they originated in the collapse of a relatively steep slope. Bar-Nun et al. (2008) proposed that they were the result of collimated ejection of ice grains during a large outburst of gas from the interior that was driven by the exothermic phase change of amorphous water ice into its crystalline phase (Fig. 13.9).

[These explanations contrast with that of Belton et al. (2007) who included the smooth terrains in their “talps” hypothesis to explain the global layering seen on 9P/Tempel 1. They proposed that the smooth terrains were laid down as part of the normal nucleus accumulation process and then recently “exhumed” by sublimation of the overlying layer as the comet moved into the inner solar system. To explain the smoothness of the terrain, they suggested that these particular layers were quickly covered up in the formation process so that they were protected from subsequent impacts and remained “smooth”].

More recently Belton and Melosh (2009) have proposed that the origin of cometary outbursts and smooth terrains are related through a common process in the interior: gas-fluidization of cometary particulate material. The idea assumes the existence of primitive gas-laden (CO and/or CO<sub>2</sub>) amorphous water ice in the interior of the nucleus that undergoes exothermic phase change to the crystalline form releasing gas and pressurizing the interior. This concept was originally proposed by Patashnik et al. (1974) and was subsequently developed by Prialnik and Bar-Nun (1990) and others. The rate at which gas is released at the phase change

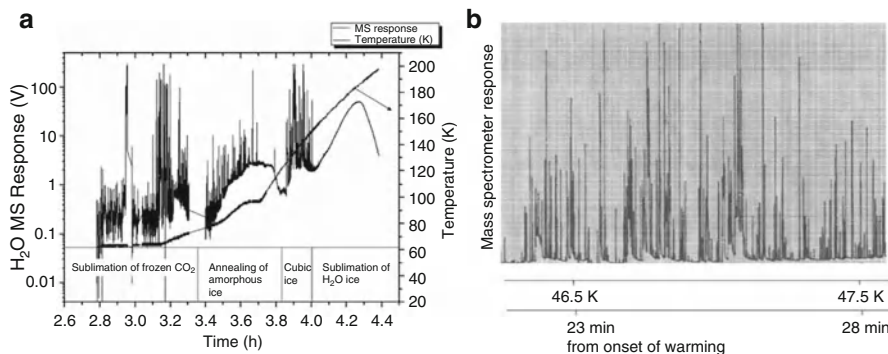


**Fig. 13.9** Ejection of ice grains by (a) the sublimation of a  $\sim 100\ \mu\text{m}$  underlying layer of frozen  $\text{CO}_2$  covered by a  $\sim 200\ \mu\text{m}$  layer of pure amorphous ice. The outflow of  $\text{CO}_2$  is governed by structural changes due to annealing of amorphous ice and transformation to cubic ice in the overlying pure ice layer, allowing increased gas flow through the ice matrix. In the latter stages, as the entire ice matrix sublimes, the structure is very open and large chunks of ice fall off the sample. (b) Ejection of ice grains from a 200- $\mu\text{m}$  Ar-laden amorphous ice sample, during the release of trapped Ar. The flux of water in the ice grains at this temperature range is  $10^{13}\text{--}10^{15}\ \text{molec. cm}^{-2}\text{s}^{-1}$  as measured by mass spectrometer (From Laufer et al. (1987))

boundary determines the outcome. At low rates the gas simply diffuses to the surface perhaps feeding an active area there. At higher rates the pressure gradient can increasingly support the weight of the overburden and inflates the interior. At some point the radial and azimuthal stress fields set up by the gas can overwhelm the strength of the overlying material and it becomes fluidized. This allows the onset of a multi-phase (gas plus solid particulates of various kinds) flow to the surface whose character depends on the magnitude of the gas flow. Possibilities include pneumatic, bubble, and spouting flow and, in addition, the phenomenon of elutriation, i.e., aerodynamic separation of particulates with different physical or compositional properties, may occur (Gidaspow 1994). These scenarios should also include the massive ejection of ice grains-fragments in an overlying ice-layer during a massive flow of gas as experimentally observed by Bar-Nun et al. (2008; Fig. 13.9).

Belton and Melosh propose that the smooth terrains are the results of localized pneumatic flow which emplaces low viscosity gas-laden material onto the surface (Fig. 13.10). Subsequent downhill flow of gas-charged dilated material quickly loses gas by diffusion thereby increasing its viscosity. Ultimately internal friction will increase to a level that halts the flow and form a scarp at its terminus. Belton and Melosh were able to show that the timescale for the emplacement of the flow was substantially longer than the timescale for the diffusive loss of gas, a necessary condition for this process to work. The loss of material from the interior leads to a collapse at the surface providing an explanation for the depression seen there. Under conditions suitable for bubble or spouting flow (Fig. 13.7), cometary outbursts are expected to be the outcome of this process.

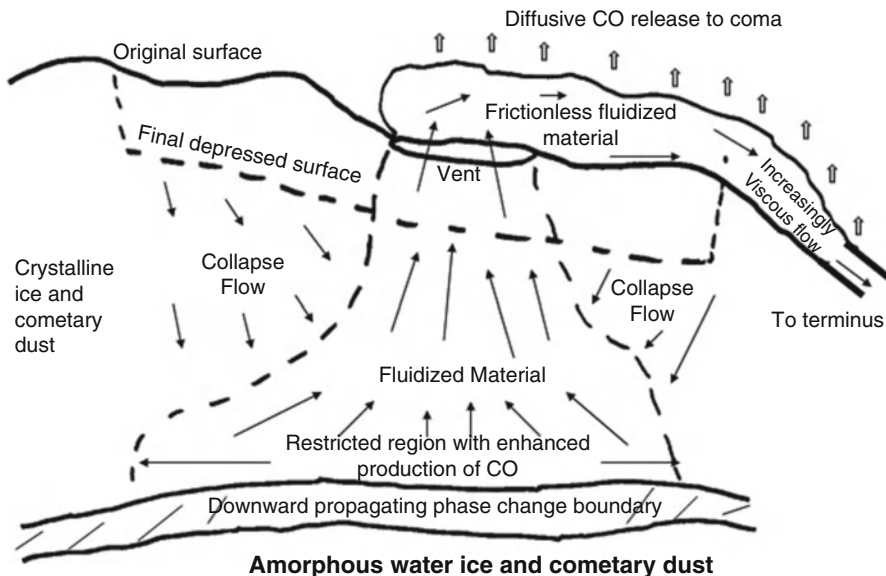


**Fig. 13.10** A cartoon illustrating the possible mode of formation of a region of smooth terrain. The production of CO and/or  $\text{CO}_2$  at an amorphous water ice phase change boundary creates a pressure gradient that overcomes the tensile strength of the crystalline ice/dust mixture above and fluidizes it. The material is extruded onto the surface at low velocity ( $\sim 0.03 - -0.003 \text{ m/sec}$ ). The gas-laden, material has low viscosity and accelerates downhill attaining an average speed of  $\sim 0.3 \text{ m}$  while continually losing its gas content. Internal friction in the flow material increases rapidly and the flow terminates forming a scarp at its terminus. As cometary material leaves the interior surrounding material collapses inward to form a depression around the source region (Figure and explanation courtesy of Belton and Melosh (2009))

### 13.3.1 Open Questions on Cometary Ices for Further Astronomical Study

1. How and where can direct, observational evidence for amorphous ice in the outer Solar system be found? What is the best way to do this, via remote sensing or in situ sampling or even sample return?
2. Are cometary ices substantially altered on the surfaces of comets, and is there a strong stratification of the ice composition and properties with respect to distance from the surface?
3. Where on the comet are outbursts initiated – on the surface, or in the interior?
4. Is the initiation of an outburst secondary to some triggering phenomenon either on the cometary surface or in the interior? Are outbursts triggered by sunlight?
5. Are patches of low boiling point, highly volatile minority ices scattered within the body of the comet responsible for outbursts?

6. Which mechanism, cryo-volcanism or gas percolation, or both, is responsible for formation of the smooth terrains?
7. What accounts for the compositional differences between carbon rich and carbon poor nuclei? Is this an artifact of formation or can it be tied the release of gas through a crystallization event?
8. What does homogeneity of nuclear ice composition (Dello-Russo et al. 2008), or the lack thereof (Feaga et al. 2008; Lederer et al. 2009) imply about interior ice structural development?

## 13.4 Laboratory Measurements of Cometary Ices

Given our current poor state of understanding from astronomical observations of the physical structure and makeup of the cometary nucleus and its component ices (e.g. Fig. 13.11; Weissman et al. 2004), what can be done to improve upon this with laboratory analogue studies? In this section we discuss past experiments on cometary ices and suggest possible future avenues of research.

### 13.4.1 The KOSI Experiments

An important early laboratory study of cometary ices mixed with frozen gas was the KOSI “Comet Simulation Experiment”, carried out at DLR Köln (Grün et al. 1993; Kölzer et al. 1995) in the early 1990s. A slurry of minerals with a trace of black carbon in water was sprayed into liquid nitrogen and mixed with solid CO<sub>2</sub> ice. When the 29 cm diameter and 13 cm high sample container was pumped on in the simulation chamber the liquid nitrogen evaporated, leaving in the container a porous sample ( $\sim 0.5 \text{ g cm}^{-3}$ ) of hexagonal ice particles with mineral dust, in which were dispersed solid CO<sub>2</sub> particles. The ice sample was tilted to 40° and irradiated by Xe arcs at a flux around one solar constant.

A flux of water vapor and CO<sub>2</sub>, initially at  $1.5 \times 10^{18} \text{ cm}^{-2} \text{s}^{-1}$  was measured, which declined gradually to  $5 \times 10^{17} \text{ cm}^{-2} \text{s}^{-1}$  after 500 min of irradiation and  $4 \times 10^{17} \text{ cm}^{-2} \text{s}^{-1}$  after 590 min. The particle count rate followed the gas flux, being initially  $\sim 60 \text{ s}^{-1}$ , falling to  $\sim 10 \text{ s}^{-1}$  after 500 min and to  $\sim 0$  after 590 min. The trajectories and speeds of the particles were followed photographically. Their highest speed was  $1.67 \text{ ms}^{-1}$ , remaining similar even 475 min after the beginning of irradiation. This speed is similar to the findings of  $1.67$  and  $1.40 \times \sin i \text{ ms}^{-1}$  for the speed of ice particles ejected from cometary ice simulants by Bar-Nun et al. (2008; Fig. 13.9). This constancy suggests that the size of the ice or ice–mineral particle which is broken from the matrix and propelled by the gas explosion is similar to the size of the cavity in which the gas resides. Namely, in a fine grained ice sample, explosions of small cavities suffice to break and propel small particles, whereas in a coarse grained ice sample, explosion of large cavities break and propel large

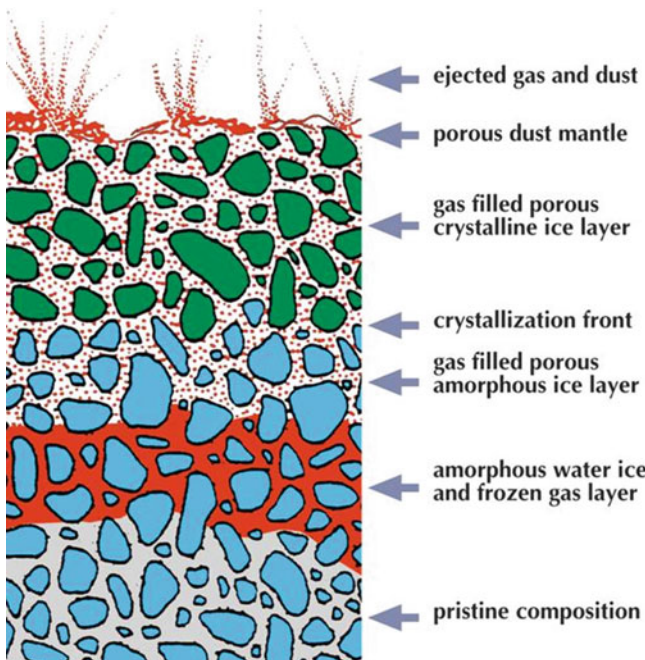


**Fig. 13.11** Schematic 1-D profile of the steady state structure of an average patch of ice in a cometary nucleus versus depth, consistent with the current state of astronomical observations described above and useful for understanding the laboratory discussion which follows. The nuclear surface is at *top*. The scale lengths in the image are, very roughly, on the order of 0.1–1 cm for the dust mantle, .01–1 m for the crystalline ice layers, and 1–10 m for the depth to pristine ice. Note that the size and structure of the large solid pieces of ice and rock have been exaggerated here for presentation purposes; in reality we expect a mix of grains of all sizes and shapes, from 0.1 um to 1.0 cm, with power law size distribution frequency and packing so that outflowing gas is in the percolation, and not free-flowing regime (After Prialnik et al. (2004))

particles. The propagation of heat derived from solar insolation inwards from the surface of a macroscopic sample of comet-like material was first experimentally measured by KOSI using thermocouples embedded throughout the large ice sample.

KOSI was notable for its application of recent findings on the nature of cometary ices and for its methodology of creating outgassing behavior in large macroscopic samples under realistic insolation and vacuum conditions. Unfortunately, more recent work has shown that the method of formation of the sample resulted in a majority of *hexagonal* ice formation, and many of the resulting measurements may not be directly related to cometary material as it is currently understood.

**Deep Impact.** NASA's Deep Impact (DI) mission was a turning point in our understanding of icy comet nuclei, and a directed astrophysical experiment. On July 4, 2005 DI sent a 364 kg impactor into the nucleus of comet 9P/Tempel 1 at  $10.2 \text{ km s}^{-1}$ . The impactor burrowed below the processed surface layers of the nucleus, releasing copious amounts of sub-surface material in a prominent ejecta

cone (A'Hearn et al. 2005; Richardson et al. 2007; Schultz et al. 2007). The vast majority of the  $\sim 10^6$  kg of material released in the impact (Lisse et al. 2006) was removed from the comet in an extremely gentle fashion, at low overpressures ( $< 1$  kPa; Stöffler et al. 1975; Melosh 1989) and temperatures, thereby preserving the mineralogical nature of the component material at the micron-scale level, although deaggregation of large ( $> 100\mu\text{m}$ ) fractal particles clearly occurred (Lisse et al. 2006). The total amount of water molecules released during DI, approximately  $5 (\pm 2) \times 10^6$  kg, corresponds to the regular output of only 0.2 days of normal activity. Together with the cratering event, which revealed the structure and composition of the upper tens of meter layer, the mission also returned observations of regular outbursts, close-up photography of surface features and surface temperature measurements.

Here we briefly compare DI's findings with the laboratory studies of Bar-Nun et al. Prior to DI, an apparatus was constructed at Tel-Aviv University (Bar-Nun and Laufer 2003), which can produce agglomerated samples of  $\sim 200\mu\text{m}$  gas laden amorphous ice particles, allowing the study of thermophysical processes occurring upon the introduction of heat energy from above. Samples as large as 20 cm diameter and 10 cm high have been studied. The good agreement between the findings of DI and the Bar-Nun et al. experimental findings provides an example of a laboratory basis for understanding the structure of comet nuclei.

*Density:* The best-fit shape model derived from DI imagery provided a total volume estimate good to 10% for the nucleus (Thomas et al. 2007). A total mass value for the nucleus was derived by Richardson et al. (2007) from estimates of the acceleration ( $\sim 10\mu\text{g}$ ) due to the nucleus' gravity on the trajectories of the DI ejecta. Richardson et al. quote an estimate for the density of 9P/Tempel 1's nucleus of  $400 +/ - 100$  kg m $^{-3}$ . Combined with other estimates of cometary bulk density, A'Hearn and Combi (2007) found a bulk mean density comets of  $\sim 350$  kg m $^{-3}$ , but with a large possible range of 100–1,000 kg m $^{-3}$ . Pat-El et al.'s (2009) reported experimental values of 250–300 kg m $^{-3}$  for porous, amorphous pure ice samples grown in the laboratory as a comet simulant are consistent with these density estimates.

*Mechanical strength:* From scaling relations for impact models of the temporal evolution of the morphology of the DI cratering event, Richardson et al. (2007) estimated a bulk tensile strength for the excavated upper layers of the comet of 1–10 kPa, while Housen and Holsapple (2007) have argued that the estimates of Richardson et al. may be low by an order of magnitude. Bar-Nun et al.'s (2009) laboratory simulations (Fig. 13.12) put the mechanical strength at 2–4 kPa, similar to that of uncompressed talcum powder, as expected for a very loose agglomerate of ice particles.

*Thermal Inertia:* Spectra and IR flux maps of the surfaces of rotating cometary bodies allow for estimates of the surface temperatures and time-scales for heat conduction into the material,  $I = (\kappa\rho c) \text{JK}^{-1}\text{m}^{-2}\text{s}^{-1/2}$ , where  $\kappa$  is the thermal conductivity,  $\rho$  the bulk density, and  $c$  the bulk heat capacity. Rotationally resolved thermal-IR observations of the whole nucleus of comet 9P/Tempel 1 at 7–35  $\mu\text{m}$  were obtained by Lisse et al. (2005) and used to show that the thermal inertia of the distant ( $r_h = 3.7$  AU) inactive

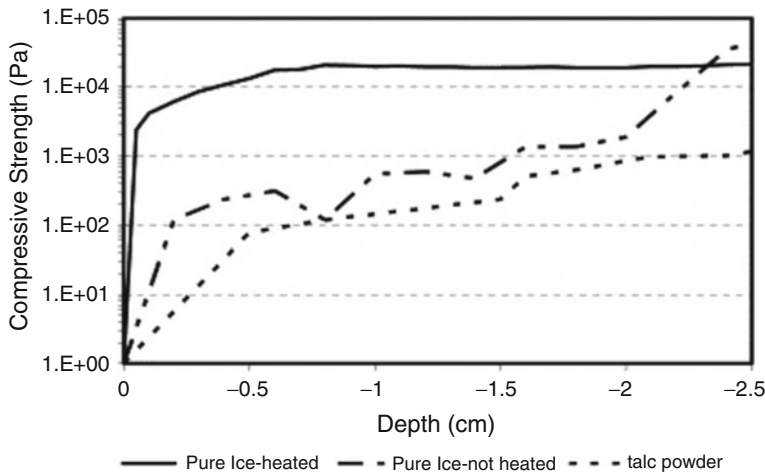


**Fig. 13.12** Measured compressive strengths of heated and not heated ice samples and that of a sample of Talcum powder (After Pat-El et al. (2009))

comet nucleus was  $<50 \text{ J K}^{-1} \text{ m}^{-2} \text{ s}^{1/2}$ . Using 3–5  $\mu\text{m}$  thermal continuum flux measurements derived from the HRI-IR spectrometer during encounter at 1.51 AU, Groussin et al. (2007) created a temperature map of the sunlit hemisphere of comet 9P/Tempel 1, and found that the best-fit thermophysical model for a slowly rotating body had a conservative upper limit for the surface thermal inertia of  $I < 100 \text{ J K}^{-1} \text{ m}^{-2} \text{ s}^{1/2}$ . From these values of the thermal inertia, scale lengths for the penetration depth of the thermal wave into the cometary nucleus due to diurnal rotation ( $\sim 1 \text{ cm}$ ) and orbital revolution ( $\sim 1 \text{ m}$ ) were derived by Groussin et al., much smaller than the  $\sim 3 \text{ km}$  radius nucleus, and the 10–100 m scale lengths for layering, flow structures, and mass wasting (Thomas et al. 2007).

In comparison, laboratory measurements of Bar-Nun et al. (2007) found a mean value of  $80 \text{ W K}^{-1} \text{ m}^{-2} \text{ s}^{1/2}$  for a macroscopic model of a cometary surface. Some variability is expected between laboratory measurements and those of real cometary nuclei, and for a given cometary nucleus at different locations in its orbit, as Bar-Nun and Laufer (2003) found that released trapped gases, as found in actively sublimating comets, increase the net thermal conductivity of ice (Fig. 13.13).

The low density, low thermal inertia, and extremely low tensile strength all point to comet Tempel 1 as being a very loose agglomerate of icy particles. Small values of the thermal inertia for cometary ices and material (by contrast the Moon and asteroids have  $I \sim 100\text{--}1000$ ) is not surprising, as the densities, volumetric thermal heat capacities, and thermal conductivities (phonon mean free paths) for loosely connected, porous fluffy material (>70% vacuum on meter-length scales) are all small (Kossacki et al. 1997; Kelly 1999; Sears et al. 1999; Lisse et al. 2005; Groussin et al. 2007; Davidsson et al. 2009). There is also good evidence from detailed observations of the Deep Impact ejecta that the water ice and refractory dust grains were mixed together as separate distinct entities rather than existing as dust frozen into patches or veins of ice (Sunshine et al. 2007).

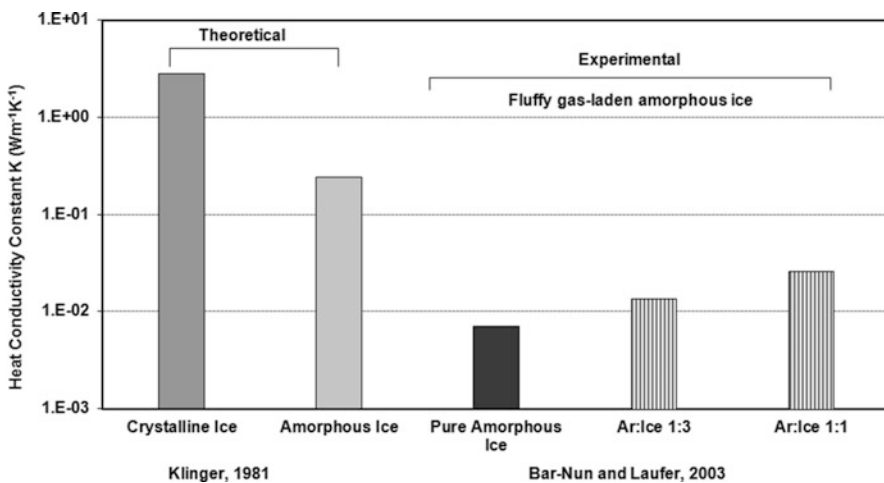


**Fig. 13.13** Thermal conductivity of various ice samples measured at different temperature ranges (After Bar-Nun and Laufer (2003)). Note the logarithmic scale on the vertical axis, and the 2–3 orders of magnitude lower conductivity values measured for amorphous ice materials

**Amorphous/Crystalline Transition.** A cometary nucleus consisting initially of a loose aggregate of dust and ice in the amorphous state and having an open low density structure is an intriguing object. This loose agglomerate may very well be a “time bomb” capable of explosive reorganization, because of the gases trapped in each amorphous grain, and because of the unstable nature of amorphous ice itself. The observed low, but finite rate of cometary splitting and disruption could be due to thermal wave penetration into a cometary body newly delivered to the inner solar system. It is amazing that such an object could survive 4.5 Gyrs from the formation of the solar system until the present day – unless there is a current sizable source population of cold comets.

On the other hand, there may be other effects that temper the effects of the water ice amorphous to crystalline transition. Low bulk thermal conductivity may allow for dissipation of the released latent heat of crystallization by radiation or evaporation, and the refractory mass component may act as a heat sink, disabling any sort of “crystallization chain reaction.”

We now also have temperature estimates for 3 cometary nuclei (Halley, Borrelly, and Tempel 1) with peak surface temperatures 350–420 K at the 0.8–1.5 AU comet-Sun distances at the time of measurement, far above the water ice crystallization temperature. Not only do these high temperatures argue for some sort of thermally insulating, non-ice surface layer to allow water ice to stably survive versus sublimation into interplanetary space, they also beg the question “Why then is there not a clear signature of crystalline ice at 1.65  $\mu\text{m}$  seen on comets?” Perhaps the thermally insulating layer (e.g., a few mm thick porous dehydrated dust layer, see Fig. 13.11) may optically mask any crystalline ice.

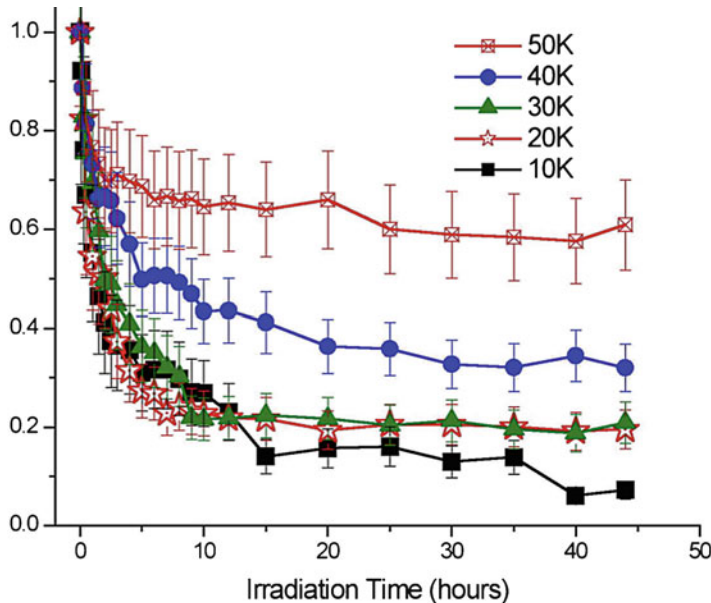


**Fig. 13.14** Effect of irradiation on the 1.65  $\mu\text{m}$  crystalline ice band of water ice. Vertical axis shows the 1.65  $\mu\text{m}$  band depth as a fraction of the initial (pre-irradiation) value. At Kuiper belt temperatures (40–50 K) the amorphization is only  $\sim 50\%$  (From Zheng et al. (2009))

The low surface coverage of water ice, and the apparent subsurface location of actively subliming ice (Sunshine et al. 2006; Groussin et al. 2007) may be another answer.

Long-term particle irradiation effects may also be important. Laboratory experiments directly show slow ice amorphization upon energetic electron irradiation. The 1.65  $\mu\text{m}$  band weakens as the fluence increases, corresponding to the destruction of the crystalline lattice. The effect is temperature dependent, however, and at higher temperatures the destructive effects of irradiation are reduced, presumably because of thermal effects (“annealing,” Zheng et al. 2009; Fig. 13.14). At 10 K, irradiated ice can be almost completely amorphized by radiation but, at the  $\sim 50$  K temperatures characteristic of the Kuiper belt, the 1.65  $\mu\text{m}$  band survives in an apparent equilibrium, with a band-depth equal to a fraction of that present in unirradiated, crystalline ice. Quantitative kinetic fits of the temporal evolution of the 1.65  $\mu\text{m}$  band clearly demonstrate that there is a balance between thermal recrystallization and irradiation-induced amorphization, with thermal re-crystallization dominant at higher temperatures. The depth of the 1.65  $\mu\text{m}$  band is thus both temperature and irradiation-dependent, and its proposed use as a thermometer (Grundy et al. 1999) may be rather complicated without good laboratory studies of its behavior. It is also possible that very different results will be found upon irradiation by energetic protons and alpha particles, also dominant in the solar wind along with energetic electrons, but providing much more momentum transfer per impact, enough to dislodge nuclei in a lattice easily.

### ***13.4.2 Open Questions on Cometary Ices for Further Laboratory Study***

1. Can a realistic laboratory model of cometary nuclear material, containing trapped gasses with boiling points as low as 30 K in vacuum be made on large scales characteristic of cometary nuclei from amorphous, porous water ice mixed with refractory dust grains? How should such a model be fabricated, by simple mixture, expensive aggregate growth from nanophase species, or by “spray-on” techniques?
2. Can these samples be made to match the very low albedo, IR water ice band depth, material strength, and thermal inertia we see for cometary materials? Can we use laboratory studies of irradiated, heated amorphous water ice to calibrate near-IR reflectance spectra of small body icy surfaces in the solar system?
3. How does the behavior of a laboratory model of cometary nuclear material change given varying amounts of dust/volatile ices, different temperature heating histories, different cosmic ray/UV irradiation histories, or different pressures of formation? I.e., what happens to this model when it is heated? Irradiated? Impacted?
4. How reliably can we scale from experiments done in the laboratory on timescales of an hour or a day to nature’s much more leisurely 4.5 Gyr timescale?
5. How reliable is Eq. 13.1 in describing the crystallization of realistic Solar system ice (i.e. ice containing impurities and in close contact with the irregular refractory surfaces of embedded dust grains)?
6. What is the true effect of energy released by the crystallization of amorphous ice on material in the nucleus, given near-surface losses and Kouchi and Sirono’s objection?

### ***13.4.3 Future Research Directions for Cometary Ices for Space Mission Study***

The results from the DS-1, STARDUST, and Deep Impact missions pose serious challenges to the current paradigm of the structure and evolution of cometary nuclei, i.e., the concept that they are collisionally processed fractal aggregates (Weissman et al. 2004). The Deep Impact and STARDUST images of 9P/Tempel 1 and 81P/Wild 2 show widespread layering in one case and massive pitting of the surface in the other. Scale lengths for thermal energy penetration and interaction are on the order of .001–1 m, yet we see surface structures and features on scales up to 10–100 m. The surfaces seem hardly consistent with our expectations based on the collisionally processed fractal model (Weaver 2004) or simple solar insolation (Groussin et al. 2007; Davidsson et al. 2009). Instead, and particularly if the layering is primitive, cometary nuclei may never have seen the kind of collisional

history on which the model is predicated. The new observations indicate active cometary interiors of a kind that urgently need to be explored. The density, mechanical strength and thermal inertia all point to a loose aggregate of ice grains which have not been compacted, but is active by either quiescent gas release, together with water vapor or explosive gas jets, accompanied by rupture of the cometary ice structure.

Such exploration will soon begin at comet 67P/Churyumov-Gerasimenko with the ESA CONCERT experiment, a microwave attenuation and propagation experiment on the Rosetta spacecraft that will probe the interior of the nucleus. In the future, powerful radar experiments that have improved volumetric resolution are possible for comet missions such as suitable modifications of the MARSIS and SHARAD radars that have been so successful in exploring the polar caps and the discovery of mid-latitude glaciation on Mars (Holt et al. 2008). Coupled with the future flight of a mapping thermal IR camera capable of making detailed measurements of the nuclear surface flux, temperature, and thermal inertia, missions that can explore the interior structure of the nucleus and relate its properties to surface activity and the geological features found there are amongst those with the highest priority for future cometary exploration (Fernandez et al. 2010; Weaver et al. 2010).

## References

- A'Hearn M et al (1995) The ensemble properties of comets: results from narrowband photometry of 85 comets, 1976–1992. *Icarus* 118:223–270
- A'Hearn MF et al (2005) Deep impact: excavating comet Tempel 1. *Science* 310:258–264
- A'Hearn MF, Combi MR (2007) Deep impact at comet Tempel 1. *Icarus* 187:1–3
- Bar-Nun A, Kleinfeld I (1989) On the temperature and gas composition in the region of comet formation. *Icarus* 80:243–253
- Bar-Nun A, Laufer D (2003) First experimental studies of large samples of gas-laden amorphous “Cometary” ices. *Icarus* 161:157–163
- Bar-Nun A, Dror J, Kochavi E, Laufer D (1987) Amorphous water ice and its ability to trap gases’. *Phys Rev B* 35:2427–2435
- Bar-Nun A, Pat-El I, Laufer D (2007) Comparison between the findings of deep impact and experimental results on large samples of gas-laden amorphous ice. *Icarus* 187:321–325
- Bar-Nun A, Pálsson F, Björnsson H (2008) Formation of smooth terrain on comet Tempel 1. *Icarus* 197:164–168
- Barucci MA, Doressoundiram A, Fulchignoni M, Florcak M, Lazzarin M, Angeli C, Lazzaro D (1998) Search for aqueously altered materials on asteroids. *Icarus* 132:388–396
- Basilevsky AT, Keller HU (2007) Craters, smooth terrains, flows, and layering on the comet nuclei. *Sol Syst Res* 41:109–117
- Belton MJS, Melosh HJ (2009) Fluidization and multiphase transport of particulate cometary material as an explanation of the smooth terrains and repetitive outbursts on 9P/Tempel 1. *Icarus* 200:280–291
- Belton MJS, Thomas P, Veverka J, Schultz P, A'Hearn MF, Feaga L, Farnham T, Groussin O, Li J-Y, Lisse C, McFadden L, Sunshine J, Meech KJ, Delamere WA, Kissel J (2007) The internal structure of Jupiter family cometary nuclei from deep impact observations: the “talps” or “Layered Pile” model. *Icarus* 187:332–344

- Belton MJS, Feldman P, A'Hearn MF, Carcich B (2008) Cometary Cryo-volcanism: source regions and a model for the UT 2005 June 14 and other mini-outbursts on comet 9P/Tempel 1. *Icarus* 198:189–207
- Biver N, Bockelée-Morvan D, Colom P, Crovisier J, Germain B, Lellouch E, Davies, JK, Dent WRF, Moreno R, Paubert G, Wink J, Despois D, Lis DC, Mehringer D, Benford D, Gardner M, Phillips, TG, Gunnarsson M, Rickman H, Winnberg A, Bergman P, Johansson LEB, Rauer H (1997) Long-term evolution of the outgassing of comet Hale-Bopp from radio observations. *Earth Moon Planet* 78:5–11
- Biver N et al (2002) The 1995–2002 long-term monitoring of comet C/1995 O1 (HALE BOPP) at radio. *Earth Moon Planet* 90(1):5–14
- Biver N, Bockelée-Morvan D, Boissier J, Crovisier J, Colom P, Lecacheux A, Moreno R, Paubert G, Lis DC, Sumner M, Frisk U, Hjalmarson Å, Olberg M, Winnberg A, Florén HG, Sandqvist A, Kwok S (2007) Radio observations of comet 9P/Tempel 1 before and after deep impact. *Icarus* 187:253–271
- Boehnhardt H (2004) Split Comets. In: Festou M, Keller HU, Weaver HA (eds) *Comets II*. University of Arizona Press, Tucson, pp 301–316
- Britt DT, Boice DC, Buratti BJ, Campins H, Nelson RM, Oberst J, Sandel BR, Stern SA, Soderblom LA, Thomas N (2004) The morphology and surface processes of comet 19P/Borrelly. *Icarus* 167:45–53
- Burbine TH (1998) Could G-class asteroids be the parent bodies of the CM chondrites? *Meteor Planet Sci* 33:253
- Campins H et al (2010) Water ice and organics on the surface of the asteroid 24 Themis. *Nature* 464:1320–1321
- Chen J, Jewitt D (1994) On the rate at which comets split. *Icarus* 108:265–271
- Chiang EI, And Brown ME (2001) Keck pencil-beam survey for faint Kuiper belt. *Astron J* 118:1411–1422
- Ciesla FJ, Cuzzi JN (2006) The evolution of the water distribution in a viscous protoplanetary disk. *Icarus* 181:178
- Cochran AL, Jackson WM, Meech KJ, Glaz M (2007) Observations of comet 9P/Tempel 1 with the Keck 1 HIRES instrument during deep impact. *Icarus* 187:156–166
- Cook JC, Desch SJ, Roush TL, Trujillo CA, Geballe TR (2007) Near-infrared spectroscopy of Charon: possible evidence for Cryovolcanism on Kuiper Belt objects. *Astrophys J* 663:1406–1419
- Davidsson BJR, Gutiérrez P, Rickman H (2009) Physical properties of morphological units on comet 9P/Tempel derived from near-IR deep impact spectra. *Icarus* 201:335–357
- Davies JK et al (1997) The detection of water ice in comet Hale-Bopp. *Icarus* 127:238–245
- Dones L et al (2004) Oort cloud formation and dynamics. In: Festou MC, Keller HU, Weaver HA (eds) *Comets II*. University Of Arizona Press, Tucson, p 745
- Ehrenfreund P, Rodgers SD, And Charnley SB (2002) Physico-chemistry of comets: models and laboratory experiments. *Earth Moon Planet* 89:221–246
- Fanale FP, Salvail JR (1984) An idealized short-period comet model – surface insolation, H<sub>2</sub>O flux, dust flux, and mantle evolution. *Icarus* 82:97
- Farnham TL, Wellnitz DD, Hampton DL, Li J-Y, Sunshine J, Groussin O, McFadden LA, Crockett CJ, A'Hearn MF, Belton MJS, Schultz P, Lisse CM (2007) Dust coma morphology in the deep impact images of comet 9P/Tempel 1. *Icarus* 187:26–40
- Feierberg MA, Lebofsky LA, Tholen DJ (1985) The nature of C-class asteroids from 3-μm spectrophotometry. *Icarus* 63:183
- Feldman PD, McCandliss SR, Route M, Weaver HA, A'Hearn MF, Belton MJS, Meech KJ (2007) Hubble space telescope observations of comet 9P/Tempel 1 during the deep impact encounter. *Icarus* 187:113–122
- Feldman P, McCandliss SR, Morgenthaler JP, Lisse CM, Weaver HA, A'Hearn MF (2010) GALEX observations of CS and OH emission in comet 9P/Tempel 1 during deep impact. *Icarus* (submitted Dec 2009)

- Fernández JA (2007) Origin of comet nuclei and dynamics. *Sp Sci Rev* 138:27–42
- Fernandez YR, et al. (2010) Centaurs and small irregular TNOs, NASA 2010 Decadal Survey Whitepaper
- Francis PJ (2005) The demographics of long-period comets. *Astrophys J* 635:1348–1361
- Gidaspow D (1994) Multiphase flow and fluidization. Academic, San Diego
- Gougen JD, Thomas PC, Veverka JF (2008) Flows on the nucleus of comet Tempel 1. In: Proceedings of the lunar and planetary sciences conference 39, abstract #1969, Houston
- Grimm RE, McSween HY Jr (1989) Water and the thermal evolution of carbonaceous chondrite parent bodies. *Icarus* 82:244–280
- Groussin O, A'Hearn MF, Li J-Y, Thomas PC, Sunshine JM, Lisse CM, Meech KJ, Farnham TL, Feaga LM, Delamere WA (2007) Surface temperature of the nucleus of comet 9P/Tempel 1. *Icarus* 187:16–25
- Grün E, Gebhard J, Bar-Nun A, Benkhoff J, Dueren H, Eich G, Hische R, Huebner WF, Keller HU, Klees G (1993) Development of a dust mantle on the surface of an isolated ice–dust mixture – results from the KOSI-9 experiment. *J Geophys Res* 98:15091–15104
- Grundy WM, Buie MW, Stansberry JA, Spencer JR, Schmitt B (1999) Near-infrared spectra of icy outer solar system surfaces: remote determination of  $\text{H}_2\text{O}$  ice temperatures. *Icarus* 142:536–549
- Gurnett DA, Ansher JA, Kurth WS, Granroth LJ (1997) Micron-sized dust particles detected in the outer solar system by the Voyager 1 and 2 plasma wave instruments. *Geophys Res Lett* 24:3125–3128
- Haghighipour N (2009) Dynamical constraints on the origin of main belt comets. *Meteor Planet Sci* 44(12):1863–1869, arXiv:0910.5746
- Hahn JM, Malhotra R (1999) Orbital evolution of planets embedded in a massive planetesimal disk. *Astron J* 117:3041–3053
- Hansen GB, McCord TB (2004) Amorphous and crystalline ice on the Galilean Satellites: a balance between thermal and radiolytic processes. *J Geophys Res* 109:E01012
- Hiroi T, Zolensky ME, Pieters CM, Lipschutz ME (1996) Thermal metamorphism of the C, G, B, and F asteroids seen from the 0.7- $\mu\text{m}$ , 3- $\mu\text{m}$ , and UV absorption strengths in comparison with carbonaceous chondrites. *Meteor Planet Sci* 31:321–327
- Holt JW et al (2008) Radar sounding evidence for buried glaciers in the southern mid-latitudes of Mars. *Science* 322:1235–1238
- Hsieh HH, Jewitt D (2006) A population of comets in the main asteroid belt. *Science* 312:561–563
- Hsieh HH, Jewitt DC, Fernández YR (2004) The strange case of 133P/Elst-Pizarro: a comet amongst the asteroids. *Astron J* 127:2997–3017
- Hsieh HH, Jewitt D, Ishiguro M (2009) Physical properties of main-belt comet P/2005 U1 (Read). *Astron J* 137:157–168
- Hughes DW (1991) Possible mechanisms for cometary outbursts. In: Newburn RL Jr, Neugebauer M, Rahe J (eds) Comets in the post-halley era, vol 2. Kluwer, Dordrecht
- Jenniskens P, Blake DF (1994) Structural transitions in amorphous water ice and astrophysical implications. *Science* 265:753–756
- Jewitt DC (1990) The persistent coma of comet 29P/Schwassmann-Wachmann 1. *Astron J* 351:277–286
- Jewitt DC (2009) The active centaurs. *Astron J* 137:4296–4312
- Jewitt DC, Haghighipour N (2007) Irregular satellites of the planets: products of capture in the early solar system. *Annu Rev Astron Astrophys* 45:261–295
- Jewitt DC, Luu J (2004) Crystalline water ice in Kuiper Belt object (50000) Quaoar. *Nature* 432:731–733
- Jewitt DC, Yang B, Haghighipour N (2009) Main-belt comet P/2008 R1 (Garradd). *Astron J* 137:4313–4321
- Jewitt DC et al (2010) A recent disruption of the main-belt asteroid P/2010A2. *Nature* 467:817–819

- Jones TD, Lebofsky LA, Lewis JS, Marley MS (1990) The composition and the origin of the C, P, and D asteroids: water as a tracer of thermal evolution in the outer belt. *Icarus* 88:172–192
- Kawakita H et al (2001) The spin temperature of NH<sub>3</sub> in comet C/1999 S4 (LINEAR). *Science* 294:1089
- Kawakita H et al (2002) Spin temperature of ammonia determined from NH<sub>2</sub> in comet C/2001 A2 (LINEAR). *Earth Moon Planet* 90:371
- Kawakita H, Watanabe JI, Furusho R, Fuse T, Capria MT, DeSanctis MC, Cremonese G (2004) Spin temperatures of ammonia and water molecules in comets. *Astrophys J* 601:1152–1158
- Keil K (2000) Thermal alteration of asteroids: evidence from meteorites. *Planet Space Sci* 48:887
- Kelly MLU (1999) Thermal properties of airless planetary regoliths. Ph.D. thesis, University of Colorado, Boulder. Source DAI-B 60/07, 118 pp
- Kölzer G, Grün E, Kochan H, Lämmerzahl P, Thiel K (1995) Dust particle emission dynamics from insolated ice/dust mixtures: results from KOSI 5 experiment. *Planet Space Sci* 43:391–407
- Kossacki KJ, Komle NI, Leliwa-Kopystynski J, Kargl G (1997) Laboratory investigation of the evolution of cometary analogs: results and interpretation. *Icarus* 128:127–144
- Kouchi A, Sirono S (2001) Crystallization heat of impure amorphous H<sub>2</sub>O ice. *Geophys Res Lett* 28(5):827–830
- Lara LM, Boehnhardt H, Gredel R, Gutiérrez PJ, Ortiz JL, Rodrigo R, Vidal-Nuñez MJ (2006) Pre-impact monitoring of comet 9P/Tempel 1, the deep impact target. *Astron Astrophys* 445:1151–1157
- Laufer D, Kochavi E, Bar-Nun A (1987) Structure and dynamics of amorphous water ice. *Phys Rev B* 36:9219–9227
- Laufer D, Pat-El I, Bar-Nun A (2005) Experimental simulation of the formation of non-circular active depressions on comet wild-2 and of ice grain ejection from cometary surfaces. *Icarus* 178:248–252
- Lebofsky LA (1980) Infrared reflectance spectra of asteroids: a search for water of hydration. *Astron J* 85:573–585
- Lebofsky LA, Feierberg MA, Tokunaga AT, Larson HP, Johnson JR (1981) The 1.7 to 4.2  $\mu\text{m}$  spectrum of asteroid 1 ceres: evidence for structural water in clay minerals. *Icarus* 48:453–459
- Lecar M, Podolak M, Sasselov D, Chiang E (2006) On the location of the snow line in a protoplanetary disk. *Astrophys J* 640:1115–1118
- Lellouch E et al (1998) Evidence for water ice and estimate of dust production rate in comet Hale-Bopp At 2.9 AU from the sun. *Astron Astrophys* 339:L9–L12
- Levison HFAnd, Morbidelli A (2003) The formation of the Kuiper Belt by the outward transport of bodies during Neptune's migration. *Nature* 426:419–421
- Licandro J et al (2011) (65) Cybele: detection of small silicate grains, water-ice, and organics. *Astron Astrophys* 525:A34
- Lisse CM, A'Hearn MF, Groussin O, Fernandez YR, Belton MJ, van Cleve JE, Charmandaris V, Meech KJ, McGleam C (2005) Rotationally resolved 8–35  $\mu\text{m}$  spitzer space telescope observations of the nucleus of comet 9P/Tempel 1. *Astrophys J Lett* 625:L139–L142
- Lisse CM, VanCleve J, Adams AC, A'Hearn MF, Fernández YR, Farnham TL, Armus L, Grillmair CJ, Ingalls J, Belton MJS, Groussin O, McFadden LA, Meech KJ, Schultz PH, Clark BC, Feaga LM, Sunshine JM (2006) Spitzer spectral observations of the deep impact ejecta. *Science* 313:635–640
- Marboeuf U, Mousis O, Petit JM, Schmitt B (2010) Clathrate hydrates formation in short-period comets. *Astrophys J* 708:812–816
- Mastrapa RME, Brown RH (2006) Ion irradiation of crystalline H<sub>2</sub>O ice: effect on the 1.65 micron band. *Icarus* 183:207–214
- McCord TB, Sotin C (2005) Ceres: evolution and current state. *J Geophys Res* 110:5009
- Meech KJ, Pittichova J, Bar-Nun A, Notesco G, Laufer D, Hainaut OR, Lowry SC, Yeomans DK, Pitts M (2008) Activity of comets at large heliocentric distances pre-perihelion. *Icarus* 201:719–739

- Melosh HJ (1989) Impact cratering: a geologic process, vol 11, Oxford monographs on geology and geophysics. Clarendon, Oxford
- Notesco G, Bar-Nun A (2005) A 25 K temperature of formation for the submicron ice grains which formed comets. *Icarus* 175:546–550
- Owen TC (2007) Planetary atmospheres. *Space Sci Rev* 130:97–104
- Patashnik H, Rupprecht G, Schuerman DW (1974) Energy sources for comet outbursts. *Nature* 250:313–314
- Pat-El I, Laufer D, Notesco G, Bar-Nun A (2009) An experimental study of the thermal inertia of comet nuclei, formation of an ice crust and migration of water vapor in a comet's upper layers. *Icarus* 201:406–411
- Prialnik D, Bar-Nun A (1990) Gas release in comet nuclei. *Astrophys J* 363:274–282
- Prialnik D, Podolak M (1999) Changes in the structure of cometary nuclei due to radioactive heating. *Space Sci Rev* 90:169–178
- Prialnik D et al (2004) Modeling the structure and activity of comet nuclei. In: Festou M, Keller HU, Weaver HA (eds) Comets II. University of Arizona Press, Tucson, pp 359–387
- Richardson JE, Melosh HJ, Lisse CM, Carcich B (2007) A ballistics analysis of the deep impact ejecta plume: determining comet Tempel 1's gravity, mass, and density. *Icarus* 190:357–390
- Rivkin AS, Emery JP (2010) Detection of ice and organics on an asteroidal surface. *Nature* 464:1322–1323
- Sasselov DD, Lecar M (2000) On the snow line in dusty protoplanetary disks. *Astrophys J* 528:995–998
- Schmitt B, Espinasse S, Grim RJA, Greenberg JM, Klinger J (1989) Physics and mechanics of cometary materials, ESA SP-302, European Space Agency, Paris, p. 65
- Schörghofer N (2008) The lifetime of ice on main belt asteroids. *Astrophys J* 682:697–705
- Schultz PH, Eberhardy CA, Ernst CM, Sunshine JM, A'Hearn MF, Lisse CM (2007) The deep impact oblique cratering experiment. *Icarus* 190:295–333
- Scott ERD, Krot AN (2005) Thermal history of silicate dust in the solar nebula: clues from primitive chondrite matrices. *Astrophys J* 623:571–578
- Scotti JV, McMillan RS, Jewitt D, Annis J, Soares-Santos M, Licandro J, Tozzi GP, Liimets T, Haver R, Buzzi L (2010a) P/2010 A2 [27338-2011/01-S2]. IAUC 9109:1
- Scotti JV, McMillan RS, Licandro J, Tozzi GP, Liimets T, Cabrera-Lavers A, Gomez G, Haver R, Caradossi A, Buzzi L (2010b) P/2010 A2 (LINEAR). CBET 2134:1
- Sears DWG, Kochan HW, And Huebner WF (1999) Invited review: laboratory simulation of the physical processes occurring on and near the surfaces of comet nuclei. *Meteor Planet Sci* 34:497–525
- Sekanina Z (1982) The problem of split comets in review. In: Wilkening L (ed) Comets. The University of Arizona Press, Tucson, pp 251–287
- Sekanina Z (1997) The problem of split comets revisited. *Astron J* 318:L5–L8
- Soderblom LA, Britt DT, Brown RH, Buratti BJ, Kirk RL, Owen TC, Yelle RV (2004) Short-wavelength infrared (1.3–2.6 μm) observations of the nucleus of comet 19P/Borrelly. *Icarus* 167:100–112
- Stern SA, Weissman PR (2001) Rapid collisional evolution of comets during the formation of the Oort Cloud. *Nature* 409:589–591
- Stöffler D, Gault DE, Wedekind J, Polkowski G (1975) Experimental hypervelocity impact into quartz sand: distribution and shock metamorphism of ejecta. *J Geophys Res* 80:4062–4077
- Strazzulla G, Baratta GA, Johnson RE, Donn B (1991) Primordial comet mantle: irradiation production of a stable organic crust. *Icarus* 91:101–104
- Sunshine JM et al (2006) Exposed water ice deposits on the surface of comet 9P/Tempel 1. *Science* 311:1453–1455
- Sunshine JM, Groussin O, Schultz PH, A'Hearn MF, Feaga LM, Farnham TL, Klaasen KP (2007) The distribution of water ice in the interior of comet tempel 1. *Icarus* 190:284–294
- Thomas PC, Veverka J, Belton MJS, Hidy A, A'Hearn MF, Farnham TL, Groussin O, Li J-Y, McFadden LA, Sunshine J, Wellnitz D, Lisse C, Schlutz P, Meech KJ, Delamere WA (2007)

- The shape, topography, and geology of Tempel 1 from deep impact observations. *Icarus* 187:4–15
- Vernazza P, Mothé-Diniz T, Barucci MA, Birlan M, Carvano JM, Strazzulla G, Fulchignoni M, Migliorini A (2005) Analysis of near-IR spectra of 1 Ceres and 4 Vesta, targets of the Dawn mission. *Astron Astrophys* 436:1113
- Vilas F, Jarvis KS, Gaffey MJ (1994) Iron alteration minerals in the visible and near-infrared spectra of low-albedo asteroids. *Icarus* 109:274
- Vitense Ch, Krivov AV, Löhne T (2010) The Edgeworth-Kuiper debris disk. *Astron Astrophys* 520:A32
- Weaver HA (2004) Not a rubble pile. *Science* 304:1760–1762
- Weaver HA, Meech KJ et al. (2010) Comets, NASA 2010 Decadal survey whitepaper
- Weidenschilling SJ (2005) Formation of the cores of the outer planets. *Space Sci Rev* 116:53–66
- Weissman PR, Asphaug E, Lowry SC (2004) Structure and density of cometary nuclei. In: Festou M, Keller HU, Weaver HA (eds) *Comets II*. University of Arizona Press, Tucson, pp 337–357
- Yeomans DK (1991) *Comets, a chronological history of observation, science, myth, and folklore*. Wiley, New York
- Zheng W, Jewitt DC, Kaiser RI (2009) On the state of water ice on Saturn's moon Titan and implications to icy bodies in the outer solar system. *J Phys Chem A* 113:11174–11181
- Zolotov MY (2009) On the composition and differentiation of Ceres. *Icarus* 204:183

# Chapter 14

## Gas Trapping in Ice and Its Release upon Warming

Akiva Bar-Nun, Diana Laufer, Oscar Rebolledo, Serguei Malyk,  
Hanna Reisler, and Curt Wittig

**Abstract** NASA’s Deep Impact was a turning point in our measurements of comet properties. For the first time we obtained direct measurements of the density, thermal inertia of the surface, and, most importantly, the tensile strength of the upper layers. The very small tensile strength of only 1–10 kPa (like that of Talcum powder) tells us that comet Tempel 1 is a loose agglomerate of fluffy ice particles (Bar-Nun et al. 2007). In what follows, we describe how gases are trapped in fluffy ice particles, how they are released from them when the temperature is increased, either by overall heating or by pulsed infrared laser irradiation and finally, what happens when deeper layers release their trapped gases when the heat wave penetrates inward. In addition, it will be shown that laboratory measurements can now be carried out that address fundamental transport issues such as the release of trapped gases in such ice environments and their transport through thin and thick ice layers.

### 14.1 Gas Trapping

When water vapor freezes at low temperatures, the ice forms an “open” amorphous structure (often referred to as amorphous solid water, ASW) with many open pores. A CO content of a few percent in comets requires the temperature of formation of the ice grains, which agglomerate to form comet nuclei, to be about 25 K (Notesco and Bar-Nun 2005). This is in agreement with the nuclear spin temperature of ~25 K derived from the ortho/para ratio of H<sub>2</sub>O in comet Halley (Mumma et al. 1988) and

---

A. Bar-Nun (✉) • D. Laufer

Department of Geophysics and Planetary Sciences, Tel-Aviv University, Tel-Aviv, Israel  
e-mail: [akivab@post.tau.ac.il](mailto:akivab@post.tau.ac.il)

O. Rebolledo • S. Malyk •

H. Reisler • C. Wittig

Department of Chemistry, University of Southern California, Los Angeles, CA 90089, USA

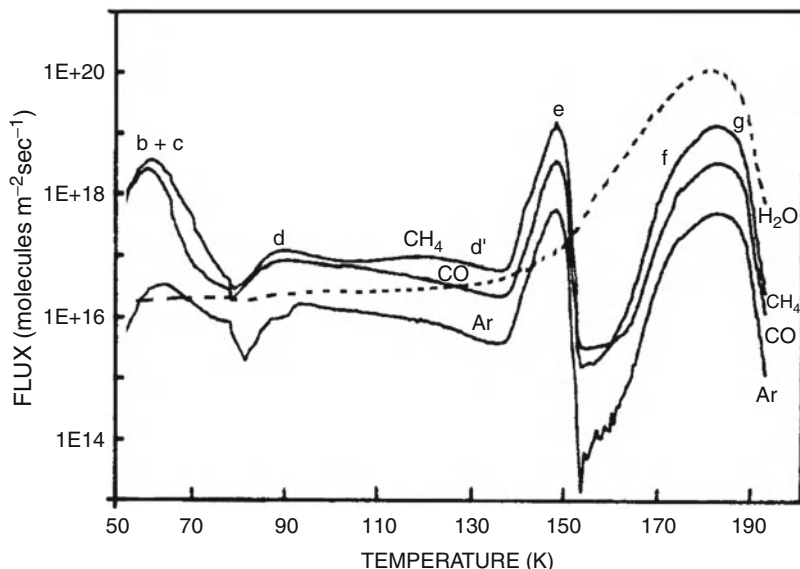


**Fig. 14.1** Fluxes of gas and water vapor versus temperature. Gas-rich amorphous ice was condensed at 50 K from the mixture  $\text{H}_2\text{O}:\text{CH}_4:\text{CO}:\text{Ar} = 1:0.33:0.33:0.33$ . Note: Changes in gas evolution occur over six orders of magnitude. Ranges *b*, *d* and *d'* – gas release due to annealing of the amorphous ice; *c* – desorption of a monolayer of adsorbed gas; *e* – gas release during the transformation of amorphous ice to cubic ice and restrained amorphous ice; *f* – gas release during the partial transformation to hexagonal ice; *g* – release of gases that were trapped even more tightly during the transformations and can be released only when the ice matrix itself sublimes (Bar-Nun et al. 1988)

Comet Hale-Bopp (Crovisier 1997), and also the temperature of  $\sim 28$  K derived from the ortho/para ratio of  $\text{NH}_3$  in Comet Linear C/1999 S4 (Kawakita et al. 2001).

At such low temperatures, water molecules stick wherever they hit the ice surface, as they do not have enough energy to migrate and form a more stable structure with more hydrogen bonds between the water molecules. This metastable structure rearranges during the annealing of the amorphous ice between 35 and 120 K, and more vigorously during transformation to the cubic structure at 120–135 K.

When amorphous ice is formed in the presence of gas, the gas molecules enter the open pores and reside there for a time that depends on the interactions with the dangling OH's on the ice walls, as well as the masses of the gas molecules and the ambient temperature. If, before escaping the pore, an overlayer of ice forms, the gas molecules become trapped, and they can escape only when the water molecules move during annealing and/or the transformation to cubic ice. Molecules such as  $\text{HCN}$ ,  $\text{NH}_3$ ,  $\text{CO}_2$ ,  $\text{CH}_4$ , etc. are trapped more efficiently than  $\text{CO}$ ,  $\text{Ar}$ ,  $\text{Kr}$ , and  $\text{Xe}$  (Bar-Nun et al. 1988). Due to the energy of the molecules in the open pores, the trapping efficiency of each gas drops exponentially with increasing temperature; see Figs. 14.1 and 14.2.

The extreme case, which demonstrated the dependence on the energy of the gas in a pore, was a comparison of the trapping of  $\text{Ar}$ ,  $\text{Kr}$ , and  $\text{Xe}$ . The ratios of residence times in the open pore were  $(m_1/m_2)^{1/2}$ , and the ratios of their trapping

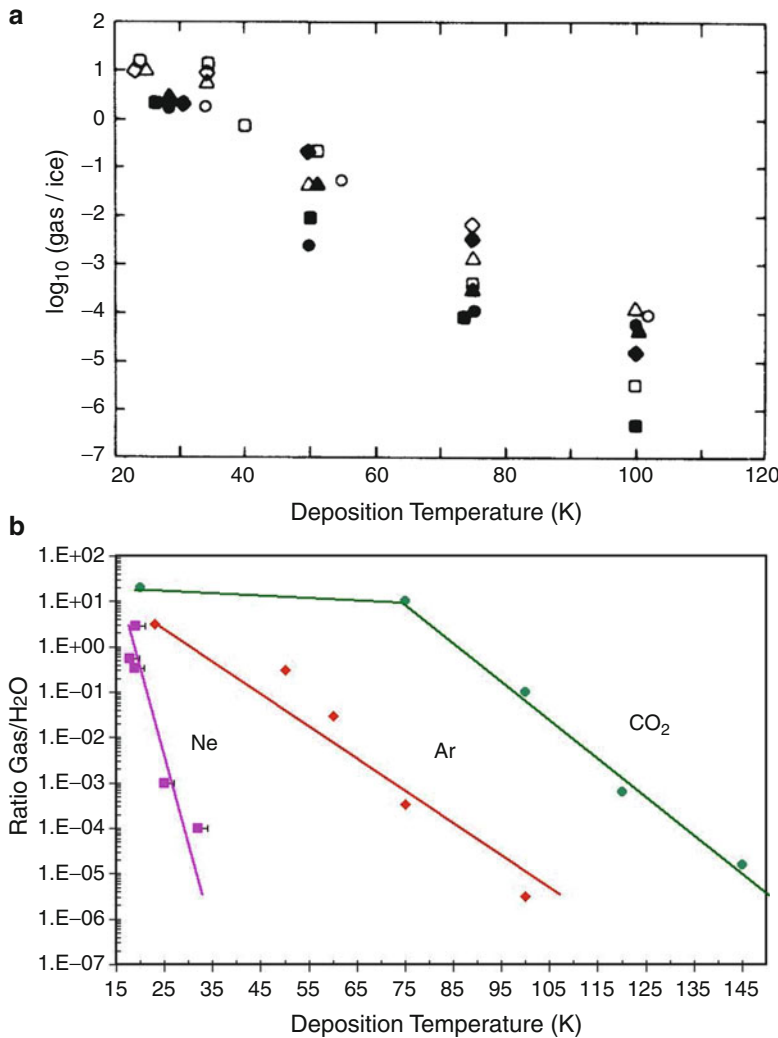


**Fig. 14.2** (a) Total amount of trapped gas versus deposition temperature for water vapor – gas mixtures.  $\diamond$  CH<sub>4</sub>,  $\Delta$  CO,  $\circ$  N<sub>2</sub>,  $\square$  Ar. Open symbols: results from deposition of a 1:1 ratio of a single gas species to water vapor. Filled symbols: results from the deposition of gas mixtures, H<sub>2</sub>O: CH<sub>4</sub>:Ar:CO (or N<sub>2</sub>) = 1:0.33:0.33 0.33. (b) Logarithmic decrease of trapping efficiency versus temperature: Ne, Ar, and CO<sub>2</sub>

efficiencies were observed to scale according to this factor for  $^{36}\text{Ar}/^{40}\text{Ar}$  and  $^{82}\text{Kr}/^{84}\text{Kr}$  (Notesco et al. 1999). The differences among the heavier Xe isotopes were too small to be significant, especially in view of their higher polarizability and consequent adherence to the ice walls.

Another mechanism of gas trapping is through the formation of clathrate hydrate, where water molecules form a cage around a guest molecule (Petrenko and Whitworth 2002). In the laboratory, ice is crushed by steel balls in the presence

of a high gas pressure (Schmitt 1991). Since steel balls were not available in the region of comet formation, we resorted to gentler procedures. In this region the gas pressures were very low, and consequently clathrate-hydrates of CH<sub>4</sub>, CO, CO<sub>2</sub>, N<sub>2</sub>, HCN, Ar, Kr, Xe could not have been formed (Davidson et al. 1987; Schmitt 1991). The only gases capable of forming clathrate-hydrates at low gas pressures are methanol, tetrahydrofuran, and oxirane (ethylene oxide) (Notesco and Bar-Nun 2000; Richardson et al. 1985), but not even the fairly polar HCN.

Another trapping mechanism involves ammonia. It is trapped in the ice like the other gases, but upon warming, H<sub>2</sub>O and NH<sub>3</sub> form a hemihydrate NH<sub>3</sub>·2H<sub>2</sub>O at ~130 K, and a hydrate NH<sub>3</sub>·H<sub>2</sub>O at 158 K (Moore et al. 2007, Notesco and Bar-Nun, unpublished). Both clathrate-hydrates and ammonia hydrates decompose at elevated temperatures and release their gases.

## 14.2 Gas Release

The entire description of gas release is shown in Fig. 14.1. The first step of gas release from its cages in the amorphous ice occurs between 35 and 120 K, where it anneals slowly, in temperature dependent steps (Bar-Nun et al. 1987). During these slow structural changes, some trapped gas is released. Gas release stops altogether when the temperature is kept constant for several days and is resumed when the temperature increases by a mere few degrees, showing that the annealing is strongly temperature dependant. This gas release can be responsible for the observed activity of comets at large heliocentric distances preperihelion (Meech et al. 2009).

Beginning at about 120 K, water molecules have enough energy to move and form the more stable cubic structure, with about 70% remaining as “restrained amorphous” ice (Jenniskens and Blake 1994). The rate of transformation increases exponentially with temperature and becomes large at ~135 K. During this process, the gases that were trapped in the amorphous ice are released from it by dynamic percolation (Laufer et al. 1987) following the increasing fraction of transformed ice.

The dependence of gas release on the thickness of the ice sample is shown in Fig. 14.3. In Fig. 14.3a, the 0.1 μm ice layer releases all its trapped gas during the transformation to cubic ice and restrained amorphous ice. However as seen in Fig. 14.3b, with a 5 μm thick ice layer, some of the gas is left in the cubic and restrained amorphous ice to be released only during the transformation of both ices to the hexagonal structure at 160 K. This is because in a thicker ice layer, movement of water molecule to form cubic and restrained amorphous structures also *closes* pores and traps some of the gases, until further movement, during the transformation to hexagonal ice releases them. In thicker ice samples, 50 μm as in Fig. 14.1, even the transformation to hexagonal ice cannot release all the gas, which is trapped at a greater depth. Only the sublimation of the entire ice layer releases the trapped gases (region “g” in Fig. 14.1).

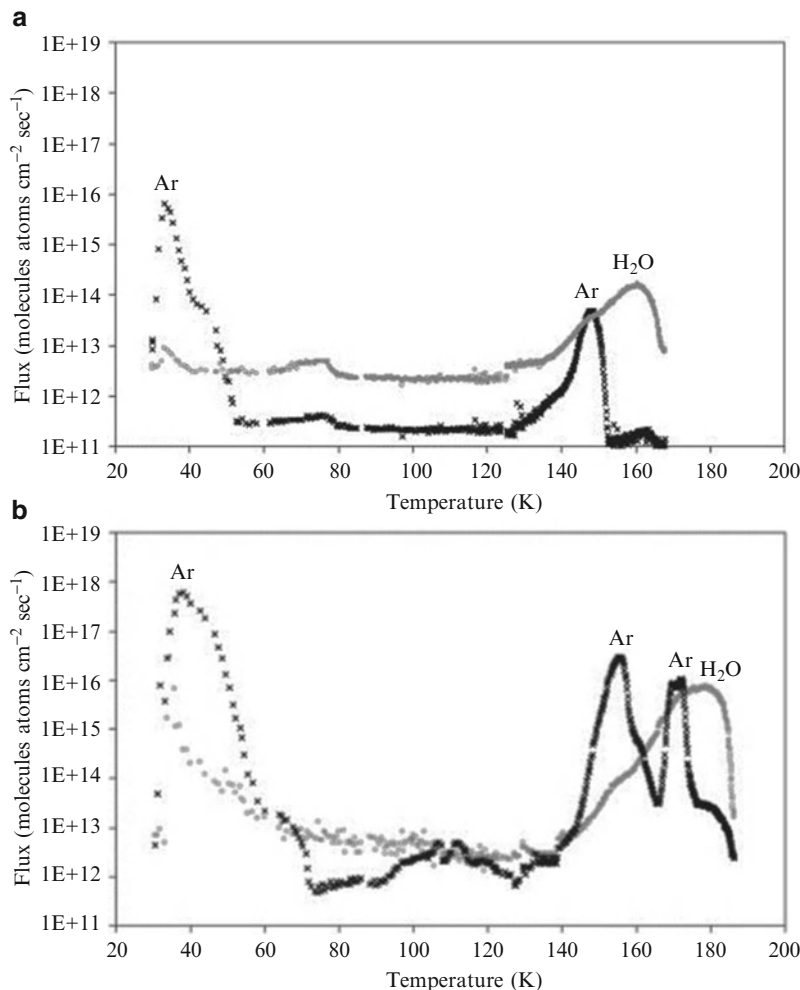


**Fig. 14.3** A plot of the fluxes of evolved Ar (black curve) and water (gray curve) during warming up of 0.1  $\mu\text{m}$  (a) and 5  $\mu\text{m}$  (b) ice layers. The gas-laden ice was deposited at 27 K from a  $\text{H}_2\text{O}$ : Ar = 1:1 mixture, at a rate of  $10^{-3} \mu\text{m min}^{-1}$ . The reason for the large amount of frozen Ar (30–40 K) compared with the amount of water was explained by Notesco et al. (2003). This frozen gas would not accumulate during ice formation in micron and sub-micron grains during  $10^5$  years

### 14.3 Laser Induced Gas Release

A complementary strategy for studying the release of trapped gas in ASW films enlists pulsed IR radiation. The idea is to trigger the release of host and guest species by heating samples that have been deposited (90 K) on an electrically insulating, but thermally conducting, substrate. The IR radiation is easily obtained by using stimulated Raman scattering (in D<sub>2</sub>) of the 1,064 nm output of a Nd-YAG laser. The resulting

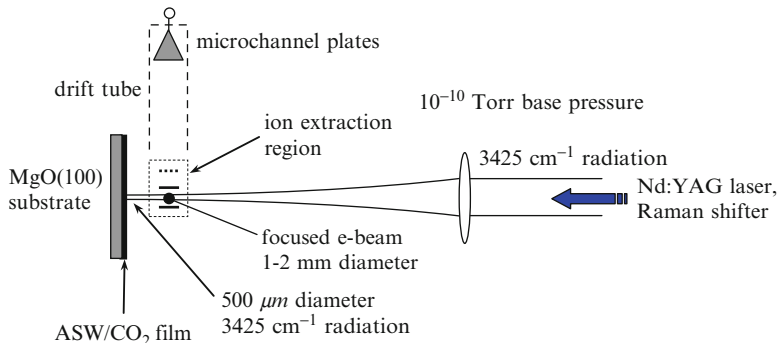


**Fig. 14.4** Arrangement for studying gas release from ASW/CO<sub>2</sub> films: The UHV chamber contains additional diagnostics: FTIR, TPD, and Auger spectroscopies (Hawkins et al. 2005; Kumi et al. 2006; Malyk et al. 2007). Samples were co-deposited at approximately 90 K

3,425  $\text{cm}^{-1}$  (second Stokes) line lies within the broad water absorption band. Specific vibrational degrees of freedom targeted by this photoexcitation are converted to heat on a picosecond time scale. For a few hundred layers, energy deposition is quite uniform because the attenuation length is an order of magnitude larger than the film thickness. Were the film on a perfectly thermally insulating substrate, photoexcitation would create a liquid that would rid itself of essentially all CO<sub>2</sub>. On the other hand, facile heat transfer to the substrate results in large temperature gradients. In this case, the release of trapped gas can vary markedly with distance from the substrate.

An important feature of the experiments is that data are acquired following a single IR pulse. Subsequent pulses address samples that, under our experimental conditions, differ markedly from the one that interacts with the first pulse. In other words, the first pulse induces qualitative changes in the sample, as discussed below.

The above ideas are best illustrated with an example. Referring to Fig. 14.4, pulsed IR radiation is incident on a CO<sub>2</sub>/ASW film, and a time-of-flight (TOF) mass spectrometer probes molecules that leave the surface. We have used a number of complementary methods to prepare films (i.e., deposit CO<sub>2</sub> first, deposit CO<sub>2</sub> last, sandwiches, co-deposition). The data reported here have all been obtained using co-deposition at approximately 90 K. Another important feature involves the TOF mass spectrometer, and the fact that packets of ions can be extracted from the ionization region at repetition rates up to 200 kHz. Specifically, these high repetition rates are achieved using a continuous electron beam whose center energy is 70 eV, with pulsed extraction of the ions. The high repetition rate capability enables temporal behavior to be recorded for different species leaving the surface.

Figure 14.5 shows TOF spectra for a single IR pulse. Each 10  $\mu\text{s}$  interval corresponds to a mass spectrum (i.e., ion extraction is carried out at 100 kHz). Good S/N enables removal efficiencies to be determined layer-by-layer. The IR beam diameter exceeds greatly the film thickness, so heat transfer takes place into the substrate.

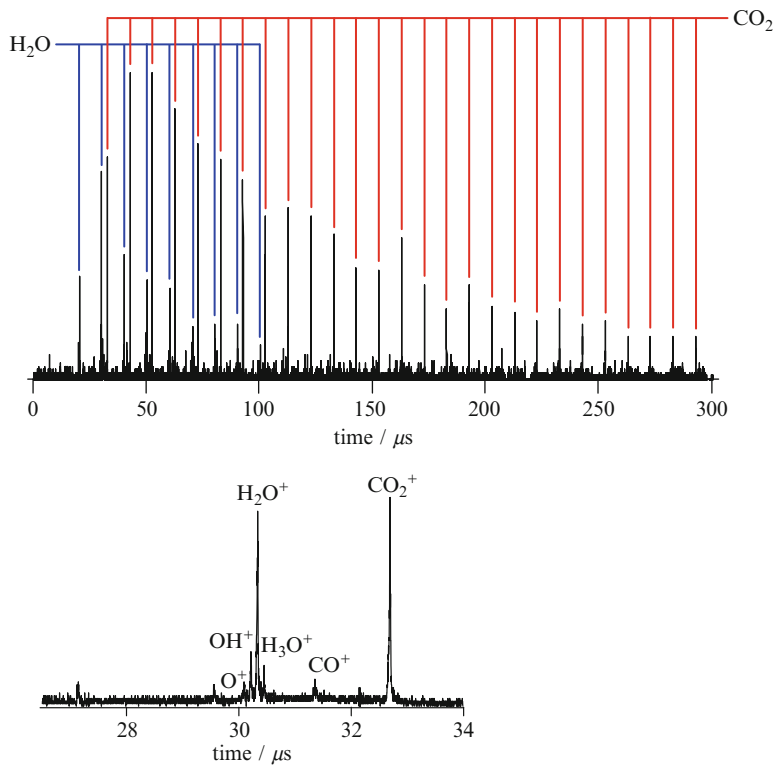


**Fig. 14.5** *Upper:* a burst of molecules produced by a single 10 ns IR pulse is analyzed by closely spaced TOF mass spectra. The sample (300 layers,  $\text{CO}_2$ :  $\text{H}_2\text{O}$  = 1:3) was co-deposited at 90 K. Blue and red lines indicate  $\text{H}_2\text{O}$  and  $\text{CO}_2$  contributions, respectively. *Lower:* the region near 30  $\mu$ s is expanded.  $\text{H}_3\text{O}^+$  indicates the presence of higher-than-monomer species. There is ~3 times more  $\text{CO}_2$  than  $\text{H}_2\text{O}$  in the released gas even though the deposited sample contains three times more  $\text{H}_2\text{O}$  than  $\text{CO}_2$ . Note that  $\text{CO}_2$  leaves the surface with lower speed than  $\text{H}_2\text{O}$

Figure 14.6 shows data from two pulses incident at the same location. The first addresses a fresh sample (300 layers,  $\text{CO}_2$ :  $\text{H}_2\text{O}$  = 1:3). Released  $\text{CO}_2$  exceeds released  $\text{H}_2\text{O}$  by a factor of ~3. Thus, the  $\text{CO}_2$  content is ~9 times higher than in the initially condensed sample. The  $\text{CO}_2$ : $\text{H}_2\text{O}$  ratio for released gas decreases with continued irradiation: (b) shows that for the sixth pulse the amounts of  $\text{CO}_2$  and  $\text{H}_2\text{O}$  are comparable. The system can be calibrated by recording signal vs. film thickness, enabling the amount of material removed per pulse to be determined.

The laser-induced temperature increase facilitates  $\text{CO}_2$  removal, whereas rapid cooling by the substrate acts to lessen  $\text{CO}_2$  removal. Consequently, material close to the substrate remains amorphous, trapping  $\text{CO}_2$  efficiently, whereas the region near the film surface has much less  $\text{CO}_2$ . The physics is the same as that of the fluffy agglomerates experiments, but here processes transpire in the presence of a

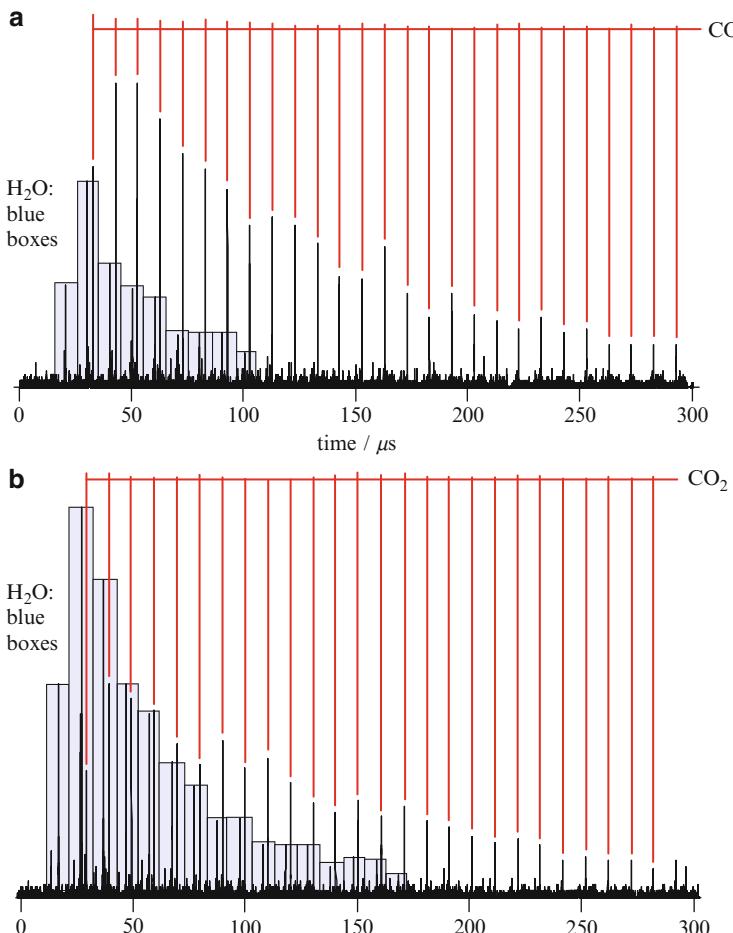


**Fig. 14.6** (a) Co-deposition (300 layers,  $\text{CO}_2$ :  $\text{H}_2\text{O} = 1:3$ ) was carried out at 90 K. A single IR pulse addresses the sample. Entry (b) is from the sixth pulse incident on the same area. The amount of  $\text{CO}_2$  exceeds the amount of  $\text{H}_2\text{O}$  by 20%. Blue boxes correspond to  $\text{H}_2\text{O}$  peaks

heat sink. On an insulating substrate, a few mJ is expected to release nearly 100% of the  $\text{CO}_2$  in a film of several hundred layers thickness, over an area  $>1 \text{ mm}^2$ .

Summing up the results of the experimental studies of gas release from thin layers of gas laden amorphous ice, we conclude that changes in the ice, due to heating the entire ice, or locally by laser heating, release the trapped gases. Yet, what happens in much thicker, comet like ice samples, composed of these gas-laden grains of amorphous ice?

**Fig. 14.7** A picture of the laboratory machine where thin ice samples are studied. Water vapor and gases flow onto a cold plate. Amorphous ice traps gases that are released during warming of the cold plate



#### 14.4 Large Ice Samples

As described above, the trapping of gas, as well as its release from ice, were studied in our laboratory with ice samples of thickness 0.1–100  $\mu\text{m}$ . The machine used for these studies is shown in Fig. 14.7.

A further step in comet simulation was achieved by constructing a unique machine capable of producing large (20 cm diameter, up to 10 cm high) samples of gas-laden amorphous ice (Fig. 14.4). One cannot produce large samples of amorphous ice by depositing water vapor on a cold plate, as is done routinely for samples up to hundreds of micrometers thick used in small-ice-sample studies. This is because it is necessary to get rid of the large heat of condensation of water vapor into ice ( $2.7 \times 10^{10} \text{ erg g}^{-1}$ ) through the growing ice sample, whose heat conductivity is poor (less than  $\sim 10^4 \text{ erg cm}^{-1} \text{ K}^{-1} \text{ s}^{-1}$ ) (Klinger 1981; Prialnik and Bar-Nun 1992; Bar-Nun and Laufer 2003) (Fig. 14.8).

If one grows an ice layer that is too thick, the heat of deposition cannot be transmitted to the cold surface, and the newly deposited ice layer reaches  $\sim 120 \text{ K}$

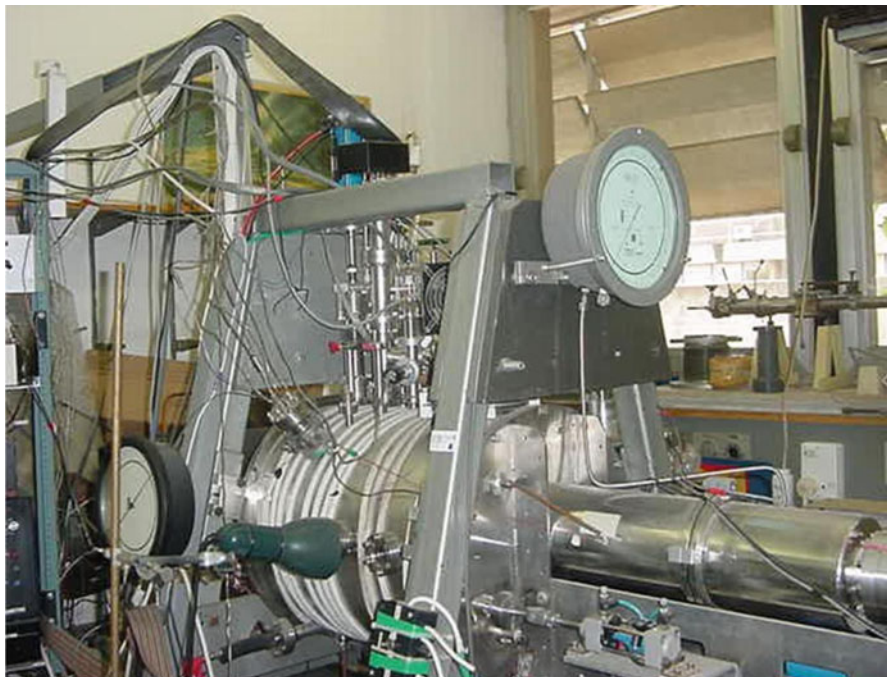


**Fig. 14.8** Picture of the laboratory machine that is used to study large ice samples

and becomes crystalline rather than amorphous. Consequently, it does not trap the gas that is flowed together with the water vapor. The solution was to slowly form thin  $\sim 200\text{ }\mu\text{m}$  ice layers on a 80 K (liquid nitrogen) cold plate, through which the heat of condensation of water could still be transmitted to the cold surface, remain amorphous, and trap the accompanying gas in it. Once a thin amorphous gas-laden ice layer is formed, it is scraped from the plate on which it is formed by an 80 K cold knife into the 80 K sample container, which is covered by an 80 K dome (Bar-Nun and Laufer 2003).

Thus a 20 cm diameter and up to 10 cm thick sample of a fluffy agglomerate of  $200\text{ }\mu\text{m}$  particles of porous amorphous gas-laden ice is formed. This sample is a good representative of the “snowball” so cleverly proposed by Fred Whipple (1987). Upon warming by the heating dome (7 in Fig. 14.9), a heat wave penetrates inward, releasing the trapped gases and sublimating the upper layer. A typical plot, together with the response of the embedded thermocouples to the penetrating heat wave, is shown in Fig. 14.10.

A major observation is that trapped Ar (which behaves like CO) emanates from the *entire* sample, whereas water vapor sublimes only from the surface, as expected. This is demonstrated by first blocking the irradiation, followed by resuming it. Whereas the surface cools quickly and ice sublimation ceases, the warmer interior releases its trapped gas. As seen in Figs. 14.1, 14.2, 14.3, 14.4, 14.5, and 14.6, the gases thus released escape quiescently. However, when more vigorous gas release

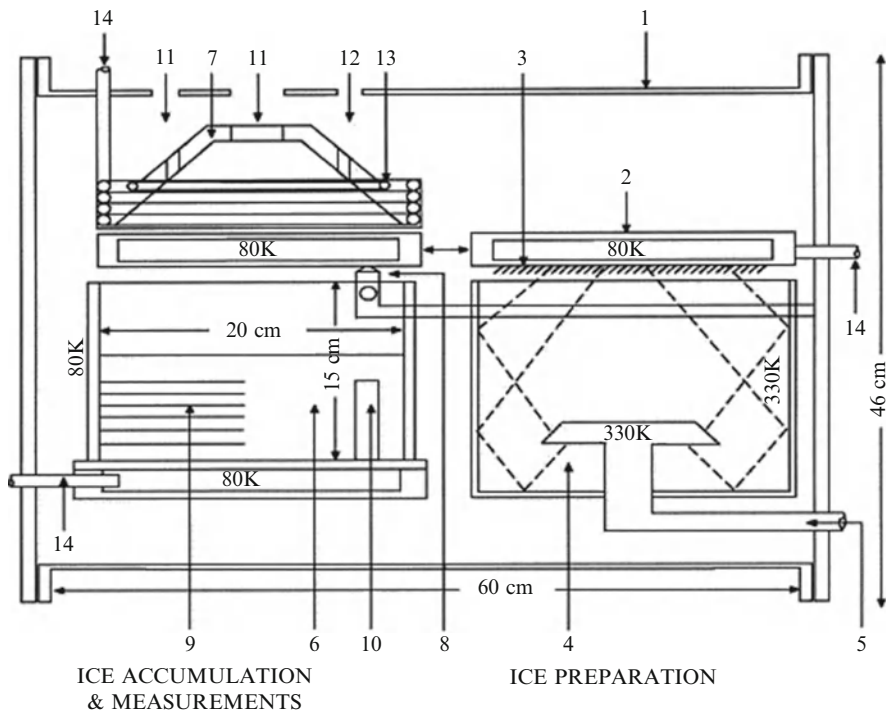


**Fig. 14.9** Schematic drawing of the machine producing large ( $200 \text{ cm}^2 \times 10 \text{ cm}$ ) gas-laden amorphous ice samples, as a “comet” simulation: (1) vacuum chamber; (2) 80 K cold plate; (3)  $200 \mu\text{m}$  amorphous gas-laden ice; (4) homogeneous flow of water vapor and gas; (5) water vapor and gas pipes; (6)  $200 \text{ cm}^2$  and 5–10 cm thick ice sample; (7) heating dome; (8) 80 K cold knife; (9) thermocouples; (10) density measurements; (11) mass spectrometer; (12) ionization gauge; (13) heating tape; (14) LN<sub>2</sub> cooling pipes

occurs, the gases carry with them huge fluxes of ice grains. These grains, each having about  $10^{10}$  water molecules, are propelled by gas jets, each having  $10^{10}$ – $10^{12}$  molecules (Laufer et al. 1987). In large samples, the gas emanating from below produces a bulge that eventually breaks, releasing a huge flux of gas and a plethora of ice grains. These phenomena are discussed in another chapter in this book.

## 14.5 Summary

The processes occurring during the formation of ice grains in the presence of gas are rather simple: At low enough temperatures around 20–50 K, the water molecules stick to the ice matrix where they hit, forming an open porous structure. Gas molecules enter these pores and reside there for a while, attracted by van der

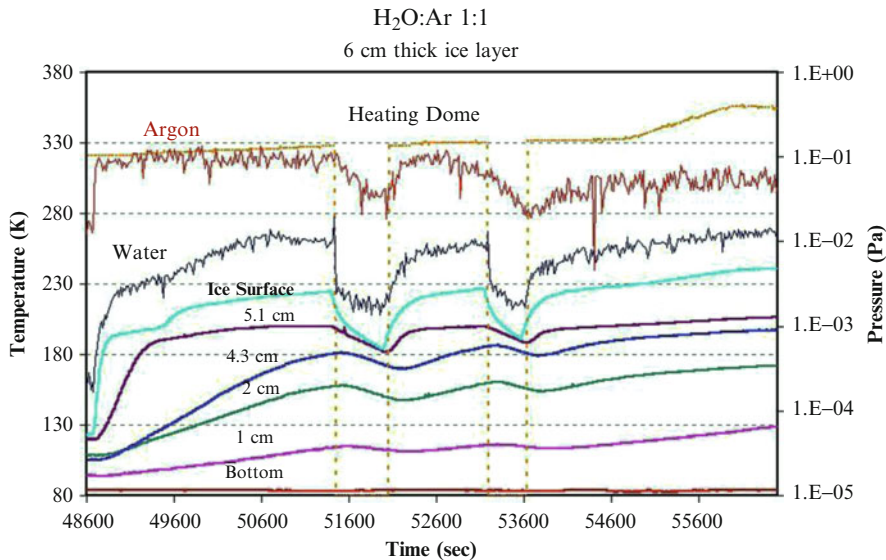


**Fig. 14.10** Evolution of trapped Ar and sublimation of water from the surface, together with temperatures measured by thermocouples in the interior

Waals forces. If before they leave the pore it is covered by a subsequent ice layer, they are trapped inside.

The trapped gases can escape the ice when the water molecules which form the cold ice move due to heating. This process occurs during the annealing of the ice between 50 and 120 K in a stepwise, temperature depended manner, and then during the vigorous transformation to cubic ice. If buried in deeper layers, further transformation of the cubic ice to hexagonal ice is needed for release another fraction of the trapped gases. All these movements of water molecules in the ice both open gas filled pores and close some. Hence the final release of all the remaining gas awaits the sublimation of the entire layer. This description encompasses the entire gas release mechanism. However, with sub-micron ice particles, all the trapped gas will be released during the transformation to cubic ice.

Another matter altogether is the release of trapped gas from a few cm thick agglomerate of  $\sim 100 \mu\text{m}$  gas-laden amorphous ice particles. Upon warming from above, gas is released from the interior while the water sublimates only from the surface. This means that the gas/water vapor in cometary comae are enriched by gas, and raises the question of what is the real composition of cometary nuclei.

Further consequences of gas release from underneath are discussed in other chapters of this book.

**Acknowledgements** This work has been supported by the US- Israel Binational Science Foundation, BSF grant 2006339 and by the U.S. Army Research Office under grant number W911NF-07-1-0081.

## References

- Bar-Nun A, Laufer D (2003) First experimental studies of large samples of gas-laden amorphous “cometary” ices. *Icarus* 161:157–163
- Bar-Nun A, Dror J, Kochavi E, Laufer D (1987) Amorphous water ice and its ability to trap gases. *Phys Rev B* 35:2427–2435
- Bar-Nun A, Kleinfeld I, Kochavi E (1988) Trapping of gas mixtures by amorphous water ice. *Phys Rev B* 38:7749–7754
- Bar-Nun A, Notesco G, Owen T (2007) Trapping of N<sub>2</sub>, CO and Ar in amorphous ice – Application to comets. *Icarus* 190:655–659
- Crovisier J (1997) Infrared observations of volatile molecules in comet Hale-Bopp. *Earth Moon Planet* 79:125–143
- Davidson DW, Desando MA, Gough SR, Handa YP, Ratcliffe CI, Ripmeester JA, Tse JS (1987) A clathrate-hydrate of carbon monoxide. *Nature* 328:418–419
- Hawkins S, Kumi G, Malyk S, Reisler H, Wittig C (2005) Temperature programmed desorption and infrared spectroscopic studies of thin water films on MgO(100). *Chem Phys Lett* 404:19–24
- Jenniskens P, Blake DF (1994) Structural transitions in amorphous water ice and astrophysical implications. *Science* 265:753–756
- Kawakita H, Watanabe J, Ando H, Aoki W, Fuse T, Honda S, Izumiura H, Kajino T, Kambe E, Kawanomoto S, Noguchi K, Okita K, Sadakane K, Sato B, Takada-Hidai M, Takeda Y, Usuda T, Watanabe E, Yoshida M (2001) The spin temperature of NH<sub>3</sub> in comet C/1999 S4 (LINEAR). *Science* 294:1089–1091
- Klinger J (1981) Some consequences of a phase transition of water ice on the heat balance of comet nuclei. *Icarus* 47:320–324
- Kumi G, Malyk S, Hawkins S, Reisler H, Wittig C (2006) Amorphous solid water films: transport and guest-host interactions with CO<sub>2</sub> and N<sub>2</sub>O dopants. *J Phys Chem A* 110:2097–2105
- Laufer D, Kochavi E, Bar-Nun A (1987) Structure and dynamics of amorphous water ice. *Phys Rev B* 36:9219–9227
- Malyk S, Kumi G, Reisler H, Wittig C (2007) Trapping and release of CO<sub>2</sub> guest molecules by amorphous ice. *J Phys Chem A* 111:13365–13370
- Meech KJ, Pittichová J, Bar-Nun A, Notesco G, Laufer D, Hainaut OR, Lowry SC, Yeomans DK, Pitts M (2009) Activity of comets at large heliocentric distances pre-perihelion. *Icarus* 201:719–739
- Moore MH, Ferrante RF, Hudson RL, Stoneb JN (2007) Ammonia–water ice laboratory studies relevant to outer Solar System surfaces. *Icarus* 190:260–273
- Mumma MJ, Blass WE, Weaver HA, Larson HP (1988) Measurements of the ortho-para ratio and nuclear spin temperature of water vapor in comets Halley and Wilson (1986 l) and implications for their origin and evolution. *Bull Am Astron Soc* 20:826
- Notesco G, Bar-Nun A (2000) The effect of methanol clathrate-hydrate formation and other gas-trapping mechanisms on the structure and dynamics of cometary ices. *Icarus* 148:456–463
- Notesco G, Bar-Nun A (2005) A 25 K temperature of formation for the submicron ice grains which formed comets. *Icarus* 175:546–550
- Notesco G, Laufer D, Bar-Nun A, Owen T (1999) An experimental study of the isotopic enrichment in Ar, Kr and Xe when trapped in water ice. *Icarus* 142:298–300
- Notesco G, Bar-Nun A, Owen T (2003) Gas trapping in water ice at very low deposition rates and implications for comets. *Icarus* 162:183–189
- Petrenko VF, Whitworth RW (2002) Physics of ice. Oxford University Press, New York
- Prialnik D, Bar-Nun A (1992) Crystallization of amorphous ice as the cause of Comet P/Halley’s outburst at 14 AU. *Astron Astrophys* 258:L9–L12
- Richardson HH, Wooldridge PJ, Devlin JP (1985) FT-IR spectra of vacuum deposited clathrate hydrates of oxirane, H<sub>2</sub>S, THF, and ethane. *J Chem Phys* 83:4387–4394
- Schmitt B (1991) Thermal and physicochemical processes in cometary nuclei. In: Benest E, Foershle C (eds) Interrelations between physics and dynamic for minor bodies in the solar system. Frontières, Gif-sur-Yvette, pp 265–307
- Whipple FL (1987) The cometary nucleus. *Astron Astrophys* 187:852–858

**Part IV**  
**Surface Ice Chemistry**

# Chapter 15

## Chemistry in Water Ices: From Fundamentals to Planetary Applications

Murthy S. Gudipati and Paul D. Cooper

**Abstract** Laboratory studies pertinent to the chemistry of ices with and without additional ingredients such as organics is critical to our understanding of how solar system icy bodies from comets and Kuiper Belt Objects far away in the outer solar system to the ices on Earth, much closer to the sun. This chapter reviews our present day understanding of the fundamental processes that occur in water-rich ices, containing organic impurities. In particular, the role of radiation – photons, electrons, and ions on the chemical evolution of solar system ices, including the newly discovered photoionization in ices, are reviewed.

### 15.1 Introduction

Understanding chemical processes in ices has implications from the interstellar medium to Earth's icy interiors and everything between – the Oort cloud, Kuiper Belt Objects (KBOs), comets, asteroids, icy outer solar system bodies, and Mars. Attempts to understand the chemistry that occurs on surfaces and in interiors of icy bodies found in these environments is by no means an easy task. This is principally due to the fact that our knowledge of such chemical processes can only be inferred from limited astronomical observations, and limited in-situ (if at all) analyses. The reflectance spectra obtained through ground or Earth-orbiting telescopes, or

---

M.S. Gudipati (✉)

Science Division, Jet Propulsion Laboratory, California Institute of Technology,  
Mail Stop 183-301, 4,800 Oak Grove Drive, Pasadena, CA 91109, USA

Institute for Physical Sciences and Technology, University of Maryland,  
Space Science Building, College Park, MD 27042, USA  
e-mail: [gudipati@jpl.nasa.gov](mailto:gudipati@jpl.nasa.gov); [gudipati@umd.edu](mailto:gudipati@umd.edu)

P.D. Cooper  
Department of Chemistry and Biochemistry, George Mason University,  
MS 3E2, 4,400 University Drive, Fairfax, VA 20186, USA  
e-mail: [pcooper6@gmu.edu](mailto:pcooper6@gmu.edu)

the small number of missions such as Voyager, Galileo and Cassini, can only sample the outer few microns of icy crust. The information gathered thus may not be representative of deeper chemical processes; especially considering the high radiation dose the outer few microns of ice receives. Chemistry of/in ice is further complicated by impurities other than H<sub>2</sub>O, such as organics, inorganics, minerals, and trapped gases (O<sub>2</sub>, CO, CO<sub>2</sub>, CH<sub>4</sub>, etc.). The parameters that expand the complexity into other dimensions are temperature, pressure, source of energy (radiation or chemical potential etc.), and boundaries with liquid or gas-phase. The analogy of the tip of an iceberg is indeed a good metaphor to represent the state of our present understanding of chemistry in ices. In this review, we focus on surface and near surface (up to ~ one meter) chemistry in ices. Studies on chemical processes in subsurface ices are still in their infancy and will not be dealt with here. Furthermore, by ice we mean the H<sub>2</sub>O molecule with usage of water vapor, liquid water, and water ice to represent the three physical forms of water.

Remote surface spectral sensing usually provides chemical information regarding the most dominant species on the surface (e.g. H<sub>2</sub>O, CO<sub>2</sub>, etc.). The infrared spectral region (~1.5–50 μm) is crowded by the absorption of water molecules and lattice vibrations, should the ice be H<sub>2</sub>O ice. Occasionally a trace chemical species can be identified either through fortuitous absorptions in the relatively transparent spectral windows spared by H<sub>2</sub>O absorption itself, or if the constituent has an unusually high intrinsic band strength. In addition to surface observations, occasionally, extra data can be obtained from icy satellites, such as measurements of tenuous atmospheres and gas plumes, that yield information about the chemical constituents of the near surface and/or satellite interior. In the case of tectonically active satellites such as Enceladus, outflows from cracks in the crust yield more detailed information about the surface/subsurface constituents.

It is important to distinguish that spectral remote sensing only provides information regarding chemical constituents and not the *chemistry itself*. Chemistry is a chain of chemical reactions that occur during the interaction of energy (radiation, energetic particles etc.) with matter (surface/subsurface ice with its constituent trace molecules). These reactions are difficult, if not impossible to observe through remote sensing, which is like taking snapshots of an event. The time lapse between these events, like that is captured by a video, can be simulated in a controlled environment in laboratory. As a result, experimentalists can put together pieces of a puzzle to get the full-story, or in other words reaction mechanisms involved in the chemical evolution of icy bodies. It is the aim of this review to use laboratory research, that is conducted with a variety of analytical tools in a controlled manner, to connect the snapshots of astrophysical observations, thereby providing the full-story of how and why chemistry happens as it happens.

Chemistry is the science of composition and structure of matter and what happens when a substance undergoes a permanent transformation. Chemistry ultimately is about redistribution of atoms and electrons in a molecule or atom involving taking or giving away energy. Electrons are responsible for the formation of chemical bonds between atoms. An atom or a collection of atoms (a molecule) prefers to be in its lowest possible electron energy configuration. And so, the electrons arrange themselves in order to minimize the energy of the system.

When nuclear repulsions are overcome by the electron-proton attractive potentials, a chemical bond between atoms results, forming molecules. This ultimately determines all chemical and physical properties of the system. This is a significantly simplified description of chemistry in terms of quantum mechanics. Advanced readers are referred to excellent graduate and undergraduate textbooks on this subject (Atkins and de Paula 2009; Szabo and Ostlund 1996).

A macroscopic view of chemistry can be expressed in terms of thermodynamics and kinetics. Thermodynamics can determine spontaneity of reactions, yet provides no details regarding how long such reactions may take to occur. Kinetics provides information regarding the rate of chemical change, but provides no information on the reaction mechanism.

When considering the chemistry of icy satellites, it is these properties that laboratory science seeks to understand, and it is these properties that make up the majority of the metaphorical iceberg. More and more laboratory studies are now emerging that look into the whole picture – from macroscopic processes to nanoscopic chemical reaction pathways and mechanisms.

## 15.2 Primary Processes in Radiation Induced Chemistry

Before we go into the details of ice chemistry, it is also important to look at the primary processes that could occur when a molecule or atom exchanges a quanta of energy (by absorbing a photon, or scattering of an electron or charged particle) resulting in an excitation process, as shown in Fig. 15.1. For clarity, rotational excitations are not shown in Fig. 15.1. Vibrational and rotational transitions and dissociation processes are limited to molecules containing a minimum of two atoms. When transitions occur through exchange of one quanta of energy that is released in the form of light, the process is called emission, the reverse of absorption.

In the solid-state, such as in ices, rotational transitions are predominantly quenched, leaving vibrational and electronic transitions. Absorption of multiple quanta of vibrational energy either at once or sequentially, could result in excitation of molecules into high vibrational levels that cross over dissociative electronic states. This is likely in heavy ion radiolysis where the kinetic energy of the incoming ion can be transferred to vibrational motion of molecules in the icy surface. Dissociative electronic states can also be reached through absorption of ultraviolet photons. Such a process where a chemical bond between two atoms is broken due to nuclear repulsions dominating the electron-proton attraction is called dissociation of a molecule. These dissociations result in the majority of cases in the formation of two fragments (radicals, such as H, O, OH, NH<sub>2</sub>, CH<sub>3</sub>, etc.).

Absorption of higher energy results in ionization of an atom or molecule. Typically, the threshold beyond which a valance electron is ejected away from the molecule (resulting in a positively charged molecular or atomic ion) is called the ionization threshold or ionization energy (IE), expressed in eV. During the ionization process a neutral molecule is converted to its ion counterpart, as shown in Fig. 15.1. Beyond the first ionization threshold, at higher energies, further resonant ionization transitions

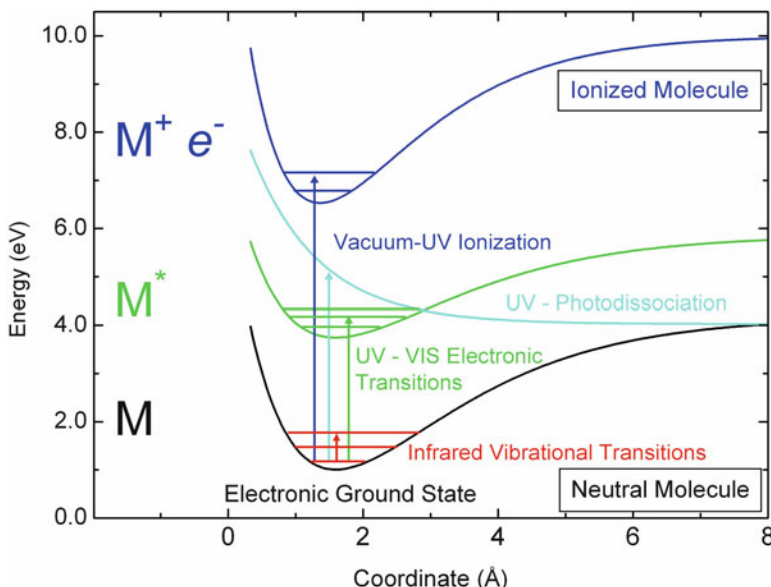


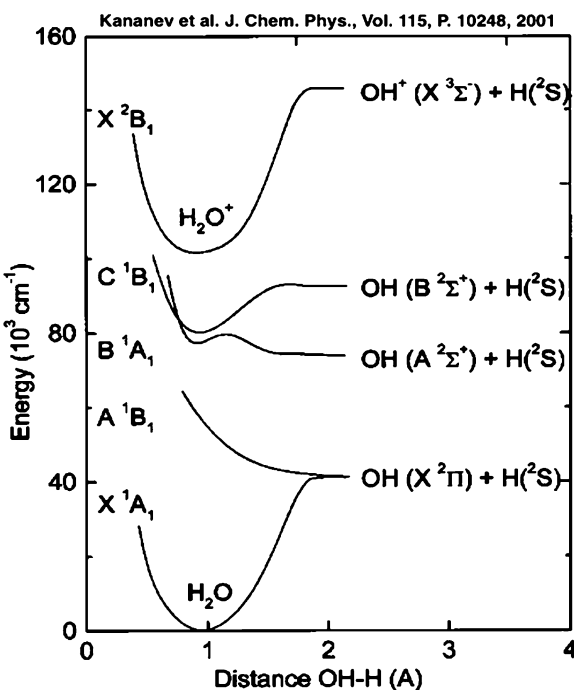
**Fig. 15.1** Excitations and subsequent processes in atoms and molecules caused by exchange of one quanta of energy.  $M$  is an atom or a molecule. These processes include ionization ( $M^+$ ), electronic excitation ( $M^*$ ), dissociation, vibrational and rotational excitations (rotational, vibrational, and dissociation processes occur only in molecules). Y-axis represents the energy involved in these processes (qualitative), whereas the X-axis represents interatomic distance in molecules (not applicable for atoms)

occur, whereby the ionized molecule finds itself in an electronically excited state. These transitions typically occur between 10 and 100 eV. At very high energies (several hundred eV), an electron from the core orbitals of a molecule (1S, 2S, etc.) can be ejected, which is followed by a valance electron filling the hole created by the first ejected electron, releasing a great amount of energy. This energy, in turn, results in ejection of another valance electron. Thus, absorption of a high-energy quantum of energy, several electrons in a molecule could be ejected which carry with them several tens to hundreds of eV kinetic energy. This whole process is called the Auger (pronounced as O-J) process (Hollas 2005). Such processes are extremely important when dealing with bombardment of MeV electrons and ions on the surfaces of icy bodies such as Europa. Each high-energy particle results in the generation of several hundreds or thousands of secondary electrons within the ice, which then can cause molecular ionizations and dissociations. This is almost like a dendrite process, which has not been studied systematically yet on ices in the laboratory.

### 15.3 Primary Chemical Processes in $H_2O$ Ice

Here we consider the possible chemical processes in  $H_2O$  ice. We do not distinguish between amorphous and crystalline forms at this point. In the solid phase, upon absorption of radiation, only two primary processes could occur to begin with:

**Fig. 15.2** Potential energy curves of  $\text{H}_2\text{O}$  dissociating to  $\text{H} + \text{OH}$ . With increasing energy, OH is formed in excited states, as can be seen from the state-symmetry in the parentheses for OH, where X is the ground-state, A is the first excited state, B the second excited state, etc. (Kanaev et al. 2001). Other channels not shown here also lead to minor amount of  $\text{O}^{(1)\text{D}} + \text{H}_2$  are formed (van Harreveld and van Hemert 2008)



(a) dissociation, and (b) ionization. Dissociation of  $\text{H}_2\text{O}$  can result in the formation of  $\text{H} + \text{OH}$  radicals or  $\text{O} + \text{H}_2$ . Similarly, ionization of  $\text{H}_2\text{O}$  results in the formation of  $(\text{H}_2\text{O})^+$  and injection of an electron into the ice. Any subsequent process is a result of the secondary and tertiary processes originating from these energy-rich and reactive radicals and ions with their surrounding molecules.

In the gas-phase,  $\text{H}_2\text{O}$  molecules are photodissociated at wavelengths shorter than 243 nm (Energy conversion:  $\text{cm}^{-1} = 1\text{e7}/\text{nm}$ ;  $\text{nm} = 1\text{e7}/\text{cm}^{-1}$ ;  $\text{eV} = 8065.5\text{ cm}^{-1}$ ). Potential energy curves that result in  $\text{H} + \text{OH}$  photodissociation are shown in Fig. 15.2, along with the ionization resulting  $\text{H}_2\text{O}^+$  molecular ground state. Minor dissociation into  $\text{O} + \text{H}_2$  is also seen when excited with  $\text{Ly}_{\alpha}$  radiation at 121.6 nm (Mordaunt et al. 1994; van Harreveld and van Hemert 2008). As seen in Fig. 15.2, the gas-phase ionization energy of  $\text{H}_2\text{O}$  to form  $\text{H}_2\text{O}^+$  is 12.6 eV, or  $101,600\text{ cm}^{-1}$ , or 98.4 nm (<http://webbook.nist.gov/chemistry/>). The electron affinity of the  $\text{H}_2\text{O}$  molecule is negative (nonbinding), meaning a single  $\text{H}_2\text{O}$  molecule in the gas-phase does not bind with an electron. However, two  $\text{H}_2\text{O}$  molecules (a water dimer) can bind with an electron. Electron binding energy increases with increasing cluster size of water, as shown in Fig. 15.3. With large enough cluster size, the binding energy is as much as 3 eV (Verlet et al. 2005). Under these conditions electrons trapped in  $\text{H}_2\text{O}$  clusters are known as “hydrated electrons”.

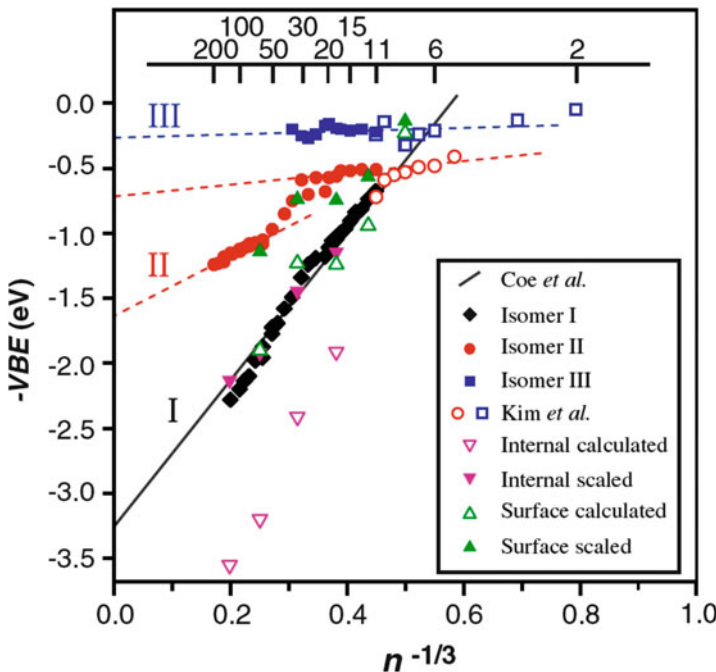


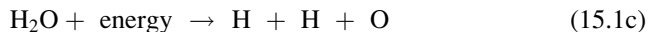
**Fig. 15.3** Vertical Binding Energy (VBE) of an electron with  $(\text{H}_2\text{O})_n$  clusters,  $n = 2-200$ . Binding energies of 3 eV or above are detected (Verlet et al. 2005). Physical meaning of VBE is that when an electron collides with  $(\text{H}_2\text{O})_n$  cluster, electron loses energy equivalent to the VBE into the cluster. If the internal energy of the electron is greater than VBE, then the electron may penetrate or escape the cluster. Several such collisions could leave the electron trapped by the water cluster. If the electron is generated within the cluster, it may or may not escape the cluster based on its internal energy and the VBE between the electron and the water cluster

## 15.4 Dissociation of Water Ice

The water ice that is present on all icy satellites in the outer solar system is exposed to some degree of damaging radiation. Due to this common feature, it is often assumed that many chemical processes are common to all icy satellites. Such processes include the formation of  $\text{H}_2\text{O}_2$  (Carlson et al. 1999; Gomis et al. 2004b; Loeffler et al. 2006a; Moore and Hudson 2000) and  $\text{O}_2$  (Johnson et al. 2005b; Spencer et al. 1995). However, the ultimate extent and complexity of the chemistry, that makes the surfaces of each icy satellite chemically distinct depends on many factors, including the amount of energy deposited in the surface, the energetic radiation type, the presence of atmospheres or magnetic fields, the primordial satellite constituents as well as other constituents formed over the history of the satellite.

The dissociation of water ice generally refers to the breaking of one or both chemical bonds in the  $\text{H}_2\text{O}$  molecule to produce neutral (uncharged) products. This process is chemically distinct from that of ionization, which produces charged

products as mentioned in the previous section. The possible primary dissociation reactions are shown below.



Surprisingly, after years of research, the branching ratios for these reactions in ice are unknown. In the gas phase there is a 10% branching ratio to reaction 15.1b. (Fillion et al. 2001; Harich et al. 2000, 2001; van Harreveldt and van Hemert 2000; van Harreveldt and van Hemert 2008; van Harreveldt et al. 2001; Yi et al. 2007). Reaction 15.1a is universally considered the most abundant in the solid state with the others almost never considered being of importance, however recent work (Cooper et al. 2010) has shown this may not be the case. The chemistry of the primary dissociation products, OH, H and O will now be addressed.

### 15.4.1 Primary Dissociation Products

#### 15.4.1.1 The OH Radical

The bond dissociation energy required to dissociate a single gas phase  $\text{H}_2\text{O}$  molecule as in Eq. 15.1a is  $\sim 5.1$  eV (Maksyutenko et al. 2006). To further dissociate the OH radical as in Eq. 15.2 requires an additional  $\sim 4.4$  eV (Joens 2001)



The bond dissociation energy and bond energy differ slightly because of this difference. By definition, the bond energy is the average of the two dissociation steps and thus is  $\sim 4.7$  eV.

This threshold energy for dissociation is interesting because the equivalent wavelength of UV light ( $\sim 243$  nm) is in a region where absorption by water in any form (gas, liquid or solid) is extremely small (Langford et al. 2001; Quickenden and Irvin 1980; Warren 1984). If water does not absorb at this threshold energy, then no dissociation is expected. Therefore around this threshold energy of  $\sim 5$  eV, one may expect a significant difference in chemistry between particle radiation that directly transfers energy to the ice and does not rely on the absorption of photons to dissociate water molecules, compared with UV photolysis at similar energies.

However, this does not explain the observations of  $\text{O}_2$  and OH luminescence phenomena in UV-irradiated ices by Quickenden and co-workers (Langford et al. 2000b; Lennon et al. 1993; Matich et al. 1993; Quickenden et al. 1982, 1985, 1988, 1996, 1997; Selby et al. 2006; Vernon et al. 1990). The technique of photon-counting weak luminescence is a particularly sensitive method of determining

chemistry – far more so than spectrometric absorption techniques. So although water is apparently “transparent” above 200 nm, there must still be weak absorption to some degree that explains the observations of Quickenden’s group.

The dissociation energy of 5.1 eV is in fair agreement with the threshold energy observed of ~6 eV for O<sub>2</sub> in electron-irradiated thin-film ices (Orlando and Sieger 2003). This value however is highly uncertain (Johnson et al. 2005a). This will also be discussed further later in this chapter.

Early measurements of OH in ice were centered on electron spin resonance (ESR) measurements (Box 1970) and observations of a 280 nm absorption band (Ghormley and Hochanadel 1971) associated with the A<sup>2</sup>Σ<sup>+</sup> ← X<sup>2</sup>Π transition in the OH radical. This corresponds to electronic excitation of OH from its ground state (X<sup>2</sup>Π) into the first excited (A<sup>2</sup>Σ<sup>+</sup>) state, as can be seen in Fig. 15.2. The Quickenden group performed an extensive series of measurements on the luminescence of OH produced from the UV-excitation of H<sub>2</sub>O ice. A comprehensive review of this field by the Quickenden group and others can be found in Langford et al. (2000a).

Although ESR, UV-absorption and luminescence studies of OH provide essential data to the spectroscopy and chemistry of OH in ice, these methods are not the most suited for rigorous planetary science remote-sensing or in-situ observations. UV-spectroscopy is widely used in planetary missions, however, due to the broadness of the absorption by ice in this region, conclusive assignments are often impossible. Instead, identification of species on a planetary surface is typically made in the near- and mid-infrared region where a molecule’s vibrational spectrum is usually quite unique – also known as the fingerprint region. However, the IR spectrum of icy bodies is dominated by water-ice absorption, which is broad by itself, leaving small non-absorbing spectral windows that can be used to detect other molecules.

In the infrared, it has so far proven impossible to detect OH radicals in an ice due to the overlapping of the OH stretch with the strong 3,200 cm<sup>-1</sup> band of water ice. A reported detection by Gerakines et al. (1996) is undoubtedly just a H<sub>2</sub>O–HO radical complex (Cooper et al. 2003c) matrix-isolated in the argon that capped their ice samples. Recently Zins et al. (2011) reported detection of OH in water ice. They assigned an infrared band at 3689 cm<sup>-1</sup> to (OH)(H<sub>2</sub>O)<sub>n</sub> bulk. This band, observed during microwave discharge of H<sub>2</sub>O diluted in He at 3.5 K, decreases in intensity monotonously upon annealing up to 35 K, almost disappearing under the absorption of ice itself. Once confirmed through other experimental work, this would be the first lab IR detection of OH in ice that could infer that OH radicals can only exist below 35 K in water ice.

Upon the initial dissociation step the OH radical can participate in a variety of chemical reactions. The simplest of these is the abstraction of H from H<sub>2</sub>O as in the following equation.



This equation is thought to be particularly important in gas-phase atmospheric chemistry (Aloisio and Francisco 2000) and should be expected to be a principle reaction of OH in ice too. If OH is trapped within the ice lattice without reacting, it is

possible that it may form a strong hydrogen bonded complex with the ice lattice, similar to that of the complex and a single water molecule ( $\text{H}_2\text{O}-\text{HO}$ ). This complex has an ab initio calculated binding energy of 5.69 kcal/mol (Cooper et al. 2003c), which is comparable to that of the water dimer binding energy of ~5 kcal/mol using similar calculations (Low and Kjaergaard 1999). This is probably the form of the “trapped OH” that is discussed in Johnson and Quickenden (Johnson and Quickenden 1997) that becomes mobile at temperatures of ~80 K where thermal energy can overcome such intermolecular forces. Chemical reactions involving OH radicals have recently been observed in ices at low temperatures and may indicate that OH may be mobile at temperatures perhaps as low as 40 K or 50 K (Cooper et al. 2008). Further research is still needed to verify the exact mechanism of OH mobility in ice.

The OH radical can potentially recombine with an H atom to re-form  $\text{H}_2\text{O}$ . The degree to which this occurs in irradiated ices is unknown. Further discussion of the H atom is dealt in the next section. OH can also react with another OH radical to form hydrogen peroxide ( $\text{H}_2\text{O}_2$ ). This will also be discussed later in the chapter.

In the presence of organic molecules in the irradiated ice, OH radicals react with organics forming hydroxylated organics (Bernstein et al. 1999; Gudipati 2004). However, there could still be some ambiguity whether the hydroxylation is due to OH radical reaction with organic molecules or the reaction of ionized organic molecules with  $\text{H}_2\text{O}$  (see below ionization section).

#### 15.4.1.2 The H-Atom

Not much is known about the stability of H atoms in  $\text{H}_2\text{O}$  ices, unlike the rare-gas cryogenic solids such as Ar, Kr, and Xe crystals in which H atom tunneling and long-range mobility has been well documented (Apkarian and Schwentner 1999; Khriachtchev et al. 2000, 2002; Tanskanen et al. 2008). Typically, H atoms are mobile in rare-gas solids at > 10 K. On the other hand, indirect evidence is available for the presence of H atoms in the ice upon radiolysis, when aromatic hydrocarbons are hydrogenated in the ice (Bernstein et al. 1999). It is expected that  $\text{H}_2$  will be the most probable product that may escape the ice at temperatures >20 K (Bar-Nun et al. 1985, 1987).

#### 15.4.1.3 The O Atom

Whereas the trapping of O atoms in rare-gas solids (Ar, Kr, & Xe) are well studied (Danilychev and Apkarian 1994; Gudipati and Kalb 1999; Gudipati et al. 2000), little data is available on the spectroscopy of O atoms in ice. Chemistry involving O atoms such as formation of ketones and hydroxylation of organics is shown to occur in the ice containing PAHs (Bernstein et al. 1999). Again, reactions due to O, OH or  $\text{H}_2\text{O}$  giving rise to hydroxylation are still not well understood. Indirect evidence for the radiolytic production of O atoms as a dissociation product of irradiated water ice has been shown (Cooper et al. 2010). In experiments containing icy mixtures of  $\text{H}_2^{16}\text{O}$  and  $^{18}\text{O}_2$ , a

variety of ozone isotopologues containing  $^{16}\text{O}$  atoms were observed upon irradiation, indicating O atoms being produced from the dissociation of water.

Perhaps the best evidence of O atoms in ices is the near edge x-ray absorption fine structure (NEXAFS) spectroscopy work by Laffon et al. (2006), where a tunable X-ray source such as synchrotron radiation is used to detect elements and their crystalline surroundings through fine-structure analysis of their X-ray absorption spectral fingerprints. They observe O atoms (as well as OH, HO<sub>2</sub>, O<sub>2</sub> and H<sub>2</sub>O<sub>2</sub>) after X-ray irradiation of crystalline water ice at 20 K. Of the oxidizing species detected, O atom is by far present in the smallest quantity, in apparent contradiction to the work of Cooper et al. (2010). This could be a result of the different irradiation methods, but with such limited data, a conclusive reason is hard to determine.

### **15.4.2 Secondary Dissociation Products**

#### **15.4.2.1 Hydrogen Peroxide (H<sub>2</sub>O<sub>2</sub>)**

Of all secondary dissociation products, H<sub>2</sub>O<sub>2</sub> has probably received the most experimental attention, especially since its observation on the surface of Europa (Carlson et al. 1999) by the Galileo spacecraft. Most recently, an assignment of H<sub>2</sub>O<sub>2</sub> on the surface of Enceladus has been suggested (Newman et al. 2007) although this has been called in to question (Loeffler and Baragiola 2009) due to band shape differences. Another possibility for this absorption may be methanol (Hodyss et al. 2009b).

The early work of Ghormley and Hochanadel (1971) showed that H<sub>2</sub>O<sub>2</sub> is produced in  $\gamma$ -irradiated pure water ice. Interestingly, they found that the maximum H<sub>2</sub>O<sub>2</sub> yield occurred at their highest irradiation temperature. However, to determine the yield of H<sub>2</sub>O<sub>2</sub>, their ices had to be melted and analyzed quantitatively for H<sub>2</sub>O<sub>2</sub>. These H<sub>2</sub>O<sub>2</sub> detections were not in-situ detections like those to follow.

In response to the Europa observations, Moore and Hudson (2000) were the first to investigate H<sub>2</sub>O<sub>2</sub> production via radiolytic methods using infrared spectroscopy in pure water ice. They found that in experiments using 800 keV H<sup>+</sup>, H<sub>2</sub>O<sub>2</sub> was only produced in comparable quantities to those observed on Europa at a temperature of 16 K. Experiments performed at 80 K yielded an undetectable amount of H<sub>2</sub>O<sub>2</sub>. This was an important result as the 80 K experiments are the more relevant to icy satellite surfaces. Moore and Hudson determined that the presence of O<sub>2</sub> or CO<sub>2</sub> as an impurity in the ice did allow the detection of H<sub>2</sub>O<sub>2</sub> in H<sup>+</sup>-irradiated ices at 80 K.

Supporting this work, Bahr et al. (2001) found only mass spectrometric evidence of H<sub>2</sub>O<sub>2</sub> formation in 200 keV H<sup>+</sup>-irradiated water ice at 80 K and 120 K. The amounts detected were sufficiently low to not observe the characteristic  $\sim 2,850\text{ cm}^{-1}$  band in the infrared. The yields from the mass spectrometry data however could not be quantitatively calculated because of the destruction of H<sub>2</sub>O<sub>2</sub> on the stainless steel walls of the vacuum chamber.

Following this work, Strazzulla and co-workers produced several papers (Gomis et al. 2004a, c; Strazzulla et al. 2005) that showed the opposite trend of H<sub>2</sub>O<sub>2</sub> production with temperature than the work of Moore and Hudson (2000). Strazzulla and co-workers performed experiments using a variety of 30 keV ions (H<sup>+</sup>, C<sup>+</sup>, N<sup>+</sup>, O<sup>+</sup> Ar<sup>+</sup>) and 200 keV ions (H<sup>+</sup>, He<sup>+</sup>, Ar<sup>++</sup>) as the bombarding energetic particles, and secondly, unlike Moore and Hudson, the ice thickness was greater than the penetrating depth of the radiation. Under such conditions, H<sub>2</sub>O<sub>2</sub> was produced at 77 K and 16 K without the need for an impurity (such as CO<sub>2</sub> or O<sub>2</sub>). For some of these ions, more H<sub>2</sub>O<sub>2</sub> was produced at the higher temperatures. Publications from this group concluded that impurities are not needed for H<sub>2</sub>O<sub>2</sub> production on icy satellites.

Following this work, the group of Kaiser investigated H<sub>2</sub>O<sub>2</sub> production in pure water ices using 5 keV electrons (Zheng et al. 2006a, b, 2007) over the temperature range 12–90 K. They found that H<sub>2</sub>O<sub>2</sub> production decreases with increasing temperature. At 90 K H<sub>2</sub>O<sub>2</sub> was not detectable in-situ using infrared spectroscopy, but was detected in their temperature-programmed-desorption (TPD) measurements. They estimate that at 90 K their column density of H<sub>2</sub>O<sub>2</sub> is of the same order of magnitude as those reported by Carlson et al. (1999) on Europa, but cannot quantify the value any further due to the lack of IR absorption data.

The radiolytic production of H<sub>2</sub>O<sub>2</sub> in water ice was also investigated by Baragiola and co-workers. They irradiated ice samples with 50 and 100 keV Ar<sup>+</sup> and 100 keV H<sup>+</sup>. Loeffler et al. (2006a) have shown that H<sub>2</sub>O<sub>2</sub> column densities decrease with increasing temperature, consistent with Moore and Hudson (Moore and Hudson 2000) and Zheng et al. (2006a, b, 2007). However, unlike Moore and Hudson (2000), this work shows that H<sub>2</sub>O<sub>2</sub> is still detectable at 80 K. Loeffler et al. explain their results in the context of previous work by asserting that the radiolytic yields of H<sub>2</sub>O<sub>2</sub> that can be produced in irradiated ices is controlled by the linear energy transfer (LET) of an energetic particle to the ice medium. LET is the amount of energy a particle loses to its surroundings as it travels through a medium (LET = ΔE/Δx). For the case of 800 keV H<sup>+</sup> (Moore and Hudson 2000), the LET is low compared with the lower energy ions used in the other experiments. The resulting low density of excitations/ionizations produces a lower yield of H<sub>2</sub>O<sub>2</sub>.

Understanding the temperature dependence of H<sub>2</sub>O<sub>2</sub> formation is critical if we are to predict the abundances of H<sub>2</sub>O<sub>2</sub> of icy surfaces in the outer solar system. However, this is not the only factor. The amount of deposited radiolytic energy and particle type also clearly play a role. For example, evidence for H<sub>2</sub>O<sub>2</sub> on Europa is strong, whereas observations of Ganymede and Callisto have failed to show its presence. It is possible that the decrease of radiation flux, in particular the heavy ion component that provides higher LET, as the distance from Jupiter increases may not yield enough H<sub>2</sub>O<sub>2</sub> for detection. But perhaps there are other unrecognized factors? Additionally of course, most icy surfaces are not pristine and contain impurities that may also affect H<sub>2</sub>O<sub>2</sub> yields. These variables make it difficult to predict whether or not H<sub>2</sub>O<sub>2</sub> will be detected on icy satellites beyond the Jovian system. If radiation and water ice are present on the majority of icy bodies, then it can be expected that H<sub>2</sub>O<sub>2</sub> will be formed. However its lifetime and the abundance in which it is formed, will depend on the nature of the icy body, its radiation environment, such as heavy or light ion, high or low flux, etc. Detailed studies in the laboratory with variable

temperatures, radiation types and fluxes, and ice impurities are required to further predict/understand the presence or absence of H<sub>2</sub>O<sub>2</sub> in our solar system.

The formation of H<sub>2</sub>O<sub>2</sub> dimers in ice was used by Cooper et al. (2003a) to predict that such clusters of H<sub>2</sub>O<sub>2</sub> molecules in an icy planetary surface may explain the observations of molecular oxygen (O<sub>2</sub>) from the icy Galilean satellites (Spencer and Calvin 2002; Spencer et al. 1995). They proposed that a dimer of H<sub>2</sub>O<sub>2</sub> could produce two H<sub>2</sub>O–O complexes that would ultimately produce O<sub>2</sub>. These could form in clusters of H<sub>2</sub>O<sub>2</sub> ice and that would aid in the trapping of volatile O<sub>2</sub>.

In order to characterize the behavior of H<sub>2</sub>O<sub>2</sub> in ice, the Baragiola group have performed experiments (Loeffler and Baragiola 2005) to determine the spectral characteristics and chemical behavior of H<sub>2</sub>O<sub>2</sub> containing ices. In particular, careful work was performed to characterize the band shapes and peak positions for amorphous and crystalline pure H<sub>2</sub>O<sub>2</sub> ice, H<sub>2</sub>O<sub>2</sub>/H<sub>2</sub>O ice mixtures, and radiolytically produced H<sub>2</sub>O<sub>2</sub> ice mixtures. Their work shows that the clusters of H<sub>2</sub>O<sub>2</sub> that were proposed to form to support O<sub>2</sub> formations may not occur on Europa due to the H<sub>2</sub>O<sub>2</sub> being too dilute. Using this data, they have assessed of the physical state of H<sub>2</sub>O<sub>2</sub> on Europa in a way that in principal can be used for all future astronomical observations of H<sub>2</sub>O<sub>2</sub> on icy planetary bodies.

#### 15.4.2.2 Molecular Oxygen (O<sub>2</sub>)

Absorption bands of molecular oxygen have been observed in visible wavelength range reflectance measurements of Ganymede (Spencer et al. 1995), Europa and Callisto (Spencer and Calvin 2002). The UV-visible region generally is not used for molecular identification due to the broadness of most electronic transitions of molecules. However, the assignment of absorption bands to O<sub>2</sub> is unambiguous due to the identification of two absorption bands that agree extremely well with literature data as discussed in Spencer et al. (1995). These astronomical measurements were further interesting because the nature of the absorption bands provided evidence that the oxygen molecules must be trapped in the icy surface.

UV-emission of molecular and atomic oxygen species has been observed from Ganymede's tenuous atmosphere (Hall et al. 1995, 1998). This is consistent with early laboratory studies that showed O<sub>2</sub> is formed in ion-irradiated ices (Brown et al. 1984). Upon its formation in ice, oxygen is sputtered out by further radiation or it can simply be sublimed from an icy surface as the freezing point of O<sub>2</sub> in a vacuum is only ~30 K, well below the surface temperature of Galilean and Saturnian Satellites. A model of the Europian atmosphere (Cassidy et al. 2007) suggests that an additional source of O<sub>2</sub> may be required to explain the observed column densities, however the large uncertainty in experimental and physical parameters makes further quantification difficult.

The nature of the absorption bands provides compelling evidence that these bands do not belong to O<sub>2</sub> present in the atmosphere, but originate from O<sub>2</sub> trapped as a solid in the icy surface. The  $a^1 \Delta_g + a^1 \Delta_g \leftarrow X^3 \sum_g^- + X^3 \sum_g^-$  double electronic transition (simultaneous excitation of two molecules that are next to each other – a cluster or a van der Waals dimer) that is assigned to the observed

absorption bands in reflectance data can only occur in O<sub>2</sub> dimers. The atmosphere of any of the icy Galilean satellites is far too tenuous for any appreciable column density of O<sub>2</sub> dimers – a molecular species held together only by weak van der Waals interactions. The detection of these absorption bands implies that O<sub>2</sub> has to be present as a solid on Ganymede’s icy surface. A comparison with the laboratory spectrum of solid O<sub>2</sub> shows (Calvin et al. 1996) that the absorption bands do indeed agree with those of solid phase O<sub>2</sub>. Cooper et al. (2003b) evaluated all O<sub>2</sub> absorption bands from the near infrared through to the vacuum UV and found that the dimer bands are in fact not the most intense absorption bands of O<sub>2</sub>, leaving the possibility that other bands may be detectable on icy satellites surfaces.

The observations of solid O<sub>2</sub> are intriguing because as stated above, the sublimation temperature of O<sub>2</sub> in a vacuum is ~30 K, yet measurements of the Galilean satellites indicate surface temperatures in the 80–130 K region. Johnson and Jesser (1997) propose that O<sub>2</sub> is trapped in gas bubbles (microatmospheres) within the icy surfaces. Such microatmospheres are produced from radiation damage, similar to processes that occur in reactor materials. They are efficient at trapping O<sub>2</sub> above its sublimation temperature. The model also accounted for UV-photolysis of O<sub>2</sub> to form O<sub>3</sub> through the well-known Chapman reactions, and was in close agreement to observations.

Early experiments from the group of Baragiola (Baragiola et al. 1999; Baragiola and Bahr 1998; Vidal et al. 1997) however show that in ices in which O<sub>2</sub> is co-deposited with H<sub>2</sub>O to form an ice, that O<sub>2</sub> did not remain trapped in sufficient quantities at relevant icy satellite surface temperatures. They concluded that measurements of surface temperature, which were measured over large regions of the surface, must in fact have much colder temperatures locally present in order for O<sub>2</sub> to remain present and not sublime. However, these experiments did not simulate the effect of radiation upon ice, a key part of the Johnson and Jesser model.

In subsequent years, detection of O<sub>2</sub> in irradiated pure water ice has become a fairly commonplace (Loeffler et al. 2006b; Teolis et al. 2005, 2009; Zheng et al. 2006b). However, at relevant surface temperatures, only small quantities have been produced. Recently though, continued work in this area by the Baragiola and co-workers (Teolis et al. 2006) has found that if an ice is irradiated concurrently while being deposited, that O<sub>3</sub> is produced, even above 100 K. These experiments are intended to simulate that water molecules are continually being deposited from the tenuous atmosphere of an icy satellite to the surface, while being bombarded by energetic particles. The presence of O<sub>3</sub> implies that a significant amount of O<sub>2</sub> must also be produced, although unfortunately they did not attempt to measure the dimer bands.

Although the deposition rates in these experiments are many orders of magnitude greater than deposition rates on any icy satellite, they highlight an important fact that is often overlooked in such laboratory simulations. That is, icy planetary surfaces are not static ice blocks that are exposed to radiation. As well as being exposed to energetic radiation, they are also being resurfaced on a molecular level by micrometeorite impacts and cryovolcanic activity that can result in deposition, sublimation and desorption of molecular species from the surface. As shown by Teolis et al. (2006), the chemical reactions occurring in irradiated ice and in ice that is being deposited and irradiated at the same time can clearly be different. In relation to the production of and trapping of O<sub>2</sub>, this phenomenon has a pronounced effect.

## 15.5 Ionization in Water Ice

Until recently ionization has been considered a passive side process, whereby ions are generated and neutralized during the bombardment of ice with energetic particles. It had been widely accepted until the early 2000s that the permanent chemical pathways of the energetic processing were through the generation of radicals within the ice through molecular dissociation. The ionization of ice was assumed to be an intermediate process, which would end up in radicals. Through a series of publications Gudipati and Allamandola have shown that ionization of polycyclic aromatic hydrocarbons embedded in ice can lead to the formation of relatively stable “*radical cations*” within the ice, injecting an electron into the ice or ejection of the electron from the ice (Gudipati 2004; Gudipati and Allamandola 2003, 2006a, b). These studies changed the paradigm of chemistry in ices from “*neutral radicals*” dominated to “*radicals and charged species*” mediated, as shown schematically in Fig. 15.4.

Ionization is a process through which one or more electrons are removed from a neutral or charged atom or molecule (see Fig. 15.1). Typically, the energy necessary for ionization is supplied either in terms of photon or particle impact energy or through catalytic activity of the medium in which autoionization can occur. Examples of the former processes are photoionization of gas-phase atmospheric molecules in the upper atmosphere of Earth and other planets, resulting in charged atmospheres, which when coupled with inherent magnetic fields of the body, result in magnetosphere. Examples of the autoionization process include removal of

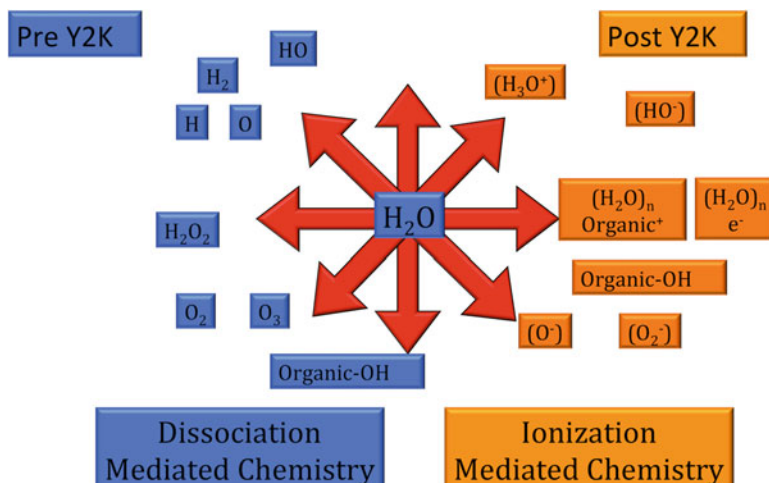


**Fig. 15.4** Schematic representation of pre and post discovery of ionization pathway in ices. Several species, especially negative ions, solvated electrons, and positive ions of  $\text{H}_2\text{O}$  byproducts are yet to be spectroscopically identified in ices. This sketch shows that radiation induced processes in ice are far more complex and diverse than mere dissociation of  $\text{H}_2\text{O}$  to  $\text{H}$ ,  $\text{O}$ , and  $\text{OH}$  radicals. Ionization and ion-mediated processes play critical role in the chemical evolution of ices in the solar system

electrons from alkali earth metals such as Sodium (Na) when added to electron deficient liquids such as liquid ammonia ( $\text{NH}_3$ ) resulting in the formation of  $\text{Na}^+$  and solvated electrons in liquid ammonia, whereby an electron is surrounded by several ammonia molecules (Meyer and van Gastel 2011).

Ionization should also be clearly distinguished from “*ionic*” molecules (salts). While ionic species such as  $\text{NaCl}$  or  $\text{MgSO}_4$  are charged counter-ions ( $\text{Na}^+$  and  $\text{Cl}^-$ ;  $\text{Mg}^{+2}$  and  $\text{SO}_4^{-2}$ ) held together through ionic (Coulombic) forces, in these species no electron is removed during a particular event. They are already depleted or enriched by electrons in a previous process. *Radiation induced ionization leads to the formation of charged species, which if stable under given conditions, can form ionic molecules in the presence of counter-ions.*

Gas-phase ionization energies of a variety of atoms and molecules can be found at the NIST *Webbook site* (<http://webbook.nist.gov/chemistry/>), where the ionization threshold for  $\text{H}_2\text{O}$  is given as 12.6 eV, which compares well with the  $\text{H}_2\text{O}^+$  potential energy surface with respect to the  $\text{H}_2\text{O}$  neutral molecule (Fig. 15.2). Atoms and molecules can be ionized several times, resulting in multiply charged species. The ionization threshold of each successive electron removal increases significantly due to tighter binding of electrons as the ratio of protons to electrons increases. Highly charged oxygen ( $\text{O}^{\text{IV}}$  etc.) and other light atom ions are a part of the solar wind and cosmic radiation. These ions can be accelerated to relativistic speeds, resulting in extremely high-energy content carried by these ions. When these ions impact a surface, the energy is released within this body through linear energy transfer (LET) that results in all the excitation processes shown in Fig. 15.1, leading to chemistry on the surface and within the ice and sputtering from the ice surface.

### 15.5.1 Ionization of $\text{H}_2\text{O}$ in Ice

Though it is widely accepted that vacuum ultraviolet (VUV,  $<190$  nm) photons and energetic electrons and ions cause ionization of  $\text{H}_2\text{O}$  molecules in the ice, followed by ejection of  $\text{H}^+$  etc., even at energies as low as 6.5 eV (Herring-Captain et al. 2005; Kimmel et al. 1994), so far there has not been direct spectroscopic evidence for the  $\text{H}_2\text{O}^+$  radical cation in the ice. Either this species is too reactive and leads to the formation of  $\text{H}^+ + \text{OH}$  in ice or not enough research has yet been devoted to obtain spectroscopic data on the  $\text{H}_2\text{O}^+$  radical cation.

### 15.5.2 Ionization of PAHs (Organics) Imbedded in Ice

Polycyclic aromatic hydrocarbons (PAHs) form a class of highly stable molecules with a benzene-like (six carbons) ring structures connected together like a honeycomb hexagonal two-dimensional mesh, with several structural permutations. These molecules are found everywhere in the Universe: In the interstellar medium as the carriers of unidentified IR (UIR) emission (Boersma et al. 2006); in interstellar dust particles (IDPs) (Quirico et al. 2005); and in meteorites (Basile et al. 1984).

PAHs also resemble, in their structural, chemical, and spectroscopic properties, biologically important molecules such as DNA bases Adenine etc., chlorophyll, and form a part of some of the amino acids such as tyrosine and tryptophan.

Recent research on ionization of polycyclic aromatic hydrocarbons (PAHs) in ices was triggered by earlier observations as follows. Bernstein et al. postulated ion-mediated chemistry to explain hydroxylation of the PAH molecule coronene imbedded in ice was VUV radiation processed, followed by warm-up (Bernstein et al. 1999). However, only the starting and product molecules were detected using mass-spectroscopic techniques. Ionized PAHs were assumed to be highly reactive in water-ice and were thought not to be detectable even at low-temperatures. Detection of any reaction intermediate using traditional infrared spectroscopy was extremely difficult, as the ice features themselves overwhelmed the mid-IR spectral region, leaving only small transparent regions. Under these conditions, Gudipati and Allamandola decided to carryout optical spectroscopy of PAHs in cryogenic ices due to the fact that PAHs have extremely strong absorption cross-section in the UV–VIS region (200–600 nm) and water-ice appropriately prepared should be transparent in this wavelength region. Against all the intuitions prevailing in the community, these initial experiments with PAHs isolated in water-ice at cryogenic conditions (Gudipati and Allamandola 2003) resulted in the detection of stable ionized PAH radical cations (Fig. 15.5). With this discovery began a new era of ionization mediated chemistry in ice, where (a) ionization of imbedded organics (PAHs) has been shown to be very facile in ices, (b) these ions are stable at 15 K indefinitely, but react with the ice medium at higher temperatures resulting in hydroxylated PAHs, (c) generation and/or storage of charge (electrons and ions) in ice is now a process that needs to be taken into account in order to understand ice physics and chemistry, (d) ionization energies of PAH impurities are lowered by several electron volts (eV) compared to their gas-phase values, making longer wavelength photons that couldn't ionize a molecule in the gas-phase now enabling ionization in ice, and (e) UV-VIS optical spectroscopy of water-ice is not only possible, but it is one of the most sensitive spectroscopic methods to study physical and chemical processes of imbedded impurities in water-ice films. It has been shown that large PAH molecules like quaterrylene can be doubly ionized (Gudipati and Allamandola 2006b) in the ice and their monocations (Gudipati and Allamandola 2006a) are stable in the ice up to very high temperatures (120 K). Further detailed discussion on the properties of water-ice that result in the above mentioned observations, kinetics of ionization of PAHs in ices as well as the formation of hydroxylated products, and analyses of the spectroscopic properties of impurities in water-ice host, can be found in the publication of Gudipati (Gudipati 2004). Detailed understanding of the mechanisms and processes at the most fundamental level are ongoing at the “Ice Spectroscopy Laboratory” of Gudipati at JPL and at other laboratories as well (Bouwman et al. 2009, 2010, 2011a, b).

The chemistry of biomolecules such as amino acids has been studied in ices. Surprisingly, UV-induced degradation of amino acids in ices was found to be effective in tens of millimeter thick ices (Orzechowska et al. 2007). It has been shown that the

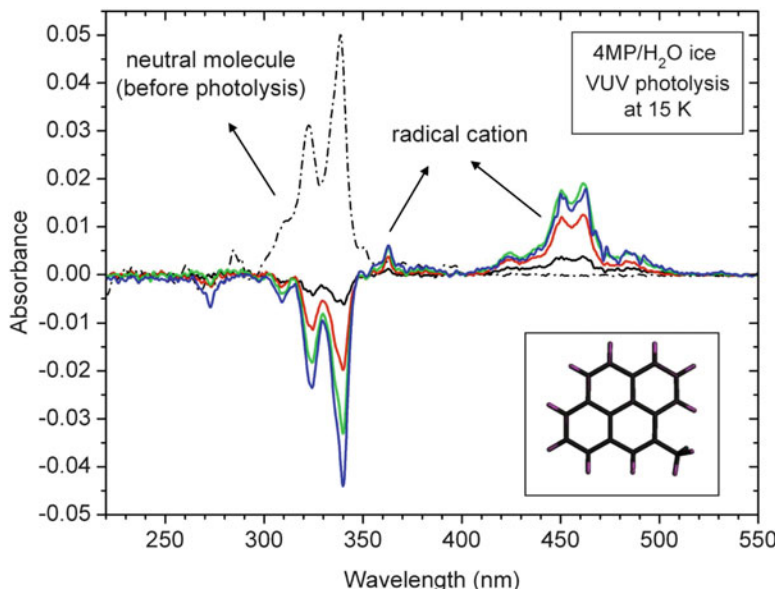


**Fig. 15.5** First detection of ionized PAHs imbedded in ice. Hydrogen discharge lamp (160–180 nm + Ly<sub>α</sub> at 121.6 nm) induced near quantitative ionization of PAH molecule 4-methylpyrene embedded in amorphous water-ice at 15 K (Gudipati and Allamandola 2003). Neutral molecules absorbing at ~340 nm are depleted (represented by negative absorbance) during the VUV radiation processing, leading to the injection of electrons in to the ice and the formation of ionized radical cation of 4-methylpyrene PAH molecule that absorbs ~460 nm

presence of methane ( $\text{CH}_4$ ) in ice could prevent the formation of OH radicals and result in oxidation of methane to carbon dioxide (Hodyss et al. 2009a; Weber et al. 2009).

### 15.5.3 Water-Ice: An Excellent Storage Medium for Charge

Why are PAHs (and by extrapolation other imbedded impurities) ionized efficiently and stabilized in water-ice? This is the first question that comes to the mind when dealing with the ionization of PAHs in ice, as we have seen in Fig. 15.5. There are two important reasons. Firstly, water molecules, possessing large molecular dipole moment, can stabilize charged species through Coulomb interactions. Secondly, the electron-ion recombination is hindered by trapping of the electron in the water-ice. It is expected that the binding energy of a trapped electron in ice can be as low as 3.5 eV (Fig. 15.3). Indeed, theoretical computations predicted lowering of ionization energy to similar extent. Woon and Park have shown that the ionization energies of  $\text{H}_2$  and small PAH molecules decrease in ice medium compared to the gas-phase (Woon and Park 2004).

### 15.5.4 Chemical Reaction Pathways involving Organics in Ice: The Oxidation

The above discussion clearly demonstrates that when a photon (perhaps an electron or ion) with sufficient energy interacts with organics imbedded in ice, the first and foremost process that occurs is *ionization of the organic, generating a charged molecule and an electron* in the ice medium. What happens to the radical cation (ionized organic molecule, here a PAH<sup>+</sup>) in the ice? What is the fate of the electron? These are the questions that are still under investigation in our laboratory. On a macroscopic scale, analysis of the reaction products has shown that PAHs are hydrogenated and oxidized, leading to the formation of hydroxyls, ketones, etc. (Baragiola et al. 1999). Our studies have shown that oxygen atom insertion occurs only at higher temperature, as in the case of naphthalene, shown in Fig. 15.6. After ionization of naphthalene at 10 K, only upon warming the ice to 125 K, is the production of hydroxylated 1-naphthol has been observed (Gudipati 2004). These studies indicate that between instantaneous ionization and further chemical reaction processes there may be an energy barrier that needs to be overcome.

### 15.5.5 Chemistry of Other Organics in Ice

Detailed mechanisms of chemical reaction pathways of non-PAH aromatic hydrocarbons such as aromatic heterocyclic (e.g. nucleic acid bases purine and pyrimidine), aliphatic hydrocarbons such as methane, ethane, propane etc., in ice upon radiation processing are not yet fully understood. Whether or not ionization is the primary process in these molecules, similar to PAHs, needs to be experimentally resolved. So far the experimental work shows that these organics in ice are oxidized upon radiation processing, similar to PAHs, leading to the formation of oxygenated species such as alcohols (Hudson and Moore 2001; Moore and Hudson 1998) and ketones (Bernstein et al. 2003). Formation of oxygenated products including CO<sub>2</sub> from simple alkanes and alkenes embedded in H<sub>2</sub>O ice subjected to 10 keV electron bombardment followed by annealing to higher temperatures has been reported recently (Hand and Carlson 2012). Deuterium exchange is also seen when aliphatic hydrocarbons trapped in D<sub>2</sub>O ice were irradiated, inferring C-H bond dissociation and abstraction of D atoms from D<sub>2</sub>O ice medium (Weber et al. 2009).

## 15.6 Conclusions

Although ice, the solid form of the triatomic molecule H<sub>2</sub>O, in its pure form should show relatively simple chemistry producing H, H<sub>2</sub>, OH, H<sub>2</sub>O<sub>2</sub>, O, O<sub>2</sub>, O<sub>3</sub>, H<sub>3</sub>O<sup>+</sup>, OH<sup>-</sup>, etc. species, the addition of carbon containing impurities in ice already leads to

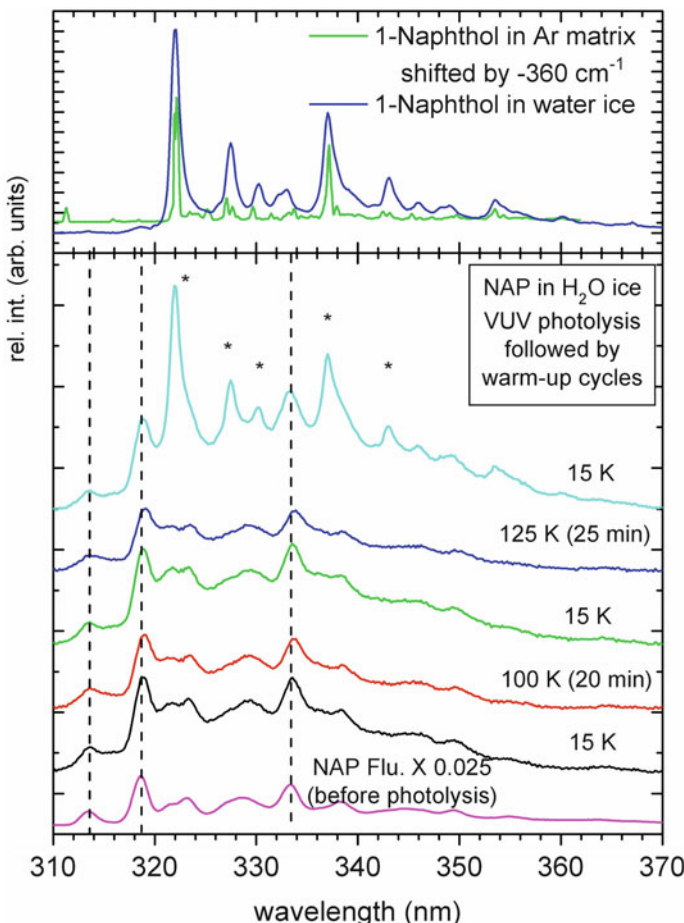


**Fig. 15.6** First observation of in-situ hydroxylation of PAH molecules subsequent to radiation induced ionization. In the ice ~80% of naphthalene was ionized prior to warming up the ice. Only after warming the ice to 125 K the oxidized product 1-naphthol is formed, which is strongly fluorescent at 15 K (not at >75 K due to excited state proton transfer – ESPT) (See (Gudipati 2004) for further details)

very rich chemistry. On the study of pure  $\text{H}_2\text{O}$  ices there are still lots of questions that need detailed answers. What role does radiation type (photons, electrons, ions) and energy have on the chemistry of irradiated ices? How does the chemistry of the primary, secondary and tertiary and higher order radiation products vary with different radiation fluxes? Are these variations linear or nonlinear with flux? What is the lifetime of such radiation products under different radiation and ice conditions? How do temperature and impurities affect the chemistry of the radiation products? How does simultaneous irradiation and ice condensation (similar to sputtering and recondensing on icy body surfaces such as Europa) affect ice

chemistry? More systematic laboratory studies are needed to resolve these questions and will help understand the evolution of pure icy surfaces in our solar system.

While the carbon containing molecules form the basis for organic chemistry/life, the small oxygenated species form the atmospheres of icy bodies in our solar system (whether CO<sub>2</sub> on Mars or small fraction of O, OH on Europa), except on Titan, which has a rich organic atmosphere. Needless to say that the complexity increases when nitrogen, sulfur, and phosphorous containing impurities are added to these ices. Indeed many solar system and interstellar ices do contain all these elements in one or other form. Complex molecules containing CHNOPS elements are the basis for life such as amino acids (CHNOS), nucleic acids (CHNO), and nucleotides of DNA and RNA (CHNOP). Two opposing processes compete with each other to make biomolecules or destroy the same under radiation. These are: Radiation processing followed by thermal processing that results in complex biomolecules molecules such as amino acids from simple starting molecules such as CO<sub>2</sub>, SO<sub>2</sub>, NH<sub>3</sub>, etc., embedded in ice (prebiotic synthesis), as shown in the laboratory (Bernstein et al. 2002; Meierhenrich et al. 2002; Muñoz Caro et al. 2002). At the same token, we have seen that large organics such as PAHs are degraded, oxidized, and perhaps destroyed by the same radiation. The answers to the question where and how life can survive will need a comprehensive and critical understanding of these competing *creation and destruction cycles* of complex organics in ices (the cosmic dance in ice). There has been tremendous progress made in the past few decades and more is in works.

**Acknowledgments** MSG thanks NASA funding through several grants (NASA Planetary Atmospheres, NASA Discovery Data Analysis, NASA Cassini Data Analysis Programs, NASA Astrobiology Institute Nodes “Icy Worlds” and “Titan Prebiotic Chemistry”), JPL’s DRDF and R&TD funding. MSG’s research was carried out at the Jet Propulsion Laboratory, California Institute of Technology, under a contract with the National Aeronautics and Space Administration. PDC acknowledges funding through the NASA Astrobiology Institute “Icy Worlds” node and the Jeffress Memorial Trust. We thank Will Grundy for critical reading and for helpful suggestions to improve the manuscript.

## References

- Aloisio S, Francisco JS (2000) Radical-water complexes in Earth’s atmosphere. *Acc Chem Res* 33(12):825–830
- Apkarian VA, Schwentner N (1999) Molecular photodynamics in rare gas solids. *Chem Rev* 99(6):1481–1514
- Atkins PW, de Paula J (2009) Atkins’ physical chemistry. Oxford University Press, Oxford
- Bahr DA, Fama M et al (2001) Radiolysis of water ice in the outer solar system: sputtering and trapping of radiation products. *J Geophys Res Planet* 106(E12):33285–33290
- Baragiola RA, Bahr DA (1998) Laboratory studies of the optical properties and stability of oxygen on Ganymede. *J Geophys Res Planet* 103(E11):25865–25872
- Baragiola RA, Atteberry CL et al (1999) “Comment on” laboratory studies of the optical properties and stability of oxygen on Ganymede “by Raul A. Baragiola and David A. Bahr – Reply”. *J Geophys Res Planet* 104(E6):14183–14187

- Bar-Nun A, Herman G et al (1985) Trapping and release of gases by water ice and implications for icy bodies. *Icarus* 63:317–332
- Bar-Nun A, Prialnik D et al (1987) Trapping of gases by water ice and implications for icy bodies. *Adv Space Res* 7(5):45–47
- Basile BP, Middelitch BS et al (1984) Polycyclic aromatic hydrocarbons in the Murchison meteorite. *Org Geochem* 5(4):211–216
- Bernstein MP, Sandford SA et al (1999) UV irradiation of polycyclic aromatic hydrocarbons in ices: production of alcohols, quinones, and ethers. *Science* 283:1135–1138
- Bernstein MP, Dworkin JP et al (2002) Racemic amino acids from the ultraviolet photolysis of interstellar ice analogues. *Nature* 416:401–403
- Bernstein MP, Moore MH et al (2003) Side group addition to the polycyclic aromatic hydrocarbon coronene by proton irradiation in cosmic ice analogs. *Astrophys J* 582(1):L25–L29
- Boersma C, Hony S et al (2006) UIR bands in the ISOSWS spectrum of the carbon star TU Tauri. *Astron Astrophys* 447(1):213–U166
- Bouwman J, Paardekooper DM et al (2009) Real-time optical spectroscopy of vacuum ultraviolet irradiated pyrene:  $\text{H}_2\text{O}$  interstellar ice. *Astrophys J* 700(1):56–62
- Bouwman J, Cuppen HM et al (2010) Photochemistry of the PAH pyrene in water ice: the case for ion-mediated solid-state astrochemistry. *Astron Astrophys* 511:10
- Bouwman J, Cuppen HM et al (2011a) Photochemistry of polycyclic aromatic hydrocarbons in cosmic water ice II. Near UV/VIS spectroscopy and ionization rates. *Astron Astrophys* 529:A46
- Bouwman J, Mattioda AL et al (2011b) Photochemistry of polycyclic aromatic hydrocarbons in cosmic water ice I. Mid-IR spectroscopy and photoproducts. *Astron Astrophys* 525:13
- Box HC (1970) Endor study of X-irradiated single crystals of ice. *J Chem Phys* 53(1059)
- Brown WL, Augustyniak WM et al (1984) Electronic sputtering of low-temperature molecular-solids. *Nucl Instrum Methods Phys Res Sect B* 229(2–3):307–314
- Calvin WM, Johnson RE et al (1996) O<sub>2</sub> on Ganymede: spectral characteristics and plasma formation mechanisms. *Geophys Res Lett* 23:673–676
- Carlson RW, Anderson MS et al (1999) Hydrogen peroxide on the surface of Europa. *Science* 283 (5410):2062–2064
- Cassidy TA, Johnson RE et al (2007) The spatial morphology of Europa's near-surface O<sub>2</sub> atmosphere. *Icarus* 191(2):755–764
- Cooper PD, Johnson RE et al (2003a) Hydrogen peroxide dimers and the production of O<sub>2</sub> in icy satellite surfaces. *Icarus* 166(2):444–446
- Cooper PD, Johnson RE et al (2003b) A review of possible optical absorption features of oxygen molecules in the icy surfaces of outer solar system bodies. *Planet Space Sci* 51:183–192
- Cooper PD, Kjaergaard HG et al (2003c) Infrared measurements and calculations on  $\text{H}_2\text{O}$  center dot HO. *J Am Chem Soc* 125(20):6048–6049
- Cooper PD, Moore MH et al (2008) Radiation chemistry of  $\text{H}_2\text{O} + \text{O}_2$  Ices. *Icarus* 194:379–388
- Cooper PD, Moore MH, Hudson RL (2010) O-atom production in water ice: implications for O<sub>2</sub> formation on icy satellites. *J Geophys Res*, accepted for publication
- Danilychev AV, Apkarian VA (1994) Atomic oxygen in crystalline Kr and Xe. 2. Adiabatic potential-energy surfaces. *J Chem Phys* 100(8):5556–5566
- Fillion JH, van Harreveld R et al (2001) Photodissociation of  $\text{H}_2\text{O}$  and  $\text{D}_2\text{O}$  in (B)over-tilde, (C) over-tilde, and (D)over-tilde states (134–119 nm). Comparison between experiment and ab initio calculations. *J Phys Chem A* 105(51):11414–11424
- Gerakines PA, Schutte WA et al (1996) Ultraviolet processing of interstellar ice analogs. I. Pure ices. *Astron Astrophys* 312:289–305
- Ghormley JA, Hochanadel CJ (1971) Production of hydrogen, hydroxide, and hydrogen peroxide in the flash photolysis of ice. *J Phys Chem* 75(1):40–44
- Gomis O, Leto G et al (2004a) Hydrogen peroxide production by ion irradiation of thin water ice films. *Astron Astrophys* 420(2):405–410
- Gomis O, Leto G, Strazzulla G (2004b) Hydrogen peroxide production by ion irradiation of thin water ice films. *Astron Astrophys* 420:405–410

- Gomis O, Satorre MA et al (2004c) Hydrogen peroxide formation by ion implantation in water ice and its relevance to the Galilean satellites. *Planet Space Sci* 52(5–6):371–378
- Gudipati MS (2004) Matrix-isolation in cryogenic water-ices: facile generation, storage, and optical spectroscopy of aromatic radical cations. *J Phys Chem A* 108(20):4412–4419
- Gudipati MS, Allamandola LJ (2003) Facile generation and storage of polycyclic aromatic hydrocarbon ions in astrophysical ices. *Astrophys J Lett* 596(2):L195–L198
- Gudipati MS, Allamandola L (2006a) Unusual stability of PAH radical cations in amorphous water-ice up to 120 K: astronomical implications. *Astrophys J Lett* 638:286–292
- Gudipati MS, Allamandola LJ (2006b) Double ionization of quaterrylene ( $C_{40}H_{20}$ ) in water-ice at 20 K with Ly(alpha) (121.6 nm) radiation. *J Phys Chem A* 110(28):9020–9024
- Gudipati MS, Kalb M (1999) Rydberg and charge-transfer states of atomic oxygen in Ar and Kr matrices: identification of two distinct sites. *Chem Phys Lett* 307(1–2):27–34
- Gudipati MS, Schouren F et al (2000) Concentration dependence of the spectroscopic and photochemical properties of atomic and molecular oxygen in argon matrices. *Spectrochim Acta A* 56:2581
- Hall DT, Strobel DF et al (1995) Detection of an oxygen tmosphere on Jupiter's Moon Europa. *Nature* 373:677–679
- Hall DT, Feldman PD et al (1998) The far-ultraviolet oxygen airglow of Europa and Ganymede. *Astrophys J* 499(1):475–481
- Hand KP, Carlson RW (2012) Laboratory spectroscopic analyses of electron irradiated alkanes and alkenes in solar system ices. *J Geophys Res Planet* 117, E03008, doi:10.1029/2011JE003888
- Harich SA, Hwang DWH et al (2000) Photodissociation of  $H_2O$  at 121.6 nm: a state-to-state dynamical picture. *J Chem Phys* 113(22):10073–10090
- Harich SA, Yang XF et al (2001) Photodissociation of  $D_2O$  at 121.6 nm: a state-to-state dynamical picture. *J Chem Phys* 114(18):7830–7837
- Herring-Captain J, Grieves GA et al (2005) Low-energy (5–250 eV) electron-stimulated desorption of  $H^+$ ,  $H-2(+)$ , and  $H + (H_2O)(n)$  from low-temperature water ice surfaces. *Phys Rev B* 72 (3):10
- Hodyss R, Johnson PV et al (2009a) Photochemistry of methane-water ices. *Icarus* 200 (1):338–342
- Hodyss R, Parkinson CD et al (2009b) Methanol on Enceladus. *Geophys Res Lett* 36:L17103
- Hollas JM (2005) Modern spectroscopy. Wiley, Chichester
- Hudson RL, Moore MH (2001) Radiation chemical alterations in solar system ices: an overview. *J Geophys Res Planet* 106(E12):33275–33284
- Joens JA (2001) The dissociation energy of  $OH(X2E\ddagger 3/2)$  and the enthalpy of formation of  $OH$  ( $X2E\ddagger 3/2$ ),  $ClOH$ , and  $BrOH$  from thermochemical cycles. *J Phys Chem A* 105 (49):11041–11044
- Johnson RE, Jesser WA (1997)  $O_2/O_3$  Microatmospheres in the surface of Ganymede. *Astrophys J* 480:L79–L82
- Johnson RE, Quickenden TI (1997) Photolysis and radiolysis of water ice on outer solar system bodies. *J Geophys Res* 102(E5):10985–10996
- Johnson RE, Cooper PD et al (2005a) Production of oxygen by electronically induced dissociations in ice. *J Chem Phys* 123(18)
- Johnson RE, Cooper PD et al (2005b) Production of oxygen by electronically induced dissociations in ice. *J Chem Phys* 123(18):8
- Kanaev AV, Museur L et al (2001) Dissociation and suppressed ionization of  $H_2O$  molecules embedded in He clusters: the role of the cluster as a cage. *J Chem Phys* 115(22):10248–10253
- Khriachtchev L, Pettersson M et al (2000) Photochemistry of hydrogen peroxide in Kr and Xe matrixes. *J Chem Phys* 112(5):2187–2194
- Khriachtchev L, Tanskanen H et al (2002) Isotopic effect on thermal mobility of atomic hydrogen in solid xenon. *J Chem Phys* 116(13):5708–5716
- Kimmel GA, Orlando TM et al (1994) Low-energy electron-stimulated production of molecular-hydrogen from amorphous water ice. *J Chem Phys* 101(4):3282–3286

- Laffon C, Lacombe S et al (2006) Radiation effects in water ice: a near edge x-ray absorption fine structure study. *J Chem Phys* 125:204714
- Langford VS, McKinley AJ et al (2000a) Identification of H<sub>2</sub>O center dot HO in argon matrices. *J Am Chem Soc* 122(51):12859–12863
- Langford VS, McKinley AJ et al (2000b) Luminescent photoproducts in UV-irradiated ice. *Acc Chem Res* 33:665–671
- Langford VS, McKinley AJ et al (2001) Temperature dependence of the visible-near-infrared absorption spectrum of liquid water. *J Phys Chem A* 105(39):8916–8921
- Lennon D, Quickenden TI et al (1993) Uv-excited luminescences from amorphous and polycrystalline H<sub>2</sub>O ices. *Chem Phys Lett* 201(1–4):120–126
- Loeffler MJ, Baragiola RA (2005) The state of hydrogen peroxide on Europa. *Geophys Res Lett* 32(17):4
- Loeffler MJ, Baragiola RA (2009) Is the 3.5 μm infrared feature on enceladus due to hydrogen peroxide? *Astrophys J Lett* 694(1):L92–L94
- Loeffler MJ, Raut U et al (2006a) Synthesis of hydrogen peroxide in water ice by ion irradiation. *Icarus* 180:265–273
- Loeffler MJ, Teolis BD et al (2006b) A model study of the thermal evolution of astrophysical ices. *Astrophys J* 639(2):L103–L106
- Low GR, Kjaergaard HG (1999) Calculation of OH-stretching band intensities of the water dimer and trimer. *J Chem Phys* 110(18):9104–9115
- Maksyutenko P, Rizzo TR et al (2006) A direct measurement of the dissociation energy of water. *J Chem Phys* 125(18):3
- Matich AJ, Bakker MG et al (1993) O<sub>2</sub> Luminescence from UV-Excited H<sub>2</sub>O and D<sub>2</sub>O Ices. *J Phys Chem* 97:10539–10553
- Meierhenrich UJ, Muñoz Caro GM et al (2002) Amino acids from ultraviolet irradiation of interstellar ice analogues. *Geochim et Cosmochim Acta* 66(15A):A505
- Meyer A, van Gastel M (2011) EPR and ENDOR study of the frozen ammoniated electron at low alkali-metal concentrations. *J Phys Chem A* 115(10):1939–1945
- Moore MH, Hudson RL (1998) Infrared study of ion-irradiated water-ice mixtures with hydrocarbons relevant to comets. *Icarus* 135(2):518–527
- Moore MH, Hudson RL (2000) IR detection of H<sub>2</sub>O<sub>2</sub> at 80 K in ion-irradiated laboratory ices relevant to Europa. *Icarus* 145(1):282–288
- Mordaunt DH, Ashfold MNR et al (1994) Dissociation dynamics Of H<sub>2</sub>O(D<sub>2</sub>O) following photoexcitation at the lyman-alpha wavelength (121.6-Nm). *J Chem Phys* 100(10):7360–7375
- Muñoz Caro GM, Meierhenrich UJ et al (2002) Amino acids from ultraviolet irradiation of interstellar ice analogues. *Nature* 416:403–406
- Newman SF, Buratti BJ et al (2007) Hydrogen peroxide on Enceladus. *Astrophys J* 670(2):L143–L146
- Orlando TM, Sieger MT (2003) The role of electron-stimulated production of O-2 from water ice in the radiation processing of outer solar system surfaces. *Surf Sci* 528(1–3):1–7
- Orzechowska GE, Goguen JD et al (2007) Ultraviolet photolysis of amino acids in a 100 K water ice matrix: application to the outer Solar System bodies. *Icarus* 187(2):584–591
- Quickenden TI, Irvin JA (1980) The ultraviolet-absorption spectrum of liquid water. *J Chem Phys* 72(8):4416–4428
- Quickenden TI, Trotman SM et al (1982) Pulse radiolytic studies of the ultraviolet and visible emissions from purified H<sub>2</sub>O ice. *J Chem Phys* 77(8):3790–3802
- Quickenden TI, Litjens RAJ et al (1985) Uv excited luminescence from crystalline H<sub>2</sub>O ice. *Chem Phys Lett* 114(2):164–167
- Quickenden TI, Litjens RAJ et al (1988) Red emission from pulse irradiated H<sub>2</sub>O ice. *Radiat Res* 115(3):403–412
- Quickenden TI, Green TA et al (1996) Luminescence from UV-irradiated amorphous H<sub>2</sub>O ice. *J Phys Chem* 100(42):16801–16807

- Quickenden TI, Hanlon AR et al (1997) Activation energy for the emission of 420 nm luminescence from UV-excited polycrystalline H<sub>2</sub>O ice. *J Phys Chem A* 101(25):4511–4516
- Quirico E, Borg J et al (2005) A micro-Raman survey of 10 IDPs and 6 carbonaceous chondrites. *Planet Space Sci* 53(14–15):1443–1448
- Selby BJ, Quickenden TI et al (2006) Isotopic effects on the time-dependences of 420 nm ice luminescence excited by UV light. *Kinet Catal* 47(5):686–698
- Spencer JR, Calvin WM (2002) Condensed O<sub>2</sub> on Europa and Callisto. *Astrophys J* 124 (December):3400–3403
- Spencer JR, Calvin WM et al (1995) Charge-coupled device spectra of the Galilean Satellites: molecular oxygen on Ganymede. *J Geophys Res* 100:19049–19056
- Strazzulla G, Leto G et al (2005) Production of oxidants by ion irradiation of water/carbon dioxide frozen mixtures. *Astrobiology* 5(5):612–621
- Szabo A, Ostlund NS (1996) Modern quantum chemistry: introduction to advanced electronic structure theory, vol 11501. Dover Publications, Mineola
- Tanskanen H, Khriachtchev L et al (2008) Formation of noble-gas hydrides and decay of solvated protons revisited: diffusion-controlled reactions and hydrogen atom losses in solid noble gases. *Phys Chem Chem Phys* 10(5):692–701
- Teolis BD, Vidal RA et al (2005) Mechanisms of O-2 sputtering from water ice by keV ions. *Phys Rev B* 72(24):9
- Teolis BD, Loeffler MJ et al (2006) Ozone synthesis on the icy satellites. *Astrophys J* 644(2): L141–L144
- Teolis BD, Shi J et al (2009) Formation, trapping, and ejection of radiolytic O-2 from ion-irradiated water ice studied by sputter depth profiling. *J Chem Phys* 130(13):9
- van Harreveld R, van Hemert MC (2000) Photodissociation of water. II. Wave packet calculations for the photofragmentation of H<sub>2</sub>O and D<sub>2</sub>O in the (B)over-tilde band. *J Chem Phys* 112(13):5787–5808
- van Harreveld R, van Hemert MC (2008) Quantum mechanical calculations for the H<sub>2</sub>O + h nu → O(D-1) + H-2 photodissociation process. *J Phys Chem A* 112(14):3002–3009
- van Harreveld R, van Hemert MC et al (2001) A comparative classical-quantum study of the photodissociation of water in the (B)over-tilde band. *J Phys Chem A* 105(51):11480–11487
- Verlet JRR, Bragg AE et al (2005) Observation of large water-cluster anions with surface-bound excess electrons. *Science* 307:93–96
- Vernon CF, Bakker MG et al (1990) The luminescence spectrum of electron-irradiated D<sub>2</sub>O ice – the effects of decay time, accumulated dose and isotopic-substitution. *Radiat Phys Chem* 36 (4):529–531
- Vidal RA, Bahr D et al (1997) Oxygen on Ganymede: laboratory studies. *Science* 276 (5320):1839–1842
- Warren SG (1984) Optical constants of ice from the ultraviolet to the microwave. *Appl Opt* 23:1206–1225
- Weber AS, Hodyss R et al (2009) Hydrogen-deuterium exchange in photolyzed methane-water ices. *Astrophys J* 703(1):1030–1033
- Woon DE, Park JY (2004) Photoionization of benzene and small polycyclic aromatic hydrocarbons in ultraviolet-processed astrophysical ices: a computational study. *Astrophys J* 607(1):342–345
- Yi WK, Park J et al (2007) Photodissociation dynamics of water at Lyman alpha (121.6 nm). *Chem Phys Lett* 439(1–3):46–49
- Zheng WJ, Jewitt D et al (2006a) Formation of hydrogen, oxygen, and hydrogen peroxide in electron-irradiated crystalline water ice. *Astrophys J* 639(1):534–548
- Zheng WJ, Jewitt D et al (2006b) Temperature dependence of the formation of hydrogen, oxygen, and hydrogen peroxide in electron-irradiated crystalline water ice. *Astrophys J* 648(1):753–761
- Zheng WJ, Jewitt D et al (2007) Electron irradiation of crystalline and amorphous D<sub>2</sub>O ice. *Chem Phys Lett* 435(4–6):289–294
- Zins EL, Joshi PR et al (2011) Production and isolation of OH radicals in water ice. *Mon Not R Astron Soc* 415(4):3107–3112

# Chapter 16

## Radiation Effects in Water Ice in the Outer Solar System

**R.A. Baragiola, M.A. Famá, M.J. Loeffler, M.E. Palumbo,  
U. Raut, J. Shi, and G. Strazzulla**

**Abstract** Water ice in the outer solar system can either have condensed from the gas phase or have been brought in by colliding bodies, such as interplanetary ice grains to comets. Since icy bodies lack a protective atmosphere, their surface is subject to irradiation by photons, ions and electrons. This chapter discusses how energetic radiation affects the physical and chemical properties of a pure water ice surface, and how the outcome of radiation processes depends on the properties of the surface and on the environment (atmosphere, particle flux and energies).

### 16.1 Introduction

Water ice in the outer solar system can either have condensed from the gas phase or have been brought in by colliding bodies, such as interplanetary ice grains to comets. Since icy bodies lack a protective atmosphere, their surface is subject to irradiation by photons, ions and electrons. This chapter discusses how energetic radiation affects the physical and chemical properties of a pure water ice surface, and how the outcome of radiation processes depends on the properties of the surface and on the environment (atmosphere, particle flux and energies). Precursors to this chapter are that by Johnson (1998), and a review by Baragiola (2003a,b); however many significant advances in our understanding have occurred since these papers were published. Radiation processes induced by low energy electrons or occurring in mixed ices are not covered here but elsewhere in this volume. Also, the chapter is not a review but a description of recent advances and should not be used for a comprehensive coverage of the history of the topic.

---

R.A. Baragiola (✉) • M.A. Famá • M.J. Loeffler • U. Raut • J. Shi  
Laboratory for Atomic and Surface Physics, University of Virginia, Charlottesville,  
VA 22904, USA  
e-mail: [raul@virginia.edu](mailto:raul@virginia.edu)

M.E. Palumbo • G. Strazzulla  
INAF-Osservatorio Astrofisico di Catania, Via S. Sofia 78, 95123 Catania, Italy

### ***16.1.1 Amorphous and Crystalline Phases***

The properties of ice applicable to surfaces in the outer solar system have been reviewed by Baragiola (2003b). The basic properties of ice are the crystallographic phase (amorphous or crystalline) and its porosity. Among the different amorphous phases, the one formed by vapor deposition is the most relevant for planetary surfaces. This phase, called ASW (amorphous solid water) is metastable, crystallizing at a rate that increases exponentially with temperature, being larger than the age of the solar system at 90 K and seconds for daytime equatorial ice in Callisto (Baragiola 2003b). That is, there is no single ‘crystallization temperature’ as assumed in many published works. Meteor impacts on icy bodies produce high transient heating that ejects water either to the exosphere or to the interplanetary space. Water vapor returning to the surface will condense as ASW below about 130 K and then crystallize or not, depending on temperature. As shown below, crystalline ice can be amorphized by radiation at temperatures prevailing in the outer solar system. On the other hand, meteor impacts can crystallize amorphous ice, since the impact heat can produce a pool of liquid water, which then cools down slowly by conduction and by radiation into space. In the periphery of the impact zone, a meteor impact also repeatedly fractures the surface and mixes the shards to a depth that depend on the size of the impact (communition).

### ***16.1.2 Optical Absorption***

Since most of our knowledge about these icy surfaces comes from studies of the reflected solar light, knowledge of the optical properties of ice is essential. Remote sensing in the infrared shows that water ice is the principal constituent of the surface of many satellites and rings (Schmitt et al. 1998), with usually minor concentrations of other condensed gases, and minerals. The sampled depth (optical skin) in optical reflectance varies with wavelength. In the far ultraviolet and mid-infrared, this depth is of the order of microns or less, while in the near ultraviolet to the near infrared, and in the far infrared and beyond, it can be centimeters or more (limited by a combination of scattering and absorption by non-ice material, e.g., minerals). The optical skin is subject to bombardment by energetic particles and Lyman- $\alpha$  radiation from the Sun, planetary magnetospheric ions, cosmic rays, and meteorites (Johnson 1998). These energetic impacts induce various effects in the surface ice, such as chemical reactions, electrostatic charging, lattice damage, desorption, and evaporation. Some of those processes alter the appearance of the surface and therefore can be identified by remote sensing.

Infrared spectroscopy, which looks at the vibrational modes of molecules, is very sensitive to the presence of water ice, because of its many strong absorption bands. The most easily detected band, due to its strength, is the fundamental OH stretching vibration at 3.1  $\mu\text{m}$ . In many cases, this feature is very nearly saturated leading to the use of weaker absorption features, combination and overtone modes,

at 1.04, 1.25, 1.5 and 2  $\mu\text{m}$ . Ratios of the intensity of these bands can be used to obtain grain size in icy regoliths (Jaumann et al. 2008). Other absorption features that can be useful lie at higher wavelengths: 6.1  $\mu\text{m}$  (bending), 12  $\mu\text{m}$  (libration) and lattice modes above 20  $\mu\text{m}$  (peak at 46  $\mu\text{m}$ ) (Warren 1984). Infrared spectroscopy is a useful tool to determine remotely whether the ice is amorphous or crystalline. This has been done from the profile (shape, width, and peak position) of the 3.1  $\mu\text{m}$  band (Hansen and McCord 2004) or from the presence and relative intensity of the 1.65  $\mu\text{m}$  band, which has been correlated with crystalline ice at low temperatures (Grundy and Schmitt 1998).

### 16.1.3 Porosity

Ice deposited below  $<100\text{ K}$  from the gas phases is microporous. Its porosity depends on experimental conditions such as temperature, deposition rate, and growth angle (e.g., Dohnálek et al. 2003; Raut et al. 2007b). Recently, Raut et al. (2007b) found that micropores are  $<1\text{ nm}$  wide and that, at large growth angles, it contains larger mesopores. Both micropores and mesopores collapse when the ice is heated above about 90 K or as a result of irradiation (see below). Since pore dimensions are much smaller than optical wavelengths, microporosity does not contribute appreciably to optical scattering. The porosity and pore size is normally measured by gas adsorption experiments (Dohnálek et al. 2003; Collings et al. 2003), which show huge effective surface areas for adsorption that can reach several hundred  $\text{m}^2/\text{g}$  for ice grown at low temperatures ( $<100\text{ K}$ ). Thus, fresh ASW acts like a high capacity vacuum pump. This pumping ability and long exposure times mean that icy surfaces in the outer solar system may be saturated with gases from their faint atmospheres. However, it also complicates laboratory studies to an extent that depends on the degree of vacuum used. Since contamination can affect properties of the amorphous deposits, it is sensible to speculate that varied vacuum conditions are a reason for the common large discrepancies in laboratory results on ice properties found in the literature.

Water molecules on the surface of the pores are incompletely coordinated, with unsaturated O or H atoms or dangling bonds (db). Porosity results in the appearance of two small, relatively sharp, blue-shifted O-H bands at 2.69 and 2.71  $\mu\text{m}$ , in addition to distortions in the bulk O-H absorption. The sharpness of the db bands is due to the decoupling from bulk vibrations; their shifted positions result from the lower coordination (three or two, respectively (Rowland et al. 1991)). The db absorption bands shift when another species (such as  $\text{N}_2$ ,  $\text{O}_2$ ,  $\text{H}_2\text{O}_2$ ,  $\text{CO}_2$ , CO,  $\text{CH}_2$ ,  $\text{SO}_2$ ) is adsorbed on the pores or co-deposited with water ice (e.g., Rowland et al. 1991; Hixson et al. 1992; Devlin 1992; Palumbo and Strazzulla 2003; Palumbo 2005, 2006; Raut et al. 2007b). The profile of the OH db band in  $\text{H}_2\text{O}:X$  mixtures has been found to be independent on the  $\text{H}_2\text{O}/X$  ratio (Palumbo 2006; Raut et al. 2007b). Measuring the intensity of the db absorption versus  $\text{CH}_4$  uptake, Raut et al. concluded the micropores are  $<3$  molecular diameters in width ( $<1\text{ nm}$ ). So far, there have been no observations of dangling bond absorptions in planetary ices.

## 16.2 Radiation Effects: Primary Processes

The icy bodies in the outer solar system are not shielded by an atmosphere from incoming energetic photons and particles, which can eject particles (sputtering) and modify the structure and chemical composition of the surface. While many radiation effects in ices have been identified in the laboratory, astronomical observations reveal a few: the generation of faint atmospheres around icy satellites by sputtering, the synthesis of hydrogen peroxide, and possibly of O<sub>2</sub> and ozone, and the charging of icy particles in Saturn's rings.

The radiation synthesis of molecules from ice and at the interface of ice and other materials may account for minor amounts of other condensed molecules. Thus, the observation of such molecules can reveal information on the environment and on surface processes. The detection of hydrogen peroxide on Europa (Carlson et al. 1999a), oxygen on Europa, Ganymede and Callisto (Calvin et al. 1996; Spencer and Calvin 2002) and possibly ozone on Ganymede (Noll et al. 1996) and on Dione and Rhea (Noll et al. 1997a) indicate that radiolysis of the surface ice is important on these bodies. The possible detection of salts on the surface of Ganymede has been thought to support the hypothesis of a subsurface ocean (McCord et al. 2001). Similar features identified as salts on Ganymede have been shown to fit to sulfuric acid spectra on Europa (Carlson et al. 1999b), which may have formed from implantation of ions from Io into the surface ice. Furthermore, the presence of CO<sub>2</sub> and O<sub>2</sub> on the surfaces of warmer Galilean satellites or CO<sub>2</sub> in the warm south polar region of Enceladus, indicate that ice can trap these relatively volatile species at temperatures much higher than those at which exposed carbon dioxide would sublime.

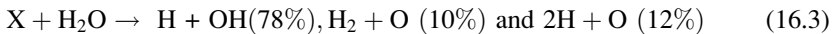
Ionizing radiation affects ice through collisions of the projectiles and of the low energy secondary electrons generated in the medium by direct ionizations. These processes are significantly different, particularly in concentration of deposited energy. For fast heavy ions, the density of ionization is so high that prompt reactions between radiation products can occur in the projectile track, which is not possible in excitations by energetic electrons or photons (LaVerne 2000; Loeffler et al. 2006d). Thus, studying surface processes induced by low energy electrons are insufficient to reveal the complexity of ion-induced effects. Photons of energy below ~8.9 eV do not produce free secondary electrons (Goulet et al. 1990) but can alter (photolyse) the ice by exciting molecules to dissociative states.

On first order, the effect of irradiation in a small volume of matter is determined by the amount of energy deposited per unit path length, called the linear energy transfer or LET. It differs slightly from the projectile energy loss per path length, dE/dx, or stopping power, due to projectile excitation and energy escape, particularly near surfaces. For fast ions, the energy is deposited mostly in ionizations and excitations, at comparable rates. Electrons from ionization events have sufficient energy to usually produce equal amounts of further ionizations and excitations than those made by the projectile in direct collisions. At lower projectile energies, knock-on (elastic) collisions with target nuclei become important. The relative importance of radiation effects in ice caused by elastic and inelastic collisions will be discussed below.

The inelastic energy deposited by the projectiles in the form of ionizations and excitations decay mostly by non-radiative processes where the energy is coupled to motion of the water molecule as a whole or to dissociation fragments.



The excited water molecule will eventually relax to the ground state or dissociate. The main dissociation channels in the gas phase for Lyman- $\alpha$  (10.2 eV) photons are (Slanger and Black 1982):



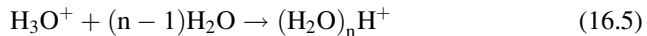
Dissociation cross-sections and fragment distribution in the solid are unknown, and should be different from those in the gas phase. This is due to the cage effect that enhances molecular recombination since the dissociation fragments can collide with the surrounding molecules (the cage), lose their energy and reform the molecule. With increasing temperatures, thermal fluctuations soften the cage making it easier for the fragments to escape recombination into  $H_2O$ . The cage effect can reduce the probability of the  $H_2 + O$  channel relative to the  $H + OH$  and  $2 H + O$  channels since it is harder for  $H_2$  than for  $H$  to leave the dissociation site.

Collisions leading to ionized fragments should be important. Direct ionizations produce electrons,  $H_2O^+$ , and ionized fragments. The electrons slow down quickly and, when their energy is below  $\sim 7$  eV (Wilson et al. 2001), they cannot produce further electronic excitations or ionizations but may still break up a water molecule by associative attachment.

Ionizations are followed by proton transfer to create a hydronium  $H_3O^+$  and OH



with further relaxation of the lattice in a hydration shell around the ion:



After this prompt physical stage, the energy evolves more slowly, governed by typical vibrational times, of the order of 0.1–1 ps. The electrons cannot recombine directly with the ions efficiently because their kinetic energy cannot be easily absorbed by the medium. They then degrade in energy slowly by excitations of intramolecular vibrations and phonons. In times  $> 1$  ps they slow down sufficiently (though not actually thermalized) that they can efficiently recombine with ions. The distance by which the electrons move from their original atom is extremely difficult to calculate since it depends on elastic scattering by atomic cores, vibrational excitations and the dynamic electric fields produced by the ion track and any

trapped charges. The latter force makes the evolution of secondary electrons highly dependent on LET. In particular, the track field destroys the tendency of isotropy produced by elastic scattering.

### 16.3 Radiation Chemistry

In the *chemical stage*, ions and neutral products interact in chemical reactions. The observation of trapped radicals in radiolyzed ice is very hard, particularly because of their low concentrations, at most a few percent. Recently Laffon et al. (2006) observed O-containing products produced by X-ray irradiation at 20 K, which modifies their samples uniformly. In their experiments, radiolysis occurs through photoelectrons and corresponds to lower LET than for incident ions. Besides H, H<sub>2</sub>, ions or trapped electrons, which their X-ray absorption technique does not detect, the two most important products are H<sub>2</sub>O<sub>2</sub> and OH. Their concentration decreases steadily with annealing temperature and OH disappears above 90 K. The less abundant O<sub>2</sub> and HO<sub>2</sub> species have a similar concentration that peaks at 40 K and then decays with temperature up to the maximum attainable, 150 K (Fig. 16.1). The signal for atomic oxygen was at the noise level. On first order, amorphous and crystalline phases of ice behaved similarly. This contrasts with studies of  $\gamma$ -irradiation of ice at 77 K that found OH is the main product in crystalline ice, and comparable amounts of OH and HO<sub>2</sub> in amorphous ice (Bednarek et al. 1998). Figure 16.1 also shows the column density of H<sub>2</sub>O<sub>2</sub> and O<sub>2</sub> produced by the irradiation of ice films by 100 keV ions, which deposit all the energy in the film (Loeffler et al. 2006d, Teolis et al. 2009). The results indicate what species are likely to be produced in outer solar system ices, depending on the local surface temperature.

Radiation effects are usually cumulative, and specified by the total radiation fluence (incident flux  $\times$  time) or dose (absorbed energy per target molecule). It needs to be used with caution in case of photolysis, since a dose of 100 eV/molecule produced by 3  $\mu$ m photons will have a negligible effect in ice, whereas the same dose produced by 30 nm photons will cause a saturation concentration of products. As will be shown below for the case of compaction, the minimum energy transfer required to produce a radiation effect is reflected in a threshold stopping power ( $dE/dx$ ) below which one cannot observe the particular radiation effect. Thus, both stopping power and dose are important in determining radiation effects. In principle, more relevant than the stopping power is the energy density, which is the stopping power divided by the area of the cylindrical track over which energy is deposited above a threshold value.

The combined role of density and dose of deposited energy, modified by threshold effects has the consequence that radiation effects depend on the type of particle (ions, electrons, photons) and their energy. For instance, the photons and electrons produce excitations and ionizations with low energy density. In those cases, formation of molecules by radical reactions (next section) requires an

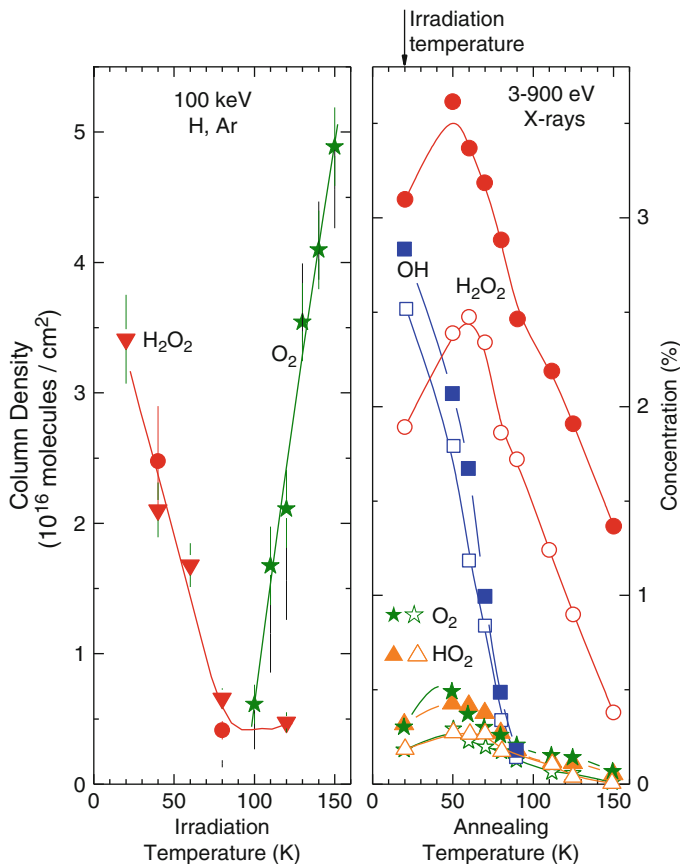


**Fig. 16.1** Left, column density of products of the deposition of 100 keV in ice films by  $\text{H}^+$  (▼) and  $\text{Ar}^+$  (●) (Loeffler et al. 2006d; Teolis et al. 2009) versus irradiation temperature. Right, concentration of radiation products created in ice by dilute, X-ray excitation at 20 K versus annealing temperature. Experiments done in amorphous (full symbols) and crystalline ice (open symbols) (Adapted from Laffon et al. (2006)). In both panels, the lines are drawn to guide the eye and have no other meaning

accumulated fluence. In contrast, fast ions produce tracks of high energy density with a high radical concentration that can lead to molecular synthesis by a single projectile.

Remote observation of long-lived radicals and stable molecular products of radiation in ice can be studied by infrared spectroscopy and compared with laboratory results. The only clear example of detection of a radiation product in ice is hydrogen peroxide in Europa (Carlson et al. 1999a) in quantities similar to those observed in irradiation experiments (Moore and Hudson 2000; Gomis et al. 2004; Loeffler et al. 2006d). A detailed analysis of laboratory  $\text{H}_2\text{O}_2$  spectra led to the conclusion that the molecule exists in Europa as di-hydrate (Loeffler and

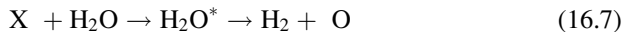
Baragiola 2005). A similar analysis shows that H<sub>2</sub>O<sub>2</sub> cannot be assigned to a feature of Enceladus (Loeffler and Baragiola 2009). In addition to radiation products inside the ice, radiation can eject molecules by sputtering. The most important synthesized molecules, H<sub>2</sub> and O<sub>2</sub> molecules have been observed during sputtering with a wide range of ions by, e.g., Reimann et al. (1984) and Teolis et al. (2005, 2009). In addition, Teolis et al. measured the depth distribution of radiolytic oxygen and its dependence on temperature and irradiation history.

Of the condensed molecules detected on the surface of planetary ices, hydrogen peroxide, oxygen and ozone are believed to form from radiolysis or photolysis of the surface water ice. We give a brief overview of the main pathways that are believed to form these three molecules. Either in dense projectile tracks or after prolonged irradiation, reactions between radicals can occur. The OH in (3) that does not recombine to form water can react to form peroxide:



To form hydrogen peroxide in (6), the OH must be close enough to one another that they react with one another rather than recombine with H or react with O to form HO<sub>2</sub>. It is thus not surprising that the amount of H<sub>2</sub>O<sub>2</sub> produced depends on the density of energy deposited by the projectile (Spinks and Woods 1990).

Oxygen and ozone can be formed through the destruction of hydrogen peroxide (Loeffler et al. 2006a) or from another destruction pathway in water ice:



Subsequent reactions in the ion track between two O atoms may lead to O<sub>2</sub> and subsequently reaction of that O<sub>2</sub> may lead to O<sub>3</sub>:



Interestingly, even though ozone is believed to be formed from oxygen that was produced by irradiation of water ice, laboratory studies have shown that irradiation of pure ice samples does not produce detectable amounts of ozone, unless sufficient amounts of O<sub>2</sub> or H<sub>2</sub>O<sub>2</sub> are initially added. The only case where ozone has been produced from only water ice is when the water was deposited on the ice *during* ion bombardment (Teolis et al. 2006). This condition is a better simulation of icy satellites, where ejected water returns by gravity to the surface rather than in all other laboratory studies where water is pumped away. The results of Teolis et al. show that the amount of ozone produced depends strongly on the type of ion used, the temperature of the ice, and the ratio of irradiation flux to the deposition rate. Thus, ozone's presence on planetary icy bodies indicates complex surface interactions and trapping of radiolytic species.

### 16.3.1 *Implantation of Chemically Reactive Ions*

A different type of radiation chemistry can result from reactions of implanted projectile ions in the surface ice. Projectiles lose energy inside the solid and, if not backscattered, stop in the material where they can trap at defect sites (implanted) or diffuse out. If the implanted ion is reactive (e.g., H, C, N, O, S), it can form new species by combining with other atoms. Lane et al. (1981) and Sack et al. (1992) proposed that implantation of sulfur ions may account for the observed ultraviolet absorption at 280 nm in Europa thought to be due to S-O bonds. However, UV spectra are not reliable identifiers since many species give broad absorption bands in that region. More reliable are infrared absorption measurements such as those made by the Galileo spacecraft. The infrared spectra at Europa, Callisto and Ganymede showed absorption features at 3.40, 3.50, 3.88, 4.05, 4.25 and 4.57  $\mu\text{m}$  (McCord et al. 1997), which also may indicate synthesis by ion implantation. The prime candidates for the five bands are: C-H,  $\text{H}_2\text{O}_2$ , S-H,  $\text{SO}_2$ ,  $\text{CO}_2$ , and CN respectively, but  $\text{H}_2\text{CO}_3$  was suggested by Hage et al. (1998) as a more likely candidate for 3.88  $\mu\text{m}$  band. Laboratory studies can address the open question of whether those species are native of the satellites or produced by exogenic processes, such as ion implantation, when detailed maps of ion fluence on the satellites become available.

A number of specific results have been obtained, mostly in Catania. Strazzulla et al. (2003) showed that C implantation into water ice forms carbon dioxide; however, this is not the dominant formation mechanism on the Galilean moons. They also showed that N implantation in pure water ice does not result in any appreciable amount of nitrogen bearing molecules, besides  $\text{N}_2$ . Sulfur implantation forms S-O compounds (Sack et al. 1992) and small amounts  $\text{SO}_2$  ( $< 0.025$  molecules/ion) and a high yield ( $0.65 \pm 0.1$  molecules/ion) of hydrated sulfuric acid (Strazzulla et al. 2007).

### 16.3.2 *Radiation Chemistry at the Interface of Ice with C- and S- Bearing Materials*

The Galileo spacecraft detected minor amounts of  $\text{CO}_2$  and  $\text{SO}_2$  (e.g., McCord et al. 1997), on the Jovian icy satellites. In particular, the spectra indicate that  $\text{CO}_2$  exists in a non-ice matrix in the surfaces of Callisto and Ganymede (Hibbitts et al. 2002, 2003).  $\text{SO}_2$  is believed to be trapped in the dark material and/or water ice (McCord et al. 1997). Carbonaceous or sulfurous materials are thought to be present on the surfaces of icy satellites because of micrometeorite bombardment. If so, such refractory materials are easily covered by water ice molecules either by deposition from the atmosphere or by sputtering followed by ballistic redistribution. Thus, it is of interest to determine if irradiation of non-icy grains coated with ice can synthesize  $\text{CO}_2$  and  $\text{SO}_2$ .

Heide (1982) showed that irradiation of ice on carbon foils by 100 keV electrons led to the etching of the foils. Recent experiments have shown that ion irradiation of water ice deposited on top of carbonaceous materials produces CO and CO<sub>2</sub> at the interface. The carbonaceous materials used are carbon, hydrogenated carbon grains, asphaltite, a natural bitumen, and solid organic residues obtained by irradiation of frozen benzene (Mennella et al. 2004, 2006; Gomis and Strazzulla 2005; Raut et al. 2005). Layered samples have been irradiated with 30 keV He<sup>+</sup>, 200 keV He<sup>+</sup> and Ar<sup>+</sup> ions and Lyman- $\alpha$  photons at 12–16 and 77–80 K. In all instances, CO and CO<sub>2</sub> are efficiently formed at low temperature (12–16 K) while a lower amount of CO is present at higher temperature (77–80 K). Remarkably, no significant amounts of CO are produced when the substrate is pure carbon. Based on the laboratory results, Gomis and Strazzulla (2005) suggested that radiolysis of mixtures of frost water and solid carbonaceous compounds could account for the quantity of CO<sub>2</sub> ice present on the surface of the Galilean satellites.

Similar experiments have recently been performed to study the formation of SO<sub>2</sub> at the interface ice/refractory material after ion irradiation of H<sub>2</sub>O on top of a solid sulfurous residue (Gomis and Strazzulla 2008). Samples have been irradiated at 80 K with 200 keV He<sup>+</sup> ions. From infrared spectra taken after irradiation only an upper limit to the SO<sub>2</sub> production yield has been obtained. Thus, the radiolysis of mixtures of water ice and sulfurous materials cannot be considered the primary mechanism responsible for the quantity of SO<sub>2</sub> present on the surfaces of the icy moons (Gomis and Strazzulla 2008) and other mechanisms have to be considered. For Callisto, where SO<sub>2</sub> is detected on the leading hemisphere, both an exogenic (Noll et al. 1997b) and an endogenic source (Lane and Domingue 1997) have been suggested. For the case of Europa, suggested mechanisms are SO<sub>2</sub> volcanism (Sack et al. 1992), SO<sub>2</sub> from an endogenic source (Noll et al. 1995), sulfur dioxide synthesized from a radiolytic cycling of sulfur (Carlson et al. 1999b), and S implantation (Lane et al. 1981; Sack et al. 1992).

## 16.4 Sputtering

The erosion or sputtering of water ice by energetic particles is an important process in the outer solar system, where icy bodies are constantly exposed to magnetospheric ions, the solar wind and cosmic rays. Sputtering, along with out-gassing, is responsible for the production of tenuous, extended neutral atmospheres of water molecules ejected from icy satellites and ice grains embedded in planetary magnetospheres (Johnson 1990; Shi et al. 1995). Such atmospheres have been detected around icy satellites of Jupiter and Saturn (Johnson 2007; McGrath et al. 2007). Atmospheric atoms and molecules are eventually ionized by solar UV photons or the local plasma, and the ions are picked-up and accelerated in the planet's rotating magnetosphere. Eventually these ions are either transported outward by plasma processes and escape, or are neutralized by charge exchange or electron recombination. Sputtering is also expected to be important for limiting the grain lifetimes of the E-ring grains orbiting Saturn (Johnson et al. 2008).

Sputtering by particle impact is caused by momentum transfer to a molecule or atom of the solid, which usually starts a cascade of internal collisions. When this collision cascade intercepts the surface, molecules and atoms are ejected if their energy is larger than the surface binding energy, 0.45 eV for ice (Sack and Baragiola 1993). The initial momentum transfer can occur indirectly through the electronic excitation of a dissociative state (electronic sputtering) (Johnson and Schou 1993, Baragiola et al. 2003) or through direct knock-on collisions between nuclei (knock-on sputtering) (Sigmund 1969). The process is characterized by the sputtering yield  $Y$ , or number of molecules ejected per incident ion, which is the sum of the electronic,  $Y_e$ , and knock-on,  $Y_k$ , components. Experiments show that not only water molecules are ejected but also H<sub>2</sub>, O<sub>2</sub> and a negligible amount of ions. The molecular oxygen synthesized in ice by ion bombardment contributes less than 10% to the total yield for temperatures below 100 K (Baragiola et al. 2003; Teolis et al. 2005). The energy distribution depends on the sputtering mechanism; for electronic sputtering, most of the ejected particles have less than 1 eV energy (Johnson 1998).

$Y_e$  is roughly proportional to the square of the energy deposited on a thin surface layer, or to  $S_e^2$  (Baragiola et al. 2003), where  $S_e = N^{-1}dE/dx$  is the electronic stopping cross section,  $dE/dx$  the energy loss per unit path length and  $N$  is the target number density. The quadratic dependence suggests that sputtering is dominated by the interaction of pairs of excitations, such as the screened Coulomb repulsion of ionized molecules. Deviations from the  $S_e^2$  at low ion velocities have been attributed to different projectile charge states and synergism between electronic and elastic collision processes, among others (Baragiola et al. 2003; Famá et al. 2007). The fewer studies on knock-on sputtering show that  $Y_k$  depends linearly on the nuclear stopping cross section,  $S_n$ , (Famá et al. 2007).

The sputtering yield depends on the angle of incidence to the surface normal  $\theta$  according to a inverse power-cosine law:  $Y(\theta) = Y(0) \cos^{-f}(\theta)$  with  $f$ , between 1 and 2 due to a forward peak in the angular distribution of deposited energy (Vidal et al. 2005; Johnson et al. 1987). Sputtering also depends on the temperature of the ice, possibly due to the formation and consequent behavior of radicals and molecular products (H<sub>2</sub>, O<sub>2</sub>) during irradiation (Bahr et al. 2001; Baragiola et al. 2003), but a detailed description is lacking. Data from the compilation of Baragiola et al. (2003) at 30 keV (mostly electronic processes) and from Famá et al. (2008) at 2 keV (elastic collisions) indicate that the sputtering yield has a universal behavior with ice temperature, irrespective of the excitation mechanism. The temperature dependent normalized yield has the form,  $Y/Y_0 = 1 + Y_1/Y_0 \exp(-E_a/kT)$  where  $Y_0$  is the constant sputtering yield in the low temperature region (<60 K),  $Y_1$  a thermal factor,  $k$  the Boltzmann constant, and  $E_a$  an activation energy with typical values below ~0.1 eV.

Based on the above discussion, the sputtering yield of water ice is linear in  $S_n(E)$  but quadratic in  $S_e(E)$ , depends on angle of incidence and temperature of the ice. It can be written as (e.g., Famá et al. 2008):

$$Y(E, m_1, z, \theta, T) = (C(E) S_n + \eta(E) S_e^2) \left( 1 + \frac{Y_1}{Y_0} e^{-E_a/kT} \right) \cos^{-f}(\theta) \quad (16.10)$$

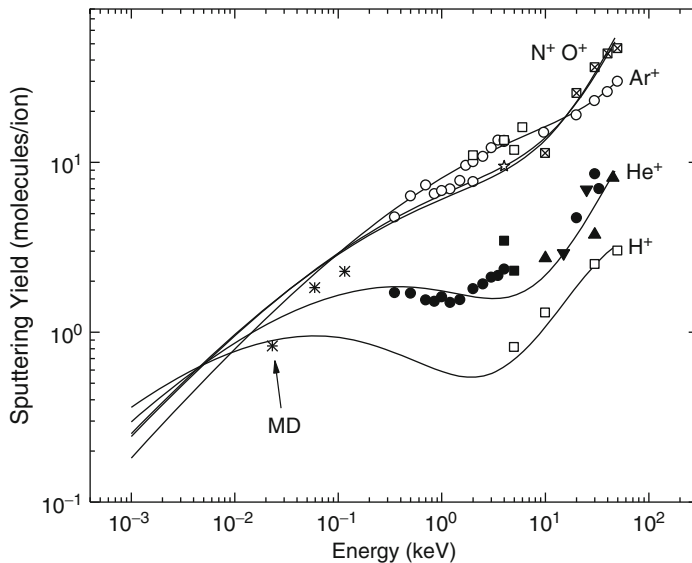


**Fig. 16.2** Solid and open symbols: experimental data for the sputtering yield of ice for H, He, N, O and Ar ions from Famá et al. (2008) and references therein. The solid lines represent the results of the empirical model from Eq. 16.8. Crosses: Molecular dynamics (MD) simulations

where  $C(E)$  is a factor that depends on the ratio of the masses of projectile and target and  $\eta(E)$  is an oscillatory function of  $z$  the atomic number of the projectile that tends to 1 at large energies.  $\eta(E)$  is needed if one uses, instead of experimental values of  $S_e$ , models that do not include known  $z$  oscillations with  $z$ .

Figure 16.2 shows a broad spectrum of data from several laboratories for the sputtering yield of ice produced by ion bombardment. For any projectile, the empirical model described by Eq. 16.10 seems to work effectively in an extended range of energies relevant to the solar system.

## 16.5 Amorphization of Crystalline Ice

Crystalline ice has been identified as a component of the surface of most of the Jovian, Saturnian and Uranian satellites (see, e.g., Grundy et al. 1999 and references therein), on Pluto's satellite Charon (Brown and Calvin 2000), and on the surface of some trans-Neptunian objects (TNO) such as Quaoar (Jewitt and Luu 2004), and Haumea (Merlin et al. 2007; Pinilla-Alonso et al. 2009). Its presence has been inferred from the near infrared (NIR) spectrum of light reflected from the Sun, using the absorption band at  $1.65\text{ }\mu\text{m}$ , which is particularly sharp in crystalline ice at low temperatures (Grundy and Schmitt 1998). The sensitivity of the relative intensity of this band to temperature has been used, not only as an indicator of the presence of the crystalline phase, but also to

measure the surface temperature (Grundy et al. 1999; Cook et al. 2007; Merlin et al. 2007). It is important to stress that extracting crystalline fraction from the 1.65  $\mu\text{m}$  band requires careful line shape analysis after background subtraction, since both amorphous and crystalline ice absorb in this spectral region (Famá et al. 2010). Such a careful procedure requires high-quality data, which is not always available in astronomical observations.

The presence of crystalline ice on any of those bodies is surprising. Due to the low maximum surface temperatures of these objects in the outer solar system (less than  $\sim 100$  K for the Saturnian satellites other than Enceladus, and less than 50 K for TNOs (Jewitt and Luu 2004)), one expects that, if the ice is accreted from the vapor, it would be amorphous in the absence of heating by high energy meteor impacts or episodic, internal heat sources. Such amorphous ice would crystallize in a few minutes above 135 K but more than  $10^7$  years at  $\sim 80$  K (Jenniskens and Blake 1996; Baragiola 2003b). Moreover, exposure to space radiation: solar UV photons and ions, cosmic rays or energetic charged particles trapped by the planetary magnetic fields, would eventually destroy crystallinity due to the accumulation of radiation effects. Golecki and Jaccard (1978) determined ion-induced disorder using channeling measurements, finding that the energy required to produce disorder—not necessarily amorphization—increased two orders of magnitude between 90 and 110 K. Amorphization has been detected by the disappearance of diffraction in the electron microscope (Lepault et al. 1983; Dubochet and Lepault 1984; Heide 1984) and using infrared absorption (Strazzulla et al. 1992; Moore and Hudson 1992; Leto and Baratta 2003; Leto et al. 2005; Baragiola et al. 2005; Mastrappa and Brown 2006). The identification of crystalline and amorphous ice by infrared spectroscopy lies in the correlation of band shapes with results from early X-ray diffraction studies.

Different experimental techniques used to detect the amorphous content of irradiated ice show that amorphization as a function of irradiation dose  $D$  follows an exponential behavior:

$$\phi_A = \phi_{A_{\max}} (1 - \exp[-KD]) \quad (16.11)$$

where  $\phi_A$  is the fraction of amorphized ice,  $\phi_{A_{\max}}$  is its maximum value, and  $K$  is a fitting parameter found to depend strongly on temperature (Fig. 16.3). The variable  $D = \langle FS \rangle$  gives the average dose over the irradiation depth. The maximum amorphous fraction  $\phi_{A_{\max}}$  is obtained for saturation doses ( $KD \gg 1$ ). While most experiments yielded full amorphization,  $\phi_{A_{\max}} = 1$ , others reported only partially amorphized ice at high fluences (e.g.,  $\phi_{A_{\max}} \sim 60\%$  with 3 keV He ions at 77 K) (Strazzulla et al. 1992). Some of the results of previous experiments are summarized in Fig. 16.3. Those by Moore and Hudson (1992) are not shown because their data was analyzed  $\phi_{A_{\max}} = 1$ , whereas it appears from their graph that  $\phi_{A_{\max}} < 1$ . Finally, Mastrappa and Brown (2006) observed full amorphization for a sample deposited at 40 K, crystallized at 160 K and cooled back to 40 K for irradiation, but not for a sample deposited at 50 K, crystallized at 160 K, cooled back at 50 K and then irradiated.

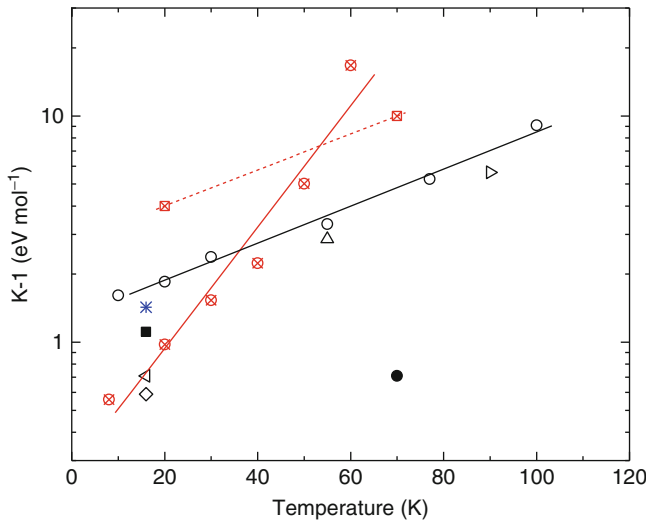


**Fig. 16.3**  $K^{-1}$  (see Eq. 16.9) versus irradiation temperature, (Adapted from Famá et al. 2010).  $K^{-1}$  (see Eq. 16.9): ○ 3 keV  $\text{He}^+$ , △ 1.5 keV  $\text{H}^+$  (Strazzulla et al. 1992); ◇ 30 keV  $\text{H}^+$ , □ 30 keV  $\text{He}^+$ , ■ 60 keV  $\text{Ar}^+$  (Leto and Baratta 2003); ▷ 200 keV  $\text{H}^+$  (Leto et al. 2005); ● 100 keV  $\text{Ar}^+$  (Baragiola et al. 2005); ▨ 100 keV  $e^-$  (Lepault et al. 1983); ▨ 100 keV  $e^-$  (Heide 1984); \* 10.2 eV photons (Leto and Baratta 2003). For electrons,  $K^{-1}$  diverges above 70 K. The low value of  $K^{-1}$  for 100 keV  $\text{Ar}^+$  may reflect the higher amorphization efficiency of nuclear vs. electronic collisions. The lines are drawn to guide the eye and have no other meaning

Since the density of energy deposition is very different for different excitation sources (ions, electrons, Lyman- $\alpha$  photons), it is perhaps surprising that  $K^{-1}$  shows similar temperature dependence. Recently, Famá et al. (2010) adapted a ‘thermal spike’ model to explain the temperature dependence of amorphization in terms of the thermal properties of ice. In this model, the incident projectile creates a liquid region that hyperquenches to the amorphous phase.

## 16.6 Compaction of Microporous Ice

Microporous ice is expected to exist on cold surfaces of satellites of the outer planets that are bombarded by solar wind and magnetospheric ions. However, ion irradiation destroys the pores and the ice is compacted (Palumbo 2005, 2006; Raut et al. 2007a, 2008). Compaction is likely caused by the energy deposited by the ions inducing molecular motion that alters the ice structure and minimizes the internal surface energy via removal of the pores. Raut et al. (2008) measured the compaction of microporous ice under irradiation with different ions in the 80–400 keV energy range. With all ions, the porosity  $P$  decreased exponentially with irradiation fluence  $F$  (Fig. 16.4) and could be fit with the expression  $P(F) = P_o \exp(-AF) + P_r$ , where

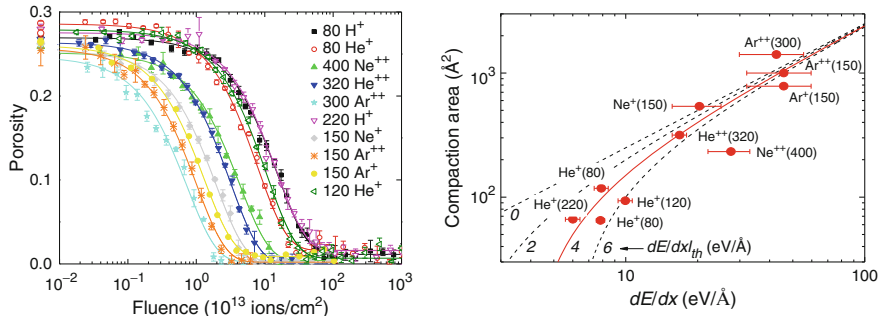


**Fig. 16.4** *Left:* Fluence dependence of compaction for ice films deposited at 30 K for different projectiles at different energies in keV. The lines are fits to the  $P(F) = P_o \exp(-AF) + P_r$ . The data points shown on the left of the axis are the initial porosities before irradiation. *Right:* Compaction area  $A$  versus stopping power  $dE/dx$ . Data points are labeled with energy in keV between parentheses. The lines are linear fits  $A = \text{const.} \times (dE/dx - dE/dx_{\text{th}})$  for different values of the threshold stopping power,  $(dE/dx)_{\text{th}}$  (Taken from Raut et al. (2008))

$P_o$  is the film porosity of unirradiated film and  $P_r$  is a small residual porosity after irradiation. This dependence arises because a region of area  $A$  around the ion track is compacted by the deposited energy in proportion to the porous fraction of the film:  $dP = -AFP$ . As seen from Fig. 16.4, the fluence dependence strongly depends on the choice of the projectile. For instance, the fluence required to compact the ice with 80 keV protons is nearly 10 times larger than for 150 keV  $\text{Ar}^{++}$ .

The key parameter determining the fluence dependence of compaction is the stopping cross section  $S$  of the projectile in the ice film, or energy deposited per unit column density in the solid. It is the sum of an electronic component,  $S_e$ , due to energy transferred into electronic excitations and ionizations, and a nuclear component,  $S_n$ , due to elastic collisions with the target nuclei. The mean compaction area  $A$  is found to increase linearly with the total stopping power ( $S = S_e + S_n$ ) of the projectile above a threshold  $S_t$ . A fit of the data with the relation  $A = (S - S_t)/\varepsilon$  gives  $\varepsilon = 1.3 \text{ eV molecule}^{-1}$  and  $S_t = 4 \text{ eV A}^{-1}$ . The parameter  $\varepsilon$  is interpreted as the effective density of deposited energy needed to break the hydrogen bonds and allow molecules to rearrange to form compact ice. Also, an important parameter typically used to compare results of different experiments is the radiation dose  $D$ ; experiments show that a dose of  $1.52 \text{ eV molecule}^{-1}$  must be delivered to the ice film to reduce its porosity by 63%.

## 16.7 Ion-Induced Gas Adsorption

A recent discovery in the laboratory is the enhanced gas trapping of nanoporous ices that have been irradiated versus those that have not been irradiated. Experiments have shown that in grown ice mixtures of oxygen and water, most

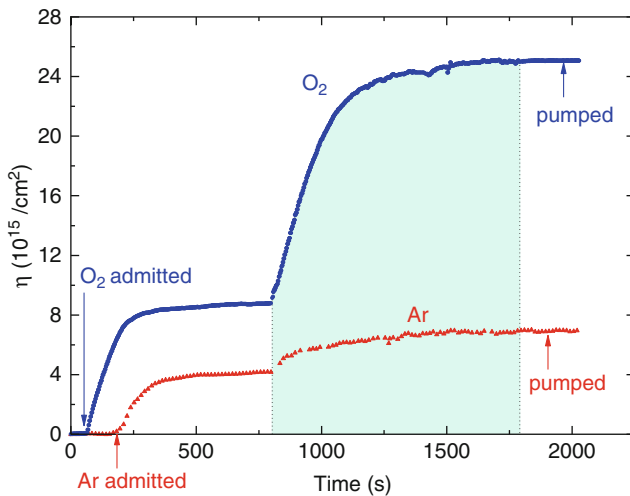


**Fig. 16.5** The  $\text{O}_2$  and Ar column densities adsorbed at 50 K at a pressure of  $7.2 \times 10^{-7}$  mbar on a  $5 \times 10^{18} \text{ H}_2\text{O}/\text{cm}^2$  thick ice film grown at 70 K. The shaded area indicates the period of irradiation with 50 keV  $\text{H}^+$  at a flux of  $1.1 \times 10^{12} \text{ H}^+ \text{ cm}^{-2} \text{ s}^{-1}$  for  $\text{O}_2$  (Ar). After the ambient gas was removed by pumping, no gas desorbed in the ice diffused out. (After Shi et al. 2009a)

of the oxygen in the sample sublimates below 40 K and that regardless of the initial gas mixture there was a maximum of 10–15% oxygen that could be retained until crystallization (Vidal et al. 1997; Baragiola and Bahr 1998). In the presence of radiation effects, up to twice the amount of oxygen can be trapped (Teolis et al. 2005; Loeffler et al. 2006b) at single defects or in bubbles (Johnson and Jesser 1997; Loeffler et al. 2006c).

In icy objects in the outer solar system, irradiation and gas adsorption are unlikely to be separated in time on a satellite surface; rather, they would take place simultaneously. However, in contrast to the case where irradiation is performed before gas exposure, irradiation enhances  $\text{O}_2$  and Ar adsorption when carried out during exposure. This phenomenon is shown in Fig. 16.5 (Shi et al. 2009a), where ice films were deposited at 70 K and then exposed to gas at 50 K. The uptake of gas molecules was measured using a quartz-crystal microbalance. After gas adsorption saturated, the ice film was irradiated with 50 keV  $\text{H}^+$  while maintaining the gas pressure. Additional gas adsorption began at the initiation of irradiation, increasing asymptotically to a new saturation level at high fluences.

The additional adsorbed gas remained in the ice after irradiation and, remarkably, even after stopping the gas exposure by removing the ambient gas. In the  $\text{O}_2$  experiments, the adsorbed  $\text{O}_2$  was retained in the film during heating until the temperature rose above 140 K, where the whole film evaporates. Thus, in contrast to the case without irradiation, the binding of the adsorbed molecule to the irradiated ice is sufficient to prevent its subsequent desorption. Also shown in Fig. 16.5 is the enhanced adsorption of Ar, which cannot be attributed to radiation chemistry. Hence, the oxygen retention is attributed mainly to trapping in collapsed nanopores.

For the low flux conditions in the outer solar system, the enhancement of adsorption is largest, as the time between ion impacts is sufficient to allow maximum oxygen adsorption between pore collapse events (Shi et al. 2009a).

## 16.8 Electrostatic Charging

The electrostatic potential of icy astronomical objects is unknown and no space mission has landed on them. The importance of surface potentials lies in their ability to deflect and even reflect magnetospheric particles from reaching the surface of the icy satellites. Charging of icy grains in planetary ring shares much of the physics with charging of planetary surfaces and can have noticeable consequence since the particles are so small that electrostatic and gravitational forces are comparable, which results in complex dynamics in the rings of Saturn (Mitchell et al. 2006).

The process of charge trapping starts with the deposition of the projectile charge and the emission of secondary electrons. When the projectiles penetrate, they create electron-ion pairs in ionization collisions of the projectile and secondary electrons with water molecules. Electrons that do not immediately recombine are much more mobile than ions. They can trap, or escape from the surface resulting in secondary electron emission. However, these electrons can be returned to a positively charged surface.

To measure charging in the laboratory, Shi et al. (2009b) use thin ice films on a grounded metal substrate to which charges may migrate. Since water ice is an insulator (band gap  $\sim 11$  eV and high resistivity), one expects electrostatic charging effects when it is irradiated by charged particles. The effects occurs when charges are trapped at defect levels (energy states located between the valence and conduction bands), where they are relatively immobile, resulting in an effective positive polarization of the insulator. The trapped charges, together with their images in the gold substrate, produce an electric field that can affect the energy and trajectory of ejected species such as secondary electrons and ions. This electric field is limited to the value at which dielectric breakdown occurs.

To study the positive electrostatic charging of ice under positive ion impact, Shi et al. (Shi et al. 2010) measured the energies of sputtered ions during irradiation with 100 keV  $\text{Ar}^+$ . The ejected ions were analyzed in mass and energy with an energy selected mass spectrometer. The ion energy is the intrinsic energy at which it is sputtered in the absence of charging, plus the electrostatic potential of the surface. For an ice films at 80 K, with thicknesses ranging from 1 to  $2.9 \times 10^{18}$   $\text{H}_2\text{O}/\text{cm}^2$ , the film voltage increases monotonically with ion fluence and saturated for fluences above  $10^{13} \text{ cm}^{-2}$  (Fig. 16.6). In all cases, the energy of secondary ions at zero fluence, the intrinsic sputtered energy  $E_0$ , is  $\sim 5$  eV. Figure 16.6 also shows that the secondary ion energy saturates at high fluences to a value that increases with film thickness.

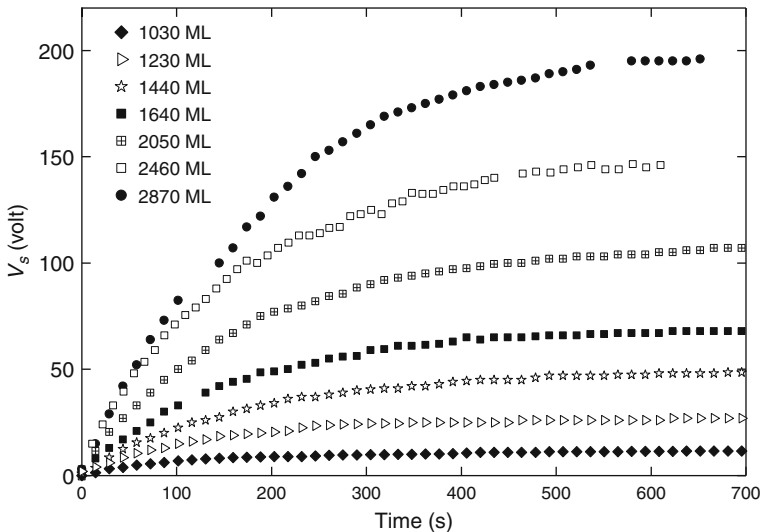


**Fig. 16.6** Charging curves for ice films *thicknesses* between  $\sim 1$  and  $\sim 3 \times 10^{18} \text{ H}_2\text{O}/\text{cm}^2$ , grown and irradiated at 80 K with 100 keV Ar ions with an ion flux  $j = 3.1 \times 10^{10} \text{ cm}^{-2} \text{ s}^{-1}$

The curves are well fit by an exponential function  $V_s(t)/V_s(\infty) = 1 - \exp(-t/\tau)$ , where  $V_s(\infty)$  is the film voltage at saturation fluence, and  $\tau$  a time constant, which describes the charging process, averaging  $150 \pm 30$  s for each different film thickness. Films thinner than  $\sim 0.6 \times 10^{18} \text{ H}_2\text{O}/\text{cm}^2$ , eject ions with  $\sim 5$  eV constant energy, even at high fluences, indicating that they do not charge.

## 16.9 Outlook

Planetary surfaces and their surrounding radiation field are a complex dynamic system. They are macroscopically and microscopically rough; temperatures vary wildly due to almost non-existent atmospheres, and depend on latitude, time of day, albedo, and exposure (some areas will be always in the shade). In addition ice grains, either in rings or as part of the surface, have unknown shapes or light scattering properties. Furthermore, grainy surfaces are eroded more slowly by sputtering due to redeposition (Cassidy and Johnson 2005).

Icy bodies in the outer solar system likely have a surface layer that has been altered by external processes such as incident radiation and micrometeorite impacts. The extent (thickness) of this layer changes with time and is mostly considered to depend on the impact processes that occur on the surface or on geologic processes that occur on or below the surface. As an example the thickness of Europa's regolith is estimated to be  $\sim 1$  m after  $10^7$  years of bombardment

(Cooper et al. 2001). Images taken from spacecraft, such as Galileo (Belton et al. 1996), and Cassini (Porco et al. 2006), reveal that there is no one typical regolith surface, as some may appear relatively featureless and uniform, while others may contain craters, cracks, and an abundant variety of large or small grains. Recognizing that each surface is unique, regardless of its bulk properties, is important since much of the information being extracted using remote sensing techniques is coming from the regolith and not the bulk.

To interpret adequately remote sensing data and results obtained from planetary scientific missions in terms of the relevant surface processes it is essential to use a combination of laboratory simulations and modeling. Laboratory simulations and modeling of processes occurring on astronomical bodies, or in their atmospheres, are crucial to support planetary scientific missions. A combination of experimental and theoretical research is required to recognize which processes are significant in astronomical environments and to provide a database for detailed analysis. The first step to interpret telescopic observations is to compare observed optical reflectance spectra with laboratory data. Although, the volume of published laboratory results is large and used constantly to support astronomical observations, the diverse and complex environments continually require new laboratory results. In addition, laboratory studies have unveiled new phenomena that had not been imagined. For instance, this chapter shows new phenomena such as synergistic effects (ice redeposition enhances the accumulation of radiation products, ion irradiation enhances adsorption of exospheric gases), molecular synthesis at interfaces, and an unexplained dependence of amorphization rates on the type of projectiles.

Since the radiation environment to which planetary ices and atmospheres are exposed includes energetic photons and charged particles, it is essential to conduct laboratory measurements using those excitation sources. Because laboratory data cannot cover the whole parameter space, modeling is needed. For instance, the dependence of different effects on stopping cross sections can be used to derive unknown information. This approach has its limitations, as exemplified in Fig. 16.3. Fluences needed for amorphization do not follow the usual scaling with the absorbed radiation dose per molecule when comparing different types of projectiles. This suggests that models need to be corrected for effects that depend on the density of initial energy deposition, charge exchange occurring for ions but not for electrons or photons, among others.

Finally, laboratory studies are needed to understand important processes occurring on planetary ices and laying a strong foundation for the direction of future planetary missions. Missions capable of *in situ* analysis by landing instruments will play a major role in advancing our fundamental understanding on what the environment is like on the surface and what causes it to change over time.

**Acknowledgments** This work was supported at Virginia by NASA Outer Solar System and Planetary Geology and Geophysics programs and by NSF Astronomy. MEP and GS acknowledge the support by Italian Space Agency contract n. I/015/07/0 (“Studi di Esplorazione Sistema Solare”).

## References

- Bahr DA, Famá M, Vidal RA, Baragiola RA (2001) Radiolysis of water ice in the outer solar system: sputtering and trapping of radiation products. *J Geophys Res* 106:33285
- Baragiola RA (2003a) Microporous amorphous water ice films and astronomical implications, In: Devlin JP, Buch B (eds) *Water in confining geometries*. Springer, Berlin (2003)
- Baragiola RA (2003b) Water ice on outer solar system surfaces: basic properties and radiation effects. *Planet Sp Sci* 51:953
- Baragiola RA, Bahr DA (1998) Laboratory studies of the optical properties and stability of oxygen on Ganymede. *J Geophys Res* 103:25865
- Baragiola RA, Vidal RA, Svendsen W, Schou J, Shi M, Bahr DA, Atteberry CL (2003) Sputtering of water ice. *Nucl Instrm Method Phys Res B* 209:294
- Baragiola RA, Loeffler MJ, Raut U, Vidal RA, Wilson CD (2005) Laboratory studies of radiation effects in water ice in the outer solar system. *Radiat Phys Chem* 72:187
- Bednarek J, Plonka A, Hallbrucker A, Mayer E (1998) Radical generation upon  $\gamma$ -irradiation of two amorphous and two crystalline forms of water at 77 K. *J Phys Chem A* 102:9091
- Belton MJS et al (1996) Galileo's first images of Jupiter and the Galilean satellites. *Science* 274:377
- Brown ME, Calvin WM (2000) Evidence for crystalline water and ammonia ices on Pluto's satellite Charon. *Science* 287:107
- Calvin WM, Johnson RE, Spencer JR (1996) O<sub>2</sub> on Ganymede spectral characteristics and plasma formation mechanisms. *Geophys Res Lett* 23:673
- Carlson RW et al (1999a) A tenuous carbon dioxide atmosphere on Jupiter's moon Callisto. *Science* 283:2062
- Carlson RW, Johnson RE, Anderson MS (1999b) Sulfuric acid on Europa and the radiolytic sulfur cycle. *Science* 286:97
- Cassidy TA, Johnson RE (2005) Monte Carlo model of sputtering and other ejection processes within a regolith. *Icarus* 176:499
- Collings MP, Dever JW, Fraser HJ, McCoustra MRS, Williams DA (2003) Carbon monoxide entrapment in interstellar ice analogs. *Astrophys J* 583:1058
- Cook JC, Desch SJ, Roush TL, Trujillo CA, Geballe TR (2007) Near-infrared spectroscopy of Charon: possible evidence for cryovolcanism on Kuiper Belt objects. *Astrophys J* 663:1406
- Cooper JF, Johnson RE, Mauk BH, Garrett HB, Gehrels N (2001) Energetic ion and electron irradiation of the icy Galilean satellites. *Icarus* 149:133
- Devlin JP (1992) Molecular interactions with icy surfaces: infrared spectra of carbon monoxide adsorbed in microporous amorphous ice. *J Phys Chem* 96:6185
- Dohnálek Z, Kimmel GA, Ayotte P, Smith RS, Kay BD (2003) The deposition angle-dependent density of amorphous solid water films. *J Chem Phys* 118:364
- Dubochet J, Lepault J (1984) Cryo-electron microscopy of vitrified water. *J Physique C* 7:85
- Fama M, Teolis BD, Bahr D, Baragiola RA (2007) Role of electron capture in ion-induced electronic sputtering of insulators. *Phys Rev B* 75:100101
- Fama M, Shi J, Baragiola RA (2008) Sputtering of ice by low-energy ions. *Surf Sci* 602:156
- Fama M, Loeffler MJ, Raut U, Baragiola RA (2010) Radiation-induced amorphization of crystal-line ice. *Icarus* 207:314
- Golecki I, Jaccard C (1978) Radiation damage in ice at low temperatures studied by Proton channelling. *J Glaciol* 21:247
- Gomis O, Strazzulla G (2005) CO<sub>2</sub> production by ion irradiation of H<sub>2</sub>O ice on top of carbonaceous materials and its relevance to the Galilean satellites. *Icarus* 177:570
- Gomis O, Strazzulla G (2008) Ion irradiation of H<sub>2</sub>O ice on top of sulfurous solid residues and its relevance to the Galilean satellites. *Icarus* 194:146
- Gomis O, Satorre MA, Strazzulla G, Leto G (2004) Hydrogen peroxide formation by ion implantation in water ice and its relevance to the Galilean satellites. *Planet Sp Sci* 52:371

- Goulet T, Bernas A, Ferradini C, Jay-Gerin J-P (1990) On the electronic structure of liquid water: conduction-band tail revealed by photoionization data. *Chem Phys Lett* 170:492
- Grundy WM, Schmitt B (1998) The temperature-dependent near-infrared absorption spectrum of hexagonal H<sub>2</sub>O ice. *J Geophys Res* 103:25809
- Grundy WM, Buie MW, Stansberry JA, Spencer JR, Schmitt B (1999) Near-infrared spectra of icy outer solar system surfaces: remote determination of H<sub>2</sub>O ice temperatures. *Icarus* 142:536
- Hage W, Liedl KR, Hallbrucker A, Mayer E (1998) Carbonic acid in the gas phase and its astrophysical relevance. *Science* 279:1332
- Hansen GB, McCord TB (2004) Amorphous and crystalline ice on the Galilean satellites: a balance between thermal and radiolytic processes. *J Geophys Res* 109:E01012
- Heide HG (1982) On the irradiation of organic-samples in the vicinity of ice. *Ultramicroscopy* 7:299
- Heide HG (1984) Observations on ice layers. *Ultramicroscopy* 14:271
- Hibbitts CA, Klemaszewski JE, McCord TB, Hansen GB, Greeley R (2002) CO<sub>2</sub>-rich impact craters on Callisto. *J Geophys Res* 107(E10):5084
- Hibbitts CA, Pappalardo RT, Hansen GB, McCord TB (2003) Carbon dioxide on Ganymede. *J Geophys Res* 108(E5):5036
- Hixson HG, Wojcik MJ, Devlin MS, Devlin JP, Buch V (1992) Experimental and simulated vibrational spectra of H<sub>2</sub> absorbed in amorphous ice: surface structures, energetics, and relaxations. *J Chem Phys* 97:753
- Jaumann R et al (2008) Distribution of icy particles across Enceladus' surface as derived from Cassini-VIMS measurements. *Icarus* 193:407
- Jenniskens P, Blake DF (1996) Crystallization of amorphous water ice in the solar system. *Astrophys J* 473:1104
- Jewitt DC, Luu J (2004) Crystalline water ice on the Kuiper belt object(50000) Quaoar. *Nature* 432:731
- Johnson RE (1990) Energetic charged-particle interactions with atmospheres and surfaces. Springer, New York
- Johnson TV (2007) Ch. 1.34 In: Davis AM (ed) Meteorites, comets and planets: treatise of geochemistry, vol 1. Elsevier, Amsterdam, The Netherlands
- Johnson RE, Jesser WA (1997) O<sub>2</sub>/O<sub>3</sub> microatmospheres in the surface of Ganymede. *Astrophys J* 480:L79
- Johnson RE, Schou J (1993) Sputtering of inorganic insulators. *Mat Fys Medd K Dan Vidensk Selsk* 43:403
- Johnson RE, Sundqvist B, Hakansson P, Hedin A, Salehpour M, Save G (1987) Incident angle dependence of electronic desorption and sputtering by energetic ions. *Surf Sci* 179:187
- Johnson RE (1998) Sputtering and Desorption from Icy Surfaces, In: Schmitt B (ed) Solar system ices. Kluwer, Dordrecht, p 303
- Johnson RE, Fama M, Liu M, Baragiola RA, Sittler EC, Smith HT (2008) Sputtering of ice grains and icy satellites in Saturn's inner magnetosphere. *Planet Sp Sci* 56:1238
- Laffon C, Lacombe S, Bournel F, Parent P (2006) Radiation effects in water ice: a near-edge x-ray absorption fine structure study. *J Chem Phys* 125:204714
- Lane AL, Domingue DL (1997) IUE's view of Callisto: detection of an SO<sub>2</sub> absorption correlated to possible torus neutral wind alterations. *Geophys Res Lett* 24:1143
- Lane AL, Nelson RM, Matson DL (1981) Evidence for sulphur implantation in Europa's UV absorption band. *Nature* 292:38
- LaVerne JA (2000) Track effects of heavy ions in liquid water. *Radiat Res* 153:487
- Lepault J, Freeman R, Dubochet J (1983) Electron beam induced "vitrified ice". *J Microsc* 132: RP3
- Leto G, Baratta GA (2003) Ly-  $\alpha$  photon induced amorphization of Ic water ice at 16 Kelvin. *Astron Astrophys* 397:7
- Leto G, Gomis O, Strazzulla G (2005) The reflectance spectrum of water ice: is the 1.65  $\mu$ m peak a good temperature probe? *Mem Soc Astron Italiana Suppl* 6:57

- Loeffler MJ, Baragiola RA (2005) The state of hydrogen peroxide on Europa. *Geophys Res Lett* 32:L172023
- Loeffler MJ, Baragiola RA (2009) Is the 3.5-micron infrared feature on enceladus due to hydrogen peroxide? *Astrophys J* 694:L92
- Loeffler MJ, Teolis BD, Baragiola RA (2006a) Decomposition of solid amorphous hydrogen peroxide by ion irradiation. *J Chem Phys* 124:104702
- Loeffler MJ, Raut U, Baragiola RA (2006b) A model study of the thermal evolution of astrophysical ices. *Astrophys J* 639:L103
- Loeffler MJ, Raut U, Baragiola RA (2006c) Enceladus: a source of nitrogen and an explanation for the water vapor plume observed by *Cassini*. *Astrophys J* 649:L133
- Loeffler MJ, Raut U, Vidal RA, Baragiola RA, Carlson RW (2006d) Synthesis of hydrogen peroxide in water ice by ion irradiation. *Icarus* 189:265
- Mastrapa RME, Brown RH (2006) Ion irradiation of crystalline H<sub>2</sub>O-ice: effect on the 1.65-μm band. *Icarus* 183:207
- McCord TB et al (1997) Organics and other molecules in the surfaces of Callisto and Ganymede. *Science* 278:271
- McCord TB, Hansen GB, Hibbitts CA (2001) Hydrated salt minerals on Ganymede's surface: evidence of an ocean below. *Science* 292:1523
- McGrath MA, Lellouch E, Strobel DF, Feldman PD, Johnson RE (2007) Ch. 19. In: Bagenal F, Dowling TE (eds) *Jupiter: the planet, satellites and magnetosphere*. Cambridge University Press
- Mennella V, Palumbo ME, Baratta GA (2004) Formation of CO and CO<sub>2</sub> Molecules by ion irradiation of water ice-covered hydrogenated carbon grains. *Astrophys J* 615:1073
- Mennella V, Baratta GA, Palumbo ME, Bergin EA (2006) Synthesis of CO and CO<sub>2</sub> molecules by UV irradiation of water ice-covered hydrogenated carbon grains. *Astrophys J* 643:923
- Merlin F, Guilbert A, Dumas C, Barucci MA, de Bergh C, Vernazza P (2007) Properties of the icy surface of the TNO 136108 (2003 EL<sub>61</sub>). *Astron Astrophys* 466:1185
- Mitchell CJ, Horanyi M, Havnes O, Porco CC (2006) Saturn's spokes: lost and found. *Science* 311:1587
- Moore MH, Hudson RL (1992) Far-infrared spectral studies of phase changes in water ice induced by proton irradiation. *Astrophys J* 401:353
- Moore MH, Hudson RL (2000) IR detection of H<sub>2</sub>O<sub>2</sub> at 80 K in ion-rradiated laboratory ices relevant to Europa. *Icarus* 145:282
- Noll KS, Weaver HA, Gonnella AM (1995) The albedo spectrum of Europa from 2200 Å to 3300 Å. *J Geophys Res* 100(E9):19057
- Noll KS, Johnson RE, Lane AL, Domingue DL, Weaver HA (1996) Detection of ozone on Ganymede. *Science* 273:341
- Noll KS, Johnson RE, McGrath MA, Caldwell JJ (1997a) Detection of SO<sub>2</sub> on Callisto with the Hubble Space Telescope. *Geophys Res Lett* 24:1139
- Noll KS, Roush TL, Cruikshank DP, Johnson RE, Pendleton YJ (1997b) Detection of ozone on Saturn's satellites Rhea and Dione. *Nature* 388:45
- Palumbo ME (2005) The morphology of interstellar water ice. *J Phys Conf Ser* 6:211
- Palumbo ME (2006) Formation of compact solid water after ion irradiation at 15 K. *Astron Astrophys* 453:903
- Palumbo ME, Strazzulla G (2003) Nitrogen condensation on water ice. *Can J Phys* 81:217
- Pinilla-Alonso N, Brunetto R, Licandro J, Gil-Hutton R, Roush TL, Strazzulla G (2009) The surface of (136108) Haumea (2003 EL{61}), the largest carbon-depleted object in the trans-Neptunian belt. *Astron Astrophys* 496:547
- Porco CC et al (2006) Cassini observes the active South pole of enceladus. *Science* 311:1393
- Raut U, Loeffler MJ, Teolis BD, Vidal RA, Baragiola RA (2005) Radiation synthesis of carbon dioxide in ice-coated grains. *Bull Am Astron Soc* 37:755
- Raut U, Teolis BD, Loeffler MJ, Vidal RA, Fama M, Baragiola RA (2007a) Compaction of microporous amorphous solid water by ion irradiation. *J Chem Phys* 126:244511

- Raut U, Fama M, Baragiola RA, Teolis BD (2007b) Characterization of porosity in vapor-deposited amorphous solid water from methane adsorption. *J Chem Phys* 127:104713
- Raut U, Fama M, Loeffler MJ, Baragiola RA (2008) Cosmic Ray compaction of porous interstellar ices. *Astrophys J* 687:1070
- Reimann CT, Boring JW, Johnson RE, Garrett JW, Farmer KR, Brown WL (1984) Ion-induced molecular ejection from D<sub>2</sub>O ice. *Surf Sci* 147:227
- Rowland B, Fisher M, Devlin JP (1991) Probing icy surfaces with the dangling-OH-mode absorption: large ice clusters and microporous amorphous ice. *J Chem Phys* 95:1378
- Sack NJ, Baragiola RA (1993) Sublimation of vapor-deposited water ice below 170 K, and its dependence on growth conditions. *Phys Rev B* 48:9973
- Sack NJ, Johnson RE, Boring JW, Baragiola RA (1992) The effect of magnetospheric ion bombardment on the reflectance of Europa's surface. *Icarus* 100:534–539
- Schmitt B, De Bergh C, Festou M (eds) (1998) Solar system ices. Kluwer, Dordrecht
- Shi M, Baragiola RA, Grosjean DE, Johnson RE, Jurac S, Schou J (1995) Sputtering of water ice surfaces and the production of extended neutral atmospheres. *J Geophys Res* 100:26387
- Shi J, Teolis BD, Baragiola RA (2009) Irradiation-enhanced adsorption and trapping of O<sub>2</sub> on nanoporous water ice. *Phys Rev B* 79:235422
- Shi J, Fama MA, Teolis BD, Baragiola RA (2010) Ion-induced electrostatic charging of ice. *Nucl Instrm Method Phys Res B* 268:2888
- Sigmund P (1969) Theory of sputtering. I. Sputtering yield of amorphous and polycrystalline targets. *Phys Rev* 184:383
- Slanger TG, Black G (1982) Photodissociative channels at 1216 Å for H<sub>2</sub>O, NH<sub>3</sub>, and CH<sub>4</sub>. *J Chem Phys* 77:2432
- Spencer JR, Calvin WM (2002) Condensed O<sub>2</sub> on Europa and Callisto. *Astron J* 124:3400
- Spinks JWT, Woods RJ (1990) An introduction to radiation chemistry. Wiley, New York
- Strazzulla G, Baratta GA, Leto G, Foti G (1992) Ion-beam-induced amorphization of crystalline water ice. *Europhys Lett* 18:517
- Strazzulla G, Leto G, Gomis O, Satorre MA (2003) Implantation of carbon and nitrogen ions in water ice. *Icarus* 164:163
- Strazzulla G, Baratta GA, Leto G, Gomis O (2007) Hydrate sulfuric acid after sulfur implantation in water ice. *Icarus* 192:623
- Teolis BD, Vidal RA, Shi J, Baragiola RA (2005) Mechanisms of O<sub>2</sub> sputtering from water ice by keV ions. *Phys Rev B* 72:245422
- Teolis BD, Loeffler MJ, Raut U, Fama M, Baragiola RA (2006) Ozone synthesis on the icy satellites. *Astrophys J Lett* 644:L141
- Teolis BD, Shi J, Baragiola RA (2009) Formation, trapping, and ejection of radiolytic O<sub>2</sub> from ion-irradiated water ice studied by sputter depth profiling. *J Chem Phys* 130:134704
- Vidal RA, Bahr D, Baragiola RA, Peters M (1997) Oxygen on Ganymede: Laboratory Studies. *Science* 276:1839
- Vidal RA, Teolis BD, Baragiola RA (2005) Angular dependence of the sputtering yield of water ice by 100 keV proton bombardment. *Surf Sci* 588:1
- Warren SG (1984) Optical-constants of ice from the ultraviolet to the microwave. *Appl Opt* 23:1206
- Wilson CD, Dukes CA, Baragiola RA (2001) Search for the plasmon in condensed water. *Phys Rev B* 63:121101

# Chapter 17

## Sputtering of Ices

Robert E. Johnson, Robert W. Carlson,  
Timothy A. Cassidy, and Marcelo Fama

**Abstract** Data obtained from the exploration of the outer solar system has led to a new area of physics: electronically induced sputtering of low-temperature, condensed-gas solids, here referred to as ices. Icy bodies in the outer solar system are bombarded by relatively intense fluxes of ions and electrons, as well as the background solar UV flux, causing changes in their optical reflectance and ejection (sputtering/desorption) of molecules from their surfaces. The low cohesive energies of ices lead to relatively large sputtering rates by both momentum transfer ('knock-on' collisions) and the electronic excitations produced by the incident particles. Such sputtering produces an ambient gas about an icy body, often the source of the local plasma. This chapter focuses on the ejection of material by ionizing radiation from a surface that is predominantly a molecular condensed gas solid. The incident radiation types considered are photons, electrons and ions with the emphasis on the ejection processes. This radiation also produces the chemical effects described in the chapters of sections II and III. The induced-chemistry can produce both more refractory and more volatile products and so affect the molecular ejection rate. The emphasis in this chapter is on the production of gas-phase species from icy surfaces in space. We describe the physics and chemistry leading to the ejection of atoms and molecules, give semi-empirical expressions based on these processes, and describe some applications.

---

R.E. Johnson (✉) • T.A. Cassidy • M. Fama  
University of Virginia, Charlottesville, VA, USA  
e-mail: [rej@virginia.edu](mailto:rej@virginia.edu); [Timothy.A.Cassidy@jpl.nasa.gov](mailto:Timothy.A.Cassidy@jpl.nasa.gov); [maf7e@virginia.edu](mailto:maf7e@virginia.edu)

R.W. Carlson  
Jet Propulsion Laboratory, California Institute of Technology, Pasadena, CA, USA  
e-mail: [Robert.W.Carlson@jpl.nasa.gov](mailto:Robert.W.Carlson@jpl.nasa.gov)

## 17.1 Introduction

We are in an exciting period of exploration of the outer solar system by spacecraft, orbiting telescopes, and remarkably improved ground-based observations. These studies have revolutionized our understanding of this region, revealing worlds very different from ours, some of which are bizarre. Because of the low surface temperatures, typically  $<120$  K, the ‘rock’ of outer-solar-system bodies is water ice. That is, excluding the four giant planets, it is the structural and thermal properties of ice that principally determine the geology of the surfaces of many of the small objects from Jupiter’s orbit and beyond. Other more volatile molecular species, such as N<sub>2</sub>, O<sub>2</sub>, CO, CO<sub>2</sub>, NH<sub>3</sub>, and CH<sub>4</sub>, form atmospheres and polar ices, or can cause the surface to be active. An interesting exception is Io, a moon of Jupiter, which does not have water ice. Owing to its tidal interactions, Io is volcanically active and has been desiccated, losing all of its water and other light volatiles which are stripped from its transient atmosphere by the Jovian plasma (Johnson 2004). Because of this, frozen SO<sub>2</sub>, a familiar, heavy volcanic gas on Earth, covers Io’s surface (e.g., Baggenstaf et al. 2004).

Since most small outer-solar-system bodies, with the exception of Titan, have either no atmospheres or tenuous ones at best, their surfaces are exposed to the solar ultraviolet radiation and local plasma. These irradiations can alter their surfaces physically and chemically (Johnson 1990; Carlson et al. 2009) and produce atmospheres (Johnson et al. 2009), such as the recent discovery of an O<sub>2</sub>–CO<sub>2</sub> atmosphere on Saturn’s moon Rhea (Teolis et al. 2010). Since the Pioneer and Voyager spacecraft found that both Jupiter and Saturn had surprisingly intense plasmas (e.g., Fig. 17.1) trapped in their giant magnetic fields, the effect of the plasma bombardment on their icy moons was investigated. Therefore, following the Pioneer encounters with Jupiter and in preparation for the Voyager encounters, W. L. Brown, L. J. Lanzerotti, and colleagues carried out a series of experiments to measure the ejection of molecules induced by energetic ion impact on ice (Brown et al. 1978; Lanzerotti et al. 1978). Their discovery that the sputtering of low temperature ice by fast, light ions is principally determined by the electronic excitations produced in the ice, rather than by knock-on collisions of the incident ions with water molecules, initiated a new area of physics, the study of electronic sputtering of low-temperature condensed-gas solids referred to here as ices.

The study of sputtering in refractory materials has a long history, as it is a tool for producing a vapor from a low-vapor-pressure solid (Sigmund 1993). Therefore the application of the standard sputtering process to ices is first discussed, followed by a description of electronic sputtering of ices and the chemical changes that effect the ejection of molecules. Finally, the relevance of sputtering to recent observations of icy bodies in the outer solar system is described.

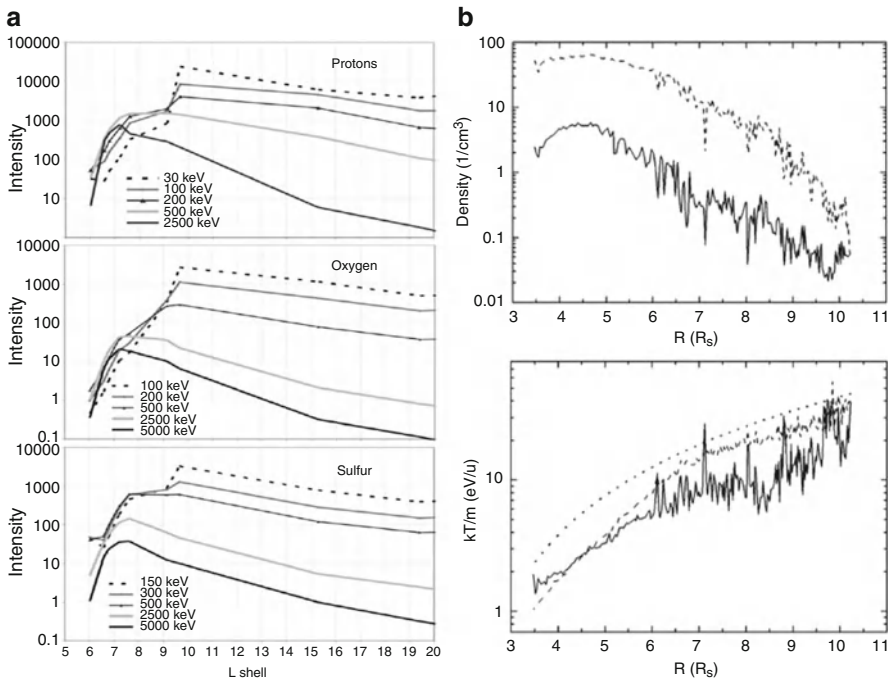


**Fig. 17.1** (a) Energetic ion intensities in ions/(cm<sup>2</sup> s sr keV) in the Jovian magnetosphere (From Paranicas et al. (2009)); thermal plasma ion densities and temperatures in the Saturnian magnetosphere: solid lines H<sup>+</sup>, dashed W<sup>+</sup> (sum of H<sub>2</sub>O<sup>+</sup>, OH<sup>+</sup> and O<sup>+</sup>); dotted line in lower panel pick-up energy (From Johnson et al. (2008))

## 17.2 Sputtering and Desorption

A fast ion or electron penetrating a solid gradually loses energy to the constituent atoms. The average rate of energy transfer is represented by a quantity  $dE/dx$ , the energy loss per unit path length of the charged particle in the solid, called the ‘stopping power’ of the material. Since an incident ion loses energy both by nuclear-elastic (knock-on) collisions and by electronic excitations and ionizations of the molecules in the material, the stopping power is often written:  $(dE/dx) \sim (dE/dx)_n + (dE/dx)_e$ . These quantities are given in Fig. 17.2a for O<sup>+</sup> incident on water ice, a system of interest in both the Jovian and Saturnian magnetospheres. Energetic electrons exhibit only a  $(dE/dx)_e$  component; for cosmic ray ions and shocks in the interstellar medium such quantities are discussed in Bringa and Johnson (2003).

Sputtering, the ejection of atoms or molecules from the solid into the vacuum, is initiated when the energy deposited by the incident particles sets atoms and molecules in motion in the surface region. The study of ion-induced sputtering by knock-on collision,  $(dE/dx)_n$ , has a long history in part due to its usefulness in materials processing such as producing a metal vapor for coatings. However, in the

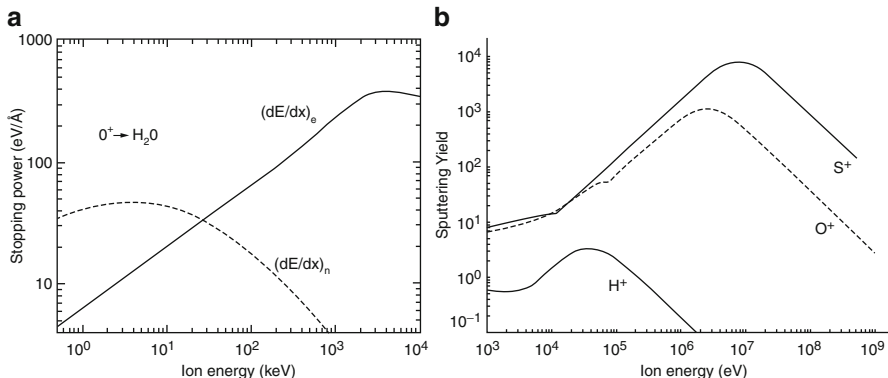


**Fig. 17.2** (a) Stopping power ( $dE/dx$ ) for  $O^+$  in  $H_2O$  is roughly the sum of two components:  $(dE/dx)_n$  nuclear-elastic (knock-on) collisions (dashed line), and  $(dE/dx)_e$  electronic excitation and ionizations (Data from Ziegler et al. (1985)). (b) Total sputtering yield given in equivalent  $H_2O$  molecules ejected per incident ion at  $T < 80$  K (Adapted from Johnson et al. (2009))

late 1970s it was discovered that weakly bound insulators such as the ices were also sputtered by the *electronic energy* deposited,  $(dE/dx)_e$  (e.g., Lanzerotti et al. 1978; Brown et al. 1978, 1982). Whereas the electronic excitations and ionizations produced are rapidly quenched in a metal, those produced in these weakly bound solid insulators can be converted to kinetic energy through a variety of pathways (Brown and Johnson 1986; Johnson 1996).

A measure of the sputtering rate for a solid is the yield,  $Y(E_i, \theta_i)$ : the number of molecules ejected per incident ion or electron with energy  $E_i$  and angle to the surface normal,  $\theta_i$ .  $Y$  is shown in Fig. 17.2b for  $\theta_i = 0$  for  $H^+$ ,  $O^{n+}$  and  $S^{n+}$  on ice. These ions, especially  $H^+$  and  $O^{n+}$ , are common in the outer planet magnetospheres. Comparing Fig. 17.2a, b it is seen that both knock-on collisions and electronic excitations sputter water ice. Although the energy deposited must act in concert,  $Y$  is usually written as a sum of two components:  $Y \sim Y_n + Y_e$ .

In metals and other refractory materials knock-on collisions are typically the dominant cause of sputtering, so that  $Y \sim Y_n$ . On the other hand, the icy surfaces in the Jovian magnetosphere are irradiated by very energetic ions. For such ions the electronic component,  $Y_e$ , is seen in Fig. 17.2b to be dominant. Below we describe the physics of electronic and knock-on sputtering. The latter is sometimes called collision cascade or nuclear sputtering.

### 17.3 Knock-on Sputtering

When an incident ion strikes an atom in a solid, setting it in motion, the recoiling atom will quickly collide with other atoms producing a cascade of collisions in the solid. At the surface some of these recoils have sufficient energy to escape from the solid contributing to the sputtering yield. In the bulk of the solid, recoils knocked

out of their lattice sites form defects (interstitials and voids). Under long term irradiation this process can also amorphize the penetrated region of a crystalline solid (e.g., Strazzulla et al. 1992; Fama et al. 2010).

### 17.3.1 Yield

Based on the picture described above,  $Y_n(E_i, \theta_i)$ , for an ion with energy incident  $E_i$  incident at an angle to the surface normal,  $\theta_i$ , is determined by the number of recoils set in motion near the surface. The recoil production is, in turn, roughly proportional to the energy deposited in the near surface region:  $(dE/dx)_n$ . Since the ability of an atom or molecule to be ejected is affected by its binding to the solid,  $Y_n$  also is, roughly, inversely dependent on the cohesive energy of the solid,  $U$ . For long term sputtering, this is the average binding energy of the atoms to the surface, which for the low energy ejecta is of the order of the sublimation energy. Therefore, the yield is often written as

$$Y_n \sim c[I(dE/dx)_n/U]^p \quad (17.1)$$

where  $I$  is the mean spacing of the molecules ( $I \sim n^{-1/3}$ ,  $n$  the molecular number density). Therefore,  $[I(dE/dx)_n]$  is the average energy deposited per molecular layer in the surface region and the term in brackets in Eq. 17.1 is dimensionless. The fraction of produced recoils moving toward the surface is roughly accounted for by  $c$  in Eq. 17.1. Since the recoils are initially forward directed,  $c \sim 0.1\text{--}0.2$  (Johnson 1990) in a number of material, and the exponent  $p$  is discussed below.

Based on Eq. 17.1, knock-on sputtering is much more efficient in ices than in refractory materials, as the value of  $U$  is an order of magnitude smaller (Johnson and Schou 1993). Although experiments clearly bear this out, using values of  $c$  based on simulations, the  $U$  extracted from measurements can differ considerably from the sublimation energy even for simple materials (Behrisch and Eckstein 2007). This is due to a number of effects, such as radiation induced damage. But for the volatile materials of interest, when a large volume of material is ejected, the sublimation energy of the individual molecule becomes irrelevant. In addition, during sputtering, the volatility of a molecular ice, hence the effective  $U$ , can be affected by the chemistry induced, as discussed shortly.

Since  $(dE/dx)_n$  roughly scales as the square of the incident ion atomic number, it is small for light ions and, therefore, produces a sparse recoil density. To first order the recoil cascade is described as ‘linear’; that is, it is assumed to be produced by a series of independent binary collisions with each collision between a recoil atom and an atom not previously struck. In this picture the probability of producing a recoil that leaves the surface is roughly proportional to the energy deposited, hence,  $p = 1$  in Eq. 17.1 above some energy threshold,  $E_t$  (Behrisch and Eckstein 2007; Johnson 1990). A threshold value of 1.48 eV for incident eV Xe ions on ice was been recently measured (Killelea et al. 2012).

The number of recoils set in motion with energy between  $E$  and  $E + dE$  is roughly proportional  $(dE/dx)_n/E^{-2}$ . This spectrum comes from a linearized particle transport equation for binary collisions between atoms described by a steeply varying interaction potential (e.g., Sigmund 1981). Molecular dynamics simulations have shown that this form is also roughly correct for low energy recoils in molecular solids (Johnson and Liu 1996), as well as for dense cascades of recoils (Bringa et al. 1999; Bringa and Johnson 2000). Integrating over the spectrum of recoils with  $E > U$  gives the term  $[(dE/dx)_n/U]$  in Eq. 17.1. Finally, at very low  $E_i$ ,  $Y_n$  rapidly decreases so that a rough threshold region is seen above some energy  $E_t$ . A recent compilation of data for atomic solids gives a table of fitting parameters based on a form like that in Eq. 17.1 with  $p = 1$  and a steep threshold dependence as  $E_i$  approaches  $E_t$  (Eckstein 2007).

At high  $(dE/dx)_n$  the density of atoms or molecules set in motion increases, so that recoils collide with other recoils. Although this leads to nonlinear energy transport, simulations and experiments show that the rough linearity in the yield in Eq. 17.1 and the form of recoil energy spectrum persist. This is even the case when a considerable number of molecules are ejected per impact event by a penetrating ion (Bringa and Johnson 1999). Since a high energy deposition density can lead to considerable dissociation in a molecular solid, the energy absorbed/released in dissociation and reactions can also contribute to sputtering. Due to this energy and the low energy recoils, the ejecta energy spectra also have a quasi-thermal component (Brown and Johnson 1986; Bringa and Johnson 1999, 2000). In addition, clusters are ejected when the yield is large, affecting the low energy component of the spectrum (Tucker et al. 2005; Anders and Urbassek 2009).

For very heavy incident ions or cluster ion impacts, the penetration depth may be quite small and the geometry of the energized region changes. In this case the full ion energy,  $E_i$ , may be deposited close to the surface so that the yield varies roughly as,  $Y_n \sim c(E_i/U)^p$ , with  $p$  near unity (e.g., Anders et al. 2004; Anders and Urbassek 2009). This process, on a microscopic scale, is similar to that occurring on a macroscopic scale in meteorite impacts on surfaces (Anders et al. 2012). The transfer of energy results in the formation of nano-craters in the surface, spallation, cluster ejection, and vaporization (Bringa et al. 2002; Anders et al. 2004; Anders and Urbassek 2009).

In the nonlinear regime, analytic models for sputtering have been constructed in which it is assumed there is a high density of random motion of the molecules in the solid (thermal-spike models) or it is assumed that net pressure is produced in the energized region (hydrodynamic models) (e.g., Johnson et al. 1989; Jakas et al. 2002). Although a good theoretical description of recoil energy transport at high  $(dE/dx)_n$  is lacking, molecular dynamics simulations have been used to reproduce many aspects of the measurements. It was shown that even in the so-called non-linear regime the yield still varied as  $\sim [(dE/dx)_n/U]$  over a range of ion energies if the radial scale of the energy density deposited is fixed (Bringa et al. 1999). Similarly, over a wide range of stopping powers, if an ion's penetration depth is greater than the depth from which the energy deposited directly contributes to sputtering, the incident angle dependence of the yield varies as  $\sim [\cos\theta_i]^{(1+x)}$  where  $\theta_i$  is the angle and  $x \sim 0.5-0.7$  (Johnson 1989; Bringa and Johnson 2001; Fama et al. 2008).

A considerable effort is still needed to describe the ejection of intact molecules versus fragments (e.g., Johnson and Sundqvist 1992), to treat the induced chemical reactions, and to describe the excitation states of the molecular ejecta. That chemical reactions affect the yield in the collision cascade regime, even when chemical products are a minor component, is clearly seen in the temperature dependence of the sputtering yield. For water ice, the yield at low T, given in equivalent molecules ejected, is typically multiplied by  $[1 + \exp(-E_a/kT)]$  as in an activated process with  $E_a$  the empirically determined activation energy. Although semi-empirical expressions are useful, understanding the physics and chemistry is critical. This is the case not only because it is an interesting problem in non-equilibrium thermodynamics, but the results can be important for describing the state of the ambient gas above the surface of an icy moon.

### 17.3.2 Ejecta Energies and Angles

The model for knock-on sputtering described above provides predictions for the energy spectra of the ejecta. There is a considerable body of data on the ejecta energy spectra for refractory material of technical interest (e.g., Behrisch and Eckstein 2007); however, this is not the case for the sputtering of molecular ices of interest in astronomy. This is unfortunate, in that modeling the fate of the ejecta in an astrophysical environment requires such spectra (e.g., Cassidy et al. 2009). When the yield is small, as is the case for sputtering of refractory solids, the number of recoils set in motion has roughly the form  $1/E^2$ , as discussed above. Therefore, the spectra of molecules with energy E ejected from a roughly planar surface would have the form

$$(dY/dE)/Y = f(E) = 2EU/(E + U)^3 \quad (17.2a)$$

where U is an effective surface binding energy (Sigmund 1981). When sputtering is averaged over a time to remove a number of monolayers of material, U in Eq. 17.2 should be the order of the sublimation energy,  $U_s$  in Table 17.1, as assumed in Eq. 17.1. In that case,  $dY/dE$  should have a maximum at  $E = U_s/2$ . Unfortunately, this is only very roughly true. More volatile solids actually do sputter more efficiently and have softer energy spectra, but in both expressions U is typically obtained by fitting to available data (e.g., Behrisch and Eckstein 2007). Using Eq. 17.2a to fit a large amount of data for refractory solids, U is found shifted always to energies lower than the theoretical U and the high energy tail can be slightly less steep than  $1/E^2$  (Gnaser 2007). Excited ejecta can have an attractive or repulsive interaction with the surface, thereby contributing to low U. Indeed ejected ions exhibit spectra that peak at  $E \sim 0$ .

For low-temperature condensed-gas solids, the experimental U extracted using Eq. 17.2a is typically much smaller than the sublimation energy. For example, in the knock-on regime,  $U \sim 0.055$  eV for sputtered D<sub>2</sub>O (Reimann et al. 1984; Brown et al. 1984); this is an order of magnitude smaller than  $U_s$  and a few times the melt

**Table 17.1** Sputter products

Ice	Products	Primary ejecta	$U_s^a$ (eV)	$\Delta H^b$ (eV)
$\text{NH}_3$	$\text{NH}_2, \text{H}$	$\text{NH}_3$	0.31	0.41
	$\text{N}_2\text{H}_4,$	$\text{N}_2$	(0.08)	
	$\text{N}_2, \text{H}_2$	$\text{H}_2$	(0.02)	
$\text{H}_2\text{O}$	$\text{OH}, \text{H}, \text{O}, \text{H}_2$	$\text{H}_2\text{O}$	0.45	2.0
	$\text{O}_2\text{H}, \text{H}_2\text{O}_2,$	$\text{O}_2$	(0.08)	
	$\text{O}_2$	$\text{H}_2$	(0.02)	
$\text{CH}_4$	$\text{CH}_3, \text{H}, \text{H}_2$	$\text{CH}_4$	0.18	0.56
	$\text{C}_2\text{H}_x, \text{C}_n\text{H}_m$	$\text{H}_2$	(0.02)	
$\text{H}_2\text{S}$	$\text{HS}, \text{H}, \text{S}, \text{H}_2$	$\text{H}_2\text{S}$	0.25	-0.13
	$\text{S}_2, \text{S}_x$	$\text{H}_2$	(0.02)	
$\text{CO}$ $(\text{CO}_2)$	$\text{C}, \text{O}, \text{CO}_2, \text{O}_2$	$\text{CO}$	0.09	1.1
	$\text{C}_x\text{O}_y$	$\text{CO}_2$	0.27	2.7
$\text{SO}_2$	$\text{SO}, \text{O}$	$\text{SO}_2$	0.28	2.7
	$\text{SO}_3, \text{O}_2, \text{S}_2\text{O}$	$\text{O}_2$	(0.08)	
	$\text{S}, \text{S}_2, \text{S}_x$	$\text{SO}$		

<sup>a</sup>Sublimation energies,  $U_s$ : brackets are energies for pure solid

<sup>b</sup>The chemical energy per equivalent molecule ejected for producing the gas phase molecules vs. the newly formed, weakly bound molecules. Rough lower bounds are given for:  $2\text{NH}_3 \rightarrow (\text{N}_2 + 3 \text{H}_2)$ ,  $2 \text{H}_2\text{O} \rightarrow \text{O}_2 + 2 \text{H}_2$ ,  $\text{CH}_4 \rightarrow \text{C} + 2 \text{H}_2$ ,  $\text{H}_2\text{S} \rightarrow \text{S} + \text{H}_2$ ,  $2\text{CO} \rightarrow \text{C}_2 + \text{O}_2$ ,  $2\text{CO}_2 \rightarrow 2\text{CO} + \text{O}_2$ ,  $\text{SO}_2 \rightarrow \text{S} + \text{O}_2$ . (e.g., <http://webbook.nist.gov/chemistry/form-ser.html>). Such processes can leave a refractory residue in a C or S containing ice

temperature. For large sputtering yields, cluster ejection occurs (Tucker et al. 2005) and the surface geometry breaks down during the ejection. Therefore, the form

$$f(E) = U/(E + U)^2 \quad (17.2b)$$

has been suggested (e.g., Johnson 1990). Indeed for large yields there appears to be either no maximum in  $f(E)$  or only a very subtle one at  $E \ll U_s/2$  (for ices, see examples in Brown and Johnson 1986). Using this spectrum to fit experimental data, the empirical values of  $U$  are still much smaller than  $U_s$ . This result, although differing from the simple analytic model is consistent with molecular dynamics simulations. That is, even in the absence of chemistry, the decay of the residual energy deposited results in a significant contribution of low energy ejecta giving a spectrum with either no maximum or one at very low energies below the melting point of the material (Bringa and Johnson 1999). Therefore, fits that include a quasi-thermal component have been explored (Kelly 1990; Urbassek and Michl 1987). However, no well-defined prescription has yet emerged.

For purpose of simulating the spatial redistribution of ejecta in a space environment, the angular distribution of the ejecta is typically assumed to be independent of the incident energy and angle. Therefore, one often uses the form,  $f(\cos\theta) = (dY/d\cos\theta)/Y \sim 2 \cos\theta$ . Although the ejecta distribution from a well prepared laboratory surface can have a very different angular distribution

(e.g., Gnaser 2007; Johnson 1989), Cassidy and Johnson (2005) have shown that for sputtering from a regolith that has a porosity typical of outer solar system icy moons (0.5–0.9), the interactions with neighboring grains is such that  $f(\cos\theta) \sim 2 \cos\theta$  is nearly always applicable. The *energy spectrum* for ejecta from a surface in space is also modified, and, hence, can differ from that on a laboratory surface affecting the redistribution of material across the surface of a body (Sieveka and Johnson 1982; Cassidy et al. 2009). Unfortunately, even for water ice, for which yields have been studied extensively, there are only a few measurements of  $f(E)$ . Since the yield depends on the chemistry induced, the surface temperature and the incident angle, the parameter space is large. However, the available data is very roughly consistent with forms like that in Eq. 17.2a or 17.2b, with a small effective  $U$ , typically an order of magnitude smaller than the sublimation energy.

## 17.4 Electronic Sputtering

Electronic sputtering is closely related to the study of photon- and electron-stimulated desorption of gases. Like knock-on sputtering, it is also the surface manifestation of radiation-induced defect production in insulators. Whereas early workers in that field concentrated on the easily detected ejected ions, Brown et al. (1982) showed that several MeV incident  $H^+$  and  $He^+$  ions ejected many more neutral molecules than ions. These ejected neutrals were representative of the electronic process induced by an incident charged particle. Depending on the incident radiation, there can be an enormous variation in the near-surface excitation density  $(dE/dx)_e$ , as was the case for knock-on sputtering. Whereas a UV photon produces  $\sim 0.001$  excitations or ionizations per monolayer in ice, relevant to the data in Fig. 17.2b, a 1-MeV  $H^+$  produces on the average  $\sim 0.3$  excitations or ionizations per molecular layer of ice penetrated and a 1-MeV  $O^+$  produces on the average  $\sim 10$  excitations/ monolayer. Electronic sputtering at high excitation densities has been used as a tool to eject intact large organic or biomolecules from samples in which such molecules are imbedded in an icy matrix (e.g., Sundqvist et al 1986; Fenyo et al. 1990). This is a process not only of interest in biochemistry but is also of interest for the proposed mission to Europa (Johnson et al. 2009) and to desorption processes in the interstellar medium (Johnson et al. 1991a).

### 17.4.1 Yield

The form used in Eq. 17.1 for knock-on sputtering is also used to fit experimental data for electronic sputtering in Fig. 17.3a, b

$$Y_e \sim c [1 f(dE/dx)_e/U]^p \quad (17.3)$$

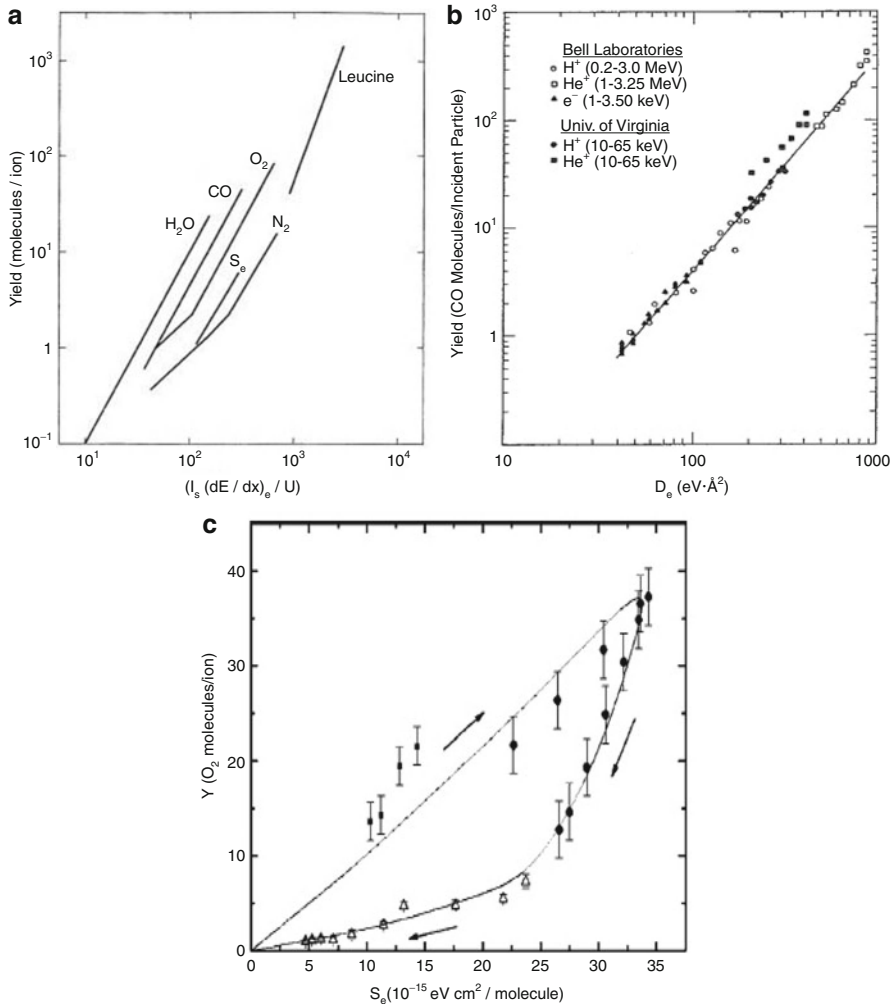


**Fig. 17.3** (a) Sputtering yield vs.  $[(I/U)(dE/dx)_e]$ , as in Eq. 17.3, for ion  $v > 2 \times 10^8$  cm/s (the Bohr velocity) showing the  $\sim$  quadratic dependence at large  $(dE/dx)_e$  for all ices but and the differences at small  $(dE/dx)_e$  (From Johnson (1990)); (b) sputtering yield of CO ice vs.  $D_e$  (i.e.,  $(dE/dx)_e$  evaluated in the near region) both at high and low speeds (filled symbols) indicating an increase in efficiency,  $f$ , in the conversion of deposited energy into molecular motion at low ion speeds (From Chrisey et al. (1990)). Similar results occur for water ice (see [www.people.virginia.edu/~rej](http://www.people.virginia.edu/~rej) for data summary); (c) electronic sputtering of solid  $O_2$  vs.  $S_e$  ( $= (dE/dx)_e n$ ): arrows indicate direction of increasing incident ion speed,  $v$ ; shows  $\sim$  linear in  $Y$  for  $O_2$  at high  $v$  & low  $S_e$ , as in (a), giving way to  $\sim$  quadratic dependence with decreasing  $v$ , and the significant enhancement in  $Y$  for this solid at the lowest  $v$  for the same value of  $S_e$  (From Fama et al. (2007))

Whereas knock-on collisions directly produce recoil motion in a solid, the electronic energy deposition does so only indirectly. Therefore, in Eq. 17.3 [ $f_e(dE/dx)_e$ ] replaces  $(dE/dx)_n$  with  $f_e$  indicating the fraction of the deposited electronic energy that is actually converted into sufficient translational motion of the molecules to produce sputtering (e.g., Johnson and Schou 1993). When an individual excitation can lead to ejection of a surface atom or a molecule, then the electronic sputtering process at low  $(dE/dx)_e$  is directly related to photon-stimulated desorption, so that  $p \sim 1$ . For large  $(dE/dx)_e$ , experiment shows that  $p > 1$ , since interactions between excited and ionized molecules occur and the energy transport is nonlinear as discussed above for knock-on collisions at high  $(dE/dx)_n$ . In this regime a nearly quadratic dependence ( $p \sim 2$ ; e.g. Fig. 17.3) is typically found with some exceptions (Johnson and Sundqvist 1992).

Therefore, the general picture resembles that discussed for knock-on sputtering, but the new problem in electronic sputtering is the efficiency of conversion of electronic excitation and ionization energy into molecular motion (Johnson and Schou 1993). In the molecular ices, which are of interest here, about half of the energy deposited by a light, fast ion [low  $(dE/dx)_e$ ] goes into the production of electron–hole pairs, and the other half into electronic and vibrational excitation of the molecules (Johnson and Schou 1993; Johnson 1990). Whereas collisions with neighbor's quench the excitations rapidly, heating the material, the recombination of the electrons with the holes can lead to reactions that release considerable kinetic energy. Although the analysis in terms of the physical and chemical processes has been discussed at length, in practice the ratio  $(f/U)$  in Eq. 17.3 is determined empirically by fitting yield data using tabulated values of  $(dE/dx)_e$ . In addition, since  $(dE/dx)_e$  is a bulk property there are surface corrections due to the anisotropy of the secondary electron production. These for the most part have been ignored, but Chrisey and Brown (1989) roughly accounted for this effect in compiling the data for sputtering of solid CO in Fig. 17.3b.

In the other extreme, a highly ionizing particle [large  $(dE/dx)_e$ ] produces a roughly cylindrical transient, high-temperature plasma around its path through the solid. This region, called the track core, has a radius of the order of nanometers that increases with increasing ion velocity. Although sputtering has proved to be one of the more useful probes of the transient energy density in the track core (Johnson and Sundqvist 1992; Johnson et al 1989), the evolution of this excited region is debated (e.g., Bringa and Johnson 2002). The energetic secondary electrons emitted radially from the track core produce a much larger region of lower excitation density of critical importance in radiation damage to biomolecules and organics. Although the data below suggest the opposite, some groups have assumed the heating of the lattice by the secondary electrons is responsible for large ion sputtering yields (e.g., Mookerjee et al. 2008).

For incident fast light ions, the yields for N<sub>2</sub> and O<sub>2</sub> were found to exhibit a linear dependence on  $(dE/dx)_e$  ( $p \sim 1$ ; Johnson and Pospieszalska 1991) at low  $(dE/dx)_e$  as seen in Fig. 17.3a. This indicates that individual excitation or ionization events *can* lead to molecular ejection in these two solids (Johnson et al. 1991b). The existence of a regime linear in  $(dE/dx)_e$  is consistent with single photon and

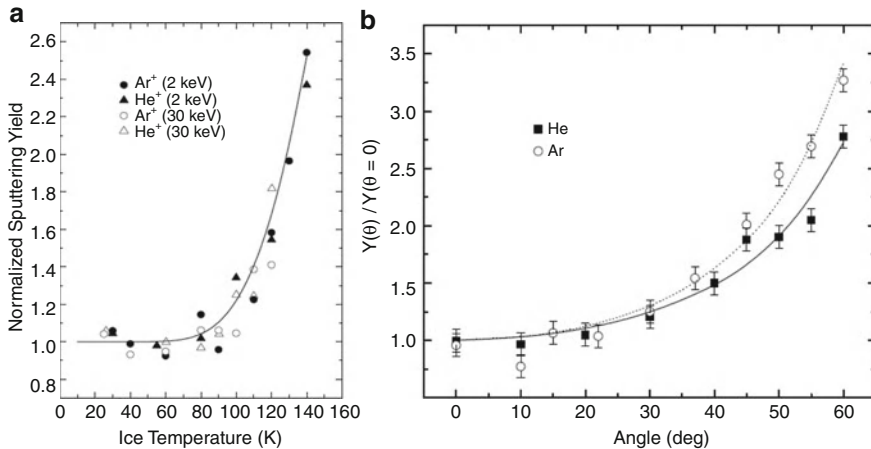


**Fig. 17.4** (a) Temperature dependence of the yield for water ice varying from the knock-on regime being totally dominant (2 keV Ar<sup>+</sup>) to the electronic regimes being dominant (30 keV He<sup>+</sup>): the curve is a fit of the form  $[1 + A \exp(-E_a/T)]$  with  $A = 220$  and  $E_a = 0.06$  eV; (b) similar comparison for the incident angle dependence of the yield:  $1/\cos^{0.45x}$  with  $x \sim 0.45$  (solid) and 0.78 (dotted) (From Fama et al. (2008), as compared to a theoretical value  $\sim 0.66$ : see also Johnson (1989); Bringa and Johnson (2001))

electron induced desorption of from these solids (e.g., Öberg et al. 2009a). In contrast to N<sub>2</sub> and O<sub>2</sub>, the yield from low-temperature S<sub>8</sub> varies steeply at low  $(dE/dx)_e$  (Torrisi et al. 1988) and CH<sub>4</sub> is rapidly converted to a refractory as discussed below. However, for low temperature H<sub>2</sub>O, SO<sub>2</sub> and CO the yields are found to be roughly quadratic down to the lowest  $(dE/dx)_e$  in Fig. 17.3a. In such frozen solids, molecular ejection appears to be dominated by processes involving more than one excitation/ ionization event that is close in space and/or time. Desorption from low temperature H<sub>2</sub>O ice *can be* produced by individual deep excitation events, but with very small cross sections: e.g., absorption of energetic photons (Heide 1984). In addition, H<sub>2</sub> is ejected in single events for the hydrogen containing molecular solids (e.g., CH<sub>4</sub>, NH<sub>3</sub>, H<sub>2</sub>O, and organics). However, desorption of the principal species (e.g., H<sub>2</sub>O from water ice) by fast ions or electrons is dominated by multiple excitation/ ionization events. This can occur by multiple excitations in the track of an individual ions or the relaxation of deep excitations by x-rays resulting in excited neighbors. However, what appears to be dominating in many instances is the fact that the erosion rates also exhibit a fluence and temperature dependence, indicative of ‘late’ ejection processes associated with the chemistry induced in these molecular solids. Therefore, not surprisingly, the component of the yield that is *temperature dependent* is similar to that discussed for knock-on sputtering as seen in Fig. 17.4a. In addition, if the incident ions penetrate sufficiently, knock-on and electronic sputtering exhibit similar incident angle dependences, as seen in Fig. 17.4b.

Two principal models have been used to describe the approximately quadratic sputtering regime. When the density of energy deposited along the ion's path remains sufficiently high for a long enough time, it has been suggested that the lattice is 'heated' leading to transient sublimation, so-called 'thermal spike' sputtering (Johnson 1989; Trautman et al. 1993). But this model cannot account for the observed non-thermal energy spectra. However, the closely spaced excitations and ionization enlarge the electron cloud along the incident ion's track resulting in a transient repulsive force caused by the *reduced screening* of the positive charges. The net force is sufficient to energize the molecules in a solid, a process often referred loosely to as a 'coulomb explosion' though a screened coulomb interaction is more accurate (Bringa and Johnson 2002). Such a model has also been used to describe ion track production in materials (Fleischer et al. 1975) a bulk manifestation of electronic sputtering. Tracks produced by solar flare ions are used to determine exposure ages for collected lunar grains (e.g., Heiken et al. 1991) and for interplanetary grains ejected from comets and collected in the earth's upper atmosphere (Bradley 1994). Molecular dynamics simulations have shown that a hybrid model describes the data (Bringa and Johnson 2000, 2002); that is, the high excitation density in track core produces a strong radial and outward mutual repulsion, which in turn energizes ('heats') an extended radial region. This gives the appropriate yield, energy spectra and incident angle dependence.

Although ejection mechanisms continue to be debated, as seen in Fig. 17.3,  $p$  in Eq. 17.2 is  $\sim 2$  above some excitation density, whereas the yields at low excitation density can differ significantly. In the quadratic ( $p \sim 2$ ) regime, whole molecules dominate the ejecta and  $f \sim 0.15\text{--}0.2$ , which is roughly the ratio of the exothermic energy release when electrons recombine with ions to the average energy required to produce and ionization in the solid, the so-called  $W$  value (Johnson and Brown 1982). Noting that  $(dE/dx)_e$  goes through a maximum in Fig. 17.2a, higher yields are found for the lower velocity ions at the same  $(dE/dx)_e$ . This is shown for the sputtering of CO plotted vs. the near surface value of  $(dE/dx)_e$  called  $D_e$  in Fig. 17.3b. The enhancement at low  $v$  occurs because the secondary electrons *do not* remove the energy from the track core, so the radial distribution of the energy deposited is narrower, hence, the energy density in the track core is higher for the same  $(dE/dx)_e$ . Therefore, the conversion of the deposited energy to molecular ejection is more efficient: i.e.,  $f$  increases to  $\sim 0.4$  at the lower  $v$  ice (Johnson and Brown 1982). The  $v$  dependence is also seen in the sputtering yield of solid oxygen bombarded with protons in Fig. 17.3c (Famá et al. 2007). For solid  $O_2$ , the dependence at high  $v$  is linear in  $S_e [= (dE/dx)/n]$  that gives way to the standard quadratic dependence for all ices, as seen in Fig. 17.3a. With decreasing  $v$  the yield goes through a maximum, as in Fig. 17.3b, exhibiting enhanced sputtering at low ion velocities. For solid  $O_2$  surface ionization produced by electron capture from the ice to the projectile can also enhance the yield at the very lowest  $v$  in Fig. 17.3c.

The excitations and ionizations produced can relax by a repulsive interaction with a neighbor or, as in a planetary atmosphere, by dissociative recombination:  $N_2^+ + e \rightarrow N + N$  releasing kinetic energy (e.g., Johnson and Schou 1993). Of course, all of the excitation energy eventually decays primarily to heat with

smaller fractions in ices to sputtering, defect formation, secondary electron emission, and luminescence. The dissociated radicals, N, produced in frozen nitrogen will preferentially be trapped in the solid due to its strong bonding. In pure nitrogen it will eventually react with another N to form N<sub>2</sub> releasing additional energy. Although these effects all lead to molecular motion, the prompt effects, such as the repulsive interactions produced by closely spaced excited molecules or following dissociative recombination have been suggested to dominate. Depending on the size of the cohesive energy, U, such processes either individually or in concert lead to the ejection of molecules from the surface.

Not surprisingly, the greatest progress in describing the sequence of events following the production of a track of excitations has been made for rare-gas solids. For such solids the relation of sputtering by ions, electrons, and photons, to secondary electron ejection and to luminescence, is roughly understood at the atomic level (e.g., Johnson and Schou 1993). For the molecular ices, which are of interest here, chemistry adds an additional level of complexity, so that a molecular level understanding of sputtering is only gradually emerging. A convenient form for the yields from the frozen solids discussed here is a sum of the low ( $dE/dx$ )<sub>e</sub> dependence, which can differ enormously between ices, plus the quadratic dependence at higher ( $dE/dx$ )<sub>e</sub>, with an incident angle dependence  $\sim 1/\cos\theta_i^{1+x}$ , as seen for ice in Fig. 17.4b. The electronic regime, for many relevant ices, unlike the nuclear regime, is typical dominated by the quadratic dependence.

### 17.4.2 Ejecta Energies and Angles

Haring et al. (e.g., 1984c; Pedrys et al. 2000) first showed that the energy distributions for the ejecta from a molecular ice at  $\sim 16$ K were not only similar in the knock-on and electronic regimes, but had a  $\sim 1/E^2$  tail at high E (Fig. 17.5). The high energy tail was predicted for knock-on collisions and subsequently shown to also occur for energy cascades initiated by electronic energy release (Johnson and Liu 1996). These spectra appeared to exhibit maxima, but at energies much less than U. In Fig. 17.5, this behavior is seen for solid CO and for dissociation products, such as N<sub>2</sub> from NH<sub>3</sub>, consistent the product being transiently trapped in the ice and then driven out by a subsequent ion. By contrast they also showed that energy spectra for the H<sub>2</sub> product, which has a very low cohesive energy in NH<sub>3</sub>, had two components: a high ejecta energy tail and a clear thermal component. The latter is associated with H<sub>2</sub> diffusion out of the solid following the decay of the transient energy density deposited by the incident ion. The H<sub>2</sub> could be newly formed or formed by a previous incident particle but remained trapped. A similar energy spectra was bound for H<sub>2</sub> from ice (Brown et al. 1984) and for the formation and loss of O<sub>2</sub> from ice (e.g., Teolis et al 2005), although the ‘thermal’ component is not as obvious in the O<sub>2</sub> energy spectra as it is for H<sub>2</sub>.

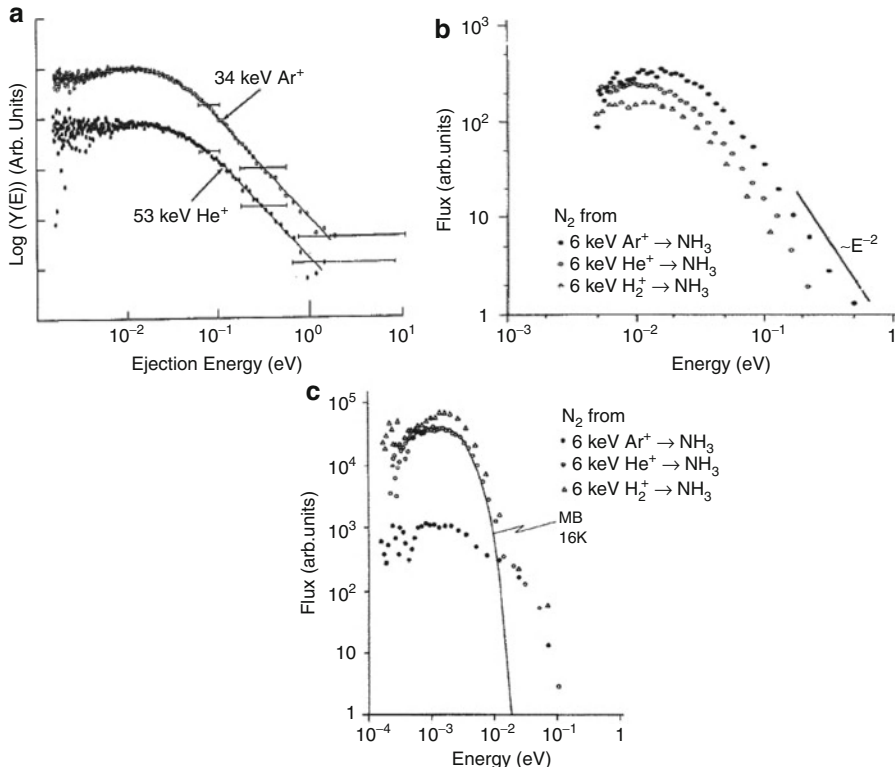


**Fig. 17.5** (a) Ejecta energy spectra vs. ejection energy  $E$ : (a) CO from a CO solid by 53 keV  $\text{He}^+$  and 34 keV  $\text{Ar}^+$  with respective bulk  $S_n/S_e$  to ratios of  $\sim 0.02$  and  $\sim 2$ ;  $T \sim 10\text{--}20\text{ K}$ . Even though the knock-on and electronic contributions differ, both spectra show similar structure and energetic tails that decay as  $\sim E^{-2}$ . Subtle peaks, well below the sublimation energy are seen (From Chrisey and Brown (1989)). (b)  $\text{N}_2$  ejected from  $\text{NH}_3$  at  $\sim 15\text{--}20\text{ K}$  after a steady state fluence; spectra similar to those in (a) even for this newly formed species consistent with the  $\text{N}_2$  being formed, trapped and subsequently ejected (Haring et al. 1984c). Similar trapping is seen for  $\text{O}_2$  formed in ice (Teolis et al 2005). (c) The ejection of  $\text{H}_2$  from  $\text{NH}_3$  clearly indicating a thermal component likely diffusing out of the solid (Haring et al. 1984c). Therefore, the volatility & the trapping of the newly formed species at a given  $T$  is important

## 17.5 Chemical/Reactive Sputtering

Chemical reactions are induced in molecular ices by both the electronic and collision energy deposited. Although reactions can occur among the transiently excited species, the chemical changes produced in molecular ices appear to be dominated by reactions that occur among radicals *after* the initial dissipation of the energy. Such reactions can also lead to erosion (sputtering) of molecular ices, consistent with the temperature dependence of the yields. These affect the yield either directly, by the exothermic energy release, or by compositional changes affecting the cohesive energy of the solid.

The term ‘chemical sputtering’ has been used for the sputtering of refractory materials by protons and other ions that react following their interaction with or implantation into a solid’s surface (Roth 1983). For example, although low doses of protons sputter refractory materials inefficiently, the implanted H can react with the matrix material. Therefore, with increasing proton dose new more volatile species, such as H<sub>2</sub> and H<sub>2</sub>O, are ejected from silicates. Similarly, O<sup>+</sup> and H<sup>+</sup> incident on graphite produces CO and CH<sub>4</sub>. It also has been used to describe the ion bombardment of a surface in an ambient gas producing enhanced surface etching.

For low-temperature ices and organic materials in the outer solar system, all incident electrons and ions leave a trail of broken bonds and trapped radicals as discussed above. When the local temperature is transiently increased, as in a thermal spike, or the density of radicals is increased, reactions can be initiated. Brown et al. (1980a, b) found the sputtering yield of water ice by several-MeV He<sup>++</sup>, He<sup>+</sup> and H<sup>+</sup> increased with increasing ambient temperature beyond 80–100 K, as seen in the data in Fig. 17.4a. From the mass spectra of the ejecta, this increase in the yield appeared to correlate with increased emission of H<sub>2</sub> and O<sub>2</sub> (e.g., Brown et al. 1982; Johnson et al. 2005). Such very volatile molecules, not initially present in the ice, must be formed and then they either diffuse out or are subsequently removed by sputtering (e.g., Reimann et al. 1984; Teolis et al. 2005, 2009) as discussed above. The temperature dependence in Fig. 17.4a suggests that processes with very low activation energies control the formation and ejection of these new species (e.g., Johnson 2011).

Although other radiation products are formed, H<sub>2</sub> and O<sub>2</sub>, which have very low binding energies in ice, are readily ejected. More refractory radiolytic products known to be present spectroscopically, such as OH, H<sub>2</sub>O<sub>2</sub>, and HO<sub>2</sub>, do not appear to contribute significantly to yield. Although the mass spectra suggest N<sub>2</sub>H<sub>4</sub> forms in NH<sub>3</sub> ice, the principal ejecta are H<sub>2</sub> and N<sub>2</sub>, and for CO<sub>2</sub> ice they are CO and O<sub>2</sub> in addition to the parent molecules NH<sub>3</sub> and CO<sub>2</sub> (e.g., see Table 17.1). For methane, after an initial transient (Lanzerotti et al. 1987) primarily H<sub>2</sub> is seen. Since hydrogen loss results in cross linking between carbon atoms, species less volatile than methane are formed. Therefore, with increasing irradiation time (fluence), cross linking efficiently converts this volatile solid into a refractory hydrocarbon. Organics and hydrocarbon are also covert to more refractory material due to loss of hydrogen. H<sub>2</sub>S is similarly converted to a sulfur polymer and irradiated carbon and sulfur oxides leave refractory residues. Radiation-induced processing appears to be occurring in many region of space (Carlson et al. 2009): it may account for the dark poles on Io and bright poles on Ganymede (e.g., Johnson 1997), as well as the UV reflectance spectra of Callisto (e.g., Hendrix and Johnson 2008). These effects are discussed in detail in other chapters; here we are interested in their effect on the erosion rates of these solids.

Radiation induced chemistry also affects the UV photon-induced erosion of water ice (Westley et al. 1995a, b). Although energetic photons that produce deep excitations in ice *can* cause desorption on photon by photon basis (Heide 1984), at low temperatures (<80 K) individual Lyman-alpha photons do not appear to directly desorb individual water molecules. However, after an incubation dose, a sufficient radical density accumulates creating new relaxation pathways and more

volatile species. For the ice *so-altered*, the subsequent irradiation leads to H<sub>2</sub>O ejection on a photon-by-photon basis. The incubation dose for this to occur is also temperature dependent. This picture has recently been disputed by Oberg et al. (2009b), but their experimental conditions might not have been ideal. In addition, consistent with recent molecular dynamics modeling (Andersson and van Dishoeck 2008; Arasa et al. 2010), Hama et al. (2010) showed that water molecules are directly desorbed, which they suggested confirmed the Oberg et al. (2009b) results. However, the models do not account for excitation quenching by and/or transfer to neighbors and the absolute yields were not well quantified, so the inefficient production of H<sub>2</sub>O at low UV fluences with the yield being eventually dominated by chemical effects is still our favored model. However, excitations of water molecules in a fluffy, under dense ice having incompletely bound surface molecules clearly can result in prompt H<sub>2</sub>O desorption by single UV photons.

## 17.6 Ice Mixtures and Impurities in Ice

Sputtering in the outer solar system and in the interstellar medium typically occurs from surfaces composed of mixed ices or ices containing impurities. This is the case for the surfaces of satellites, comets, Kuiper Belt Objects, and Oort cloud bodies. The bombardment can also disrupt small grains (Bringa and Johnson 2003) and produce chemical changes, as discussed above and as shown for example in Fig. 17.6 for H<sub>2</sub>O:CO<sub>2</sub> mixture. Consistent with what occurs in a pure molecular ice, both more volatile (here CO) and less volatile (H<sub>2</sub>CO<sub>3</sub>) species are created affecting the sputtering yield (erosion rate) of the surface. Sputtering related phenomena include the population of tenuous atmospheres by the more volatile

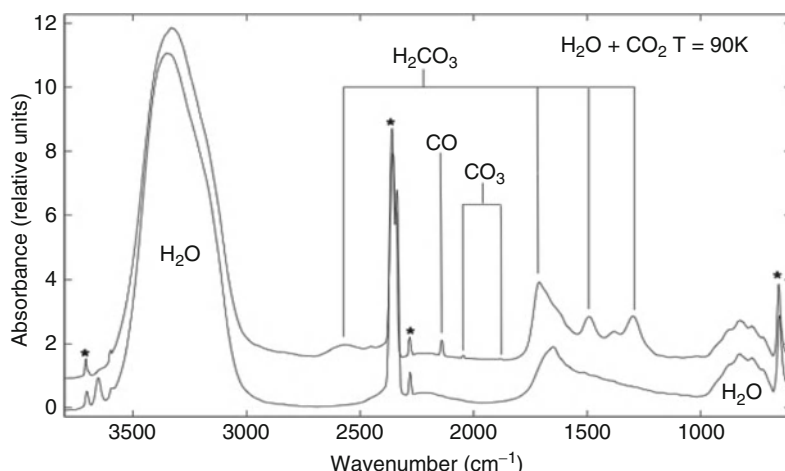


**Fig. 17.6** Electron radiolysis of CO<sub>2</sub> + H<sub>2</sub>O ices at 90 K. The film was deposited at 50 K and then warmed to 90 K. The *bottom* spectrum shows the ice before irradiation; the *upper* spectrum shows the ice after irradiation. Primary products are CO<sub>2</sub>, CO, and H<sub>2</sub>CO<sub>3</sub>, (From Hand et al. (2007))

species produced and ejected, as observed on Jupiter's satellites, as well as the redistribution of materials over their surfaces and even among these satellites (Cassidy et al. 2010). Sputtering of such surfaces has been proposed as a means to investigate their composition through observations of the gas-phase species produced, either from remotely sensed emissions or by direct sampling from by spacecraft (Johnson et al. 1998). Therefore, it is important to establish the relationship between the surface composition and the gas-phase ejecta. The radiolysis and radiation chemistry of planetary and interstellar ice analogs has been extensively studied, but only a small fraction of that work is on sputtering of multi-component ices. When ices are co-deposited, in space or prior to carrying out a laboratory experiment, it is often not clear, unless the ice is directly monitored, how much segregation occurs on deposition or following irradiation (e.g., Oberg et al. 2009c).

Measurements of the sputtered neutrals using mass spectroscopy (SNMS) were performed by de Vries (1984a, b), Haring et al. 1983, 1984a, b) for mixed NH<sub>3</sub>:CO and H<sub>2</sub>O:CO ices. Irradiation of isotopically labeled CO<sub>2</sub>:H<sub>2</sub>O ices was suggested to produce formaldehyde, CH<sub>2</sub>O, as a sputter product (Pirronello et al. 1982, 1984). Later, Farenzena et al. (2005) and Ponciano et al. (2005) investigated CO<sub>2</sub>:H<sub>2</sub>O ices by measuring positive and negative sputtered ions using mass spectroscopy (SIMS). Loeffler et al. (2006) recently investigated NH<sub>3</sub> + H<sub>2</sub>O ices.

Sputtering in mixed ices is expected to be different than in the pure component end-members, having different chemistry, yields, and energy distributions of the products. This, of course, can depend upon the whether the sputtering is predominantly collisional or electronic. In addition, the ejection efficiency of trace species embedded in an ice matrix, such as alkalis in the surface of Europa, can depend on the size of the sputtering yield. Although the sodium atom is likely present as a strongly-bound hydrate in the ice matrix, it is readily removed from the surface as a neutral even by relatively low ( $dE/dx$ )<sub>e</sub> radiations (Johnson et al. 2002), similar to what was observed for ejection of Na from a mineral (Madey et al. 1998, 2002). When this is the case, the changing surface concentration, discussed below, and replenishment become issues, issues that we describe for one case in the next section. However, when the sputtering yields are large, then trace species can be carried off with the significant volume of ejected matrix (Cassidy et al. 2009). Such a model appears to be consistent with models for the observation of Na at Europa (Cipriani et al. 2008; Leblanc et al. 2005). Cassidy et al. (2010) used this assumption to describe the sputter-produced gas-phase density and redistribution of SO<sub>2</sub> at Europa. Because of the importance of this process, a recent laboratory study of the sputtering of SO<sub>2</sub> in ice is described below as a model for mixed ices.

### 17.6.1 *Sputtering of a Mixed Ice: Knock-on Regime*

When a heavy ion is incident on an SO<sub>2</sub>:D<sub>2</sub>O ice mixture the knock-on (collisional) sputtering products will include the parent molecules and, depending on the amount of dissociation produced, new radiolytic products. In SO<sub>2</sub>:D<sub>2</sub>O sputtering by 5-keV

argon ions, which we describe in this section, the major products were seen to be SO<sub>2</sub> and D<sub>2</sub>O, with few or no radiolytic products or hydrates (mSO<sub>2</sub> • nD<sub>2</sub>O). This observation is consistent with collision cascade sputtering particularly when the volume of material ejected is significant. Electronic sputtering by fast ions is expected to produce radiolytic products much more efficiently as discussed shortly.

In the absence of new product formation in a two component material a simple expression for the sputtering yield is available: e.g., (Sigmund 1981; Johnson 1990, 1998). The yields ( $Y_A$ ,  $Y_B$ ) for the components of a mixed material A:B can be thought of as proportional to the number fractions ( $c_A$ ,  $c_B$ ) and inversely proportional to the molecules' effective binding energies ( $U_A$ ,  $U_B$ ) as in Eqs. 17.1 and 17.3 above:

$$Y_A \propto c_A/U_A \text{ and } Y_B \propto c_B/U_B. \quad (17.4)$$

Based on our discussion for pure ices above, the effective binding energies obtained from fits to the energy spectra are strictly empirical and their relationship to the actual surface binding energy is not well understood. However, from Eq. 17.4 it is seen that the molecule with the smaller binding energy (higher volatility, which we will denote as A) will be preferentially sputtered, depleting the surface concentration of A and enhancing that of the less volatile molecule B (e.g., Lanzerotti et al. 1984). As the irradiation time increases, the surface concentration and, hence, the yields, will evolve with time as shown in Fig. 17.7. After a significant irradiation time, the steady state surface number fractions ( $c'_A$ ,  $c'_B$ ) are such that the yields ( $Y'_A$ ,  $Y'_B$ ) have, roughly, the same proportions as the bulk concentration:

$$Y'_A/Y'_B = \frac{(c'_A/U_A)}{(c'_B/U_B)} = (c_A/c_B) \quad (17.5)$$

a fact suggested as useful for analysis of space data (Johnson and Sittler 1990). Assuming that  $U_A$  and  $U_B$  are constant, we can experimentally determine the ratios  $c'_A/c_A$  and  $c'_B/c_B$  from the mass spectrometer signals in Fig. 17.7, and then use those results to derive the ratio of effective binding energies for the species in the mixed ice:

$$U_A/U_B = \frac{(c'_A/c_A)}{(c'_B/c_B)} \quad (17.6)$$

For sputtering of a SO<sub>2</sub>:D<sub>2</sub>O film at a nominal bulk concentration of 1:3, we use the data in Fig. 17.7 and find  $U_{\text{SO}_2}/U_{\text{D}_2\text{O}} = 0.15$ . While these energies probably differ from the binding energies of the pure components, it is interesting to compare their ratio to the corresponding yield ratios of the pure ices. Argon ion sputtering of pure H<sub>2</sub>O (assumed to be sputtered like D<sub>2</sub>O) at low temperatures and in the collision cascade regime (30 keV incident energy) exhibits a yield of ~25 molecules/ion (Baragiola et al. 2003), while SO<sub>2</sub> at the same conditions sputters at a rate of ~180 molecules/ion (Boring et al. 1984a). From these yields, the inferred ratio of the

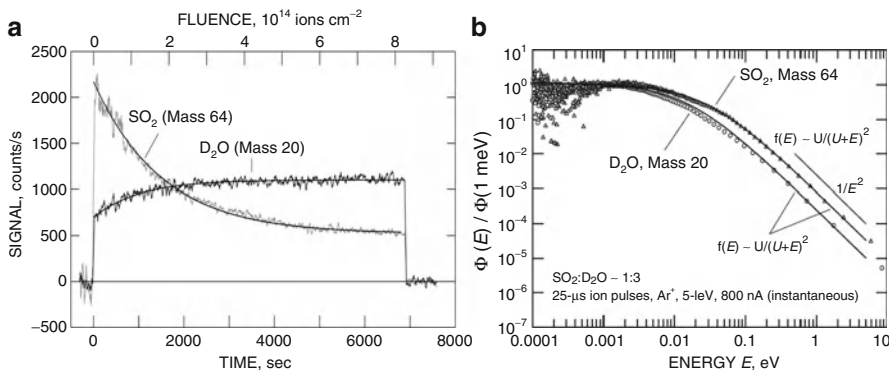


**Fig. 17.7** (a) Time (fluence) profile for sputtering of a pristine SO<sub>2</sub>:D<sub>2</sub>O sample. SO<sub>2</sub> is preferentially sputtered at the beginning, resulting in a surface concentration that eventually *sputters* with a yield ratio equal to the bulk concentration. Sample was deposited on a 50 K aluminum surface using a nominal 1:3 SO<sub>2</sub>:D<sub>2</sub>O composition and irradiated with 50-μs pulses of 5-keV Ar<sup>+</sup> at 60 Hz. The instantaneous current was 800 nA. A gated quadrupole mass spectrometer (Hidden IDP) with low voltage (45 eV) electron ionization detects the ms-wide pulse of ejected neutral molecules and the background which is subtracted. Irradiation started at t = 0 and stopped at t ~ 6,900 s. Exponential fits are for initial and equilibrium values of 2,170 and 520 counts s<sup>-1</sup> for SO<sub>2</sub> and 700 and 1,100 counts s<sup>-1</sup> for D<sub>2</sub>O. (b) Energy profile of sputtered SO<sub>2</sub> (*triangles*) and D<sub>2</sub>O (*circles*), normalized at 1 meV. Irradiation described in (a) but with 25-μs pulses, counts accumulated in a 1,600-channel multi-channel scalar using 10-μs bins. Velocity is determined using the path length between the sample and mass spectrometer's ionizer (7.57 cm) and by accounting for the flight times through the quadrupole. The fits shown for SO<sub>2</sub> (*upper curve*) and D<sub>2</sub>O (*lower curve*) use the expression in Eq. 17.2b which is consistent with a break down in the planar binding

effective binding energies of SO<sub>2</sub> and D<sub>2</sub>O for pure materials 0.14, compared our measured value of to 0.15 for SO<sub>2</sub> in D<sub>2</sub>O. Although this is consistent with the simple model, we note that the binding of SO<sub>2</sub> in an H<sub>2</sub>O matrix is likely to be somewhat larger than it is in a SO<sub>2</sub> matrix, consistent, for instance, with tendency for SO<sub>2</sub> to form hydrates (Schriver et al. 1988; Schriver-Mazzuoli et al. 2003). For comparison, the chemical binding energy ratio of SO<sub>2</sub> and H<sub>2</sub>O from Table 17.1 is 0.62, another indication that the effective “binding energy” used in sputtering theory has little to do with the classically defined chemical binding energy.

It is also seen in Fig. 17.7a that the fluence needed to reach equilibrium surface concentrations is about 2 × 10<sup>14</sup> ions cm<sup>-2</sup> consistent with ~one incident ion for ~five times the unit area subtended on the surface by the molecules (~10<sup>-15</sup> cm<sup>2</sup>). For the average concentrations during this period the total yield is about 15 molecules/ion, so about 3 × 10<sup>15</sup> molecules cm<sup>-2</sup> are sputtered away, amounting to about three monolayers.

The energy profiles (normalized at 1 meV) for the two major ejected species, SO<sub>2</sub> and D<sub>2</sub>O, are shown in Fig. 17.7b. Both exhibit the expected 1/E<sup>2</sup> dependence at the higher ejecta energies. Since there is no clear maximum, we use the form in

Eq. 17.2b for which the planar surface binding has broken down. The characteristic energies (and velocities) for D<sub>2</sub>O and SO<sub>2</sub> are 15 meV ( $3.9 \times 10^4$  cm s<sup>-1</sup>) and 28 meV ( $2.9 \times 10^4$  cm s<sup>-1</sup>), respectively. As discussed for pure substances, these energies are much smaller than the sublimations energies and the energy ratio is very different from the ratio discussed above.

### 17.6.2 Sputtering of a Mixed Ice: Electronic Excitation

Although a number of authors, beginning with Haring et al. (1984a, b, c), have studied the *ejecta* from a mixed ice in the electronic regime, there is no analysis of the type described above. Considerable effort has been spent on the chemical alterations as discussed in other chapters. Haring, Pedrys, deVries and coworkers considered the ejecta from a number of mixtures in *both* the predominantly knock-on (incident keV Ar<sup>+</sup>) and predominantly electronic regimes (incident H<sub>2</sub><sup>+</sup> and He<sup>+</sup>) as seen in Table 17.2. They found the differences between the regimes were not major. In all cases, in addition to initial molecules present, the ejecta included the most volatile radiolytic products: e.g., O<sub>2</sub>, N<sub>2</sub>, H<sub>2</sub>, CO etc. They also showed that the energy spectra are similar in form to those described above for both the principal species and the products. Moore and Khanna (1990) irradiated H<sub>2</sub>O + CO<sub>2</sub> ice mixtures which were thought to form formaldehyde (Pirronello et al. 1982) but found carbonic acid. Loeffler et al. (2006) irradiated a 2:1 (H<sub>2</sub>O: NH<sub>3</sub>) mixture at 80 K with 100 keV protons and found a peak sputtering yield  $\sim$ 110 molecules/ion (assuming mass = 17 amu) at a fluence of  $\sim$ 3  $\times$  10<sup>15</sup> ions/cm<sup>2</sup>, with the yield first increasing and then decreasing with ion dose. This fluence dependence is related to the formation new species, H<sub>2</sub> and N<sub>2</sub>, in the ice matrix and the concomitant destruction of NH<sub>3</sub>, as expected from the sputtering of pure samples. However, unlike the sputtering of ammonia ice, the ejecta from the ammonia-water sample in the electronic regime appeared to contain very little NH<sub>3</sub>. Similarly, irradiation of ice mixtures with carbon containing frozen gases, again results in the formation of volatile products (H<sub>2</sub>, O<sub>2</sub>, CO) results with the refractory residues forming more efficiently in the electronic vs. the knock-on regime (e.g., see summary in Cassidy et al. 2010). The dearth of useful data on the efficiencies of the production of gas-phase products from ice mixtures is striking and needs to be addressed.

## 17.7 Summary

Following the realization that icy objects in the outer solar system are exposed to relatively intense fluxes of ions and electrons, a large number of laboratory measurements were carried out on the sputtering/ desorption of ices. Such measurements have shown that the sputtering rates can be large and that, in addition to ejection by knock-on collisions, sputtering is produced by the electronic energy

**Table 17.2** Summary of measurements of sputtering/desorption yields for pure ices and ice mixtures

Ice	Measurements for <i>sputtering/desorption</i> by ions, electrons and UV
H <sub>2</sub> O, D <sub>2</sub> O	Akin et al. (2009); Ayotte et al. (2001); Bar Nun et al. (1985); Benit et al. (1987); Benit and Brown (1990); Boring et al. (1984a, b); Brown et al. (1978), (1980a, b, 1982, 1984); Chrisey et al. (1986); Christensen et al. (1986); Cooper and Tombrello (1984); de Vries et al. (1984a); Fama et al. (2008); Grieves and Orlando (2005); Haring et al. (1983, 1984a, b, c); Oberg et al. (2009b); Orlando and Sieger (2003); Pedrys et al. (2000); Petrik and Kimmel (2003, 2004, 2005); Petrik et al. (2006a, b); Kimmel and Orlando (1995); Kimmel et al. (1994); Reimann et al. (1984); Rocard et al. (1986); Seiberling et al. (1982); Sieger et al. (1997, 1998); Shi et al. (1995a); Strazzulla et al. (1992); Teolis et al. (2005, 2006, 2009); Zheng et al. (2006a, b)
CH <sub>4</sub>	Bennett et al. (2006); Calcagno et al. (1986); de Vries et al. (1984b); He et al. (2010); Foti et al. (1987); Lanzerotti et al. (1985, 1987); Pedrys et al. (1986); Strazzulla et al. (1988)
NH <sub>3</sub>	de Vries et al. (1984a); Haring et al. (1983, 1984a, b, c), Johnson et al. (1983b); Lanzerotti et al. (1984); Zhang et al. (2008)
H <sub>2</sub> S	Boring et al. (1985)
H <sub>2</sub> , D <sub>2</sub> , HD	Erents and McCracken (1973); Pedrys et al. (1997); Schou et al. (1984, 1995, 2001); Stenum et al. (1990, 1991a, b); Thestrup et al. (1994)
O <sub>2</sub>	Balaji et al. (1995); Ellegaard et al. (1986, 1994); Fama et al. (2007); Gibbs et al. (1988); Hudel et al. (1992); Pedrys et al. (1989); Rook et al. (1985)
N <sub>2</sub>	Balaji et al. (1995); Brown et al. (1984); Ellegaard et al. (1986, 1993, 1994); Hudel et al. (1992); Oberg et al. (2009a); Pedrys et al. (1989); Rook et al. (1985); Shi et al. (1995b); Stenum et al. (1991b)
CO	Balaji et al. (1995); Brown et al. (1984, 1986); Chrisey et al. (1986, 1989; 1990); de Vries et al. (1984a); Haring et al. (1983, 1984a, b, c); Oberg et al. (2009a); Schou et al. (1984); Schou and Pedrys (2001); Shi et al. (1995b)
CO <sub>2</sub>	Boring et al. (1983); Brown et al. (1982); Christensen et al. (1986); Farenzena et al. (2005); Johnson et al. (1983b); Ponciano et al. (2005); Oberg et al. (2009a)
SO <sub>2</sub>	Boring et al. (1983, 1984a); Brown et al. (1982); Lanzerotti et al. (1982); LePorire et al. (1983); Melcher et al. (1982); Moore (1984)
S <sub>8</sub> (S <sub>2</sub> )	Chrisey et al. (1987, 1988a); deJonge et al. (1986); Strazzulla et al. (1987); Torrisi et al. (1988)
Na <sub>2</sub> S	Chrisey et al. (1988b)
SF <sub>6</sub>	Pedrys et al. (1984)
CO + N <sub>2</sub>	Oberg et al. (2009a)
H <sub>2</sub> O + CO	de Vries et al. (1984a); Haring et al. (1983, 1984b)
H <sub>2</sub> O + CO <sub>2</sub>	Pirronello et al. (1982, 1984); Moore and Khanna (1990); Siller et al. (2003)
NH <sub>3</sub> + CO	de Vries et al. (1984a); Haring et al. (1983, 1984a, b, c)
H <sub>2</sub> O + NH <sub>3</sub>	Loeffler et al. (2006)
D <sub>2</sub> O + SO <sub>2</sub>	This chapter

deposited by incident ions, electrons, and ultraviolet photons and the rates are affected by the radiation-induced chemistry.

There is now extensive laboratory data on the sputtering of ice by incident ions and electrons, as indicated in Table 17.2, and there are a number of summaries of this data (e.g., [www.people.virginia.edu/~rej](http://www.people.virginia.edu/~rej)). Although there still are large gaps in

our understanding, a generally agreed upon semi-empirical model is obtained as described above. The data for the yields can roughly be approximated by  $Y \sim Y_e + Y_n$ , with each component fit to the data as described following Eqs. 1 and 2. For water ice, the electronic and collision components have been combined in the form

$$Y \sim Y_e + Y_n \sim \{c_n S_n + c_{e2} S_e^2\} \{1 + A \exp(-E_a/kT)\} / \cos\theta^{1+x}$$

With  $S_{n,e} = (dE/dx)_{n,e}/n$  where  $n$  is the molecular number density. Fitting to a large amount of experimental data for *low ion velocities* ( $v \ll 2 \times 10^8 \text{ cm/s}$ ) gave  $A \sim 220$  and  $E_a \sim 0.06 \text{ eV}$  with the other parameters varying somewhat with the incident ion mass ( $m_i$ ) and nuclear charge ( $Z_i$ ):  $c_n \sim 0.033 - 0.146 c_n(m_i) \approx 0.0332 [1 + 4.9 \exp(-0.870m_i) + 1.48 \exp(-0.105m_i)] (\text{eV A}^2)^{-1}$ ,  $c_{e2} \sim (0.0005 - 0.0035)/(\text{eV}^* \text{A}^2)^2 c_{e2} \approx 0.0004939 + 0.0029613 \sin^2[2.72923(Z_i - 1)^{0.31812}] (\text{eV A}^2)^{-2}$ , and  $x \sim 0.3 - 0.78x \approx 0.3 + 0.13 \ln(m_i)$  (Fama et al. 2008; see, Johnson et al. 2008 for application to ices in Saturn's magnetosphere). A term linear in the electronic sputtering, an important contribution for O<sub>2</sub> and N<sub>2</sub> ices, was not included, since it is thought to be a very small contribution in water for most radiation environments. Of course, for x-ray flux onto ice grains in an accretion disc such a term could dominate. For a number of other icy materials an expression like that above can be a useful form for modeling. However, in modeling sputtering in a radiation environment, actual data should be used whenever possible for a particular radiation type/energy and surface sample composition.

Such models have been applied to determine the production of ambient neutrals for the Jovian (e.g., reviews: Johnson et al. 2004, 2009) and Saturnian (Johnson et al. 2008) magnetosphere by sputtering of the embedded icy moons and the grains. These sources of gas add to that supplied by direct outgassing from Enceladus and the loss of atmosphere from Io and Titan. Ionization of the ejected neutrals is then a principal source of the local plasma which in turn bombards and alters the surfaces of the moons and grains in an interesting feedback and exchange process (Burger et al. 2010). For Europa instruments are being developed to collect the sputter ejecta and the local ions as a means of determining the surface composition by an orbiting spacecraft (Carlson et al. 2009).

Based on laboratory measurements of O<sub>2</sub> production by irradiation of low-temperature ice, Johnson et al. (1982) predicted that the ice-covered moon Europa was should have an extremely tenuous O<sub>2</sub> atmosphere. This was observed using the Hubble Space Telescope (e.g., review McGrath et al. (2009)). Radiolytic ice products have since been observed on a number of the icy moons of Jupiter and Saturn appear to have, H<sub>2</sub>O<sub>2</sub>, O<sub>2</sub> and O<sub>3</sub> formed and trapped in the radiation produced defects and voids in their icy surfaces (Johnson and Jesser 1997; review Johnson 2011). Therefore, plasma bombardment, leading to implantation, chemistry and sputtering, can result in both dramatic and subtle alterations of the optical reflectance, the ambient gas and plasma environment of icy materials in space.

**Acknowledgments** REJ acknowledges support for the work at Virginia from: NASA Geology & Geophysics Program; NASA Origins Program; & NASA Planetary Atmospheres program. RWC: portions of this work were performed at the Jet Propulsion Laboratory, California Institute of Technology, under contract with NASA

## References

- Akin MC, Petrik NG, Kimmel GA (2009) Electron-stimulated reactions and O<sub>2</sub> production in methanol-covered amorphous solid water films. *J Chem Phys* 130:104710
- Anders C, Urbassek HM (2009) Cluster-induced sputtering of molecular targets. *Nucl Instrum Methods* B267:3227–3231
- Anders C, Bringa EM, Ziegenhain G, Graham GA, Hansen FJ, Park N, Teslich NE, Urbassek HM (2012) Why Nanoprojectiles Work Differently than Macroimpactors: The Role of Plastic Flow. *Phys Rev Letts.* 108:027601. <http://prl.aps.org/abstract/PRL/v108/i2/e027601>
- Andersson S, van Dishoeck EF (2008) Photodesorption of water ice: a molecular dynamics study. *Astron Astrophys* 491:907–916
- Anders C, Urbassek HM, Johnson RE (2004) Linearity and additivity in cluster-induced sputtering: a molecular-dynamics study of van-der-Waals bonded systems. *Phys Rev B70:*155404-1-4
- Arasa C, Andersson S, Cuppen HM, van Dishoeck EF, Kroes G-J (2010) Molecular dynamics simulations of the ice temperature dependence of water ice photodesorption. *J Chem Phys* 132:184510. doi:10.1063/1.3422213
- Ayotte P, Smith RS, Stevenson KP, Dohnálek Z, Kimmel GA, Kay BD (2001) Effect of porosity on the adsorption, desorption, trapping, and release of volatile gases by amorphous solid water. *J Geophys Res* 106:33387
- Bagenal F, Dowling T, McKinnon W (2004) Jupiter: the planet, satellites and magnetosphere. Cambridge University Press, Cambridge
- Balaji V, David DE, Tian R, Michl J, Urbassek HM (1995) Nuclear sputtering of condensed diatomic molecules. *J Phys Chem* 99:15565–15572
- Baragiola RA, Vidal RA, Svendsen W, Schou J, Shi M, Bahr DA, Atteberry CL (2003) Sputtering of water ice. *Nucl Instrum Methods* B209:294–303
- Bar-Nun A, Hermann AG, Rappaport ML, Mekler Y (1985) Ejection of H<sub>2</sub>O, O<sub>2</sub>, H<sub>2</sub> and H from water ice by 0.5–6 keV H<sup>+</sup> and Ne<sup>+</sup> ion bombardment. *Surf Sci* 150:143–156
- Behrisch R, Eckstein W (2007) Sputtering by particle bombardment. Springer, Berlin
- Benit J, Brown WL (1990) Sputtering of isotopically labeled H<sub>2</sub>O. *Nucl Instrum Methods* B46:448–454
- Benit J, Bibring JP, Della-Negra S, Le Beyec Y, Mendenhall M, Roccard F, Standing K (1987) Erosion of ices by ion irradiation. *Nucl Instrum Methods* B19(20):838–842
- Bennett CJ, Jamieson CS, Osamura Y, Kaiser RI (2006) Laboratory studies on the irradiation of methane in interstellar, cometary, and solar system ices. *Astrophys J* 653:792–811
- Boring JW, Nansheng Z, Chrisey DB, O'Shaughnessy DJ, Phipps JA, Johnson RE (1985) The production and sputtering of S<sub>2</sub> by keV ion bombardment. In: Rickman H et al (eds) Asteroids, comets, and meteors II. University Uppsala Press, Uppsala, pp 229–234
- Boring JW, Garrett JW, Cummings TA, Johnson RE (1984a) Sputtering of solid SO<sub>2</sub>. *Nucl Instrum Methods* B1:321–326
- Boring JW, Garrett J, Cummings TA, Johnson RE, Brown WL (1984b) Ion-induced molecular ejection from D<sub>2</sub>O ice. *Surf Sci* 147:227–240
- Boring JW, Johnson RE, Reimann CT, Garrett JW, Brown WL, Marcantonio KJ (1983) Ion-induced chemistry in condensed gas solids. *Nucl Instrum Methods* 218:707–711

- Bradley JP (1994) Chemically anomalous, preaccretionaly irradiated gains in interplanetary dust from comets. *Science* 265:925–929
- Bringa EM, Johnson RE (2003) Ion interaction with solids: astrophysical application. In: Pirronello V, Krelowaky J (eds) Solid state astrochemistry. Kluwer, Netherlands, pp 357–393
- Bringa EM, Johnson RE (2002) Coulomb explosion and thermal spikes. *Phys Rev Lett* 88:165501-1–4
- Bringa EM, Johnson RE (2001) Angular dependence of the sputtering yield from cylindrical track. *Nucl Instrum Methods* B180:99–104
- Bringa EM, Johnson RE (2000) Electronic sputtering of solid O<sub>2</sub>. *Surf Sci* 451:108–115
- Bringa EM, Johnson RE (1999) Molecular dynamics study of non-equilibrium energy transport from a Ccylindrical track: part II. Models for the sputtering yield. *Nucl Instrum Methods* 152:267–290
- Bringa EM, Johnson RE, Papaleo RM (2002) Crater formation by single ions in the electronic stopping regime: comparison of molecular dynamics simulation with experiments on organic films. *Phys Rev B* 65:094113-1–8
- Bringa EM, Johnson RE, Jakas M (1999) Molecular-dynamics simulation of electronic sputtering. *Phys Rev B* 60:15107–15116
- Brown WL, Johnson RE (1986) Sputtering of ices: a review. *Nucl Instrum Methods* B13:295–303
- Brown WL, Augustyniak WM, Marcantonio KJ, Simmons EN, Boring JW, Johnson RE, Reimann CT (1984) Electronic sputtering of low temperature molecular solids. *Nucl Instrum Methods* B1:307–314
- Brown WL, Augustyniak WM, Simmons E, Marcantonio KJ, Lanzerotti LJ, Johnson RE, Boring JW, Reimann CT, Foti G, Pirronello V (1982) Erosion and molecular formation in condensed gas films by electronic energy loss of fast ions. *Nucl Instrum Methods* 198:1–8
- Brown WL, Augustyniak WM, Brody E, Cooper B, Lanzerotti LJ, Ramirez A, Evatt E, Johnson RE (1980a) Energy dependence of the erosion of H<sub>2</sub>O ice films by H and He ions. *Nucl Instrum Methods* 170:321–325
- Brown WL, Augustyniak WM, Lanzerotti LJ, Johnson RE, Evatt R (1980b) Linear and nonlinear processes in the erosion of H<sub>2</sub>O Ice by fast light ions. *Phys Rev Lett* 45:1632–1635
- Brown WL, Lanzerotti LJ, Poate JM, Augustyniak WM (1978) “Sputtering” of ice by MeV light ions. *Phys Rev Lett* 49:1027–1030
- Burger MH, Wagner R, Jaumann R, Cassidy TA (2010) Effects of the external environment on icy satellites. *Space Sci Rev* 153:349–374
- Calcagno L, Oostra DJ, Pedrys R, Haring A, de Vries AE (1986) Erosion of methane induced by energetic electron bomdradment. *Nucl Instrum Methods* B17:22–24
- Carlson RW, Calvin WM, Dalton JB, Hansen GB, Hudson RL, Johnson RE, McCord TB, Moore MH (2009) Europa’s surface composition. In: Pappalardo R et al (eds) Chapter in Europa. University of Arizona Press, Tucson, pp 283–327
- Cassidy TA, Johnson RE (2005) Monte Carlo model of sputtering and other ejection processes within a regolith. *Icarus* 176:499–507
- Cassidy T, Coll P, Raulin F, Carlson RW, Johnson RE, Loeffler MJ, Hand KH, Baragiola RA (2010) Radiolysis and photolysis of icy satellite surfaces: experiments and theory. *Space Sci Rev* 115:299–315. doi:[10.1007/s11214-009-9625-3](https://doi.org/10.1007/s11214-009-9625-3), Chapter in Exchange Processes in the Outer Solar System
- Cassidy TA, Johnson RE, Tucker OJ (2009) Trace constituents of Europa’s atmosphere. *Icarus* 201:182–190
- Christey DB, Brown WL, Boring JW (1990) Electronic excitation of condensed CO: sputtering and chemical change. *Surf Sci* 225:130–142
- Christey DB, Brown WL (1989) Electronic excitation of condensed CO: sputtering and chemical change. *Surf Sci* 225:130–142
- Christey DB, Boring JW, Johnson RE, Phipps JA (1988a) Molecular ejection from low temperature sulfur by keV ions. *Surf Sci* 195:594–618
- Christey DB, Johnson RE, Boring JW, Phipps JA (1988b) Ejection of sodium from sodium sulfide by the sputtering of the surface of Io. *Icarus* 75:233–244

- Chrisey DB, Johnson RE, Phipps JA JA, McGrath MA, Boring WJ (1987) Sputtering of sulfur by keV ions: application to the magnetospheric plasma interaction with Io. *Icarus* 70:111–123
- Chrisey DB, Boring JW, Phipps JA, Johnson RE (1986) Sputtering of molecular gas solids by keV ions. *Nucl Instrum Methods B* 13:360–364
- Christiansen JW, Capini DD, Tsong IST (1986) Sputtering of ices by keV ions. *Nucl Instrum Methods B* 15:218–221
- Cipriani F, Leblanc F, Witasse O, Johnson RE (2008) Sodium recycling at Europa: what do we learn from the sodium cloud variability. *Geophys Res Lett* 35:L19201. doi:[10.1029/2008GL035061](https://doi.org/10.1029/2008GL035061)
- Cooper B, Tombrello TA (1984) Sputtering of water ice by MeV ions. *Radiat Eff* 80:203–209
- de Jonge R, Baller T, Tenner MG, de Vries AE, Snowden KJ (1986) Internal energy distribution of sputtered sulfur molecules. *Nucl Intrum Methods B* 17:213
- de Vries AE, Haring RA, Haring A, Klein FS, Kummel AC, Saris FW (1984a) Synthesis and sputtering of newly formed molecules by kiloelectronvolt ions. *J Phys Chem* 88:4510–4512
- de Vries AE, Haring RA, Haring A, Saris FW, Pedrys R (1984b) Emission of large hydrocarbons from frozen CH<sub>4</sub> by keV proton irradiation. *Nature* 311:39–40
- Eckstein W (2007) Sputtering yields. In: Behrisch R, Eckstein W (eds) Topics in applied physics, vol 110, Sputtering by particle Bombardment. Springer, Berlin/New York, pp 33–185
- Ellegaard O, Schou J, Stenum H, Pedrys R, Warczak B, Oostra DJ, Haring A, de Vries AE (1994) Sputtering of solid nitrogen and oxygen by keV hydrogen ions. *Surf Sci* 302:371–377
- Ellegaard O, Schou J, Sorensen H, Pedrys R, Worcyak B (1993) Sputtering of solid nitrogen by keV helium ions. *Nucl Instrum Methods B* 78:192–197
- Ellegaard O, Schou J, Sivensen H, Birgesen P (1986) Electronic sputtering of solid nitrogen and oxygen by keV electrons. *Surf Sci* 147:474–492
- Erents SK, McCracken GM (1973) Desorption of solid hydrogen by energetic protons, deuterons, and electrons. *J Appl Phys* 44:3139–3145
- Famá M, Loeffler MJ, Raut U, Baragiola RA (2010) Radiation-induced amorphization of crystalline ice. *Icarus* 207:314–319
- Famá M, Shi J, Baragiola RA (2008) Sputtering of ice by low-energy ions. *Surf Sci* 602:156–161
- Famá M, Teolis BD, Bahr DA, Baragiola RA (2007) Role of electron capture in ion-induced electronic sputtering of insulators. *Phys Rev B* 75(10), 10.1103/PhysRevB.75.100101
- Farenzena LS, Collado VM, Ponciano CR, da Silveira EF, Wien K (2005) Secondary ion emission from CO<sub>2</sub>–H<sub>2</sub>O ice irradiated by energetic heavy ions Part I. Measurement of the mass spectra. *Int J Mass Spectrom* 243:85–93
- Fenyö D, Sundqvist BUR, Karlsson BK, Johnson RE (1990) Molecular-dynamics study of electronic sputtering of large organic molecules. *Phys Rev B* 42:1895–1902
- Fleischer RL, Price PB, Walker RM (1975) Nuclear tracks in solids, Principles and applications. University of California, Berkley
- Foti G, Calcagno L, Zhou FZ, Strazzulla G (1987) Chemical evolution of frozen gases by keV ion bombardment. *Nucl Instrum Methods B* 24(25):522–525
- Gibbs K, Brown WL, Johnson RE (1988) Electronic sputtering of condensed O<sub>2</sub>. *Phys Rev B* 38:1–7
- Gnaser H (2007) Energy and angular distributions of *A* sputtered Species. In: Behrisch R, Eckstein W (eds) Topics in applied physics, vol 110, Sputtering by particle Bombardment. Springer, Berlin/New York, pp 231–323
- Grieves GA, Orlando TM (2005) The importance of pores in the electron stimulated production of D<sub>2</sub> and O<sub>2</sub> in low temperature ice. *Surf Sci* 593:180
- Hama T, Yokoyama M, Yabushita A, Kawasaki M, Andersson S, Western CM, Ashfold MNR, Dixon RN, Watanabe N (2010) A desorption mechanism of water following vacuum-ultraviolet irradiation on amorphous solid water at 90 K. *J Chem Phys* 132:164508. doi:[10.1063/1.3386577](https://doi.org/10.1063/1.3386577)
- Hand KP, Carlson RW, Chyba CF (2007) Energy, chemical disequilibrium, and geological constraints on Europa. *Astrobiology* 7:1006–1022

- Haring RA, Kolfschoten AW, de Vries AE (1984a) Chemical sputtering by keV ions. *Nucl Instrum Methods* B2:544–549
- Haring RA, Pedrys R, Oostra DJ, Haring A, deVries AE (1984b) Reactive sputtering of simple condensed gases by keV ions II: mass spectra. *Nucl Instrum Methods* B5:476–482
- Haring RA, Pedrys R, Oostra DJ, Haring A, de Vries AE (1984c) Reactive sputtering of simple condensed gases by keV ions III: kinetic energy distributions. *Nucl Instrum Methods* B5:483–488
- Haring RA, Haring A, Klein FS, Kummel AC, De Vries AE (1983) Reactive sputtering of simple condensed gases by keV heavy ion bombardment. *Nucl Instrum Methods* 211:529–533
- He J, Gao K, Vidali G, Bennett CJ, Kaiser RI (2010) Formation of molecular hydrogen from methane ice. *Astrophys J* 721:1656–1662
- Hendrix AR, Johnson RE (2008) Callisto: new insights from Galileo disk-resolved UV measurements. *Astrophys J* 687:706–713
- Heiken G, Vaniman D, French BM (1991) *Lunar sourcebook: a user's guide to the moon*. Cambridge University Press, Cambridge/New York
- Heide HG (1984) Electron microscopical results on cryoprotection of organic materials obtained with cold stages. *Ultramicroscopy* 14:271–278
- Hudel E, Steinacker E, Feulner P (1992) Kinetic energy distributions of particles desorbed from solid N<sub>2</sub>, O<sub>2</sub>, and NO by electron impact. *Surf Sci* 273:405–410
- Jakas MM, Bringa EM, Johnson RE (2002) Fluid dynamics calculation of Sputtering from a cylindrical thermal spike. *Phys Rev* B65:165425-1–9. doi:[10.1029/2002GL015855](https://doi.org/10.1029/2002GL015855)
- Johnson RE (2011) Photolysis and radiolysis of water ice. In: Khriachtchev L (ed) *Chapter in physics and chemistry at low temperatures*. World Scientific, Singapore
- Johnson RE (2004) The magnetospheric plasma-driven evolution of satellite atmospheres. *Astrophys J* 609:L99–L102
- Johnson RE (1998) Sputtering and desorption from icy surfaces. In: Schmitt B, de Bergh C (eds) *Solar system ices*. Kluwer, Dordrecht, pp 303–334
- Johnson RE (1997) Polar ‘Caps’ on Ganymede and Io revisited. *Icarus* 128:469–471
- Johnson RE (1996) Sputtering of ices in the outer solar system. *Rev Mod Phys* 68:305–312
- Johnson RE (1990) *Energetic charged-particle interactions with atmospheres and surfaces*. Springer, Berlin
- Johnson RE (1989) Electronic sputtering: angular and charge-state dependence of the yield via superposition. *J Phys Colloque* C2:251–257, Tome 50
- Johnson RE, Jesser WA (1997) O<sub>2</sub>/O<sub>3</sub> micro-atmospheres in the surface of Ganymede. *Astrophys J Letts* 480:L79–L82
- Johnson RE, Liu M (1996) Molecular dynamics studies of mini-cascades in electronically stimulated sputtering of condensed-gas solids. *J Chem Phys* 104:6041–6051
- Johnson RE, Schou J (1993) Sputtering of inorganic insulators. In: Sigmund P (ed) *Fundamental processes in the sputtering of atoms and molecules*, vol 43, Matematisk-fysiske Meddelelser. The Royal Society, Copenhagen, pp 403–494
- Johnson RE, Sundqvist BUR (1992) Electronic sputtering: from atomic physics to continuum mechanics. *Phys Today* 45(3):28–36
- Johnson RE, Pospieszalska M (1991) Linear-to-quadratic transition in electronically stimulated sputtering of solid N<sub>2</sub> and O<sub>2</sub>. *Phys Rev* B44:7263–7272
- Johnson RE, Sittler EC (1990) Sputter-produced plasma as a measure of satellite surface composition: the Cassini mission. *Geophys Res Lett* 17:1629–1632
- Johnson RE, Brown WL (1982) Electronic mechanisms for sputtering of condensed-gas solids by electronic ions. *Nucl Instrum Methods* 198:103–118
- Johnson RE, Burger MH, Cassidy TA, Leblanc F, Marconi M, Smyth WH (2009) Composition and detection of Europa’s sputter-induced atmosphere. In: Pappalardo R et al (eds) *Chapter 20 in Europa*. University of Arizona Press, Tucson, pp 507–527
- Johnson RE, Fama M, Liu M, Baragiola RA, Sittler EC Jr, Smith HT (2008) Sputtering of ice grains and icy satellites in Saturn’s inner magnetosphere. *Planet Space Sci* 56:1238–1243

- Johnson RE, Cooper PD, Quickenden TI, Grieves GA, Orlando TM (2005) Production of oxygen by electronically induced dissociations in ice. *J Chem Phys* 123:184715
- Johnson RE, Carlson RW, Cooper JF, Paranicas C, Moore MH, Wong MC (2004) Radiation effects on the surface of the Galilean satellites. In: Bagenal F, Dowling T, McKinnon WB (eds) *Jupiter—the planet, satellites and magnetosphere*. Cambridge University, Cambridge, pp 485–512, Chapter 20
- Johnson RE, Leblanc F, Yakshinskiy BV, Madey TE (2002) Energy distributions for desorption of sodium and potassium from ice: the Na/K ratio at Europa. *Icarus* 156:136–142
- Johnson RE, Killen RM, Waite JH, Lewis WS (1998) Europa's surface composition and sputter-produced ionosphere. *Geophys Res Lett* 25:3257–3260
- Johnson RE, Pirronello V, Sundqvist BUR, Donn B (1991a) Desorption of large molecules from grains in dense clouds. *Astrophys J* 379:L75–L77
- Johnson RE, Pospieszalska MK, Brown WL (1991b) Linear-to-quadratic transition in electronically stimulated sputtering of solid N<sub>2</sub> and O<sub>2</sub>. *Phys Rev B* 44:7263–7272
- Johnson RE, Sundqvist BUR, Hedin A, Fenyo D (1989) Sputtering by fast ions based on a sum of impulses. *Phys Rev B* 40:49–53
- Johnson RE, Boring JW, Reimann CT, Barton LA, Seiveka EM, Garrett JW, Farmer KR, Brown WL, Lanzerotti LJ (1983a) Plasma Ion-induced molecular ejections on the Galilean satellites: energies of ejected molecules. *Geophys Res Lett* 10:892–895
- Johnson RE, Lanzerotti LJ, Brown WL, Augustyniak WM, Mussil C (1983b) Charged particle erosion of frozen volatiles in ice grains and comets. *Astron Astrophys* 123:343–346
- Johnson RE, Lanzerotti LJ, Brown WL (1982) Planetary applications of ion induced erosion of condensed-gas frosts. *Nucl Instrum Methods* 198:147–157
- Kelly R (1990) On the dual role of the Knudsen layer and unsteady, adiabatic expansion in pulse sputtering phenomena. *J Chem Phys* 92:5047–5056
- Killelea DR, Gibson KD, Hanqiu Yuan, James S. Becker, SibenerJ SJ (2012) Dynamics of the sputtering of water from ice films by collisions with energetic xenon atoms. *Chem Phys* 136:144705. doi:[10.1063/1.3699041](https://doi.org/10.1063/1.3699041)
- Kimmel GA, Orlando TM, Vizina C, Sanche L (1994) Low-energy electron-stimulated production of molecular hydrogen from amorphous water ice. *J Chem Phys* 101:3282
- Kimmel GA, Orlando TM (1995) Low-energy (5–120 eV) electron-stimulated dissociation of amorphous D<sub>2</sub>O Ice: D(2S), O(3P<sub>2,1,0</sub>), and O(1D<sub>2</sub>) yields and velocity distributions. *Phys Rev Lett* 75:2606
- Lanzerotti LJ, Brown WL, Marcantonio KJ (1987) Experimental study of erosion of methane ice by energetic ions and some considerations for astrophysics. *Astrophys J* 313:910–919
- Lanzerotti LJ, Brown WL, Johnson RE (1985) Laboratory studies of ion irradiation of water, sulfur dioxide and methane ices. In: Klinger J et al (eds) *Ices in the solar system*. Riedel, Dordrecht, pp 317–333
- Lanzerotti LJ, Brown WL, Marcantonio KJ, Johnson RE (1984) Production of ammonia-depleted surface layers on the saturnian satellites by ion sputtering. *Nature* 312:139–140
- Lanzerotti LJ, Brown WL, Augustyniak WM, Johnson RE (1982) Laboratory studies of charged particle erosion of SO<sub>2</sub> ice and applications to the frosts of Io. *Astrophys J* 259:920–929
- Lanzerotti LJ, Brown WL, Poate JM, Augustyniak WM (1978) On the contribution of water products from Galilean satellites to the Jovian magnetosphere. *Geophys Res Lett* 5:155–158
- Leblanc F, Potter A, Killen R, Johnson RE (2005) Origins of Europa's Na cloud and torus. *Icarus* 178:367–385
- Lepoire DJ, Cooper BH, Melcher CL, Tombrello TA (1983) Sputtering of SO<sub>2</sub> by high energy ions. *Rad Effects* 71:245–255
- Loeffler MJ, Raut U, Baragiola RA (2006) Enceladus: a source of nitrogen and an explanation for the water vapor plume observed by Cassini. *Astrophys J* 649:L133–L136
- Madey TE, Johnson RE, Orlando TM (2002) Far-out surface science radiation-induced surface processes in the solar system. *Surf Sci* 500:838–858

- Madey TE, Yakshinskiy BV, Ageev VN, Johnson RE (1998) Desorption of alkali atoms and ions from oxide surfaces: relevance to origins of Na and K in atmospheres of Mercury and the Moon. *J Geophys Res* 103:5873–5888
- McGrath MA, Hansen CJ, Hendrix AR (2009) Observations of Europa's tenuous atmosphere. In: Pappalardo R et al (eds) Chapter in *Europa*. University of Arizona Press, Tucson, p 85
- Melcher CL, LePoire DJ, Cooper BH, Tombrello TA (1982) Erosion of frozen sulfur dioxide by ion bombardment – applications to Io. *Geophys Res Lett* 9:1151–1154
- Moore MH (1984) Studies of proton-irradiated SO<sub>2</sub> at low temperatures: implications for Io. *Icarus* 59:114–128
- Moore MH, Khanna RK (1990) The infrared and mass spectra of proton irradiated H<sub>2</sub>O and CO<sub>2</sub> ices: identification of carbonic acid. *Spec Chem Acta* 479:255–262
- Mookerjee S, Beuve M, Khan SA, Toulemonde M, Roy A (2008) Sensitivity of ion-induced sputtering to the radial distribution of energy transfers: a molecular dynamics study. *Phys Rev B* 78:045435
- Öberg KI, van Dishoeck EF, Linnartz H (2009a) Photodesorption of ices I: CO, N<sub>2</sub>, and CO<sub>2</sub>. *Astron Astrophys* 496:281–293
- Öberg KI, Linnartz H, Visser R, van Dishoeck EF (2009b) Photodesorption of Ices II. H<sub>2</sub>O and D<sub>2</sub>O. *Astrophys J* 693:1209–1218
- Öberg KI, Fayolle EC, Cuppen HM, van Dishoeck EF, Linnartz H (2009c) Quantification of segregation dynamics in ice mixtures. *Astron Astrophys* 505:183–194
- Orlando TM, Sieger MT (2003) The role of electron-stimulated production of O<sub>2</sub> from water ice in the radiation processing of outer solar system surfaces. *Surf Sci* 528:1–7
- Paranicas C, Cooper JF, Grarrett HB, Johnson RE, Sturnet SJ (2009) Europa's radiation environment and its effects on the surface. In: Pappalardo R et al (eds) *Europa*. University of Arizona Press, Tucson
- Pedrys R, Krok F, Leskiewicz P, Schou J, Podschaske U, Cleff B (2000) Time-of-flight study of water ice sputtered by slow xenon ions. *Nucl Instrum Meth* B164:861–867
- Pedrys R, Warczak B, Schou J, Stenum B, Ellegaard O (1997) Ejection of molecules from solid deuterium excited by keV electrons. *Phys Rev Lett* 79:3070–3073
- Pedrys R, Oostra DJ, Haring A, de Vries AE (1989) Energy distributions for electronic sputtering of solid nitrogen. *Radiat Eff Defect S* 109:239–244
- Pedrys R, Oostra DJ, Haring RA, Calcagno L, Haring A, de Vries AE (1986) Emission of large molecules from methane by ion bombardment. *Nucl Instrum Methods* B17:15–21
- Pedrys R, Haring RA, Haring A, de Vries AE (1984) Erosion of frozen SF<sub>6</sub> by electron bombardment. *Nucl Instrum Meth* B2:573
- Petrik NG, Kimmel GA (2003) Electron-stimulated reactions at the interfaces of amorphous solid water films driven by long-range energy transfer from the bulk. *Phys Rev Lett* 90:166102
- Petrik NG, Kimmel GA (2004) Electron-stimulated production of molecular hydrogen at the interfaces of amorphous solid water films on Pt(111). *J Chem Phys* 121:3736
- Petrik NG, Kimmel GA (2005) Electron-stimulated sputtering of thin amorphous solid water films on Pt(111). *J Chem Phys* 123:054702-1–7
- Petrik NG, Kavetsky AG, Kimmel GA (2006a) Electron-stimulated production of molecular oxygen in amorphous solid water. *J Phys Chem* B110:2723
- Petrik NG, Kavetsky AG, Kimmel GA (2006b) Electron-stimulated production of molecular oxygen in amorphous solid water on Pt(111): precursor transport through the hydrogen bonding network. *J Chem Phys* 125:124702
- Pirronello V, Strazzulla G, Foti G, Brown WL, Simmons E (1984) Formaldehyde formation in cometary nuclei. *Astron Astrophys* 134:204–206
- Pirronello V, Brown WL, Lanzerotti LJ, Marcantonio KJ, Simmons E (1982) Formaldehyde formation in a H<sub>2</sub>O/CO<sub>2</sub> ice mixture under irradiation by fast ions. *Astrophys J* 262:636–640
- Ponciano CR, Farenzena LS, Collado VM, da Silveira EF, Wien K (2005) Secondary ion emission from CO<sub>2</sub>–H<sub>2</sub>O ice irradiated by energetic heavy ions Part II: analysis–search for organic ions. *Int J Mass Spectrom* 244:41–49

- Reimann CT, Johnson RE, Brown WL (1984) Sputtering and luminescence in electronically excited solid argon. *Phys Rev Lett* 53:600–603
- Rocard F, Benit J, Bibring JP, Meuneir R (1986) Erosion of ices: physical and astrophysical discussion. *Rad Effects* 99:97–104
- Rook FL, Johnson RE, Brown WL (1985) Electronic sputtering of solid N<sub>2</sub> and O<sub>2</sub>: a comparison of non-radiative relaxation processes. *Surf Sci* 164:625–639
- Roth J (1983) In: Behrisch R (ed) *Sputtering by particle bombardment II*. Springer, Berlin
- Schrivier-Mazzuoli L, Chaabouni H, Schriver A (2003) Infrared spectra of SO<sub>2</sub> and SO<sub>2</sub>: H<sub>2</sub>O ices at low temperature. *J Mol Struct* 644:151–164
- Schrivier A, Schriver L, Perchard JP (1988) Infrared matrix isolation studies of complexes between water and sulfur dioxide: identification and structure of the 1:1, 1:2, and 2:1 species. *J Mol Spectr* 127:125–142
- Schou J, Pedrys R (2001) Sputtering of carbon monoxide ice by hydrogen ions. *J Geophys Res* 106:33309–33314
- Schou J, Stenum B, Pedrys R (2001) Sputtering of solid deuterium by He-ions. *Nucl Instrum Meth B* 182:116–120
- Schou J, Stenum B, Ellegaard O, Dutkiewicz L, Pedrys R (1995) Sputtering of the most volatile solids: the solid hydrogen. *Nucl Instrum Methods* B100:217–223
- Schou J, Sorensen H, Borgesen P (1984) The measurement of electron-induced erosion of condensed gasses: experimental methods. *Nucl Instrum Methods* B5:44–57
- Seiberling LE, Meins CK, Cooper BM, Griffith JE, Mendenhal MH, Tombrello TA (1982) The sputtering of insulating materials by fast heavy ions. *Nucl Instrum Methods* 198:17–25
- Shi M, Baragiola RA, Grosjean DE, Johnson RE, Jurac S, Schou J (1995a) Sputtering of water ice surfaces and the production of extended neutral atmospheres. *J Geophys Res* 100:26387–26395
- Shi H, Cloutier P, Sanche L (1995b) Low-energy-electron stimulated desorption of metastable particles from condensed N<sub>2</sub> and CO. *Phys Rev B* 52:5385–5391
- Sieger MT, Simpson WC, Orlando TM (1998) Production of O<sub>2</sub> on icy satellites by electronic excitation of low-temperature water ice. *Nature* 394:554
- Sieger MT, Simpson WC, Orlando TM (1997) Electron-stimulated desorption of D<sup>+</sup> from D<sub>2</sub>O ice: surface structure and electronic excitations. *Phys Rev B* 56:4925–4937
- Sieveka E, Johnson RE (1982) Thermal- and plasma-induced molecular redistribution on the icy satellites. *Icarus* 51:528–548
- Sigmund P (ed) (1993) Fundamental processes in the sputtering of atoms and molecules. Royal Danish Academy, Copenhagen
- Sigmund P (1981) Sputtering by particle bombardment. Theoretical concepts. In: Behrisch R (ed) *Sputtering by particle bombardment I*. Springer, Berlin, pp 9–72
- Sigmund P, Claussen C (1981) Sputtering from elastic-collision spikes in heavy-ion-bombarded metals. *J Appl Phys* 52:990–993
- Šiller L, Sieger MT, Orlando TM (2003) Electron-stimulated desorption of D<sub>2</sub>O coadsorbed with CO<sub>2</sub> ice at VUV and EUV energies. *J Chem Phys* 118:8898–8904
- Stenum B, Schou J, Ellegaard O, Sorensen H, Pedrys R (1991a) Sputtering of solid hydrogenic targets by keV hydrogen ions. *Phys Rev Lett* 67:2842–2845
- Stenum B, Ellegaard O, Schou J, Sørensen H, Pedrys R (1991b) Sputtering of frozen gases by molecular hydrogen ions. *Nucl Instrum Methods* B58:399–403
- Stenum B, Ellegaard O, Schou J, Sørensen H (1990) Sputtering of solid hydrogenic targets by keV hydrogen ions. *Nucl Instrum Methods* B48:530–533
- Strazzulla G, Baratta GA, Leto G, Foti G (1992) Ion-beam-induced amorphization of crystalline water ice. *Europhys Lett* 18:517
- Strazzulla G, Torrisi L, Foti G (1988) Light scattering from ion-irradiated frozen gases. *Europhys Lett* 7:431–434
- Strazzulla G, Torrisi L, Coffa S, Foti G (1987) Sputtering of sulfur: experiments and consequences for Io. *Icarus* 70:379–382

- Sundqvist B, Hedin A, Hakansson P, Salehpour M, Save G, Johnson RE (1986) Sputtering of biomolecules by fast heavy ions. *Nucl Instrum Methods* B14:429–435
- Teolis BD, Jones GH, Miles PF, Tokar RL, Magee BA, Waite JH, Rousso E, Young DT, Crary FJ, Coates AJ, Johnson RE, Tseng WL, Baragiola RA (2010) Cassini finds an oxygen–carbon dioxide atmosphere at Saturn’s Icy Moon Rhea. *Science* 330:1813–1815
- Teolis BD, Shi J, Baragiola RA (2009) Formation, trapping, and ejection of radiolytic O<sub>2</sub> from ion-irradiated water ice studied by sputter depth profiling. *J Chem Phys* 130:134704, 1–92009
- Teolis BD, Loeffler MJ, Raut U, Fama M, Baragiola RA (2006) Ozone synthesis on the icy satellites. *Astrophys J* 644:L141
- Teolis BD, Vidal RA, Shi J, Baragiola RA (2005) Mechanisms of O<sub>2</sub> sputtering from water ice by keV ions. *Phys Rev* B72:245422
- Thestrup B, Svendsen W, Schou J, Ellegaard O (1994) Sputtering of thick deuterium films by KeV electrons. *Phys Rev Lett* 73:1444–1447
- Torrisi L, Coffa S, Foti G, Johnson RE, Chrisey DB, Boring JW (1988) Threshold dependence in the electronic sputtering of condensed sulfur. *Phys Rev* B38:1516–1519
- Tucker OJ, Ivanov DS, Johnson RE, Zhigilei LV, Bringa EM (2005) Molecular dynamics simulation of sputtering from a cylindrical track: EAM versus pairpotentials. *Nucl Instrum Methods* B228:163–169
- Trautman C, Spohn R, Toulemonde M (1993) Stopping power dependence of ion track etching in amorphous metallic Fe<sub>81</sub>B<sub>13.5</sub>Si<sub>3.5</sub>C<sub>2</sub>. *Nucl Instrum Methods* B83:513–517
- Urbassek HM, Michl J (1987) A gas-flow model for the sputtering of condensed gases. *Nucl Instrum Methods* B22:480–490
- Westley MR, Baragiola A, Johnson RE, Barratta G (1995a) Photodesorption from low-temperature water ice in interstellar and circumsolar grains. *Nature* 373:405–407
- Westley MS, Baragiola RA, Johnson RE, Barratta GA (1995b) Ultraviolet photodesorption from water ice. *Planet Space Sci* 43:1311–1315
- Zheng W, Jewitt D, Kaiser RI (2006a) Formation of hydrogen, oxygen and hydrogen peroxidized in electron-irradiated water ice. *Astrophys J* 639:534–548
- Zheng W, Jewitt D, Kaiser RI (2006b) Temperature dependence of the formation of hydrogen, oxygen, and hydrogen peroxide in electron-irradiated crystalline water ice. *Astrophys J* 648:753–761
- Zheng W, Jewitt D, Osamura Y, Kaiser RI (2008) Formation of nitrogen and hydrogen-bearing molecules in solid ammonia and implications for solar system and interstellar ices. *Astrophys J* 674:1242–1250
- Ziegler JF, Biersack JP, Littmark U (1985) The stopping and range of ions in solids. Pergamon, New York

# Chapter 18

## Photochemistry in Terrestrial Ices

Cort Anastasio, Michael Hoffmann, Petr Klán, and John Sodeau

**Abstract** Terrestrial ices contribute to the delicate balance between reflected and absorbed solar heat on Earth. Chemical and physical processes occurring in terrestrial ices, whether during the formation of crystalline ice from cooling water or in the form of snow or in ice cores, are some of the important processes that need to be well understood. The presence of organic and inorganic pollutants – whether through natural events or through human activity – influences both the physics and chemistry of terrestrial ices. Our understanding of thermal, pressure induced, and photochemical transformations of impurities in terrestrial ices are reviewed in this chapter.

### 18.1 Introduction

Water ice is the most abundant solid on Earth (Petrenko and Whitworth 1999). Terrestrial and atmospheric ice and snow are practically always contaminated with various species of both anthropogenic and biogenic origin. Some of them can undergo chemical changes upon direct solar irradiation, and some may be degraded via dark or photochemically initiated secondary chemical processes. Their reactivity

---

C. Anastasio (✉)

Department of Land, Air, and Water Resources, University of California, Davis, CA, USA  
e-mail: [canastasio@ucdavis.edu](mailto:canastasio@ucdavis.edu)

M. Hoffmann

W. M. Keck Laboratories, California Institute of Technology, Pasadena, CA, USA  
e-mail: [mrh@caltech.edu](mailto:mrh@caltech.edu)

P. Klán

Department of Chemistry, Masaryk University, Brno, Czech Republic  
e-mail: [klan@sci.muni.cz](mailto:klan@sci.muni.cz)

J. Sodeau

Department of Chemistry, University College Cork, College Road, Cork, Ireland  
e-mail: [j.sodeau@ucc.ie](mailto:j.sodeau@ucc.ie)

depends on many factors, such as light absorption properties, chemical constitution, the presence of other species, phase properties of the guest matrix, or temperature. The low concentrations of contaminants and the complexity of the system remains a profound challenge to both experimentalists and theoreticians to study and describe the physical and chemical processes occurring in natural ice or snow. Laboratory simulations are being compared with field observations; nevertheless, many questions are still unanswered. This chapter discusses the physico-chemical properties of terrestrial ice/snow and the course and extent of photochemical transformations of its contaminants as well as possible implications of these processes for the environment. Several recent reviews can also serve the reader as additional, more detailed sources of information (Domine et al. 2008; Grannas et al. 2007; Klán and Holoubek 2002; Simpson et al. 2007; Steffen et al. 2008).

## 18.2 Physico-Chemical Properties of Ice and Snow

### 18.2.1 *Properties of Bulk Ice*

The dielectric properties of the ice/water system are unique among polar liquids. The dielectric constant of water,  $\epsilon$ , is very high and increases at lower temperature (Rick 2001; Suresh and Naik 2000). Remarkably,  $\epsilon$  keeps increasing in the solid; a direct indication that its dielectric properties are not associated with rotating dipoles, but with the long-range polarization of the entire lattice, probably via H-bonding chains. “Normal” liquids experience a drastic drop of the dielectric constant upon freezing.

The electrical properties of ice are also unique and may be very important in trying to understand its role as a reaction medium. Ice provides a good example of electrical conduction by protons, which have mobilities of about an order of magnitude larger than those characteristic of normal ionic conductors. Protons become immobile below 190 K on the surface of ice (Cowin et al. 1999). In fact, many analogies can be established between protonic conduction in ice and electronic conduction in metals and intrinsic semiconductors. Ionic impurities can have drastic effects on the dielectric and conduction properties, particularly at low frequencies.

Several dynamical processes occurring in ice exhibit intriguing similarities in activation energies and rate constants, such as dielectric and elastic relaxation, self-diffusion, spin-lattice relaxation, and motion narrowing of magnetic resonance lines (Onsager and Runnels 1969). Interestingly, oxygen and hydrogen diffuse at the same rate, suggesting that the primary diffusing species is not an ion, but an intact water molecule.

### 18.2.2 *Freezing and Ice Polymorphs*

Ice can adopt many crystalline structures, more than any other known material. At ordinary pressures the stable phase of ice is called ice I, which exists in two

closely related variants: hexagonal ice ( $I_h$ ), with hexagonal symmetry, and cubic ice ( $I_c$ ), which has a diamond-like structure.  $I_h$  is the usual form of ice.  $I_c$  is formed by deposition at very low temperatures, below 140 K, which are beyond the environmental range. Amorphous ice can be made by depositing water vapor onto a substrate at still lower temperatures, and therefore does not qualify either as a simile for environmental ices. Environmental ices can grow from the vapor phase, or by freezing water or aqueous solutions (Hobbs 1974). The properties and morphologies of the ices formed depend on nucleation and growth kinetics, which are a function of the degree of supersaturation and the presence of solutes (Wettlaufer 1999a). Sparse ice aerosols may settle into polycrystalline aggregates having distinct mesoscopic characteristics (Hobbs 1974). The degree of crystallinity of the ice formed by vapor deposition is known to depend on the deposition rate (Olander and Rice 1972). In past studies it has been found that the phase of ice may affect the chemistry of molecules adsorbed on its surface (Gertner and Hynes 1996). Remarkably, heterogeneous freezing on  $(\text{NH}_4)_2\text{SO}_4$  depends on its morphology (Zuberi et al. 2001). If the solid is in the form of microcrystals, freezing begins at the eutectic temperature, but on large ammonium sulfate crystals heterogeneous freezing occurs at the normal melting point. Thus, ice cores, ice clouds, snow, and oceanic ice caps actually represent different reaction media.

From the viewpoint of experimental design it should be emphasized that the structure and properties of thin ice films markedly depend on the properties and morphology of the substrate, as revealed by IR spectroscopy (Trakhtenberg et al. 1997), and therefore are not, in general, valid surrogates for materials formed by unconstrained freezing, such as snow or marine ice caps (Bluhm and Salmeron 1999; Bluhm et al. 2000a, b; Delzeit et al. 1996; Chaabouni et al. 2000a, b; Miranda et al. 1998; Salmeron and Bluhm 1999; Su et al. 1998). The phenomenon of interfacial premelting of ice, so important from the environmental point of view since the quasi-liquid layer will be the location of most solutes, will occur when, loosely speaking, the polarizability of water lies between that of the ice and the substrate (Wilen et al. 1995). The polarizability of a material is a function of its refractive index and, therefore, results obtained in thin ice films deposited on optical materials such as Ge ( $n = 4.0$ ) will have to be qualified regarding its transportability to environmental ice. The novelty of the ice/water system stems from the fact that the polarizability of ice is greater than that of water at high frequencies, while at lower frequencies is smaller. The effect of retardation is to attenuate the high-frequency contributions. Thus, ice on a surface having a low-frequency polarizability larger than water will melt completely. If the third phase is water vapor, surface melting is limited to a finite thickness (Israelachvili 1992; Wilen et al. 1995).

Sintering is an important process occurring in ice at finite rates above about  $-35^\circ\text{C}$ , which must be taken into account to ensure experimental reproducibility. It has been found that the radius of the neck  $x$  that forms between two ice spheres of radius  $r$  is given by the expression:

$$\left(\frac{x}{r}\right)^n = \frac{A(T)}{r^m}$$

where  $n$  and  $m$  are integers, the values of which depend on the dominant mechanism by which material is transferred to the neck, and  $A(T)$  is a function of temperature and mechanism (Hobbs 1974).

A fundamental parameter in the growth of ice from the vapor phase is the condensation coefficient  $\alpha_c$ , which is defined as the probability that an  $H_2O(g)$  molecule will stick to ice surfaces. Typical  $\alpha_c$  values decrease with temperature between 0.2 below  $-90^\circ C$ , to 0.01 above  $-13^\circ C$  (Haynes et al. 1992). The latter value approaches  $\alpha_c$  in water near the melting point, consistent with the existence of a liquid film over ice. Mass accommodation coefficients  $\alpha_c$  of  $H_2O(g)$  on water as a function of temperature were recently measured (Li et al. 2001).

### 18.2.3 *The Quasi-Liquid Layer*

Faraday suggested in 1859 that ice is covered by a “liquid-like” layer. The existence of such a layer does not contradict the phase rule, as it has been argued before, which in its simple form for bulk phases,  $F = C + 2 - P$ , states that there is only a single ( $F = 0$ ) state (specified by two parameters  $P, T$ ) in which three macroscopic phases ( $P = 3$ ) can coexist in a one-component system ( $C = 1$ ). In fact, the consideration of surfaces as distinct phases requires specifying an additional intensive parameter, the surface tension  $\gamma$ , which naturally increases the number of intensive variables. Hence, the phase rule has to be cast in the form  $F = C + 3 - P$ . In other words, it is thermodynamically possible to have three phases – gas, solid, and liquid film – over a range of temperatures below the normal freezing point (Baker and Baker 1996; Knight 1996).

Bulk ice is covered by a quasi-liquid layer of variable thickness down to about 240 K (Doppenschmidt and Butt 2000; Doppenschmidt et al. 1998). The thickness of the liquid layer markedly depends on the presence of ice impurities (Dash et al. 1995; Wettlaufer 1999b; Wettlaufer and Dash 2000). However, the onset of ice surface disordering depends on the technique used to monitor the changes (Mantz et al. 2000). The critical temperature will also vary depending on the conditions under which the experiments are performed, the presence of surface impurities, and the different nature and sensitivity of the techniques employed. For example, atomic force microscopy indicates that at temperatures below 243 K supercooled water droplets form on top of a nm-thick ice layer in contact with a cleaved mica substrate. After annealing, a continuous flat film is formed. Between 263 and 253 K and a relative humidity of 83% the film consists of a solid ice layer about 0.7 nm thick, covered with a liquid-like layer about 5 nm thick (Bluhm and Salmeron 1999). Rejected solutes will populate such layer, which is more akin to a fluid than to a solid medium, or accumulate into veins and nodes (Cullen and Baker 2000; Huthwelker et al. 2001). Solute mobility in the top two or three bilayers is substantially faster than in the bulk, even at low temperatures (Bolton and Pettersson 2000).

### 18.2.4 Solute Rejection, Partitioning, Migration and Conformational Behavior During Freezing

Freezing at or below eutectic temperatures can create solid solutions, depending on the extent of ice-solution equilibration. It should be emphasized that a system is completely solid only below its eutectic point. In the range of temperatures between the freezing and eutectic points, ice and fluid solution coexist (Pincock 1969). At the eutectic point, ice and solute may separate as independent solid phases or not, depending on their compatibility. It is always possible to reach such a condition by cooling the solutions sufficiently fast, i.e., by preventing solvent freezing at temperatures above the eutectic point (van der Ham et al. 1999). In general, with a few exceptions such as NH<sub>4</sub>F, polar, non-polar, or ionic solutes are segregated from ice upon freezing above the eutectic point (Killawee et al. 1998). The existence of solid solutions in which ice is the major component has only been demonstrated for NH<sub>4</sub>F, HF, and a few organic acids. However, ammonium also enhances the solubility in ice of anions that do not fit easily into the ice structure.

Thus, freezing aqueous solutions of most of the organic and inorganic compounds causes that ice and solute molecules separate (Cohen et al. 1996; Dash et al. 1995; Doppenschmidt and Butt 2000; Finnegan and Pitter 1997; Giannelli et al. 2001; Gross et al. 1987; Heger et al. 2005; Cho et al. 2002; Petrenko and Whitworth 1999; Smith and Pounder 1960; Takenaka et al. 1996; Vrbka and Jungwirth 2005; Wang 1961, 1964). The solute local (microscopic) concentrations in the layers surrounding the crystal walls significantly increase causing a considerable depression of the freezing point (Bhatnagar et al. 2005); the layers eventually solidify as temperature further decreases.

The precise location of solutes in ice matrices remains controversial (Gross and Svec 1997; Gross et al. 1987). Atmospheric or aerosolized marine species can be deposited on growing ice surfaces, and their local environment within the solid being formed will change as they become buried under successive layers (Conklin and Bales 1993; Huthwelker et al. 2001; Choi et al. 2000; Kawamura et al. 1996, 2001; Oremp and Adamson 1969). In the important case of clouds, it has been shown that the relationship between fresh snow and air composition will depend on the growth rate of snow crystals (Thibert and Domine 1998).

In most aqueous solutions studied (Gross et al. 1987), ice grown from solution remains nearly pure. Even within the liquid layer, solute distribution within micro-crystalline ice aggregates is not homogeneous, but tends to peak at the triple intersection of grain boundaries (Nye 1989). Information on the distribution of these ions, i.e., whether they are disseminated through the crystals or concentrated in a liquid phase at the triple junctions between the crystals, is essential to model these systems (Potts et al. 1992). It has been found that liquid H<sub>2</sub>SO<sub>4</sub> is concentrated at the junctions, but that NaCl and its ions could not be detected inside ice crystals. The relationship between the degree of ionization and the environment of a strong acid is also of great importance. Often this relationship reduces to the interdependence of ion/acid hydration and proton transfer. Even in the presence of pure water, the surface of crystalline ice, particularly at cryogenic temperatures, is one of

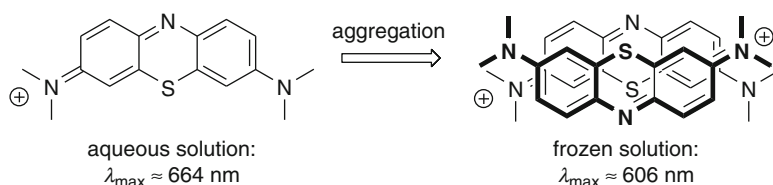
limited water availability. Recent infrared spectroscopic work has found that the surface of free-standing ice particles is badly disordered, with a range of water-ring sizes and an increased level of H-bond saturation relative to an ordered ice surface. DCl and DBr are present as molecular adsorbates.  $\text{HNO}_3$ , however, behaves differently even at 135 K (Devlin et al. 1999).

There is indirect evidence on the liquid nature of the ice/air interface via  $\text{SO}_2$  uptake on ice spheres (Conklin and Bales 1993). Physical studies on the adsorption of simple, non-polar hydrocarbon vapors on ice reveal that below  $-35^\circ\text{C}$  adsorption is characterized by low adsorption energies, with isosteric heats lower than the heat of condensation at low coverage. Above that temperature, adsorption changes dramatically to that of adsorption on liquid water, implying a discontinuity in the properties of ice at  $-35^\circ\text{C}$ , above which it becomes covered with a liquid film (Oremp and Adamson 1969). The phenomenon is an equilibrium one because it is not history-dependent, despite the fact that the total surface available for adsorption decreases at higher temperatures due to sintering.

Escape of insoluble gasses out of the aggregates will take place mainly by diffusion through the lattice voids, and therefore the length of the diffusive path will depend on tortuosity, i.e., the mesoscopic structure of the ice pack. Diffusion under simultaneous concentration and temperature gradients leads to isotopic fractionation within ice pores. Post-depositional migration can certainly influence the interpretation of paleoclimatic information (Livingston and George 2001; Livingston et al. 2000). Conflicting reports on nitric acid diffusion on ice surfaces attest to the difficulty of characterizing ice structures (Domine and Thibert 1998; Laird et al. 1999; Sommerfeld et al. 1998; Thibert and Domine 1998). Post-depositional loss of nitrate has been observed in surface snow layers of the Antarctic ice-sheet (Fabre et al. 2000; Nakamura et al. 2000).

Organic compounds are also rejected from the growing ice phase upon freezing their aqueous solutions. Spectroscopic methods have been used for studying the aggregation process of some organic dyes, such as Methylene Blue (MB), a cationic redox indicator, which self-organizes to give sandwich-type associations exhibiting a blue shift of the spectral band of the  $\pi - \pi^*$  transition compared to that of a monomer (Lewis et al. 1943) (Scheme 18.1) (Heger et al. 2005). The extent of MB aggregation was found to depend on the freezing rate and initial MB concentration: compared to in liquid solution, the occurrence of aggregated dye molecules increased by 3–4 orders of magnitude upon fast freezing at 77 K, and by more than by six orders of magnitude upon slow freezing at 243 K. The analysis of the protonation degree of an acid–base indicator, Cresol Red (CR), in frozen aqueous solutions of mineral or organic acids (such as HF, HCl,  $\text{HNO}_3$ ,  $\text{H}_2\text{SO}_4$ , and *p*-toluenesulfonic acid) revealed that production of a protonated form of CR in solidified solutions was enhanced by 2–4 orders of magnitude compared to the liquid solutions, which was apparently also connected to an increase in the microscopic concentration of acids at the grain boundaries (Heger et al. 2006).

The chemical transformations of the environmental species trapped in snow and ice actually take place in micro-fluids (QLL's) wetting polycrystalline ice grains. These inter-granular fluids are not concentrated replicas of the solutions to be frozen



**Scheme 18.1** Aggregation of methylene blue

as is often assumed. For example, the acidity of the micro-fluids in ice is usually different from that of the bulk solutions before freezing and, to a large extent, driven by ion fractionation at the ice-water interface during freezing. Upon freezing electrolyte solutions, a few ( $\sim 1$  in  $10^4$ ) ions are selectively trapped into the ice lattice as substitutional impurities, thereby creating electrical imbalances between the ice and fluid phases that can only relax via migration of the intrinsic  $\text{H}^+/\text{HO}^-$  ice carriers (see also later). Thus, preferential incorporation of cations into the ice lattice leads to acidification of the remaining liquid, whereas preferential incorporation of anions has the opposite effect. Since the local acidity of the interstitial micro-fluids determines whether weak, volatile acids or bases can be exchanged between ice and the gas phase, and whether reactions between dopants are inhibited or catalyzed in frozen media, it is important to understand the factors that control ice acidity.

Hoffmann and co-workers have provided direct experimental evidence of the universal phenomenon known as freezing hydrolysis by measuring the magnitude of pH changes as a function of ice freezing rate, electrolyte composition and concentration (Robinson et al. 2006). The acidity of electrolyte solutions before, during, and after freezing is measured by means of confocal laser scanning microscopy (CLSM) in conjunction with the dual emission pH indicator carboxy-seminaphthorhodafluor-1 (C-SNARF-1). This approach makes it possible to probe, with temporal and spatial resolution, the freezing-induced pH changes in the aqueous electrolyte samples. The fluorescence emission spectra of C-SNARF-1 show two emission peaks around 580 and 640 nm, corresponding to the protonated and deprotonated species, respectively. Therefore, the ratio of the fluorescence intensities at these two emission wavelengths can be used for quantitative determinations of pH. This approach effectively eliminates problems associated with photo-bleaching, sample heterogeneity, and concentration changes during freezing. The calibration of the emission ratio for the C-SNARF-1 as a function of solution pH using both a CLSM and a luminescence spectrophotometer yielded similar results (Fig. 18.1). Differences in spectra are most likely due to differences in instrumental conditions and optical setup. It was also found that the emission ratio is not sensitive to sample concentration, temperature, and instrumental parameters such as excitation laser intensity, pinhole size, and detector gain.

As the ice front moves radially inward toward the center of the sample well upon freezing, the fluorescent probe is rejected by the ice and trapped in the liquid channels, whose morphology depends markedly on the presence of electrolytes. C-SNARF-1 in MilliQ water freezes into thin liquid channels arranged in a

**Fig. 18.1** Fluorescence emission ratio versus pH measured a fluorometer (blue line;  $\lambda_1 = 587$  nm,  $\lambda_2 = 634$  nm) and with a cryogenic confocal laser microscope (CLSM) (red line;  $\lambda_1 = 581$  nm,  $\lambda_2 = 635$  nm)

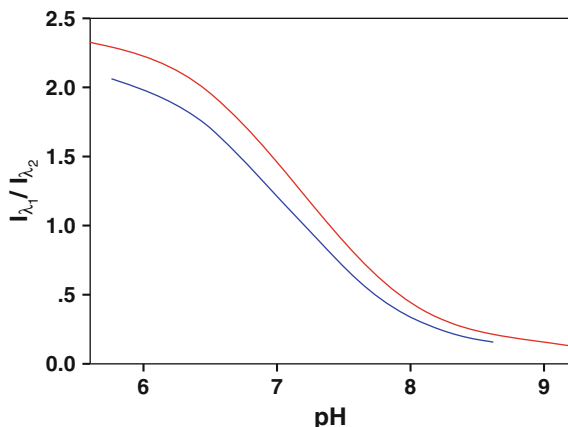
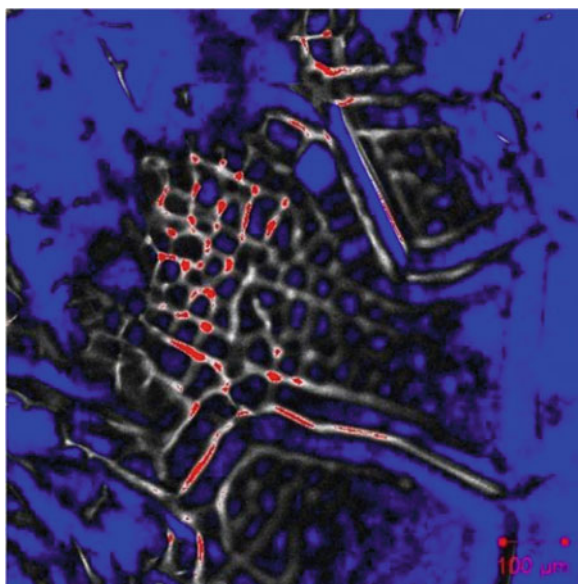


**Fig. 18.2** C-SNARF-1 in hexagonal ice veins during freezing. Fluorescence intensity is indicated by a color scale (blue: low intensity, red: high intensity)



hexagonal network of veins and nodes (Fig. 18.2), whereas in freezing solutions containing electrolytes such as NaCl and  $(\text{NH}_4)_2\text{SO}_4$  at a concentration above 1 mM, C-SNARF gets concentrated in seemingly more randomly-distributed pools and dendritic channels. The observed morphologies are determined by both thermodynamic and mass transport effects.

The pH change in the liquid channels during the freezing of a solution containing 10  $\mu\text{M}$  C-SNARF-1 and 0.1 mM NaCl with an initial pH of 6.38 were determined by the emission ratio (Fig. 18.3). When freezing begins, C-SNARF-1 is observed to accumulate up to 20  $\mu\text{m}$  ahead of the freezing front, demonstrating that mass diffusion is slow relative to the speed of progression of the freezing front, which

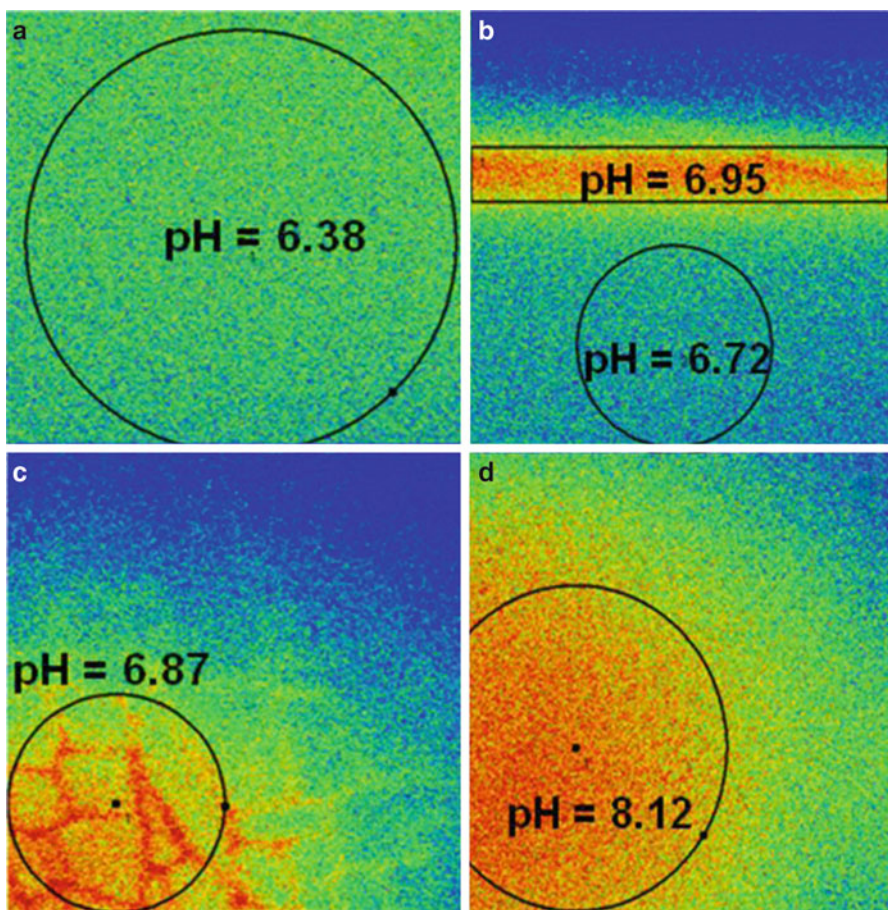


**Fig. 18.3** Fluorescence emission spectra of an aqueous solution containing 10  $\mu\text{M}$  C-SNARF-1 and 0.1 mM NaCl (a) before freezing, (b) 9.8 s after freezing was initiated, (c) 52.4 s after the start of freezing, and (d) 20 s after thawing started. The pH values shown are based on the emission ratio averaged over the area of interest. Each frame size is 225  $\mu\text{m} \times 225 \mu\text{m}$

is estimated to be  $50 \mu\text{m s}^{-1}$ . Consequently, the pH changes induced by freezing are largely confined to the interfacial region rather than uniformly across the fluid. The fast freezing rates also limit the magnitude of pH changes observed during the entire freezing process. However, when the sample is partially thawed after remaining frozen for 10 min, the pH is observed to rise by up to 1.8 units, suggesting the interfacial migration of  $\text{H}^+/\text{HO}^-$  in the frozen sample. The pH returns to the initial value when the sample is completely thawed. The freezing-induced pH increase has been consistently observed for NaCl solutions at concentrations from 0.1 to 1 mM, in accordance with expectations based on

freezing hydrolysis. In contrast, the pH of a 0.05 mM CH<sub>3</sub>COONH<sub>4</sub> solution was observed to drop from 7.91 to 6.80 due to preferential incorporation of NH<sub>4</sub><sup>+</sup> into the ice during freezing.

### 18.2.5 Chemical Properties of Ice/Vapor and Ice/Water Interfaces

Ice surfaces are chemically distinct phases. For example, although proton transfer between ammonia and hydronium proceeds instantaneously in the aqueous phase, it never reaches equilibrium on ice surfaces due to restrictions on ion mobility (Park et al. 2001). The reason is that at high coverage NH<sub>3</sub> encounters not only H<sub>3</sub>O<sup>+</sup> but also, increasingly, NH<sub>4</sub><sup>+</sup>, with which it forms ammoniated, immobile clusters.

Hydrogen chloride becomes less than 50% dissociated on ice at temperatures below 120 K. On the other hand, NaCl readily dissociates to Na<sup>+</sup> and Cl<sup>-</sup> ions on a condensed water surface, even at 100 K (Park et al. 2000). However, the temperature dependence of solute interactions with water-ice is so steep that it is unwarranted to extrapolate very low-temperature data to field conditions (Hynes et al. 2001).

Inorganic ions are not necessarily incorporated in ice in the proportion originally present in aqueous solutions during freezing. Such a non-equilibrium process can generate a substantial electrical potential difference between the solid ice and an unfrozen liquid layer. This uneven ion distribution during freezing generate a substantial electrical potential difference between the solid ice and an unfrozen liquid layer (Bronshteyn and Chernov 1991; Finnegan and Pitter 1997; Sola and Corti 1993). It depends on the rate of freezing and affects pH of the liquid layer surrounding the (nearly) pure ice crystals. For example, in case of NaCl, Cl<sup>-</sup> incorporates more into the ice lattice as HCl, whereas Na<sup>+</sup> and OH<sup>-</sup> remain in the liquid phase (Workman and Reynolds 1950). The pH of the brine layer can be as high as 9 (Sola and Corti 1993), which has also been confirmed by absorption measurements using Cresol Red as an acid–base indicator (Heger et al. 2006) or used in base-catalyzed oxidative decomposition of gallic acid in aqueous solution containing NaCl induced by freezing (Takenaka et al. 2006).

The equilibrium electrical properties of ice/water interfaces have been investigated by (Kallay and Cakara 2000). The reversible electrostatic potential is created by protonation equilibria involving atmospheric OH groups, and therefore is pH-dependent. The isoelectric point of ice, i.e., the conditions under which ice particles suspended in water are electrophoretically quiescent, i.e.,  $\zeta = 0$ , was found to be close to pH = 4 using an ice electrode (Doe et al. 1995; Glenn and Ingram 1994; Kallay and Cakara 2000). In an interesting approach, the electrophoretic mobility and zero point charge (zpc) were determined for D<sub>2</sub>O (mp = 3.8°C) ice particles suspended in H<sub>2</sub>O (Drzymala et al. 1999). In 1 mM NaCl, 3.5°C,  $\zeta = 0$  at pH = 3.0, and zpc is reached at pH = 7.0. The inference is that chloride ions are specifically adsorbed at the ice/water interface.

### 18.2.6 Non-photochemical Processes Occurring upon Freezing

Chemical reactions may take place on preformed ice or during freezing (Kiosky and Pincock 1966; Pincock 1969). The differential incorporation of ions in ice during the freezing of solutions generates transiently charged interfaces (Sola and Corti 1993). The extent of non-equilibrium, which depends on the rate of freezing, may induce thermodynamically forbidden reactions. It has been shown that concentration of the rejected solutes remaining in the liquid phase during freezing (Honda 2001; O'Driscoll et al. 2008; Sato et al. 2003; Takenaka et al. 1992, 1996, 1998, 2003) accounts for the acceleration of chemical rates in most cases, but this is a rather trivial effect. There are remarkable findings that cannot be accommodated by concentration effects alone. A maximum at about  $-15^{\circ}\text{C}$  in the rate constant of nitrite and sulfite oxidation has been ascribed to the interplay of the increased electrolyte concentration and the lower reaction rate constant at lower temperatures (Betterton and Anderson 2001).

In binary systems it is simple to distinguish between a true solid-state reaction and a liquid-phase process by determining whether products are still formed below the eutectic temperature. In complex multicomponent systems, as they arise in the environment, the lowest temperature at which liquid may exist is often far below the eutectic point of the major component. However, the absence of discontinuities in the dependence of the correlated overall rate constant for the kinetics of Fe(III)-Fe(II) electron transfer in 0.55 perchloric acid media above and below its eutectic point at  $-55^{\circ}\text{C}$  was interpreted as evidence against diffusion control, and in favor of electron transfer mediated by the ice matrix (Horne 1963). The Fe(III)/Fe(II) equilibrium is also modified by freezing (Sinner et al. 1994). The effect of freezing on a variety of acidified and neutral, nitrite ion and halide-containing mixtures has been investigated. Several trihalide ions were formed, including  $\text{I}_2\text{Cl}^-$ ,  $\text{I}_2\text{Br}^-$ ,  $\text{ICl}_2^-$ , and  $\text{IBr}_2^-$ , and the mechanism may involve INO and the nitroacidium ion,  $\text{H}_2\text{ONO}^+$  (O'Driscoll et al. 2006).

It should be emphasized that the above reactions are thermodynamically allowed, i.e., exclusion from the ice matrix only enhances their rates. More interesting is the finding that some endoergic reactions, such as the reduction of  $\text{CO}_2$  to formate and formaldehyde, occur under the non-equilibrium conditions prevailing during fast freezing (Finnegan et al. 1991, 2001; Finnegan and Pitter 1991, 1997). The transient charge separation that develops at the advancing ice front provides the overpotential required to drive the otherwise uphill redox process:



for which a free energy defect  $\Delta G_2 > 300 \text{ kJ} \sim 3 \text{ V}$  was estimated under neutral conditions,  $p_{\text{O}_2} = 0.21 \text{ Pa}$ , and  $T = 300 \text{ K}$ . Clearly, this reaction would not proceed to any detectable extent under equilibrium conditions in homogeneous, uncharged phases. Formally, reductions will take place on ice if it were positively

charged by the preferential incorporation of H<sup>+</sup> relative to OH<sup>-</sup>. Finnegan et al. have argued forcibly in favor of H<sup>+</sup> and OH<sup>-</sup> as the ions involved in charge separation, in dissidence with previous reports (Bronshteyn and Chernov 1991; Gross and Svec 1997; Gross et al. 1975, 1987; Lodge et al. 1956; Shibkov et al. 2001; Workman and Reynolds 1950). One last possibility is that high pressure could trigger certain reactions above a certain threshold level. However, 130 m ice depths amount to 1 MPa, which is far below the typical pressures required to modify reactivity in solids (Hemley 2000).

It has long been known that some other diffusion-controlled events, such as enzymatic degradation or ice recrystallization, occur during freezing foods (Fennema 1975; Goff 1992; Goff and Sahagian 1996; Lee et al. 2002, 2008). In this context, denaturation of proteins during freezing, microscopic ice crystals formation, or large pH shifts are also often observed during freeze-drying process (lyophilization), which is one of the favored ways of stabilizing biological materials and some therapeutic proteins (Bhatnagar et al. 2007, 2008; Cao et al. 2003; Carpenter et al. 1993; Engstrom et al. 2008; Chang et al. 1996; Cheftel et al. 2000; Pikal 2004; Regand and Goff 2005; Sarciaux et al. 1999; Strambini and Gonnelli 2008). However, some cells are known to adopt a strategy in protecting their proteins by the production of osmolytes, low molecular weight organic substances, such as carbohydrates, polyols, or methylamine derivatives (Yancey 2005; Yancey et al. 1982).

Some “dark” chemical reactions can take an entirely different course in ice. For example, the addition of Cl<sub>2</sub> to propene yields 1,2-dichloropropane, rather than 2-chloro-1-propanol, the dominant product in water (Graham and Roberts 2000).

## 18.3 Photochemistry of Inorganic Species in Ice and Snow

### 18.3.1 Rates of Snow Photochemical Processes

Photochemical processes involve two steps: absorption of light by a chromophore (light absorbing molecule) to form an excited state, followed by decomposition of the excited state to form new products (or relaxation back to ground state) (Gilbert and Baggott 1991). Thus the rate of any photochemical process – regardless of phase – depends upon three variables: (1) the flux of light, (2) the extent to which the chromophore absorbs light, and (3) the efficiency of the chromophore excited state to form products. For condensed phases in the environment, these variables correspond to, respectively, the spherically integrated solar actinic flux ( $I_{\lambda}$ ), the (base-10) molar absorptivity of chromophore C ( $\varepsilon_{C,\lambda}$ , L mol<sup>-1</sup> cm<sup>-1</sup>), and the quantum yield for formation of product  $i$  ( $\Phi(C \rightarrow i)_{\lambda}$ , molecules of  $i$  formed per photon absorbed by C). In the snowpack, the rate of a photochemical reaction is determined by the product of these variables, summed over all of the wavelengths

of sunlight. For example, the rate of formation of  $i$  during sunlight illumination of C is (Chu and Anastasio 2005):

$$R(C \rightarrow i)_{SUN} = (2.303 \times 10^3 / N_A) \times \Sigma (I'_\lambda \varepsilon_{C,\lambda} \Phi(C \rightarrow i)_\lambda \Delta\lambda) \times [C] \quad (18.1)$$

where  $N_A$  is Avogadro's number, the factor  $(2.303 \times 10^3 / N_A)$ ; units of  $\text{cm}^3 \text{ mol L}^{-1} \text{ molecule}^{-1}$ ) is for units and base conversion,  $\Delta\lambda$  is the size of each actinic flux wavelength interval (nm), and  $[C]$  is the molar concentration of C in the bulk (melted) snow. The rate of  $i$  formation is in units of  $\text{mol L}^{-1} \text{ s}^{-1}$ , expressed in terms of the bulk (melted) snow volume. The right-hand side of Eq. 18.1 is often re-expressed as the first-order photochemical rate constant,  $j(C \rightarrow i)_{SUN} (\text{s}^{-1})$ :

$$R(C \rightarrow i)_{SUN} = \Sigma (j(C \rightarrow i)_\lambda \Delta\lambda) [C] = j(C \rightarrow i)_{SUN} [C] \quad (18.2)$$

Calculating the rate of disappearance of C is simply done by replacing the quantum yield  $\Phi(C \rightarrow i)_\lambda$  in Eq. 18.1 with the quantum efficiency for loss of C.

Values of the actinic flux in snowpacks have been derived from measurements of irradiance as a function of depth in the snow (Galbavy et al. 2007a; Simpson et al. 2002). But since there are relatively few actinic flux measurements, values of  $I'_\lambda$  in the surface snow are more commonly obtained from models such as the NCAR TUV model (Madronich and Flocke 1998). For example, Fig. 18.4 shows TUV model output for four polar locations during summer or spring. Note that the shortest wavelength of sunlight present in polar locations is approximately 300 nm. As these values are actinic fluxes for the snow surface – while snow photochemical reactions can occur to depths of 10s of cm into the snowpack – actinic fluxes as a function of depth must be determined in order to determine the full rate of a process in the snowpack. This can either be done using measured e-folding depths for actinic flux or photolysis rate constants (i.e., the depth at which the actinic flux (or  $j$ ) is 1/e (37%) of its surface value) (Galbavy et al. 2007a, b; King and Simpson 2001) or through modeling (Lee-Taylor and Madronich 2002; Peterson et al. 2002; France et al. 2007).

### 18.3.2 Overview of Inorganic Chromophores

Most inorganic constituents in snow do not absorb tropospheric sunlight and thus have no direct photochemistry. This is the case, for example, with many of the inorganic compounds that are used as tracers in snow and ice cores, including the alkali metals (e.g., Li, Na, and K), alkali earth metals (e.g., Mg and Ca), and a wide array of non-metals (e.g.,  $\text{NH}_4^+$ ,  $\text{CO}_2(\text{aq})/\text{HCO}_3^-/\text{CO}_3^{2-}$ ,  $\text{SO}_4^{2-}$ ,  $\text{Br}^-$ , and  $\text{Cl}^-$ ). Some of these species – most notably  $\text{Br}^-$  and  $\text{Cl}^-$ , but also the carbonate species – are susceptible to indirect photochemical reactions, i.e., with photoformed oxidants such as  $\cdot\text{OH}$  (NIST 2002). But most of the rest are quite unreactive, whether with highly reactive  $\cdot\text{OH}$  or less reactive photooxidants.

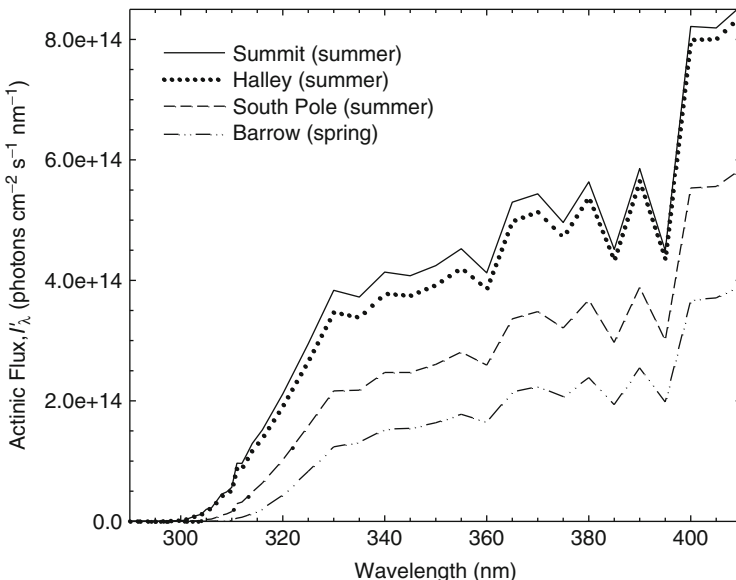


**Fig. 18.4** Modeled actinic fluxes from TUV (Madronich and Flocke 1998) for surface snow at four polar sites at solar noon: Summit, Greenland ( $72.6^{\circ}\text{N}$ ,  $38.5^{\circ}\text{W}$ ; June 21; 308 DU  $\text{O}_3$ ; 3.2 km elevation); Halley, Antarctica ( $75.6^{\circ}\text{S}$ ,  $26.5^{\circ}\text{W}$ ; Dec. 21; 270 DU; 33 m); South Pole ( $90^{\circ}\text{S}$ ; Dec. 21; 308 DU; 2.8 km); and Barrow, Alaska ( $71.3^{\circ}\text{N}$ ,  $156.8^{\circ}\text{W}$ ; Mar. 21; 460 DU; 9 m). Snow albedo was set at a wavelength-independent value of 0.90 (Halley and Barrow) or 0.93 (Summit and South Pole). The TUV model is available online at <http://cprm.acd.ucar.edu/Models/TUV/>

On the other hand, there are several snowpack inorganic compounds that do undergo direct photochemistry, most notably nitrate ( $\text{NO}_3^-$ ), nitrite ( $\text{NO}_2^-$ , and its acid forms), and hydrogen peroxide ( $\text{HOOH}$  or  $\text{H}_2\text{O}_2$ ). As shown in Fig. 18.5, all of these compounds absorb tropospheric sunlight, ranging from very weakly absorbing  $\text{HOOH}$  (which has a molar absorptivity at 300 nm of approximately  $1 \text{ M}^{-1} \text{ cm}^{-1}$ ) to modestly absorbing  $\text{HONO}$  (which has a peak molar absorptivity of  $57 \text{ M}^{-1} \text{ cm}^{-1}$  at 370 nm). Because the rate constant for photolysis depends on the product of  $I_\lambda$  times  $\epsilon_{\text{C},\lambda}$  (Eq. 18.1), chromophores which absorb at longer wavelengths – where there are more photons (Fig. 18.4) – are more likely to undergo rapid photolysis. Of course the rate of photolysis also depends upon the quantum yield and concentration of chromophore (Eq. 18.1); thus although  $\text{HOOH}$  is the weakest absorbing of the five chromophores shown in Fig. 18.5, values of  $\Phi_{\text{HOOH},\lambda}$  and  $[\text{HOOH}]$  are relatively large, and thus  $\text{HOOH}$  photolysis ends up being quite significant, as described below.

The snow photochemistries of the five species ( $\text{NO}_3^-$ , nitrite and its N(III) brethen, and  $\text{HOOH}$ ) are described below, with a particular focus on nitrate, since there are still some significant uncertainties about its photochemical fate. There are likely a number of other inorganic chromophores in snow, including peroxynitrite, peroxynitrate, and transition metals complexed with inorganic (and organic) ligands,

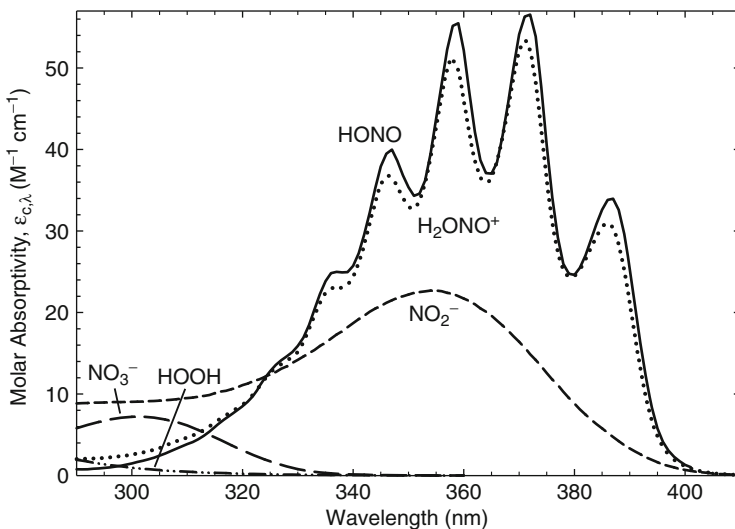


**Fig. 18.5** Base-10 molar absorptivities of five inorganic chromophores (C) in solution at 1°C: HONO (solid line; (Anastasio and Chu 2009)),  $\text{H}_2\text{ONO}^+$  (dotted line; (Anastasio and Chu 2009)),  $\text{NO}_2^-$  (short dash line; (Chu and Anastasio 2007)),  $\text{NO}_3^-$  (long dash line; (Chu and Anastasio 2003)), and HOOH (dash dot dot line; (Chu and Anastasio 2005))

such as  $\text{Fe(OH)(H}_2\text{O)}_5^{2+}$  and Fe-carboxylic acid complexes. Although these compounds are photoactive in solution (Faust and Hoigné 1990; Faust and Zepp 1993; Pehkonen et al. 1993), their photochemistry has not been examined on snow or ice and thus they are not included here.

### 18.3.3 Photochemistry of Nitrate

The current interest in snow photochemistry was largely ignited by field observations that sunlit snow at Summit, Greenland is a source of  $\text{NO}_x$  (i.e., NO and  $\text{NO}_2$ ) to the overlying atmosphere (Honrath et al. 1999). This is significant because  $\text{NO}_x$  plays a key role in a number of tropospheric reactions, including the formation of ozone, nitric acid and particulate nitrate (Finlayson-Pitts and Pitts 2000). The original observations were soon followed by a flurry of studies showing photochemical release of  $\text{NO}_x$  – as well as nitrous acid (HONO) – not only at Summit (Dibb et al. 2002; Honrath et al. 2002), but also at other Arctic locations (Beine et al. 2002; Zhou et al. 2001), in the Antarctic (Davis et al. 2001; Jones et al. 2000), and in mid-latitude snow (Honrath et al. 2000b).

From the initial field observations it was suggested that photolysis of nitrate ( $\text{NO}_3^-$ ) and/or nitrite ( $\text{NO}_2^-$ ) on snow grains was the source of snowpack  $\text{NO}_x$ , based on their photochemistries in solution (Honrath et al. 1999, 2000a). Subsequent work has strengthened this hypothesis and suggested that nitrate

**Table 18.1** Quantum yields for products from nitrate photolysis in liquid water and water ice<sup>a</sup>

Reference and year	Quantum yields						Notes	
	NO <sub>2</sub> + •OH	NO <sub>2</sub> <sup>-</sup> + O( <sup>3</sup> P)	^-OONO	T (K)	$\lambda$ (nm)	pH		
<i>Solution values</i>								
$\lambda \sim 200$ nm								
Goldstein and Rabani (2007)	0.13	0.21	0.28	297	205	4, 13	<sup>b</sup>	
Madsen et al. (2003)	$\leq 0.05$	$\leq 0.07$	0.48	—	200	—	<sup>c</sup>	
$\lambda \sim 250$ nm								
Goldstein and Rabani (2007)	0.037	0.065	0.102	297	254	4, 13	<sup>b</sup>	
Herrmann (2007)	0.094	—	—	298	248	8.5		
Mark et al. (1996)	0.09	<0.001	0.1	—	254	4–13	<sup>d</sup>	
	—	0.06	—	—	254	5	<sup>d</sup>	
$\lambda \geq 300$ nm								
Roca et al. (2008)	—	0.005; 0.008	—	298	310	4	<sup>e</sup>	
Goldstein and Rabani (2007)	~0.009	0.0094	<0.002	297	300	4, 13	<sup>b</sup>	
Chu and Anastasio (2003)	0.012	—	—	298	313	5	<sup>f</sup>	
Dubowski et al. (2002)	—	0.006	—	294	313	—	<sup>g</sup>	
Zellner et al. (1990)	0.017	—	—	298	308	4–9	<sup>h</sup>	
Warneck and Wurzinger (1988)	0.012	0.010; 0.012	—	295	305	3–11	<sup>i</sup>	
Zepp et al. (1987)	0.0092	0.0011	—	295	305	3–11	<sup>i</sup>	
	0.015	—	—	297	313	6.2, 8.2	<sup>j</sup>	
<i>Ice values</i>								
$\lambda > 300$ nm								
Chu and Anastasio (2003)	0.0040	—	—	263	313	5	<sup>f</sup>	
Dubowski et al. (2002)	0.0015	—	—	238	313	5	<sup>f</sup>	
Dubowski et al. (2001)	—	0.0015; 0.009	—	263	313	—	<sup>k</sup>	
	—	0.0006; 0.003	—	238	313	—	<sup>k</sup>	
	>0.005	0.0048	—	263	313	—	<sup>l</sup>	

<sup>a</sup>Values not reported in a given study are indicated by a dash here<sup>b</sup>Values of  $\Phi(\text{NO}_2 + \bullet\text{OH})$  were calculated based on the quantum yields for the other two channels; the value at 300 nm was not reported by the authors but was calculated here using their equation. Values of  $\Phi(\text{NO}_2^- + \text{O}(\text{P}^3))$  were measured in pH 4.2–4.5 solutions containing 10 mM formate as an  $\bullet\text{OH}$  scavenger. Values of  $\Phi(\text{^-OONO})$  were measured in pH 13 solutions containing 20 mM 2-propanol as an  $\bullet\text{OH}$  scavenger<sup>c</sup>Primary photoproducts measured over timescales of picoseconds.—OONO was identified as the cis isomer. The quantum yield for  $\bullet\text{O}_2^-$  and NO (or possibly  $\text{NO}^-$  and  $\text{O}_2$ ) was estimated as 0.08, while 44% of excited state  $\text{NO}_3^-$  decays to ground state. The temperature and solution pH were not specified, although solution pH was likely near neutral since experiments were performed on 14 mM aqueous  $\text{KNO}_3$  solutions<sup>d</sup>Data on the first line are quantum yields determined in the absence of an  $\bullet\text{OH}$  scavenger. In the second line the nitrite quantum yield was determined in the presence of 10 mM methanol as an  $\bullet\text{OH}$  scavenger<sup>e</sup>The first value for  $\Phi(\text{NO}_2^- + \text{O}(\text{P}^3))$  is for solutions containing 0.01 M  $\text{NaNO}_3$  with no added formate. The second value is the result from 0.01 M  $\text{NaNO}_3$  solutions with 0.01 M formate as an  $\bullet\text{OH}$  scavenger

(continued)

**Table 18.1** (continued)

<sup>f</sup>Values of  $\Phi(\text{NO}_2 + \cdot\text{OH})$  were determined in solutions containing 450  $\mu\text{M}$  benzoate/benzoic acid and 200  $\mu\text{M}$   $\text{NO}_3^-$ . In the frozen samples at 263 K the calculated nitrate concentration in the QLL is 0.85 M. Listed pH values for the ice experiments are for the sample solutions prior to freezing. On ice, quantum yields for  $\cdot\text{OH}$  decreased with increasing acidity in samples made from solutions with pH values below 5

<sup>g</sup>Solutions contained 10 mM  $\text{NaNO}_3$  and no  $\cdot\text{OH}$  scavenger

<sup>h</sup>Solutions contained 3 mM  $\text{KNO}_3$  and 300 mM thiocyanate as an  $\cdot\text{OH}$  scavenger

<sup>i</sup>On the first line: (1) the listed  $\Phi(\text{NO}_2 + \cdot\text{OH})$  value is the average for all experiments over the entire range of 2-propanol concentrations employed (1.3–130 mM; pH 3–11), and (2) the two  $\Phi(\text{NO}_2^- + \text{O}(\text{P}^3))$  values are for experiments with pH 4–5.6 and pH 9–11, respectively, in solutions containing 130 mM 2-propanol as an  $\cdot\text{OH}$  scavenger. On the second line: (1) the  $\Phi(\text{NO}_2 + \cdot\text{OH})$  value is an average from experiments using the lowest 2-propanol concentrations (1.3 and 13 mM), and (2)  $\Phi(\text{NO}_2^- + \text{O}(\text{P}^3))$  was determined by measuring  $\text{O}(\text{P}^3)$  production using 5 mM added cyclohexene (pH 5.6)

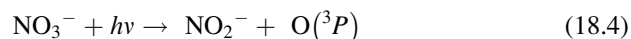
<sup>j</sup>Solutions contained 0.2–4.0 mM  $\text{NaNO}_3$  and < 300  $\mu\text{M}$  of organics used as  $\cdot\text{OH}$  scavengers and probes

<sup>k</sup>The first entry in each pair of  $\Phi(\text{NO}_2^- + \text{O}(\text{P}^3))$  values was measured in ice pellets made from solutions containing 10 mM  $\text{NaNO}_3$  and no added formate. The second entry in each pair was measured in ice pellets made from solutions containing 1 mM  $\text{NaNO}_3$  and 10 mM formate as an  $\cdot\text{OH}$  scavenger

<sup>l</sup>Solutions contained 10 mM  $\text{NaNO}_3$  and no added  $\cdot\text{OH}$  scavenger. The value for  $\Phi(\text{NO}_2 + \cdot\text{OH})$  is the calculated primary quantum yield for  $\text{NO}_2$  based on the measured  $\text{NO}_2$  flux after correcting for photolytic losses due to slow diffusion from the ice matrix

photolysis is also responsible for release of HONO (Anastasio and Chu 2009; Boxe et al. 2006; Cotter et al. 2003; Dubowski et al. 2001; Chu and Anastasio 2003; Jacobi and Hilker 2007, Simpson et al. 2002). Nitrate is one of most abundant trace constituents in snow, with typical snow concentrations on the order of 1–5  $\mu\text{M}$  (expressed in terms of the melted snow volume) (Burkhart et al. 2004, 2009; Mulvaney et al. 1998).

In aqueous solution, nitrate irradiation results in three reaction channels (Mack and Bolton 1999):



Note that the  $\cdot\text{O}^-$  in Eq. 18.3 is rapidly protonated to form  $\cdot\text{OH}$ . Despite this apparent simplicity, nitrate photolysis is complicated by a number of factors. The first complicating factor is illumination wavelength: as shown in Table 18.1, for any given channel the quantum yield for the strong  $\pi \rightarrow \pi^*$  transition (peak  $\lambda \approx 200$  nm) is significantly higher than the value in the weak  $n \rightarrow \pi^*$  transition (peak  $\lambda = 301$  nm; Fig. 18.4). The second complicating factor is that the products from each channel can react, which makes the experimental results dependent both upon

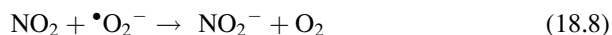
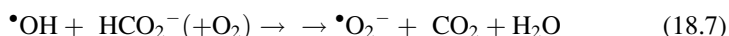
the timescale of measurement as well as the composition of the solution. For example, because the hydroxyl radical formed in Eq. 18.3 reacts rapidly with  $\text{NO}_2^-$  (the product from Eq. 18.4), the quantum yield for the nitrite channel is higher in the presence of  $\cdot\text{OH}$  scavengers. Table 18.1 summarizes the reported quantum yields for each of these nitrate photolysis channels.

As shown in Table 18.1, there are some discrepancies in the quantum yields for formation of  $\text{NO}_2$  and  $\cdot\text{OH}$  from nitrate illumination (Eq. 18.3) with shorter wavelengths ( $\lambda \leq 254$  nm), as described by (Goldstein and Rabani 2007). But for tropospherically relevant wavelengths ( $\lambda \geq 300$  nm) there is good agreement that  $\Phi(\text{NO}_2 + \cdot\text{OH})$  is approximately 0.01 at room temperature. In addition, the quantum yields for ice and solution samples fit the same temperature dependence equation, suggesting that the photochemistry on ice is occurring in a liquid-like environment, i.e., in quasi-liquid layers (QLL's) (Dubowski et al. 2001; Chu and Anastasio 2003); similar behavior has also been seen for  $\text{HOOH}$  and  $\text{H}_2\text{ONO}^+$  (Anastasio and Chu 2009; Chu and Anastasio 2005). Although the quantum yield for nitrite decreases at very high nitrate concentrations (above approximately 1 M) (Roca et al. 2008), in the study of (Chu and Anastasio 2003) the solution and ice quantum yields for  $\text{NO}_2$  and  $\cdot\text{OH}$  are described by the same Arrhenius equation even though the nitrate concentration in the QLL of the frozen sample is approximately 1 M, much higher than in solution (Table 18.1). Finally, although  $\Phi(\text{NO}_2 + \cdot\text{OH})$  is different between the 200- and 300-nm absorbance bands (Table 18.1), this quantum yield is independent of illumination wavelength within the 300-nm band (Chu and Anastasio 2003; Zellner et al. 1990).

As seen for the  $\text{NO}_2 + \cdot\text{OH}$  channel, quantum yields for the second channel of nitrate photolysis, producing  $\text{NO}_2^-$  and  $\text{O}({}^3P)$  (Eq. 18.4), are also higher for the 200-nm band compared to the 300-nm band (Table 18.1). In the 300-nm band at room temperature, quantum yields for nitrite range from approximately 0.005–0.01. The 0.001 value for this channel determined by measuring  $\text{O}({}^3P)$  seems anomalously low (Table 18.1; Warneck and Wurzinger data) and is not recommended. For experiments where nitrite was measured, quantum yields are higher in samples that contained an organic compound to scavenge  $\cdot\text{OH}$ , which is produced from Eq. 18.3. There are two reasons for this (Dubowski et al. 2002; Goldstein and Rabani 2007). The first is that, in the absence of a scavenger,  $\cdot\text{OH}$  reacts at diffusion-controlled rates with  $\text{NO}_2^-$  (Eq. 18.6) to decrease nitrite concentrations (and the apparent nitrite quantum yield):



The second reason is that organic scavengers such as formate ( $\text{HCO}_2^-$ ) also convert  $\cdot\text{OH}$  into  $\cdot\text{O}_2^-$ , which can react with  $\text{NO}_2$  to form  $\text{NO}_2^-$ :



In solution (298 K) the value of  $\Phi(\text{NO}_2^- + \text{O}^{(3P)})$  in the presence of formate is 1.6 times higher than the value determined in the absence of formate (Table 18.1; Roca et al. data). However, there is a greater effect in ice samples, with  $\Phi(\text{NO}_2^- + \text{O}^{(3P)})$  larger by a factor of 5–6 in the presence of formate (Table 18.1, Dubowski et al. 2002 ice data).

Which condition – with or without formate – is more representative of environmental samples? In natural water samples, whether liquid or frozen, organic compounds will generally be the major sink for  $\cdot\text{OH}$ , whereas nitrite will be a minor sink (Anastasio et al. 2007; Arakaki and Faust 1998; Zepp et al. 1987). On the other hand, while organic compounds in solution generally convert  $\cdot\text{OH}$  into  $\cdot\text{O}_2^-$  (Graedel and Weschler 1981), the extent of this conversion varies with different organic molecules (Hullar and Anastasio 2011). Furthermore, the dominant fate of  $\cdot\text{O}_2^-$  in natural samples is unlikely to be reaction with  $\text{NO}_2$  (Eq. 18.8), but rather is probably disproportionation of  $\cdot\text{O}_2^-/\text{HO}_2^\bullet$  into  $\text{HOOH}$ , at least at pH values of 6 or below where this reaction is rapid (Bielski et al. 1985). Thus values of  $\Phi(\text{NO}_2^- + \text{O}^{(3P)})$  determined in the absence of an  $\cdot\text{OH}$  scavenger most likely underestimate the actual values in environmental samples, but quantum yields determined in the presence of formate as an  $\cdot\text{OH}$  scavenger likely overestimate the actual values in environmental samples. The environmental value of the nitrite quantum can be estimated by subtracting the influence of formate-mediated  $\text{NO}_2^-$ -formation (via Eqs. 18.7 and 18.8) from the nitrite quantum yield measured in the presence of formate. Assuming that every  $\cdot\text{OH}$  formed reacts with formate to ultimately produce  $\text{NO}_2^-$ , this yields:

$$\Phi(\text{NO}_2^- + \text{O}^{(3P)})_{\text{ENVT}} \approx \Phi(\text{NO}_2^- + \text{O}^{(3P)})_{\text{FORMATE}} - \Phi(\text{NO}_2 + \cdot\text{OH}) \quad (18.9)$$

where the first term is the estimated nitrite quantum yield in environmental samples, the second term is the measured nitrite quantum yield in the presence of formate, and the third term is the measured quantum yield for  $\cdot\text{OH}$  (and  $\text{NO}_2$ ). Substituting in values for the second (0.009) and third (0.0040) terms from Table 18.1, gives an estimated value for  $\Phi(\text{NO}_2^- + \text{O}^{(3P)})_{\text{ENVT}}$  of 0.005 at 263 K. The fact that this estimated “environmental” nitrite quantum yield is slightly larger than the  $\text{NO}_2 + \cdot\text{OH}$  quantum yield (i.e., the “major” channel) is somewhat surprising because in solution the nitrite quantum yield in the presence of formate (or other  $\cdot\text{OH}$  scavenger) is no larger than the  $\text{NO}_2 + \cdot\text{OH}$  quantum yield. Thus a value of  $\Phi(\text{NO}_2^- + \text{O}^{(3P)})_{\text{ENVT}}$  of 0.005 is likely too high, probably because the value for  $\Phi(\text{NO}_2^- + \text{O}^{(3P)})_{\text{FORMATE}}$  at 263 K (0.009; Table 18.1) is incorrectly high. Indeed, comparing the 263 K nitrite quantum yield with the room temperature solution values (all with  $\cdot\text{OH}$  scavengers) suggests the 263 K value is too high since it is as large as the solution values (Table 18.1). In contrast, the value of  $\Phi(\text{NO}_2 + \cdot\text{OH})$  at 263 K is a factor of 3 lower than the 298 K value. Thus at the present time, the value 0.0015, determined in the absence of formate, is recommended for  $\Phi(\text{NO}_2^- + \text{O}^{(3P)})$  on ice at 263 K. But clearly there is a need for further study of this reaction on ice.

**Table 18.2** Photolysis of inorganic chromophores in snow under conditions at Halley, Antarctica (75.6°S, 26.5°W) on the austral summer solstice (Dec. 21) at midday (263 K)

Chromophore	$j_C^a$ ( $10^{-6}$ s $^{-1}$ )	$\tau_C^b$ (hr)	Chromophore conc. in snow <sup>c</sup> (nmol L $^{-1}$ )	Kinetics of product ( $P$ ) formation		
				Product(s)	$j(C \rightarrow i)^d$ ( $10^{-6}$ s $^{-1}$ )	Rate (nmol L $^{-1}$ h $^{-1}$ )
HOOH	2.0	140	5,000	•OH	3.9	70
$\text{NO}_3^-$	$0.3^e$	$1000^e$	2,600	$\text{NO}_2 + \cdot\text{OH}$	0.20	1.9
				$\text{NO}_2^- + \text{O}({}^3P)$	$0.08^e$	$0.7^e$
				$\text{OONO}^-$	<0.04	<0.3
$\text{NO}_2^-$	27	11	33	$\text{NO} + \cdot\text{OH}$	27	3.2
HONO <sup>f</sup>	490	0.57	0.2	$\text{NO} + \cdot\text{OH}$	500	0.4
$\text{H}_2\text{ONO}^{+f}$	66	4.2	0.0001	$\text{NO} + \cdot\text{OH}$	70	0.00002

<sup>a</sup>Rate constant for photolytic loss of chromophore C. For hydrogen peroxide the rate constant for •OH formation is twice the rate constant for HOOH loss ( $\text{HOOH} + h\nu \rightarrow 2 \cdot\text{OH}$ ). For nitrate the rate constant for loss of nitrate is equal to the sum of the rate constants of the three product channels

<sup>b</sup>Lifetime for chromophore with respect to direct photolysis at midday, calculated as  $1/j_C$

<sup>c</sup>Typical surface snow concentrations in coastal Antarctica during midsummer. References: HOOH (Neumayer data from Jacob and Klockow (1993)),  $\text{NO}_3^-$  and  $\text{NO}_2^-$  (Halley data from Jones et al. (2008)). Note that the measured nitrite concentration likely represents all three forms of N(III), although it is dominated by nitrite

<sup>d</sup>Rate constant for formation of product  $i$  from photolysis of chromophore C

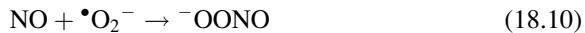
<sup>e</sup>These italicized values are uncertain because of the uncertainty in the quantum yield for nitrite formation from nitrate photolysis (see text). A value of  $\Phi(\text{NO}_2^- + \text{O}({}^3P))$  of 0.0015 was used here, but this quantum yield might be as high as 0.005 (see text)

<sup>f</sup>Italicized values are uncertain because of great uncertainty in the concentrations of HONO and  $\text{H}_2\text{ONO}^+$ , which were estimated using the measured  $\text{NO}_2^-$  concentration and assuming that the QLLs of the snow grains have a pH of 5. Based on reported pKa values for N(III) in solution (Riordan et al. 2005), at pH 5 the mole fractions of  $\text{NO}_2^-$ , HONO, and  $\text{H}_2\text{ONO}^+$  are 0.99, 0.0063, and  $3.1 \times 10^{-6}$ , respectively. The concentrations and photolysis rates for HONO and  $\text{H}_2\text{ONO}^+$  are strongly dependent upon QLL pH: for example, compared to pH 5, at pH 4 the concentrations of HONO and  $\text{H}_2\text{ONO}^+$  (and their photolysis rates) would be higher by 10 and 100 times, respectively, while  $\text{NO}_2^-$  would only decrease by approximately 5%

The quantum yield for the third channel of nitrate photolysis, to form peroxynitrite ( $\text{OONO}^-$ ), is also somewhat uncertain. At short illumination wavelengths, this is the dominant channel, accounting for 48% of nitrate excited states at picosecond time scales during 200 nm irradiation (Table 18.1; Madsen et al. data). At longer time scales (minutes), the quantum yield is somewhat lower (28%, Table 18.1), but still very large at these short wavelengths. It has been suggested that this channel is also significant during illumination of nitrate with tropospherically relevant wavelengths, but recent results (Goldstein and Rabani 2007) indicate that this is a minor pathway, accounting for the fate of less than 0.2% of the nitrate excited state formed during illumination with 300 nm radiation (Table 18.1). Adjusting this upper bound to ice temperatures using the activation energy for channel 1 (20 kJ mol $^{-1}$  (Chu and Anastasio 2003)), gives a quantum yield for  $\text{OONO}^-$  at 263 K of < 0.0007, i.e., at least 6 times lower than the corresponding quantum yield for  $\text{NO}_2^- + \cdot\text{OH}$ .

Table 18.2 shows calculated rates of nitrate photolysis on snow grains at 263 K under midday, summer solstice conditions at Halley, Antarctica. Based on the recommended quantum yields for the three channels of nitrate photolysis (Fig. 18.6 and text above), the rate of  $\text{NO}_2$  formation (Eq. 18.3) is nearly 3 times faster than the rate of  $\text{NO}_2^-$  formation (Eq. 18.4), while direct formation of peroxy nitrite (Eq. 18.5) is, at most, 15% of the  $\text{NO}_2$  rate. Given the relatively inefficient quantum yields for nitrate photolysis, the lifetime for  $\text{NO}_3^-$  with respect to direct photolysis is quite long, on the order of 1,000 h (of midday, summer solstice sunlight).

Although the formation of peroxy nitrite directly from nitrate photolysis appears to be insignificant in polar snow, this molecule is likely formed on snow grains via other pathways, and it is probably significant in snow photochemistry (Anastasio and Chu 2009; Honrath et al. 2000a). The most likely formation pathway on snow grains is, by analogy to solution reactions (NIST 2002), via the combination of NO (formed from N(III) photolysis, e.g., Eq. 18.14) with superoxide ( $\cdot\text{O}_2^-$ ) or hydroperoxyl radical ( $\text{HO}_2^\bullet$ ):



These two forms – peroxy nitrite and peroxy nitrous acid (HOONO) – are an acid–base pair, with a pKa of 6.5 (Mack and Bolton 1999). The pH values of quasi-liquid layers in most snowpacks are probably acidic (although perhaps not in regions with high sea-salt inputs and low acid inputs), thus HOONO is likely the most abundant form. HOONO is unstable, rapidly converting to nitrate with a lifetime on the order of 1 s (Mack and Bolton 1999), although Goldstein and Rabani (2007) suggest that a portion also decomposes to  $\cdot\text{OH}$  and  $\text{NO}_2$ . Thus HOONO is unlikely to be an important reactant on the snow grains. However, a significant portion of QLL HOONO likely evaporates to the firn air, since mass transport from surface quasi-liquid layers might have characteristic times smaller than 1 s (Anastasio and Chu 2009). Thus snow-grain reactions might be a significant source of HOONO to the firn air and overlying boundary layer. Similarly, snow-grain reactions of  $\text{NO}_2$  (from nitrate photolysis, Eq. 18.3) with  $\cdot\text{O}_2^-$  or  $\text{HO}_2^\bullet$  can form peroxy nitrous acid (HOONOO), which could then evaporate to the firn air (Anastasio and Chu 2009).

### 18.3.4 Photochemistry of N(III) (Nitrite, Nitrous Acid, and Nitrous Acidium Ion)

Nitrite in snowpacks is formed via the photolysis of nitrate (Eq. 18.4) as well as from the reduction of  $\text{NO}_2$  (e.g., by  $\cdot\text{O}_2^-$  in Eq. 18.8). While it had been thought that nitrate photolysis is the dominant source of  $\text{NO}_x$  and HONO from sunlit snowpacks, recent modeling and field work has shown that photolysis of nitrite

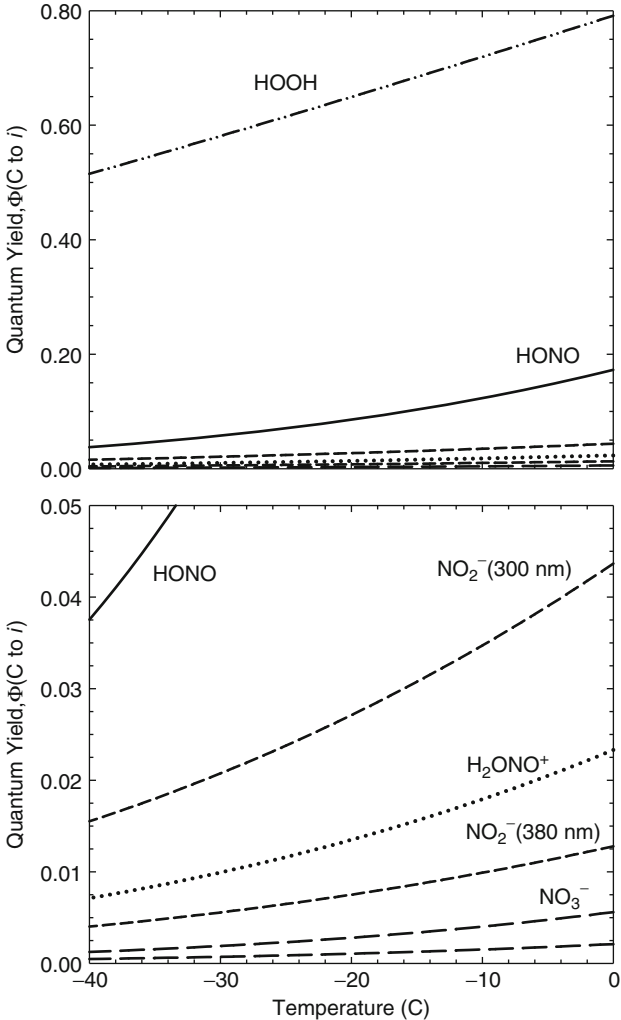


**Fig. 18.6** Quantum yields for product  $i$  ( $\bullet\text{OH}$ ,  $\text{NO}$ , and/or  $\text{NO}_2$ ) from photolysis ( $\lambda \geq 300 \text{ nm}$ ) of five chromophores (C):  $\text{HOOH}$  (dash dot dot line (Chu and Anastasio 2005)),  $\text{HONO}$  (solid line (Anastasio and Chu 2009)),  $\text{NO}_2^-$  at 300 and 380 nm (short dash line (Chu and Anastasio 2007)),  $\text{H}_2\text{ONO}^+$  (dotted line (Anastasio and Chu 2009)), and  $\text{NO}_3^-$  (long dash line (Chu and Anastasio 2003)). The top panel shows all of the data (with all but  $\text{HOOH}$  and  $\text{HONO}$  nearly indistinguishable from the x-axis), while the bottom panel focuses on the bottom portion of the quantum yield range. The two lines for  $\text{NO}_3^-$  represent the two photolysis channels:  $\text{NO}_2 + \bullet\text{OH}$  (Eq. 18.3; top long dashed line) and  $\text{NO}_2^- + \text{O}(\text{P})$  (Eq. 18.4; bottom long dashed line). The lines represent regression equations to laboratory solution and ice data for each of the chromophores, except for  $\text{HONO}$ , which was studied only in solution (1–10°C), and the second channel of nitrate photolysis ( $\text{NO}_3^- \rightarrow \text{NO}_2^- + \text{O}(\text{P})$ ), which combines the 0.0015 value at 263 K from (Dubowski et al. 2002) with the temperature dependence for the first channel (Chu and Anastasio 2003). These quantum yields are independent of wavelength ( $\lambda \geq 300 \text{ nm}$ ) except for  $\text{NO}_2^-$ , whose quantum yield decreases with increasing wavelength between approximately 300 and 380 nm (Chu and Anastasio 2007). Note that the quantum yields for  $\bullet\text{OH}$  and  $\text{NO}_2$  from  $\text{NO}_3^-$  photolysis are for ices made from solutions of pH 5; quantum yields decrease with increasing acidity (Chu and Anastasio 2003)

and other N(III) species can make important contributions (Anastasio and Chu 2009; Chu and Anastasio 2007; Jones et al. 2008). This was initially unexpected since the concentrations of nitrite in snow are approximately 100 times smaller than those of nitrate.

There are three major N(III) species: nitrite ( $\text{NO}_2^-$ ), nitrous acid (HONO), and nitrous acidium ion ( $\text{H}_2\text{ONO}^+$ ). In solution (or, presumably, in QLLs), these three forms are in acid–base equilibrium:



with pKa values for HONO and  $\text{H}_2\text{ONO}^+$  of 2.8 and 1.7, respectively (Anastasio and Chu 2009; Riordan et al. 2005). Compared to nitrate, the N(III) species have higher molar absorptivities, and absorb at longer wavelengths (Fig. 18.5), which leads to higher rates of sunlight absorbance for N(III). In addition, the N(III) species – especially aqueous HONO – have higher quantum yields than nitrate (Fig. 18.6). The quantum yields for  $\text{NO}_2^-$  photolysis are somewhat complicated as they are dependent upon wavelength as well as temperature; at 263 K they range from 0.046 at 290 nm to 0.012 at  $\lambda > 370$  nm (Fischer and Warneck 1996; Chu and Anastasio 2007). In contrast, quantum yields for HONO and  $\text{H}_2\text{ONO}^+$  are wavelength independent (for  $\lambda > 300$  nm), with values at 263 K of 0.18 and 0.024, respectively (Anastasio and Chu 2009).

Photolysis of N(III), whether in solution or ice, forms NO and  $\bullet\text{OH}$  (Anastasio and Chu 2009; Chu and Anastasio 2007). For example, in the case of nitrite, this process is



where, again,  $\bullet\text{O}^-$  is rapidly protonated to  $\bullet\text{OH}$ . Based on modeling (Anastasio and Chu 2009; Chu and Anastasio 2007) and measurements (Jones et al. 2008), even though concentrations of N(III) are 100–1,000 times lower than  $\text{NO}_3^-$  in surface snow, the rate of NO release from N(III) photolysis can be comparable to the rate of  $\text{NO}_2$  release from nitrate photolysis. For example, under the summer solstice conditions at Halley shown in Table 18.2, the rate constant for nitrite photolysis ( $2.7 \times 10^{-5} \text{ s}^{-1}$ ) is 100 times greater than the combined rate constants for nitrate photolysis ( $2.8 \times 10^{-7} \text{ s}^{-1}$ ). Because of this, the rate of NO release from nitrite photolysis is comparable to the combined rates of  $\text{NO}_2$  and  $\text{NO}_2^-$  release from nitrate photolysis. Furthermore, because the photolysis rate of aqueous-phase HONO is approximately 20 times greater than that of nitrite (Table 18.2), nitrous acid can also contribute significantly, even under conditions where it is only a very small portion of N(III) in the QLL. For example, for a QLL pH of 5 under these Halley conditions, HONO photolysis accounts for 10% of NO release from N(III) photolysis, even though HONO accounts for only 0.6% of N(III) (Table 18.2).

In more acidic snow, this contribution will increase (because of a higher mole fraction of HONO), although this also suppresses the total amount of N(III) in snow grains because of the rapid photolysis and volatilization of HONO (Anastasio and Chu 2009). In very acidic snow grains, the dominant N(III) species becomes  $\text{H}_2\text{ONO}^+$ , which is both a photochemical source of NO (Table 18.2) as well as a thermal source of oxidized halogens and HOONO (Anastasio and Chu 2009; Hellebust et al. 2007b).

### 18.3.5 Photochemistry of Hydrogen Peroxide

Hydrogen peroxide ( $\text{HOOH}$  or  $\text{H}_2\text{O}_2$ ) is a moderately stable tracer of the atmosphere's oxidizing capacity, whose snow concentration is often highest in summer and lowest in winter (Hutterli et al. 2003; Jacob and Klockow 1993). Although it only very weakly absorbs tropospheric sunlight (Fig. 18.5), HOOH has the highest quantum yield of the identified inorganic chromophores (Fig. 18.6), and, typically, one of the highest concentrations compared to other trace species in polar snowpacks (Grannas et al. 2007). Thus the product of these three parameters (Eq. 18.1) leads to the highest rate of photolysis among the inorganic chromophores considered here. As shown in Table 18.2 for Halley conditions, the rate of  $\cdot\text{OH}$  formation from HOOH photolysis is  $70 \text{ nmol L}^{-1} \text{ h}^{-1}$ , which is an order of magnitude higher than the sum of the rates of  $\cdot\text{OH}$  (or  $\text{NO}_x$ ) formation from photolysis of  $\text{NO}_3^-$  and  $\text{NO}_2^-$ . This has two main ramifications. The first is that, in contrast to what was initially predicted, nitrate and nitrite are minor sources of  $\cdot\text{OH}$  that are dwarfed by HOOH photolysis (Anastasio et al. 2007; Chu and Anastasio 2005). The second ramification is that the flux of  $\cdot\text{OH}$  in snow grains is much greater (by a factor of approximately 10) than the flux of  $\text{NO}_x$ , which is important for understanding the overall chemical budget of snowpacks. For example, since the major sink for  $\cdot\text{OH}$  is likely organic compounds, the high photochemical flux of  $\cdot\text{OH}$  implies rapid oxidation of snow-grain organics, which likely leads to release of volatile organics such as formaldehyde into the firn air and boundary layer (Anastasio et al. 2007; Sumner et al. 2002).

### 18.3.6 Unresolved Issues

#### 18.3.6.1 Light Absorbance by Chromophores in/on Ice

There are currently only a very few measurements of light absorbance by chromophores on ice and none of the measurements are quantitative. Based on these data, it appears that light absorption by frozen chromophores is qualitatively very similar to solution data (Dubowski et al. 2001; Matykiewiczová et al. 2007b), but this is an issue that has not been examined critically. A few measurements in

solution have shown that molar absorptivities for many inorganic chromophores are nearly independent of temperature down to 1°C (Chu and Anastasio 2003, 2005, 2007). However, it would be very useful to have quantitative molar absorptivity measurements of inorganic and organic chromophores in ice as a function of temperature and ice composition, especially as related to differences in quasi-liquid layer thicknesses and QLL pH values. Furthermore, bulk light absorbance measurements on (melted) snow from Summit, Greenland and Dome C, Antarctica, have revealed that  $\text{NO}_3^-$ , HOOH, and N(III) together typically account for only approximately half of total light absorbance by soluble chromophores (Anastasio and Robles 2007), indicating that there are likely many other species that need to be identified and characterized.

### 18.3.6.2 Quantum Yields for Nitrite and Peroxynitrite Formation from Nitrate Photolysis

There is a large amount of uncertainty in values of  $\Phi(\text{NO}_2^- + \text{O}({}^3P))$  determined on ice, with values determined in the presence of formate 5–6 times greater than those determined in the absence of formate (Table 18.1). As described above, while the quantum yield for this reaction in the environment is likely intermediate between these values, that leaves a significant range of uncertainty. In addition, the temperature dependence of this quantum yield is unclear. There is also the question of the quantum yield for peroxy nitrite formation (Eq. 18.5). At present, the upper bound for this reaction is high enough that it could lead to a minor, but still significant, flux of reactive N from nitrate photolysis. A better understanding of both of these quantum yields would help constrain snowpack nitrogen chemistry and its impacts upon boundary layer  $\text{NO}_x$ , HONO, and HOONO.

### 18.3.6.3 pH Values of Snow-Grain Quasi-Liquid Layers

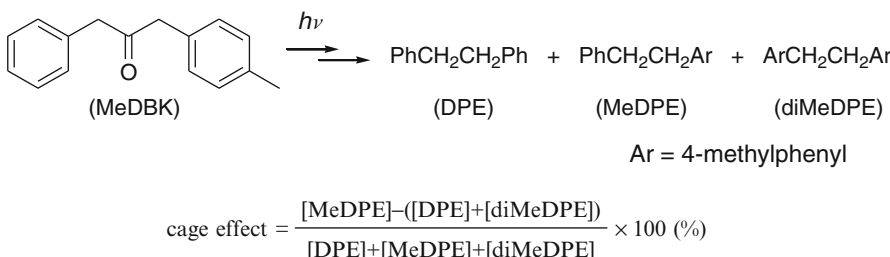
Constraining the fluxes of  $\text{NO}_x$  and HONO from sunlit snowpacks requires that the speciation of N(III) is understood, which in turn requires knowledge of the pH of snow-grain quasi-liquid layers. Similarly, there are many other condensed-phase reaction systems that are pH dependent, from halide oxidation (Anastasio and Matthew 2006) to acid–base speciation and volatilization of small organic acids (Dibb and Arsenault 2002). Despite this, there are currently no measurements of QLL pH values in authentic snow samples. There has been progress made on measuring pH in the QLLs of laboratory ices (Robinson et al. 2006), but a technique for measuring pH in ambient samples, especially *in situ*, is an important component that is missing from our toolkit.

## 18.4 Photochemistry of Organic Compounds in Ice and Snow

Organic compounds are significant constituents of the atmosphere (Heintzenberg 1989). Dicarboxylic acids, for example, which are very abundant in aerosols (Sempere and Kawamura 1994), have been proposed to play an important role in ice nucleation processes in the atmosphere (Andreae and Rosenfeld 2008; Du and Ariya 2008). Despite little data, it is now also evident that organic compounds are present in terrestrial snow and ice at significant concentrations (Grannas et al. 2006, 2007). The total organic carbon (TOC) in snow was found in concentrations in the order of  $0.1 \text{ mg L}^{-1}$  at remote high latitude sites (Grannas et al. 2004; Twickler et al. 1986). Many natural and anthropogenic organic compounds, such as polycyclic aromatic hydrocarbons (Jaffrezo et al. 1994; Masclet et al. 2000), phthalates and phenols (Grollert and Puxbaum 2000), carbonyl compounds (Houdier et al. 2002; Perrier et al. 2002), carboxylic acids (Dibb and Arsenault 2002; Legrand and Deangelis 1995; Narukawa et al. 2003), persistent organic pollutants (Blais et al. 1998; Garbarino et al. 2002; Herbert et al. 2005; Lode et al. 1995; Villa et al. 2003), and humic-like compounds (Calace et al. 2001; Grannas et al. 2004), have been identified in cold regions. Snow at closer proximity to urban sources will undoubtedly be even more polluted. There are field evidences that some of the organic compounds are photochemically produced or processed in polar snowpacks (Bottenheim et al. 2002; Boudries et al. 2002; Grannas et al. 2007; Guimbaud et al. 2002; Hutterli et al. 2004; Klán et al. 2003; Swanson et al. 2002).

### 18.4.1 *Organic Compounds on the Surface of Ice and Snow Crystals*

In general, adsorption, desorption, the magnitude and type of intermolecular interactions, as well as diffusion of the chemical species (contaminants) in/on ice are temperature- and phase-dependent variables (Abbatt 2003; Heger et al. 2005; Cho et al. 2002; Roth et al. 2004). Ice surface and organic contaminant–ice interactions were studied by various methods, including infrared and Raman spectroscopy, combined with computer modeling (Devlin 1992; Devlin and Buch 1995). Three different types of surface water molecules have been identified, including those with dangling hydrogen or oxygen atoms. The adsorbed states of some organic molecules, such as acetonitrile, chloroform (Schaff and Roberts 1999), acetone (Bartels-Rausch et al. 2004, 2005; Schaff and Roberts 1998), benzene derivatives (Borodin et al. 2004), or formic and acetic acids (Hellebust et al. 2007a) were examined by desorption mass, electron, or absorption spectroscopy, revealing the importance of hydrogen-bonding or dipolar interactions. The nature and magnitude of the intermolecular interactions of some dipolar organic solvatochromic (Reichardt 1994) indicators in frozen solutions at 253 or 77 K was also studied using empirical solvent polarity parameters (Heger and Klán 2007). A solvatochromic effect originates from a different degree of solvent



**Scheme 18.2** Photochemistry of 4-methyldibenzyl ketone and the cage effect

molecules orientation around a dipolar ground state probe and from the dipole moment change when the chromophores are electronically excited. This work suggested that hydrogen-bond and electron-pair donating ice–contaminant interactions are substantially larger than those found in liquid aqueous solutions.

Until the layers surrounding the crystal walls containing rejected organic solutes are solidified, molecular translational motion (diffusion) and large conformational changes are possible (Klán et al. 2000a), although with still increasing restrictions as temperature further drops. The freezing process in terrestrial ices can never be too fast due to moderate temperatures; therefore, organic hydrophobic compounds should have sufficient time to self-organize. Klán and coworkers studied the Norrish type I reaction of 4-methyldibenzyl ketone (MeDBK), producing the primary benzyl radicals and subsequently their recombination products (Scheme 18.2) in frozen aqueous solutions over a temperature range of 273–193 K (Ruzicka et al. 2005). It was found that heterogeneous environment caused a remarkable cage effect (Ramamurthy 1991) (the equation in Scheme 18.2, where the photoproduct concentrations are in moles (Engel 1970)) on the product mixture due to restricted diffusion of the radical intermediates. The cage effect was found to increase consistently with decreasing temperature, and eventually leveled off to 100% below 203 K (Fig. 18.7). The data points were closely fitted with a Boltzmann sigmoidal curve which allowed estimating the inflection point at ~223 K, at which the rates of radical diffusion and recombination become equal. The concept of “reactive cavity” as a time-independent structural constraint imposed by the medium must be qualified in the case of ice, and more so for the environment provided by the quasi-liquid layer. The “effective reaction cavity” will depend on the lifetime of the chromophore excited state and the dynamics of the cavity. The actual geometry of ice cavities may be two- or three-dimensional. The quasi-liquid layer may actually behave as a two-dimensional supercage. In other words, the effective constraints will depend on the solute as well. How easily a medium responds to shape changes or volume demands that occur during the course of a reaction depends on the microviscosity of the medium and the cooperativity of motions involving host and guest molecules. The cavity may be active (water molecules of ice could interact with polar and H-bonding species) or passive (non-reactive). Finally, it should be borne in mind that geometry and polarizability of the excited states are in general different from ground states.

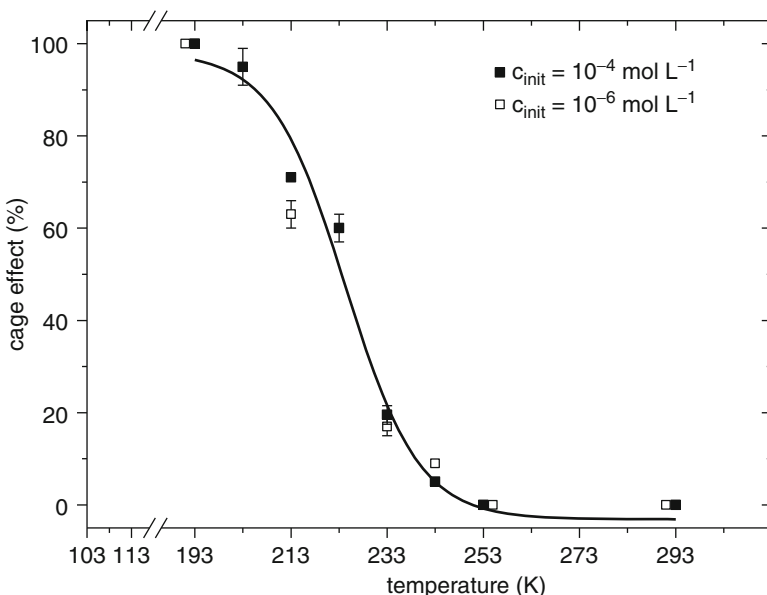


**Fig. 18.7** Temperature dependence of the cage effect in the photolysis of MeDBK in ice (Ruzicka et al. 2005)

During snow precipitation, falling ice (snow) crystals can scavenge atmospheric aerosols and gaseous compounds (Hoff et al. 1995; Wania et al. 1998, 1999a, b). Trapping of volatile and semi-volatile organic compounds by ice surfaces at moderate temperatures can be illustrated as their dissolution in the quasi-liquid layer (QLL) (Compoint et al. 2002; Domine et al. 2008; Jedlovszky et al. 2008; von Hessberg et al. 2008) or as simple adsorption on solid surfaces in case they are poorly soluble (Sokolov and Abbatt 2002; Winkler et al. 2002). Contaminants in the QLL are available for rapid exchange with the atmosphere or snow interstitial air, while revolatilization of those adsorbed onto the snow crystals depends on their partial pressure and ambient temperature (Domine et al. 2007, 2008). Desorption is thus less probable for compounds that possess relatively higher snow/air interfacial partitioning coefficients or Henry's law constants (Herbert et al. 2006a, b; Matykiewiczová et al. 2007a). Adsorbed small organic compounds can also diffuse within the ice crystalline lattice to some extent. For example, formaldehyde was found to have the diffusion coefficient of  $8 \times 10^{-11} \text{ cm}^2 \text{ s}^{-1}$  at 258 K (Perrier et al. 2003).

#### 18.4.2 Photochemistry of Organic Molecules in Ice

The early interest in the subject originated from evidence revealing that ice is a unique chemical environment. In 1957 Szent-Gyorgyi reported dramatic spectral emissive changes caused by freezing aqueous solutions of a number of dyes

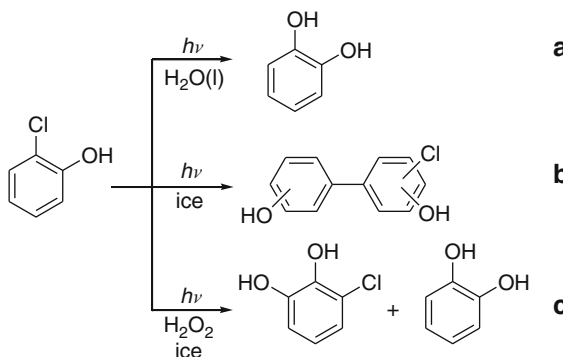
(Szent-Gyorgyi 1957). He found that crystalline ice is essential for the quenching of the emitting triplet state into a dark singlet ground state (Szent-Gyorgyi 1957). The results represent genuine matrix effects on electronic states and radiationless transitions in polyatomic species, and specifically rule out alternative interpretations based on enhanced solute-solute intermolecular interactions via concentration effects from solute rejection by the freezing solution (Kiovsky and Pincock 1966; Pincock 1969). Concentration effects cause electron magnetic resonance (EMR) line broadening upon slow freezing. The removal of the responsible solute-solute intermolecular interactions is partially achieved by rapid freezing and requires glass-forming additives (Leigh and Reed 1971). These observations highlight the crucial role of the freezing protocol in the experiment outcome.

Photodimerization reactions of thymine, pyrimidine, or uracil derivatives in frozen media were investigated since the 1960s in order to understand the photodeactivation mechanism of DNA (Beukers et al. 1959; Bose et al. 1984; Rahn and Hosszu 1969; Sasson and Wang 1977; Szent-Gyorgyi 1957; Varghese 1970; Wacker et al. 1961; Wang 1961, 1963, 1964). Isolated hydrated DNA molecules in aqueous solutions are transformed by freezing to ordered molecular aggregates dispersed in an ice matrix, which increases the probability of such bimolecular chemical processes (Montenay-Garestier et al. 1976). These reactions were also utilized for synthetic purposes, especially because the ice-mediated photoreactions are often regioselective. In addition, fast spontaneous (dark) replication of RNA was recently reported to occur at sub-freezing temperatures without the presence of usual enzymes (Vogel and Richert 2007).

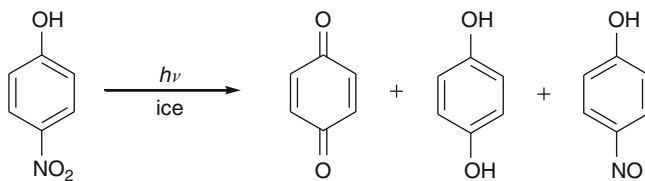
Photochemical transformations are also believed to occur in cometary ices in interstellar space. Comets are ices made of simple molecules, such as  $\text{H}_2\text{O}$ ,  $\text{CH}_3\text{OH}$ ,  $\text{NH}_3$ ,  $\text{CO}$ , and  $\text{CO}_2$ , although more complex species, including nitriles, ketones, esters, or aromatic hydrocarbons, can be also present. Chemical changes can be promoted due to penetrating cosmic radiation or absorbed stellar radiation to produce more complex organic molecules, such as amino acids (Bernstein et al. 2002; Caro et al. 2002). This topic is covered by the other chapters of this book.

Unusual photobehavior of halobenzenes, such as chlorobenzene, 2- or 4-dichlorobenzene, bromobenzene, or 1,4-dibromobenzene, in frozen aqueous solutions was reported by Klán and coworkers (Klán and Holoubek 2002; Klán et al. 2000b, 2001). Photolysis of relatively concentrated ( $c > 10^{-4} \text{ mol L}^{-1}$ ) frozen solutions below  $\sim 265 \text{ K}$  gave dehalogenation, coupling (halogenated biphenyls or terphenyls), or rearrangement products, instead of photosolvolytic products (phenols) which are formed in irradiated liquid aqueous solutions. Predominant coupling product formation is related to a substantial concentration effect and still efficient diffusion of reactive intermediates. Similarly, chlorobiphenyldiols were the major products obtained by UV-irradiation of halophenols in ice (e.g., 2-chlorophenol in Scheme 18.3a, b) (Klánová et al. 2003a, b).

It was shown that photolysis of 4-nitrophenol in both ice pellets and liquid aqueous solutions afford the same photoproducts, i.e., hydroquinone, benzquinone, or 4-nitrosophenol (Scheme 18.4) suggesting that similar mechanisms of the decomposition may occur in the two phases (Dubowski and Hoffmann 2000).



**Scheme 18.3** Photochemistry of 2-chlorophenol in water and ice

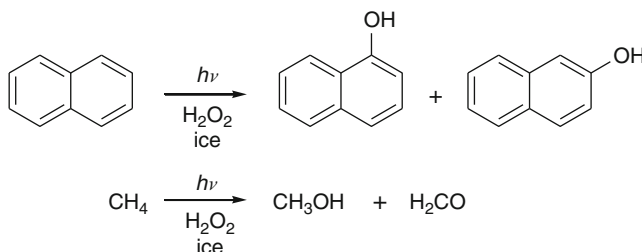


**Scheme 18.4** Photochemistry of 4-nitrophenol in ice

The authors discussed this reaction as an archetypal process for photochemical behavior of organic compounds in polar ice and snow.

The photodegradation of the most abundant snow-pack PAHs – phenanthrene, pyrene, and fluoranthene – has also been examined in laboratory ices (Ram and Anastasio 2009). Because of their very high molar absorptivities, the major loss process for these compounds in the field is direct photodegradation, while  $\cdot\text{OH}$ -mediated reactions are minor. However, the laboratory lifetimes are much shorter than the values inferred from field observations, suggesting that PAHs in polar snowpacks are present in particles where PAH photochemistry is much less efficient compared to in ice quasi-liquid layers.

Irradiation of chlorophenols in frozen aqueous solutions in the presence of hydrogen peroxide, a source of hydroxyl radicals, gave chlorobenzenediols or dihydroxybenzenes as the major products (Scheme 18.3) (Klánová et al. 2003b). Since both chlorophenols and  $\text{H}_2\text{O}_2$  are photoactive chromophores, a competition of different photoreaction mechanisms was observed. Aromatic and saturated aliphatic hydrocarbons and their derivatives can also be photooxidized in the presence of  $\text{H}_2\text{O}_2$  (Scheme 18.5) (Dolinová et al. 2006). While aromatic molecules principally undergo addition–elimination reactions to form the corresponding hydroxy compounds, saturated hydrocarbons (cyclohexane, butane, methane) are converted to alcohols or carbonyl compounds via initial hydrogen abstraction and subsequent radical termination reactions.



**Scheme 18.5** Photochemistry of naphthalene and methane in ice

The oxidation and radical substitution reactions of organic compounds by OH has been suggested to occur in nature because  $\text{H}_2\text{O}_2$  has been identified as one of the important trace constituents of polar or atmospheric ices (Anastasio and Jordan 2004; Hutterli et al. 2001; Chu and Anastasio 2005; Jacobi et al. 2004; Yang et al. 2002); such photoreactions could be an important sink for organic anthropogenic pollutants in cold environments (Boudries, Bottemheim, Guimbaud et al. 2002; Grannas et al. 2004; Klán and Holoubek 2002; Klán et al. 2003). When frozen solutions of aromatic compounds, such as phenol or 4-methoxyphenol, are photolyzed in the presence of inorganic nitrite or nitrate, nitration, hydroxylation, and radical coupling reaction were their major degradation processes (Matykiewiczová et al. 2007b). At  $\lambda_{\text{irr}} > 290$  nm, the reactions predominantly proceeded by the nitrite or nitrate photoexcitation. These results suggest that photolysis of nitrate in the snowpack (Honrath et al. 1999; Zhou et al. 2001) could contribute to oxidation of organic ice/snow contaminants, although, as described above, photolysis of  $\text{HOOH}$  appears to be the dominant source of  $\cdot\text{OH}$  in polar snowpacks. Based on a preliminary  $\cdot\text{OH}$  steady-state concentration in the QLL of illuminated Summit snow of  $10^{-15}$  M, lifetimes of organics with respect to  $\cdot\text{OH}$  reaction will be on the order of days to weeks during summer in the surface snow (Anastasio et al. 2007; Sumner et al. 2002).

The laboratory simulation of photochemical behavior of persistent organic pollutants, such as polychlorinated biphenyls (PCBs), in artificial snow at environmentally relevant concentrations recently enabled simultaneous monitoring of their photochemical changes and volatilization fluxes from the solid matrix (Matykiewiczová et al. 2007a). PCBs underwent the reductive dehalogenation reactions upon irradiation at  $\lambda > 290$  nm which competed with a desorption process responsible for the pollutant loss from snow, especially in case of lower molecular-mass derivatives produced during photolysis. Snow/air exchange has been previously suggested to be an important process responsible for pollutant loss from the snowpack (Hansen et al. 2006; Herbert et al. 2005), yet the question of the actual quantities of chemicals released back to the atmosphere which competes with photochemical changes is still open to debate.

### 18.4.3 Photochemistry of Natural Organic Matter and Its Photodegradation Products

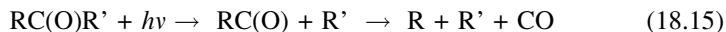
Carbon monoxide is emitted by decaying plant matter exposed to sunlight (Schade and Crutzen 1999; Schade et al. 1999). The system displays hysteresis and a quadratic dependence of CO production rates on photon flux. Both phenomena are consistent with the build-up of the intermediate CO precursors under high-irradiance conditions. The proposed mechanism involves the photocleavage of the  $\alpha$ -glycosidic bonds of the cellulose chain into free radicals, followed by decarbonylation and the formation of non-cyclic hydroxyketones (Schade and Crutzen 1999; Schade et al. 1999). Thus, cellulose-based organic matter of natural origin undergoes progressive degradative photochemical oxidation into simpler species and releases CO in the process. The shift of the absorption spectra towards the blue is the result of the progressive loss of conjugation in the remaining species.

Carbon monoxide is also produced by photodegradation of dissolved organic matter (DOM) in rain (Zuo and Jones 1996) and snow (Haan et al. 2001). The mechanisms involved are not completely understood, but CO photochemical formation rates were found to be strongly correlated with the concentrations of dissolved organic carbon (DOC), its UV absorbance, and its fluorescence yield (Zuo and Jones 1997). These observations implicate carbonyl functional groups associated with the relevant chromophores. Formaldehyde is also produced from illuminated snowpacks, but the mechanism of this process probably involves indirect photooxidation, rather than direct photodecomposition of organic material (Sumner and Shepson 1999). It has been demonstrated that the photochemical production of CO and carbonyl sulfide (OCS) from dissolved organic matter in natural waters share a common acyl radical intermediate (Pos et al. 1998). Addition of model carbonyl compounds such as acetylacetone, pyruvate, and glyoxylate enhance the production rates of both species, whereas the addition of cysteine or bisulfide as reduced sulfur-containing substrates increase OCS formation at the expense of CO. Reductive pretreatment of fulvic acid with NaBH<sub>4</sub>, which is expected to reduce carbonyl groups, induces a sharp decrease in the photochemical CO production from this surrogate of natural dissolved organic matter.

Dissolved organic matter is degraded by sunlight into a variety of products, such as CO, CO<sub>2</sub>, and organic photoproducts that, although smaller in size than the parent species, remain part of DOM pool (Moran and Zepp 1997) and share some of its properties. Aquatic humic substances are refractory to microbial oxidation, but are the major chromophores in natural waters. Photoproducts become biologically more available than the original material. About 17 low molecular weight species have been identified as photoproducts, including C<sub>1</sub>–C<sub>3</sub> aldehydes, formate and acetate, glyoxalate, levulinic acid, malonate, and pyruvate. The quantum yields for the production of CO and H<sub>2</sub>O<sub>2</sub> from DOM photoreactions are about 0.1% near 300 nm and display similar action spectra. The results are nearly independent of the source of natural water (Valentine and Zepp 1993). Dissolved iron increases dramatically CO photoproduction, e.g., 90 µg Fe/L increased CO photoproduction eightfold.

A similar effect was found in the photodecomposition of oxalic, glyoxalic and pyruvic acids (Zuo and Hoigne 1994). Thus, the water-soluble natural organic matter is expected to be photodegraded into simpler, but functionally related species, by sunlight, while being incorporated into atmospheric aerosol, rain, or snow.

The photochemistry of simple carboxylic acids in aqueous solution has been investigated. Processes that lead to CO production via photochemical decarbonylation are well known and involve an excited carbonyl moiety (Kagan 1993). In one type of these photoprocesses, the so-called Norrish type I mechanism, the  $\alpha$ -bond to the carbonyl group is broken, and a pair of free radicals is formed:



Two types of excited states,  $n-\pi^*$  or a  $\pi-\pi^*$ , can participate in this reaction, depending on the conditions. The rate constants for Norrish type I reactions are much faster for  $n-\pi^*$  states. However, in aqueous solution the reactivity pattern may be reversed due to stabilization of carbonyl non-bonding electrons by water molecules. This is not the only issue that should be taken into account. Other factors, such as the stability of the acyl  $\text{RC(O)}$  radicals, are also important in condensed media. Unless the acyl radical decomposes, there is always the possibility of reactant reformation via cage recombination. In natural systems, metal chelation to dicarbonyls may substantially affect their photoreactivity via a ligand-to-metal charge transfer mechanism. Actually, the increased production of CO upon addition of ketoacids to natural waters, but not to pure water, implies photosensitization rather than direct photolysis above 300 nm (Guzmán et al. 2006a, b, 2007, ). Studies on direct photolysis of  $\alpha$ -ketoacids in pure water have demonstrated that the neutral rather than anionic species are involved. Because most ketoacids have  $pK_a$  values lower than about 4, photodecomposition at neutral pH will be inhibited. In addition, the lower enhancement of CO production rates by glyoxylic vs. pyruvic acid addition suggest that enolization of the aldehydic group  $-\text{C(O)H}$  is also detrimental. At seawater pH, more than 90% of glyoxylate is in the hydrated form, which does not lend itself to CO formation. In many cases it was found that more than one mole of  $\text{CO}_2$  was produced in the decarboxylation of  $\alpha$ -ketoacids in the presence of oxygen (Davidson and Goodwin 1980). Bimolecular electron transfer between two molecules of pyruvic acid, or between pyruvic acid and  $\text{O}_2$ , has been postulated, and they may be feasible in the concentrated solutions that accrue from solute rejection into the quasi-liquid layer.

Most ketones lacking  $\gamma$ -H's undergo decarbonylation with nearly unitary quantum yields (Kagan 1993). Such  $\alpha$ -diketones as glyoxal extend their absorption into the red, with strong bands about 430 nm, in addition to the characteristic  $\text{C} = \text{O}$  absorptions at about 280 nm. Their decomposition not only yields CO, but is expected to generate free alkyl radicals as well:



Decomposition quantum yields in solution might be as large as in the gas phase, if the lifetime of the primary HCO radical were very short. Acyl radical decomposition is not an easily reversed process i.e., radical addition to a closed-shell species such as CO has sizable activation energy, rendering cage effects inoperative (see below), while in the gas phase pyruvic acid undergoes quantitative decarboxylation into CO<sub>2</sub> and CH<sub>3</sub>CHO (Leermakers and Vesley 1963; Vesley and Leermakers 1964):



with a quantum yield of  $\Phi = 0.8$  at 366 nm. On the other hand, dimethyltartaric acids are formed in methanol as a solvent. The products of the photoreaction in water are very different. Pyruvic acid in water shows two near-ultraviolet absorption maxima; an n- $\pi^*$  band with  $\lambda_{\max} = 321.2$  nm with a small extinction coefficient ( $\epsilon = 11.3 \text{ M}^{-1} \text{ cm}^{-1}$ ), and a  $\pi-\pi^*$  band at  $\lambda_{\max} = 200.0$  nm ( $\epsilon = 2,100 \text{ M}^{-1} \text{ cm}^{-1}$ ) (Leermakers and Vesley 1963). In the past it has been reported that aqueous solutions of pyruvic acid upon ultraviolet irradiation under anoxic conditions evolve carbon dioxide, leaving 3-hydroxy-2-butanone, “acetoin”, as the only organic product remaining in solution:



based on gas chromatography (GC) retention times in which water eluted simultaneously with acetoin (Leermakers and Vesley 1963). The quantum yield for this process was measured based on ultraviolet absorbance changes before and after irradiation at 366.6 nm:  $\Phi = 0.79 \pm 0.05$  at 298 K (Leermakers and Vesley 1963). The 320 nm band photodecarboxylation of pyruvic acid in water solutions has actually been extensively restudied to find the reaction products (Guzmán et al. 2006a). Pyruvic acid is photochemically inert in benzene, a solvent unable to donate hydrogens, probably via deactivation of the excited state by the solvent, but in the presence of oxygen undergoes photooxidation into peracetic acid (50%), H<sub>2</sub>O<sub>2</sub> (10%), and CH<sub>4</sub> (~ 20%) (Sawaki and Ogata 1981). Pyruvate is photochemically unreactive under the same conditions:  $\Phi < 0.04$  (Leermakers and Vesley 1963). In the presence of hydrogen-donating organic solvents like methanol, pyruvic acid is photoreduced into 2,3-dimethyltartaric acid and at least a 1:1 solvent adduct (2-methyl-2,3-dihydroxypropanoic acid) without significant decarboxylation (Barton et al. 1958).

The photolysis of aqueous biacetyl, the prototypical  $\alpha$ -dicarbonyl, in the presence of O<sub>2</sub> leads to acetic acid, peroxyacetic acid, and hydrogen peroxide (Faust et al. 1997). The reaction in aqueous media yields stabilized acetyl radicals, which become hydrated and react with O<sub>2</sub> to produce acetylperoxide radicals. In contrast, the gas-phase photolysis of biacetyl is a source of acetyl radicals and yields CO, H<sub>2</sub>, and formaldehyde (Finlayson-Pitts and Pitts 1986).

The photooxidation of organic and inorganic substrates during UV photolysis of nitrite anion in aqueous solutions has been studied by EMR spin trapping (OH radicals by DMPO, NO<sub>2</sub> by aci-nitromethane), and O<sub>2</sub> consumption

techniques (Arakaki et al. 1999; Bilski et al. 1992; Pace and Carmichael 1997; Zuo and Deng 1998). Since nitrite is a major product of nitrate anion photolysis in water and ice (Dubowski et al. 2001) above 300 nm (Eq. 18.4), and the secondary decomposition of nitrite by •OH radicals is efficiently inhibited by formate (Dubowski et al. 2002), it is interesting to speculate about the possibility that the photochemically produced •OH radicals could drive organic oxidations in ice. NO<sub>2</sub>, another product of nitrate anion photolysis (Eq. 18.3), can add to double bonds to initiate the oxidation of unsaturated fatty acids (Pryor and Lightsey 1981) to abstract hydrogen from alkenes (Pryor et al. 1982), and to oxidize thiols to disulfides;  $\gamma$ -irradiation of ice also produces •OH radicals that have been trapped by DMPO (Yoshioka and Hasegawa 1996) or by organic aromatic substrates (Klánová et al. 2003b).

The toxic effects of photoproducts formed upon the laboratory photolysis of 2- and 4-chlorophenol in frozen aqueous solutions were determined with a bacterial luminescence test and in vitro biomarker assay for dioxin-like effects, and they were compared to those of products formed in the liquid phase (Blaha et al. 2004). The irradiated ice samples elicited significant inductions of dioxin-like effects, which supported the assumptions that the photochemistry of organic compounds in ice/snow might have important environmental consequences, especially in polar regions where persistent organic pollutants are common trace constituents (Grannas et al. 2007; Klán and Holoubek 2002).

## 18.5 (Photo)chemistry in/on Atmospheric Ices

Photochemical processes which occur in the gas phase and solution have been explored in detail for many years due to their relevance in our atmosphere and for industrial synthesis. Less general recognition has been provided to photo-active materials in/on solid environments for which molecular motion is restricted, even though the work underpins our understanding of highly important phenomena such as photosynthesis and photochromic optics. The substrate solids and surfaces involved can range from the truly organized (i.e. crystalline) through to low-temperature, inert “gas matrices” in which random orientations between guests and the host are apparent. Monographs have been devoted to these specialized fields of research in constrained media over many years as discussed in the first section of this review (Hallam 1973; Moskovits and Ozin 1976; Ramamurthy 1991).

However until the last decade, studies of constrained photochemistry in waterices and on their surfaces had been far fewer in number. The increase in activity can be directly related to the discovery of the Antarctic ozone “hole” about 20 years ago and its origins with stratospheric, cold/frozen water droplets present as Polar Stratospheric Clouds (PSCs) (Farman et al. 1985; Solomon et al. 1986). Their heterogeneous influence on the Earth’s atmosphere quickly became clear but it is only within the last 5–10 years that similar effects related to cold tropospheric aerosols and the land-based snowpack, altogether termed the cryosphere, has

become fully realized (Grannas et al. 2007). Indeed these studies on *terra firma* and their findings are fully complementary to related phenomena observed for ices found in our prebiotic past and more distant planetary/interstellar locations (Sodeau and Horn 2003).

One potentially important reason for the further detailed study of heterogeneous photochemistry in/on water ices is because its science has three times caught the atmospheric science community off-guard: the first regarding stratospheric ozone depletion, the second because of unexpected emissions from snowpacks and the third because of tropospheric ozone/mercury “sudden” depletion events (Grannas et al. 2007; Simpson et al. 2007; Steffen et al. 2008). Therefore the purpose of this section of the review is to link work that has been published to date on the photochemistry of materials constrained within and on the surface of ices, to atmospheric phenomena found on planet Earth. The local environments to which the “guests” are bound to or located in/on do exert some control upon outcomes and are therefore addressed first before considering some specific examples relevant to cryoprocessing.

### 18.5.1 Water-Ices

Several mechanisms are operative in the atmosphere to produce the water-ice surfaces and particles, which lead to the (photo)-chemical processes discussed in this review. Hence: (1) water vapor can condense onto an ice-forming nucleus, which can be chemical or biological in nature and (2) growing ice crystals can themselves promote the nucleation of super-cooled water droplets. For both routes, impurities can readily become integrated into the ice. Furthermore crystals can grow by simple vapor condensation, a process that often takes place in a discontinuous manner, with new layers of water condensing at the crystal edges. These varying growth mechanisms lead to a rich variety of possibilities into/onto which chemicals can interact with, or perhaps become constrained in, before photolysis can take place (Pruppacher and Klett 1997).

Several studies have shown that the interfacial water-ice sites are sensitive to occluded molecules and that the type and magnitude of interaction can be monitored using infrared spectroscopy: the extent can be well-quantified in terms of the resulting spectral position of the so called “dangling bond” of the water (Cocke et al. 2004; Holmes and Sodeau 1999). Classically, of course, water is capable of forming four hydrogen bonds to other water molecules but in amorphous water-ice the coordination sites may not be fully saturated and so “guest” molecules can interact, whether they are carbonyl-containing species or halocarbons, for example (Sodeau and Horn 2003). Very often as a function of temperature, the surface can become disrupted in terms of hydrogen bonding leading to the formation of nanometer thick quasi-liquid layers (QLL), which were first postulated by Faraday (Faraday 1859). Such a disordered air/surface/bulk interface (or grain boundary) is still not fully characterized and its quantitative effect on (photo)chemical observations is unclear.

Of further complication is the fact that the resultant multi-component systems are only completely solid below the eutectic point; between their freezing point and eutectic point both liquid and solid co-exist in equilibrium (Pincock and Kiovsky 1966). Under the latter condition, liquid can reside in the surface QLL or in small structural holes known as “micropockets” or “microveins” between the grains of solid ice (Betterton and Anderson 2001). These locations are not a theoretical notion: they have been observed in both laboratory and field ice samples using techniques such as NMR spectroscopy. They can also act as sites for “freeze concentration” and microacidity changes, which can lead to unexpected results (Cho et al. 2002; Takenaka et al. 1996).

From the above discussion it is possible to describe a fairly encompassing picture in which a “typical” atmospheric ice sample (whether originating from a PSC, cirrus cloud, snowflake or hailstone) would be formed with a frozen morphology consisting of a number of potential reaction regimes. To a first approximation the resultant water-ices would comprise mainly a solid structure containing microcavities with a disordered, liquid-like layer or islands distributed over the surface. Wherever sited, the reactive fate of the “guests” would be expected to be controlled to some extent by hydrogen bonding and or cage effects, which would hinder product escape and promote recombination or “new” pathways. The first type of reactions that may have taken place in such environments date to prebiotic times as discussed below.

### 18.5.2 Prebiotic Mechanisms

Many key biochemical building blocks such as hydrogen cyanide, formamide, formaldehyde, hydrogen peroxide and various amino acids can become concentrated in strong salt eutectics at temperatures well below 0°C. Resulting condensation reactions can then drive polynucleotide formation in frozen lakes and other water masses as a prelude to the evolution of life (Bernstein et al. 2002; Caro et al. 2002; Sanchez et al. 1966). (The freeze-concentration and subsequent reaction of molecules and ions in “micropockets” will be further discussed below in relation to halogen releases over the Arctic and Antarctic troposphere.) The proposed prebiotic mechanisms contrast significantly with the classic Urey-Miller proposals (Miller 1953) but are plausible. Hence HCN ices and HCN/ammonia/water frozen mixtures irradiated with light in the wavelength range 110–250 nm produce a rich set of products including isocyanic acid, cyanate ions and formamide (Gerakines et al. 2004). Furthermore, related nitrile-containing compounds in water ices give rise to a complex suite of amino acids upon ion irradiation (Hudson et al. 2008). The formation of carbohydrates is also possible in low-temperature media involving the photolysis of formaldehyde to produce its recently spectroscopically characterized tautomer, hydroxymethylene (HCOH) (Schreiner et al. 2008). Glycoaldehyde is formed by the reaction together of both isomers in a frozen solid (Hudson 2006; Sodeau and Lee 1978); condensation to sugars can subsequently occur in the presence of phosphates (Simonov et al. 2007).

### 18.5.3 Stratospheric Mechanisms

As mentioned above, stratospheric heterogeneous chemistry catalyzed by PSC (water-ice) surfaces is now well-established as playing an important role in the processes which mediate polar ozone levels (Farman et al. 1985; Sodeau 1995; Solomon et al. 1986). Indeed the experimental strategies used in these investigations have subsequently driven laboratory studies related to unusual observations found throughout the cryosphere. Since about 1995 a number of publications have also centered on the water-ice *photochemistry* of the main surface species involved in stratospheric ozone depletions such as chlorine nitrate (Schrivener-Mazzuoli et al. 2003), chlorine oxides (Inglese et al. 2005), hydrochloric acid (Woittequand et al. 2005), nitric acid (Koch and Sodeau 1995; Koch et al. 1996) and dinitrogen pentoxide (Koch and Sodeau 1996).

For example the heterogeneous photochemistry of chlorine nitrate ( $\text{ClONO}_2$ ) adsorbed on HCl-doped crystals has been studied at 181 K and at 190 K. Under the experimental conditions employed the main gaseous products found at 181 K were  $\text{Cl}_2\text{O}$  and  $\text{Cl}_2$ , while at 190 K,  $\text{Cl}_2\text{O}$  was mainly observed. At both temperatures a net enhancement in the rate of gaseous product formation was observed when light of wavelength longer than 350 nm was used for photolysis (Faraudo and Weibel 2001). The photodissociation of the closely related  $\text{CINO}_2$  molecule embedded in argon and water low-temperature clusters has also been investigated by detecting the chlorine atom photo-fragments using resonance enhanced multiphoton ionization time-of-flight spectroscopy (REMPI-TOF). By utilizing various cluster formation conditions the measured speed distributions of the products show that, in contrast to monomer photolysis, only one decay channel is found to be active. The implication to atmospheric chemistry is that  $\text{CINO}_2$  embedded in water clusters represents a photolytic source of Cl and NO radicals (Li and Huber 2002).

Given the prevalence of condensed nitric acid hydrates in the atmosphere, reflection-absorption infrared spectroscopy (RAIRS) has been employed in order to investigate the low-temperature photochemistry (90–140 K) of thin films of appropriate composition (as well as ammonium nitrate) grown *in vacuo*. Photolysis of amorphous nitric acid hydrate, the crystalline dihydrate (NAD) and trihydrate (NAT) at  $\lambda > 230$  nm results in the formation of molecular nitric acid due to rapid protonation of the excited nitrate ion. Secondary photolysis of  $\text{HONO}_2$  produces  $\text{NO}_2$  and NO. Similarly, when neat films of molecular, anhydrous nitric acid are irradiated, nitrate and nitronium ions are observed. In contrast, ammonium nitrate photolysis at 140 K did not result in a proton transfer to produce  $\text{NH}_3$  and  $\text{HONO}_2$  but in the formation of the peroxynitrite ion ( $\text{ONOO}^-$ ) as a precursor for  $\text{NO}_2^-$ . Molecular dinitrogen tetroxide and nitrous oxide were also detected in the film (Koch et al. 1996). What these measurements show is that in favorable optical conditions, transformations of these materials into less benign (and more reactive) forms are possible, and that photochemistry may result not only in additional surface reactions but also in the modification of the reactive surface. As expected the results are quite different from those determined in conventional matrix

isolation experiments in which nitric acid was dispersed in an argon host at low temperatures (Koch and Sodeau 1995). It can be concluded that photochemistry in water-ices is an area which requires much more detailed scrutiny, since few atmospheric models include potential “new pathway” effects.

Other  $\text{NO}_x$  and  $\text{ClO}_x$  compounds have been photolyzed in ice systems over the last few years in order to determine whether the processes might impinge on the chemical composition of the atmosphere. For example, monolayer coverages of  $\text{N}_2\text{O}_4$  have been prepared *via* the adsorption of gaseous  $\text{NO}_2$  at *ca.* 100 K on 5–10 monolayers of condensed  $\text{H}_2\text{O}$  in a high vacuum system. Exposure to continuous near-UV irradiation resulted in the photo-desorption of  $\text{NO}_2$  from the surface. The interaction with the ice was determined to be purely physical in character and there was no reaction observed between  $\text{NO}_2$  and the water surface. The temporal profiles of both the  $\text{NO}_2$  photodesorption rate and of the surface-bound  $\text{N}_2\text{O}_4$  concentration exhibited simple monotonic decays and were explained within a simple kinetic scheme for the photochemistry of adsorbed  $\text{N}_2\text{O}_4$ . The wavelength dependence of the  $\text{NO}_2$  yield was shown to be comparable to the gas-phase absorption cross-section for  $\text{N}_2\text{O}_4$ . The experiments show that the photochemistry of  $\text{N}_2\text{O}_4$  physisorbed on low-temperature ice is not significantly different to that of its gas-phase counterpart. The dynamics of photodissociation in physisorbed  $\text{N}_2\text{O}_4$  have also been investigated by time-of-flight mass spectrometry. It was shown that the photodissociation dynamics are dependent on the unique properties of the ordered physisorbed system (Rieley et al. 1996, 1997a, b).

In a separate set of studies, the photochemistry of  $\text{NO}_2$  adsorbed on an Au(111) surface has been investigated at <120 K in an ultrahigh vacuum system. The adsorption states of the molecules were characterized by thermal desorption spectroscopy and IR reflection absorption spectroscopy. It was concluded that the photolysis of physisorbed  $\text{N}_2\text{O}_4$  is inhibited significantly when the Au surface is covered with a thin water ice film, suggesting that the photolysis is enhanced by metal substrate photoexcitation or electron transfer from the substrate to the adsorbates (Sato et al. 1999).

The photochemistry of chlorine dioxide,  $\text{OCIO}$ , in amorphous ice has also been investigated using IR and UV-vis spectroscopy. Exposure to ultraviolet light (360 nm) quantitatively converted the  $\text{OCIO}$  to the chlorine peroxy radical,  $\text{ClOO}$ . Under the dilute conditions used, the only photoproduct appeared to be  $\text{ClOO}$ , in contrast with the gas-phase photolysis which yields predominantly  $\text{ClO}$ . It was suggested that these findings have implications for stratospheric ozone loss because the photochemical conversion of  $\text{OCIO}$  to  $\text{ClOO}$  in stratospheric ice particles may represent a new ozone-depleting mechanism. Thus, under the very dilute conditions that would exist on polar stratospheric ice particles, the photochemical conversion of  $\text{OCIO}$  to  $\text{Cl}$  atoms and  $\text{O}_2$  would represent a new source of active halogen radicals for ozone depletion (Pursell et al. 1995, 1996). In a separate TOF-QMS/RAIR study it was shown that the predominant photoproduct retained in the ice films at coverages between 0.5 and 2 monolayers was  $\text{ClClO}_2$  without formation of other photoproducts of formula  $\text{Cl}_x\text{O}_y$ . A third research group has also investigated the  $\text{OCIO}$  system using RAIR spectroscopy and mass

spectrometry. It was confirmed that photolysis of a neat film of OCIO ( $\lambda > 300$  nm, 90–110 K) produces chloryl chloride, ClClO<sub>2</sub>. However it was also shown that irradiation of a co-deposited OCIO/H<sub>2</sub>O film produces chlorine superoxide, ClOO. This result suggests that OCIO isomerization is the first step in the process which produces ClClO<sub>2</sub>. Photolysis of Cl<sub>2</sub>O was also undertaken and shown to produce OCIO, initially, which is subsequently converted to ClClO<sub>2</sub>. (Graham et al. 1996) Recently the photodissociation of ClOOCl has been simulated using a semiclassical representation of the excited state; it was suggested that the absorption cross sections of this molecule change by interaction with ice particularly at longer wavelengths (Inglese et al. 2005). This prediction would be interesting to confirm experimentally.

The photodissociation of HCl on ice has also been study by computational methods recently. The results indicate that the hydrogen fragment diffuses into an ice cavity, presumably of the “micropocket” type. The photodecomposition of CFCl<sub>3</sub> on an ice surface on Ru(001) has been studied using infrared absorption spectroscopy. It appears that so-called anionic chlorine coordinated to free OH species is formed as a result. If extrapolated to the field, the mechanism would enable the highly concentrated storage of chlorine on ice surfaces (Woittequand et al. 2005).

Of final note in this section is the reports that various spectroscopic and spectrometric methods have been used to study O<sub>3</sub>, OCS and CS<sub>2</sub> trapped in water-ice (Chaabouni et al. 2000b; Ikeda et al. 2008). The photochemistry of ozone in excess ice was investigated using laser irradiation at 266 nm. H<sub>2</sub>O<sub>2</sub> was shown to be produced at low-temperatures through a hydrogen-bonded complex between ozone and free OH bonds. At higher temperatures, when a solid solution of ozone in water exists, the H<sub>2</sub>O<sub>2</sub> was apparently formed by the reaction of an excited oxygen atom O(<sup>1</sup>D<sub>2</sub>) with its nearest water molecules. In contrast only sulfur and its dimers were observed to be formed at the surface when OCS and CS<sub>2</sub> were photolyzed at 193 nm on water-ice.

#### 18.5.4 Tropospheric Ice and Snowpack Mechanisms

Measurements at Summit, Greenland, performed from June-August 1999, showed significant enhancement in concentrations of several trace gasses in the snowpack (firn) pore air relative to the atmosphere. Measurements have been reported of alkenes, halocarbons, and alkyl nitrates that are typically a factor of 2–10 higher in concentration within the firn air than in the ambient air 1–10 m above the snow. Profiles of concentration to a depth of 2 m into the firn show that maximum values of these trace gasses occur between the surface and 60 cm depth. The alkenes show highest pore mixing ratios very close to the surface, with mixing ratios in the order ethene > propene > 1-butene. Mixing ratios of the alkyl iodides and alkyl nitrates peak slightly deeper in the firn, with mixing ratios in order of methyl > ethyl > propyl. It was suggested that these variations are likely consistent with different near-surface

photochemical production mechanisms (Swanson, Blake, Dibb et al. 2002). These polar field observations are not the only ones which indicate unusual (photo)chemical activities related to tropospheric water-ice (Grannas et al. 2007; Sumner and Shepson 1999; Sumner et al. 2002; Yang et al. 2002). Other parts of this review discuss those phenomena in more detail and therefore this section will concentrate simply on several mimic laboratory studies which may prove relevant to understand the mechanisms, which underpin the wide-range of monitoring observations that have been made in the polar regions.

Firm air does contain elevated levels of nitrogen dioxide and therefore the mechanisms discussed in Sect. 18.3.3, which involve nitrate ion photolysis are likely to be important. Further to that discussion, the effects of photolysis on frozen thin films of water-ice containing nitrogen dioxide (as its dimer, dinitrogen tetroxide) have been investigated using a combination of Fourier transform reflection-absorption infrared spectroscopy and mass spectrometry. Under these circumstances HONO can be released from the ice by a mechanism involving the nitrosonium nitrate ion ( $\text{NO}^+\text{NO}_3^-$ ) and its solvated, protonated product  $\text{H}_2\text{ONO}^+$  (the nitroacidium ion). Related experiments in a low-temperature argon matrix have also been performed (Hellebust et al. 2007b).

The photolysis of nitrate ions to nitrite ions has also received attention in the past but recently the reaction in the presence of formate, formaldehyde, methane sulfonate and chloride ion has been evaluated. The rate is found to be enhanced, particularly in the presence of formate and formaldehyde and it was speculated that the origin of the effect is related to the protection of nitrite ions from oxidation. Indeed organic-nitrate materials may be formed (Minero et al. 2007). In fact the photolysis of the most important organic nitrate, peroxyacetyl nitrate (PAN), has received little experimental attention on actual ice surfaces (Ford et al. 2002). However a computer modeling study has been performed, which indicates that an important sink for PAN is related to sunlight-exposed snowpack surfaces (Dassau et al. 2004).

The photoconversion of *p*-chlorophenol in ice in the presence of nitrite ions and as a function of pH has been recently discussed (Kang et al. 2008). Serious effects on the photo-conversions were observed and the work provides an indication of the potential effects of acidity/basicity on snowpack chemistry. Related measurements on halogen-containing materials in ices have also been made with respect to interhalogen release to polar atmospheres particularly with regard to ozone depletion events as discussed below.

Tropospheric ozone depletion events observed during polar spring in the Northern Hemisphere have been ascribed to the release of “active” (photolytic) bromine following reaction between HOBr and bromide ions in acidic solutions. However the release of bromine and chlorine interhalogens promoted by the freezing of known sea-salt components in the presence of nitrite ions, has also been proposed. Hence the freeze-concentration effect (referred to above) can initially operate in liquid “micropockets” within the ice structure (thereby bringing reactants close together) and then the nitroacidium ion acts as an efficient proton transfer chaperone to the chloride- and bromide-containing interhalide ions. Furthermore the

known room-temperature, solution-phase reaction between nitrite ions and iodide ions, which occurs in acidic conditions ( $\text{pH} < 5.5$ ) has been shown to be accelerated when neutral aqueous solutions are frozen. The reaction is also proposed to occur in liquid “micropockets” within the ice structure at temperatures between the freezing point and the eutectic temperature. The products, nitric oxide and molecular iodine, are known to play significant roles in atmospheric compositional change and, therefore, the results obtained here may impact on observed snow-pack chemistry. Investigation of the effect of oxygen on the chemical processing indicated that a chain-reaction mechanism operates (O’Driscoll et al. 2006, 2008).

The adsorption and photochemistry of various halogenocarbons (Grecea et al. 2006; Sohn et al. 2008) and ethanol (Tang et al. 2006) on water-ice has also recently been explored. The works are not necessarily connected to any yet discovered tropospheric ice/snow events but the community has been caught off-guard before. Hence using a combination of RAIRS, temperature programmed desorption and time of flight measurements, with photolysis at 266 nm, a number of new halogenocarbon chemical species with O-bonds were formed (Grecea et al. 2006). This contrasts with experiments performed with ethyl chloride and tert-butyl iodide in water-ice for which no O-bonded materials were observed (Sohn et al. 2008). Perhaps of more interest is the fact that  $\text{CH}_3\text{CHO}$ , when photolyzed on water-ice, produces about 50% less of the HCO radicals produced in the gas-phase or on an aluminum surface held at the same low temperature (243 K) (Tang et al. 2006). Many more photochemical experiments need to be made in order to provide good contrast between water-ice surfaces, other cold surfaces and the gas-phase.

## 18.6 Chemistry in Ice Cores

### 18.6.1 *Čerenkov Radiation*

While field studies show that ice dopants and pollutants undergo chemical and photochemical modification, and there is a certain source of UV radiation of cosmic origin at all depths, the current understanding of the photochemical processes that may take place in ice media is rudimentary. The fact that ice cores in glaciers, Greenland, Arctic and the Antarctic are completely shielded from direct exposure to sunlight (Hondoh 2000) does not necessarily rule out photochemical transformations. The reason is that relativistic muons of cosmic origin weakly emit continuous Čerenkov radiation throughout ice cores. The faint bluish glow emitted by transparent substances in the neighborhood of strong radioactive sources is the visible manifestation of Čerenkov radiation (Andres et al. 2001; Jelley 1958; Thompson 1973), which is generated as the medium is perturbed by relativistic charged particles. Although particles cannot move faster than the speed of light in the vacuum, they can still exceed the speed of light in a dense medium such as ice. With a refractive index of  $n \sim 1.32$  over most of the UV spectral region, the speed of light in ice is

$c_{\text{ice}} = c/1.32 = 0.757 c$ . Thus, charged particles moving faster than  $c_{\text{ice}}$  would induce a macroscopic polarization field about a plane moving with the particle and perpendicular to its trajectory. The reason is that the medium cannot relax fast enough to maintain instantaneous electroneutrality (Jelley 1958). The resultant dipole field will be felt even at large distances from the track. The emissions will be spread over a band of frequencies corresponding to the various Fourier components of the pulse generated by the relativistic particle. All charged particles with velocities  $v = \beta c > c_{\text{ice}}$  will induce Čerenkov emissions in the medium.

The classical theory of Frank and Tamm, based on the above considerations about the origin of the Čerenkov radiation, leads to the following expression for  $N$ , the number of photons emitted by the particle in the range of wavelength  $[\lambda_1, \lambda_2]$  as it traverses the distance  $L$  (Jelley 1958):

$$N = 2\pi\gamma L \left( \frac{1}{\lambda_1} - \frac{1}{\lambda_2} \right) \left( 1 - \frac{1}{\beta^2 n^2} \right) \quad (18.19)$$

where  $\gamma = 1/137$  is the fine structure constant and  $n$  is the average refractive index of the medium. Muons, produced by the interaction of cosmic rays with matter, are positively charged elemental particles with a rest mass of  $m_0 = 1.88 \times 10^{-28}$  Kg, i.e., about 206 times heavier than the electron. Their typical kinetic energies  $T$  exceed 1 GeV, which is much larger than the threshold energy for Čerenkov emissions in ice at about 65 MeV. From the relativistic expression for  $\beta$ :

$$\beta = \sqrt{1 - \frac{1}{[1 + (T/m_0 c^2)]^2}} \quad (18.20)$$

and  $m_0 c^2 = 105$  MeV for the muon, it was found that muons with  $T > 1$  GeV, have  $\beta > 0.996 > 0.757$  and are, therefore, Čerenkov active. Using the above equations with  $230 < \lambda/\text{nm} < 400$ ,  $n = 1.32$ ,  $\beta \sim 1$ , it was estimated that about  $\sim 322$  photons  $\text{cm}^{-1}$  are continuously emitted along the track of the muon. An integral flux of energetic muons ( $T > 0.5$  GeV) at the sea level of about 0.04 muons  $\text{cm}^{-2} \text{s}^{-1}$  will therefore generate  $0.04 \times 322 \sim 13$  actinic photons  $\text{cm}^{-3} \text{s}^{-1}$  uniformly in the ice cores. The weakly attenuated muons will travel hundreds of meters in ice before their kinetic energies drop below the Čerenkov threshold. This mechanism represents a homogeneous, steady production at all depths. The estimated photon dose over a millennium amounts to  $4 \times 10^{11}$  photons  $\text{cm}^{-3} = 0.7 \text{nM}$ , which is in the range of chemically detectable concentrations.

### 18.6.2 Optical Properties of Deep Ice

The attenuation of sunlight through snow is due to absorption and mainly to scattering (Beukers et al. 1959; Wolff et al. 1998). The directional properties of the photon field also affect its spectral distribution as a function of depth

(Glendinning and Morris 1999). The optical properties of snow covering the Arctic tundra were investigated (Gerland et al. 1999) showing that photosynthetically active radiation decreases nearly exponentially with depth, dropping by an order of magnitude within the first 10–20 cm. Extinction coefficients of  $\alpha = 35 \text{ m}^{-1}$  and  $17 \text{ m}^{-1}$  were measured before and after melting, confirming that after the onset of melting light penetrates deeper into the snowpack. The visual albedo of the snowpack dropped from 0.75 in early June to 0 within 2 weeks. Light at  $\lambda < 500 \text{ nm}$  is largely reflected by snow, but longer wavelengths are able to penetrate it. Above  $\lambda > 1,250 \text{ nm}$ , the albedo drops to zero. Therefore, the photochemical transformation of snow dopants by sunlight occurs close to the snow/air interface rather than in the bulk (Franchy 1998; Glendinning and Morris 1999). From this viewpoint, dopants become isolated from sunlight after being buried a couple of meters.

The optical properties of deep ice are very different from those of snow and firn. The absorption coefficients of bubble-free ice obtained by freezing ultra purified water in the laboratory were measured in the range 250–500 nm (Perovich and Govoni 1991), and display a minimum of about  $0.04 \text{ m}^{-1}$  at about 450 nm. However, these data have been dramatically superseded by field measurements on deep ice. The optical properties of deep ice in the UV-visible range were investigated in connection with the AMANDA (Antarctic Muon and Neutrino Detector Array) experiment. The experiment involves the detection of Čerenkov radiation emitted by energetic neutrinos that penetrate the ice cap from underneath, rather than from the top, using the earth as a filter to eliminate interference from other cosmic particles. At depths of 800–1,000 m, scattering is dominated by residual air bubbles, while absorption is due to the ice itself and to impurities. Photons experience a random walk from the emitter to the detectors, bouncing specularly at each ice-bubble interface, while being absorbed along the magnified path. In this way, neutrinos were actually detected via their Čerenkov emissions by sensors buried in Antarctic ice (Weller et al. 1999).

From a molecular point of view, photon absorption by water-ice in the visible and near-UV is dominated by dipolar transitions involving overtones of intermolecular and intramolecular vibrations. However, the probability of higher-order multiphoton processes decays exponentially, leading to absorption coefficients smaller than  $0.001 \text{ m}^{-1}$  below 500 nm. On the other hand, the tail of the ultraviolet absorptions due to excited states of molecular water as perturbed by intermolecular interactions within the ice matrix, the so-called Urbach tail, drops steeply above 200 nm. Absorption in the intervening spectral region is largely due to atmospheric impurities incorporated into the snow and subsequently processed in the firn layer. These results are quite relevant because they lead to intrinsic ice absorption coefficients in the photochemically useful region that are orders of magnitude smaller than previous data obtained in laboratory ice. In other words, while Čerenkov radiation shorter than 230 nm is largely absorbed by ice, near-UV photons will be exclusively absorbed by embedded contaminants (Belzile et al. 2000; Moran and Zepp 1997; Zuo and Jones 1997).

### 18.6.3 Chemical Identity of Organic and Inorganic Chromophores in Ice Cores

Colored organic matter found in ice cores derives from the water-soluble component of atmospheric aerosol. However, there is very little information on its chemical functionalities. Short chain carboxylic and dicarboxylic acids, as well as complex organic compounds were reported (Baboukas et al. 2000; Legrand and Deangelis 1995; Yu 2000). Humic acid, i.e., the brown material consisting of multifunctional oxygenated organic compounds has been found in the aerosol (Krivacsy et al. 2000). A homologous series of  $\alpha,\omega$ -dicarboxylic acids ( $C_2$ – $C_{10}$ ), among other species such as oxoacids and dicarbonyls, were determined in Greenland ice core samples (206 m deep, 450 years old) (Kawamura et al. 1996, 1999, 2001). This study identified succinic acid as the most abundant species, with a mean concentration of  $4.8 \text{ ng g}^{-1}$ . Much less organic material is found in Antarctic ice, due to its remoteness from continental landmasses. The fact that oxalic, rather than succinic, is the most abundant diacid in the atmosphere (Sempere and Kawamura 1996) clearly suggests post-depositional processing in ice cores. The photoinduced atmospheric oxidation of unsaturated fatty acids is expected to be initiated at the site of unsaturation. For example, the photochemical oxidation of oleic (9-octadecenoic) acid in snow and ice is the plausible source of azelaic acid ( $C_9$ ) (Kawamura et al. 1999). It should be emphasized that saturated carboxylic acids are resistant to oxidation by atmospheric  $O_3$  (Bailey 1972). The recent characterization of polar organic compounds in fog water by liquid chromatography with UV diode array and mass spectrometry detection revealed that most of the UV active organic compounds in fog water are largely acidic and polyfunctional. The acidic organic components absorb between 200 and 450 nm (Fuzzi et al. 2001; Kiss et al. 2001; Krivacsy et al. 2000). A simplified model of the water-soluble organic component of atmospheric aerosols includes neutral compounds such as dialkyl ketones (16%), acids such as alkanedioic acids (15%), hydroxyalkanoic acids (15%), and polycarboxylic acids such as fulvic acid (41%) (Fuzzi et al. 2001).

Since carbonylic compounds can enolize and/or hydrate in aqueous media, and considering that light absorption by carbonyl functionalities extends above 300 nm, whereas *gem*-diols are transparent down to 230 nm, it is very important to establish the actual form of carbonylic species in the quasi-liquid layer. The thermodynamics of the exothermic carbonyl hydration in aqueous solutions favors hydration at lower temperatures (Xu et al. 1993), but the solutes rejected into the quasi-liquid layer will find limited water availability. Solid-state  $^1\text{H}$  NMR of frozen solutions is a suitable technique to elucidate this crucial phenomenon.

For example, it was found that UV absorption by aqueous biacetyl corresponds to about 25% of the dicarbonyl form, the remaining being due to the monocarbonylic species resulting from partial hydration (Faust et al. 1997):



The degree of hydration of the carbonyl group of glyoxylic acid C(O)HC(O)OH ( $pK_a = 3.3$ ) markedly depends on the ionization state. The longest wavelength absorption of the glyoxylate anion is centered at 357 nm, indicative of substantial carbonyl character. However, undissociated glyoxylic acid does not absorb above 275 nm (Steenken et al. 1975). Thus, the temperature dependence of the  $pK_a$ 's of the  $\alpha$ -oxocarboxylic acids will also affect the extent of hydration of the carbonyl group.

The extent to which all the above factors are modified in ice relative to aqueous solutions remains an open field. Solute segregation will in principle shift the hydration equilibrium of aldehydes and ketones to the keto forms, but the issue whether solutes are really immersed in a quasi-liquid layer down to  $-50^{\circ}\text{C}$  will strongly qualify such a tentative conclusion. Acid–base equilibria may also shift upon freezing.

Some inorganic species can absorb solar actinic radiation within ice cores, such as O<sub>3</sub>, H<sub>2</sub>O<sub>2</sub>, NO<sub>2</sub>, HONO, HONO<sub>2</sub>, NO<sub>2</sub><sup>-</sup>, and NO<sub>3</sub><sup>-</sup> (Finlayson-Pitts and Pitts 1986). At 340 nm, their respective optical absorption coefficients are  $\varepsilon$  (base 10, L mole<sup>-1</sup> cm<sup>-1</sup>): 2.0, 0.11, 359, 45, < 0.005, 17, and < 0.9, respectively. However, their photochemical contributions could be substantially larger under the short wavelength Čerenkov radiation ( $\lambda > 230$  nm) transmitted through glacial ice.

#### 18.6.4 Photochemistry of Ice Cores

Ice itself can undergo photochemical decomposition into H and OH radicals. The long-wavelength cutoff of ice is shifted to the blue ( $\lambda < 190$  nm) relative to that of helium-purged liquid water ( $\lambda < 200$  nm). O<sub>2</sub>-saturated water absorbs above 200 nm, with an extinction coefficient of about 0.03 cm<sup>-1</sup> at 210 nm, 298 K (Ghormley and Hochanadel 1971). Langford et al. showed that crystalline, polycrystalline, and amorphous ices irradiated at 220 and 260 nm, i.e., longer than the dissociation threshold at 242 nm in the gas phase, displaying luminescence that has been ascribed to Herzberg band emissions from O<sub>2</sub>\* at 340 nm, and from spin-forbidden  $^4\Sigma \rightarrow X ^2\Pi$  transition of OH radicals (Langford et al. 2000). Thermodynamically, dissociation of H<sub>2</sub>O in ice can occur for wavelengths as long as 270 nm, due to the stabilization of the OH photoproducts in the ice lattice. The implication is that radiation close to the atmospheric ozone cutoff can induce excited state photochemistry in ice.

Assuming that Čerenkov radiation is absorbed exclusively by organic ice dopants, which in turn undergo decarbonylation with nearly unitary quantum efficiency, it has been estimated that about  $4 \times 10^{11}$  CO molecules cm<sup>-3</sup> can be produced over 1,000 years (see above). From the ~100 ppbv CO excess found in 1,000 year old Greenland ice cores with respect to data obtained in the Antarctic (Haan and Raynaud 1998), which are simultaneous with 20 ppmv CO<sub>2</sub> excesses corresponding to about 0.08  $\mu\text{mol kg}^{-1}$  (Tschumi and Stauffer 2000), (Colussi and Hoffmann 2003) obtained a CO concentration excess of  $2 \times 10^{11}$  CO molecules

cm<sup>-3</sup>, i.e., in fair agreement with their estimates. In other words, given the uncertainties associated with some of these assumptions, photochemistry in deep ice cores driven by Čerenkov radiation could account for a substantial fraction of excess CO and CO<sub>2</sub>.

**Acknowledgments** This chapter is dedicated to the memory of Richard E. Honrath – a pioneer in the field of snow photochemistry – in honor of his many achievements and in recognition of the great loss that we feel at his untimely passing.

This work was made possible by funding from the U.S. National Science Foundation (C. A.: ANT-0636985; M. R. H.: ATM-0714329 and ATM-0534990), the Czech Ministry of Education, Youth and Sport (P. K.: MSM0021622412), Science Foundation Ireland (J. S.).

## References

- Abbatt JPD (2003) Interactions of atmospheric trace gases with ice surfaces: adsorption and reaction. *Chem Rev* 103(12):4783–4800
- Anastasio C, Chu L (2009) Photochemistry of nitrous acid (HONO) and nitrous acidium ion ( $\text{H}_2\text{ONO}^+$ ) in aqueous solution and ice. *Environ Sci Technol* 43(4):1108–1114
- Anastasio C, Jordan AL (2004) Photoformation of hydroxyl radical and hydrogen peroxide in aerosol particles from Alert, Nunavut: implications for aerosol and snowpack chemistry in the Arctic. *Atmos Environ* 38(8):1153–1166
- Anastasio C, Matthew BM (2006) A chemical probe technique for the determination of reactive halogen species in aqueous solution: part 2 – chloride solutions and mixed bromide/chloride solutions. *Atmos Chem Phys* 6:2439–2451
- Anastasio C, Robles T (2007) Light absorption by soluble chemical species in Arctic and Antarctic snow. *J Geophys Res-Atmos* 112(D24):D24304
- Anastasio C, Galbavy ES, Hutterli MA, Burkhardt JF, Friel D (2007) Photoformation of hydroxyl radical on snow grains at Summit, Greenland. *Atmos Environ* 41:5110–5121
- Andreae MO, Rosenfeld D (2008) Aerosol-cloud-precipitation interactions. Part 1. The nature and sources of cloud-active aerosols. *Earth-Sci Rev* 89(1–2):13–41
- Andres E, Askebjer P, Bai X, Barouch G, Barwick SW, Bay TC, Becker KH, Bergstrom L, Bertrand D, Bierbaum D, Biron A, Booth J, Botner O, Bouchta A, Boyce MM, Carius S, Chen A, Chirkin D, Conrad J, Cooley J, Costa CGS, Cowen DF, Dailing J, Dalberg E, DeYoung T, Desiati P, Dewulf JP, Doksy P, Edsjo J, Ekstrom P, Erlandsson B, Feser T, Gaug M, Goldschmidt A, Goobar A, Gray L, Haase H, Hallgren A, Halzen F, Hanson K, Hardtke R, He YD, Hellwig M, Heukenkamp H, Hill GC, Hulth PO, Hundertmark S, Jacobsen J, Kandhadai V, Karle A, Kim J, Koci B, Kopke L, Kowalski M, Leich H, Leuthold M, Lindal P, Liubarsky I, Loaiza P, Lowder DM, Ludvig J, Madsen J, Marciniewski P, Matis HS, Mihalyi A, Mikolajski T, Miller TC, Minaeva Y, Miocinovic P, Mock PC, Morse R, Neunhoffer T, Newcomer FM, Niessen P, Nygren DR, Ogelman H, De los Heros CP, Porrata R, Price PB, Rawlins K, Reed C, Rhode W, Richards A, Richter S, Martino JR, Romenesko P, Ross D, Rubinstein H, Sander HG, Scheider T, Schmidt T, Schneider D, Schneider E, Schwarz R, Silvestri A, Solarz M, Spiczak GM, Spiering C, Starinsky N, Steele D, Steffen P, Stokstad RG, Usechak N, Vander Donckt M, Walck C, Weinheimer C, Wiebusch CH, Wischniewski R, Wissing H, Woschnagg K, Wu W, Yodh G, Young S (2001) Observation of high-energy neutrinos using Čerenkov detectors embedded deep in Antarctic ice. *Nature* 410 (6827):441–443
- Arakaki T, Faust BC (1998) Sources, sinks, and mechanisms of hydroxyl radical (OH) photoproduction and consumption in authentic acidic continental cloud waters from Whiteface

- Mountain, New York: the role of the Fe(r) ( $r = \text{II}, \text{III}$ ) photochemical cycle. *J Geophys Res-Atmos* 103(D3):3487–3504
- Arakaki T, Miyake T, Hirakawa T, Sakugawa H (1999) pH dependent photoformation of hydroxyl radical and absorbance of aqueous-phase N(III) ( $\text{HNO}_2$  and  $\text{NO}_2^-$ ). *Environ Sci Technol* 33 (15):2561–2565
- Baboukas ED, Kanakidou M, Mihalopoulos N (2000) Carboxylic acids in gas and particulate phase above the Atlantic Ocean. *J Geophys Res* 105(D11):14459–14471
- Bailey PS (1972) Ozone reactions with organic compounds. In: 161st meeting of the American Chemical Society, Los Angeles, 29–30 March 1971
- Baker M, Baker MB (1996) A model for the ice-vapor interface at equilibrium. *J Cryst Growth* 169 (2):393–404
- Bartels-Rausch T, Guimbaud C, Gaggeler HW, Ammann M (2004) The partitioning of acetone to different types of ice and snow between 198 and 223 K. *Geophys Res Lett* 31(16):L16110
- Bartels-Rausch T, Huthwelker T, Gaggeler HW, Ammann M (2005) Atmospheric pressure coated-wall flow-tube study of acetone adsorption on ice. *J Phys Chem A* 109(20):4531–4539
- Barton DHR, De Mayo P, Shafiq M (1958) Photochemical transformations. 2. The constitution of lumisantonin. *J Chem Soc* 140:140–146
- Beine HJ, Honrath RE, Dominé F, Simpson W, Fuentes JD (2002)  $\text{NO}_x$  during background and ozone depletion periods at Alert: fluxes above the snow surface. *J Geophys Res-Atmos* 107(D21):4584
- Belzile C, Johannessen S, Gosselin M, Demers S, Miller W (2000) Ultraviolet attenuation by dissolved and particulate constituents of first-year ice during late spring in an Arctic polynya. *Limnol Oceanogr* 45(6):1265–1273
- Bernstein MP, Dworkin JP, Sandford SA, Cooper GW, Allamandola LJ (2002) Racemic amino acids from the ultraviolet photolysis of interstellar ice analogues. *Nature* 416(6879):401–403
- Betterton EA, Anderson DJ (2001) Autoxidation of N(III), S(IV), and other species in frozen solution – a possible pathway for enhanced chemical transformation in freezing systems. *J Atmos Chem* 40(2):171–189
- Beukers R, Ijlstra J, Berends W (1959) The effect of ultraviolet light on some components of the nucleic acids: II: in rapidly frozen solutions. *Recl Trav Chim Pays-Bas* 77:729–732
- Bhatnagar BS, Cardon S, Pikal MJ, Bogner RH (2005) Reliable determination of freeze-concentration using DSC. *Thermochimica Acta* 425(1–2):149–163
- Bhatnagar BS, Bogner RH, Pikal MJ (2007) Protein stability during freezing: separation of stresses and mechanisms of protein stabilization. *Pharm Dev Technol* 12(5):505–523
- Bhatnagar BS, Pikal MJ, Bogner RH (2008) Study of the individual contributions of ice formation and freeze-concentration on isothermal stability of lactate dehydrogenase during freezing. *J Pharm Sci* 97(2):798–814
- Bielski BHJ, Cabelli DE, Arudi RL, Ross AB (1985) Reactivity of  $\text{HO}_2/\text{O}_2^-$  radicals in aqueous solution. *J Phys Chem Ref Data* 14(4):1041–1100
- Bilski P, Chignell CF, Szychlinski J, Borowski A, Olewsky E, Reszka K (1992) Photooxidation of organic and inorganic substrates during UV-photolysis of nitrite anion in aqueous solution. *J Am Chem Soc* 114(2):549–556
- Blaha L, Klánová J, Klán P, Janousek J, Skarek M, Ruzicka R (2004) Toxicity increases in ice containing monochlorophenols upon photolysis: environmental consequences. *Environ Sci Technol* 38(10):2873–2878
- Blais JM, Schindler DW, Muir DCG, Kimpe LE, Donald DB, Rosenberg B (1998) Accumulation of persistent organochlorine compounds in mountains of western Canada. *Nature* 395 (6702):585–588
- Bluhm H, Salmeron M (1999) Growth of nanometer thin ice films from water vapor studied using scanning polarization force microscopy. *J Chem Phys* 111(15):6947–6954
- Bluhm H, Inoue T, Salmeron M (2000a) Formation of dipole-oriented water films on mica substrates at ambient conditions. *Surf Sci* 462(1–3):L599–L602
- Bluhm H, Inoue T, Salmeron M (2000b) Friction of ice measured using lateral force microscopy. *Phys Rev B* 61(11):7760–7765

- Bolton K, Pettersson JBC (2000) A molecular dynamics study of the long-time ice Ih surface dynamics. *J Phys Chem B* 104(7):1590–1595
- Borodin A, Hofft O, Kahnert U, Kempfer V, Krischok S, Abou-Helal MO (2004) The interface between benzenes ( $C_6H_6$ ;  $C_6H_5Cl$ ; 2- $C_6H_4OHCl$ ) and amorphous solid water studied with metastable impact electron spectroscopy and ultraviolet photoelectron spectroscopy ( $He^I$  and  $II^+$ ). *J Chem Phys* 120(11):5407–5413
- Bose SN, Kumar S, Davies RJH, Sethi SK, McCloskey JA (1984) The photochemistry of d(T-A) in aqueous solution and in ice. *Nucleic Acids Res* 12(20):7929–7947
- Bottenheim JW, Boudries H, Brickell PC, Atlas E (2002) Alkenes in the Arctic boundary layer at Alert, Nunavut, Canada. *Atmos Environ* 36(15–16):2585–2594
- Boudries H, Bottenheim JW, Guimbaud C, Grannas AM, Shepson PB, Houdier S, Perrier S, Domine F (2002) Distribution and trends of oxygenated hydrocarbons in the high Arctic derived from measurements in the atmospheric boundary layer and interstitial snow air during the ALERT2000 field campaign. *Atmos Environ* 36(15–16):2573–2583
- Boxe CS, Colussi AJ, Hoffmann MR, Perez IM, Murphy JG, Cohen RC (2006) Kinetics of NO and  $NO_2$  evolution from illuminated frozen nitrate solutions. *J Phys Chem A* 110(10):3578–3583
- Bronshteyn VL, Chernov AA (1991) Freezing potentials arising on solidification of dilute aqueous-solutions of electrolytes. *J Cryst Growth* 112(1):129–145
- Burkhart JF, Hutterli M, Bales RC, McConnell JR (2004) Seasonal accumulation timing and preservation of nitrate in firn at Summit, Greenland. *J Geophys Res-Atmos* 109(D19):D19302
- Burkhart JF, Bales RC, McConnell JR, Hutterli MA, Frey MM (2009) Geographic variability of nitrate deposition and preservation over the Greenland Ice Sheet. *J Geophys Res-Atmos* 114: D06301
- Calace N, Petronio BM, Cini R, Stortini AM, Pampaloni B, Udisti R (2001) Humic marine matter and insoluble materials in Antarctic snow. *Int J Environ Anal Chem* 79(4):331–348
- Cao EH, Chen YH, Cui ZF, Foster PR (2003) Effect of freezing and thawing rates on denaturation of proteins in aqueous solutions. *Biotechnol Bioeng* 82(6):684–690
- Caro GMM, Meierhenrich UJ, Schutte WA, Barbier B, Segovia AA, Rosenbauer H, Thiemann WHP, Brack A, Greenberg JM (2002) Amino acids from ultraviolet irradiation of interstellar ice analogues. *Nature* 416(6879):403–406
- Carpenter JF, Prestrelski SJ, Arakawa T (1993) Separation of freezing-induced and drying-induced denaturation of lyophilized proteins using stress-specific stabilization. 1. enzyme-activity and calorimetric studies. *Arch Biochem Biophys* 303(2):456–464
- Chaabouni H, Schriver-Mazzuoli L, Schriver A (2000a) FTIR studies of annealing processes and irradiation effects at 266 nm in ozone-amorphous ice mixtures. *Low Temp Phys* 26 (9–10):712–718
- Chaabouni H, Schriver-Mazzuoli L, Schriver A (2000b) Infrared spectroscopy of neat solid ozone and that of ozone in interaction with amorphous and crystalline water ice. *J Phys Chem A* 104 (30):6962–6969
- Chang BS, Kendrick BS, Carpenter JF (1996) Surface-induced denaturation of proteins during freezing and its inhibition by surfactants. *J Pharm Sci* 85(12):1325–1330
- Cheftel JC, Levy J, Dumay E (2000) Pressure-assisted freezing and thawing: principles and potential applications. *Food Rev Int* 16(4):453–483
- Cho H, Shepson PB, Barrie LA, Cowin JP, Zaveri R (2002) NMR investigation of the quasi-brine layer in ice/brine mixtures. *J Phys Chem B* 106(43):11226–11232
- Choi J, Conklin MH, Bales RC, Sommerfeld RA (2000) Experimental investigation of  $SO_2$  uptake in snow. *Atmos Environ* 34(5):793–801
- Chu L, Anastasio C (2003) Quantum yields of hydroxyl radical and nitrogen dioxide from the photolysis of nitrate on ice. *J Phys Chem A* 107:9594–9602
- Chu L, Anastasio C (2005) Formation of hydroxyl radical from the photolysis of frozen hydrogen peroxide. *J Phys Chem A* 109(28):6264–6271
- Chu L, Anastasio C (2007) Temperature and wavelength dependence of nitrite photolysis in frozen and aqueous solutions. *Environ Sci Technol* 41:3626–3632

- Cocke DL, Gomes JAG, Gossage JL, Li KY, Lin CJ, Tandl S (2004) Water-related matrix isolation phenomena during NO<sub>2</sub> photolysis in argon matrix. *Appl Spectrosc* 58(5):528–534
- Cohen SR, Weissbuch I, PopovitzBiro R, Majewski J, Mauder HP, Lavi R, Leiserowitz L, Lahav M (1996) Spontaneous assembly in organic thin films spread on aqueous subphase: a scanning force microscope (SFM) study. *Israel J Chem* 36(1):97–110
- Colussi AJ, Hoffmann MR (2003) In situ photolysis of deep ice core contaminants by Čerenkov radiation of cosmic origin. *Geophys Res Lett* 30(4):1195
- Compoint M, Toubin C, Picaud S, Hoang PNM, Girardet C (2002) Geometry and dynamics of formic and acetic acids adsorbed on ice. *Chem Phys Lett* 365(1–2):1–7
- Conklin M, Bales RC (1993) SO<sub>2</sub> uptake on ice spheres: liquid nature of the ice-air interface. *J Geophys Res* 98(D9):16851–16855
- Cotter ESN, Jones AE, Wolff EW, Bauguitte SJB (2003) What controls photochemical NO and NO<sub>2</sub> production from Antarctic snow? Laboratory investigation assessing the wavelength and temperature dependence. *J Geophys Res* 108(D4):4147
- Cowin JP, Tsekouras AA, Iedema MJ, Wu K, Ellison GB (1999) Immobility of protons in ice from 30 to 190 K. *Nature* 398:405
- Cullen D, Baker I (2000) The chemistry of grain boundaries in Greenland ice. *J Glaciol* 46(155):703–706
- Dash JG, Fu HY, Wetzlaufer JS (1995) The premelting of ice and its environmental consequences. *Rep Prog Phys* 58(1):115–167
- Dassau TM, Shepson PB, Bottenheim JW, Ford KM (2004) Peroxyacetyl nitrate photochemistry and interactions with the Arctic surface. *J Geophys Res-Atmos* 109(D18)
- Davidson RS, Goodwin D (1980) The direct photo-oxidative decarboxylation of alpha-hydroxy-carboxylic acids. *Tetrahedron Lett* 21:4943
- Davis D, Nowak JB, Chen G, Buhr M, Arimoto R, Hogan A, Eisele F, Mauldin L, Tanner D, Shetter R, Lefer B, McMurry P (2001) Unexpected high levels of NO observed at South Pole. *Geophys Res Lett* 28(19):3625–3628
- Delzeit L, Devlin M, Rowland B, Devlin J, Buch V (1996) Adsorbate-induced partial ordering of the irregular surface and subsurface of crystalline ice. *J Phys Chem* 100(24):10076–10082
- Devlin JP (1992) Molecular interactions with icy surfaces – infrared spectra of CO absorbed in microporous amorphous ice. *J Phys Chem* 96(15):6185–6188
- Devlin JP, Buch V (1995) Surface of ice as viewed from combined spectroscopic and computer modeling studies. *J Phys Chem* 99(45):16534–16548
- Devlin J, Uras N, Rahman M, Buch V (1999) Covalent and ionic states of strong acids at the ice surface. *Israel J Chem* 39(3–4):261–272
- Dibb JE, Arsenault M (2002) Shouldn't snowpacks be sources of monocarboxylic acids? *Atmos Environ* 36(15–16):2513–2522
- Dibb JE, Arsenault M, Peterson MC, Honrath RE (2002) Fast nitrogen oxide photochemistry in Summit, Greenland snow. *Atmos Environ* 36(15–16):2501–2511
- Doe H, Kobayashi T, Sawada H (1995) Characterization of ice electrodes. *J Electroanal Chem* 383:53
- Dolinová J, Ruzicka R, Kurková R, Klánová J, Klán P (2006) Oxidation of aromatic and aliphatic hydrocarbons by OH radicals photochemically generated from H<sub>2</sub>O<sub>2</sub> in ice. *Environ Sci Technol* 40(24):7668–7674
- Domine F, Thibert E (1998) Comment on diffusion of HNO<sub>3</sub> in ice. *Geophys Res Lett* 25(23):4389–4390
- Domine F, Cincinelli A, Bonnaud E, Martellini T, Picaud S (2007) Adsorption of phenanthrene on natural snow. *Environ Sci Technol* 41(17):6033–6038
- Domine F, Albert M, Huthwelker T, Jacobi HW, Kokhanovsky AA, Lehning M, Picard G, Simpson WR (2008) Snow physics as relevant to snow photochemistry. *Atmos Chem Phys* 8(2):171–208
- Doppenschmidt A, Butt H-J (2000) Measuring the thickness of the liquid-like layer on ice surfaces with atomic force microscopy. *Langmuir* 16:6709–6714

- Doppenschmidt A, Kappel M, Butt H-J (1998) Surfaces properties of ice studied by atomic force microscopy. *J Phys Chem B* 102:7813–7819
- Drzymala J, Sadowski Z, Holysz L, Chibowski E (1999) Ice/water interface: zeta potential, point of zero charge, and hydrophobicity. *J Colloid Interface Sci* 220:229
- Du R, Ariya PA (2008) The test freezing temperature of C<sub>2</sub>–C<sub>6</sub> dicarboxylic acid: the important indicator for ice nucleation processes. *Chin Sci Bull* 53(17):2685–2691
- Dubowski Y, Hoffmann MR (2000) Photochemical transformations in ice: implications for the fate of chemical species. *Geophys Res Lett* 27(20):3321–3324
- Dubowski Y, Colussi AJ, Hoffmann MR (2001) Nitrogen dioxide release in the 302 nm band photolysis of spray-frozen aqueous nitrate solutions. Atmospheric implications. *J Phys Chem A* 105:4928
- Dubowski Y, Colussi AJ, Boxe C, Hoffmann MR (2002) Monotonic increase of nitrite yields in the photolysis of nitrate in ice and water between 238 and 294 K. *J Phys Chem A* 106(30):6967–6971
- Engel PS (1970) Photochemistry of dibenzyl ketone. *J Am Chem Soc* 92(20):6074–6076
- Engstrom JD, Lai ES, Ludher BS, Chen B, Milner TE, Williams RO, Kitto GB, Johnston KP (2008) Formation of stable submicron protein particles by thin film freezing. *Pharm Res* 25(6):1334–1346
- Fabre A, Barnola JM, Arnaud L, Chapellaz J (2000) Determination of gas diffusivity in polar firn: comparison between experimental measurements and inverse modeling. *Geophys Res Lett* 27:557–560
- Faraday M (1859) On regulation, and on the conservation of force. *Philos Mag* 17:162–169
- Faraudo G, Weibel DE (2001) Effect of HCl addition and temperature on the heterogeneous chemistry and photochemistry of ClONO<sub>2</sub> adsorbed on ice crystals. *Prog React Kinet Mech* 26(2–3):179–199
- Farman JC, Gardiner BG, Shanklin JD (1985) Large losses of total ozone in Antarctica reveal seasonal ClO<sub>x</sub>/NO<sub>x</sub> interaction. *Nature* 315(6016):207–210
- Faust BC, Hoigné J (1990) Photolysis of Fe(III)-hydroxy complexes as sources of OH radicals in clouds, fog and rain. *Atmos Environ* 24A(1):79–89
- Faust BC, Zepp RG (1993) Photochemistry of aqueous iron(III) polycarboxylate complexes – roles in the chemistry of atmospheric and surface waters. *Environ Sci Technol* 27(12):2517–2522
- Faust B, Powell K, Rao C, Anastasio C (1997) Aqueous-phase photolysis of biacetyl (an alpha-dicarbonyl compound): a sink for biacetyl, and a source of acetic acid, peroxyacetic acid, hydrogen peroxide, and the highly oxidizing acetylperoxyl radical in aqueous aerosols, fogs, and clouds. *Atmos Environ* 31(3):497–510
- Fennema O (1975) Reaction kinetics in partially frozen aqueous systems. In: Duckworth RG (ed) *Water relations of foods*. Academic, London, pp 539–556
- Finlayson-Pitts BJ, Pitts JN (1986) *Atmospheric chemistry*. Wiley, New York
- Finlayson-Pitts BJ, Pitts JN (2000) *Chemistry of the upper and lower atmosphere: theory, experiments, and applications*. Academic, San Diego
- Finnegan WG, Pitter RL (1991) Preliminary study of coupled oxidation-reduction reactions of included ions in growing ice crystals – reply. *Atmos Environ* 25(12):2912–2913
- Finnegan W, Pitter R (1997) Ion-induced charge separations in growing single ice crystals: effects on growth and interaction processes. *J Colloid Interface Sci* 189(2):322–327
- Finnegan WG, Pitter RL, Young LG (1991) Preliminary study of coupled oxidation reduction reactions of included ions in growing ice crystals. *Atmos Environ A-Gen Top* 25(11):2531–2534
- Finnegan W, Pitter R, Hinsvark B (2001) Redox reactions in growing single ice crystals: a mechanistic interpretation of experimental results. *J Colloid Interface Sci* 242(2):373–377
- Fischer M, Warneck P (1996) Photodecomposition of nitrite and undissociated nitrous acid in aqueous solution. *J Phys Chem* 100(48):18749–18756
- Ford KM, Campbell BM, Shepson PB, Bertman SB, Honrath RE, Peterson M, Dibb JE (2002) Studies of Peroxyacetyl nitrate (PAN) and its interaction with the snowpack at Summit, Greenland. *J Geophys Res-Atmos* 107(D10):4102

- France JL, King MD, Lee-Taylor J (2007) Hydroxyl (OH) radical production rates in snowpacks from photolysis of hydrogen peroxide ( $H_2O_2$ ) and nitrate ( $NO_3^-$ ). *Atmos Environ* 41(26):5502–5509. doi:[10.1016/j.atmosenv.2007.03.056](https://doi.org/10.1016/j.atmosenv.2007.03.056)
- Franchy R (1998) Surface and bulk photochemistry of solids. *Rep Prog Phys* 61:691
- Fuzzi S, Decesari S, Facchini MC, Matta E, Mircea M, Tagliavini E (2001) A simplified model of the water soluble organic component of atmospheric aerosols. *Geophys Res Lett* 28(21):4079–4082
- Galbavy ES, Anastasio C, Lefer B, Hall S (2007a) Light penetration in the snowpack at Summit, Greenland: part 1. Nitrite and hydrogen peroxide photolysis. *Atmos Environ* 41(24):5077–5090
- Galbavy ES, Anastasio C, Lefer B, Hall S (2007b) Light penetration in the snowpack at Summit, Greenland: part 2. Nitrate photolysis. *Atmos Environ* 41(24):5091–5100
- Garbarino JR, Snyder-Conn E, Leiker TJ, Hoffman GL (2002) Contaminants in arctic snow collected over northwest Alaskan sea ice. *Water Air Soil Pollut* 139(1–4):183–214
- Gerakines PA, Moore MH, Hudson RL (2004) Ultraviolet photolysis and proton irradiation of astrophysical ice analogs containing hydrogen cyanide. *Icarus* 170(1):202–213
- Gerland S, Winther JG, Orbaek JB, Liston GE, Oritsland NA, Blanco A, Ivanov B (1999) Physical and optical properties of snow covering Arctic tundra on Svalbard. *Hydrol Process* 13(14–15):2331–2343
- Gertner BJ, Hynes JT (1996) Molecular dynamics simulation of hydrochloric acid ionization at the surface of stratospheric ice. *Science* 271:1563
- Ghormley JA, Hochanadel CJ (1971) Production of H, OH,  $H_2O_2$ , in the flash photolysis of ice. *J Phys Chem* 75(1):40–44
- Giannelli V, Thomas DN, Haas C, Kattner G, Kennedy H, Dieckmann GS (2001) Behaviour of dissolved organic matter and inorganic nutrients during experimental sea-ice formation. *Ann Glaciol* 33:317–321
- Gilbert A, Baggott J (1991) Essentials of molecular photochemistry. CRC Press, Boca Raton
- Glendinning JHG, Morris EM (1999) Incorporation of spectral and directional radiative transfer in a snow model. *Hydrol Process* 13:1761
- Glenn DF, Ingram JC (1994) Electrodeposition at an ice-coated electrode. *J Electrochem Soc* 141(9):L113
- Goff HD (1992) Low-temperature stability and the glassy state in frozen foods. *Food Res Int* 25(4):317–325
- Goff HD, Sahagian ME (1996) Glass transitions in aqueous carbohydrate solutions and their relevance to frozen food stability. *Thermochimica Acta* 280:449–464
- Goldstein S, Rabani J (2007) Mechanism of nitrite formation by nitrate photolysis in aqueous solutions: the role of peroxynitrite, nitrogen dioxide, and hydroxyl radical. *J Am Chem Soc* 129(34):10597–10601
- Graedel TE, Weschler CJ (1981) Chemistry within aqueous atmospheric aerosols and raindrops. *Rev Geophys Sp Phys* 19(4):505–539
- Graham J, Roberts J (2000) Chemical reactions of organic molecules adsorbed at ice 1. Chlorine addition to propene. *J Phys Chem B* 104(5):978–982
- Graham JD, Roberts JT, Anderson LD, Grassian VH (1996) The 367 nm photochemistry of OCIO thin films and OCIO adsorbed on ice. *J Phys Chem* 100(50):19551–19558
- Grannas AM, Shepson PB, Filley TR (2004) Photochemistry and nature of organic matter in Arctic and Antarctic snow. *Global Biogeochem Cycles* 18(1):GB1006
- Grannas AM, Hockaday WC, Hatcher PG, Thompson LG, Mosley-Thompson E (2006) New revelations on the nature of organic matter in ice cores. *J Geophys Res-Atmos* 111(D4):D04304
- Grannas AM, Jones AE, Dibb J, Ammann M, Anastasio C, Beine HJ, Bergin M, Bottenheim J, Boxe CS, Carver G, Chen G, Crawford JH, Domine F, Frey MM, Guzman MI, Heard DE, Helmig D, Hoffmann MR, Honrath RE, Huey LG, Hutterli M, Jacobi HW, Klán P, Lefer B, McConnell J, Plane J, Sander R, Savarino J, Shepson PB, Simpson WR, Sodeau JR, von Glasow R, Weller R, Wolff EW, Zhu T (2007) An overview of snow photochemistry: evidence, mechanisms and impacts. *Atmos Chem Phys* 7:4329–4373

- Grecea ML, Backus EHG, Kleyn AW, Bonn M (2006) Adsorption and photochemistry of multilayer bromoform on ice. *Surf Sci* 600(16):3337–3344
- Grollert C, Puxbaum H (2000) Lipid organic aerosol and snow composition at a high alpine site in the fall and the spring season and scavenging ratios for single compounds. *Water Air Soil Pollut* 117(1–4):157–173
- Gross G, Svec R (1997) Effect of ammonium on anion uptake and dielectric relaxation in laboratory-grown ice columns. *J Phys Chem B* 101(32):6282–6284
- Gross GW, McKee C, Wu C-H (1975) Concentration dependent solute distribution at the ice/water phase boundary. *J Chem Phys* 62:3080–3092
- Gross GW, Gutjahr A, Caylor K (1987) Recent experimental work on solute redistribution at the ice water interface – implications for electrical-properties and interface processes. *Journal De Physique* 48(C-1):527–533
- Guimbaud C, Grannas AM, Shepson PB, Fuentes JD, Boudries H, Bottenheim JW, Domine F, Houdier S, Perrier S, Biesenthal TB, Splawn BG (2002) Snowpack processing of acetaldehyde and acetone in the Arctic atmospheric boundary layer. *Atmos Environ* 36(15–16):2743–2752
- Guzmán MI, Colussi AJ, Hoffmann MR (2006a) Photoinduced oligomerization of aqueous pyruvic acid. *J Phys Chem A* 110:3619–3626
- Guzmán MI, Hildebrandt L, Colussi AJ, Hoffmann MR (2006b) Cooperative hydration of pyruvic acid in ice. *J Am Chem Soc* 128(32):10621–10624
- Guzmán MI, Hoffmann MR, Colussi AJ (2007) Photolysis of pyruvic acid in ice: possible relevance to CO and CO<sub>2</sub> ice core record anomalies. *J Geophys Res-Atmos* 112(D10):D10123
- Haan D, Raynaud D (1998) Ice core record of CO variations during the last two millennia: atmospheric implications and chemical interactions within the Greenland ice. *Tellus* 50B:253
- Haan D, Zuo Y, Gros V, Brenninkmeijer C (2001) Photochemical production of carbon monoxide in snow. *J Atmos Chem* 40(3):217–230
- Hallam HE (1973) Vibrational spectroscopy of trapped species: infrared and raman studies of matrix-isolated molecules, radicals and ions. Wiley, New York
- Hansen KM, Halsall CJ, Christensen JH (2006) A dynamic model to study the exchange of gas-phase persistent organic pollutants between air and a seasonal snowpack. *Environ Sci Technol* 40(8):2644–2652
- Haynes DR, Tro NJ, George SM (1992) Condensation and evaporation of H<sub>2</sub>O on ice surfaces. *J Phys Chem* 96(21):8502–8509
- Heger D, Klán P (2007) Interactions of organic molecules at grain boundaries in ice: a solvatochromic analysis. *J Photochem Photobiol A-Chem* 187:275–284
- Heger D, Jirkovský J, Klán P (2005) Aggregation of methylene blue in frozen aqueous solutions studied by absorption spectroscopy. *J Phys Chem A* 109(30):6702–6709
- Heger D, Klánová J, Klán P (2006) Enhanced protonation of cresol red in acidic aqueous solutions caused by freezing. *J Phys Chem B* 110(3):1277–1287
- Heintzenberg J (1989) Fine particles in the global troposphere - a review. *Tellus B Chem Phys Meteorol* 41:149–160
- Hellebust S, O'Riordan B, Sodeau J (2007a) Cirrus cloud mimics in the laboratory: an infrared spectroscopy study of thin films of mixed ice of water with organic acids and ammonia. *J Chem Phys* 126(8):084702
- Hellebust S, Roddis T, Sodeau JR (2007b) Potential role of the nitroacidium ion on HONO emissions from the snowpack. *J Phys Chem A* 111(7):1167–1171
- Hemley R (2000) Effects of high pressure on molecules. *Ann Rev Phys Chem* 51:763–800
- Herbert BMJ, Halsall CJ, Villa S, Jones KC, Kallenborn R (2005) Rapid changes in PCB and OC pesticide concentrations in Arctic snow. *Environ Sci Technol* 39(9):2998–3005
- Herbert BMJ, Halsall CJ, Jones KC, Kallenborn R (2006a) Field investigation into the diffusion of semi-volatile organic compounds into fresh and aged snow. *Atmos Environ* 40(8):1385–1393
- Herbert BMJ, Villa S, Halsall C (2006b) Chemical interactions with snow: understanding the behavior and fate of semi-volatile organic compounds in snow. *Ecotoxicol Environ Saf* 63(1):3–16

- Herrmann H (2007) On the photolysis of simple anions and neutral molecules as sources of  $\text{O}^-/\text{OH}$ ,  $\text{SO}_x^-$  and  $\text{Cl}$  in aqueous solution. *Phys Chem Chem Phys* 9(30):3935–3964
- Hobbs PV (1974) *Ice physics*. Clarendon Press, Oxford
- Hoff JT, Wania F, Mackay D, Gillham R (1995) Sorption of nonpolar organic vapors by ice and snow. *Environ Sci Technol* 29(8):1982–1989
- Holmes NS, Sodeau JR (1999) A study of the interaction between halomethanes and water-ice. *J Phys Chem A* 103(24):4673–4679
- Honda K (2001) Acceleration of sulfurous acid oxidation by freezing of aqueous solution. *Nippon Kagaku Kaishi* 2:125–127
- Hondoh T (ed) (2000) *Physics of ice core records*. Hokkaido University Press, Sapporo
- Honrath RE, Peterson MC, Guo S, Dibb JE, Shepson PB, Campbell B (1999) Evidence of  $\text{NO}_x$  production within or upon ice particles in the Greenland snowpack. *Geophys Res Lett* 26(6):695–698
- Honrath RE, Guo S, Peterson MC, Dziobak MP, Dibb JE, Arsenault MA (2000a) Photochemical production of gas phase  $\text{NO}_x$  from ice crystal  $\text{NO}_3^-$ . *J Geophys Res-Atmos* 105(D19): 24183–24190
- Honrath RE, Peterson MC, Dziobak MP, Dibb JE, Arsenault MA, Green SA (2000b) Release of  $\text{NO}_x$  from sunlight-irradiated midlatitude snow. *Geophys Res Lett* 27(15):2237–2240
- Honrath RE, Lu Y, Peterson MC, Dibb JE, Arsenault MA, Cullen NJ, Steffen K (2002) Vertical fluxes of  $\text{NO}_x$ ,  $\text{HONO}$ , and  $\text{HNO}_3$  above the snowpack at Summit, Greenland. *Atmos Environ* 36(15–16):2629–2640
- Horne RA (1963) Kinetics of the iron(II)-iron(III) electron exchange reaction in ice media. *J Inorg Nucl Chem* 25:1139
- Houdier S, Perrier S, Domine F, Cabanes A, Legagneux L, Grannas AM, Guimbaud C, Shepson PB, Boudries H, Bottenheim JW (2002) Acetaldehyde and acetone in the Arctic snowpack during the ALERT2000 campaign. Snowpack composition, incorporation processes and atmospheric impact. *Atmos Environ* 36(15–16):2609–2618
- Hudson RL (2006) Astrochemistry examples in the classroom. *J Chem Educ* 83(11):1611–1616
- Hudson RL, Moore MH, Dworkin JP, Martin MP, Pozun ZD (2008) Amino acids from ion-irradiated nitrile-containing ices. *Astrobiology* 8(4):771–779
- Hullar T, Anastasio C (2011) Yields of hydrogen peroxide from the reaction of hydroxyl radical with organic compounds in solution and ice. *Atmos Chem Phys* 11:7209–7222
- Huthwelker T, Lamb D, Baker M, Swanson B, Peter T (2001) Uptake of  $\text{SO}_2$  by polycrystalline water ice. *J Colloid Interface Sci* 238(1):147–159
- Hutterli MA, McConnell JR, Stewart RW, Jacobi HW, Bales RC (2001) Impact of temperature-driven cycling of hydrogen peroxide ( $\text{H}_2\text{O}_2$ ) between air and snow on the planetary boundary layer. *J Geophys Res-Atmos* 106(D14):15395–15404
- Hutterli MA, McConnell JR, Stewart RW, Bales RC (2003) Sensitivity of hydrogen peroxide ( $\text{H}_2\text{O}_2$ ) and formaldehyde (HCHO) preservation in snow to changing environmental conditions: implications for the interpretation of ice core records. *J Geophys Res-Atmos* 108(D12):4023
- Hutterli MA, McConnell JR, Chen G, Bales RC, Davis DD, Lenschow DH (2004) Formaldehyde and hydrogen peroxide in air, snow and interstitial air at South Pole. *Atmos Environ* 38(32):5439–5450
- Hynes R, Mossinger J, Cox R (2001) The interaction of  $\text{HCl}$  with water-ice at tropospheric temperatures. *Geophys Res Lett* 28(14):2827–2830
- Ikeda A, Kawanaka N, Yabushita A, Kawasaki M (2008) Photodissociation dynamics of OCS and CS<sub>2</sub> adsorbed on water ice films at 193 nm. *J Photochem Photobiol A-Chem* 195(2–3):330–336
- Inglese S, Granucci G, Laino T, Persico M (2005) Photodissociation dynamics of chlorine peroxide adsorbed on ice. *J Phys Chem B* 109(16):7941–7947
- Israelachvili J (1992) *Intermolecular and surface forces*. Academic, San Diego
- Jacob P, Klockow D (1993) Measurements of hydrogen peroxide in Antarctic ambient air, snow, and firn cores. *Fresenius J Anal Chem* 346(4):429–434

- Jacobi HW, Hilker B (2007) A mechanism for the photochemical transformation of nitrate in snow. *J Photochem Photobiol A-Chem* 185(2–3):371–382
- Jacobi HW, Bales RC, Honrath RE, Peterson MC, Dibb JE, Swanson AL, Albert MR (2004) Reactive trace gases measured in the interstitial air of surface snow at Summit, Greenland. *Atmos Environ* 38(12):1687–1697
- Jaffrezo JL, Clain MP, Masclet P (1994) Polycyclic aromatic hydrocarbons in the polar ice of Greenland – geochemical use of these atmospheric tracers. *Atmos Environ* 28(6):1139–1145
- Jedlovszky P, Hantal G, Neurohr K, Picaud S, Hoang PNM, von Hessberg P, Crowley JN (2008) Adsorption isotherm of formic acid on the surface of ice, as seen from experiments and grand canonical Monte Carlo simulation. *J Phys Chem C* 112(24):8976–8987
- Jelley JV (1958) Cerenkov radiation. Pergamon, New York
- Jones AE, Weller R, Wolff EW, Jacobi H-W (2000) Speciation and rate of photochemical NO and NO<sub>2</sub> production in Antarctic snow. *Geophys Res Lett* 27(3):345–348
- Jones AE, Wolff EW, Salmon RA, Bauguitte SJB, Roscoe HK, Anderson PS, Ames D, Clemithshaw KC, Fleming ZL, Bloss WJ, Heard DE, Lee JD, Read KA, Hamer P, Shallcross DE, Jackson AV, Walker SL, Lewis AC, Mills GP, Plane JMC, Saiz-Lopez A, Sturges WT, Worton DR (2008) Chemistry of the Antarctic boundary layer and the interface with snow: an overview of the CHABLIS campaign. *Atmos Chem Phys* 8(14):3789–3803
- Kagan J (1993) Organic photochemistry, principles and applications, vol chapter 4. Academic, San Diego
- Kallay N, Cakara D (2000) Reversible charging of the ice-water interface – I. Measurement of the surface potential. *J Colloid Interface Sci* 232(1):81–85
- Kang CL, Gao HJ, Guo P, Tang XJ, Zhang GS, Liu XJ, Dong DM (2008) Photoconversion of *p*-chlorophenol in ice and the presence of nitrite. *Chem J Chin Univ-Chin* 29(4):705–709
- Kawamura K, Suzuki I, Fujii Y, Watanabe O (1996) Ice core record of fatty acids over the past 450 years in Greenland. *Geophys Res Lett* 23(19):2665–2668
- Kawamura K, Yokoyama K, Fujii Y, Watanabe O (1999) Implication of azelaic acid in a Greenland ice core for oceanic and atmospheric changes in high latitudes. *Geophys Res Lett* 26:871
- Kawamura K, Yokoyama K, Fujii Y, Watanabe O (2001) A Greenland ice core record of low molecular weight dicarboxylic acids, ketocarboxylic acids, and alpha-dicarbonyls: a trend from Little Ice Age to the present (1540 to 1989 AD). *J Geophys Res* 106(D1):1331–1345
- Killawee JA, Fairchild IJ, Tison JL, Janssens L, Lorrain R (1998) Segregation of solutes and gases in experimental freezing of dilute solutions: implications for natural glacial systems. *Geochim Cosmochim Acta* 62:3637
- King MD, Simpson WR (2001) Extinction of UV radiation in Arctic snow at Alert, Canada (82 degrees N). *J Geophys Res-Atmos* 106(D12):12499–12507
- Kiovsky TE, Pincock RE (1966) Demonstration of a reaction in frozen aqueous solutions. *J Chem Edu* 43:361
- Kiss G, Varga B, Gelencser A, Krivacsy Z, Molnar A, Alsberg T, Persson L, Hansson HC, Facchini MC (2001) Characterisation of polar organic compounds in fog water. *Atmos Environ* 35(12):2193–2200
- Klán P, Holoubek I (2002) Ice (photo)chemistry. Ice as a medium for long-term (photo)chemical transformations – environmental implications. *Chemosphere* 46:1201–1210
- Klán P, Janousek J, Kriz Z (2000a) Photochemistry of valerophenone in solid solutions. *J Photochem Photobiol A-Chem* 134(1–2):37–44
- Klán P, Ansorgová A, Del Favero D, Holoubek I (2000b) Photochemistry of chlorobenzene in ice. *Tetrahedron Lett* 41(40):7785–7789
- Klán P, Del Favero D, Ansorgová A, Klánová J, Holoubek I (2001) Photodegradation of halobenzenes in water ice. *Environ Sci Pollut Res* 8(3):195–200
- Klán P, Klánová J, Holoubek I, Cupr P (2003) Photochemical activity of organic compounds in ice induced by sunlight irradiation: the Svalbard Project. *Geophys Res Lett* 30(4):1313
- Klánová J, Klán P, Nosek J, Holoubek I (2003a) Environmental ice photochemistry: monochlorophenols. *Environ Sci Technol* 37(8):1568–1574

- Klánová J, Klán P, Heger D, Holoubek I (2003b) Comparison of the effects of UV,  $\text{H}_2\text{O}_2/\text{UV}$  and gamma-irradiation processes on frozen and liquid water solutions of monochlorophenols. *Photochem Photobiol Sci* 2(10):1023–1031
- Knight CA (1996) Surface layers on ice. *J Geophys Res-Atmos* 101(D8):12921–12928
- Koch TG, Sodeau JR (1995) Photochemistry of nitric acid in low-temperature matrices. *J Phys Chem* 99(27):10824–10829
- Koch TG, Sodeau JR (1996) Photochemistry of dinitrogen pentoxide in low-temperature matrices. *J Chem Soc-Faraday Trans* 92(13):2347–2351
- Koch TG, Holmes NS, Roddis TB, Sodeau JR (1996) Low-temperature photochemistry of submicrometer nitric acid and ammonium nitrate layers. *J Phys Chem* 100(27):11402–11407
- Krivacsy Z, Kiss G, Varga B, Galambos I, Sarvari Z, Gelencser A, Molnar A, Fuzzi S, Facchini M, Zappoli S, Andracchio A, Alsberg T, Hansson HC, Persson L (2000) Study of humic-like substances in fog and interstitial aerosol by size-exclusion chromatography and capillary electrophoresis. *Atmos Environ* 34(25):4273–4281
- Laird S, Buttry D, Sommerfeld R (1999) Nitric acid adsorption on ice: surface diffusion. *Geophys Res Lett* 26(6):699–701
- Langford V, McKinley A, Quickenden T (2000) Luminescent photoproducts in UV-irradiated ice. *Acc Chem Res* 33(10):665–671
- Lee S, Cornillon P, Kim YR (2002) Spatial investigation of the non-frozen water distribution in frozen foods using NMR SPRITE. *J Food Sci* 67(6):2251–2255
- Lee S, Moon S, Shim JY, Kim YR (2008) Freezing behaviors of frozen foods determined by  $^1\text{H}$  NMR and DSC. *Food Sci Biotechnol* 17(1):102–105
- Leermakers PA, Vesley GF (1963) The photochemistry of  $\alpha$ -keto acids and  $\alpha$ -keto esters. I. Photolysis of pyruvic acid and benzoylformic acid. *J Am Chem Soc* 85:3776–3779
- Lee-Taylor J, Madronich S (2002) Calculation of actinic fluxes with a coupled atmosphere-snow radiative transfer model. *J Geophys Res-Atmos* 107(D24):4796
- Legrand M, Deangelis M (1995) Origins and variations of light carboxylic acids in polar precipitation. *J Geophys Res-Atmos* 100(D1):1445–1462
- Leigh JS, Reed GH (1971) Electron paramagnetic resonance studies in frozen aqueous solutions. Elimination of freezing artifacts. *J Phys Chem* 75:1202
- Lewis GN, Goldschmid O, Magel TT, Bigeleisen J (1943) Dimeric and other forms of methylene blue: absorption and fluorescence of the pure monomer. *J Am Chem Soc* 65(6):1150–1154
- Li Q, Huber JR (2002) The photodissociation of  $\text{ClNO}_2$  in argon and water clusters studied at 235 nm by the REMPI-TOF method. *Chem Phys Lett* 354(1–2):120–127
- Li YQ, Davidovits P, Shi Q, Jayne JT, Kolb CE, Worsnop DR (2001) Mass and thermal accommodation coefficients of  $\text{H}_2\text{O(g)}$  on liquid water as a function of temperature. *J Phys Chem A* 105:10627–10634
- Livingston F, George S (2001) Diffusion kinetics of  $\text{HC}_1$  hydrates in ice measured using infrared laser resonant desorption depth-profiling. *J Phys Chem A* 105(21):5155–5164
- Livingston F, Smith J, George S (2000) Depth-profiling and diffusion measurements in ice films using infrared laser resonant desorption. *Anal Chem* 72(22):5590–5599
- Lode O, Eklo OM, Holen B, Svensen A, Johnsen AM (1995) Pesticides in precipitation in Norway. *Sci Total Environ* 161:421–431
- Lodge JP, Baker ML, Pierrard JM (1956) Observations on ion separation in dilute solutions by freezing. *J Chem Phys* 24:716
- Mack J, Bolton J (1999) Photochemistry of nitrite and nitrate in aqueous solution: a review. *J Photochem Photobiol A-Chem* 128:1–13
- Madronich S, Flocke SJ (1998) The role of solar radiation in atmospheric chemistry. In: Boule P (ed) *Handbook of environmental chemistry*, vol 2 L. Springer, Heidelberg, pp 1–26. [www.acd.ucar.edu/TUV](http://www.acd.ucar.edu/TUV)
- Madsen D, Larsen J, Jensen S, Keiding S, Thøgersen J (2003) The primary photodynamics of aqueous nitrate: formation of peroxynitrite. *J Am Chem Soc* 125(50):15571–15576
- Mantz Y, Geiger F, Molina L, Molina M, Trout B (2000) First-principles molecular-dynamics study of surface disordering of the (0001) face of hexagonal ice. *J Chem Phys* 113(23):10733–10743

- Mark G, Korth H-G, Schuchmann H-P, von Sonntag C (1996) The photochemistry of aqueous nitrate ion revisited. *J Photochem Photobiol A-Chem* 101:89–103
- Masclet P, Hoyau V, Jaffrezo JL, Cachier H (2000) Polycyclic aromatic hydrocarbon deposition on the ice sheet of Greenland. Part I: superficial snow. *Atmos Environ* 34(19):3195–3207
- Matykieviczová N, Klánová J, Klán P (2007a) Photochemical degradation of PCBs in snow. *Environ Sci Technol* 41(24):8308–8314
- Matykieviczová N, Kurková R, Klánová J, Klán P (2007b) Photochemically induced nitration and hydroxylation of organic aromatic compounds in the presence of nitrate or nitrite in ice. *J Photochem Photobiol A-Chem* 187(1):24–32
- Miller SL (1953) A production of amino acids under possible primitive Earth conditions. *Science* 117(3046):528–529
- Minero C, Maurino V, Bono F, Pelizzetti E, Marinoni A, Mailhot G, Carlotti ME, Vione D (2007) Effect of selected organic and inorganic snow and cloud components on the photochemical generation of nitrite by nitrate irradiation. *Chemosphere* 68(11):2111–2117
- Miranda PB, Xu L, Shen YR, Salmeron M (1998) Icelike water monolayer adsorbed on mica at room temperature. *Phys Rev Lett* 81(26):5876–5879
- Montenay-Garestier T, Charlier M, Helene C (1976) Aggregate formation, excited-state interactions, and photochemical reactions in frozen aqueous solutions of nucleic acid constituents. In: Wang SY (ed) *Photochemistry and photobiology of nucleic acids*, vol 1. Academic, New York, pp 381–417
- Moran MA, Zepp RG (1997) Role of photoreactions in the formation of biologically labile compounds from dissolved organic matter. *Limnol Oceanogr* 42(6):1307–1316
- Moskovits M, Ozin GA (1976) *Cryochemistry*. Wiley, New York
- Mulvaney R, Wagenbach D, Wolff EW (1998) Postdepositional change in snowpack nitrate from observation of year-round near-surface snow in coastal Antarctica. *J Geophys Res-Atmos* 103 (D9):11021–11031
- Nakamura K, Masayoshi N, Ageta Y, Goto-Azuma K, Kamiyama K (2000) Post-depositional loss of nitrate in surface snow layers of the Antarctic ice sheet. In: Hondoh T (ed) *The physics of ice core records*. Hokkaido University Press, Sapporo, p 214
- Narukawa M, Kawamura K, Hatsushika H, Yamazaki K, Li SM, Bottenheim JW, Anlauf KG (2003) Measurement of halogenated dicarboxylic acids in the Arctic aerosols at polar sunrise. *J Atmos Chem* 44(3):323–335
- NIST (2002) NIST Standard Reference Database 40, Solution Kinetics. <http://kinetics.nist.gov/solution/>. Accessed April 2009
- Nye JF (1989) The geometry of water veins and nodes in polycrystalline ice. *J Glaciol* 35:17
- O'Driscoll P, Lang K, Minogue N, Sodeau J (2006) Freezing halide ion solutions and the release of interhalogens to the atmosphere. *J Phys Chem A* 110(14):4615–4618
- O'Driscoll P, Minogue N, Takenaka N, Sodeau J (2008) Release of nitric oxide and iodine to the atmosphere from the freezing of sea-salt aerosol components. *J Phys Chem A* 112(8):1677–1682
- Olander DS, Rice SA (1972) Preparation of amorphous solid water. *Proc Natl Acad Sci USA* 69:98–100
- Onsager L, Runnels LK (1969) Diffusion and relaxation phenomena in ice. *J Chem Phys* 50:1089
- Oremp MW, Adamson AR (1969) Physical adsorption of vapor on ice. II, n-alkanes. *J Colloid Interface Sci* 31:278
- Pace MD, Carmichael AJ (1997) Quantitative EPR spin trapping. 1. Nitrogen dioxide radicals and nitrite ions from energetic materials in alkaline aqueous solution. *J Phys Chem A* 101:1848
- Park S, Pradeep T, Kang H (2000) Ionic dissociation at NaCl on frozen water. *J Chem Phys* 113(21):9373–9376
- Park S-C, Maeng K-W, Pradeep T, Kang H (2001) Unique chemistry at ice surfaces: incomplete proton transfer in the H<sub>3</sub>O<sup>+</sup>–NH<sub>3</sub> system. *Angew Chem Int Ed* 40:1497–1500
- Pehkonen SO, Siebert R, Erel Y, Webb S, Hoffmann MR (1993) Photoreduction of iron oxyhydroxides in the presence of important atmospheric organic compounds. *Environ Sci Technol* 27(10):2056–2062

- Perovich DK, Govoni JW (1991) Absorption coefficients of ice from 250 to 400 nm. *Geophys Res Lett* 18(7):1233–1235
- Perrier S, Houdier S, Domine F, Cabanes A, Legagneux L, Sumner AL, Shepson PB (2002) Formaldehyde in Arctic snow. Incorporation into ice particles and evolution in the snowpack. *Atmos Environ* 36(15–16):2695–2705
- Perrier S, Sassin P, Domine F (2003) Diffusion and solubility of HCHO in ice: preliminary results. *Can J Phys* 81(1–2):319–324
- Peterson M, Barber D, Green S (2002) Monte Carlo modeling and measurements of actinic flux levels in Summit, Greenland snowpack. *Atmos Environ* 36(15–16):2545–2551
- Petrenko VF, Whitworth RW (1999) Physics of ice. Oxford University Press, Oxford
- Pikal MJ (2004) Mechanisms of protein stabilization during freeze-drying and storage: the relative importance of thermodynamic stabilization and glassy state relaxation dynamics. In: Rey L, May JC (eds) Freeze-drying/lyophilization of pharmaceutical and biological products. Marcel Dekker, New York, pp 63–107
- Pincock RE (1969) Reactions in frozen systems. *Acc Chem Res* 2:97
- Pincock RE, Kiovsky TE (1966) Kinetics of reactions in frozen solutions. *J Chem Educ* 43(7):358–360
- Pos WH, Riemer DD, Zika RG (1998) Carbonyl sulfide (OCS) and carbon monoxide (CO) in natural waters: evidence of a coupled production pathway. *Mar Chem* 62(1–2):89–101
- Potts WTW, Oates K, Wolff EW, Mulvaney R (1992) The distribution of impurities in Antarctic ice. *Scanning Microsc* 6(1):295–299
- Pruppacher HR, Klett JD (1997) Microphysics of clouds and precipitation. Springer, New York
- Pryor WA, Lightsey JW (1981) Mechanisms of nitrogen-dioxide reactions – initiation of lipid-peroxidation and the production of nitrous acid. *Science* 214:435–437
- Pryor WA, Lightsey JW, Church DF (1982) Reaction of nitrogendioxide with alkenes and poly-unsaturated fatty-acids – addition and hydrogen abstraction mechanisms. *J Am Chem Soc* 104:6685–6692
- Pursell CJ, Conyers J, Alapat P, Parveen R (1995) Photochemistry of chlorine dioxide in ice. *J Phys Chem* 99(26):10433–10437
- Pursell CJ, Conyers J, Denison C (1996) Photochemistry of chlorine dioxide in polycrystalline ice ( $T = 140\text{--}185\text{ K}$ ): production of chloryl chloride,  $\text{Cl}(\text{OClO})$ . *J Phys Chem* 100(38):15450–15453
- Rahn RO, Hosszu JL (1969) Photochemical studies of thymine in ice. *Photochem Photobiol* 10(2):131–137
- Ram K, Anastasio C (2009) Photochemistry of phenanthrene, pyrene, and fluoranthene in ice and snow. *Atmos Environ* 43(14):2252–2259
- Ramamurthy V (1991) Photochemistry in organized and constrained media. Wiley-VCH, Weinheim
- Regand A, Goff HD (2005) Freezing and ice recrystallization properties of sucrose solutions containing ice structuring proteins from cold-acclimated winter wheat grass extract. *J Food Sci* 70(9):E552–E556
- Reichardt C (1994) Solvatochromic dyes as solvent polarity indicators. *Chem Rev* 94(8):2319–2358
- Rick SW (2001) Simulations of ice and liquid water over a range of temperatures using the fluctuating charge model. *J Chem Phys* 114:2276
- Riley H, McMurray DP, Haq S (1996) Adsorption and photochemistry of dinitrogen tetroxide on low temperature ice layers. *J Chem Soc-Faraday Trans* 92(6):933–939
- Riley H, Colby DJ, McMurray DP, Reeman SM (1997a) Photochemistry in ordered physisorbed monolayers of dinitrogen tetroxide. *Surf Sci* 390(1–3):243–249
- Riley H, Colby DJ, McMurray DP, Reeman SM (1997b) Photodissociation dynamics in ordered monolayers: physisorbed  $\text{N}_2\text{O}_4$ . *J Phys Chem B* 101(25):4982–4991
- Riordan E, Minogue N, Healy D, O'Driscoll P, Sodeau JR (2005) Spectroscopic and optimization modeling study of nitrous acid in aqueous solution. *J Phys Chem A* 109(5):779–786
- Robinson C, Boxe CS, Guzman MI, Colussi AJ, Hoffmann MR (2006) Acidity of frozen electrolyte solutions. *J Phys Chem B* 110(15):7613–7616. doi:[10.1021/jp061169n](https://doi.org/10.1021/jp061169n)

- Roca M, Zahardis J, Bone J, El-Maazawi M, Grassian VH (2008) 310 nm irradiation of atmospherically relevant concentrated aqueous nitrate solutions: nitrite production and quantum yields. *J Phys Chem A* 112(51):13275–13281. doi:[10.1021/jp809017b](https://doi.org/10.1021/jp809017b)
- Roth CM, Goss KU, Schwarzenbach RP (2004) Sorption of diverse organic vapors to snow. *Environ Sci Technol* 38(15):4078–4084
- Ruzicka R, Baráková L, Klán P (2005) Photodecarbonylation of dibenzyl ketones and trapping of radical intermediates by copper(II) chloride in frozen aqueous solutions. *J Phys Chem B* 109(19):9346–9353
- Salmeron M, Bluhm H (1999) Structure and properties of ice and water film interfaces in equilibrium with vapor. *Surf Rev Lett* 6(6):1275–1281
- Sanchez R, Ferris J, Orgel LE (1966) Conditions for purine synthesis – did prebiotic synthesis occur at low temperatures? *Science* 153(3731):72–73
- Sarciaux JM, Mansour S, Hageman MJ, Nail SL (1999) Effects of buffer composition and processing conditions on aggregation of bovine IgG during freeze-drying. *J Pharm Sci* 88(12):1354–1361
- Sasson S, Wang SY (1977) Photochemistry of 5-bromouridine and 5-bromo-2'-deoxyuridine in ice and in “puddles”. *Photochem Photobiol* 26(4):357–361
- Sato S, Senga T, Kawasaki M (1999) Adsorption states and photochemistry of NO<sub>2</sub> adsorbed on Au(111). *J Phys Chem B* 103(24):5063–5069
- Sato K, Furuya S, Takenaka N, Bandow H, Maeda Y, Furukawa Y (2003) Oxidative reaction of thiosulfate with hydrogen peroxide by freezing. *Bull Chem Soc Jpn* 76(6):1139–1144
- Sawaki Y, Ogata Y (1981) Mechanism of the photoepoxidation with and photodecarboxylation of  $\alpha$ -keto acids. *J Am Chem Soc* 103:6455–6460
- Schade GW, Crutzen PJ (1999) CO emissions from degrading plant matter (II). Estimate of a global source strength. *Tellus B* 51(5):909–918
- Schade GW, Hofmann RM, Crutzen PJ (1999) CO emissions from degrading plant matter (I). Measurements. *Tellus B* 51(5):889–908
- Schaff JE, Roberts JT (1998) The adsorption of acetone on thin films of amorphous and crystalline ice. *Langmuir* 14(6):1478–1486
- Schaff JE, Roberts JT (1999) Interaction of acetonitrile with the surfaces of amorphous and crystalline ice. *Langmuir* 15(21):7232–7237
- Schreiner PR, Reisenauer HP, Pickard FC, Simonett AC, Allen WD, Matyus E, Csaszar AG (2008) Capture of hydroxymethylene and its fast disappearance through tunnelling. *Nature* 453(7197):906–942
- Schrivener-Mazzuoli L, Schriver A, Coanga JM, Steers M (2003) Vibrational spectra and 266 nm photochemistry of ClNO<sub>2</sub> thin films and ClNO<sub>2</sub> in amorphous water ice. *J Phys Chem A* 107(26):5181–5188
- Sempere R, Kawamura K (1994) Comparative distributions of dicarboxylic-acids and related polar compounds in snow rain and aerosols from urban atmosphere. *Atmos Environ* 28(3):449–459
- Sempere R, Kawamura K (1996) Low molecular weight dicarboxylic acids and related polar compounds in the remote marine rain samples collected from western Pacific. *Atmos Environ* 30:1609
- Shibkov A, Golovin Y, Zheltov M, Korolev A (2001) Pulsed electromagnetic and acoustic emission accompanying fast crystallization of supercooled water droplets. *Chrystallogr Rep* 46(1):144–147
- Simonov AN, Pesturlova OP, Matvienko LG, Snytnikov VN, Snytnikova OA, Tsentalovich YP, Parmon VN (2007) Possible prebiotic synthesis of monosaccharides from formaldehyde in presence of phosphates. *Adv Space Res* 40(11):1634–1640
- Simpson W, King MD, Beine HJ, Honrath RE, Zhou X (2002) Radiation-transfer modeling of snow-pack photochemical processes during ALERT 2000. *Atmos Environ* 36:2663–2670
- Simpson WR, von Glasow R, Riedel K, Anderson P, Ariya P, Bottenheim J, Burrows J, Carpenter LJ, Friess U, Goodsite ME, Heard D, Hutterli M, Jacobi HW, Kaleschke L, Neff B, Plane J, Platt U, Richter A, Roscoe H, Sander R, Shepson P, Sodeau J, Steffen A, Wagner T, Wolff E (2007) Halogens and their role in polar boundary-layer ozone depletion. *Atmos Chem Phys* 7(16):4375–4418

- Sinner T, Hoffmann P, Knapp CP, Ortner HM (1994) Influence of freezing of aqueous samples on the Fe(II)/Fe(III) equilibrium. *Fresenius J Anal Chem* 349:334–335
- Smith M, Pounder ER (1960) Impurity concentration profiles in ice by an anthrone method. *Can J Phys* 38:354–368
- Sodeau JR (1995) Atmospheric cryochemistry. In: Clark RJH, Hester RE (eds) Spectroscopy in environmental science. Advances in spectroscopy. Wiley, New York
- Sodeau JR, Horn AB (2003) Interactions and photochemistry of small molecules on ice surfaces. In: Buch V, Devlin JP (eds) Water in confining geometries. Cluster physics. Springer, New York, pp 295–334
- Sodeau JR, Lee EKC (1978) Intermediacy of hydroxymethylene (HCOH) in low-temperature matrix photochemistry of formaldehyde. *Chem Phys Lett* 57(1):71–74
- Sohn Y, Wei W, White JM (2008) Thermal and photochemistry of *tert*-butyl iodide on ice films. *Surf Sci* 602(15):2706–2712
- Sokolov O, Abbatt JPD (2002) Adsorption to ice of n-alcohols (ethanol to 1-hexanol), acetic acid, and hexanal. *J Phys Chem A* 106(5):775–782
- Sola MI, Corti HR (1993) Freezing induced electric potentials and pH changes in aqueous solutions of electrolytes. *An Asoc Quim Argent* 81(6):483–498
- Solomon S, Garcia RR, Rowland FS, Wuebbles DJ (1986) On the depletion of Antarctic ozone. *Nature* 321(6072):755–758
- Sommerfeld RA, Knight CA, Laird SK (1998) Diffusion of HNO<sub>3</sub> in ice. *Geophys Res Lett* 25 (6):935–938
- Steenken S, Sprague ED, Schulte-Frohlinde D (1975) Photofragmentation of alpha-oxocarboxylic acids in aqueous solutions. An EPR study. *Photochem Photobiol* 22:19–27
- Steffen A, Douglas T, Amyot M, Ariya P, Aspmo K, Berg T, Bottenheim J, Brooks S, Cobbett F, Dastoor A, Dommergues A, Ebinghaus R, Ferrari C, Gardfeldt K, Goodsite ME, Lean D, Poula AJ, Scherz C, Skov H, Sommar J, Temme C (2008) A synthesis of atmospheric mercury depletion event chemistry in the atmosphere and snow. *Atmos Chem Phys* 8(6):1445–1482
- Strambini GB, Gonnelli M (2008) Specific anions effects on the stability of azurin in ice. *J Phys Chem B* 112(33):10255–10263
- Su X, Lianos L, Shen YR, Somorjai G (1998) Surface-induced ferroelectric ice on Pt(111). *Phys Rev Lett* 80(7):1533
- Sumner AL, Shepson PB (1999) Snowpack production of formaldehyde and its effect on the Arctic troposphere. *Nature* 398(6724):230–233
- Sumner AL, Shepson PB, Grannas AM, Bottenheim JW, Anlauf KG, Worthy D, Schroeder WH, Steffen A, Domine F, Perrier S, Houdier S (2002) Atmospheric chemistry of formaldehyde in the Arctic troposphere at Polar Sunrise, and the influence of the snowpack. *Atmos Environ* 36(15–16):2553–2562
- Suresh SJ, Naik VM (2000) Hydrogen bond thermodynamic properties of water from dielectric constant data. *J Chem Phys* 113:9727
- Swanson AL, Blake NJ, Dibb JE, Albert MR, Blake DR, Rowland FS (2002) Photochemically induced production of CH<sub>3</sub>Br, CH<sub>3</sub>I, C<sub>2</sub>H<sub>5</sub>I, ethene, and propene within surface snow at Summit, Greenland. *Atmos Environ* 36(15–16):2671–2682
- Szent-Gyorgyi A (1957) Bioenergetics. Academic, New York
- Takenaka N, Ueda A, Maeda Y (1992) Acceleration of the rate of nitrite oxidation by freezing in aqueous solution. *Nature* 358(6389):736–738
- Takenaka N, Ueda A, Daimon T, Bandow H, Dohmaru T, Maeda Y (1996) Acceleration mechanism of chemical reaction by freezing: the reaction of nitrous acid with dissolved oxygen. *J Phys Chem* 100(32):13874–13884
- Takenaka N, Diamon T, Ueda A, Sato K, Kitano M, Bandow H, Maeda Y (1998) Fast oxidation reaction of nitrite by dissolved oxygen in the freezing process in the tropospheric aqueous phase. *J Atmos Chem* 29:135–150
- Takenaka N, Furuya S, Sato K, Bandow H, Maeda Y, Furukawa Y (2003) Rapid reaction of sulfide with hydrogen peroxide and formation of different final products by freezing compared to those in solution. *Int J Chem Kinet* 35(5):198–205

- Takenaka N, Tanaka M, Okitsu K, Bandow H (2006) Rise in the pH of an unfrozen solution in ice due to the presence of NaCl and promotion of decomposition of gallic acids owing to a change in the pH. *J Phys Chem A* 110(36):10628–10632
- Tang YX, Zhu L, Chu LT, Xiang B (2006) Cavity ring-down spectroscopic study of acetaldehyde photolysis in the gas phase, on aluminum surfaces, and on ice films. *Chem Phys* 330(1–2):155–165
- Thibert E, Domine F (1998) Thermodynamics and kinetics of the solid solution of HNO<sub>3</sub> in ice. *J Phys Chem B* 102(22):4432–4439
- Thompson MG (1973) Energetic muons. In: Wolfendale AW (ed) *Cosmic rays at ground level*. The Institute of Physics, London, p 17
- Trakhtenberg S, Naaman R, Cohen SR, Benjamin I (1997) Effect of the substrate morphology on the structure of adsorbed ice. *J Phys Chem B* 101:5172
- Tschumi J, Stauffer B (2000) Reconstructing past atmospheric CO<sub>2</sub> concentration based on ice-core analyses: open questions due to in situ production of CO<sub>2</sub> in the ice. *J Glaciol* 46(152):45–53
- Twickler MS, Spencer MJ, Lyons WB, Mayewski PA (1986) Measurement of organic carbon in polar snow samples. *Nature* 320(6058):156–158
- Valentine EL, Zepp RG (1993) Formation of carbon monoxide from the photodegradation of terrestrial dissolved organic carbon in natural waters. *Environ Sci Technol* 27:409
- van der Ham F, Witkamp GJ, de Graauw J, van Rosmalen GM (1999) Eutectic freeze crystallization simultaneous formation and separation of two solid phases. *J Cryst Growth* 198/199:744
- Varghese AJ (1970) Photochemistry of thymidine in ice. *Biochemistry* 9(24):4781–4787
- Vesley GF, Leermakers PA (1964) The photochemistry of  $\alpha$ -keto acids and  $\alpha$ -keto esters. III. Photolysis of pyruvic acid in the vapor phase. *J Phys Chem* 68(8):2364–2366
- Villa S, Vighi M, Maggi V, Finizio A, Bolzacchini E (2003) Historical trends of organochlorine pesticides in an Alpine glacier. *J Atmos Chem* 46(3):295–311
- Vogel SR, Richert C (2007) Adenosine residues in the template do not block spontaneous replication steps of RNA. *Chem Commun* 19:1896–1898
- von Hessberg P, Pouvesle N, Winkler AK, Schuster G, Crowley JN (2008) Interaction of formic and acetic acid with ice surfaces between 187 and 227 K. Investigation of single species- and competitive adsorption. *Phys Chem Chem Phys* 10(17):2345–2355
- Vrbka L, Jungwirth P (2005) Brine rejection from freezing salt solutions: a molecular dynamics study. *Phys Rev Lett* 95(14):148501
- Wacker A, Weinblum D, Traeger L, Moustafa Z (1961) Photochemical reactions of uracil and uridine. *J Mol Biol* 3:790–793
- Wang SY (1961) Photochemical reactions in frozen solutions. *Nature* 190:690–694
- Wang SY (1963) Humidity and photochemistry. *Nature* 200:879–880
- Wang SY (1964) The mechanism for frozen aqueous solution irradiation of pyrimidines. *Photochem Photobiol* 3(4):395–398
- Wania F, Hoff JT, Jia CQ, Mackay D (1998) The effects of snow and ice on the environmental behaviour of hydrophobic organic chemicals. *Environ Pollut* 102(1):25–41
- Wania F, Mackay D, Hoff JT (1999a) The importance of snow scavenging of polychlorinated biphenyl and polycyclic aromatic hydrocarbon vapors. *Environ Sci Technol* 33(1):195–197
- Wania F, Semkin R, Hoff JT, Mackay D (1999b) Modelling the fate of non-polar organic chemicals during the melting of an Arctic snowpack. *Hydrol Process* 13(14–15):2245–2256
- Warneck P, Wurzinger C (1988) Product quantum yields for the 305-nm photodecomposition of NO<sub>3</sub><sup>−</sup> in aqueous solution. *J Phys Chem* 92(22):6278–6283
- Weller R, Minikin A, Konig-Langlo G, Schrems O, Jones AE, Wolff EW, Anderson PS (1999) Investigating possible causes of the observed diurnal variability in Antarctic NO<sub>y</sub>. *Geophys Res Lett* 26(18):2853–2856
- Wettlaufer JS (1999a) Ice surfaces: macroscopic effects of microscopic structure. *Phil Trans R Soc Lond, A* 357:3403
- Wettlaufer JS (1999b) Impurity effects in the premelting of ice. *Phys Rev Lett* 82(12):2516–2519
- Wettlaufer JS, Dash JG (2000) Melting below zero. *Sci Am* 282(2):50–53

- Wilen LA, Wetlaufer JS, Elbaum M, Schick M (1995) Dispersion force effects in interfacial premelting of ice. *Phys Rev B* 52:12426
- Winkler AK, Holmes NS, Crowley JN (2002) Interaction of methanol, acetone and formaldehyde with ice surfaces between 198 and 223 K. *Phys Chem Chem Phys* 4(21):5270–5275
- Woittequand S, Toubin C, Pouilly B, Monnerville M, Briquez S, Meyer HD (2005) Photodissociation of a HCl molecule adsorbed on ice. *Chem Phys Lett* 406(1–3):202–209
- Wolff EW, Hall JS, Mulvaney R, Pasteur EC, Wagenbach D, Legrand M (1998) Relationship between chemistry of air, fresh snow and firm cores for aerosol species in coastal antarctica. *J Geophys Res* 103(D9):11057–11070
- Workman EJ, Reynolds SE (1950) Electrical phenomena occurring during the freezing of dilute aqueous solutions and their possible relationship to thunderstorm electricity. *Phys Rev* 78(3):254–259
- Xu H, Wentworth PJ, Howell NW, Joens JA (1993) Temperature dependent near-UV molar absorptivities of aliphatic aldehydes and ketones in aqueous solution. *Spectrochim Acta* 49A(8):1171–1178
- Yancey PH (2005) Organic osmolytes as compatible, metabolic and counteracting cytoprotectants in high osmolarity and other stresses. *J Exp Biol* 208(15):2819–2830
- Yancey PH, Clark ME, Hand SC, Bowlus RD, Somero GN (1982) Living with water-stress – evolution of osmolyte systems. *Science* 217(4566):1214–1222
- Yang J, Honrath RE, Peterson MC, Dibb JE, Sumner AL, Shepson PB, Frey M, Jacobi HW, Swanson A, Blake N (2002) Impacts of snowpack emissions on deduced levels of OH and peroxy radicals at Summit, Greenland. *Atmos Environ* 36(15–16):2523–2534
- Yoshioka H, Hasegawa K (1996) Solid-state spin trapping of the hydroxyl radical formed by gamma-irradiation in ice and the scavenging effect of sodium L-ascorbate. *Biosci Biotechnol Biochem* 60(12):1971–1975
- Yu SC (2000) Role of organic acids (formic, acetic, pyruvic and oxalic) in the formation of cloud condensation nuclei (CCN): a review. *Atmos Res* 53(4):185–217
- Zellner R, Exner M, Herrmann H (1990) Absolute OH quantum yields in the laser photolysis of nitrate, nitrite and dissolved H<sub>2</sub>O<sub>2</sub> at 308 and 351 nm in the temperature range 278–353 K. *J Atmos Chem* 10(4):411–425
- Zepp RG, Hoigné J, Bader H (1987) Nitrate-induced photooxidation of trace organic chemicals in water. *Environ Sci Technol* 21(5):443–450
- Zhou XL, Beine HJ, Honrath RE, Fuentes JD, Simpson W, Shepson PB, Bottenheim JW (2001) Snowpack photochemical production of HONO: a major source of OH in the Arctic boundary layer in springtime. *Geophys Res Lett* 28(21):4087–4090
- Zuberi B, Bertram A, Koop T, Molina L, Molina M (2001) Heterogeneous freezing of aqueous particles induced by crystallized (NH<sub>4</sub>)<sub>2</sub>SO<sub>4</sub>, ice, and letovicite. *J Phys Chem A* 105(26):6458–6464
- Zuo Y, Deng Y (1998) The near-UV absorption constants for nitrite ion in aqueous solution. *Chemosphere* 36(1):181–188
- Zuo YG, Hoigne J (1994) Photochemical decomposition of oxalic, glyoxalic and pyruvic acids catalyzed by iron in atmospheric waters. *Atmos Environ* 28(7):1231–1239
- Zuo Y, Jones RD (1996) Formation of carbon monoxide by photolysis of dissolved marine organic material and its significance in the carbon cycling of the oceans. *Geophys Res Lett* 23:2769
- Zuo YG, Jones RD (1997) Photochemistry of natural dissolved organic matter in lake and wetland waters – production of carbon monoxide. *Water Res* 31(4):850–858

# Index

## A

- Abe, O., 211  
Ab initio molecular dynamics, 152  
Adamson, A.W., 418  
Adisasmito, S., 418, 420  
A'Hearn, M.F., 475  
Allamandola, L.J., 10  
Allen, M.P., 152  
Ammonia ice  
  optical constants, 82  
  reflectance measurements, 83  
Amorphization, of crystalline ice, 538–540  
Amorphous phase, water ice  
  formation conditions, 377  
  infrared spectroscopy, 391  
  phases of, 372–373  
  structure, 375  
  thermally induced phase change, 380–382  
Anastasio, C., 600  
Anderson, R.C., 76, 82  
Andrade, E.N.D., 209  
Andrade model, 209–211  
Angell, C.A., 378  
Antarctic ice sheet, 229  
Asteroids, 16  
Atmospheric ices, photochemistry of  
  prebiotic mechanisms, 619  
  snowpack mechanisms, 622–624  
  stratospheric mechanisms, 620–622  
  tropospheric ice, 622–624  
  water-ices, 618–619  
Atreya, S.K., 432, 433  
Attenuation properties, planetary ices  
  anelasticity impact, 215–217  
  Cole model, 188  
  definition, 186

- dissipation models  
  material response, 204  
  Maxwell model, 204–205  
  Voigt/Kelvin model, 206  
elasticity, 186  
forced oscillation tests, 187  
Iapetus' evolution to spin-orbit resonance,  
  217–218  
inelasticity, 186  
internal friction, 186  
laboratory measurements  
  amorphous ice, 199  
  dopants and soluble impurities, 195  
  material aging, 199  
  partial melting and slurries, 195–197  
  porosity, 197–198  
  solid particles and second phases, 197  
linear and non-linear deformation, 194  
Maxwell body approximation, 214–215  
mechanisms driving dissipation, 212–214  
microcreep, 187  
phase lag and attenuation, 202–203  
primary creep, 186  
processes, 186  
shear *vs.* bulk viscoelasticity, 193–194  
stress-strain relationships  
  in frequency domain, 201–202  
  in time domain, 200–201  
tidal dissipation modeling, 211–212  
tidal forcing frequency and cyclic peak  
  stress, 184, 185  
transient creep component  
  Andrade model, 209–211  
  Burgers model, 206–207  
  Caputo model, 208  
  Cole model, 208–209

Attenuation properties (*cont.*)

- extended Burgers model, 207
- standard anelastic solid, 206
- viscoelastic dissipation
  - defect-related mechanisms, 188
  - dislocation-driven attenuation, 190–192
  - grain-boundary sliding (GBS), 192–193
  - proton reorientation, 189

Auger process, 506

Autoionization process, 516. *See also* Ionization, water ice**B**

- Bader, R., 157
- Bahr, D.A., 512
- Baragiola, R.A., 382, 515, 527, 528, 537
- Barkume, K.M., 131, 136
- Barnes, P., 172, 237
- Bar-Nun, A., 470, 471, 473, 475, 476
- Barr, A.C., 213, 434
- Barrer, R.M., 418
- Barucci, M.A., 124, 128
- Basilevsky, A.T., 470
- Beeman, M., 173, 178, 305
- Belton, M.J.S., 468–472
- Berland, B.S., 85
- Bernstein, M.P., 120
- Bertie, J.E., 389, 390
- Betts, B.H., 10
- Blake, D.F., 377, 380
- Bowell, E., 56, 113
- Boyce, J.M., 301
- Bradley, E.T., 93
- Brandt, R.E., 76, 79
- Bringa, E.M., 553
- Browell, E.V., 76, 82
- Brown, M.E., 132, 133, 135, 137
- Brown, R.H., 539
- Brown, W.L., 559, 561, 566
- Brunetto, R., 111, 118, 120, 122
- Buch, V., 389
- Buratti, B.J., 25, 95
- Burgdorf, M.J., 121
- Burgers model, 206–207
- Byerlee's rule, 172
- C**
- Cage effect, 531
  - photolysis, MeDBK, 609, 610
  - water ice, 386–388
- Callisto, 22–23, 429–431
- Calvin, W.M., 133
- Campbell, J.M., 418, 420
- Caputo model, 208
- Carbon monoxide, 118, 614
- Carlson, R.W., 513
- Cassel, E.J., 76
- Cassidy, T.A., 559, 568
- Cassini, G.D., 25
- Castelnau, O., 200
- Castillo-Rogez, J.C., 204, 212, 214, 217
- Centaurs. *See* Transneptunian objects (TNOs)
- Chandrasekhar, S., 59
- Chapman, C.R., 336
- Chastain, B.K., 411
- Chemical/reactive sputtering, 565–567
- Cheng, A.F., 327
- Chevrier, V., 411
- Chew, H.A.M., 240
- CH<sub>4</sub> ice, 13–14
- Choukroun, M., 410, 414, 435
- Chrisey, D.B., 561
- Chronology models
  - ages, 301–302
  - cometary impact, 301
  - late heavy bombardment (LHB), 300
  - methods, 299
  - Neukum lunar-like impact, 300–301
  - Nice impact, 301
- Chu, L., 600
- Clark, R.N., 6, 8, 12–14, 16, 26, 27, 108, 116, 117, 331, 394
- Clathrate hydrates
  - description, 410
  - Enceladus
    - interpretations, 439–441
    - observations, 437–438
    - visibility, 436
  - hydrogen bonds, 411
  - on icy satellites, 427–431
  - implications
    - gas-laden amorphous ice model, 425
    - snow line, 424–425
  - molecular structure
    - cavity types and arrangements, 412, 413
    - crystallographic information, 412, 413
    - structural transitions, 412, 414
  - occurrence, 410–411
  - potential storage medium, 411
  - stability of
    - factors, 417
    - phase behavior, 419–421
    - pressure-temperature plot, 418, 419
    - thermodynamic modeling, 421–424

- Titan  
clathrate-rich crust formation, 434–435  
cryovolcanic release of methane, 435–436  
methane problem, 431–433  
van der Waals interactions, 411–412  
*vs.* water ice  
density values, 416–417  
mechanical behavior, 415–416  
thermal conductivity, 415
- Coherent backscatter opposition effect  
(CBOE), 61
- Cold faithful model, 439
- Cold ice, friction coefficients  
barring melting, 176  
brittle-ductile transition, 173–174  
brittle fault, 172  
deformation-induced plastic shear fault, 173  
ductile-brittle-like transition, 177  
fresh-water ice sliding, smooth interface,  
174, 175  
*internal cohesion vs. sliding velocity,*  
174, 177  
vs. sliding speed, 174, 176  
strain rate, 178  
tiger stripe faults, 172  
yield strength, 172
- Cole, D.M., 194, 196, 199, 208, 209, 237
- Cole model, 188, 208–209
- Collins, G.C., 302, 303, 305, 311, 317,  
319, 323
- Combi, M.R., 475
- Cometary ices  
KOSI experiments  
amorphous/crystalline transition, 477–478  
deep impact, 474–475  
density, 475  
hexagonal ice formation, 473–474  
mechanical strength, 475  
thermal inertia, 475–477  
nature of ices  
crystalline state, 461–462  
fluxes of gas and water vapor *vs.*  
temperature, 459–460  
gas production rate *vs.* heliocentric  
distance, 460  
reservoirs of  
MBCs, 457, 458  
near infrared spectrum, of Charon, 456,  
457  
Oort cloud comets, 456  
for space mission, 479–480  
water ice  
amorphous and crystalline, 462–465  
outbursts (*see* Outbursts, comets)  
outgassed ices, 465  
smooth terrains, 469–472
- Cometary impact chronology, 301
- Comets, 16, 399–400
- Compaction, microporous ice, 540–541
- Conamara chaos, 323
- Conca, J., 298
- Condensation coefficient, 586
- Cook, J.C., 137, 457
- Cooper, J.F., 87, 90
- Cooper, P.D., 512, 514, 515
- Cooper, R.F., 185
- Coulomb explosion, 563
- Croft, S.K., 287
- Cruikshank, D.P., 25, 113, 114,  
121, 130
- Cryovolcanism  
cantaloupe terrain, 331  
Enceladus, 329  
gaseous N<sub>2</sub> and CH<sub>4</sub>, 331  
paterae, 329  
principle, 328  
regions of volcanic activity, 329–330  
rheologies, 332
- Crystalline phase, water ice  
formation conditions, 377  
infrared spectroscopy, 391–392  
phases of, 373–374  
structure, 375–376  
thermally induced phase change, 382
- Cuffey, K.M., 238
- Curchin, J.M., 13
- D**
- Dangling bonds, 529, 618
- Daniels, J., 76
- Davidson, D.W., 416
- Davies, J.K., 16, 400
- Davy, H., 410
- Dawes, A., 83, 84, 99
- Deaton, W.M., 418, 420
- de Bergh, C., 112, 116
- Delsemme, A.H., 411, 418
- Density-functional perturbation theory  
(DFPT), 152–155
- Density-functional theory (DFT)  
core and the valence electrons, 151  
electron density, 150  
homogeneous electron gas, 151  
Khon-Sham wavefunctions, 151–152  
parameters, 152

- Density values, clathrate hydrates, 416–417  
 Dermott, S.F., 305, 432  
 de Roo, J.L., 418, 420  
 Devlin, J.P., 389  
 de Vries, A.E., 568  
 Diepen, G.A.M., 418, 420  
 Dissociation, water ice  
     description, 508–509  
     primary products  
         H-atom, 511  
         O atom, 511–512  
         OH radical, 509–511  
     secondary products  
         hydrogen peroxide, 512–514  
         molecular oxygen, 514–515  
 Dombard, A.J., 172, 327  
 Domingue, D.L., 91  
 Douté, S., 113, 114  
 Dressler, K., 76, 80, 82, 85  
 Durell, G.D., 194, 196, 199, 209  
 Durham, W.B., 197, 200, 228, 305, 410  
 Duval, P., 200, 209, 237, 238  
 Dyadin, Y.A., 418, 420
- E**  
 Edge, A.V.J., 418  
 Efroimsky, M., 204, 212  
 Ehrenfreund, P., 455  
 Eiben, K., 82  
 Ejecta energy spectra *vs.* ejection energy,  
     564, 565  
 Electron diffraction patterns, water ice, 379  
 Electronic sputtering  
     ejecta energies and angles, 564–565  
     yield, 559–564  
 Electron radiolysis, 567  
 Electrostatic charging, 543–544  
 Emery, J.P., 128  
 Enceladus, clathrate hydrates  
     interpretations, 439–441  
     observations, 437–438  
     visibility, 436  
 Europa, 20–21, 428–429  
 Evans, D.C.B., 172  
 Extended Burgers model, 207
- F**  
 Facile heat transfer, 492  
 Falabella, B.J., 418, 420  
 Famá, M.A., 537, 538, 540  
 Farenzena, L.S., 568
- Filled-ice structure (FIS), 413  
 Fink, U., 391, 395  
 First-Principles Molecular Dynamics, 152  
 Fischer, D.A., 239  
 Flasar, F.M., 432  
 Fluorescence emission spectra, carboxy-  
     seminalphorhodafluor-1  
     (C-SNARF-1), 589–591  
 Fortes, A.D., 164, 410, 434, 439  
 Fortes model, 439  
 Fortt, A.L., 174, 177  
 Four-element model, 206–207  
 Fourier transform, water ice, 376  
 Fray, N., 419  
 Freezing hydrolysis, 589  
 Frenkel, D., 152  
 Frictional sliding, 171  
 Frigid faithful model, 439–441  
 Frost, E.M., 418, 420  
 FTIR spectra, CO<sub>2</sub> trapped in Ar crystal  
     lattice, 388  
 Fulvio, D., 120
- G**  
 Galilean satellites, planetary ices  
     absorption characteristics, 86  
     Callisto, 90–92  
     complex interactions  
         and interconnections, 88  
     complex surface chemistry, 86  
     Europa, 89  
     Ganymede, 90  
     hemispherical albedo dichotomy, 87  
     Io, 88–89  
     sputtering and volatilization, 87  
 Galileo, 16, 17  
 Galloway, T.J., 418, 420  
 Ganymede, 21–22, 429–431  
 Gas-laden amorphous ice model, 425  
 Gas release  
     annealing, 490  
     dependence of, 490–491  
     laser induced, 491–493  
 Gas trapping  
     ammonia, 490  
     clathrate hydrate formation, 489–490  
     fluxes of gas and water vapor *vs.*  
         temperature, 488  
     large ice samples, 495–498  
     trapped gas *vs.* deposition temperature,  
         488, 489  
 Gautier, D., 425

- Geometric albedo model spectra, water ice, 395  
Ghormley, J.A., 512  
Giese, B., 292, 308, 329  
Gioia, G., 441  
Glass transition, 378  
Goguen, J., 56, 113  
Goldsby, D.L., 200, 213, 228, 236–238, 245  
Golecki, I., 539  
Gomis, O., 536  
Goodman, D.J., 200  
Gougen, J.D., 470  
Gow, A.J., 229  
Grain-boundary sliding (GBS), 192–193  
Granato, A.V., 191  
Greeley, R., 317, 319, 323  
Greenberg, J., 76  
Greenland ice sheet, 229  
Greenstein, J., 58  
Groussin, O., 476  
Grundy, W.M., 32, 117, 118, 391, 395, 399  
Grynkov, Y.S., 113  
Gudipati, M.S., 386, 518  
Gunderson, K., 57
- H**
- Hage, W., 535  
Hama, T., 567  
Hansen, G.B., 84, 396  
Hapke, B.W., 56–60, 62, 63, 65, 66, 79, 80, 83, 113, 114, 394  
Hapke model  
macroscopic roughness parameter, 59–61  
multiple scattering, 59  
opposition effect, 61–62  
phase curve, 63–64  
powders, 62  
regolith particles, 64  
single scattering, 58–59  
Hardin, A.H., 390  
Haring, R.A., 564, 568, 571  
Harvey, K.B., 390  
Head, J.W., 317  
Heide, H.G., 536  
Helfenstein, P., 57, 59, 61, 62, 65, 68, 113  
Hendrix, A.R., 92, 93, 95, 98  
Henyey, C., 58  
Hersant, F., 421, 424, 425  
Hessinger, J., 199  
Hirai, H., 432  
Hirai, S., 414  
Hirshfeld, F.H., 157  
Hobbs, P.V., 14  
Hochanadel, C.J., 512  
Hodyss, R., 79  
 $\text{H}_2\text{O}$  ice. *See* Water ice  
Holder, G.D., 418, 420  
Holsapple, K.A., 475  
Housen, K.R., 475  
Hudgins, D.M., 117, 390  
Hudson, R.L., 82, 122, 512, 513, 539  
Hughes, D.W., 466, 468  
Hurford, T., 302, 319  
Hussmann, H., 214, 304  
Huygens, 27  
Hydrated electrons, 507  
Hydrocarbon ice, 11–13  
Hydrocode modelling, 264–265  
Hyper-quenched glassy water (HGW)  
creation, 382  
X-ray diffraction, 377
- I**
- Ice cores  
Čerenkov radiation, 624–625  
optical properties, of deep ice, 625–626  
organic and inorganic chromophores,  
chemical identity of, 627–628  
photochemistry, 628–629  
Ice rules, crystalline ice, 375  
Icy volcanism. *See* Cryovolcanism  
Impact cratering  
basins  
Evander, 290, 292  
Gertrude, 290, 292  
Gilgamesh, 291  
morphologies, 293  
multi-ring, 289  
Odysseus, 290–291  
pictorial representation, 289  
Valhalla, 289–290  
catastrophic disruption, 270–274  
chronology models  
ages, 301–302  
cometary impact, 301  
late heavy bombardment  
(LHB), 300  
methods, 299  
Neukum lunar-like impact, 300–301  
Nice impact, 301  
comet nuclei  
deep impact mission, 269  
lighting and image resolution, 268  
pictorial representation, 267–268  
81P/Wild 2, 269

- Impact cratering (*cont.*)
   
complex craters, 285–288
   
crater chains, 293–295
   
craters on Titan, 298–299
   
electrostatic accelerator
   
    light gas guns, 261
   
    particle mass vs. speed, 261
   
    projectile velocity, 260
   
    rail guns, 262
   
equation of state (EOS), 257
   
geological material density, 256
   
hydrocode modelling, 264–265
   
hydrodynamic processes, 254
   
internal energy, 257
   
laboratory experiments, 262–263, 302
   
light flash, 262
   
palimpsest craters, 288
   
perlite, 264
   
pit and dome craters, 266
   
porosity, 256
   
Pwyll, 267
   
ray craters
   
    Creusa, 297
   
    dome crater Osiris, 295
   
    Inktomi, 297
   
    magnetospheric particles, 298
   
    modes of origin, 297
   
    pictorial representation, 295–296
   
regular complex craters, 282–285
   
sequence of, 254–255
   
shock Hugoniot measurements, 258
   
shock pressures, 257–258
   
simple craters, 282, 283
   
size, 254–255
   
speeds, 258–259
- Ingersoll, A.P., 331
- Inverse power-cosine law, 537
- Io, 18–20
- Ion-induced gas adsorption, 541–543
- Ionization, water ice
   
    charge storage, 518
   
    non-polycyclic aromatic hydrocarbons, 520
   
    oxidation, 520
   
    pathway, 516
   
    polycyclic aromatic hydrocarbons, 516–518
   
    radical cations, 516
- Iro, N., 411
- J**
- Jaccard, C., 539
- Jackson, I., 185
- Jarvis, K.S., 25
- Jaumann, R., 302
- Jenniskens, P., 375–380
- Jesser, W.A., 515
- Jewitt, D.C., 133
- Jhaveri, J., 418, 420
- Johari, G.P., 199
- Johnson, R.E., 92, 515, 527, 553, 559
- Johnson, T.V., 302
- Jones, B.R., 418
- Jones, K.B., 288
- Jones, S.J., 240
- Jupiter system
   
    Callisto, 22–23
   
    Europa, 20–21
   
    Ganymede, 21–22
   
    gas-starved nebula model, 18
   
    infrared spectra, Galilean satellites, 16–17
   
    Io, 18–20
   
    magnetic dynamo, 18
- K**
- Kaasalainen, S., 55
- Karato, S., 185, 191, 207
- Kargel, J., 439
- Kattenhorn, S.A., 302, 319
- Katz, D.L., 418, 420
- Keller, H.U., 26, 470
- Kelvin model, 206
- Kennedy, F.E., 174, 176
- Kennedy, G.C., 418, 420
- Khanna, R.K., 119, 571
- Kieffer, H.H., 395
- Kieffer, S.W., 439
- Kirby, S.H., 240, 243
- Knock-on sputtering
   
    ejecta energies and angles, 557–559
   
    yield, 555–557
- Kobayashi, R., 418, 420
- Koerner, R.M., 239
- Koh, C., 410, 416, 417
- Kohlstedt, D.L., 200, 213, 228, 236–238, 245
- KOSI experiments, cometary ices
   
    amorphous/crystalline transition, 477–478
   
    deep impact
   
        density, 475
   
        mechanical strength, 475
   
        thermal inertia, 475–477
   
        hexagonal ice formation, 473–474
- Kossacki, K.J., 432
- Kouchi, A., 380, 426, 464
- Krasnopol'sky, V.A., 97, 98, 130

- Kuhs, W.F., 419, 420  
Kuiper belt objects (KBOs). *See*  
Transneptunian objects (TNOs)  
Kuiper, G.P., 431
- L**  
Laffon, C., 512, 532  
Lainey, V., 204  
Lambert, J.H., 55  
Lane, A.L., 91, 535  
Langford, V.S., 509, 510  
Larson, H.P., 391, 395  
Larson, S.D., 418, 420  
Laser induced gas release  
from ASW/CO<sub>2</sub> film, 492  
co-deposition, 493, 494  
TOF spectra, 492, 493  
LeGac, H., 238  
Leinhardt & Stewart, 274  
Lellouch, E., 16, 400, 463  
Lisse, C.M., 475  
Loeffler, M.J., 513, 568, 571  
Lopes, R.M.C., 432  
Lorenz, R.D., 432  
Loveday, J.S., 432  
Lücke, K., 191  
Lu, H.-C., 76, 79, 83, 84  
Lumme, K., 56, 113  
Lunine, J.I., 432, 433  
Lunine, M.G., 432  
Luu, J.X., 133  
Lynch, M.J., 76
- M**  
Madden, W.G., 392  
Maeno, N., 174  
Mahaffy, P.R., 425  
Main-belt comets (MBCs), 457, 458  
Makogon, T.Y., 418, 420  
Marboeuf, U., 411, 460  
Mars, 14–16  
Marshall, D.R., 420  
Martinez, R.D., 164  
Martonchik, J.V., 82–84, 119  
Mason, N.J., 76, 84  
Mass wasting processes, 333  
Masterson, C.M., 119  
Mastrapa, E., 390  
Mastrapa, R.M.E., 8, 117, 539  
Max, M.D., 410  
Maxwell model, 204–205
- McCarthy, C., 212  
McCord, T.B., 396  
McGetchin, T.R., 302  
McGuire, A., 58, 59  
McKinnon, W.B., 172, 298  
McLeod, H.O., 418, 420  
Mechanical behavior, clathrate hydrates,  
415–416  
Mega-outbursts, 467–468  
Mehta, B.R., 418, 420  
Melosh, H.J., 470, 472  
Mercier, E., 324  
Merlin, F., 124, 133  
Meteor impacts, 528  
Methane clathrate hydrate, 416, 417  
Methane ice, 13–14  
Mével, L., 324  
Microporous ice, compaction of, 540–541  
Miller, S.L., 410, 418  
Mini-outbursts, 468  
Minnaert, M., 55  
Minton, A.P., 76, 79  
Miranda, 314–315  
Mischenko, M.I., 113  
Mitri, G., 326  
Mohammadi, A.H., 419  
Montagnat, M., 177  
Moore, J.M., 287, 307, 308, 310, 342, 345  
Moore, M.H., 82, 119, 512, 513, 539, 571  
Mousis, O., 425  
Müller, T.G., 49  
Murray, C.D., 305
- N**  
Nakamura, T., 211  
Nash, D.B., 10, 84  
Near-infrared reflectance spectrum, 6–7  
Nebula condensation, 425  
Nelson, R.M., 90, 94, 432  
Neptune system  
Charon, 33  
Kuiper belt, 31–32  
Triton and Pluto, 30–31  
Neukum, G., 301, 302  
Neukum lunar-like impact chronology,  
300–301  
Newman, S.F., 397  
Ng, H.-J., 418, 420  
Nice impact chronology model, 301  
Niemann, H.B., 431, 432  
Nimmo, F., 198, 323  
Nitrogen (N<sub>2</sub>) ice, 10–11

- Noll, K.S., 89–91, 93  
 Non-photochemical processes, freezing, 593–594  
 Normal-outbursts, 467–468  
 Norrish type I mechanism, 615  
 Notesco, G., 491
- O**  
 Öberg, K.I., 567  
 Ockman, N., 389, 390  
 Ohmura, R., 419  
 Onaka, R., 76  
 Oort cloud comets, 456  
 Optical absorption, 528–529  
 Otto, A., 76  
 Outbursts, comets  
     cometary cryo-volcanism, 466–467  
     deep impact mission, 465–467  
     MBCs, 468–469  
     mechanisms, 468, 469  
     mega-outbursts, 467–468  
     mini-outbursts, 468  
     normal-outbursts, 467–468  
     swelling, time sequence of, 465, 466  
 Outgassed ices, 465  
 Owen, T.C., 25
- P**  
 Pappalardo, R.T., 172, 213, 311, 313–315, 317  
 Passey, Q.R., 288  
 Patashnik, H., 470  
 Pat-El, I., 475  
 Patterson, G.W., 319  
 Peak Lambert absorpt., 11  
 Peale, S.J., 211, 217  
 Pearl, J., 119  
 Persson, B.N.J., 172  
 Petrenko, V.F., 305  
 Photochemistry  
     atmospheric ices  
         prebiotic mechanisms, 619  
         snowpack mechanisms, 622–624  
         stratospheric mechanisms, 620–622  
         tropospheric ice, 622–624  
         water-ices, 618–619  
     ice cores, 628–629  
     inorganic species  
         hydrogen peroxide, 606  
         inorganic chromophores, 595–597  
         light absorbance, by chromophores, 606–607  
         of N(III), 603–606  
         of nitrate, 597–603  
         pH values, snow-grain quasi-liquid layers, 607  
         quantum yields, nitrite and peroxy nitrite formation, 607  
         snow photochemical processes, rates of, 594–595  
     organic compounds  
         in ice, 610–613  
         on ice and snow crystal surface, 608–610  
         natural organic matter and degradation products, 614–617  
 Photodimerization, 611  
 Photolysis  
     cage effect, 609, 610  
     inorganic chromophores, 602, 603  
     4-nitrophenol, 611–612  
     quantum yields, nitrate, 598–599  
 Photometric properties, icy surface  
     ejecta exchange, 68  
     energy balance, 48  
     geometric albedo, 52  
     giant planet magnetosphere, 52  
     Kuiper belt object, 54  
     Miranda and Ariel, 54  
     models  
         components, 56  
         empirical equations, 55  
         Hapke (*see* Hapke model)  
         quasi-fractal, 65–68  
         radiance factors, 55  
     phase function parameter, 52  
     quantities, 49–51  
     reflectance vs. solar phase angle, 49  
     TNO systems, 55  
     types of, 53  
 Piatek, J., 64  
 Pieters, C.M., 14  
 Pinilla-Alonso, N., 133, 134  
 Pipes, J.G., 79–81, 83  
 Planetary ices  
     ab initio molecular dynamics, 152  
     attenuation properties (*see* Attenuation properties, planetary ices)  
     crystalline nitrogen, 159–160  
     density-functional perturbation theory (DFPT), 152–155  
     density-functional theory (DFT)  
         core and the valence electrons, 151  
         electron density, 150  
         homogeneous electron gas, 151

- Khon-Sham wavefunctions, 151–152  
parameters, 152  
hydrous and anhydrous salts, 164  
physical properties  
    crystal structures, 157  
    dielectric properties, 158  
    dynamical properties, 158–159  
    elastic constants, 158  
    electron density, 157  
    plasticity, 158  
thermodynamic functions, 155–156  
UV properties (*see* Ultraviolet properties,  
    planetary ices)  
water ice, 160–163  
WURM project, 164–165
- Planetary photometry. *See* Photometric properties, icy surface
- Platteauw, J.C., 422
- Plescia, J.B., 301
- Pneumatic flow, smooth terrains, 471–472
- Polar ice sheets and deep ice cores, 228–229
- Polychlorinated biphenyls (PCBs), 613
- Polycrystalline ice  
    creep behavior  
        internal friction, 235  
        normalized strain rate, 233, 234  
        primary creep, 233–235  
        secondary creep, 235–241  
        tertiary creep, 242–244  
    rate-controlling processes  
        secondary creep with  $n \leq 2$ , 245  
        secondary creep with  $n=3$ , 244–245  
        tertiary creep, 246
- Ponciano, C.R., 568
- Potential energy curves, water ice, 507
- Poulet, F., 113, 115
- Prialnik, D., 470
- Principal models, electronic sputtering, 563
- Prockter, L.M., 319, 335, 337
- Proton order-to-disorder transition, 386
- Protopappa, S., 121
- Q**
- Quasi-fractal photometric models, 65–68
- Quickenden, T.I., 509, 510
- Quirico, E., 118–120
- R**
- Rabinowitz, D.L., 55
- Radebaugh, J., 326
- Radiation effects, water ice
- amorphization, 538–540  
amorphous and crystalline phases, 528  
chemically reactive ions,  
    implantation of, 535  
column density,  $H_2O_2$  and  $O_2$ , 532, 533  
compaction, 540–541  
electrostatic charging, 543–544  
at interface of ice, 535–536  
ion-induced gas adsorption, 541–543  
optical absorption, 528–529  
porosity, 529  
primary processes, 530–532  
radiolysis, 532  
sputtering, 536–538  
stopping power, 532
- Ragozzine, D., 135
- Rambaux, N., 212
- Raut, U., 529, 540
- Ray craters  
    Creusa, 297  
    dome crater Osiris, 295  
    Inktomi, 297  
    magnetospheric particles, 298  
    modes of origin, 297  
    pictorial representation, 295–296
- Reactive cavity, 609
- Reimann, C.T., 534
- Remote surface spectral sensing, 504
- Richardson, J.E., 475
- Richon, D., 419
- Ripmeester, J.A., 416
- Rist, M.A., 173
- Roberts, O.L., 418, 420
- Robinson, D.B., 418, 420
- Roush, T.L., 95, 97, 122
- S**
- Sack, N.J., 81, 382, 535
- Sagan, C., 432
- Sandwell, D.T., 328
- Sanford, S.A., 10
- Satorre, M.A., 120
- Saturn system  
    coloring agent, 23  
     $CO_2$  on icy objects, 23–24  
    Dione satellite, 23–24  
    Iapetus, 23, 25  
    Titan, 26–28
- Scattering models  
    airless particulate surface, 113  
    ammonia hydrates, 119  
    carbon dioxide, 118–119

- Scattering models (*cont.*)
   
  carbon monoxide, 118
   
  ethane, 119
   
Grenoble Astrophysics and Planetology
   
  Solid Spectroscopy and
   
  Thermodynamics database, 123
   
Heidelberg-Jena-St Petersburg Database of
   
  Optical Constants, 122
   
hydrogen cyanide, 119
   
ices mixed with non-icy materials, 120–121
   
icy mixtures, 120
   
irradiated ices, 121–122
   
laboratory transmission spectra, 116
   
methane diluted in nitrogen, 117–118
   
methanol, 119
   
nitrogen, 118
   
particulate surface, 114
   
photometry, 113
   
pure methane, 117
   
reflectance spectra, 112
   
spectrum of 5145 Pholus, 114–115
   
surface configuration, 114
   
unirradiated ices, 116
   
water ice, 117
   
Schenk, P.M., 285, 287, 294, 298, 307, 308, 342
   
Schmitt, B., 10, 113, 116–120, 391, 392, 395, 418
   
Schnepp, O., 76, 80, 82
   
Schroeder, S.E., 26
   
Schubert, G., 328
   
Schulson, E.M., 174, 177, 178
   
Secondary creep, polycrystalline ice
   
  behavior at low stresses, 236–237
   
  confining pressure effect, 240
   
  grain size effect, 237–238
   
  ice anisotropy, 241
   
  particles and impurities effect, 238–240
   
  strain rate, 235
   
  temperature effect and liquid phase, 237
   
Seki, M., 76, 79, 80
   
Selleck, F.T., 418
   
Shadow hiding opposition effect (SHOE), 61
   
Shepard, M.K., 57, 59, 61, 62
   
Shibaguchi, T., 76, 79
   
Shi, J., 543
   
Shkuratov-Helfenstein (S-H) model
   
  elemental scatterers, 66
   
  fractally-structured aggregates, 65
   
  multiply-scattered light, 68
   
  quantity, 66
   
Shkuratov, Y.G., 56, 57, 65, 68, 113
   
Shoemaker, E.M., 288, 301
   
Single ice crystals, viscoplastic behavior
   
  basal and non-basal slip, 229–230
   
  dislocation dynamics, 230–231
   
  flow law and rate-controlling processes, 232–233
   
  internal friction, 232
   
Sintering, 585
   
Sirono, S., 464
   
Slip windows, 172
   
Sloan, E.D., 410, 413, 416–418, 420
   
Smith, B.A., 288
   
Smith-Konter, B., 172
   
Smooth terrains, comets
   
  origin, 470–472
   
  9P/Tempel1, nucleus of, 469, 470
   
  talps hypothesis, 470
   
Smythe, W.D., 395, 418
   
SO<sub>2</sub> ice, 10
   
Solvatochromic effect, 608–609
   
Sotin, C., 432
   
Souchon, A., 59
   
Spencer, J.R., 337
   
Spencer, J.R., 302, 313, 318, 329, 514
   
Spetzler, H.A., 207
   
Spohn, T., 214
   
Sputtering
   
  chemical/reactive sputtering, 565–567
   
  and desorption, 553–554
   
  electronic sputtering
   
    ejecta energies and angles, 564–565
   
    yield, 559–564
   
  energetic ion intensities, 552, 553
   
  ice mixtures and impurities in ice, 567–568
   
  knock-on sputtering
   
    ejecta energies and angles, 557–559
   
    yield, 555–557
   
  mixed ice
   
    electronic excitation, 571, 572
   
    knock-on regime, 568–571
   
    water ice, 536–538
   
Stansberry, J., 49
   
Steinemann, S., 243
   
Stephan, K., 298
   
Stern, L.A., 200, 305
   
Stern, S.A., 97
   
Stevenson, D.J., 432, 433
   
Stofan, E.R., 432
   
Stopping power, 553, 554
   
Strazzulla, G., 513, 535, 536
   
Strom, R.G., 300
   
Sugisaki, M., 381
   
Sunshine, J.M., 16, 470
   
Sunshine, J.S., 14

- Surface erosion and degradation  
  impact gardening, 333–335  
  mass wasting, 333  
  sputtering, 335–336  
  sublimation, 337–338  
  surface-atmosphere interaction, 338–341
- Swings, P., 411
- T**
- Takahashi, T., 76
- Takenouchi, S., 418, 420
- Talps hypothesis, smooth terrains, 470
- Tatibouet, J., 199, 232
- Taub, I.A., 82
- Taylor, F.W., 119
- Tectonic features, Enceladus, 438
- Tectonic resurfacing, icy satellites  
  assemblages, 303  
  bands, 319–321  
  brittle material, 305  
  coronae, 314–315  
  folds  
    bands and faults, 326  
    Cassini Regio, 327  
    compressive tectonics, 324–325  
    contractional deformation, 326  
    ductile material, 328  
    massive ring, 327  
  fractures  
    degraded impact basin, 307–308  
    Ithaca Chasma, 306–307  
    multi-ring impact basins, 306  
  graben-like structures  
    Europa and Enceladus, 309  
    tidal stresses, 310  
    wispy terrain, 308  
grooves  
  brittle surface layer, 314  
  extensional stress, 311  
  Harran Sulcus, 313  
  schematic representation, 311, 313  
  strike-slip motion, 313  
  sulci, 311–312  
  terrain, 310  
landforms, 302  
lenticulae and chaotic terrain,  
  321–324  
mechanisms, 303  
ridges, 315–319  
rotation and tides, 304  
strike-slip faulting, 303  
symmetric stress pattern, 304
- Teolis, B.D., 82, 515, 534
- Tera, F., 301
- Terrestrial ice/snow  
  conformational behavior, 587–592  
  dielectric and electrical properties, 584  
  freezing and ice polymorphs, 584–586  
  ice/vapor and ice/water interface, chemical  
    properties of, 592  
  non-photochemical processes, 593–594  
  photochemistry (*see also* Photochemistry)  
    hydrogen peroxide, 606  
    inorganic chromophores, 595–597  
    light absorbance, by chromophores,  
      606–607  
    of N(III), 603–606  
    of nitrate, 597–603  
    organic compounds, 608–617  
    pH values, snow-grain quasi-liquid  
      layers, 607  
    quantum yields, nitrite and peroxy nitrite  
      formation, 607  
    snow photochemical processes, rates of,  
      594–595  
  quasi-liquid layer, 586  
  solute rejection, partitioning and migration,  
      587–592
- Terrestrial planets, 14–16
- Tetragonal structure, clathrate hydrates, 414
- Thakore, J.L., 418, 420
- Thermal conductivity, clathrate hydrates, 415
- Thermal spike sputtering, 563
- Thermodynamic modeling, clathrate hydrates  
  fugacity coefficients, 422  
  inhibitors, 424  
  Kihara parameters, 423  
  stability conditions, 421  
  stability curves, 423, 424  
  statistical thermodynamic approach,  
      422–423
- Thomas, P.C., 470
- Thorsteinsson, T.H., 229
- Tidal model, 437
- Tildesley, D.J., 152
- Titan, clathrate hydrates  
  clathrate-rich crust formation, 434–435  
  cryovolcanic release of methane, 435–436  
  methane problem, 431–433
- TNOs. *See* Transneptunian objects (TNOs)
- Tobie, G., 212, 214
- Tomasko, M.G., 26
- Track core region, electronic sputtering, 561
- Trafton, L.M., 97
- Transient creep, 186

Transneptunian objects (TNOs)  
 bulk densities, 398, 399  
 characteristics, 111  
 classification, 109  
 cold classical Kuiper belt objects, 136  
 colors of Centaurs, 137–138  
 component model, 131  
 dynamically hot populations, 137  
 H-band reflectance spectra, 398  
 medium-sized Kuiper belt objects, 136–137  
 objects with featureless to nearly  
     featureless spectra, 131  
 objects with moderate water ice spectra,  
     131–132  
 objects with strong water ice spectra,  
     132–135  
 particle irradiation, 112  
 scattering models (*see* Scattering models)  
 signatures, 110  
 taxonomic classification, 135  
 visible-near infrared reflectance spectra,  
     123, 124  
 with volatile ices  
     atmospheric loss model, 129  
     Eris spectrum, 124, 128  
     Makemake spectrum, 127–128  
     photochemistry, 130  
     Quaoar spectrum, 127, 129  
     Sedna, 127–129  
 Trujillo, C.A., 134  
 Tryka, K.A., 118, 331  
 TUV model, 595, 596

**U**

Ultraviolet properties, planetary ices  
 absorption and in reflectance, 75  
 ammonia ice  
     optical constants, 82  
     reflectance measurements, 83  
 application, 98–100  
 carbon dioxide ice, 84  
 Galilean satellites  
     absorption characteristics, 86  
     Callisto, 90–92  
     complex interactions and  
         interconnections, 88  
     complex surface chemistry, 86  
     Europa, 89  
     Ganymede, 90  
     hemispherical albedo dichotomy, 87  
     Io, 88–89  
     sputtering and volatilization, 87

hydrogen peroxide, 85  
 instrumentation, 74–75  
 methanol, 86  
 Pluto and Charon, 97–98  
 Saturn satellites and rings, 92–94  
 sulfur dioxide frost, 84  
 Triton, 97  
 Uranus satellites, 94–97  
 water ice  
     amorphous and crystalline ice, 80–81  
     laboratory measurements, 76–78  
     radiolysis effects, 81–82  
     reflectance spectra, 79–80  
     refraction index, 76  
     wavelength ranges, 73–74  
 Unruh, C.H., 418, 420  
 Uranus system, 28–30

**V**

Vaida, V., 85  
 van Cleef, A., 418, 420  
 van der Waals, J.H., 422  
 Verbiscer, A.J., 55, 93–95, 99, 113  
 Verma, V.K., 418, 420  
 Vertical binding energy (VBE), 508  
 Vilas, F., 25  
 Vitreous ice. *See* Amorphous phase, water ice  
 Voigt model, 206

**W**

Waite, J.H., 423, 424, 431, 432, 439  
 Wall, S.D., 432  
 Warren, S.G., 76, 79–81, 84, 119  
 Water ice, 7–10  
     amorphous ice  
         formation conditions, 377  
         phases of, 372–373  
         structure, 375  
     Auger process, 506  
     comets  
         amorphous and crystalline, 462–465  
         outbursts (*see* Outbursts, comets)  
         outgassed ices, 465  
         smooth terrains, 469–472  
     crystalline phase  
         formation conditions, 377  
         phases of, 373–374  
         structure, 375–376  
     crystallization rates, 381  
     density-functional perturbation theory  
         (DFPT), 160–163

- diffraction techniques, 374–375  
dissociation  
description, 508–509  
H-atom, 511  
hydrogen peroxide, 512–514  
molecular oxygen, 514–515  
O atom, 511–512  
OH radical, 509–511  
electron diffraction patterns, 379  
excitation process, 505  
Fourier transform, 376  
geometric albedo model spectra, 395  
impact induced phase change, 384  
implications, of phase  
cavity volume/cage effect, 386–388  
thermal properties, 385  
thermal/radiation history, 385  
infrared spectroscopy  
amorphous ice, 391  
amorphous *vs.* crystalline ice, 392–393  
assignment of bands, 389, 390  
crystalline ice, 391–392  
laboratory needs, 394  
model mixtures, 393–394  
relevant absorptions, 390–391  
ionization  
charge storage, 518  
non-polycyclic aromatic hydrocarbons,  
    520  
oxidation, 520  
pathway, 516  
polycyclic aromatic hydrocarbons,  
    516–518  
primary chemical processes in, 506–508  
radiation effects, in outer solar system  
amorphization, 538–540  
amorphous and crystalline phases, 528  
chemically reactive ions, implantation  
    of, 535  
column density, H<sub>2</sub>O<sub>2</sub> and O<sub>2</sub>, 532, 533  
compaction, 540–541  
electrostatic charging, 543–544  
at interface of ice, 535–536  
ion-induced gas adsorption, 541–543  
optical absorption, 528–529  
porosity, 529  
primary processes, 530–532  
radiolysis, 528–532  
sputtering, 536–538  
stopping power, 532  
radiation induced phase change, 383–384  
in solar system  
comets, 399–400  
EJSM mission, 401  
origin, 396  
satellites, 396–397  
TNOs, 397–399  
thermally induced phase change  
amorphous-amorphous, 379–380  
amorphous-crystalline, 380–382  
crystalline-crystalline, 382  
glass transition, 378  
UV properties  
amorphous and crystalline ice, 80–81  
laboratory measurements, 76–78  
radiolysis effects, 81–82  
reflectance spectra, 79–80  
refraction index, 76  
Weertman, J., 185, 200  
Wenger, A., 411, 418  
Whalley, E., 389, 390, 392  
Whipple, F.L., 496  
Whitworth, R.W., 305  
Williams, J.G., 212  
Williamson, T., 229  
Wolfe, R.F., 301  
Wood, C.A., 298, 299  
WURM project, 164–165
- Y**  
Yasuda, K., 419  
Young, L.A., 97
- Z**  
Zahnle, K., 301, 336, 343, 432  
Zheng, W.J., 513